JOURNAL OF APPLIED PHYSICS

Vol. 31, No. 5 May, 1960

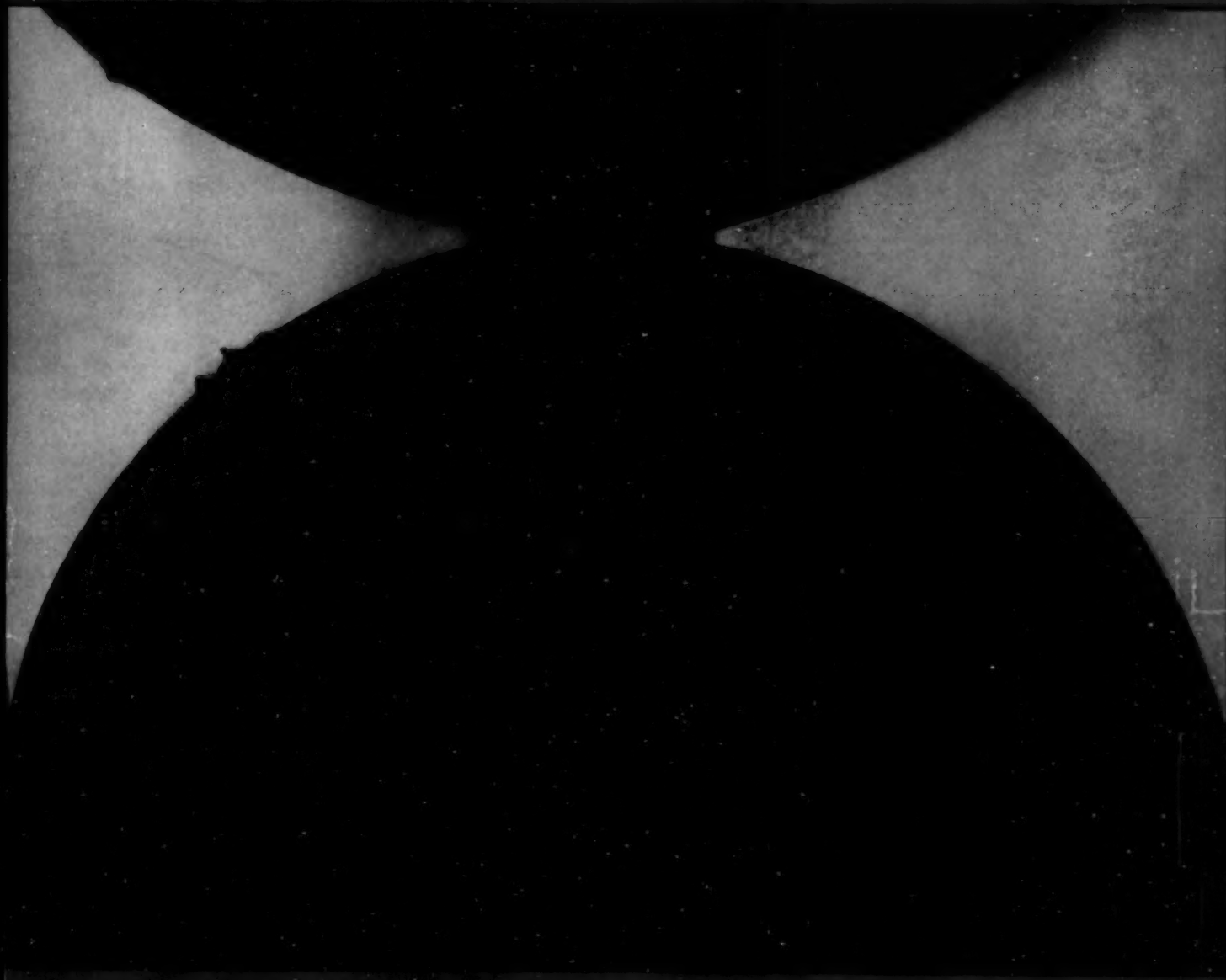

Photomicrograph of Neck Area between Ice Spheres.
See Page 833.

HARSHAW MANUFACTURES A COMPLETE LINE OF SCINTILLATION AND OPTICAL CRYSTALS

SCINTILLATION *Mounted* NaI(T1) *Crystals*

Crystal detectors designed for the most sophisticated counting problems. Our physics and engineering group are available to assist you in your special detector problems.

More detailed information is contained in our 32-page book, "Harshaw Scintillation Phosphors." We invite you to write for your free copy!

STANDARD LINE
(Hermetically Sealed Crystal Assemblies)

- The accepted standard of the industry
- Proven through years of service in research, medical and industrial applications
- unparalleled performance
- dependability
- consistent good quality.

INTEGRAL LINE
(Crystal photo multiplier tube combination assembly)

- Improved resolution
- Ready to use plug-in unit
- Permanently light sealed
- Capsule design facilitates decontamination
- Close dimensional tolerances
- Harshaw guaranteed

Large Crystal **MATCHED WINDOW LINE**
(Designed primarily for crystals 4" dia. and larger)

- "Small crystal" performance achieved through improved optical design
- Low mass containers
- Available in standard aluminum or complete low background assemblies
- Convenient mounting flange
- Ready to use

Every Harshaw crystal is a product of our experience in crystal growing technology since 1936

Other Phosphors Available from The Harshaw Chemical Company

ROUGH CUT THALLIUM ACITVATED SODIUM IODIDE CRYSTAL BLANKS • EUROPIUM ACTIVATED-LITHIUM IODIDE (NORMAL) • EUROPIUM ACTIVATED LITHIUM IODIDE (96% Li^6 ENRICHED) • THALLIUM ACTIVATED CESIUM IODIDE • THALLIUM ACTIVATED POTASSIUM IODIDE • ANTHRACENE • PLASTIC PHOSPHORS

OPTICAL *Crystals*

For Infrared and Ultra Violet Transmitting Optics

"HARSHAW QUALITY" INHERENT IN EACH HARSHAW-GROWN CRYSTAL GUARANTEES THE MOST EFFICIENT OPTICAL TRANSMISSION POSSIBLE THROUGH:

1) Negligible light scattering in crystals, permitting higher sensitivity and improved resolution
2) Freedom from absorptions caused by trace impurities in crystal optics
3) Minimum strain

"HARSHAW QUALITY" meets the demand for uniformity of optical properties such as dispersion and refractive index. Prices, specifications, or other information will be sent in answer to your inquiry.

The following infrared and ultra violet transmitting crystals are available; others are in the process of development:

SODIUM CHLORIDE • SODIUM CHLORIDE MONOCHROMATOR PLATES POTASSIUM BROMIDE • POTASSIUM BROMIDE PELLET POWDER • (through 200 on 325 mesh) • POTASSIUM CHLORIDE • OPTICAL SILVER CHLOFIDE • THALLIUM BROMIDE IODIDE • LITHIUM FLUORIDE • LITHIUM FLUORIDE MONOCHROMATOR PLATES • CALCIUM FLUORIDE • BARIUM FLUOFIDE • CESIUM BROMIDE • CESIUM IODIDE

Additional information on the physical and optical properties of the above crystals is available in our 36-page booklet "Synthetic Optical Crystals". Send for your free copy.

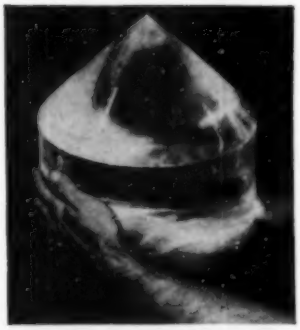

HARSHAW

THE HARSHAW CHEMICAL CO.
Crystal Division • Cleveland 6, Ohio

JOURNAL OF APPLIED PHYSICS

Vol. 31, No. 5 MAY, 1960

In This Issue

Specific Ionization Measurements and Energy Requirements for *F*-Center Formation . . . . . R. D. Jordan and R. S. Alger 747

Influence of Transverse Modes on Photoconductive Decay in Filaments . J. S. Blakemore and K. C. Nomura 753

Studies in Partial Switching of Ferrite Cores . . . . . Roger H. Tancrell and Robert E. McMahon 762

External Fields from Domain Walls of Cobalt Film . . . . . B. Kostyshyn, J. E. Brophy, I. Oi, and D. D. Roshon, Jr. 772

Optical Constants of Germanium in the Region 0–10 ev . . . . . M. P. Rimmer and D. L. Dexter 775

High Power Effects on Ferrimagnetic Resonance . . . . . M. T. Weiss 778

Stable, High Density Field Emission Cold Cathode . . . . . E. E. Martin, J. K. Trolan, and W. P. Dyke 782

Electrical Stability and Life of the Heated Field Emission Cathode . . . . . W. P. Dyke, F. M. Charbonnier, R. W. Strayer, R. L. Floyd, J. P. Barbour, and J. K. Trolan 790

Scattering of a Plane Transverse Wave by a Spherical Obstacle in an Elastic Medium . . . . . Norman G. Einspruch, E. J. Witterholt, and Rohn Truell 806

Photoelastic Properties of Polystyrene in the Glassy State. III. Styrene Derivatives and Copolymers . . . . . J. F. Rudd and R. D. Andrews 818

Orientation Density and Its Use in Quantitative Texture Studies . . . . . C. G. Dunn and J. L. Walter 827

Regelation, Surface Diffusion, and Ice Sintering . . . . . W. D. Kingery 833

Etching of Surfaces with 8-Kev Argon Ions . . . . . R. L. Cunningham, P. Haymann, C. Lecomte, W. J. Moore, and J. J. Trillat 839

Explosively Loaded Metallic Cylinders. I . . . . . F. E. Allison and R. W. Watson 842

Explosively Loaded Metallic Cylinders. II . . . . . F. E. Allison and J. Thomas Schriempf 846

Intensities of λ1850 and λ2537 in Low-Pressure Mercury Vapor Lamps with Rare Gas Present . . . . . Bentley T. Barnes 852

Ultrasonic Viscoelastic Properties of Associated Liquids . . . . . R. Meister, C. J. Marhoeffer, R. Sciamanda, L. Cotter, and T. Litovitz 854

Theory of a Negative-Resistance Transmission Line Amplifier with Distributed Noise Generators . . . . . K. K. N. Chang 871

Thermal Emission of Alkali Ion Pulses from Clean and Oxygenated Tungsten . . . . . Robert E. Minturn, Sheldon Datz, and Ellison H. Taylor 876

Thermal Positive Ion Emission and the Anomalous Flicker Effect . . . . . S. Datz, R. E. Minturn, and E. H. Taylor 880

Acoustic Resonance in Solid Propellant Rockets . . . . . F. T. McClure, R. W. Hart, and J. F. Bird 884

Detection of Metastable Atoms and Ions . . . . . Homer D. Hagstrum 897

Bounds on the Elements of the Equivalent Network for Scattering in Waveguides. I. Theory . . . . . Larry Spruch and Ralph Bartram 905

Bounds on the Elements of the Equivalent Network for Scattering in Waveguides. II. Application to Dielectric Obstacles . . . . . Ralph Bartram and Larry Spruch 913

Stacking Faults in Zinc . . . . . A. Fourdeux, A. Berghezan, and W. W. Webb 918

Evolution of Gases and Ions from Different Anodes Under Electron Bombardment . . . . . J. R. Young 921

Energy Distribution and Cooling Effect of Electrons Emitted from an Arc Cathode . . . . . T. H. Lee 924

Recovery of Internal Friction in Aluminum after Plastic Deformation . . . . . Ivar Holwech 928

Effect of Atomic Interaction Potential on Defect Production in Metals . . . E. Brown and G. H. Goedecke 932

Letters to the Editor:

"Foldover" Effects Caused by Spin Wave Interactions in Ferromagnetic Resonance . . . . . H. Suhl 935

Terraces on Etchpits . . . . . J. J. Gilman 936

Effect of Nuclear Polarization on the Behavior of Solid State Masers . . . . . G. Makhov, L. G. Cross, R. W. Terhune, and J. Lambe 936

Microwave Measurement of Semiconductor Carrier Lifetimes . . . . . H. A. Atwater 938

High-Temperature Hall Coefficient in GaAs . . . . . L. W. Aukerman and R. K. Willardson 939

Film Stripping Technique for Making Thin Silica Windows . . . . . E. Tannenbaum 940

Influence of Negative Ions on Ambipolar Diffusion of Electrons . . . Hendrik J. Oskam and Verlyn R. Mittlestadt 940

Proposed Molecular Amplifier and Coherent Generator for Millimeter and Submillimeter Waves . . . . . Walter Gordy and Monroe Cowan 941

Erratum: Magnetization of the Compound TiFe . . . . . M. V. Nevitt 942

Errata: Alternative Forms of Some Exponential and Power Functions for Graphical Representation . C. C. Harris 942

Errata: Reviving the Classical Theory of Friction by a Modern Dislocation Theory of Deformation Revision . . . . . John H. Dismant 942

Books Reviewed 943

Books Received 943

JOURNAL OF APPLIED PHYSICS

A journal of general physics and its applications to other sciences and to industry

Published by the

American Institute of Physics

GOVERNING BOARD

Ralph A. Sawyer, *Chairman*

J. G. Baker
R. H. Bolt
W. R. Brode
Harvey Brooks
Dirk Brouwer
J. W. Buchta
Vernet E. Eaton
J. H. Elliott
Herbert A. Erf
S. A. Goudsmit
W. W. Havens, Jr.
Winston E. Kock
R. Bruce Lindsay
H. V. Neher
C. J. Overbeck
G. E. Pake
Ray Pepinsky
R. A. Sawyer
F. W. Sears
Frederick Seitz
John Strong
G. E. Uhlenbeck
M. E. Warga
V. F. Weisskopf
W. R. Willets

ADMINISTRATION

Elmer Hutchisson
Director

Henry A. Barton
Associate Director

Wallace Waterfall
Secretary and Treasurer

Ruth F. Bryans
Publication Manager

W. C. Kelly
Director of Education Projects

Eugene H. Kone
Director of Public Relations

Alice Mastropietro
Circulation Manager

Kathryn Setze
Assistant Treasurer

Edward Tober
Manager, Production and Distribution

Theodore Vorburger
Advertising Manager

Emily Wolf
Office Manager

Editor
James A. Krumhansl

Assistant Editor
Ethel McMillan

Editorial Board

J. H. Crawford
Arthur Kantrowitz
A. F. Kip
J. E. Goldman
J. L. Tuck
C. A. Wert
Herman A. Haus
C. Lester Hogan
R. S. Rivlin

THE JOURNAL OF APPLIED PHYSICS is devoted to general physics and its applications to other sciences, to engineering, and to industry. Previous to 1937, this journal was called PHYSICS.

The JOURNAL OF APPLIED PHYSICS welcomes articles of two distinct kinds: (1) Descriptions of new results in experimental or theoretical physics which are of general interest to physicists. The author should explain his contribution in such a way that a physicist or engineer in another field of specialization can appreciate its objectives and essential features. (2) Critical reviews of particular areas of physics or surveys of extensive investigations at a single laboratory. Authors contemplating writing such should correspond with the Editor before they begin writing.

The JOURNAL OF APPLIED PHYSICS welcomes letters to the editor which describe in a few words the content of laboratory reports and theses and which tell readers how they may obtain copies of such reports.

Manuscripts should be submitted to the Editor, James A. Krumhansl, Rockefeller Hall, Cornell University, Ithaca, New York. Authors should read the "Information for Contributors," facing page 1 of the January issue, before writing articles or letters. The *Style Manual* of the American Institute of Physics is also helpful to writers preparing manuscripts for journals published by the American Institute of Physics. It can be obtained for $1.00 from the American Institute of Physics, 335 East 45 Street, New York 17, New York.

Corrected proofs and all correspondence concerning papers in the process of publication should be addressed to the Publication Manager, American Institute of Physics, 335 East 45 Street, New York 17, New York.

Subscriptions, renewals, and orders for back numbers should be addressed to the American Institute of Physics, 335 East 45 Street, New York 17, New York.

Subscription Price	U.S. and Canada	Elsewhere
To members of member organizations of the American Institute of Physics and Affiliated Societies ..	$12.00	$13.00
To all others	14.00	16.00

Back Number Prices

Yearly back number rate when complete year is available: $17.00.
Single copies: $1.75 each (exception: March, 1958—$3.00 each).

Changes of address should be sent to the American Institute of Physics.

Advertising rates supplied on request. Orders, advertising copy, and cuts should be sent to the American Institute of Physics.

The Journal of Applied Physics is published monthly at Prince and Lemon Streets, Lancaster, Pennsylvania.

Second-class postage paid at Lancaster, Pa.

ARNOLD: WIDEST SELECTION OF MO-PERMALLOY POWDER CORES FOR YOUR REQUIREMENTS

For greater design flexibility, Arnold leads the way in offering you a full range of Molybdenum Permalloy powder cores . . . 25 different sizes, from the smallest to the largest on the market, from 0.260" to 5.218" OD.

In addition to pioneering the development of the cheerio-size cores, Arnold is the exclusive producer of the largest 125 Mu core commercially available. A huge 2000-ton press is required for its manufacture, and insures its uniform physical and magnetic properties. This big core is also available in three other standard permeabilities: 60, 26 and 14 Mu.

A new high-permeability core of 147 Mu is available in most sizes. These cores are specifically designed for low-frequency applications where the use of 125 Mu cores does not result in sufficient Q or inductance per turn. They are primarily intended for applications at frequencies below 2000 cps.

Most sizes of Arnold M-PP cores can be furnished with a controlled temperature coefficient of inductance in the range of 30 to 130° F. Many can be supplied temperature stabilized over the MIL-T-27 wide-range specification of −55 to +85° C . . . another special Arnold feature.

Graded cores are available upon special request. All popular sizes of Arnold M-PP cores are produced to a standard inductance tolerance of + or −8%, and many of these sizes are available for immediate delivery from strategically located warehouses.

Let us supply *your* requirements for Mo-Permalloy powder cores (*Bulletin PC-104C*). Other Arnold products include the most extensive line of tape-wound cores, iron powder cores, permanent magnets and special magnetic materials in the industry. • Contact *The Arnold Engineering Co., Main Office and Plant, Marengo, Illinois.*

ADDRESS DEPT. J-5

ARNOLD

SPECIALISTS in MAGNETIC MATERIALS

BRANCH OFFICES and REPRESENTATIVES in PRINCIPAL CITIES • *Find them FAST in the YELLOW PAGES*

1187

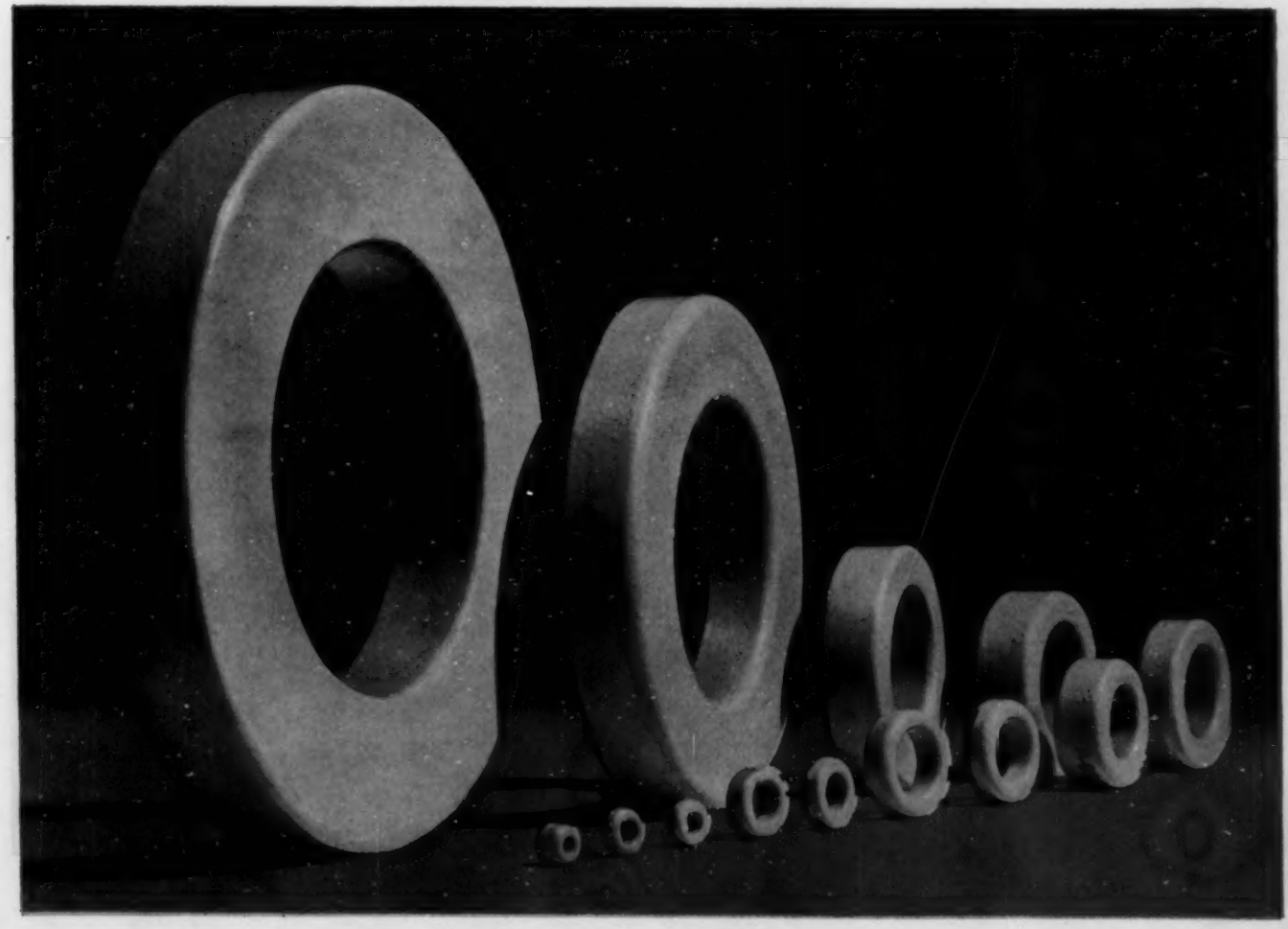

plasma physics

new research programs at Hughes Research Laboratories

New means for generating and containing highly ionized dense plasmas—new processes to produce controlled fusion power—new concepts on the interaction of electro-magnetic waves with plasmas... these are some of the expanding projects pursued at the Hughes Research Laboratories in the field of plasma physics.

Openings currently exist in the field of plasma physics for SCIENTISTS and ENGINEERS—at senior and junior levels—at the Hughes Research Laboratories.

In Malibu, California... just above the Pacific in the foothills of the Santa Monica Mountains... this new facility has been specifically designed for effective research effort with private offices and complete research laboratories. In this uniquely creative atmosphere, Hughes scientists and engineers will continue their record of accomplishment in electronics and physics research.

Your inquiry regarding staff openings may be directed in confidence to Dr. Malcolm R. Currie, **HUGHES RESEARCH LABORATORIES,** *Malibu 4, California.*

Creating a new world with ELECTRONICS

HUGHES

© 1960, HUGHES AIRCRAFT COMPANY

RESEARCH LABORATORIES

HAROLD S. BLACK, LAMME MEDALIST

A MAN WINS A MEDAL . . . AND STRENGTHENS A PHILOSOPHY

The search for the "hitherto unattainable" sometimes ends in strange places.

For years Bell Laboratories engineer Harold S. Black pondered a problem: how to rid amplifiers of the distortion which unhappily accumulated as signal-transmission paths were made longer and amplifiers were added. There had been many approaches but all had failed to provide a practical answer.

Then one day in 1927 the answer came —not in a research laboratory, but as he traveled to work on the Lackawanna Ferry. On a newspaper, Mr. Black jotted down those first exciting calculations.

Years later, his *negative feedback principle* had revolutionized the art of signal amplification. It is a principal reason why telephone and TV networks can now blanket the country, the transoceanic cable is a reality, and military radar and missile-control systems are models of precision.

For this pioneer achievement, and for numerous other contributions to communications since then (some 60 U. S. patents are already credited to him), Mr. Black received the 1957 Lamme Medal from the American Institute of Electrical Engineers. He proved that the seemingly "unattainable" often *can* be achieved, and thus strengthened a philosophy that is shared by all true researchers.

He is one of many Bell Telephone Laboratories scientists and engineers who have felt the challenge of telephony and have risen to it, ranging deeply into science and technology. Numerous medals and awards have thus been won. Two have been Nobel Prizes, a distinction without equal in any other industrial concern.

Much remains to be done. To create the communication systems of the future, we must probe deeper still for new knowledge of Nature's laws. We must continue to develop new techniques in switching, transmission and instrumentation for every kind of information-bearing signal. As never before, communications offer an inspiring challenge to creative men.

BELL TELEPHONE LABORATORIES

WORLD CENTER OF COMMUNICATIONS RESEARCH AND DEVELOPMENT

Timely McGRAW-HILL Books

Beranek—NOISE REDUCTION. *Ready in August*

Chernov—WAVE PROPAGATION IN A RANDOM MEDIUM. *Now Available*

Clement and Johnson—ELECTRICAL ENGINEERING SCIENCE. 601 pages. $9.50

Goertzel and Tralli—SOME MATHEMATICAL METHODS OF PHYSICS. 312 pages. $8.50

Ledley—DIGITAL COMPUTER AND CONTROL ENGINEERING. *Ready in June*

Lindsay—MECHANICAL RADIATION. 415 pages. $10.00

Meghreblian and Holmes—REACTOR ANALYSIS. *Ready in July*

Nielsen—MISSILE AERODYNAMICS. 346 pages. $12.50

Overman and Clark—RADIOISOTOPE TECHNIQUES. 496 pages. $10.00

Slater—QUANTUM THEORY OF ATOMIC STRUCTURE. Volume I. *Ready in July*

Send for copies on approval

McGraw-Hill
BOOK COMPANY, INC.
330 West 42nd Street New York 36, N.Y.

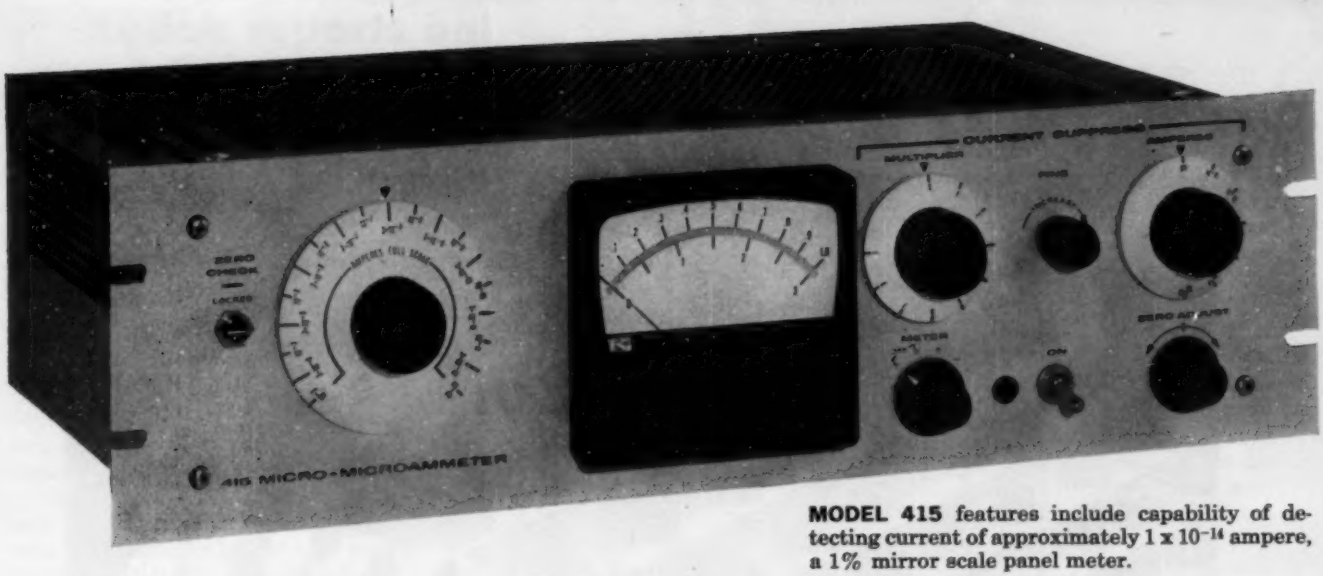

MODEL 415 features include capability of detecting current of approximately 1×10^{-14} ampere, a 1% mirror scale panel meter.

new high-speed research micro-microammeter

Model 415 offers high speed of response, accuracy, and zero suppression.

The new Model 415 incorporates advanced high-speed circuitry developed by Keithley Instruments for rocket and satellite experimentation — where measurements of Lyman-Alpha night glow and upper air density require fast response.

A speed response of less than 600 milliseconds to 90% of final value at 10^{-12} ampere is possible where external circuit capacity is 50 picofarads ($\mu\mu$f). Critical damping of the circuit, with any input capacity, is maintained on all ranges through one infrequent adjustment. There is no possibility of oscillation or poor response, on any range.

Accuracy is ±2% of full scale on 10^{-3} through 10^{-8} ampere ranges, and ±3% of full scale on 3×10^{-9} through 10^{-12} ampere ranges.

The 415 also provides zero suppression up to 100 full scales, permitting full scale display of one per cent variations of a signal. Once suppressed to zero, such variations may be observed on any of the next four more sensitive ranges without resetting the suppression.

Excelling other Keithley 400 Series Micro-micro-ammeters in speed of response, the 415 is ideal for current measurements in ion chambers, photomultipliers, gas chromatography, mass spectrometry.

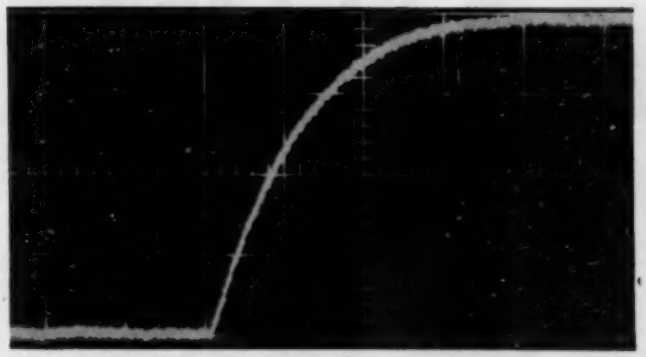

AN OSCILLOGRAM demonstrating response to a current step of 10^{-12} ampere. Input capacity is 35 picofarads ($\mu\mu$f). One major horizontal division equals 200 milliseconds.

BRIEF SPECIFICATIONS

RANGES: 10^{-12}, 3×10^{-12}, 10^{-11}, 3×10^{-11}, etc. to 10^{-3} ampere f.s.

ACCURACY: ±2% f.s. 10^{-3} thru 10^{-8} ampere ranges; ±3% f.s. 3×10^{-9} thru 10^{-12} ampere ranges.

ZERO DRIFT: Less than 2% of f.s. per day after warmup.

INPUT: Grid current less than 5×10^{-14} ampere.

OUTPUT: 1 v f.s. at up to 5 ma. Noise less than 20 mv.

RISE TIME: Typical values given in sec. to 90% of final values.

Range amps f.s.	C_{in} = 50 $\mu\mu$f seconds	C_{in} = 150 $\mu\mu$f seconds	C_{in} = 1500 $\mu\mu$f seconds
10^{-12}	.600	.800	2.5
3×10^{-12}	.200	.300	1.0
10^{-11}	.060	.080	.250
3×10^{-11}	.020	.030	.100
10^{-10}	.006	.010	.030
3×10^{-10}	.002	.003	.010
10^{-9}	.001	.001	.003
3×10^{-9} and above	.001	.001	.001

PRICE: Model 415, $750.00

For complete details, write:

KEITHLEY INSTRUMENTS, INC.
12415 EUCLID AVENUE
CLEVELAND 6, OHIO

Honeycomb, a critical assembly device, is one of many research tools developed through the cooperation of Los Alamos scientists and engineers to enhance the Laboratory's constant quest for knowledge.

For employment information write: Personnel Director Division 60-48

los alamos
scientific laboratory
OF THE UNIVERSITY OF CALIFORNIA
LOS ALAMOS, NEW MEXICO

Kodak reports on:

and and . . . a little literature before the 11 o'clock news . . lenses for the new phosphors

Infrared detectors for sale

Our involvement in infrared detectors has deepened.

Pictured at the top of this page are, respectively, the simplest kind of *Kodak Ektron Detector* with a rectangular sensitive area of any reasonable dimensions, available either in a 3-pin miniature cable socket or unmounted with re-solderable leads; an "immersed" detector with detecting substance deposited on the plano surface of a radiation-collecting lens; a detector mounted in a Dewar for cooling by cryostat. We also deposit detecting substance in separated or intricate configurations as ingenuity, under necessity's goad, may provide.

Since any of these physical forms can now be provided with any of six different kinds of lead sulfide or lead selenide depositions, as governed by spectral sensitivity, response time, temperature, and ambient humidity, the print gets quite fine in a folder we have just published to guide the selection of *Kodak Ektron Detectors*.

A free copy is available from Eastman Kodak Company, Apparatus and Optical Division, Rochester 4, N. Y. It is designed to make the sale with minimum further correspondence. To give you an idea, the off-the-shelf, one-only price scale starts from $14.50.

Metallography and other matters

You would think we had nothing better to do than write letters and be friendly, helpful, and cheerful.

Though this policy hasn't sunk us yet, we do go through motions to put the dispensing of technical photographic wisdom on a slightly self-sustaining basis. For those who have not yet delved deep enough to frame specific questions, we publish what we call *Kodak Data Books* and print on the cover a small cash price, like 50c.

Just issued is a new one, "Photomicrography of Metals." It contains 13 pages on the metallographic microscope (unbiased toward any particular make of instrument, since we are not in that business), 3 pages on illumination, 5 on filters, 3 on photographic materials (which we do make), 5 on exposure determination, and 8 on processing and printing—just enough for thoughtful perusal between the evening paper and the 11 o'clock news. The pages are meaty; the illustrations are there to explain, not just fill space; the author (anonymous) is a photomicrographer, not an ad-writing hack.

Also just published is the 8th edition of one that has taught many thousands of people since 1933 the rock-bottom facts about the photographic emulsion as a scientific device. The title, "Kodak Photographic Films and Plates for Scientific and Technical Use," dissembles a wee bit. In the old days astronomy was regarded as too thin and unworldly a market to justify commercial literature; therefore the title was devised as a shield from the beady eyes of hard-headed accountants. They find it hard to understand that addressing ourselves to the needs of men with their minds inside stars strengthens the capabilities of photographic technology in general. The edition reveals some constriction from the sprawling diversity of *Kodak "Spectroscopic" Plates and Films* hitherto offered, and these pages show how the present lineup fills the bill.

Theoretically the purchase of these data books from your Kodak dealer draws him and you closer together. Those willing to forego the personal touch can obtain them from Special Sensitized Products Division, Eastman Kodak Company, Rochester 4, N. Y., which is also the place to address specific questions.

Heat from the tubes

Create a stream of electrons, focus them into a sharp pencil, and write or draw with it. Great Zeus! *There* is an idea worth noting in the history of man's climb upward from the slime! Whither it will lead tomorrow can only be guessed at. Today there are contracts to be fulfilled (and possibly money to be made) by finding a lens to image some smart writing from a cathode-ray tube to photographic material and then doing something further smart from there.

A lens? It so happens that you have come to the right place, you there with the black boxes. Your suspicion may well be justified that the old photo-enlarging lens which images your c-r tube on a piece of drugstore film could be missing some of the voluminous detail being poured forth so ferociously by your black boxes. (Better not to disclose what happens in them. Kodak, too, makes mysterious black boxes. It's the American way.)

Formula M-236 is our designation for a beaut of a lens. It represents our response to the heat being put on our end of the c-r recording business by the tube makers. As long as their phosphors couldn't show any finer detail than 10 lines per millimeter on the tube face, it was silly to fuss over the lens. Now that they can put down 100 lines per millimeter, a basic fact of lens design must be faced. A lens designed for distant objects, as most photographic lenses are, cannot function at its best for 4:1 reduction.*

M-236 is designed for 4:1 reduction. Here, for the guidance of the man who needs to design equipment around the finest cathode-ray tube lens currently available on special order, and to the intense boredom of the man who doesn't, are the dimensions:

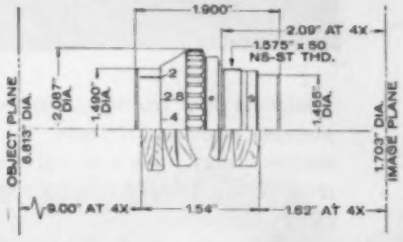

The lens is achromatized for P-16 phosphor. When the diaphragm is wide open to the *f*/2.0 mark, the edge of the 1.700″-diameter image gets 35% as much illumination as the center. If that image size is too small, or if you use P-11 instead of P-16, we have several other c-r lens designs of longer focal length and for lesser reduction.

As to the resolution, we could quote a lot of numbers that are obviously supposed to make your jaw hang slack but don't mean a thing until you pick the film to use with the lens. For this you must be prepared to answer questions on how much voltage to light the tube, how much time to record, how many seconds to process (!), how to be read, etc.

Then you get in touch with Eastman Kodak Company, Special Products Division, Rochester 4, N. Y. No obligation, of course, but what did you say the color of your money was?

*Visitors to Rochester are sometimes permitted a glimpse at a mathematician of ours who thinks, after some years of immersion in matrix algebra, that by and by he will be able to write a computer program which, for any set of circumstances whatever, will design the best possible lens.

Price quoted is subject to change without notice.

Kodak
TRADE MARK

This is another advertisement where Eastman Kodak Company probes at random for mutual interests and occasionally a little revenue from those whose work has something to do with science

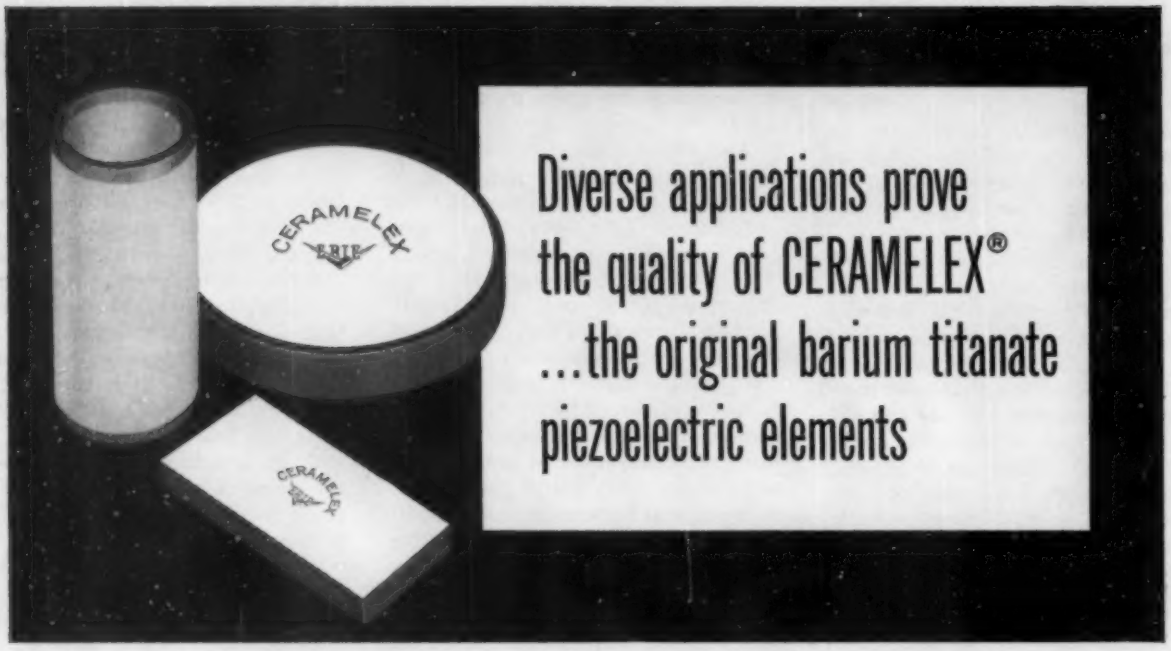

Diverse applications prove the quality of CERAMELEX® ...the original barium titanate piezoelectric elements

Designers and manufacturers of ultrasonic microphones, phono cartridges, IF transformers, sonic devices, delay lines and ultrasonic cleaning devices rely on CERAMELEX piezoelectrics for efficient energy conversion.

Barium titanate, first artificially polarized* by Erie Resistor, is the base material of CERAMELEX. This precision-produced material has qualities not found in the conventional single crystal piezoelectrics:

Variety of sizes and shapes . . . ceramic composition allows molding and pressing;

Wide temperature range . . . operating temperatures as high as 100°C;

Efficient performance . . . higher degree of energy conversion than possible with natural crystals.

You're invited to contact Department 81 of Erie Technical Ceramics for literature and information regarding further capabilities, tolerances and availability of Erie CERAMELEX products.

*U.S. Patent 2,486,560

NOMINAL CHARACTERISTICS OF CERAMELEX® BODIES

	PZ 1005	PZ 1006	PZ 1007*	PZ 1009
Density gm/cc	5.6	5.5	5.4	5.6
Young's Modulus X 10^{10} Newton/m^2	10.2	11.5	10.1	11.0
Dielectric Constant	1800	1200	1200	1400
Diss. Factor %	0.8	0.9	2.5	0.8
Radial Coup. Coeff. k_r	.33	.31	.37	.32
k_p	0.20	0.18	0.22	0.19
k_{33}	.47	.48	.55	.52
d_{31} x 10^{-12} m/v	77	56	71	62
d_{33} x 10^{-12} m/v	180	148	177	168
g_{31} x 10^{-3} v.m/New.	4.9	5.2	6.7	5.1
g_{33} x 10^{-3} v.m/New.	11.5	13.7	16.7	13.8
Frequency Constant (fc) cyc. m	1440	1560	1465	1500
Aging %/decade	2	1	4	1½
Maximum Temperature 1°C	100	100	45	110

*Phono Pick-up units only

Write for Erie Bulletin 454, which gives complete technical data on CERAMELEX.

ERIE

TECHNICAL CERAMICS
DIVISION

ERIE RESISTOR CORPORATION
Erie, Pennsylvania

IN TOUCH WITH NEW HORIZONS

Another achievement of IBM Applied Scientists: computer program for distillation tower design

Making hard realities out of ideas is a task of the IBM Applied Scientist. Through unique and creative applications of data processing, he is changing the worlds of science, industry and business.

One team of Applied Scientists worked closely with IBM customers to develop a new, far more efficient method of designing distillation towers. They created a program for computer analysis of towers with any number of feed and side streams.

Other teams are investigating computer techniques for mathematical physics, machine tool programming, taxonomy, advanced forecasting methods, and information retrieval. The variety of projects is unlimited.

You too may make a vital contribution to this challenging profession. There are openings in many cities for men and women with advanced degrees in engineering, mathematics, or a physical science; or with a degree in one of these areas plus a Master's degree in business administration or experience in computer programming.

For a confidential interview at your convenience, contact any IBM Branch Office or one of these Regional Managers of Applied Science:

L. M. Fulton
IBM Corporation
425 Park Avenue
New York 22, N. Y.

R. W. De Sio
IBM Corporation
618 S. Michigan Ave.
Chicago 5, Ill.

L. C. Hubbard
IBM Corporation
3424 Wilshire Bld.
Los Angeles 5, Cal.

DATA PROCESSING DIVISION **IBM**®

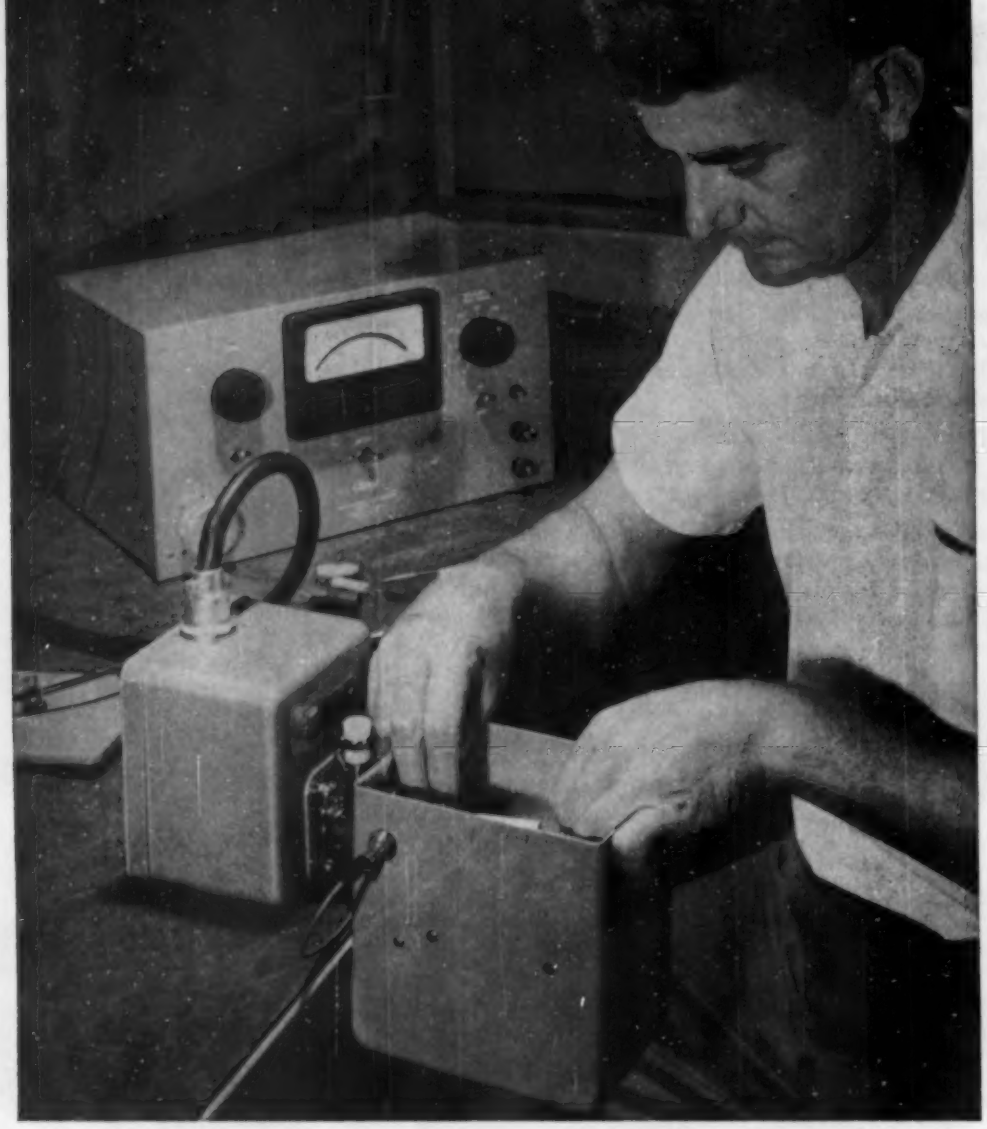

Cary Electrometers measure insulation resistance of 10^{15} ohms at potentials of one volt or less with ±1% accuracy

Provide fast accurate leakage measurements; eliminate instrument loading of the test circuit

In addition to measuring large resistance values Cary Electrometers are used for measuring charging phenomena, hysteresis and photo effects of semi-conductors and insulating materials. Applications include air ionization studies, measurement of ion currents in mass spectrometry, radioactivity measurements of solids, liquids and gases and Hall effect studies.

Cary Electrometers detect currents as small as 10^{-17} amperes; charges to 6×10^{-16} coulombs; and voltages as low as 20 microvolts.

High stability (less than 5×10^{-17} amperes steady drift), high accuracy (±0.25% using a precision potentiometer), and operation independent of changes in vacuum tube and component characteristics are just a few of the features contributing to the superior performance of Cary Electrometers.

Choose from several models: MODEL 31 for measuring currents from grounded sources and voltages from ungrounded sources; MODEL 31V for voltage measurements from grounded sources; MODEL 31-31V for measuring voltage or current from grounded sources.

Cary INSTRUMENTS

Additional information on Cary Electrometers and Accessories is yours for the asking. Write for data file R14-50

Electrometers • UV—Visible—Near IR and Raman Spectrophotometers

APPLIED PHYSICS CORPORATION • 2724 So. Peck Rd., Monrovia, Calif.

New from RCA...X-Ray Vacuum Spectrometer

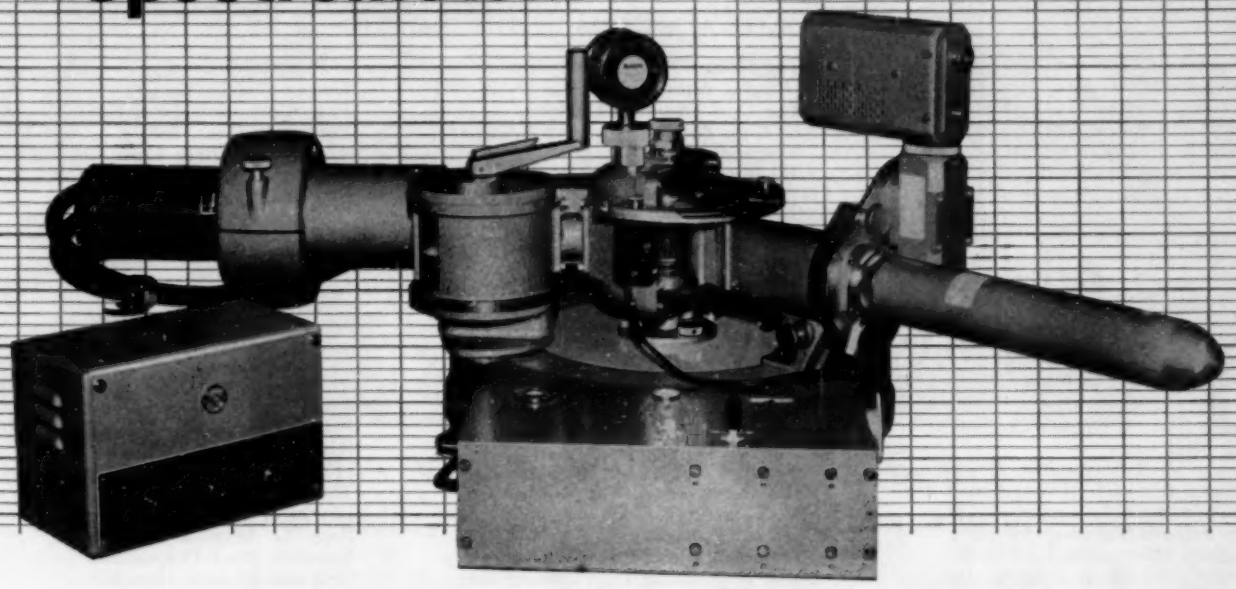

for analysis of the lighter elements

Especially suited to the X-ray spectro-chemical analysis of elements below atomic number 22, RCA's new Vacuum Spectrometer permits the use of three samples at one time. Samples—powders or solids—can be moved in and out of the vacuum path without breaking vacuum. The need for helium is eliminated, but air or helium can be used when desired. A flange connects the sample chamber directly to the X-ray tube, making higher intensities possible, and eliminating the need for a second beryllium window. From a cold start the recommended vacuum of 0.1mm or 100 microns can be reached in less than two minutes. Designed primarily for the analysis of lighter elements, the Vacuum Spectrometer can be used to advantage with heavy elements to give higher intensities.

The Vacuum Spectrometer is one of a wide range of attachments and accessories available for RCA X-Ray Diffraction and Spectroscopy equipment which contribute to its extreme flexibility of application. Installations already made in some of the nation's leading research laboratories are demonstrating the efficiency, technical excellence and versatility of these instruments.

Installation supervision and contract service for RCA Electron Microscopes and X-Ray Diffraction and Spectroscopy Equipment are available through the RCA Service Company.

For details on the new Vacuum Spectrometer or RCA's full line of X-Ray Diffraction and Spectroscopy equipment, write to RCA, Dept. G-65, Building 15-1, Camden, New Jersey.

Vacuum Spectrometer and a Diffractometer mounted on Crystalloflex IV and connected to Electronic Circuit Panel

The Most Trusted Name in Electronics
RADIO CORPORATION OF AMERICA

Corporate Associates

American Institute of Physics

The Corporate Associates of the American Institute of Physics are a group of corporations, institutions, and laboratories who believe it is valuable to them and to America to maintain a vigorous advance in the physical sciences. By their membership dues they aid the Institute significantly in carrying out its purpose: the advancement and diffusion of knowledge of the science of physics and its application to human welfare. The Institute is grateful for their assistance.

CORPORATE ASSOCIATES OF THE INSTITUTE

Abbott Laboratories
Academic Press Inc.
Airborne Instruments Laboratory, Inc.
Allegheny Ludlum Steel Corporation
Allen-Bradley Company
Allied Chemical Corporation
Allied Research Associates, Inc.
Allis-Chalmers Manufacturing Co.
Aluminum Company of America
American Can Company
American Cyanamid Company
American Machine & Foundry Co.
American Optical Company
American Radiator & Standard Sanitary Corp.
American Viscose Corporation
Ampex Corporation
Ansco Div. of General Aniline & Film Corp.
Armco Steel Corporation
Armour Research Foundation
Armstrong Cork Company
The Atlantic Refining Company
Atomics International Division North American Aviation, Inc.
Avco-Everett Research Laboratory
Avco Research & Advanced Development Division
Baird-Atomic, Inc.
Basic Books, Inc.
Battelle Memorial Institute
Bausch & Lomb Optical Company
Bell Telephone Laboratories, Inc.
Bendix Aviation Corporation
Bethlehem Steel Company, Inc.
Boeing Airplane Company
Bodine Soundrive Company
Bolt Beranek and Newman Inc.
Borg-Warner Corporation
Bulova Research and Development Laboratories, Inc.
Burroughs Corporation
California Research Corporation
Caterpillar Tractor Company
CBS Laboratories
Celanese Corporation of America
Central Scientific Company
Chance Vought Aircraft, Inc.
The Chemstrand Corporation
Chrysler Corporation
The Cincinnati Milling Machine Company
Clevite Corporation
Collins Radio Company
Combustion Engineering, Inc.
Consolidated Electrodynamics Corp.
Continental Can Company, Inc.
Continental Oil Company
Convair
Cornell Aeronautical Laboratory, Inc.
Corning Glass Works
Crane Company
The Detroit Edison Company
Douglas Aircraft Co., Inc.
The Dow Chemical Company
E. I. du Pont de Nemours & Co., Inc.
Eastman Kodak Company
Thomas A. Edison Research Laboratory
The Eppley Laboratory, Inc.
Esso Research & Engineering Company
Farrand Optical Co., Inc.
The Firestone Tire & Rubber Co.
Ford Motor Company
The Foxboro Company
General Dynamics Corporation General Atomic Division
General Electric Company
General Motors Corporation
General Radio Company
General Telephone Laboratories, Inc.
The Gillette Company
The B. F. Goodrich Company
The Goodyear Tire & Rubber Co.
W. R. Grace & Co.
Grinnell Corporation
Grumman Aircraft Engineering Corp.
Gulf Research & Development Co.
Haller, Raymond and Brown, Inc.
Halliburton Oil Well Cementing Co.
Haloid Xerox Inc.
Hercules Powder Company
Hewlett-Packard Company
High Voltage Engineering Corp.
Hoffman Electronics Coporation
Hughes Aircraft Co.
Humble Oil & Refining Company
International Business Machines Corp.
International Harvester Company
International Minerals & Chemical Corp.
International Nickel Co., Inc.
Itek Corporation
ITT Laboratories
Joslyn Mfg. & Supply Co.
Knowles Electronics, Inc.
Lear, Incorporated
Leeds & Northrup Company
Libbey-Owens-Ford Glass Co.
Arthur D. Little, Inc.
Lockheed Aircraft Corporation
McGraw-Hill Book Company, Inc.
The Martin Company
Massachusetts Institute of Technology
Merck Sharp & Dohme Research Labs.
Minneapolis-Honeywell Regulator Co.
Minnesota Mining & Manufacturing Co.
Monsanto Chemical Company
The National Cash Register Company
National Research Corporation
Northrop Corporation
Nuclear Development Corporation of America
The Ohio Oil Company
Olin Mathieson Chemical Corp.
Outboard Marine Corporation
Owens-Corning Fiberglas Corporation
Owens-Illinois Glass Co.
Page Communications Engineers, Inc.
Pergamon Press, Inc.
The Perkin-Elmer Corp.
Philco Corporation
Philips Laboratories, Div. of North American Philips Co., Inc.
Phillips Petroleum Company
Pilkington Brothers Limited
Pitney-Bowes, Inc.
Pittsburgh Corning Corp.
Pittsburgh Plate Glass Company Glass Division
Polaroid Corporation
The Procter & Gamble Company
The Pure Oil Company
Radio Corporation of America
Ramo-Wooldridge Division Thompson Ramo Wooldridge Inc.
The Rand Corporation
Raytheon Mfg. Co.
Republic Aviation Corporation
Republic Steel Corporation
Sangamo Electric Company
Schering Corporation
Schlumberger Well Surveying Corp.
Scientific American
Shell Development Company
Shockley Transistor Corporation
Smyth Research Associates
Socony Mobil Oil Company, Inc.
Space Technology Laboratories, Inc.
Sperry Rand Corporation
Sprague Electric Company
A. E. Staley Manufacturing Co.
Standard Oil Company (Indiana)
Stanford Research Institute
Sun Oil Company
Sylvania Research Laboratories Div. of Sylvania Electric Products, Inc.
Technical Operations, Inc.
Texaco, Inc.
Texas Instruments, Inc.
Tung-Sol Electric Inc.
Union Carbide Corporation
Union Oil Company of California
Union Switch & Signal Div. of Westinghouse Air Brake Co.
United Gas Corporation
United States Rubber Company
United States Steel Corp.
Universal Oil Products Company
The Upjohn Company
Varian Associates
Veeco Vacuum Corp.
Vitro Laboratories Division of Vitro Corp. of America
Western Union Telegraph Company
Westinghouse Electric Corporation
Whirlpool Corporation
Zenith Radio Corporation

The American Institute of Physics cordially invites interested corporations and institutions to make application for Corporate Associate membership and will welcome their inquiries addressed to the Secretary.

Physicists, Engineers, EE's

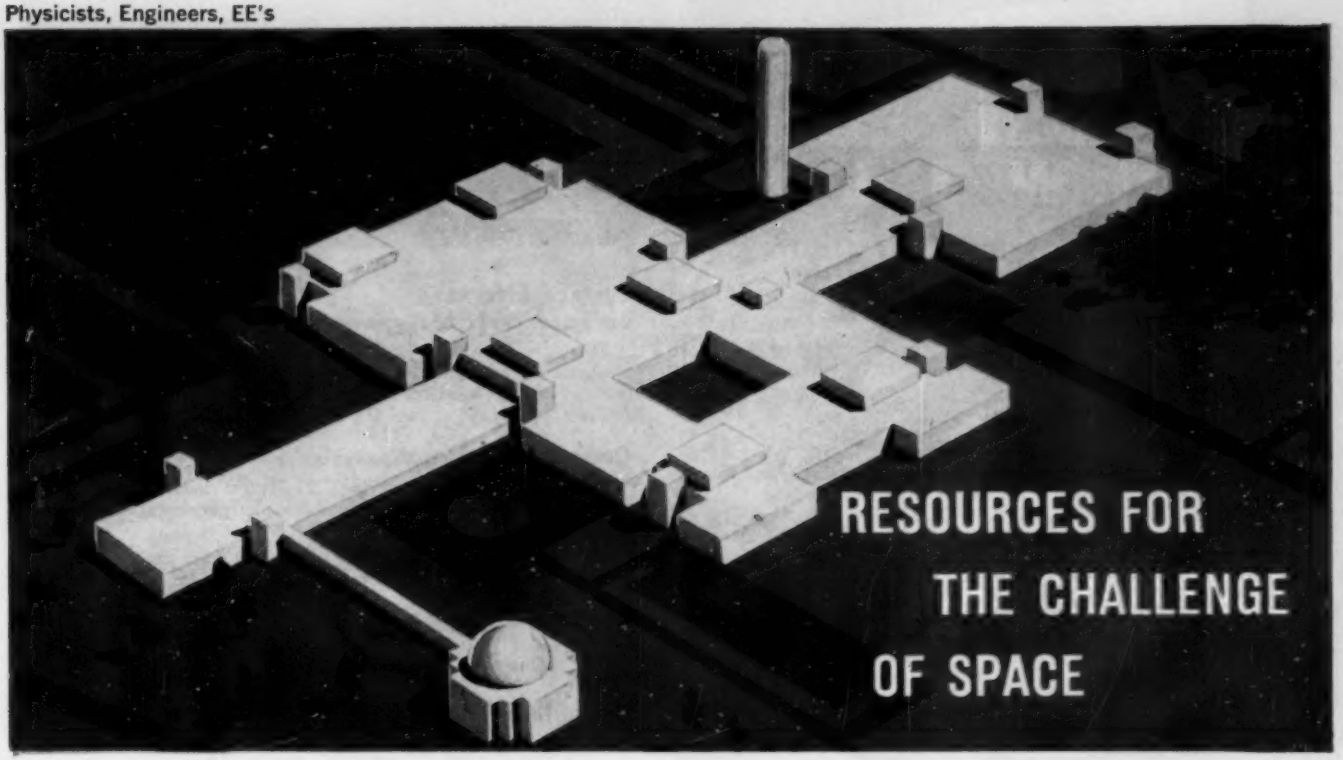

...General Electric's New $14,000,000 Space Research Center, to be built near Valley Forge Park 17 miles from Philadelphia

The Missile and Space Vehicle Department invites scientists and engineers with previous records of accomplishment in the space sciences to review the positions described on this page.

These positions are with our Space Sciences Laboratory, which will move to suburban Valley Forge upon the completion of the Department's new Space Research Center. Unique equipment—in addition to the six inch shock tunnel and water stabilized arc now in our Philadelphia facility—will be installed to further long range studies in the areas indicated below:

THEORETICAL GAS DYNAMICS

A Physicist with PhD degree or equivalent in aerodynamics, gas dynamics, or the physics of fluids in high temperature and high altitude regimes is sought. This scientist will perform theoretical investigations of the following areas of gas dynamics: magneto-gas dynamics, non-equilibrium effects in gas dynamics at high altitudes, mass transfer and heat transfer, boundary layer theory and flow field analysis.

THEORETICAL PLASMA INVESTIGATIONS

Opening for scientist with PhD degree or equivalent experience in physics or any of the related fields of electro-magnetic phenomena or gaseous electronics. He will perform theoretical investigations associated with the generation and diagnosis of plasmas. And, he will be offered the opportunity to study the interactions of plasmas with magnetic fields and microwave radiation and many-body and collective phenomena in plasmas.

INTERPLANETARY AND LUNAR TRAJECTORY RESEARCH

A number of opportunities exist at the PhD level of Mathematics, Astronomy and Applied Mechanics to conduct analytical and computer studies in the following areas: applied mechanics, applied mathematics, celestial dynamics, analytical dynamics.

ADVANCED STRUCTURAL RESEARCH

Research in the fields of dynamic buckling, radiation shielding, high speed particle impact, etc. A doctoral degree in engineering, applied mechanics or applied mathematics is required.

ADVANCED COMMUNICATIONS

To work primarily on problems of interaction of electromagnetic waves with partially ionized high-temperature gases. A PhD degree with general physics background and special competence in electro-magnetic theory is essential. An appreciation for the techniques, problems and results of aerodynamics and thermodynamics is also desirable.

For further information regarding opportunities here, write Mr. Thomas H. Sebring, Div. 37ME.
You will receive an answer within 10 days.

MISSILE & SPACE VEHICLE DEPARTMENT

GENERAL ELECTRIC

3198 Chestnut Street, Philadelphia 4, Pa.

WILEY BOOKS

Elementary Introduction to Nuclear Reactor Physics

By SALOMON E. LIVERHANT, *State University of New York. 1960. Approx. 472 pages. Prob. $9.75.*

Physics for Students of Science and Engineering

By DAVID HALLIDAY, *University of Pittsburgh, and* ROBERT RESNICK, *R.P.I.* VOLUME I: By Resnick and Halliday. *1960. 594 pages. $6.00.* VOLUME II: by Halliday and Resnick. *1960. 528 pages. $6.00.* COMBINED: *1960. Approx. 1064 pages. $10.50.*

Thermodynamics

By HERBERT B. CALLEN, *University of Pennsylvania.* Develops the theory of thermodynamics as a self-contained, logical structure. *1960. 376 pages. $8.75.*

Optical Crystallography

Third Edition

By ERNEST E. WAHLSTROM, *University of Colorado. 1960. 356 pages. $7.00.*

Physics and Medicine of the Atmosphere and Space

Edited by Major General OTIS O. BENSON *and* HUBERTUS STRUGHOLD, *both of the Aviation School of Medicine. 1960. 645 pages. $12.50.*

Radiation Pyrometry and Its Underlying Principles of Radiant Heat Transfer

By THOMAS R. HARRISON, *Minneapolis-Honeywell Regulator Co.* Presents the theoretical principles of radiation pyrometry and the methods for its practical application. *1960. 234 pages. $12.00.*

Mechanics and Properties of Matter

Second Edition

By REGINALD J. STEPHENSON, *The College of Wooster. 1960. Approx. 384 pages. Prob. $7.95.*

Magnesium and Its Alloys

By C. SHELDON ROBERTS, *Fairchild Semiconductor Corp. 1960. 230 pages. $9.00.*

Direct Conversion of Heat to Electricity

Edited by JOSEPH KAYE *and* JOHN A. WELSH, *both of M.I.T.* A collection of papers by leading scientists and engineers currently working in this new technological field. *1960. 377 pages. $8.75.*

Basic Data of Plasma Physics

By SANBORN C. BROWN, *M.I.T.* A Technology Press Book, M.I.T. *1959. 336 pages. $6.50.*

Surface Effects on Spacecraft Materials

Edited by FRANCIS J. CLAUSS, *Lockheed Aircraft Corp.* Proceedings of a symposium held in May, 1959, on the temperature-control behavior of material surfaces in space. *1960. 404 pages. $11.50.*

Crystal-Structure Analysis

By MARTIN J. BUERGER, *M.I.T.* Offers theoretical and practical discussion of all the available analytical procedures. *1960. Approx. 664 pages. $16.00.*

Progress in Dielectrics

Volume I

Edited by J. B. BIRKS, *Manchester University; and* J. H. SCHULMAN, *U. S. Naval Research Laboratory. 1960. 225 pages. $11.00.*

Probability Theory and Its Applications

By EMANUEL PARZEN, *Stanford University. 1960. 464 pages. $9.00.*

Electromagnetic Energy Transmission and Radiation *

By RICHARD B. ADLER, LAN JEN CHU, *and* ROBERT M. FANO, *all of M.I.T. 1960. 621 pages. Prob. $12.00.*

Electromagnetic Fields, Energy and Forces *

By ROBERT M. FANO, LAN JEN CHU, *and* RICHARD B. ADLER, *all of M.I.T. 1960. 520 pages. $10.00.*

Progress in Semiconductors

Volume IV

Edited by ALAN F. GIBSON, *Radar Research Establishment;* R. E. BURGESS, *University of British Columbia; and* F. A. KRÖGER. *1960. 292 pages. $10.50.*

Theory of Thermal Stresses

By BRUNO A. BOLEY *and* JEROME H. WEINER, *both of Columbia University. 1960. Approx. 560 pages. Prob. $15.50.*

Mathematical Methods for Digital Computers

Edited by ANTHONY RALSTON, *the Bell Telephone Laboratories; and* HERBERT S. WILF, *University of Illinois. 1960. 293 pages. $9.00.*

Theory of Mechanical Vibration

By KIN S. TONG, *Syracuse University. 1960. 348 pages. $9.75.*

* *A Volume in the M.I.T. "Core Curriculum" Program in Electrical Engineering.*

Send for examination copies.

JOHN WILEY & SONS, Inc. **440 Park Avenue South, New York 16, N.Y.**

ENGINEERS • SCIENTISTS

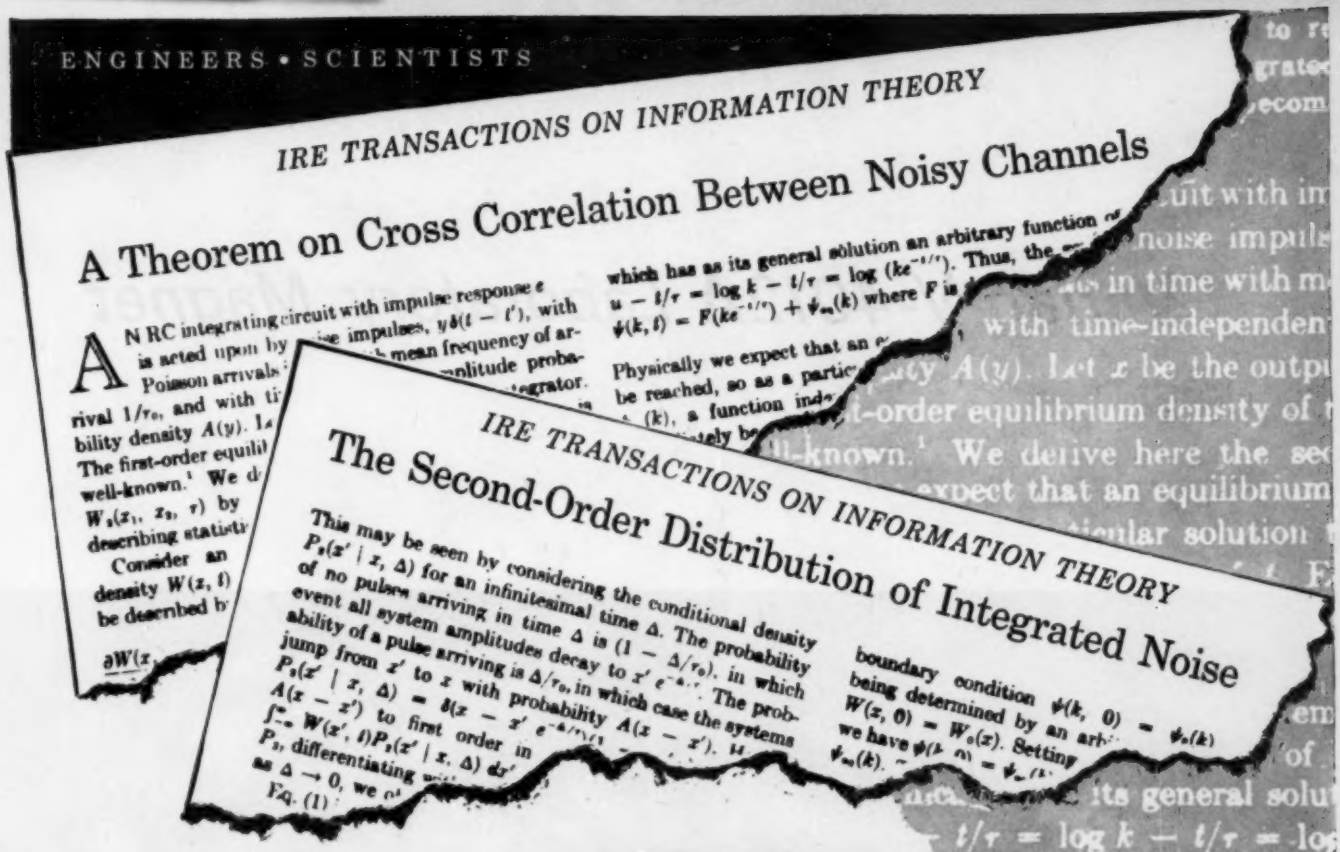
IRE TRANSACTIONS ON INFORMATION THEORY
A Theorem on Cross Correlation Between Noisy Channels
IRE TRANSACTIONS ON INFORMATION THEORY
The Second-Order Distribution of Integrated Noise

SYLVANIA'S ARL Applied Research Laboratory

Is engaged in diversified, active programs that afford broad individual participation

The Applied Research Laboratory is directing its growing capability toward theoretical and experimental investigations that will lead to major state-of-the-art advances in the field of military and commercial electronic systems. The opportunity for individual recognition in this challenging technological area is typified by the titles of the two recent technical papers, by ARL staff members, which are depicted here.

If you possess superior qualifications (an advanced degree is desirable) and would like to join this highly professional group, you are invited to inquire about career positions in these areas:

- **RADIO PHYSICS ▪ ELECTROMAGNETIC PROPAGATION**
- **HYPERSONIC GAS DYNAMICS ▪ MICROELECTRONICS**
- **MATHEMATICAL ANALYSIS & OPERATIONS RESEARCH**
- **INFORMATION & COMMUNICATION THEORY**

For further information about research work in the above areas, and other technical publications by ARL engineers, you are invited to write to:
Dr. L. S. Sheingold, Director, Applied Research Laboratory

Waltham Laboratories / SYLVANIA ELECTRONIC SYSTEMS
A Division of SYLVANIA
Subsidiary of GENERAL TELEPHONE & ELECTRONICS
100 First Avenue, Waltham 54, Massachusetts

Varian V-4012A Laboratory Magnet

UNMATCHED PERFORMANCE

AS FURNISHED OR AS CONVERTED

From the standard Varian V-4012A 12-inch Laboratory Magnet, performance is unmatched in providing the user with a ***maximized product*** of the three important magnetic-field parameters: (1) field strength, (2) permissible sample volume in the air gap, and (3) field uniformity over the sample volume.

Because when one magnet parameter goes up another goes down, the true measure of the magnet's quality and usefulness is the ***field-volume-uniformity*** combination and the wide range over which each may be varied. The typical field plot at the right demonstrates that even at a field as high as 20,000 gauss, the Varian V-4012A can accommodate a useful-sized sample within its volume of high-homogeneity field. This 20,000 gauss performance is an achievement that has utilized highly advanced design and shimming techniques. It reflects Varian Associates' unique understanding acquired from years of continuous and productive research in magnet technology.

But the full extent of the inherent quality of the V-4012A is revealed by its convertibility to another highly useful but specialized type of magnet. Any new Varian V-4012A can now be converted in the

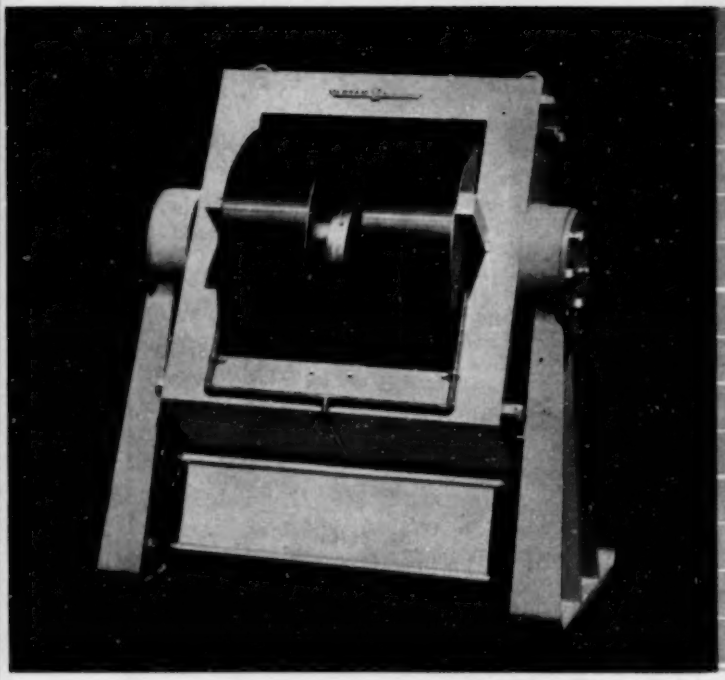

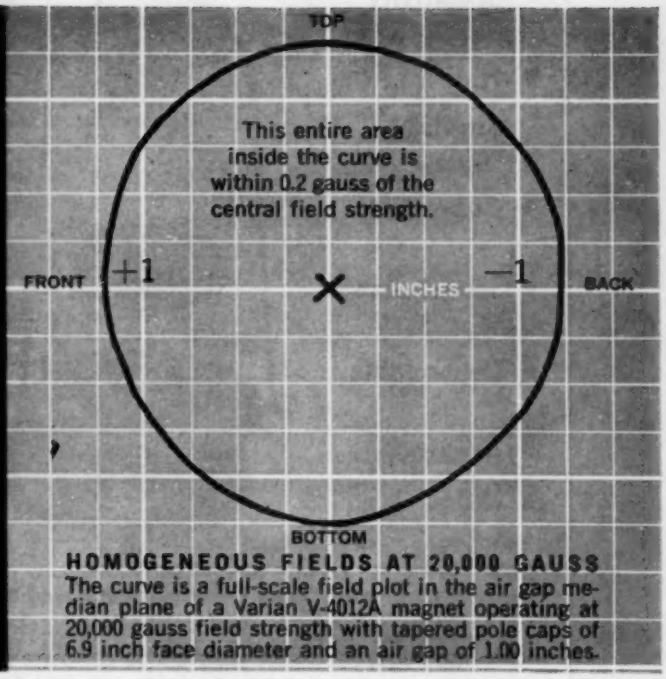

HOMOGENEOUS FIELDS AT 20,000 GAUSS
The curve is a full-scale field plot in the air gap median plane of a Varian V-4012A magnet operating at 20,000 gauss field strength with tapered pole caps of 6.9 inch face diameter and an air gap of 1.00 inches.

field to what we designate as a V-4013 – the ultra-precise magnet that Varian developed to make possible the 60-megacycle High Resolution NMR Spectrometer. The magnet-dependent resolution of this spectrometer is as high as one part in 200,000,000 for a spinning cylindrical proton sample of 4 mm diameter in a 14,100 gauss field.

Choosing a Varian Magnet for your laboratory is an act of foresight. Not only will its performance serve for today's uses, but tomorrow's can be accommodated as well.

Varian Associates manufactures a line of 4, 6, and 12-inch laboratory magnet systems including rotating models and adjustable yoke types. For literature describing all types, write the Instrument Division.

The Varian Magnet Standard:
Unmatched performance through unique understanding.

VARIAN associates
PALO ALTO 36, CALIFORNIA

NMR & EPR SPECTROMETERS, MAGNETS, MAGNETOMETERS, GRAPHIC RECORDERS, FLUXMETERS, MICROWAVE TUBES, MICROWAVE SYSTEM COMPONENTS, HIGH VACUUM EQUIPMENT, LINEAR ACCELERATORS, RESEARCH AND DEVELOPMENT SERVICES

• *Fast, Accurate Weighing* • *Rugged Construction*

Welch TRIPLE BEAM BALANCE

All Exposed Parts of *Stainless Steel*

Corrosion-Resistant

- Good Sensitivity
- High Stability
- Convenient
- Serviceable
- Dependable
- Accuracy-tested

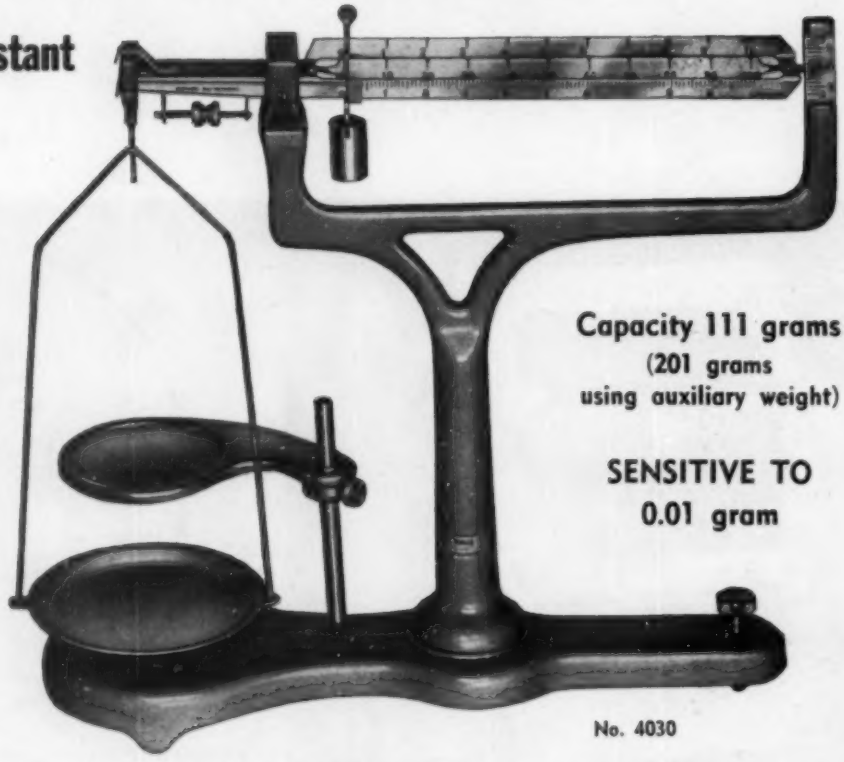

Capacity 111 grams
(201 grams using auxiliary weight)

SENSITIVE TO 0.01 gram

No. 4030

3 Graduated Scale Levels for easy reading. Riders move easily. Hard, Cobalite Knife Edges maintain true edge indefinitely. Grooved Agate Bearings are protected against damage, yet highly resistant to corrosive action of laboratory fumes. One-Piece Beam Construction—Silver-Gray Hammerloid Finish Rapid Zero Setting.

4030. TRIPLE-BEAM BALANCE, High Form. Each, $27.50

4031. AUXILIARY WEIGHT. For use on the 100-gram notch of No. 4030 Balance to increase weighing capacity from 111 grams to 201 grams. Each, $1.50

4030C. PLASTIC COVER, For No. 4030. Each, $1.10

W. M. WELCH SCIENTIFIC COMPANY

DIVISION OF W. M. WELCH MANUFACTURING COMPANY

ESTABLISHED 1880

1515 Sedgwick Street, Dept. C-1 Chicago 10, Illinois U. S. A.

Manufacturers of Scientific Instruments and Laboratory Apparatus

Journal
of
Applied Physics

Volume 31, Number 5 May, 1960

Specific Ionization Measurements and Energy Requirements for *F*-Center Formation

R. D. JORDAN* AND R. S. ALGER
U. S. Naval Radiological Defense Laboratory, San Francisco, California
(Received December 9, 1959; revised manuscript received February 1, 1960)

Measurements were made of the energy required to produce *F* centers in pure and sensitized alkali halide crystals by bombardment with electrons and deuterons accelerated in a Van de Graaff generator. In KBr+KH exposed to 1.2-Mev electrons, 35 ev were required per *F* center. This value is in agreement with other published data. A value of approximately 100 ev was required with deuterons and KBr+KH. Slightly lower yields were found for several other salts. The specific ionizations of electrons, deuterons, and gamma rays were investigated and used to determine the accelerator beam size and penetration. The ranges of electrons in KBr, KCl, and NaCl were measured as a function of accelerator voltage and found to agree well with ranges predicted by the Feather rule. Energy transport and features of the specific ionization pattern are discussed in terms of the Seitz synthesis of crystal imperfections.

INTRODUCTION

WHEN crystals containing sensitizing or activating centers are bombarded with ionizing radiation, most of the energy is absorbed and dissipated by the host material, but a portion is transported to the impurity centers. The efficiency of this transfer is of prime importance in the practical application and use of these materials; consequently, the literature on the scintillation crystals, conductivity crystal counters, and color centers in the alkali halides frequently touches on the problem of energy transport. It has been established that the final distribution of the energy is strongly influenced by the condition of the host material, the type of ionizing particle, and the nature of the activating atoms. Generally, it is inconvenient to obtain direct quantitative measurements of the efficiency of this energy transport. The conversion of *U* centers, in alkali halide crystals, to *F* centers is one of the simpler reactions for quantitative measurements of this transport efficiency. The objectives of this study are: (a) to examine the influence of host material and bombarding particle on the energy requirements for *F*-center production, and to compare these results with values obtained using gamma rays; and (b) to determine the feasibility of using color-center production for the measurement of specific ionization and range of high-energy electrons.

A number of investigators have found that photochemical reactions employing ionizing radiations are about 10% efficient.[1] (See Table I.) The wide range of efficiencies obtained is indicative of the difficulty encountered in obtaining reproducible quantitative results. Qualitatively it is apparent that the most sensitive systems in the case of alkali halides are those containing suitable impurities, and that ionization by heavy particles leads to much lower efficiencies than those produced by gamma and beta rays.

EXPERIMENTAL PROCEDURE

Single crystals of KBr+KH, KCl+KH, and NaCl +KH, mixed crystals of KBr and KCl, and pure KBr, KCl, and NaCl were bombarded with electrons and deuterons to produce *F* centers under conditions which permitted the measurement of the energy absorbed by the crystal. The electrons and deuterons were accelerated by a Van de Graaff generator and could be given energies between 0.5 and 2.3 Mev. Figure 1 shows the

* Now at the U. S. Naval Postgraduate School, Monterey, California.

[1] R. Frerichs, "A study of the older literature related to the coloring of crystals by radiation with x-rays or nuclear radiation," Northwestern University Report, September, 1950 (unpublished).

Copyright © 1960 by the American Institute of Physics.

TABLE I.

Alkali halide	*F*-center conc (F/cm^3)	*U*-center conc (U/cm^3)	Radiation	Radiation energy	Energy/*F*-center (ev/*F* ctr)	Remarks
NaCl[a]	0	0	electrons	...	35	
NaCl[a]	10^{15}	0	electrons	...	39	
NaCl[a]	10^{16}	0	electrons	...	150	
KBr[b]	initial	$>10^{17}$	x rays	...	35	
KBr[c]	initial	$<25\times10^{17}$ $>2\times10^{17}$	x rays	50–60 kev	41	
KCl[c]	initial	$<6\times10^{17}$ $>2\times10^{17}$	x rays	50–60 kev	26	
NaCl[d]	initial	0	Co^{60} γ	1.27 Mev 191 000 r/hr	98[f]	annealed, Harshaw
NaCl[e]	0	0	x rays	40 kvp	98	Harshaw
KCl[g]	initial	0	x rays	...	18	
KCl[g]	$<5\times10^{17}$	0	x rays	...	53	
KCl[h]	...	...	x rays	...	120	
KBr[i]	$<10^{16}$	$>10^{17}$	Co^{60} γ	1.27 Mev	26	
KBr[i]	initial	0	Co^{60} γ	1.27 Mev	92	estimated from curves
KBr[i]	10^{15}–10^{16}	0	Co^{60} γ	1.27 Mev	154	
KBr	$\approx10^{16}$	$>10^{17}$	electrons	1.2 Mev	35	
NaCl	$\approx10^{16}$	10^{16}–10^{17}	Co^{60} γ	1.2 Mev	44	
KCl	$\approx10^{16}$	10^{16}–10^{17}	Co^{60} γ	1.2 Mev	51	
KBr	...	10^{17}	deuterons	1.2 Mev	100	estimated from curves

[a] K. Przibram, *Irradiation Colours and Luminescence* (Pergamon Press, New York, 1956), p. 71.
[b] W. Martienssen and H. Pick, Z. Physik **135**, 309 (1953).
[c] W. Martienssen and H. Mette, Naturwissenschaften **41**, 331 (1954).
[d] A. S. Nowick, Phys. Rev. **111**, 16 (1958).
[e] H. W. Etzel and J. G. Allard, Phys. Rev. Letters **2**, 452 (1959).
[f] Corrected to energy absorption coefficient of 0.055 cm^{-1}.
[g] E. E. Schneider, *Photographic Sensitivity* (Butterworths Scientific Publications Ltd., London, 1951).
[h] H. -U. Harten, Z. Physik **126**, 619 (1949); Nachr. Akad. Wiss. Göttingen IIa **3**, 15 (1950).
[i] R. S. Alger and R. D. Jordan, Phys. Rev. **97**, 277 (1955).

device used to collimate and reduce the beam diameter to $\frac{5}{16}$ in. The exposure chamber at the bottom of the collimator served as a Faraday cup. Beam currents of about 10^{-9} amp were integrated over a total exposure of approximately 10^{-8} coulomb with an external capacitor, and measured with a vibrating reed electrometer. Between exposures the condenser and electrometer were calibrated with a constant current source, consisting of a battery in series with a 10^{11}-ohm calibrated resistor.

The total number of *F* centers produced was determined from the peak height and half-bandwidth of the *F*-absorption band, using the classical expression of Smakula

$$N_{\text{salt}} = (\text{Numerical factor of salt})KL,$$

where K = absorption coefficient at the *F*-band maximum in cm^{-1}, L = crystal thickness in cm.[2] The optical densities of the crystals used in the absolute and relative energy-absorption-efficiency studies were measured with a Cary Model 11 spectrophotometer. Owing to variations in the intensity of the charged particle beam, the exposure area was not uniformly colored. A plot of the distribution in optical density was obtained by scanning the colored spot with a 0.020×0.125-in. slit in the spectrophotometer beam. The *F*-center population was determined from a graphical integration of this plot.

The curves showing relative *F*-center concentrations (Figs. 2–4) were obtained with the spectrophotometer, using a $\frac{3}{16}$-in. diam iris to sample the center of the colored spot. The absorption spectrum from 3000 to 8000 A was measured in all cases to insure a reliable reference level for the different salts.

The specific-ionization and depth-of-penetration curves were obtained with a nuclear-track-plate microscope for deuterons and a microdensitometer for electrons. Slices about 0.010 in. thick from the center of the colored spot were split parallel to the path of the incident particles and scanned along the path of the incident beam. Care was exercised in exposing the sensitized KBr crystals used for the specific ionization curves to avoid *F*-center saturation in the more highly ionized volumes.

All crystals compared were grown by the same process and were given similar thermal histories prior to exposure. Crystals grown in air using the Kyropoulos technique were used for Figs. 3 and 4. The other results were obtained with Harshaw crystals which were annealed in air or additively colored. In determining the energy requirements for *F*-center formation with deuterons and electrons, adjacent slices from the same original crystals were used. In the specific-ionization study the crystals used were cleaved from several

[2] K. Przibram, *Irradiation Colors and Luminescence* (Pergamon Press, New York, 1956), p. 260.

larger pieces that were originally part of a single crystal. All crystals were given a slow anneal before cleaving and were left unpolished, i.e., the cleaved surfaces were considered adequate.

RESULTS

$U \rightarrow F$ Transition

Two methods of irradiation were used to obtain upper and lower limits for the energy required to produce an F center in sensitized salt. At energies around 1 Mev both gamma and beta ionization are essentially electronic processes. As reported previously[3] a determination of the energy-absorption efficiency using gamma rays resulted in a value which was somewhat low due to several approximations made in calculating the energy absorbed. Electrons, however, will give a value which is high if a correction is not made for bremsstrahlung loss (Fig. 5).

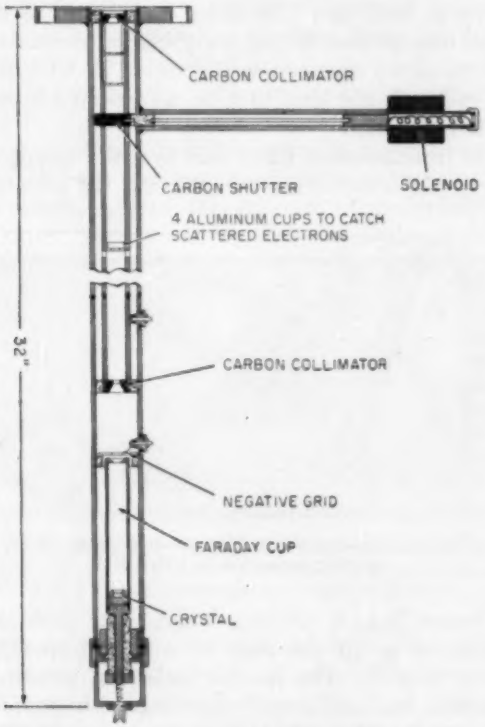

FIG. 1. Irradiation chamber with electron-beam collimator.

KBr+KH gave the most reliable results. The yields with gamma rays and electrons were quite reproducible and in general agreement with several published values (see Table I). The gamma value was 26 ev per F center and the electron value 35 ev per F center for an accelerating voltage of 1.2 Mev. The results of the work on deuterons would seem to indicate that approximately 100 ev were needed to produce an F center, but the value is somewhat high because the saturation concentration of F centers develops at extremely small doses. This saturation was on account of the small penetration and high specific ionization produced by the deuterons. The 100 ev value was estimated from the slope of a line through the origin (Fig. 5) and tangent to a curve plotted for several very short deuteron exposures. The crystal scanning technique could not be used in this case owing to the small optical densities obtained before saturation occurred, and therefore it is not known if the density observed through the crystal and the estimated colored area are appropriate to the measured charge.

[3] R. S. Alger and R. D. Jordan, Phys. Rev. 97, 277 (1955).

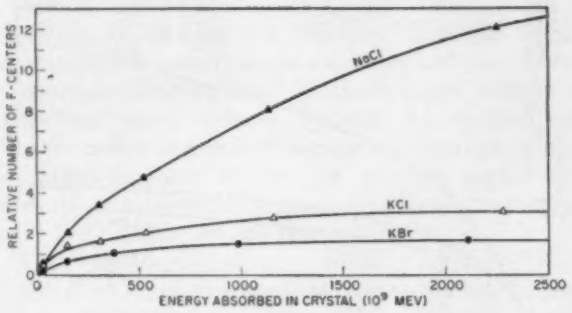

FIG. 2. Effect of crystal material on the yield and saturation concentration of F centers.

Measurements of the absorbed energy required to produce an F center were made for NaCl+KH and KCl+KH. The values obtained for NaCl+KH and KCl+KH were 43.7 ev per F center and 51.0 ev per F center, respectively. Neither of these results is as reliable as the KBr+KH data since there was a tendency for the crystals to saturate at lower optical densities. The low yields were caused by insufficient initial U-center concentrations (10^{16} to 10^{17} per cc). The values of energy absorption per F center obtained by extrapolating the NaCl+KH and KCl+KH coloring curves to the origin would still be higher than the KBr value.

Pure Crystals

Comparisons of the coloring efficiencies of KBr, KCl, and NaCl using electrons were made, and it was found that the energy absorbed per F center was least in NaCl, slightly larger in KCl and quite a bit larger in

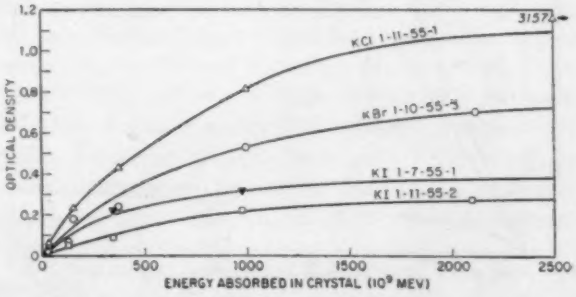

FIG. 3. Effect of Halogen ion on the yield and saturation concentration of F centers in K salts.

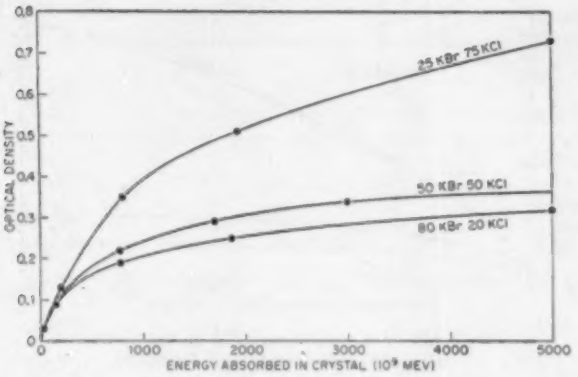

FIG. 4. Relative *F*-center production in mixed crystals of KBr and KCl.

KBr (Fig. 2), which agreed with results obtained in previous work using gamma and x rays. Comparisons of KCl, KBr, and KI to determine the effect of the halogen ion on energy absorbed per *F* center with electron radiation show that, for the same alkali ion (Fig. 3), the coloring efficiency decreases with a halogen of increasing atomic number. These results also agree with previous work using gamma and x rays.

Mixed crystals of KCl and KBr were investigated and it was found that the various mixtures (Fig. 4) corresponded to points between the pure KCl and KBr.

Specific Ionization and Range

The most reproducible specific ionization data were obtained for KBr+KH. A family of curves representing the specific ionization at various distances from the crystal surface is shown in Fig. 6. These curves were taken from microdensitometer traces of thin slices of the crystal. In general, the curves are shaped as would be expected from theory, and have extrapolated ranges which are a few percent less than those predicted by Feather rule as modified by Glendenin and Coryell. There is an unusual feature at the maximum penetration which was observed in most of the samples. It consists of one or more secondary maxima. These humps in the curve are definitely present as shown by Fig. 7, and are well above any deviations produced by the densitometer or by crystal surface defects. The curves do not approach the abscissa tangentially at the ends of the humps as they would for idealized beta absorption curves (see Fig. 6).

The ranges of electrons and deuterons were investigated as a function of accelerator voltage. Electron ranges were determined by extrapolating the linear portion of the microdensitometer traces as indicated by the dashed lines in Fig. 6. It was found that the penetration increased linearly with energy from 0.8 to 2.3 Mev in KBr, and probably also in NaCl and KCl. The experimental determinations of range were not as accurate in NaCl and KCl, since the crystals used were either unsensitized or had low *U*-center concentrations. The range of electrons was greatest in KCl, slightly less in NaCl, and least in KBr, as expected from their relative densities.

The irradiations of KBr+KH by deuterons produced a very high color density in the first few mils of salt,

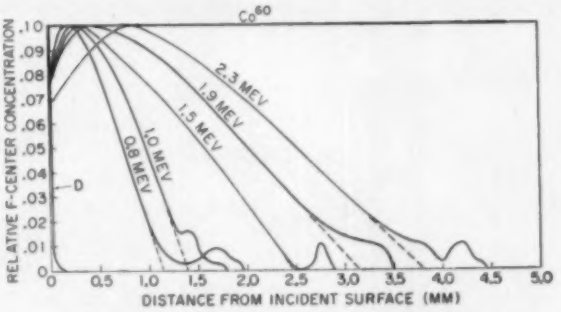

FIG. 6. Influence of particle type and energy on the specific ionization in KBr+KH.

and some lighter coloring which was probably on account of recoil electrons or x rays deeper in the crystal (Fig. 6). The specific ionization produced by deuterons was estimated from visual observations on the crystal with a microscope. The color distribution appeared to be similar to that of crystals with a saturation dose of electrons, except that the penetration was approximately two orders of magnitude less.

The range of deuterons in KBr+KH, as measured with a microscope equipped with a reticule eyepiece, was approximately 0.002 cm for 1.2-Mev energy. In addition to the volume inside this range in which most of the coloring occurred, there was a lightly colored region which extended out to approximately 0.01 cm.

The optical densities of the Co^{60}-irradiated samples were measured in the microdensitometer, and showed no difference in intensity throughout the 1-cm thickness of crystals.

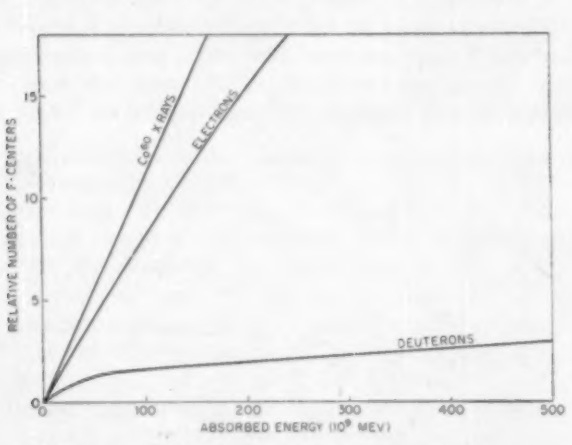

FIG. 5. Comparison of *F*-center yields using gamma rays, electrons, and deuterons to convert *U* centers to *F* centers in KBr+KH.

DISCUSSION AND CONCLUSIONS

The reactions relevant to the measurements of yield, specific ionization, and range will be discussed in terms

of the Seitz synthesis of crystal imperfections.[4] For convenience, the resident and transient imperfections are divided into four groups:

1. phonons, excitons, free electrons, and holes
2. vacancies, dislocations, and foreign atoms
3. photons and charged particles
4. reaction products resulting from combinations of of the foregoing; e.g., U centers are type 2, and F centers are type 4.

When a crystal is exposed to ionizing radiations, the initial reactions occur primarily between transient, type-3 defects and normal ions of the crystal. Since U centers and other type-2 imperfections account for only 10^{-4} to 10^{-6} of the total number of available lattice sites, the probability of their direct ionization or excitation by transient defects is small. Consequently, the initial effect of ionization is the production of type-1 defects. To obtain efficient activation of U centers and other sensitizing centers, energy must be transferred from the host crystal to these centers. The type-1 defects perform this function. A multiplicity of

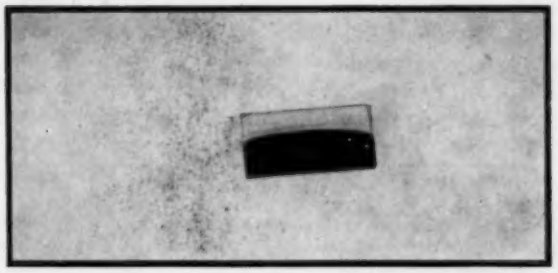

FIG. 7. Photograph of the central section from a KCl crystal after bombardment with 2-Mev electrons. The anomalous coloring at the end of the maximum electron range is apparent.

reactions are possible between the type-1 defects and other crystal constituents; therefore, the absorbed energy may be dissipated in a variety of products: e.g., a hole may be annihilated by a free electron; it may react with a U center to liberate a hydrogen atom and form an F center; it may be captured by a vacancy to form a V center.

Obviously, the type and concentration of resident defects have a strong influence on the efficiency of color-center formation, and are responsible for much of the divergence in the published yield values. The defect population also changes during irradiation, leading to a reduction in the F-center yield with increasing dose, as illustrated in Figs. 2–5. In pure crystals the hole population increases as the vacancies are filled to produce F centers. This change in concentration favors the back reaction, e+hole → normal ion, and leads to saturation. The $U \rightarrow F$-center reaction offers a twofold advantage in avoiding this difficulty. First, the initial population of U centers can be regulated and established at concentrations at least 10 times larger than the competing type-2 defects. Second, the competition from the radiation products is reduced, since the hydrogen atom liberated during the reaction apparently moves to an interstitial lattice position and shows relatively little affinity for the free electrons.[5]

When the U-center concentration is above 10^{17} per cc, the $U \rightarrow F$ reaction predominates under irradiation, and the yield remains constant at exposures well above the minimum for detectability. Of the results reported here, the yield values for KBr+KH are most reliable because these crystals contained high, uniform U-center concentrations. The value of 35 ev per F center obtained with 1.2 Mev electrons is the same as the results Martienssen and Pick[6] obtained with low-energy x rays (see Table I). The difference (Fig. 5) between this value and the value of 26 ev per F center obtained with Co^{60} gamma rays can be explained in part by the approximations made in the energy-loss calculations. The only factor neglected in the electron determinations was the bremsstrahlung loss, which would make the 35-ev value about 4% higher than the true value. For this reason the electron results are much more reliable than the Co^{60} determinations. If the minimum energy for the $U \rightarrow F$ reaction in KBr+KH is 5.4 ev, the efficiency of F-center formation is about 15%.

The pure and mixed crystals of Figs. 2–4 show the influence of competing reactions. Saturation of F-center production has commenced by the time sufficient centers are present for reliable measurements. Presumably, the first F centers are formed with efficiencies approaching those observed in the $U \rightarrow F$ reaction, but by the time a detectable concentration has been produced (10^{15} per cc), the energy expenditure per F center has risen to over 100 ev.

During the interval between the initial reporting of the material on specific ionization and range measurements and their inclusion in this paper, other crystals and glasses have been suggested and used to determine the energy and distribution of accelerator beams.[7,8]

If the color-center distribution is to convey a true picture of the specific ionization, a change in yield efficiency resulting from saturation must be avoided. With heavy particles such as deuterons, the high specific ionization and short range lead to saturation before measurable numbers of F centers are produced. Even with electrons, portions of pure crystals may be easily saturated. Figure 8 shows the apparent change in the specific ionization pattern in a pure KCl crystal as saturation develops. Saturation flattens the peak and extends the detectable range slightly. Crystals contain-

[4] F. Seitz, *Imperfections in Nearly Perfect Crystals*, edited by W. Shockley, Chairman (John Wiley & Sons, Inc., New York, and Chapman and Hall, Ltd., London, England, 1952).

[5] C. J. Delbecq, B. Smaller, and P. H. Yuster, Phys. Rev. **104**, 599 (1956).

[6] W. Martienssen, and H. Pick, Z. Physik **135**, 309 (1953).

[7] R. S. Alger and R. D. Jordan, Phys. Rev. **98**, 1550 (A) (1955).

[8] C. J. Delbecq *et al.*, Rev. Sci. Instr. **26**, 543 (1955).

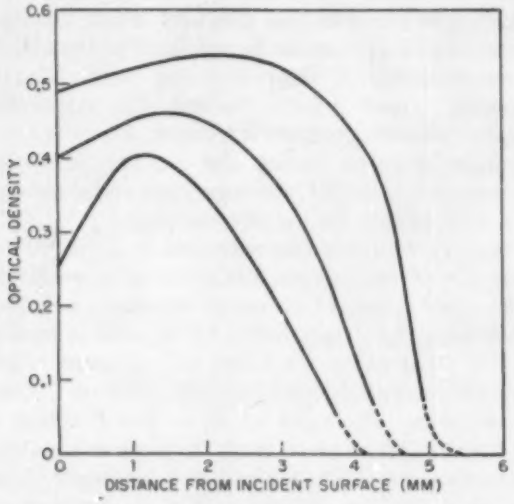

FIG. 8. Effect of *F*-center saturation on the specific ionization pattern and the observable range.

ing *U* centers, such as KBr+KH, are superior for specific ionization measurements because they offer more sensitivity and latitude before saturation commences. The specific ionization curves in Fig. 6 obtained with KBr+KH appear to be free from saturation.

The extrapolated ranges obtained from curves such as those in Fig. 6 were found to be in good agreement with values calculated by the Feather rule as modified by Glendenin and Coryell for the range between 0.8 and 2.3 Mev. Figure 9 compares the calculated electron ranges, which give linear plots, with experimental points obtained from extrapolated ranges. KBr+KH shows the least dispersion in the experimental points, which was due to the use of exposures below the saturation level in all cases. Owing to the low sensitivities of NaCl and KCl, various degrees of saturation were permitted in these crystals, and there is a large spread in the observed penetrations. Figure 9 illustrates the effect of saturation on range, and the necessity of proper exposures to obtain reproducible results.

The tails observed in Figs. 6 and 7 are not normally encountered in conventional measurements of electron penetration or range; however, it should be possible to explain their presence in terms of the four types of defects. Two general possibilities will be considered here. First, there is the "pleochroic halo" approach. The appearance of the tails is similar to the halos which surround alpha-emitting radioactive particles in natural crystals, although the magnitudes are quite different. One of the theories proposed to explain these rings is based on sensitization and desensitization of various regions of the crystals by mechanical strains induced by the radiation.[2] In the case of the halos, the distortion in the lattice presumably develops because of accumulated helium from the alpha particles. Crystals also expand when irradiated, because of the increase in vacancy population caused by high-energy radiations. Since only parts of the crystal sample color under electron irradiation, an inhomogeneous expansion takes place. This nonuniform distortion should produce regions which are stressed to various degrees and hence have different coloring sensitivities.

Second, there is the Lichtenberg pattern approach. When high-energy electrons are shot into an insulating medium, they become trapped and form a space charge. Although electrons may be expected to be trapped throughout the colored volume of the crystal, the evidence from Lichtenberg patterns in plastics such as lucite and polystyrene indicates that a substantial charge is deposited just short of the extrapolated range. The electric field resulting from this space charge can become very large, and is limited only by the insulating

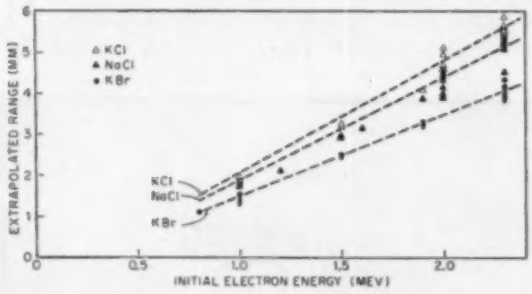

FIG. 9. Comparison of measured electron ranges to range-versus-energy curves computed by the Feather rule as modified by Glendenin and Coryell.

properties of the dielectric and the energy of the incident electrons. The electrical breakdown which generates the Lichtenberg pattern is evidence of the high field produced. Such a field would repel secondary electrons and cause them to move toward the anode or back surface of the crystal. *F* centers excited by appropriate illumination are quite mobile in an electric field. Presumably, suitable electrostatic forces could extend the colored regions of the crystal and hence produce the observed tails.

The supporting evidence casts doubt on the halo mechanism, and provides no obvious objections to the Lichtenberg approach. Tails were observed in crystals containing substantial *U*-center concentrations where it would be expected that the $U \rightarrow F$-center reaction should predominate by an order of magnitude over other reactions involving resident defects. This should be particularly true near the end of the electron range where the *F*-center concentration is low.

Influence of Transverse Modes on Photoconductive Decay in Filaments

J. S. Blakemore and K. C. Nomura
Honeywell Research Center, Hopkins, Minnesota

(Received April 13, 1959)

The roles of high order modes are discussed for the decay of excess carriers in a semiconducting filament. A general solution is given for the strength of the various modes when excess generation (i.e., illumination) is any function of time and space. Solutions for several specific cases are illustrated in graphical and tabular form. It is well known from the discussions of Shockley and of Stevenson and Keyes that odd-numbered modes can augment the surface recombination of the fundamental mode: the present calculations show that for typical generative procedures this increased recombination is considerably more serious than has been generally supposed. The role is noted of even numbered (antisymmetric) modes, which contribute nothing to filament photoconductance, but which arise under antisymmetric generation conditions to describe transverse diffusion (and usually to disturb the relative amplitudes of the odd modes). Attention is drawn to the fact that some odd modes can have a *generative* behavior when carrier creation is a suitable function of position. This is turned to advantage in suggesting how lifetime may be measured in a filament with minimum interference from the surface.

I. INTRODUCTION

When excess current carriers are created in a semiconducting filament they immediately start to decay, through recombination in the bulk and on the surface. Shockley[1] showed that the situation can always be described as a superposition of excess carrier modes, whose wave numbers are related to the sample dimensions. He pointed out that the decay rate of a mode depends on its wave numbers, but was preoccupied mainly with the fundamental mode (smallest wave numbers) since this decays less rapidly than any of the others.

Stevenson and Keyes[2] discussed the influence of various modes at some length, but they left an impression that high order modes serve only to speed up recombination in the early stages of decay. While this is their most obvious function, we intend to show in the following pages how these modes can also express tendencies for transverse diffusion and even surface generation.[3]

We use the method of Green's functions to obtain a general solution for excess carrier modes when the generation rate is an arbitrary function $g=g_0\sigma(x_0,y_0,z_0)s(t_0)$ of space and time. In order to make the partial differential equation of continuity linear, and hence solvable analytically, we assume that the semiconductor is isotropic and uniform (i.e., the thermal carrier densities n_0 and p_0 and the bulk recombination rate ν_b are everywhere the same). We further assume that no trapping occurs, and that ν_b is not dependent on the local excess carrier density $n_1=(n-n_0)=(p-p_0)$.

The general solutions may be expressed in terms of any set of separable coordinates. Our emphasis is not so much on the geometry of the *sample* (as has been the case in the discussions of Stevenson and Keyes,[2] McKelvey,[4] and Sim[5]) but rather on the importance of the initial *carrier* distribution within a sample. The relative importance of bulk and surface properties depends in a marked fashion on the initial spatial distribution.

To demonstrate these ideas, it is both convenient and practical to use Cartesian coordinates and to treat the problems of a filamentary sample which is a rectangular parallelepiped, bounded in length by the planes $x=0$, $x=2A$; in width by $y=0$, $y=2B$; and in thickness by $z=0$, $z=2C$. It is quite possible to solve the problem for any longitudinal electrical field, but this is an almost unnecessary complication. The solutions of greatest interest are those which hold when the electric field is small[2] so that carrier migration occurs by diffusion alone (with diffusion constant D). This then is the case we shall treat.

II. SPACE-TIME CARRIER DISTRIBUTION

In the presence of an excess generation rate g, excess carriers tend to diffuse and suffer bulk recombination subject to a continuity equation,

$$\partial n_1/\partial t = g - (1/q)\,\mathrm{div}\mathbf{I} - n_1\nu_b. \tag{1}$$

We may choose to describe the boundary conditions in terms of a surface recombination velocity $\mathbf{s}(x,y,z,t)$; then at the various faces,

$$\mathbf{I} = q\mathbf{s}n_1. \tag{2}$$

Suppose the initial condition is that $n_1=0$ at $t=0$. Then, subject to the conditions discussed in Sec. I, the solution of (1) in terms of a Green's function is

$$n_1=\int_0^t\int_0^{2C}\int_0^{2B}\int_0^{2A} g(x_0,y_0,z_0,t_0) \times G(x,y,z,t\,|\,x_0,y_0,z_0,t_0)\,dx_0dy_0dz_0dt_0, \tag{3}$$

[1] W. Shockley, *Electrons and Holes in Semiconductors* (D. Van Nostrand Company, Inc., Princeton, New Jersey, 1950).
[2] D. T. Stevenson and R. J. Keyes, J. Appl. Phys. **26**, 190 (1955).
[3] J. S. Blakemore and K. C. Nomura, Bull. Am. Phys. Soc. Ser. II, **4**, 179 (1959).
[4] J. P. McKelvey, IRE Trans. on Electron Devices **ED-5**, 260 (1958).
[5] A. C. Sim, J. Electronics and Control **5**, 251 (1958).

where

$$G=\frac{1}{ABC}\sum_{ijk}\omega_i(x)\omega_i(x_0)\omega_j(y)\omega_j(y_0)\omega_k(z)\omega_k(z_0)\times\exp\left\{(t_0-t)\left[\nu_b+\frac{D}{4}\left(\frac{\xi_i^2}{A^2}+\frac{\eta_j^2}{B^2}+\frac{\zeta_k^2}{C^2}\right)\right]\right\}. \quad (4)$$

The ω's and ξ_i, η_j, ζ_k are respectively the eigenfunctions and eigenvalues of the homogeneous part of Eq. (1). A full treatment of this kind of problem is given by Morse and Feshbach[6]; general solutions are not unduly difficult analytically, but are computational very laborious. This complexity arises largely from the non-simple relationships of mode wave numbers in the general case. Fortunately, the most important case (that of large s) happens also to be the simplest. Situations of large recombination velocity are important in that many experimental situations involve polished, ground, sandblasted or numerous kinds of etched surfaces for which $s\gg1000$ cm/sec. It is interesting to note that while such surfaces are easy to prepare the eigenvalues are insensitive to variations in the procedure provided that s remains very large.[1] For $s\rightarrow\infty$ the relative mode wave numbers become a series of integers and the eigenfunctions reduce to sine functions.

In order to further clarify the issues, we shall, for the remainder of this paper, quote the solution for a two-dimensional problem, neglecting variations of n_1 in the x direction. This is certainly justifiable for a reasonably long filament which is uniformly illuminated over a region long compared with lateral dimensions. For the two-dimensional case with $s=\infty$, Eq. (3) becomes

$$n_1=\frac{1}{BC}\exp[-\nu_b t]\sum_{jk}\gamma_{jk}\times\exp[-\nu_{jk}t]\sin\left(\frac{j\pi y}{2B}\right)\sin\left(\frac{k\pi z}{2C}\right), \quad (5)$$

where we use the conventional notation

$$\nu_{jk}=\frac{\pi^2 D}{4}\left[\frac{j^2}{B^2}+\frac{k^2}{C^2}\right], \quad (6)$$

to signify the surface recombination rate of the jk mode.

For the kind of problem we shall concern ourselves with, the time-dependent Fourier coefficient γ_{jk} can be written as a product of time and space integrals[7]

$$\gamma_{jk}=\left\{\int_0^t s(t_0)\exp[t_0(\nu_b+\nu_{jk})]dt_0\right\}\times\left\{\int_0^{2B}\int_0^{2C} g_0 r(y_0,z_0)\times\sin(j\pi y_0/2B)\sin(k\pi z_0/2C)dy_0dz_0\right\}. \quad (7)$$

[6] P. M. Morse and H. Feshbach, *Methods of Theoretical Physics* (McGraw-Hill Book Company, Inc., New York, 1953).

[7] Obviously, if the space and time coordinates are related (as they are in the case of a flying spot scanner), then γ_{jk} must be treated as a triple integral.

The relative importance of a given mode depends on a number of factors, including time. When generation ceases, the distribution of n_1 as a function of y and z does not decay uniformly as time progresses since the modes of high order are attenuated rapidly through the action of a large ν_{jk}. Eventually, the 11 mode ($j=1$, $k=1$) retains more influence than all the others.

When generation occurs during a very brief period only, the initial relative amplitudes of modes are controlled exclusively by the spatial distribution function $g_0 r(y,z)$. But if generation proceeds at a uniform rate for a finite period t^*, it can readily be seen from (7) and (5) that the relative amplitudes of the modes as they start their decay are modified by factors $(\nu_b+\nu_{jk})^{-1}\{1-\exp[-t^*(\nu_b+\nu_{jk})]\}$, which serve to attenuate the high order modes of large ν_{jk}. It is worth noting this since for the most part we shall be considering examples involving generation at a uniform rate followed by an abrupt cutoff at t^*.

The importance of various types of modes, and how these are created by the function $r(y,z)$ is best discussed in relation to the macroscopic properties of a filament, a topic we pursue in the next section.

III. FILAMENT PHOTOCONDUCTANCE AND THE EFFECTS OF VARIOUS KINDS OF MODES

When a semiconducting filament experiences temporary excess generation, the most obvious change in the observable filament properties is an increase in total conductance. This is a measure of the total number of excess carriers per unit length, which we may denote

$$N(t)=\int_0^{2B}\int_0^{2C} n_1 dydz. \quad (8)$$

There is a convenient way we can express $N(t)$ during decay if the generative process is such that $g=0$ at all times later than t^*. From (7) and (5), we can see that in such a case

$$N(t)=\frac{16}{\pi^2}\exp[-\nu_b(t-t^*)]\times\sum_{jk}\sin^2\left(\frac{j\pi}{2}\right)\sin^2\left(\frac{k\pi}{2}\right)\Gamma_{jk}(t), \quad t>t^*, \quad (9)$$

where

$$\Gamma_{jk}(t)=\frac{\gamma_{jk}}{jk}\exp[-(\nu_{jk}t+\nu_b t^*)], \quad t>t^*. \quad (10)$$

This quantity $\Gamma_{jk}(t)$, which may at first seem a little elusive, forms a very useful part of the notation for discussion of surface recombination, as will be developed shortly.

Now we are discussing a filament in which there was definitely an excess of carriers at $t=t^*$; then $N(t)$ must clearly decline as time goes on. It does not follow, however, that every mode which was initially present will assist in the recombination.

First, we should mention the bizarre modes for which j or k (or both) are even; these can perform no recombination since the presence of $\sin^2(j\pi/2)$ and $\sin^2(k\pi/2)$ in Eq. (8) ensures that the contribution of such modes to $N(t)$ is zero at all times. Stevenson and Keyes remarked on this and did not discuss even modes any further. Yet they merit some brief attention for they have a function to perform.

The amplitude (as well as the integral) of each even mode is zero when the pattern of generation is symmetrical with respect to the center of the filament. But when more carriers are created in one half of the cross-section than the other, antisymmetrical even numbered modes must be invoked *as well as* odd numbered modes. The influence of the even modes is crudely that of diffusion within the filament, trying to make the distribution more nearly symmetrical. When a given number of carriers is distributed in a nonsymmetrical manner, the decay scheme is liable to be different from that of a uniform distribution, since even modes must be used *and* the amplitudes of some recombinative odd modes adjusted accordingly. Section IV provides illustrations of this.

At any rate, so far as filament photoconductance is concerned, only the odd modes need be considered, or

$$N(t)=\frac{16}{\pi^2}\exp[-\nu_b(t-t^*)]\sum_{\text{odd } j,k}\Gamma_{jk}(t),\quad t>t^*. \tag{11}$$

It is evident that when j and k are both odd, the contribution of the jk mode to photoconductance can be nonzero, and is then a quantity which decays with time. But a given mode has a recombinative effect only if $\Gamma_{jk}>0$, which is dependent on the spatial dependence of the generation function.

For many distributions of generation in space (including that of complete uniformity), all odd modes have positive γ_{jk} and every such mode assists in recombination. On the other hand, there are ways $g_0\sigma(y,z)$ can be distributed to produce a superposition of some odd modes (including the lowest) with positive γ_{jk} and others with *negative* coefficients. Then surface recombination by some modes is at least partially compensated by *surface generation* of the others.

This occurs for instance when generation is produced with light which is restricted to a central strip of the filament's front face.[8] Since excess carriers are not created near the side faces, no recombination can occur there at first. Eventually, some carriers will diffuse out to these surfaces, but by this time the diffusion front will be quite gradual, characteristic mainly of the lowest mode. The lessened importance of surface recombination in the early stages is described in mode terms as a compensation of *recombinative* by *generative* modes.

The decay of $N(t)$ is not a simple exponential, yet it can be decomposed into the sum of the bulk recombination rate ν_b and a surface recombination rate $\nu_s(t)$ which changes with the progression of the decay,

$$-d/dt[\ln N(t)]=\nu_b+\nu_s(t)$$
$$=\nu_b-\frac{\sum_{jk\text{ odd}}[d\Gamma_{jk}(t)/dt]}{\sum_{jk\text{ odd}}\Gamma_{jk}(t)}, \tag{12}$$

or

$$\nu_s(t)=-\left\{\frac{\sum_{jk\text{ odd}}[d\Gamma_{jk}(t)/dt]}{\sum_{jk\text{ odd}}\Gamma_{jk}(t)}\right\}\quad\text{for}\quad t>t^*. \tag{13}$$

At times sufficiently removed from t^*, $\nu_s(t)$ will reduce to ν_{11}, but in the earlier stages of decay it will usually be strongly influenced by the higher modes.

Note that $\nu_s(t)$ is the logarithmic decrement of a quantity we may write as

$$F(t)=\frac{\sum_{jk\text{ odd}}\Gamma_{jk}(t)}{\sum_{jk\text{ odd}}\Gamma_{jk}(t^*)}. \tag{14}$$

This is the fraction of the excess population existent at time t^* which have been spared by surface recombination up to the time t. In treating the various numerical cases and considering the effects of changing dimensions, spatial distribution and the time dependence of generation, the most useful quantities to follow are often $F(t)$ and its decay rate $\nu_s(t)$.

IV. DECAY PATTERNS FOR TYPICAL TRANSVERSE DISTRIBUTIONS

The influence of the surface during the decay process in a filament is controlled by a whole series of variables, and the examples of this section can only touch on a few of the most typical configurations. However, these examples do demonstrate phenomena which will occur to a greater or lesser extent in any experimental arrangement. Awareness of their importance should help in making more meaningful measurements of a quantity such as bulk recombination rate ν_b from observations of photoconductive decay.

It is not a particularly arduous matter to calculate the form of decay for any cross-sectional geometry, but there are certain advantages in making calculations for a sample of square cross section. Thus, the surface decay rate of the fundamental mode is $\nu_{11}=\pi^2D/2C^2$ while for any higher mode, $\nu_{jk}=\frac{1}{2}(j^2+k^2)\nu_{11}$ and $[d\Gamma_{jk}(t)/dt]=-\frac{1}{2}(j^2+k^2)\Gamma_{jk}(t)$. In order to take advantage of these simplifications, we suppose a square geometry in the following examples. In every case, it is evident what changes in behavior would occur for a different geometry.

[8] As previously recommended for measurements on silicon, J. S. Blakemore, Phys. Rev. **110**, 1301 (1958).

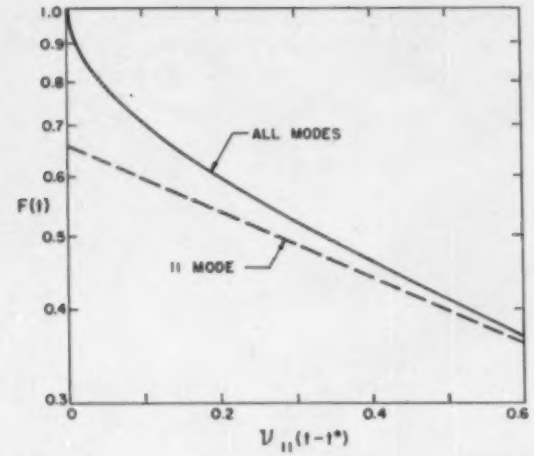

FIG. 1. Progression of $F(t)$ with time following a delta function pulse of generation which is uniform through the filament. (The data for this and all subsequent figures and tables are calculated for a filament with square cross section.)

1. Spatially Uniform Generation

Experimental results are often interpreted as though the generation rate were the same throughout a specimen cross section. Such an assumption is usually not justified, since uniform generation is an ideal which can be but imperfectly approached. Thus if light is supposed incident on the face $z=0$, the rate g will decrease with increasing z if the light has an appreciable absorption coefficient. A monochromator or filter may be used to present only those spectral components with very small absorption coefficients, but if the filtering action is sufficiently efficient to eliminate all nonpenetrating light there are no photons left capable of inducing a photoconductive signal! In the usual compromise, a filter of moderate thickness is used[8]: this passes a fair proportion of the semi-penetrating wavelengths to make g a slowly varying function of z. Aside from this question of whether strictly uniform generation is possible, it is a useful case for us to explore first.

The series of Fourier coefficients which makes $r(y,z)$ constant over a cross section is well known; the even modes all vanish and the odd modes have positive coefficients,

$$\gamma_{jk}=\frac{16BCg_0}{\pi^2 jk}\sin^2\left(\frac{j\pi}{2}\right)\sin^2\left(\frac{k\pi}{2}\right)\times\int_0^t s(t_0)\exp[t_0(\nu_b+\nu_{jk})]dt_0, \quad \text{for all } t. \quad (15)$$

The corresponding filament modes have coefficients which depend on the form of generation as a function of time. We shall consider the consequences for two important limiting cases.

When the generative procedure consists of a very short but very intense pulse, $s(t_0)=\delta(t-t_0)$, then the various coefficients of the filament modes which decay are (for odd jk, of course)

$$\Gamma_{jk}(t)=\frac{16BCg_0}{\pi^2 j^2k^2}\exp[-\nu_{jk}(t-t^*)], \quad t>t^*\sim 0. \quad (16)$$

$F(t)$ and $\nu_s(t)$ for this case then become

$$F(t)=\frac{64}{\pi^4}\left\{\sum_{\text{odd } jk}\left(\frac{1}{k^2}\right)\exp[\tfrac{1}{2}k^2\nu_{11}(t^*-t)]\right\}^2, \quad t>t^*, \quad (17)$$

and

$$\nu_s(t)=\nu_{11}\left\{\frac{\sum_{\text{odd } jk}\exp[\tfrac{1}{2}k^2\nu_{11}(t^*-t)]}{\sum_{\text{odd } jk}(1/k^2)\exp[\tfrac{1}{2}k^2\nu_{11}(t^*-t)]}\right\}, \quad t>t^*, \quad (18)$$

with a filament of square cross section. The decay of $F(t)$ (and of the portion contributed by the lowest mode) for this configuration is shown in Fig. 1; while Fig. 2 displays the progression of the rate constant ν_s over the same time range. We use ν_{11} to normalize the scales. To give some sense of perspective, we might remark that with a filament of N-type germanium 0.5 cm $\times$0.5 cm, $\nu_{11}\sim 3600$ sec^{-1} and the time range covered in Figs. 1 and 2 is about 170 μsec.

As expected all along, a considerable time has to elapse before the surface decay rate can be fairly approximated to ν_{11}. This is important when an attempt is made to deduce the bulk recombination rate ν_b from the slope of photoconductive decay. A compromise must usually be struck between the requirements of letting high order modes die out, yet making the measurement before the signal voltage becomes too small.

In the usual accomplishment of this compromise, the total decay rate is measured as soon as the signal drops to a given fraction $N(t)/N(t^*)$ of its peak value,[9] and is

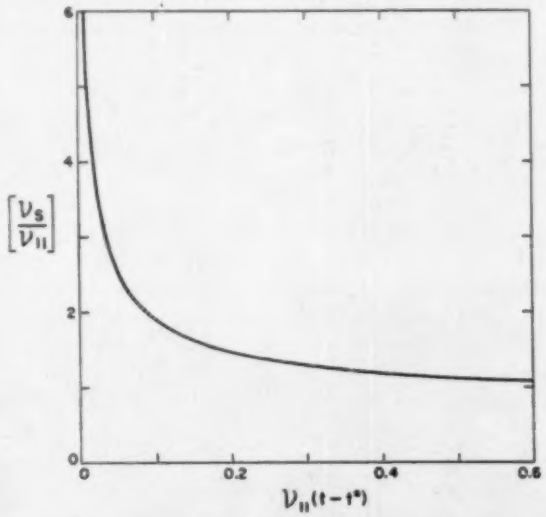

FIG. 2. Variation of ν_s with time for the decay of Fig. 1.

[9] This fraction can of course equally well be written as $F(t)\exp[-\nu_b(t-t^*)]$; it diminishes at a rate set by both surface and bulk recombination.

supposed equal to the sum of ν_{11} and a quantity we shall call ν_m. Unless the decay has gone on for a considerable time prior to the moment of the measurement, ν_s will be larger than ν_{11} and ν_m will differ from the true bulk recombination rate,

$$\nu_m=\nu_b+(\nu_s-\nu_{11}). \tag{19}$$

It is not generally recognized that the measured ν_m is liable to differ from ν_b whether bulk processes are relatively slow or not. For a filament composed of material with a small ν_b, it is obviously necessary to wait until decay is far advanced before making a measurement, since *any* interference from high order surface modes will cause a serious discrepancy between ν_m and the true ν_b. But the problem is still serious when ν_b is many times larger than ν_{11}. For then the signal voltage becomes small compared with its peak value at a time when high order modes still comprise an important part of the total surface effort.

This point is amply demonstrated by the data of Table I, which enumerates the percentage error in a measurement of ν_b for square filaments at various stages of decay from a brief period of uniform generation. Four possible values are chosen for the ratio of bulk recombination rate ν_b to the minimum surface rate ν_{11}. [A high value for (ν_b/ν_{11}) is indicative of a large filament cross section and/or of material containing many active recombination centers.] The possible errors are monstrously large for measurements made in the early stages of decay when (ν_b/ν_{11}) is small; and even if $(\nu_b/\nu_{11})\gg 1$, quite undesirably large errors will be made if measurements are made too early in the decay.

Some rather surprising figures in Table I are those in the column for measurements made at $N(t)/N(t^*)=0.10$. Interference from high order modes is then very slight even when (ν_b/ν_{11}) is quite small.[10] This column also brings out the point that the change in error with falling (ν_b/ν_{11}) is not a monotonically increasing function when measurements are made late in the decay.

TABLE I. The error involved in a measurement of bulk recombination rate if it is assumed that the surface rate is only ν_{11} when the photoconductance has dropped to a given fraction of its peak value. For a filament of square cross section, when generation is very brief and spatially uniform.

Ratio of bulk rate to the surface rate of the fundamental mode (ν_b/ν_{11})	Percentage error in measurement of bulk rate $100[(\nu_m/\nu_b)-1]\%$ Measured when $N(t)/N(t^*)=0.75$	Measured when $N(t)/N(t^*)=0.50$	Measured when $N(t)/N(t^*)=0.25$	Measured when $N(t)/N(t^*)=0.10$
0.1	1250%	270%	27%	1.0%
1.0	160%	50%	12%	2.1%
10	33%	17%	8.9%	5.3%
100	9.5%	5.6%	3.8%	2.7%

[10] Not that we would recommend attempting to deduce ν_b from a measurement of $(\nu_b+\nu_s)$ in a filament, where ν_b/ν_{11} is smaller than unity. High order modes may not cause error if the measurement is sufficiently delayed, but any uncertainty in dimensions or diffusion constant would jeopardize the possibility of expressing ν_{11} itself with the required accuracy.

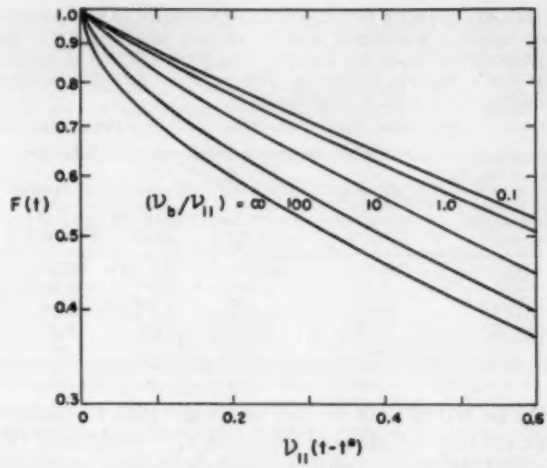

FIG. 3. Decay of $F(t)$ following a very long period of spatially uniform generation, for various ratios of ν_b to ν_{11}.

The tendency for error to show a maximum, then a minimum, then a continued rise as (ν_b/ν_{11}) goes to zero does not have an opportunity to develop when measurements are made in the early stages of decay; but it is a natural consequence of the way the measuring point shifts along the surface decay curve.

The preceding discussion has painted an alarming picture of the troubles which arise even with the use of penetrating illumination if all the generation occurs within an extremely short interval. But very few illumination sources satisfy these criteria in any case—most deliver their light over an appreciable interval of time. This can in fact be of some assistance if the generation rate is constant for some time and then ceases *very abruptly*.

When uniform generation goes on for a finite time, the carrier population and its Fourier modes build up and eventually saturate when the period becomes long compared to $(\nu_b+\nu_{11})^{-1}$. If generation now ceases abruptly at $t=t^*$, then during the course of decay $\Gamma_{jk}(t)$ becomes

$$\Gamma_{jk}(t)=\frac{16BCg_0}{\pi^2 j^2k^2}\left\{\frac{1-\exp[-t^*(\nu_b+\nu_{jk})]}{\nu_b+\nu_{jk}}\right\} \times\exp[-\nu_{jk}(t-t^*)],\quad t>t^*. \tag{20}$$

When t^* is now made very large, the first exponential term vanishes and the expressions for $F(t)$ and $\nu_s(t)$ become

$$F(t)=\left\{\frac{\sum_{\text{odd } jk}[1/j^2k^2(\nu_b+\nu_{jk})]\exp[-\nu_{jk}(t-t^*)]}{\sum_{\text{odd } jk}[1/j^2k^2(\nu_b+\nu_{jk})]}\right\}, \tag{21}$$

and

$$\nu_s(t)=\left\{\frac{\sum_{\text{odd } jk}[\nu_{jk}/j^2k^2(\nu_b+\nu_{jk})]\exp[-\nu_{jk}(t-t^*)]}{\sum_{\text{odd } jk}[1/j^2k^2(\nu_b+\nu_{jk})]\exp[-\nu_{jk}(t-t^*)]}\right\}. \tag{22}$$

TABLE II. The error involved in a measurement of bulk recombination rate if it is assumed that the surface rate is only ν_{11} when the photoconductance has dropped to a given fraction of its peak value. For a filament of square cross section, when generation is spatially uniform and of long duration.

Ratio of bulk rate to the surface rate of the fundamental mode (ν_b/ν_{11})	Percentage error in measurement of bulk rate $100[(\nu_m/\nu_b)-1]\%$			
	Measured when $N(t)/N(t^*)=0.75$	Measured when $N(t)/N(t^*)=0.50$	Measured when $N(t)/N(t^*)=0.25$	Measured when $N(t)/N(t^*)=0.10$
0.1	84%	26%	1.5%	0.05%
1.0	21%	8.8%	2.2%	0.36%
10	12%	8.2%	5.2%	3.3%
100	4.7%	3.6%	2.8%	2.2%

It will be noted that we can no longer plot a universal curve for the variation of $F(t)$ and $\nu_s(t)$ with $\nu_{11}(t-t^*)$ as we did for the case of very brief generation, since now the shapes of these curves depend also on ν_b. In Fig. 3, $F(t)$ has been plotted as a family of curves corresponding to different values of ν_b/ν_{11} ranging from 0.1 to 100. [The final curve indicated by $\nu_b/\nu_{11}=\infty$ is indentical with $F(t)$ of Fig. 1.] It is readily seen that when ν_b/ν_{11} is small, $F(t)$ consists almost entirely of the fundamental mode, even in the initial stages of decay. It will be surmised that measurements of ν_b should thus be liable to much less error than was the case for brief generation: a comparison of Tables I and II confirms this hypothesis. Physically, this means that when surface recombination dominates bulk recombination *during* the generative process, the carriers assume a distribution rather similar to that of the fundamental mode. High order modes are then needed only for small corrections.

However, when (ν_b/ν_{11}) is large, the spatial distribution of excess carriers tends to look like the spatial distribution of generation itself, irrespective of the duration t^*. From the tables, it will be noted that with large values of (ν_b/ν_{11}), a lengthy illuminating pulse does not permit much more accuracy in measurement of ν_b than does a short one.

2. Decay Following Exposure to Nonpenetrating Light

It can confidently be expected that if generation occurs mostly near one surface of the specimen, this surface will contribute vigorously to the ensuing decay. Such is the case if generation occurs with light which tends to be heavily absorbed in the semiconductor. We cannot hope to discuss every possibility, and confine our remarks to one type of generation pattern; that produced with monochromatic radiation of absorption coefficient α, incident on the $z=0$ face. Then,

$$g=g_0 s(t)\exp(-\alpha z). \tag{23}$$

Ridley[11] has discussed the transient photoconductance of a specimen which is infinite in both length and width, following exposure to light of this type. He too was concerned with the ability to measure bulk properties, but developed this mainly through an extension of DeVore's result[12] for the explicit dependence of photoconductance on absorption coefficient. Our main objectives here are a little different. For our usual rectangular filament, the generation procedure of (23) sets up excess carrier modes with Fourier coefficients,

$$\gamma_{jk}=-\frac{8BCg_0}{\pi^2 jk}\sin^2\left(\frac{j\pi}{2}\right)\left[\frac{1-\cos(k\pi)\exp(-2C\alpha)}{1+(2C\alpha/k\pi)^2}\right]$$
$$\times\int_0^t s(t_0)\exp[t_0(\nu_b+\nu_{jk})]dt_0, \quad \text{for all } t. \tag{24}$$

It will be noted that modes are now present for even values of k. Their presence indicates the tendency for carriers to diffuse in the direction of increasing z. These even modes do not, of course, contribute to the photoconductance of the filament [$\Gamma_{jk}(t)$ is still identically zero for all of them], but as a result of the antisymmetric generation procedure which brought the even modes into being, odd modes of high k are represented more strongly than they were for uniform generation [Eq. (15)]. Thus the fundamental mode describes only a small part of the excess carrier population when decay starts, and $\nu_s \gg \nu_{11}$ for a considerable time.

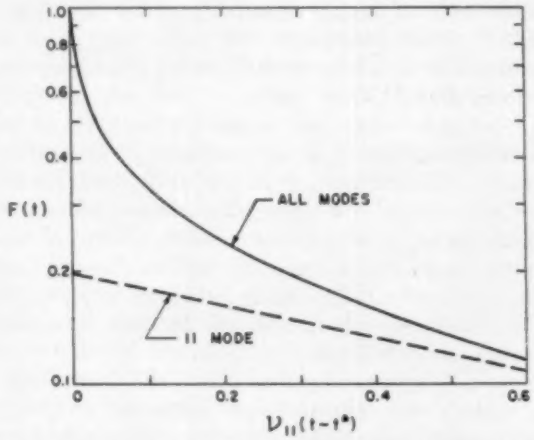

FIG. 4. Time dependence of $F(t)$ following illumination with a delta function pulse of light having an absorption coeff $\alpha=5\pi/2C$.

This is amply demonstrated by Figs. 4 and 5, showing the progression of $F(t)$ and $\nu_s(t)$ following a delta function pulse of moderately absorbing illumination. It was supposed for this calculation that $\alpha=(5\pi/2C)$ [corresponding with $\alpha\sim30$ cm^{-1} for a typical filament thickness of ~0.5 cm] and the influence of high order modes could easily have been made to appear much more formidable by choosing a larger value for α. No further evidence is needed that absorbing light (even with α as small as was supposed here) is highly unsuitable for a

[11] B. K. Ridley, J. Electronics and Control **5**, 549 (1958).

[12] H. B. DeVore, Phys. Rev. **102**, 86 (1956).

measurement of bulk recombination rate. Any attempt to do so will encounter errors of the magnitude listed in Table III. Even at quite a late stage of the decay the error cannot be reduced to an acceptable margin.

It might be imagined that a decay so heavily tainted with higher modes could never be mistaken for $\exp[-(\nu_b+\nu_{11})(t-t^*)]$; and that conditions involving serious error would always be recognized as such. That this is not necessarily so is illustrated in Fig. 6, where we

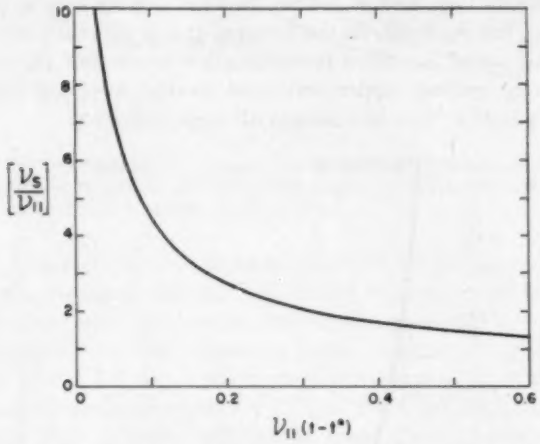

FIG. 5. Variation of ν_s with time for the decay of Fig. 4.

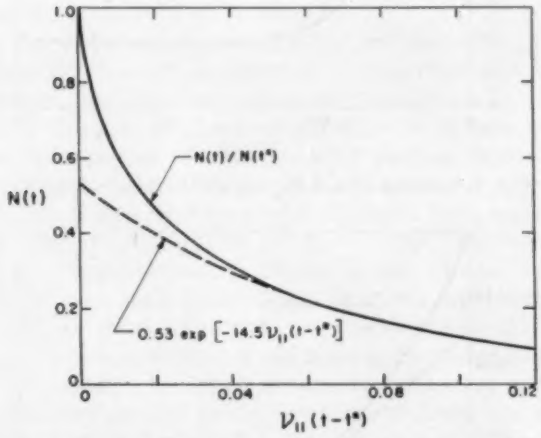

FIG. 6. How $N(t)$ diminishes when $F(t)$ is as described in Fig. 4 and the bulk recombination rate $\nu_b=10\nu_{11}$. The dashed curve shown for comparison is a pure exponential, but with a rate faster than $(\nu_b+\nu_{11})$.

have calculated the decay of $N(t)$ for a filament in which $\nu_b=10\nu_{11}$, if excitation occurs via a short pulse of non-penetrating light. Within normally acceptable limits of error, the decay for times beyond $(0.06/\nu_{11})$ is indistinguishable from that of an exponential with rate constant $14.5\nu_{11}$. Yet for this filament $(\nu_b+\nu_{11})=11\nu_{11}$, and an attempt to measure ν_b under the conditions shown would be in error by some 35%!

As with uniform generation, so with absorbing light also the high order modes are less strongly represented

TABLE III. The error involved in a measurement of bulk recombination rate if it is assumed that the surface rate is only ν_{11} when the photoconductance has dropped to a given fraction of its peak value. For a filament of square cross section following very brief generation by absorbing light whose absorption coefficient is $\alpha=(5\pi/2C)$.

Ratio of bulk rate to the surface rate of the fundamental mode (ν_b/ν_{11})	Percentage error in measurement of bulk rate $100[(\nu_m/\nu_b)-1]\%$ Measured when $N(t)/N(t^*)=0.50$	Measured when $N(t)/N(t^*)=0.25$	Measured when $N(t)/N(t^*)=0.10$
1.0	900%	250%	63%
10	130%	58%	30%
100	27%	17%	12%

if generation occurs over a finite period. Figure 7 shows that for a filament in which $\nu_b=10\nu_{11}$, the fundamental mode can be improved to account for some 33% of the initial signal if the illumination persists for a duration $(0.05/\nu_{11})$; and the remaining higher modes are not so heavily loaded with exceedingly fast constituents. This is not enough, however, to make such a form of light useful for bulk rate measurements. The error in attempting to measure ν_b is still 54% at $N(t)/N(t^*)=0.50$, 33% at 0.25 and 20% at 0.10; which is distinctly unfavorable compared with what can be achieved using a pulse of penetrating light, either long or short in duration.

3. Use of Penetrating Light with Specimen Masking

From the foregoing, it is evident that penetrating radiation is highly important in the measurement of bulk recombination rate from filament properties. The influence of high order modes on filament behavior can be further reduced by judicious masking of the specimen. We refer here not to masking of the regions adjacent to the end contacts (a precaution which is always advisable) but to the masking of strips extending the whole length of the front face[8] for some distance from the edges $y=0$, $y=2B$. The reason for such a

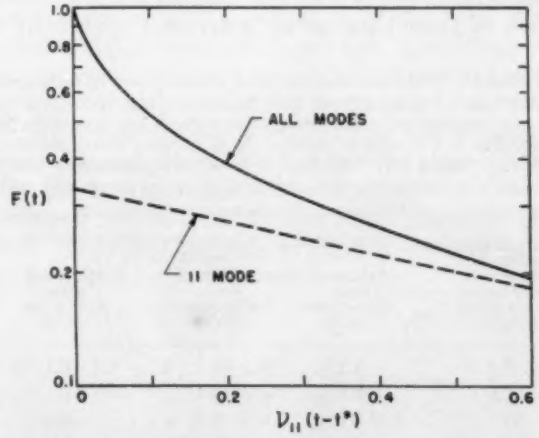

FIG. 7. The decay of $F(t)$ when absorbing light $(\alpha=5\pi/2C)$ is incident for a finite duration $t^*=0.05/\nu_{11}$. For $\nu_b=10\nu_{11}$.

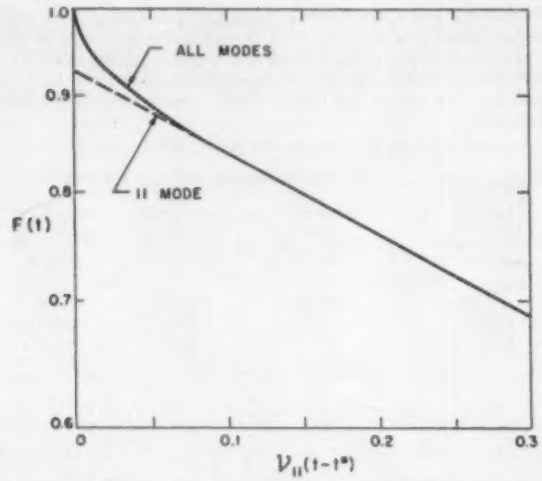

FIG. 8. Progression of $F(t)$ following a delta function pulse of generation which is uniform in depth but which is permitted to reach only the center half of the filament's width.

suggestion becomes apparent if it is noted that when

$$\left.\begin{aligned} &g=g_0 s(t_0), \quad (B-a)<y<(B+a), \\ &g=0, \quad \text{elsewhere} \end{aligned}\right\} \tag{25}$$

the various modes have coefficients

$$\gamma_{jk}=\frac{16BCg_0}{\pi^2 jk}\sin^2\left(\frac{k\pi}{2}\right)\sin\left(\frac{j\pi}{2}\right)\sin\left(\frac{j\pi a}{2B}\right)$$

$$\times\int_0^t s(t_0)\exp[t_0(\nu_b+\nu_{jk})]dt_0 \quad \text{for all } t. \tag{26}$$

We see from (26) that γ_{jk} may be either positive or negative. Modes for which $\gamma_{jk}<0$ are referred to as *generative* modes, since they have an effect on the filament photoconductance which becomes *less negative* as time goes by. When excess carriers have been created, the net photoconductance must of course be positive, but this is achieved through a partial cancellation of recombinative by generative modes. In the final result, the fundamental mode assumes a highly dominant position.

Aside from mathematical arguments, it is intuitively obvious that when carriers are created in a region which stops short of the side faces by a diffusion length or more, the decay will initially correspond with the form of that for a filament which has nonrecombinative side faces ($s=0$ for $y=0$, $2B$). For a filament like this, ν_s is half of that prescribed by Eq. (18). At later stages of the decay, the side faces begin to contribute to recombination, and of course the final surface rate is not $\frac{1}{2}\nu_{11}$, but ν_{11} itself. In the interim, it will generally dip a little below ν_{11}, when recombination at the side faces is barely getting under way and modes involving high values of k have lost almost all their influence.

TABLE IV. The error involved in a measurement of bulk recombination rate if it is assumed that the surface rate is only ν_{11} when the photoconductance has dropped to a given fraction of its peak value. For a filament of square cross section, when generation occurs through a very brief flash of penetrating radiation, which is permitted to reach only the central half of the specimen's width.

Ratio of bulk rate to the surface rate of the fundamental mode (ν_b/ν_{11})	Percentage error in measurement of bulk rate $100[(\nu_m/\nu_b)-1]\%$ Measured when $N(t)/N(t^*)=0.50$	Measured when $N(t)/N(t^*)=0.25$	Measured when $N(t)/N(t^*)=0.10$
0.1	−1.1%	$<\lvert-0.1\rvert\%$	$<\lvert-0.1\rvert\%$
1.0	−0.9%	$<\lvert-0.1\rvert\%$	$<\lvert-0.1\rvert\%$
10	+1.9%	$<\lvert-0.1\rvert\%$	−0.2%
100	+2.3%	+1.3%	+0.8%

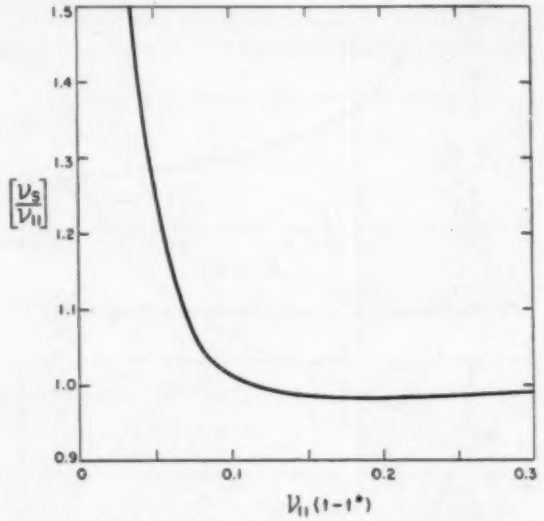

FIG. 9. Variation of ν_s with time for the decay of Fig. 8.

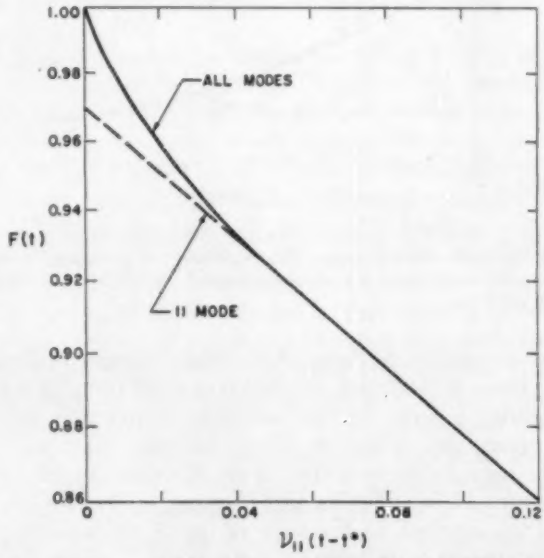

FIG. 10. Decay of $F(t)$ when penetrating light (restricted to the center half of the specimen's width) causes generation for a finite duration $t^*=0.05/\nu_{11}$. For $\nu_b=10\nu_{11}$.

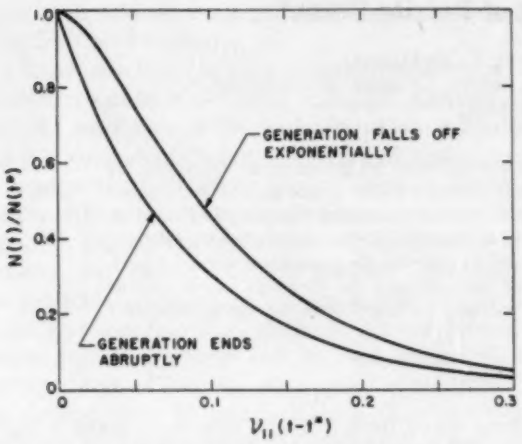

FIG. 11. Showing how the decay is modified when generation decreases at a finite rate following lengthy uniform illumination prior to t^*. For $\nu_b=10\nu_{11}$ and $\nu_g=30\nu_{11}$.

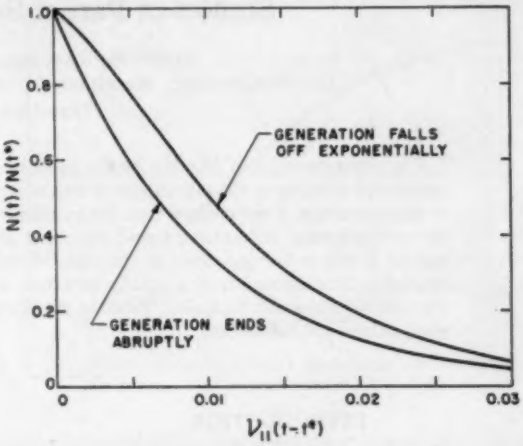

FIG. 12. Illustrating the same phenomenon as in Fig. 11, but for $\nu_b=100\nu_{11}$ and $\nu_g=300\nu_{11}$.

This behavior can be seen quite well for the numerical example illustrated by Figs. 8 and 9 for a square cross section, with the center half of the specimen's width exposed to a delta function pulse of penetrating light ($a=\frac{1}{2}B=\frac{1}{2}C$). Even at the start of the decay, the fundamental mode accounts for 92% of the total population, and $F(t)$ is indistinguishable from the fundamental after a short time. (It will be noted that both the vertical and horizontal scales in Fig. 8 are more expanded than previous figures.)

The effective decay rate ν_s is just half that of Eq. (18) up to $(t-t^*)\sim 0.07/\nu_{11}$, when $\nu_s\sim 1.1\nu_{11}$. From this time onward, the decay rate slackens more gradually than for a filament with nonrecombinative side faces, and gently increases towards ν_{11} after passing through a minimum of about $0.98\nu_{11}$. In mode terms, we can say of this example that for $a=\frac{1}{2}B$, all modes have negative γ_{jk} when $j=3, 5, 11, 13, 19, 21, \cdots$, etc. Thus, the 31 and 13 modes cancel, as do the 51 and 15 modes and many more such pairs. Apart from the fundamental itself, the most long-lived components are the 33, 53, and 35 modes, all three of which are generative in action.

Since ν_s approaches ν_{11} so soon after the decay begins, it becomes possible to measure filament decay rate with $N(t)/N(t^*)$ as large as 0.5 and still get a reliable value for ν_b from the data. Errors may now be either positive or negative, as shown in Table IV, but these are all small enough to be ignored compared with other sources of error in any experimental arrangement.

It is possible to make the fundamental mode even more dominant by illuminating for a finite interval, as illustrated by Fig. 10 for $t^*=0.05\nu_{11}$ when $\nu_b=10\nu_{11}$, but this is an almost superfluous refinement. Whether the illumination period be short or long, there seems every reason to believe that a filament photoconductance decay rate can be reliably associated with $(\nu_b+\nu_{11})$ if penetrating light is used in conjunction with the suggested masking procedure.

In making this statement, we of course imply that the experimental arrangement is free from other undesirable attributes, such as that discussed in 4.

4. Effect of Finite Tail to Generative Process

Up to this point, we have assumed in all our examples that generation ceases abruptly at $t=t^*$. When this is not so, and g decreases at a finite rate, it is evident that this rate will frustrate attempts to measure the fast decay of a semiconducting filament.

Figures 11 and 12 illustrate how the decay is retarded when a very lengthy period of uniform generation (uniform in both time and space) is followed by

$$g=g_0\exp[-\nu_g(t-t^*)], \quad t>t^*. \tag{27}$$

For the first example, bulk recombination is supposedly reasonably dominant ($\nu_b=10\nu_{11}$, $\nu_g=30\nu_{11}$) and in the second is highly dominant ($\nu_b=100\nu_{11}$, $\nu_g=300\nu_{11}$) over the fundamental surface rate, but in the two cases the distortion of the decay by a finite generative tail is roughly comparable. It is evident that any attempt to measure $(\nu_b+\nu_{11})$ from the decrement of photoconductance at any reasonable value of $N(t)/N(t^*)$ will be worthless. This is an important point to keep in mind when considering possible sources of error in photoconductive decay experiments.

Studies in Partial Switching of Ferrite Cores*

ROGER H. TANCRELL AND ROBERT E. MCMAHON
Lincoln Laboratory, Massachusetts Institute of Technology, Lexington, Massachusetts
(Received October 12, 1959)

The characteristics of Mg Mn ferrite cores in a partially switched state are investigated. Questions are considered relating to the percentage of flux switched at various locations within a core as well as the speed of this switching. Results show that the amplitude and duration of the set pulse has a pronounced effect on the core behavior. It has been found that most of the variation of the switching waveform among different regions is due to the geometry of the core. Models are proposed to describe the behavior observed experimentally. The operation of partially switched cores in a fast memory and the investigation of various memory schemes are discussed. Possible applications of the partially switched cores for digital computer applications are mentioned.

INTRODUCTION

THE reversal of magnetization of a ferrite core requires a finite time to go to completion, the duration of this time being dependent upon the amplitude of the driving field. If the driving field is removed before the core has had time to completely switch into saturation, a partially switched condition exists. It is the purpose of this work to investigate the properties of the cores as related to their partially switched characteristics.

The partial switching characteristics of cores have been utilized in a memory of cycle time less than one microsecond,[1] and the mode of operation of the cores in this memory is discussed in detail. Certain questions on partial switching can not be answered with simple observation of the switching of a memory core and special cores have been fabricated. A description is given of some possible applications of partially switched cores. These applications result from a better understanding of the relationship among the saturated states, partially switched states, and the reversible processes.

In this investigation the approach has been primarily experimental. The actual switching waveform of the core under different levels of driving field supplies a clue to the switching process within the core. Attempts have been made to formulate the data in a consistent manner by postulating models to represent the observed results, although such models are not necessarily based on basic physical considerations. It is hoped that these models will still represent the switching process when further data is taken in hitherto uninvestigated areas.

LINEAR SELECTION, PARTIAL SWITCHING CORE MEMORY

Ferrite cores have been investigated to study their fast switching characteristics as related to their use in a fast memory. One method of obtaining increased switching speed from a ferrite core is to apply a high-driving field. Also improvement in signal-to-noise ratio can be obtained at highdrive levels. The switching speed characteristic of a ferrite core of 30 mils-i.d. and 50-mils o.d. (RCA XF 3018H) has been carefully measured and is shown in Fig. 1. This core switches in 1.0 μsec under normal coincident-current drive of 500-ma full current. This switching characteristic curve is taken for the reset current equal in both amplitude and width to the read current. From the curve it can be seen that the switching speed of the core can be increased by a factor of 10 by increasing the driving current from 500 ma to 2.0 amp. A photo of the switching waveform for a read current of 500 ma is shown in Fig. 2 along with the noise output of the core disturbed by a write current of 377 ma. Note the high initial peak in the output due to the reversible component of magnetization which switches during the fast rise-time of the driving current. With a high read current of 1.32 amp, the output of the core for complete switching and that for the core when disturbed with the same current of 377 ma is shown in Fig. 3. A comparison of the two photos points out the improvement in signal-to-noise ratio for the cases of high and low read-out current. With the highdrive current, the noise peaks early in relation to the peaking of the signal but the peak of the signal has been increased over the low read-current case. The plot of Fig. 4 shows the improve-

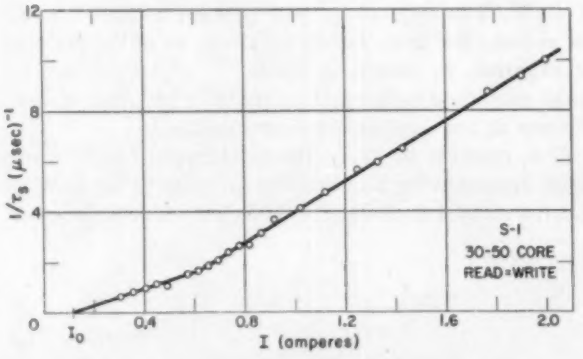

FIG. 1. Switching speed characteristic curve for core of 30–50 mil dimensions.

* The work reported in this paper was performed by Lincoln Laboratory, a center for research operated by Massachusetts Institute of Technology with the joint support of the U. S. Army, Navy, and Air Force.

[1] R. E. McMahon, *Solid-State Circuits Conference Digest* (February, 1959), pp. 16–17.

ment in signal-to-noise ratio that can be achieved by using high read currents.

A linear selection (or word selection) memory scheme provides a means of obtaining increased memory speed since the amplitude of the read current is not limited as it is in a coincident-current scheme, and a read current as large as desired can be used. The main limitations remain only with the available power and the driving circuitry. During the write time of the memory cycle, however, any memory scheme depends upon selecting one particular core out of the array and writing a bit of information into that core. A normal coincident-current selection scheme can be used where two half-currents (each of 250 ma) are applied in coincidence to the desired core to switch it into the "one" state. However, with this scheme the cycle time is not greatly improved since the write operation requires 1.0 μsec.

Two methods of increasing the speed of the write cycle will be discussed here. One method uses two narrow high-amplitude current pulses, one on the X selection line and one on the Y line, which occur at adjacent

FIG. 2. Read output of a saturated core and of a write disturbed core for $I_{read}=500$ ma. Rise-time of drive current is 30 mμsec; time scale, 0.10 μsec/cm.

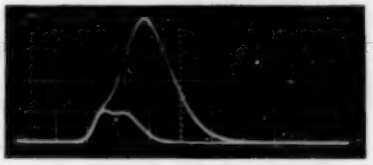

FIG. 3. Read output of a saturated core and of a write disturbed core for $I_{read}=1.32$ amp. Time scale, 0.040 μsec/cm.

positions in time so that the selected core receives a current of double the width of one pulse. The unselected cores receive a narrow pulse which does not switch the core at all because of its narrow width but only produces changes which are reversible. This effect on metallic tape cores has been reported in the literature.[2] For ferrite cores the pulse width must be carefully controlled at a width much less than that for tape cores (less than 0.1 μsec) in order not to produce any nonreversible effects on the unselected cores. Because of the critical nature of the widths of both pulses as well as the timing between them, this method was not used in the memory.

The second method has been studied in detail. It has been found that, if the write current is of large amplitude (say 600 ma) but of narrow width (say 0.15 μsec), only a small portion of the core is switched. If the amplitude of this 600-ma pulse is increased by about 200 ma, a much greater percentage of the core is switched. For example, a core receiving a write-current pulse of 800 ma at 0.15-μsec width produces a signal

[2] V. L. Newhouse, Proc. Inst. Radio Engrs. **45**, 1484 (1957).

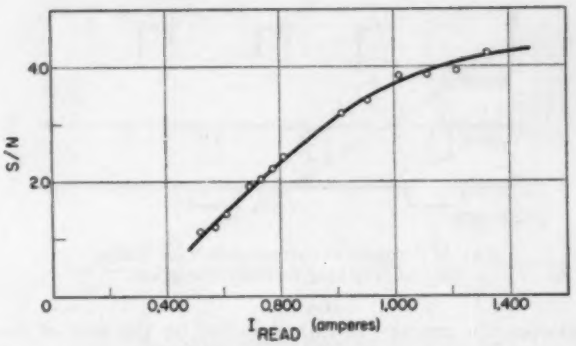

FIG. 4. Signal-to-noise ratio (based upon peak core output) for a 30–50 core, write disturbed with 377 ma.

3 times larger during the subsequent read-out than the output from a core having received only 600 ma at this same width. Therefore, a memory-write-scheme can be devised in which the selected core receives two currents coincident in time. One of the currents is a narrow pulse of amplitude above 600 ma called the write current and a second current which is 250 ma or below called the exciter current. The only requirement is that the two currents occur coincident in time. The 250-ma current can be of arbitrary width just as long as it is as wide as the narrow write pulse. The selected core then is switched by a current which has the pedestal appearance of Fig. 5. Switching takes place only during the time that the write current is being applied. The core that is to be written into the "one" state switches by the addition of the exciter current and the impulse of write current. This same impulse of write current when not coincident with an exciter current switches very little of the core. Due to the narrow width of this high current, the core exhibits an increased coercive force over the normal coercive force of the material. The exciter current, of course, is below the coercive force of the core so that no switching occurs no matter how many times the exciter current is repeatedly applied.

PARTIAL SWITCHING FOR MEMORY APPLICATIONS

For optimum memory design, the use of this technique requires quantitative knowledge of the core properties as related to the drive currents. In order to find the combination of width and amplitude of the write and exciter currents which gives the best selection ratio, RCA XF 3018H cores were carefully tested. One of the most important parameters is the relationship

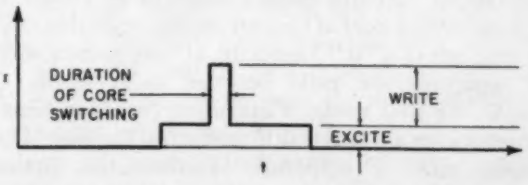

FIG. 5. Pedestal appearance of current on selected core during write time.

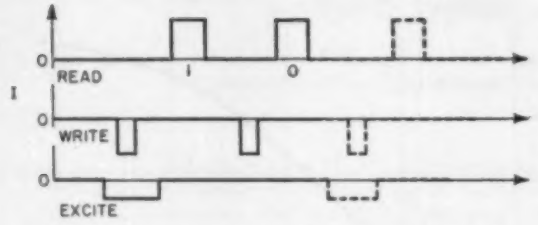

FIG. 6. Program of current pulses for testing partial switching memory operation.

between the amount of flux switched by the sum of the write and exciter currents and that switched by the write current alone. The program for testing the cores has two read currents for observing the "one" and the "zero" outputs as shown in Fig. 6. The peak value of the core output was measured during both of these read pulses along with the switching time of the core. Note that the noise output or "0" is defined as that signal which occurs during the read-out of the core after it has been disturbed by the write current alone. For these tests the exciter current was maintained at its maximum permissible value of 250 ma and the *width* of the write current was varied.

EXPLANATION OF RESULTS

For the purpose of examining the data shown in Fig. 7, consider the set of curves for the write current equal to 600 ma. At large write-current widths (above 0.6 μsec) the core is being entirely switched by the write current with the aid of the exciter current. Furthermore, the write current is of sufficient width by itself to switch the entire core, so that the output of the "0" is as large as that of the "1" and the signal-to-noise ratio is unity. At a narrower width of write current of about 0.25 μsec the current is no longer capable of switching the entire core in the time that it is applied even with the aid of the exciter current. At this same width the write current alone is switching a smaller portion of the core and the signal-to-noise ratio has increased to 2.5. As the width is further decreased, less of the core is switched during write time and the peak "1" output decreases. Note that the width of the output-switching-waveform also decreases. The signal-to-noise ratio reaches a maximum of over 4.0 at a width of 0.15 μsec. With further narrowing of the write-current width, the signal-to-noise ratio begins to decrease since at these widths such a small percentage of the core is being switched to produce a "1" that the read output becomes small enough to be comparable to the reversible part of the core output occurring during the read-out of a "0." Therefore, at very narrow widths the signal-to-noise ratio becomes unity again. Obviously, the best mode of operating cores for memory purposes uses a write width producing the best signal-to-noise ratio, if amplitude discrimination between sensing a "1" and a "0" is used.

A series of these curves have been plotted for different levels of write current ranging from 400 ma to 1 amp. Three curves of this series are shown in Fig. 7. It can be seen that with high write-current amplitude, narrower widths of the write current are required (1) to achieve partial switching operation and (2) for maximum signal-to-noise ratios. In addition to varying the write current as shown in Fig. 7, the read current also has been varied from 1.0 to 2.0 amp with the result that better signal-to-noise ratios are obtained with high read current, and the switching speed and peak output are increased. Also the exciter current, which determines the additional current which a selected core receives over an unselected core, has been decreased to 100 ma. Surprisingly good selection ratios can be obtained with signal-to-noise ratios of about 5, although with this low-exciter speed is sacrificed. The exact details involved in the use of this partial (impulse) switching and the special considerations needed in building a memory of this type are reported in another paper.[3] The only demand that is made by this memory scheme is that the read current always must switch all the flux which has been set by the write current so that the core is in the saturated "0" state at the end of the read time, in order to avoid spurious "ones" from accumulating in a core.

SPECIAL NOTES ON PARTIAL SWITCHING CURVES

In addition to giving the memory designer a means of deciding the best mode for operating cores and also

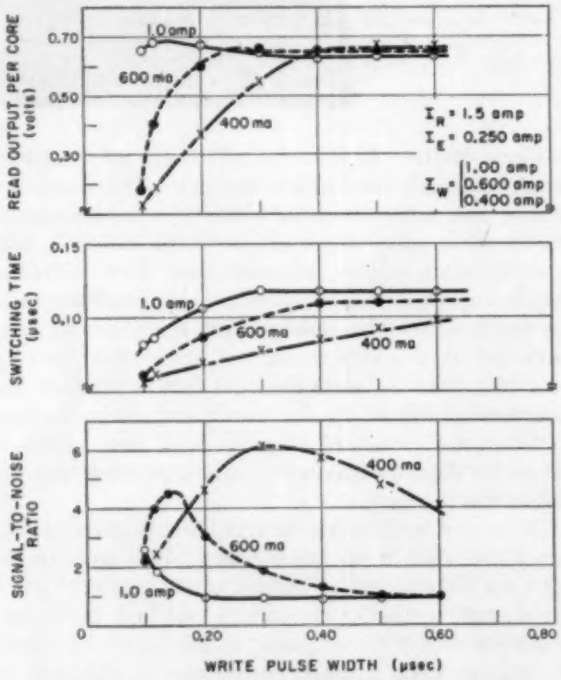

FIG. 7. Core output as a function of write-pulse width for impulse switching.

[3] V. J. Sferrino, WESCON Convention Record, part 4, (August 18, 1959), pp. 3–15.

the demands on the driving circuitry, these curves give some indication as to the process of flux reversal within the core for partial switching conditions. It can be noted that as the write width is reduced the read output increases in amplitude slightly before falling off. The switching time of the read output has decreased at this peak output point so that no greater amount of flux is being switched than at long current widths, however. This point occurs at a width of 0.25 μsec for the case considered above of 600-ma write current. This is the point, therefore, at which the core just begins to go into a partially switched state. The fact that the speed of the switching process has increased indicates that the read-out of a core which has not been fully saturated occurs faster than that from a saturated core. The flux is switched at a faster rate probably because a greater number of domains of reverse magnetization are present in the unsaturated core as would be indicated by Menyuk and Goodenough's theory.[4] A further point of interest is the fact that the read-output curves for the three levels of write current cross over one another as they go into saturation. The read peak output is highest for cores which have been reset by the lowest value of write-current amplitude. This effect again is related to the number of domains of reverse magnetization in the core at the time of the application of the read current. A further clue as to the domain configuration within the core under these partial switching conditions has been reported by McKay[5] by measuring the reversible output at various levels of residual flux.

TEMPERATURE CONSIDERATIONS

Increasing the temperature of the surrounding atmosphere of the core can change the percentage of flux which a given combination of current and width can switch. Data was taken on the change in the peak output due to changes in temperature. More elaborate testing is needed to determine accurately the effect of temperature on the partial switching characteristic. The most interesting characteristic is the change in operation when the repetition rate is increased to 1 Mc. The resulting increase in the internal temperature of the core is extremely difficult to measure. The energy loss in the core is related to the percentage of flux switched, but the temperature does not increase linearly with the energy loss because of the relation between core surface area and percentage of flux switched.

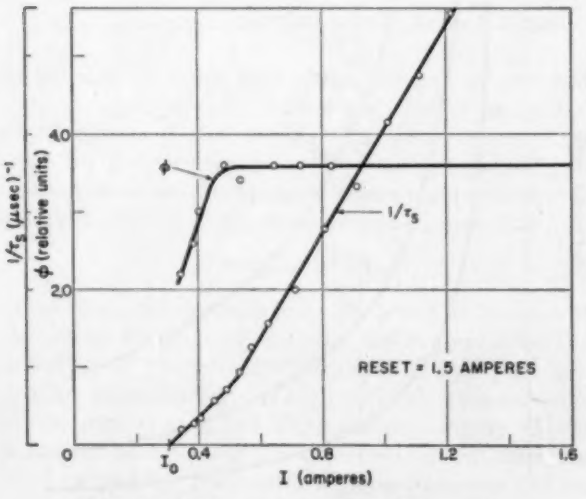

FIG. 8. Switching speed characteristic curve for large reset (write) current.

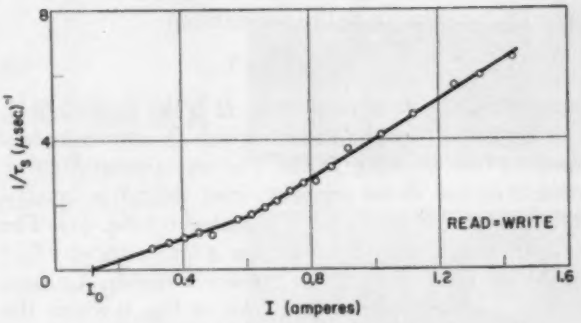

FIG. 9. Switching speed characteristic curve for read current equal to write current.

STUDIES IN CORE SWITCHING CHARACTERISTICS

A careful study has been made of the dynamic reversal of flux in a ferrite core of square-loop material. An indication of this switching characteristic can be found by measuring the switching time (τ_s) of the core for different driving conditions. In Fig. 9 the inverse-switching-time ($1/\tau_s$) is shown plotted against the driving current for a 30–50 core of Mg Mn material. The cores used throughout this investigation all have the composition $Mg_{0.81}Mn_{0.47}Fe_{1.71}O_4$. For this curve the core was reset into a saturated state by a high write current before the application of each read current. The switching time is defined here as the duration of time that the rate of change of flux of the core ($d\phi/dt$) is larger than 10% of its peak value. Another definition in common use[6] defines the switching time as the time required for the flux to change from 10% to 90% of its final value. During this investigation, data was taken using both definitions and it was found that the second definition of switching time resulted in τ_s being from 0.58 to 0.60 times that as measured using the first definition. Since the two results only differ by a constant multiplier, the first definition (10% of $d\phi/dt$) shall be used throughout this paper.

A linear relationship between the inverse-switching-time and the applied field is predicted by Menyuk and Goodenough's theory which defines a switching coeffi-

[4] N. Menyuk and J. B. Goodenough, J. Appl. Phys. **26**, 8 (1955).

[5] R. W. McKay, J. Appl. Phys. **30**, 56S (1959).

[6] E. M. Gyorgy, J. Appl. Phys. **28**, 1011 (1957).

cient (S_w) according to the relationship

$$\mathcal{T}_s(H-H_0)=S_w, \quad (1)$$

where $\mathcal{T}_s$ is the switching time, H is the applied field, and H_0 is the threshold field which is approximately equal to the coercive force. The experimental curve consists of two linear segments over the range investigated instead of just one as indicated by Eq. (1). The manner of resetting the core has a pronounced effect on the slope of the curve in the lower region. An illustration of this difference is shown in Fig. 9 where the write current is held at the same width and amplitude as the read current. With the large reset current (Fig. 8) the break is less definite and the value of the intercept (noted as I_0 in the curves) is at a higher value. Measurement of the actual flux being reversed during switching shows that the core is not being fully saturated (not all the flux is being reversed), unless the read current is at a value greater than that at the break in both Figs. 8 and 9. In the upper portion of the curve, the slope is determined entirely by the increased speed of the reversal mechanism as the current is increased by a small increment, whereas in the lower portion of the curve, in addition to the increased speed of the switching process, a greater amount of flux is also being switched for an incremental increase in current. Thus, the slopes are different for the segment in saturation and that not in saturation.

The difference in the intercepts (I_0) between Figs. 8 and 9 gives an indication of the changes in H_0 and also the change in the apparent coercive force of the material when the core is saturated and when it is not being fully switched (i.e., when it is operating on a minor hysteresis loop). When the core is being used in a coincident-current memory mode it is operating in the lower region of Fig. 9, at 500 ma, and is not operating in saturation. The value of S_w for this lower portion is 1.0 oe-μsec and is 0.6 oe-μsec for the upper portion of Fig. 8. These numbers indicate that, in addition to the expected gain in speed, driving with a high current results in operation on a more favorable portion (lower S_w) of the switching characteristic curve.

No additional breaks in the linearity of the switching characteristic curve have been found in this work. Workers in other laboratories have noted further breaks for ferrite cores than that mentioned above. Gyorgy and Hagedorn[7] and Shevel[8] show a third region in the curve beginning at about 8 oe, for a Mg Mn core. In this work we are concerned only with fields below 6 oe which can be achieved with presently available current drivers. The exact mechanism of flux reversal by wall motion, rotation, or a combination thereof is not considered; rather only the observable results are examined.

[7] E. M. Gyorgy and F. B. Hagedorn, J. Appl. Phys. suppl. **30**, 308S (1959).
[8] W. L. Shevel, Jr., J. Appl. Phys. suppl. **30**, 47S (1959).

PARTIAL SWITCHING PHENOMENON

Certain core properties remain in doubt with the information given by the switching characteristic curve. Since the core is not being fully switched in the lower region the question remains as to whether it is because the coercive force is different throughout the core, or whether it is due to the geometry of the core. It is in this lower portion of the curve that the core can be partially switched due to a low-driving current. The core can also be partially switched due to a narrow width of a high current. The relationship between these two methods of partial switching is of interest.

In order to answer some of these questions, a group of cores of dimensions other than 30–50 were examined. The characteristic curve of the standard 50–80 core was plotted and the break in the curve occurred at the same value of current that switched all the flux. The break was less pronounced than for the small core, however.

If the question is posed whether the break in the curve is related to the geometry of the core, it implies that there is a nonuniformity of the driving field (H) across the core. Because of the circular symmetry of the core, it can be assumed that a current passing through a wire in the center hole produces concentric circles of magnetic intensity. The magnitude of the H field is determined by the length of the magnetic path and can be expressed in terms of the dimensions of the core,

$$H=0.2I/2.54R, \quad (2)$$

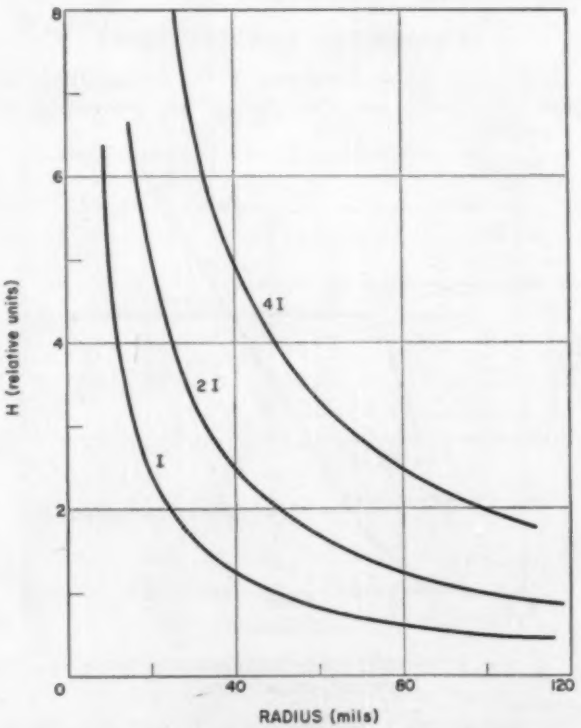

FIG. 10. Variation of driving field intensity across dimensions of core.

where H is the field in oersteds, I is the driving current in amperes, and R is the distance from the center of the core in inches. The variation in magnitude of the field across the core has the shape shown in Fig. 10.

An experimental check of this idea has been made on cores having small sense holes at various locations within the body of the toroid. The electrical output from a wire placed through these holes measures the amount of flux being switched in a particular region and also the speed of switching. The body of the core was made large in order to facilitate fabrication of the core and it was cut from a $\frac{1}{4}$-in. diam disk with a 0.030-in. center hole and with four 5-mil diam sense holes, as shown in Fig. 11. It was assumed that the small sense holes through the body of the core do not affect the switching process. This assumption was found to be adequate by experimentally comparing the behavior of cores with and without the small holes.

The inverse R relationship predicts that at low levels of current (below the break in the $1/\mathcal{T}_s$ vs current

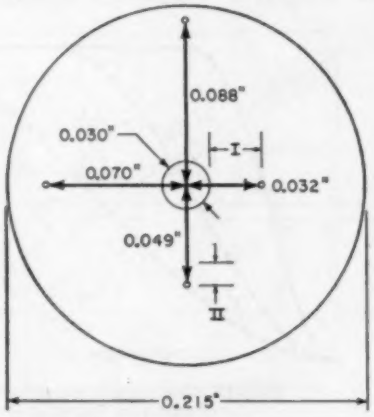

FIRST TWO REGIONS SHOWN I AND II

FIG. 11. Sketch of 0.215–0.030-in. core with four sense holes, each of 5-mil diam.

curve) only an inside ring of the core can be switched since at more distant regions the field is below the coercive force of the material. To obtain a numerical value for the coercive force, the intercept I_0 of Fig. 8 is interpreted as the value of current which will just initiate switching at the *inside diameter*, such that

$$H_0 = 0.2I_0/2.54R_{id}, \tag{3}$$

where R_{id} is the distance from the center of the core to the inside diameter of the core. Photographs for the switching of the two inner regions of the $\frac{1}{4}$-in. o.d. core are shown in Fig. 12. Figure 12 (a) is the read-out of the core after a full write current. Figure 12 (b) shows the read-out for the same read current after the write current has been reduced in *amplitude* to 450 ma with a 100-μsec duration. Note that the amount of flux switched in the second region has decreased almost to zero, whereas the flux switched in the first region has been affected only slightly by the reduction in write current. Since I_0 for this core equals 200 ma, this value

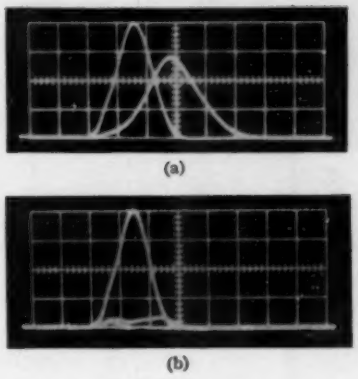

(a)

(b)

FIG. 12. (a) Read output for complete switching of first two regions of 215–30 core. (b) Read output of first two regions for partial switching due to small write current. Time scale: 0.040 μsec/cm. voltage scale: 0.36 v/cm.

of 450 ma checks well with the calculated value of 425 ma (from Eq. (3)) to produce H_0 at the first sense hole.

Further agreement for this partial switching due to very low current was found with a smaller core of 37 to 82-mil dimensions which has one sense hole in the body of the core. The two traces of Fig. 13 (a) show the switching waveform for the inner and outer regions for complete switching, and those for switching due to low write current are shown in Fig. 13 (b).

Evidence that the driving field is low at the outer regions of a core can be noted from Figs. 12 (a) and 13 (a) in that the outer portion switches slower and peaks at a later time than does the inner region. These results indicate that in the lower segment of the switching characteristic curve the core is being partially switched, and the switching is almost complete in the inner portion with little or no switching in the outer region, and there is a rather sharp demarcation between the switched and unswitched regions. This same model predicts that the break in the $1/\mathcal{T}_s$ curve occurs when the value of H at the outside diameter reaches H_0 in magnitude. This prediction agrees well with the experimental data if the value of H_0 is taken from the curve of Fig. 8 where the reset current is very large, but the agreement is poor when the H_0 is determined from Fig. 9 where not all the flux is being reset. For the test in Fig. 9, the degree to which the core is being pulled into saturation by the write current varies over the lower segment of the curve and the

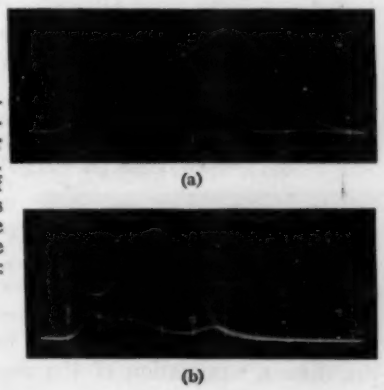

(a)

(b)

FIG. 13. (a) Read output for complete switching of inner and outer regions of 37–82 core. (b) Read output of inner and outer regions for partial switching due to low-amplitude write current. Time scale: 0.040 μsec/cm.

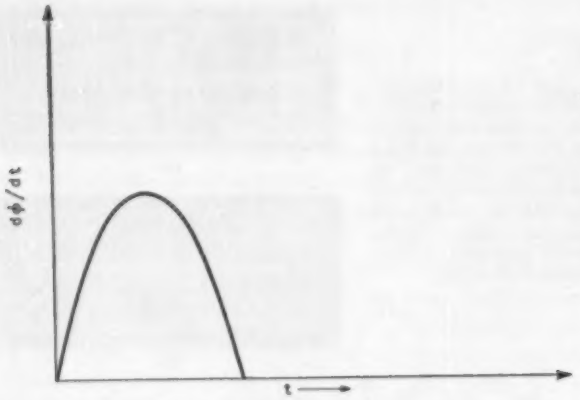

FIG. 14. Sinusoidal switching waveform for small element of core.

effective value of I_0 (or H_0) is also changing for each setting in drive current. The value of H_0 obtained by the intercept of this latter curve, therefore, has little meaning.

PREDICTIONS OF A DYNAMIC MODEL

The above description for low-current amplitudes describes the situation only for the end states of the switching process when switching is allowed to go to completion since the duration of the currents are extremely long. To describe the end states for partial switching due to high-current drive with a narrow width, a dynamic model is necessary. Partial switching by this mode is not as simple as the case for low currents since the whole core has sufficient field to start switching throughout the core, but the process is not allowed to go to completion. To fully describe this partial switching process, the dynamic model must describe the switching waveform.

Different dynamic models have been proposed and studied; the one which gives the best results shall be discussed. A model was assumed for the reversal of the magnetization at each point of distance R from the center of the core. It was assumed that for an infinitesimal portion of the core dR in width, the switching waveform has a *sinusoidal* shape in time as sketched in Fig. 14. The flux of the core at that radius therefore changes according to a cosine relationship. The flux switches slower at greater distances away from the center as sketched in Fig. 15 since the effective field $(H-H_0)$ is smaller at the distant regions. The flux at a given radius can be expressed as

$$\phi_{at\ R}=-\phi_s \cos K(H-H_0)t \quad \text{for} \quad t<\mathcal{T}_s, \tag{4}$$

where

$$H=0.2I/2.54R, \tag{2}$$

and ϕ_s is the saturation flux, t is time, $\mathcal{T}_s$ is the switching time, and K and H_0 are determined experimentally for a given material. The switching for the whole core is therefore a summation of the magnetization changes over the total radius. The total flux can be found by integrating from the initial radius (R_i) to the final radius (R_f),

$$\phi(t)=\int_{R_i}^{R_f}\psi(R,t)dR, \tag{5}$$

where

$$\psi(R,t)=-B_s(d)\cos K(H-H_0)t \quad \text{for} \quad 0<t<T(R), \tag{6}$$

and

$$\psi(R,t)=+B_s(d) \quad \text{for} \quad t>T(R). \tag{7}$$

where B_s is the flux density of the material and d is the depth of the core. The parameter $T(R)$ is the time at which the switching has gone to completion for a particular R, that is when the following relationship is satisfied:

$$\pi=K\left(\frac{0.2I}{2.54R}-H_0\right)T(R). \tag{8}$$

Computer computation is necessary for an evaluation of integral 5. Numerical integration methods were

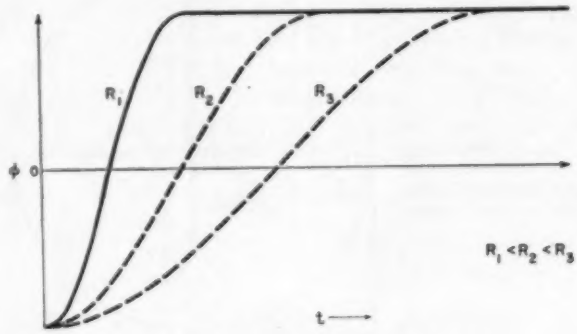

FIG. 15. Flux change for different elements of core as a function of time.

used for performing this integration on CG 24, a general purpose transistor digital computer of the Lincoln Laboratory. With this integration program the switching waveform for a total core, or any portion of that core, can be determined easily. The value of K is not readily determined by inspection of the data. To obtain a numerical value for K, the switching time of a core using an arbitrary value of K was measured and compared with the experimental results. Successive changes in K led to the best value to describe the switching time.

The model does not account for the incomplete switching when the current is less than that required to produce H_0 at the outside diameter. For currents above this value, however, the model should give the observed linear relationship between $1/\mathcal{T}_s$ and the driving current. The switching time as determined by computer computation was measured as the time that $\Delta\phi/\Delta t$ was above 10% of its peak value and calculations were made for several values of drive current for a core of 30–50 dimensions. Nominal values of K equal to 5.00 rad/oe-μsec and H_0 equal to 1 oe were used.

The result of this computation is plotted in Fig. 16. The curve is linear and its slope is approximately that of Fig. 8, but the curve is too high indicating that a lower value of K is needed to obtain a better fit with experiment.

One of the most critical requirements of the model is that it describe the switching waveform for cores of different sizes. To examine this feature the switching of four regions of the large (0.215 in.-0.030 in.) core with four sense holes located as in Fig. 11 was determined from the model and compared with the observed results. Computer computation was made using a drive current of 2.4 amp and taking the dimension between two adjacent sense holes R_{initial} and R_{final} as the limits on the integral. Nominal values of K and H_0 were taken without any special effort to obtain the exact constants. The computer results are plotted in Fig. 17. The actual waveforms for this drive current are shown in the photo of Fig. 18(a) for five regions of the core, along with the output of the total core in Fig. 18(b). A comparison between the switching times

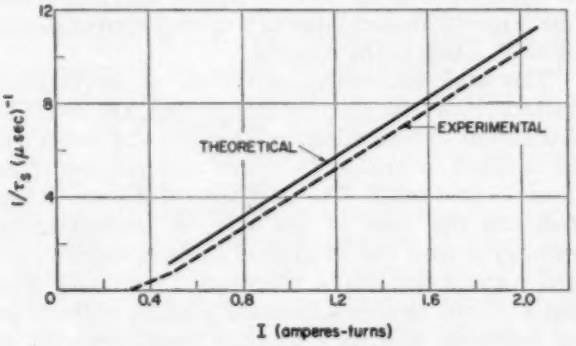

FIG. 16. Theoretical switching characteristic curve for core of 30–50 mil dimensions.

determined experimentally and theoretically shows agreement within 10%. The peak amplitudes compare as follows:

	Computed units	Experimental units
1st region	5.9	5.9
2nd region	3.25	3.74
3rd region	2.20	2.66
4th region	1.25	1.18

The measurements of the physical dimensions of the core as used for computation by the computer are accurate to about 10%.

The initial peak in the experimental waveform is due to the reversible portion of the switching process, and is not taken into account by the model. Other than for this portion of the waveform, the theory and experiment are in good agreement, both in the duration of the switching for each region and the switching waveform.

A very interesting check on the ideas involved in a study of the geometry effects is to investigate the prop-

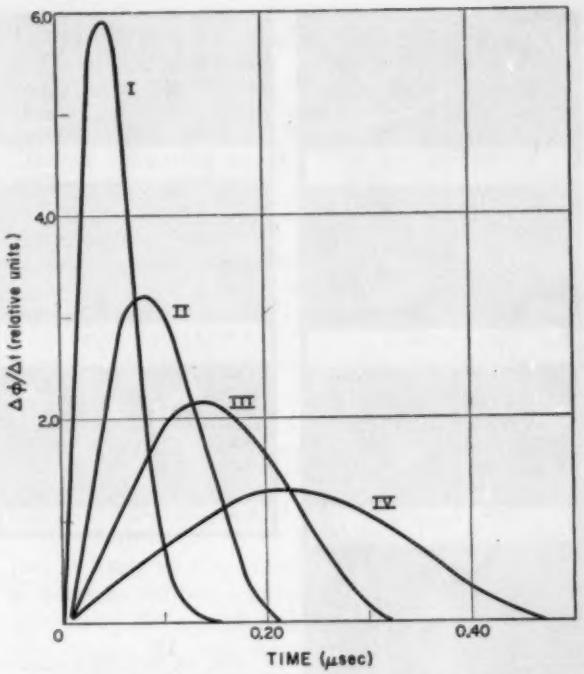

FIG. 17. Theoretical switching waveforms of first four regions of 215–30 core. Numerical integration performed on digital computer.

erties of cores which have the same outside diameter but with different inside diameters. The effects of changes in geometry, limited to changes in the inside diameter only, become evident. A group of cores all of 0.215-in. o.d., but with inside diameters of 0.056, 0.100, 0.130, and 0.158 in., were fabricated. The switching characteristic curves for these cores show certain similarities and differences. All the curves have breaks at the value of current which produces saturation and this break occurs at approximately the same value of current (to within 100 ma) for all cores. The intercept I_0, however, varies considerably for the cores mentioned above. Values of I_0 range from 300 ma to 1.1 amp for the above cores. If the *inside diameter* is used to calculate the value of H_0 by Eq. (3), the following values of H_0 are found: 1.14, 1.10, 1.09, and 0.92 oe. These values

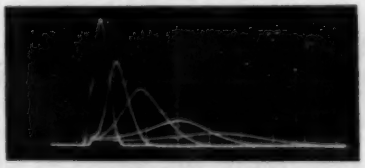

(a)

(b)

FIG. 18. (a) Experimental switching waveform of five regions of 215–30 core. Time scale: 0.10 μsec/cm. Voltage scale: 0.36 v/cm. (b) switching waveform for total core. Time scale: 0.10 μsec/cm. Voltage scale: 0.46 v/cm. Drive current equal to 2.4 amp.

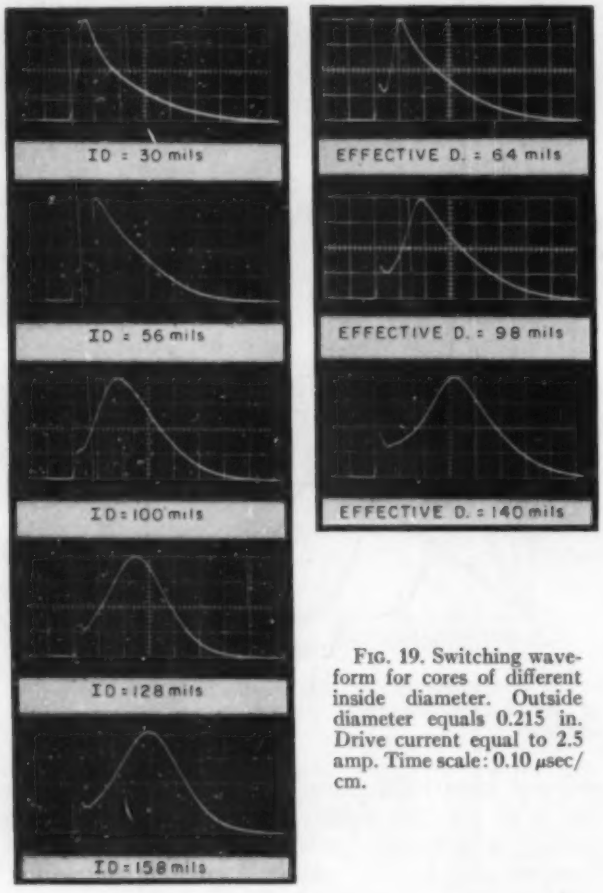

FIG. 19. Switching waveform for cores of different inside diameter. Outside diameter equals 0.215 in. Drive current equal to 2.5 amp. Time scale: 0.10 μsec/cm.

are close, considering the accuracy to which the data can be taken, and indicate that the lower intercept is related to the inside of the cores, whereas the break is a function of the outside diameter. The slope of the upper portion of the curves is the same for all cores and indicates that the switching time of the entire core is determined primarily by the switching of the outside region.

Further experimental and theoretical examination of this set of cores shows other evidence of the relation between the switching speed and the distance from the drive winding. The switching waveform at a current level of 2.5 amp for the four cores were examined experimentally and theoretically. A comparison of the experimental outputs for these cores is shown in Fig. 19. Note that the time of peaking is later for the cores with the largest center hole. The switching time, however, changes only slightly for all the cores. The calculated waveform from the model exhibits the same trends. Additional comparison is made in this figure with the output from a core with a small center hole and with four sense holes (Fig. 11). The electrical outputs from these holes at various points are the changes in flux from that point to the outside edge. The effective diameter can be considered as twice the distance from the core center to the sense hole under consideration. There is little difference between these outputs and those of a core with the center area removed, indicating that the presence of the material on the inside of the core does not appreciably affect the switching at the more distant points.

CONCLUSIONS AND APPLICATIONS

For ferrite cores of the material and geometry studied, the nonuniformity of the driving field over the core produces the major differences in the switching waveform for various regions of the core. For partial switching conditions the proposed model predicts the amount of flux switched in any given region as well as the relative switching speeds of the regions. Understanding these ideas is a necessary tool for applying magnetic material to engineering applications.

If the geometry is changed from the toroidal form to a nonsymmetric shape, for example, an elliptical form, the problem of calculating the exact driving field H at a particular point becomes difficult. The inverse distance relationship is no longer valid. The problem is one of finding the locus of equi-H lines throughout the magnetic material due to a driving current passing through a hole in the material.

This work has motivated the use of the magnetic material in several practical applications. The reversible component of magnetization, as mentioned earlier, can be obtained by applying a narrow-current pulse of less than 0.1 μsec width. The amplitude of the core output indicates the state of the core. A nondestructive-memory-scheme can be devised utilizing narrow pulse drives and a core can be interrogated repeatedly without a rewrite operation. Intricate selection methods can be developed whereby a group of these narrow pulses are added adjacent in time so that one particular core receives the sum of many pulses adding to a long pulse.

If the read-current width is increased beyond 0.1 μsec in width, a part of the core will be irreversibly switched. If the core is in a saturated "1" state several of these current pulses can be applied before all the flux has been reversed. For a certain amplitude and width of this current, the output has the same peak amplitude for about eight successive applications of this current pulse. Thus a memory can be designed for extreme reliability since each readout of a core can be sensed eight times instead of once. Reliability is achieved by redundancy. A photo of the output for the first eight successive applications of a current of 800 ma at

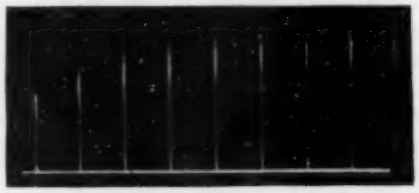

FIG. 20. Eight successive read outputs of 30-50 core for narrow read current of 800 ma in amplitude.

0.06 μsec is shown in Fig. 20. An interesting point to note is that the first output of the eight is the lowest in amplitude. This phenomenon is due to the fact that the first pulse must first nucleate reverse domains, whereas succeeding pulses need only continue the reversing process.

The inverse of this readout process can be used to store successive amounts of flux during the write operation. The application of a series of similar narrow pulses switches more and more of the core until it reaches saturation. The core is acting as an accumulator, and the percentage of flux which has been switched is an indication of the number of pulses received. This write technique can also be used on cores which have a series of small sense holes drilled in them. The output from a particular hole indicates that a certain number of narrow pulses has been received and thus the location of the switched region of the core tells the number of pulses received.

The application of very narrow pulses can be extended to the continuous ac situation. If a current around 10 Mc in frequency is applied to the core, the output of the core is also ac and is nondestructive of the state of the core. The amplitude of the reversible component is the largest when there is the greatest number of domain walls present in the core, as reported by Becker.[9] He showed experimentally that during the switching process the greatest number of domain walls are present in the core at the time that the rate of charge of flux is a maximum. Therefore, if the switching process is interrupted at the peak in $d\phi/dt$, the greatest number of domain walls exists in this partially switched core. The response of the partially switched core to an alternating current will be much larger than that of a saturated core. A sketch of the ac output for different states of the core is shown in Fig. 21. Note that the ac output is over three times greater in magnitude after partial switching than before.

It has been found that a core partially switched with a very high, narrow current gives a higher ac output than one which has been switched by the same percentage with a lower current. This follows from the fact that the high current can nucleate many domains throughout the core. If the frequency of the ac current which is superimposed on a pulse of switching current

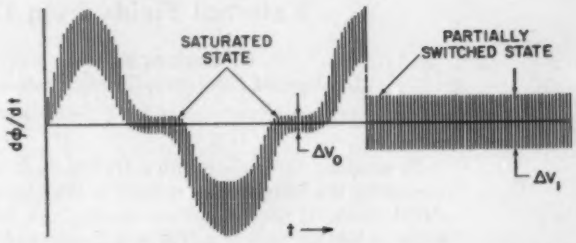

FIG. 21. Output from core when driven with a 10-Mc alternating current in addition to switching current. ΔV_0 is ac output from saturated core, ΔV_1 is ac output from partially switched core.

is above 10 Mc, the ac component does not interfere with ordinary switching of the core. This technique can be used to perform logical function with ferrite cores incorporating nondestructive sensing the state of the core. The ac output can be rectified and used directly to set the state of another core.

This high-frequency ac technique is also a valuable tool in studying magnetization processes. The response of cores in various degrees of partial switching to the ac current tells a great deal about the domain configuration within the core. Also the percentage of partially switching at different locations within a core can be seen by measuring the magnitude (and possibly the phase) of the ac output at those points.

One further application of ferrite cores of some material is related to its behavior to an impulse of current. When S-1 material is driven by a current having the pedestal appearance of Fig. 5, it only switches during the period that the impulse of current is applied and stops at the end of the impulse. Some materials, however, continue to switch after the impulse has been removed under the field of the low current. If the low current is applied alone, however, the core does not switch and does not begin until the switching process is initiated with a high impulse of current. Cores of this type require a high nucleating field and only a much smaller field is required to continue the reversal process. Both memory and logic systems can be designed on this phenomenon where the selection scheme is the initiating impulse of current applied to one particular core.

ACKNOWLEDGMENT

The authors wish to thank R. H. Baker for his encouragement during this work and J. C. Henry for assistance with the computer computation.

[9] J. J. Becker, J. Appl. Phys. **30**, 387 (1959).

External Fields from Domain Walls of Cobalt Film

B. KOSTYSHYN, J. E. BROPHY, I. OI, AND D. D. ROSHON, JR.
Development Laboratory, General Products Division, IBM Corporation, Endicott, New York

(Received June 25, 1959)

By scanning the surface with a Hall probe, domain patterns on thin cobalt films have been mapped by measuring the fringing flux normal to the film surface. The samples studied were cobalt approximately 2000A thick. At the domain boundaries, peak fields ranged in intensity from less than 0.5 to 4.5 oe. The probe to film gap was 13 μ. The sensitive area of the probe was a square of bismuth 20 μ on a side. It was observed that along specific boundaries, reversal of flux direction occurs. The boundaries exhibiting low peak fields were generally parallel to the easy direction of magnetization, whereas the boundaries exhibiting high fields were skewed relative to the easy direction of magnetization. Kerr effect and Hall probe patterns for the same domain configuration are shown to agree.

INTRODUCTION

DOMAIN patterns have been observed on thin ferromagnetic films by use of magnetic powder patterns,[1] the Kerr and Faraday effects[2,3] and electron beam microscopy.[4] Domain structure on tin samples at liquid helium temperatures have been observed by use of the magneto-resistive effect in bismuth wire.[5]

In the following paper, an alternative technique for determining domain structure of thin films by employing the Hall effect is described. The technique used consists of mapping the surface of the thin film with a Hall probe of high resolution and sensitivity. At the domain boundaries there are, in general, measurable fields normal to the surface of the film which may be plotted and analyzed.

The Hall probe used in determining the field configurations is shown in Fig. 1. The probe amplifier used is to be described in detail elsewhere.[6] The sensitive area of the probe used was a square, 20 μ on each side with a thickness of 12 μ. The probe currents were of the order of 10^{-3} amp, and the material used to construct the probe was bismuth. The probe amplifier system enabled determination of fields down to 0.2 oe in intensity with a signal-to-noise ratio of three to one.

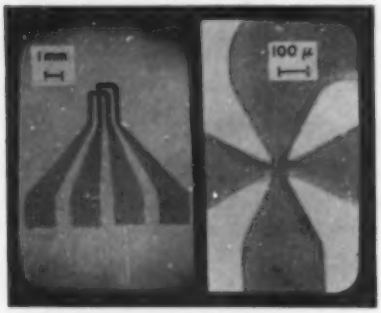

FIG. 1. Hall probe with enlarged view of sensitive area.

The specimens studied were thin cobalt films of approximately 2000 A in thickness and of surface dimension of $\frac{1}{4}\times\frac{1}{4}$ in. A uniaxial direction of easy magnetization was observed. The specimens were prepared in the manner outlined by Williams and Sherwood[3] in 1957. The direction of easy magnetization was determined by employing a Kerr effect apparatus and by observing the growth pattern of the domains as the specimen was rotated relative to the direction of the energizing field. The domains nucleate and grow in a unique manner when the energizing field is in the direction of easy magnetization.[3]

The specimen and probe were mounted on a modified Gaertner microscope stage. The stage was driven by a synchronous motor such that the probe was moving at the rate of 15 mm per min relative to and parallel to the surface of the specimen. The probe to film gap was 13 μ. The surface of each specimen was scanned along the length approximately forty times at intervals of 125 μ. Smaller intervals were used as required.

In the samples studied, the domain shapes observed roughly corresponded to triangles. A hypothetical film is shown in Fig. 2 in which the triangular domains labeled I, II, and III described are separated from the

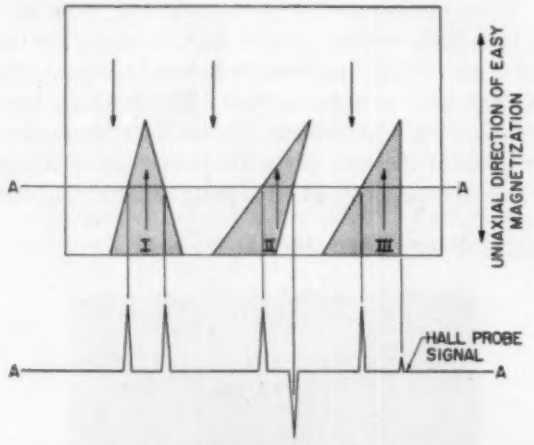

FIG. 2. Hypothetical film with a uniaxial direction of easy magnetization showing a domain structure with the expected output from a Hall probe scan.

[1] H. J. Williams, R. M. Bozorth, and W. Shockley, Phys. Rev. **75**, 155 (1949).
[2] G. A. Fowler and E. M. Frye, Phys. Rev. **94**, 526 (1954).
[3] H. J. Williams and R. C. Sherwood, J. Appl. Phys. **28**, 548 (1957).
[4] L. Mayer, J. Appl. Phys. **29**, 658 (1958).
[5] A. Shalnikov, Physics (U.S.S.R.) **9**, 202 (1945).
[6] D. D. Roshon, Rev. Sci. Instr. (to be published).

remainder of the film by 180° remainder of the film by 180° Bloch walls. The direction of magnetization assumed is shown by the arrows. Domain I is in the shape of an isosceles triangle; domain II, in the shape of an obtuse triangle, and domain III, in the shape of a right triangle.

At the domain boundaries, there will be fringing fields normal to the film surface. The fringing fields are due to a combination of domain magnetization (comparable to the fringing fields of two opposing bar magnets) and Bloch wall magnetization (comparable to the fringing field of a dipole). If the surface of the film were scanned with a Hall probe in the direction *A-A*, a probe signal as shown in the bottom of Fig. 2 would be expected.

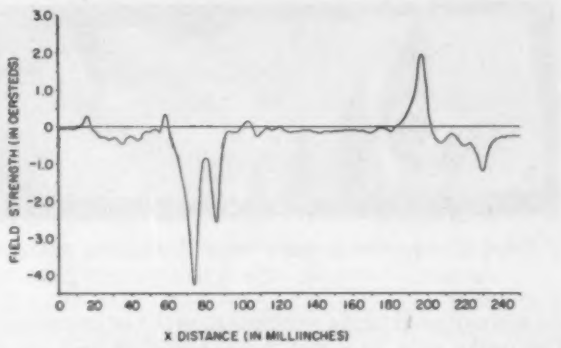

FIG. 3. Hall probe output for a typical scan over the film surface shown in Fig. 5. Output represents the component of field normal to the film surface. Probe to film gap: 13 μ.

EXPERIMENTAL RESULTS

An actual scan of a Hall probe on a typical sample is shown in Fig. 3. These data were taken from a sample which did not contain a domain with a canted boundary (center domain, Fig. 2). The peaks observed, ranging in intensity from 0.2 to 4.5 oe, are the peak field predicted by the simplified model of Fig. 2 without the center domain. The sample does not have equal intensity peaks as shown in the simple case.

Assuming that the presence of a peak represents the boundary of a domain, the plot of the peaks of a series of scans would indicate the domain pattern. In Fig. 4, the plot of a series of scans is shown with the corresponding Kerr pattern shown in Fig. 5.

The agreement between the Hall pattern and the Kerr pattern is good except in the case of the small nucleations at the edges of the sample. This is due to the masking of the small fringing fields from the nucleated structures by the inherently large fields present at the edges of the film.

Three points of interest are apparent from the plot shown in Fig. 4.

(1) There are a multiplicity of peaks not associated with any observable domain structure in certain regions.

(2) Along certain domain boundaries (in the regions labeled *A*), there are no peaks associated with the boundary.

(3) Along other domain boundaries (in the regions labeled *C*) there are reversals in the direction of the fringing field.

The above observations may be explained by considering the topographical map of the normal component of the fringing field as shown in Fig. 6. In the map, shown, the fringing field is plotted in levels of 0.5 oe. The shaded regions indicate the domain structure of Fig. 4 and the heavy lines represent the zero field level.

In the map shown, it is seen that the region occupied by the large number of unassociated peaks described above is essentially void of detail. This indicates that

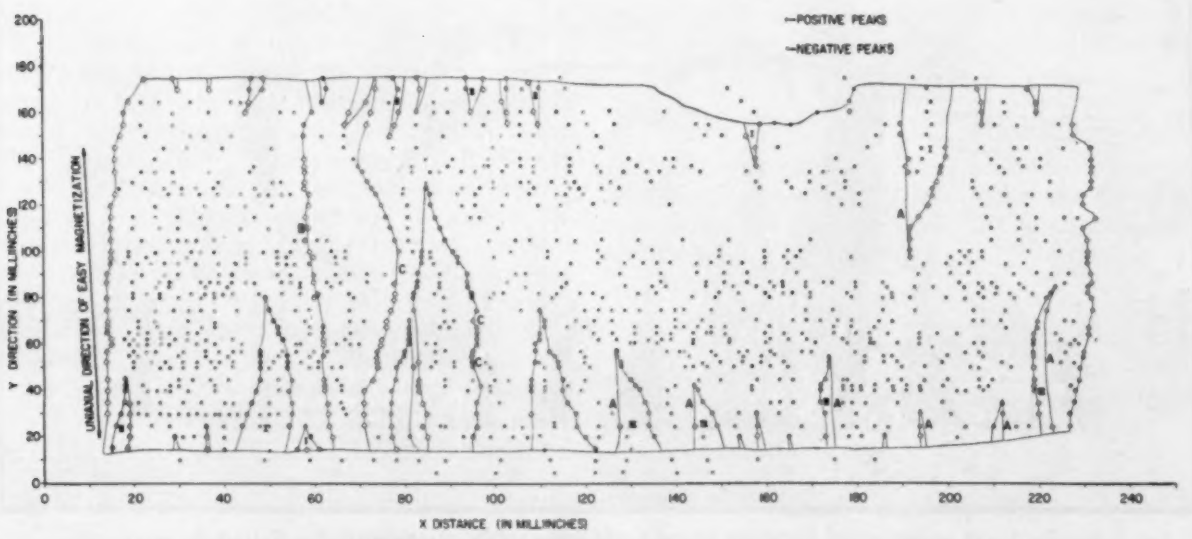
—POSITIVE PEAKS
—NEGATIVE PEAKS
Y DIRECTION (IN MILLIINCHES)
UNIAXIAL DIRECTION OF EASY MAGNETIZATION
0 20 40 60 80 100 120 140 160 180 200 220 240
X DISTANCE (IN MILLIINCHES)

FIG. 4. Distribution of the position of peak fields for scans over the film surface shown in Fig. 5.

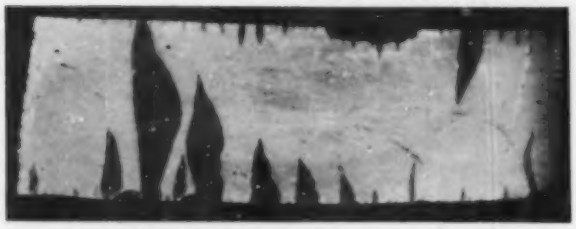

FIG. 5. Kerr pattern of cobalt film. Film thickness 2000 A.

the unassociated peaks were less than 0.5 oe in intensity. The peaks may be called "surface noise" and are attributable to small surface defects in the film.

In considering the boundaries not indicated by peaks (labeled *A* in Fig. 4), it is noted that they are all approximately parallel to the uniaxial direction of easy magnetization. It is seen from Fig. 6 that in general the regions that display high fields and high gradients are at the edges of the film (expected because of the physical discontinuity) and also at the domain boundaries canted relative to the direction of easy magnetization.

From considerations of flux closure (referring to the model shown in Fig. 2), it is expected that at the canted boundaries the fringing fields will be dominated by flux originating in the domain, whereas at the boundaries parallel to the direction of easy magnetization, the contribution due to domain magnetization will be small. In most cases where the boundaries are not indicated by peaks, there is a canted boundary in the immediate vicinity. The effect of the canted boundary is to mask the fringing fields of its neighbor. This is clearly shown in Fig. 6.

From the foregoing, it is apparent that it would be impossible to examine the fringing fields due to Bloch wall magnetization at a canted boundary or at any boundary masked by fields dominated by flux originating in the domain proper. To examine the fringing fields due to Bloch wall magnetization, it is necessary to examine a domain structure where the flux closure patterns are limited. Such a domain is the large domain shown in Figs. 4 and 6. One wall labeled B is approximately parallel to the direction of easy magnetization, whereas the opposite wall is irregular. Along the irregular wall as seen in Fig. 6, the high fields and gradients associated with flux closure are present, whereas on the wall labeled B the peak fields are in the region of 0.5 to 1.0 oe. No attempt has been made to correlate the observed fields with the expected fields due to domain wall magnetization.

In considering the boundaries where reversal of flux direction takes place (labeled C in Figs. 4 and 6) it is noted that in the specific region of reversal, the domain wall is always irregular. Consider a hypothetical domain structure as shown in Fig. 7. The domain shown is approximately triangular with an irregularity on one leg of the triangle. On the basis of flux closure considerations, a series of three Hall probe scans, A-A, B-B, and C-C would yield signals showing a reversal in the direction of the peak at the wall containing the irregularity. The reversal of the fringing field observed is thereby due to the flux seeking the shortest possible return path to the film surface. Similar irregularities in the domain wall have been shown by Williams and Sherwood[3] to be due to observable surface defects in the film.

SUMMARY

Magnetic domain patterns have been measured on cobalt films 2000 A in thickness by plotting the component of the fringing fields perpendicular to the surface of the film with a Hall probe. The domain patterns

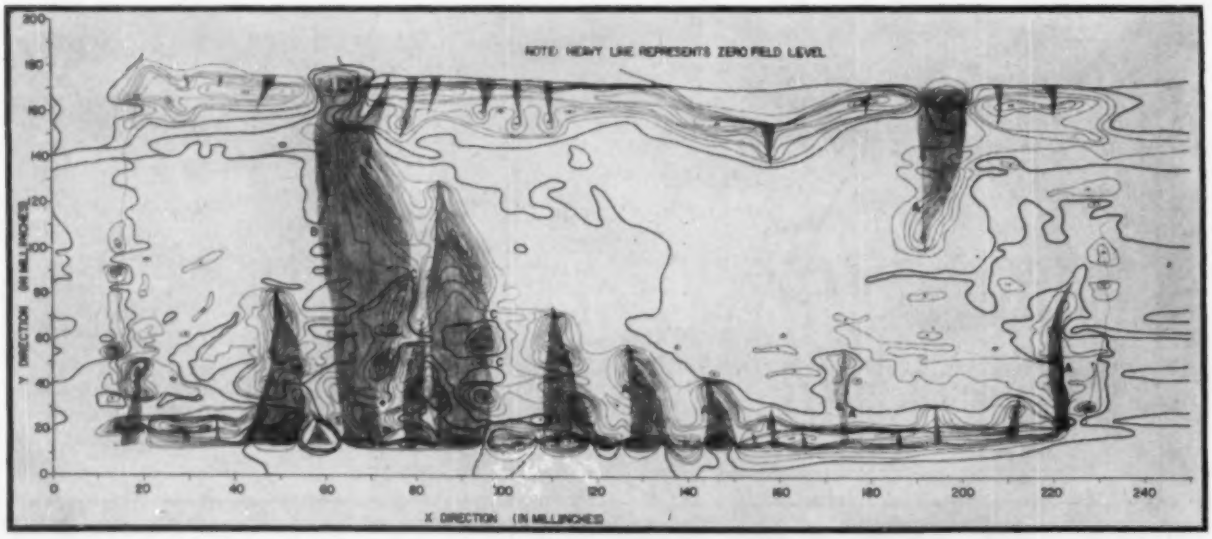

FIG. 6. Distribution of magnetic field component normal to the surface of the film shown in Fig. 5. Dark line represents the zero field level. Field distribution plotted in 0.5 oe levels.

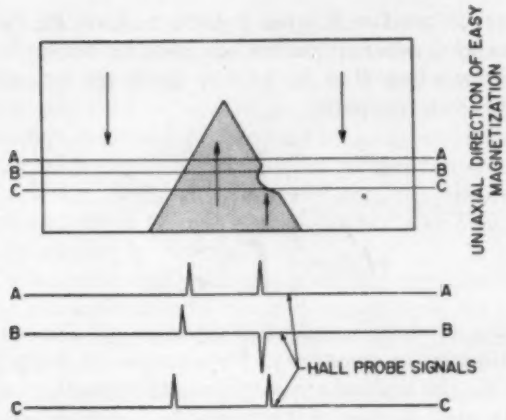

FIG. 7. Hypothetical film with a uniaxial direction of easy magnetization showing a domain with an irregularity in the boundary.

studied were formed by partially magnetizing the film in the uniaxial direction of easy magnetization.

The magnetic fields observed varied in intensity and direction. In general, the fields normal to the surface in the region of boundaries parallel to the uniaxial direction of easy magnetization were small (0.5 oe or less), whereas the fields from all other boundaries were larger (up to 4.5 oe). The agreement between the Hall probe plots and the Kerr photographs of identical domain patterns was good except in the details of small domains present at the edges of the samples. In these cases, the large fields inherently present at the sample edge masked the fields due to the small domains.

In some cases, the observed flux along a Bloch wall changed direction. In the cases observed, the reversals occurred at an irregularity in the Bloch wall. Similar irregularities have been attributed by other investigators to observable surface imperfections in the film.

ACKNOWLEDGMENTS

The authors wish to thank Mr. Gerald C. Olson of the Simpson Optical Company for the preparation of the films used, and Mr. Bruce Bertelsen of IBM for aid in the Kerr apparatus used.

JOURNAL OF APPLIED PHYSICS VOLUME 31, NUMBER 5 MAY, 1960

Optical Constants of Germanium in the Region 0–10 ev*

M. P. RIMMER AND D. L. DEXTER
Institute of Optics, University of Rochester, Rochester, New York
(Received December 2, 1959)

A program has been written for the IBM 650 Digital Computer to evaluate the Kramers-Kronig dispersion relation between real and imaginary parts of the index of refraction, n and k. By this means measurement of the reflection coefficient over a sizable energy range allows the determination of n and k throughout most of this region. Reflection data of Philipp and Taft on germanium have been analyzed in this way, and the results are compared with those of Philipp and Taft obtained by another method. The results are similar, minor differences occurring in the fine structure. The computer program is available on request.

AN accurate determination of the optical absorption coefficient and refractive index of a material in a strongly absorbing region is a difficult task for several reasons. In transmission measurements, the sample must be thin, say 100–1000 A, and the perfection of the sample is suspect. Furthermore, a very large fraction of the atoms is close to a surface, there subject to unknown influences. In addition, it is necessary to measure the thickness of the film, which again is not easy. No completely satisfactory solution to these problems has been found.

One method which has been receiving increased attention recently is based on the Kramers-Kronig relation of dispersion theory, which relates the real and imaginary parts of the dielectric constant. If either part is known over the entire energy spectrum, the other is determined by the principle of causality.

The following procedure may be used: If we define the complex index of refraction by $n-ik$, we make use of the Fresnel equation for the amplitude of reflected light at normal incidence from a flat surface

$$r=(n-ik-1)/(n-ik+1)=|r|e^{i\theta}. \tag{1}$$

The reflection coefficient, or reflected intensity is given by $R=|r|^2$, and this is the quantity whose measured value is required in this method. The Kramers relation may be expressed in the form,[1]

$$\theta(E)=\frac{E}{\pi}\int_0^\infty \frac{\ln R(E')dE'}{E'^2-E^2}, \tag{2}$$

and the real and imaginary parts of the refractive index are computed from Eq. (1), or its equivalent form,

$$\begin{aligned}(n-1)^2+k^2/(n+1)^2+k^2&=R,\\ \tan\theta&=-2k/n^2+k^2-1.\end{aligned} \tag{3}$$

* Research supported in part by the U. S. Air Force through the Air Force Office of Scientific Research, A.R.D.C.

[1] F. S. Jahoda, Phys. Rev. **107**, 1261 (1957).

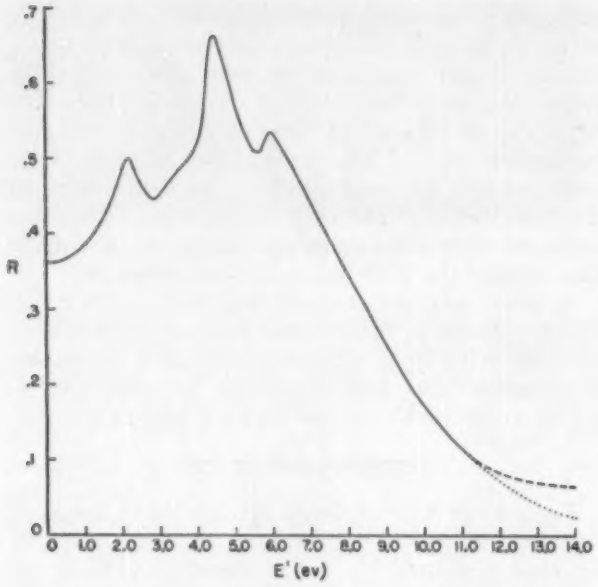

FIG. 1. Measured reflectance from clean Ge surfaces, (footnotes 2 and 3) solid curve. Extrapolation of footnote reference 2, dashed curve, of the present work, dotted curve.

The absorption coefficient μ is then computed from the definition $\mu=4\pi k/\lambda$, where λ is the wavelength of the light *in vacuo*.

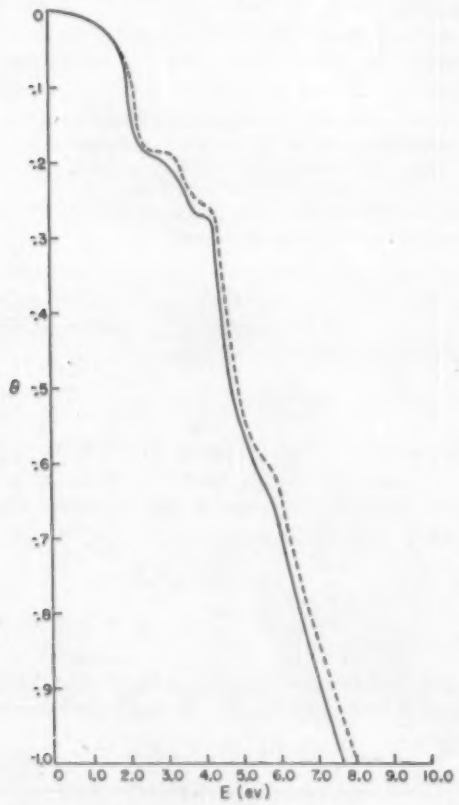

FIG. 2. Phase angle [see Eq. (1)] computed from Eq. (2) for Ge. Solid curve, present work; dashed curve, footnote 2.

Since in practice it is not possible to know $R(E')$ for all energies, some approximation must be employed. If R is known from 0 to E_1, we may divide the integral in Eq. (2) into two parts,

$$\theta_1(E)=\frac{E}{\pi}\int_0^{E_1}\frac{\ln R\,dE'}{E'^2-E^2},$$
$$\theta_2(E)=\frac{E}{\pi}\int_{E_1}^{\infty}\frac{\ln R\,dE'}{E'^2-E^2}, \tag{4}$$

the first of which is computed directly, and the second is estimated in some way. For energies E much less than E_1, the limit of measurement, the contribution θ_2 will be small because of the energy denominator, and no serious error will be incurred even by a crude approximation to the function R. For energies $E\sim E_1$, R would

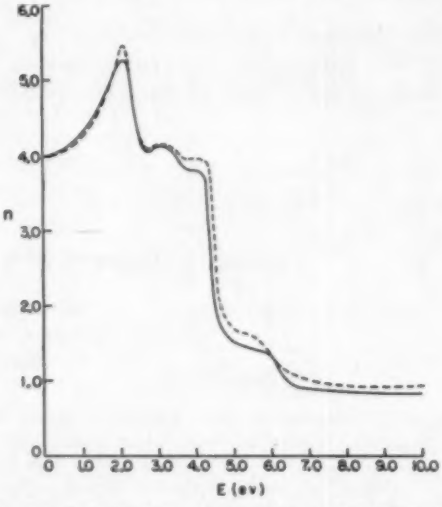

FIG. 3. Real part of the index of refraction, n, for Ge. Solid curve, present work; dashed curve, footnote 2.

have to be accurately estimated at energies above E_1. Accordingly, the expected error in the results of this technique increases with increasing energy.

Philipp and Taft[2] have measured R throughout the energy range 0.6–11.3 ev on freshly etched surfaces of single crystals of germanium. At lower energies, where k is essentially zero, R may be computed from measured values of the (real) index of refraction.[3] The experimental results from 0–11.3 ev are shown in Fig. 1 in the solid line. The dashed curve is the assumed extrapolation used by Philipp and Taft of the form $\ln R=A\ \ln E'+B$ from 11.4 ev. to 30 ev, the integral being terminated at that point.[4] On approximating the function $\ln R$ vs $\ln E'$ by a series of straight lines from 0–30 ev, they evaluated the integral for θ, solved Eqs. (3), and obtained the

[2] H. R. Philipp and E. A. Taft, Phys. Rev. **113**, 1002 (1959).
[3] C. Salzberg and J. Villa, J. Opt. Soc. Am. **47**, 244 (1957); H. B. Briggs, Phys. Rev. **77**, 287 (1950).
[4] Dr. Philipp has kindly informed us in a private communication that this is the functional form utilized, rather than that cited in footnote 2.

results shown in dashed lines in Figs. 2–5. The results are in good agreement with the measured values of Archer[5] in the range $E<3.5$ ev, with measured index values below 0.7 ev,[3] and with the measured absorption coefficient below 1.8 ev. They are in disagreement above 3.5 ev with conclusions drawn by Archer based on results in the literature. In particular, the absorption coefficient drops off much more slowly above 5 ev than was concluded by Archer.

Background and indications of the significance of these measurements for the understanding of the properties of germanium are given in footnote references 2 and 5.

In connection with other problems, we have written a program for the IBM 650 Digital Computer for the determination of n, k, and μ from reflectance data. Copies of this program are available on request. We felt that it would be of interest to repeat the analysis of the data of Philipp and Taft in view of the disagreement with the conclusions of Archer at high energies; first, because of a possible uncertainty in the method of

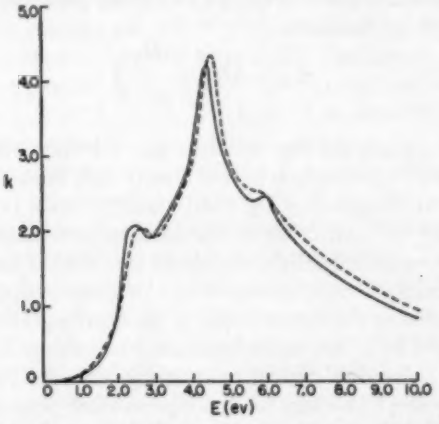

FIG. 4. Imaginary part of the index of refraction, k, for Ge. Solid curve, present work; dashed curve, footnote reference 2.

evaluating the integral in the earlier analysis, and second, as pointed out by Philipp and Taft, because of the arbitrariness of any extrapolation procedure. In particular, we wondered about a possible effect of the large discontinuity in slope in R at 11.3 ev.

Accordingly, we repeated the analysis on the 650 computer, by using tables of data kindly supplied by Philipp and Taft. Our extrapolation procedure was to assume a functional form $\ln R=aE'+b$ for the region $E>11.3$ ev, to require continuity at 11.3 ev, and to require a fit to the measured absorption coefficient in the region 0.6–1.7 ev. This was achieved with the parameters $a=-0.552$ ev^{-1}, $b=4.000$. The dotted curve of Fig. 1 indicates our extrapolation of R, and it is seen that the slope of R is nearly continuous at 11.3 ev. This last circumstance would not be expected to make much difference at low energies, but might be expected to extend to higher energies than previously the region of validity of the results for the optical constants.

[5] R. J. Archer, Phys. Rev. **110**, 354 (1958).

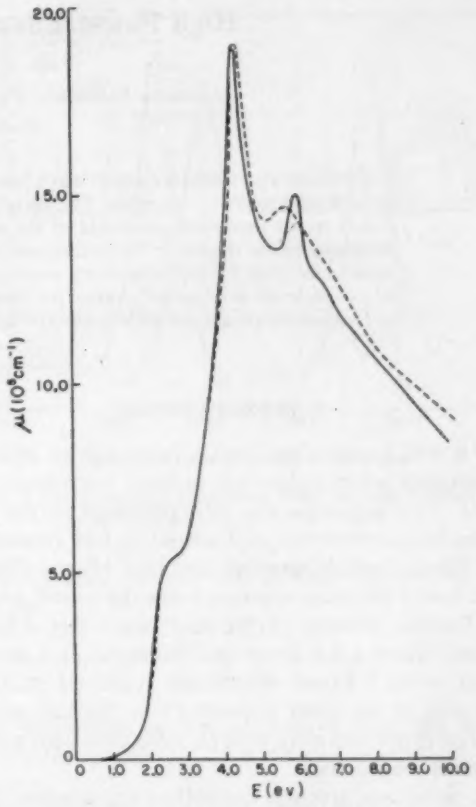

FIG. 5. Absorption coefficient for Ge. Solid curve, present work; dashed curve, footnote reference 2.

The measured and extrapolated values of R were punched on the input deck of cards, at intervals of 0.1 ev from 0 to 6 ev, and at successively larger intervals to 30 ev, where the integral was terminated; a trapezoidal rule was employed in the integration procedure. The accuracy of this type of integration is well within experimental error.

In this program the IBM 650 computes at selected intervals similar to those above, namely 0.1–0.4 ev, depending on the structure in R, the phase angle θ, and solves Eqs. (3) for n, k, and μ. The results are shown in Figs. 2–5 in solid curves. The agreement with the earlier analysis (shown in broken curves) is seen to be very good below about 3 ev, somewhat sharper structure appearing in the extinction and absorption coefficients at higher energy. Accordingly, we confirm all the principal results of the analysis of Philipp and Taft, and conclude that their methods of graphical integration and also, probably, of extrapolation, are within experimental error; an obvious corollary is that if the measured values of R fall within the estimated error, the absorption coefficient remains above 10^6 cm^{-1} to energies beyond 8 ev, in contrast to the views expressed in footnote 5.

ACKNOWLEDGMENTS

We are indebted to Dr. H. R. Philipp and Dr. E. A. Taft for a preprint of their work and for private correspondence.

High Power Effects on Ferrimagnetic Resonance

M. T. Weiss*
Microwave Laboratory, Hughes Aircraft Company, Culver City, California
(Received December 11, 1959)

Ferrimagnetic resonance experiments have been performed on single-crystal spheres of manganese ferrite at high microwave power levels. The variation of susceptibility with power level is in good agreement with Suhl's recent theoretical treatment of the saturation process in which scattering of the uniform precession into spin waves caused by impurities and imperfections is taken into account. Our results show that the ratio of intrinsic to scattering decay constants is close to zero, so that the susceptibility decreases gradually at power levels substantially below the theoretical critical signal level. At very high power levels, various anomalous effects appear such as absorption line asymmetries, bistabilities, and flat-topped absorption lines.

I. INTRODUCTION

IT is well known that ferrites behave in an anomalous manner when subjected to high microwave signal levels. This behavior was first observed in the cavity resonance experiments of Damon[1] and of Bloembergen and Wang,[2] which revealed two new effects. First, the peak loss of the main resonance line decreased, while the line became broader as the microwave signal level increased above a certain critical value. Second, at similar power levels a broad absorption appeared on the low field side of the main resonance line. In this paper we shall be concerned only with the effects of high power on the main resonance.

H. Suhl[3] has given a theoretical explanation for the above two anomalies. Because of thermal vibrations or impurity scattering, the precession of the magnetization vector about the dc field is not entirely uniform throughout the sample of ferrite. In addition to the uniform precession, spin waves are set up in which part of the magnetization vector in the ferrite breaks up into laminas with adjacent laminas precessing with different phase relationships. The spin waves of importance in the saturation of the main resonance are z directed and have a resonant frequency given by

$$\omega_k=\gamma H_s-\gamma N_z M+\gamma H_{ex} l^2 k^2,$$

where H_s is the applied magnetic field in the z direction, H_{ex} is the effective exchange field, l is the lattice spacing (of the order of 10^{-7} cm), and the other symbols have their usual meaning. The spin wave number k is $2\pi/\lambda_k$, with the wavelength λ_k being of the order of 10^{-5} cm for the spin waves of importance in the present discussion. Of course, the above expression for ω_k is not applicable for small values of k for which the magnetostatic modes become important.

Spin waves of high k number may become degenerate with the $k=0$ uniform precession. Because of thermal effects, there will be coupling between the uniform precession and the degenerate spin waves which will cause an increase in the line width even at low signal levels. At high signal levels, however, nonlinear coupling arises from the essential nonlinearity of the motion of the total magnetization vector. When the signal level exceeds a certain critical value, this coupling increases so that the amplitudes of the degenerate spin waves increase exponentially with time. The value of this critical rf magnetic field for circularly polarized signals is given by Suhl as

$$h_{crit}=\Delta H\left(\frac{2\Delta H_k}{M}\right)^{\frac{1}{2}},$$

where ΔH_k is the line width of the kth spin wave.

More recently, the above theory has been extended by Schlömann[4] and by Suhl,[5] and it now takes into account the scattering of the uniform precession at impurities and imperfections in the material. Thus, if the scattering decay constant η_{sc} becomes appreciable compared to the intrinsic decay constant η_0, then saturation effects at the main resonance can occur at rf field levels below the critical value given above. Theoretical curves of χ'' as a function of rf power are given by Suhl[5] for various values of the ratio of intrinsic to scattering decay constants.

II. EXPERIMENTAL METHOD FOR MAIN RESONANCE EFFECTS

As a check on the theory and as a guide for future work on the behavior of ferrites under high microwave signal levels, cavity experiments were performed on a single crystal spherical sample of manganese ferrite of 0.022-in. diam. The approximate composition of the sample was $Mn_{1.4}Fe_{1.6}O_4$ and its saturation magnetization approximately 3300 oe. The sphere was mounted on a quartz rod with a [110] axis along the rod. When the sample was rotated about this axis, the static field could be made parallel to the [100], [110], or [111] axis of the crystal.

A block diagram of the experimental setup is shown in Fig. 1. A tunable magnetron (Litton Industries Type 6543) was used as the microwave power source. This

* This paper is based on data obtained while the author was at the Bell Telephone Laboratories, Holmdel, New Jersey.
[1] R. W. Damon, Revs. Modern Phys. **25**, 239 (1953).
[2] N. Bloembergen and S. Wang, Phys. Revs. **93**, 1 (1954).
[3] H. Suhl, J. Phys. Chem. Solids **1**, 209 (1957).
[4] E. Schlömann, Bull. Am. Phys. Soc. **4**, 53 (1959).
[5] H. Suhl, J. Appl. Phys. **30**, 1961 (1959).

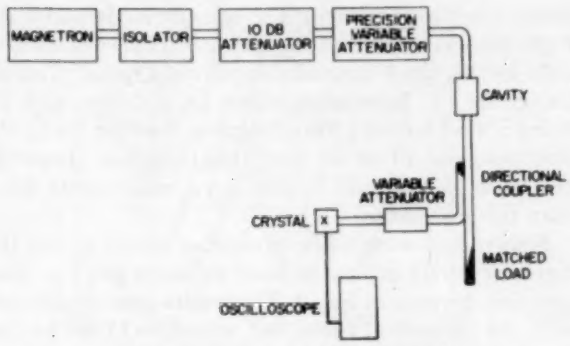

FIG. 1. Block diagram of experimental equipment.

was followed by a resonance isolator which eliminated reflections that might affect the magnetron frequency and output power. A fixed 10 db pad lowered the power level sufficiently (to 1.2 kw peak) to permit the use of a precision rotating vane attenuator (Hewlett-Packard) without fear of burnout. The ferrite sphere was placed in the center of a full wavelength transmission cavity having a loaded Q of 500. Part of the cavity output was fed to a crystal detector through a directional coupler and a variable attenuator. The crystal output was observed on a (Type 531 Tektronix) oscilloscope having a 10 Mc bandwidth.

The magnetron was operated at a pulse width of 0.8 μsec and at a repetition rate of 35 pulses per sec. This low repetition rate was used to prevent heating of the ferrite sample which might affect the results. The pulse was not flat-topped, but had a scalloped top with amplitude variations in the scallops of about 0.5 db. The rf power level input to the precision attenuator was measured by the usual water calorimeter technique.

Attenuation data on the ferrite sphere were taken as a function of applied dc magnetic field in the following manner. With zero applied field, the crystal detector output level was set at a fixed level on the oscilloscope. As the dc field was varied, the crystal output was kept constant by means of the precision variable attenuator. (It should be noted that in order to keep the power level constant at the ferrite sample, the variable attenuator must be placed before the cavity and not after the cavity.) The magnetic field was applied by a 6-in. Varian magnet and measured with a Numar nuclear resonance probe.

From the above measurements the value of μ'' can be computed as a function of the applied field by the use of the following equation in mks units:

$$\mu''=\frac{\mu_0}{4}\frac{V_c}{V_s}\frac{\lambda_g^2}{\lambda^2}\frac{1}{Q_L}\left(\frac{P_{\text{in}}}{P_{\text{in}}'}\right)^{\frac{1}{2}}-1,$$

where V_c=cavity volume; V_s=sample volume; λ_g =guide wavelength; λ=free space wavelength; Q_L =loaded Q of cavity; P_{in}=incident power with ferrite loss; and P_{in}'=incident power with no ferrite loss. For

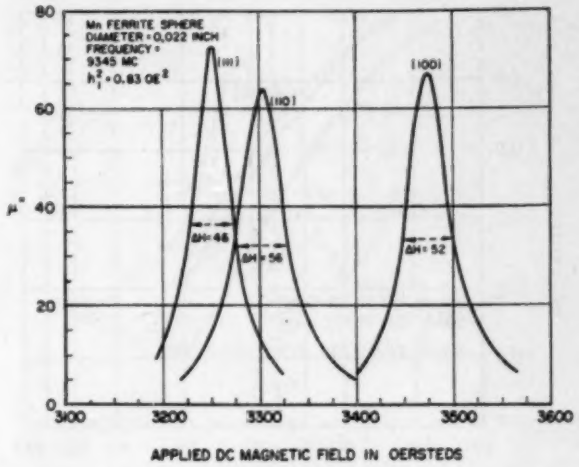

FIG. 2. Ferrimagnetic absorption lines for three crystalline orientations at a low-power level.

the cavity and sample used in this experiment, μ'' is given by

$$\mu''=110\left(\frac{P_{\text{in}}}{P_{\text{in}}'}\right)^{\frac{1}{2}}-1.$$

The magnitude of the microwave magnetic field at the ferrite sample is determined by the following equation:

$$h^2=\frac{P_{\text{diss}}Q_u}{\omega_0\mu_0(V_c/4)(\lambda_g^2/\lambda^2)},$$

where P_{diss}=power dissipated in cavity and Q_u=unloaded Q of cavity.

III. EXPERIMENTAL RESULTS ON MAIN RESONANCE

Figure 2 shows a plot of μ'' as a function of the applied field for three orientations of the ferrite sphere. The data were taken at 9345 Mc at a power level of several db below saturation with $h_1^2=0.83$ oe^2. Several interesting facts can be noted from these curves. First, the anisotropy field causes resonance to occur at different values of applied field for different crystal orientations so that the difference between H_{100} and H_{111} is 226 oe. Thus, K_1/M is -68 oe, where K_1 is the first order anisotropy constant. Second, the line widths for the three directions are not identical. For this sample the [111] line is the narrowest and the [110] line is the broadest. Dillon, Geschwind, and Jaccarino[6] reported different results on a $Mn_{0.98}Fe_{1.86}O_4$ ferrite sphere. Their results showed that the [100] line was the narrowest while the [111] line was the broadest. No theory is as yet available to explain the reason for the different line widths obtained in different crystal orientations.

Furthermore, we note that the maximum value of μ'' for the [111] line is 72, agrees with simple theory which predicts a value of $(M/\Delta H)=(3300/46)=72$. The products of μ'' and ΔH should be constant for all orienta-

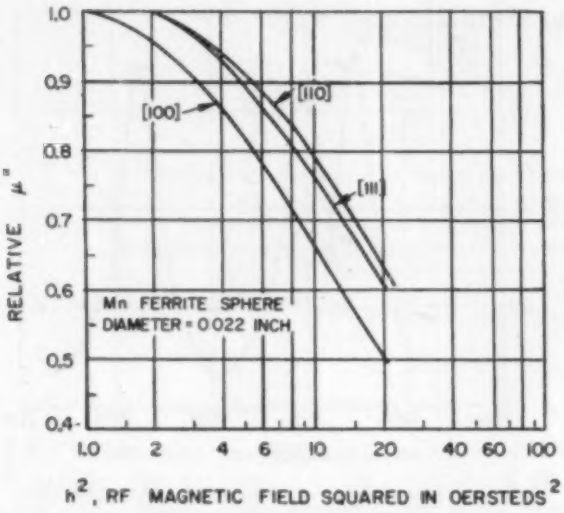

FIG. 3. Variation of normalized susceptibility with power level.

tions of the crystal. In this experiment these products are constant to better than 10%.

As the signal level is increased beyond a certain power point, the maximum value of μ'' drops. Figure 3 shows a plot of normalized μ'' as a function of the square of the microwave magnetic field. Although data were taken for power levels with h^2 as high as 83 oe^2, the curves in Fig. 3 are plotted only to $h^2=20$. For higher power, various unusual effects were noted which, as shown later, make a maximum μ'' determination of questionable validity.

As a check of the foregoing data against Suhl's theory, a plot was made of μ''/μ_0'' as a function of P/P_c, where P_c is a "critical" power level chosen so as to give a best fit with one of Suhl's[5] saturation curves. The experimental results are shown in Fig. 4 together with the theoretical curve for a ratio of intrinsic to scattering decay constants of zero. The agreement between the experimental points and the theoretical curve is remarkable for all three orientations of the crystal. The P_c values for the three orientations are different with h_c^2 being 5.9 oe^2 for the [100] direction, 9 oe^2 for the [111] direction, and 10 oe^2 for the [110] direction. However, no choice of P_c would fit any η_0/η_{sp} value curve other than the zero curve.

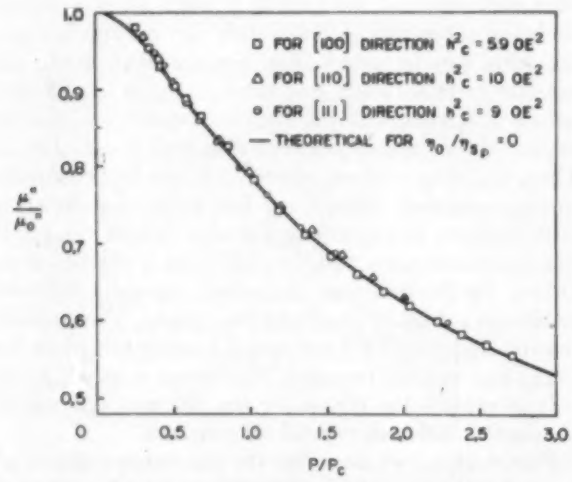

FIG. 4. Variation of normalized susceptibility with normalized power level. The power level has been normalized with respect to the "critical" power level.

Similar data were taken on another sphere of half the diameter (0.011 in.) taken from the same boule as that used for the data of Fig. 4. These data also agreed well with the theoretical curve, but with $h_c^2=11$ oe^2 for the [100] direction and $h_c^2=14$ oe^2 for the [100] and [111] directions. No explanation is as yet available for the variation of P_c with orientation.

Another interesting effect is shown in Fig. 5, which is a plot of the dc magnetic field required for resonance (defined as the field at which μ'' is at a maximum) as a function of power level. For all crystalline orientations there is a general tendency for the required field to increase with increasing power level. This effect and the resulting asymmetry in line shape has been tentatively explained in a previous publication[6] as caused by a variation in g factor with spin temperature.

Figure 6 shows plots of μ'' as a function of applied field for the three crystal orientations and for various high power levels. All of these curves are given in detail because they reveal a variety of unusual effects and there is no guide available to determine what are the essential data in these curves. Thus, one notes that for power levels sufficient to give an h^2 of 8.3 oe^2 or higher [Figs. 6(a) to 6(c)] the asymmetry referred to above becomes apparent, with the high field side dropping more rapidly than the low field side. At still higher power levels, with an h^2 of 33 oe^2 and higher, an unstable

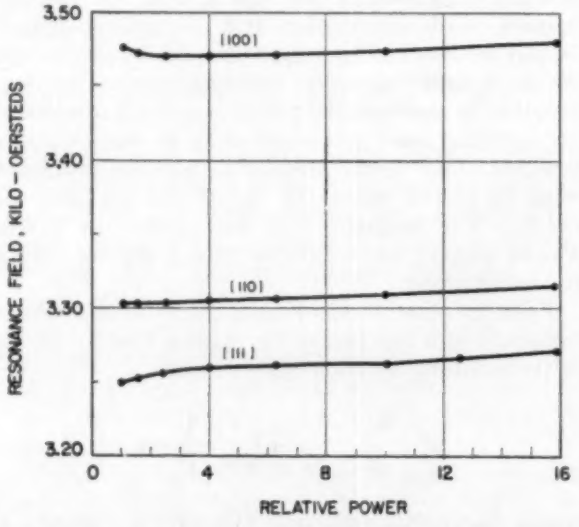

FIG. 5. Dc magnetic field required to produce ferrimagnetic resonance with increasing power level.

[6] M. T. Weiss, J. Appl. Phys. 30, 2014 (1959).

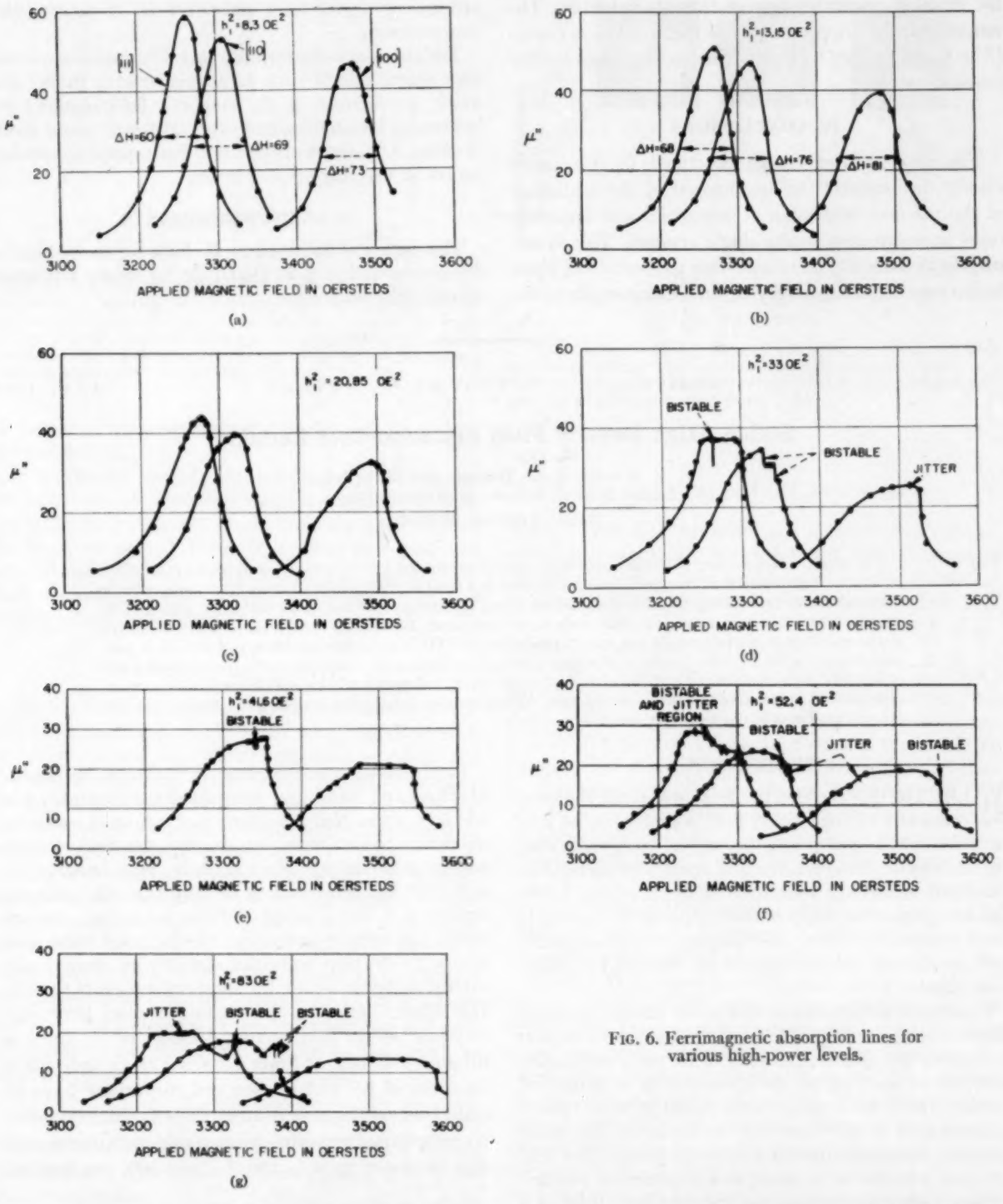

FIG. 6. Ferrimagnetic absorption lines for various high-power levels.

situation arises as seen in Figs. 6(d) to 6(f). Over a wide range of fields, the output pulse from the cavity shows a pronounced jitter, while at certain critical fields and power levels the ferrite absorption appears to have two different values so that two pulses of different heights are observed simultanously on the oscilloscope. This denotes an instability in the ferrite and is so recorded on the curves. The curves for the [100] direction show the least amount of this instability while the [111] direction is most susceptible to this instability. This effect is probably related in a general way to that described in earlier papers,[6,7] but more work is required

[7] M. T. Weiss, Phys. Rev. Letters **1**, 239 (1958); and J. Appl. Phys. Suppl. **30**, 146S (1959).

for detailed understanding of these instabilities. The remarkable flat-topped nature of the absorption curves [Fig. 6(g)] at very high power levels also needs further investigation.

IV. CONCLUSIONS

The experimental results described in this paper clearly demonstrate the importance of the scattering of the uniform precession at impurities and imperfections in manganese ferrite single crystals. This in not surprising since these crystals were grown by the flame fusion process. The validity of the Suhl analysis of the saturation of the main resonance is, of course, also demonstrated.

The above experiments also reveal various unexpected high power effects such as an asymmetry in the line shape, an increase in the magnetic field required for resonance, bistabilities and jitter arising at power levels of about 5 db above critical, and flat-topped absorption curves at very high power levels.

V. ACKNOWLEDGMENTS

The author is indebted to H. Suhl for many helpful discussions and to J. F. Dillon, Jr. for kindly supplying several oriented spheres.

JOURNAL OF APPLIED PHYSICS VOLUME 31, NUMBER 5 MAY, 1960

Stable, High Density Field Emission Cold Cathode*

E. E. Martin, J. K. Trolan, and W. P. Dyke
Linfield Research Institute, McMinnville, Oregon
(Received October 28, 1959)

The practical application of the field emission electron source has heretofore been impeded by insufficient reliability. Instability (i.e., changes in emitted current at a fixed applied voltage) results from changes in the cold cathode surface associated with contamination and sputtering. The cold clean cathode is shown to be electrically stable at dc emission densities up to 10^7 amp/cm^2. Techniques are discussed which permitted stable operation of a single needle tungsten cathode during 1000 hr at an average beam power of 35 w (corresponding to a beam power density of 35 billion w per unit cathode area). A simple method is described which permits reconditioning of the cathode surface when required, and apparently extends life indefinitely; operating periods in excess of 12 000 hr are reported. An explanation is suggested for the small, gradual residual changes observed in the emitted current.

INTRODUCTION

ELECTRONS are emitted from metals in the presence of a strong electric field, a process called field emission which has properties suited to several electronic devices[1]; however, the field emitter has heretofore exhibited insufficient reliability for applications. In the present paper the smooth clean cathode is shown to have electrical stability and longevity; contamination and sputtering are recognized as sources of earlier difficulties.

Improved environments described herein have enabled a cold, microscopic, needle shaped field emitter to yield stably a current density of 10^7 amp/cm^2 during 1000 hr of unattended dc operation in a sealed off vacuum tube. An average beam power of 35 w from a cathode area of 10^{-9} cm^2 can be exploited for either extreme miniaturization or very high power. The field emission gun can be as small as a hypodermic needle[1]; a related emission process has recently been used in a 300 megawatt flash x-ray tube.[2]

Field emission was discovered in 1897 by R. W. Wood.[3] Millikan and Lauritsen[4] recognized the dependence of stability upon high vacuum, and achieved sufficient reliability to determine empirically the field current-voltage relationship. More recently, field emission microscopy[5] has been used to identify the clean emission surface and conventional electron microscopy has revealed the emitter geometry. Haefer[6] used these techniques to develop sufficient stability to draw stable current densities up to 10^6 amp/cm^2 for short periods. The application of pulse techniques and very high vacuums[7] led to field current densities of the order of 10^8 amp/cm^2 and, at lower densities, to cathode life of the order of 100 hr.[8] Elinson and co-workers[9] have investigated ion trapping in an attempt to obtain stability at conventional pressures; while stable operating periods were increased by a factor of about 100, the reported

* This work was sponsored by ARDC, United States Air Force, through The Electronic Components Laboratory, Wright Air Development Center.

[1] W. P. Dyke, Proc. Inst. Radio Engrs. 43, 162 (1955); IRE Trans. on Military Electronics, MIL-4, 38–45 (1960).

[2] F. J. Grundhauser, *et al.*, paper presented at Field Emission Symposium, 1959 (to be published).

[3] R. W. Wood, Phys. Rev. **5**, 1 (1897).

[4] R. A. Millikan and C. C. Lauritsen, Proc. Natl. Adac. Sci. (U.S.) **14**, 45 (1928).

[5] E. W. Müller, Z. Physik **106**, 541 (1937).

[6] R. H. Haefer, Z. Physik **116**, 604 (1940).

[7] R. T. Bayard and D. Alpert, Rev. Sci. Instr. **21**, 571 (1950).

[8] W. P. Dyke and W. W. Dolan, *Advances in Electron Physics*, **8**, 89 (1956).

[9] M. I. Elinson, V. A. Gor'kov, and G. F. Vasiliev, Radiotekh. i. Elektron **2**, 205 (1957).

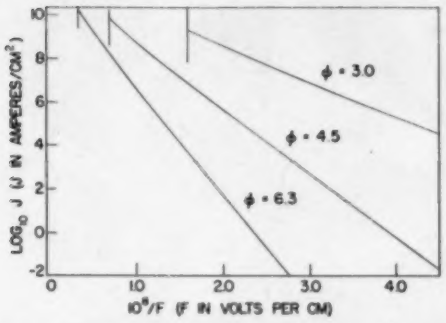

FIG. 1. Graph of the modified Fowler-Nordheim equation for field emission, showing field current density J as a function of applied surface electric field F, for several values of the work function ϕ in ev. The vertical line at the upper end of each curve corresponds to a field sufficient to lower the top of the surface potential barrier down to the Fermi level.

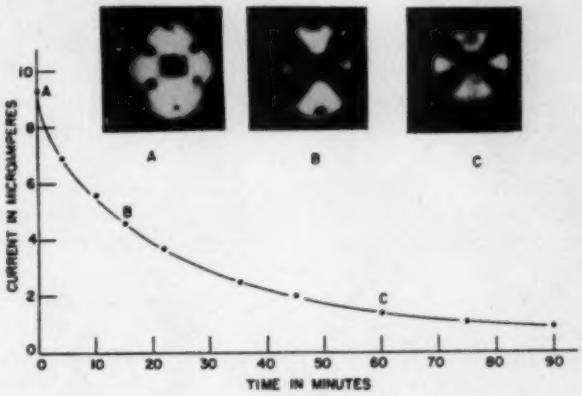

FIG. 2. A graph showing decrease of emission current with time at constant voltage when work function is increased by adsorption of an electronegative gas such as oxygen; emission patterns show preferential adsorption on different surfaces.

performance was considerably less than that required in most devices.

In the present work, further improvements in vacuum are combined with ion and electron trapping to yield the stability mentioned above together with emitter life in excess of 12 000 hr. It appears that sufficient stability and life are thus available for several applications including a new tetrode structure which will amplify microwave signals.[10]

CAUSES OF INSTABILITY

The term "electrical stability" is used herein to describe the condition in which the relationship between field current and applied voltage remains essentially unchanged with time. It will be helpful first to examine the causes of instability (i.e., effects which alter the current-voltage relationship), and then to note how such effects may be reduced or avoided.

Field emission instability usually arises through changes in two variables on which the electron current density has a sensitive dependence, namely ϕ, the work function of the emitting surface, and β, a geometric factor having units of cm^{-1} and defined as the ratio of the electric field F at the cathode to the applied potential V. An indication of the dependence of this ratio on the electrode geometries can be gained from the expression[11]

$$\beta = 2[r \ln(4R/r)]^{-1}, \qquad (1)$$

which is based on the approximation of the field emitter geometry as a hyperboloid of revolution. Here r is the emitter tip radius, and R is the anode to cathode spacing, both in cm. The importance of ϕ and β is seen in the following variation of the Fowler-Nordheim equation expressing the emission current density J at zero or low temperature[12,13]:

$$J = (K_1\beta^2V^2/\phi)\exp[-K_2\phi^{3/2}f(y)/\beta V], \qquad (2)$$

where K_1 and K_2 are constants, V is the applied voltage, and $f(y)$ is an elliptic function which takes account of the image force. A good treatment of the theory leading to this relationship is given by Sommerfeld and Bethe,[14] and tables of current density as a function of F and ϕ have been published by Dolan.[15]

Figure 1, which presents a graph of Eq. (2), further illustrates the strong dependence of current density on β and ϕ. For a typical field strength of 5×10^7 v/cm and a work function of 4.5 ev (the central region of the figure), a 1% change in β results in about a 15% change in J, ϕ and V remaining constant. For the same field and work function, a 1% change in ϕ results in a change of about 20% in J, β and V remaining constant. Clearly, both ϕ and β must be carefully controlled in order to stabilize the emission mechanism described by Eq. (2). In the present work, stability was achieved by holding the ratio $\phi^{3/2}/\beta$ constant by maintaining a clean smooth cathode surface of constant configuration.

Changes in the work function of metal surfaces caused by the adsorption of various contaminants are well established. Sources of such contaminants are residual gases, materials adsorbed on electrode surfaces, decomposition products formed at tube envelope surfaces during electron bombardment, etc. The corresponding rate of contamination observed during operation of a field cathode is large at conventional tube pressures, e.g., 10^{-7} mm of Hg. In fact, even in tubes having very low static residual gas pressures, contamination may occur when an electronic discharge is drawn from the cathode. A typical example of instability arising from changes in

[10] F. M. Charbonnier, J. E. Henderson, and W. P. Dyke (to be published).
[11] C. F. Eyring, S. Mackeown, and R. A. Millikan, Phys. Rev. **31**, 900 (1928).
[12] R. H. Fowler and L. W. Nordheim, Proc. Roy. Soc. (London) **A119**, 173 (1928).
[13] L. W. Nordheim, Proc. Roy. Soc. (London) **A121**, 626 (1928).
[14] A. Sommerfeld and H. Bethe, *Handbuch der Physik* (Springer-Verlag, Berlin, Germany, 1933), Vol. XXIV, Part 2, p. 441.
[15] W. W. Dolan, Phys. Rev. **91**, 510 (1953).

emitter work function is shown in Fig. 2. The current-voltage relationship and emission patterns were observed during the operation of a conventional diode electron projection tube consisting of a needle shaped tungsten cathode at the center of a hemispherical aluminized phosphor anode. Localized changes in cathode work function, caused by the selective adsorption of electronegative gas such as oxygen, resulted in changes in the emission pattern and a decrease of total current with time.

Changes in β are also frequently observed in practice. At the highly curved field emitter, both strong surface forces and large opposing electrostatic forces are present, so that deformation of the surface is possible when energy is added. The deformation may merely alter the current-voltage relationship, as for example when a heated cathode is dulled in the absence of electrostatic forces, or it may also lead to a destructive vacuum arc[16] when increasing surface roughness causes localized increases in β and, correspondingly, excessive values of current density.[17]

A common deformation mechanism is surface migration[18] which is appreciable at intermediate temperatures for tungsten emitters of conventional size. The time rate of change of length dz/dt of a small projection of length z and tip radius r is given by

$$dz/dt=\frac{-\Omega_0^2\,\Delta_0\exp(-Q/RT)}{A_0\qquad r^2kT}\left[\frac{\gamma}{r}-\frac{F^2}{8\pi}\right], \qquad (3)$$

where Ω_0 is the atomic volume in cm³/atom, γ is the surface tension in d/cm, A_0 is the surface area in cm²/atom, Δ_0 is the diffusivity constant in cm²/sec, Q is the activation energy in cal/mole, T is the temperature of the projection in °K, and F is the applied electric field in v/cm.[19] At the field strengths needed for appreciable emission, and with tungsten emitters of conventional size (i.e., $F>3\times10^7$ v/cm and $r>3\times10^{-6}$cm), the term in brackets is negative; hence dz/dt is positive and a surface projection tends to grow outward or extrude when either the temperature is high enough to cause appreciable surface migration or when surface atoms gain energy from ionic bombardment. It is observed that extrusion usually increases β, and hence current density at a given voltage; this in turn may further increase the emitter temperature through such processes as resistive heating and bombardment by ions formed in the residual gas. The process is thus regenerative, leading to further increases of both the extrusion rate and current density and ultimately to a low impedance vacuum arc and cathode damage. It is convenient to refer to this process as extrusion breakdown.[20]

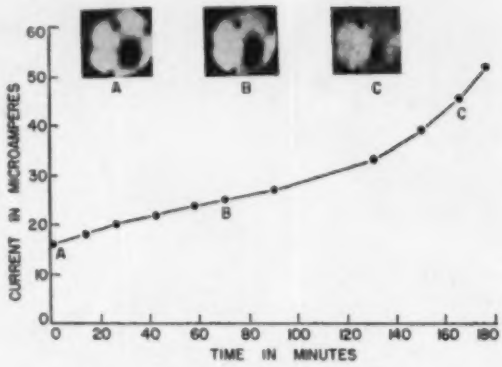

FIG. 3. A graph showing the increase of emission current with time at constant voltage, attributed to cathode sputtering by helium ions.

Extrusion breakdown can be initiated when sufficiently large surface projections are formed by cumulative cathode sputtering. This occurs for example when energetic helium ions impinge on the cold tungsten surface in the presence of a high field, a phenomenon which is commonly observed in tubes having envelopes of Corning 7740 Pyrex glass, or other similar glasses, and results from diuffsion of helium from the atmosphere. Figure 3 illustrates effects which can be attributed to this mechanism. At a constant applied voltage, emission from the smooth, clean cathode (at A) is stable except for a gradual increase of current with time which is accompanied by changes in the emission pattern (as at B and C). Small areas develop (bright spots) at which current density is increased by several orders of magnitude as estimated from emission pattern analysis. When the current increase exceeds about a factor of five, the current-voltage relationship usually fluctuates erratically and cathode damage is likely. Sudden current decreases are accompanied by the disappearance of the brightest spots whose corresponding surface projections are presumably "burned off" during localized vacuum arcs initiated by resistive heating. The criteria which determine whether such an arc merely removes the initiating projection or spreads to the entire emitting tip have not been fully determined.

In experiments with a tube having a Corning 7740 glass envelope which was sealed off with an ion gauge, the relative time rate of increase of the current at fixed voltage was found to be proportional to helium pressure and approximately to the current level, as may be seen in Fig. 4 which presents data taken in the range $10^{-8}<p<10^{-6}$ mm Hg, $10^{-7}<I<5\times10^{-5}$ amp. Insta-

[16] W. P. Dyke, *et al.*, Phys. Rev. **91**, 1043 (1953).
[17] W. W. Dolan, W. P. Dyke, and J. K. Trolan, Phys. Rev. **91**, 1054 (1953).
[18] J. L. Boling and W. W. Dolan, J. Appl. Phys. **29**, 556 (1958).
[19] J. P. Barbour, F. M. Charbonnier, W. W. Dolan, W. P. Dyke, E. E. Martin, and J. K. Trolan, Phys. Rev. **117**, 1452 (1960).

[20] Extrusion is complicated by the dependence of surface migration on crystallographic detail, a fact which is ignored in Eq. (3) without serious effect on the foregoing generalization. In practice, extrusion leads to a polyhedral cathode form whose planes are crystal surfaces with low Miller indices. β is increased at the ridges formed by the intersections of these planes, leading as before to extrusion breakdown.

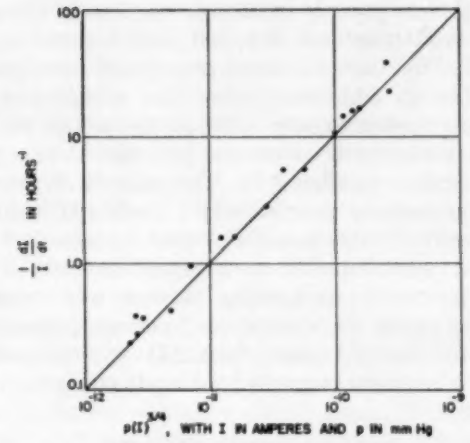

FIG. 4. A graph of the relative time rate of change of field emission current at fixed voltage as a function of the partial pressure of helium within the tube and emission current level; the solid line graphs the empirical equation $I^{-1}dI/dt=10^{11}p(I)^{\frac{3}{4}}$. (Pressure values are equivalent nitrogen pressure.)

bility was appreciable at pressures as low as 10^{-9} mm of Hg, a pressure which is supplied by the diffusion of helium from the atmosphere in a period less than 1 hr in a one liter sealed envelope made of Corning 7740 Pyrex glass.[21] Although ionic pumping helpfully reduced the helium pressure, it was not found adequate to maintain stability in such envelopes.

EXPERIMENTAL METHODS

Envelope Material

The diffusion of atmospheric gases into the tube envelope was effectively reduced at room temperatures by use of high density glass selected on the basis of data given by Norton,[22] which identifies a number of glasses having helium permeation rates several orders of magnitude lower than that of Corning 7740 Pyrex. In the present series of tests, both Corning 0120 lead glass and Corning 1720 alumino-silicate glass were satisfactory in this respect. However, the latter material is considerably superior for ultra-high vacuum work for two reasons: first, the rate of release of gas from the heated glass is very low as compared to that from alternate glasses[23]; and second, its annealing point of 712°C makes possible high bakeout temperatures. Except where otherwise noted, all tests reported herein were in tubes having envelopes of this material. Some difficulty was initially experienced with fabrication of envelopes and electrical inseals from the alumino-silicate glass; however, it was found that it could be satisfactorily sealed to molybdenum leads and, if thoroughly clean and free of fingerprints, could be readily worked in a slightly reducing hydrogen-oxygen flame. Detailed procedures for working alumino-silicate glass of different manufacture have been outlined and are generally applicable to the above material.[24]

Evacuation

Experimental tubes were sealed off following evacuation with a three stage, 70 liters/sec, all glass mercury diffusion pump with liquid nitrogen traps. Metal electrodes were fabricated from molybdenum or tungsten and during evacuation were heated to a temperature of approximately 2000°C until a pressure of the order of 10^{-9} mm Hg could be maintained while the metal was hot. The glass was baked and the metals were heated alternately. Satisfactory evacuation of alumino-silicate glass envelopes was achieved using both 500° and 650°C oven temperatures. During the latter treatment, the tubes were contained in a stainless steel muffle filled with nitrogen derived from the boiling liquid. Such an atmosphere protected the exposed portions of the molybdenum leads from excessive oxidation and was found to be almost completely free of helium. The resultant low level of dissolved helium in the envelope walls reduced the subsequent diffusion of that gas into the tube when the envelope became heated during either post-seal-off heating of electrodes or operation of the tube at higher power levels. In most cases evacuation was continued for periods as long as 50 or 100 hr; however, equivalent results can probably be achieved in a much shorter period if glass and metal are treated simultaneously insofar as possible and if bake periods are not unnecessarily prolonged.

Pressure prior to seal-off was in most cases at or below the x-ray limit of a Bayard-Alpert type ionization gauge, i.e., of the order of 10^{-10} mm Hg. The pressure increased momentarily to 10^{-8} mm at the instant of seal-off, but returned to the lower value thereafter. Gettering by evaporation of titanium from a previously degassed filament and brief heating of the electrodes established the final environment. In most cases no change in the electrical characteristics of initially clean tungsten field emitters was observable after inoperative shelf periods of 1000 hr or more. A conservative estimate of residual pressure of chemically active gas based on kinetic theory reveals that the static pressure could not have exceeded 10^{-13} mm Hg during that period. Absence of pronounced sputtering of the cathode during prolonged operation, as reported later herein, indicates that the partial pressure of inert gases was similarly low.

Tube Design

Although some work was done in more complex structures, as for example in field emission tetrodes, the stability tests reported herein were made in simple diodes employing well outgassed metal anodes and some form of secondary electron trapping to inhibit bombardment of envelope surfaces.

In tubes of the type shown schematically in Fig. 5

[21] D. Alpert and R. S. Buritz, J. Appl. Phys. **25**, 202 (1954).
[22] Francis J. Norton, J. Appl. Phys. **28**, 34 (1957).
[23] B. J. Todd, J. Appl. Phys. **27**, 1209 (1956).
[24] M. Hillier and R. L. Bell, British J. Appl. Phys. **9**, 94 (1958).

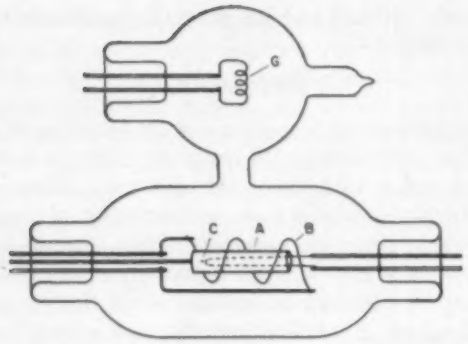

FIG. 5. Schematic diagram of experimental field emission diode tube which provides electrostatic trapping of secondary electrons. Envelope of Corning type 1720 glass; *A*, tungsten anode; *B*, bombardment filament; *C*, cathode; *G*, getter.

secondary electron trapping was achieved through use of a coaxial anode-cathode configuration in which secondary electrons were returned to the anode by the radial electric field between the cylindrical anode skirt and the emitter support filament. The effectiveness of such trapping can be estimated by calculation of electron trajectories. In the present series of tests anodes having a length to diameter ratio of approximately five were used, a configuration which insured that even those elastically deflected primary electrons having optimum direction for escape interacted a minimum of three times with the anode. Envelope bombardment is believed to have been reduced by about four orders of magnitude from that which would have occurred if a planar anode had been used.

A second tube was developed to provide similar electron trapping with an additional provision to view the emission pattern periodically in order to judge the condition of the emitter surface; the electrode configuration and typical electron trajectories for this tube are illustrated in Fig. 6. The anodes consisted of two parallel 5-mil tungsten plates each 3×5 cm and spaced 2 cm apart. The field emitter was placed midway between the plates with the emitter axis normal to an aluminum backed willemite phosphor screen. During prolonged periods of operation, a one kilogauss magnetic field supplied by a permanent magnet constrained the electrons to helical paths which terminated near the midpoints of the plates and inhibited secondary electron bombardment of the envelope walls. The use of a magnetic field also led to reduced bombardment of the cathode by anode formed ions. The emission pattern could be viewed at will by removing the magnetic field.

Instrumentation

Stability was judged on the basis of the current response at a fixed value of the applied voltage during both steady state and pulsed operation. The sensitivity of field current to small changes of either ϕ or β has been previously noted; since current was similarly sensitive to the value of the applied voltage, several precautions were taken to prevent its fluctuation. Steady voltage in the kilovolt range was supplied from a power supply controlled by a series array of gaseous voltage regulator tubes. As an additional precaution, a Sola constant voltage transformer was used in the ac circuit and output voltage was monitored periodically as a safeguard against possible drift. The emitted dc currents were continuously recorded with a Leeds and Northrup Speedomax G chart recorder. Pulsed voltages of 1 μsec duration were supplied at a repetition rate of 120 pulses/sec by a pulseforming network with resonant charging. Both the current and voltage pulses were monitored by Tektronix type 511 oscilloscopes. A Sorensen regulator controlled the input voltage of these circuits.

EXPERIMENTAL RESULTS

First, it may be of interest to note the general effect of electron trapping on emitter stability which was demonstrated by the following simple experiment. Two nearly identical emitters were operated in the same Corning 0120 glass envelope, which contained a tubular molybdenum anode, closed near one end by a partition as shown in Fig. 7. The emitters were so positioned, one inside and one outside the anode enclosure, that the entire primary emission of each would fall on the corresponding and opposite sides of the partition; thus they were presumably exposed to the same anode conditions but to different sources of ions and gas at other surfaces since secondary electrons were trapped in one case and not in the other. Figure 8 compares the stability observed during the independent operation of the enclosed emitter (curve *A*) and the exposed emitter (curve *B*), i.e., emission was drawn first from one and then from the other. Curve *C* displays data from the enclosed emitter which was taken at the same time that its companion was yielding curve *B*, i.e., both emitters were operated simultaneously. It is seen that the current from the enclosed emitter was, in both cases, relatively stable while that from the external emitter decreased rapidly. These data illustrate the improvement of field emission stability by use of electron trapping.

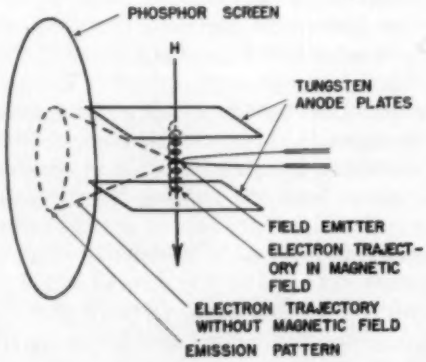

FIG. 6. Schematic diagram of electrode configuration and electron trajectories in magnetically switched tube, which allows optional viewing of the emission pattern.

Second, even in the presence of electron trapping, there are apparently residual mechanisms which affect the emitter stability at a lower rate and over a longer time period; the data may be used to identify and evaluate such residual mechanisms. Figure 9 presents typical data obtained from fixed voltage operation of electrostatically trapped field cathodes in tubes of the type shown in Fig. 5. The data are presented in semilogarithmic form in order both to compare performance over a wide range of currents and to relate the current changes to the ratio $\phi^{3/2}/\beta$ on which they depend exponentially in view of Eq. (2). These data are characterized by a small initial current increase of short duration followed by a long period of essentially stable operation during which the current gradually decreased in some tubes and increased in others. The behavior of a given tube was reproducible, i.e., its operation could be repeated after cleaning the emitter by momentarily heating it to 2000°C; similar behavior was also noted over a wide range of currents.

However, in a given tube, the rate of change of current was usually found to depend directly on the average current during both the initial transient and the later gradual change, provided that the anode temperature was less than about 1000°C, i.e., when the power was limited to a level of 5 to 10 w in tubes of the type shown in Fig. 5. This observation led to the assumption that the rate of arrival of foreign material at the cathode of a given tube was proportional to the emitted current. This suggests two possible mechanisms: ionization of residual gas and release of surface material by electron bombardment through a momentum transfer process. The following experiment was performed to evaluate the relative contributions of these mechanisms.

Two emitters were mounted in a field emission microscope tube having an aluminum backed willemite phosphor anode. During operation of the tube both

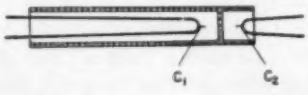

FIG. 7. Schematic diagram of anode used in experimental tube to determine the effectiveness of electrostatic trapping of secondary electrons by comparing the stability of cathodes C_1 and C_2.

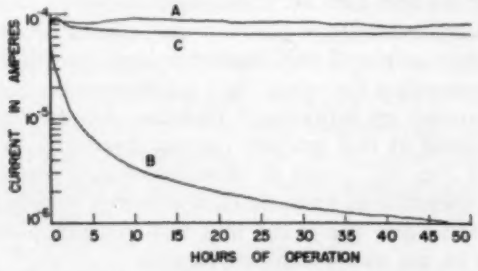

FIG. 8. Comparison of the operation of the enclosed emitter C_1 of Fig. 7, curve A, with that of the exposed emitter C_2, curve B; curve C shows performance of C_1 during simultaneous operation of C_2.

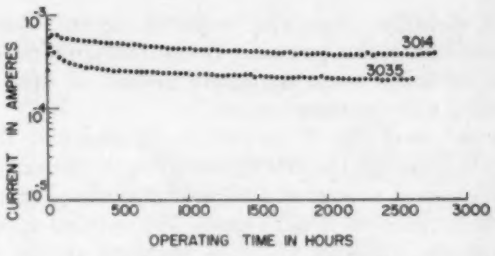

FIG. 9. Graphs of the current emitted at fixed voltage in two test diodes of the type shown in Fig. 5.

emitters were equally exposed to contaminants originating at the anode; however, one emitter was subject to bombardment by ions formed in the residual gas while the other was relatively isolated from such bombardment. By a proper choice of emitter radii, and hence electric field strengths at a common voltage, one emitter could be operated while the other, although also cathodic, was quiescent. During the test the smaller cathode was operated and its current-voltage relationship was continuously monitored; the larger cathode was quiescent, except during brief intervals when current was drawn to check its characteristics. For that purpose the sharper emitter was electrically connected to the anode and the voltage was increased. Because of the configuration of the electric field in the vicinity of a needle-shaped emitter, only ions formed near the needle axis follow trajectories which terminate on the emitting portion of the needle and thus affect subsequent emission. In view of the divergence of the electron beam and the decrease in ionization probability with increased electron energy, the majority of such ions originate near the electron source. Thus, the quiescent needle was considerably less subject to bombardment by ions formed in the gas than the emitting needle, resulting from the use of an inter-emitter spacing which was large compared to the emitter dimensions. Figure 10 indicates that the two emitters exhibited

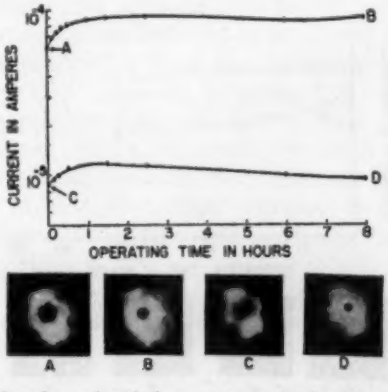

FIG. 10. Graphs and emission patterns obtained from two emitters held at the same voltage in a common tube; upper curve (A to B) was obtained during operation of the smaller tip while the lower curve (C to D) was obtained by periodic monitoring of the normally nonemitting larger tip.

similar stability; thus, the observed current changes were apparently due primarily to contaminants arriving at the cathodes from the anode instead of from the residual gas in the tube.

The curves of Fig. 10 are sufficiently similar to those of Fig. 9, although the rate of change in the former case is much higher, to suggest that similar mechanisms may have been involved in both cases. The mottled appearance of the emission patterns obtained during the present test indicated that the surface was roughened by ionic bombardment (note the similarity to the patterns from the sputtered emitter shown in Fig. 3). That this was indeed the case was confirmed by a second experiment during which one needle was, except for periodic monitoring, maintained at anode potential. The curves and patterns obtained during this test are shown in Fig. 11; the behavior of the emitting tip was essentially the same as before, while both the emission pattern and current-voltage relationship for the non-emitting needle underwent changes characteristic of adsorption of electronegative gas (note the similarity to Fig. 2). Thus, in this tube and probably in the metal anode tubes which yielded the curves of Fig. 9 as well, both sputtering and adsorption processes were active at the emitting surface. Therefore, both neutral and ionized material appear to have been released during electron bombardment of the anode. It is interesting to note that the relative effects caused by these two constituents remained essentially constant over long periods of time, over an appreciable range of current, and furthermore, apparently did not vary greatly between different anode surfaces.

The electrical stability of cold tungsten emitters in electro-statically trapped tubes was also studied during pulsed operation. Curve *A* of Fig. 12 describes 5000 hr of operation at a peak current of approximately 45 ma from a single needle at an applied voltage of 17.1 kv. The overall rate of current drift during this test did not exceed 1%/100 hr. Curve *B* shows the similar operation of another single needle emitter at a pulsed current in the order of 100 ma and an applied voltage of 24.9 kv. An over-all current drift at the rate of 3%/100 hr was observed in this case and the test terminated with failure of the cathode after 850 hr of operation. The reason for this failure has not been established; however, the pulsed current density in both of these tests was of the order of 10^7 amp/cm², i.e., approaching the resistive heating limit for tungsten emitters of this size. The curves of Fig. 11 show random current variations of the order of 10%, superimposed on the systematic drift. It is felt that these variations are not related to changes in $\phi^{3/2}/\beta$, but rather to small fluctuations in applied voltage (less than 1% voltage fluctuation would account for the observed current fluctuation). The limited accuracy of the voltage measurement by oscillographic techniques did not allow this assumption to be verified.

In more recent tests with magnetically switched tubes, having the electrode configuration shown in Fig. 6, a further increase in the milliampere hours of unattended operation has been observed during dc operation. Figure 13 shows the observed current during two 1000 hr tests of such a tube at two different fixed levels of applied voltage. The tungsten emitter used in these tests had a terminal radius of approximately 1.5×10^{-5} cm, hence, an emitting area of approximately 7×10^{-10} cm²; an average current of 7.5 ma was emitted during the first 1000 hr. This corresponded to an emission current density of 10^7 amp/cm², a level which was heretofore achieved only during pulsed operation[25]; it also approaches the upper limit set by resistive heating and vacuum arc initiation.[16] Emission pattern changes were noted at this extreme current density as can be seen in Fig. 13, A and B. However, during the subsequent operation at 2 ma, the current varied by only 10% in 1000 hr and the initial and final pattern pictures, C and D, are nearly indistinguishable.

The greatly improved performance observed in magnetically trapped tubes has not yet been completely

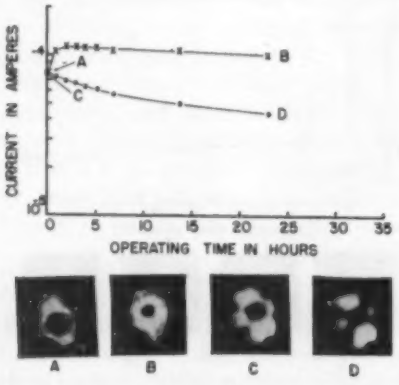

FIG. 11. Graphs and emission patterns obtained with the same tube as in Fig. 10 but with the larger emitter held at anode potential. (*Note.* on the vertical axis, the upper coordinate should read 10^{-4} instead of -4.)

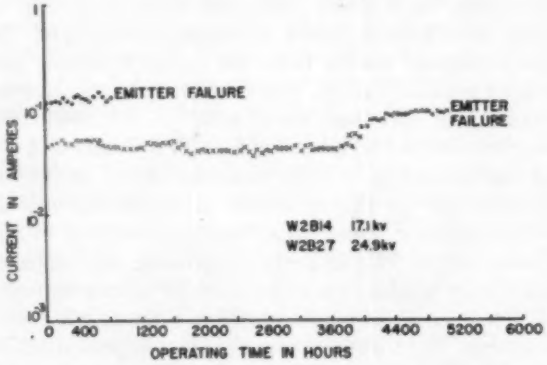

FIG. 12. Graphs of the pulse currents obtained during pulsed operation of tungsten emitters in tubes of the type shown in Fig. 5; micro-second voltage pulses of fixed magnitude were applied at a repetition rate of 120 pps.

[25] W. P. Dyke and J. K. Trolan, Phys. Rev. 89, 799 (1953).

explained; however, the following generalizations can apparently be made: increased anode area led to improved heat dissipation; increased anode to cathode distance (by about a factor of 4) led to decreased probability of neutral material reaching the tip from the anode, and the combined influence of magnetic and electric fields apparently reduced the incidence of ions on the emitting surface. The latter effect is also assumed to have accounted for the reduced initial transient current increase which was reported earlier in the curves of Fig. 9.

Thus, the unattended operation of the cold field emission cathode has been extended to a level of approximately 10^4 ma-hr (Fig. 13); however, the useful life of the cathode is much longer. The initial cathode condition may be restored and the operation repeated when the cathode is resmoothed and cleaned by heating

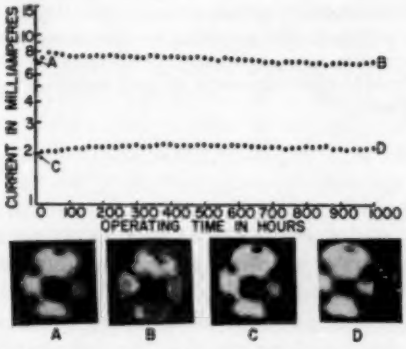

FIG. 13. Graphs and emission patterns obtained during fixed voltage operation of a magnetically switched tube having electrodes as shown in Fig. 6.

it briefly at say 2000°K. Contaminants are evaporated and roughness is smoothed by surface migration during a heat flash of a msec duration which can be supplied by discharging a condenser through the cathode support filament. Provided that the period of heating is short, the reconditioning may be done without interrupting the electron emission; surface migration is preferential at small projections, which can be smoothed in a time short compared with that required for buildup, i.e., the deformation of the heated tip by electrostatic forces.[2] By periodic reconditioning, cathodes have been operated for periods up to 12 000 hr without any indication of a limit on further operation. It is probable that the actual cathode life is much longer than any period yet reached. Clearly, this observed longevity of the field emitter is due at least in part to its ability to yield useful currents at low temperatures where a number of

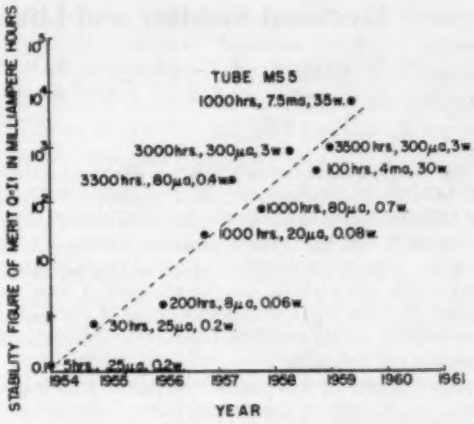

FIG. 14. Improvement with time of the stability figure of merit $Q=It$ for a single needle cold field cathode operated dc at fixed applied voltage. I is the dc emitted current, and t is the period of continuous operation without cathode reconditioning. The cathode current density in tube MS 5 exceeds 10^7 a/cm². The rate of progress over the past 5 years has been exponential with a time constant of $\frac{1}{3}$ year.

disturbing mechanisms are minimized, e.g., chemical changes, transport mechanisms, etc.

In summary, the clean, smooth, cold tungsten field emitter is electrically stable; it is possible to maintain stability during periods of the order of 1000 hr of unattended operation at useful levels of current and power. By a simple reconditioning process, the operation may be repeated; cathode life thus appears to be indefinite; operating periods in excess of 12 000 hr have been demonstrated.

Longevity and stability have been observed at a dc current density of 10^7 amp/cm² which corresponded to 35 billion w of beam power per unit cathode area. Attention has been called to the possibility of utilizing this cathode in an electron gun having either extreme miniaturization at conventional power levels or unusually high peak power[25]; several possible applications were noted in the same reference.

In general, the emission current level and the period during which the cathode can be operated stably without attention are found to be reciprocal quantities. Thus, the product of these two variables serves as a useful figure of merit for judgment of stability. In Fig. 14 are shown values of this product which had been obtained during the course of the work for dc operation of cold tungsten field emitters. If the performance of the cold cathode continues to increase at the rate shown, a number of additional applications may soon be possible.

[25] W. P. Dyke, "Field Emission A Newly Practical Electron Source" (to be published); this is a reference to footnote 1.

Electrical Stability and Life of the Heated Field Emission Cathode*

W. P. Dyke, F. M. Charbonnier, R. W. Strayer, R. L. Floyd, J. P. Barbour, and J. K. Trolan
Linfield Research Institute, McMinnville, Oregon

(Received October 28, 1959)

The cold tungsten field cathode exhibits electrical stability and long life (12 000 hr demonstrated) at dc emission densities up to 10^7/cm², when operated in vacuum tubes with a residual gas pressure below 10^{-12} mm Hg; with a provision for periodic reconditioning of the cathode surface by a brief flash heating, satisfactory operation of the cold cathode may be achieved at tube pressures up to about 10^{-9} mm Hg. Continuous heating of the field cathode is shown to yield useful electrical stability at conventional tube pressures, e.g., 10^{-6} mm Hg.

The theory of transport phenomena in heated metals is applied to a quantitative study of the geometrical stability of the heated field cathode. Expressions are derived for the time rate of change of cathode tip radius in the presence or absence of dc and pulsed electric fields at the cathode surface, and long-term geometrical stability of the cathode surface is predicted when the average applied field has the proper value. Large cathodes operated at high current level will only tolerate pulsed emission, and expressions are obtained for the maximum allowed duty cycle and pulse length in this case; small heated cathodes are capable of stable dc emission.

Occurrence of a vacuum arc is proposed as the cause of cathode failure. Considerations based on this assumption lead to predictions concerning the dependence of average cathode life on temperature, and to quantitative expressions for the statistical distribution and average value of life for unbiased field cathodes operated at high temperatures.

Experimental results yielded by the operation of 85 cathodes show good agreement with the theory. The heated cathode shows constant performance over a long period after which cathode failure occurs abruptly, and the statistical nature of cathode life is confirmed. The statistical distribution of cathode life and the measured effect of various parameters on average life show good agreement with theoretical predictions. Unbiased tungsten cathodes yielded an average life of 250 hr at an optimum cathode temperature of 2040°K. With the application of a suitable bias both long-term stability and an average life of 487 hr at 1970°K have been achieved, and according to the theory a substantial further increase in average life may be obtained by the use of a higher cathode temperature and of cathode materials with reduced impurity content.

INTRODUCTION

IN the previous paper[1] concerning the cold field emission cathode, two essential results were demonstrated: first, the cathode exhibits electrical stability and longevity, even at dc emission densities as high as 10^7 amp/cm², if its surface can be maintained smooth and clean; second, techniques have been developed and used in field emission tubes to maintain a clean and smooth cathode surface during prolonged operation at a relatively high power level. The conditions for good performance of the cold tungsten field cathode, at emitted current densities $\leqslant 10^7$ amp/cm², reduce in effect to a single requirement: a very high vacuum (of the order of 10^{-12} mm Hg) must be achieved and also maintained during operation. This has been obtained in practical field emission tubes by effective evacuation and processing techniques, by the use of vacuum envelopes impervious to helium, and by the confinement of electron bombardment (both primary and secondary electrons) to clean and well outgassed metal surfaces.

However, there may be practical devices where the distinctive properties of the field cathode could be used to advantage, but where the conditions for longevity and stability of the cold cathode are not readily reconciled with effective and economic design. This may occur, for instance, when the average power dissipation becomes very large, or when substantial amounts of power must be dissipated in phosphors or dielectrics which cannot be well outgassed or release decomposition products under electron bombardment, or again in devices such as electron microscopes where operation is desired after the shortest possible evacuation time. The heated field emission cathode or "*T-F* cathode"[2,3] has been developed for use in such cases; it retains the essential properties and advantages of the field emission cathode, and in addition, it exhibits useful electrical stability at conventional residual tube pressures.

The effect of heating on the electrical stability of the field emission cathode is readily understood from a consideration of the basic field emission law

$$J = A \exp\left(-B\frac{\phi^{3/2}}{F}\right), \tag{1}$$

where J, F, and ϕ are the local values of the emitted current density, the applied electric field and the work function at any point of the cathode surface, and B is a constant; the parameter A depends on field and work function, but as in the case of thermionic emission the exponential term exercises a predominant influence. Electrical instability of the field cathode usually arises through the strong dependence of the emission density J on the values of F and ϕ; for typical operating conditions, a 1% increase in F (at constant ϕ) causes approximately a 10% increase in J, and a 1% increase in ϕ (at constant F) causes a 15% decrease in J. When the cathode is cold, ion bonbardment causes a gradual

* This work was sponsored by the Office of Naval Research; it was reported in part at the 1955, 1956, and 1957 Field Emission symposia, and published in part in Advances in Electronics and Electron Phys. 8, 90–185.

[1] E. E. Martin, J. K. Trolan, and W. P. Dyke, J. Appl. Phys. **31**, 782 (1960).

[2] W. W. Dolan and W. P. Dyke, Phys. Rev. **95**, 327 (1954); also W. P. Dyke and J. P. Barbour, J. Appl. Phys. **27**, 356 (1956).

[3] W. P. Dyke, J. P. Barbour, *et al.*, Phys. Rev. **99**, 1192 (1955); also W. P. Dyke and W. W. Dolan, Advances in Electronics and Electron Phys. **8**, (1956).

roughening of the emitting surface through cumulative sputtering, resulting in local increases of the electric field (at constant applied voltage) and an over-all increase of the emitted current; also a fraction (equal to the sticking probability) of the chemically active neutral particles which strike the initially clean surface becomes chemisorbed, and affects the emission through a local change in work function. Thus, large rates of contamination and sputtering preclude satisfactory operation of the cold cathode.

Heating of the cathode surface serves to reduce the effects of contamination and sputtering to a level consistent with sufficient electrical stability of the emission. For this purpose, the cathode temperature must be high enough to cause rapid evaporation of the surface contaminants, and to activate transport processes (usually surface migration) which smooth out surface roughness caused by sputtering. In the case of tungsten field cathodes, which are at present used in most applications, experiments described below show that a cathode temperature equal to at least 1800°K is required to achieve the desired objectives. This value is consistent with estimates based on the rate of desorption of chemisorbed contaminants: barring the presence of carbon (which is carefully avoided in field emission tubes), oxygen appears to be the most tightly bound among the usual contaminants of the tungsten surface, and the rate of desorption of chemisorbed oxygen becomes very rapid above about 1800°K.[4] This minimum value of cathode temperature is also consistent with estimates of the rate at which surface migration smooths out sharp projections resulting from sputtering, as shown in a later section.

The choice of cathode temperature deserves careful consideration. The requirement that a nearly clean and smooth surface be maintained determines a lower limit T_m, since the rates for evaporation of contaminants and smoothing out of sputtering must be large compared to the rates of contamination and sputtering; it will be noted that T_m is not a sensitive function of environment since the latter rates vary linearly with tube pressure, whereas the former rates vary exponentially with temperature. Thus, a suitable value of T_m may be found which is sufficient in the great majority of practical cases. On the other hand, the use of a cathode temperature much larger than the minimum T_m required for a clean and smooth surface usually has undesirable effects on the electrical stability and longevity of the cathode because, as shown in a later section, it increases the rate at which gross changes in cathode geometry (such as dulling or build-up) will occur. Thus, in practice, the optimum cathode temperature lies very close to the minimum required T_m.

When the field cathode is operated at the proper temperature, the microgeometry and the work function of the emitting surface become essentially constant; under such conditions, possible changes in the macroscopic geometry of the cathode become the most important factor contributing to electrical instability. Thus, it was recognized that a determination of the optimum operating conditions of the heated field cathode required the identification and quantitative study of the basic transport mechanisms at the heated cathode surface. Surface migration was identified as the predominant transport mechanism under the usual operating conditions[5]; both the activation energy and diffusivity constants for the process, and also the surface tension, were measured in the case of tungsten.[6] As a result of this work, quantitative expressions became available to determine the rate of kinetic change of the heated field cathode geometry as a function of the experimental parameters.

In the present paper, the extension to field emission cathodes[6] of Herring's theory of transport phenomena in heated metals[7] is applied to a quantitative theoretical discussion of the electrical stability and life of heated emission cathodes as a function of operating parameters. Conditions are derived which yield electrical stability by providing a time-independent emitter geometry through proper balance of surface tension and electrostatic forces. Also reported are data from the operation of 85 experimental tubes, which provide a verification and an extension of the theory.

THEORY

The technique described in this paper provides a means of obtaining electrical stability and useful performance of field emission cathodes despite an unfavorable environment. This desired purpose is achieved by heating the cathode to a temperature sufficient to maintain a clean and smooth surface in spite of bombardment by neutral or ionized particles. Under such conditions, it becomes necessary to study the changes in emitter geometry which may occur as a result of transport phenomena activated by the heating of the cathode, as such changes are the main source of electrical instability of the heated field emission cathode.

A. Stability of the Heated Field Cathode

Herring[7] has applied the principles of thermodynamics to the theoretical study of transport phenomena and the associated geometrical changes in heated crystals of pure metals. The field emission cathode consists of a very sharp hemispherical tip smoothly fitted to a conical shank and it has symmetry of revolution, as shown in Fig. 1. The tip radius (normally less than 1 μ) is much smaller than average crystal dimensions in the cathode material, so that the fraction of the emitter,

[4] J. A. Becker, Advances in Catalysis **7**, 136 (1955).

[5] J. L. Boling and W. W. Dolan, J. Appl. Phys. **29**, 556 (1958).

[6] J. P. Barbour, F. M. Charbonnier, W. W. Dolan, W. P. Dyke, E. E. Martin, and J. K. Trolan, Phys. Rev. **117**, 1452 (1960); also, W. P. Dyke and W. W. Dolan, Advances in Electronics and Electron Phys. **8** (1956).

[7] C. Herring in "Structure and Properties of Solid Surfaces," ed. by R. Gomer and C. S. Smith (University of Chicago Press, Chicago, 1953).

FIG. 1. Electron microscope shadowgraphs of a typical field emitter; *B* shows emitter rotated 90° from position of *A*; magnification 3000 *X*.

which is of interest from the standpoint of emission and stability normally consists of a single crystal to which Herring's theory may be applied.

Scaling laws derived by Herring[5] have been used[5] to establish that under normal experimental conditions surface migration is the transport process primarily responsible for the geometrical changes observed in field cathodes. Surface tension forces and electrostatic forces are the two motivating forces for the migration, and they have opposite effects: when surface tension forces predominate there is a net migration of atoms from the emitter tip toward the shank, and the emitter dulls as its tip recedes; when electrostatic forces predominate the direction of net migration is reversed and a phenomenon called "build-up" occurs. Geometrical and hence electrical stability of the heated field cathode may be achieved by balancing the surface tension forces against the electrostatic forces.

The case where the migration is controlled by surface tension forces and leads to emitter dulling has been studied in some detail and appears well understood. A fairly complete discussion may be found in a recent publication.[6] When the net migration is directed from the emitter tip toward the shank, cathode materials of interest here behave in first approximation as though they were isotropic. The migration current at any point M is proportional to the gradient at that point of a chemical potential μ derived by Herring and equal to

$$\mu=\mu_0+\Omega_0\left[\gamma\left(\frac{1}{R_1}+\frac{1}{R_2}\right)-P_{zz}\right] \tag{2}$$

for an isotropic material. μ_0 is an arbitrary constant (corresponding to a plane stress-free surface), Ω_0 is the volume per atom, γ is the surface tension, R_1 and R_2 are the principal radii of curvature of the surface, and P_{zz} is the normal component of any surface stress which may be present, these latter quantities being evaluated at the point M under consideration.

1. Migration in the Absence of Appreciable Field Forces

This case applies in practice to the migration of field cathodes either in the absence of applied electric field, or for very low duty cycle pulsed emission. In this case the time average of the surface stress is either zero or negligibly small, and the net chemical potential $(\mu-\mu_0)$ is proportional to the total surface curvature $1/R_1+1/R_2$, which in view of the emitter shape decreases steadily from the emitter apex toward the shank. Surface atoms will migrate from regions of high μ toward regions of low μ, i.e., from the emitter apex toward the shank. As shown in footnote reference 6, the following expression may be derived for the rate dz/dt at which the emitter tip (axial coordinate z) recedes with time as a result of the surface tension induced surface migration

$$\frac{dz}{dt}=\frac{\Omega_0^2}{A_0}\frac{D_0\exp-(Q/kT)}{kT}\frac{1.25\gamma}{r^3}\equiv\frac{C}{r^3}, \tag{3}$$

where A_0 is the average surface area per atom, k is the Boltzmann constant, T is the tip temperature in °K, D_0 and Q are the diffusivity constant and activation energy for surface migration, r is the tip radius, and 1.25 is the average value of a diminsionless factor determined by the shape of the emitter profile. The substituting of appropriate values for tungsten (see reference 6) yields

$$\frac{dz}{dt}=-2.6\times10^4\frac{\exp-(36\,300/T)}{Tr^3}, \tag{4}$$

where dz/dt is in cm/sec, r is in cm, and T is in °K. Equation (4) leads to the curves of Fig. 2. For convenience, the receding rate is given in centimeters per second and also in atom layers per second, i.e., by counting the number per second of atom layers dissolved by surface migration at the tungsten emitter tip, assuming the usual tip crystallographic orientation of the cathode in which the emitter axis coincides with a (110) direction. As shown in Fig. 2, the receding rate is a sensitive function of both tip radius and tip temperature.

In practice the emitted current is controlled by the voltage V_0 applied between the cathode and a nearby electrode (control grid). The emitted current density is a sensitive function of the electric field at the cathode surface; thus, for a fixed value of V_0, variations in the tip

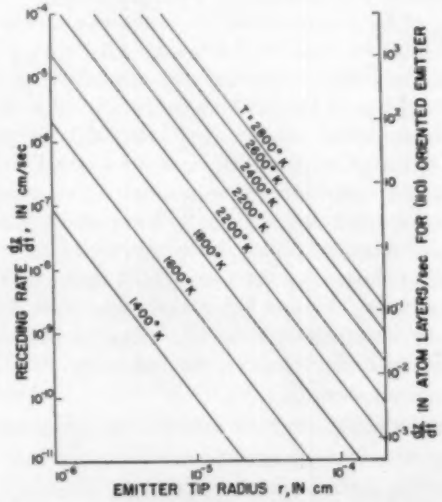

FIG. 2. Tungsten emitter tip receding rate, vs tip radius r and tip temperature T (°K).

[5] C. Herring, J. Appl. Phys. **21**, 301 (1950).

radius r cause variations in the field which in turn affect the emitted current, and the variations of r with time are of particular interest in connection with the long-term electrical stability of the cathode. As the emitter recedes, its radius changes because of the cathode shape, and in first approximation the emitter dulling rate dr/dt is simply equal to $-\alpha dz/dt$, where α is the half angle of the conical cathode shank. By using Eq. (4) for the receding rate, one readily obtains

$$[r(t)]^4 - r_0^4 = 4C\alpha(t-t_0), \tag{5}$$

where r_0 is the initial value of emitter tip radius at time t_0. This expression has important practical implications, as it shows that the rate of increase of the tip radius is not uniform but decreases rapidly with increasing radius. Under a suitable choice of experimental conditions, several advantageous properties result: First, the dulling rate is negligibly small for the larger emitters ($r > 10^{-4}$ cm) when the tip temperature is made just large enough (e.g., $T \cong 1800°$K for tungsten) to establish, through evaporation of impurities, a clean surface with time-independent work function. Second surface roughness (small r) caused by ion sputtering is rapidly smoothed out while the gross surface (larger r) remains relatively unchanged. Third, preselected values of the tip radius and operating voltage of the cathode may be achieved by heating for a suitable period an initially sharp emitter. Finally, when large currents are desired it is possible to use multiple needle arrays consisting of a large number of field emitters operated in parallel and mounted on a common support; effective parallel operation requires highly uniform tip radii, which can be obtained after suitable heat treatment even though the emitters may initially exhibit large variations in radius.

These various considerations are illustrated in Fig. 3 and Table I, which show the variations with time of the radii of two tungsten field cathodes with widely different initial tip radii $r_0 = 10^{-6}$ cm and $r_0' = 20\, r_0$, for $T = 1800°$K and $\alpha = 0.1$ rad.

As shown, the rate of relative change of the emitter radius decreases very rapidly with emitter radius, and

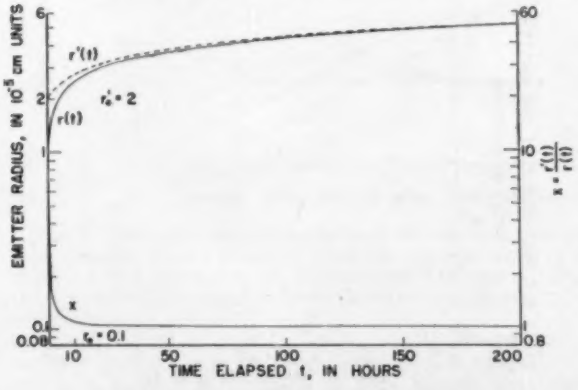

FIG. 3. Variations of emitter tip radius with time, for $T = 1800°$K and $\alpha = 0.1$ rad.

TABLE I. Variation of emitter tip radius with time.

Time elapsed (hr)	0	0.1	1	10	10^2	10^3	10^4
$r(t)$ in 10^{-5} cm units $r_0 = 0.1$		0.77	1.36	2.42	4.31	7.66	13.6
$r'(t)$ in 10^{-5} cm units $r_0' = 2$		2.01	2.1	2.66	4.36	7.67	13.6
$x(t) = r'(t)/r(t)$	20	2.63	1.54	1.1	1.011	1.0016	1.00016
$y(r') = \frac{1}{r'}\frac{dr'}{dt}$ (%/hr)	5.4	5.3	4.4	1.7	0.24	0.025	0.0052

is reduced to 0.01% per hr for $r = 10^{-4}$ cm. It may be noted also that the ratio x of the two tip radii, even though initially quite large, decreases rapidly and approaches unity for large values of t. At 1800°K, x is reduced to 1.01 after approximately 115 hr; in practice, a much higher temperature is used during emitter fabrication in order to reduce the time required to achieve a high degree of radius uniformity in multiple emitter cathodes, e.g., x is reduced to 1.01 after only 8 min of heating at 2800°K. The use of heating to equalize by surface migration the tip radii of a multiple emitter cathode is particularly effective when all emitters have the same angle, as assumed above; however, it remains useful even when the emitters have different cone angles, since Eq. (5) shows that $r(t)$ is proportional to $\alpha^{\frac{1}{4}}$, and therefore, is relatively insensitive to cone angle variations. Finally, uniform heating of the various emitters is required for good results, because of the sensitive dependence on temperature of the surface migration rates, e.g., a 5% variation in temperature will cause a spread of about 20% in the final values of radius.

Thus, emitter dulling, caused by surface migration controlled by surface tension forces, can be used to considerable practical advantage in the control and improvement of cathode performance. However, in view of Eq. (5), only the larger emitters exhibit geometric and therefore electrical stability when heated in vacuum in the absence of large electrostatic forces; sharper emitters, often desired for low-voltage operation, dull rapidly and then require increasing voltage for a given current. In the next section, a method is presented by which the emitter geometry can be stabilized for a wide range of tip radii and temperatures.

2. *Migration in the Presence of Steady State Electric Fields*

a. Small fields. When a voltage is applied to a nearby electrode, there results at any point M an electric field F_M and a corresponding electrostatic stress $P_{zz} = F_M^2/8\pi$ in electrostatic units. In view of the shape of the cathode, the electric field is maximum at the emitter apex and normally decreases steadily at increasing distances from the apex. Thus, in view of Eq. (2), the surface tension forces and electrostatic forces have opposite effects on the gradient of the chemical potential, and application of a field as the cathode surface reduces the net migration rate. As shown in footnote reference 6, the receding rate in the presence of a steady state field F_0 at the emitter apex is approximately

$$\left(\frac{dz}{dt}\right)_{F_0} \cong \left(\frac{dz}{dt}\right)_0 \left(1 - \frac{1}{c_0^*} \frac{rF_0^2}{16\pi\gamma}\right), \tag{6}$$

where c_0 is the value at the emitter apex of a dimensionless coefficient, which is determined by the shape of the emitter profile; more specifically, c_M is the ratio at point M of the relative variations with position of the total surface curvature and the electrostatic stress. Experimental results confirm[6] the predicted dependence of the emitter receding rate on the applied electric field. A detailed examination of field cathode profiles further shows that the relative variation of the total curvature near the apex is only about one-half the relative variation of the electrostatic stress, and therefore $c_0 \cong 0.5$. Thus, it is possible to stop the emitter dulling by application at the emitter apex of a steady state electric field F_{01} equal to

$$F_{01} \cong \left(\frac{8\pi\gamma}{r}\right)^{\frac{1}{2}}, \tag{7}$$

where F_{01} is in electrostatic units, γ is in d/cm, and r is in cm.

This method has been used to determine the value of the surface tension of tungsten and other metals in the solid phase.[6] Figure 4 shows the dependence of F_{01} on r obtained from Eq. (7) for tungsten field cathodes ($\gamma \cong 2900$ d/cm, thus $(F_{01})\text{v/cm} = 8.1 \times 10^4 r_{\text{cm}}^{-\frac{1}{2}}$).

b. Intermediate fields. Experiments show that if a field F_0 slightly larger than F_{01} is applied at the emitter apex the emitter dulling stops only temporarily, and is resumed after a period of time which increases rapidly with the difference $F_0 - F_{01}$. This phenomenon can be explained theoretically by referring to the basic expression (2) for the chemical potential μ. Since a local gradient of μ causes a local surface migration current, true geometric stability of the heated field cathode requires that the chemical potential have the same value at all points on the emitter surface. Thus, a necessary condition for true equilibrium is that the chemical potential be the same at the emitter apex A and at some distant point B on the emitter shank, i.e.,

$$\frac{2\gamma}{r} - \gamma\left(\frac{1}{R_1} + \frac{1}{R_2}\right)_B = \frac{F_{02}^2}{8\pi} - \frac{F_B^2}{8\pi}, \tag{8}$$

where F_{02} is the value of the electric field required at the apex to produce true equilibrium, and $2/r$ is the total curvature at the apex of the axially symmetrical emitter. However, at point B, both the curvature and the field stress are negligibly small compared to their values at the apex, and the necessary condition for true geometric equilibrium of the heated emitter is

$$F_{02} \cong \left(\frac{16\pi\gamma}{r}\right)^{\frac{1}{2}} = F_{01}\sqrt{2}. \tag{9}$$

The fields F_{01} and F_{02} differ because the "annealed" form of field cathodes (i.e., the profile obtained by heating the cathode in the absence of electric field) corresponds to $c_0 \neq 1$, and $F_{01} = (c_0)^{\frac{1}{2}} F_{02}$. The schematic diagram of Fig. 5 appears helpful in discussing the situation. In the absence of applied field the chemical potential decreases steadily from a maximum value $\mu_A = \mu_0 + (2\gamma\Omega_0/r)$ at the emitter apex. Application of a field $F_0 < F_{01}$ causes a reduction in both μ and $|\nabla\mu|$, but since $\nabla\mu$ remains everywhere "negative" (i.e., directed away from the apex) migration toward the shank proceeds at a reduced rate. Application of a field $F_0 = F_{01}$ is sufficient to reduce $\nabla\mu$ to zero at the apex, thus stopping the migration there; however, away from the apex, $\nabla\mu$ remains negative and surface migration proceeds toward the emitter shank; the effect of this surface migration is to reduce the local value of the chemical potential, and therefore after a short time a negative gradient reappears at the apex and surface migration resumes at the apex. Application of a field F_0 larger than F_{01} but smaller than F_{02} results in a value $\mu_A > \mu_0$, but also in a maximum μ_M in the μ curve; thus, initially, the direction of migration at some point P depends on the location of P with respect to the maximum μ_M; this migration reduces the maximum μ_M until eventually $\nabla\mu$ is negative everywhere and general migration toward the shank is resumed; the larger F_0 in this region the longer the time interval between the time when the field is applied and the time when migration toward the shank is resumed near the apex. When $F_0 = F_{02}$ the same situation prevails, but now the end points correspond to the same value of μ; whether or not long-term geometric stability can be achieved under this condition depends on whether the emitter can attain by local migration a modified profile for which $\mu = \mu_0$ everywhere; it does not seem possible to demonstrate theoretically the existence of such a profile, but experiments seem to indicate that long-term geometric stability of heated field cathode is indeed achieved after initial rearrangement of the surface when a field of the order of F_{02} is applied at the apex. Finally, when F_0 exceeds F_{02} the net migration is directed from the shank toward the apex, a situation discussed in the next paragraph.

c. Large fields. In the case of small fields ($F_0 < F_{01}$), migration is directed away from the emitter apex and

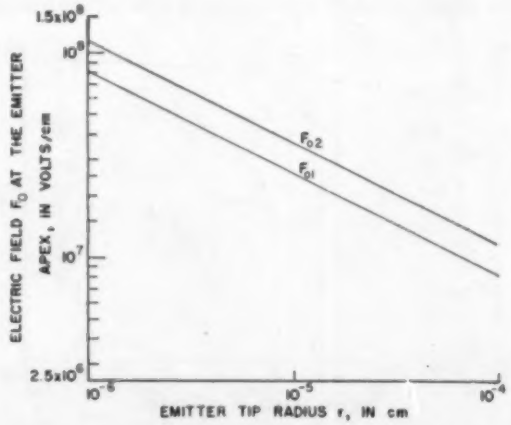

FIG. 4. Dependence on emitter radius of the dc bias fields F_{01} and F_{02}, for heated tungsten cathodes ($\gamma \cong 2900$ d/cm).

Herring's theory, simplified by the assumption that tungsten behaves as though it were an isotropic material, is successful in predicting correctly by Eq. (6) the receding rate of the emitter apex. In view of Eq. (6) one might expect the heated field cathode to extrude when fields in excess of F_{01} are applied at the emitter apex; however, simple extrusion does not occur because of the difficulty of nucleating new atom layers in certain crystallographic orientations [such as (110), and to a lesser extent (100) and (211)] corresponding to close-packed and relatively smooth surfaces. This difficulty causes a very small relative rate of growth of the emitter in the corresponding directions, and as a result the heated field cathode subjected to fields larger than F_{02} does not remain smoothly rounded, but gradually builds up into a polyhedral shape, shown in Fig. 6, in which the emitter surface eventually consists of large plane facets separated by sharp edges and corners. This process is called "build-up" and will be discussed in some detail in a forthcoming publication.[9]

From a practical standpoint, the build-up of field cathodes with controlled crystallographic orientation may find useful applications in cases where special beam geometries are desired; however, in general, build-up of the field cathode must be avoided during operation, since for a constant applied voltage the build-up process leads to large increases in local electric field at the edges and corners; these in turn result in extreme emitted current densities, which preclude electrical stability and may eventually cause cathode destruction by a vacuum arc.[10,11]

The field emission process is a very nonlinear process characterized by a very sensitive dependence of the emitted current density on the applied field. The useful range of emitted current densities ($J=10^4$ to 10^8 amp/cm^2) corresponds to apex fields F_0 in the range of 4×10^7 to 8×10^7 v/cm for materials such as tungsten which have an effective work function of the order of

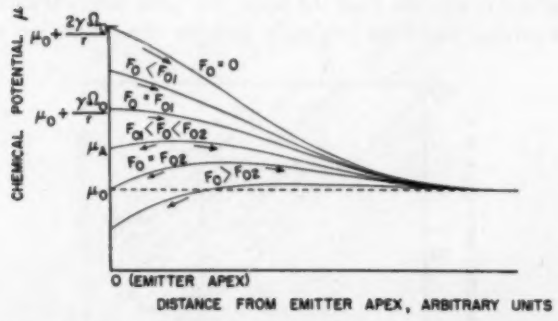

FIG. 5. Schematic illustration showing the chemical potential μ vs distance from the emitter apex, for various values of the electric field F_0 applied at the emitter apex. The arrows indicate the direction of the migration immediately after application of the electric field.

[9] P. C. Bettler and F. M. Charbonnier (to be published).
[10] W. P. Dyke, J. K. Trolan, *et al.*, Phys. Rev. **91**, 1043 (1953).
[11] W. W. Dolan, W. P. Dyke, and J. K. Trolan, Phys. Rev. **91**, 1054 (1953).

FIG. 6. Electron microscope shadowgraphs of a typical field cathode, showing the effect of build-up. (a) Smoothly rounded cathode profile obtained by heating without field; (b) cathode profile after extensive build-up; (c) cathode profile after extensive build-up, at 90° from profile (b).

4.5 ev. In view of Fig. 4, the necessity to avoid build-up precludes dc operation of heated field cathodes with radii in excess of 8×10^{-6} cm, since such radii correspond to values of F_{02} lower than 4×10^7 v/cm. It may be noted however that other cathode materials with lower work function may allow dc operation of larger heated cathodes, since according to the Fowler-Nordheim law of field emission [see Eq. (1)] the field required to yield a given current density is approximately proportional to $\phi^{3/2}$.[12]

Thus, successful dc operation of the heated cathode is restricted to cathodes having a radius small enough to preclude the occurrence of build-up. Larger cathodes may be heated during operation to maintain electrical stability despite contamination or sputtering of the emitting surface, but the necessity to avoid build-up restricts such cathodes to pulsed operation, and places limitations on duty cycle and pulse length which are discussion in the next section.

3. Migration in the Presence of Both Steady State and Pulsed Fields

In most applications of the field cathode one seeks to achieve the highest beam current or beam conductance consistent with electrical stability and sufficient life of the cathode. The use of pulsed rather than dc emission allows substantially higher values of beam current and conductance, and it becomes of interest to study the behavior of the heated field cathode in the more general case, where the electric field applied at the emitter apex consists of both a relatively small steady state component F_0 and a superimposed pulsed field resulting in a total applied field $F_p \gg F_0$ during the pulse. Under such conditions, the necessity to preserve cathode electrical stability by avoiding build-up imposes upper limits on the pulse duty cycle and pulse length, which may be estimated from the theory. These limits will hold in practice, unless other more severe

[12] Even though the cathode surface exhibits gross deformations caused by build-up, it appears to remain atomically smooth for the values of applied field and temperature of interest in the operation of heated tungsten field cathodes. At still higher fields ($>10^8$ v/cm), Drechsler has shown that the atomically smooth surface becomes unstable and changes to a hill and valley structure.

limitations exist (arising for instance from consideration of power dissipation).

a. Maximum allowed duty cycle. Let x be the pulse duty cycle, i.e., the average fraction of the total time during which the pulsed field F_p is applied. The maximum duty cycle is readily estimated from the theory when the pulse duration t_p is short compared with the time t_M required for critical build-up at the pulsed field value F_p; t_M will be estimated in the next section. In practice the pulse duration t_p is always much longer than the vibration time t_0 of the surface atoms (which is of the order of 10^{-13} sec), so that the direction of the migration at any instant is always determined by the value of the surface electric field at that instant. During the period between pulses surface tension forces predominate (since obviously the steady state component F_0 of the field at the emitter apex must be smaller than F_{02} if build-up is to be prevented) and the net migration is directed away from the emitter apex; during the pulse the direction of migration may be reversed if F_p exceeds F_{02}.

Even though a time-independent surface geometry cannot be achieved in a strict sense since the surface field is discontinuous, a quasi-equilibrium situation can be achieved (in which the emitter surface pulsates by a small amount about a constant average geometry) when the various parameters F_0, F_p, and x satisfy the proper relationship given by Eq. (11) below. This relationship is simply obtained by noting that, under the condition $t_0 \ll t_p \ll t_M$, the average surface migration rate is equal to that resulting from the dc electric field F which yields the same time average of the electrostatic stress, i.e.,

$$\frac{F^2}{8\pi} = (1-x)\frac{F_0^2}{8\pi} + x\frac{F_p^2}{8\pi}. \tag{10}$$

A time-independent average emitter geometry will be achieved when $F = F_{02}$, i.e., in view of Eqs. (9) and (10), when

$$x_0 = \frac{(16\pi\gamma/r) - F_0^2}{F_p^2 - F_0^2}, \tag{11}$$

where all quantities are in cgs esu units. The duty cycle is in first approximation independent of cathode temperature. Emitter dulling occurs when $x < x_0$ and emitter build-up occurs when $x > x_0$. In practice, the duty cycle and the pulse field are predetermined by the proposed application, and Eq. (11) then determines the proper value of dc bias field F_0, which should be used to achieve a time-independent geometry of the heated cathode.

If $F_p < F_{02}$, Eq. (11) yields a value larger than unity for the duty cycle; this is readily understood since in such a case surface tension forces always predominate and build-up cannot occur even at unit duty cycle. In the usual case where $F_p > F_{02}$ the duty cycle x_0 increases as the dc bias field F_0 is reduced, and the maximum duty cycle x_M allowed for a given pulsed field F_p is obtained by setting $F_0 = 0$ in Eq. (11). In the case of tungsten ($\gamma = 2900$ d/cm) one obtains

$$x_M = \frac{F_{02}^2}{F_p^2} = \frac{1.3\times10^{10}}{rF_p^2}, \tag{12}$$

where r is in cm and F_p is in v/cm. Figure 7 shows the dependence of the maximum duty cycle x_M on the tip radius of heated tungsten cathodes for various values of the pulse field covering the range used in practice; the corresponding emitted current density J_p at 2000°K is also shown for convenience. The higher the emitted current density the smaller the maximum allowed duty cycle; values in the range 5% to 10% are typical of usual experimental conditions for the heated emitter.

b. Maximum allowed pulse length. During the pulse electrostatic forces predominate and the surface migration currents are directed toward the emitter apex when F_p exceeds F_{02}. As noted in the foregoing, simple extrusion does not occur in this case because of the difficulty of nucleating new atom layers in certain crystallographic directions, and a more complicated process called "build-up" takes place in which the emitter geometry gradually assumes a polyhedral shape in which the emitter surface consists of plane facets with (110) and (100) or infrequently (211) orientation, connected by sharp edges and corners. If a constant potential is applied between the field cathode and a control grid, excessive local emitted current densities causing emitter destruction by vacuum arc will result shortly before complete build-up is reached. Thus, for satisfactory operation of the heated field cathode the pulse length t_p must be kept short compared to the time t_M required for complete build-up.

The build-up process is markedly anisotropic, and therefore cannot be fully treated by the simple theory given above; however, an experimental study of the phenomenon[9] seems to indicate that, whereas the initial stages of the build-up process are the result of local surface migration near the apex, the later stages leading to critical build-up probably involve the migration of

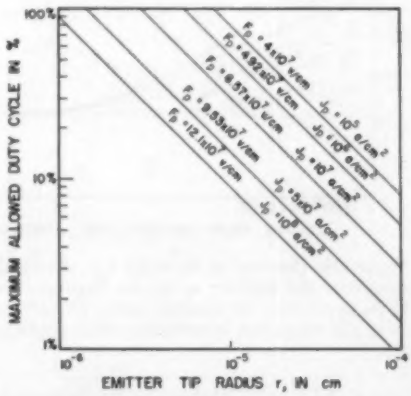

FIG. 7. Maximum allowed duty cycle vs emitter tip radius, for heated tungsten field cathodes operated at various values of pulsed field F_p and peak emitted current density J_p.

additional material from the emitter shank toward the tip. Thus, a rough theoretical estimate of the build-up time t_M may be obtained by assuming that the rate of nucleation of additional atom layers with (110) or (100) orientation is negligibly small and that the emitter shank supplies the major fraction of the additional volume of material v required near the tip for completion of the build-up process ($v \cong 0.02r^3$). Since in practice the pulse length will be limited to a small fraction of t_M for reliable cathode operation, an approximate determination of t_M serves a useful purpose even though it may not be accurate.

For a typical emitter profile the rate dV/dt at which material is transferred by migrating atoms across a plane perpendicular to the emitter axis and located just below the build-up region may be estimated from the foregoing theory; the corresponding estimate of t_M is simply

$$t_M \cong \frac{v}{(dV/dt)} \cong 0.2 \frac{A_0 k}{D_0 \Omega_0^2} T e^{(Q'/kT)} \frac{r^3}{F_p^2 - F_{02}^2}, \quad (13)$$

where Q' is the effective activation energy for the build-up process and other quantities have been defined previously; t_M goes to infinity when $F_p \leqslant F_{02}$, since in that case field forces no longer predominate and critical build-up does not occur. The dependence of t_M on the parameters T, F_p, and r is complicated because F_{02} is a function of r [as shown by Eq. (9)] and because a variation in applied field F_p may cause an appreciable variation of the activation Q' at the large field values required for build-up to occur[13]; if the latter effect is ignored in the present approximate derivation of t_M the curves of Fig. 8 are obtained for the build-up time t_M as a function of radius and temperature, by using the value 3.14 ev/atom for Q' (see footnote 6), and assuming a constant applied field $F_p = 7\times10^7$ v/cm typical of pulsed cathode operation. As seen, the dependence of t_M on cathode temperature is very sensitive and straightforward. The dependence on radius is more complicated: for large values of the radius t_M is approximately proportional to r^3, but as r decreases the field F_{02} increases and t_M becomes infinity where F_{02} becomes equal to F_p; Figure 4 yields the corresponding value r_m of the tip radius (2.7×10^{-6} cm in Fig. 8, where $F_p = 7\times10^7$ v/cm); the minimum of t_M corresponds to $r = 4/3\, r_m$. The effect of the applied field on build-up is usually small, except near r_m, because the practical range of emitted current densities (10^5 to 10^8 amp/cm^2) corresponds to a narrow range of applied fields (5.5×10^7 to 8×10^7 v/cm for tungsten); it is illustrated by the dotted curve of Fig. 8, which corresponds to $F_p = 6\times10^7$ v/cm.

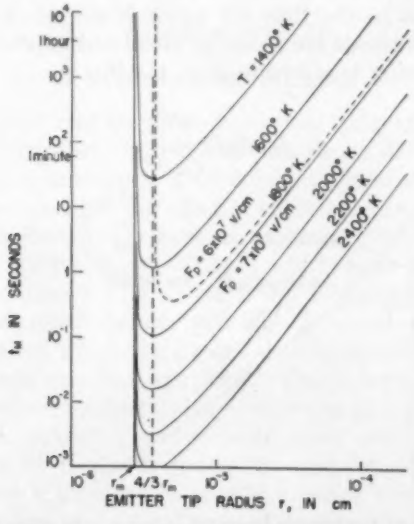

FIG. 8. Time t_M required for critical build-up, as a function of tip radius and temperature, for an applied field $F_p = 7\times10^7$ v/cm (full curves) or 6×10^7 v/cm (dotted curve). Below $r_m = 2.7\times10^{-6}$ cm, build-up does not occur and t_M is infinite.

[13] M. Drechsler, Z. Elektrochem. **61**, 48 (1957).

The operating conditions most frequently selected for the heated field cathode ($r = 3$ to 6×10^{-5} cm, $T = 1800$ to 2000°K, $F = 6$ to 7×10^7 v/cm) correspond to values of t_M in the range 1 sec to 1 min; preliminary experiments indicate this estimate of t_M to be correct within an order of magnitude, but somewhat conservative. Thus under normal conditions build-up effects do not preclude satisfactory performance of the heated cathode during pulsed operation, when the pulse length does not exceed a fraction of a second; when required, satisfactory operation for somewhat longer pulses may be achieved by reducing the cathode temperature.

B. Life of the Heated Field Cathode

1. Life Termination Mechanism

In the previous section the theory of transport processes in heated metals was applied to a discussion of the geometrical and therefore electrical stability of the heated cathode. The same theory may be used, together with an assumed life terminating mechanism suggested by the experimental results, to provide an estimate of the statistical distribution and average value of life for unbiased field cathodes.

An experimental study of pulsed field emission from heated field cathodes indicates no gradual deterioration of the cathode; the emission characteristics are essentially constant for a long period, after which life termination occurs abruptly as a result of a catastrophic event which can develop within a single microsecond pulse. In view of previous experiments[10] this behavior suggests life termination by occurrence of a vacuum arc initiated by excessive local values of the emitted current density. With this interpretation, life termination is associated with either a sudden local increase in electric field or a sudden local decrease in work function, which may result from causes internal or external to the cathode. Two main external causes have been previously recognized: sputtering of the emitting surface by ion bombardment or contamination by low work function material; thus, the average cathode life would be ex-

pected to be sensitive to environment and to increase rapidly with emitter temperature, until the cathode temperature reaches a value T_m sufficient to yield rapid evaporation of contaminants and rapid smoothing of sputtering by surface migration. For temperatures above T_m sputtering and contamination have little effect on the condition of the emitting surface and life termination must be caused by agents within the cathode.

Thus, for sufficient cathode temperature ($T>T_m$), cathode life is expected to be independent of environment and closely related to the degree of purity of the cathode material. It is postulated that life termination occurs when a sufficiently large cluster of impurities becomes exposed at the emitting surface, causing either a decrease in local work function or an increase in local electric field (the latter as a result of evaporation and subsequent ionization by the electron beam of the impurities, which produces a positive space charge cloud near the cathode surface). Such clusters of impurities may reach the surface by volume diffusion, and also as a result of emitter dulling. If this interpretation is correct, a longer average life would be expected when the heated field cathode is biased to prevent emitter dulling, and the average life should decrease rapidly with increasing cathode temperature (above T_m) for both biased and unbiased cathode operation, since volume diffusion and surface migration rates increase rapidly with temperature.

Experimental results concerning the effect of environment, cathode temperature and bias field on average cathode life agree with the foregoing conclusions, and thus appear to support the validity of the mechanism proposed for life termination.

2. *Statistical Distribution and Average Value of Cathode Life*

When the heated field cathode is biased to prevent emitter dulling, it assumes a time-independent geometry, and impurity clusters can reach the surface only by volume diffusion within the cathode material. Thus, when the cathode temperature is high enough to reduce the effect on cathode life of environmental factors to a relatively small level, the statistical distribution of life, for a large number of cathodes with identical tip radius and temperature, will depend on the density and spatial distribution of impurities, and also on whether the motion of impurities by volume diffusion within the cathode is directed or random. The average cathode life is expected to vary exponentially with inverse temperature, and a measurement of this effect will yield the activation energy for volume diffusion of the impurities in the tungsten lattice. The average life is also expected to decrease when either the tip radius or the density of impurities is increased.

A more quantitative discussion can be made in the case of heated field cathodes operated under conditions (e.g., low duty cycle pulsed emission in the absence of cathode bias), where surface tension forces predominate on the average and cause emitter dulling. In this case the average life is found experimentally to be much shorter than when emitter dulling is prevented; thus, emitter dulling rather than volume diffusion is primarily responsible for exposing impurities at the emitter surface, and in first approximation the motion of impurities by volume diffusion may be neglected. Impurity clusters large enough to cause life termination by vacuum arc are assumed to have random spatial distribution with an average density n_0 per cm^3. The probability dP that emitter dulling will expose a cluster in time dt is

$$dP=n_0dV\cong n_0\pi r^2(dz/dt)dt, \tag{14}$$

where dz/dt is the receding rate given by Eq. (6). Thus, if we consider a large number N_0 of identical cathodes placed into operation at time $t_0=0$, the number of cathodes which are destroyed between times t and $t+dt$ is $dN=-N(t)dP$. A straightforward integration yields the number $N(t)$ of cathodes still operating at time t

$$N(t)=N_0\exp-(\pi n_0/3\alpha)[(r_0^4+4C\alpha t)^{\frac{3}{4}}-r_0^3], \tag{15}$$

where r_0 is the initial emitter radius, α is the half angle of the conical cathode shank, and C is a function of temperature and bias field defined by: $dz/dt=C/r^3$. According to this expression, $N(t)$ is initially an exponential function of time (when $4C\alpha t\ll r_0^4$) and then decreases more slowly with time. Figure 9 shows the statistical life distribution curve $N(t)$ calculated by means of Eq. (15), for a typical cathode ($r_0=3\times10^{-5}$ cm, $\alpha=0.1$ rad) operated at 2200°K; the value $n_0=10^{11}$ cm^{-3} is obtained by means of Eq. (17).

In most experimental cases, the cathode life is long compared to the time for which $4C\alpha t=r_0^4$. Thus, the average cathode life t_0 can be calculated approximately by assuming $4C\alpha t\gg r_0^4$ in $N(t)$, yielding

$$t_0\cong0.28\frac{\alpha^{1/3}}{Cn_0^{4/3}}. \tag{16}$$

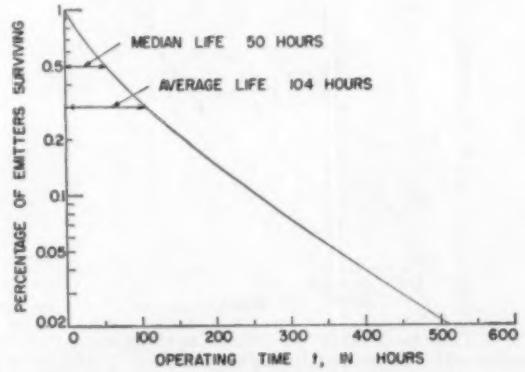

FIG. 9. Calculated statistical percentage of heated field cathodes surviving after t hours of operation at 2200°K, assuming typical cathode geometry ($r_0=3\times10^{-5}$ cm, $\alpha=0.1$ rad) and $n_0=10^{11}$ cm^{-3}.

For the case of low duty cycle pulsed emission from unbiased tungsten cathodes, the average life is approximately

$$t_0 \cong 10^{-5} \frac{T \exp(36\,300/T)\alpha^{1/3}}{n_0^{4/3}}, \qquad (17)$$

where t_0 is in seconds, T is the cathode temperature in °K, α is the half angle of the conical cathode shank in radians, and n_0 is the average number of impurity clusters large enough to cause a vacuum arc in each cubic centimeter of cathode material. This expression is useful in showing the dependence of average cathode life on cathode parameters; it does not yield a numerical value of t_0 since n_0 is not known. Conversely, the experimental determination of average cathode life at 2200°K can be used to estimate $n_0 \cong 10^{11}$ cm^{-3} by means of Eq. (17): this would correspond to an average of one large impurity cluster in a cube of cathode material 2.2 μ or 7000 lattice parameters on the side.[14]

In conclusion, cathode life is expected to be a random quantity with an exponential like statistical distribution. As the cathode temperature is gradually increased, the average cathode life is expected to increase rapidly at first with temperature (resulting from the more effective removal of the external causes of life termination) and then to decrease rapidly with temperature because of the increasing rate of diffusion and migration processes at the cathode. Thus, the cathode should be operated within a well defined and relatively narrow range of temperatures for maximum average life. The most important other factor affecting cathode life is expected to be the degree of purity of the cathode material, e.g., Eq. (16). Finally, the average cathode life is expected to increase slowly with cathode cone angle.

EXPERIMENTS

A. Experimental Methods

The tubes used for the experimental study of the life and stability of the heated field cathode are diodes with Pyrex glass envelopes. Two different types of anodes were used to check the effect of environment.

The majority of the tubes were modified Müller field emission microscopes ("FEM") which have been described earlier.[10] The anode is an aluminum-backed phosphor screen which provides a visual emission pattern from which the current density distribution at the cathode may be determined.[15] The emission pattern reveals effects at the cathode surface due to contamination and sputtering, and is particularly useful for the detection of localized changes in emission characteristics, which may not be readily detected through the measurement of the total emitted current; the emission pattern also allows the use of a sensitive technique for the measurement of small changes in emitter geometry,[16] which affect the electrical stability of the cathode. However, a disadvantage of the projection tube is the liberation, caused by electron bombardment of the phosphor screen and the glass envelope, of contaminants which deteriorate the emitter environment. Hence several tubes of another type were used in which the cathode and the electron discharge were enclosed in a well-outgassed metal box anode; these tubes permitted increased power dissipation at the anode with a reduced deterioration of the environment, and information on the effect of environment on cathode life and stability could be obtained by a comparison of the respective performance of the two types of tubes.

Very sharp needle-shaped tungsten field cathodes, mounted on hairpin support filaments, were fabricated by electrolytic etch[17]; high purity wire stock, Phillips type HCA, was used in all tests unless otherwise noted. The very sharp emitters were then dulled to the desired radius by heating in vacuum, in accord with Eq. (5); for this purpose, the cathode support filament was heated by passing a current through it, and the emitter tip was heated from the supporting filament by thermal conduction.

All experimental tubes were evacuated on a mercury diffusion pump system and sealed off at pressures in the range 10^{-9} to 10^{-10} mm of Hg, as measured on a Bayard-Alpert ionization gauge. A tantalum getter was then used to reduce the pressure of chemically active gases, until pressures in the range 10^{-10} to 10^{-12} mm Hg were reached, judged by the rate of contamination of the cold field cathode surface.[18] Following this, the partial pressure of inert gases increased with time since helium is known to diffuse into a one liter Pyrex flask at the rate of about 10^{-9} mm Hg/hr at room temperature[19]; the partial pressure of chemically active gas also increased during operation, reaching maximum values in the range 10^{-6} to 10^{-8} mm Hg in the case of FEM tubes and of emission at relatively high current level, e.g., 0.2 amp peak.

The electrical stability of the cathode was evaluated from the time variation of the field emission current-voltage relationship, and also from the characteristics of the emission pattern in the case of FEM tubes. A total of 85 single needle tungsten cathodes were operated until their useful lives were terminated by a vacuum arc. All emitters were maintained at a constant temperature while field emission currents were drawn during microsecond intervals at a repetition rate of 120 pps. Temperatures in the range of 1500°K to 2300°K, and peak current density levels approximately 0.1 to 0.2 of the maximum level imposed by resistive heating[11] were used. Fifteen of the emitters were operated with

[14] This value of n_0 might at first appear unreasonably large; however, it is smaller (by a factor of at least 10^7) than the average number of impurity atoms per cm^3 in the Phillips type HCA tungsten wire commonly used in the fabrication of field cathodes.

[15] W. P. Dyke, J. K. Trolan, *et al.*, J. Appl. Phys. **25**, 106 (1954).

[16] J. K. Trolan, J. P. Barbour, *et al.*, Phys. Rev. **100**, 1646 (1955).

[17] W. P. Dyke, J. K. Trolan, *et al.*, J. Appl. Phys. **24**, 570 (1953).

[18] R. Gomer, J. Chem. Phys. **19**, 1072 (1951).

[19] Rogers, Buritz, and Alpert, J. Appl. Phys. **25**, 868 (1954).

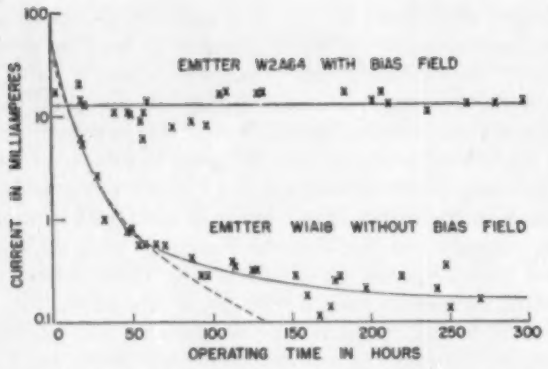

FIG. 10. Effect of a dc bias voltage on the electrical stability of the heated field emitter.

an additional continuous bias field adjusted at a level to eliminate emitter dulling and achieve a time-independent emitter geometry, in accordance with Eqs. (5) and (8). Of the 85 cathodes, 70 were operated in field emission projection microscope (FEM) tubes; 13 were operated in tubes with copper box anodes; and two were operated in tubes with cylindrical molybdenum anodes.

B. Experimental Results and Discussion

The present experiments were intended to evaluate and improve the life and stability of the heated field emission cathode through identification and control of the mechanisms involved, thereby providing both an experimental test of the foregoing theory and engineering data useful for practical applications of the heated field cathode to electron devices. A range of values was used for those controllable variables which according to the theory might influence emitter life and stability. A statistically valid experimental determination of the effect on life of each pertinent parameter was unfortunately beyond the scope of this work, as it would have required the testing of several hundred cathodes in view of the statistical nature of emitter life under given conditions. Nevertheless, sufficient data were obtained to permit conclusions which are presented in the following sections.

1. Electrical Stability of the Heated Field Cathode

As noted the purpose of heating the cathode is to eliminate electrical instabilities due to surface contamination and sputtering. Inspection of the current-voltage relationship and observation of the emission pattern showed the absence of appreciable contamination and sputtering over operating periods of up to several hundred hours when the tungsten cathode was heated above 1800°K, even though in some cases the tube pressure rose to 10^{-6} mm Hg during operation at relatively high current level; thus, the effectiveness of the technique is clearly demonstrated, since according to the kinetic theory of gases the cold tungsten surface would be completely covered by a monolayer of contaminants in approximately 30 sec, assuming a tube pressure of 10^{-6} mm Hg and a sticking probability of 0.1.

Gross changes in emitter geometry, caused by surface migration and discussed in the theory, are the main factors contributing to electrical instability of the heated field cathode. Such changes introduce limitations in the operation of the heated cathode; for instance, they limit the duty cycle and pulse length of the larger cathodes. However, if the theory is correct these geometrical changes can be predicted and in some cases eliminated (e.g., by the use of a dc cathode bias in the case of low duty cycle pulsed emission) and therefore they do not preclude satisfactory operation of the cathode.

An earlier report[6] has discussed the experimental verification of the basic theoretical expressions for the rate dz/dt at which the tip of the heated cathode recedes, in the case of low duty cycle pulsed emission with or without dc cathode bias [Eqs. (3), (4), and (6)]. The corresponding rate of variation of emitter radius with time, given by Eq. (5), is of more direct interest from the standpoint of electrical stability. Figure 10 shows a comparison of the measured (full curve) and calculated (dotted curve) time dependence of the peak emitted current for emitter W1A18, for low duty cycle pulsed emission without bias field and at fixed anode pulsed voltage. The calculated curve is obtained by using Eq. (5) to predict the tip radius as a function of time, and then using electrostatic theory and the field emission law to calculate the corresponding pulsed values of the electric field at the tip, of the emitted current density and of the total emitted current. As seen the calculated and measured values of peak emitted current are in close agreement for the first 50 hr, corresponding to a current variation by a factor of almost 100, thus supporting the validity of the theoretical expression for $r(t)$. The departure observed at subsequent time shows that the tip radius then increased more slowly with time than Eq. (5) would predict; similar departures have been observed in several instances and have been

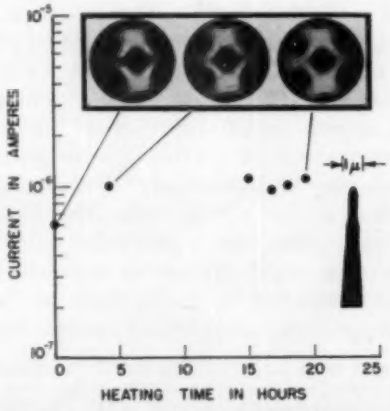

FIG. 11. Variations with time of the emitted current and emission pattern, for dc emission from a heated field cathode.

shown to occur when emitter dulling exposes a grain boundary at the emitter tip.

The theory predicts that geometrical stability may be achieved by application of a suitable dc bias voltage to the cathode, which suppresses surface migration by a compensation of surface tension and electrostatic forces. This possibility has been verified in a number of instances, and is illustrated by the performance of emitter W2A64, also shown in Fig. 10. Finally, the theory indicates that continuous electron emission may be reconciled with geometrical stability of the heated field cathode when the dc field at the cathode tip has the proper value F_{02} [given by Eq. (9)]. This useful property has also been verified experimentally, as illustrated in Fig. 11, for a field cathode heated at 2000°K and having an initial tip radius $r=2\times10^{-5}$ cm (corresponding to $F_{02}\cong2.6\times10^{7}$ v/cm). When the corresponding dc voltage was applied at the anode, both the current response and the emission pattern show that, after an initial rearrangement of its profile, the heated cathode reached a stable geometry corresponding to the electron microscope shadowgraph shown in Fig. 11. During the fifteen hours preceding completion of the test only small changes in emitted current were observed; for comparison, emitter dulling would reduce the emitted current by a factor 2 in approximately 10 min if the applied field were removed, and critical build-up would occur in approximately one second if the applied field were increased to 7×10^{7} v/cm.

When a gradually increasing dc electric field is applied to the heated field cathode, the theory predicts that emitter dulling will stop immediately but only temporarily when the field at the apex reaches the value F_{01} (see Fig. 4), whereas long-term geometrical stability requires application of a larger field F_{02}, approximately equal to $\sqrt{2}F_{01}$ for typical emitter shapes; thus, for an intermediate applied field F_0 it is expected that emitter dulling will resume after a time t_s which increases from zero to infinity as F_0 increases from F_{01} to F_{02}. Preliminary experiments appear to confirm this prediction to the theory, as shown in Table II.

As shown in the theory, the maximun allowed values of duty cycle and pulse length are closely related to the geometrical instability of the heated field cathode. Experimental results to data are incomplete; however, a preliminary study of build-up indicates that the theoretical estimate of the maximum pulse length [see Eq. (13) and Fig.8] is correct within an order of magnitude. The lack of a pulser with sufficient duty cycle has so far prevented an experimental verification of the calculated maximum duty cycle [see Eq. (12) and Fig. 7]; however, the satisfactory agreement between theory and experiment concerning the value of dc field required to yield geometrical stability of the cathode provides a verification of the theoretical predictions for the limiting case where the duty cycle becomes unity.

TABLE II. Effect of dc bias electric field on cathode geometrical stability.

Emitter	F_0/F_{01}	t_s
W3A23	1.079	4 hr
W3A23	1.103	21 hr
W3A26	1.111	26 hr

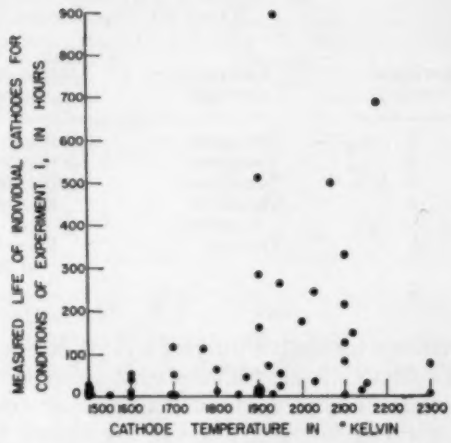

FIG. 12. Dependence of life on temperature, for unbiased tungsten cathodes continuously heated and operated in projection microscope tubes (phosphor anode).

2. Life of the Heated Field Cathode

During the present tests the life of the heated field cathode, for low duty cycle pulsed emission at a peak current level of the order of 0.1 amp, has been measured in a total of 85 instances. Several parameters were varied to determine their effect on cathode life, leading to the classification of the experiments performed, as shown in Table III. The first experiment was primarily intended to determine the effect on life of the cathode temperature. The other experiments were intended to determine the effect on cathode life of other parameters, and were generally performed at a fixed cathode temperature of 2000°K in order to reduce the number of measurements required for a statistically significant result. Experiment 2 showed the effect of environment; experiment 3 compared the respective effectiveness of intermittent and continuous heating of the field cathode; experiment 4 tested the effect of low work function impurities in the tungsten cathode, and finally experiment 5 tested the effect on cathode life of the application of a dc field adjusted to the value F_{02} yielding geometrical stability of the heated cathode.

a. Dependence of average life upon temperature. Figure 12 is a plot of cathode life as a function of temperature. In order to eliminate the effect of other parameters, only the data obtained from the 52 cathodes tested in experiment 1 are shown in this plot. The statistical nature of cathode life is clearly apparent. The dependence of the average life on cathode temperature is obtained from the raw data of Fig. 12, by dividing the over-all temperature range investigated into intervals small enough to permit averaging of the individual

TABLE III. Experimental conditions for the various life test experiments.

Experiment number	Cathode material	Anode material	Type of heating	dc Bias applied	Number of cathodes tested
1	Tungsten	Phosphor	Continuous	No	52
2	Tungsten	Copper	Continuous	No	9
3	Tungsten	Phosphor	Intermittent	No	5
4	Thoriated tungsten	Phosphor	Continuous	No	4
5	Tungsten	Phosphor or copper	Continuous	Yes	15

measurements within this interval and yet large enough to reduce statistical uncertainties to an acceptable level. The average life and corresponding average temperature, calculated for each interval, are shown by the points labeled 1 in Fig. 13; the boundaries between successive intervals are labeled *a*, *b*, *c*, *d*, *e*. Also indicated is the approximate statistical uncertainty associated with each average value of life; in this and all subsequent instances the uncertainty shown corresponds to the standard deviation of an assumed Poisson distribution of cathode life. Finally, the full curve of Fig. 13 connects the average points and represents the present estimate of the average cathode life as a function of temperature, for the conditions of experiment 1. The dotted curve shows the average cathode life at high temperature, calculated from the theoretical expression (17) with $n_0 = 10^{11}$ cm^{-3} and $\alpha = 0.1$ rad. The close agreement found between the measured and predicted dependence of average cathode life on temperature supports the validity of the theory.

Thus, in the case of unbiased tungsten cathodes continuously heated and operated in projection microscope tubes with a phosphor anode, the following conclusions are proposed:

(1) A cathode temperature lower than 1800°K is ineffective in correcting the effects of contamination and sputtering, as is also confirmed by direct observation of the emission pattern. The average cathode life is very short and life termination results from poor surface conditions normally due to environment, even though in some cases surface migration of contaminants from the cathode shank toward the tip may be a contributing factor.

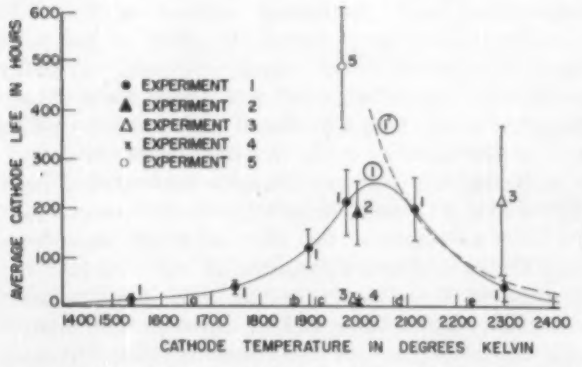

FIG. 13. Life of the heated field emission cathode—summary of the results; Full curve 1—experimentally determined average life for the conditions of experiment 1; dotted curve 1—average life calculated from Eq. (17) for the same conditions.

(2) In the range 1800 to 2000°K cathode life increases rapidly due to improved cleanliness and smoothness of the emitting surface, and the average cathode life becomes gradually insensitive to environment.

(3) At temperatures above 2100°K the surface is essentially clean and smooth, and is not appreciably improved with further increases in temperature. Thus, cathode life is controlled by the degree of purity of the cathode material, and for a given degree of purity the average life decreases rapidly with temperature, in the manner predicted by the theory [see Eq. (17)], because of the rapid increase in emitter dulling rate.

(4) In the range 2000 to 2100°K an intermediate situation prevails, in which surface condition and cathode material purity both affect the cathode life and have opposite variations with temperature. The maximum average life is found in this range, and corresponds approximately to 250 hr at 2040°K for the cathodes tested in experiment 1.

This discussion also suggests that further increases in average life may be achieved through improved environment (for $T \leqslant 2100$°K) and/or through the use of high purity cathode material (for $T \geqslant 2000$°K).

b. Dependence of average life upon environmental factors. The purpose of experiment 2 was to provide a preliminary check on the dependence of life upon environmental factors. For this purpose 9 unbiased continuously heated tungsten field cathodes were operated in diodes with a copper anode box. The experimental result is shown in Fig. 13; the cathode temperature was 2000°K, and an average life of 191 hr was found, with a statistical uncertainty of ±63 hr. Thus, at 2000°K this test showed no statistically significant difference between the average life of the cathode in tubes having either a phosphor or a copper anode. Whereas this result would at first seem surprising, it appears satisfactorily explained by the following considerations:

(1) The possibility of a higher average life in copper tubes is not precluded by the experimental results, in view of the relatively large statistical uncertainties caused by the limited number of tubes tested. Assuming a Poisson distribution of cathode life for given experi-

TABLE IV. Effect on average life of cathode pretreatment by heating in vacuum.

Case	Number of emitters	Duration of heat treatment time	Average operating temperature	Average life	Statistical uncertainty
1	5	None	2084°K	231 hr	±103 hr
2	7	33 to 58 hr (av 53 hr)	2043°K	249 hr	±94 hr
1 and 2 combined	12	0 to 58 hr (av 30 hr)	2060°K	242 hr	±70 hr
3	9	>110 hr (av 133 hr)	2056°K	145 hr	±48 hr

mental conditions, there is a probability of 16% that an accurate measurement based on a large number of tubes would yield an average cathode life in excess of 254 hr for the conditions of experiment 2.

(2) The discussion of the previous section indicates that the effect of environment on cathode life decreases rapidly with temperature above 1800°K, and is expected to be relatively small at 2000°K.

(3) The environment appears to affect cathode life through contamination and sputtering of the emitting surface. Most of the common contaminants (e.g., oxygen) increase the work function and lower the emission, and thus reduce cathode stability rather than cathode life. In the present experiments, which used Pyrex envelopes permeable to helium, the main environmental factor reducing cathode life is expected to have been sputtering by helium ions, and this factor was unchanged by the use of a copper anode.

Thus, the experimental study of the dependence of cathode life upon environmental factors is at present incomplete, but nevertheless seems to confirm the effectiveness of heating the tungsten cathode above 2000°K in protecting the cathode from the effects of an unfavorable environment.

c. Dependence of average life upon heating cycle. According to the interpretation given earlier the average cathode life is controlled at low temperatures by the effect of environmental factors on the condition of the emitting surface, and at high temperatures by the emitter dulling rate and the degree of purity of the cathode material. If this is correct, one would expect a reduction in average life at low temperatures and an increase in average life at high temperature when the field cathode is heated intermittently instead of continuously. Experimental results seem to confirm this prediction; 5 unbiased tungsten cathodes in phosphor tubes were heated periodically for 4 sec out of every minute; three cathodes heated at 2000°K show an average life of 17 hr, as opposed to 235 hr for continuously heated cathodes, whereas the other two cathodes heated at about 2300°K show an average life of 215 hr, as opposed to 40 hr for continuous heating. Whereas the statistical uncertainties are large because of the small number of measurements, the expected trend appears confirmed. From a practical standpoint, intermittent heating at a relatively high cathode temperature might permit an appreciable increase in the maximum average life of the heated field cathode, and further experiments are planned to test this possibility.

d. Dependence of the average life upon the degree of purity of the cathode material. According to the theory the major cause of life termination at high cathode temperature is the occurrence of a vacuum arc following the appearance at the emitting surface of a sufficiently large cluster of impurities with either low work function or low melting point.[20] An attempt was made to test this hypothesis by two different experiments.

First the average cathode life was compared for cathodes made of either raw untreated wire (Phillips type HCA) or of initially similar wire which had been heated to 2700°K in vacuum for various periods of time. The results of this comparison are shown below. The data presented are restricted to unbiased cathodes continuously heated during operation to a temperature in the range 2000° to 2180°K; this range was made as narrow as possible because of the dependence of cathode life on temperature, and was limited to $T \geqslant 2000$°K since at lower temperatures cathode life appears controlled by factors other than cathode material purity. See Table IV.

As shown, the difference between the average life for cases 1 and 2 is not statistically signficant. However, when these two cases are combined to reduce the statistical uncertainty, comparison with case 3 indicates a significant decrease of cathode life with prolonged preheating of the tungsten wire stock. It is thought that prolonged heating, even though it decreases the total impurity content, also tends to segregate the remaining impurities, and therefore increases the number of impurity clusters large enough to cause a vacuum arc when exposed to the surface.

A conclusive result was also obtained by measuring the life of four cathodes fabricated from tungsten wire containing 2% thoria (experiment 4). These cathodes were operated unbiased at 2000°K and yielded an average life of 9.5 hr, as compared with 235 hr for the pure tungsten cathodes operated under the same conditions. This pronounced difference seems to indicate that at 2000°K the average cathode life decreases rapidly as the impurity content increases; an even larger effect would

[20] Characteristic effects occasionally observed on emission patterns, and reported by Dyke and Barbour (see footnote reference 2) appear to provide experimental evidence of the eruption of internal impurities onto the surface of heated tungsten field cathodes.

TABLE V. Effect of cathode cone angle on average life.

Case	Number of emitters	Cone half angle	Average operating temperature	Average life	Statistical uncertainty
1	10	1° to 7°, av 5°	2070°K	130 hr	±41 hr
2	11	7.5° to 11.5°, av 9.5°	2047°K	264 hr	±80 hr

be expected at higher cathode temperatures where the relative importance of cathode purity as a life termination factor is increased.

Since the presence of internal impurities appears to be the main factor limiting cathode life at high temperature, the use of highly pure cathode materials is particularly desirable. Floating zone melting techniques have been used here recently to produce tungsten wire with a controlled crystallographic orientation. Life testing of field cathodes fabricated from zone melted tungsten wire is proposed, as such cathodes should have a reduced content of internal impurities, and would be expected to exhibit relatively long life when operated at a sufficiently high temperature.

e. Dependence of average life upon cathode cone angle. According to the theory the average cathode life at high temperatures should be proportional to the one-third power of the half-angle α of the cathode conical shank. The experimental results are shown below, restricted to unbiased cathodes continuously heated and operated in a narrow temperature range (2000° to 2180°K) for reasons stated earlier. See Table V.

Thus, the increase with cone angle of the average life is statistically significant. The rate of increase appears more rapid than that predicted by the theory, even though the difference is not statistically significant; a possible explanation is that the diffusion of impurities to the surface is facilitated in the case of field cathodes with small cone angle, and therefore with small cross section.

f. Dependence of average life upon the presence of a dc bias field. According to the theory, the average life of the heated cathode is expected to increase at high temperatures when a dc bias field is applied to reduce the emitter dulling rate. This prediction has been confirmed experimentally by a measurement of the average life of 15 tungsten cathodes continuously heated and biased to the correct level for geometrical stability (corresponding to a dc field F_{02} at the emitter apex). The experimental results are shown in Fig. 13; the average cathode temperature was 1970°K and an average life of 487 hr was measured, with a statistical uncertainty of ±125 hr, as opposed to approximately 200 hr for unbiased cathodes operated under otherwise identical conditions. Thus, a very substantial increase in average life is achieved by the use of a dc bias. The scope of this work did not permit a detailed investigation of the temperature dependence of average life for biased cathodes; however some indications may be derived from the results obtained with unbiased cathodes. At a temperature of 1970°K the effect on cathode life of environmental parameters affecting the condition of the emitting surface remains quite important, and if this were the only cause of life termination a substantial increase in average life would be obtained by increasing the cathode temperature. On the other hand at 2100°K the average life of unbiased cathodes is about 200 hr and the good agreement of theory and experiment leads to expect that emitter dulling plays a major role in reducing cathode life; thus the use of a bias would be expected to yield a large increase in average life at 2100°K. In view of these considerations, the optimum operating temperature of biased tungsten cathodes is probably appreciably larger than 1970°K, and the corresponding average life may be well in excess of 500 hr. Finally, as noted earlier, the use of zone melted tungsten wire is expected to yield a substantial further increase in average cathode life.

g. Statistical distribution of cathode life. The number of cathodes tested for any given set of operating conditions was too limited to permit an accurate check of the theoretical predictions concerning the statistical distribution of cathode life. However, preliminary results are presented in Fig. 14 for both biased and unbiased cathodes. In the case of unbiased cathodes, the data used were obtained from 36 pure tungsten cathodes heated continuously at temperatures in the range 1900° to 2180°K; whereas this temperature range is wider than would be desirable in view of the temparature dependence of cathode life, it was felt that selection of a more restricted temperature range would yield a sample too small to be statistically significant. Figure 14 shows the percentage of emitters surviving as a function

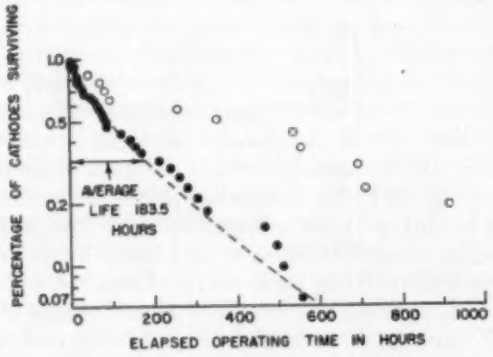

FIG. 14. Statistical distribution of heated field cathode life; ● experimental data points, unbiased cathodes; ○ experimental data points, biased cathodes; dashed curve: statistical distribution calculated by Eq. (15) for an average life of 183.5 hr.

of elapsed operating time, and a logarithmic scale is used for the ordinate to show possible departures of the distribution from the straight line, which would be obtained for a purely random process with time independent probability of cathode failure.

The solid circles represent the data from the 36 unbiased cathodes; the measured average life for these cathodes is 183.5 hr. As shown, the distribution appears to depart significantly from a straight line. In the theory an expression was derived for the statistical distribution of cathode life [see Eq. (15)] based on the assumptions that life termination occurs when a sufficiently large impurity cluster is exposed at the emitting surface, that such clusters have random spatial distribution and that they become exposed primarily as a result of emitter dulling. The dotted curve of Fig. 14 represents the statistical distribution calculated by Eq. (15) when the parameters are adjusted to yield the measured value of average life; this curve departs from a straight line, even though the clusters are assumed to be randomly distributed, because the emitter dulling rate varies with time. A close agreement is found between the calculated and measured distributions, supporting the validity of the assumptions underlying the theory.

The open circle represents the data from 15 biased cathodes (two points are not shown as they correspond to lives in excess of 1000 hr); the measured average life is 487 hr. Interpretation of the data is difficult because the number of cathodes tested is too small to have statistical validity. The study of the temperature dependence of the average life of unbiased cathodes shows that, at the average operating cathode temperature of 1970°K, environmental factors certainly have an important effect on cathode life. The data seem to indicate a rapid initial decrease followed by an approximately linear variation; the latter would suggest a time-independent probability of cathode failure, and is consistent with the hypothesis that the effect of environmental factors on the emitting surface played a major role in causing life termination at the operating temperature used.

SUMMARY AND CONCLUSIONS

The theory of transport phenomena in heated metals has been applied to a quantitative study of the geometrical stability of the heated field cathode in the presence of dc and pulse fields. Experimental results seem to be in good agreement with the theory, and confirm the possibility of achieving geometrical and therefore electrical stability of the heated cathode by application of a suitable dc bias field at the cathode surface.

An experimental study of pulsed emission from heated field cathodes shows constant performance over a long period, after which cathode failure occurs abruptly. Occurrence of a vacuum arc is thought to be the cause of cathode failure; on this basis the dependence of average life on experimental parameters can be predicted, and quantitative expressions can be derived concerning the statistical distribution and average values of life for unbiased cathodes operated at high temperatures. A complete experimental study of the effect on life of all pertinent parameters would require the testing of a very large number of cathodes because of the statistical nature of cathode life; preliminary tests involving 85 cathodes show good agreement with the theoratical predictions and thus lend confidence in the validity of the basic assumptions concerning the nature and causes of cathode failure.

The experimental results also yield useful information for the evaluation of the heated field cathode as a high emission density electron source for practical devices. The heated cathode remains stable in a conventional vacuum (up to 10^{-6} mm Hg) at peak current densities of the order of 10^7 amp/cm^2. For unbiased tungsten cathodes the optimum cathode temperature is approximately 2040°K and corresponds to a measured average life of 250 hr. With the application of a suitable bias both long term stability and an average life of approximately 500 hr at 2000°K have been achieved. The theory leads one to expect a substantial further increase in the average life of the biased tungsten cathode, by the use of a higher cathode temperature and of cathode materials with a reduced density of internal impurities.

ACKNOWLEDGMENTS

The authors gratefully acknowledge considerable assistance from several staff members of this laboratory, including E. E. Martin, L. M. Perry, F. M. Collins, and J. L. Boling.

Scattering of a Plane Transverse Wave by a Spherical Obstacle in an Elastic Medium*

NORMAN G. EINSPRUCH,† E. J. WITTERHOLT, AND ROHN TRUELL
Metals Research Laboratory, Division of Applied Mathematics, Brown University, Providence 12, Rhode Island

(Received August 28, 1959)

An analysis of the scattering of transverse elastic waves by spherical obstacles is presented. The scatterer is taken to be (a) a cavity, (b) a rigid sphere, (c) a fluid-filled cavity, and (d) to consist of an elastic material with properties different from those of the surrounding material. The problems are carried as far as possible analytically without approximations and are reported as matrix equations. The solution of these equations yields the expansion coefficients that describe the waves which are scattered outward from the obstacle and which are excited within the scatterer. A general expression for the scattering cross section offered to a transverse wave has been derived. The Rayleigh approximation is then considered in detail for three of the cases.

I. INTRODUCTION

THE scattering of elastic (sound) waves by obstacles has been studied by numerous investigators for almost a century. Since problems in which the medium supporting the sound wave is a compressible inviscid fluid are of a less complicated nature, most of the work found in the literature deals with fluids rather than with solids. Early work was done by Rayleigh[1] on the scattering of sound by elastic discontinuities of small size; in scattering problems, the significant parameter is (ka) (where a=radius of spherical scatterer, and $k=2\pi/\lambda$=wave number, λ =wavelength); cases in which $ka\ll 1$ are generally referred to as Rayleigh scattering. Recently, Ying and Truell,[2] using techniques similar to those of Herzfeld,[3] studied the scattering of compressional waves by an elastic scatterer in an elastic medium. They considered the cases in which the scatterer is an elastic sphere of properties different from those of the surrounding matrix material, a rigid sphere, and a spherical cavity. The Rayleigh case was considered in detail. The present authors have considered the case in which the scatterer is a cavity filled with a compressible nonviscous fluid[4]; they have also considered scattering by a layered sphere[5] in which the core has the four elastic properties studied by Ying and Truell and by themselves.

A great deal of the recent theoretical work on sound scattering has been motivated by the development of ultrasonic techniques as laboratory and engineering tools. Mason and McSkimin,[6] Roth,[7] and Roney[8] all attempted to attribute the attenuation of ultrasonic waves in polycrystalline solids to scattering at the boundaries of differently oriented anisotropic grains. The theoretical work of Ying and Truell mentioned above was undertaken in conjunction with experimental work by those authors on sound absorption in samples of single crystal alloys containing precipitates.[9] The most recent work on multiple scattering was done by Waterman and Truell.[10] They used an integral equation method of Foldy[11] to describe the over-all properties of a medium containing a statistical array of scattering regions in terms of the scattering properties of a single scatterer.

The present work is a consideration of the scattering of a shear wave by a spherical discontinuity. In particular, the cases are analyzed in which the scatterer is (a) a cavity, (b) a rigid sphere, (c) a fluid-filled cavity, and (d) of an elastic material having acoustic properties different from those of the surrounding medium. The analysis is carried as far as possible without the introduction of approximate methods. Since the range of the parameters (ka) of interest is frequently beyond the region of validity of the Rayleigh approximation, in the megacycle frequency range, the exact equations for the expansion coefficients must be solved by numerical techniques. These equations, which arise from systematic application of the appropriate boundary conditions, are presented for each case listed above.

Finally, the Rayleigh approximation is considered in detail. The scattering cross section in the limit $(ka)\ll 1$ is reported for three of the cases.

* The work reported here was supported by contracts with the Office of Ordnance Research and the U. S. Atomic Energy Commission.

† Present address: Texas Instruments Incorporated, Central Research Laboratories, Dallas, Texas.

[1] Lord Rayleigh, *The Theory of Sound* (Dover Publications, New York, 1945), 1st American ed.

[2] C. F. Ying, and R. Truell, J. Appl. Phys. **27**, 1086 (1956).

[3] K. F. Herzfeld, Phil. Mag. **9**, T41 (1930).

[4] N. G. Einspruch and R. Truell, J. Acoust. Soc. Am. **32**, 214 (1960).

[5] N. G. Einspruch and R. Truell, "Scattering of a plane longitudinal wave by a layered spherical obstacle in an elastic medium," (to be published).

[6] W. P. Mason and H. J. McSkimin, J. Acoust. Soc. Am. **19**, 464 (1947); and J. Appl. Phys. **19**, 940 (1948).

[7] W. Roth, J. Appl. Phys. **19**, 901 (1948).

[8] R. K. Roney, "The influence of metal grain structure on the attenuation of an ultrasonic wave", Ph.D. Thesis, California Inst. Technol. (1950).

[9] C. F. Ying and R. Truell, "Ultrasonic attenuation in vacuum annealed internally oxidized single crystals of dilute copper alloys," Tech. Rept. No. 2 (July, 1954) and Quarterly Repts, No. 10 (August, 1954) and No. 11 (November, 1954), for Office of Ordnance Research, U. S. Army under contract.

[10] P. C. Waterman and R. Truell, "Multiple scattering of waves," Tech. Rept. WAL 143/14–49 (October, 1957) for Watertown Arsenal under contract, and for Office of Ordnance Research, U. S. Army under contract.

[11] L. L. Foldy, Phys. Rev. **67**, 107 (1945).

II. SOME GENERAL CONSIDERATIONS

A. Wave Equation

For a review of the basic concepts of infinitesimal elasticity theory, the classic book by Love[12] and the more modern one by Sokolnikoff[13] should be consulted. From the equation of motion of an elastic solid and the linear (Hooke) stress-strain law for a homogeneous isotropic elastic medium, the following equation can be derived:

$$(\lambda+\mu)\nabla(\nabla\cdot\mathbf{S})+\mu\nabla^2\mathbf{S}=\rho(\partial^2\mathbf{S}/\partial t^2), \tag{1}$$

where $\mathbf{S}$ = displacement vector, ρ = density, ∇ = "del" operator, t = time, and λ, μ = Lamé constants for the material. If simple harmonic time dependence

$$\mathbf{S}=\mathbf{s}e^{iwt}$$

is assumed, where $\mathbf{s}$ = spatial part of displacement vector, w = angular frequency of the elastic wave, and $i=(-1)^{\frac{1}{2}}$, Eq. (1) becomes

$$\frac{1}{k^2}\nabla(\nabla\cdot\mathbf{s})+\frac{1}{\mathrm{K}^2}[\nabla^2\mathbf{s}-\nabla(\nabla\cdot\mathbf{s})]+\mathbf{s}=0, \tag{2}$$

where

$$k=w[(\lambda+2\mu)/\rho]^{-\frac{1}{2}}$$

and

$$\mathrm{K}=w[\mu/\rho]^{-\frac{1}{2}}.$$

Since the vector $\mathbf{S}$ will not be used in any further discussion, the vector $\mathbf{s}$ may be called the displacement vector without fear of confusion.

The decomposition of a vector into a solenoidal part $\mathbf{s}''$ and an irrotational part $\mathbf{s}'$ generally can be effected.

$$\mathbf{s}=\mathbf{s}'+\mathbf{s}'', \tag{3}$$

where

$$\nabla\cdot\mathbf{s}''=0 \tag{4}$$

$$\nabla\times\mathbf{s}'=0. \tag{5}$$

The irrotational part of the displacement $\mathbf{s}'$ [i.e., the part for which Eq. (5) is satisfied] corresponds to a compressional (longitudinal, dilatational) wave. The solenoidal part of the displacement $\mathbf{s}''$ [i.e., the part for which Eq. (4) is satisfied] corresponds to a shear (transverse, distortional) wave. After substitution of Eq. (2), application of conditions (4) and (5), and use of the vector identity

$$\nabla\times\nabla\times\mathbf{s}=\nabla(\nabla\cdot\mathbf{s})-\nabla^2\mathbf{s},$$

two equations are obtained,

$$\nabla^2\mathbf{s}'+k^2\mathbf{s}'=0 \tag{6}$$

and

$$\nabla^2\mathbf{s}''+\mathrm{K}^2\mathbf{s}''=0; \tag{7}$$

hence, k and K, defined previously, are the wave numbers for compressional and shear waves, respectively. The remainder of this work involves solution of Eqs. (6) and (7) and satisfaction of certain appropriate boundary conditions.

B. Boundary Conditions

In an infinite homogeneous isotropic elastic solid, both plane compressional and plane shear waves may propagate independently, each at its characteristic velocity, provided the displacements produced by the wave satisfy Eqs. (6) and (7). However, if the medium contains discontinuities in elastic properties (i.e., in ρ, λ, μ) the waves no longer may travel independently of each other. If a wave of either type is incident upon a scattering obstacle, waves of both types are scattered from the obstacle. If the scatterer is an elastic solid, waves of both types are excited within the scatterer as well. The process of redistribution of energy from a given type of elastic wave to a wave of the other type is known as *mode conversion*. The existence of mode conversion is experimentally verifiable and is a mathematical requirement for the satisfaction of the conditions that must be fulfilled at the interface between the scatterer and the matrix material in which the scatterer is embedded. A discussion of the reflection and refraction of plane waves at a plane interface between two semi-infinite elastic media can be found in Kolsky's[14] monograph.

The boundary conditions that must hold at the interface between an elastic scattering obstacle and the elastic medium in which it is implanted will now be discussed. The scatterer is assumed to be in intimate contact with the surrounding material at all times, hence, an obvious condition that must be satisfied is that the displacement vector $\mathbf{s}$ is continuous across the boundary; this condition is equivalent to three scalar boundary conditions to be satisfied by the components of the displacement vector. If a small volume element is constructed across a portion of the interface, material from both media will be enclosed in the element, which may be taken as roughly a cylinder with altitude perpendicular to the enclosed portion of interface. If the altitude of the cylinder is made to decrease from both ends toward the interface, the mass contained in the cylinder will decrease as well. Examination of the equation of motion for an elastic medium shows that in order to have noninfinite accelerations in this limiting case, the stresses acting on the boundary must be continuous. Continuity of the interface traction is a vector boundary condition, and is equivalent to three scalar boundary conditions to be satisfied by the three stress components acting on the spherical boundary. Hence, in the case under discussion, scattering by an

[12] A. E. H. Love, *A Treatise on the Mathematical Theory of Elasticity* (Dover Publications, New York, 1944), 1st Am. ed.
[13] I. S. Sokolnikoff, *Mathematical Theory of Elasticity* (McGraw-Hill Book Company, Inc., New York, 1956), 2nd ed.
[14] H. Kolsky, *Stress Waves in Solids* (Oxford University Press, London, 1953).

elastic obstacle, six scalar boundary conditions must be satisfied.

If the interface lies between a rigid fixed scattering obstacle and the surrounding elastic material, fewer boundary conditions are needed in order to solve the problem since no wave is excited inside the sphere. A complete description of the waves resulting from the scattering and mode conversion processes can be obtained by using a lesser number of wave functions than were necessary in the previous case in which the scatterer was an elastic medium. By definition, a rigid body is one in which the distance between any pair of points in the body remains constant at all times. In particular, this means that there are no displacements on the surface of the rigid obstacle. Since the displacements across the interface must be continuous, the condition that must hold is that the displacements produced by the incident and scattered waves must vanish at the boundary. This is a vector boundary condition and is equivalent to three scalar boundary conditions.

If the interface lies between an obstacle which is a cavity and the surrounding elastic material, the situation is again simplified since there is no wave excited inside the scatterer because a vacuous obstacle will not support a stress. Since the stress must be continuous across the interface, the condition that must hold is that the combined stresses produced by the incident and scattered waves must vanish at the boundary. This is a vector boundary condition and is equivalent to three scalar boundary conditions. The similarity of this problem to the problem of the rigid scatterer is manifest by the common number of boundary conditions to be satisfied in each case.

If the cavity scatterer considered above is filled with a nonviscous fluid, a different combination of boundary conditions will apply. The fluid material will support a compressional wave, hence, two of the conditions that must be satisfied are that the normal components of displacement and stress must be continuous across the boundary. Since an inviscid fluid will not support a shear wave, the shear stress must vanish at every point in the scatterer. The shear stress, in particular, vanishes at the surface of the fluid obstacle. Since the stresses acting across the interface must be continuous, the condition that must hold is that the combined shear stresses produced by the incident and scattered waves must vanish at the boundary. The total number of scalar boundary conditions that must be specified is thus seen to be four.

III. SOLUTION OF WAVE EQUATION

A. Decomposition of Vector Solutions

The problems under consideration in this paper are discussed in a spherical polar coordinate system with the origin at the center of the spherical obstacle. Since the literature contains many definitions of a spherical coordinate system in terms of a rectangular coordinate system, Fig. 1 is included for reference. In the work on the scattering of a compressional wave by a spherical obstacle, the situation was greatly simplified as a result of the azimuthal symmetry of the incident wave. The solutions were independent of the coordinate ϕ; moreover, the problem was reduced to that of finding solutions of two scalar Helmholtz equations satisfying the appropriate boundary conditions. One of these solutions is the scalar potential giving rise to the compressional part of the displacement vector, and the shear portion of the displacement vector is constructed from the other scalar solution.

In the problems in which the incident wave is a shear wave, the azimuthal symmetry is no longer present since the shear wave has a definite polarization. The polarization of the incident wave results in dependence of the description of the wave on the angle ϕ, and the simplification of the vector potential is no longer possible. Consequently, the vector Helmholtz equation must be solved, and the solutions must be chosen to satisfy boundary conditions of the type discussed in Sec. II.B. A thorough discussion of the vector wave equation can be found in Morse and Feshbach.[15] Many of the mathematical tools used in this section of the present work are discussed in that text.

In a rectangular coordinate system, the vector Helmholtz equation separates readily into three scalar Helmholtz equations each involving one and only one of the rectangular components of the unknown vector. Unfortunately, the vector Helmholtz equation expressed in a spherical coordinate system does not separate simply into three scalar Helmholtz equations each involving only one spherical component of the unknown vector. The coupling among the component

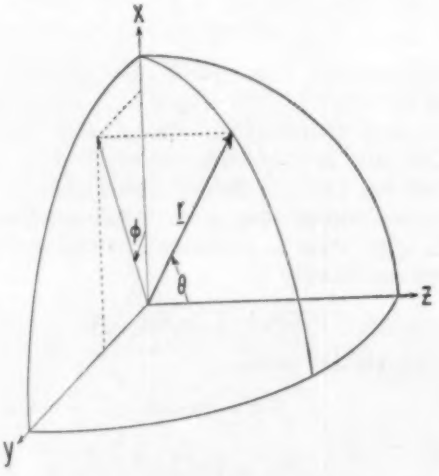

FIG. 1. Spherical coordinate system.

[15] P. M. Morse and H. Feshbach, *Methods of Theoretical Physics* (McGraw-Hill Book Company, Inc., New York, 1953).

equations can be seen readily by examining the vector Helmholtz equation given below in spherical coordinates

$$\nabla^2\mathbf{u}+K^2\mathbf{u}$$

$$=\boldsymbol{e}_r\left[\nabla^2 u_r-\frac{2}{r^2}u_r-\frac{2}{r^2\sin\theta}\frac{\partial}{\partial\theta}(\sin\theta u_\theta)-\frac{2}{r^2\sin\theta}\frac{\partial u_\phi}{\partial\phi}\right]$$

$$+\boldsymbol{e}_\theta\left[\nabla^2 u_\theta-\frac{u_\theta}{r^2\sin\theta}+\frac{2}{r^2}\frac{\partial u_r}{\partial\theta}-\frac{2\cos\theta}{r^2\sin^2\theta}\frac{\partial u_\phi}{\partial\phi}\right]$$

$$+\boldsymbol{e}_\phi\left[\nabla^2 u_\phi-\frac{u_\phi}{r^2\sin\theta}+\frac{2}{r^2\sin\theta}\frac{\partial u_r}{\partial\phi}+\frac{2\cos\theta}{r^2\sin^2\theta}\frac{\partial u_\theta}{\partial\phi}\right]$$

$$+K^2[\boldsymbol{e}_r u_r+\boldsymbol{e}_\theta u_\theta+\boldsymbol{e}_r u_\phi]=0,$$

where $\boldsymbol{e}_r$, $\boldsymbol{e}_\theta$, and $\boldsymbol{e}_\phi$ are the unit vectors in the spherical coordinate system, and $\mathbf{u}$ is a solution of the equation. Solving the component equations, which are coupled to each other, by a separation of variables technique does not look promising since this would lead to the problem of simultaneous solution of a system of ordinary differential equations, hence other devices will be used.

Any solution of the vector Helmholtz equation $\mathbf{u}$ can be decomposed into a longitudinal solution and a transverse solution. The longitudinal solution can be simply derived as the gradient of a scalar function which is a solution of the scalar Helmholtz equation. The transverse part of the field is derivable from a vector potential and is related to two scalar fields which are solutions of the scalar Helmholtz equation. A third scalar potential is not required in order to specify the vector potential completely since the requirement that the vector potential be solenoidal provides the third condition. The decomposition of the vector solution $\mathbf{u}$ into longitudinal and transverse portions is given below. It should be pointed out that this decomposition of vector solutions into longitudinal and transverse portions can be effected only in a limited number of coordinate systems; fortunately, the spherical polar coordinate system can be treated in this manner in order to solve the vector Helmholtz equation. For other vector equations, a decomposition of the present type can be accomplished in even fewer coordinate systems. Let

$$\mathbf{u}=\mathbf{L}+\mathbf{M}+\mathbf{N},$$

where $\mathbf{L}$, $\mathbf{M}$, and $\mathbf{N}$ satisfy the vector Helmholtz equation. $\mathbf{L}$ is the longitudinal portion of the solution and is derivable as the gradient of a scalar potential function which satisfies the scalar Helmholtz equation. The vectors $\mathbf{M}$ and $\mathbf{N}$ compose the transverse portion of the solution and are also related to scalar potential functions which satisfy the scalar Helmholtz equation; they are derived as the curl and curl curl of a simple vector function constructed from the scalar potential functions. All three of the scalar potential functions are formed from the basic solutions of the scalar Helmholtz equation. The major difference, however, between the functions applicable to the problem of scattering of shear waves and the functions in the cases in which compressional waves are scattered, is the presence of azimuthal terms in the basic scalar solutions of the shear wave case, while azimuthal terms were absent in the compressional case. It should be recalled that the solutions in the compressional wave problem were independent of the coordinate ϕ as a result of the axial symmetry of the incident wave. It is due to the polarization, or lack of axial symmetry, that the problem of the scattering of shear waves is a much more difficult one to treat mathematically.

The vector solutions are related to the scalar functions as follows:

$$\mathbf{L}=\nabla\Phi/k,$$

$$\mathbf{M}=\nabla\times(\boldsymbol{e}_r r\Psi),$$

and

$$\mathbf{N}=\nabla\times\nabla\times(\boldsymbol{e}_r r\chi)/k,$$

where

$$(\nabla^2+k^2)(\Phi,\Psi,\chi)=0.$$

The factor $1/k$ is included in the construction of $\mathbf{L}$ and $\mathbf{N}$ in order that the three scalar functions may have the same dimensions.

The particular vector Helmholtz equations of interest here are Eqs. (6) and (7). The requirements have been imposed that $\mathbf{s}'$ and $\mathbf{s}''$ be compressional wave and shear wave solutions, respectively, of the vector Helmholtz equation satisfying certain boundary conditions at the surface of the spherical scatterer. The vectors $\mathbf{s}'$ and $\mathbf{s}''$ will now be decomposed into basic vector solutions as was the general vector solution $\mathbf{u}$ in the previous paragraph.

For the longitudinal wave solution, the decomposition of $\mathbf{s}'$ reduces to

$$\mathbf{s}'=\mathbf{L},$$

since the condition (5) must hold; obviously,

$$\nabla\times\mathbf{L}=0$$

since $\mathbf{L}$ is the gradient of a scalar function, and the curl of a gradient vanishes identically; the curl of the $\mathbf{M}$ and $\mathbf{N}$ terms do not vanish in general, hence they are dropped. The compressional wave solution, $\mathbf{s}'$, thus has the desired form; it is expressed solely as the gradient of a potential function which satisfies the scalar Helmholtz equation. $\mathbf{s}'$ certainly satisfies (6) since $\mathbf{L}$ was chosen to be a solution of the vector Helmholtz equation. For the transverse wave solution, the decomposition of $\mathbf{s}''$ reduces to

$$\mathbf{s}''=\mathbf{M}+\mathbf{N}$$

since the condition (4) must hold; obviously,

$$\nabla\cdot(\mathbf{M}+\mathbf{N})=0,$$

since both $\mathbf{M}$ and $\mathbf{N}$ are constructed as the curl and

curl curl of a simple vector function, and the divergence of a curl vanishes identically; the divergence of $\mathbf{L}$ does not vanish in general, hence the $\mathbf{L}$ term is dropped. The transverse wave solution thus has the desired form; it is expressed solely as the sum of two vector functions which are derived by taking the curl of two vector potential functions. $\mathbf{s}''$ certainly satisfies (7) since $\mathbf{M}$ and $\mathbf{N}$ were chosen to be solutions of the vector Helmholtz equation. Since the compressional and shear waves travel at different velocities, constants appearing in the solution for the total displacement vector $\mathbf{s}$ which depend on the velocity, will have to be labeled accordingly; this is obvious since the wave number in (6) is k and the wave number in (7) is K.

The basic vector solutions in the spherical coordinate system are given in Morse and Feshbach and are written below. The solutions have an abundance of indices which will first be explained. The index n appears as index for the radial functions (such as the $j_n(kr)$) as well as "lower" index for the spherical harmonics (the $Y_{\sigma mn}$ or P_n^m); the range of n is zero to infinity. The index m appears as the "upper" index for the spherical harmonics and also as the index for the azimuthal functions (the $e^{im\phi}$); the range of m is zero to n. These two indices are the ones usually obtained from the separation of variables solution of the scalar Helmholtz equation in three dimensions. The label σ is either e (even) or o (odd) and designates whether the even (real) or odd (imaginary) part of the azimuthal function is to be employed. The superscript 1 indicates that the radial functions to be used are those which are nonsingular at the origin. The vector functions which represent outgoing waves contain Hankel functions as the radial functions and will be labeled by superscript 3. The functions $Y_{\sigma mn}(\theta,\phi)$ are the total angular functions. The vector functions $\mathbf{B}_{mn}(\theta,\phi)$, $\mathbf{C}_{mn}(\theta,\phi)$, and $\mathbf{P}_{mn}(\theta,\phi)$ are the vector spherical harmonics; their definitions are also included below.

$$\mathbf{L}_{\sigma mn}^{1}=(1/k)\nabla[Y_{\sigma mn}(\theta,\phi)j_n(kr)]$$

$$=\mathbf{P}_{mn}{}^{\sigma}\frac{1}{k}\frac{d}{dr}[j_n(kr)]+[n(n+1)]^{\frac{1}{2}}\mathbf{B}_{mn}{}^{\sigma}\frac{1}{kr}[j_n(kr)] \quad (8)$$

$$\mathbf{M}_{\sigma mn}{}^{1}=\nabla\times[\mathbf{r}Y_{\sigma mn}(\theta,\phi)j_n(kr)]$$

$$=[n(n+1)]^{\frac{1}{2}}\mathbf{C}_{mn}{}^{\sigma}j_n(kr)=(1/k)\nabla\times\mathbf{N}_{\sigma mn}{}^{1}(\mathbf{r}) \quad (9)$$

$$\mathbf{N}_{\sigma mn}{}^{1}=(1/k)\nabla\times\mathbf{M}_{\sigma mn}{}^{1}(\mathbf{r})$$

$$=n(n+1)\mathbf{P}_{mn}{}^{\sigma}\frac{1}{kr}j_n(kr)+[n(n+1)]^{\frac{1}{2}}\mathbf{B}_{mn}{}^{\sigma}\frac{1}{kr}\frac{d}{dr}[rj_n(kr)], \quad (10)$$

where the vector spherical harmonics are defined as

$$\mathbf{P}_{mn}=\mathbf{e}_r X_n{}^m(\theta,\phi)$$

$$\mathbf{B}_{mn}=\frac{[n(n+1)]^{\frac{1}{2}}}{(2n+1)\sin\theta}\times\left\{\mathbf{e}_\theta\left[\frac{n-m+1}{n+1}X_{n+1}{}^m-\left(\frac{n+m}{n}\right)X_{n-1}{}^m\right]+\mathbf{e}_\phi\frac{m(2n+1)}{n(n+1)}iX_n{}^m\right\}$$

$$=\mathbf{e}_r\times\mathbf{C}_{mn}$$

$$\mathbf{C}_{mn}=\frac{[n(n+1)]^{\frac{1}{2}}}{(2n+1)\sin\theta}\left\{\mathbf{e}_\theta\frac{m(2n+1)}{n(n+1)}iX_n{}^m-\mathbf{e}_\phi\left[\left(\frac{n-m+1}{n+1}\right)X_{n+1}{}^m-\left(\frac{n+m}{n}\right)X_{n-1}{}^m\right]\right\},$$

where

$$X_n{}^m(\theta,\phi)=e^{im\phi}P_n{}^m(\cos\theta)=Y_{mn}{}^e(\theta,\phi)+iY_{mn}{}^o(\theta,\phi).$$

B. Scattering by a Rigid Sphere

The simplest type of scattering obstacle that can be considered is the rigid sphere. The boundary conditions that must be satisfied are that the components of the displacement vector must vanish at the spherical surface; three scalar boundary conditions must hold. The incident plane wave must first be described before the solutions describing the scattered wave can be constructed. There is, of course, no wave excited within the scatterer.

The most general expansion for a plane wave propagating in the z direction and expressed in spherical coordinates is given by

$$\mathfrak{I}e^{ikz}=\sum_n\frac{(2n+1)i^n}{n(n+1)}\{\mathbf{e}_x[\mathbf{M}_{o1n}{}^{1}(\mathbf{r})-i\mathbf{N}_{e1n}{}^{1}(\mathbf{r})]+\mathbf{e}_y[\mathbf{M}_{e1n}{}^{1}(\mathbf{r})+i\mathbf{N}_{o1n}{}^{1}(\mathbf{r})]-in(n+1)\mathbf{e}_z\mathbf{L}_{eon}{}^{1}(\mathbf{r})\},$$

where

$$\mathfrak{I}=\text{unit dyadic}=\mathbf{e}_x\mathbf{e}_x+\mathbf{e}_y\mathbf{e}_y+\mathbf{e}_z\mathbf{e}_z$$

and it should be noted that $m\leqslant n$; hence the sums representing the $\mathbf{e}_x$ and $\mathbf{e}_y$ terms (i.e., the shear wave terms) must range from one to infinity.

Since the incident wave is a shear wave propagating in the z direction and is polarized such that the displacements are in the x direction, forming the inner product of $\mathbf{e}_x$ and $\mathfrak{I}e^{iK_1z}$ will yield the desired representation for the incident wave,

$$\mathbf{s}_i=\mathbf{s}_i''=\mathbf{e}_x e^{iK_1 z}$$

$$=\sum_n \frac{(2n+1)i^n}{n(n+1)}[\mathbf{M}_{o1n}^{1}(\mathbf{r})-i\mathbf{N}_{e1n}^{1}(\mathbf{r})], \quad (11)$$

where the range of the index n in the sum will be omitted for convenience in all of the work.

The general character of the shear portion of the scattered wave may be inferred from Eq. (11); a different linear combination of vector solutions similar to those that appear in Eq. (11) will be formed. Solutions having superscript three, indicating that Hankel functions will be used as radial functions, will be employed in the sum. The shear portion of the scattered wave is given by

$$\mathbf{s}_s''=\sum_n \frac{(2n+1)i^n}{n(n+1)}[a_n\mathbf{M}_{o1n}^{3}(\mathbf{r})-ib_n\mathbf{N}_{e1n}^{3}(\mathbf{r})], \quad (12)$$

where the a_n and the b_n are expansion coefficients to be determined by applying the boundary conditions. As a result of the mode conversion process which takes place at the boundary, the scattered wave has a compressional portion. The polarization of the incident wave along the x axis precludes the use of the highly symmetric functions which describe a purely compressional incident wave for the construction of the longitudinal portion of the scattered wave. Functions in which the azimuthal index is unity, as in the transverse portion of the solution, will be used to describe $\mathbf{s}_s'$;

$$\mathbf{s}_s'=\sum_n \frac{(2n+1)i^n}{n(n+1)}d_n\mathbf{L}_{e1n}(\mathbf{r}), \quad (13)$$

where the d_n are expansion coefficients to be determined by application of the boundary conditions.

By using the definitions of the vector functions Eqs. (8)–(10) and the vector spherical harmonics following Eq. (10), the expressions for both the incident and scattered waves may be written in terms of simple scalar functions. From Eq. (11) and the definitions, one obtains expressions for the components of the displacement vector. In order to condense these expressions, abbreviations for the radial functions are introduced. The summation over n is understood.

$$s_{ri}=\cos\phi P_n^1 E_1(r) \quad (14a)$$

$$s_{\theta i}=\cos\phi\frac{1}{\sin\theta}\left\{P_n^1 F_1(r)+\left[\frac{n}{n+1}P_{n+1}^1-\frac{n+1}{n}P_{n-1}^1\right]F_2(r)\right\} \quad (14b)$$

$$s_{\phi i}=\sin\phi\frac{1}{\sin\theta}\left\{P_n^1 G_1(r)+\left[\frac{n}{n+1}P_{n+1}^1-\frac{n+1}{n}P_{n-1}^1\right]G_2(r)\right\}, \quad (14c)$$

where

$$E_1(r)=-(i)^{n+1}(2n+1)\frac{1}{K_1 r}j_n(K_1 r)$$

$$F_1(r)=(i)^n\frac{(2n+1)}{n(n+1)}j_n(K_1 r)$$

$$F_2(r)=-(i)^{n+1}\frac{1}{K_1 r}\frac{d}{dr}[r j_n(K_1 r)]$$

$$G_1(r)=(i)^{n+1}\frac{(2n+1)}{n(n+1)}\frac{1}{K_1 r}\frac{d}{dr}[r j_n(K_1 r)]$$

$$G_2(r)=-(i)^n j_n(K_1 r).$$

In a similar manner, the expressions for the components of the displacement vector produced by the outgoing wave are developed. The spherical Hankel functions $h_n(x)$ used here are the $h_n^{(1)}(x)$, where

$$h_n^{(1)}(x)=j_n(x)+in_n(x).$$

$$\mathbf{s}_s=\mathbf{s}_s'+\mathbf{s}_s''=\sum_n \frac{(2n+1)i^n}{n(n+1)}\times[a_n\mathbf{M}_{o1n}^{3}(\mathbf{r})-ib_n\mathbf{N}_{e1n}^{3}(\mathbf{r})+d_n\mathbf{L}_{e1n}^{3}(\mathbf{r})].$$

In terms of the abbreviated radial functions,

$$s_{rs}=\cos\phi P_n^1[b_n A_1(r)+d_n A_2(r)] \quad (15a)$$

$$s_{\theta s}=\cos\phi\frac{1}{\sin\theta}\left\{a_n P_n^1 B_1(r)+\left[\frac{n}{n+1}P_{n+1}^1-\frac{n+1}{n}P_{n-1}^1\right]\times[b_n B_2(r)+d_n B_3(r)]\right\} \quad (15b)$$

$$s_{\phi s}=\sin\phi\frac{1}{\sin\theta}\left\{a_n\left[\frac{n}{n+1}P_{n+1}^1-\frac{n+1}{n}P_{n-1}^1\right]D_1(r)+P_n^1[b_n D_2(r)+d_n D_3(r)]\right\}, \quad (15c)$$

where

$$\mathrm{A}_1(r)=-(\mathrm{i})^{n+1}(2\mathrm{n}+1)\frac{1}{K_1 r}\mathrm{h}_n(K_1 r)$$

$$A_2(r)=\frac{(i)^n(2n+1)}{n(n+1)}\frac{1}{k_1}\frac{d}{dr}h_n(k_1 r)$$

$$B_1(r)=\frac{(i)^n(2n+1)}{n(n+1)}h_n(K_1 r)$$

$$B_2(r)=-(i)^{n+1}\frac{1}{K_1 r}\frac{d}{dr}[r h_n(K_1 r)]$$

$$B_3(r)=(i)^n\frac{1}{k_1 r}h_n(k_1 r)$$

$$D_1(r)=-(i)^n h_n(\mathrm{K}_1 r)$$

$$D_2(r)=(i)^{n+1}\frac{(2n+1)}{n(n+1)}\frac{1}{\mathrm{K}_1 r}\frac{d}{dr}[r h_n(\mathrm{K}_1 r)]$$

$$D_3(r)=-(i)^n\frac{(2n+1)}{n(n+1)}\frac{1}{k_1 r}h_n(k_1 r).$$

The boundary conditions that must hold at the surface of the rigid sphere are

$$s_{ri}+s_{rs}=0 \tag{16a}$$

$$s_{\theta i}+s_{\theta s}=0 \quad r=a. \tag{16b}$$

$$s_{\phi i}+s_{\phi s}=0 \tag{16c}$$

The substitution of Eqs. (14) and (15) into Eqs. (16), and introduction of the notation

$$df(a)/da\equiv df(r)/dr|_{r=a}$$

yields the following set of equations:

$$\cos\phi P_n^1\{b_n A_1(a)+d_n A_2(a)+E_1(a)\}=0$$

$$\cos\phi\frac{1}{\sin\theta}\left\{a_n P_n^1 B_1(a)+\left[\frac{n}{n+1}P_{n+1}^1-\frac{n+1}{n}P_{n-1}^1\right]\times[b_n B_2(a)+d_n B_3(a)]+P_n^1 F_1(a)+\left[\frac{n}{n+1}P_{n+1}^1-\frac{n+1}{n}P_{n-1}^1\right]F_2(a)\right\}=0$$

$$\sin\phi\frac{1}{\sin\theta}\left\{a_n\left[\frac{n}{n+1}P_{n+1}^1-\frac{n+1}{n}P_{n-1}^1\right]D_1(a)+P_n^1[b_n D_2(a)+d_n D_3(a)]+P_n^1 G_1(a)+\left[\frac{n}{n+1}P_{n+1}^1-\frac{n+1}{n}P_{n-1}^1\right]G_2(a)\right\}=0.$$

Consider each of the boundary condition equations above; the dependence on the azimuthal variable is common to each term appearing in a given equation, and this dependence may be factored out. Since $\cos\phi$ and $\sin\phi$ are nonzero in general, the coefficients of $\cos\phi$ and $\sin\phi$ must vanish in order to satisfy the equations. The three equations are then multiplied by $P_n^1\sin\theta$, $P_n^1\sin^2\theta$, and $P_n^1\sin^2\theta$, respectively, and are integrated with respect to θ over the range $[0,\pi]$ in order to remove the dependence on the angle θ. The orthogonality relation for the associated Legendre polynomials [see Eq. (A.1)] is utilized to obtain

$$b_n A_1(a)+d_n A_2(a)+E_1(a)=0 \tag{17a}$$

$$a_n B_1(a)+F_1(a)=0 \tag{17b}$$

$$b_n D_2(a)+d_n D_3(a)+G_1(a)=0. \tag{17c}$$

Equations (17) constitute a set of three linear algebraic equations in three unknowns, the expansion coefficients, for each allowed value of n. The equations are solved readily and the solutions are as follows,

$$a_n=-j_n(\mathrm{K}_1 a)/h_n(\mathrm{K}_1 a) \tag{18a}$$

$$b_n=\frac{\frac{1}{k_1}\left\{\frac{d}{da}h_n(k_1 a)\right\}\frac{1}{\mathrm{K}_1 a}\frac{d}{da}\{a j_n(\mathrm{K}_1 a)\}-n(n+1)\frac{1}{\mathrm{K}_1 a}j_n(\mathrm{K}_1 a)\frac{1}{k_1 a}h_n(k_1 a)}{n(n+1)\frac{1}{\mathrm{K}_1 a}h_n(\mathrm{K}_1 a)\frac{1}{k_1 a}h_n(k_1 a)-\frac{1}{k_1}\left\{\frac{d}{da}h_n(k_1 a)\right\}\frac{1}{\mathrm{K}_1 a}\frac{d}{da}\{a h_n(\mathrm{K}_1 a)\}} \tag{18b}$$

$$d_n=\frac{\frac{1}{(\mathrm{K}_1 a)^2}n(n+1)\left[h_n(\mathrm{K}_1 a)\frac{d}{da}\{a j_n(\mathrm{K}_1 a)\}-j_n(\mathrm{K}_1 a)\frac{d}{da}\{a h_n(\mathrm{K}_1 a)\}\right]}{n(n+1)\frac{1}{\mathrm{K}_1 a}h_n(\mathrm{K}_1 a)\frac{1}{k_1 a}h_n(k_1 a)-\frac{1}{k_1}\left\{\frac{d}{da}h_n(k_1 a)\right\}\frac{1}{\mathrm{K}_1 a}\frac{d}{da}\{a h_n(\mathrm{K}_1 a)\}} \tag{18c}$$

The expansion coefficients describing the wave scattered by a rigid sphere have thus been determined explicitly. It should be noted that the expressions (18) are exact and are valid for any value of n, and for any values of the parameters $(k_1 a)$ and $(\mathrm{K}_1 a)$, since no approximations were made in the process of evaluating the expansion coefficients. Techniques similar to those developed in this section are employed in later work on the analysis of scattering by spherical obstacles other than rigid spheres.

C. Scattering by a Spherical Cavity

Since the boundary conditions appropriate to the problem in which the scatterer is a cavity, are that the components of the stress acting on the spherical boundary must vanish, expressions for the appropriate stress components must be developed. Equations relating the strains and displacements in a spherical coordinate system are given in Sokolnikoff's text.

The expressions for the stresses produced by both the incident and scattered waves are obtained by substi-

tuting the equations for the displacement components, Eqs. (14) and (15) into the strain equations, and systematically applying Hooke's Law for a homogeneous isotropic elastic solid.

The boundary conditions to be satisfied are

$$\sigma_{rri}+\sigma_{rrs}=0 \tag{19a}$$

$$\sigma_{r\theta i}+\sigma_{r\theta s}=0 \quad r=a. \tag{19b}$$

$$\sigma_{r\phi i}+\sigma_{r\phi s}=0. \tag{19c}$$

The explicit expressions for the stresses are substituted into Eqs. (19), and the boundary condition equations are obtained. The dependence of the terms in these equations on the angular variables is treated as in case of the rigid sphere. However, the orthogonality relation used previously will not cover all of the integrals of interest in this section. A number of definite integrals involving associated Legendre polynomials are evaluated in Appendix A and the results of these integrations are used in this and the following sections. A set of three linear equations in three unknowns is again obtained; it is readily solved for the expansion coefficients,

$$a_n=-\frac{(d/da)[j_n(\mathrm{K}_1a)/a]}{(d/da)[h_n(\mathrm{K}_1a)/a]} \tag{20a}$$

$$b_n=\Delta_b{}^n/\Delta^n$$
$$d_n=\Delta_d{}^n/\Delta^n, \tag{20b}$$

where the Δ are the appropriate determinants formed from the matrix equation representing the set of linear equations. The equations are solved simply by application of Cramer's rule. In matrix form, the equations are written as

$$\begin{bmatrix} E_{11} & E_{12} \\ E_{21} & E_{22} \end{bmatrix}\begin{bmatrix} b_n \\ d_n \end{bmatrix}=\begin{bmatrix} \delta_1 \\ \delta_2 \end{bmatrix},$$

where (21a)

$$E_{11}=(\lambda_1+2\mu_1)\frac{2n(n+1)}{2n+1}\frac{d}{da}A_1(a)$$
$$+\lambda_1\frac{4n(n+1)}{2n+1}\frac{A_1(a)}{a}+\lambda_1(1-2n^2)\frac{B_2(a)}{a}$$
$$+\lambda_1 n(n+1)\frac{D_2(a)}{a}$$

$$E_{12}=(\lambda_1+2\mu_1)\frac{2n(n+1)}{2n+1}\frac{d}{da}A_2(a)$$
$$+\lambda_1\frac{4n(n+1)}{2n+1}\frac{A_2(a)}{a}+\lambda_1(1-2n^2)\frac{B_3(a)}{a}$$
$$+\lambda_1 n(n+1)\frac{D_3(a)}{a}, \tag{21b}$$

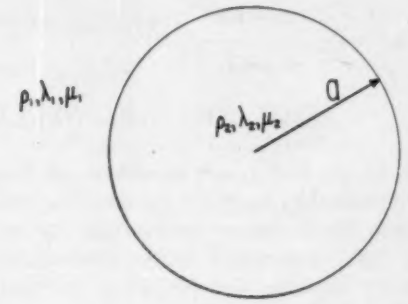

FIG. 2. Properties of elastic scatterer and elastic matrix material.

$$E_{21}=a^2\frac{d}{da}\left[\frac{D_2(a)}{a}\right]-A_1(a), \tag{21c}$$

$$E_{22}=a^2\frac{d}{da}\left[\frac{D_3(a)}{a}\right]-A_2(a), \tag{21d}$$

$$\delta_1=-\Bigg[(\lambda_1+2\mu_1)\frac{2n(n+1)}{2n+1}\frac{d}{da}E_1(a)$$
$$+\lambda_1\frac{4n(n+1)}{2n+1}\frac{E_1(a)}{a}+\lambda_1(1-2n^2)\frac{F_2(a)}{a}$$
$$+\lambda_1 n(n+1)\frac{G_1(a)}{a}\Bigg], \tag{21e}$$

$$\delta_2=E_1(a)-a^2\frac{d}{da}\frac{G_1(a)}{a}. \tag{21f}$$

D. Scattering by an Elastic Sphere

The problem in which the scattering obstacle is a homogeneous isotropic elastic sphere of elastic properties different from those of the elastic matrix in which the scatterer is embedded is considered next. The physical arrangement is shown in Fig. 2. The expressions for the displacements and stresses produced by the incident wave and outward propagating scattered wave are of the same form as considered previously in Sec. III.B,C. However, in the present case, there is a wave propagating within the scattering obstacle. As a result of the scattering and mode conversion processes, both compressional and shear waves are excited within the scatterer. The scattering region contains the origin of the spherical coordinate system; hence, radial functions which are nonsingular at the origin (i.e., the set $j_n(pr)$, where p is k_2 or K_2 are used to describe the wave. The subscript q is used to label the wave excited within the scatterer, and the subscript 2 is used to describe the elastic properties of the scatterer. The wave propagating within the scatterer is given by

$$\mathbf{s}_q=\mathbf{s}_q'+\mathbf{s}_q''=\sum_n \frac{(2n+1)i^n}{n(n+1)}$$

$$\times[e_n\mathbf{M}_{o1n}{}^1(\mathbf{r})-if_n\mathbf{N}_{e1n}{}^1(\mathbf{r})+g_n\mathbf{L}_{e1n}{}^1(\mathbf{r})],$$

where the e_n, f_n, and g_n are expansion coefficients and will be determined by applying the boundary conditions. The q wave displacement vector may be written in terms of its components using abbreviated radial functions by making the following substitutions in Eqs. (15),

Substitute		For
λ_2, μ_2		λ_1, μ_1
k_2, K_2		k_1, K_1
$j_n(\rho r)$		$h_n(\rho r)$
R_i	$i=1, 2$	A_i
S_i	$i=1, 2, 3$	B_i
T_i	$i=1, 2, 3$	D_i
e_n, f_n, g_n		a_n, b_n, d_n.

The stresses are then calculated as in Sec. III.C. The boundary conditions that must be satisfied are

$$s_{ri}+s_{rs}=s_{rq} \tag{22a}$$

$$s_{\theta i}+s_{\theta s}=s_{\theta q} \tag{22b}$$

$$s_{\phi i}+s_{\phi s}=s_{\phi q} \quad r=a. \tag{22c}$$

$$\sigma_{rri}+\sigma_{rrs}=\sigma_{rrq} \tag{22d}$$

$$\sigma_{r\theta i}+\sigma_{r\theta s}=\sigma_{r\theta q} \tag{22e}$$

$$\sigma_{r\phi i}+\sigma_{r\phi s}=\sigma_{r\phi q} \tag{22f}$$

The appropriate expressions for the displacement and stress components are then inserted in Eqs. (22) and the boundary condition equations are thus obtained. These equations are similar in form to the boundary condition equations derived in Sec. III.B, C. The problem in which the scatterer is an elastic solid can be regarded in a sense as a combination of the rigid sphere and the cavity problems. The significant difference between the boundary condition equations derived in this section and those equations derived previously, is the presence of additional terms in each equation resulting from the wave which is excited within the scatterer. The boundary condition equations are then integrated in order to eliminate the angular dependence in the same manner as was previously done. Again, the definite integrals needed for this integration are found in Appendix A. A set of six linear algebraic equations in six unknowns, the expansion coefficients, is thus derived. Simultaneous solution of the equations is a somewhat less formidable problem than it would seem at first glance. The expansion coefficients a_n and e_n appear only in the second and fifth equations, hence, they may readily be determined,

$$a_n=\frac{\mu_2F_1(a)\dfrac{d}{da}\left[\dfrac{S_1(a)}{a}\right]-\mu_1S_1(a)\dfrac{d}{da}\left[\dfrac{F_1(a)}{a}\right]}{\mu_1S_1(a)\dfrac{d}{da}\left[\dfrac{B_1(a)}{a}\right]-\mu_2B_1(a)\dfrac{d}{da}\left[\dfrac{S_1(a)}{a}\right]},$$

and

$$e_n=\frac{\mu_1F_1(a)\dfrac{d}{da}\left[\dfrac{B_1(a)}{a}\right]-\mu_1B_1(a)\dfrac{d}{da}\left[\dfrac{F_1(a)}{a}\right]}{\mu_1S_1(a)\dfrac{d}{da}\left[\dfrac{B_1(a)}{a}\right]-\mu_2B_1(a)\dfrac{d}{da}\left[\dfrac{S_1(a)}{a}\right]}.$$

The remaining four equations may be written in matrix notation,

$$\begin{bmatrix} E_{11} & E_{12} & E_{13} & E_{14} \\ E_{21} & E_{22} & E_{23} & E_{24} \\ E_{31} & E_{32} & E_{33} & E_{34} \\ E_{41} & E_{42} & E_{43} & E_{44} \end{bmatrix} \begin{bmatrix} b_n \\ d_n \\ f_n \\ g_n \end{bmatrix} = \begin{bmatrix} \delta_1 \\ \delta_2 \\ \delta_3 \\ \delta_4 \end{bmatrix},$$

where

$$E_{11}=D_2(a) \qquad E_{21}=D_2(a)$$

$$E_{12}=D_3(a) \qquad E_{22}=D_3(a)$$

$$E_{13}=-R_1(a) \qquad E_{23}=-T_2(a)$$

$$E_{14}=-R_2(a) \qquad E_{24}=-T_3(a)$$

$$E_{31}=(\lambda_1+2\mu_1)\frac{2n(n+1)}{2n+1}\frac{d}{da}A_1(a)+\lambda_1\frac{4n(n+1)}{2n+1}\frac{A_1(a)}{a}$$

$$+\lambda_1(1-2n^2)\frac{B_2(a)}{a}+\lambda_1n(n+1)\frac{D_2(a)}{a}$$

$$E_{32}=(\lambda_1+2\mu_1)\frac{2n(n+1)}{2n+1}\frac{d}{da}A_2(a)+\lambda_1\frac{4n(n+1)}{2n+1}\frac{A_2(a)}{a}$$

$$+\lambda_1(1-2n^2)\frac{B_3(a)}{a}+\lambda_1n(n+1)\frac{D_3(a)}{a}$$

$$E_{33}=-\left[(\lambda_2+2\mu_2)\frac{2n(n+1)}{2n+1}\frac{d}{da}R_1(a)\right.$$

$$+\lambda_2\frac{4n(n+1)}{2n+1}\frac{R_1(a)}{a}+\lambda_2(1-2n)^2\frac{S_2(a)}{a}$$

$$\left.+\lambda_2n(n+1)\frac{T_2(a)}{a}\right]$$

$$E_{34}=-\left[(\lambda_2+2\mu_2)\frac{2n(n+1)}{2n+1}\frac{d}{da}R_2(a)\right.$$

$$+\lambda_2\frac{4n(n+1)}{2n+1}\frac{R_2(a)}{a}+\lambda_2(1-2n^2)\frac{S_3(a)}{a}$$

$$\left.+\lambda_2n(n+1)\frac{T_3(a)}{a}\right]$$

$$E_{41}=\mu_1\left\{a\frac{d}{da}\left[\frac{D_2(a)}{a}\right]-\frac{A_1(a)}{a}\right\}$$

$$E_{42}=\mu_1\left\{a\frac{d}{da}\left[\frac{D_3(a)}{a}\right]-\frac{A_2(a)}{a}\right\}$$

$$E_{43}=-\mu_2\left\{a\frac{d}{da}\left[\frac{T_2(a)}{a}\right]-\frac{R_1(a)}{a}\right\}$$

$$E_{44}=-\mu_2\left\{a\frac{d}{da}\left[\frac{T_3(a)}{a}\right]-\frac{R_2(a)}{a}\right\}$$

$$\delta_1=-E_1(a)\quad\delta_2=-G_1(a)$$

$$\delta_3=-\left[(\lambda_1+2\mu_1)\frac{2n(n+1)}{2n+1}\frac{d}{da}E_1(a)+\lambda_1\frac{4n(n+1)}{2n+1}\frac{E_1(a)}{a}+\lambda_1(1-2n^2)\frac{F_2(a)}{a}+\lambda_1 n(n+1)\frac{G_1(a)}{a}\right]$$

$$\delta_4=-\mu_1\left\{a\frac{d}{da}\left[\frac{G_1(a)}{a}\right]-\frac{E_1(a)}{a}\right\}.$$

E. Scattering by a Fluid-Filled Cavity

The problem in which the scattering obstacle is a spherical cavity which is filled with a compressible inviscid fluid will be considered next. As a result of the mode conversion and scattering processes, which take place at the boundary, both compressional and shear waves would be expected to propagate within the scatterer; however, due to the nature of the scatterer, only the compressional wave is excited. The subscript q is again used to label the wave inside the scatterer, and the subscript f is used to describe the properties of the fluid material. Obviously,

$$\mathbf{s}_q''=0;$$

hence

$$\mathbf{s}_q=\mathbf{s}_q'=\sum_n\frac{(2n+1)i^n}{n(n+1)}g_n\mathbf{L}_{e1n}^1(\mathbf{r}),$$

where the g_n are expansion coefficients and will be determined. The boundary conditions that must be satisfied at the solid-fluid interface are

$$s_{ri}+s_{rs}=s_{rq} \tag{23a}$$

$$\sigma_{rri}+\sigma_{rrs}=\sigma_{rrq} \tag{23b}$$

$$\sigma_{r\theta i}+\sigma_{r\theta s}=0\quad r=a \tag{23c}$$

$$\sigma_{r\phi i}+\sigma_{r\phi s}=0. \tag{23d}$$

The normal components of displacement and stress for the q wave are given by

$$s_{rq}=\cos\phi P_n^1 g_n R_2(r)$$

$$\sigma_{rrq}=\lambda_f\cos\phi\left\{P_n^1 g_n\frac{d}{dr}R_2(r)+2P_n^1 g_n\frac{1}{r}R_2(r)-\frac{1}{\sin\theta}g_n\left[\frac{n}{n+1}P_{n+1}^2-\frac{n+1}{n}P_{n-1}^2\right]\frac{S_2(r)}{r}+\frac{1}{\sin^2\theta}P_n^1 g_n\frac{T_2(r)}{r}+\frac{\cos\theta}{\sin\theta}g_n\left[\frac{n}{n+1}P_{n+1}^1-\frac{n+1}{n}P_{n-1}^1\right]\frac{S_3(r)}{r}\right\}.$$

The normal stress is then calculated as in Sec. III.C. The appropriate expressions for the displacement and stress components are then inserted into Eqs. (23), and the boundary condition equations are thus obtained. The boundary condition equations are then integrated in order to remove the angular dependence in the same manner as was previously done. A set of four linear algebraic equations in four unknowns, the expansion coefficients, is thus derived. The third equation is solvable immediately for a_n,

$$a_n=-\frac{d/da[F_1(a)/a]}{d/da[B_1(a)/a]};$$

this is precisely the expression derived for the a_n in the case in which the scatterer is a cavity. The remaining three equations may be written in matrix notation

$$\begin{bmatrix}E_{11}&E_{12}&E_{13}\\E_{21}&E_{22}&E_{23}\\E_{31}&E_{32}&E_{33}\end{bmatrix}\begin{bmatrix}b_n\\d_n\\g_n\end{bmatrix}=\begin{bmatrix}\delta_1\\\delta_2\\\delta_3\end{bmatrix},$$

where

$$E_{11}=A_1(a)$$

$$E_{12}=A_2(a)$$

$$E_{13}=-R_2(a)$$

$$E_{21}=(\lambda_1+2\mu_1)\frac{2n(n+1)}{2n+1}\frac{d}{da}A_1(a)+\lambda_1\frac{4n(n+1)}{2n+1}\frac{A_1(a)}{a}+\lambda_1(1-2n^2)\frac{B_2(a)}{a}+\lambda_1(n+1)\frac{D_2(a)}{a}$$

$$E_{22}=(\lambda_1+2\mu_1)\frac{2n(n+1)}{2n+1}\frac{d}{da}A_2(a)+\lambda_1\frac{4n(n+1)}{2n+1}\frac{A_2(a)}{a}+\lambda_1(1-2n^2)\frac{B_3(a)}{a}+\lambda_1 n(n+1)\frac{D_3(a)}{a}$$

$$E_{23}=-\left[\lambda_f\frac{2n(n+1)}{2n+1}\frac{d}{da}R_2(a)+\lambda_f\frac{4n(n+1)}{2n+1}\frac{R_2(a)}{a}\right.$$
$$\left.+\lambda_f(1-2n^2)\frac{S_2(a)}{a}+\lambda_f n(n+1)\frac{T_2(a)}{a}\right]$$

$$E_{21}=a\frac{d}{da}\left[\frac{D_2(a)}{a}\right]-\frac{A_1(a)}{a}$$

$$E_{22}=a\frac{d}{da}\left[\frac{D_2(a)}{a}\right]-\frac{A_2(a)}{a}$$

$$E_{23}=0$$

$$\delta_1=-E_1(a)$$

$$\delta_2=-\left[(\lambda_1+2\mu_1)\frac{2n(n+1)}{2n+1}\frac{d}{da}E_1(a)\right.$$
$$+\lambda_1\frac{4n(n+1)}{2n+1}\frac{E_1(a)}{a}+\lambda_1(1-2n^2)\frac{F_2(a)}{a}$$
$$\left.+\lambda_1 n(n+1)\frac{G_1(a)}{a}\right]$$

$$\delta_3=-\left\{a\frac{d}{da}\left[\frac{G_1(a)}{a}\right]-\frac{E_1(a)}{a}\right\}.$$

IV. SHEAR WAVE SCATTERING CROSS SECTION

The scattering cross section for an elastic wave is defined as the ratio of the energy scattered per unit time by the obstacle to the energy per unit area carried per unit time by the incident wave. The latter quantity will be evaluated first. The displacements produced by the incident wave are given by

$$s_{xi}=e^{iK_1z},\quad s_{yi}=s_{zi}=0.$$

It should be noted that the displacements in the present discussion are taken to be dimensionless. It is readily seen that the only nonvanishing stress in the field of the incident wave is σ_{zz}, which is given by

$$\sigma_{zzi}=2\mu_1 e_{zzi}=iK_1\mu_1 e^{iK_1z},$$

where the strain component e_{xz} is defined as

$$e_{xz}=\frac{1}{2}\left(\frac{\partial s_x}{\partial z}+\frac{\partial s_z}{\partial x}\right).$$

The energy flux expression derived by Ying and Truell is then utilized to obtain

$$\dot{F}_i=-\rho_1 w^3/K_1.$$

In order to calculate the total energy scattered by the spherical obstacle, a sphere of radius b, $(b\gg a)$, is constructed concentric with the scatterer. The rate of transport of energy across the larger sphere is then obtained by integrating over the sphere as was done in the previous work on compressional waves by Ying and Truell and by the present authors.

$$\dot{Q}_s=\frac{iw}{2}\int_0^{\pi}\int_0^{2\pi}[(\sigma_{rrs}\bar{s}_{rs}+\sigma_{r\theta s}\bar{s}_{\theta s}+\sigma_{r\phi s}\bar{s}_{\phi s})$$
$$-(\bar{\sigma}_{rrs}s_{rs}+\bar{\sigma}_{r\theta s}s_{\theta s}+\bar{\sigma}_{r\phi s}s_{\phi s})]b^2d\phi\sin\theta d\theta,\quad(24)$$

where $\bar{s}_r$ indicates complex conjugate of s_r, etc. The expression developed for the displacements and the stresses produced by the scattered wave are inserted into Eq. (24) and the integrations are performed. The integrations with respect to the azimuthal variable are particularly simple

$$\int_0^{2\pi}\sin^2\phi d\phi=\int_0^{2\pi}\cos^2\phi d\phi=\pi.$$

The result of this integration is merely multiplication of the remaining integral by π. The integrations with respect to θ involve products of the associated Legendre polynomials. These integrals are evaluated in the Appendix and the results are utilized in the calculation of $\dot{Q}_s$. The two integrations eliminate all of the dependence of $\dot{Q}_s$ on the angular variables, and only the radial functions remain. Up to this point, nothing has been said about the magnitude of b, except that b is much greater than a. Since the material surrounding the scattering obstacle has been taken to be homogeneous, isotropic and ideally elastic, there is no attenuation of the scattered wave due to viscous or thermal damping, or any other conceivable loss mechanism. Consequently, the rate at which energy is transported across a sphere concentric with the scatterer is independent of b. If b is taken to be sufficiently large such that

$$k_1b,\quad K_1b\gg1\quad(\text{and } b\gg a),$$

the asymptotic forms provide reasonable representations for the spherical Hankel functions, which are used to describe the scattered wave. The asymptotic expansions for $h_n(x)$ is given by Watson[15] as follows

$$h_n(x)\underset{x\to\infty}{\longrightarrow}\frac{1}{x}e^{[ix-\frac{1}{2}i\pi(n+1)]},$$

where x is k_1r or K_1r.

The asymptotic forms are then used to evaluate the functions $A_1(K_1b)$, $A_2(k_1b)$, $\cdots$ etc., which appear in $\dot{Q}_s$. The details of the calculation are not shown here; the result is indicated and the summation sign is included in the result.

$$\dot{Q}_s=-2\rho_1w^3\pi\sum_{n=1}^{\infty}(2n+1)\left\{\frac{1}{K_1^3}a_n\bar{a}_n+\frac{1}{K_1^3}b_n\bar{b}_n\right.$$
$$\left.+\frac{1}{n(n+1)k_1^3}d_n\bar{d}_n\right\}.$$

The scattering cross section is defined as

$$\gamma = \dot{Q}_s / \dot{F}_i.$$

The scattering cross section obviously has dimensions of [length]^2. The normalized scattering cross section, defined as the ratio of γ to the geometrical cross section, is given by

$$\gamma_N = \gamma/\pi a^2$$

$$= 2\sum_{n=1}^{\infty}(2n+1)\left\{\frac{1}{(\mathrm{K}_1 a)^2}a_n\bar{a}_n + \frac{1}{(\mathrm{K}_1 a)^2}b_n\bar{b}_n + \frac{(\mathrm{K}_1 a)}{n(n+1)(k_1 a)^3}d_n\bar{d}_n\right\},$$

where γ_N is dimensionless and depends only on $(k_1 a)$ and $(\mathrm{K}_1 a)$ and is not dependent on k_1, K_1, or a alone. It should be noted that the scattering cross section appears as the sum of squares of the expansion coefficients. There is no coupling between the two shear modes since the cross terms vanish in the $b \to \infty$ limit. There is also no coupling between the compressional mode and either of the shear modes since the phase velocities differ.

V. RAYLEIGH LIMIT APPROXIMATION

The well-known series definitions of the spherical Bessel and Hankel functions are

$$j_n(x) = 2^n x^n \sum_{m=0}^{\infty}(-1)^m \frac{(n+m)!}{m![2(n+m)+1]!}x^{2m}$$

$$h_n(x) = h_n^{(1)}(x)$$

$$= \frac{e^{ix}}{x^{n+1}}\sum_{m=0}^{n}(-i)^{n-m+1}\frac{(n+m)!}{m!(n-m)!2^m}x^{n-m}.$$

In the Rayleigh limit, $x \ll 1$, terms of order x^2 and higher orders are neglected with respect to those of order x^0. This is the criterion used in calculating the limiting forms of the scattering cross sections. The cross section for the Rayleigh scattering of transverse elastic waves by spherical obstacles are tabulated below.

Rigid sphere

$$\gamma_N = 6\frac{[1+\frac{1}{2}k_1^3/\mathrm{K}_1^3]}{[1+k_1^2/\mathrm{K}_1^2]^2} + \frac{4}{3}\frac{[12+12k_1^2/\mathrm{K}_1^2+8k_1^4/\mathrm{K}_1^4+5k_1^5/\mathrm{K}_1^5]}{[3+4k_1^2/\mathrm{K}_1^2]^2}(\mathrm{K}_1 a)^4$$

Cavity

$$\gamma_N = \left\{\frac{8}{27}[1+\tfrac{1}{2}k_1^3/\mathrm{K}_1^3] + 10\left[\frac{2}{4k_1^2/\mathrm{K}_1^2-9}\right]^2[1+\tfrac{1}{6}k_1^5/\mathrm{K}_1^5]\right\}(\mathrm{K}_1 a)^4$$

Elastic sphere

$$\gamma_N = \frac{8}{3}\left[1+\frac{1}{2}\frac{k_1^3}{\mathrm{K}_1^3}\right](\mathrm{K}_1 a)^4 \times \frac{\left[3\frac{\mathrm{K}_1^2}{\mathrm{K}_2^2} - 3\frac{\mathrm{K}_2^2}{\mathrm{K}_1^2} - 4\frac{k_2^2\mathrm{K}_1^2}{\mathrm{K}_2^4} + 10\frac{k_2^2}{\mathrm{K}_2^2} - 6\frac{k_2^2}{\mathrm{K}_1^2}\right]}{\left[1-10\frac{\mathrm{K}_1}{k_1}+6\frac{k_2}{k_1}-6\frac{k_2\mathrm{K}_2^2}{k_1\mathrm{K}_1^2}+9\frac{\mathrm{K}_2^2}{\mathrm{K}_1^2}\right]^2}$$

Note that the classical dependence of the cross section on the fourth power of the frequency is obtained in each case for the transverse wave. In the scattering by a rigid sphere, it is obtained as a perturbation on a term of zero order. The zero order dependence alone is reported in the work of Ying and Truell. As was noted in the problem of scattering by an elastic sphere of a longitudinal wave, the cross section for a transverse wave vanishes if the obstacle and the medium are composed of the same material; i.e., no scatterer.

APPENDIX I. SOME DEFINITE INTEGRALS INVOLVING ASSOCIATED LEGENDRE POLYNOMIALS

In order to remove the angular dependence of the boundary condition equations in the shear wave scattering problems, integrations with respect to the variable θ are performed. The integrals involve products of the associated Legendre polynomials $P_n^m(x)$, where $x = \cos\theta$, and some power of x. Two of the required integrals are to be found in standard texts; the results for these commonly found integrals are

$$\int_0^{\pi} P_n^1 P_m^1 \sin\theta d\theta = \frac{2n(n+1)}{2n+1}\delta_{mn} \qquad (A.1)$$

$$\int_0^{\pi} \frac{P_n^1 P_n^1}{\sin^2\theta}\sin\theta d\theta = n(n+1). \qquad (A.2)$$

Necessary additional integrations have been carried out. Several of the integrals are easily shown to vanish; others are more difficult and apparently not to be found in the literature. Only the results of the integrations are

given below.

$$\int_0^\pi P_n^1 P_n^2 d\theta = 0 \qquad \text{(A.3)}$$

$$\int_0^\pi P_n^1 P_n^1 \cos\theta \sin\theta d\theta = 0 \qquad \text{(A.4)}$$

$$\int_0^\pi \frac{P_n^1 P_n^1}{\sin^2\theta} \cos\theta \sin\theta d\theta = 0. \qquad \text{(A.5)}$$

$$\int_0^\pi P_n^1 P_n^2 \sin^2\theta d\theta = 0 \qquad \text{(A.6)}$$

$$\int_0^\pi \frac{P_n^1}{\sin\theta}\left[\frac{n}{n+1}P_{n+1}^2 - \frac{n+1}{n}P_{n-1}^2\right]\sin\theta d\theta = 2n^2 \qquad \text{(A.7)}$$

$$\int_0^\pi \frac{P_n^1}{\sin^2\theta}\left[\frac{n}{n+1}P_{n+1}^1 - \frac{n+1}{n}P_{n-1}^1\right]\cos\theta \sin\theta d\theta = 1 \qquad \text{(A.8)}$$

The final integral is given as an exercise in Whittaker and Watson.[16]

$$\int_0^\pi \frac{P_{n+1}^1 P_{n-1}^1}{\sin^2\theta} \sin\theta d\theta = n(n-1) \qquad \text{(A.9)}$$

[16] E. T. Whittaker and G. N. Watson, *A Course of Modern Analysis* (Cambridge University Press, Cambridge, England, 1935), 4th ed.

JOURNAL OF APPLIED PHYSICS VOLUME 31, NUMBER 5 MAY, 1960

Photoelastic Properties of Polystyrene in the Glassy State. III. Styrene Derivatives and Copolymers*

J. F. Rudd and R. D. Andrews†
Physical Research Laboratory, The Dow Chemical Company, Midland, Michigan

(Received May 22, 1959)

The stress-optical coefficient, Young's modulus, and strain-optical coefficient at room temperature (27°C) have been determined for several styrene derivatives, for two copolymer systems (styrene/α-methyl styrene and styrene/methyl methacrylate) over the entire composition range, and for several copolymers of styrene with acrylates and methacrylates of varying composition. The results indicate that steric effects, particularly in the immediate neighborhood of the chain backbone, have a very important influence on the nature of the molecular motions (and, consequently, on the photoelastic behavior) during glassy distortions. The stress-optical coefficient becomes more negative (phenyl rings less free to orient) as a result of α-substitution on the chain or ortho-substitution on the phenyl ring. Substitution in the para-position of the phenyl ring, or increasing the separation of the phenyl ring from the chain backbone makes the stress-optical coefficient more positive (phenyl rings more free to orient); plasticizers (including residual monomer and solvents) or decreasing molecular weight have an effect in the same direction. Copolymer systems show nonideal mixing, photoelastically, indicating that interaction effects between neighboring monomer units along the chain are of significant magnitude. This may provide a means of studying the nature of the monomer sequences in copolymers (e.g., of block and graft copolymers), and also of observing stereospecific structure in polymers.

INTRODUCTION

THE photoelastic properties of a polymer seem to hold great promise as a means of investigating the configurational changes taking place in the molecules during mechanical deformation processes. However, this type of measurement cannot be used as an effective tool for this purpose until the relationship between the stress-birefringence and the details of molecular structure, and other variables of the system, have been established. This has been the aim of the present series of investigations, in which attention has been centered on the photoelastic behavior of polystyrene in the glassy state.

In the first two papers of this series,[1,2] the effects of molecular orientation and of temperature, respectively, on the photoelastic properties (stress-optical coefficient, Young's modulus, and strain-optical coefficient) of glassy polystyrene were investigated. In the present paper the effects of details of molecular structure are investigated, by the use of several styrene derivatives, and copolymer systems of two types (styrene/α-methyl styrene and styrene/acrylic). The results obtained cast considerable light on the essential nature of the phenomenon and the most significant factors involved.

EXPERIMENTAL

The general principle of the experimental method was the same as in previous work, involving the application

* Presented in part before the Eighth Canadian High Polymer Forum at MacDonald College, St. Anne de Bellevue, Quebec, May 14, 1958.

† Present address: Plastics Research Laboratory, Room 7-006, M.I.T., Cambridge 39, Massachusetts.

[1] R. D. Andrews and J. F. Rudd, J. Appl. Phys. **28**, 1091 (1957), Part I.

[2] J. F. Rudd and E. F. Gurnee, J. Appl. Phys. **28**, 1096 (1957), Part II.

of dead loads to the samples and measurement of the birefringence produced, by use of a Sénarmont compensator arrangement. However, the equipment was set up in the present case as a table-top arrangement with the optical components mounted on an optical bench support rod. The sample hung vertically from a cross bar, the height of which could be varied, and was gripped at the ends by clamps with roughened inner surfaces, which were attached by essentially swivel-type connections to the support frame above and a slotted weight holder below. A mercury thermometer was mounted with bulb next to the sample. A sketch of the experimental arrangement is given in Fig. 1. All measurements were carried out at room temperature (27°±2°C).

The samples used were compression molded, to avoid molecular orientation as much as possible (in Part I it was shown that molecular orientation affects the photoelastic properties in a very significant way). Typical sample dimensions were of ⅛0.1 in.-thickness, 0.5 in.-width, 4 in.-length, although samples of various sizes were employed. Slotted weights in the range of 0.5 to 5 kg were applied to the samples to give simple tensile stresses. The analyzer was first set at extinction with no added weights (this took into account the effect of the weight of the lower clamp and weight holder, plus any initial birefringence in the sample). Then various weights were added and the change in extinction angle (or change in birefringence) resulting from the added weights was determined. Results of a typical experiment are shown in Fig. 2. A linear relation was obtained in all cases and the stress-optical coefficient was calculated from the slope, as the ratio of birefringence to stress, in the conventional units of Brewsters (1 Brewster = 10^{-13} reciprocal d/cm²).

Time effects were largely absent or negligible. Slight drifts in the analyzer reading ("optical creep") were occasionally observed; these were usually most noticeable just after application or removal of the load. Zero readings were taken before and after each load, and the two values averaged in computing the change produced by the load. In addition, a number of duplicate readings were taken at each load (and each zero) and an average reading computed from these; this was necessary because of the limited precision of individual readings.

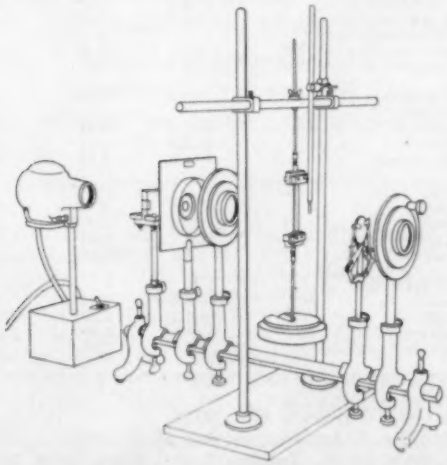

FIG. 1. Sketch of experimental arrangement.

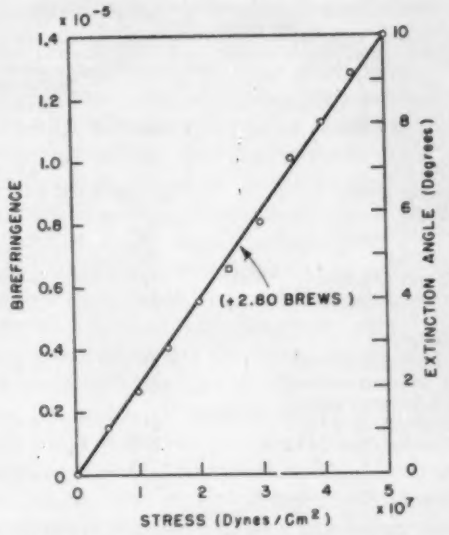

FIG. 2. Results of a typical stress-optical experiment, on a styrene/methyl methacrylate copolymer (containing 68.2 mole % styrene).

Young's modulus was determined by the beam flexure method described in Part II. The strain-optical coefficient was calculated simply by multiplying the values of stress-optical coefficient and Young's modulus, as in Parts I and II.

Copolymer compositions were determined directly by spectroscopic analysis. The styrene/α-methyl styrene copolymers were dissolved in carbon tetrachloride (2% solution) and analyzed by determining the concentration of α-methyl groups, from the infra-red absorption at 3.4 μ (antisymmetrical CH_3 stretch). The values obtained are believed to be accurate to within about ±0.5%. The styrene-acrylic copolymers were analyzed for the concentration of phenyl rings using ultra-violet. The polymers were dissolved in tetrahydrofuran (0.1% solution) and the absorption measured at 259 mμ. This latter procedure was essentially the same as that used by Dunn and Melville[3,4] and more recently by Tobolsky, Eisenberg, and O'Driscoll[5] to analyze the composition of styrene/methyl methacrylate copolymers; however, these other authors used chloroform as their solvent.

EXPERIMENTAL RESULTS

A. Polystyrene

Values for the stress-optical coefficient of polystyrene in the glassy state have been obtained by several in-

[3] A. S. Dunn and H. W. Melville, Nature **169**, 699 (1952).
[4] A. S. Dunn, B. D. Stead, and H. W. Melville, Trans. Faraday Soc. **50**, 279 (1954).
[5] A. V. Tobolsky, A. Eisenberg, and K. F. O'Driscoll, Anal. Chem. **31**, 203 (1959).

TABLE I. Stress-optical coefficient of polystyrene in the glassy state.

Author	Temp (°C)	Stress-optical coefficient (Brewsters)
Müller (1941)[a]	—	+6.5
Trapeznikova (1948)[b]	12°–32°	+9 to +11
Bailey (1948)[c]	25°	+7.0
Kolsky (1950)[d]	16°	∼+10
Kawata (1956)[e]	20°	∼+10.5
Bhagavantam and Murty (1956)[f]	32°	+9.56
Tsvetkov and Krim (1956)[g]	18°	+7.6
Present Series		
Part I (monofilaments)[h]	27°	+10.1
Part II (extruded sheet)	27°	+9.5
Part III (present paper)		
(isothermal, $M=145\,000$)	27°	+8.7
(isothermal, $M=225\,000$)	27°	+8.3

[a] See footnote 102 of reference 6.
[b] Values of $+\Delta\epsilon$ from Table I of footnote 7.
[c] Computed from his value of 490 psi per order per inch (p. 231 and Fig. 12 of footnote 8), assuming white light with an average wavelength of 6000 A.
[d] Measured on Transpex II polystyrene. Sign "∼" indicates "approximately."
[e] Taken from dashed curve in Fig. 1-1 of footnote 10.
[f] Computed as $n^3(q_{11}-q_{12})/2$, by using data from Tables I and III of footnote 11.
[g] From Table I of footnote 12.
[h] Extrapolated to zero orientation.

vestigators (including Müller,[6] Trapeznikova,[7] Bailey,[8] Kolsky,[9] Kawata,[10] Bhagavantam and Murty,[11] and Tsvetkov and Krim[12]). These values available in the published literature, together with values from the present series of investigations, have been collected in Table I. Some measuremtens have also been made by Hiltscher,[13] but it was not possible to compute the stress-optical coefficient from his data because the wavelength of the light used was not given (temperature was also not specified).

A significant variation is observed in the different values—even in the values which we have measured ourselves. The samples used in the present study were two polymers of different molecular weight made by a thermal polymerization method carried out under isothermal conditions[13a]; for simplicity, these polymers will be referred to as "isothermal." The intrinsic viscosities of these polymers in toluene at 25°C were 0.653 and 0.881 dl/g, which would correspond to average molecular weights of 145 000 and 225 000, respectively. It was difficult to prepare compression moldings from these polymers which were optically homogeneous, and values of stress-optical coefficient were obtained at different positions on the same sample which varied as much as 2–3 Brewsters. Consequently, readings were taken at several positions on two samples of each polymer and the results averaged. This effect was probably caused by localized states of orientation in the moldings. Difficulties of this sort were not ordinarily encountered, but appeared in a few cases, showing that sample preparation can sometimes be a significant problem in work of this kind.

B. Styrene Derivatives

Measurements of the photoelastic constants of several polystyrene derivatives were carried out, and the results are listed in Table II. This table lists values for alkyl- and chloro-derivatives of polystyrene, as well as values of all three constants for the various polystyrene samples which we have measured, and for a few methacrylate polymers of special interest.

One striking result, which is immediately evident, is the effect of adding a methyl group to the chain of polystyrene, to give poly-α-methyl styrene. This causes the stress-optical coefficient to completely change sign, from approximately +9 to −2 Br. Let us assume as a provisional hypothesis that the photoelastic effect in glassy polymers is caused by the orientation of molecular groups having anisotropic polarizabilities, just as in the rubbery state and in solution. (This may be contrasted with a theory involving the distortion of interatomic distances, which has been proposed by Mueller[14,15] and Weyl[15a] to explain the photoelastic

TABLE II. Photoelastic constants of polystyrene, polystyrene derivatives and methacrylates.

Polymer of	Stress-optical coefficient (Brewsters)	Young's modulus (psi $\times 10^{-5}$)	Strain-optical coefficient ($\times 10^{5}$)
Styrene			
Part I (monofilaments)	+10.1	4.25	+29.6
Part II (extruded sheet)	+9.5	4.65	+30.5
Part III (present paper)			
(isothermal, $M=145\,000$)	+8.7	5.14	+31.0
(isothermal, $M=225\,000$)	+8.3	4.60	+26.4
α-Methyl styrene	−2.0	5.74	−8.0
Vinyl toluene			
Dow Q406.3	+15.5	3.81	+40.7
Cymac 400	+11.6	3.82	+30.6
p(tert-Bu) styrene	+11.0	3.53	+26.8
p-Cl styrene			
pptd once	+32.6	4.25	+95.6
pptd twice	+22.9	5.07	+80.1
pptd 3 times	+23.7	4.81	+78.6
2,5 di-Cl styrene	+7.2	5.64	+27.8
Methyl methacrylate			
Plexiglas II	−3.8	5.29	−13.8
Lucite 130	−2.7	4.30	−8.1
Phenyl methacrylate	+39.8	4.87	+133.6
Cyclohexyl methacrylate	+5.9	3.55	+14.4

[6] F. H. Müller, Kolloid-Z. **95**, 138, 306 (1941).
[7] O. N. Trapeznikova, J. Phys. Chem. (U.S.S.R.) **22**, 395 (1948). An English translation of this article by Mrs. V. Tolkmith and R. D. Andrews has been put on file in the Crerar Library, Chicago.
[8] J. Bailey, India Rubber World **118**, 225 (1948).
[9] H. Kolsky, Nature **166**, 235 (1950).
[10] K. Kawata, J. Polymer Sci. **19**, 359 (1956).
[11] S. Bhagavantam and Y. K. Murty, Proc. Indian Acad. Sci. **A43**, 203 (1956).
[12] V. N. Tsvetkov and I. A. Krim, Vestnik Leningrad University, Physics and Chemistry Series, No. 16, p. 5 (1956). An English translation of this article by Mrs. V. Tolkmith and J. F. Rudd is on file in the Crerar Library.
[13] R. Hiltscher, VDI Zeitschrift **95**, 777 (1953). These data are also reprinted in R. Hiltscher, VDI Zeitschrift **97**, 49 (1955).
[13a] U. S. Patent 2,769,804 to A. W. Hanson, Dow Chemical Company (1956).
[14] H. Mueller, Physics **6**, 179 (1935).
[15] H. Mueller, J. Am. Ceramic Soc. **21**, 27 (1938).
[15a] Described by M. Tashiro, J. Soc. Glass Tech. **40**, 353 T (1956).

effect in inorganic silicate glasses.) The phenyl ring has a particularly high polarizability anisotropy and it is largely responsible for the photoelastic effect in polystyrene. The polarizability anisotropy of the hydrocarbon chain is relatively much smaller, and this is true also of the methyl group. In fact, the slight anisotropy of the methyl group will tend to neutralize that of the backbone chain, so that the chain and α-methyl groups taken as a whole probably have an almost zero anisotropy.

The effect of the methyl group in poly-α-methyl styrene must, therefore, be primarily a steric one, influencing the freedom to orient of the phenyl rings. The negative sign indicates that the phenyl rings are actually orienting *laterally*, rather than in the direction of the strain. Benzene rings, which were free to orient in an optically neutral elastic suspending medium, would give a positive effect. Molecular models of polystyrene and poly-α-methyl styrene confirm the large steric effect of the α-methyl group; i.e., the polystyrene chain is fairly flexible, whereas the poly-α-methyl styrene chain is so crowded sterically that a model will hardly stay together. A similar increase of steric crowding and chain stiffness is produced when an α-methyl group is added to an acrylate chain to give a methacrylate chain, as has been noted by several authors.[16–22]

The substitution of a methyl group on the phenyl ring to give vinyl toluene seems to have a less drastic effect. Values are given for two polymers, an American Cyanamid polymer, Cymac 400 (48% ortho-, 5% meta-, 47% para-vinyl toluene) and a Dow polymer (0% *o*-, 65% *m*-, 35% *p*-).[23] The stress-optical coefficient seems to be slightly more positive for these polymers, particularly for the Dow polymer. A sample of pure ortho-monomer was obtained and polymerized, but no useable samples could be prepared from this polymer either by compression molding or solvent casting—the polymer was extremely brittle. This brittleness was undoubtedly caused by low molecular weight; the intrinsic viscosity of this polymer (in toluene at 25°C) was 0.248 dl/g, which would indicate an average molecular weight (based on polystyrene) of only 40 000. The polymer of pure para-tert-butyl styrene was also somewhat brittle, but could be measured; the value of +11.0 Br obtained for this polymer is again slightly higher than polystyrene.

Two chloro-derivatives of styrene were also examined —a pure para isomer of mono-chlor styrene and 2,5 (ortho, meta)-dichlorostyrene. The poly p-Cl styrene had a pronounced monomer odor after polymerization, precipitation from solution, drying, and molding. A high value (+32.6 Br) of stress-optical coefficient was obtained for this sample. The polymer was reprecipitated and the value of the stress-optical coefficient dropped to +22.9 Br. However, a faint monomer odor could still be detected. A third, very thorough precipitation was therefore carried out (using a Waring blendor), and this was followed by extended drying in a vacuum oven. This successfully removed all monomer odor from the polymer. However, it was difficult to obtain an optically useable molding from this last polymer by the usual molding procedure. A molding made with a positive pressure mold was reasonably satisfactory, and this gave a value of +23.7 Br, which differed little from the previous value. The strain-optical coefficient shows a regular decrease with decreasing monomer content. The third modulus value looks slightly out of line—one would expect this to be the highest value of all. Nevertheless, it can be concluded from these results, first, that the stress-optical coefficient for poly p-Cl styrene (approximately +23 Br) is significantly higher than the value for polystyrene; and, second, that the presence of monomer (and probably of any low molecular weight plasticizing material) in the polymer has a considerable effect on the photoelastic properties, making the stress-optical coefficient (and strain-optical coefficient) more positive, indicating that the freedom of the phenyl rings to orient has been increased.

The stress-optical coefficient for poly-2,5-dichlorostyrene differs from polystyrene in the opposite direction; the value here is +7.2 Br. Comparison of strain-optical values indicates that this is mostly an effect of the higher modulus, which in turn probably reflects a significant amount of dipole-dipole attraction in the solid state. The contrast between this polymer and the poly p-Cl styrene is interesting, however, and deserves further investigation.

An over-all comparison of these various ring-substituted derivatives suggests some tentative conclusions. Substitution in the orthoposition appears to have a similar effect to substitution in the α-position on the chain; i.e., it causes the stress-optical coefficient to change in the negative direction. Substitution in the para-position, on the other hand, causes the stress-optical coefficient to become more positive. In the polyvinyl toluene samples, both effects are present. That orthosubstitution should have an effect similar to α-substitution is not surprising if steric effects are important, since an orthosubstituent will occupy a spatial position much like that of an α-substituent, relative to the chain backbone, and will probably produce a similar crowding effect. The effect of para substitution may come from the fact that the para substituent tends to push neighboring chains further away, and thus gives the phenyl ring more "effective room" for orientation.

[16] R. F. Tuckett, Trans. Faraday Soc. **38**, 310 (1942).
[17] E. Jenckel, Kolloid-Z. **100**, 163 (1942).
[18] G. D. Coumoulos, Proc. Roy. Soc. (London) **A182**, 166 (1943).
[19] D. J. Crisp, J. Colloid Sci. **1**, 161 (1946).
[20] J. Heyboer, P. Dekking, and A. J. Staverman, *Proceedings of the Second International Congress on Rheology* (Butterworths Scientific Publications, Ltd., London, 1954), p. 123.
[21] S. Iwayanagi, J. Sci. Research Inst. (Tokyo) **49**, 23 (1955).
[22] A. Silberberg, J. Eliassaf, and A. Katchalsky, J. Polymer Sci. **23**, 259 (1957).
[23] The ortho/meta/para ratio was determined for these polymers from infrared absorption at 13.75, 12.78, and 12.29 μ, respectively (1% solution in carbon disulfide).

These effects of ring substitution are generally smaller than the effect of α-substitution, except in the case of the p-Cl polymer. The explanation for this latter case is not completely clear; one factor involved may be that a chlorine substituent probably increases the polarizability anisotropy of the phenyl ring more than a methyl substituent does.

C. Related Acrylic Polymers

The methacrylate samples in Table II are also of considerable interest. Polyphenyl methacrylate, which may be considered a homolog of polystyrene (or, more accurately, of poly-α-methyl styrene) is found to have a strikingly high stress-optical coefficient of +39.8 Br. Evidently, the fact that the phenyl ring has been separated from the main chain backbone by two intermediate atoms has very greatly increased the freedom of the phenyl ring to orient. The value for polycyclohexyl methacrylate is only +5.9 Br, showing that the polarizability anisotropy of the aromatic phenyl ring is in fact making the principal contribution to the birefringence. The value of the stress-optical coefficient of polymethyl methacrylate seems to be slightly different for Plexiglas (Rohm & Haas) and for Lucite (duPont); the values are roughly −3 Br, however.

Measurements of the stress-optical behavior in the glassy state (at 20–25°C) have been carried out for several methacrylates, and also for polystyrene, by Dvořák and Majer.[24,25] However, they computed their results in terms of an "optical sensitivity constant" K, and the defining equation which they give for this quantity is dimensionally incorrect. If it is assumed that their constant K is simply an inverse stress-optical coefficient, a transformation equation of the following form can be written:

$$\text{Stress-optical coeff (Br)} = 500/K, \qquad (1)$$

where the constant 500 is chosen so that polystyrene ($K = 50$) will have a value of +10 Br. Some polymers which the present work and their work have in common, and stress-optical values computed by use of Eq. (1), are the following:

Polymer of	K	Stress-opt coeff (Brewsters)
Styrene	(+50)	(+10.0)
Methyl methacrylate	−140	−3.6
Phenyl methacrylate	+13	+39
Cyclohexyl methacrylate	+100	+5.0

The agreement here with our own values of stress-optical coefficient is very good, indicating that Eq. (1) is correct.

Three other polymers which they studied, and which are also of particular interest here, are the following:

Polymer of	K	Stress-opt coeff (Brewsters)
Chlorethyl methacrylate	+90	+5.6
o-Nitrophenyl methacrylate	+23	+22
Benzyl methacrylate	+11	+45

They say that the chlorethyl methacrylate listed shows a larger birefringence than plain ethyl methacrylate, though no exact value could be obtained for the latter polymer because it was somewhat soft and showed time-effects. The stress-optical coefficient is also positive, whereas the value for polymethyl methacrylate is negative. This more positive value may be related to the more positive value of poly p-Cl styrene as compared with polystyrene.

The effect of orthosubstitution (making the stress-optical coefficient more negative, or less positive) seems to be observed in poly-o-nitrophenyl methacrylate, comparing this with polyphenyl methacrylate, even though the phenyl ring is somewhat separated from the chain backbone; this is perhaps a result of the size of the nitro group.

The value of the stress-optical coefficient for benzyl methacrylate, compared with that for phenyl methacrylate, indicates that the phenyl rings in this polymer are still more free to orient than the phenyl rings in phenyl methacrylate, though the difference is actually not great. The phenyl rings have apparently been freed from the larger part of their steric hindrance by the time that they have been separated from the chain backbone by two intermediate atoms,[26] so that a third intermediate atom has relatively little additional effect. This is illus-

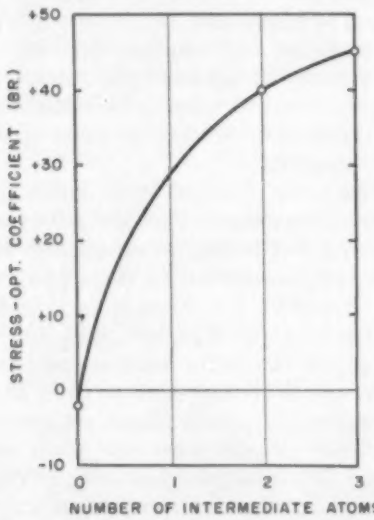

FIG. 3. Plot of stress-optical coefficient vs number of intermediate atoms separating the phenyl ring from the chain backbone, for chains with complete α-methyl substitution.

[24] J. Dvořák and J. Majer, Collection Czechoslov. Chem. Commun. **22**, 379 (1957). (Text in German.)

[25] J. Majer and J. Dvořák, Kunststoff-Rundschau **4**, 345 (1957).

[26] *Note added in proof.*—Some photoelastic measurements on poly(p-tert-butyl) phenyl methacrylate have been reported by Tsvetkov and Verkhotina [J. Tech. Phys. (U.S.S.R.) **28**, 97 (1958); English translation in Soviet Phys.-Tech. Phys. **3**, 87 (1958)] which are of interest in this connection. They give a value of +36 Br for the stress-optical coefficient of this polymer in the glassy state, which is not greatly different from that of the unsubstituted polyphenyl methacrylate.

TABLE III. Photoelastic constants for styrene copolymers.

Copolymer of Styrene with	% Styrene Wt %	% Styrene Mole %	Stress-optical coefficient (Brewsters)	Young's modulus (psi×10^{-5})	Strain-optical coefficient (×10^{3})
α-Methyl styrene	16.8	18.7	+3.0	5.17	+10.6
α-Methyl styrene	36.0	39.0	+0.7	6.16	+2.8
α-Methyl styrene	42.7	45.8	+0.1	4.22	+0.2
α-Methyl styrene	56.0	59.1	+0.6	5.06	+2.1
α-Methyl styrene	71.5	74.0	+3.5	4.87	+11.6
α-Methyl styrene (isothermal)	90.0	91.1	+5.7	3.83	+15.1
Methyl methacrylate	17.1	16.6	−2.2	4.04	−6.2
Methyl methacrylate	33.3	32.5	−1.0	4.30	−3.1
Methyl methacrylate	34.2	33.1	−0.7	4.76	−2.2
Methyl methacrylate	49.4	48.4	+0.5	4.34	+1.5
Methyl methacrylate	69.0	68.2	+2.8	4.77	+9.2
Methyl methacrylate	86.4	85.9	+4.9	4.96	+16.8
Acrylates					
Acrylic acid	85.3	80.1	+9.6	4.96	+32.7
Acrylic acid	90.3	88.1	+8.7	5.31	+31.9
Acrylic acid	93.2	90.5	+8.6	5.09	+30.2
Methyl acrylate	74.1	70.3	+10.7	4.38	+32.3
Butyl acrylate	71.1	75.2	+8.4	3.82	+22.2
Butyl acrylate	80.3	83.4	+8.0	3.96	+21.8
Decyl acrylate	77.8	87.7	+9.3	3.95	+25.4
Methacrylates					
Methacrylic acid	83.3	80.5	+5.6	4.79	+18.3
Methacrylic acid	91.3	89.7	+6.7	4.96	+23.0
Ethyl methacrylate	79.2	80.7	+6.5	3.91	+17.5
Hexyl methacrylate	76.4	84.1	+5.8	4.22	+16.7
Hexyl methacrylate	79.9	86.7	+5.4	4.28	+15.9

trated graphically in Fig. 3, where values of stress-optical coefficient for poly-α-methyl styrene, polyphenyl methacrylate, and polybenzyl methacrylate are plotted vs distance of separation of the phenyl ring from the chain backbone (the chain backbone here has complete α-methyl substitution in all cases). It is clear that the hindrance to phenyl orientation is most pronounced, and slight steric effects will have the most influence, in the immediate neighborhood of the chain backbone.

D. Molecular Weight Effect

Dvořák and Majer also made photoelastic measurements on five different polystyrene samples of different molecular weight. Their data, when converted by use of Eq. (1), indicate that the stress-optical coefficient has an essentially constant value of about +9 Br at high molecular weights ($MW > 80\,000$), and increases with decreasing molecular weight; i.e., a value of +11.6 Br was found for the lowest molecular weight sample, which had a molecular weight of about 50 000.

This effect of molecular weight can probably be explained by the observation that when a molecular model of polystyrene (or any similar polymer) is built, the monomer units near the end of the chain have more flexibility and freedom to change their configuration than monomer groups which lie well within the chain. The phenyl rings near the end of the polystyrene chain are thus probably more free to orient than the phenyl rings in the interior of the chain, and these end rings will tend to make the over-all stress-optical coefficient more positive, to an extent depending on the concentration of chain ends in the polymer, which is determined by the number average molecular weight.

E. Styrene Copolymers

Photoelastic measurements were also carried out on two copolymer systems (styrene/α-methyl styrene and

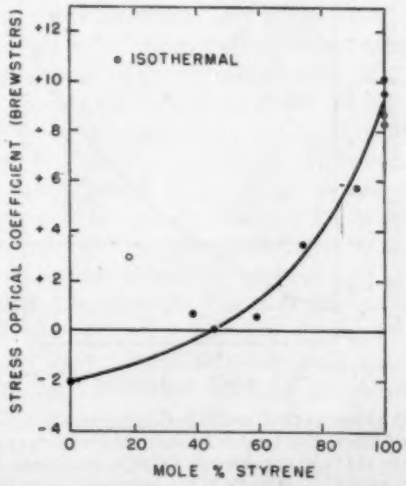

FIG. 4(a). Stress-optical coefficient vs composition for styrene/α-methyl styrene copolymers.

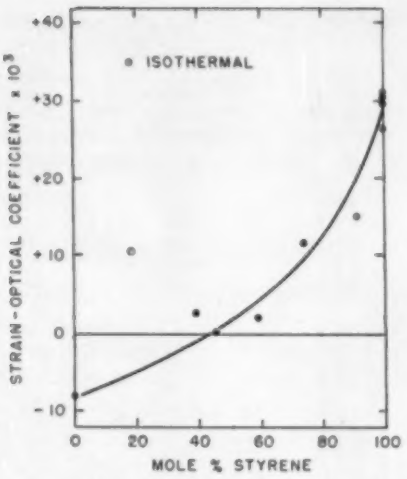

FIG. 4(b). Strain-optical coefficient vs composition for styrene/α-methyl styrene copolymers.

styrene/methyl methacrylate) over the entire composition range. The data obtained are presented in Table III and in Figs. 4 and 5.

Figs. 4(a) and 4(b) show the stress-optical and strain-optical coefficients for the styrene/α-methyl styrene system plotted vs mole % styrene content. The copolymers shown here were obtained from different sources and were polymerized in different ways; this probably accounts for the scatter in the points. Samples prepared by "isothermal" polymerization are indicated by special points.

The sample with 18.7 mole % styrene was prepared in a special way. This polymer for some reason did not form compression moldings which were optically usable, so several thin films were cast from toluene solution and dried; these were laid on top of each other and the whole "sandwich" compressed under heat and pressure. The resulting sample was satisfactory for optical measurements; however, the values obtained (open circles) do not fall smoothly in line with the other data. The values are too high in the positive direction suggesting that solvent was probably not completely removed from the cast films. The data for this polymer must therefore be disregarded, but are included in the figures to illustrate that caution is probably necessary in using solvent-cast films in experiments of this type (as has been done, for example, by Trapeznikova[7]).

Since the two monomers in this system differ only by the presence or absence of the α-methyl group, the abscissa scale in Figs. 4(a) and 4(b) can also be read backwards as percent of α-methyl substitution in polystyrene. It is clear that neither the stress-optical nor strain-optical coefficient gives a linear relation vs mole

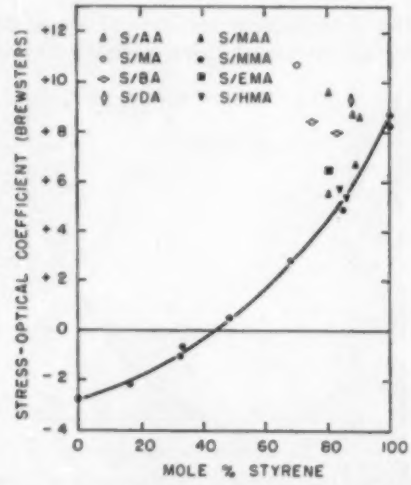

FIG. 5(a). Stress-optical coefficient vs composition for styrene/acrylic copolymers. Solid curve is drawn through data for methyl methacrylate (MMA) copolymers. Other comonomers are acrylic acid (AA), methyl acrylate (MA), butyl acrylate (BA), decyl acrylate (DA), methacrylic acid (MAA), ethyl methacrylate (EMA), and hexyl methacrylate (HMA).

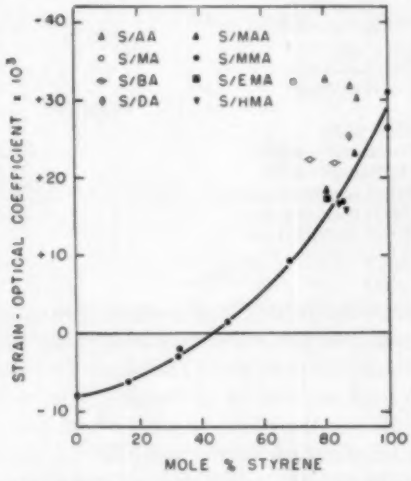

FIG. 5(b). Strain-optical coefficient vs composition for styrene/acrylic copolymers. Code same as in Fig. 5a.

% composition: both plots show a pronounced curvature toward the side of more negative values. The optical behavior of a copolymer thus cannot be described as a simple additive function of the optical behavior of the component monomers, which is of considerable interest from a theoretical standpoint. This provides additional evidence that neighboring side groups along the chain interfere sterically with each other.

Very similar results are obtained for the styrene/methyl methacrylate system, as seen from Figs. 5(a) and 5(b). In fact, this and the preceding copolymer system are almost quantitatively identical. This copolymer series (including the 100% styrene polymers, but not the 100% methyl methacrylate sample, where the Lucite value is used) were all isothermal polymers, and the uniform method of preparation seems to result in less scatter of the points than in the α-methyl styrene case. The smoothed curves for both stress-optical and strain-optical coefficients again show a definite curva-

ture (toward the negative side) when plotted vs mole % composition.

Scattered measurements were made on several acrylic and methacrylic copolymers with styrene (all isothermal copolymers), and these are also plotted in Figs. 5(a) and 5(b). The numerical values are given in Table III. While these copolymers all have a relatively high styrene content and do not cover the whole composition range, they show some interesting trends which are most evident in the plot of strain-optical coefficient [Fig. 5(b)].

One generalization which is immediately evident is that the methacrylate copolymers (methacrylic acid, methyl, ethyl, hexyl) all lie very nearly on the curve drawn for the methyl methacrylate copolymers; the nature of the end group seems to make little difference. The acrylate copolymers, on the other hand, lie off the methyl methacrylate curve and show much more effect of the nature of the end group (hydrogen, methyl, butyl, decyl). The acrylate copolymers have values which are more positive than the methacrylate copolymers, and the copolymers of acrylic acid and methyl acrylate actually have values more positive than polystyrene itself. The values move in the negative direction as the size of the end group increases, but never reach the methacrylate curve. The decyl acrylate copolymer seems out of line with the others, since it lies above the butyl acrylate copolymers. This particular copolymer (unlike the others) was quite milky in appearance, resulting perhaps from the presence of microcrystallites produced by crystallization of the decyl groups. The orientation of such crystallites, or the plasticizing effect of the decyl groups, probably accounts for the anomalous behavior of this copolymer.

These results can be understood on the basis of the same sort of steric effects as have been postulated previously. The fact that the methacrylate copolymers all behave similarly, and show little change in effect when the end group is changed, can be explained by the fact that the α-methyl group, which they all contain, is exerting the controlling influence here. This methyl group probably crowds the chain so tightly that the end group on the ester is forced to stand out away from the chain and thus exerts little influence on the freedom of rotation of the phenyl rings. In the acrylate copolymers the absence of the α-methyl group gives the phenyl rings more freedom to orient; the stress-optical (and strain-optical) coefficient is therefore more positive than for the methacrylate copolymers. Also, since the α-methyl group is absent, it is probable that the ester end group can fold back into the neighborhood of the chain backbone to some extent, and thus exert a crowding effect similar to that of an α-methyl group; and the crowding will be greater, the larger the size of this end group. This increase in the size of the end group will therefore produce a progressively greater interference with phenyl ring orientation, causing the photoelastic constants to move in the negative direction. The values approach but never reach the methacrylate curve indicating that the steric effect of the ester end group never becomes quite as great as that of an α-methyl group attached directly to the chain backbone.

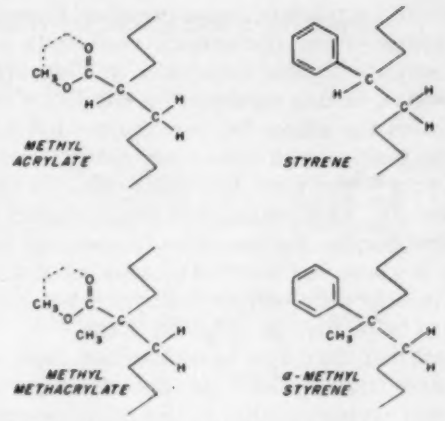

FIG. 6. Sketch of structures of monomeric units in styrene and acrylic polymers, with and without α-methyl substitution.

DISCUSSION

The copolymer results above also allow some conclusions to be drawn regarding the photoelastic behavior of acrylic-type polymers. Taking polymethyl methacrylate as an example, the polarizability anisotropy is centered in the carboxyl (–COO–), and particularly in the carbonyl (>C=O) group. The orientation of this group should produce a *positive* birefringence, whereas the optical effect observed for polymethyl methacrylate in the glassy state is actually *negative*. The explanation for this is probably to be found in the analogy of the structure of this polymer with that of poly-α-methyl styrene, both polymers containing an α-methyl group on the chain. Monomer units for these two polymers, together with the corresponding polymers which do not contain the α-methyl group, are sketched in Fig. 6. The carboxyl group is planar just like the inner half of the phenyl ring in polystyrene, and is therefore probably very similarly affected by any steric effects in the immediate neighborhood of the chain backbone (such as those produced by introduction of an α-methyl group). The similarity of the ester group to the phenyl ring has been emphasized in Fig. 6 by drawing in the remainder of a hexagon with dashed lines. Actually, the terminal methyl group is free to rotate, but this probably has only a secondary effect on either the polarizability or the steric behavior of the ester group.

We would therefore predict that the stress-optical coefficient of polymethyl acrylate should be positive in the glassy state, like polystyrene. This appears to be in conflict with a statement made by Trapeznikova and Zhurina[27] to the effect that the stress-optical coefficient

[27] O. N. Trapeznikova and M. N. Zhurina, J. Phys. Chem. (U.S.S.R.) **24**, 1471 (1950). An English translation of this paper by Mrs. V. Tolkmith and J. F. Rudd is on file with the Crerar Library.

of polymethyl acrylate is always negative. Examination of the values of the photoelastic coefficients for the methyl acrylate/styrene copolymer in Figs. 5(a) and 5(b), however, further reinforces the conclusion that by extrapolation the values for pure polymethyl acrylate should be positive with values not too different from those of pure polystyrene. This point should be checked experimentally. Low-temperature measurements would be required because the transition temperature for this polymer is about +4°C.[28,29] The stress-optical coefficient of nearly pure polyethyl acrylate has been observed[30] to be positive in the glassy state.

The fact that the curves vs composition (both stress-optical and strain-optical) for the styrene/α-methyl styrene and styrene/methyl methacrylate systems are almost identical quantitatively is also a very interesting result. The α-methyl group is of course a common feature of both comonomers, but one is also forced to conclude from this that the ester and phenyl groups have almost identical optical effects, and are thus optically equivalent in a photoelastic sense. This lends further weight to the prediction that the photoelastic coefficients for glassy polymethyl acrylate should be positive. This also indicates that the contribution of the ester group is probably small in the case of the two methacrylate polymers in Fig. 3. Also of interest in this connection are the recent results of Lamble and Dahmouch,[31] showing that the addition of plasticizer to polymethyl methacrylate causes the stress-optical coefficient to change in the positive direction, and actually assume positive values if sufficient plasticizer is added; this illustrates a further analogy of behavior of the ester and phenyl groups.

The fact that the curves of stress-optical and strain-optical coefficient vs composition for the two complete copolymer systems are not linear leads to some additional conclusions. As mentioned previously, this result indicates that the photoelastic constants of a copolymer cannot be described as a simple additive function of contributions from the two types of monomer unit. Evidently interaction effects between neighboring monomer units are present. The most pronounced interactions are probably between nearest neighbors. In a copolymer with monomer units *A* and *B*, there will be six different types of nearest-neighbor configurations, three with an *A* unit in the center (–AAA–, –AAB–, –BAB–) and three with a *B* unit in the center (–ABA–, –ABB–, –BBB–). The chain can thus be described as consisting of six different types of unit, rather than two. And since these will probably all make contributions of different magnitude to the optical effect, the existence of a curved relation rather than a straight line can readily be explained in this way.

If this interpretation is correct, the curvature in such a plot should give information on the type of monomer sequences present in the polymer; and anything affecting the nature of the monomer sequences should affect the curvature. Block copolymers, for example, where the blocks are fairly long should contain essentially only two of the six types of nearest-neighbor groupings, i.e., –AAA– and –BBB–. A block copolymer system of this sort should give curves vs composition which are much nearer straight lines. The same should be true of graft copolymers where the grafted branches are fairly long. And if the system were carefully enough calibrated, it should be possible, conversely, to deduce from the curvature of plots vs composition (or even from individual values at a known composition) information on the lengths of the blocks or grafted branches present in the polymer, or on the nature of the monomer sequences in general. This method would probably be most sensitive in the range of shorter lengths or sequences, as is probably also true of the sensitivity to molecular weight.

Photoelastic measurements might similarly be useful in the study of stereospecific polymers, since the different isomeric forms undoubtedly have somewhat different steric characteristics in the immediate neighborhood of the chain backbone. The side groups should probably have greatest freedom to orient in a "syndiotactic" molecule (alternate *D*,*L*), and least in an "isotactic" (all *D* or all *L*). An "atactic" molecule (random *D*,*L*) should lie somewhere between these other two. Precautions would have to be taken against the complicating effects of crystallinity in this particular application, however.

ACKNOWLEDGMENTS

Appreciation is expressed to all those in the Dow Company, too numerous to mention individually, who contributed to this work by supplying monomers or polymers, carrying out spectroscopic analyses, and molding samples. Particular thanks are due R. M. Nowak and P. L. Brissette of the Physical Research Laboratory for polymerization of several of the special monomers used.

[28] E. Jenckel, Z. Phys. Chem. **A190**, 24 (1941).
[29] R. H. Wiley and G. M. Brauer, J. Polymer Sci. **3**, 455 (1948).
[30] R. S. Stein, S. Krimm, and A. V. Tobolsky, Textile Research J. **19**, 8 (1949).
[31] J. H. Lamble and E. S. Dahmouch, Brit. J. Appl. Phys. **9**, 388 (1958).

Orientation Density and Its Use in Quantitative Texture Studies

C. G. DUNN AND J. L. WALTER
General Electric Research Laboratory, Schenectady, New York
(Received December 7, 1959)

An equation is derived from a definition of *orientation density*, $Q=\delta\zeta/1.4\rho^3$, where Q is the average orientation density in an orientation state of size ρ centered on a particular orientation and $\delta\zeta$ is the measured volume fraction of the sample with orientations within the orientation state. An approximate relationship between orientation density and (100) pole density for a strong single component texture is obtained, namely, $Q_0=1.08P_0^4$, where Q_0 is the maximum orientation density and P_0 is the maximum pole density. Samples that include the orientations of a large number of grains are used to illustrate the application of orientation density to the study of textures. Orientation density results are considered to be especially valuable when the texture has many components.

ACCORDING to Burgers[1] and common usage, the word *texture* may be taken to specify the crystallographic arrangement of all the crystals (or crystallites) of a sample. Often the question arises, during the analysis of data, whether or not the final description of the texture gives the crystallographic arrangement correctly and completely. An example of a correct and complete description would be that of a wire with complete fibering[2] with the crystallographic arrangement specified in an axis-density plot, showing the quantitative pole density of every possible $\{hkl\}$ pole parallel to the fiber axis.[3] Correct but not as complete would be a description in terms of all the $\{hkl\}$ pole concentrations parallel to the fiber axis, i.e., a description giving information about the $\langle hkl\rangle$ components of the fiber texture. It is in the description of textures such as those appearing in rolled materials, however, that difficulty arises. The crystallographic arrangement required involves orientations and orientation concentrations[4,5] and this immediately suggests the need for a quantitative term such as orientation density.

Qualitatively the term *orientation density*, for a given orientation in a polycrystalline sample, is a measure of the fraction of a sample in a small orientation range about the given orientation. In Sec. I this term is defined more precisely for its quantitative use in the study of textures.

An orientation may be described by three angle coordinates (see Appendix) or by numbers giving both the (hkl) plane in the plane of rolling and the $[uvw]$ direction in the direction of rolling. A quantitative pole figure, however, gives only the pole density as a function of direction (i.e., two angle coordinates) and this, of course, is not in the form of orientation data. Pole figures, as is well known, have to be analyzed or interpreted to obtain orientation results. The extent of possible errors in the interpretations is not known, but certainly should be more for complex textures than for simple textures. It has been pointed out previously[4] that information about orientations is lost when a (100) pole figure or a set of axis density figures is used to summarize many individually determined orientations in a multicomponent texture. The present paper is in part an extension of this type of treatment, making use of additional data and the concept of orientation density (Sec. II).

The usual definition of pole density[4] is given at the beginning of Sec. I in order to develop, by analogy, the present definition of orientation density.

SECTION I. DEFINITIONS OF POLE DENSITY, ORIENTATION DENSITY, AND ORIENTATION CONCENTRATION

Pole Density

Let $\delta\omega$ be an element of solid angle for a direction (θ,ϕ) and δf be the volume fraction of a polycrystalline sample with (hkl) poles within $\delta\omega$. The average (hkl) pole density within $\delta\omega$ is then given by

$$P=b\delta f/\delta\omega, \tag{1}$$

where b is a constant. The pole density is constant for all values of (θ,ϕ) if the sample is one of randomly oriented crystals. We set $P=1$ for the value of the constant pole density and obtain

$$1=b(\delta f)_r/\delta\omega, \tag{2}$$

where $(\delta f)_r$ now refers to the random-orientation sample, or simply the *r-o* sample.

The division of (1) by (2) eliminates both b and $\delta\omega$ and gives

$$P=\delta f/(\delta f)_r \text{ in "times random" units.} \tag{3}$$

Since the intensity of diffracted monochromatic x rays is proportional to the volume fraction of a sample correctly oriented for diffraction, a practical substitute to (3) is

$$P=I_a/I_r, \tag{4}$$

where I_a is the corrected intensity of diffracted x rays

[1] W. G. Burgers, "Rekristallisation, Verformter Zustand und Erholung" in Masing, *Handbuch der Metallphysik* (Leipzig, Becker and Erler 1941), Vol. III, p. 2.
[2] *Metals Handbook* (ASM, Cleveland, 1948), p. 17.
[3] L. K. Jetter, C. J. McHargue, and R. O. Williams, J. Appl. Phys. **27**, 368 (1956).
[4] C. G. Dunn, J. Appl. Phys. **30**, 850 (1959).
[5] C. G. Dunn and J. L. Walter, J. Appl. Phys. **30**, 1067 (1959).

from the sample and I_r is the similar quantity for an r-o sample.

There are other situations where Eq. (1) must be used. The value of b therefore has to be determined. This number, which depends on (hkl), is obtained by integrating (2) over a solid angle of 2π. Thus

$$P=(2\pi/n)\delta f/\delta\omega, \tag{5}$$

where n is a multiplicity factor with values of 3, 4, 6, 12, and 24 for (100), (111), (110), (112), and (123) poles, respectively.

If $\delta\omega$ is in the form of a conical solid angle (i.e., is a circle in stereographic projection of angular ratius ρ), it has a value of $2\pi(1-\cos\rho)$. When ρ is not too large, the solid angle may be written simply as $\pi\rho^2$. For this case, (5) reduces to

$$P=(2/n)\delta f/\rho^2. \tag{6}$$

The units of P in both (5) and (6) are "times random."

If P has a maximum point for some direction (θ,ϕ), this direction locates a pole concentration.

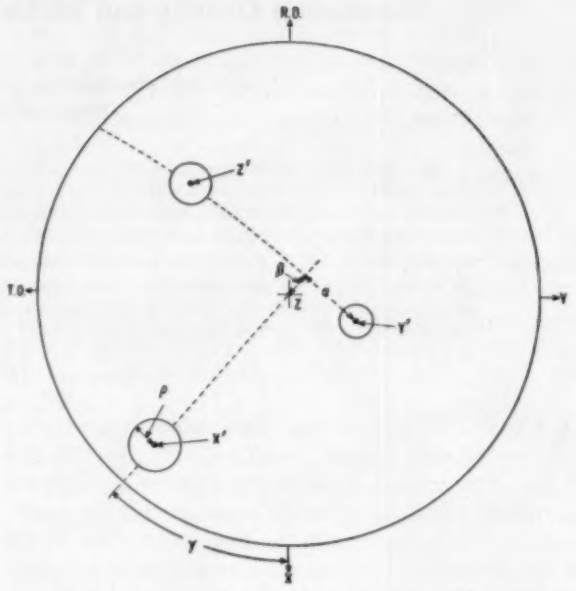

FIG. 1. Stereographic projection showing an orientation (α,β,γ) or $X'Y'Z'$ and an orientation state of size ρ.

Orientation Density

Expressions and equations entirely analogous to the above (except Eq. 4) may now be written for orientation density. The analogue of direction (θ,ϕ) is orientation (α,β,γ) and the analogue of element of solid angle $\delta\omega$ is element of orientation space $\delta\nu$; i.e., a range of orientations $\delta\alpha\delta\beta\delta\gamma$. Therefore, let $\delta\nu$ be an element of orientation space at an orientation (α,β,γ), and $\delta\zeta$ be the volume fraction of a polycrystalline sample with orientations within $\delta\nu$. The average orientation density within $\delta\nu$ by definition is then given by

$$Q=c\delta\zeta/\delta\nu, \tag{7}$$

where c is a constant. The orientation density $Q(\alpha,\beta,\gamma)$ is constant for all orientations if the sample is an r-o sample. We set $Q=1$ for such a sample and obtain

$$1=c(\delta\zeta)_r/\delta\nu, \tag{8}$$

where $(\delta\zeta)_r$ refers to the r-o sample. The division of (7) by (8) eliminates both c and $\delta\nu$ and gives

$$Q=\delta\zeta/(\delta\zeta)_r \text{ in "times random" units.} \tag{9}$$

Since the intensity of diffracted monochromatic x rays depends only on the volume fraction of crystals with a given (hkl) plane in position for diffraction and not on crystallographic directions in the (hkl) plane, there is no simple x-ray procedure associated with the use of Eq. (9). However, if the volumes and orientations of enough grains in a sample are determined individually, values of $\delta\zeta$ can be calculated for chosen orientations within an orientation range $\delta\nu$. Furthermore, the value of $(\delta\zeta)_r$ for the same orientation range can be calculated for an r-o sample. To do this we fix both the orientation and the size of $\delta\nu$ by using a specific orientation state of size ρ. Such an orientation state is illustrated in a stereographic plot in Fig. 1. The orientation is specified by the positions of three mutually perpendicular directions X', Y', Z' while the orientation state includes all orientations with {100} poles within ρ radians of X', Y', and Z', respectively. For example, any orientation with its {100} poles within the three circles is in this particular $X'Y'Z'$ orientation state. If ρ is not too large, the probability that an orientation, selected from a random group, will lie in this specific orientation state is $1.43\rho^3$.[6] Consequently,

$$(\delta\zeta)_r=1.43\rho^3. \tag{10}$$

If we drop the third digit and substitute in (10) we get

$$Q=\delta\zeta/1.4\rho^3. \tag{11}$$

This equation may be applied directly in the determination of orientation densities. An alternative equation is derived in the Appendix.

Orientation Concentration

If the orientation density Q has a maximum point for some orientation $X'Y'Z'$, then the position $X'Y'Z'$ locates an orientation concentration. In order that Q be a maximum it is necessary for $Q(X'Y'Z')>Q(X''Y''Z'')$ for all sufficiently small deviations of $X''Y''Z''$ from $X'Y'Z'$. If this condition is met, it follows from (11) that Q increases towards a maximum as ρ decreases. Let us also write $(\delta\zeta)_2-(\delta\zeta)_1$ for the volume fraction increase of orientations as ρ increases from ρ_1 to ρ_2 and Q^* for the average orientation density associated with the increase of ρ. It follows, from the definition of an average,

[6] C. G. Dunn, Phys. Rev. 66, 215 (1944).

that

$$Q^*=\frac{(\delta\zeta)_2-(\delta\zeta)_1}{1.4(\rho_2^2-\rho_1^2)}. \tag{12}$$

Thus, if $X'Y'Z'$ locates an orientation concentration, Q^* must increase as both ρ_2 and ρ_1 decrease.

Pole Density vs Orientation Density

In general, no unique relation exists between pole density and orientation density. On the other hand, it is clear that an orientation concentration for an orientation $X'Y'Z'$ in a single component texture must have (100) pole concentrations in the three X', Y', Z' directions, or must have (hkl) pole concentrations at proper (θ,ϕ) positions for the particular orientation.

Perhaps of greatest interest are the probable relations between Q and P when P refers to (100) poles having a normal distribution for a strong single-component texture. Let each pole concentration be of the form

$$P_0\exp\{-(x^2+y^2)/2\sigma^2\}$$

with $\sigma^2=1/3P_0$. We consider one relation only—namely, how the maximum value of the orientation density Q_0 depends on the maximum value of the pole density P_0. From (5) the fraction of the sample for a solid angle $\delta x\delta y$ at one peak pole position is $(3/2\pi)P_0\delta x\delta y$. We assume that this fraction is normally distributed along an arc 90° away with maxima points at the peaks of the other two pole concentrations. Integration over one pole concentration requires that $(3/2\pi)P_0\delta x\delta y=\int g\exp(-\lambda^2/2\sigma^2)d\lambda$, and $g=(3P_0/2\pi)^{\frac{1}{2}}\delta x\delta y$.

The fraction of the sample $\delta\zeta$ in a range $\delta\lambda$ (or in an element of space $\delta v=\delta x\delta y\delta\lambda$) at the peak position is $g\delta\lambda$. Thus $\delta\zeta=(3P_0/2\pi)^{\frac{1}{2}}\delta x\delta y\delta\lambda$. But $Q_0=c\delta\zeta/\delta x\delta y\delta\lambda$, where $c=\pi^2/3$ (see Appendix). Therefore,

$$Q_0\simeq 1.08P_0^{\frac{1}{2}}. \tag{13}$$

This equation, of course, is not valid for values of P_0 near 1.

An alternate form of (13) is

$$Q_0\simeq 36P_0/\sigma \tag{14}$$

when σ is expressed in degrees. Although (13) applies only to single component textures, (14) may apply also to multicomponent textures if the P_0 is interpreted as the peak height of a completely isolated (100) pole concentration with a distribution parameter σ. Furthermore, if the fraction of this component of the texture is f, then

$$f=3P_0\sigma^2 \tag{15}$$

when σ is in radians.

TABLE I. Average (100) pole density, P, and average orientation density, Q. (X represents the times random unit.)

ρ	P	Q
10°	15X	54X
7°	16.5X	66X
5°	21X	99X

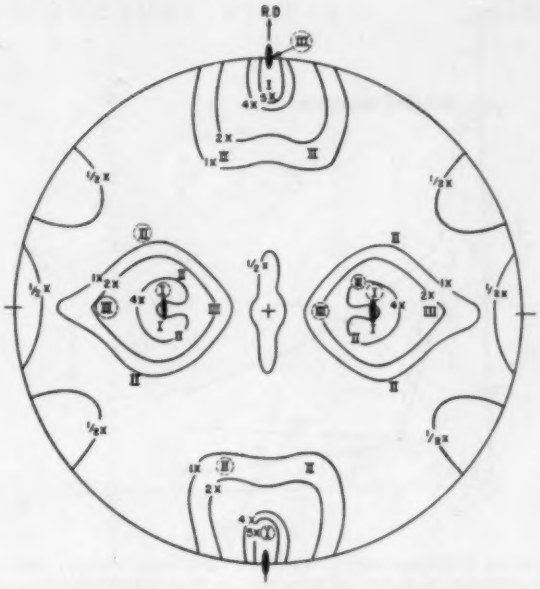

FIG. 2. (100) pole density figure[4] and positions of eight components (three types of components) of the texture.

SECTION II. APPLICATIONS OF ORIENTATION DENSITY CONCEPTS

Single-Component Texture

The orientations of 42 grains, representative of a moderately strong (110) [001] texture,[4] were used to calculate both (100) pole densities and orientation densities for the expected maximum densities. Table I summarizes the results. These results show that both P and Q increase with decrease in the value of ρ, as required for a pole concentration and an orientation concentration. If the largest value of P, 21X, is taken for P_0 then the value of Q_0 calculated from (13) is 104X. This value may be compared with the largest value of Q in Table I since the distribution of poles was approximately a normal distribution. Although the agreement is good, more data, which include a range of value of Q, are needed to determine the applicability of Eq. (13).

Multicomponent Textures

Figure 2 shows a synthesized (100) pole figure for a texture having two type I components, four type II components, and two type III components, i.e., having a total of eight components.[4] Figure 3 gives the analysis of original orientation data using Eq. (12) for orientations $X'Y'Z'$ located at the estimated maximum density points for types I, II, and III components and for the (110) [001] orientation. The symmetrization of the texture in Fig. 2 leads to superimposed curves in Fig. 3. Thus, curve I is to be considered as two superimposed

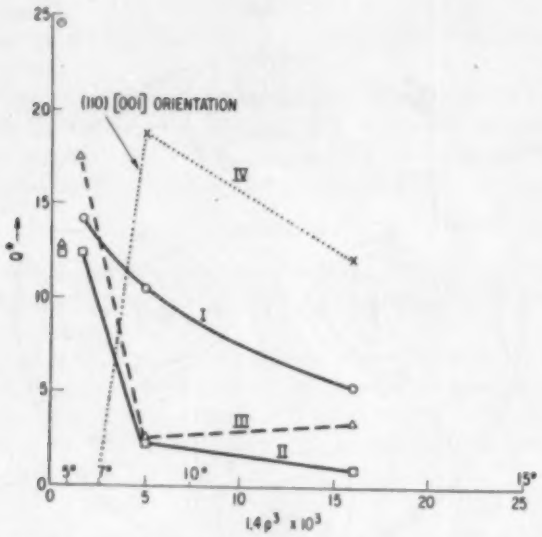

FIG. 3. Curves showing results of orientation density tests for the presence of either orientations or orientation concentrations at the (110) [001] orientation or at the type *I*, type *II*, and type *III* orientations.

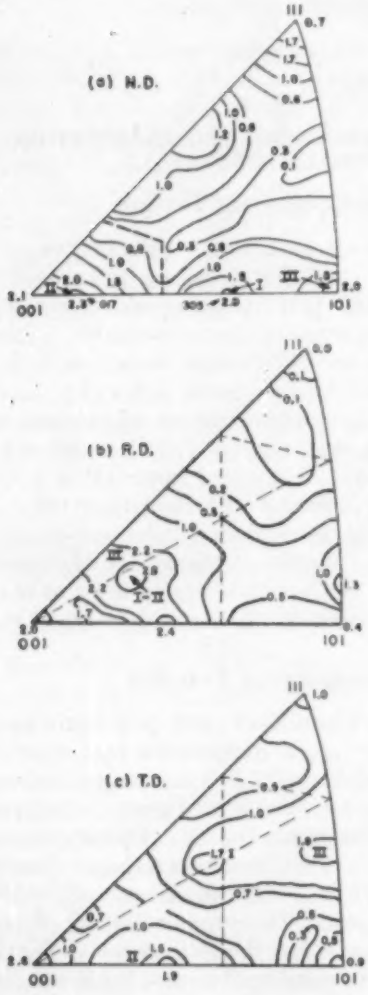

FIG. 4. Axis density figures for (a) normal direction, (b) rolling direction, and (c) transverse direction.[6]

curves, curve *II* as four curves, and curve *III* as two curves.

Before discussing Fig. 3, it should be pointed out that plots of axis densities[4] for the normal direction, the rolling direction, and the transverse direction came much closer to resolving the texture into these components than did the (100) pole figure. Figure 3, however, may be seen to summarize most of the arguments set forth earlier[4] for the existence of eight orientation concentrations and the absence of a (110) [001] component. For example, the orientation density is seen to increase as ρ decreases for the eight components, whereas the orientation density drops to zero for $\rho = 7°$ in a plot testing for the presence of a (110) [001] component. It is necessary also to consider the data on a probability basis. Thus, the zero value of orientation density for (110) [001] may have been due in part to insufficient orientation data. Nevertheless, the fact that the associated (100) pole densities (see Fig. 2) were $3X$ or more does show the possibility of Q being zero or nearly zero when P is quite far from zero. Also it is doubtful that the additional construction of a (111) pole figure would settle such a point (in this connection Sharp and Dunn[7] discussed a texture in copper, with cube and near cube orientations missing despite the presence of both {100} and {111} poles in the correct positions for cube orientations).

Some further points regarding the usefulness of orientation density may be illustrated for a second multicomponent texture. The data included 191 orientations and their volume fractions.[5] Figure 4 is a reproduction

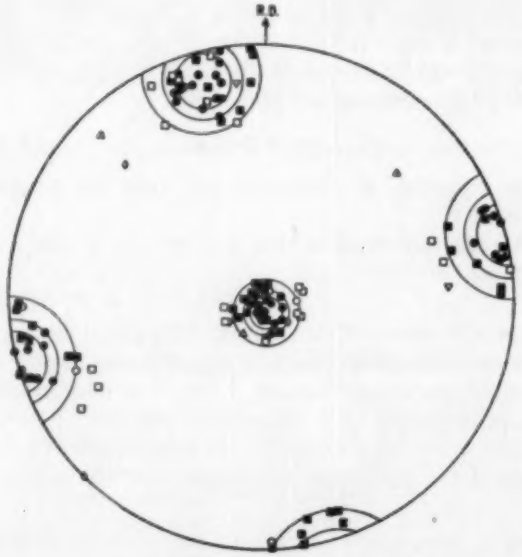

FIG. 5. Combined (100) plot of four (017) [$27\bar{1}$] type components (all orientations for the area near 001 outlined in Fig. 4). Large circles show orientation states of 7°, 10°, and 15° size. Orientations within 10° state: small closed circles; within 15° state: small closed squares; edge of 15° state: small open circles; beyond 15° state: other symbols.

[7] M. Sharp and C. G. Dunn, Trans. AIME **194**, 42 (1952).

of the axis density plots, with some added lines, which will be referred to later. Figure 5 is a plot of cube poles of four (017) [27$\bar{1}$] type components combined into one, together with all orientations in the outlined region of Fig. 4(a) near 001. More precisely, since 34 orientations are involved but more than 34 appear, the plot shows those that must be considered in a symmetrized group of four times 34 orientations. The first point to note is that many of the orientations in Fig. 5 are either identical with or close to those found in a (017) [2$\bar{7}$1] component, which can be described in terms of a 180° rotation of Fig. 5 about the normal direction. In fact, (017) [27$\bar{1}$] and (017) [2$\bar{7}$1] orientation states are completely separated only when $\rho < 7°$.

When the orientations for Fig. 5 and their volume fractions were used to calculate Q^*, the results plotted in Fig. 6 were obtained. Q^* has been plotted at the midpoint of each range. The curve drawn through these points is one of four superimposed curves; it clearly shows an orientation concentration for (017) [27$\bar{1}$]. A too high value of Q^* at large ρ, resulting from overlapping orientation states, creates no serious problem here.

A plot of orientation density for a 45° range of orientations, all with a common crystallographic direction, provides further information on the (017) [27$\bar{1}$] identification as well as information on (305) [5 21 $\bar{3}$] type components. The common direction is [010], but located 15° counterclockwise from R. D. At a zero angle of tilt or rotation [3 11 0] is parallel to R. D. and [100] is in a direction 85° clockwise from R. D. The angle of tilt is the angle between [001] and the normal direction. Figure 7 gives the plot of Q based on average values in either 5° or 7° states. The first point to note from the plot is the elimination of (001) [3 11 0] as an orientation concentration; this orientation not only is 7° from (017) [27$\bar{1}$] but is exactly halfway between (017) [27$\bar{1}$] and (017) [2$\bar{7}$1], the close pair discussed earlier. The second point is the identification of four (305) [5 21 $\bar{3}$] type components in the texture. The third point involves (110) [1$\bar{1}$5] which previously[5] was called a component.

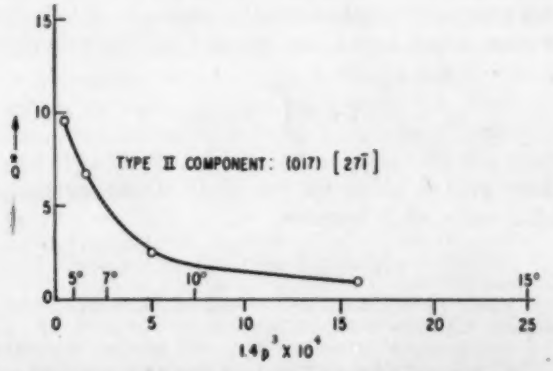

FIG. 6. Curve showing decrease of orientation density with increased disorientation from (017) [27$\bar{1}$], using Eq. 12.

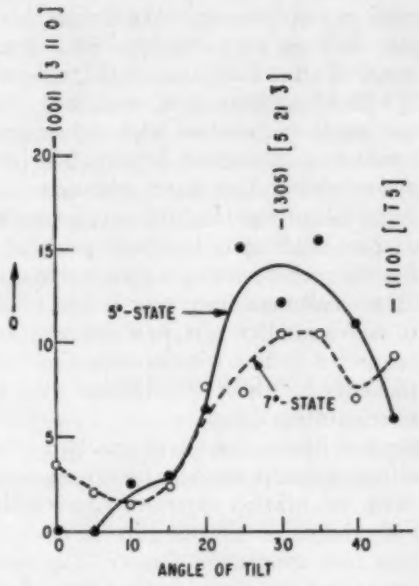

FIG. 7. Illustrative curves showing variation in average orientation density in a 45° tilt range that includes one (305) [5 21 $\bar{3}$] type orientation concentration.

Lack of a clear maximum point indicates that (110) [1$\bar{1}$5] does not completely meet the test of an orientation concentration and therefore is probably not a component. The appreciable orientation density at (110) [1$\bar{1}$5] may be caused by orientation spread from (305) [5 21 $\bar{3}$] components.

Some further information on the (305) [5 21 $\bar{3}$] type components as well as information on orientations of low orientation density is obtained in a plot of orientation density for rotations about [305] parallel to the normal direction. Statistically, use of a larger state such as $\rho = 10°$ is preferred in the regions of low orientation density, even though this lowers the value of Q at (305) [5 21 $\bar{3}$] from 12X (see Fig. 7) to 6X, as shown in Fig. 8. The angle of rotation is measured in terms of the angle swept by [010] starting with [010] parallel to R. D. Thus, in a rotation of 360° the curve shown in Fig. 8 would repeat four times. The traces that the axis directions parallel to the rolling direction and to the trans-

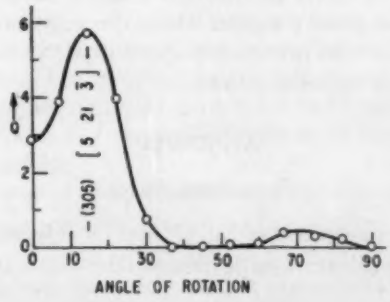

FIG. 8. Illustrative curve showing variation in average orientation density (a 10° state) in a 90° rotation that includes one (305) [5 21 $\bar{3}$] type orientation concentration.

verse direction, respectively, make during this rotation are outlined in Figs. 4(b) and 4(c). Since a maximum point is reached after a rotation of 15°, the presence of a (305) [5 21 $\bar{3}$] component is confirmed. Also there clearly are many orientations with either zero or less than 1X values of orientation density. The presence of many adjacent orientation states with zero orientation density is an indication that the present texture does not have a part made up of randomly oriented crystals, except possibly such a part with almost zero orientation density. The small maximum near 70° in Fig. 8 either belongs to such a random part, in which case the density would be expected to drop with more data, or it indicates real components for these orientations with very low maximum orientation densities.

The foregoing illustrations have provided information of a quantitative nature not only for orientation concentrations with orientation densities appreciably above the level of random or 1X but also for orientations of zero or near zero orientation density. The second illustration treated only eight components of a multicomponent texture. The maximum orientation densities were approximately ten or more times the orientation density of a random-orientation sample (Figs. 6 and 7). On the other hand, the axis density figures (Fig. 4) showed that the maximum pole densities were less than three times random. The extent of departure of the texture from a random-orientation texture is therefore much more clearly revealed by orientation density data than by axis density data.

At present, there is a quantitative limitation to the use of orientation density. This limitation stems from the fact that orientation density cannot be calculated without knowing the orientations of individual grains. On the other hand, the relationship given in Eq. (13) between maximum orientation density Q_0 and maximum (100) pole density P_0 suggests that further probability relationships may be found between orientation densities and pole densities.

Finally, it is of interest to point out that orientation density data might also be shown in a three-dimensional (α,β,γ) plot. Whereas pole densities are shown by a series of constant density contour lines in the two-dimensional pole figure, orientation densities would be shown by a series of constant density surfaces in an orientation density figure. Thus, the complete texture could be seen in orientation space in terms of the distribution of the orientations.

APPENDIX

Orientation Space

The rearrangement of Eq. (7) and the integration over all possible orientations determines the constant c. Thus,

$$\int\int\int Q d\alpha d\beta d\gamma = c, \tag{A1}$$

because the sum of the $\delta\zeta$'s is one. For a random orientation sample $Q=1$, so

$$\int\int\int d\alpha d\beta d\gamma = c. \tag{A2}$$

The value of c then, in units of radians raised to the third power, is a measure of the orientation space. To evaluate (A2) we follow Bitter[8] and describe an orientation $X'Y'Z'$ in terms of three rotations α, β, γ, from a standard or initial orientation XYZ. Bitter lets X, Y, and Z coincide with such coordinates in the sample as rolling direction, transverse direction, and normal direction; i.e., R. D.$\|X$, T. D.$\|Y$, and N. D.$\|Z$.

The two rotations α and β determine an axis direction in $X'Y'Z'$ that lies parallel to N. D. The corresponding direction in XYZ lies in one of eight unit triangles nearest Z. When $|\alpha| \geqslant |\beta|$, the rotations are: α about R. D. followed by β about T. D. When $|\beta| > |\alpha|$, the rotations are: β about T. D. followed by α about R. D. The value of $\int\int d\alpha d\beta$ for this range is eight times the area of one unit triangle, i.e., $2\pi/3$ sr. The range required for γ is from $-\pi/4$ to $\pi/4$ or $\pi/2$. Therefore,

$$c = \pi^3/3. \tag{A3}$$

The substitution of this value of c in (7) gives

$$Q = (\pi^3/3)\delta\zeta/\delta v. \tag{A4}$$

Let us take δv as a small sphere of volume $(4/3)\pi\eta^3$ in orientation space, η being the range of disorientation[9] (see also later comment). Substitution in (A4) gives

$$Q = \delta\zeta/(4/\pi)\eta^3. \tag{A5}$$

This equation is similar but not identical to Eq. (11). When $Q=1$,

$$(\delta\zeta)_r = (4/\pi)\eta^3 \simeq 1.3\eta^3. \tag{A6}$$

Equation (A6) is similar but not identical to Eq. (10). Incidentally, (A6) may be derived directly from a distribution function developed by Mackenzie[10] in the following way: We consider all orientations in the range zero to η from an initial orientation $X'Y'Z'$ when η is small; this involves Mackenzie's cumulative distribution function, which here is designated $P(\eta)$. Accordingly,

$$P(\eta) = \int_0^{\eta} p(\psi) d\psi,$$

where $p(\psi)$ is given by Eq. (5.3) of Mackenzie. In radian units, (5.3) becomes

$$p(\psi) = (24/\pi)(1-\cos\psi).$$

[8] F. Bitter, *Introduction to Ferromagnetism* (McGraw-Hill Book Company, Inc., New York, 1937), p. 214.

[9] A disorientation between $X'Y'Z'$ and another orientation $X''Y''Z''$ is the smallest rotation possible about a common axis (see footnote reference 10).

[10] J. K. Mackenzie, Biometrika **45**, 229 (1958).

For small values of ψ, $p(\psi)=(24/\pi)(\psi^2/2)$. The value of $P(\eta)$ therefore is

$$P(\eta)=(4/\pi)\eta^3. \quad \text{(A7)}$$

Thus, (A7) is the same as (A6). $P(\eta)$ is obviously the fraction of space that has a volume of unity, since it is a probability number. The value of δv, however, is this fraction times the total volume, $\pi^2/3$; i.e.,

$$\delta v=(4/\pi)\eta^3\times\pi^2/3 \text{ or } (4/3)\pi\eta^3.$$

Therefore, the small sphere of radius η in orientation space is equivalent to taking all orientations in the range 0 to η from $X'Y'Z'$.

A few comments about Eqs. (10) and (A6) may be made. When $\rho=\eta$, Eq. (10) obviously gives the larger number; $(\delta\zeta)_r$ is larger calculated from (10) because the orientation state includes some disorientations that are greater than ρ. For example, it is easily confirmed that a rotation of ρ about a $\langle 111\rangle$ axis of $X'Y'Z'$ lies well within the orientation state of size ρ. Regarding the validity of Eq. (10), Mackenzie[11] has recently verified this equation by calculating a $P(\rho)$ such that no cube axis is more than ρ from $X'Y'Z'$.

Since $P(\rho)$ is only about 12% larger than $P(\eta)$ when $\rho=\eta$, it makes little difference which of these expressions is used to obtain $(\delta\zeta)_r$. There are a number of reasons based on expediency, however, for use of the orientation state of size ρ rather than the disorientation state of size η. On the other hand, if orientation data could be programmed for high-speed machine calculations, $P(\eta)$ probably would be preferred in automatic calculations of orientation densities.

ACKNOWLEDGMENTS

The authors express their appreciation to R. H. Pry for a critical reading of the manuscript and to H. Brandhorst for calculating orientation densities.

[11] J. K. Mackenzie (private communication).

JOURNAL OF APPLIED PHYSICS VOLUME 31, NUMBER 5 MAY, 1960

Regelation, Surface Diffusion, and Ice Sintering

W. D. KINGERY
Ice Research Laboratory, Department of Metallurgy, Massachusetts Institute of Technology, Cambridge, Massachusetts
(Received October 30, 1959)

The freezing together of ice particles when they are brought into contact, originally described by Faraday and called regelation, is shown to occur not only at the freezing point, but also at temperatures as low as −25°C. It is shown that pressure melting is not essential to the process, nor is the presence of any unique liquid film. The welding together of ice particles occurs as a result of surface diffusion, as indicated by the time dependence and particle size dependence for the process. Surface diffusion of H_2O molecules over an ice surface is found to be rapid. Equations for the kinetics of the process are closely related to those derived for sintering phenomena, but a quantitative derivation of the surface diffusion coefficient is not obtained.

I. INTRODUCTION

WHEN two pieces of solid ice are brought together at 0°C, they become firmly cemented; this cementation occurs in air, *in vacuo*, and even under water. The phenomena was described by Faraday[1] and the term "regelation" applied to it by Tyndall.[2] Dorsey[3] states that the "generally accepted" explanation for the phenomena is that sufficient compressive stresses exist at the contact area to cause melting when the pieces of ice are brought together, and when this stress is released solidification occurs. This was originally proposed by J. Thomson[4] and endorsed by his brother, Lord Kelvin.[5]

These early investigators observed that ice did not readily adhere at temperatures well below the melting point. Faraday commented on the difficulty of forming snowballs at low temperatures. They concluded that the effect was present only for ice at the melting point and for "thawing" ice with a superficial coating of liquid. However, Nakaya and Matsumoto[6] observed that a cohesive force did develop between ice spheres in contact at −7°C. Similarly, we have observed microscopically that fine ice particles adhere when brought into contact at temperatures as low as −20°C. At this temperature, no liquid is expected to be present on the surface and the classical discussion of regelation can hardly apply.

These observations have led to the present examination of phenomena related to the sticking of solid ice particles to each other, and to more general aspects of ice sintering. In anticipation of our results we may say

[1] M. Faraday, Proc. Roy. Soc. (London) **10**, 440 (1860).
[2] J. Tyndall, Proc. Roy. Soc. (London) **9**, 76 (1858).
[3] N. E. Dorsey, *Properties of Ordinary Water-Substance* (Reinhold Publishing Corporation, New York, 1940), p. 413.
[4] J. Thomson, Proc. Roy. Soc. (London) **10**, 152 (1859); **11**, 473 (1861).
[5] W. Thomson (Lord Kelvin), Proc. Roy. Soc. (London) **9**, 141 (1858).
[6] U. Nakaya and A. Matsumoto, J. Colloid. Sci. **9**, 41 (1954).

that surface diffusion is found to be an important consideration.

II. REGELATION

The fact that an increase in pressure lowers the melting point of ice is well known[7] and quantitative measurements are available for the effect of pressure on the melting point. Various phenomena that depend on this relationship have been described. Perhaps the best known of these is the experiment of Bottomley[8] in which it was reported that a weighted wire could pass through a block of ice without severing it. The pressure on the wire induces melting below it, chilling the wire and water; water flows around and freezes above the wire where it is not under stress. The heat liberated by freezing maintains the system in dynamic equilibrium so that the wire passes through the ice block without damaging it. The experiment does not work if (a) the cold water is drained off before freezing so that heat is not reliberated or (b) if the wire is replaced by a string or other poor heat conductor. Turpin and Warrington[9] repeated this experiment and found that the wire velocity increases as its thermal conductivity is raised and also as the load is raised. This and other similar experiments make it clear that pressure melting and resolidification do indeed occur and can give a redistribution of material.

However, the regelation experiments of Faraday were carefully carried out in such a way as to minimize the pressure employed. In one series of measurements, two rounded pieces of ice were anchored under water and then brought together with but very slight pressure. They were found to adhere. Faraday explained this process in terms of a liquid layer stable on a free surface of ice, but which was transformed into a solid layer when it was between two pieces of ice. On the other hand, Thomson argued that even though the pressure was slight, it was sufficient to cause pressure melting and resolidification of the ice. In both cases, the major difficulty requiring explanation was assumed to be the source of the heat absorbed during solidification by which the ice samples adhere. The main reason that Thomson's explanation was favored is that it implies a process first of melting, then of solidification, so that the net heat change is zero.

The process can be considered from another point of view by considering the relative energies of the initial two samples of ice in a liquid medium relative to the two samples of ice joined together as a solid unit with a grain boundary between them. If sticking is to take place at all, it is essential that the system with a grain boundary be the stable one rather than the two samples of ice with a liquid layer between them. Thus, the fact that the two ice particles stick together requires that the grain boundary energy be less than twice the solid-liquid interface energy. As long as this is the case, the two ice particles will stick together, the boundary being filled in by processes of material transfer that do not require the freezing of new material. These processes might consist of volume diffusion, viscous or plastic flow of the solid, surface diffusion, or dissolution at the surface of the large particle and solidification at the small negative radius of curvature. Unless this surface energy relationship holds, then even though melting occurs when pressure is applied, the liquid present will tend to penetrate between the particles after resolidification, reforming the system of low surface energy.

TABLE I. Characteristics of different mechanism of material transfer.

Process	Rate of neck growth	Shrinkage
1. Viscous flow	$\left(\frac{x}{r}\right)^2 = \frac{A(T)}{r}t$	$\frac{\Delta L}{L_0} = \left[\frac{A^*(T)}{r}\right]t$
2. Evaporation condensation	$\left(\frac{x}{r}\right)^3 = \frac{B(T)}{r^2}t$	none
3. Volume diffusion	$\left(\frac{x}{r}\right)^5 = \frac{C(T)}{r^3}t$	$\frac{\Delta L}{L_0} = \left[\frac{C^*(T)}{r^3}\right]^{2/5} t^{2/5}$
4. Surface diffusion	$\left(\frac{x}{r}\right)^7 = \frac{D(T)}{r^4}t$	none

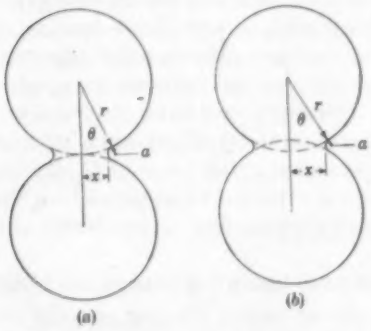

FIG. 1. Configurational changes for (a) evaporation-condensation and surface diffusion and (b) viscous flow and volume diffusion.

That is, neither the pressure-melting process nor a special kind of liquid is necessary to describe what is comparable to a "cold-welding" process known to occur when many clean surfaces are brought together. Instead, the special requirements of the ice-water system lie in the relationship between the solid-solid and solid-liquid surface energies.

III. SINTERING PROCESSES

Sintering is normally defined as a process in which a powdered compact increases its strength and density on being heated to elevated temperatures. Temperatures near the freezing point are already high relative

[7] P. W. Bridgeman, J. Chem. Phys. 5, 964 (1937).
[8] J. T. Bottomley, Nature 5, 185 (1872).
[9] G. S. Turpin and A. W. Warrington, Phil. Mag. 18, (5), 120 (1884).

temperatures for ice, so that whenever powdered particles are brought together there is a tendency for this kind of process to take place. The major energy change during sintering is the decrease in surface energy which is initially high in a fine particle size material. If we consider the initial stages of sintering for two spherical particles brought into contact, such as illustrated in Fig. 1, the decrease in surface area is initially accomplished by a growth of a neck between particles. Material continually flows into this neck area under the influence of a chemical potential gradient arising from the differences in curvature of the surface. This results from the surface energy, since there is a pressure difference across a curved surface given by

$$\Delta P=\gamma[(1/R_1)+(1/R_2)], \tag{1}$$

where R_1 and R_2 are the principal radii of curvature. This can be viewed as giving rise to a change in the chemical potential,

$$\mu-\mu_0=RT\ln(a/a_0)=\Delta PV_0, \tag{2}$$

where μ is chemical potential, a is the chemical activity, and V_0 the molar volume. In the present case, since the radius of curvature of the neck area is much smaller than that of the particle surface,

$$\mu-\mu_0=\gamma V_0/\rho. \tag{3}$$

Neck growth occurs by the most rapid mechanism of material transport available; possible processes include evaporation-condensation, viscous flow within the solid phase, volume diffusion within the solid phase, and surface diffusion along the solid surface. (See Fig. 1) The resulting rate of neck growth between spheres and the shrinkage, or approach of sphere centers, has been discussed by a number of authors[10–14] and results are summarized in Table I. Each of these material transfer processes has been experimentally observed to predominate in at least one system with kinetics as given in Table I.

There are five tests by which the kinetics of neck growth and shrinkage between particles in contact can be employed to determine what sort of process occurs during sintering. First, the time dependence of neck growth varies, depending on the process taking place, from the one-half to the one-seventh power of time. Second, the particle size dependence varies from the first to the fourth power of the particle diameter. Third, there is no shrinkage for evaporation-condensation and surface diffusion, while the time dependence of shrinkage for viscous flow and volume diffusion is different. Fourth, the temperature dependence of the sintering rate varies, and finally, quantitative calculations can be made of the sintering rate for some processes and compared with experimental measurements. Each of these tests should be in agreement with experimental measurements in order to give confidence that a proposed process is actually occurring.

FIG. 2. Photomicrograph of neck area between ice spheres.

IV. EXPERIMENTAL OBSERVATIONS

Experimental measurements consisted of preparing spherical particles of ice and observing the rate of neck growth and rate of shrinkage of different size particles at different temperatures. From these measurements, the relationships in Table I can be tested as a means of determining the mechanism of sintering taking place.

Spherical samples have been prepared by spraying liquid water into a liquid oxygen or liquid nitrogen bath. For the measurements reported here liquid oxygen was used because it happened to be readily available. Spherical samples over the size range 0.1 to 3 mm radius could be readily selected from the solid product. Samples were observed by placing two or more spherical particles in a line on a glass slide under a microscope. The particles were brought together lightly, and configurational changes measured directly with a micrometer ocular.

Measurements were carried out with the entire apparatus in a constant temperature room so that no separate enclosure for the particles or cold stage for the microscope was required. The largest number of measurements were carried out at a temperature of −17.8°C; other measurements were employed over the temperature range from −2.2 to −25.1°C. At −2.2°C difficulty was encountered in handling spheres without causing plastic deformation or surface melting on account of pressure or temperature effects. At −25.1°C, the process was slow and the low ambient temperature made manipulations difficult for the observer.

Experimental results for the rate of neck growth are collected in Fig. 3 and Table II. The experimentally observed measurements were found to show a time dependence in which the neck growth rate followed a relationship,

$$(x/r)\sim t^{1/6.1-7.1}. \tag{4}$$

The average value for −17.8°C at which the largest

[10] G. C. Kuczynski, Trans. A.I.M.E. **185**, 169 (1949).
[11] C. Herring, J. Appl. Phys. **21**, 301 (1950).
[12] W. D. Kingery and M. Berg., J. Appl. Phys. **26**, 1205 (1955).
[13] R. L. Coble, J. Am. Ceram. Soc. **41**, 55 (1958).
[14] W. D. Kingery, editor, *Kinetics of High-Temperature Processes* (Massachusetts Institute of Technology Press, Cambridge, Massachusetts, 1959), Part IV.

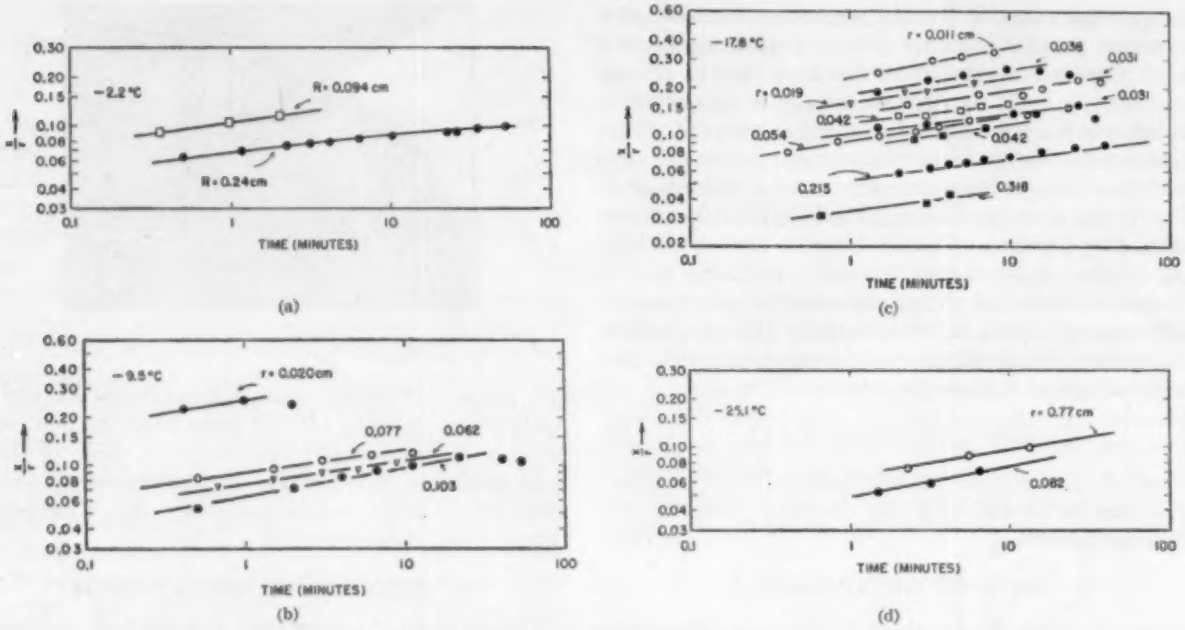

FIG. 3. Measurements of neck growth between spheres at four different temperatures. Sphere radii are indicated for each experiment.

number of observations was made was $(x/r)\sim t^{1/6.9}$, in close agreement with the value to be expected from surface diffusion as indicated in Table I.

Measurements of the distance separating contact points between three or four spheres lined up in a row showed that no shrinkage took place between centers, indicating that the process was one of evaporation-condensation, or surface diffusion rather than viscous flow, or volume diffusion.

The effect of particle size can best be illustrated by comparing the time required to reach a given configuration. Taking a ratio of $x/r=0.1$ for comparison, since this value is observed in most of the measurements, results are plotted in Fig. 4. As shown there, the time is closely proportional to the one-fourth power of the particle size as required by Herring's scaling law for surface diffusion,[11] and indicated in Table I.

TABLE II. Time dependence of neck growth.

Temperature (°C)	Particle radius (cm)	Inverse slope $n\left(\frac{x}{r}\sim t^{1/n}\right)$	
−2.2	0.093	7.0	mean = 7.1
	0.24	7.2	
−9.5	0.020		
	0.062	6.5	
	0.077	6.7	mean = 6.2
	0.103	5.5	
−17.8	0.011	5.5	
	0.019	6.5	
	0.031	6.7	
	0.031	7.2	
	0.038	6.6	mean = 6.9
	0.042	8.5	
	0.042	6.8	
	0.054	6.4	
	0.215	7.2	
	0.328	7.0	
−25.1	0.077	6.4	mean = 6.1
	0.082	5.7	

The temperature dependence of the process can be satisfactorily represented by an Arhennius plot of the log rate vs $1/T$, as illustrated in Fig. 5. The slope of this line gives an experimental activation energy of 27.5 kcal/mole.

V. DISCUSSION

The time dependence and particle size dependence of neck growth between spherical particles and the lack of approach between spherical particles are only consistent with the sintering process in which surface diffusion under the influence of surface energy gives rise to the adhesion between particles. All of the data are in agreement with this hypothesis and none are contradictory.

Confirmation that the process occurs more rapidly than for viscous flow or evaporation-condensation can be obtained by calculating the rates for these two processes which can be satisfactorily derived from theory. The rate of growth of a contact area between centers by a viscous flow of process is given by

$$(x/r)^2=3\gamma t/2\eta r, \qquad (5)$$

where η is the viscosity. Values for the apparent viscosity reported in the literature vary between 0.1 and 900×10^{12} poise according to Dorsey.[3] If we take the lowest viscosity value (corresponding to the most rapid

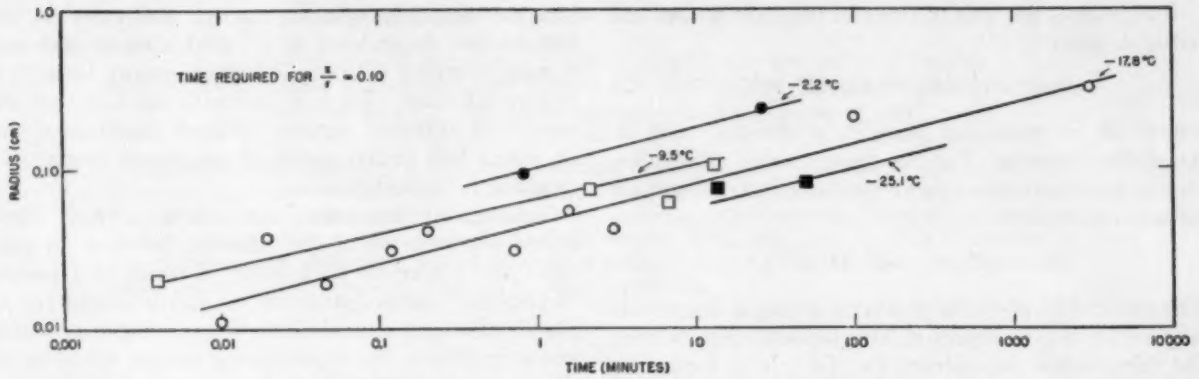

FIG. 4. Effect of sphere radius on time required to reach a specific geometry, $x/r=0.10$.

sintering) and $\gamma=90$ erg/cm², we calculate that about 1.5×10^4 min would be required for 1 mm spheres to reach $x/r=0.1$ at -17.8°C. This is about 1000 times larger than experimentally observed, indicating that viscous or plastic flow is a negligible contribution to the observed process.

Similarly, it has been shown[12] that for the most rapid case of material transfer in a vacuum, the rate of interface growth by evaporation-condensation is given by

$$\left(\frac{x}{r}\right)^3=\frac{3\pi M\gamma(M/2\pi RT)^{\frac{1}{2}}P_o}{r^2d^2RT}t, \qquad (6)$$

where M is the molecular weight, P_0 the vapor pressure, and d the density of the material. Equation (6) is derived from the Langmuir equation assuming that vaporization and condensation take place *in vacuo*; under a positive pressure, the rate of vaporization is decreased as a result of diffusion through a boundary layer. Consequently, Eq. (6) gives a result an order of magnitude larger than that expected under atmospheric pressure. Since the vapor pressure of ice is quite high (reaching 3.816 mm at -2.2°C), the evaporation-condensation process is relatively rapid; calculated rates are included in Fig. 5 in comparison with those experimentally observed. Even under *vacuo* the expected rate of material transfer by evaporation-condensation is less than that experimentally observed at temperatures above -20°C. Under atmospheric conditions, the evaporation-condensation mechanism is even less important. However, there may be some contribution from this mechanism at -25°C, as evidenced by the somewhat larger inverse slope of neck growth versus time than that expected from pure surface diffusion.

Two aspects of the experimental results are somewhat puzzling. First is the very high value of the surface diffusion coefficient, and second the large temperature dependence for surface diffusion. Kuczynski[10] and also Cabrera[15] and Schmed[16] have derived relationships between the rate of neck growth and the surface diffusion coefficient. Each of these suffers from the difficulty that the effective diffusion length from the nearly flat sphere surface to the highly concave neck area is either blandly assumed as some fixed fraction of the particle size or else introduced as an unknown parameter. This diffusion path will be determined by the rate at which mobile surface atoms are made available either from the vapor phase or from the interior of the crystal. From the rapid surface diffusion occuring in this case, we can conclude that the replenishment of surface atoms from the interior must be very rapid, but we have no information on which to base more quantiative observations. While at any one temperature the surface diffusion path is fixed, it will be variable with temperature. The large activation energy experimentally observed suggests that this surface equilibrium relaxation time is strongly temperature dependent.

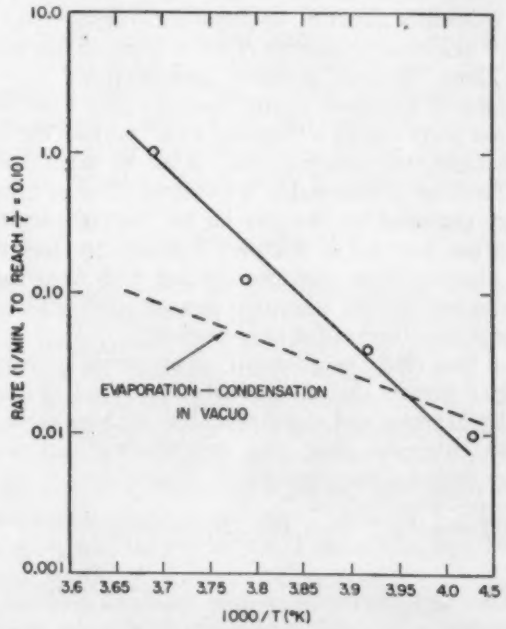

FIG. 5. Temperature dependence of the rate of neck growth between ice spheres.

[15] N. Cabrera, Trans. A.I.M.E. **188**, 667 (1950).
[16] P. Schmed, Trans. A.I.M.E. **191**, 245 (1951).

Kuczynski's analysis of the rate constant for surface diffusion gives

$$D_s = (x/r)^7 r^4 RTN^{\frac{1}{2}}/64\gamma(M/d)^{\frac{1}{2}}t, \quad (7)$$

where M is molecular weight, d density, and N Avogadro's number. For the present case, calculation on this basis results in a value for the "effective" surface diffusion coefficient,

$$D_s = 10^{22} \exp(-27\,500/RT). \quad (8)$$

The value of D_0 observed is several orders of magnitude larger than is to be expected. This probably results from the temperature dependence for the rate of formation of mobile surface atoms. That is, the value obtained in Eq. (8) is not a true diffusion coefficient.

An alternative explanation for the high activation energy and large absolute value for D_s is a change in surface structure with temperature. The large value of the apparent surface diffusion coefficient calculated from Eq. (7) would correspond to jump distances of many molecular diameters. It may be that the surface structure changes with decreasing temperature in such a way that the mean free path of the diffusing molecule decreases.

The high surface mobility of molecules on the surface of ice is not unreasonable in view of the unique structure of the ice crystal. Each oxygen in the crystal is tetrahedrally coordinated to other oxygen ions by means of hydrogen bonds in which hydrogen atoms alternate between equivalent positions. Molecules on the surface are presumably bonded to the crystal by two hydrogen bonds in which the hydrogen atoms also have two equivalent positions. These hydrogen bonds provide a reasonable mechanism by which rapid mobility of surface molecules might be anticipated. Murphy[17] has discussed electrical properties of ice in terms of ion migration along "internal surfaces" and proposed that the swinging of hydrogen bonds from one lattice oxygento another gives rise to a "bipedal walk" surface diffusion mechanism; this analysis was, as in the present case, put forth as a reasonable hypothesis. The activation energy proposed by Murphy for his "internal surface" migration was 5.2 kcal/mole; considerably less than that observed here and more in line with what might be expected for the migration process itself (this value is about half the heat of vaporization).

The fact that the observed experimental activation energy is greater than that ascribed to boundary migration by Murphy and also larger than the heat of vaporization suggests that the experimental activation energy includes the temperature dependence of the relaxation time for replacing surface molecules on the temperature dependence of a variable mean path and is more complex than an activation energy for simple surface diffusion. This is in line with the fact that the calculated apparent surface diffusion coefficients give D_0 values four or five orders of magnitude larger than expected for diffusion alone.

Nakaya and Matsumoto[6] and also Weyl[18] have interpreted observations of the adhesion between ice particles and regelation phenomena in terms of a mobile "liquid-like" surface structure. If this is considered as a layer of several atomic dimensions having appreciable atomic mobility, the experimental results would be as expected here; this would provide a mechanism for rapid surface diffusion. At the same time, there is nothing in the present experimental results that is not adequately explained on the basis of a surface layer one or a few molecules thick having high mobility, as is to be expected for surface molecules in any case. The structure of water and the nature of the hydrogen bonding between water molecules make it likely that surface molecules have an unusually high degree of mobility. This does not require, however, an appreciable thickness of liquid on the surface. It is difficult for us to accept the fact that we have a liquid layer at a temperature some 25 deg below the melting point. Since no discontinuity in properties or surface diffusion phenomena are observed between this low temperature and the melting point, we see no reason for introducing the concept of liquidity or suggesting that there is a second phase present on the surface of the crystalline particles.

Finally, while the Bottomley experiment of passing a weighted wire through an ice block adequately demonstrates that pressure melting and subsequent solidification—a regelation process—can occur when sufficient pressure is applied, this mechanism is not necessary for adherence between ice particles as carried out here at temperatures below the melting point, or as described by Faraday in 1850. These results instead require that liquid water (and air) at equilibrium does not penetrate a grain boundary between ice particles. When this is the case, surface diffusion is sufficiently rapid for cold welding to occur, giving rise to cementation without requring heat transfer either for melting or solidification.

ACKNOWLEDGMENT

This research was carried out at the Climatic Laboratory, Eglin Air Force Base, as a project of the Arctic Institute of North America, with support from the Air Force Cambridge Research Center under a U. S. Air Force contract.

[17] E. J. Murphy, J. Chem. Phys. **21**, 183 (1953).

[18] W. A. Weyl, J. Colloid. Sci. **6**, 389 (1951).

Etching of Surfaces with 8-Kev Argon Ions

R. L. CUNNINGHAM, P. HAYMANN, C. LECOMTE, W. J. MOORE, AND J. J. TRILLAT
Laboratoire de Microscopie Electronique, Centre National de la Recherche Scientifique, Bellevue, S. et. O., France
(Received August 3, 1959; revised manuscript received January 18, 1960)

Methods of optical and electron microscopy were used to study the effects on solid surfaces of bombardment with argon ions of 8-kev energy. The targets were crystals of aluminum, zinc and α-corundum, and polycrystalline gold and aluminum. At oblique ionic incidence, etch hillocks were formed that were invariably oriented along the surface component of the direction of the ionic beam. Crystals were etched by ionic bombardment while being heated at elevated temperatures; this technique revealed dislocations widely spaced along the direction of growth in aluminum crystals.

VARIOUS observations of the effects of ionic bombardment on metal surfaces have recently been described.[1–5] It was shown by Haymann[6] in this laboratory that the bombardment of electropolished uranium surfaces with argon ions of 4- to 10-kev energy at glancing angles caused a characteristic pattern of grooves oriented parallel to the surface component of the direction of the beam. In the present work, microscopic techniques have been used to study the effects of similar bombardments on surfaces of zinc, aluminum, gold, and aluminum oxide.

EXPERIMENTAL

The ionic bombardments were carried out with the gun developed by Gervais and Trillat[7] for mounting on the Trüb-Taüber electron-diffraction apparatus. The positive ions passed through a hole of 1.0-mm diam in the cathode, and traveled about one cm before striking the target. The accelerating voltage was set at 8 kev. The current density at the target was 50 to 200 μa cm^{-2}, with the cross section of the beam 2×4 mm. The ionic intensity varied across the beam, being a maximum at the center, and about half-maximum midway between the center and edge. This estimate was obtained by examining the effects of the beam on layers of tantalum oxide on tantalum that were uniformly colored by interference, and correlating the intensity profile of the beam with the colors of the concentric patterns formed by sputtering of the oxide layers. Effects of variations in the intensity of the beam could be eliminated, when so desired, by means of a device for rocking the gun so as to sweep the beam back and forth across the target.

The samples for bombardment were about 5 mm square. They were mounted in a holder that permitted adjustment of the azimuthal angle, rotation, and linear displacements in two degrees of freedom. The maximum temperature rise resulting from bombardment was less than 100°. The background impurity pressure did not seem to have any significant effect on the sputtering phenomena. It was possible, for example, to observe the electron diffraction pattern of a monocrystalline aluminum specimen during bombardment with argon ions, either at ordinary temperature or with heating to 550°. This result shows that the rate of removal of surface layers by the ionic impacts must be higher than the rate at which impurities or oxidizing agents strike the surface.

After bombardment, the surfaces of the specimens were examined by optical and electron microscopy. Several different replica techniques were used, but usually one of the following: (a) The surface of the sample was pressed into the surface of a section of 0.3 mm thick Rhodoid sheet, which had been moistened with acetone. (Rhodoid is a cellulose acetate from the Rhone-Poulenc Company). After drying, the Rhodoid imprint was peeled from the specimen, shadowed with chromium at 45°, and coated with carbon by vertical evaporation. The replica was then placed face downwards on a copper grid and the plastic dissolved in warm condensing acetone. (b) Direct replicas were made by simultaneous evaporation of carbon and platinum onto the specimen, which was then covered with a thin layer of a viscous solution of Alcolene-100 in toluene. (Alcolene is a polystyrene from the Pechiney Company). The dried film was stripped from the specimen, placed on a grid, and the plastic removed by solution in toluene.

Materials

Zinc specimens were obtained by cleavage of a large single crystal after it had been chilled in liquid air. The surface for bombardment was the basal plane (0001). The crystal sections were electropolished in 17% aqueous chromic acid for about 20 sec at 8 v.

Gold foil about 0.5 mm thick was annealed for 6 hr at 850°, attaining an average grain size of 2 to 3 mm. The specimens were polished mechanically and finally electropolished in a bath consisting of 8 g KCN, 5 g $AuCl_3$, 4 g K_2CO_3, and H_2O to 100 ml. Typical conditions were 10 v for 4 min.

Aluminum was used both as polycrystalline foil and as single crystals. Fine grained foil with a purity of 99.9997% was supplied by the Pechiney Co. This could

[1] W. Bayh, Z. Physik **151**, 281 (1958).
[2] G. Möllenstadt and M. Keller, Radex Rundschau **153**, (1956).
[3] V. E. Yurasov, Kristallografiya **2**, 770 (1957).
[4] G. Wehner, J. Appl. Phys. **29**, 217 (1958).
[5] H. E. Farnsworth, R. E. Schlier, T. H. George, and R. M. Burger, J. Appl. Phys. **29**, 1150 (1958).
[6] P. Haymann and J. J. Trillat, Compt. rend. **248**, 2472 (1959).
[7] H. Gervais and J. J. Trillat, Vide **12**, 416 (1957).

be electropolished without preliminary mechanical polishing. The bath was 78 ml $HClO_4$, 700 ml ethanol, 120 ml H_2O, and 100 ml Butyl Cellosolve (ethylene glycol monobutylether). A pointed stainless steel anode was used, with typical conditions 25 to 35 v for 2 min. Single crystals of aluminum were kindly supplied by Professor G. Craig, University of Toronto. These had been grown from oriented seed crystals by progressive solidification from one end of the melt. The growth axis was the [100] direction, and the surfaces of the specimens were formed by (100) planes. The growth rate had been such that the lineage structure as described by Teghtsoonian and Chalmers[8] was developed. From these crystals samples were cut so that either a (100) or a (111) plane was close to the surface. Mechanical polishing was followed by electropolishing, for up to 6 min in order to eliminate strained material at the surface.

Aluminum oxide was obtained as disks 2 mm thick cut from a single crystal boule of alpha corundum prepared by the Verneuil process in the Speedway Laboratory of the Union Carbide Company. These had been polished with fine diamond dust, and were used without further preparation.

RESULTS

Gold

A photomicrograph of a gold surface after bombardment for 30 min with Ar^+ ions at 8 kev and angle of incidence $\alpha=60°$ from the normal is shown in Fig. 1. The arrow-shaped hillocks were always pointed exactly in the direction of the lateral component of the incident beam, but on different grains they differed considerably in shape. The superficial density of hillocks also differed from grain to grain, some being heavily covered, whereas others were almost free of markings.

Two different mechanisms for the formation of such hillocks can be envisaged. They may be patterns formed in relief as the result of a more rapid removal of surrounding material. On the other hand, they may represent the recrystallization and growth of newly formed crystallites, as a result of a process of nucleation on special sites, followed by the transport of atoms along the surface to the growing nuclei. This latter process was suggested by Meckel and Swalin[9] to account for their observations on the effects of argon ions of much lower energy (~300 ev) normally incident on germanium crystals.

It is not easy to distinguish these two mechanisms by experimental tests, but at present we prefer the mechanism of selective attack because many of the etch patterns clearly indicate a selective attack, and the invariable congruence between the direction of ionic incidence and the direction of orientation of the hillocks seems to be more readily related to the removal of sputtered material than to an effect of ionic incidence on the direction of recrystallization. Argon ions at kilovolt energies penetrate the surface and the sputtering is caused by displaced metal atoms coming from subsurface regions.[10] The sputtering rate in these systems is fairly high, at least one atomic layer per sec.

The effect of a longer time of bombardment at a higher ion intensity, in the Au/Ar^+ system, is shown in Fig. 2. The grooves in the surface are always exactly in the direction of the beam. Perpendicular bombardment at the same energy and intensity does not produce such an oriented pattern of attack. This effect, therefore, provides visual evidence that the sputtering process is governed by the transfer of momentum from the ions to the solid, and not simply the transfer of energy. It is a vectorial process.

Zinc

In the experiments on zinc, the bombardments were made at $\alpha=75°$ on the cleavage planes (0001). In this case, no triangular hillocks were observed, but simply elongated lines or grooves of attack, oriented along the direction of the beam. In many cases, the attack appeared to originate at slip lines and to continue as parallel striations from these lines.

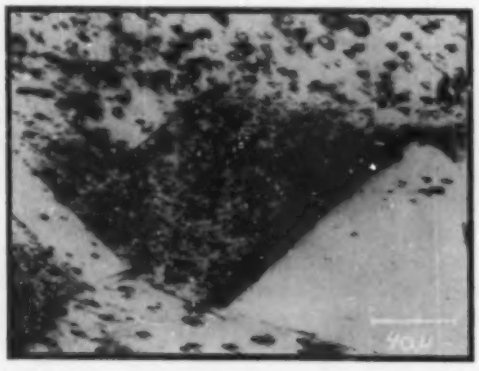

FIG. 1. Photomicrograph of polycrystalline gold bombarded with Ar^+ of 8 kev for 30 min at 60° incidence.

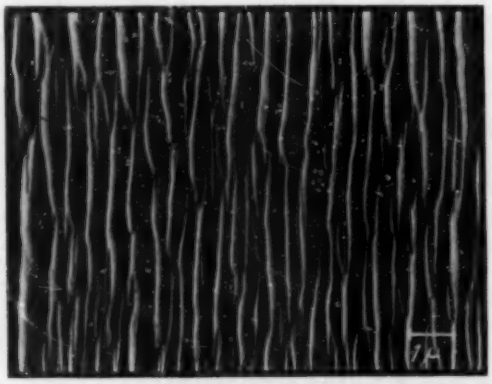

FIG. 2. Electron micrograph (Rhodoid replica) of polycrystalline gold bombarded with Ar^+ of 8 kev for 120 min at 70° incidence.

[8] E. Teghtsoonian and B. Chalmers, Can. J. Phys. **29**, 370 (1951); **30**, 388 (1952).

[9] B. B. Meckel and R. A. Swalin, J. Appl. Phys. **30**, 89 (1959).

[10] F. Keywell, Phys. Rev. **97**, 1611 (1955).

Aluminum

The first experiments on aluminum were made with long durations of bombardment on polycrystalline specimens. The typical pattern of elongated furrows in the direction of the ionic incidence was quite similar to that observed with gold under similar conditions.

The effects of angle of incidence on the attack patterns were studied systematically with the polycrystalline aluminum targets. Other factors being the same, the lower the angle α, the more selective did the attack appear. Thus, grain boundaries, subgrain boundaries, and other features were sharply distinguished at lower angles of incidence, at which terraced surfaces were revealed that differed markedly with crystallite orientation. Sometimes one surface grain was attacked in the form of terraces and an adjacent grain in the form of furrows. One example of the phenomena observed is shown in Fig. 3.

With the single crystals, there was a selective attack on both the (100) and the (111) faces, with the development of terraces, but in the case of the (111) face the steps appeared to be considerably deeper. An explanation would be that in both instances (100) planes were selectively exposed, so that the sputtering was more rapid from the closest packed planes (111).

There is evidence that the shock of an ionic collision inside a solid is selectively propagated along closest packed rows of atoms. Such an effect was indicated by the calculations of Silsbee[11] on the focusing of momentum in solid-state collisions and by the experimental demonstration of such focusing in the work of Thompson[12] on the ejection of atoms from gold crystals during proton irradiation. Such focusing might also serve to explain the more rapid sputtering of (111) planes in fcc crystals, and why defects often appear in relief above an ionically bombarded surface. The more perfect regions would be selectively sputtered by the focused collisions, whereas collisional chains would be scattered from the neighborhood of defects. Since the ionic etching is caused by collisions of displaced atoms coming from below the surface, if a raised region was nucleated on the

FIG. 3. Selective etching of a polished aluminum surface by 8 kev Ar^+ ions at angle of incidence of 30°, 2 hr at 100 $\mu A/cm^2$.

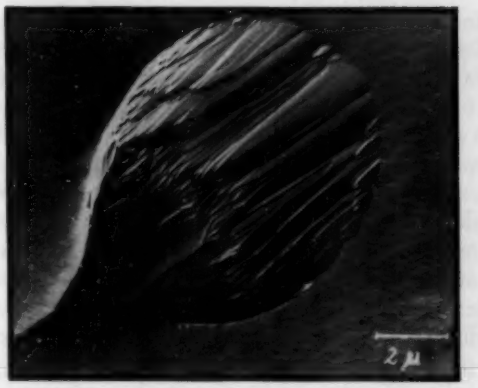

FIG. 4. Electron micrograph (Carbon-platinum direct replica) of (100) face of aluminum crystal bombarded with Ar^+ of 8 kev for 85 min at 70° incidence.

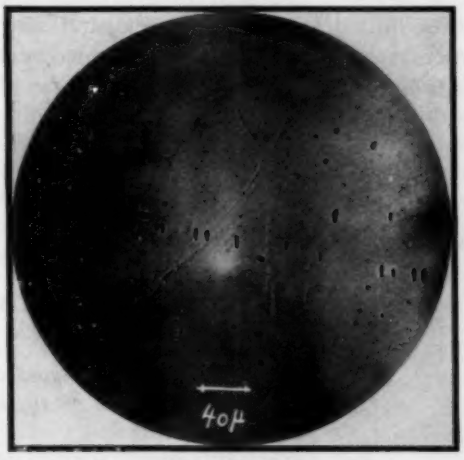

(a)

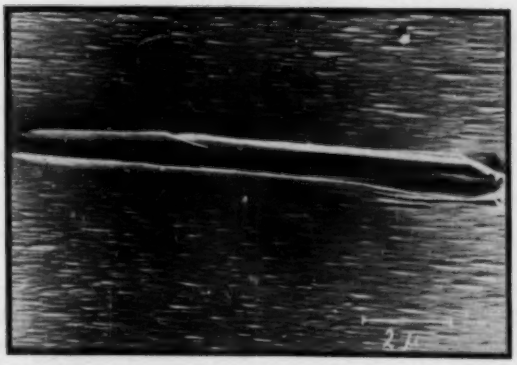

(b)

FIG. 5. Ionic attack at an elevated temperature: Ar^+ of 8 kev for 120 min at 70° incidence on (100) face of aluminum at 500°C. (a)Photomicrograph, (b) electron micrograph (carbon-platinum) of an individual hillock.

[11] R. H. Silsbee, J. Appl. Phys. **28**, 1246 (1957).

[12] M. W. Thompson, Phil. Mag. **4**, 139 (1959).

surface, it would tend to grow in height to a certain limiting value. The absence of oriented hillocks on the (1000) surfaces of zinc is also in accord with this mechanism.

We have found some experimental evidence for a lowered sputtering rate at lattice imperfections in observations on (100) faces of aluminum at lower ionic intensities. Such faces often reveal characteristic relief patterns such as that shown in Fig. 4. The arrows on the surface of the hillock all point along the direction of ionic incidence. The largest of these hillocks are about 5 μ in diam, but they grow from smaller embryos that often seem to be nucleated at grain boundaries or other imperfections. The direction of the ionic attack was from the wider ends of the hillocks towards their points, and the points of many of the smallest distinct hillocks appeared to originate on subgrain boundaries at the crystal surface.

A (100) surface was cut parallel to the direction of growth and hence parallel to the lineage structure of these aluminum crystals. This was bombarded with argon ions at 8 kev and $\alpha = 70°$ for 120 min at 500°. The method of ion bombardment thus provides the possibility of attacking the surfaces of crystals while they are being heated at appreciable temperatures, an important extension of the techniques provided by oridnary methods of chemical etching. In this case, rows of evenly spaced elongated hillocks occurred in the direction of the crystal growth, as shown in Fig. 5. These hillocks may be associated with individual edge dislocations; however, the distance between them is of the order of 20 μ, so that the alinement must result from details in the lineage structure of the aluminum crystal with a long repeat distance in the growth direction.

Aluminum specimens from the same crystal were bent around a cylinder of 5-cm radius. Two sets of slip lines were thus introduced, which cut the (100) planes at 90° to each other. After bombardment at room temperature, no preferential attack on these slip lines was detected. The same specimen was then repolished and bombarded again, but the slip lines were not revealed by the ionic attack. It was reported[3] that bombardment with Ne^+ at 2 kev revealed slip lines in cadmium and zinc, and this effect was noted with Ar^+ at 8 kev on zinc. It is therefore interesting to find that the effect is not general, since it was not observed with aluminum or gold.

Aluminum Oxide (α-corundum)

The bombardment of a smooth surface of monocrystalline corundum with Ar^+ at 8 kev and $\alpha = 20°$ for 135 min, led to an attack notably less rapid than that on Al, but similar surface features were revealed, especially the occurrence of elongated hillocks similar to that in Fig. 4 with typical striations, and also the shallow terraces perpendicular to the direction of orientation of the hillocks.

JOURNAL OF APPLIED PHYSICS VOLUME 31, NUMBER 5 MAY, 1960

Explosively Loaded Metallic Cylinders. I*

F. E. Allison and R. W. Watson
Carnegie Institute of Technology, Pittsburgh, Pennsylvania
(Received December 16, 1959)

Recent experiments using thin-walled metal cylinders internally loaded with high explosives have been performed in an effort to show that the casing velocity vector bisects the angle formed by the expanding cylinder and the undisturbed portion. This relation, which was first derived by Sir Geoffrey Taylor, can be expressed by the equation $\delta = \theta/2$, where δ is the angle between the velocity vector and the normal to the undisturbed casing, and θ is the angle formed by the normals to the moving and undisturbed portions of the casing. Although this relation forms a part of most theories pertaining to the acceleration of thin liners by high explosives, direct experimental verification of the relation has been difficult. In an attempt to verify Taylor's relation, values of δ were determined by inspecting the fragmentation patterns produced on cylindrical witness targets surrounding the charges. The values of δ determined in this manner are within the range of recent measurements by Singh using similar charges. Values of θ were independently determined from Kerr Cell photographs of the expanding cylinders. The experimental observations are in good agreement with the relation $\delta = \theta/2$.

INTRODUCTION

IT has long been known that the pressure produced by conventional high explosives greatly exceeds the yield strength of solid materials. Recent studies[1,2] have shown that the Chapman-Jouget pressure for 64RDX/36TNT is roughly 30 000 times the critical shear stress of bulk copper crystals and 35 times the maximum shear stress of small perfect crystals.[3] Under such extremely high pressure, the motion of materials such as copper and steel can be treated by classical hydrodynamics.

* This work was performed under a contract with the Ballistics Research Laboratories, Aberdeen Proving Ground, Maryland.
[1] R. E. Duff and E. Houston, J. Chem. Phys. **23**, 1268 (1955).
[2] W. E. Deal, J. Chem. Phys. **27**, 796 (1957).
[3] S. S. Brenner, J. Appl. Phys. **27**, 1484 (1956).

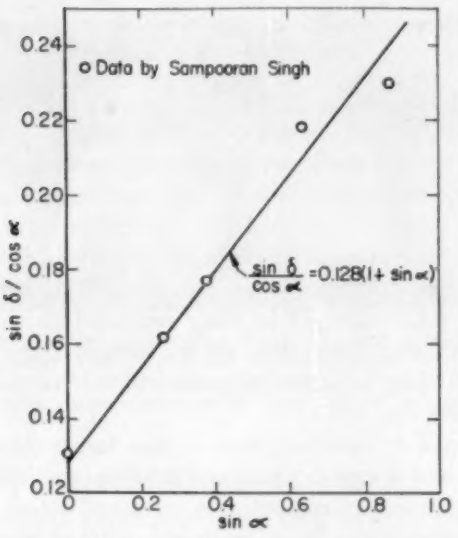

FIG. 1. Singh's data relating the angle between the velocity vector and the normal to the undisturbed liner (δ) with the angle between the propagation vector of the detonation wave and the normal to the undisturbed tangent to the undeformed liner (α). The data are in good agreement with the equation $\sin\delta/\cos\alpha = V(0)\,(1+\sin\alpha)/2D$, which can be derived from Taylor's relation $\sin\delta = V(\cos\alpha)/2D$ and Singh's relation $V(\alpha) = V(0)\,(1+\sin\alpha)$.

The steady-state theory of shaped-charge liner collapse[4] is an excellent example of the successful application of incompressible fluid theory to a practical situation. In discussing the collapse of a shaped-charge liner, use is made of the fact that the liner velocity V bisects the angle between the perpendicular to the original liner surface and the perpendicular to the collapsing liner surface. Since G. I. Taylor[5] was the first to derive such a relation, the mathematical formula that describes the direction of V has become known as Taylor's relation. For a conventional shaped charge, Taylor's relation takes the form

$$\sin\delta = V(\cos\alpha)/2D, \tag{1}$$

where δ is the angle between the velocity of a liner element after being struck by the detonation wave and the normal to the undisturbed liner surface, α is the half angle of the conical liner, and D is the detonation velocity of the explosive. The steady-state theory has since been generalized to include nonsteady liner collapse[6]; however, Taylor's relation remains one of the fundamental equations. The experimental verification of the nonsteady theory of jet formation[7,8] has provided considerable indirect evidence supporting Taylor's relation.

[4] G. Birkhoff, D. P. MacDougall, E. M. Pugh, and G. Taylor, J. Appl. Phys. **19**, 563 (1948).
[5] The original analysis of explosively loaded cylinders by G. I. Taylor appeared in an unpublished British report (R. C. 193) in 1941.
[6] E. M. Pugh, R. J. Eichelberger, and N. Rostoker, J. Appl. Phys. **23**, 532 (1952).
[7] R. J. Eichelberger and E. M. Pugh, J. Appl. Phys. **23**, 537 (1952).
[8] R. J. Eichelberger, J. Appl. Phys. **26**, 398 (1955).

Some recent experiments by Singh[9] provide additional evidence supporting Taylor's relation. In one experiment steel cylinders having an internal diameter of $1\frac{1}{2}$ to $2\frac{1}{2}$ in. and a wall thickness of $\frac{1}{8}$ to $\frac{3}{8}$ in. were filled with 60RDX/40TNT and detonated at the center of a large circular test area. The fragmentation pattern was observed on steel witness plates located tangentially along an arc. Most of the fragments were found to have been projected at angles corresponding to a δ of 6 to 9°. Other than showing that δ is not zero, this experiment provides little verification of the theory. However, Singh performed an additional experiment with liners inclined at an angle α with the propagation direction of the detonation wave. By using, in addition to Taylor's relation, an empirical equation of the form

$$V(\alpha) = V(0)(1+\sin\alpha), \tag{2}$$

Singh was able to account for the observed variations in δ. It should be pointed out, however, that Eq. (2) was based on data obtained under several different sets of experimental conditions and should be regarded as an empirical approximation.[10] Nevertheless, as shown in Fig. 1, Singh's data are well represented by Eqs. (1) and (2), and his experiment indirectly verifies Taylor's relation to within the accuracy of Eq. (2).

Experiments were recently undertaken at Carnegie Institute of Technology in an effort to obtain direct verification of Eq. (1). For this purpose, thin-walled copper cylinders were filled with explosive and detonated at one end. If the motion of the metal cylinder is represented by Fig. 2(a), then Taylor's relation requires that the velocity vector bisect the angle between the two normals. This requirement can be expressed mathe-

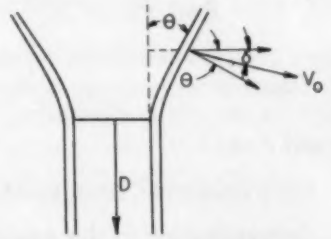

(a) Motion as viewed in the laboratory system of co-ordinates.

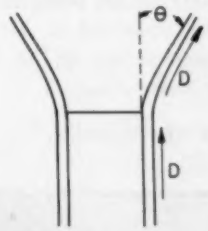

(b) Motion as viewed in a co-ordinate system moving with the detonation front.

FIG. 2. Motion of an internally loaded metal cylinder. The region shown is in the immediate neighborhood of the detonation front.

[9] Sampooran Singh, Proc. Phys. Soc. (London) **B69**, 1089 (1956).
[10] Sampooran Singh, Proc. Phys. Soc. (London) **B68**, 785 (1955).

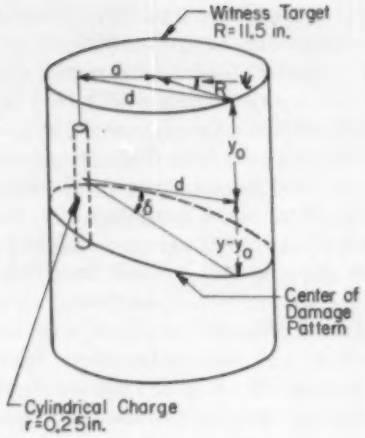

FIG. 3. Diagram illustrating the experimental arrangement used to determine the angle δ.

matically by the equation $\delta=\theta/2$. A simple derivation of this relation follows, as shown in Fig. 2(b), from the fact that a pressure acting perpendicular to the motion of the casing does not change the magnitude of its velocity but only its direction of motion. Thus, in the coordinate system moving with the detonation front, the radial and tangential components of velocity are

$$v_r=D\sin\theta$$
$$v_z=D\cos\theta. \tag{3}$$

A transformation to the laboratory system of coordinates gives

$$V_r=D\sin\theta$$
$$V_z=D(1-\cos\theta) \tag{4}$$
$$V=2D\sin(\theta/2).$$

Since $\tan\delta=V_z/V_r$, it immediately follows that $\delta=\theta/2$. In our experiment an attempt has been made to verify the theory by a direct experimental determination of the two angles θ and δ.

EXPERIMENTAL PROCEDURES

Determination of the Angle δ

The angle δ was determined from an analysis of the fragmentation pattern obtained in tests using the experimental arrangement shown in Fig. 3. An examination of the geometry shows that

$$y=y_0+(\tan\delta)d, \tag{5}$$

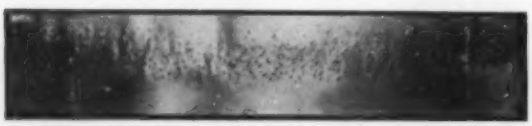

FIG. 4. Fragmentation pattern obtained in tests with an explosively loaded copper cylinder having a 0.040-in. wall thickness. This pattern is typical of the fragmentation patterns used to compute the angle δ.

where

$$d=(R^2+a^2+2aR\cos\psi)^{\frac{1}{2}}-r. \tag{6}$$

Thus, y is a linear function of d whose slope is $\tan\delta$, and the offset arrangement shown in Fig. 3 has an advantage over the circularly symmetrical arrangement in that δ can be determined without accurate knowledge of y_0. This technique was used to determine δ for copper cylinders having wall thicknesses of 0.030, 0.040, and 0.050 in. All cylinders had an internal diameter of $\frac{1}{2}$ in. and a total length of 6 in. They were filled with 60RDX/40TNT and fitted with a $\frac{1}{2}$-in. pressed tetryl pellet, which was initiated by means of a No. 8 electric blasting cap.

Figure 4 shows a typical witness target obtained in tests with a cylinder having a 0.040-in. wall thickness. For purposes of computing δ, values of y (see Fig. 3) corresponding to the approximate center of mass of the damage pattern were determined at 14 intervals equally spaced around the periphery of the witness target. Equivalent values of y obtained in three separate tests with each cylinder thickness were averaged and plotted against the associated values of d computed from Eq. (6). The regression line of y on d was then used to determine the values of $\tan\delta$ corresponding to the three thicknesses. The results of these tests are presented in Fig. 5. Linear correlation coefficients were computed for each of the three data sets and their high values indicate that the experimental results are well represented by Eq. (5).

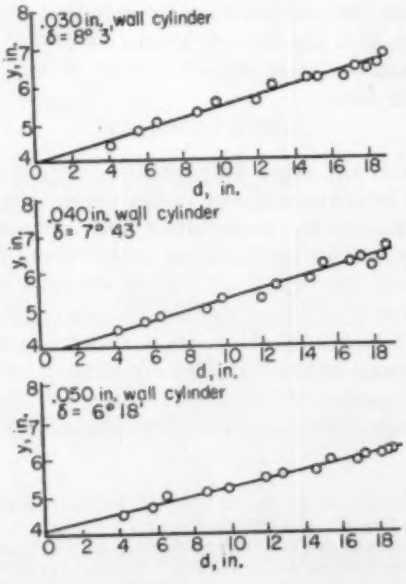

FIG. 5. Experimental results obtained with the witness-target arrangement shown in Fig. 3. These data are fitted with a least-squares line of the form $y=y_0+(\tan\delta)d$. For cylinders of a given wall thickness, each value of y represents the average obtained from three separate tests.

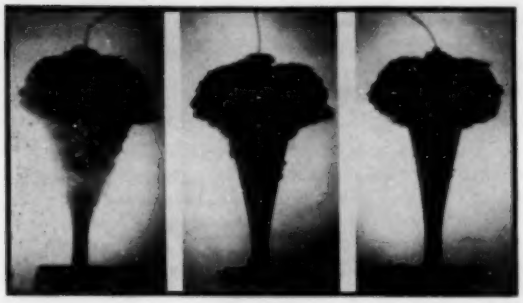

FIG. 6. Kerr Cell photographs of exploding charges confined in copper cylinders having different wall thicknesses. From left to right the wall thicknesses are 0.030, 0.040, and 0.050 in. These photographs are representative of those used to determine the angle θ.

Determination of the Angle θ

The angle θ was determined in a separate series of tests using charges similar to those previously described. In these tests a high-speed Kerr Cell camera[11,12] was used to photograph the exploding charges. The timing was arranged to record the phenomena while detonation was in progress. Three photographs were obtained for each cylinder thickness; typical photographs are shown in Fig. 6. In order to effect a direct comparison with the values of δ obtained in the tests using the cylindrical witness target, the angle θ was defined as that angle between the charge axis and the tangent to the expanding casing drawn through the point at which the casing ruptures. It is assumed that δ remains constant once the casing has ruptured. The angle θ, so defined, was measured from enlargements of the Kerr Cell photographs, and the values of θ for three charge types are presented in Table I. For comparison purposes the values of δ are also presented.

[11] R. v. Heine-Geldern, "Kerr cell photography of high speed phenomena," Carnegie Institute of Technology, Department of Physics, June 1952 (unpublished thesis).

[12] E. M. Pugh, R. v. Heine-Geldern, S. Foner, and E. C. Mutschler, J. Appl. Phys. **22**, 487 (1951).

TABLE I. Experimentally determined values of the angles δ and θ for thin-walled, internally loaded copper cylinders. The probable errors indicated in this table represent the authors' estimate of the accuracy that would be obtained from the experiments.

Wall thickness (in)	θ	θ (average)	$\theta/2$ (average)	δ (average)
0.030	14.8°			
	13.5°			
	13.5°	13.6°	6.8°±2.0°	8.1°±0.3°
0.040	11.8°[a]			
	14.4°			
	14.0°	14.2°	7.1°±0.5°	7.7°±0.3°
0.050	11.8°			
	12.0°			
	12.0°	11.9°	6.0°±0.5°	6.3°±0.3°

[a] The cylinder for which this value of θ was computed fractured prematurely. For this reason the value recorded here was omitted in the computation of the average.

CONCLUSIONS

Although different charge geometries were used, the experimental values of δ presented in Table I fall within the range reported by Singh. However, agreement with Singh's data should be anticipated since both experiments were performed with charges having approximately the same ratio of explosive mass to casing mass. A further examination of Table I shows that the values of δ are nearly equal to the values of $\theta/2$. The agreement is especially good for the thicker walled cylinders. The discrepancies in the case of the thinner walled cylinders can be attributed to a larger error in the determination of θ resulting from their rapid expansion and early rupture. In any case, the values of δ and $\theta/2$ agree sufficiently well to show that the trajectory of the fragments is adequately described by Taylor's relation.

ACKNOWLEDGMENTS

The authors wish to thank Prof. Emerson M. Pugh of the Carnegie Institute of Technology and Dr. R. J. Eichelberger of the Ballistics Research Laboratories for many helpful and stimulating discussions.

Explosively Loaded Metallic Cylinders. II*

F. E. Allison and J. Thomas Schriempf
Carnegie Institute of Technology, Pittsburgh, Pennsylvania
(Received December 16, 1959)

High-speed oscillographic pin technique was used to determine the radial displacement as a function of time for thin-walled copper cylinders internally loaded with high explosive (60RDX/40TNT). The results were compared with theoretical calculations based on G. I. Taylor's model for the expansion of an incompressible cylinder and on the additional assumption that the detonation products behaved as an adiabatically expanding polytropic gas. Theoretical calculations and experimental measurements were made for cylinders having a 0.500-in. inside diameter and seven different wall thicknesses ranging from 0.030 in. to 0.122 in. Although the experimental results agree with the calculated velocities at the larger radii, the data do not follow the theory in detail. During the initial expansion, the measurements show that the cylinder does not behave as an incompressible fluid, but is accelerated in a step-wise fashion characteristic of motion produced by shock waves.

INTRODUCTION

In the preceding paper it was shown that Taylor's relation describes the trajectory of the fragments from internally loaded, thin-walled, metal cylinders. However, Taylor's analysis of explosively loaded cylinders is more complete and gives, in addition to a relation between V and δ, a method for calculating the velocity of the casing. He assumes that, when the explosive is initiated at one end, a plane steady-state detonation front propagates parallel to the walls of the cylinder. The calculations are simplified by assuming that the chemical reaction occurs instantaneously at the detonation front and the casing behaves as an incompressible fluid. Even though explosively loaded metals are now known to behave as compressible fluids[1] and calculations that take into account the compressible nature of the metal have been made for certain geometries, detailed calculations have not been made for an axially symmetric geometry such as those encountered in a conventional shaped charge.[2] It is therefore important to make observations of the radial displacement as a function of the time and compare them with the approximate theory. High-speed oscillographic pin technique was used to determine the radial displacement as a function of time for copper cylinders internally loaded with 60RDX/40TNT. The experimental results are compared with calculations based on Taylor's theory and on the additional assumption that the detonation products follow the thermodynamic relations for a polytropic gas. Because his work is not widely distributed, the theory is described in detail with the general procedure closely following Taylor's original work.[3]

* This work was performed under a contract with the Ballistic Research Laboratories, Aberdeen Proving Ground, Maryland.
[1] R. G. Shreffler and W. E. Deal, J. Appl. Phys. **24**, 44 (1953); R. W. Goranson, D. Bancroft, B. L. Burton, T. Blechar, E. E. Houston, E. F. Gittings, and S. A. Landeen, J. Appl. Phys. **26**, 1472 (1955).
[2] G. Birkhoff, D. P. MacDougall, E. M. Pugh, and G. Taylor, J. Appl. Phys. **19**, 563 (1948).
[3] The original analysis of explosively loaded cylinders by G. I. Taylor appeared in an unpublished British Report (R. C. 193) in 1941.

THEORY

For an observer moving with the detonation front, the pressure of the burned gases will not impart energy to the casing. Rather, each element of the casing will follow an equilibrium path in which the centrifugal force is always balanced by the instantaneous pressure exerted by the detonation products. Thus, for a plane perpendicular to the axis and located a distance z behind the detonation front,

$$2\pi r p = mDd\theta/dt = mD^2(\cos\theta)d\theta/dz, \qquad (1)$$

where m denotes the mass per unit length of the cylinder; p, the instantaneous pressure; r, the instantaneous inside radius; D, the detonation rate of the explosive; θ, the angle of inclination of the wall to the axis; and t, the time. At the detonation front, the chemical reaction is assumed to be completed without expanding the cylinder; i.e., t, z, and θ equal zero, r equals r_0, and p equals p_1. In order to integrate Eq. (1) consider the relation

$$(\sin\theta)d\theta/dz = -d(\cos\theta)/dz = -\tan\theta d(\cos\theta)/dr,$$

or

$$(\cos\theta)d\theta/dz = -d(\cos\theta)/dr.$$

By substituting for $(\cos\theta)d\theta/dz$ in Eq. (1), one obtains

$$2\pi r p = -mD^2 d(\cos\theta)/dr,$$

which can be integrated to give

$$\sin^2(\theta/2) = \frac{\pi}{mD^2}\int_{r_0}^{r} pr'dr' = \frac{\pi}{2mD^2}\int_{r_0}^{r} pd(r^2). \qquad (2)$$

If the integral in Eq. (2) is now integrated by parts, one obtains

$$\sin^2(\theta/2) = \frac{\pi}{2mD^2}\left(pr^2 - p_1 r_0^2 + \int_{p}^{p_1} r^2 dp'\right). \qquad (3)$$

This relation represents the equation of motion for the casing. In order to proceed further, it is necessary to consider the motion of the detonation products.

Since the process is assumed to be steady-state, the conservation of mass can be expressed by the relation,

$$\rho_0 D r_0^2 = \rho(D-u)r^2, \tag{4}$$

where u is the particle velocity associated with the detonation products when observed in the laboratory system of coordinates, ρ, the density of the detonation products, and ρ_0, the density of the undetonated explosive. Equation (4) can now be used to eliminate r from Eq. (3) to give

$$\sin^2(\theta/2) = \frac{\pi\rho_0 r_0^2}{2mD}\left[\frac{p}{\rho(D-u)} - \frac{p_1}{\rho_0 D} + \int_{p_1}^{p} \frac{dp'}{\rho(D-u)}\right]. \tag{5}$$

The chemical reaction has been assumed to take place instantaneously at the detonation front (producing an initial pressure p_1). If it is further assumed that the product gases then expand adiabatically, one can write Bernoulli's equation in the form

$$\int_{p_1}^{p} \frac{dp'}{\rho} + \tfrac{1}{2}(D-u)^2 = \tfrac{1}{2}(D-u_1)^2, \tag{6}$$

which can be simplified by means of Eq. (4) to

$$2\int_{p}^{p_1} \frac{dp'}{\rho} = (D-u)^2 - D^2(\rho_0/\rho_1)^2. \tag{7}$$

By taking the derivative of Eq. (7), one obtains

$$dp/\rho = (D-u)du. \tag{8}$$

Equation (8) can now be used to evaluate the remaining integral in Eq. (5) which then reduces to

$$\sin^2(\theta/2) = \frac{\pi\rho_0 r_0^2}{2mD}\left[\frac{p}{\rho(D-u)} - \frac{p_1}{\rho_0 D} + u_1 - u\right]. \tag{9}$$

Equation (9) can be simplified further by noting that the conservation of momentum across the detonation front requires that

$$p_1 = \rho_0 D u_1, \tag{10}$$

where atmospheric pressure is neglected. By substituting for p_1, Eq. (9) can be reduced to

$$\sin^2(\theta/2) = \frac{\pi\rho_0 r_0^2}{2mD}\left[\frac{p}{\rho(D-u)} - u\right]. \tag{11}$$

If the ratio of the mass of the explosive to the mass of the casing is designated by ϕ, then

$$\phi = \rho_0 \pi r_0^2/m,$$

and Eq. (11) becomes

$$4\sin^2(\theta/2) = \frac{2\phi}{D}\left[\frac{p}{\rho(D-u)} - u\right]. \tag{12}$$

But, according to Eq. (4) of paper I, $2D\sin(\theta/2)$ is equal to the magnitude of the velocity imparted to the casing. Thus, Eq. (12) can be written

$$V = 2D\sin(\theta/2) = \left\{2\phi D\left[\frac{p}{\rho(D-u)} - u\right]\right\}^{\frac{1}{2}}. \tag{13}$$

In order to obtain numerical values for the velocity of the casing, it is necessary to evaluate the pressure, density, and particle velocity as a function of the radius of the expanding cylinder. This is easily accomplished when suitable thermodynamic data for the detonation products are available. In the following analysis it has been assumed that the detonation products obey the thermodynamic relations for a polytropic gas; i.e., an ideal gas for which the internal energy is directly proportional to the temperature. For such a gas, the pressure and density during an adiabatic process are related by the equation

$$p = a\rho^{\gamma}. \tag{14}$$

In addition to Eq. (14) there are four other equations that must be satisfied for an idealized detonation wave. They are the following:

Conservation of mass	$\rho_0 D = \rho_1(D-u_1)$	(15)
Conservation of momentum	$p_1 = \rho_0 D u_1$	(16)
Chapman-Jouget condition	$D = c + u_1$	(17)
Definition of sound velocity	$c^2 = (dp/d\rho)_{\text{adiabatic}}$.	(18)

Thus, there are a total of five equations connecting the eight quantities: ρ_0, D, ρ_1, u_1, p_1, c, a, and γ. Only three quantities need be chosen arbitrarily or determined experimentally in order to completely specify the conditions at the detonation front. Since ρ_0 and D can be determined experimentally, it is convenient to regard these two quantities as known. One must now assign a numerical value to one other quantity in order to completely specify the conditions at the detonation front. It appears to be most convenient to specify a numerical value for γ. Since recent work at Los Alamos[4] has shown that the detonation products of Grade A Composition B (64/35/1: RDX/TNT/Wax) are suitably described by a polytropic equation with $\gamma = 2.77$, this value was chosen for these calculations. Separate experiments were used to determine ρ_0 and the detonation rate of the explosive in the copper cylinders; values of 1.68 g/cm^3 and 0.793 cm/μsec were used for these parameters.

The independent parameter was taken as r_0/r, and corresponding values of ρ, p, u, and $\{p/[\rho(D-u)]-u\}$ were calculated. The last quantity is proportional to V^2. The results of calculations for $\gamma = 2.77$ and $\gamma = 3.00$ are

[4] W. E. Deal, Phys. Fluids **1**, 523 (1958).

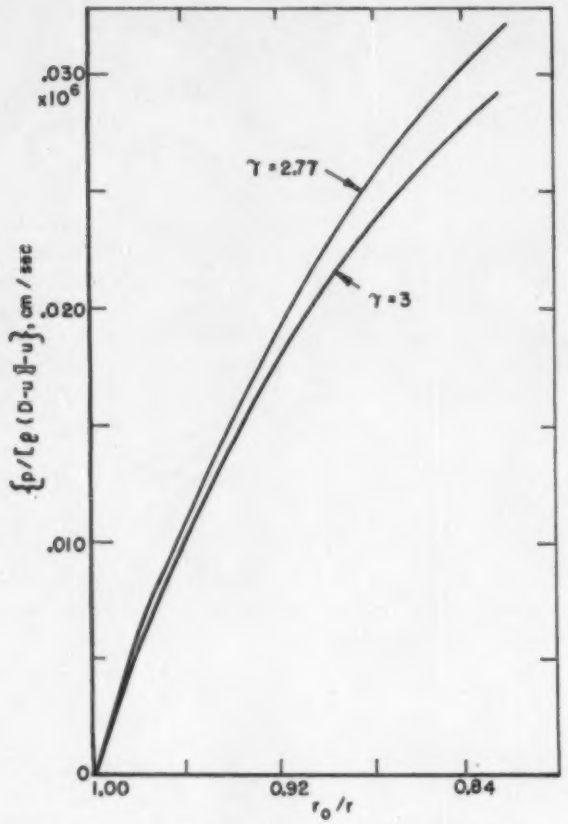

FIG. 1. Comparison between the theoretical calculations for $\gamma=2.77$ and $\gamma=3.00$. The quantity of $\{p/[\rho(D-u)]-u\}$ is proportional to the square of the casing velocity; r_0 is the initial inside radius of the cylinder and r, the instantaneous inside radius of the expanding cylinder.

presented in Fig. 1. For an increase of 0.050 in. in the radius of a casing with an original radius of 0.250 in., the quantity $\{p/[\rho(D-u)]-u\}$ is about 8% larger for $\gamma=2.77$ than it is for $\gamma=3$. A simple calculation based upon Eq. (13) shows that V would be only 4% larger. Thus, for many practical purposes, $\gamma=3$ may be an excellent approximation.

These calculations give V as a function of r_0/r, with the nature of the casing entering only through the parameter ϕ. However, it is not feasible to measure V directly with the techniques employed. Therefore, it is necessary to put the theoretical calculations in a form more suitable for an experimental check. This was done by using the calculated values of V to compute the profile of the casing from the equation,

$$z=\int_{r_0}^{r}\frac{dr'}{\tan\theta}, \tag{19a}$$

where

$$\tan\theta\cong 2\sin(\theta/2)+3\sin^3(\theta/2). \tag{19b}$$

From Eq. (13), V is directly proportional to $\sin(\theta/2)$. Although the integral cannot be evaluated in closed form it can be evaluated by mechanical quadratures. However, there is one difficulty introduced by the fact that the integrand becomes infinite at r_0. Although with sufficient effort one can approach arbitrarily close to r_0, the point itself must always be excluded from the quadratures. Thus, in reality, one is evaluating a quantity $(z-\delta z)$ given by the equation,

$$z-\delta z=\int_{r_0+\delta r}^{r}\frac{dr'}{\tan\theta}. \tag{20}$$

However, since $V=0$ for $z=0$ and $dV/dz>0$ for $z=0$, it was possible to extrapolate to $V=0$ and estimate δz.

The description of the casing will be complete when the outside radius of the casing has been specified. The conservation of mass for the metal casing can be written in the form

$$\pi\rho_l[(r_0')^2-(r_0)^2]=\pi\rho_l[(r')^2-(r)^2]D\cos\theta, \tag{21}$$

where r' is the outside radius of the casing and ρ_l is the density of the casing. For practical purposes $\cos\theta$ may be regarded as unity, and Eq. (21) reduces to

$$r'=\{r^2+[(r_0')^2-(r_0)^2]\}^{\frac{1}{2}}. \tag{22}$$

Values of V, z, and r' were computed for the charge designs used in the experimental tests.

As an illustration of these calculations, a scale drawing of the casing profile for a 0.122-in. thick copper cylinder having an initial internal radius of 0.250 in. is shown in Fig. 2. A curve showing the pressure as a function of the distance behind the detonation front is also shown in this figure. It is interesting to note that the pressure has dropped to one-half its initial value at a point 0.75 cm behind the detonation front. Since the detonation velocity is greater than 0.75×10^6 cm/sec, one observes that the pressure drops to one-half its initial value in less than 10^{-6} sec after the detonation front passes.

EXPERIMENTAL TECHNIQUES

The charge design used was the same as that considered in the theoretical analysis, and the data obtained

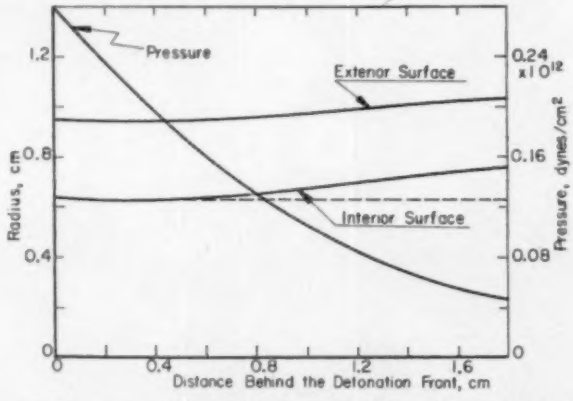

FIG. 2. Scale drawing of the casing profile for a 0.122-in. thick copper cylinder having an initial radius of 0.250 in. The pressure is also shown as a function of the distance behind the detonation front.

from these experiments can be compared directly with results obtained from the numerical analysis. The position of the exterior surface of the casing was determined as a function of time by a high-speed oscillographic pin technique similar to that developed at other installations for the study of explosive phenomena. Probes (pins) were placed at known distances from the initial position of the tube wall. As shown in Fig. 3(a), the probes lie in a plane perpendicular to the tube and point directly at its axis. When the wall of the tube, which is electrically grounded, makes contact with a probe, it discharges a condenser and forms an electric pulse. The series of pulses resulting from the shorting of successive probes is fed to an oscilloscope and recorded in a photograph. Since the horizontal sweep of the oscilloscope can be calibrated with an oscillator, the time interval between pulses can be accurately determined. The radial positions of the cylinder's exterior surface, which correspond to the radial positions of the probes, can now be plotted as a function of the corresponding times.

It should be emphasized that values of the time determined from the oscillogram will correspond to the radial positions of the exterior surface of the tube in a fixed plane and not to the radial position of a fixed element of the tube. This difference results from the fact that the probes are all located in a single plane perpendicular to the tube axis, while the trajectory of a fixed element of the cylinder does not lie in a single plane. The time at which a given probe should make contact with the surface can be obtained from the profile of the expanding case. One has only to consider the process in a coordinate system moving with the detonation front. As shown in Fig. 3(b), the probes, when viewed from this coordinate system, will be moving parallel to the axis of the casing with a velocity D. Since the casing will have assumed a steady-state contour, a probe with radial position r will reach the exterior surface at time

$$t=z/D, \tag{23}$$

where z is the distance measured from the plane of the

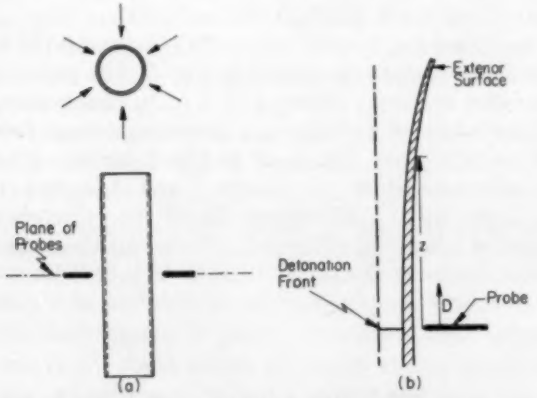

FIG. 3. Diagram illustrating (a) the arrangement of the probes, and (b) the initial position of a probe relative to its point of contact with the expanding cylinder.

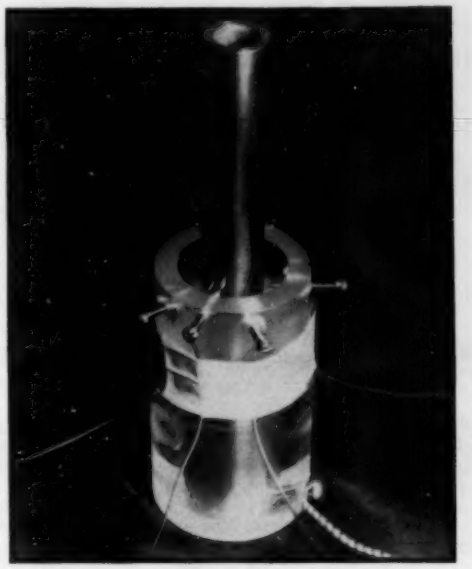

FIG. 4. Photograph of a tube and probe assembly prior to loading with the explosive.

detonation wave and t is the time measured from the instant the probes pass the plane of the detonation wave. Thus, the experimental measurements can be compared directly with the casing profile obtained from the above calculations.

Copper bus-bar was machined into 6-in. long tubes having seven different wall thicknesses—0.030, 0.040, 0.050, 0.066, 0.085, 0.104, and 0.122 in. Variations in wall thickness were kept within ± 0.001 in. and the inside diameters were maintained at 0.500 ± 0.0005 in. Each tube was positioned inside a machined lucite fixture, which was used to hold the probes in proper position with respect to the copper tubes. The probes, which were made from 2-56 brass screws, were adjusted by means of gauge blocks and an ohmmeter. The leads, which were to be connected to the pulse-forming circuit, were soldered to the probes and taped into position as shown in Fig. 4. The completed assembly was then sent to the hot-melt laboratory and filled with Composition B (60RDX/40TNT). As soon as the explosive had solidified, the loaded assemblies were sent directly to the test chamber where they were connected to the pulse-forming circuit. The pulse-forming circuit was kept close to the loaded assembly in order to minimize effects of stray capacitance. A-$\frac{1}{4}$ in. thick steel plate was placed between the pulse-forming circuit and the loaded assembly in order to protect the circuit from blast and fragments. The possibility of ionized gases prematurely shorting the probes was minimized by flushing the region around the probes with propane. The explosive was initiated by a No. 8 detonator used in conjunction with a $\frac{1}{4}$-in. long by $\frac{1}{2}$-in. diam tetryl booster. The output from the pulse-forming circuit was fed through coaxial cable to a Spencer-Kennedy oscilloscope located in an adjacent laboratory. The oscilloscope was triggered by an

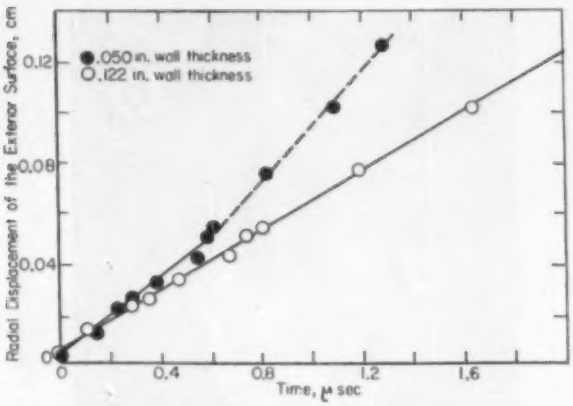

FIG. 5. Measured values of the radial displacement of 0.500-in. i.d. copper cylinders loaded with 60RDX/40TNT. The acceleration produced by the first reflected shock is evident in the data obtained with the 0.050-in. cylinders.

auxiliary circuit connected to a probe placed $\frac{1}{8}$ in. above the plane of the other probes. The traces produced on the oscilloscope were photographed on 35 mm film. The distances between pulses were measured on an optical comparator and subsequently converted to intervals of time with the aid of a calibration obtained by feeding the output of a 10-Mc crystal oscillator into the oscilloscope. New calibrations were taken frequently throughout the experiment. A careful comparison of the calibrations showed that variations in the horizontal sweep of the oscilloscope were less than 2%.

Although the oscillograms could be read to the nearest thousandth of a μsec, the time measurements were not that accurate. The greatest source of error in the time measurements was the variation of the probes from a single plane perpendicular to the axis of the cylinder. If the probes deviate from the mean plane by ±0.002 in., Eq. (23) shows that the time measurements will deviate from the average by ±0.006 μsec. Since a metal fixture was used as a guide for drilling holes for the probes, a systematic error of this magnitude could be introduced in the resulting data.

Variations in positioning the probes in the radial direction will also contribute to the scatter in the experimental data. By substituting z from Eq. (19a) into Eq. (23) one finds that r and t are related by

$$t=\int_{r_0}^{r}\frac{dr'}{D\tan\theta}. \tag{24}$$

The mean-value theorem of the integral calculus can be used to write Eq. (24) in the form,

$$t=(r-r_0)/D\tan\theta(\xi), \tag{25}$$

where $r_0<\xi<r$. Since $\tan\theta(\xi)$ is of the order of 0.1, a variation of ±0.001 inches in the radial position of the probes will be reflected in a variation of ±0.030 μsec. Thus, the largest source of variability, as far as the experimental time data are concerned will result from errors in the radial position of the probes. However, since errors in setting the radial position of the probes can be expected to occur at random, useful experimental results can be obtained by averaging a sufficient number of observations. For this reason the experimental results to be discussed in the next section are based on 5 to 10 observations for each individual pin configuration.

EXPERIMENTAL RESULTS

Kerr cell photographs shown in Paper I indicated that the tubes fracture at radial expansions greater than 0.050 in. In order to cover the range from 0 to 0.050 in., two groups of pin settings were used: one group was set at distances of 0.0015, 0.005, 0.009, 0.013, 0.017, and 0.021 in. from the initial position of the tube wall, and the other group at 0.0015, 0.010, 0.020, 0.030, 0.040, and 0.050 in. In the first group, adjacent pins were as close as possible without serious loss of experimental

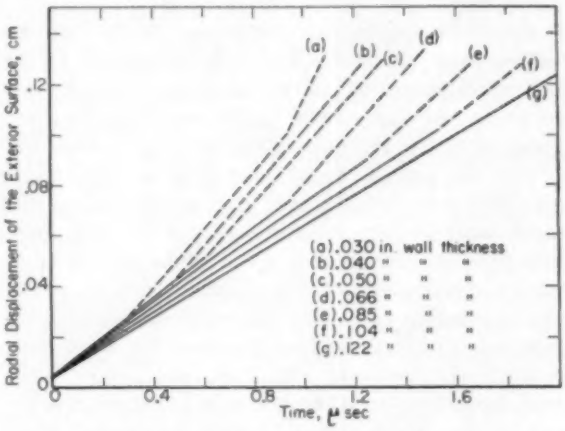

FIG. 6. Graphs illustrating the effect of wall thickness on the radial displacement of 0.500-in. i.d. copper cylinders loaded with 60RDX/40TNT.

accuracy. Measurements were taken on a total of 115 tubes, with seven different wall thicknesses corresponding to explosive mass to cylinder mass ratios of 0.747, 0.550, 0.432, 0.318, 0.239, 0.189, and 0.157.

The data for cylinders having 0.050-in. and 0.122-in. wall thicknesses are presented in Fig. 5. The points in this figure represent averages of 8 to 10 observations, and the standard deviation per observation range from 0.01 to 0.05 μsec. The data obtained for the other cylinders have about the same amount of scatter. In Fig. 6 the radial displacement for all the cylinders is plotted as a function of the time, illustrating the general characteristics of the initial motion. As is well known, the distance-time plot for the acceleration of a compressible fluid consists of a series of straight lines connecting the points where the shocks reach the exterior surface, each line having a higher slope than the ones preceding it. This general behavior is evident in the data shown in Fig. 6. Although the data do not permit a

quantitative evaluation of such parameters as the radial shock velocity, calculations of the average shock velocity are in qualitative agreement with more accurate measurements reported by Walsh and Christian.[5]

For comparison purposes, both the theoretical curves and the data for tubes having 0.050- and 0.122-in. wall thicknesses are plotted in Fig. 7. It is clear that both the theoretical and experimental curves approach the same slope in the limit of large expansions. Within the limits of experimental error there is no discrepancy between the calculated and measured slopes for all the wall thicknesses studied.

In Fig. 7 the calculated and experimental curves are matched by extrapolating to the initial external radius of the tube. When this is done, one observes that both curves can be brought into agreement at the larger radii by shifting the experimental curve to the right. The amount of shift necessary for agreement decreases as wall thickness decreases. The theoretical curve is based

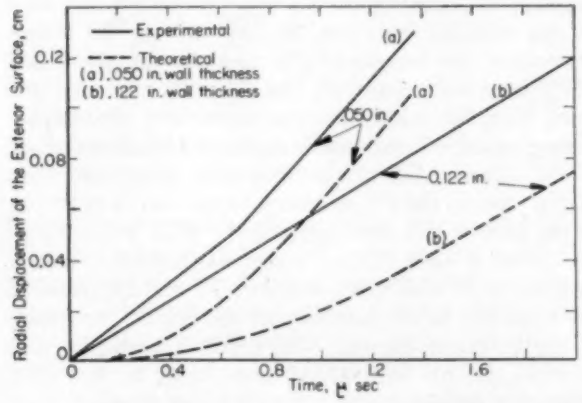

FIG. 7. Comparison between the measured radial displacement and that calculated from Taylor's theory, which assumes that the copper cylinders behave as an incompressible fluid.

on an incompressible model which requires the initial motion of the exterior surface to begin at the instant the detonation front passes a radially opposite point on the inner surface. However, in a compressible fluid picture the outer surface does not begin moving until the shock travels through the wall of the tube. Thus, the necessary time shift should be equal to the wall thickness divided by the shock velocity in copper.

Figure 8 is a somewhat idealized comparison between the motion predicted by the compressible and incompressible models. For the tubes having a 0.050-in. wall

[5] J. M. Walsh and R. H. Christian, Phys. Rev. **97**, 1544 (1955); J. M. Walsh, M. H. Rice, R. G. McQueen, and R. L. Yarger, Phys. Rev. **108**, 196 (1957).

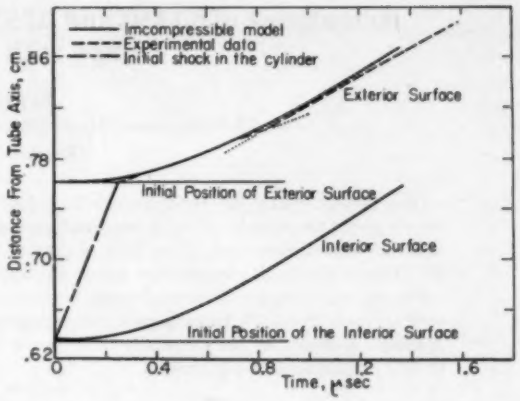

FIG. 8. Comparison between the measured radial displacement and that calculated from the incompressible fluid model. Note that the measured radial displacements have been translated along the time axis by an amount equal to the time required for the initial shock to reach the outer surface. The data shown are for cylinders having a 0.050-in. wall thickness.

thickness and a shock velocity of 0.45×10^{6} cm/sec, 0.23×10^{-6} sec will be required for the initial shock to travel through the tube. When the experimental data are shifted by this amount, as shown in Fig. 8, they agree quite well with the calculated curves at the larger radii. The dashed line indicates the data, and the broken line suggests the motion of the first shock through the tube wall.

CONCLUSIONS

Even though the metal is being accelerated in a stepwise fashion by the successive reflection of a shock wave, the theoretical analysis outlined in this paper, which treats the metal cylinders as an incompressible fluid and the detonation products as a polytropic gas having $\gamma=2.77$, is a good limiting approximation. Taylor's relation ($\delta=\theta/2$), though not applicable to the motion produced by individual shocks, was shown in Paper I to be a good approximation for the fragments produced by the copper cylinders used in these experiments. In order to approach the limiting conditions for which Taylor's relation is applicable, it is only necessary that a sufficient number of shock reflections occur before the cylinders rupture.

ACKNOWLEDGMENTS

The authors gratefully acknowledge the assistance of Prof. Emerson M. Pugh of the Carnegie Institute of Technology and Dr. R. J. Eichelberger of the Ballistics Research Laboratory who have contributed by many helpful and stimulating discussions.

Intensities of λ1850 and λ2537 in Low-Pressure Mercury Vapor Lamps with Rare Gas Present

BENTLEY T. BARNES
Lamp Development Department, General Electric Company, Cleveland, Ohio
(Received January 12, 1960)

The radiant flux in the Hg resonance lines just inside the wall of a lamp with an inside diameter of 35–36 mm is given for currents 0.4–2.0 amp and various bulb temperatures and rare gas fillings. The intensity of the 1850 line ranges from 12 to 34% of that of the 2537 one, with the highest ratios occurring when both arc current and bulb temperature are at the upper end of the ranges used. Since this result is contrary to what one would expect with single-stage excitation of the 1850 line, one must assume that this line is excited mainly by $6\,^3P-6\,^1P_1$ transitions when arc current and mercury vapor pressure are both relatively high. A rough estimate of the frequency of $6\,^3P_2-6\,^1P_1$ transitions, compared to those from the ground level to $6\,^1P_1$ confirms this conclusion.

MANY articles have given data on the relative intensity of λ2537 under various conditions of operation of a low-pressure mercury vapor discharge with rare gas present; a few have listed absolute values. Corresponding data for the 1850-A line are meager because few laboratories have had suitable equipment for measuring it. In 1948 Butaeva and Fabrikant[1] published some data for a lamp with argon filling at 4 mm (Hg) pressure.

By the use of phototubes calibrated with the aid of a monochromator with prisms and lenses of Corning high purity vitreous silica, we have obtained fairly extensive data on the intensities of λ1850 and λ2537.

EQUIPMENT AND PROCEDURE

The optical parts of the monochromator mentioned above absorbed about 50% of the flux in the central ray for λ1850, but very little at λ2537. The instrument was flushed with a continuous flow of dry N_2 to eliminate absorption by air and water vapor, The source for phototube calibrations was a low-pressure mercury vapor lamp with neon filling gas at 2 mm (Hg) pressure. This lamp had a window of Corning silica flush with the wall. Just outside this window there was a diaphraghm with an opening 8 mm in diam located in the plane normally occupied by the monochromator slit and used as the entrance aperture. At the exit of the monochromator, the images of this aperture for λ1850 and λ2537 were well separated. The flux in the spectral line being used for calibration passed without obstruction through an aperture 9 mm in diam, and irradiated most of the cathode disk of the phototube which had been placed close to the exit aperture. Stray 2537-A radiation in the 1850-A line was negligible ($<\frac{1}{2}\%$). Intensity at the center of each spectral image was measured with a thermocouple with CaF_2 window. To find the ratio of the total flux to the intensity at the center, the image of the entrance aperture was scanned vertically and horizontally, for both λ2537 and λ1850, by use of a phototube provided with a 1.0×1.5-mm aperture.

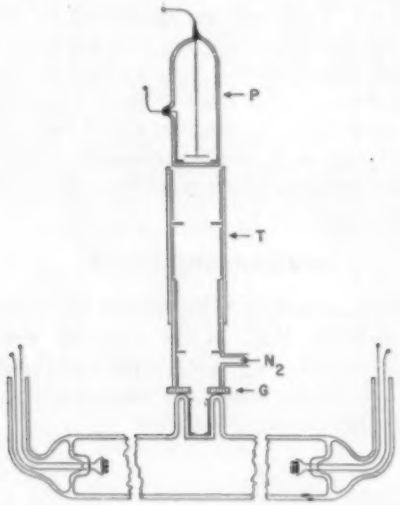

FIG. 1. Setup for intensity measurements. *P*, phototube; *T*, steel tube lined with felted black paper; *G*, soft rubber gasket.

The phototubes had nickel cathode disks coated with either tellurium, for measurement of λ1850, or cadmium, for λ2537. These cathode disks had a sensitivity variation of only a few percent over their surface. (A tube with cadmium on the rear wall, and with a cathode lead sealed in the glass at the center of the irradiated area had a 2:1 range of sensitivity over an area 1 cm in diam. Reliable calibration was practically impossible.) The Te tube had negligible sensitivity for λ2537; response of the Cd tube for λ1850 was eliminated by use of a Vycor filter.

For measurement of the spectral intensity from a lamp, the setup shown in Fig. 1 was used. Nitrogen flowing through tube *T* eliminated oxygen and water vapor which absorb λ1850, and prevented the formation of ozone, which absorbs λ2537. Blackened diaphragms and a lining of felted black paper in tube *T* and in the side tube above the lamp window eliminated errors due to reflection of radiation. The main part of the lamp was immersed in a water bath. A heating coil around the reentrant tube supporting the window prevented condensation of mercury in this region. The lamp was operated in series with a variable inductance, with the

[1] F. Butaeva and V. A. Fabrikant, J. Tech. Phys. U.S.R.R. 18, 1127 (1948).

TABLE I. Intensities per unit area inside window (milliw/steradian, cm²).

Filling gas Pressure (mm)	t*	λ1850 Kr 2.0	λ1850 Kr 1.0	λ1850 A 3.0	λ1850 A 1.0	λ1850 Ne 2.0	λ2537 Kr 2.0	λ2537 Kr 1.0	λ2537 A 3.0	λ2537 A 1.0	λ2537 Ne 2.0
0.40 amp	20°C	0.238	0.372				1.93	2.31			
	30	0.43	0.56	0.74	0.84		3.2	3.7	4.5	5.0	
	40	0.55	0.57	0.78	0.77	1.04	4.0	4.0	4.9	4.9	6.1
	50	0.56	0.57	0.74	0.70	0.94	3.8	3.6	4.5	4.4	5.4
	60			0.73	0.66	0.90			3.8	3.6	4.7
	70					0.87					4.1
0.80 amp	20°C	0.280	0.50				2.47	3.33			
	30	0.65	0.87	1.18	1.48		4.7	5.8	7.2	8.0	
	40	0.89	1.07	1.37	1.49	2.11	6.1	6.8	7.6	8.0	10.4
	50	1.01	1.11	1.42	1.42	1.94	6.0	5.7	7.2	7.2	9.2
	60			1.46	1.35	1.90			5.9	5.8	7.8
	70					1.86					6.6
1.50 amp	20°C	0.36	0.60				3.2	4.4			
	30	0.70	1.15	1.58	2.20		5.8	7.6	9.3	12.5	
	40	1.21	1.65	2.08	2.40	3.40	7.6	9.1	10.4	12.3	16.1
	50	1.54	1.82	2.20	2.44	3.34	7.7	7.6	9.4	10.4	14.0
	60			2.27	2.38	3.30			7.5	8.3	11.4
	70					3.21					9.4
2.00 amp	20°C	0.37	0.70				3.5	5.2			
	30	0.70	1.27	1.73	2.58		6.1	8.6	10.4	14.6	
	40	1.28	1.90	2.31	2.84	3.88	8.1	10.3	11.6	14.2	18.5
	50	1.69	2.04	2.48	2.97	3.96	8.4	8.5	10.2	12.0	16.4
	60			2.58	2.85	4.00			8.0	9.9	13.4
	70					3.94					10.7

* t = bulb wall temperature.

line voltage (rms) adjusted to be double the lamp voltage. To permit the use of various filling gases, the lamp was not sealed off, but a mercury cutoff prevented passage of contaminating vapors into the lamp during operation. After measurements had been completed, the window was cut out of each lamp and its transmittance for λ1850 and λ2537 was determined by use of a beam of radiant flux of sufficiently small diameter that none of it struck the wall of the tube on which the window was mounted.

RESULTS

The intensity per cm² in a radial direction, just inside the lamp window is listed in Table I. Since the intensity of resonance radiation at the tube wall probably falls off a little faster than the cosine of the angle which the rays make with the perpendicular to the tube wall, particularly for directions nearly tangential, the integration factor required to convert the values in Table I to total flux per cm² would be a few percent less than π. An additional factor of $2\pi R$ would be required to change from flux per cm² to total flux per cm of arc. (R, the inside radius of the lamp, is about 1.8 cm.)

As shown by Table I, the intensities of both the 1850- and the 2537-A line increase with a decrease of either the pressure or the atomic weight of the filling gas. This effect, well known for λ2537, is caused by the increase of electron temperature required to compensate for the more rapid loss of ions and electrons to the wall. The factor by which the 1850-A intensity is increased is in each case greater than that for the 2537 line. Similarly, the rate of rise of the intensity of λ1850 with increasing arc current and constant filling gas and bulb temperature is always greater than that for λ2537.

For bulb temperatures above 40°C, the intensity of the 1850 line either falls off much less rapidly than the 2537 output, with increasing bulb temperature, or actually increases. (In the two cases where the 2537 output increases in the 40–50° range, the output at λ1850 rises at a greater rate). At 0.40 amp, the increase

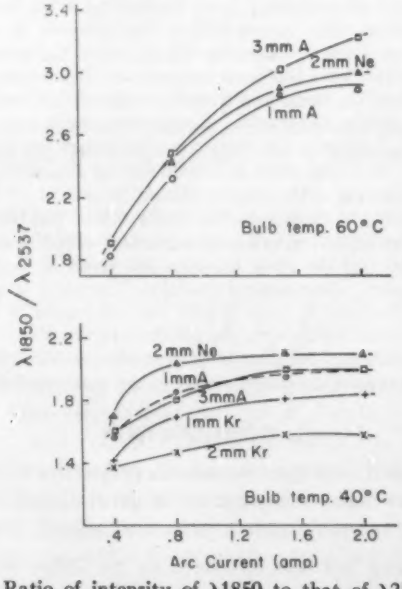

FIG. 2. Ratio of intensity of λ1850 to that of λ2537 vs arc current for two bulb temperatures. Rare gas used, and filling pressure at 25°C, are indicated on curves. (Ordinate scales incorrect; multiply by 0.1.)

TABLE II. Calculated ratio[a] of $6\,^3P_2-6\,^1P_1$ transitions to those from $6\,^1S_0$ to $6\,^1P_1$.

Bulb temperature (°C)	40	40	60
Arc current (amp)	0.40	1.50	1.50
Ratio	0.7	1.2	3.0

[a] Assumed proportional to integrals throughout lamp of number of atoms in lower energy level per cm³ times number of electrons per cm³ with sufficient energy. Computation made for argon filling gas at 3.5 mm (Hg) pressure.

is observed only with krypton present; at 1.50 amp, only with neon filling was there a decrease for the change from 40 to 50°C.

The intensity ratio, λ1850/λ2537 is plotted vs arc current in Fig. 2, for two bulb temperatures and the various gas contents indicated in Table I. The highest ratio is obtained when both the arc current and the bulb temperature are relatively high. Because of decreasing electron temperature T_e, this ratio would decrease with increasing current or with increasing mercury vapor pressure if excitation of the $6\,^1P_1$ level were entirely single stage. Although the probabilities of $6\,^3P-6\,^1P_1$ transitions are not known, some indication of the importance of two-stage excitation of the $6\,^1P_1$ line is given by a rough calculation. For this purpose, only the $6\,^3P_2-6\,^1P_1$ transitions were considered in appraisal of the two-stage process, since the rates of the other $6\,^3P-6\,^1P_1$ transitions are less. The product of the number of atoms in the lower level for a particular transition and the number of electrons with sufficient energy to cause the transition was used as a measure of its probability. Electron temperature values required for this calculation were obtained from probe measurements. Density of excited atoms in the $6\,^3P_2$ level vs distance from the tube axis was determined by computing the balance between excitation to the $6\,^3P$ levels, radial flow of 2537 radiation, and return of excitation energy to the electrons. The procedures described by Kenty[2] were used in this calculation. The results are listed in Table II. Although the ratios listed in this table may be far from the true values, they do show that multistage excitation of the $6\,^1P_1$ level probably plays a major role, and that it becomes more important when either the mercury vapor pressure or the arc current is increased. Thus, increased multistage excitation tends to offset the reduction in T_e that accompanies these changes in operating conditions.

[2] C. Kenty, J. Appl. Phys. **21**, 1309 (1950).

JOURNAL OF APPLIED PHYSICS VOLUME 31, NUMBER 5 MAY, 1960

Ultrasonic Viscoelastic Properties of Associated Liquids*

R. MEISTER,† C. J. MARHOEFFER,‡ R. SCIAMANDA,§ L. COTTER,‖ AND T. LITOVITZ
Physics Department, Catholic University of America, Washington, D. C.

(Received October 26, 1959)

Measurements of ultrasonic propagation of longitudinal and shear waves over a wide frequency and temperature range were made in an homologous series of associated liquids, butanediol 1,3, 2-methyl pentanediol 2,4 and hexanetriol 1,2,6. In each case, the absorption data demonstrated the presence of shear and structural or volume viscosities which are of the same order of magnitude and have the same temperature dependence. In order to account for the shear and compressional data, it was necessary to assume that a distribution of relaxation times excited. It was found that a different distribution was necessary for the compressional data than that used in accounting for the shear relaxation data. Comparison of the average relaxation time of structural and shear processes in the associated liquids shows that they are very close in value departing by a maximum of a factor of 4. In addition, it was found that the shear modulus was about 20 to 30% of the high-frequency compressional modulus. The ratio of shear compressional modulus in these liquids was very close to the values found in typical solids, even though the magnitudes of the moduli of the liquids was about a factor of 10 smaller than found in typical solids. The temperature dependence of the shear modulus and the relaxation part of the compressional modulus was found to be the same. The moduli linearly increase with decreasing temperature in a manner which is not accounted for by the Eyring-Hirai theory. It was found that the Tobolsky-Leaderman Ferry reduction formula, which is based on the assumption that the moduli are proportional to temperature, does not hold for these liquids and probably not for any high frequency visco-elastic data not associated with an "entropy" modulus. The data in the associated liquids were reduced by using the proper temperature dependence of the moduli. In considering the data of high frequencies, the absorption could not be accounted for by the same distribution which was used to fit the velocity data. At frequencies well above the dispersion region it was found that an attenuation set was independent of frequency. This appears to be characteristic of these liquids at very high frequencies and viscosities. At this time, there seems to be no acceptable mechanism to explain this type of loss. The latter authors have suggested that the hysteresis effect is not related to the viscous flow mechanism causing absorption at the lower frequencies and viscosities.

I. INTRODUCTION

ALTHOUGH the viscoelastic properties of polymers have been investigated in great detail,[1,2] similar studies in nonpolymeric liquids are limited. The associated organic liquids offer interesting possibilities for investigation because they exhibit both shear and volume viscosities. The latter appears to be caused by structural relaxation effects involving the liquid lattice.

* This work has been sponsored by the Office of Ordnance Research.

† Electrical Engineering Department, Catholic University of America.

‡ Presently at DePaul University, Chicago, Illinois.

§ Presently at Gannon College, Erie, Pennsylvania.

‖ Presently at Wadhams Hall, Ogdensburg, New York.

[1] T. Alfrey, Jr., *Mechanical Behavior of High Polymers* (Interscience Publishers, Inc., New York, 1948).

[2] W. P. Mason, Phys. Rev. **73**, 1074 (1948).

There are indications that the structural (or volume) and shear relaxation processes in these liquids are closely related. For example, in glycerol the volume and shear viscosity are equal. The relaxation times associated with these two processes are close in value, and have the same temperature dependence.

Investigation of the ultrasonic propagation in these liquids allows one to measure such quantities as the shear rigidity of a liquid and the relaxational part of the compressibility of the liquid lattice in addition to shear and compressional relaxation times.

In this paper, measurements using ultrasonic shear and longitudinal waves are used to investigate three associated liquids, butanediol 1,3, hexanetriol 1,2,6, and 2-methyl pentanediol 1,2 are reported. These results, in addition to previously reported data, allow some conclusions to be drawn about the dynamic mechanical properties of associated liquids.

II. RELAXATION THEORY

The most general behavior of an isotropic fluid is described by linear combination of the time derivatives of stress and of strains.[3] The numerical coefficient appearing in the linear relationship are the physical constants to be determined by measurements. Combining the equation of continuity, Newton's Law, and the single relaxation stress strain relationships, one can obtain the wave equation in terms of complex moduli given here in one dimension for the longitudinal sound wave,

$$\rho\frac{\partial^2 u_1}{\partial t^2}=\left[K^*+\tfrac{4}{3}G^*\right]\frac{\partial^2 u_1}{\partial x^2}, \tag{1}$$

where the coefficients ρ, K^*, G^* are the density, the complex compressional modulus, and the complex shear modulus, respectively. Since a longitudinal stress involves both shear and compressional stress, the coefficient appearing in Eq. (1) $[K^*+\frac{4}{3}G^*]/\rho$ is equal to the square of the complex longitudinal phase velocity. The sum $K^*+\frac{4}{3}G^*$ is called the longitudinal modulus M^* and may be written in the complex form,[4]

$$M^*=M'+iM''. \tag{2}$$

By solving the one-dimensional wave equation, the real and imaginary parts of M^* can be found in terms of the phase velocity and the loss. On assuming an exponential type solution,

$$u=u_0\exp\left(i\omega\left[t-\frac{x}{v_L^*}\right]\right) \tag{3}$$

and

$$\frac{1}{v_L^*}=\frac{1}{v_L}-\frac{\alpha}{\omega}i,$$

where α=nepers/unit dist., v_L, phase velocity, ρ, density, $\omega=2\pi\times$frequency, and substituting into the wave equation the real and imaginary parts of the longitudinal modulus are found in terms of α and v_L,

$$M'=\rho v_L^2[1-(\alpha\lambda/2\pi)^2]/[1+(\alpha\lambda/2\pi)^2]^2 \tag{4}$$

$$M''=2\rho v_L^2(\alpha\lambda/2\pi)/[1+(\alpha\lambda/2\pi)^2]^2. \tag{5}$$

For the case of pure shear stress one obtains the wave equation,

$$\rho(\partial^2 u_2/\partial t^2)=G^*(\partial^2 u_2/\partial x^2). \tag{6}$$

Again, on assuming a solution of this equation to be a sinusoidal damped plane wave,

$$u_2=A\exp\left(i\omega\left[t-\frac{x}{C_s^*}\right]\right), \tag{7}$$

where

$$\frac{i}{C_s^*}=\frac{1}{v_s}-\frac{i\alpha_s}{\omega}. \tag{8}$$

α_s, v_s, C_s^* are the absorption coefficient, the shear velocity, and the complex shear velocity, respectively. C^* equals $(G^*/\rho)^{\frac{1}{2}}$ and ρC_s^* is the complex shear impedance.

The properties of a liquid can be studied by means of the real and imaginary parts of both the shear and compressional moduli, if the relations between complex moduli and the measurable quantities are known.

The measurable quantities of the shear wave are the real and imaginary parts of the shear impedance, $\rho C_s'$ and $\rho C_s''$, respectively, where C' and C'' are the real and imaginary parts of the complex shear velocity. C' and C'' are related to the complex shear modulus by the following[5]:

$$\rho C_s'^2=G'/2[1+\{1+(G''/G')^2\}^{\frac{1}{2}}] \tag{9}$$

$$\rho C_s''=G'/2[\{1+(G''/G')^2\}^{\frac{1}{2}}-1], \tag{10}$$

where $G'=\mathrm{Re}G^*$ and $G''=\mathrm{Im}G^*$ and $G^*=G'+iG''$. From these relations, it is seen that the real part of the shear modulus G' is determined by a combination of $\rho C_s'^2$ and $\rho C_s''^2$.

Since propagation of a shear wave in a liquid is possible for only a few thousandths of a centimeter, the attenuation α_s, and the phase velocity v_s cannot be measured directly as in the longitudinal case. Therefore, as will be described in Sec. IV, a reflection method[6] is used to determine the real part of the acoustic impedance $\rho C_s'$. Then, by using methods described in Sec. III, G' and G'' are calculated from the $\rho C_s'$ data.

We shall now consider the elastic moduli in more detail. For a viscoelastic substance, a general stress strain relationship which includes time derivatives must be used.[1] Treating the pure compressional moduli considering a single relaxation process, the stress strain relation

[3] H. Kolsky, *Stress Waves in Solids* (Clarenden Press, Oxford, England, 1953).

[4] R. S. Marvin, R. Aldrich, and H. S. Sack, J. Appl. Phys. **25**, 1213 (1954).

[5] W. P. Mason, Phys. Rev. **75**, 936 (1949).

[6] In these measurements $\rho C_s''$, the imaginary part of the acoustic impedance, was not measured.

is written,

$$p+\tau_v\dot{p}=K_0\epsilon+\tau_vK_\infty\epsilon \tag{11}$$

where p is the applied pressure, ϵ, the fractional condensation, K_0, the static compressional modulus, K_∞, the high-frequency compressional modulus, and τ_v, the relaxation time for structural rearrangement in the liquid. K_0, K_∞, τ_v have one set of values if the process is isothermal, and another if adiabatic.[7] When considering ultrasonic waves, the latter are of interest.

If one applies a sinusoidal pressure $p=p_0e^{i\omega t}$ to this fluid, then (11) becomes

$$p_0(1+i\omega\tau_v)=\epsilon_0(K_0+i\omega\tau_vK_\infty) \tag{12}$$

and one obtains a complex adiabatic modulus of compression

$$K^*=\frac{p}{\epsilon}=K_0+\frac{K_2\omega^2\tau_v^2}{1+\omega^2\tau_v^2}+i\frac{K_2\omega\tau_v}{1+\omega^2\tau_v^2}, \tag{13}$$

where $K_2=K_\infty-K_0$; K_2 is the relaxational part of the modulus. Rewriting (12) the stress strain relation is obtained in the form

$$p=K^*\epsilon=[K'+i\omega\eta_v(\omega)]\epsilon. \tag{14}$$

K' is the real part of K^* and $\eta_v(\omega)=K_2\tau_v/1+\omega^2\tau_v^2$ plays the role of a frequency dependent volume viscosity. At low frequencies this term becomes

$$\eta_v=K_2\tau_v, \tag{15}$$

which is the "unrelaxed" volume viscosity.

The shear components of the stress-strain relation can be expressed in an equation of the same form as Eq. (11). Assuming the static shear rigidity of a liquid is zero, this is written

$$p_{ij}+\tau_s\dot{p}_{ij}=G_\infty\tau_s\dot{\epsilon}_{ij}, \tag{16}$$

where τ_s is the shear relaxation time G_∞, and the high-frequency shear rigidity.

When considering the effect of a sinusoidal applied stress one obtains as in the foregoing a complex shear modulus

$$G^*=\frac{p_{ij}}{\epsilon_{ij}}=\frac{G_\infty\omega^2\tau_s^2}{1+\omega^2\tau_s^2}+\frac{i\omega G_\infty\tau_s}{1+\omega^2\tau_s^2}, \tag{17}$$

where $G_\infty\tau_s/1+\omega^2\tau_s^2$ is the frequency dependent shear viscosity, which at low frequencies reduces to the unrelaxed shear viscosity,

$$\eta_s=G_\infty\tau_s. \tag{18}$$

The longitudinal modulus M^* for the single relaxation process is now determined using Eq. (1).[8]

$$M^*=\left[K_0+\frac{K_2\omega^2\tau_v^2}{1+\omega^2\tau_v^2}+\frac{4}{3}\frac{G_\infty\omega^2\tau_s^2}{1+\omega^2\tau_s^2}\right]+i\left[\frac{K_2\omega\tau_v}{1+\omega^2\tau_v^2}+\frac{4}{3}\frac{G_\infty\omega\tau_s}{1+\omega^2\tau_s^2}\right]. \tag{19}$$

From this relationship, the limiting longitudinal moduli are obtained. The M^* at low frequency is $M_0=K_0$, and at high frequency the limiting modulus is $M_\infty=K_0+K_2+\frac{4}{3}G_\infty$. The relaxation part of the longitudinal modulus is $M_2=M_\infty-M_0$.

If we solve Eqs. (4) and (5) for α, we obtain in terms of the relaxation moduli K_2 and G_∞ in the low-frequency limit, where $(\alpha v/\omega)^2\ll1$

$$\alpha=\frac{\omega^2}{2\rho v^3}[K_2\tau_v+\tfrac{4}{3}G_\infty\tau_s]. \tag{20}$$

From Eqs. (15) and (18) the attenuation in terms of the shear and compressional viscosity is obtained

$$\alpha=\frac{\omega^2}{2\rho v^3}[\eta_v+\tfrac{4}{3}\eta_s], \tag{21}$$

where

$$\alpha_{\text{stokes}}=\frac{2\omega^2\eta_s}{3\rho v^3}. \tag{22}$$

By using Eqs. (21) and (22) the ratio of the volume to the shear viscosity may be found

$$\frac{\eta_v}{\eta_s}=\frac{4}{3}\left[\frac{\alpha}{\alpha_{\text{stokes}}}-1\right]. \tag{23}$$

III. REDUCTION OF THE DATA

A. Longitudinal Data

It is possible to define a real reduced part of the total dilatational modulus by the ratio,

$$\mathfrak{M}=\frac{M'-M_0}{M_\infty-M_0}=f(\omega\tau) \tag{24}$$

M_0 = static modulus

$M_\infty-M_0$ = relaxational contribution to the total modulus.

$\mathfrak{M}'$ is a function of temperature only through the variable $\omega\tau$[9,10] since dividing by $M_\infty-M_0$ accounts for

[7] K. F. Herzfeld and T. Litovitz, *Absorption and Dispersion of Ultrasonic Waves* (Academic Press, Inc., New York, 1959).

[8] T. Litovitz, T. Lyon, and L. Peselnick, J. Acoust. Soc. Am. **26**, 566 (1954).

[9] After using the real part of Eq. (19) and introducing $a=(\tau_v/\tau_s)$, the real part of the longitudinal modulus may be written as

$$M'=M_0+M_2\frac{\omega\tau_s}{1+(\omega\tau_s)^2}\left\{\frac{(1-a^2)[1-\frac{4}{3}(G_\infty/M_2)]}{1+(a\omega\tau_s)^2}\right\}$$

from which Eq. (24) is obtained. It is seen here that $\mathfrak{M}'$ is a func-

the effect on M' of the temperature dependence of $(M_\infty - M_0)$. The advantage of reducing the date with the proper variable is that measurements at different temperatures may be reduced to a single curve. Similarly, a reduced imaginary part may be written

$$\mathfrak{M}'' = \frac{M''}{M_\infty - M_0} = f_1(\omega\tau). \tag{25}$$

If this is the case, all the measurements at the different frequencies and viscosities should reduce to the same curve as a function of the variable $\omega\tau$.

The reduction of $\mathfrak{M}'$ and $\mathfrak{M}''$ data does not depend on the functional form of M but only on whether or not it is a function of $\omega\tau$ alone. The description of the process until now has only considered a single relaxation time associated with the mechanism for absorption, but even if distribution of relaxation times exist, as long as these times each have the same temperature dependence it can be shown that a reduction of the data is possible. The criteria for reduction is found to exist if the ratio of the average compressional to average shear time $(\tau_v)_{av}/(\tau_s)_{av}$ and the ratio of the relaxation moduli G_∞/M_2 are independent of temperature.

It should be mentioned here that if attenuation data are not available to calculate M' as in Eq. (4), then ρv_L^2 may be used instead, leading to the reduced form,

$$\frac{\rho v_L^2 - M_0}{M_2} = \mathfrak{M}' - \frac{M'}{M_2}\left\{\frac{(\alpha v_L/\omega)^2[3+(\alpha v_L/\omega)]}{1-(\alpha v/\omega)^2}\right\}, \tag{26}$$

where the second term explicitly depends on temperature. However, in the liquids discussed below $(\alpha v_L/\omega)^2$ at the maximum is less than 0.08, which leads to a difference of less than 6% between $\rho v_L'^2$ and M'.

(Note that in this highly viscous region the value of v_L' can be measured only to about 3%.)

B. Shear Data Reduction

Since only the real part of the shear impedance is measured for the liquids discussed, the problem becomes one of finding a theoretical function for G' and G'', which when combined according to Eq. (9) produces $\rho C_s'^2$. The fact that the real and imaginary parts of the complex moduli are integrally related makes a considerable simplification.

A reduced plot of the $\rho C_s'^2$ data is made by defining a quantity

$$S(\omega\tau_s) = \frac{\rho C_s'^2}{G_\infty} \tag{27}$$

where the limiting modulus G_∞ is determined at high frequencies and low temperature. In liquids the data are often insufficient to adequately fix the temperature dependence of G_∞. From the criteria that the temperature dependence of G_∞ and M_2 must be equal for a reduction to be possible, it is possible to adequately determine the temperature dependence of G_∞ if M_2 data are available.

In the viscous liquids studied it is found that limiting values can be approached only by measuring over several decades of the variable. In contrast to the single relaxation process which reaches limiting values in two decades, the constructed theoretical function must then contain a distribution of relaxation times rather than a single relaxation time. The function having a relaxation character and also containing the distribution of times may be written[4]

$$G^* = G_\infty \int_0^\infty \frac{g(\tau/\tau_s')i\omega\tau}{1+i\omega\tau} d(\tau/\tau_s'),$$

or in terms of real and imaginary parts.

$$G' = G_\infty \int_0^\infty \frac{g(\tau/\tau_s')(\omega\tau)^2}{1+\omega^2\tau^2} d(\tau/\tau_s')$$

and (28)

$$G'' = G_\infty \int_0^\infty \frac{g(\tau/\tau_s')\omega\tau}{1+\omega^2\tau^2} d(\tau/\tau_s'),$$

where $g(\tau/\tau_s')$ is the normalized contribution to the shear modulus of a group of molecules having individual relaxation times in a range $d\tau$ near τ. The τ_s' represents some intermediate value of τ. The combination of G' and G'' in Eq. (9) produces $\rho C_s'^2$. Further examination of the reduced data $\rho C_s'^2/G_\infty$ will show whether or not there is symmetry around the half value of the reduced modulus and with this information a guess at the type of distribution function of relaxation times may be made. Satisfactory results are obtained below with two types of distribution functions. There may be other functions that will give a satisfactory representation of the data over the range of the variable measured.[11,12] The functions used below are:

(a) A symmetrical Gaussian distribution of relaxation times given by[13]

$$g(\tau/\tau_s') = \frac{b}{(\pi)^{\frac{1}{2}}}\frac{\tau_s'}{\tau}\exp\left[-b\ln\left(\frac{\tau}{\tau_s'}\right)^2\right] \quad 0<\tau<\infty. \tag{29a}$$

This function is logarithmically symmetric and exhibits a maximum at $\tau=\tau_s'$. The width of the distribution is determined by (b). [See Fig. 1(a).]

(b) An assymetrical distribution of relaxation times

tion of temperature through $\omega\tau_s$ alone if τ_v/τ_s and G_∞/M_2 are constant with temperature.

[10] R. Piccirelli and T. A. Litovitz, J. Acoust. Soc. Am. **29**, 1009 (1957).

[11] Tobolsky, Dunnell, and Andrews, J. Textile Research **21**, 404 (1951).

[12] Considerable success has been obtained with measurements on long chain polymers using rectangular and trapezoidal distribution functions.

[13] W. A. Yager, J. Appl. Phys. **7**, 434 (1936).

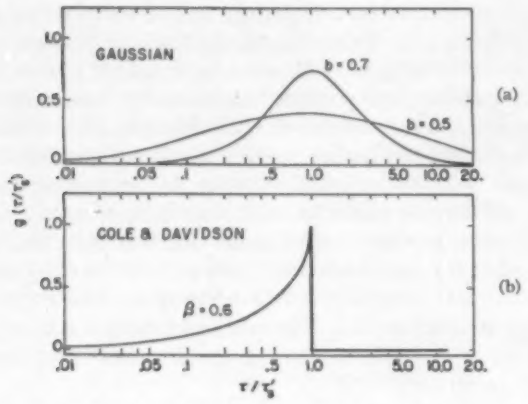

FIG. 1. (a) Gaussian function $g(\tau/\tau_s')$ for distribution of relaxation times in the interval $d\ln(\tau/\tau_s')$ computed for $b=0.7$ and 0.5. (b) Cole & Davidson distribution function $g(\tau/\tau_s')$ for distribution of relaxation times in the interval $d\ln(\tau/\tau_s')$ computed for $\beta=0.6$.

due to Cole-Davidson, where[14]

$$g(\tau/\tau_s')=\tau_s'/\tau\,\sin\beta\pi/\pi[\tau/\tau_s'/1-\tau/\tau_s']^\beta;\quad 0\leq\tau/\tau_s'<1 \tag{29b}$$

$$g(\tau/\tau_s')=0;\quad 1\leq\tau/\tau_s'$$

β and τ_s' are parameters which determine the width and position of the maximum, respectively. This function has maximum value at $\tau=\tau_s'$. τ_s' is the longest relaxation present, and β determines the width of the curve. [See Fig. 1(b).] From the imaginary part of Eq. (28) one obtains for the shear viscosity in the low frequency limit,

$$\eta_{s\text{theor}}=\frac{G''}{\omega}=G_\infty\int_0^\infty \tau g(\tau/\tau_s')d(\tau/\tau_s'). \tag{30}$$

It can be seen that the integral represents the average relaxation time $\tau_{s_{av}}$. Thus, when a distribution exists $\eta_s=G_\infty\tau_{s_{av}}$. By substituting Eq. (29a) into the integral in Eq. 30, one finds that for a Gaussian distribution of relaxation times

$$\tau_{s_{av}}=\tau_s'\exp\frac{1}{4b^2}=\frac{\eta_{s\text{theor}}}{G_\infty}. \tag{30a}$$

If instead one uses the Cole-Davidson distribution, Eq. 30 gives

$$\tau_{s_{av}}=\tau_s'\beta. \tag{30b}$$

It can be seen that in neither type of distribution is τ_s' numerically equal to $\tau_{s_{av}}$ the average relaxation time.

(c) Determination of the compressional modulus using shear modulus. If both the measured value of the dilatational modulus and the shear modulus are known, then by the subtraction $M^*-\frac{4}{3}G^*$ the K^* modulus can be obtained by using Eq. 1.

The real and imaginary parts of the compressional moduli may be plotted as a single reduced curve by defining reduced compressional moduli,

$$\text{(a)}\quad \mathcal{K}'=\frac{K'-K_0}{K_\infty-K_0}=\mathfrak{F}(\omega\tau_v)$$
$$\text{(b)}\quad \mathcal{K}''=\frac{K''}{K_\infty-K_0}=\mathfrak{F}_1(\omega\tau_v), \tag{31}$$

where $K_0=M_0$. On dividing by the total relaxation part of the compressional modulus K_2 the reduced quantities K' and K'' are obtained. When a distribution of times exists, this modulus may be written

$$K^*(\omega\tau_v)=K_0+K_2\int_0^\infty \frac{k(\tau/\tau_v')i\omega\tau}{1+i\omega\tau}d(\tau/\tau_v'), \tag{32}$$

where $k(\tau/\tau_v')$ is the normalized contribution to the static compressional modulus of a group of molecules having individual relaxation times in a range $d\tau$ near τ. The τ_v' represents some intermediate value of τ. The imaginary part of Eq. (32) gives in the low frequency limit the value of compressional viscosity,

$$\eta_{v\text{theor}}=\frac{K''}{\omega}=K_2\int_0^\infty \tau k\left(\frac{\tau}{\tau_v'}\right)d\left(\frac{\tau}{\tau_v'}\right),$$

where the integral represents the average value of τ_v, and thus

$$\eta_{v\text{theor}}=K_2\tau_{v_{av}}. \tag{33}$$

Note that for the compressional case τ_v' is substituted for τ_s' in Eq. 29.

IV. EXPERIMENTAL METHODS

A. Sample Preparation

Samples of butanediol 1,3 and 2-methyl-pentanediol 2,4 of the C.P. grade were obtained from Eastman Organic Chemicals. These samples were prepared by boiling at low pressure to free the sample of water. The sample of Hexanetriol 1,2,6, a technical grade obtained from Carbon and Carbide Chemicals, was dried by fractional distillation. In order to obtain a high purity, the process was repeated twice using the indicated B.P. 156°C at a pressure of 5 mm, taking the middle third fraction each time.

B. Viscosity and Density

The viscosities and densities of the liquids were measured as a function of temperature. The Ostwald and Hoeppler Viscometers were both used and these measurements were performed in a temperature bath which was controlled to ±0.1°C with the resulting accuracy in the viscosity of about ±1%.

C. Longitudinal Absorption and Velocity

The pulse technique was used for measurement of longitudinal ultrasonic velocity and absorption over a

[14] D. W. Davidson and R. H. Cole, J. Chem. Phys. **19**, 1484 (1951).

TABLE I. Summary of density and viscosity data.[a]

	Structure[b]	Density g/cc	Shear viscosity[c] (poise) $\ln_e\eta$
Butanediol 1,3	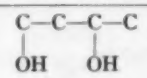	$1.015-6.4\times10^{-4}T$	$-5.898+\frac{1.552\times10^3}{(T+273)^2}$
2-methyl-Pentanediol 2,4	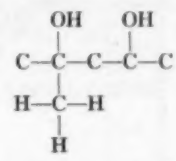	$1.132-7.0\times10^{-4}T$	$-5.090+\frac{1.441\times10^3}{(T+273)^2}$
Hexanetriol 1,2,6	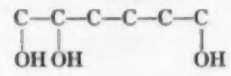	$1.109-5.5\times10^{-4}T$	$-5.63-+\frac{2.2098\times10^3}{(T+273)^2}$
Glycerol[d]	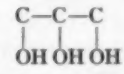	$1.273-5.8\times10^{-4}T$	$-1.627+\frac{2.204\times10^3}{(T+273)^2}$

[a] Equations obtained from best fit of experimental data and used to extrapolate to determine values needed in calculations outside measured range.
[b] For simplicity, H atoms not part of OH groups have been omitted.
[c] Range of measurement (in degrees centigrade):

Hexanetriol 1,2,6	density (−10° to +40°C)	viscosity (−20° to +39°C)
Butanediol 1,3	density (−50° to +40°C)	viscosity (−45° to +40°C)
2-methyl-Pentanediol 2,4	density (−48° to +5°C)	viscosity (−53° to +5°C)

[d] R. Piccirelli and T. Litovitz, J. Acoust. Soc. Am. 29, 1009 (1957).

frequency range from 1 to 100 Mc/sec. A full description of the method is found in a paper by Litovitz, Lyon, and Peselnick.[8]

D. Shear Impedance

In this method, the reflection coefficient for normal incidence of shear waves (generated by ac cut quartz transducer) on liquid quartz interface is obtained directly from the db loss/echo, a measurable quantity. This reflection coefficient is related to the acoustic impedances of the quartz and the liquid under test.

In terms of the complex shear impedance, the reflection coefficient is given by

$$Re^{-i\theta}=Zq-\rho C_s^*/Zq+\rho C_s^*, \tag{34}$$

where Zq and ρC_s^* are the shear impedances of the quartz and liquid, respectively. R is the absolute magnitude of the reflection coefficient and θ is its phase angle. By treating only the absolute magnitude R, the following relation may be written

$$\rho C_s'^2=Zq/\rho[1-R/1+R]^2. \tag{35}$$

Since the absolute value of the reflection coefficient for the quartz air interface is unity, the loss per echo in db may be written in terms of the difference $D_\omega(T)$ between the liquid quartz and the liquid air interface, ω is the angular frequency and T is the temperature

$$D_\omega(T)=20\log_{10}R. \tag{36}$$

Algebraic manipulation leads directly to

$$\rho C_s'^2=Zq^2\tanh^2[D_\omega(T)/20\log_{10}e]. \tag{37}$$

This method and the analysis is fully discussed by Piccirelli[15] and Mason.[16]

V. DISCUSSION OF EXPERIMENTAL DATA

A. Density and Shear Viscosity

The density and viscosity data for the temperature ranges covered in this work are given in Table I.[17] The equations given there represent the best fit to the experimental data. $Ln\eta_s$ was found to be proportional to T^{-3}.

B. Velocity Dispersion

The longitudinal velocity data plotted vs frequency are shown in Fig. 2. It can be seen that considerable dispersion is present. The data indicate typical relaxational behavior, but unfortunately the experimentally available frequency range did not allow a measurement of both the limiting low and high frequencies at any given temperature. The values of V_∞ and V_0 shown in Fig. 2 are obtained by calculation from the extrapolated values of M_∞ and M_0 from the higher and lower temperatures, respectively. The ultrasonic longitudinal velocities as a function of temperature at various frequencies are found in Fig. 3. They all show a similar behavior in that low- and high-frequency limiting velocities V_∞ and V_0, respectively, are reached. This is

[15] R. Piccirelli, Ph.D. Dissertation, Catholic University, Washington, D. C. (1957).
[16] W. Mason and H. McSkimin, Bell System Tech. J. 25, 122 (1951).
[17] In most of the tables which appear throughout this paper other associated liquids will be included, where appropriate, for purposes of comparison.

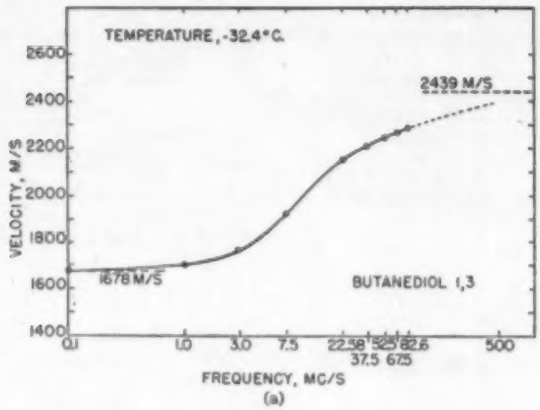

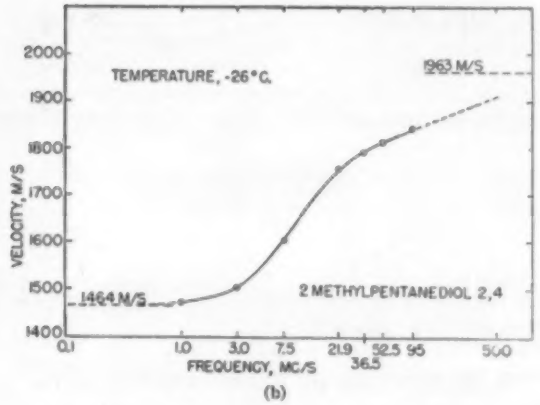

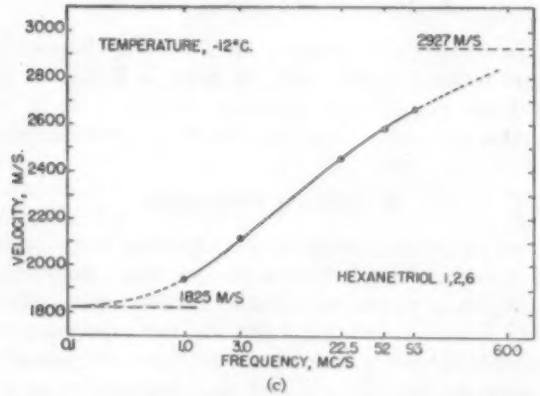

FIG. 2. (a–c) The longitudinal velocity plotted against frequency at a given temperature as noted on figures. The upper and lower dashed horizontal lines represent V_∞ and V_0, respectively. These limiting velocities are obtained from extrapolation of the limiting moduli M_∞ and M_0.

shown by the absence of dispersion at low and high temperatures. Experimental difficulties limited the accuracy of the velocity measurements in the very viscous or low-temperature region. The temperature dependence of V_∞ was obtained by extrapolations of M_0 and M_∞, which best reduced the data. It is evident that the temperature dependence of V_∞ is larger than that of V_0.

In Table II are tabulated the values of V_∞ and V_0 obtained by extrapolating the M data from upper and lower temperatures, respectively. The magnitude of the

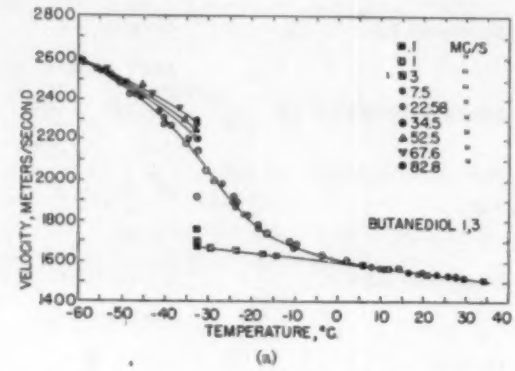

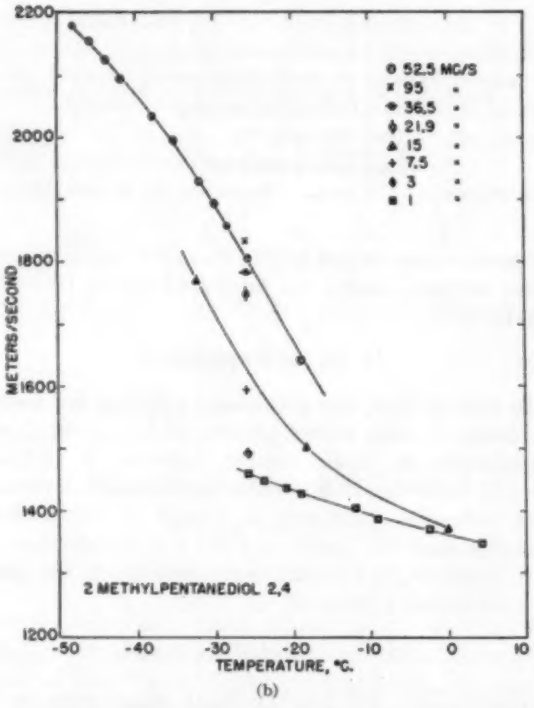

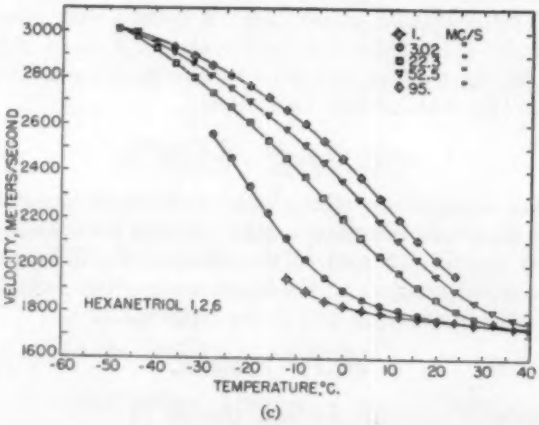

FIG. 3. (a–c) Longitudinal velocity plotted against temperature for various frequencies.

dispersion $V_\infty - V_0/V_0$ varies between 15 and 60%, most of the liquids exhibiting a value larger than 25%.

The thermal coefficients of the velocity and density are tabulated in Table III. For the liquids listed the temperature dependences of V_0 lie between two and four times the temperature dependence of the density, in only rough agreement with the observations of Rao[18] who suggests a factor of three. It can be seen that the temperature dependence of V_∞ ranges from about two to eight times the temperature dependence of the density.

C. Longitudinal Absorption

The measurement of absorption associated with the longitudinal wave is plotted in Fig. 4, as a function of temperature and at various frequencies. All the curves show a similar behavior exhibiting a bell shape typical of a relaxation process. As the temperature is lowered, the absorption coefficient exhibits a maximum, the magnitude and position of which depends upon the ultrasonic frequency used. The higher frequencies have a correspondingly higher maximum value. The peaks of the curves shift toward lower temperatures at lower frequencies. This, of course, indicates that the relaxation time increases as the temperature is lowered (or as the viscosity is increased). In Table II the values of the ratio $\alpha_{obs}/\alpha_{stokes}$ in the nondispersion region are tabulated. The values are independent of temperature (in the nondispersion region) and lie between 1.5 and 3.5. These results are typical of associated liquids and indicate the

TABLE II. Velocity dispersion data in associated liquids.

	T °C	η_s poise	α/α_{stokes}[a]	v_0 M/sec	v_∞ M/sec	$\frac{v_\infty - v_0}{v_0}$
Butanediol 1,3	−32.2	189	1.76	1695	2331	0.375
2-methyl-Pentanediol 2,4	−26.0	42.3	3.38	1460	1865	0.280
Hexanetriol 1,2,6	−10.5	720	1.65	1820	2740	0.515
Glycerol[b]	−14.0	616	1.78	1990	3150	0.59
Propanediol 1,2[c]	−37.8	905	2.08	1650	2360	0.43
n-Propanol[d]	−130.0	450	1.77	1860	2160	0.15
Diphenyl pentachloride[e]	34.5	12	3.28	1310	1690	0.29

[a] The values of α/α_{stokes} listed are those measured in the nondispersion region.
[b] See footnote d, Table I.
[c] R. Meister (private communication).
[d] T. Lyon and T. Litovitz, J. Appl. Phys. **27**, 179 (1956).
[e] T. Litovitz, T. Lyon, and L. Peselnick, J. Acoust. Soc. Am. **4**, 566 (1954).

TABLE III. Temperature dependence of the density and of high- and low-frequency limiting velocities.[a]

	$\frac{1}{\rho}\frac{\partial\rho}{\partial T}$[b]	$\frac{1}{v_0}\frac{\partial v_0}{\partial T}$[b]	$\frac{1}{v_0}\frac{\partial v_0}{\partial T}\Big/\frac{1}{\rho}\frac{\partial\rho}{\partial T}$	$\frac{1}{\rho}\frac{\partial\rho}{\partial T}$[c]	$\frac{1}{v_\infty}\frac{\partial v_\infty}{\partial T}$[c]	$\frac{1}{v_\infty}\frac{\partial v_\infty}{\partial T}\Big/\frac{1}{\rho}\frac{\partial\rho}{\partial T}$
Butanediol 1,2	0.658	1.70	2.58	0.628	2.08	3.31
2-methyl-Pentanediol 2,4	0.630	2.64	4.18	0.602	4.50	7.50
Hexanetriol 1,2,6	0.543	1.26	2.29	0.484	1.07	2.22
Glycerol[d]	0.455	1.15	2.53	0.448	1.98	4.43
Diphenyl pentachloride[e]	0.649	1.94	2.99	0.649	3.84	5.92

[a] Units $[°C]^{-1}\times10^3$.
[b] Data at 20°C.
[c] Data at −50°C $[(1/\rho)\partial\rho/\partial T$ is given for two different temperatures in order to avoid extrapolation of the limiting velocities V_∞ and $v_0]$.
[d] See footnote d, Table I.
[e] See footnote e, Table II.

[18] M. R. Rao, Indian J. Phys. **14**, 109 (1940).

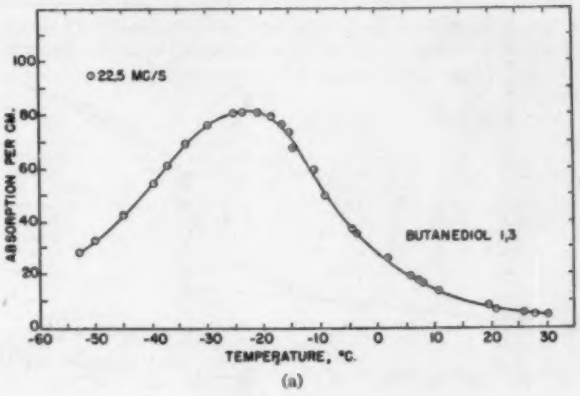

(a)

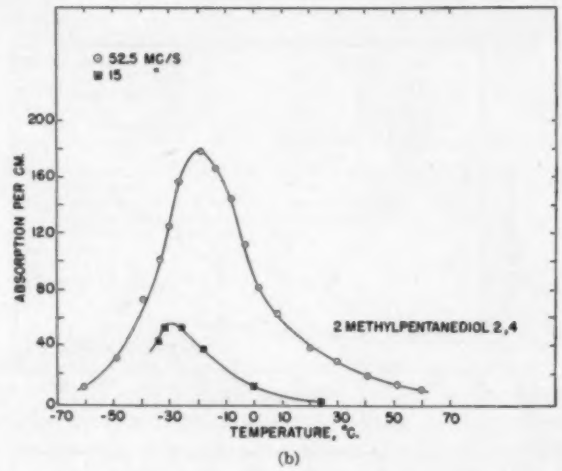

(b)

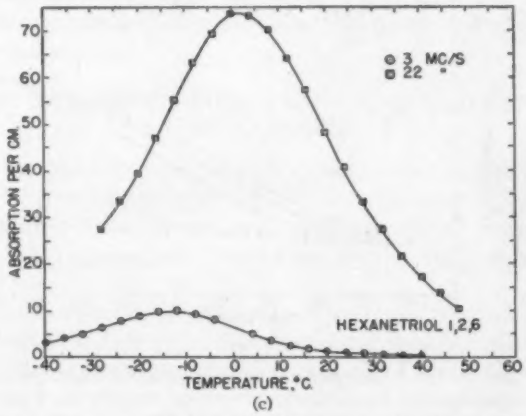

(c)

FIG. 4. (a–c) Longitudinal absorption coefficient plotted as a function of temperature.

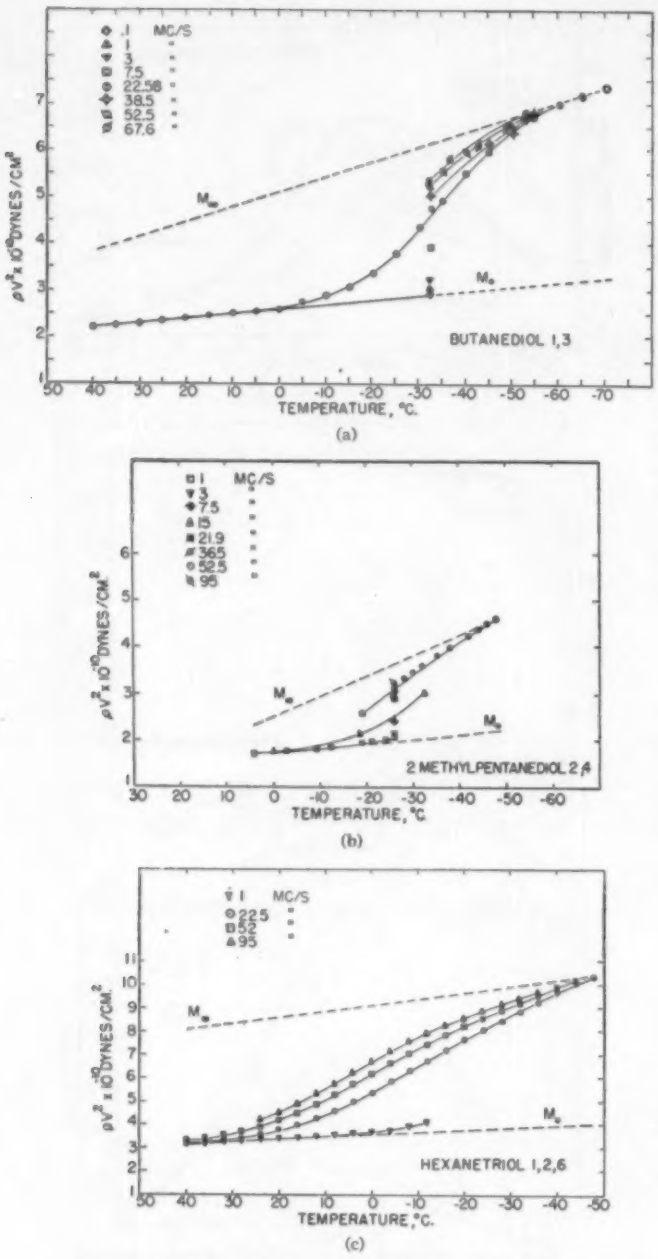

FIG. 5. (a–c) Longitudinal velocity squared times the density plotted against temperature for various frequencies. Upper and lower dashed lines represent extrapolations of M_∞ and M_0 respectively for best fit of data.

presence of a structural relaxation mechanism in addition to shear viscosity effects.

VI. LIMITING MODULI

In Fig. 5 the values of ρv_L^2 are plotted. It can be seen that ρv_L^2 exhibits both high- and low-frequency limiting values in the low- and high-temperature regions, respectively. It can be shown using Eq. (26) that in the limiting high- and low-frequency regions ρv_L^2 is equal to M' within experimental accuracy. Therefore, the data in these regions can be used directly to determine the limiting longitudinal moduli M_0 and M_∞.

For extrapolation purposes, M_0 and M_∞ are assumed to vary linearly with the temperature over the entire temperature range. (The validity of this assumption is borne out by the fact that the data reduce.) The values of G_∞ are obtained from the limiting values of $\rho C_s'^2$ found in the data of Fig. 6. K_∞ can now be calculated from the relation

$$K_\infty = M_\infty - \tfrac{4}{3}G_\infty. \tag{38}$$

The limiting elastic moduli are tabulated in Table IV for seven typical associated liquids. It can be seen that M_∞ varies from about 1.3 to almost 3.0 times M_0 (or K_0). The measured values of K_2/K_∞ vary between 0.25

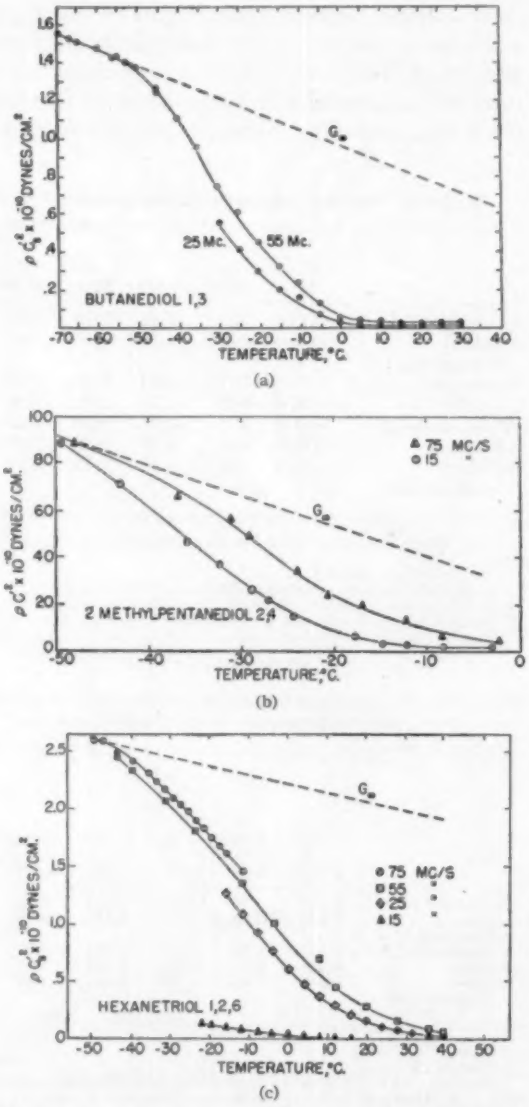

FIG. 6. (a–c) The square of the real part of the shear impedance plotted against temperature for various frequencies. Dashed line represents extrapolation of G_∞ for best fit of data.

and 0.43. Note that the ratio K_2/K_∞ is equal to the ratio $\mathcal{K}'/\mathcal{K}$ where $\mathcal{K}'$ is the relaxational part of the normal liquid compressibility, $\mathcal{K}$. The data indicate that about 30% of the total normal compressibility of these liquids is due to structural relaxation effects. Also listed in Table IV is a value of K_2/K_∞ for water calculated using Hall's theory.[19] This value is 0.61, which is over 50% larger than any of the values measured for the other associated liquids listed. This difference is in agreement with the concept that water has a very open structure and therefore, larger, structural volume changes would be possible. In Table IV the values of G_∞ found in the hydrogen bonded liquids are compared with a polymeric liquid (polyisobutylene) and an organic glass (sucrose octa-acetate),[20] and come hydrocarbon oils.[21] It can be seen that no significant difference exists in the values of G_∞. Because K_∞ and G_∞ are often called the "solid-like" moduli of the liquids it is of interest to compare values found in the organic liquids with those for amorphous and crystalline solids. The organic liquid values run about 1/10th the values found for fused quartz and sodium chloride and less than 1/20th the values of G_∞ found in nickel.

The values of K_∞ found in the organic liquids are roughly the same as the K_∞ found for the polymer polyisobutylene. However, K_∞ for the organic liquids runs about 1/10th of that of fused quartz and sodium chloride and 1/100th the value found for nickel. After comparing the ratio G_∞/K_∞ for the organic liquids and the solids, it can be seen that even though the values of G_∞ and K_∞ vary by factors of 10 or 100 from organic liquid to crystalline solid, the ratio G_∞/K_∞ remains constant to within a factor of about three. (This factor is actually less than 1.5 when compared to most solids. Note the value of G_∞/K_∞ for fused quartz is unusually high compared to typical solids). This indicates that the same factors which cause the organic liquid lattice to be more compressible than the inorganic solid affect the shear rigidity of the liquid in the same manner. Unfortunately, the shear rigidity of the crystalline form of these organic liquids is not known. However, it is probable that the G_∞ and K_∞ measured here in the liquid state is of the order of magnitude of the value the organic crystal would have. This reasoning is supported by the fact that elastic moduli of glycerol in the liquid and glassy state do not differ by more than a factor or two.[22] It is well known that the values of the elastic moduli for crystalline substances do not differ markedly from the values found in the glassy or amorphous form. An example of this can be seen in a comparison of the elastic constants of amorphous or fused silica and crystalline silica.

TABLE IV. Comparison of the magnitude of elastic moduli in associated liquids with various solids. (Units are d/cm²×10⁻¹⁰)

	T°C	K_0	M_∞	K_∞	K_2	K_2/K_∞	G_∞	G_∞/K_∞
Butanediol 1,3	−32.2	2.93	6.17	4.53	1.59	0.35	1.23	0.270
2-methyl-Pentanediol 2,4	−26.0	2.04	3.67	2.86	0.82	0.29	0.62	0.217
Hexanetriol 1,2,6	−10.5	3.71	9.53	6.46	2.75	0.43	2.31	0.357
Glycerol[a]	−14.0	5.04	12.79	8.79	3.75	0.37	3.00	0.366
Propanediol[b] 1,2	−37.8	3.14	6.16	4.65	1.51	0.32	1.13	0.24
n-Propyl alcohol[c]	−130	3.2	4.3	4.3	1.1	0.255	...	...
Diphenyl pentachloride[d]	+34.5	2.78	4.2	4.1	1.3	0.317	...	...
Water[e,f]	+20	...	...	...	...	0.61	...	...
Polyisobutylene[g]	+25	...	...	2.68	...	...	0.58	0.17
Fused quartz[h]	+25	...	...	37.3	...	...	31.2	0.84
Nickel[i]	+25	...	...	371	...	...	73.5	0.20
Sodium chloride[j]	+25	...	...	48.5	...	...	12.5	0.26
LVI[k]		...	...	...	...	...	0.70	...
MVI[k]		...	...	...	...	...	0.78	...
HVI[k]		...	...	...	...	...	0.70	...
Organic glasses[l]		...	...	...	...	...	1.50	...

[a] See footnote d, Table I.
[b] See footnote c, Table II.
[c] See footnote d, Table II.
[d] See footnote e, Table II.
[e] L. Hall, Phys. Rev. **78**, 775 (1948).
[f] Calculated from Hall's theory for structual relaxation in water, where $K_0=4.58\times10^{-11}$ d/cm², $=2.78\times10^{-11}$ d/cm².
[g] W. P. Mason, W. O. Baker, H. J. McSkimmin, and J. H. Heiss, Phys. Rev. **75**, 936 (1949).
[h] H. J. McSkimmin, J. Appl. Phys. **24**, 988 (1953).
[i] C. D. Hodgman, *Handbook of Chemistry and Physics* (Chemical Rubber Company, Cleveland, Ohio, 1956), 36 ed.
[j] See reference i.
[k] See footnote 21.
[l] See footnote 20.

VII. TEMPERATURE DEPENDENCE OF LIMITING ELASTIC MODULI

The limiting shear, compressional, and longitudinal moduli are tabulated in Table V as a function of temperature. These moduli are found to depend linearly on the temperature, increasing as the temperature decreases.

The temperature coefficients of the elastic moduli are tabulated in Table VI. Inspection of the data here shows that the temperature coefficients of K_∞, K_2, and G_∞ are

TABLE V. Temperature dependence of limiting elastic moduli (moduli in d/cm²×10⁻¹⁰; T in °C).

	M_0	M_∞	G_∞	K_∞
Butanediol 1,3	$2.61-0.010T$	$5.13-0.032T$	$0.962-0.00847T$	$3.85-0.02098T$
2-methyl-Pentanediol 2,4	$1.77-0.0102T$	$2.54-0.0437T$	$0.294-0.0124R$	$2.148-0.0272T$
Hexanetriol 1,2,6	$3.61-0.0094T$	$9.24-0.28T$	$2.23-0.0075T$	$6.28-0.018T$
Glycerol[a]	$4.91-0.0122T$	$11.96-0.059T$	$2.75-0.0183T$	$8.30-0.035T$
Diphenyl pentachloride[b]	$3.20-0.012T$	$5.82-0.0448T$	...	...

[a] See footnote d, Table I.
[b] See footnote e, Table II.

[19] L. Hall, Phys. Rev. **73**, 775 (1948).
[20] S. Crawford, Proc. Phys. Soc. (London) **B69**, 1312 (1956).
[21] A. Barlow and J. Lamb (to be published).
[22] T. Litovitz and T. Lyon, J. Acoust. Soc. Am. **30**, 856 (1958).

TABLE VI. Temperature coefficients of elastic moduli.[a]

	$\alpha/\alpha_{\text{stokes}}$	$\frac{1}{M_0}\frac{\partial M_0}{\partial T}$	$\frac{1}{M_\infty}\frac{\partial M_\infty}{\partial T}$	$\frac{1}{G_\infty}\frac{\partial G_\infty}{\partial T}$	$\frac{1}{K_\infty}\frac{\partial K_\infty}{\partial T}$	$\frac{1}{G_\infty}\frac{\partial G_\infty}{\partial T}$ / $\frac{1}{K_\infty}\frac{\partial K_\infty}{\partial T}$	$\frac{1}{K_2}\frac{\partial K_2}{\partial T}$
Butanediol 1,3	1.76	−3.83	−6.24	−8.8	−5.45	+1.61	−8.85
2-methyl-Pentanediol 2,4	3.38	−5.76	−7.20	−42.10	−12.66	+3.33	−44.9
Hexanetriol 1,2,6	1.65	−2.59	−3.03	−3.34	−2.88	+1.16	−3.27
Glycerol[b]	1.78	−2.48	−4.93	−6.65	−4.22	+1.57	−6.72
Diphenyl pentachloride[c]	3.27	−3.75	−7.69	−12.51	···	···	−12.51

[a] Calculated from Table V for a temperature of 0°C.
[b] See footnote *d*, Table I.
[c] See footnote e, Table II.

greater than that for K_∞. This decrease in G_∞ with increasing temperature is similar to that found by Mason[23] for the high-frequency, shear stiffness of polyisobutylene. This point emphasizes the difference between the "entropy" modulus (which is proportional to temperature) found in polymers and the "energy" modulus found here in associated liquids. It also indicates that the Tobolsky-Leaderman-Ferry[24] reduction formula can not hold for the associated liquids. One can compare the temperature coefficients of the "solid-like" moduli of these liquids with that found for a typical solid. In aluminum,[25] for example, the value of $(1/G_\infty)(\partial G_\infty/\partial T)$ is equal to $-0.72\times10^{-3}C^{-1}$. This shows that these liquid moduli have a temperature dependences about one order of magnitude greater than the temperature of those for metallic solids. This fact can be understood if one realizes that changing the temperature of a solid changes only the interatomic spacings; however, when one changes the temperature of a liquid both the interatomic spacings and the degree of short range order of the liquid change. It is reasonable to expect that the elastic constants of a lattice whose order is changing with temperature would be more temperature dependent than that lattice where only interatomic spacings change.

It can be seen in Table VI that the temperature dependence of G_∞ for every liquid listed is very close to the temperature dependence of K_2. This result was determined by the fact that a reduction in the data (obtained below) could only be found when it was assumed that $1/M_2[\partial M_2/\partial T]_{T_0}=1/G_\infty[\partial G_\infty/\partial T]_{T_0}$.[26] Since $M_2=K_2+\frac{4}{3}G$ it follows that for these liquids $1/K_2[\partial K_2/\partial T]_{T_0}=1/G_\infty[\partial G_\infty/\partial T]_{T_0}$.

It can be further seen in Table VI that the ratio of $\alpha_{\text{obs}}/\alpha_{\text{stokes}}$ is approximately equal to the ratio $(1/G_\infty)(\partial G_\infty/\partial T)/(1/K_\infty)(\partial K_\infty/\partial T)$. The reason for this relationship is not understood at this time.

Hirai and Eyring[27] offer a theory of compressional—(structural) viscosity for associated liquids based on

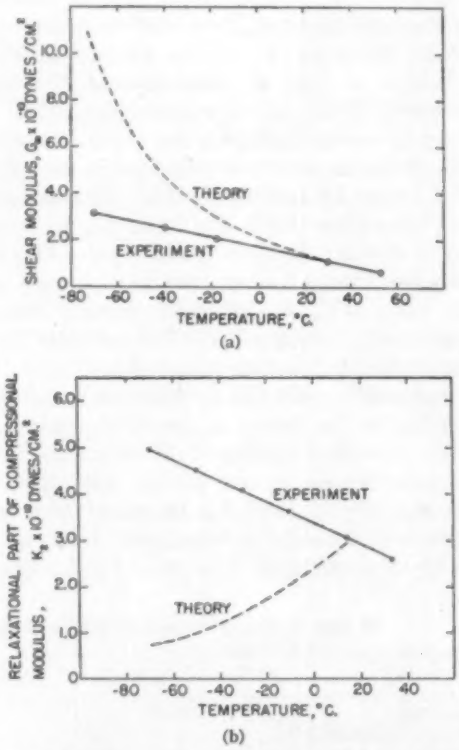

FIG. 7. (a) Temperature dependence of limiting shear modulus G_∞ for glycerol. The dashed line represents the theoretical values calculated from Hirai and Eyring theory. The solid line represents values of G_∞ used in reduction of experimental data. (b) Temperature dependence of the relaxational part of the compressional modulus K_2 for Glycerol. The dashed line represents theoretical values. The solid line represents values of K_2 used in reduction of experimental data.

[23] W. P. Mason, Phys. Rev. **73**, 1074 (1948).
[24] A. Tobolsky and R. Andrews, J. Chem. Phys. **11**, 125 (1943); H. Leaderman, Textile Foundation, 30 (Washington, D. C., 1943); J. Ferry, J. Am. Chem. Soc. **72**, 3746 (1950).
[25] C. M. Zener, "Elasticity and anelasticity of metals," University Chicago Press, Chicago, Illinois, 1948).
[26] Because of the limited data on G_∞ (obtained at low temperatures and high frequencies) there is some difficulty in fixing the temperature dependence of G_∞ and M_∞. Therefore, an iterative process was used. A straight line anchored at the low-temperature region of the curve (see Fig. 5) was drawn from which $M_\infty-M_0$ was obtained. There was no difficulty encountered in extrapolating M_0. By using $(\omega\eta_s/M_\infty-M_0)$ as abscissa, a reduction of the longitudinal data was attempted. Successive trials produced M_2 and G_∞ values which adequately reduced the data. Within experimental error, the fractional slopes of M_2 and G_∞ were equal.
[27] N. Hirai and H. Eyring, J. Appl. Phys. **29**, 810 (1958).

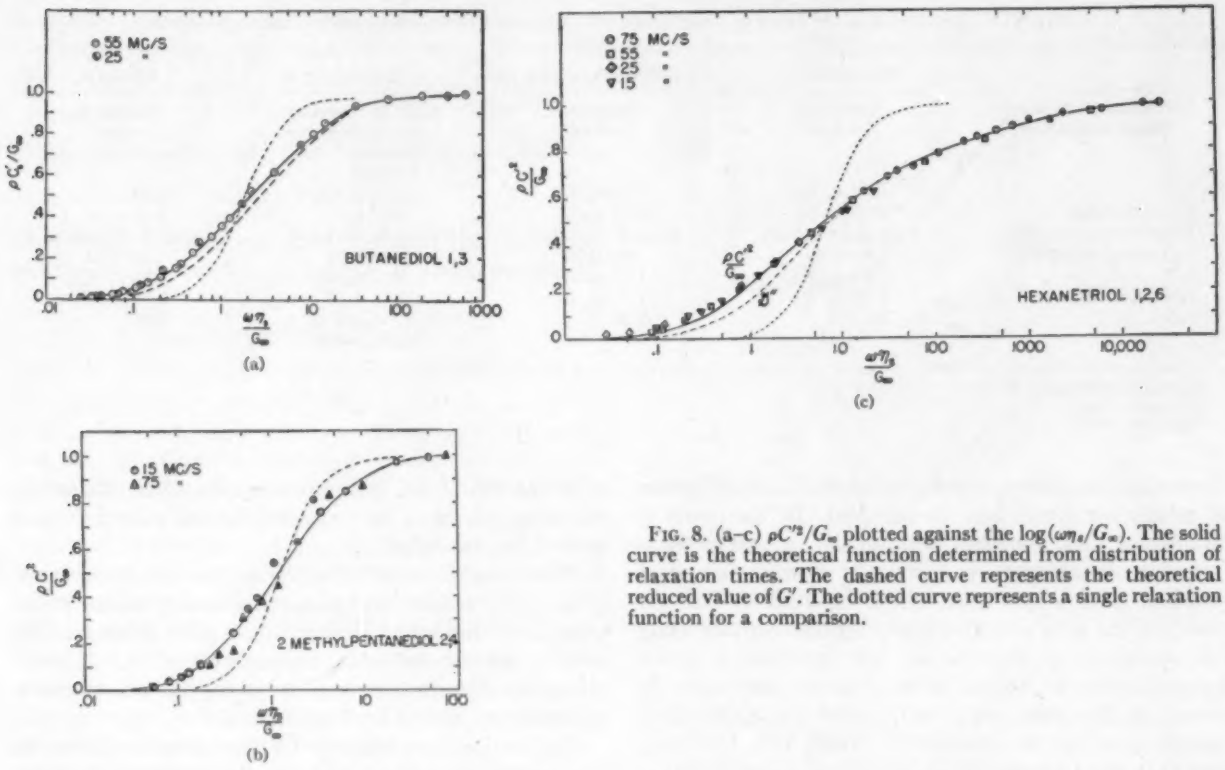

FIG. 8. (a–c) $\rho C^{\prime 2}/G_\infty$ plotted against the $\log(\omega\eta_s/G_\infty)$. The solid curve is the theoretical function determined from distribution of relaxation times. The dashed curve represents the theoretical reduced value of G'. The dotted curve represents a single relaxation function for a comparison.

chemical rate process theory from which they deduce expressions for the shear and compressional relaxational moduli G_∞ and K_2. These are given by

$$G_\infty=\frac{kT}{v_0}\exp[\epsilon n/kT] \tag{39}$$

$$K_2=K_0\left[\frac{kT}{K_0 v_n}\exp(\epsilon n/kT)-1\right], \tag{40}$$

where ϵ_n is equal to the energy necessary to create a hole in the liquid, v_n is the volume of a hole, k is the Boltzman's constant, v_0 is the volume the liquid would have without holes. In Fig. 7(a) the values predicted by Eqs. (39) and (40) are plotted and compared with the experimental values obtained for glycerol. On considering the data for G_∞, it can be seen that the Eyring and Hirai theory gives reasonably close agreement with the experimental values at temperatures above 0°C. However, at the lower temperatures there is considerable disagreement between the theoretical and experimental data. It can be seen that at −70° the theoretical value exceeds the experimental one by a factor of three. This disagreement is due to the exponential temperature dependence of G_∞ deduced by Eyring and Hirai, whereas the data here indicate that G_∞ varies linearly with the temperature.

When considering data for K_2 in Fig. 7(b) it can be seen that the theory gives the right order of magnitude but the wrong temperature dependence (see appendix). It is apparent that the Hirai and Eyring theory for shear and structural relaxation in associated liquids is inadequate to account for the data on the relaxational part of the elastic moduli which have been found here. This conclusion extends to all the liquids which have been measured because in every case G_∞ has varied with temperature in a linear manner and in every case K_2 has decreased with temperature whereas the Hirai and Eyring theory predict an increase.

VIII. DETERMINATION OF THE SHEAR MODULUS

In Sec. III it was shown that by using reduced parameters the moduli data at different temperatures and frequencies should reduce to a single curve when plotted as a function of $\omega\tau_s$. For the data τ_s is not directly known, but Eq. 18 shows that $\tau_s=\eta_s/G_\infty$, or if a distribution of relaxation times is present $(\tau_s)_{av}=\eta_s/G_\infty$ [see Eq. (30)]. Therefore, if the reduced parameters are plotted against the reduction of data to one curve should be achieved. The reduced shear impedance $\rho C_s^{\prime 2}/G_\infty$ is plotted against $\omega(\eta_s/G_\infty)$ for hexanetriol 1,2,6, butanediol 1,3, and 2-methyl-pentanediol 2,4, in Fig. 8. In all cases, the data reduces to a single curve within experimental accuracy.

In all three liquids the parameter $\rho(C_s^{\prime 2}/G_\infty)$ reaches a limiting value. To cover the range from 10 to 90% of the limiting value, a little over two decades of the variable $\omega(\eta_s/G_\infty)$ must be covered. It can be seen that in every liquid a single relaxation time theory is inadequate to account for the data. In order to obtain a

TABLE VII. Comparison of the types of distribution functions used to represent the relaxation processes.

	Butanediol 1,3	2-methyl-Pentanediol 2,4	Hexanetriol 1,2,6	Glycerol[a]
Distribution function (shear relaxation)	Gaussian $b=0.46$	Gaussian $b=0.60$	Cole & Davidson and a single relaxation time $b=0.32$	Gaussian $b=0.42$
$\tau_s'^{[b]}$	$0.31\ \eta_s/G_\infty$	$0.53\ \eta_s/G_\infty$	$1.22\ \eta_s/G_\infty$	$0.24\ \eta_s/G_\infty$
τ_s' (empirical)	$0.38\ \eta_s/G_\infty$	$0.55\ \eta_s/G_\infty$	$0.67\ \eta_s/G_\infty$	$0.28\ \eta_s/G_\infty$
Distribution function (volume relaxation)	Cole & Davidson $\beta=0.49$	Cole & Davidson $\beta=0.60$	Cole & Davidson $\beta=0.24$	Cole & Davidson $\beta=0.32$
$\tau_v'^{[c]}$	$2.04\ \eta_v/K_2$	$1.67\ \eta_v/K_2$	$4.17\ \eta_v/K_2$	$3.14\ \eta_v/K_2$
τ_v (empirical)	$1.81\ \eta_v/K_2$	$1.21\ \eta_v/K_2$	$5.86\ \eta_v/K_2$	$2.86\ \eta_v/K_2$
τ_v/τ_s	0.79	2.38	$\tau_v/\tau_{s2}=0.41$ $\tau_v/\tau_{s1}=4.6$	0.81

[a] See footnote d, Table I.
[b] Equation (30a).
[c] Equation (30b).

theoretical function to represent the data, a distribution of relaxation times has to be used. In the case of butanediol and 2-methyl pentanediol, a symmetrical Gaussian distribution of relaxation times is assumed [see Eq. (29a)], and when this is inserted in Eqs. (9) and (28) the data are adequately represented. In using this symmetrical distribution, the constant b which determines the broadness of the reduced curve must be chosen. In Fig. 8(a) and 8(b) the solid line is the curve calculated using the constants in Table VII. It can be seen that the assumption of this distribution of relaxation times gives an excellent fit to the data.

For the two liquids butanediol and methyl pentanediol $b=0.46$ and 0.60 respectively give the best fit to the shape of the experimental reduced curves. The values of τ_s' is the theoretically related to η_s/G_∞ by Eq. (30a) and can be evaluated once b is chosen. (See Table VII for a summary of the distribution data.)

On comparing the theoretical values with the empirical values of τ_s in Table VII it may be argued that two factors contribute to the discrepancy. One, the Gaussian distribution probably does not give the exact distribution of relaxation times and two, there is an uncertainty in the value of G_∞ of about $\pm 10\%$.

One could assume that only part of the shear viscosity has relaxed. If this is so then the value of η_s used in Eq. (30a) would be some fraction of the total "static" shear viscosity. However, this leads to even smaller calculated values of τ_s', and therefore to larger discrepancies with the empirical values of τ_s'. It must be concluded, therefore, that the total shear viscosity is relaxing here. This is of interest when one considers the data on polymers, where the quasi-static viscosity relaxes in two different frequency ranges and is associated with two types of shear moduli. The high frequency or "solid-like" modulus has properties similar to those found here for the associated liquids. For example, it has a value around 10^{10} d/cm^2. The other polymer shear modulus is known as a "rubber-like" modulus relaxing at much lower frequencies than the "solid-like" modulus (by factors of 100 or more) and has values of the order of 10^6 to 10^7 d/cm^2. In the two associated liquids in the foregoing, there is no evidence for the existence of a rubber-like modulus.

When one considers the shear data for hexanetriol [Fig. 8(c)] a more complicated situation exists. However, it is somewhat similar to polymer behavior. To account for the shear data the presence of two different relaxation distributions must be assumed, each of which is associated with a limiting modulus.

The major contribution to the shear modulus is represented by a Cole-Davidson distribution of relaxation times whose average time is $\tau_{s\text{av}}$. [See Eq. (30b).] In addition, another shear relaxation process represented by a single relaxation function must be assumed. This second process has a relaxation time τ_{s2} which is longer than the value of τ_{s1}'.

The function G^* is constructed by superimposing these two shear processes as follows:

$$G^*=G_{\infty 1}\int_0^\infty \frac{g(\tau/\tau_{s1}')}{1+i\omega\tau}d(\tau/\tau_{s1}')+G_{\infty 2}\frac{i\omega\tau_{s2}}{1+i\omega\tau_{s2}}, \quad (41)$$

where $G_{\infty 1}$ and $G_{\infty 2}$ are the contributions to the high-frequency limiting modulus of the two processes respectively. The total high-frequency modulus is given by

$$G_\infty=G_{\infty 1}+G_{\infty 2}.$$

To adequately fit the data the following empirical values were chosen:

$$G_{\infty 1}=0.9G_\infty \quad \beta=0.32$$
$$G_{\infty 2}=0.1G_\infty \quad \tau_{s2}=5.3\tau_{s1}'.$$

Some uncertainty in the choice of constants (especially for the single relaxation process) is caused by the fact that the two relaxation times are close in value, and because the data in the low range of $\omega\tau$ has rather large uncertainties.

That part of the "quasi-static" shear viscosity η_s associated with the relaxation processes measured here may be determined theoretically by considering the

imaginary part of Eq. (41) and is given by

$$G''=G_{\infty 1}\int_0^\infty \frac{g(\tau/\tau_s')\omega\tau}{1+\omega^2\tau^2}d(\tau/\tau_s')+G_{\infty 2}\frac{\omega\tau_{s2}}{1+\omega^2\tau_{s2}^2}. \quad (42)$$

In the low-frequency limit $(\omega\tau)^2\ll 1$, integration leads to

$$G''=G_{\infty 1}\omega\tau_{s1}'\beta+G_{\infty 2}\omega\tau_{s2}. \quad (43)$$

That shear viscosity η_s associated with the relaxation process can be found by using Eq. 30 and becomes

$$\eta_{s\text{theor}}=\frac{G''}{\omega}=G_{\infty 1}\tau_{s1}'\beta+G_{\infty 2}\tau_{s2}.$$

On substituting $\tau_{s2}=5.3\tau_{s1}'$, $\beta=3.2$, then $\eta_{s\text{theor}}=0.818\ \tau_{s1}'G_\infty$ the data show that $\eta_s=1.5\tau_{s1}'G_\infty$ thus, $\eta_{s\text{theor}}=0.54\eta_s$. The fact that the viscosity determined by the viscoelastic theory for hexanetriol 1,2,6, is about half as large as the "quasi-static" shear viscosity may be explained in two ways. First, the fit of the $\rho C_s'^2$ with the theoretical function is approximate. The theoretical function is low in the range of low values of $\omega\tau_{s1}'$, and high in the middle range of $\omega\tau_{s1}'=10$. [See Fig. 8(c).] Thus, the distribution function does not exactly describe the data. Secondly, there may have been other relaxation processes at longer times which would account for the additional viscosity $\eta_s=\eta_1+\eta_2+\eta_3$. The $G_{\infty 2}$ modulus is smaller, the contribution to the total shear viscosity associated with the different moduli are each of the same order of magnitude.

IX. REDUCTION OF THE LONGITUDINAL DATA

According to Eqs. 24 and 25, it is possible to reduce the longitudinal data when the following conditions hold.

$$\frac{1}{G_\infty}\left[\frac{\partial G_\infty}{\partial T}\right]_{T_0}=\frac{1}{M_2}\left[\frac{\partial M_2}{\partial T}\right]_{T_0},$$

and τ_v/τ_s is independent of temperature. As noted in Eq. (24) under the above conditions M' and M'' are a function of temperature through $\omega\tau_s$ or $\omega\eta_s/G_\infty$. Since η_s and G_∞ are known this becomes a convenient parameter against which to plot the longitudinal data.

In Fig. 9 it can be seen that a reduction of the longitudinal data is achieved for each liquid. In addition, it was empirically found that best reduction of the data was achieved when it was assumed that $1/M[\partial M_2/\partial T]_{T_0}=1/G_\infty[\partial G_\infty/\partial T]_{T_0}$. This reduction of the longitudinal data is the best indication that τ_v and τ_s do have the same temperature dependence. Because a distribution of times exists this reduction indicates that $(\tau_v)_{av}$ and $(\tau_s)_{av}$ have the same temperature dependence.

X. COMPRESSIONAL RELAXATION IN ASSOCIATED LIQUIDS AND COMPARISON WITH SHEAR RELAXATION

By use of Eqs. (24) and (28), longitudinal and shear data can be combined to obtain the frequency and

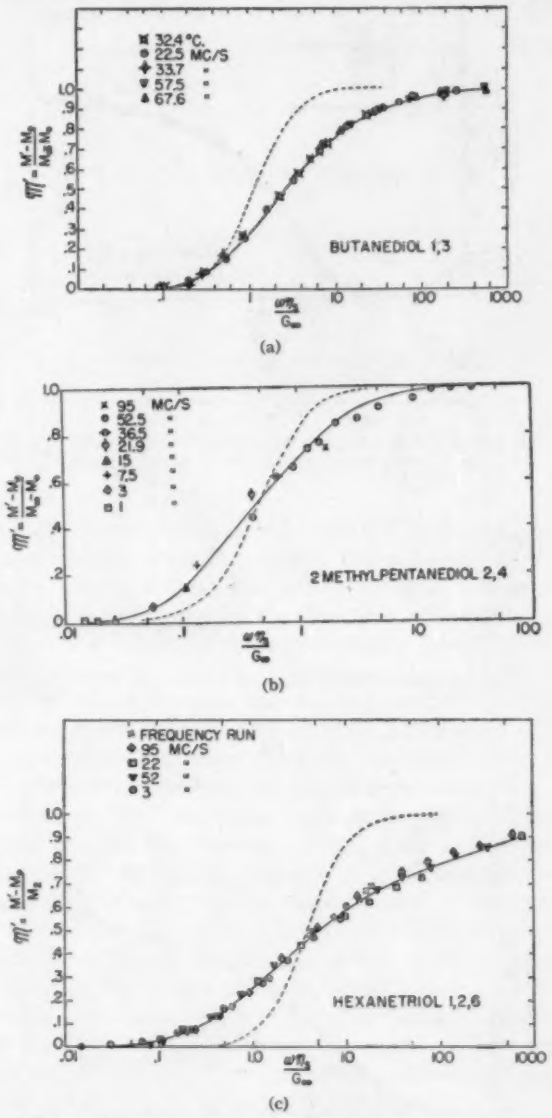

FIG. 9. (a–c) M' plotted against the $\log(\omega\eta_s/G_\infty)$. The solid curve is a smooth curve drawn through the data. The dotted curve represents a single relaxation function.

temperature dependence of the compressional modulus of a liquid. The reduced relaxational part of the compressional modulus has been calculated and the results are plotted in Fig. 10 as a function of $\omega(\tau_v)_{av}$. The average relaxation time is obtained using the relation $(\tau_v)_{av}=\eta_v/K_2$, where the value η_v is evaluated by using Eq. (23) and data on the ratio of α/α_{stokes} in the classical region. It is seen in Fig. 10 that the single relaxation theory is inadequate to describe the results.

It is found that by choosing a distribution function this compressional reduction is adequately represented. In each liquid the reduced compressional modulus is logarithmically assymmetric about its inflection point. Because of this a Cole-Davidson distribution function was chosen to represent the distribution of times. By

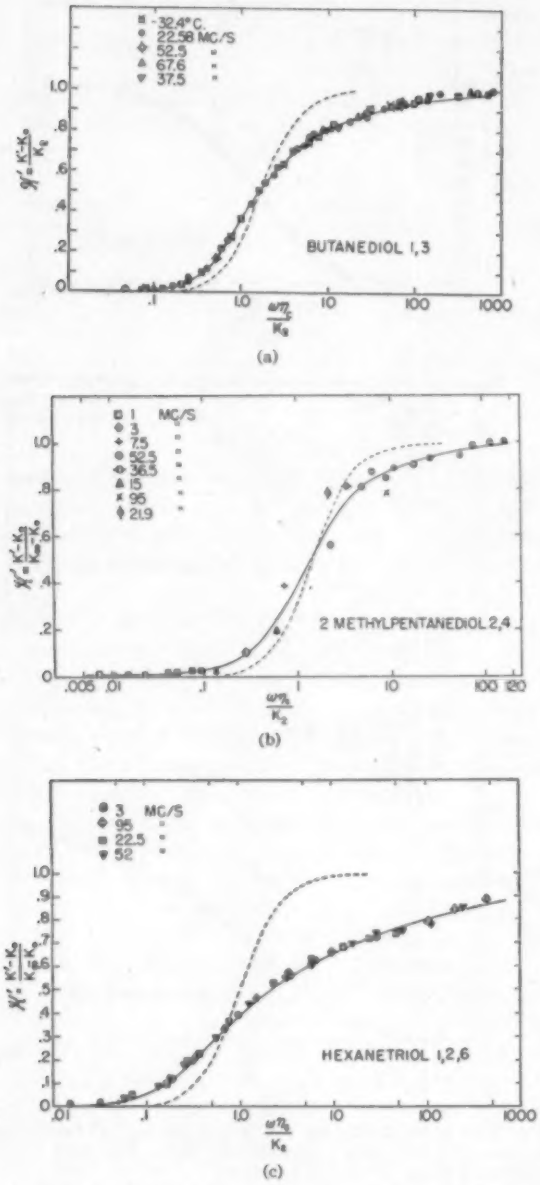

FIG. 10. (a–c) K' plotted against $\log\omega\eta_c/K_2$. The solid curve represents the theoretical value of K' using Cole and Davidson distribution function. The dotted curve represents a single relaxation function.

substituting this distribution into Eq. (32), integrating and separating into real and imaginary parts, the reduced compressional function is obtained,

$$K'=1-\cos^{\beta}(\arctan\omega\tau_v')\cos(\beta\arctan\omega\tau_v')$$

$$K''=\cos^{\beta}(\arctan\omega\tau_v')\sin(\beta\arctan\omega\tau_v').$$

The parameter β is tabulated in Table VII.

In each case there is reasonable good agreement between the shape of the experimental and theoretical curves when the β's listed in Table VII are used. Theoretically, τ_v' is related to η_v and K_2 by the relation,

$$\tau_v'=\frac{\eta_v^{\text{theor}}}{\beta K_2}.$$

It is found empirically, however, that the position of the theoretically curve fits the data best for the various cases considered if τ_v is assumed equal to $\eta_v/\beta'(K_\infty-K_0)$, where β' differs by as much as 35% from the value of β. This discrepancy can be due to several factors such as (1) how well the M data reduce; (2) the accuracy of the calculated values of G' and G'' (errors here may cause serious discrepancies since K' is found by a subtraction of $\frac{4}{3}G'$ from M'); (3) uncertainties in the value of $\alpha/\alpha_{\text{stokes}}$ used in determining the variable $\eta_v[\alpha/\alpha_{\text{stokes}}$ has an estimated uncertainty of about $\pm5\%$ and could lead to about a $\pm15\%$ uncertainty in the calculation of $\eta_v]$; (4) uncertainty in the value of β (a small range of β could have been used in each case without detecting significant change in the theoretical function). On considering all these uncertainties, the agreement is quite good between the value of β and the value of β', except in the case of hexanetriol. But here, since there was difficulty in the fitting of the shear data, the discrepancy is understandable.

The ratio of τ_v/τ_s and the type of distribution function used to reduce the data are tabulated in Table VII.

XI. IMAGINARY PART OF THE DILATATIONAL MODULUS

On using the distribution functions found above one can calculate G'' and K'' for each liquid. By adding these two quantities according to Eq. 19 one can calculate a theoretical value of M''. In Fig. 11 the experimental and calculated values of M'' are plotted for the liquids hexanetriol 1,2,6 and butanediol 1,3. Good agreement is found between the measured and calculated values of M'' up to values of $\omega(\eta_s/G_\infty)\cong1$. The theoretical curve peaks at $\omega(\eta_s/G_\infty)\cong1.5$. The measured values of M'' rise to a maximum, but at value of $\omega(\eta_s/G_\infty)=3$ and then stay above the theoretical curve for larger values of $\omega(\eta_s/G_\infty)$. In Fig. 12 $\mathfrak{M}_{\text{exp}}''-\mathfrak{M}_{\text{theor}}$ is plotted. It can be seen that this value approaches a constant at large values of $\omega(\eta_s/G_\infty)$. Since M'' is proportional to $\alpha\lambda$, the absorption per wave length, this result indicates that the loss per cycle approaches a constant independent of frequency and viscosity. This type of loss known as hysteresis is typical of highly viscous liquids when measured at frequencies well above the dispersion region. This hysteresis was first noted by Mason[28] et al. in measurements on polyisobutylene. Litovitz and Lyon[29] have reported extensive measurements on this type of loss in glycerol and pentachlorobiphenyl. The latter authors have suggested that the hysteresis effect is not related to the viscous flow

[28] W. Mason, W. Baker, H. McSkimin, and J. Heiss, Phys. Rev. 73, 1074–1091 (1948).
[29] T. Litovitz and T. Lyon, J. Acoust. Soc. Am. 26, 577 (1954).

mechanism causing absorption at the lower frequencies and viscosities. Mason and coauthors offer the suggestion that the acoustic hysteresis loss in polyisobutylene is related to the fact that molecules or chains no longer have time to accumulate the heat energy necessary to jump to adjacent stable potential wells. It is proposed that on one part of the compression cycle the molecules can jump to intermediate potential minima, which probably consist simply of the internal twisting of a molecule rather than a rotation of a whole molecule. The twisted portion of the molecule is held in this new position till some later part of the stress cycle and then returns to its original position. To accomplish this Mason suggests that the acoustic wave exerts an extreme biasing force in the direction of twisting of motion. This biasing force would effectively reduce the activation energy to zero. The studies of Litovitz and Lyon do not agree with this concept for two reasons. They point out that if a biasing force is necessary then the absorption coefficient should be amplitude dependent. There is no evidence for this in either the polyisobutylene or the associated liquids measured. Another difficulty with the biasing concept arises when one attempts to explain the apparently large temperature dependence of this constant loss term, which was noted by Litovitz and Lyon in glycerine and diphenylpentachloride. In the two liquids, butanediol 1,2, and hexanetriol 1,3,6, the temperature range covered was insufficient to detect any small temperature variation in the constant loss term. There was no question, however, that the loss was much less temperature dependent than in the liquid studies by Litovitz and Lyon.

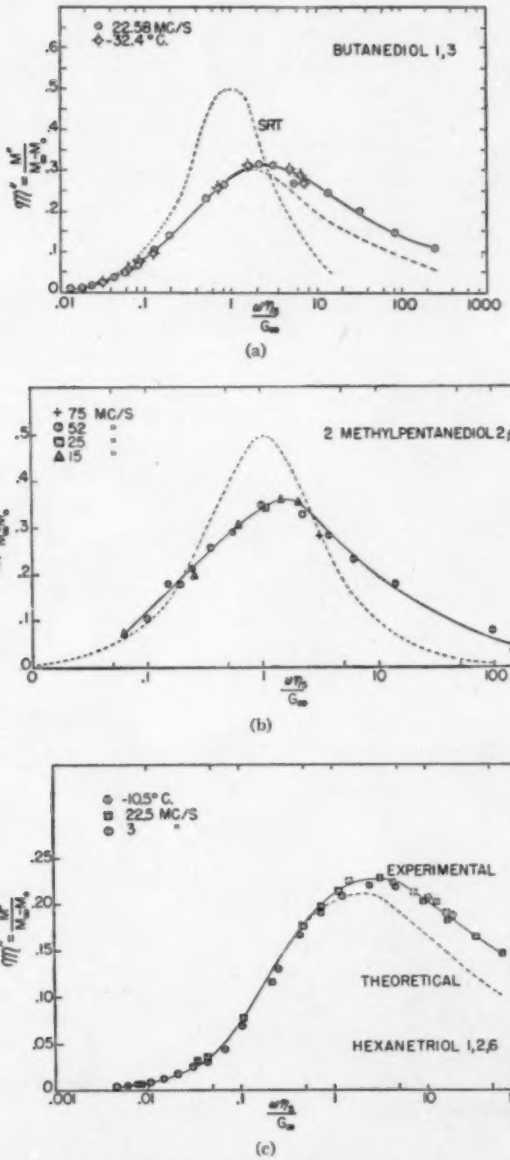

FIG. 11. (a–c) M'' plotted against the $\log(\omega\eta_s/G_\infty)$. The line is a plot of the experimental values of M''. The dashed line is a plot of the theoretical values of M'' obtained from a combination of the distribution functions used for the shear and compressional processes. The dotted curve represents a single relaxation function (SRT)

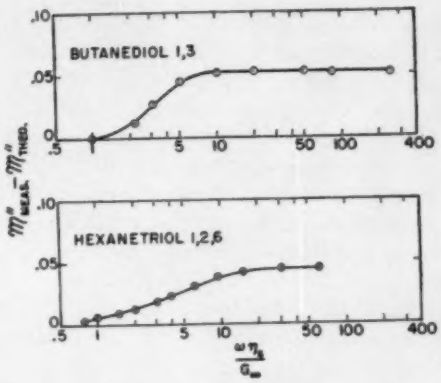

FIG. 12. Normalized difference between the experimental and theoretical values of M'' plotted against $\log\omega\eta_s/G_\infty$.

The absorption measurements in this work emphasize the widespread appearance of this hysteresis type loss in viscous liquids above the dispersion region; however, there is still no adequate explanation for the origin of this loss.

SUMMARY

Ultrasonic longitudinal and shear measurements have been measured in three associated liquids, hexanetriol 1,2,6, butanediol 1,3, and 2-methyl pentanediol 2,4. This data has been compared with other associated liquids and certain conclusions about the dynamic mechanical behavior of these liquids can be made. These are as follows:

1. The absorption of ultrasonic longitudinal waves in the nondispersion region demonstrates the presence of both shear and volume viscosities, which are about the same order of magnitude and have the same temperature dependence.

2. Ultransonic shear data indicates that the shear

viscosity is related to a relaxation process and that at sufficiently high frequencies these liquids exhibit a shear rigidity. This rigidity has a value of about 10^{10} d/cm^2, which is an order of magnitude less than that found in typical inorganic solids, but is about the same value as found in organic solids such as polymers. One characteristic of the liquid's shear rigidity is its relatively large temperature dependence. For example, $(1/G_\infty)(\partial G_\infty/\partial T)$ for the associated liquids is about a factor of ten greater than that found in a typical metal.

It was found that the Eyring-Hirai theory predicted an exponential temperature dependence for G_∞, whereas a linear dependence was found for these liquids.

In order to account for the data on shear relaxation a distribution of relaxation times had to be assumed. In most of the associated liquids a Gaussian type distribution function fit the data. However, in hexanetriol, 1,2,6, the longest chain molecule measured (6 carbons) required the assumption of both a single relaxation time in addition to an assymmetric (Cole-Davidson) type distribution function.

It would appear that this molecule is large enough to begin showing elastic behavior somewhat similar to long chain polymers.

It was found that the shear data at different frequencies and viscosities could be reduced to one curve if plotted vs $\omega\tau_{sv}$. In this case τ_{sv} is equal to η_s/G_∞. G_∞ has a negative temperature dependence of the form $G=a-bT$, thus τ_{sv} varies as $\eta_s/a-bT$. This result differs from that found in polymers for the "entropy" shear modulus, which has a positive temperature dependence and varies linearly with temperature, and which led Ferry to propose a reduction of the form $\omega\eta(T_0/T)$. The reduction for the associated liquid shear data is similar to that which would be necessary for the high-frequency ultrasonic shear data found for polyisobutylene by Mason.

3. The longitudinal velocity data show dispersions of between 15 to 60% which are much larger than that found in any other type of ultrasonic relaxation. In every case, the high-frequency limiting velocity, is more temperature dependent than the low frequency values.

4. On combining the longitudinal and shear data, the real and imaginary parts of the compressional moduli were determined. An asymmetric distribution of relaxation times was needed to fit the compressional data in each case. This was in contrast to the shear behavior. Comparison of the average shear and compressional relaxation times for several associated liquids showed that the ratio of these times do not differ by more than a factor of 5. Furthermore, they have the same temperature dependence which emphasizes the close relationship of the shear and compressional relaxation processes in these liquids.

Consideration of the compressional data showed that anywhere from 25 to 60% of the "static" compressibility of these liquids is due to structural relaxation. The instantaneous (high frequency) compressional modulus of these liquids are a factor of ten less than that found in typical inorganic solids. However, the ratio of G_∞/K_∞ of these liquids are approximately the same as one finds in solids. This result indicates that the factors which reduce the compressional modulii of the liquid lattice affects the shear modulus in the same way. The temperature dependence of K_2 was found to be the same as that for G_∞, and it also is not in agreement with the Eyring-Hirai theory.

5. From the absorption data the imaginary part of the longitudinal modulus M'', was calculated. The distribution functions which were used to fit the shear and compressional dispersion data gave good agreement with the M'' data only up to the region where $\omega\tau_{sv}\approx 1$. At higher values of $\omega\tau_{sv}$ there existed a loss per cycle which was independent of frequency and viscosity. The origin of this "hysteresis" loss is not completely understood.

APPENDIX

Hirai and Eyring offer two mechanical models for bulk viscosity as shown in Fig. 13, where (from model A), K_n is the part of the compressional modulus associated with the elimination of holes and K_s is caused by the compression of the lattice structure. Model B represents the values of the modulii obtained from the ultrasonic measurement. Since the models are equivalent, the relationships of the modulii are given as

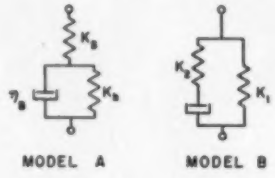

FIG. 13. Mechanical models for viscoelastic liquid.

$$K_1=K_sK_n/K_s+K_n \tag{A.1}$$

$$K_2=K_s^2/K_s+K_n, \tag{A.2}$$

where

$$K_n=(kT/v_n)\exp[(\epsilon_n+pv_n)/kT]. \tag{A.3}$$

The identification between these modulii and those used in this paper are

$$K_1=K_0 \tag{A.4}$$

$$K_2=K_\infty-K_0. \tag{A.5}$$

The relaxational compressional modulus is according to our notation given by

$$K_2=\frac{K_0K_\infty}{K_n}=K_0K_\infty\frac{v_n}{kT}\exp[-(\epsilon_n+pV)/kT]. \tag{A.6}$$

Theory of a Negative-Resistance Transmission Line Amplifier with Distributed Noise Generators*

K. K. N. CHANG
RCA Laboratories, Princeton, New Jersey
(Received January 8, 1960)

A transmission line with distributed positive and negative resistances as well as with distributed noise generators is treated. Gain and noise factor are derived as a function of boundary conditions, matching conditions and distributed noise. It is found that low-noise amplification can be achieved on such a line provided the line is characterized by high gain per unit length, high total gain, good matching, and low distributed noise. A distortionless active line for such low-noise amplifiers appears attractive.

I. INTRODUCTION

PRESENT negative-resistance devices, such as parametric diodes[1] and tunnel diodes,[2] because of their one-port property, require auxiliary isolators for low-noise applications. To convert from one-port to two-port operation, traveling-wave circuitry[3] has been suggested. However, previous circuit analysis has been limited to the lossless case and the circuit has been assumed free from any distributed Johnson noise or shot-effect noise, and also any input or output reflection.

The purpose of this paper is to treat a transmission line with distributed negative-resistances in a more general way. First, the line is considered to be lossy, with both series resistances and shunt conductances. Secondly, distributed noises voltages and currents are introduced. These noise voltages and currents may be caused by not only to thermal noise in the lossy elements, but also by shot noise in the active elements. Gain and noise factor are then derived as a function of the input and output conditions.

II. TRANSMISSION LINE

The transmission line under investigation is shown in Fig. 1. The line has the following distributed parameters:

R = net series resistance per unit length;

L = series inductance per unit length;

G = net shunt conductance per unit length;

C = shunt capacitance per unit length;

$|v_n|^2$ = noise voltage squared per unit length;

$|i_n|^2$ = noise current squared per unit length.

These parameters are either smoothly distributed or are made of lumped constants so closely spaced that a smooth-line approach is still valid. In addition, both R and G are generalized to include negative values. It is when R and/or G are negative that the line behaves as the active device, which is of main interest here.

III. BASIC EQUATIONS

The usual transmission line equations in voltage V and current I are

$$-\frac{\partial V}{\partial z}=(R+j\omega L)I \tag{1}$$

$$-\frac{\partial I}{\partial z}=(G+j\omega C)V. \tag{2}$$

However, because the problem of essential interest involves uncorrelated noise sources, the square of the voltage $(|V|)^2$ and the power P, instead of the voltage (V) and the current (I), are chosen as the working electrical parameters. Let

$$VI^*+V^*I=2P_r \tag{3}$$

$$VI^*-V^*I=2P_x, \tag{4}$$

where P_r is the real power and P_x is the reactive power.

By ignoring the distributed noise, a set of four working equations is derived from (1), and (2),

$$-\frac{\partial}{\partial z}|V|^2=2RP_r+2\omega LP_x \tag{5}$$

$$-\frac{\partial}{\partial z}|I|^2=2GP_r-2\omega CP_x \tag{6}$$

$$-\frac{\partial}{\partial z}P_r=R|I|^2+G|V|^2 \tag{7}$$

$$-\frac{\partial}{\partial z}P_x=(\omega L)|I|^2-(\omega C)|V|^2 \tag{8}$$

These equations are quite similar to the noise equations which were treated in the electron stream of traveling wave tubes.[4] Equations (5), (6), (7), and (8) can be

* The research reported in this paper has been sponsored by the Electronics Research Directorate of the Air Force Cambridge Research Center, Air Research and Development Command, under contract.

[1] L. J. Giacolletto and J. O'Connell, RCA Review **17**, 68 (March, 1956); also, A. Uhlir, Jr., Proc. I.R.E. **46**, 1099–1115 (June, 1958).

[2] H. S. Sommers, Proc. I.R.E. **47**, 1201 (July, 1959).

[3] P. K. Tien, J. Appl. Phys. **29**, No. 9, 1347–1357 (September, 1958).

[4] J. Berghammer and S. Bloom, J. Appl. Phys. **31**, 454 (1960).

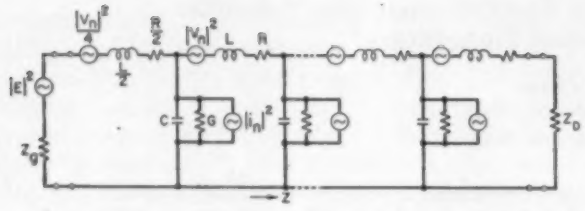

FIG. 1. Lossy transmission line with distributed negative resistances and noise sources. Each section or unit length is less than $\frac{1}{8}$ wave length.

transformed into the following common equation:

$$\left[\frac{\partial^4}{\partial z^4}+4(\omega^2LC-RG)\frac{\partial^2}{\partial z^2}-4(\omega LG+\omega CR)^2\right](|V|^2,\ |I|^2,\ P_r,\text{ or } P_z)=0. \quad (9)$$

Equation (9) is the differential equation of $|V|^2$, $|I|^2$, P_r, or P_z for an ordinary transmission line in the absence of distributed noise. If the line, which is of length D, with a characteristic impedance $Z_0(=R_0+jX_0)$, is terminated by an impedance $Z_D(=R_D+jX_D)$ and is driven by a signal voltage source $|E|^2$ with a generator impedance Z_g, the solution of (9) can be readily determined[5]; it is

$$|V|^2=\frac{P_0}{R_0}|Z_0|^2\left[\frac{a_z+b_z}{a_0+b_0}\right] \quad (10)$$

$$|I|^2=\frac{P_0}{R_0}\left[\frac{a_z-b_z}{a_0+b_0}\right] \quad (11)$$

$$P_r=\frac{P_0}{2R_0(a_0+b_0)}[Z_0(\bar{a}_z+j\bar{b}_z)+Z_0^*(\bar{a}_z-j\bar{b}_z)] \quad (12)$$

$$P_z=\frac{P_0}{2R_0(a_0+b_0)}[Z_0(\bar{a}_z+j\bar{b}_z)-Z_0^*(\bar{a}_z-j\bar{b}_z)], \quad (13)$$

where

$$P_0=\frac{|E|^2}{|Z_0+Z_g|^2}R_0 \quad (14)$$

$$\left.\begin{matrix}\bar{a}_z\\ a_z\end{matrix}\right\}=e^{-\alpha_1 z}\mp|N|^2e^{\alpha_1(z-2D)} \quad (15)$$

$$\left.\begin{matrix}\bar{b}_z\\ b_z\end{matrix}\right\}=-2e^{-D\alpha_1}|N|\begin{matrix}\sin\\ \cos\end{matrix}[|\alpha_2|(z-D)+\theta_2] \quad (16)$$

$$a_0=1+|MN|^2e^{-2D\alpha_1} \quad (17)$$

$$b_0=-2e^{-D\alpha_1}|MN|\cos[\theta_1+\theta_2-D|\alpha_2|] \quad (18)$$

[5] S. Goldman, *Transformation Calculus and Electrical Transients* (Prentice-Hall, Inc., Englewood Cliffs, New Jersey), pp. 396–415.

$$\alpha_1=\omega(2LC)^{\frac{1}{2}}\{(XY-1)+[(1+X^2)(1+Y^2)]^{\frac{1}{2}}\}^{\frac{1}{2}} \quad (19)$$

$$\alpha_2=\omega(2LC)^{\frac{1}{2}}\{(XY-1)-[(1+X^2)(1+Y^2)]^{\frac{1}{2}}\}^{\frac{1}{2}} \quad (20)$$

$$X=\frac{R}{\omega L} \quad (21)$$

$$Y=\frac{G}{\omega C} \quad (22)$$

$$Z_0=\left(\frac{L}{C}\right)^{\frac{1}{2}}\left(\frac{X+j}{Y+j}\right)^{\frac{1}{2}} \quad (23)$$

$$M=\frac{Z_0-Z_g}{Z_0+Z_g}=|M|e^{j\theta_1} \quad (24)$$

$$N=\frac{Z_0-Z_D}{Z_0+Z_D}=|N|e^{j\theta_2}. \quad (25)$$

In (19), α_1 has a positive sign if the line is passive; i.e., if both R and G are positive. For an active line, (i.e., the case where R and/or G is negative), it is noted from (20) that α_2 is always a pure imaginary number. Thus, α_1 is either an amplification constant or an attenuation constant, while α_2 is a phase constant.

M and N are coefficients of reflection for the input and for the output, respectively. Containing these two reflection coefficients, the denominators of (10), (11), (12) and (13) can be expanded into a power series in $|MN|$ when $|MNe^{-D\alpha_1}|<1$ or in $|MN|^{-1}$ when $|MNe^{-D\alpha_1}|>1$. The successive terms of these series are the contributions due to multiple reflections back and forth from the ends of the line.

TRANSMISSION LINE WITH DISTRIBUTED NOISE GENERATORS

Now assume that a noise mean voltage $|\hat{v}_n|^2$ and a noise mean square current $|\hat{\imath}_n|^2$ are distributed along the line. Equations (5), (6), (7), and (8) can be then written, for noise alone, as

$$-\frac{\partial}{\partial z}|\hat{V}|^2=2R\hat{P}_r+2\omega L\hat{P}_z-|\hat{v}_n|^2 \quad (26)$$

$$-\frac{\partial}{\partial z}|\hat{I}|^2=2G\hat{P}_r-2\omega C\hat{P}_z-|\hat{\imath}_n|^2 \quad (27)$$

$$-\frac{\partial}{\partial z}\hat{P}_r=R|\hat{I}|^2+G|\hat{V}|^2 \quad (28)$$

$$-\frac{\partial}{\partial z}\hat{P}_z=(\omega L)|\hat{I}|^2-(\omega C)|\hat{V}|^2, \quad (29)$$

where the crowns designate the noise case. The noise sources $|\hat{v}_n|^2$ and $|\hat{\imath}_n|^2$ can be, for instance, the Johnson noise due to the losses of the line, and whatever noise

the negative-resistance devices contribute. $|\hat{v}_n|^2$ and $|\hat{\imath}_n|^2$ are assumed not to be functions of the line distance z. Equations (26), (27), (28), and (29) have almost the same form as (5), (6), (7), and (8), except for the presence of the noise generator terms. By making the following substitutions:

$$|\hat{\hat{V}}|^2=|\hat{V}|^2 \tag{30}$$

$$|\hat{\hat{I}}|^2=|\hat{I}|^2 \tag{31}$$

$$\hat{\hat{P}}_r=\hat{P}_r-\hat{p}_r \tag{32}$$

$$\hat{\hat{P}}_x=\hat{P}_x-\hat{p}_x \tag{33}$$

$$\hat{p}_r=\frac{1}{X+Y}\left[\frac{|\hat{v}_n|^2}{2\omega L}+\frac{|\hat{\imath}_n|^2}{2\omega C}\right] \tag{34}$$

$$\hat{p}_x=\frac{1}{X+Y}\left[Y\frac{|\hat{v}_n|^2}{2\omega L}-X\frac{|\hat{\imath}_n|^2}{2\omega C}\right] \tag{35}$$

one arrives at the same differential equation as (9) for $|\hat{\hat{V}}|^2$, $|\hat{\hat{I}}|^2$, $\hat{\hat{P}}_r$, or $\hat{\hat{P}}_x$. A set of solutions similar to (10), (11), (12), and (13) will be obtained in the noise case provided Z_D and N are respectively replaced by $\hat{Z}_D$ and $\hat{N}$, where

$$\hat{Z}_D=\hat{R}_D+j\hat{X}_D \tag{36}$$

$$\hat{R}_D=R_D\left(1-\frac{\hat{p}_r}{\hat{P}_{rD}}\right) \tag{37}$$

$$\hat{X}_D=X_D\left(1-\frac{\hat{p}_x}{\hat{P}_{xD}}\right) \tag{38}$$

$$\hat{N}=\frac{Z_0-\hat{Z}_D}{Z_0+\hat{Z}_D}=|\hat{N}|e^{j\hat{\theta}_2}. \tag{39}$$

Here $\hat{P}_{rD}$ and $\hat{P}_{xD}$ denote respectively the real noise power and the reactive noise power at the termination. Equations (36), (37), (38), and (39) have an inportant physical meaning; namely, as far as the electrical performance is concerned, a line with distributed noise generators and a passive terminating impedance is equivalent to the same line without such noise generators but with a fictitious termination $\hat{Z}_D$, which is a function of the driving powers $\hat{P}_{rD}$ and $\hat{P}_{xD}$.

GAIN AND NOISE FACTOR

The real signal and noise powers, P_r and $\hat{P}_r$, which have been derived as (12), are now used for the computation of the gain and noise factor.

If we use (12), the power gain G_p, which is defined as the ratio of the output power P_{rD} to the available input power P_a, is

$$G_P=\frac{P_{rD}}{P_a}=\frac{P_0}{P_a(a_0+b_0)}\left[\bar{a}_D-\frac{X_0}{R_0}\bar{b}_D\right], \tag{40}$$

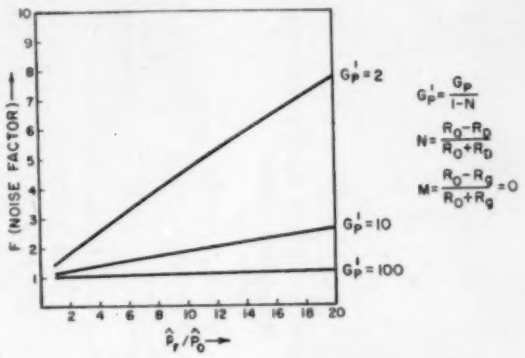

FIG. 2. Noise factor of a matched-input line with distributed noise sources.

where

$$\left.\begin{aligned} P_a&=\frac{|E|^2}{4R_g}\\ \bar{a}_D&=(\bar{a}_z)|_{z=D}\\ \bar{b}_D&=(\bar{b}_z)|_{z=D}\end{aligned}\right\}. \tag{41}$$

The equation for the output noise power P_r is

$$\hat{P}_{rD}=\hat{P}_0\left(\frac{1}{\hat{a}_0+\hat{b}_0}\right)\left[\hat{\bar{a}}_D-\frac{X_0}{R_0}\hat{\bar{b}}_D\right]. \tag{42}$$

Here $\hat{a}_0$, $\hat{b}_0$, $\hat{\bar{a}}_D$ and $\hat{\bar{b}}_D$ are derived from (17), (18), and (41) by substituting $|\hat{N}|$ for N. Since $|\hat{N}|$ is a function of $\hat{P}_{rD}$, (42) is a polynominal equation in $\hat{P}_{rD}$. The solution is rather involved. Only a few special cases are illustrated in the examples to be shown.

By using the solution of $\hat{P}_{rD}$ from (42), the noise factor F is

$$F=(\hat{P}_{rD}/\hat{P}_aG_P). \tag{43}$$

Examples

To show the noise performance of an active transmission line distributed with noise generators, three simple cases are illustrated in Table I. They are a matched line, a mismatched input line, and a mismatched output line. The lines are distortionless; i.e., $X=Y$. An isolated load is assumed for the termination in all three cases.

The case for a nonisolated bilateral transmission line with both mismatched input and output is rather complex. The output noise would be the sum of the noises resulting from multiple reflections at the input and output plus the distributed noise. Consider the special case where the load is matched to the line; i.e., $N=0$. Then the input noise power originating from the nonisolated load, which generates a noise power $\hat{P}_l$ is

$$\hat{P}_L=\hat{P}_l\hat{M}^2e^{-D\alpha_1}=\hat{P}_l\frac{\hat{M}^2}{1-\hat{M}^2}G_P. \tag{50}$$

TABLE I.

Case	Matched input and output $X=Y=$Neg	Mismatched input $X=Y=$Neg	Mismatched output $X=Y=$Neg
Given	$R_g=R_0=R_D$ $X_g=X_0=X_D=0$ $\hat{p}_x=0$	$R_g\neq R_0,\quad R_0=R_D$ $X_g=X_0=X_D=0$ $\hat{p}_x=0$	$R_g=R_0,\quad R_0\neq R_D$ $X_g=X_0=X_D=0$ $\hat{p}_x=0$
a_0	1	1	1
b_0	0	0	0
$\hat{a}_D$	$e^{-\alpha_1 D}$	$e^{-\alpha_1 D}$	$(1-\lvert N\rvert^2)e^{-\alpha_1 D}$
$\hat{a}_0$	1	$1+\lvert M\hat{N}\rvert^2 e^{-\alpha_1 D}$	1
$\hat{b}_0$	0	$\pm 2e^{-D\alpha_1}\lvert M\hat{N}\rvert$; Assume $D\lvert\alpha_2\rvert=n\pi$	0
$\hat{a}_D$	$(1-\lvert\hat{N}\rvert^2)e^{-\alpha_1 D}$	$(1-\lvert\hat{N}\rvert^2)e^{-\alpha_1 D}$	$(1-\lvert N\rvert^2)e^{-\alpha_1 D}$
G_P	$e^{-\alpha_1 D}$	$(1-M^2)e^{-\alpha_1 D}$	$(1-\lvert N\rvert^2)e^{-\alpha_1 D}$
$\hat{P}_{rD}$	$\frac{1}{2}[\hat{p}_r+G_P\hat{P}_0]\cdot\left[1+\left(1-\left(\frac{\hat{p}_r}{\hat{p}_r+G_P\hat{P}_0}\right)^2\right)^{\frac{1}{2}}\right]$ (44)	$\frac{1}{2}\left[\hat{p}_r+\frac{G_P}{1-M^2}(\hat{P}_0\pm M\hat{p}_r)\right]\cdot\left[1+\left(1-\left\{\frac{\hat{p}_r[1\pm(M/1-M^2)G_P]}{\hat{p}_r+(G_P/1-M^2)(\hat{P}_0\pm M\hat{p}_r)}\right\}^2\right)^{\frac{1}{2}}\right]$ (45)	$\frac{1}{2}\left[\hat{p}_r+G_P\frac{\hat{P}_0}{1-N^2}\right]\cdot\left[1+\left(1-\left(\frac{\hat{p}_r}{p_r+(G_P/1-N^2)\hat{P}_0}\right)^2\right)^{\frac{1}{2}}\right]$ (46)
F	$\frac{1}{2}\left[1+\frac{\hat{p}_r}{\hat{P}_0G_P}\right]\cdot\left[1+\left(1-\left(\frac{\hat{p}_r/\hat{P}_0}{\hat{p}_r/\hat{P}_0+G_P}\right)^2\right)^{\frac{1}{2}}\right]$ (47)	$\frac{1}{2}\left[1+\frac{\hat{p}_r}{\hat{P}_0G_P}(1-M^2)\pm\frac{\hat{p}_r}{\hat{P}_0}M\right]\cdot\left[1+\left(1-\frac{(1\pm MG_P/1-M^2)^2}{\{1+(G_P/1-M^2)[(\hat{p}_0/\hat{p}_r)\pm M]\}^2}\right)^{\frac{1}{2}}\right]$ (48)	$\frac{1}{2}\left[1+\frac{\hat{p}_r}{\hat{P}_0}\frac{1-N^2}{G_P}\right]\cdot\left\{1+\left[1-\left(\frac{\hat{p}_r/\hat{P}_0}{\hat{p}_r/\hat{P}_0+(G_P/1-N^2)}\right)^2\right]^{\frac{1}{2}}\right\}$ (49)

The new input noise power now becomes

$$\hat{P}_0' = \hat{P}_0 + \hat{P}_I \frac{\hat{M}^2}{1-\hat{M}^2} G_P. \tag{51}$$

Therefore, the actual values of the noise factor are the same as those obtained by (43) provided $\hat{P}_0$ is replaced by $\hat{P}_0'$.

Equations (47) and (49) are plotted in Fig. 2 for the case $M=0$. Equation (48) is plotted for two cases; $N=0$, $M=0.2$ (Fig. 3) and $N=0$, $M=0.5$ (Fig. 4). When the line is mismatched at the input, (i.e., M is not equal to zero), the noise factor will be a function of the phase angles of the reflection coefficients and the number of electrical wave lengths of the line. At some particular line lengths, as shown by a dotted curve of Fig. 3, the noise factors are even lower than those in the matched case (Fig. 2). This is due to a partial noise cancellation in the course of reflection. However, since the noise cancellation depends upon the line length or the frequency, those low noise factors are often accompanied by narrow bandwidths.

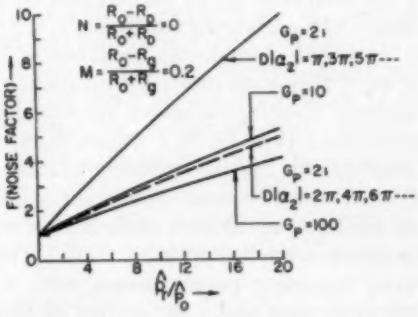

FIG. 3. Noise factor of a mismatched-input line with distributed noise sources ($M=0.2$).

As expected, the curves all indicate that the noise factor tends to increase at low gains, and at high reflection coefficients. The magnitude of $\hat{p}_r/\hat{P}_0$ used in these curves can be ealily computed from (34) and (35). For a distortionless transmission line, that is $X=Y$

$$\frac{\hat{p}_r}{\hat{P}_0} = \left[\frac{R_d+R_n}{\left| |R_a|-R_d \right|} + \frac{G_d+G_n}{\left| |G_a|-G_d \right|} \right], \tag{52}$$

where R_d, G_d = line positive resistance, conductance per unit length; R_a, G_a = introduced negative resistance, conductance per unit length; and R_n, G_n = equivalent noise resistance, conductance per unit length. Equation (52) reveals that low negative resistances and conductances per unit length would result in relatively high noise powers on the line and thus high noise factors according to Figs. 3 and 4. In cases where the distributed

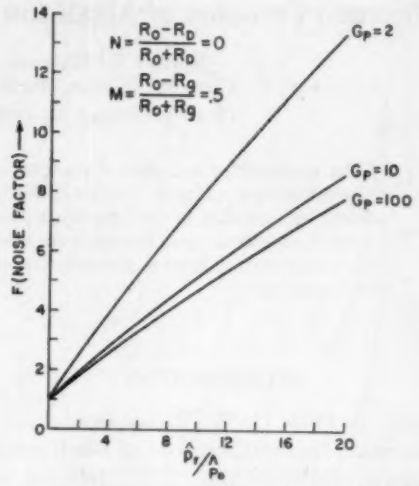

FIG. 4. Noise factor of a mismatched-input line with distributed noise sources ($M=0.5$).

negative resistance just overcomes the distributed positive resistance, the noise factor becomes extremely large. In addition, since the gain per unit length is small, because of the small net negative resistance, a large total gain is possible only when the line is long.

CONCLUSIONS

For a transmission line with both positive and negative distributed resistances as well as distributed random noise sources, low-noise amplification can be achieved via the line provided that (1) the line is operated at sufficiently high gain, (2) the line is well matched at both the input and the output, and (3) the net negative resistance and/or the net negative conductance is large; i.e., that gain per unit length is large. These conditions, which have been deduced from a quantitative analysis, are the necessary ones for low noise amplification. They accord with expectations from qualitative deduction. It is to be noted that for condition (2) to be satisfied over a wide range of frequencies the line must be distortionless.

In the case of a nonisolated load, a slight mismatch at the input will considerably increase the over-all noise factor. For instance, according to (51), neglecting $\hat{p}_r$, an input mismatch of 10% ($M=0.1$) at a power gain of 20 db will increase the noise factor by 3 db; while a 20% input mismatch will increase the noise factor by 7 db. Therefore, it is desirable to isolate the output load through a undirectional isolator. In those negative-resistance transmission lines where negative resistance is formed only in the forward direction, such as the traveling wave parametric amplifier, undirectional isolation coexists with undirectional amplification, and hence no additional isolator is necessary.

Thermal Emission of Alkali Ion Pulses from Clean and Oxygenated Tungsten

ROBERT E. MINTURN, SHELDON DATZ, AND ELLISON H. TAYLOR
Chemistry Division, Oak Ridge National Laboratory, Oak Ridge, Tennessee*
(Received August 28, 1959; revised manuscript received January 5, 1960)

The spontaneous emission of positive ions from a heated tungsten filament occurs as pulses, a single pulse releasing as many as 10^6 ions in less than 100 μsec. The pulses are composed mainly of potassium ions, present as impurities in the tungsten lattice. It is suggested that the emission of positive ions in the form of bursts is dependent upon the existence of edge dislocations in the metal. At temperatures where the formation of an adsorbed layer is possible, oxygen has a very pronounced effect upon the rate of emission of positive ion pulses.

INTRODUCTION

As early as 1913, O. W. Richardson[1] came to the conclusion that positive ions of alkali metals were emitted from heated metals. J. P. Johnson in 1925[2] correlated the positive ion emission with the "anomalous flicker effect" found in diodes under space charge limited operation, and postulated that the ions were emitted in bursts of about 10^5 ions. Much more recently, Lindemann and van der Ziel[3] have described a more comprehensive study of the anomalous flicker effect, and have proposed that the effect is the result of the trapping of bursts of positive ions in the electron space charge surrounding the filament.

The undesirable effects on electron emission caused by positive ion eruptions may be eliminated by the use of appropriately placed ion traps.[3] However, in the application of the surface ionization gauge to the detection of atomic and molecular beams,[4,5] positive ion noise cannot be eliminated in any simple way, and is the limitation in sensitivity of the method at low beam intensities. In addition, when the filament surface is oxygenated in order to increase the ionization efficiency for atoms of higher ionization potential, the positive ion noise is greatly increased. The present work was undertaken in an attempt to find a mechanism which is consistent with the observations.

EXPERIMENTAL

The tungsten filament to be studied was mounted in a surface ionization gauge, the construction and operation of which have been described previously.[5] The filament was a well aged, two-mil wire of high-purity tungsten, obtained from the General Electric Company Wire Works. When in operation, the gauge was surrounded by a liquid-nitrogen-cooled trap. Filament temperatures were calculated from the current vs temperature relations given in the Jones-Langmuir tables.[6] The pressures reported are those indicated by an ionization gauge. The low pressures ca 10^{-7} mm Hg represent the lowest total pressure attainable in the system, and do not accurately represent the partial pressure of oxygen, which must be considerably lower. The characteristics of the pulses were established with the instrumentation shown schematically in Fig. 1. F is the filament and P is the collector plate of the gauge. The potential difference across the gauge was supplied by a 45-v battery at E. The electrical capacitance and resistance are indicated by C_1 and R_1 and include the input values of the measuring oscilloscope. CRO was a Tektronix Type 531 cathode-ray oscilloscope, utilizing a type 53/54 E high-gain plug-in preamplifier, with a 0.047 μf external blocking capacitor, for the analysis of pulse heights and a type 53/54 L preamplifier, with its 0.01 μsec rise time, for the determination of pulse shapes.

Measurements of the general noise trace as a function of temperature (see Fig. 2) were made with a vibrating reed electrometer (Applied Physics Corp., Model 13) and a Brown recording potentiometer with a 4½-sec full-scale traverse time and a sensitivity of 10 mv full scale. The input resistance to the electrometer was 10^9 ohms.

The types of ions emitted and their relative abundances under different conditions were determined by use of modified General Electric 6-in. radius, 60° sector, first-order-focusing mass spectrometer with an electron-multiplier detector. The instrument has been described by Wells and Melton.[7] The thermal ion source consisted of tungsten filament wire, identical to that used in the surface ionization gauge, mounted in the ionization chamber of the instrument. It was positioned to allow the use of the electron beam to ionize evaporated neutrals.

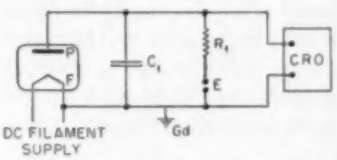

FIG. 1. Schematic diagram of apparatus to establish characteristics of thermal positive ion pulses from tungsten filaments.

* Operated by Union Carbide Corporation for the U. S. Atomic Energy Commission.

[1] O. W. Richardson, Proc. Roy. Soc. (London) **89**, 507 (1913).
[2] J. P. Johnson, Phys. Rev. **26**, 71 (1925).
[3] W. W. Lindemann and A. van der Ziel, J. Appl. Phys. **28**, 448 (1957).
[4] J. B. Taylor, Z. Physik **57**, 242 (1929).
[5] S. Datz and E. H. Taylor, J. Chem. Phys. **25**, 389 (1956).
[6] H. A. Jones and I. Langmuir, Gen. Elec. Rev. **30**(6), 310 (1927).
[7] G. F. Wells and C. E. Melton, Rev. Sci. Instr. **28**, 1065 (1955).

RESULTS

The mass spectrometric results indicate that the thermal positive ion emission from well-aged tungsten at temperatures from 1200° to 2400°K is composed mainly of potassium with a small amount of sodium and traces of rubidium, calcium, and aluminum. When an unaged filament is heated, much larger amounts of Na^+ appear, but this emission decays with time much more rapidly than that of K^+, sizable amounts of which remain throughout the lifetime of the filament. This effect may be due to the similarity in size of the K^+ ion ($d=1.33$ A) and the W atom in the metal ($d=1.37$ A). The Na^+ ion ($d=0.95$ A), however, may be small enough to diffuse rapidly through the lattice and be lost during the high-temperature aging process. Thermal ions of W^+ and WO^+ could be observed only when the temperature was raised to 2650°K at an oxygen pressure of 6×10^{-5} mm Hg. Even under these conditions, the abundance of these ions relative to that of K^+ (ca 10^{-13} amp) was 6×10^{-5} for W^+ and 5×10^{-4} for WO^+. No additional ions could be observed by electron bombardment of the evaporated neutrals, but this absence is probably caused by the inefficiency of this process.

The temperature dependence of the positive ion emission may be seen in Figs. 2 and 3. Figure 2 indicates the noise traces made by chart recording the output of the vibrating reed electrometer when it was placed directly across the surface ionization gauge. The trace in Fig. 2(A) is characteristic of filament noise at low oxygen pressure, while Fig. 2(B) indicates the effect of higher pressure. The ragged displacement of the noise trace in the 1600–2300° temperature range of Fig. 2(B)

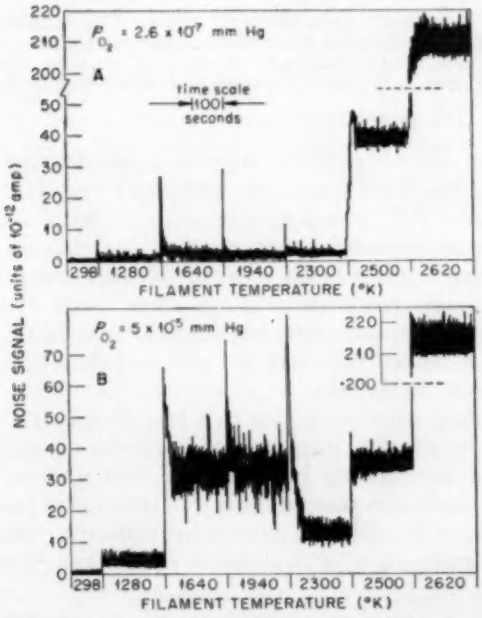

FIG. 2. Thermal positive ion noise traces at several temperatures and two pressures made by chart recording the output of the vibrating reed electrometer.

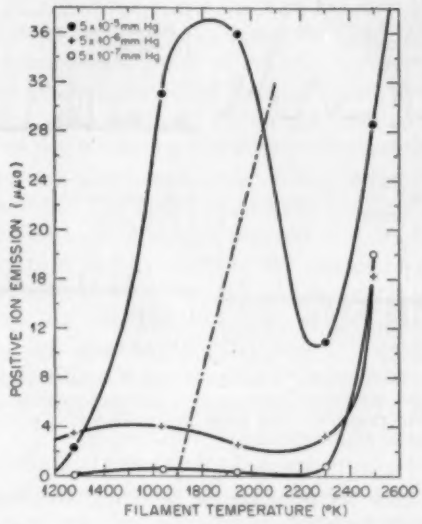
5 x 10⁻⁵ mm Hg
5 x 10⁻⁶ mm Hg
5 x 10⁻⁷ mm Hg
POSITIVE ION EMISSION (μμa)
FILAMENT TEMPERATURE (°K)
1200 1400 1000 1800 2000 2200 2400 2600

FIG. 3. Thermal positive ion emission as a function of temperature at three different oxygen pressures. The dashed line intersects the individual curves at a point representing monolayer coverage by adsorbed oxygen.

above the corresponding value of Fig. 2(A) reflects the inability of the measuring instruments to follow the large rapid fluctuations in noise signal that occur under these conditions. The displacement of the entire trace to higher values at the higher temperatures is thought to be caused mainly by the emission of photoelectrons from the collector. The enhanced noise associated with an abrupt change in filament temperature is also indicated in Fig. 2. This extra noise is characteristic of abrupt decreases as well as increases in temperature, and in each case soon decays to the noise level characteristic of the filament at the new temperature. An increase in the rate of emission of pulses, very similar to that accompanying changes in temperature, was also noted when the heated filament was mechanically strained. This effect had been observed by Richardson.[1] Figure 3 indicates the rate of positive ion emission as a function of temperature for three different oxygen pressures. The points on the curves were obtained by measuring the average amplitude, at a given temperature, of noise traces such as illustrated in Fig. 2, and subtracting from that the signal due to photoelectric emission. Each curve goes through a maximum in the temperature region between 1500° and 1800°K. The dashed line intersects the individual curves at a point representing monolayer coverage by adsorbed oxygen at the given pressure, assuming a heat of adsorption of 5 ev.[8] Thus, the maximum emission occurs under conditions where the surface is covered by at least a monolayer of adsorbed oxygen. As the temperature is increased, the surface coverage decreases and the noise-level decreases. Above 2400°K, the emission begins to increase rapidly,

[8] J. A. Becker and R. G. Brandes, J. Chem. Phys. **23**, 1323 (1955).

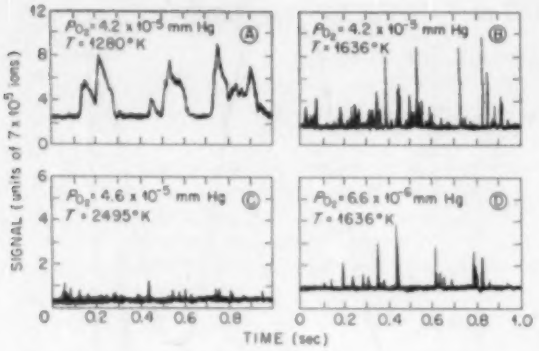

FIG. 4. Oscillographic tracings of the thermal emission noise from a heated tungsten filament under different conditions of temperature and pressure. Unit peak height is equivalent to about 7×10^5 positive ions.

and at higher temperatures it becomes independent of oxygen pressure.

Figure 4 is a set of oscillographic tracings of the thermal-emission noise from a heated tungsten filament. Each tracing is a recording of a single, one-second sweep of the oscilloscope, and a unit pulse height is equivalent to 7×10^5 positive ions. Figures 4(b), 4(c), and 4(d) indicate clearly that the positive ions are emitted in discrete bursts of short duration. Figure 4(a) represents the emission pattern at relatively low temperature and relatively high oxygen pressure. Under these conditions, several bursts often occur almost simultaneously and the instrument cannot differentiate clearly one from another. Tracings 4(a), 4(b), and 4(c) illustrate the effect of temperature on the pulses emitted at high oxygen pressure ($\sim5\times10^{-5}$ mm Hg) while 4(d) indicates the effect of a diminished oxygen pressure. The results of several observations made at each set of experimental conditions are averaged in Table I. With the amplification available, pulses of less than about 10^5 ions would not be observed, but the ion currents that may be calculated by multiplying the frequency of the bursts by the number of ions per burst agree quite well

TABLE I. Average values for thermal positive ion emission from W filaments.[a]

PO_2(mm Hg)	Filament °K	Pulses/sec	Ions/pulse
4.2×10^{-5}	1280	—[b]	$\sim2\times10^{6}$[b]
	1640	115	1.24×10^{6}
	1940	200	0.65×10^{6}
	2300	42	0.47×10^{6}
	2500	35	0.21×10^{6}
	2620	24	0.17×10^{6}
6.6×10^{-6}	1280	—[b]	$\sim2\times10^{6}$[b]
	1640	23	0.74×10^{6}
	1940	18	0.57×10^{6}
	2300	5	0.36×10^{6}
7.0×10^{-7}	1280	1	0.37×10^{6}
	1640	2	0.96×10^{6}
	1940	2	0.30×10^{6}
	2300	5	0.13×10^{6}

[a] For a filament 0.005 cm in diameter and 3.5 cm in length.
[b] For these cases, the complexity of the oscillogram [see Fig. 3(A)] precludes an accurate estimate.

with those derived from vibrating reed measurements of the noise amplitude, such as those presented in Fig. 3.

In Fig. 5, Curve *A* is an oscillographic tracing of the instantaneous voltage across the capacitance C_1 of Fig. 1 resulting from a single pulse. Note the much expanded time scale. Since the time constant of the circuit was long compared to the duration of the pulse, the shape of the pulse may be obtained from Curve *A* by differentiation with respect to time and multiplication by the capacitance. Curve *B* is the result. The pulse depicted in Fig. 5 emanated from a tungsten filament at 2090°K and had a rise-time of less than 2 μsec. Pulse decay-times were found to vary inversely with temperature, with a range from about 20 to 200 μsec at 1640°K and from 1 to 10 μsec at 2400°K. The decay-times were independent of oxygen pressure.

DISCUSSION

After extensive annealing at high temperatures, the tungsten wire was observed to consist of a series of

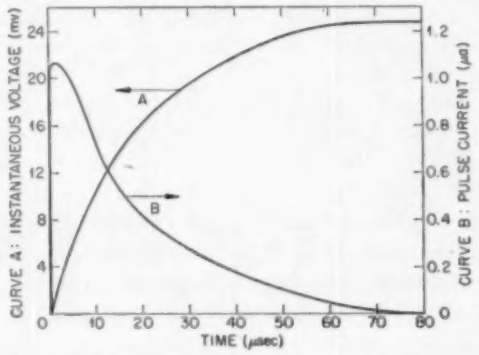

FIG. 5. Curve *A* is an oscillographic tracing of the instantaneous voltage across the capacitance of the measuring system due to a single pulse. Curve *B* indicates the shape of the pulse, obtained from Curve *A* by differentiation and multiplication by the capacitance.

monocrystals one or two wire diameters in length, in accord with observations previously reported by others.[9,10] It is typical of even annealed metal crystals to contain many lattice imperfections, and in particular, they may contain of the order of 10^{10} edge dislocations per square centimeter.[11] Edge dislocations may be made to move under very low stresses,[11] and the number of such dislocations may be increased drastically by cold-working the metal.

When a stress is applied to a heated tungsten wire, either by abruptly increasing or decreasing its temperature or by suddenly increasing its tension, there is a corresponding increase in the rate of emission of positive ion pulses. In addition, unannealed filaments showed a much greater rate of emission of pulses than do those

[9] R. P. Johnson, Phys. Rev. **54**, 459 (1938).
[10] N. F. Kravtsova, Dopovidi L'viv Derzhav. Univ. im I. Franka **6**, 2, 124 (1955).
[11] C. Kittel, *Introduction to Solid State Physics* (John Wiley & Sons, Inc., New York, 1953), 323 ff.

which have been thermally aged for a considerable time. Thus, the factors which are known to affect the number and movement of dislocations in a metallic lattice show a corresponding effect on the rate of pulse emission. Furthermore, impurity atoms are known to concentrate at (decorate) edge dislocations.[11–13] We are therefore led to the conclusion that the emission of positive ions in the form of bursts is dependent upon the existence of decorated edge dislocations in the metal crystal. Thus, the rapid rise of the pulse can be related to the initial contact of the decorated dislocation with the surface, and the slower exponential decline to the depletion of the impurity ions by diffusion along the dislocation channel.

Additional substantiating evidence may be inferred from the work of Dyke and Barbour with a pulsed-field emission microscope.[14] They reported observing the evolution of about 10^5 impurity atoms from a surface fissure of atomic dimensions in a single-crystal tungsten cathode at 2000°K. Also, the large number of ions in the burst indicates that the concentration of ions in the dislocation is high (i.e., 1 to 10 per atom layer), and the observation by Reynolds and Michel[15] of small amounts of the polymeric ions K_2^+ $K_3^+ \cdots K_{15}^+$ from heated tungsten is in accord with conditions of high concentration.

The effect of oxygen on the emission is caused, in part, by the increased work function of the oxygen covered surface, which increases the surface ionization efficiency.[5] However, the effect is much greater than that attributable to this cause, since the ion current was composed primarily of potassium even under the most highly oxygenated conditions and the increase in surface ionization efficiency for potassium upon oxygenation is only 30%. In addition, the large increase in total ion emission does not result primarily from an increase in the size of individual pulses but from an increase in the number of pulses (Table I). Since the effect of oxygen is most pronounced under conditions favorable to formation of an oxide film (Fig. 3), a possible cause for the increase in pulse rate may lie in the additional stress applied to the crystal by the formation of an oxide film with the attendant mismatch of the oxide and substrate lattices. The bunching of pulses observed under conditions of relatively high pressure and low temperature may then be the result of the release of a pile-up of dislocations at a stable oxide film barrier.

Because of the relatively few grain boundaries which exist in a well-annealed tungsten wire, it is unlikely that they constitute a major source of positive ion bursts. The role of evaporation of tungsten atoms in the liberation of impurity pockets, as proposed by Lindemann and van der Ziel,[3] must be considered negligible in the absence of oxygen, since bursts were observed at temperatures where the tungsten evaporation rate is only a few atoms per sec.

The presence of the positive ion bursts severely limits the use of the tungsten filament in surface ionization detectors for molecular beams, and the elimination of erratic signals caused by such bursts could extend the range of these detectors to lower beam intensities and to elements having higher ionization potentials. Attempts to make tungsten wire completely free of alkali impurities have not yet succeeded. However, since the noise has been shown to consist of relatively infrequent bursts of short duration, it is possible to discriminate against it by the use of appropriate clipping circuits. This has been attempted at Bonn University (Physikalische Institut) and some success has been achieved.[16]

ACKNOWLEDGMENTS

It is a pleasure to acknowledge the contributions of R. H. Dilworth and E. Fairstein to the design of the instrumentation used in this investigation, and of C. E. Melton to the mass spectroscopic analysis.

[12] A. J. Dekker, *Solid State Physics* (Prentice-Hall, Inc., Englewood Cliffs, New Jersey, 1957), 95 ff.
[13] A. H. Cottrell, "Theory of dislocations" in *Progress in Metal Physics*, edited by B. Chalmers (Interscience Publishers, Inc., New York, 1949), Vol. 1.
[14] W. P. Dyke and J. P. Barbour, J. Appl. Phys. **27**, 356 (1956).
[15] F. L. Reynolds and M. C. Michel, USAEC Rept. (1957).
[16] K. Berkling, Physik. Institut, Universität Bonn (private communication).

Thermal Positive Ion Emission and the Anomalous Flicker Effect

S. Datz, R. E. Minturn, and E. H. Taylor
Chemistry Division, Oak Ridge National Laboratory, Oak Ridge, Tennessee*
(Received August 28, 1959)

The correlation between the anomalous flicker effect in space charge limited diodes and the positive ion pulses which generate it is studied in the light of recent measurements of the size and shape of thermal positive ion pulses from tungsten filaments. It is shown that the positive ion pulses, although smaller than the electron pulses, have similar duration times, and that the periodic structure of the electron pulses may be quantitatively explained by reflection of the positive ion bursts back and forth through the region of maximum space charge.

INTRODUCTION

ANOMALOUS flicker noise, which consists of pulses of 10^5 to 10^6 electrons emitted in tungsten filament diodes under space charge limited conditions, was first reported by Johnson in 1925[1] and was attributed by him to the emission of positive ions from the filament which acted to disturb the space charge. Lindemann and van der Ziel[2] recently studied the individual electron pulses over a wide frequency range and deduced from the results some properties of the causative positive ion pulses. They proposed that the positive ion bursts were of very short duration (<1 μsec) and that these ions were trapped in the space charge for many μsecs. The postulated size and shape of the positive ion pulses were not in agreement with measurements made by the present authors.[3] In particular, the positive ion pulses observed by MDT had duration times very similar to those of the electron pulses observed by LZ at comparable temperatures, and the electron pulses were only a factor of ten or a hundred larger than the positive ion pulses, not a factor of 10^4 as postulated.

The present work was carried out in an attempt to determine the mechanism which correlates the two types of emission. Positive ion pulses and the corresponding anomalous flicker pulses were studied in both the Sylvania 5722 noise diode and a surface ionization gauge.

EXPERIMENTAL

The apparatus used to observe the pulses has been described previously.[3] The Sylvania 5722 noise diode contains a tungsten hairpin filament 0.0096 cm in diam and about 3.0 cm in length. The anode is a rectangular steel box, 0.198 cm by 1.11 cm by 1.27 cm, open on two ends. At a filament voltage of 4 v, the filament carries about 1.33 amp, and reaches a temperature of about 2390°K, as calculated from the tables of Jones and Langmuir.[4] When the anomalous flicker electron pulses were being observed, the 5722 diode was operated at a plate current of 1 ma with the plate about 2.22 v positive with respect to the midpoint of the filament. When positive ion bursts were being observed, the plate was 45 v negative with respect to ground.

The surface ionization gauge was similar to those previously described.[5] It is a cylindrical diode with a 2-mil tungsten wire filament about 3.5 cm long and a nickel cylinder collector 6.7 cm long and 1.90 cm inside diam. Two square holes, 1.6 cm on edge, are cut out of opposite sides of the cylinder at the midpoint of the filament. Electron pulses were observed at two different temperatures and at several plate currents, and the positive ion bursts had been observed previously[3] with -45 v accelerating potential.

RESULTS

The characteristics of the anomalous flicker electron pulses in the 5722 diode observed by us under similar conditions are consistent with the observations of LZ. At 2390°K, there appear to be about 500- to 1000-electron bursts per sec, each burst rising in a few tenths of a μsec, and decaying in 8 or 10 μsecs. The bursts contain 10^6 to 10^8 electrons, determined separately by measuring the peak heights utilizing a circuit having a time constant of 19 μsecs. The shapes of the pulses, on the other hand, were observed with a circuit having a time constant small compared with the lengths of the pulses. Figure 1(a) is a typical oscillogram of three anomalous flicker effect pulses. The sweep speed was 1 μsec/cm and the instantaneous current is given in μamp. Over 95% of the negative pulses observed had the periodic structure demonstrated by LZ. The rise times of the anomalous flicker pulses varied with the size of the pulses, but the time between succeeding peaks of a given pulse was constant at about 0.6 μsec for all pulses. Figure 1(b) illustrates typical positive ion pulses in the 5722 diode at the same conditions under which Fig. 1(a) was observed, except that the polarity was reversed to collect positive ions. The curves of Fig. 1(b) were derived from the slopes of curves on oscillograms which recorded the instantaneous voltage across the inherent electrical capacitance of the measuring circuit. Since the time

* Operated by Union Carbide Corporation for the United States Atomic Energy Commission.

[1] J. B. Johnson, Phys. Rev. **26**, 71 (1925).

[2] W. W. Lindemann and A. van der Ziel, J. Appl. Phys. **28**, 448 (1957), hereinafter referred to as LZ.

[3] R. E. Minturn, S. Datz, and E. H. Taylor, J. Appl. Phys. **31**, 876 (1960), (this issue), hereafter referred to as MDT.

[4] H. A. Jones and I. Langmuir, Gen. Elec. Rev. **30** (6), 310 (1927).

[5] S. Datz and E. H. Taylor, J. Chem. Phys. **25**, 389 (1956).

constant of the measuring circuit was 60 μsecs in this case, little signal was lost by leakage through the high impedance to ground.[3] About 200 positive ion pulses per sec were observed, but the amplification was such that pulses of less than 10^5 ions would not be seen.

Anomalous flicker effects observed in the surface ionization gauge, Fig. 2, also exhibited a periodic structure, although the times involved were much longer. Figure 2(a) is an oscillogram of typical surface ionization gauge electron pulses with the filament at 2390°K and the plate current at 0.01 ma. The electron pulses of Fig. 2(b) are representative of the same diode with the filament at 2625°K and the plate current at 0.115 ma.

DISCUSSION

The emission of charged particles from heated tungsten filaments was studied under two distinct modes of operation in this investigation. In Case *A*, the collector was positive with respect to the filament, and electrons

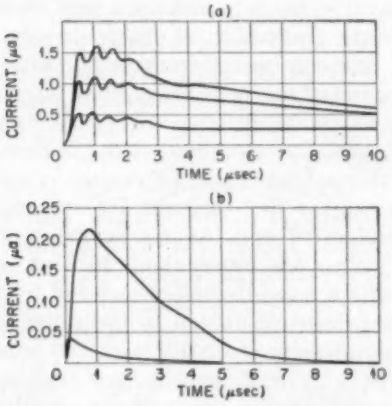

FIG. 1. Current pulses in the 5722 diode at a filament temperature of 2390°K; (a) Anomalous flicker effect pulses at 1-ma plate current, and (b) positive ion pulses with the collector 45-v negative with respect to the filament.

were collected under space-charge-limited conditions. In Case *B*, the collector was 45-v negative with respect to the filament, and positive ions were collected. Figure 3 indicates schematically the variation in potential with distance in the 5722 diode for the two cases, assuming a cylindrical shape for the diode. Curve *A* goes through a minimum of magnitude V_m at distance r_m from the axis of the filament, which has a radius r_o. The effective voltage across the diode V_e has the magnitude $V_A+(\Psi_f-\Psi_c)$, where V_A is the applied voltage, and Ψ_f and Ψ_c are the work function of the filament and collector, respectively. Since, at distances less than r_m, the potential gradient is negative for both modes of operation, conclusions drawn about the shape of the positive ion bursts leaving the surface under negative polarization should apply equally well to the case of positive polarization.

Under the space charge limited conditions of Case *A*, a positive ion leaving the surface with initial thermal

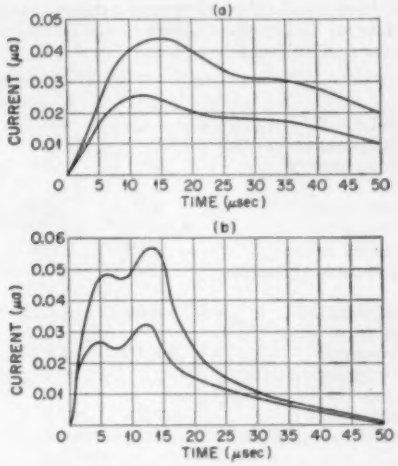

FIG. 2. Anomalous flicker effect pulses in the surface ionization gauge; (a) with the filament at 2390°K and 0.01-ma plate current, and (b) with the filament at 2625°K and 0.115-ma plate current.

kinetic energy V_o would be accelerated to a maximum kinetic energy (V_o-V_m) at r_m, and then decelerated to its position of maximum displacement at r_f. The particle would then be reflected back through r_m and either strike the filament or, if it had sufficient initial kinetic energy normal to the radial field, it would pass the filament and proceed through r_m to r_f to be reflected again. Those ions which strke the filament would re-evaporate as either ions or atoms according to the probabilities dictated by the Saha-Langmuir equation,[6] and the ions thus formed would again follow the paths outlined

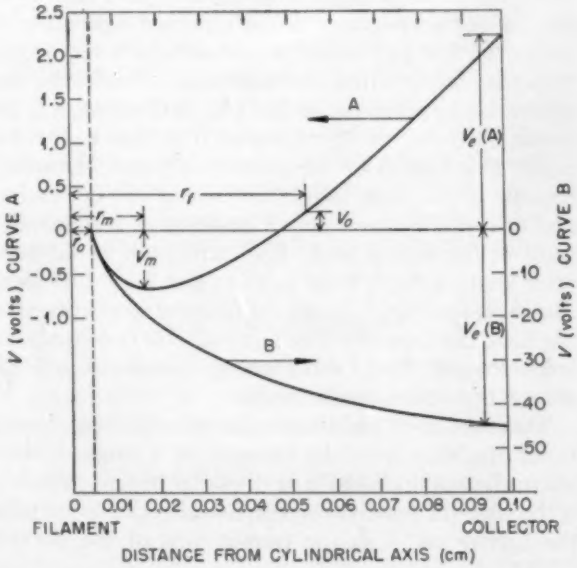

FIG. 3. Schematic diagram of the variation in potential with distance in the 5722 noise diode with the filament at 2390°K. Curve *A*, positive polarization with 1 ma plate current; curve *B*, 45 v negative polarization.

[6] I. Langmuir and K. H. Kingdon, Proc. Roy. Soc. (London) **A107**, 61 (1925).

TABLE I. Numerical values of several parameters characteristic of the anomalous flicker effect pulses in the Sylvania 5722 noise diode and the surface ionization gauge.

	5722	SIG	
Filament temperature, T(°K)	2390	2390	2625
Total emission current, I_e(ma)[a]	9.9	5.9	49.8
Plate current, I(ma)	1.0	0.01	0.115
Filament radius, r_o(cm)	4.8×10^{-3}	2.5×10^{-3}	2.5×10^{-3}
Collector radius, r_c(cm)	0.097	0.952	0.952
Radius of potential minimum, r_m(cm)[a]	0.017	0.183	0.062
Potential at potential minimum, V_m(volts)[a]	−0.66	−1.57	−1.63
Electron density at potential minimum, ρ_m(electrons cm^{-3})[a]	4×10^9	4×10^7	5×10^8
Pulse rise time (μsec)	~0.2	~15	~5
Peak-to-peak time (μsec)	0.6	~22	7

[a] Calculated values.

above. While in the region of the space charge maximum, the positive ion would locally lower the barrier V_m and more electrons would reach the collector. The peaks in the electrons pulse would correspond to the passage of the peak of the ion pulse through this region. A prediction of the peak-to-peak times may then be obtained from this mechanism by a calculation of the traverse times. For these calculations, r_m and V_m were calculated from equations derived by Wheatcroft for cylindrical diodes,[7,8] and their values are listed in Table I. A value for $r_f \cong 0.053$ cm in the 5722 diode at 2390°K can be estimated from Fig. 3 for an average thermal energy $V_e = 0.21$ ev. For potassium ions, the calculated time of flight from r_m to r_f and back is 0.7 μsec, which corresponds to the expected separation between the first and second peaks and agrees very closely with the observed time of 0.6 μsec. To estimate the time separation between the second and third peaks, it is also necessary to calculated the transit time from r_m to r_o and back. This time is in the order of 0.15 μsec. However, because of the peak width, this would not be resolved and one would expect only a broadening and enhancement of the second peak. The third peak would occur after another flight from r_m to r_f and back (0.7 μsec). For those ions which strike the filament after traversing the field, the expected time necessary for re-evaporation is less than 10^{-7} sec,[9] and therefore would not radically change the peak-to-peak times.

The number of additional electrons reaching the collector resulting from the presence of a single positive ion in the space charge is in the order of t_+/t_e, where t_+ is the time the positive ion remains effective in lowering the barrier and t_e is the transit time of the electron across the diode.[2] For the 5722 under the space charge limited conditions of the present experiments, t_e is ca. 1.7×10^{-9} sec as calculated from Wheatcroft's equations.[7,8] The maximum value of t_+ corresponding to the average lifetime of the ion in the tube can be estimated from the average traverse time between peaks and the number of peaks observed, and is the order of 4×10^{-6} sec. This value is also consistent with the positive ion escape mechanism given below. The resulting amplification factor is about 2×10^3 electrons per positive ion. Experimentally, the largest positive ion pulses contained about 10^6 ions while the largest electron pulses consisted of about 10^8 electrons, giving an observed factor of 10^2. This lower factor suggests that the effectiveness of the positive ion in lowering the barrier is a function of its position in the space charge and the overall amplification represents a weighted average of the times spent in regions of high and low efficiency.

In addition, it must be remembered that this estimate of the amplification factor assumes that the positive ion density is so low as to constitute only a minor perturbation on the electron space charge density. That this is not the case may be seen from the following considerations. The initial source of the positive ion burst is contained in very small emitting area ($<10^{-12}$ cm^2).[3] If one were to assume free two dimensional flow over the surface at a thermal velocity of 10^5 cm/sec for an estimated residence time of 10^{-8} sec,[9] the average emitting area would be 3×10^{-6} cm^2. At the peak intensity of an average positive ion burst, about 10^5 ions are emitted per μsec with a mean thermal velocity of 10^5 cm/sec. If all the ions came off normal to the emitting area,[10] a positive ion density of 3×10^{11} ions/cm^3 would be obtained. That this ion density is more than sufficient to neutralize the electron space charge density may be demonstrated by calculating ρ_m, its approximate value at the potential minimum, by means of an equation which can be derived from relations given by Wheatcroft[7]

$$\rho_m = \frac{6.28\times10^{15} I_e \exp(\ln r_m/r_c - V_m\epsilon/kT)}{r_m l(2\pi kT/m)^{\frac{1}{2}}},$$

where I_e is the total emission current, l is the filament length, and m and ϵ are the mass and charge of the electron. From this equation, a value of $\rho_m = 4\times10^9$ electrons/cm^3 is obtained. Although the effect of the positive ion excess would be to deplete the electron space charge in neighboring areas, thereby increasing the collector current, the amplification per positive ion in this case may be less than that expected for the isolated positive ion. Such a "saturation" effect may be inferred from Fig. 1 in that the apparent amplification is less at the beginning of the pulse than in the trailing edge.

[7] E. L. E. Wheatcroft, J. Inst. Elec. Engrs. (London) **86**, 473 (1940).

[8] E. L. E. Wheatcroft, J. Inst. Elec. Engrs. (London) **87**, 692 (1940).

[9] S. Datz and E. H. Taylor, "Some applications of molecular beam techniques to chemistry" in *Recent Research in Molecular Beams*, edited by I. Estermann (Academic Press, Inc., New York, 1959), pp. 166–167.

[10] Although the thermal velocities would be expected to have cosine distribution with respect to a normal to the surface, resulting in a decrease in density, the radial form of the accelerating field and the small distance involved (from r_o to r_m) makes this attenuation negligible in this approximation.

Of the possible mechanisms for the loss of the ions from the region of interest, those requiring charge exchange, gaseous recombination, or collisions seem not to be feasible upon consideration of the cross sections for such processes. Since the ionization efficiency for potassium on tungsten at this temperature is about 0.75,[5] some attenuation of ions should occur every time part of the ion burst strikes the filament. However, the principal loss mechanism appears to be that of drift through the open ends of the collecting region. The impetus for this drift is simply the randomly oriented thermal velocity component imparted to the particle upon leaving the surface. Thus, a particle whose thermal velocity component is directed at 45° to the surface will travel a distance of $2r_f$ toward the open end of the tube in each cycle. In the 5722, an ion starting from a burst at the center of the collector region would require about five such displacements to escape, in good agreement with the observed number of peaks in a typical burst.

Contrary to the supposition of Lindemann and van der Ziel, it is not necessary to postulate an extremely short positive ion pulse to account for the observed shape of the anomalous flicker pulses. In Fig. 4 is a demonstration of the synthesis of an anomalous flicker pulse from a positive ion burst of the shape indicated by curve A. The ordinate on the left represents the flux, in arbitrary units, of positive ions through a cylinder of radius r_m at the time t where the zero time is that at which the first ions of the burst reach r_m. After reflection at r_f, the leading ions will add to the flux of those going through r_m for the first time and the total flux will peak again, as indicated by curve B. Subsequent peaks are generated in a similar manner. The electron pulses, one of which is illustrated by the dashed line in Fig. 4, then mirror this positive ion flux through the region of maximum space charge, with the peaking damped by the dispersion and loss of the ions.

The oscillatory behavior was also observed in the surface ionization gauge, but, due to the difference in space charge distribution and electrode geometry, the pulse shapes were considerably modified. Thus, at 2390° in the SIG, the space charge density at the maximum is much less and it's spatial distribution is more diffuse. The effect of these conditions may be seen in Fig. 2(a), in which the second peak is barely discernable. The peaking becomes much more pronounced when the space charge density is increased by raising the temperature to 2625° [Fig. 2(b)]. The peak-to-peak times, which are some ten times greater than those observed in the 5722,

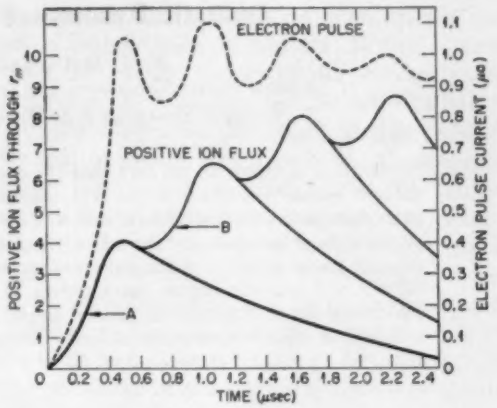
ELECTRON PULSE
POSITIVE ION FLUX
B
A
POSITIVE ION FLUX THROUGH r_m
ELECTRON PULSE CURRENT (μa)
TIME (μsec)
0 0.2 0.4 0.6 0.8 1.0 1.2 1.4 1.6 1.8 2.0 2.2 2.4
0 1 2 3 4 5 6 7 8 9 10
0 0.1 0.2 0.3 0.4 0.5 0.6 0.7 0.8 0.9 1.0 1.1

FIG. 4. The generation of an anomalous flicker electron pulse, dashed curve, by a burst of positive ions. Curve A represents the flux of positive ions going through a cylinder of radius r_m for the first time, while curve B and subsequent curves represent the increased in flux through r_m caused by ions which have been reflected and are crossing r_m for the second, third, and subsequent times.

can be anticipated from time-of-flight calculations, since the distance is also ten times greater. In addition, an estimate of escape time based on the same mechanism given above for the 5722 would predict the formation of only two peaks in the electron pulse. Numerical values for the characteristic parameters of the two diodes are given in Table I.

CONCLUSIONS

A mechanism has been proposed to correlate the emission of positive ion pulses from a tungsten filament and their subsequent oscillation in the space charge region with the resultant transmission of electrons. The mechanism appears to adequately explain the observed electron pulse shape, peak-to-peak times, total number of peaks, amplification factor, and escape probability. The results may find application in the use of "Kingdon cage"[11] detectors for molecular beams in which the effect will be a major contributor to the noise background, and in work on space charge neutralization in diodes.

ACKNOWLEDGMENT

The authors wish to thank Mr. R. H. Dilworth for his contribution to the instrumentation and for his many helpful discussions concerning this investigation.

[11] I. Estermann and O. Stern, Z. Physik 85, 135 (1933).

Acoustic Resonance in Solid Propellant Rockets*

F. T. McClure, R. W. Hart, and J. F. Bird
Applied Physics Laboratory, The Johns Hopkins University, Silver Spring, Maryland
(Received November 5, 1959; revised manuscript received January 25, 1960)

Attention is drawn to the fact that the solid propellant must, in general, be considered as one of the acoustic media in a rocket motor. The viscoelastic properties of the solid along with those of the burned gases determine the characteristic modes of the system corresponding to the particular boundary conditions imposed on these media by the metal components. In addition, these properties of the media contribute strongly to the selection of the regions of stability and instability of the system and therefore to the intermittent and sporadic nature characteristic of resonant burning in solid propellant motors. Calculations are carried out to illustrate the general nature of the phenomenon, and the relationship of these studies to a variety of experimental observations is discussed.

I. INTRODUCTION

DESPITE the considerable activity in the field of solid propellant combustion instability, such phenomena remain as one of the more important and least understood aspects of combustion since the advent of modern solid fuel rocketry.[1] In general, it is evident that a rocket chamber (cf. Fig. 1) comprises an acoustic cavity containing a reacting surface which is frequently capable of amplifying small pressure disturbances.[2,3] If the acoustic losses are sufficiently small in one or more frequency intervals, these frequency components are reinforced and acoustic oscillation in the cavity results. As would be expected, it is found empirically that many of the frequencies at which such oscillations occur correspond closely to acoustic normal modes of the gas filled part of the chamber. However, it is also found that these modes typically appear, disappear, and reappear, etc. with (burning) time forming an intricate and rather haphazard pattern which is difficult to reproduce from one experiment to the next. Apparently, the root of this intermittent behavior lies in cavity geometry, which alone appears strongly sensitive to time, but its explanation has remained an important challenge to theory. Our principal concern here is with furthering the development of the theory at least to the point where it is capable of predicting and describing this *apparently* sporadic behavior.

In principle, a theoretical analysis of acoustic instability should consist in first obtaining expressions for the acoustic fields in the burning zone, as well as in the gas and solid phase regions, and second, in determining and applying proper boundary conditions at all boundaries. But it will immediately be recognized that an exact treatment, including all effects of the spatially nonhomogeneous flow field and the highly complex chemical reactions, faces formidable difficulties. It is possible to circumvent some highly complicating features by taking advantage of the fact that, insofar as its acoustic properties are concerned, the chamber may be regarded as consisting of two regions, the solid and the gas, which are separated by a transition zone which is extremely thin compared with the wavelength of sound.[4] By collapsing this region, the analysis of the acoustic problem is separated conceptually into two parts, namely: 1. The acoustic interaction with a burning propellant, whose solution would supply the boundary equations connecting the sound field at the interface between the solid and the gas regions, and 2. The sound field itself, including the determination of its stability or instability.[5]

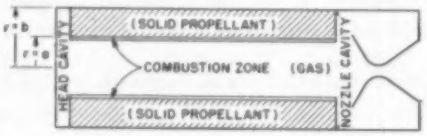

FIG. 1. Schematic representation of solid propellant rocket.

Attention previously has been devoted to both of these problems. With respect to problem 1, it now appears that the pressure (rather than the velocity) variation at the burning surface is usually the primary cause of amplification. It is to be expected that the burning region will be capable of acoustic amplification of pressure disturbances over a wide range of frequencies and a wide range of physical circumstances.[2] Furthermore, the amplification factor ordinarily should be insensitive to minor fluctuations in the environment; therefore, it appears unlikely, that the explanation of the observed erratic behavior lies buried in problem 1.

With respect to problem 2, attention previously has been devoted entirely to the gas filled portion of the chamber, with the solid propellant itself regarded as incompressible. Even with this simplification, the modes

* This work supported by the Bureau of Ordnance, Department of the Navy.
[1] E. W. Price, Astronautica Acta **V**, 63–72 (1959).
[2] R. W. Hart and F. T. McClure, J. Chem. Phys. **30**, 1501–1514 (1959).
[3] J. Bird, L. Haar, F. T. McClure, and R. W. Hart, J. Chem. Phys. **32**, 1423 (1960).
[4] At typical rocket chamber pressures, for example, the thickness of the reaction region is believed to be of order 10^{-4} to 10^{-2} cm, compared with the wavelength of sound at, say, 10^{4} cps, which is approximately 10 cm.
[5] While problems 1 and 2 are not entirely independent analytically, because the burning rate is modified to some extent by the compressibility and thermal expansion coefficient of the solid phase, their effect on problem 1 is calculated to be ordinarily less than 10%, at least for pressures less than ~70 atm (see footnote 3).

are difficult to obtain exactly, partly because of the nonisotropic mean gas flow, and partly because of the complexities introduced by the head and nozzle cavities (cf., Fig. 1). However, it seems likely and has generally been accepted that, at least insofar as frequency is concerned, the normal modes of the gas filled chamber are approximated adequately by neglecting the flow field, and that nozzle losses can be approximated by assigning an appropriate (scalar) impedance to the port plane. An approximate calculation of such a port impedance apparently has been published only for the axial cavity modes, but both experimental and elementary theoretical considerations tend to support this view. However, the important effect of the nozzle cavity as a low pass acoustic filter has apparently escaped notice.

Let us consider the assumption that the solid is incompressible. Although this may appear very plausible at first glance, since the solid is much less compressible than the gas, it must be examined critically because it is the pressure amplitude at the *burning surface* which is amplified. One sees that this assumption would place a velocity node (i.e., pressure maximum) at the most strategic point in the entire cavity. If the solid is able to share in the acoustic motion to the extent that the pressure maximum is significantly displaced from the propellant surface, the amplification would thereby be reduced, and stability enhanced. In such an event, it is possible that large amplification factors would occur only in such frequency regions for which a velocity node for the composite (solid-gas) system lies near the burning surface. Since the dimensions of the gas and solid filled portions of the cavity change with burning time, we may possibly have an orderly cause of intricate and erratic appearing phenomena.

The concept of a velocity node at a solid-gas interface is ordinarily a valid one, because the velocity of sound is ordinarily very much greater in solids than in gases. The velocity of propagation of elastic waves in solid propellants is not customarily measured, but may readily be estimated in the usual way from Young's modulus data.[6] This velocity is found to be relatively low and indeed comparable to that of the gas. From a theoretical point of view, then, it seems essential that, in contrast to the customary picture of a gas filled cavity having for its boundaries the surface of the powder and the end faces of the casing, we should now consider an acoustic cavity having as its boundaries the entire surface of the casing, and filled with two media—the gas and the solid.

Before proceeding with a lengthy theoretical analysis, it would clearly be reassuring to possess some direct experimental evidence of the two-part (solid and gas) nature of the acoustic problem. One of the consequences of the present concept is quite striking, namely that the acoustic modes of the cavity will strongly depend on whether the powder is in contact with the wall of the chamber or not. In fact, one must discuss several degrees of intimateness of contact. Is the contact so poor that the outside surface of the powder is able to move freely in the axial direction?—in the radial direction?—in the tangential direction? Are the ends of the powder free to move? The answers to these questions determine what kind of axial, radial, or tangential modes the solid propellant can support. Since the propellant is simply one of the media of the chamber, these answers also make a similar determination for the system as a whole. Because of the high density of the solid relative to the gas, it turns out that a few thousandths of an inch clearance (at high frequencies) makes a complete change in some of these boundary questions, and therefore, in the location of the pressure nodes within the cavity. As a result, we expect that the exact nature of the mounting of the grain in the chamber could be very important in determining the properties of the system.

In particular, the thought that a small clearance between the (inhibited) outer surface of the solid propellant and the chamber wall should exert a major influence on the resonance properties can be readily verified by experiment. In fact, a group of such definitive experiments has recently been performed which dramatically confirms these concepts.[7] In summary, both theoretical and experimental considerations now appear to force the treatment of the solid propellant as a participating element in the acoustic motion.

II. FORMULATING THE PROBLEM

In order to make the problem tractable, we find it necessary to treat a model for which the gas and solid have highly idealized acoustic properties. Although the bridging equations which connect the acoustic fields at the two "sides" of the burning surface may readily be formulated in general, it would seem inappropriate not to take advantage also of simplifications in this area, when it appears that they can be accomplished without serious error.

1. Gas Region

We shall begin by confining our attention to the central chamber cavity. The nozzle cavity is regarded as a low pass acoustic filter, which tends to isolate the central cavity from acoustic loss via the throat, except near the end of burning when this filter vanishes. The theory of such a filter, including the mean flow field, is a problem which we do not want to investigate in detail in this paper. Accordingly, we shall ignore nozzle losses entirely and regard the port plane as a perfect sound reflector. We will also ignore the head cavity, although the occasional ringing of such a cavity may, in reality, contribute to the observed phenomena.

[6] R. Houwink, *Elasticity, Plasticity, and Structure of Matter* (Dover Publishing Company, New York, 1953), p. 231.

[7] T. Angelus, presented at the panel session on Unstable Burning; the American Rocket Society Solid Propellants Conference, January 28–29, 1960.

With respect to the differential equations for the sound field in the gas, we shall regard the gas as isotropic, neglecting any residual chemical reactions persisting outside the immediate neighborhood of the burning surface. Since the stationary state flow field is ordinarily at small Mach number (usually $<\frac{1}{10}$), we also neglect its effect on the acoustic field. Since inhomogeneities ordinarily increase losses, it may be supposed that the principal effect of these approximations is to underestimate losses by an amount which is expected to increase with decreasing sound wavelength. In general, the propagation constant k of the gas is complex, with an imaginary part $i\alpha^1$ accounting for absorption.[8] The acoustic pressure p and particle velocity $\mathbf{u}$ in the gas satisfy the familiar relationships

$$(\nabla^2+k^2)p=0, \tag{2.1a}$$

$$\mathbf{u}=[(1/-i\omega\rho)-(2\alpha^1 c/\rho\omega^2)]\nabla p, \tag{2.1b}$$

where ρ is the (mean) gas density, ω the angular frequency, and

$$k=\omega/c=(\omega/c^0)-i\alpha^1, \tag{2.1c}$$

where $c^0=(\gamma\bar{P}/\rho)^{\frac{1}{2}}$, $\bar{P}$ the mean gas pressure, and γ the specific heat ratio of the gas. The index, α^1, is the reciprocal absorption length characteristic of gas phase damping.

2. Solid Region

While we shall treat the solid as a homogeneous medium there still remain the well-known unsolved difficulties associated with the general elastic motion of thick cylindrical shells. These are of two kinds: (1) analytical, in that for not all boundary conditions are separable solutions of the equation of motion possible; (2) numerical, in that even when separable solutions do exist, the amount of computation required is large. With the aid of modern high-speed computing devices, however, difficulty (2) is greatly alleviated, so in this work, we shall only need to avoid encountering nonseparability.

The displacement $\mathbf{S}$ satisfies the usual differential equation[9]

$$c_d^2 \text{ grad div}\mathbf{S}-c_s^2 \text{ curl curl}\mathbf{S}+\omega^2\mathbf{S}=0, \tag{2.2a}$$

where we have used the time dependence $\exp(i\omega t)$, and where c_d is the velocity of propagation of waves of dilation ("longitudinal"), and c_s is the velocity of propagation of waves of distortion ("shear"); in general, both of these velocities are complex because of viscoelastic losses.

If in fact, λ^+, μ^+ are the usual (real) Lamé moduli, and if λ^1, η are the coefficients of expansive friction and shear viscosity, respectively, we have

$$c_d^2=\frac{(\lambda^++2\mu^+)+i\omega(\lambda^1+4\eta/3)}{\rho_s}, \tag{2.2b}$$

and

$$c_s^2=(\mu^++i\omega\eta)/\rho_s, \tag{2.2c}$$

and the complex Lamé moduli λ and μ are

$$\lambda=\lambda^++i\omega\lambda^1-(2i\omega\eta/3), \tag{2.2d}$$

and

$$\mu=\mu^++i\omega\eta. \tag{2.2e}$$

3. Boundary Conditions at the Outer Surface of the Propellant ($r=b$)

With respect to the conditions to be applied to the displacement vector ($\mathbf{S}$) and stress tensor ($\mathbf{P}$) at ($r=b$), we shall consider in detail only three cases, involving various tightnesses of fit. In each case the chamber wall itself will be regarded as rigid (perhaps thick steel).

Case A. Here, we consider a propellant "case-bonded" to a rigid chamber wall, so that both tangential and radial displacements are zero, i.e.,

$$\mathbf{S}=0 \quad \text{at} \quad r=b. \tag{2.3a}$$

This boundary condition requires the existence of shear waves, so that elementary "sound wave" theory (scalar pressure) is not directly applicable.

Case B. Here, we again consider a tight fit at a rigid chamber wall, but let the surfaces be ideally smooth, so that no tangential tractions are exerted, i.e., a "supported" boundary, where

$$(\mathbf{S}\cdot\hat{\mathbf{r}})=(\mathbf{P}\cdot\hat{\mathbf{r}})\times\hat{\mathbf{r}}=0 \quad \text{at} \quad r=b, \tag{2.3b}$$

where $\hat{\mathbf{r}}$ is the unit vector in the radial direction.

Case C. Finally, let the propellant fit sufficiently loosely that its outer surface is separated from the chamber wall by a cylindrical shell of gas of uniform thickness s. By our assumption that the gas exerts only a normal pressure, we have zero tangential traction

$$(\mathbf{P}\cdot\hat{\mathbf{r}})\times\hat{\mathbf{r}}=0 \quad \text{at} \quad r=b, \tag{2.3c}$$

while for the normal components of stress and displacement at this surface, continuity of normal force and velocity across $r=b$ requires

$$p=-(\mathbf{P}\cdot\hat{\mathbf{r}})\cdot\hat{\mathbf{r}}, \quad \text{at} \quad r=b, \tag{2.3d}$$

and

$$\mathbf{u}\cdot\hat{\mathbf{r}}=i\omega\mathbf{S}\cdot\hat{\mathbf{r}}, \quad \text{at} \quad r=b. \tag{2.3e}$$

Finally, the ratio of radial velocity to acoustic pressure at $r=b$ is to be expressed in terms of the admittance presented to the solid by the layer of gas.

4. Boundary Conditions at the Inner Surface of the Propellant ($r=a$)

Here, we are concerned with the equations which bridge the combustion zone, and connect the acoustic

[8] Since only sinusoidal time dependence need be treated in a linearized analysis, all time derivatives are replaced by $i\omega$, and it is understood that real parts of the dependent variables correspond to the physical quantities.

[9] W. P. Mason, *Physical Acoustics and the Properties of Solids* (D. Van Nostrand Company, Princeton, New Jersey, 1958), p. 14; or P. Morse and H. Feshbach, *Methods of Theoretical Physics* (McGraw-Hill Book Company, Inc., New York, 1953), p. 142.

field in the burned gas with the elastic motion in the homogeneous solid. The region to be bridged is depicted schematically in Fig. 2. On the one side of the zone, the solid propellant is essentially at ambient temperature T_c, while on the other side, the gaseous products of combustion are essentially at the asymptotic flame temperature T_f.

If it were not for the transpiration of solid to gas, we would entirely ignore the small thickness of the transition region between T_c and T_f, recognizing that its effects would then be indistinguishable from errors in cavity radius of the same order of magnitude as the thickness of the transition region. However, the existence of transpiration alters the relative phase of velocity and pressure, and thereby introduces a net energy flux which is vital to the question of stability.

The effect of transpiration on the pressure is in fact negligible because of the extremely small pressure increments associated with the mass transport. We shall identify the pressure at T_c with that at T_f; i.e., we require

$$(\mathbf{P}\cdot\hat{\mathbf{r}})\times\hat{\mathbf{r}}=0, \quad (\text{at } r=a), \tag{2.4a}$$

which is the condition for no tangential traction (shear) at the solid surface, and

$$-(\mathbf{P}\cdot\hat{\mathbf{r}})\cdot\hat{\mathbf{r}}=p, \quad \text{at} \quad r=a, \tag{2.4b}$$

which is the requirement that the normal pressure on the solid surface be equal to the gas pressure.

We next derive the relationships between the (incremental) radial particle velocities on the gas (u_f) and solid (u_a) sides, respectively. The flow field in the gas phase region is the province of what was termed in the introductory section "problem 1," and we may assume that the solution of this problem is available to us in the present treatment of acoustic amplification in a cavity. Therefore, in the notation of footnote (2), the fractional increment in (radial) mass flow is

$$\mu=\delta v/\bar{v}+\delta\rho/\bar{\rho}, \tag{2.4c}$$

where v is radial particle velocity relative to the moving solid-gas interface, and bars denote time average values. (All radial velocities positive if directed in the positive r direction.) Thus, if V_0 is the surface velocity in the laboratory system,

$$u=\delta v+\delta V_0.$$

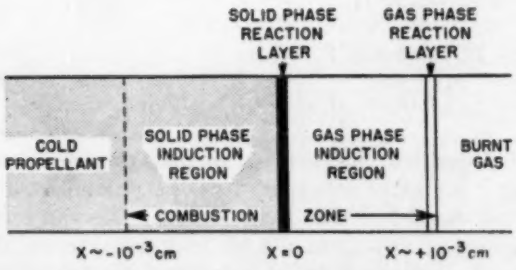

FIG. 2. Schematic representation of combustion zone of the solid propellant.

We apply Eq. (2.4c) twice, first on the homogeneous gas side, where $T=T_f$, and second, at the unreacted (but heated) solid surface, where $T=T_{0s}$. If we multiply the first by $\bar{v}_f$, and the second by $-\bar{v}_{0s}=\bar{V}_0$, the mean surface regression speed, we obtain

$$u_f-u_{0s}=\bar{v}_f\left(\mu_f-\frac{\epsilon}{\gamma}\right)+\bar{V}_0\left[\mu_{0s}-\frac{\delta\rho_{0s}}{\bar{\rho}_{0s}}\right], \tag{2.4d}$$

where $\epsilon=p/\bar{P}$ evaluated at $r=a$. Of course, the functions μ_f and μ_{0s} and $\delta\rho_{0s}/\bar{\rho}_{0s}$ are to be obtained from the time dependent solution of problem 1. Such solutions have been found only for sufficiently fast gas phase reactions that the thickness of the region between ignition and essentially complete reaction is very much smaller than the induction region. In that case, μ_f and μ_1 become equal. For the cases of interest, the mean surface regression speed is much less than the speed of the burned gases ($\sim 1/100$) so that the second term on the right-hand side of Eq. (2.4d) may be dropped (from footnote 2, μ_1/ϵ and μ_{0s}/ϵ are typically of order unity; $\delta\rho_{0s}/\bar{\rho}_{0s}$ is somewhat smaller than this for propellants of typical compressibilities).

Finally, we must complete the bridge by spanning the induction region in the solid. But no transpiration occurs in this region, so that insofar as the sound field is concerned, we may collapse it entirely—with an ignorable error equivalent to that introduced by an incorrect determination of the thickness of the solid by an amount of the same order as that of the solid phase induction region, say 10^{-3} cm. We shall approximate Eq. (2.4d) by

$$u_f-u_a=\bar{v}_f[\mu_1-(\epsilon/\gamma)]. \tag{2.4e}$$

5. Boundary Conditions at Propellant End-Faces

In this paper we shall carry out detailed calculation only for modes having no axial component, i.e., for an infinitely long cylindrical system. Actually, the equations may be separated for the case of supported ends on a finite cylinder, and for completeness the boundary equations for this case are included in this section.[10]

(*a*) *Infinite length—no axial modes.* In many rocket firings it is apparent that axial modes of oscillation are not predominant. As an approximation to this state of affairs, we may treat an infinitely long cylindrical system. We then require no axial dependence of $\mathbf{S}$, i.e., $\partial\mathbf{S}/\partial z=0$.

(*b*) *Finite length with supported end-faces.* In this case we suppose that the two ends of the cylinder fit tightly against an inflexible but frictionless surface. Then, we must require

$$\mathbf{S}\cdot\hat{\mathbf{z}}=(\mathbf{P}\cdot\hat{\mathbf{z}})\times\hat{\mathbf{z}}=0 \quad \text{at} \quad z=0,L. \tag{2.5}$$

[10] The solution for finite length requires the solution of a 6×6 determinantal system as against a 4×4 for infinite length and the additional computation does not seem necessary to illustrate the phenomenon.

We have now completed our specification of boundary conditions.

Before proceeding to the formal solution of the problem we have set, it is worth noting that, despite the many assumptions and approximations we have made, we are left with an extremely complicated physical model. In brief, we are proposing to solve for the acoustic modes of a cylindrical cavity which contains a gas surrounded by a thick shell of elastic solid. This thick shell, for which we will consider waves of distortion as well as dilation, is bounded outside by an inflexible casing which either supports it, or clamps it, or is separated from it by a blanket of gas. At the inner surface of the solid cylindrical shell we have introduced a thin combustion zone in which solid-gas phase change and chemical energy release occur. Finally, we plan to discuss the stability of the oscillation modes of this entire system as determined by the balance between acoustic amplification at the combustion zone and attenuation of sound in the solid and the burned gas.

Thus, despite our simplifications, we are left with a somewhat exotic model, which apparently retains many of the important features of the actual physical situation in a rocket chamber. We have the further satisfaction that none of the features retained turns out to have a trivial effect.

III. FORMULATING THE SOLUTION

As formulated in the previous section, the present analysis differs from the conventional rocket acoustics primarily in that the acoustic pressure is not arbitrarily assumed to have a maximum at the burning surface. Instead, the acoustic field (in the entire chamber containing both solid and gas) is to be determined by analysis. The transpiring boundary condition itself will be formulated in terms of an impedance condition and the resultant acoustic field analyzed by small loss perturbation analysis, after the method of Grad[11] and Cheng.[12] But, as would now be expected, the elastic motion of the solid introduces substantial new difficulties, which force us to a more elaborate analysis.

It has already been indicated that the formal solution of the fundamental elastic equations for a cylindrical shell can be obtained, provided only that the boundary conditions permit separable characteristic functions. Nevertheless, it will appear that there are important conceptual advantages to be gained (as well as a saving in machine time), by taking advantage of the smallness of the absorption and pyrolysis terms, in order to obtain an approximate solution of a general nature, rather than an exact solution for a specific set of conditions. Accordingly, we shall regard pyrolysis and viscosity as perturbing influences, retaining only their first order effects. We begin by formulating the zero-order (no loss, no pyrolysis) case.

1. Elastoacoustic Modes in the Absence of Losses and Pyrolysis

The principles of the method of solution of the elastic problem are well known, so that the details need not be reproduced here. We shall merely summarize the method in the process of displaying the solutions for the several cases considered.

For cylindrical geometry, the characteristic solutions in the gas region are evidently:

For the acoustic pressure

$$p_{m,k,h}=e^{i\omega t}p_0\cos(m\phi)\cos(hz+\psi)J_m(\alpha r), \quad (3.1a)$$

and for the radial component of the particle velocity, (cf., Eq. 2.1b),

$$u_{m,k,h}=\frac{\omega p_0[1-(h^2/k^2)]e^{i\omega t}}{-i(c^0)^2\alpha\rho_f}\times\cos(m\phi)\cos(hz+\psi)J_m'(\alpha r),$$

where

$$\alpha=(k^2-h^2)^{\frac{1}{2}}, \quad (3.1b)$$

m is an integer, and the characteristic values of k and h, as well as the amplitude p_0 and the axial phase angle ψ, are yet to be determined. In the following, the subscripts on p and u will be suppressed in order to simplify the notation. The normal admittance $\mathbf{Y}_m(a)\equiv(-u/p)_a$ presented by the gas to the solid is readily obtained from Eq. 3.1b

$$\mathbf{Y}_m(a)=\frac{\omega[1-(h^2/k^2)]}{+i\alpha(c^0)^2\rho_f}\frac{J_m'(\alpha a)}{J_m(\alpha a)}. \quad (3.1c)$$

The normal acoustic impedance to be associated with the m'th "tangential" mode at the outer surface of the solid will be denoted by $\mathbf{Y}_m(b)=(u/p)_{r=b}$. A routine calculation shows that for the case of a rigid chamber wall, separated from the propellant by a thin cylindrical shell of thickness s,

$$\mathbf{Y}_m(b)=\frac{1}{-i\rho_b c_b}\left\{\frac{Y_m'[K(b+s)]J_m'(Kb)-J_m'[K(b+s)]Y_m'(Kb)}{Y_m'[K(b+s)]J_m(Kb)-J_m'[K(b+s)]Y_m(Kb)}\right\}, \quad (3.1d)$$

where $K=\omega/c_b$, ρ_b and c_b are the density and sound velocity in the space between the propellant and the chamber wall. Except at very low frequencies the results will be essentially independent of the parameter s providing it is greater than a few tens of thousandths of an inch and much less than a wavelength. This can easily be verified by expansion of 3.1d. In physical terms, this comes about because the thin layer of gas offers little impedance to the small solid surface motion character-

[11] H. Grad, Comm. Pure Appl. Math. **2**, 79 (1949).
[12] S. I. Cheng, Jet Propulsion **24**, 27–32 and 102–109 (1954).

istic of high frequency modes. Thus, in the actual calculations for the unsupported grains reported here, we have used the "free" boundary condition.

If we take advantage of the fact that the radial velocities are required to satisfy the impedance condition for every ϕ and z at the inner surface, we can identify the tangential and axial wave numbers and the tangential and axial phases in the solid with those in the gas. With this simplification, the characteristic solutions for the particle displacement in the solid become,[13]

$$S_r=+\frac{i\alpha_1 e^{i\omega t}}{k_c}\cos(hz+\psi)\cos(m\phi)\left\{A_1J_m'(\alpha_1 r)+A_2Y_m'(\alpha_1 r)+\frac{mk_c}{k_s\alpha_1 r}[B_1J_m(\alpha_2 r)+B_2Y_m(\alpha_2 r)]\right.$$
$$\left.-\frac{ihk_c\alpha_2}{k_s^2\alpha_1}[C_1J_m'(\alpha_2 r)+C_2Y_m'(\alpha_2 r)]\right\}, \quad (3.2a)$$

$$S_\phi=-\frac{ime^{i\omega t}}{k_c r}\cos(hz+\psi)\sin(m\phi)\left\{A_1J_m(\alpha_1 r)+A_2Y_m(\alpha_1 r)+\frac{k_c}{k_s}\frac{\alpha_2 r}{m}[B_1J_m'(\alpha_2 r)+B_2Y_m'(\alpha_2 r)]\right.$$
$$\left.-\frac{ihk_c}{k_s^2}[C_1J_m(\alpha_2 r)+C_2Y_m(\alpha_2 r)]\right\}, \quad (3.2b)$$

$$S_z=\frac{-ihe^{i\omega t}}{k_c}\sin(hz+\psi)\cos(m\phi)\left\{A_1J_m(\alpha_1 r)+A_2Y_m(\alpha_1 r)+\frac{ik_c}{h}\left(1-\frac{h^2}{k_s^2}\right)\left[C_1J_m(\alpha_2 r)+C_2Y_m(\alpha_2 r)\right]\right\}, \quad (3.2c)$$

where

$$\alpha_1^2=k_c^2-h^2, \quad \alpha_2^2=k_s^2-h^2, \quad k_c^2=\frac{\omega^2}{c_d^2}, \quad k_s^2=\frac{\omega^2}{c_s^2},$$

and the amplitudes $A_{1,2}$, $B_{1,2}$, $C_{1,2}$, and the axial phase angle ψ and wave number h are yet to be determined.

The normal pressure $-P_{rr}$ and the azimuthal and axial tractions $P_{r\phi}$, P_{rz} on a radial face are given by

$$P_{rr}=-\frac{i\alpha_1 2\mu e^{i\omega t}}{k_c r}\cos(hz+\psi)\cos(m\phi)\left\{A_1j_r(\alpha_1 r)+A_2y_r(\alpha_1 r)+\frac{k_c}{k_s}\frac{\alpha_2}{\alpha_1}[B_1j_1(\alpha_2 r)+B_2y_1(\alpha_2 r)]\right.$$
$$\left.+\frac{ik_ch}{k_s^2}\frac{\alpha_2}{\alpha_1}(\alpha_2 r)\left[C_1J_m''(\alpha_2 r)+C_2Y_m''(\alpha_2 r)\right]\right\}, \quad (3.3a)$$

$$P_{r\phi}=+\frac{2\mu i\alpha_1 e^{i\omega t}}{k_c r}\cos(hz+\psi)\sin(m\phi)\left\{A_1j_1(\alpha_1 r)+A_2y_1(\alpha_1 r)+\frac{k_c}{k_s}\frac{\alpha_2}{\alpha_1}[B_1j_\phi(\alpha_2 r)+B_2y_\phi(\alpha_2 r)]\right.$$
$$\left.-\frac{ihk_c\alpha_2}{k_s^2\alpha_1}\left[C_1j_1(\alpha_2 r)+C_2y_1(\alpha_2 r)\right]\right\}, \quad (3.3b)$$

and

$$P_{rz}=\frac{-i\alpha_1 2\mu he^{i\omega t}}{k_c}\sin(hz+\psi)\cos(m\phi)\left\{A_1J_m'(\alpha_1 r)+A_2Y_m'(\alpha_1 r)+\frac{mk_c}{2\alpha_1 k_s r}[B_1J_m(\alpha_2 r)+B_2Y_m(\alpha_2 r)]\right.$$
$$\left.-\frac{ihk_c\alpha_2}{\alpha_1 k_s^2}\left(1-\frac{k_s^2}{2h^2}\right)[C_1J_m'(\alpha_2 r)+C_2Y_m'(\alpha_2 r)]\right\}, \quad (3.3c)$$

where

$$j_1(x)=m\left[\frac{J_m(x)}{x}-J_m'(x)\right], \quad (3.3d)$$

$$j_r(x)=J_m'(x)+xJ_m(x)\left[1+\frac{(\lambda/2\mu)(k_c r)^2-m^2}{x^2}\right], \quad (3.3e)$$

$$j_\phi(x)=J_m'(x)+xJ_m(x)\left(\tfrac{1}{2}-\frac{m^2}{x^2}\right), \quad (3.3f)$$

and the y functions similar but with $J_m\rightarrow Y_m$.

[13] P. M. Morse and H. Feshbach, loc. cit., p. 1840.

The normal pressure and tangential tractions on an end face are given by[13]

$$P_{zz}=-\frac{2\mu ih^2e^{i\omega t}}{k_c}\cos(hz+\psi)\cos(m\phi)\left\{\left[1+\frac{\lambda k_c^2}{2\mu h^2}\right]\times[A_1J_m(\alpha_1 r)+A_2Y_m(\alpha_1 r)]+\frac{ik_c}{h}\left[\frac{k_s^2-h^2}{k_s^2}\right][C_1J_m(\alpha_2 r)+C_2Y_m(\alpha_2 r)]\right\}, \quad (3.4a)$$

$$P_{z\phi}=\frac{2\mu ihme^{i\omega t}}{k_c r}\sin(hz+\psi)\sin(m\phi)\left\{A_1J_m(\alpha_1 r)+A_2Y_m(\alpha_1 r)+\frac{1}{2}\left(\frac{k_c}{k_s}\right)\left(\frac{\alpha_2 r}{m}\right)[B_1J_m'(\alpha_2 r)+B_2Y_m'(\alpha_2 r)]-\frac{ihk_c}{k_s^2}\left[1-\frac{k_s^2}{2h^2}\right][C_1J_m(\alpha_2 r)+C_2Y_m(\alpha_2 r)]\right\} \quad (3.4b)$$

and of course

$$P_{zr}=P_{rz}, \quad (3.4c)$$

where λ and μ are the Lamé elastic moduli, related to c_d and c_s by the familiar relationships

$$c_d=\left(\frac{\lambda+2\mu}{\rho_s}\right)^{\frac{1}{2}} \quad \text{and} \quad c_s=\left(\frac{\mu}{\rho_s}\right)^{\frac{1}{2}}.$$

Let us now consider the explicit evaluation of the remaining six amplitudes $(A_1,A_2,B_1,B_2,C_1,C_2)$, and the axial phase and wave number (ψ and h). Only if the boundary conditions are consistent with separable characteristic functions will these eight constants be sufficient to satisfy the twelve boundary equations—three (scalar) conditions on each of the four faces of the solid.

As has been indicated we shall consider in numerical detail the particularly simple case of infinite length. Setting $h=0$, and $C_1=C_2=0$, therefore, the dimensionality of the problem reduces to two, and the number of boundary conditions and arbitrary constants reduces to four. If we use the boundary conditions stated previously for the radial boundaries [Eqs. (3.1c), (3.1e)], we find the solution to be expressed by

$$0=(P_{r\phi})_{r=a}=A_1j_1(k_ca)+A_2y_1(k_ca)+B_1j_\phi(k_sa)+B_2y_\phi(k_sa) \quad (3.5a)$$

$$0=(iP_{r\xi}\mathbf{Y}_m(a)+\omega S_r)_{r=a}=\{+[2\mu\mathbf{Y}_m(a)/ia][A_1j_r(k_ca)+A_2y_r(k_ca)+B_1j_1(k_sa)+B_2y_1(k_sa)]+\omega[A_1J_m'(k_ca)+A_2Y_m'(k_ca)+(m/k_sa)(B_1J_m(k_sa)+B_2Y_m(k_sa))]\} \quad (3.5b)$$

$$0=[(P_{r\phi}/Z_{b\phi})-Z_{b\phi}\omega S_\phi]_{r=b}=\{[2\mu/bZ_{b\phi}][A_1j_1(k_cb)+A_2y_1(k_cb)+B_1j_\phi(k_sb)+B_2y_\phi(k_sb)]+Z_{b\phi}[\omega m/bk_c[A_1J_m(k_cb)+A_2Y_m(k_cb)]+\omega[B_1J_m'(k_sb)+B_2Y_m'(k_sb)]]\} \quad (3.5c)$$

and

$$0=(-iP_{rr}\mathbf{Y}_m(b)+\omega S_r)_{r=b}=\{+[i2\mu\mathbf{Y}_m(b)/b][A_1j_r(k_cb)+A_2y_r(k_cb)+B_1j_1(k_sb)+B_2y_1(k_sb)]+\omega[A_1J_m'(k_cb)+A_2Y_m'(k_cb)+(m/k_sb)(B_1J_m(k_sb)+B_2Y_m(k_sb))]\}, \quad (3.5d)$$

where $(Z_{b\phi})$ is to be taken infinite for an immobilized surface, and zero for a freely slipping surface. In these equations, $\mathbf{Y}_m(a)$ and $\mathbf{Y}_m(b)$ are to be obtained from Eqs. (3.1c) and (3.1d); $k_c=\omega/c_d$, $k_s=\omega/c_s$. These four simultaneous, homogeneous equations will evidently have a nontrivial solution only if the determinant of the coefficients vanishes. This vanishing condition is the eigenvalue equation for ω, and is already expressed in a form readily handled by machines such as the Univac-1103A.

The configurations of finite length which are both tractable and of real interest correspond to the propellant constrained axially, but not subject to tangential traction, at its ends (cf., Sec. II),

$$S_z=P_{zr}=P_{z\phi}=0 \quad \text{at} \quad z=0, \quad z=L.$$

This configuration can also be handled by the present approach, although one would have to solve six simultaneous equations. After considering the condition $S_z=0$ at $z=0$, $z=L$ and referring to Eq. (3.2c) for the axial velocity, we must require $\psi=0$, and

$$h=l\pi/L, \quad l=0, 1, 2, \cdots.$$

Now considering the tangential tractions P_{zr} and $P_{z\phi}$ on the end faces [Eqs. (3.4b), (3.4c), or (3.3c)] we note that they are also satisfied because of the specification $h=l\pi/L$, so that we have six constants $(A_1,A_2,B_1,B_2,C_1,C_2)$ to satisfy the remaining six boundary equations,

$$(P_{r\phi})_{r=a}=0,$$
$$(P_{rz})_{r=a}=0,$$
$$(-P_{rr}\mathbf{Y}_m(a)+i\omega S_r)_{r=a}=0,$$
$$(P_{rr}\mathbf{Y}_m(b)+i\omega S_r)_{r=b}=0,$$
$$[(P_{r\phi}/Z_{b\phi})-Z_{b\phi}\omega S_\phi]_{r=b}=0,$$
$$[(P_{rz}/Z_{bz})-Z_{bz}\omega S_z]_{r=b}=0,$$

where $Z_{b\phi}=Z_{bz}=0$ for a freely slipping surface and $Z_{b\phi}=Z_{bz}=\infty$ for a clamped surface. These equations could be expressed in terms of the A's, B's and C's by using the general expressions Eqs. (3.2) and (3.3).

2. Pyrolysis and Viscoelastic Losses

It is clear that the acoustic response of the burning surface, as introduced through μ_1/ϵ, and the contributions of the viscosities must be known in order to carry out the determination of the characteristic frequencies exactly. Actually, however, the principal characteristics of the solution may be obtained without explicit knowledge as to the frequency dependence of μ_1/ϵ, by taking advantage not only of the smallness of the losses, but also of the smallness of the coefficient which multiplies the terms involving $(\mu_1/\epsilon)-(1/\gamma)$. The result of this is that the characteristic frequencies are essentially those of the purely elastic system[11,12], while the stability is determined by the net of the gains and losses. For each mode the criterion for instability, written in admittance form, is:

$$\frac{(-\bar{v}_f)}{\rho_f(c^0)^2}\left(\gamma\,\mathrm{Re}\frac{\mu_1}{\epsilon}-1\right)-\mathrm{Re}\left[\mathbf{Y}_m(a)+\left(\frac{i\omega S_r}{-P_{rr}}\right)_a\right]>0. \quad (3.6)$$

where it should be noted that $\bar{v}_f$ is a *negative* number, cf. Eq. (2.4e.)

The evaluation of the real part of μ_1/ϵ is the province of what was termed in the introduction, problem 1, and may be considered performed, for the purposes of the present study. For each mode, the real part of the admittance presented to the burning zone by the gas is readily determined to first order in the absorption (to terms linear in α^1) by expanding Eq. (3.1c) about $\alpha^1=0$. We obtain the positive definite quantity,

$$\text{Real of } \mathbf{Y}_m(a)=\frac{\alpha^1 a}{\rho_f c^0}\left[1-\frac{m^2}{(\alpha^0 a)^2}+\left(\frac{J_m'(\alpha^0 a)}{J_m(\alpha^0 a)}\right)^2\right], \quad (3.7)$$

where

$$\alpha=\left[\left(\frac{\omega}{c^0}-i\alpha^1\right)^2-h^2\right]^{\frac{1}{2}}\approx\alpha^0-i\frac{\omega\alpha^1}{c^0\alpha^0},$$

with

$$\alpha^0\equiv\left(\frac{\omega^2}{(c^0)^2}-h^2\right)^{\frac{1}{2}}.$$

For each mode, the real part of $(i\omega S_r/-P_{rr})_a$ is obtained similarly, by expanding in powers of η,λ^1. To first order,

$$\text{Re of}\left(\frac{i\omega S_r}{-P_{rr}}\right)_a=-\left\{\omega^2\eta\left[\frac{\partial}{\partial\mu}\left(\frac{S_r}{-P_{rr}}\right)-\frac{2}{3}\frac{\partial}{\partial\lambda}\left(\frac{S_r}{-P_{rr}}\right)\right]+\omega^2\lambda^1\frac{\partial}{\partial\lambda}\left(\frac{S_r}{-P_{rr}}\right)\right\}_a. \quad (3.8)$$

Because of the intractable form of the analytic solution, we evaluate the partial derivatives numerically.

IV. APPLICATION OF THE THEORY—A SAMPLE CALCULATION

1. Selection of Parameters

We need merely specify the dimensions, the elastic constants of the media, and the propellant amplification function,

$$\mathrm{Re}\left[\left(\frac{\mu_1}{\epsilon}-\frac{1}{\gamma}\right)\frac{|\bar{v}_f|}{\bar{P}}\right]$$

in order to complete the calculation and apply the results of Sec. III in detail.

The selection of a geometry presents no difficulty. We note that the inner and outer radii (a,b) appear in the combinations $k_c a$, $k_s a$, b/a, $\omega a/c$, so that in the normal course of exploring the burning of a charge $(a\to b)$, we will obtain a sequence of b/a ratios. In the remaining combinations, a is multiplied by frequency, so that scaling is possible. For a specific case, then, we have selected a chamber radius $b=5.75$ cm, containing a charge with initial radius $a=2.87$ cm.

Although both dilatational (c_d) and shear (c_s) velocities are ordinarily not known for propellants, the order of magnitude is readily estimated from Young's modulus and plausible Poisson's ratio. We choose $c_d=7.0\times10^4$ cm/sec, and $c_s=3.1\times10^4$ cm/sec. The velocity of sound (c^0) in the burned gas (molecular wt$\sim$26) at 80 atm, 2500°K is taken to be 10^5 cm/sec.

An estimate of viscosities on the basis of presently available data is subject to more uncertainty. Insofar as the attenuation length (α^1) in the gas is concerned, we must continue to ignore the (possibly large) effects of incomplete chemical reactions on sound absorption. But even if nonreacting, the burned gases constitute an impressive mixture of several gases under conditions of high temperature and pressure, for which the sound absorption has not been measured. It would appear, however, that nitrogen, for example, would be an effective absorber of sound at elevated temperatures (in contrast to room temperature). We shall make a crude estimate of the absorption for a rather typical gas composition containing 10% N. Extrapolating to 2500°K the empirical temperature relationship found by Young and Mawardi[14] (who did not go beyond

[14] J. E. Young and O. K. Mawardi, J. Chem. Phys. 24, 1109 (1956).

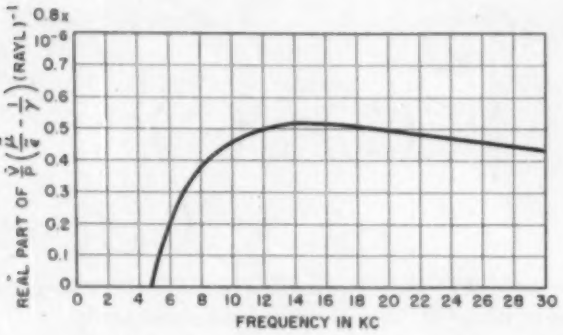

FIG. 3. Real part of the negative of the specific acoustic admittance of the burning boundary. (On the vertical axis, 0.8× and 10^{-6} should be reversed.)

1000°K), and boldly extrapolating from 1 to 80 atmospheres in the usual way, we obtain $\alpha^1=1.07\,f^2\,10^{-12}$ nepers/cm (where f is the frequency). An independent estimate may be obtained, based on the usual sound absorption theory and the measured relaxation times in nitrogen in the neighborhood of 2500°K.[15] The value so obtained actually agrees with the previous estimate to within a factor of two. It is also true that carbon monoxide could be an efficient absorber at rocket temperatures, so that the above estimate for the propellant gas might easily be low by a factor of five. However, the gases also contain water and hydrogen, both of which tend to lower vibrational relaxation times of typical absorbers.[16] Thus, it is quite difficult to make a realistic estimate of the absorption coefficient of the propellant gases, and we shall content ourselves with the value of $\alpha^1=1.07f^2\times10^{-12}$ nepers/cm for the illustrations in this paper.

With respect to the dilational viscosities, no information is available for propellant-like materials. For one rigid polymer for which this coefficient has been measured,[17] it has been found comparable in magnitude to the coefficient of shear viscosity. With respect to the shear viscosity, itself, little information which is directly pertinent to solid propellant-like materials is available. Data on a plasticized cellulose nitrate[18] suggests that the frequency dependence of the shear viscosity is not simply described in terms of the usual visco-elastic model of solids, in the frequency range of interest. In the absence of an attractive guide, we shall adopt constant values of $\eta=\lambda^1=200$ poises, in order to carry through the sample application of the theory.

In the selection of a propellant amplification function, we must rely entirely on theory. It appears, however, that such amplification functions can be expected to show amplification at frequencies above the order of 1000 cycles. For the present purpose, the precise frequency dependence is of little concern, and it will be sufficient to adopt one of the amplification functions presented in footnote 2. Accordingly, we adopt the curve of Fig. 2 of footnote reference 2 (a hypothetical propellant having a pressure index $n=0$), scaled to correspond to a pressure of 80 atmospheres, a mean mass flow of 1.9 g/sec cm^2, $\gamma=1.25$, gas heat conductivity $\lambda=3.46\times10^{-4}$ (cal/cm sec °K), and a burned gas molecular weight of 26, as shown in Fig. 3.

We have used the above values of the parameters and investigated the characteristic modes in the frequency interval 1.0 to 25 kc, for three boundary conditions at the outer surface of the propellant ($r=b$),

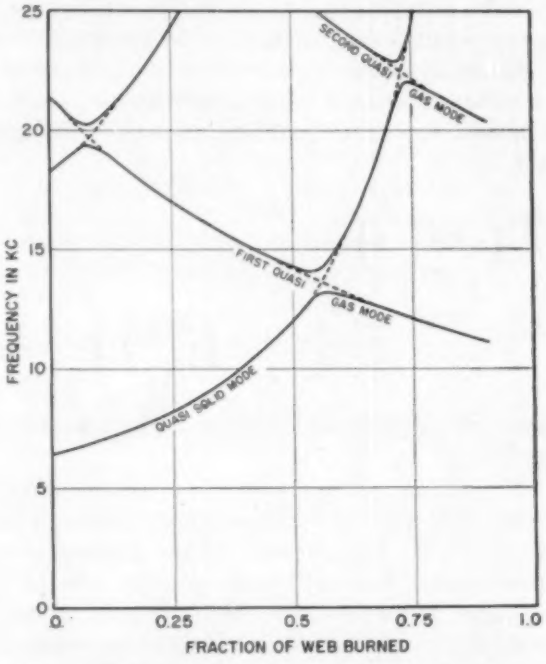

FIG. 4a. The radial mode map for a clamped boundary condition at the exterior surface of the propellant.

namely, (a) clamped, (b) supported, and (c) free boundaries.

2. Characteristic Modes

The solid lines in Fig. 4(a) display the radial ($m=0$) dilatational modes for case (a). The pure shear modes having pressure nodes on the propellant-gas interface are not shown, since the absence of shear at this interface means that these modes are not coupled to the gas and are, therefore, not excited (at least, in first order). As might be expected, the mode frequencies correspond rather closely to either the quasi-solid or quasi-gas modes (i.e., the modes corresponding to the solid shell with a free interior surface, or the modes of a gas filled cavity with a rigid surface). These quasi-modes, where different from the actual modes, are indicated

[15] V. Blockman, J. Fluid Mech. **1**, 61–85 (1956).

[16] A small amount of water vapor is known to reduce drastically the absorption coefficient of CO at elevated temperatures— see M. Windsor, N. Davidson, and R. Taylor, Seventh International Symposium on Combustion (Butterworth's Scientific Publications, Ltd., London, 1959).

[17] W. O. Baker and J. H. Heiss, Bell System Tech. J. **31**, 318 (1952).

[18] I. L. Hopkins, Trans. ASME **73**, 195–204 (1951).

by the dashed lines. Since the interface boundary conditions for the quasi-modes are mutually exclusive, the modes of the real system avoid the intersection of dashed lines, and change their character in such neighborhoods from quasi-solid to quasi-gas. The "splitting" of the modes is influenced both by the mismatch in acoustic properties of the solid and gas media, and by the relative amounts of shear and dilatational motion in the solid.

For tangential modes ($m \neq 0$), the mode maps are considerably complicated by the fact that the real modes of the system are not individually pure shear or pure dilatation, but are combinations of both. Figures 5(a), 5(b), 5(c) illustrate the second tangential modes for the three types of boundary conditions (a,b,c), respectively.

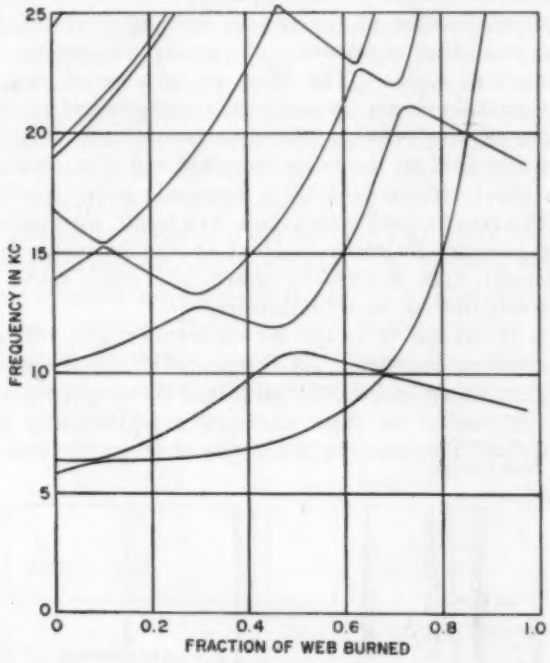

FIG. 5(a). The second tangential mode map for a clamped boundary condition at the exterior surface of the propellant.

3. Stability or Instability

The question of stability or instability is now to be decided by determining whether or not the amplification at the burning surface is sufficient to overcome the viscous losses. As formulated in Sec. III, this question, in turn, is to be answered by whether or not the real part of the admittance presented by the burning surface exceeds the sum of the real parts of the specific acoustic admittance contributed by the gas and solid media. An answer must be determined for each mode and for each configuration assumed during the course of burning. The real parts of the admittances [cf., Eqs. (3.8a), (3.8b), and Fig. 3] are illustrated for the second tangential modes (Figs. 6(a), (b), and (c)). The lines labelled

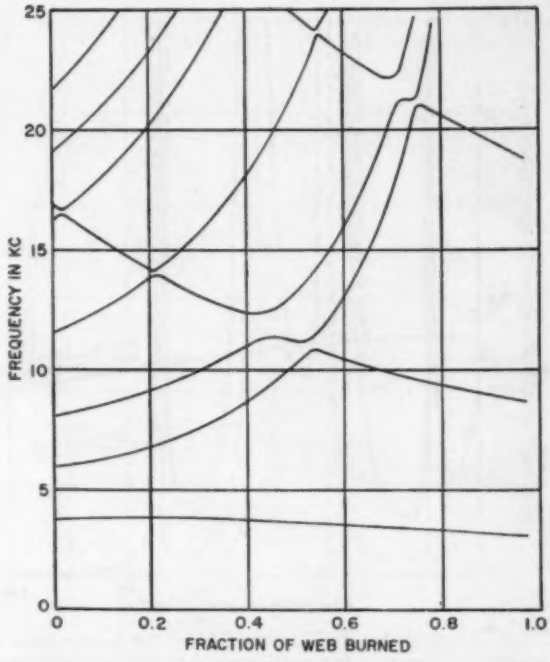

FIG. 5(b). The second tangential mode map for a supported boundary condition at the exterior surface of the propellant.

"gas attenuation" are really the admittance of the gas quasi-modes and are not correct for the real modes for geometries such that a pressure node lies in the immediate neighborhood of the burning surface. The correct admittance of the gas actually rises sharply to infinity at the same places where the solid admittances become

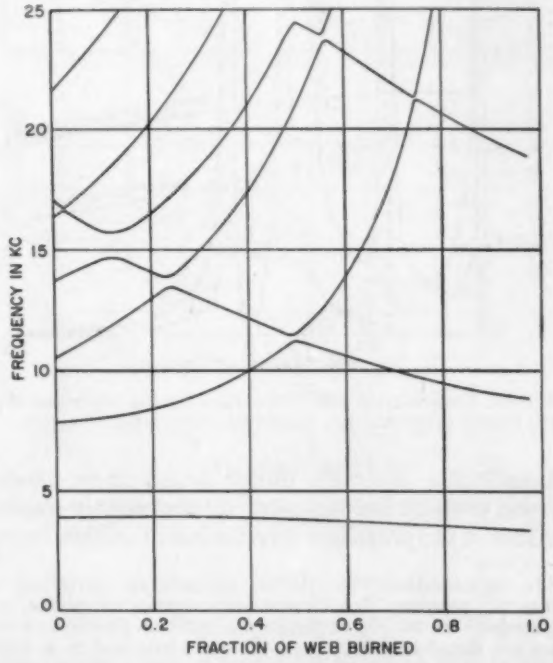

FIG. 5(c). The second tangential mode map for a free boundary condition at the exterior surface of the propellant.

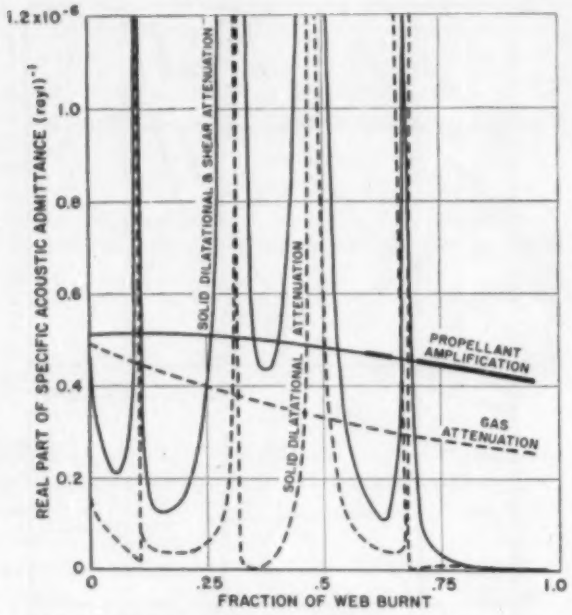

FIG. 6(a). Amplification and attenuation for the fundamental of the second tangential gas quasi-mode (clamped boundary).

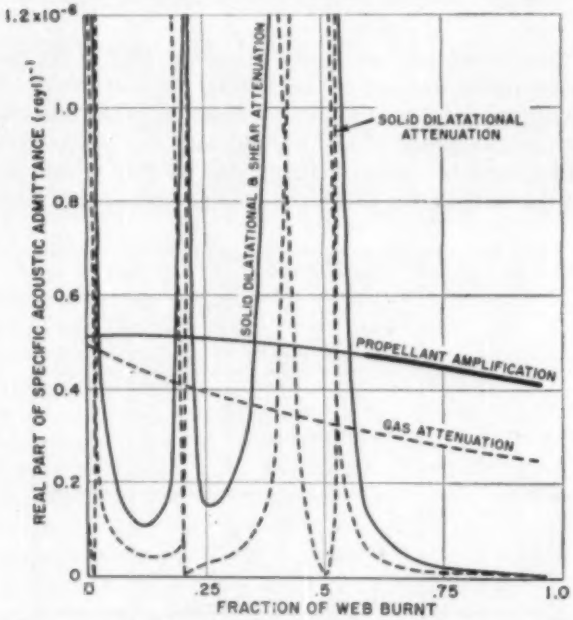

FIG. 6(b). Amplification and attenuation for the fundamental of the second tangential gas quasi-mode (supported boundary).

infinite.[19] The intervals during which these modes become unstable are indicated by the heavily shaded portions of the propellant amplification function curve.

[19] In the admittance form the loss and gain are normalized to unit surface pressure. Thus, for a pressure node on the surface, the amplitude of the motions in the gas and solid are infinite, and the losses are therefore infinite, also. If one normalized to a fixed amplitude of excitation of the system, the losses would remain finite but the surface amplification would be zero for a pressure node on the burning surface.

The effect on stability of the boundary conditions imposed on the outer surface of the propellant is indicated most graphically by consolidating the findings for the several modes on a single figure for each of the three boundary conditions. The result is indicated in Figs. 7(a), 7(b), and 7(c), where the intervals of instability, and the corresponding frequencies, are shown by the solid curves. For purposes of illustration, we have arbitrarily cut off the instability near the end of burning in order to illustrate the effect of increased coupling of the central chamber to the nozzle. As we have previously indicated, this increased coupling occurs as the radius of the central cavity approaches that of the nozzle cavity, which then loses its effectiveness as an acoustic filter. The dashed lines in Figs. 7(a), 7(b), and 7(c) indicate the second harmonics of the fundamental modes. These harmonics will also occur, in general, because of the erosive burning produced by the oscillating components of velocity tangent to the propellant surface. The effect on burning of such a tangential velocity is necessarily independent of the sense of the velocity. Superposition of the acoustic velocity field on the mean flow field will thus produce an effect representable in a harmonic series starting with a zero frequency (dc) term. As a result, corresponding pressure fluctuations occur at the harmonic frequencies, even though the system is actually stable to perturbations at such frequencies.

It is difficult to escape the observation that for the parameters considered, the theoretical effects of boundary conditions at the outer surface of the propellant are rather similar to those obtained experimentally by Angelus.[7] The presence or absence of severe instability

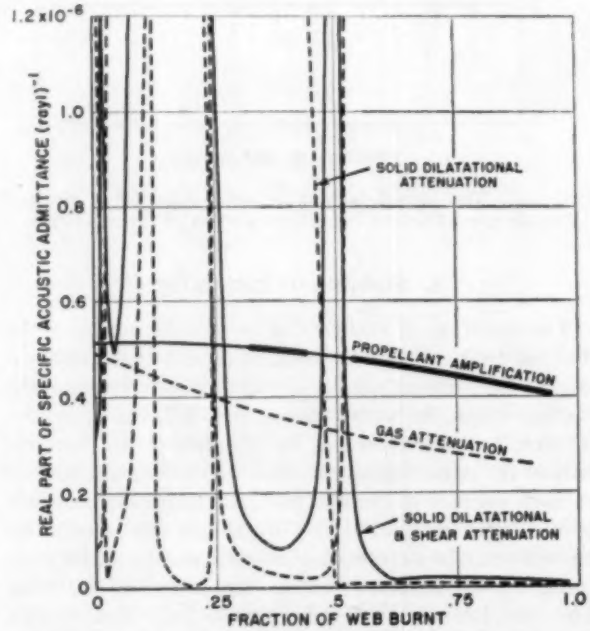

FIG. 6(c). Amplification and attenuation for the fundamental of the second tangential gas quasi-mode (free boundary).

in the second tangential mode is perhaps the major feature of the experimental results, and in this respect, the coincidence between the theoretical case and experiment is striking. (We tend to ignore the first tangential mode in this comparison, because its relative stability as observed experimentally is known to be due in large part, at least, to the presence of four equi-spaced radial slots cut in the end of the grain in order to obtain a relatively flat pressure-time curve.)

It would be attractive to believe that the agreement in gross features between theory and experiment is not entirely coincidence, and we are able to note several features of the theory which lend us encouragement. In the first place, it should be mentioned that the density, and the low frequency elastic moduli of the solid propellant were determined for the appropriate temperature in crude experiments, and used for the theoretical calculations. The pressure and gas phase sound velocity corresponding to the experimental conditions were, of course, rather well known and used in the theoretical calculations. Nevertheless, the values assigned to propellant surface amplification and the gas and solid phase dynamic viscosities, while possibly of the correct order of magnitude, can otherwise only be regarded as picked out of a hat. Fortunately, however, as shown in Figs. 6(a), (b), and (c), the locations of the major unstable regions are insensitive to our choice of these quantities. In fact, it now seems plausible that the unstable regions might be predicted in some detail, if only the necessary parameters were known.

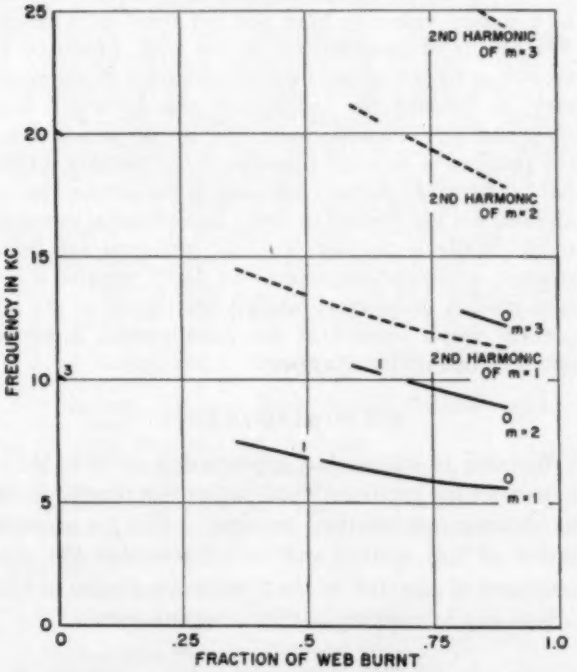

FIG. 7(a). Composite instability map for the clamped exterior boundary. 0, 1 indicate the number of nodes occurring in the solid shell.

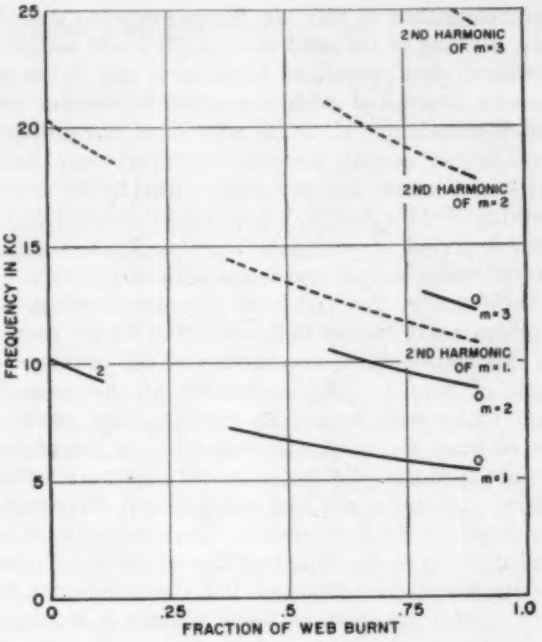

FIG. 7(b). Composite instability map for the supported exterior boundary. 0, 2, 3 indicate the number of nodes occurring in the solid shell.

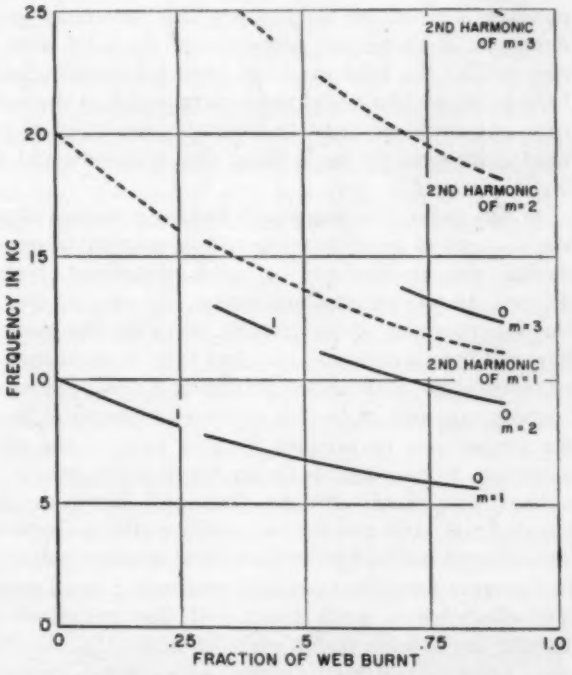

FIG. 7(c). Composite instability map for the free exterior boundary. 0, 1 indicate the number of nodes occurring in the solid shell.

V. DISCUSSION

It is evident from the foregoing that during intense oscillation of the system we frequently may expect to have stress waves of considerable amplitude in the solid propellant. If the propellant is one that permits only a

small elongation to fracture, we may expect a considerable cracking of the solid to occur. It is not surprising, therefore, that propellant break-up is one of the phenomena associated with resonance in motors using brittle propellants. If, on the other hand, the propellant is not brittle, we may, nevertheless, expect some changes in its temperature and properties caused by the acoustic working of the material. The common observation that after a period of resonance the propellant is slightly altered ballistically is consistent with this picture.

Incidentally, the fact that the wave motion is a combination of motion in the solid and the gas provides an explanation for the variability of the phenomenon. Lack of precision in the control of the geometry, particularly with respect to the boundary conditions placed upon the solid, and variability in the physical properties of the solid due to lack of accurate control of mixing and curing will lead to significant differences in the details of the phenomenon. The importance of controlled curing to the reproducibility of this phenomenon has frequently been reported. It is clear, therefore, why very careful attention to these features is required if complete reproducibility is desired.

As the particular example above indicates, the viscosities of the solid play a very important part in producing regions of stability. This feature leads to another possible method of suppressing this resonance phenomenon. If the elastic properties of the solid were so chosen that the solid would be expected to participate fully in the oscillations of the system, and if at the same time one could contrive to have the viscosities of the solid appropriately high, then the system would be highly damped.

At this point, it seems worth making a remark about the changes in mean burning rate frequently observed during the oscillations in solid propellant rocket motors. As was pointed out earlier, the erosion due to the superposition of an acoustic wave on the general flow will have a constant (dc) first term in its harmonic representation. This term contributes a change in mean burning rate and, in fact, it appears in general to be of the proper size to account for this part of the phenomenon. It accounts both for the positive effects in normal propellants (where "erosion" increases the burning rate) and also for the negative effects observed for moderate oscillations in the case of mesa propellants. In the mesa propellants erosion produces a small negative effect for a small velocity if the propellant is burning in the mesa region while for large velocities the effect becomes positive. If a mesa propellant is burning well below the mesa, the negative effect can be carried to larger values before it ultimately becomes positive at large velocities, i.e., large acoustic oscillations. Above the mesa only positive effects occur. Thus we see that for mesa propellants we expect either increased or decreased mean burning rate in various degrees depending upon the steady state condition and the amplitude of the oscillations in the tangential modes.

While the results of our study have to some extent a rather startling correlation with experimental observations, it should be remembered that the prediction of all the details of experiments on the oscillations of rockets is a task for which neither the basic information nor an adequately complete theory exists. We must recall that the stability against small oscillations which we have considered is a necessary but not sufficient condition for stability of a system, and we should consider ourselves fortunate indeed if the results of such a simple theory proved to be generally valid. Some encouragement may be drawn, however, from the observation that solid rockets which are stable to small fluctuations are not generally known to become unstable when subjected to large perturbations in contradistinction to liquid rockets which sometimes exhibit the phenomenon of being stable against small, but not large, perturbations. The complexity of the geometries customarily encountered produces problems in solution of wave theory which are indeed formidable. That the flow field introduces nonhomogeneity into the acoustic medium which will have a significant effect on the propagation and dissipation of the waves must be recognized. There is no adequate treatment of the coupling of the various cavities to the system, particularly the cavity involving the nozzle with its flow field reaching sonic value. The properties of erosive burning under an oscillating velocity field (in contrast to a steady velocity) have not yet been investigated. The effects of irregularities in low field, produced by erosion or by jets of gas from irregularities in the geometry, in limiting the oscillations also have not been quantitatively treated. Last, but by no means least, the problem of acoustic response of the burning surface has been treated theoretically only in the simplest model and has not yet yielded to direct experimental measurement. While a number of these problems are being studied, a theory complete in all detail remains a distant goal. A satisfactory unified description of the important major aspects of the phenomenon, however, seems to be rapidly emerging.

ACKNOWLEDGMENTS

We wish to express our appreciation to Mrs. M. E. Lynam for her persistence and patience in programming the delicate computations required to find the acoustic modes of this system and to acknowledge the able assistance of the staff of the Computing Center of this Laboratory in carrying out the computations.

JOURNAL OF APPLIED PHYSICS VOLUME 31, NUMBER 5 MAY, 1960

Detection of Metastable Atoms and Ions

HOMER D. HAGSTRUM
Bell Telephone Laboratories, Inc., Murray Hill, New Jersey
(Received January 18, 1960)

Experimental work is presented concerning the detection of metastable singly charged ions by means of electron ejection from contaminated metal surfaces. By the use of suitable retarding potentials one can cause the current of reflected ions to cancel very nearly the current of electrons ejected by the ground state ions. This method increases the ratio of metastable signal to background signal by a factor of 300 or more and is comparable to what can be done by modulation of the metastable component. Some comments concerning the detection of metastable atoms by means of Auger electron ejection processes are included.

I. INTRODUCTION

THE electrical effects which accompany the interaction of an atomic particle with a solid surface have been used extensively as detectors of such particles. Surface ionization of neutral unexcited atoms or molecules depends upon the particle being ionized by the loss of an electron to the surface. The method requires the work function of the metal to be greater than the ionization energy of the atom or molecule and condensation of atoms on the surface, with consequent change in work function, must be prevented. Clean and oxygenated refractory metals held at sufficiently high temperatures to prevent condensation have been widely used to detect molecular beams.[1,2] The surface ionization process involves the tunneling of one electron through the barrier between the metal and the atom.

Excited atoms, principally metastables, have also been detected by the electrical effects they produce at surfaces. Webb[3] first showed that metastable mercury atoms can eject electrons from metals. The phenomenon has been studied experimentally by others.[4–7] Theoretical investigations have been carried out by Massey,[8] Cobas and Lamb,[9] Shekhter,[10] Hagstrum,[11] and Sternberg.[12] It is recognized that we are dealing here with a two-electron process of an Auger type, in which one of the two electrons involved is excited and as a consequence has a finite chance of leaving the solid. The metastable atom is detected by observing these Auger electrons. This method has been used in gaseous electronics studies by Dorrestein[13] and Schulz and Fox,[14] by Lamb and Retherford[15] in their work on the fine structure of the hydrogen atom, and by Novick and Commins[16] who modulated the metastable component in a beam of He^+ ions. Other methods have involved light absorption[17] and quenching followed by detection of the emitted photon.[16,18,19]

It is the purpose of the present paper to present further work on the detection of metastable ions by means of Auger de-excitation and neutralization at a solid surface.[20] In a previous publication,[21] studies were reported on the formation of such ions by a single electron impact in the noble gases and their interaction with atomically clean metal surfaces. The metastable ions are detected by their greater ability, with respect to unexcited ions, to eject electrons from the metal. The present paper extends this work to a study of: (1) The detection of metastable ions by electron ejection at contaminated metal surfaces (Sec. III); (2) Means of increasing the detection sensitivity (Sec. IV). It is obvious that the worker with molecular beams not only prefers to, but perhaps must use contaminated rather than atomically clean surfaces.

The second part of the present study, listed above, arose from a suggestion by Novick and Commins[16] that retarding potential discrimination among the ejected electrons might improve detection sensitivity for the metastable ion over the ever-present background of electrons ejected by the ground state ions. The present work shows that for the contaminated metal surfaces used no significant improvement in detection sensitivity is achieved in this way. However, in the course of these

[1] J. B. M. Kellogg and S. Millman, Revs. Modern Phys. **18**, 323, 331–333 (1946).
[2] N. F. Ramsey, *Molecular Beams* (Oxford University Press, New York, 1956).
[3] H. W. Webb, Phys. Rev. **24**, 113 (1924).
[4] M. L. E. Oliphant, Proc. Roy. Soc. (London) **A124**, 228 (1929).
[5] S. Sonkin, Phys. Rev. **43**, 788 (1933).
[6] R. Dorrestein, Physica **9**, 433 (1942).
[7] D. Greene, Proc. Phys. Soc. (London) **B63**, 876 (1950).
[8] H. S. W. Massey, Proc. Cambridge Phil. Soc. **26**, 386 (1930); **27**, 460 (1931).
[9] A. Cobas and W. E. Lamb, Jr., Phys. Rev. **65**, 327 (1944).
[10] S. S. Shekhter, J. Exptl. Theoret. Phys. (U. S. S. R.) **7**, 750 (1937).
[11] H. D. Hagstrum, Phys. Rev. **96**, 336 (1954).
[12] D. Sternberg, Ph.D. Dissertation, Columbia University, New York, N. Y. (1957), unpublished.
[13] R. Dorrestein, Physica **9**, 447 (1942).
[14] G. J. Schulz and R. E. Fox, Phys. Rev. **106**, 1179 (1957).
[15] W. E. Lamb, Jr., and R. C. Retherford, Phys. Rev. **79**, 549 (1950).
[16] R. Novick and E. D. Commins, Phys. Rev. **111**, 822 (1958). Note that the last term of Eq. (7) in this paper should be $\gamma_{2S}{}^{1}\Phi I_{2S}{}^{0}$.
[17] A. V. Phelps, Phys. Rev. **99**, 1307 (1955); A. V. Phelps and J. L. Peck, Rev. Sci. Instr. **26**, 45 (1955); in these papers references to a number of other works are to be found.
[18] W. E. Lamb, Jr., and M. Skinner, Phys. Rev. **78**, 539 (1950).
[19] R. Novick, E. Lipworth, and P. F. Yergin, Phys. Rev. **100**, 1153 (1955).
[20] A metastable ion here means an ion which is metastable with respect to radiative transition to the ground state. The term has also been used for complex ions which are metastable with respect to dissociation into one or more molecular fragments. See J. A. Hipple, R. E. Fox, and E. Y. Condon, Phys. Rev. **69**, 347 (1946); J. A. Hipple, Phys. Rev. **71**, 594 (1947); J. Phys. and Colloid Chem. **52**, 456 (1948).
[21] H. D. Hagstrum, Phys. Rev. **104**, 309 (1956).

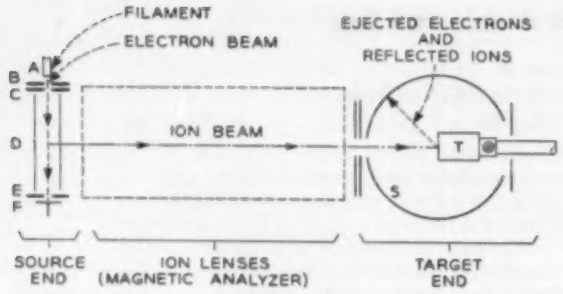

FIG. 1. Schematic diagram of experimental apparatus.

studies, a method of cancelling the effect of ground state ions was devised which increases the specific detection sensitivity for the metastable ion by a large factor. Novick and Commins used an elegant means of discrimination which involved modulating the metastable component in the ion beam at 280 cps and observing the modulated component in the ejected electron current with a narrow-band detector. It is shown that the new method presented here is comparable in sensitivity to this modulation scheme of Novick and Commins (Sec. V).

For completeness, a few comments are made in Sec. VI concerning the detection of metastable atoms by means of Auger electron ejection.

II. EXPERIMENT AND APPARATUS

The experimental work has been performed with apparatus like that used in the earlier work.[21] A schematic diagram is shown in Fig. 1. Ions formed by electron impact are focussed into an ion beam, which falls on a metal ribbon target T situated at the center of a spherical electron collector S. The measurements made on the ejected electrons are total yield γ_i in electrons per incident ion and kinetic energy distribution $N_0(E_k)$ obtained using retarding fields between electrodes S and T. Pressure of background gases in the instrument during the experiment was about 1×10^{-9} mm Hg with liquid nitrogen on the traps, 1×10^{-8} mm Hg with CO_2 and acetone on the traps. It was not necessary to obtain lower pressures as all the work was done with contaminated target surfaces.

All of the experimental results to be discussed in this paper are obtained from the so-called retarding potential curve for the ejected electrons. Such a plot for He^+ ions of 100 ev incident kinetic energy on contaminated tungsten is shown in Fig. 2. It is a plot of the quantity $\rho=I_S/(I_T+I_S)$ as a function of V_{ST}, the voltage between collector sphere S and target T. In the expression for ρ, I_S, and I_T are the algebraic currents to collector and target, respectively. The curve of Fig. 2 is representative in the following general respects of such curves obtained for ion-target combinations (whether the surface is contaminated or not) for which ion reflection at the target surface as ions or as metastable atoms is small:

1. For $V_{ST}<0$, where electrons are accelerated toward the collector, ρ is essentially constant. For V_{ST} negative but near zero, $-\rho=\gamma_i$, the total electron yield per ion.

2. For $V_{ST}>0$ the ejected electrons are retarded and $d\rho/dV_{ST}=N_0(E_k)$ is their kinetic energy distribution. The $N_0(E_k)$ function obtained from the data of Fig. 2 is plotted in Fig. 3.

3. For sufficiently large positive V_{ST} (Fig. 2) ρ reverses sign. The asymptotic value of ρ at large positive V_{ST} is designated as R. R is the sum, per unit incoming current, of all secondary and tertiary currents resulting from the reflection of incoming ions at the target surface as ions or as metastable atoms.[22] The reflected particles can eject electrons from the inside surface of the sphere, which electrons are then accelerated to T and also contribute to R. For He^+ on contaminated tungsten, R is small.

When reflection at the target surface is large, the ρ vs V_{ST} characteristic is changed drastically as is illustrated in Fig. 4 for the case of A^+ on contaminated tungsten. Here are shown ρ curves for two values of the bombarding electron energy in the ion source (V_{AC}). We note two new features of the curves in Fig. 4 when compared with Fig. 2. First, the values of R are very large. Second, the curve continues to rise as V_{ST} becomes increasingly negative. When all currents are analyzed, it can be shown that $d\rho/dV_{ST}$ for $V_{ST}<0$ is the kinetic

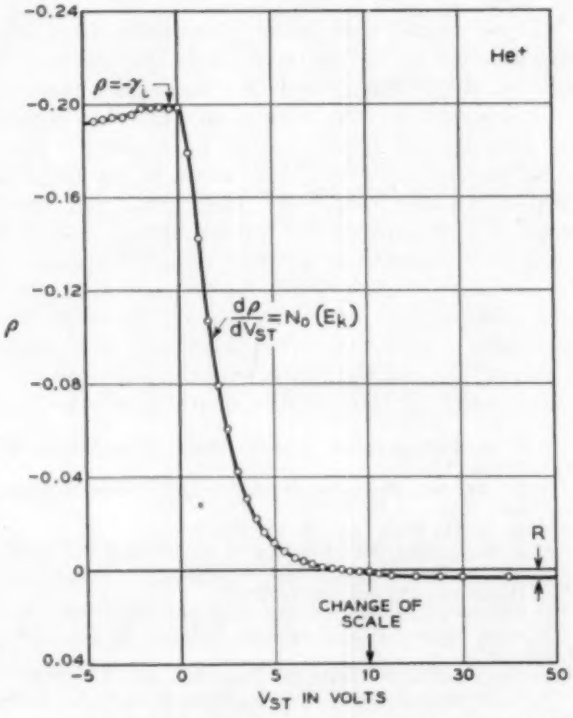

FIG. 2. Plot of the quantity $\rho=I_S/(I_T+I_S)$ as a function of V_{ST}, the voltage between the electron collector and the target, for 60 ev He^+ ions incident on contaminated tungsten.

[22] H. D. Hagstrum, Rev. Sci. Instr. 24, 1122 (1953).

energy distribution of reflected ions. This is indicated in Fig. 5, where $d\rho/dV_{ST}$ from the data of Fig. 4 are plotted. For $V_{ST}>0$ in Fig. 4, $d\rho/dV_{ST}$ is, as before, the kinetic energy distribution of electrons ejected from the target. The total electron yield γ_i is the asymptote of $-\rho$ at large negative V_{ST}. This is the same as the quantity $|\rho-R|=\int_{V_{ST}}^{\infty} N_0(E_k)dE_k$, evaluated at $V_{ST}=0$.

When R is large, particle loss through the entrance aperture of the spherical collector is large. This is illustrated in Fig. 6. Here ρ is plotted for A^+ ions on contaminated tungsten for a series of V_{ST} values indicated on the curves. These data are plotted against $V_{M_1M_2}$, the cross voltage between the last set of plates of the ion lens just outside the spherical collector. $V_{M_1M_2}$ determines the centering of the beam upon the front face of the target. Data are plotted against the experimentally convenient scale on the vernier dial of the $V_{M_1M_2}$ voltage divider. Actual values of $V_{M_1M_2}$ are indicated by the vertical, dashed equivoltage lines. It is observed that for $V_{ST}>-6$ v ρ passes through a maximum when the ion beam is centered on the target face and the loss of ejected electrons through the entrance aperture is a maximum. For this reason, data reported here were taken with the beam offset, say at a $V_{M_1M_2}$ scale reading of 58 or thereabouts.

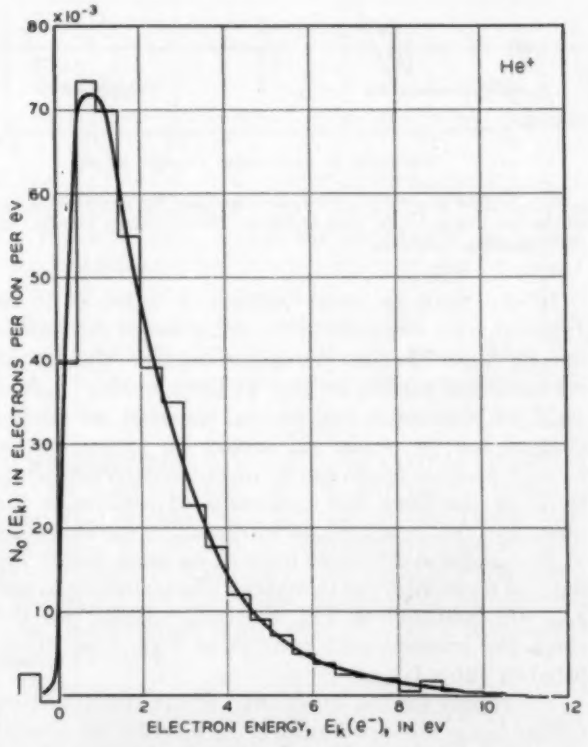

FIG. 3. Kinetic energy distribution of electrons ejected by 60 ev He^+ ions from contaminated tungsten. The stepped curve is obtained from point to point differentiation of the data of Fig. 2. The smooth curve represents the most probable true distribution.

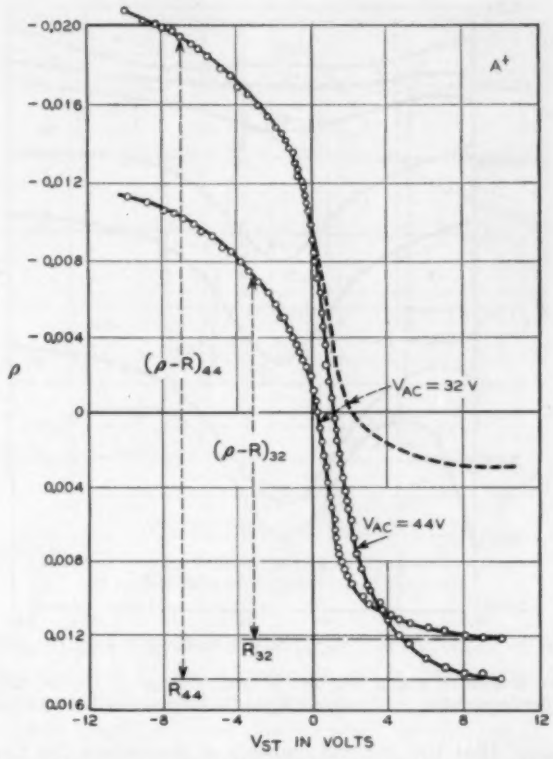

FIG. 4. Retarding potential plots for 100 ev A^+ ions incident on contaminated tungsten. Curves are shown for ions generated by 32 and 44 ev bombarding electrons in the ion source. The dashed curve is the $V_{AC}=32$ v curve shifted vertically by an amount sufficient to bring it into coincidence with the $V_{AC}=44$ v curve over the range $V_{ST}=-10$ v to zero.

III. DETECTION OF METASTABLE IONS AT CONTAMINATED SURFACES

We discuss now the experimental results for metastable ions incident on contaminated metal surfaces and recall from the earlier work on atomically clean sur-

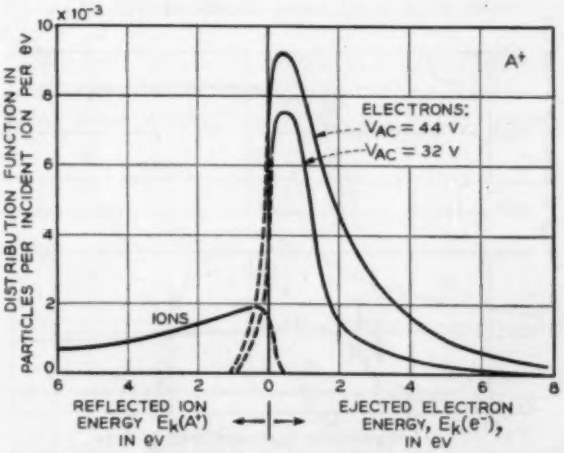

FIG. 5. Plots of $d\rho/dV_{ST}$ from the data of Fig. 4. The distribution in energy of reflected ions (which is the same for $V_{AC}=32$ v and $V_{AC}=44$ v) lies to the left of zero on the abscissa scale. To the right of zero lie the distributions for electrons ejected by ions formed in the ion source at the bombarding energies shown.

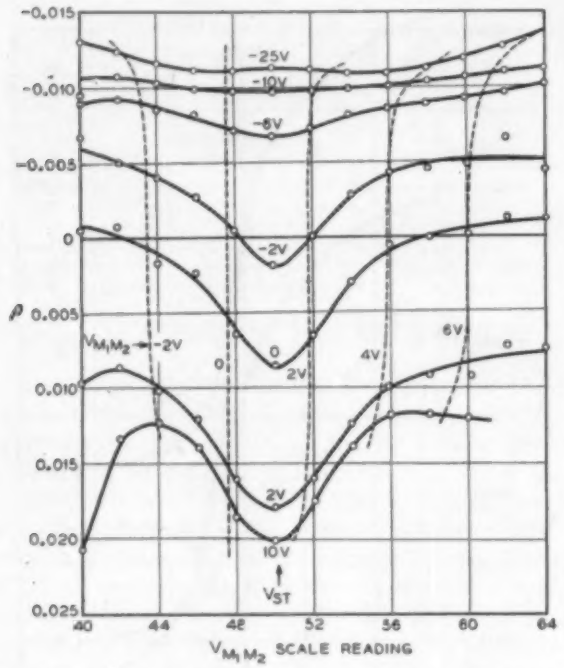

FIG. 6. Plot of ρ as a function of cross voltage on the ion beam (hence position on the target face) for different values of V_{ST}.

faces[21] that the method consists of measuring the electron yield as a function of bombarding electron energy in the ion source. It was shown in the earlier paper that the observed yield may be written

$$\gamma_{obs}=(1-f_{im})\gamma_{i1}+f_{im}\gamma_{im},$$

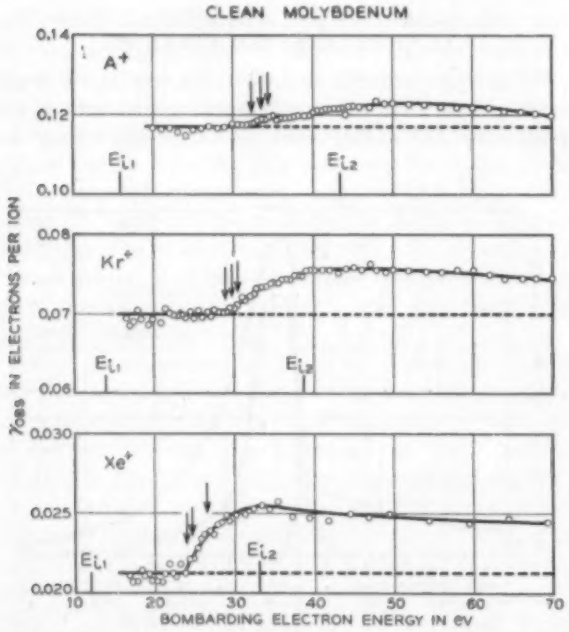

FIG. 7. Plots of γ_{obs} vs bombarding electron energy (V_{AC}) in the ion source for A^+, Kr^+, Xe^+ ions of 100 ev kinetic energy incident on atomically clean molybdenum ($V_{ST}=-2$ v). Arrows indicate the energies of metastable ionic states. This figure is reproduced from the paper of footnote 21.

where f_{im} is the fraction of the ion beam which is in a metastable excited state, γ_{i1} is the electron yield per incident normal ion, and γ_{im} the yield per metastable ion. To illustrate the method and for comparison with the present results, we reproduce here in Fig. 7 the results for A^+, Kr^+, and Xe^+ on atomically clean molybdenum.

In presenting the results for contaminated surfaces, we shall plot ρ at $V_{ST}=-2$ v, not calling it $-\gamma_{obs}$ because in general it is not. This is the result of the large reflection of ions at the contaminated surface. We shall see that ρ at $V_{ST}=-2$ v may even be positive, as in the case for krypton. In Figs. 8–10 are plotted the results for A^+, Kr^+, and Xe^+ on contaminated tungsten, respectively. The general behavior is the same as for the clean surface (Fig. 7), but the detection sensitivity is increased. The ρ values measured are about an order of magnitude lower than the γ_{obs} for the clean surface. However, the percentage change in this quantity is considerably greater.

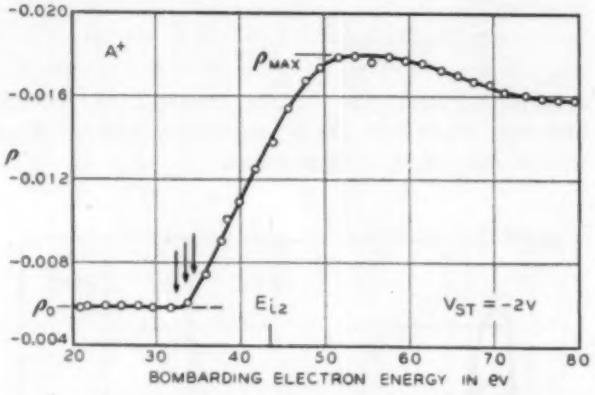

FIG. 8. Plot of $\rho=I_S/(I_T+I_S)$ vs bombarding electron energy in the ion source for A^+ ions of 100 ev kinetic energy incident on contaminated tungsten.

In the work on clean surfaces, a figure of merit $(\gamma_{im}-\gamma_{i1})/\gamma_{i1}$ was defined for detection of metastable ions by Auger ejection. We cannot calculate this for the contaminated surface because we know neither γ_{im}, the yield per metastable ion, nor γ_{i2}, the yield per doubly charged ion to which γ_{im} should be approximately equal.[23] Another relative measure of the detection sensitivity of the clean and contaminated surfaces is the quantity $|(\rho_{max}-\rho_0)/\rho_0|$, in which ρ_{max} is the value of ρ at its maximum deviation from ρ_0, its value before the onset of metastable ion formation. The quantities ρ_0 and ρ_{max} are indicated on Fig. 8. $|(\rho_{max}-\rho_0)/\rho_0|$ for the clean and contaminated surfaces of Figs. 7 to 10 are listed in Table I.

The reason for the superiority of the contaminated surface lies in the fact that for it the yield for the normal ion is relatively less than that for the metastable ion. This also accounts for the general increase in detection

[23] H. D. Hagstrum, Phys. Rev. **104**, 672 (1956).

sensitivity in going from A^+ to Xe^+. The method outlined above was still not sensitive enough to detect He^{+m} at the contaminated surface. This required the method to be discussed in Sec. IV. For Ne no deviation from ρ_0 was found since there are no Ne^+ metastable levels.

IV. MEANS OF INCREASING DETECTION SENSITIVITY

The basic drawback of the method of detecting metastable ions by Auger electron ejection is the fact that one must detect the metastable ions in the presence of the relatively large electron yield from the much greater number of normal ions present in the ion beam. Novick and Commins[16] suggested trying to improve this situation by means of a retarding potential which discriminates against "the low-energy electrons ejected with neutralization of the ground state ion." Their attempt was apparently not successful. The same experiment was tried in the present work with the same results.

We shall discuss retarding potential discrimination in terms of two ρ vs V_{ST} curves, one taken below and the other somewhat above the onset of metastable ion formation. Such curves for argon at bombarding electron energies (V_{AC}) of 32 and 44 ev are shown in Fig. 4.

TABLE I. Comparison of $|(\rho_{max}-\rho_0)/\rho_0|$ as a measure of sensitivity of detection of metastable ions at clean and contaminated metal surfaces.

	A^+	Kr^+	Xe^+
Clean	0.05	0.09	0.2
Contaminated	2	4	320

If the $V_{AC}=44$ v curve is shifted vertically, it can be brought into coincidence with the $V_{AC}=32$ v curve in the region $V_{ST}<0$, Hence the distribution in kinetic energy of reflected ions is independent of electron energy in the ion source as it should be.

We now compare for these curves the total numbers of electrons of energy greater than a given value, say V_{ST}, as V_{ST} is increased positively from zero. This number of electrons is $\int_{V_{ST}}^{\infty} N_0(E_k)dE_k=\rho-R$. Thus, we compare $\rho-R$ for the $V_{AC}=44$ v curve of Fig. 4 with that for the $V_{AC}=32$ v curve by plotting the quantity $|(\rho-R)_{44}/(\rho-R)_{32}|$ as a function of V_{ST}. This is done in Fig. 11. We see that this quantity does not increase greatly above its value of 1.5 for $V_{ST}\ll 0$. It reaches a value of 2.5 at $V_{ST}=+2$ v, representing an improvement in detection sensitivity of only a little more than 1.5.

We have seen that for the contaminated metal surface used here the retarding potential discrimination among ejected electrons will not increase detection sensitivity for the metastable ion appreciably. The method fails because the kinetic energy distributions for neutralization of metastable and normal ions are not sufficiently

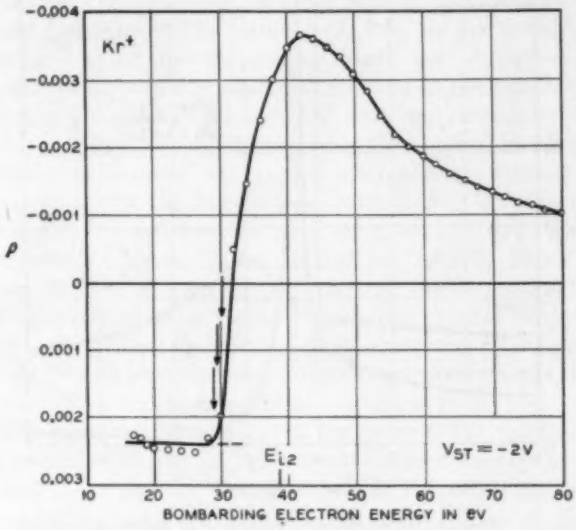

FIG. 9. Plot of ρ vs bombarding electron energy for 100 ev Kr^+ ions on contaminated tungsten.

different (see Fig. 5). This latter fact is the result of the neutralization of the metastable ion in two steps. As discussed elsewhere,[23] it is probable that the first step involves transit to the ground state of the ion in a process of Auger deexcitation, followed in the second step by transit to the ground state of the atom in a process of Auger neutralization. For the heavier noble gas ions the potential energies available in these steps, metastable excitation energy vs first ionization energy, are comparable so the kinetic energies of the ejected electrons should be comparable. It would be a different story if the metastable ion were neutralized directly in one jump to the ground state of the atom with all the energy thus released going into the ejected electron. In the case of He^+ these energies are in the ratio of 2 to 1, but this apparently does not result in a sufficient difference in the energy distributions for the contaminated surface.

As has been said in the foregoing, the problem really is to depress the background of electrons released by neutralization of the ground state ions. In the course of

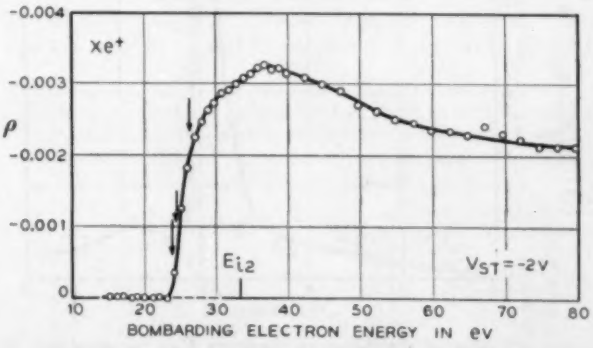

FIG. 10. Plot of ρ vs bombarding electron energy for 100 ev Xe^+ ions on contaminated tungsten.

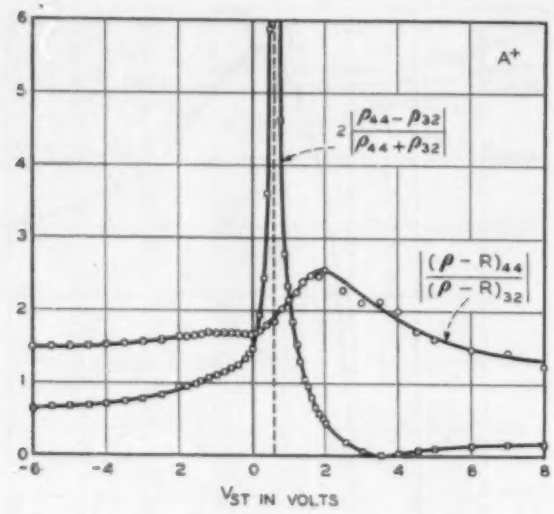

FIG. 11. Plots of the figures of merit vs V_{ST} for detecting metastable A^+ ions by two schemes discussed in the text.

the measurements just discussed, it occurred to the writer that the reflected ion current which causes ρ to change sign provides just the mechanism needed for balancing out the unwanted electron current ejected by the ground state ions. Thus, at the point ($V_{ST}=+0.6$ v) where the ρ curve for $V_{AC}=32$ v in Fig. 4 goes through zero, this balance has been achieved. If one then measures changes in ρ from this point with bombarding electron energy, a considerably enhanced detection sensitivity for the metastable ion results.

A reasonable figure of merit for this scheme is $|(\rho-\rho_0)/(\rho+\rho_0)/2|$, the change in ρ from the preonset value divided by the average value of ρ. Applied to the two curves of Fig. 4, it is $|(\rho_{44}-\rho_{32})/(\rho_{44}+\rho_{32})/2|$, which quantity is also plotted in Fig. 11. This figure of merit becomes infinite when $\rho_{44}=-\rho_{32}$. The method is thus a sort of cancellation method which consists of using the reflected ion current to depress the zero on the I_S current scale.

A crucial test of the method outlined above comes when it is applied to the detection of the metastable helium ion. ρ measurements at $V_{AC}=60$ and 100 v, below and above the expected metastable ion onset at 65.4 v, yield the figure of merit $|(\rho_{100}-\rho_{60})/(\rho_{100}+\rho_{60})/2|$ plotted in Fig. 12. This indicates that the V_{ST} value at which one should operate is near 8.6 ev where ρ_{60} changes sign (Fig. 2). Measurements of ρ vs V_{AC}, the bombarding electron energy in the ion source, have been made with V_{ST} held constant at +6 v and +8 v and are plotted in Fig. 13. The onset of formation of metastable He^+ ions is clearly evident. Calculation of the figure of merit from these data yields a value about half that of Fig. 12 for $V_{ST}=8$ v. Experimental variations of this kind most likely rsulted from variations in setting the voltage $V_{M_1M_2}$. See Fig. 6 and discussion concerning it.

V. COMPARISON OF VARIOUS METHODS OF DETECTING METASTABLE IONS

Several methods of detecting metastable helium ions have now been tried and it is instructive to compare them. These methods are: (1) photoelectric detection of the Lyman-alpha radiation emitted on decay of the metastable ion (Lamb and Skinner,[18] Novick and Commins,[16] Novick, Lipworth, and Yergin[19]); (2) surface detection of electrons ejected by the modulated metastable ion component in the total ion beam (Novick

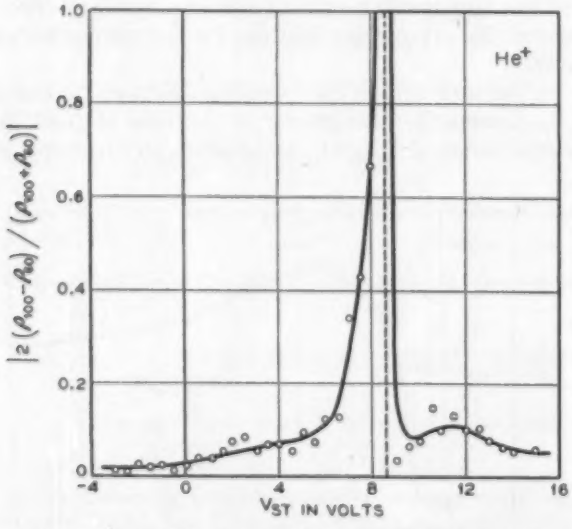

FIG. 12. Plot of the figure of merit vs V_{ST} for detection of $He^+(2S)$ at a contaminated tungsten surface by the scheme discussed in the text.

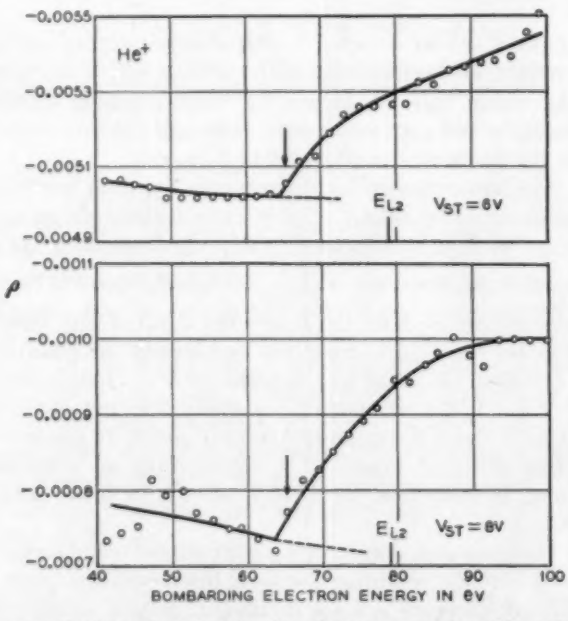

FIG. 13. Plots of ρ vs bombarding electron energy for 100 ev He^+ ions incident on contaminated tungsten. V_{ST} was held constant at the values shown. The arrows indicate the threshold for onset of formation of the metastable ion $He^+(2S)$.

and Commins[16]); (3) surface detection of a dc beam by collecting all ejected electrons (Hagstrum,[21] present work); (4) surface detection of a dc beam employing cancellation of electrons ejected by the ground state ions (present work).

We shall discuss these methods for the case of contaminated metal surfaces first and in terms of the example used by Novick and Commins (abbreviated N. C.).[16] In this example we have an initial current of ground state ions, I_{1S}^0, of 2×10^{-8} amp, an initial current of metastable ions, I_{2S}^0, of 2×10^{-10} amp at a bombarding electron energy of 250 v, and yield parameters $\gamma_{1S}^+=0.30$, $\gamma_{2S}^+=0.81$.

Novick and Commins estimate useful metastable ion signal and background signal for methods (1) and (2). Novick[24] has suggested that in the dc detection schemes of methods (3) and (4), one would operate the apparatus with polarizer and analyzer on continuously and look for changes produced by switching the field in the hfs transition region on and off. Equations for signal and background currents for the four methods are given below.

(1) *Photoelectric detection*

$S_p=(\Phi'''-\Phi'')I_{2S}^0T\eta\Omega/4\pi$ [N. C. Eq. (11)]
$=2.6\times10^{-15}$ amp. [N. C. Eq. (22)]
B_p may be reduced to a very low level. [N. C. p. 832]

(2) *Surface detection using modulated metastable component*

$S_S=(\gamma_{2S}^+-\gamma_{1S}^+)(\Phi'''-\Phi'')I_{2S}^0$ [N. C. Eq. (9)]
$=7.0\times10^{-12}$ amp. [N. C. p. 833]
$B_S=(\gamma_{2S}^+-\gamma_{1S}^+)(\Phi''-\Phi')I_{2S}^0$ [N. C. Eq. (10)]
$=1.8\times10^{-11}$ amp. [N. C. p. 833]

(3) *Surface detection of total beam*

$S_S=(\gamma_{2S}^+-\gamma_{1S}^+)(\Phi'''-\Phi'')I_{2S}^0$
$=7.0\times10^{-12}$ amp.
$B_S=\gamma_{1S}^+I_{1S}^0+[\gamma_{1S}^++\Phi''(\gamma_{2S}^+-\gamma_{1S}^+)]I_{2S}^0$
$=6.0\times10^{-9}$ amp.

(4) *Surface detection at* $\rho_{1S}\sim0$

$S_S=(\rho_{2S}-\rho_{1S})(\Phi'''-\Phi'')I_{2S}^0$
$=1.8\times10^{-12}$ amp.
$B_S=\rho_{1S}I_{1S}^0+[\rho_{1S}+\Phi''(\rho_{2S}-\rho_{1S})]I_{2S}^0$
$=5.6\times10^{-12}$ amp.

In the above tabulation, Novick and Commins' notation has been used. The quantities Φ', Φ'', and Φ''' are fractional transmissions of Novick and Commins' apparatus under the three conditions listed on their page 827. S_S for methods (3) and (4) is the same as that for method (2). B_S may be obtained from Eq. (7) of Novick and Commins.[16] The term $\gamma_{1S}^+I_{1S}^0$ in B_S for the electrons ejected by the ground state ions completely swamps out the metastable component in the signal S_S and is the cause of the very low detection sensitivity of this method. Novick[24] has very kindly supplied the individual value for $\Phi''=0.141$ needed to calculate a numerical value for the background current B_S. Differences between various Φ values only are given in Novick and Commins' paper. These are for the $\Delta F=1$, $\Delta m_F=0$ transition with optimum polarizer and analyzer settings.

The equations for method (4) are like those of method (3), except that the total yield parameters γ have been replaced by the quantities ρ since the measurements are made at a retarding potential as discussed in Sec. IV. The numerical values listed for method (4) were obtained as follows: In Table II are listed values of $|\rho_{60}|$ and $|\rho_{100}-\rho_{60}|$ for several values of the retarding potential V_{ST} appraoching the condition when $\rho_{60}\sim0$. We use the data at $V_{ST}=8.5$ v as closest to the point at which $\rho_{60}=-\rho_{100}$ and the detection sensitivity by this method is optimum. From the equation,

$$\rho_{\text{obs}}=\rho_{1S}I_{1S}/(I_{1S}+I_{2S})+\rho_{2S}I_{2S}/(I_{1S}+I_{2S}),$$

which holds at the target in the present apparatus, we obtain for $V_{AC}=60$ v; $I_{2S}=0$, $\rho_{\text{obs}}=\rho_{60}=\rho_{1S}$, and $\rho_{1S}=0.94\times10^{-4}$. At $V_{AC}=100$ v, we take the fraction of metastables to ground state ions to be 40% of Novick and Commins' value at 250 ev bombarding electron energy. This makes use of the cross-section data plotted in Novick and Commins' Fig. 6. Thus $I_{2S}/(I_{1S}+I_{2S})=0.004$ and $I_{1S}/(I_{1S}+I_{2S})\cong1$, again at the target in the present experiment, from which we obtain $\rho_{2S}=250(\rho_{100}-\rho_{60})=0.13$. By using these ρ values and $(\Phi'''-\Phi'')=0.069$, $\Phi''=0.141$, one obtains the signal strengths listed. All of these estimated signal strengths are given in Table III. As expected, method (3) is relatively poor. Methods (2) and (4) are comparable. Method (1) has excellent background but relatively small useful signal.

In Sec. III it was stated that detection by method (3) at a clean surface is poorer than for a contaminated surface. No work has been done on a clean surface with method (4) or, in fact, with Novick and Commins' suggested retarding potential discrimination method. Comparison of Figs. 3 and 12 of footnote reference 23 indi-

TABLE II. Values of ρ parameters and figure of merit for several retarding potentials using method (4) listed in the text.

V_{ST}	$\lvert10^4\rho_{60}\rvert$	$\lvert10^4(\rho_{100}-\rho_{60})\rvert$	$\left\lvert\frac{2(\rho_{100}-\rho_{60})}{(\rho_{100}+\rho_{60})}\right\rvert$
6.5	36.0	5.1	0.13
7.0	20.5	9.5	0.35
7.5	12.1	6.5	0.42
8.0	4.3	4.3	0.67
8.5	0.94	5.2	1.5

[24] R. Novick (private communication).

TABLE III. Comparison of useful metastable signal S and background signal B for four detection schemes applied to the example of Novick and Commins' apparatus.

Method	S	B	S/B
Photoelectric	2.6×10^{-15}	~0	...
Modulated surface	7.0×10^{-12}	1.8×10^{-11}	0.4
Unmodulated surface	7.0×10^{-12}	6.0×10^{-9}	0.001
Unmodulated surface with compensation	1.8×10^{-12}	5.6×10^{-12}	0.3

cates that the kinetic energy distributions of the doubly-charged ions (which the metastable singly-charged ion distributions should resemble) project to considerably larger energies than do those of the ground state singly-charged ions. Thus, the simple retarding potential discrimination of Novick and Commins may well work, but its detailed sensitivity has not been tested. As Novick[24] has suggested, this would require low reflection of the doubly and singly charged ions as ions which unpublished work of the author shows to be the case when the incident energy of the ions is 40 ev or less. Since, in general, ρ changes sign for the singly-charged ions on the clean surface, method (4) should also work but has not been tested.

Novick[24] has raised the important question of the stability of the cancellations method [(4) in the foregoing]. Surface changes, brought about by poor vacuum conditions, for example, could cause appreciable and annoying drift in the background current. What little experience has been gained relating to this problem in the present work would indicate that the contaminated surface is a particularly stable one, once a reasonable pressure, say 10^{-7} mm Hg has been attained, but no test of stability as such has been carried out.

VI. DETECTION OF METASTABLE ATOMS

As indicated in the introduction, an uncharged, metastable atom may also be detected by the electrons which it ejects from a metal. These electrons need not, as we shall see, arise in the so-called direct Auger de-excitation of the metastable. It is possible, if energy levels are appropriate, that the metastable atom will be converted to an ion by resonance tunneling of the metastable electron into an unfilled state in the metal before the Auger transition probabilities become appreciable. Although the resonance (one-electron) and Auger (two-electron) processes have been understood, the possibilities of their interplay in any particular situation has not been generally appreciated.

It is apparent, both theoretically and experimentally, that the one-electron process has a greater probability than does the two-electron process at a given distance of atomic particle from the metal surface. This means that the nature of the particle (as between ion and metastable) at the mean distance from the surface where the Auger process occurs is independent of what the nature of the particle was at large distances from the metal surface.[25,26] Thus, it appears that Greene[7] was actually observing electrons ejected by the helium ion rather than the helium metastable atom with which he bombarded the tungsten surface.[23] Lamb and Retherford[15] in discussing the detection of metastable hydrogen atoms recognized the possibility of surface ionization of the metastable atom, but apparently didn't realize that the ion thus formed would almost immediately undergo Auger neutralization explaining their failure to observe H^+ ions formed from the metastable atoms. Lamb and Retherford quote Bühl[27] who reports observing conversion of metastable Hg atoms to ions at a hot, oxidized metal surface. Certainly at a clean surface one can see no reason why the ion should not almost immediately undergo Auger neutralization. Perhaps the oxidized surface accounts for Bühl's observation.

ACKNOWLEDGMENTS

It is a pleasure to thank C. D'Amico for technical assistance and George E. Moore and Robert Novick for critical reading of the manuscript. The author is particularly grateful to Professor Novick for help and criticism by private communication which is acknowledged at several places in the text.

[25] H. D. Hagstrum, Phys. Rev. **91**, 543 (1954), Sec. V. See also footnote 11, Sec. XI.
[26] L. J. Varnerin, Jr., Phys. Rev. **91**, 859 (1953).
[27] A. Bühl, Helv. Phys. Acta **6**, 231 (1933).

Bounds on the Elements of the Equivalent Network for Scattering in Waveguides. I. Theory*†

LARRY SPRUCH AND RALPH BARTRAM
Physics Department, Washington Square College, New York University, New York 3, New York
(Received June 8, 1959)

For a few particular waveguide problems, standard variational expressions have previously been shown to be upper or lower bounds on the quantities of interest. However, bounds have not previously been obtained for any truly three-dimensional problem; that is, where the fields cannot be derived from a single scalar potential. An example is a three-dimensional obstacle which contacts only one waveguide surface. As one consequence, no straightforward procedure exists for improving the approximations. Recently, Kato devised a rather general method for bounding the cotangent of the phase shift for a given angular momentum in a quantum mechanical central potential scattering problem. This method should be applicable whenever a system can be analyzed in terms of uncoupled standing waves each characterizable by one real phase shift. The method is here adapted to waveguides, including truly three-dimensional problems. The obstacle must be symmetric about a plane perpendicular to the waveguide axis, with certain exceptions only one mode should propagate, and the system should be lossless. Analysis is then possible in terms of η_e and η_0, the real uncoupled phase shifts associated with the even and odd standing waves, respectively. The bounds obtained on $\cot\eta_e$ and $\cot\eta_0$ determine bounds on the equivalent network elements.

1. INTRODUCTION

THE introduction of variational techniques has greatly facilitated the solution of scattering problems in various fields. They were originally applied by Schwinger to scattering in an analysis of waveguide problems[1,2] and quantum mechanical problems[3] and, independently, by Hulthén[4] in an analysis of quantum mechanical problems.[5] These techniques have subsequently proved to be useful in a wide variety of fields including optics, acoustics, and water waves. Though they are clearly superior to previously used techniques, variational techniques as applied to scattering theory suffer a major defect as compared to variational techniques as applied to the determination of point eigenvalues such as the resonant frequencies of vibrating systems or the bound state energy eigenvalues of quantum mechanical systems. This defect is that while the expressions are stationary, they are in general neither an upper nor a lower bound. Thus, given two different trial functions, one cannot generally know which of the two variational results is better; in particular, the incorporation of additional parameters in a given trial function does *not* guarantee a better result. Consequently, it would be very desirable to be able to deduce bounds on the quantities of interest. Now, in fact in some particular waveguide problems the variational expressions themselves have been shown to be upper or lower bounds.[1,2] However, these problems are not sufficiently general to include all cases of practical interest. For example, no technique seems to have been devised which is capable of giving bounds on the relevant quantities for a truly three-dimensional case, that is, where the fields cannot be derived from a single scaler potential.

Now a rather general approach has been devised by Kato[6–9] for obtaining bounds on $\cot(\eta-\theta)$, where η is the phase shift for a given angular momentum in a quantum mechanical central potential scattering problem and θ is a parameter chosen for convenience. This method should be applicable to any problem which can be analyzed in terms of uncoupled standing waves each of which can be characterized by one real phase shift. It is the purpose of this paper to adapt the Kato formalism to scattering by obstacles in waveguides, including the truly three-dimensional problem. The problems to be considered, for reasons which will be discussed later, are subject to the following restrictions: (1) The waveguide is uniform in the asymptotic region; (2) only the dominant mode propagates, with exceptions which will be mentioned later; (3) the obstacle is symmetrical about a plane perpendicular to the axis of the waveguide; and (4) the waveguide and obstacle are lossless.

* The research reported in this document has been supported in part by the Geophysics Research Directorate of the Air Force Cambridge Research Center, Air Research and Development Command.

† Submitted by Ralph Bartram in partial fulfillment of the requirements for the degree of Doctor of Philosophy at New York University.

[1] David S. Saxon, "notes on lectures by Julian Schwinger: Discontinuities in waveguides" (unpublished, 1945).

[2] Nathan Marcuvitz, *Waveguide Handbook* (McGraw Hill Book Company, Inc., New York, 1951), M.I.T. Radiation Laboratory Series, Vol. 10.

[3] J. M. Blatt and J. D. Jackson, Phys. Rev. **76**, 18 (1949). See also B. A. Lippmann and J. S. Schwinger, Phys. Rev. **79**, 469 (1950).

[4] L. Hulthén, Kgl. Fysiograf. Sällskap. Lund, Förh. **14**, 257 (1944).

[5] H. S. W. Massey, "Theory of atomic collisions" in *Encyclopedia of Physics* (Springer-Verlag, Berlin, Germany, 1957), Vol. 36.

[6] T. Kato, Progr. Theoret. Phys. **6**, 394 (1951).

[7] L. Spruch, Phys. Rev. **109**, 2149 (1958).

[8] L. Spruch and M. Kelley, Phys. Rev. **109**, 2144 (1958).

[9] L. Spruch and L. Rosenberg consider scattering by a compound system (to be submitted for publication). The problem of *zero* energy scattering by compound systems has been attacked by a method which is simpler than that of Kato. See L. Spruch and L. Rosenberg, Phys. Rev. **116**, 1034 (1959); Rosenberg, Spruch, and O'Malley, Phys. Rev., to be published.

In the companion paper,[10] the Kato formalism is applied to some specific problems involving dielectric obstacles and it is found that with a simple trial function and a moderate amount of work one can obtain upper and lower bounds on cot $(\eta_0-\theta)$ and cot $(\eta_e-\theta)$, where η_e and η_0 are the real uncoupled phase shifts associated with the even and odd standing waves, respectively. These bounds differ from one another by only a few percent, even for obstacles whose dimensions are comparable with the transverse dimensions of the waveguide. In addition, for the obstacles considered, bounds can be obtained directly on the phase shifts themselves and on the elements of the equivalent T network.

2. APPLICABILITY OF THE KATO METHOD

Before proceeding to the waveguide case, it will be helpful to outline Kato's approach. A standard technique in the quantum theory of scattering of a particle by a central potential, $V(\mathbf{r})=V(r)$, is to separate the wave into partial waves, i.e., the eigenfunctions of the angular momentum operator. For a specified angular momentum and energy, the effect of the potential on each incident partial wave is completely characterized by one real number, the phase shift. For the case of zero orbital angular momentum, which is the closest analogue to the waveguide case we are ultimately interested in, the phase shift η is determined by the equations

$$\mathfrak{L}'u_\theta\equiv\left[\frac{d^2}{dr^2}+k^2+W(r)\right]u_\theta=0, \quad 0\leq r\leq\infty \tag{1a}$$

$$u_\theta(0)=0 \tag{1b}$$

$$u_\theta(r)\rightarrow\cos(kr+\theta)+\cot(\eta-\theta)\sin(kr+\theta), \quad r\rightarrow\infty \tag{1c}$$

In the above expressions, k^2 and $W(r)$ are proportional to the total energy and the negative of the potential energy, respectively, and the normalization constant θ satisfies $0\leq\theta<\pi$, but is otherwise arbitrary. The introduction of θ provides an additional element of freedom.

Let $u_{\theta t}$ be a trial wave function which satisfies the boundary condition (1b) and has the asymptotic form (1c) with a trial phase shift η_t; $u_{\theta t}$ need not of course satisfy the wave equation (1a). (Trial quantities will be distinguished from their exact counterparts by a subscript t.) From Green's theorem,

$$\int_0^\infty(u_\theta\mathfrak{L}'u_{\theta t}-u_{\theta t}\mathfrak{L}'u_\theta)dr=\left[u_\theta\frac{du_{\theta t}}{dr}-u_{\theta t}\frac{du_\theta}{dr}\right]_0^\infty, \tag{2}$$

and from the asymptotic forms of u_θ and $u_{\theta t}$, it follows that

$$k\cot(\eta-\theta)=k\cot(\eta_t-\theta)-\int u_{\theta t}\mathfrak{L}'u_{\theta t}dr+\int w_\theta\mathfrak{L}'w_\theta dr, \tag{3}$$

where

$$w_\theta(r)=u_{\theta t}(r)-u_\theta(r). \tag{4}$$

Equation (3) is an identity. If $u_{\theta t}$ is a good approximation to u_θ, then w_θ is a small term of first order, and the error term $\int w_\theta\mathfrak{L}'w_\theta dr$ is of second order. If the error term is neglected in Eq. (2), the remaining two terms on the right hand side can be evaluated explicitly and constitute a variational expression for $k\cot(\eta-\theta)$. (For certain values of θ, this expression reduces to previously known variational principles.)

Kato's major contribution was the determination of upper and lower bounds on the error term and, hence, on $k\cot(\eta-\theta)$.[6] Kato derives the inequality,

$$-\alpha_\theta^{-1}\int\rho^{-1}(\mathfrak{L}'u_{\theta t})^2dr\leq\int w_\theta\mathfrak{L}'w_\theta dr\leq\beta_\theta^{-1}\int\rho^{-1}(\mathfrak{L}'u_{\theta t})^2dr, \tag{5}$$

where ρ is some nonnegative weight factor to be chosen for convenience; α_θ is the smallest positive eigenvalue and β_θ the smallest (in absolute value) negative eigenvalue of the associated eigenvalue problem,

$$\mathfrak{L}'\phi_n(r)+\mu_n\rho(r)\phi_n(r)=0, \quad 0\leq r\leq\infty. \tag{6}$$

The eigenfunctions ϕ_n and eigenvalues μ_n are determined by the boundary conditions that ϕ_n vanish at the origin and have the asymptotic phase shift $\delta(\mu_n)$ given by

$$\delta(\mu_n)=\theta+n\pi, \quad n=0, \quad \pm1, \cdots. \tag{7}$$

Even quite crude lower bounds on α_θ and β_θ in Eq. (5) will provide close bounds on the error term in Eq. (3), and hence on the phase shift provided the error integral $\int\rho^{-1}(\mathfrak{L}'u_{\theta t})^2dr$, which vanishes for the exact wave function, can be made sufficiently small. Comparison potentials for which Eq. (6) can be solved exactly are employed in the estimation of α_θ and β_θ, together with a theorem which states that the phase shift increases monotonically with increasing "potential", $W(r)$[6-8] (decreasing potential energy).

Let us now consider a one-dimensional quantum mechanical scattering problem, which is a still closer analogue to the waveguide problem. This differs from the previous case in that the range of the independent variable extends from $-\infty$ to $+\infty$. The difference is fundamental, however, since there are now two channels, i.e., two sets of incoming and outgoing waves. In a scattering problem which contains n channels, the remote effects of the scattering process are characterized by an $n\times n$ scattering matrix relating the amplitudes of the n outgoing waves to those of the n incoming waves. Since the n^2 elements of the scattering matrix are complex, there are $2n^2$ quantities in all. However, not all of these quantities are independent. It follows

[10] R. Bartram and L. Spruch, J. Appl. Phys. **31**, 913 (1960).

from conservation of probability (energy in the electromagnetic case) and time reversibility that the scattering matrix is unitary and symmetric, which reduces the number of independent quantities to $\frac{1}{2}n(n+1)$.[11,12] In the case of scattering by a central potential, there is a channel corresponding to each value of the angular momentum, but since the potential does not couple the waves of different angular momentum there is a separate scattering problem for each channel characterized by a single real number, the phase shift. In the one dimensional problem there are two channels; hence, three independent quantities are required to characterize the scattering. For this case, the Kato method does not appear to be applicable. However, if we restrict ourselves to an even potential, $W(x)=W(-x)$, the number of independent parameters is reduced to two. Further, the two independent solutions of the wave equation can be taken as standing waves which are even and odd in x, each characterized by one real number, the phase shifts η_e and η_0, respectively. The even and odd solutions can be regarded as solutions to two completely independent scattering problems, distinguished by the boundary conditions. The odd solution is identical with the solution of the radial wave equation for zero angular momentum (an odd function vanishes at the origin), except that the integrals are multiplied by $\frac{1}{2}$ because the range of integration has been doubled. The Kato method can also be applied to the even solution with minor modifications. The details will not be presented here because of the close correspondence to the waveguide case which will now be treated.[13]

In the waveguide problem two additional formal complications arise. Firstly, the problem is three-dimensional, so that the line integrals which appear in the variational principle are replaced by volume integrals. Secondly, the wave functions are vectors rather than scalars. It will be seen that these two complications do not cause any difficulty in principle; in particular, the assumed uniformity of the waveguide in the asymptotic region makes the problem effectively one-dimensional in this region. However, there are two channels corresponding to each propagating mode. If the Kato method is to be applicable, then in line with the previous discussion the waveguide and obstacle must be such that it is possible to reduce the scattering problem to completely independent problems each characterized by one real number. The number of channels can be reduced to two by requiring that the waveguide have only one propagating mode, which is not a serious restriction in most applications. Then, as in the one-dimensional case, the number of independent parameters can be reduced from three to two, and the scattering problem to completely independent problems for even and odd solutions if the obstacle is symmetrical about a plane perpendicular to the axis of the waveguide.

More than one mode can be allowed to propagate if the obstacle is such that it does not couple these modes. As an example, consider a metallic or uniform dielectric obstacle in a rectangular waveguide in the form of a right circular cylinder centered in the guide, oriented parallel to the direction of polarization of the dominant mode, and extending in that direction to the conducting boundaries. It is possible to select the dimensions of the waveguide in such a way that in some range of frequencies there are only three propagating modes, usually designated TE_{10}, TE_{20}, and TE_{01}.[12] These three modes are not coupled to one another by such an obstacle, nor are the even and odd standing wave solutions corresponding to each mode coupled. Thus, there is a total of six channels such that the scattering in each channel is a separate problem characterized by a single phase shift. A simpler example is that of a dielectric obstacle whose permittivity is an even function of the coordinate parallel to the axis of the waveguide only. The problem is then one-dimensional and we can consider an arbitrary number of propagating modes, for the various channels are uncoupled and each is characterized by a single phase shift. The problem of multiple propagating modes will not be considered further. It will henceforth always be understood that just the dominant mode propagates.

In some cases the symmetry of the obstacle is such that the scattering can be described in terms of a scalar wave function rather than a vector wave function, which may result in considerable simplification. For example, in a rectangular waveguide the dominant mode can be described variously as a TE wave propagating parallel to the axis of the waveguide, as a TM wave propagating parallel to the axis of polarization, or as a TE wave propagating in a direction perpendicular to both of these axes. Any finite obstacle destroys uniformity in the direction of the waveguide, but it may possess sufficient symmetry to preserve uniformity in one of the perpendicular directions, in which case the TE or TM description still applies. Now TE and TM waves can be derived from Hertzian electric and magnetic vector potentials, respectively, which are parallel to the propagation direction of the TE and TM waves, respectively. Thus, the fields are characterized by a single scalar function, the component along the appropriate axis of propagation of the Hertzian vector potential. If the symmetry of the obstacle permits description of the fields in terms of a TM wave propagating parallel to the axis of polarization, the electric field is proportional to the vector potential, and the vector equations derived below go over to scalar equations directly. For the symmetry which permits description in terms of a

[11] John M. Blatt and Victor F. Weisskopf, *Theoretical Nuclear Physics* (John Wiley & Sons, Inc., New York).

[12] C. G. Montgomery, R. H. Dicke, and E. M. Purcell, *Principles of Microwave Circuits* (McGraw-Hill Book Co., Inc., New York, 1948), M.I.T. Radiation Laboratory Series, Vol. 8.

[13] *Note added in proof.*—It has proved possible to obtain bounds on the elements of the 2×2 scattering matrix for the one-dimensional problem for $w(x)$ arbitrary.

TE wave, there is no such simple correspondence and the scalar formulation of the problem requires a separate derivation starting directly from the Hertzian vector potential formulation. Only the vector formulation will be presented here, though in the TE case it might be simpler to use the scalar formulation.

3. VARIATIONAL PRINCIPLES FOR WAVEGUIDES

In this section we shall derive the variational principle for a waveguide for both metallic and dielectric obstacles, with the four restrictions noted in the Introduction. In line with the previous discussion, it then follows that the general scattering problem reduces to two independent scattering problems, each of which can be characterized by just one real phase shift.

On assuming a time dependence $\exp(-i\omega t)$, the electric field intensity $\mathbf{E}(\mathbf{r})$ satisfies the equations,

$$\mathfrak{L}\mathbf{E}=-\nabla\times\nabla\times\mathbf{E}+(\omega^2/c^2+W)\mathbf{E}=0 \qquad (8a)$$

$$\nabla\cdot\epsilon\mathbf{E}=0, \qquad (8b)$$

where c is the velocity of light, ϵ is the relative permittivity, and the potential W is defined by $W=\omega^2(\epsilon-1)/c^2$; the quantum mechanical analogue of W is proportional to the negative of the potential. In addition, $\mathbf{E}$ is required to be normal to all conducting surfaces including any metallic obstacles. Let the z coordinate be parallel to the axis of the waveguide. It follows from restriction (3) that $W(z)=W(-z)$, and the general solution can be expressed as a linear combination of standing wave solutions which are even and odd functions of z. In what follows, subscripts e and o will be used to denote quantities associated with the even and odd functions respectively, but will be omitted wherever the formalism is the same for both functions. The solutions are required to have the asymptotic forms for $z\to+\infty$,

$$\mathbf{E}_{\theta e}(\mathbf{r})=\mathbf{e}(x,y)[-\sin(kz+\theta)+\cot(\eta_e-\theta)\cos(kz+\theta)] \qquad (9a)$$

$$\mathbf{E}_{\theta o}(\mathbf{r})=\mathbf{e}(x,y)[\cos(kz+\theta)+\cot(\eta_o-\theta)\sin(kz+\theta)], \qquad (9b)$$

where $\mathbf{e}(x,y)$ is the form function for the dominant mode, and where θ satisfies $0\leq\theta<\pi$. The utility of the parameter θ will become apparent as we go along.

The trial functions are distinguished from the exact functions by the subscript t, and are required to be even and odd and to have the asymptotic forms given by Eqs. (9), except for the substitution of trial phase shifts η_{et} and η_{ot} for the exact phase shifts η_e and η_o. In addition, the trial function is required to be normal to all conducting surfaces and both the function and its first derivatives are required to be continuous in the interior of the waveguide.

Consider the integral (the subscript θ will occasionally be dropped),

$$\int(\mathbf{E}\cdot\mathfrak{L}\mathbf{E}_t-\mathbf{E}_t\cdot\mathfrak{L}\mathbf{E})d\tau=-\int(\mathbf{E}\cdot\nabla\times\nabla\times\mathbf{E}_t-\mathbf{E}_t\cdot\nabla\times\nabla\times\mathbf{E})d\tau, \qquad (10)$$

where the range of integration is over the interior of the waveguide. (It is to be understood, from here on, that the interior of the waveguides excludes any metallic obstacles.) The second term in the integrand on the left-hand side of Eq. (10) vanishes by virtue of Eq. (8a), and the right-hand side can be transformed by Green's theorem to give

$$\int\mathbf{E}\cdot\mathfrak{L}\mathbf{E}_t d\tau=\int(\mathbf{E}\times\nabla\times\mathbf{E}_t-\mathbf{E}_t\times\nabla\times\mathbf{E})\cdot\mathbf{d}\sigma. \qquad (11)$$

The surface integral vanishes on the conducting surfaces since $\mathbf{E}$ and $\mathbf{E}_t$ are required to be normal to these surfaces, and the contribution from the asymptotic region is

$$\int\mathbf{E}_\theta\cdot\mathfrak{L}\mathbf{E}_{\theta t}d\tau=2k\Big[\cot(\eta_t-\theta)-\cot(\eta-\theta)\Big]\times\int\Big[\mathbf{e}(x,y)\times\mathbf{a}_z\Big]^2\mathbf{d}\sigma, \qquad (12)$$

where $\mathbf{a}_z$ is the unit vector in the z direction and the surface integral is over the cross section of the wave guide.

In the preceding derivation, it has been tacitly assumed that the potential W is continuous in the interior of the waveguide. However, in the case of a discrete dielectric obstacle, W is discontinuous and as a consequence of Eq. (8b) the component of the electric field normal to the surface of the dielectric is also discontinuous. The curl of the electric field is still continuous, however, since it is proportional to the magnetic field and we are assuming that the permeability of the obstacle is the same as that of free space. In this case the volume integral on the left-hand side of Eq. (11) must be split into two volume integrals, one over the interior of the obstacle and the other over the remainder of the interior of the waveguide. In addition to the integral over the conducting surfaces and end surfaces, the right-hand side of Eq. (11) now includes two integrals over the surface of the obstacle, one with an inward directed element of surface $\mathbf{d}\sigma$, and the other with an outward directed element of surface. It can now be seen that these additional integrals make no net contribution if $\mathbf{E}_t$ is required to satisfy the same continuity conditions as $\mathbf{E}$. Both the tangential component of $\mathbf{E}$ and its curl are continuous and the normal component plays no role since the vector product of the normal component with the curl is perpendicular to the element of surface. Thus, the derivation of Eq. (12) is still valid in the case of discrete dielectric obstacles. This exception to the continuity requirements, that the normal component of a

vector function may be discontinuous at the surface of a discrete dielectric obstacle, is applicable in the following sections as well, although it will not be stated there explicitly.

It is convenient at this point to adopt a normalization and notation conforming more closely to that of Kato.[6] Let $\mathbf{u}_\theta$ and $\mathbf{w}_\theta$ be defined by

$$\mathbf{u}_\theta \equiv \left\{ \int [\mathbf{e}(x,y)\times \mathbf{a}_z]^2 d\sigma \right\}^{-\frac{1}{2}} \mathbf{E}_\theta \tag{13a}$$

$$\mathbf{w}_\theta = \mathbf{u}_{\theta i} - \mathbf{u}_\theta. \tag{13b}$$

With these definitions, Eq. (12) can be written as

$$k\cot(\eta-\theta) = k\cot(\eta_i-\theta) - \tfrac{1}{2}\int \mathbf{u}_{\theta i}\cdot \mathfrak{L}\mathbf{u}_{\theta i} d\tau + \tfrac{1}{2}\int \mathbf{w}_\theta \cdot \mathfrak{L}\mathbf{w}_\theta d\tau \tag{14}$$

in analogy with Eq. (3). The factor $\frac{1}{2}$ arises because the range of integration has been doubled. The first two terms on the right-hand side of Eq. (14) can be calculated by specifying the trial function, and constitute a variational approximation for $k\cot(\eta-\theta)$. The third term, $\frac{1}{2}\int \mathbf{w}_\theta \cdot \mathfrak{L}\mathbf{w}_\theta d\tau$, is the error term and is of the order of the square of the error in the trial function.

We now derive one consequence of Eq. (14). We have η as the phase shift associated with W. We let $\eta+d\eta$ be the phase shift associated with $W+dW$, where $dW(\mathbf{r})\geq 0$ for all $\mathbf{r}$. On applying Eq. (14) to the determination of $\eta+d\eta$, we choose for our trial function the *exact* solution $\mathbf{u}_\theta$ associated with W. We find

$$d\eta = (\tfrac{1}{2}\sin^2\eta/k)\int \mathbf{u}_\theta^2(\mathbf{r}) dW(\mathbf{r}) d\tau \geq 0,$$

where the inequality is a consequence of the nonnegativeness of $dW(\mathbf{r})$ and the reality of $\mathbf{u}_\theta(\mathbf{r})$. More generally, it then follows that if $W_2(\mathbf{r})\geq W_1(\mathbf{r})$, then $\eta_2\geq\eta_1$. This result is generally referred to as the monotonicity theorem.

4. RIGOROUS BOUNDS ON THE ERROR

Kato's method for obtaining rigorous bounds on the error term, and hence on $\cot(\eta-\theta)$, can be applied to the waveguide case with minor modification. In order to accomplish this, we make use of the following information about $\mathbf{w}_\theta$:

$$\mathfrak{L}\mathbf{w}_\theta = \mathfrak{L}\mathbf{u}_{\theta i} \tag{15a}$$

$$\mathbf{w}_{\theta e} \to C_e'\mathbf{e}(x,y)\cos(kz+\theta), \quad z\to+\infty \tag{15b}$$

$$\mathbf{w}_{\theta o} \to C_o'\mathbf{e}(x,y)\sin(kz+\theta), \quad z\to+\infty \tag{15c}$$

where C_e' and C_o' are unknown constants. Also, $\mathbf{w}_{\theta e}$ and $\mathbf{w}_{\theta o}$ are even and odd functions of z, respectively; $\mathbf{w}_\theta$ is normal to all conducting surfaces, and $\mathbf{w}_\theta$ and its first derivatives are continuous in the interior of the waveguide. Consider the equation

$$\mathfrak{L}\boldsymbol{\phi}(\mathbf{r}) + \mu\rho(\mathbf{r})\boldsymbol{\phi}(\mathbf{r}) = 0. \tag{16}$$

The function $\boldsymbol{\phi}(\mathbf{r})$ is required to be normal to all conducting surfaces. The weight function $\rho(\mathbf{r})\geq 0$ is an even function of z and tends to zero at large distances from the obstacle in such a way that $\int \rho(\mathbf{r})d\tau$ converges. Equation (16) may be regarded as a scattering problem of the type of Eq. (8) with a potential $W+\mu\rho$. The even and odd standing wave solutions are associated with entirely separate problems and the distinction between them is not relevant to the following discussion. Let $\delta(\mu)$ be the phase shift corresponding to this potential. (The choice of ρ must be such that this problem also satisfies the four restrictions listed in the introduction in order that there be just one phase shift $\delta(\mu)$ associated with each value of μ.) Equation (16) will be referred to as the associated eigenvalue problem with eigenvalues μ_n and eigenfunctions $\boldsymbol{\phi}_n(\mathbf{r})$ when $\delta(\mu_n)$ is restricted by the condition

$$\delta(\mu_n) = \theta + n\pi. \tag{17}$$

If $\mathbf{f}$ and $\mathbf{g}$ are two functions which satisfy the boundary conditions appropriate to $\boldsymbol{\phi}_n$, then it follows from Green's theorem that

$$\int \mathbf{f}\cdot\mathfrak{L}\mathbf{g}\, d\tau = \int \mathbf{g}\cdot\mathfrak{L}\mathbf{f}\, d\tau, \tag{18}$$

where the integrals are over the interior of the waveguide. Thus, the operator $\mathfrak{L}$ restricted by these boundary conditions is hermitian; it follows that the eigenvalues are real and the eigenfunctions satisfy orthogonality relations,

$$k\int \boldsymbol{\phi}_m\cdot\boldsymbol{\phi}_n\rho d\tau = \delta_{mn}, \tag{19}$$

where $\delta_{mn}=1$ if $m=n$ and $\delta_{mn}=0$ if $m\neq n$ and the normalization is chosen for convenience.

By using the monotonicity theorem discussed earlier, it follows since $\rho(r)\geq 0$ for all r that

$$(d\delta(\mu)/d\mu)\geq 0. \tag{20}$$

The eigenvalues therefore satisfy the relationship

$$\mu_{n+1}\geq\mu_n. \tag{21}$$

It can be shown that the eigenfunctions $\boldsymbol{\phi}_n$ form a complete set in the sense that the Parseval identities hold for any functions $\mathbf{F}$, $\mathbf{G}$, which satisfy certain symmetry conditions to be discussed in the following section, which are normal to all conducting surfaces, and which are continuous and have continuous first derivatives; that is

$$k\int \mathbf{F}^2\rho d\tau = \sum a_n^2, \quad k\int \mathbf{F}\cdot\mathbf{G}\rho d\tau = \sum a_n b_n, \quad k\int \mathbf{G}^2\rho d\tau = \sum b_n^2; \tag{22}$$

the a_n and b_n are Fourier coefficients defined by

$$a_n=k\int \boldsymbol{\phi}_n\cdot\mathbf{F}\rho d\tau,\quad b_n=k\int\boldsymbol{\phi}_n\cdot\mathbf{G}\rho d\tau. \tag{23}$$

Now let $\mathbf{F}$ satisfy the boundary conditions (17) and set $\mathbf{G}=\rho^{-1}\mathfrak{L}F$. Then

$$b_n=k\int\boldsymbol{\phi}_n\cdot\mathfrak{L}\mathbf{F}d\tau=k\int\mathfrak{L}\boldsymbol{\phi}_n\cdot\mathbf{F}d\tau=-\mu_n k\times\int\boldsymbol{\phi}_n\cdot\mathbf{F}\rho d\tau=-\mu_n a_n, \tag{24}$$

where we have made use of the hermitian property of $\mathfrak{L}$, Eq. (18). The Parseval identities become

$$k\int F^2\rho d\tau=\sum\mu_n^{-2}b_n^2 \tag{25a}$$

$$k\int\mathbf{F}\cdot\mathfrak{L}\mathbf{F}d\tau=-\sum\mu_n^{-1}b_n^2 \tag{25b}$$

$$k\int(\mathfrak{L}\mathbf{F})^2\rho^{-1}d\tau=\sum b_n^2. \tag{25c}$$

Let α_θ be the smallest positive eigenvalue and $-\beta_\theta$ the smallest (in absolute value) negative eigenvalue, so that

$$-\alpha_\theta^{-1}\leq-\mu_n^{-1}\leq\beta_\theta^{-1}.$$

Then it follows from Eqs. (25) that

$$-\alpha_\theta^{-1}\int(\mathfrak{L}\mathbf{F})^2\rho^{-1}d\tau\leq\int\mathbf{F}\cdot\mathfrak{L}\mathbf{F}d\tau\leq\beta_\theta^{-1}\int(\mathfrak{L}\mathbf{F})^2\rho^{-1}d\tau. \tag{26}$$

The point is that while $\mathfrak{L}$ is an unbounded operator, $\mathfrak{L}^{-1}$ is a bounded operator, its eigenvalues ranging from $-\beta_\theta^{-1}$ to α_θ^{-1}. If we identify $\mathbf{F}$ with $\mathbf{w}_\theta$ defined by Eq. (13b) and recognize that $\mathfrak{L}\mathbf{w}_\theta=\mathfrak{L}\mathbf{u}_{\theta t}$, Eq. (26) implies that

$$-\tfrac{1}{2}\alpha_\theta^{-1}\int(\mathfrak{L}\mathbf{u}_{\theta t})^2\rho^{-1}d\tau\leq\tfrac{1}{2}\int\mathbf{w}_\theta\cdot\mathfrak{L}\mathbf{w}_\theta d\tau\leq\tfrac{1}{2}\beta_\theta^{-1}\int(\mathfrak{L}\mathbf{u}_{\theta t})^2\rho^{-1}d\tau. \tag{27}$$

The quantity $\frac{1}{2}\int(\mathfrak{L}\mathbf{u}_{\theta t})^2\rho^{-1}d\tau$ is determined by specifying the trial function $\mathbf{u}_{\theta t}$. Thus, the problem of obtaining rigorous upper and lower bounds on the error term in Eq. (14) is reduced to that of obtaining rigorous lower bounds on α_θ and β_θ. If the trial function $\mathbf{u}_{\theta t}$ is a good approximation to the exact function $\mathbf{u}_\theta$, $(\mathfrak{L}\mathbf{u}_{\theta t})^2$ is a small term of second order, and even crude lower bounds on α_θ and β_θ can provide close bounds on the error term, and hence on $\cot(\eta-\theta)$.

5. COMPLETENESS

The question of completeness is rather more complicated for the present waveguide case than for the one independent variable quantum mechanical case discussed by Kato. In particular, it will be shown that the $\boldsymbol{\phi}_n$ as defined by the differential Eq. (16) and by the boundary condition Eq. (17), are *not* necessarily complete. Limitations are thereby imposed on the trial function, in addition to the boundary conditions stated in Sec. 3, if the bounds deduced in Sec. 4 on $\cot(\eta-\theta)$ are to be valid. It will be seen, however, that the limitations are in no sense severe; on the contrary, it will only be required that the trial function have the same symmetry properties as the true function. Clearly, no restrictions whatever are thereby introduced on the accuracy of the bounds that can be achieved. The fact remains that each of the symmetry properties must be recognized if the Kato bounds are to be valid.

That the $\boldsymbol{\phi}_n$ are not always complete can be seen by considering the simple example of a waveguide for which the obstacle is a dielectric slab, which extends to the conducting boundaries of the waveguide and whose permittivity is independent of x and y. Then *each* of the $\boldsymbol{\phi}_n$ will *everywhere* (not only asymptotically) have the same x and y dependence. In particular, each $\boldsymbol{\phi}_n$ can be expressed as a product of $\mathbf{e}(x,y)$ and a function of z, where $\mathbf{e}(x,y)$ is the form function appropriate to the dominant mode, and the problem is then effectively one dimensional. In this example, the $\boldsymbol{\phi}_n$ are obviously not a complete set; however, this need cause no concern. It is clear that the true solution $\mathbf{u}$ would also have the same x,y dependence as the dominant mode. One would then choose the trial function $\mathbf{u}_t$ to have this x,y dependence, in which case $\mathbf{w}=\mathbf{u}_t-\mathbf{u}$ would also have this x,y dependence, and this $\mathbf{w}$ *could* be expanded in terms of the $\boldsymbol{\phi}_n$. On the other hand, if one failed to recognize the one dimensionality of the problem and used any x,y dependence other than that given by $\mathbf{e}(x,y)$, $\mathbf{w}$ could *not* be expanded in terms of the $\boldsymbol{\phi}_n$ and the bounds obtained on $\cot(\eta-\theta)$ in Sec. 4 would not be rigorous.

In discussing the question of completeness for an arbitrary $W(x,y,z)$, it is assumed for simplicity of presentation that W and ρ both vanish identically beyond $|z|=d$. It is believed, however, that the conclusions of this section can be established under more general circumstances. Now it can be shown that the eigenfunctions of a positive definite hermitian operator form a complete set.[14] Actually, the essential point is not that the operator be positive definite but rather that there be a minimum negative eigenvalue. That there is a

[14] Philip M. Morse and Herman Feshbach, *Methods of Theoretical Physics* (McGraw-Hill Book Co., Inc., New York, 1953), Part I, pp. 771–777.

minimum negative eigenvalue in the associated eigenvalue problem follows from the assumption that W and ρ vanish identically beyond $|z|=d$, since there is a minimum number of nodes which the wave functions can have in the region $-d<z<d$.

It remains to determine the boundary conditions for which $\mathfrak{L}$ is hermitian. It follows from Green's theorem that for two functions $\mathbf{f}(\mathbf{r})$ and $\mathbf{g}(\mathbf{r})$, which are continuous and have continuous first derivatives, and which are normal to the conducting boundaries of the waveguide,

$$\int(\mathbf{f}\cdot\mathfrak{L}\mathbf{g}-\mathbf{g}\cdot\mathfrak{L}\mathbf{f})d\tau=\int(\mathbf{f}\times\nabla\times\mathbf{g}-\mathbf{g}\times\nabla\times\mathbf{f})\cdot\mathbf{d}\sigma,$$

where the surface integral is over end surfaces of the waveguide in the asymptotic region. Consider a set of eigenfunctions ψ_m of the differential equation

$$\mathfrak{L}\psi_m+\lambda_m\rho\psi_m=0$$

defined by the boundary condition

$$\int(\psi_m\times\nabla\times\psi_n-\psi_n\times\nabla\times\psi_m)\cdot\mathbf{d}\sigma=0$$

for all m and n. Then the operator $\mathfrak{L}$ is hermitian with respect to the set of functions ψ_m and it follows that these functions form a complete set. The set of functions ψ_m can be divided into two subsets. The first subset consists of functions which have the asymptotic form of the dominant mode and whose phase shifts $\delta(\lambda_m)$ differ by integral multiples of π. This subset is identical with a set of associated eigenfunctions ϕ_n with $\lambda_m=\mu_n$. The second subset consists of functions which vanish asymptotically. These functions do not occur in the one independent variable quantum mechanical problem with fixed, positive energy, and it follows that for that problem each of the ψ_m equals one of the ϕ_n which then form a complete set. However, in the waveguide problem the functions which vanish asymptotically can exist under special circumstances which will now be considered.

In the region of large $|z|$, where W and ρ are zero, each ψ_m is a superposition of evanescent waveguide modes and of the dominant waveguide mode. (The term waveguide mode will be used for modes in the absence of an obstacle.) The coefficient of the dominant waveguide mode will be denoted by C_m. There are two alternative possibilities. (1) If each C_m is different from zero, each ψ_m equals one of the ϕ_n and each λ_m equals one of the μ_n. The ϕ_n then form a complete set. (2) If $C_m=0$ for any m, the corresponding ψ_m vanishes asymptotically and the ϕ_n do not then form a complete set.

The condition $C_m=0$ can only arise if some of the evanescent waveguide modes are not coupled to the dominant waveguide mode. This lack of coupling can only occur if W and ρ have some special symmetry property. We have already given one example in which W and ρ are independent of the transverse coordinates. As another example, we consider a rectangular waveguide where the z axis is the axis of the waveguide, the y axis is the axis of polarization of the dominant mode, and the waveguide extends from $x=0$ to $x=a$. We further specify that W and ρ are independent of y and are even functions of $x-\frac{1}{2}a$. Then the functions ϕ_n share the polarization of the dominant mode, are independent of y, and are even functions of $x-\frac{1}{2}a$; the ϕ_n are not, therefore, a complete set. The set of functions ψ_m which is complete includes functions which are odd functions of $x-\frac{1}{2}a$, functions which depend upon y and whose polarization is not along the y axis, and functions with both of these properties, all of which vanish asymptotically. However, the exact solution $\mathbf{u}$ is also polarized parallel to the y axis, is independent of y, and is an even function of $x-\frac{1}{2}a$. If the trial function $\mathbf{u}_t$ is chosen to have the same properties it will be possible to expand $\mathbf{w}$ in terms of the *incomplete* set ϕ_n.

In summary, if W and ρ have no symmetry properties, the ψ_n are identical with the ϕ_n so the latter form a complete set. On the other hand, if W and ρ do have some symmetry properties, the functions ϕ_n have some common symmetry properties and do not then form a complete set. The set of functions ψ_n is complete, however, since it then contains functions which vanish asymptotically and have different symmetry properties. For an arbitrary trial function $\mathbf{u}_t$ the difference function $\mathbf{w}$ could only be expanded in terms of the ψ_n; one could not then use the monotonicity theorem to order the eigenvalues in terms of the phase shifts, an ordering which is essential for the applicability of the method used in the following section for the determination of bounds on α_θ and β_θ. It is of course quite possible that methods could be devised for the determination of bounds on α_θ and β_θ even for the case for which evanescent modes must be included; if, however, $\mathbf{u}_t$ is chosen with the correct symmetry, $\mathbf{w}$ can be expanded in terms of the ϕ_n and the question does not then arise.[15]

6. LOWER BOUNDS ON α_θ AND β_θ

The general procedure for obtaining lower bounds on α_θ and β_θ involves the use of comparison potentials for which the scattering problem can be solved exactly, and the use of the monotonicity theorem, Eq. (20). A number of cases have been treated in the literature.[6,8] In this section we will consider just three special cases applicable to a wide variety of waveguide scattering problems. We restrict ourselves to waveguides which are of uniform cross-section everywhere. These three cases are particularly simple to apply.

In the context of the following discussion, metallic obstacles may be regarded as dielectric obstacles with infinite negative permittivity. (This comment does not

[15] Some further discussion on completeness is contained in a paper referred to in footnote 9.

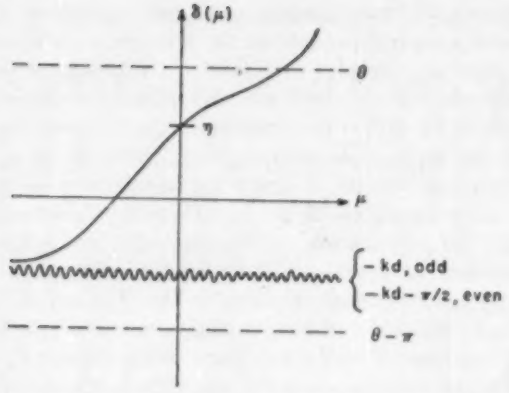

FIG. 1. Determination of a lower bound on β_θ assuming $\eta<\theta$, and assuming $-kd>\theta-\pi$ in the odd case and $-kd-\frac{1}{2}\pi>\theta-\pi$ in the even case. Since $\delta(\mu)$ must exceed $\theta-\pi$, β_θ is infinite.

apply to the preceding discussion of the variational principle and associated eigenvalue because the integrals would be divergent with an infinite "potential".) Suppose the obstacle does not extend beyond $z=\pm d$, and that ρ is identically zero for $|z|>d$ and positive for $|z|<d$.

We will first obtain a lower bound on β_θ. As μ approaches $-\infty$, it is evident that the phase shift $\delta(\mu)$ of the associated eigenvalue problem approaches $-kd$ in the odd case and $-kd-\frac{1}{2}\pi$ in the even case. Now if $-\mathrm{kd}>\theta-\pi$ in the odd case or $-kd-\frac{1}{2}\pi>\theta-\pi$ in the even case and if $\eta<\theta$, then as shown in Fig. 1, there can be no negative eigenvalues and β_θ can be regarded as infinite. In this case the error term in Eq. (14) is always negative, and the variational approximation to $k\cot(\eta-\theta)$ is always an upper bound on the exact value.

A lower bound on α_θ can be obtained as follows. We know from the monotonicity theorem, Eq. (20), that the phase shift $\delta(\mu)$ is less than the phase shift $\delta'(\mu)$ which would result if the obstacle were replaced by a dielectric slab which fills the space $-d<z<d$ out to the conducting boundaries of the waveguide, and whose potential is equal to the maximum value of $W+\mu\rho$. This phase shift is given by

$$\delta_e'(\mu)=-kd+\tan^{-1}(k'd/kd\,\tan k'd) \tag{28a}$$

$$\delta_o'(\mu)=-kd+\tan^{-1}(kd/k'd\,\tan k'd) \tag{28b}$$

$$k'=k'(\mu)=[k^2+(W+\mu\rho)_{\max}]^{\frac{1}{2}} \tag{28c}$$

It can be seen from Fig. 2 that a useful lower bound on α_θ is provided by the value of μ, to be denoted by α_θ', defined by $\delta'(\alpha_\theta')\equiv\theta$, provided that $\eta'\equiv\delta'(0)<\theta$ and $\eta>\theta-\pi$. For a dielectric obstacle η will always be greater than zero and the last condition will automatically be satisfied.

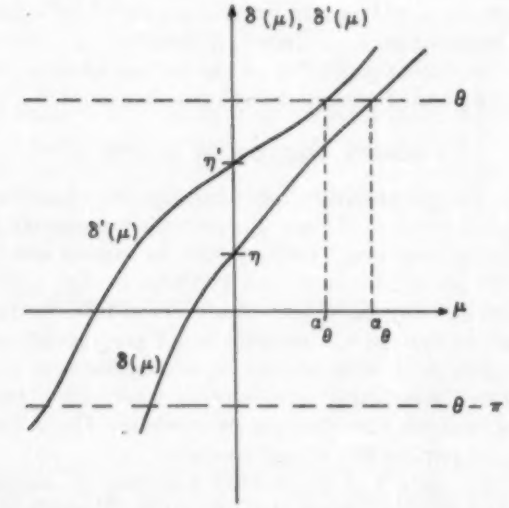

FIG. 2. Determination of a lower bound on α_θ assuming $\eta'<\theta$ and $\eta>\theta-\pi$. The upper curve corresponds to a dielectric slab filling the guide in the range $-d<z<d$, whose "potential" equals the maximum "potential" of the obstacle. From the monotonicity theorem, $\delta'(\mu)>\delta(\mu)$ and therefore $\alpha_\theta'<\alpha_\theta$.

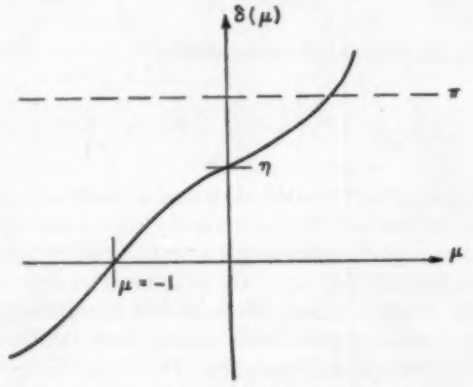

FIG. 3. Determination of the exact value of β_θ assuming $W>0$, $\rho=W$, $\theta=0$, and $\eta<\pi$. In this case, β_0 is given exactly by $\beta_0=1$.

From the rough bounds already obtained on η,

$$-kd-\tfrac{1}{2}\pi<\eta_e<\eta_e', \tag{29a}$$

$$-kd<\eta_o<\eta_o', \tag{29b}$$

it follows that a sufficient condition for obtaining lower bounds on α_θ and β_θ by the procedure described in the foregoing is that $d(k^2+W_{\max})^{\frac{1}{2}}$ be less than $\frac{1}{2}\pi$ in the even case and less than π in the odd case. An equivalent statement is that $2d$ must be less than $\frac{1}{2}\lambda$ in the even case and λ in the odd case, where λ is the smallest guide wavelength in the dielectric. However, it should be noted that these restrictions are by no means fundamental, since there are many more possibilities for obtaining lower bounds on α_θ and β_θ.

There is one case of interest in which β_θ can be determined exactly.[6] If W is everywhere positive we can choose $\rho=W$. Then the potential of the associated eigenvalue problem, $W+\mu\rho$, vanishes when $\mu=-1$; $\delta(-1)$ vanishes then also. If we choose $\theta=0$, it is evident that $\mu=-1$ is an eigenvalue. Furthermore, if we know that $\eta<\pi$, it is the smallest (in absolute value)

negative eigenvalue as can be seen from Fig. 3. Thus, for the case in which $W>0$, $\rho=W$, $\theta=0$, and $\eta<\pi$, the eigenvalue β_0 is given exactly by

$$\beta_0=1. \tag{30}$$

(More generally, if $W>0$, if $\rho=W$, and if $\eta<\theta$, then $\beta_\theta\geq 1$.) Equation (30) is applied in Part 2 to a problem in which a special trial function is used which generates the Schwinger integral variational principle.

ACKNOWLEDGMENTS

We would like to thank Dr. Martin Kelly, Leonard Rosenberg, and Kalman Kalikstein for a helpful discussion.

JOURNAL OF APPLIED PHYSICS VOLUME 31, NUMBER 5 MAY, 1960

Bounds on the Elements of the Equivalent Network for Scattering in Waveguides. II. Application to Dielectric Obstacles*†

RALPH BARTRAM AND LARRY SPRUCH

Physics Department, Washington Square College, New York University, New York 3, New York

(Received June 8, 1959)

The theory developed in the companion article for obtaining rigorous bounds on $\cot\eta$, where η the phase shift, is applied to scattering by dielectric obstacles in rectangular waveguides. For the obstacles considered here, bounds are also obtained on the phase shifts directly and on the elements of the equivalent T network. The exact solution for a dielectric slab of finite length, which extends to the conducting boundaries of the waveguide and completely encloses the obstacle, is introduced as a convenient trial function. The permittivity of the slab is retained as a parameter which is varied to improve the bounds. In the expressions for the bounds on $\cot\eta_s$ and $\cot\eta_0$, the particular obstacle configuration appears only in certain integrals of relatively simple form. Numerical results are obtained for large and small obstacles of various shapes, including some truly three-dimensional cases. The upper and lower bounds on the phase shifts and on the elements of the equivalent circuit are found to be quite close to one another. In one case, the bounds obtained by using the simple trial function are compared with the bounds obtained by using the trial function which generates the Schwinger integral variational principle.

1. INTRODUCTION

IN the preceding paper,[1] the Kato[2] method for obtaining rigorous variational bounds on the phase shifts was adapted to scattering by obstacles in waveguides. In this paper the theory is applied to several specific examples of obstacles in a rectangular waveguide. The application to metallic obstacles is complicated by the requirement that the trial function $\mathbf{u}_t$ be normal to the surface of the obstacle, and therefore, it seemed preferable to limit ourselves in the present paper to dielectric obstacles.

In principle, there is a great deal of freedom in the choice of a trial function. In practice, the trial function must of course be one for which the integrals in Eq. (14), Part I can be performed. We have gone further and sought a trial function which leads to an uncomplicated final analytic form from which numerical results can be fairly readily obtained. A particularly simple trial function, which has been found to provide reasonably close bounds, is the exact solution for a homogeneous dielectric slab of finite extent in the axial direction which completely encloses the obstacle and extends to the conducting boundaries of the waveguide. It should be noted that this trial function contains all of the symmetry properties that could be required with any obstacle to ensure completeness of the associated eigenfunctions.

We have also given some consideration to the trial function which generates the Schwinger integral variational principle.

Both the variational principle and the method for obtaining bounds are equally applicable to relatively large and very small obstacles, and include multiple, hollow, and composite obstacles. For simplicity, we have considered only examples of uniform permittivity, but this is by no means necessary. We have also considered obstacles whose maximum axial extent is a half wavelength in the dielectric; this enables us to use the lower bounds on the associated eigenvalues α_θ and β_θ developed in Part I, but as noted there, bounds on α_θ and on β_θ can be obtained under much more general conditions. Finally, the scattering problems satisfy the four conditions listed in the Introduction to Part I; these conditions are essential to the applicability of the method. The variational principle and the method

* The research reported in this document has been supported in part by the Geophysics Research Directorate of the Air Force Cambridge Research Center, Air Research and Development Command.

† Submitted by Ralph Bartram in partial fulfillment of the requirements for the degree of Doctor of Philosophy at New York University.

[1] L. Spruch and R. Bartram, 31, 905, J. Appl. Phys. (1960) previously published as New York University Report No. Em 132, (1959).

[2] T. Kato, Progr. Theoret. Phys. 6, 394 (1951).

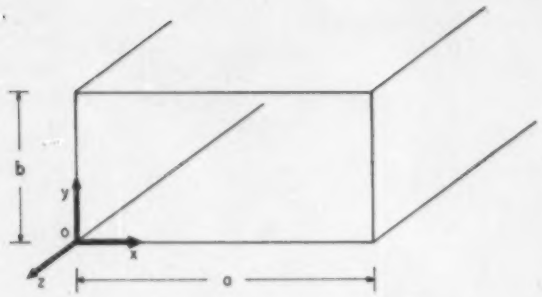

FIG. 1. Rectangular waveguide showing dimensions and coordinate system.

for obtaining bounds are valid even when the problem cannot be reduced to a scalar problem, as, for example, when the obstacle does not extend between opposite walls of the waveguide.

2. TRIAL FUNCTION FOR DIELECTRIC OBSTACLES

In this section, the theory of Part I will be applied to scattering from dielectric obstacles in a rectangular waveguide. The dimensions of the waveguide and the coordinate system are defined in Fig. 1. The polarization of the dominant mode is parallel to the y axis. We will take as the trial function the exact function for a homogeneous dielectric slab, which fills the region $-d\leq z\leq d$, where $2d$ is the greatest extent of the obstacle in the z direction, and extends to the conducting boundaries of the waveguide. Since the obstacle is symmetric about $z=0$, the slab completely encloses the obstacle. The permittivity of the slab, or, equivalently, the 'potential' of the slab is retained as a parameter to be varied to improve the bounds on the phase shifts η_e and η_0 associated with the even and odd standing wave solutions, respectively. The normalization constant θ can also be varied. However, it is more convenient, and it will prove to be sufficient, simply to take $\theta=\pi-kd$ in the odd case and in the determination of a lower bound on $k\cot(\eta_e-\theta)$ in the even case, and $\theta=\frac{1}{2}\pi-kd$ in the determination of the upper bound in the even case. With this choice of θ, β_θ can be regarded as infinite in Eq. (27) of Part I. Note that the variation of either the potential or of θ to improve the upper bound is independent of the variation of these quantities to improve the lower bound.

The trial functions for $-d<z<d$ with the above choices for θ are

odd, both bounds

$$\mathbf{u}_{ot}=-\mathbf{j}(2/ab)^{\frac{1}{2}}\frac{\sin(\pi x/a)\sin Kz}{\sin Kd} \tag{1a}$$

even, lower bound

$$\mathbf{u}_{et}=-\mathbf{j}(2/ab)^{\frac{1}{2}}(kd/Kd)\frac{\sin(\pi x/a)\cos Kz}{\sin Kd} \tag{1b}$$

even, upper bound

$$\mathbf{u}_{et}=-\mathbf{j}(2/ab)^{\frac{1}{2}}\frac{\sin(\pi x/a)\cos Kz}{\cos Kd}, \tag{1c}$$

where $\mathbf{j}$ is the unit vector in the y direction. The parameter K which is to be varied is related to the 'potential' W' of the dielectric slab by

$$K=(k^2+W')^{\frac{1}{2}}. \tag{2}$$

The normalization of the trial functions in Eq. 1a–c is determined by matching the tangential components of $\mathbf{E}$ and $\mathbf{H}$ at $z=\pm d$ to the asymptotic forms defined by Eqs. (9) and (13a) of Part I. The trial phase shifts, η_{ot} and η_{et}, are obtained by the same procedure. It is also convenient to take the weight function ρ to be constant for $-d\leq z\leq d$ and to be zero for $|z|>d$. Substitution of the trial functions and trial phase shifts in Eqs. (14) and (27) of Part I then yields as the bounds on $\cot\eta_e$ and $\cot\eta_0$,

$$-\tfrac{1}{2}\csc^2(Kd)[P^2Q^-+(2PR+R^2)I_0]/(\pi^2-k^2d^2-R)\leq kd\cot(\eta_0-\pi+kd)-Kd\cot(Kd)+\tfrac{1}{2}\csc^2(Kd)(PQ^-+RI_0)\leq 0 \tag{3a}$$

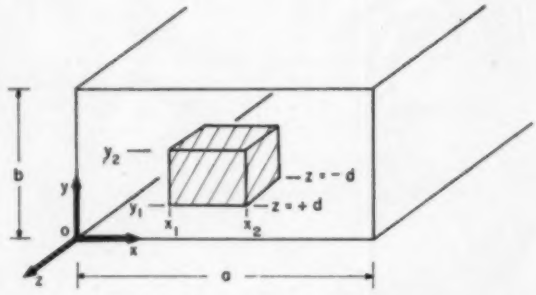

FIG. 2(a). A dielectric obstacle in a rectangular waveguide, in the form of a rectangular parallelopiped oriented parallel to the axes of the waveguide.

$$kd\cot(\eta_e-\tfrac{1}{2}\pi+kd)\leq -Kd\tan(Kd)-\tfrac{1}{2}\sec^2(Kd)(PQ^++RI_e) \tag{3b}$$

$$\left.\begin{aligned}Kdkd\cot(Kd)-\tfrac{1}{2}kd\csc^2(Kd)(PQ^++RI_e)\\ -\tfrac{1}{2}kd\csc^2(Kd)[P^2Q^++(2PR+R^2)I_e]/\\ (\pi^2-k^2d^2-R)\leq(Kd)^2\cot(\eta_e-\pi+kd),\end{aligned}\right\} \tag{3c}$$

where

$$P\equiv(kd)^2-(Kd)^2 \tag{4a}$$

$$Q^{+,-}\equiv 1\pm\sin 2Kd/2Kd \tag{4b}$$

$$R\equiv Wd^2 \tag{4c}$$

$$I_0\equiv(2/abd)\int_{obst}\sin^2(\pi x/a)\sin^2(Kz)d\tau \tag{4d}$$

$$I_e\equiv(2/abd)\int_{st}\sin^2(\pi x/a)\cos^2(Kz)d\tau. \tag{4e}$$

The range of integration in Eqs. (4d) and (4e) is over

the volume of the obstacle. With the specified values of θ, it follows from Eqs. (28) of Part I that a lower bound on α_θ is given by

$$\alpha_\theta \rho d^2 > \pi^2 - k^2 d^2 - W d^2. \tag{5}$$

We have incorporated this lower bound in the inequalities (3).

The inequalities (3) are quite general; it can be seen that the specific geometry of the obstacle enters only in the integrals I_0, I_e defined by Eqs. (4d) and (4e), respectively. The integrals I_0 and I_e are evaluated below for four obstacle geometries: a rectangular parallelopiped and right circular cylinders oriented parallel to each of the coordinate axes.

(a) A rectangular parallelopiped, extending from x_1 to x_2, y_1 to y_2, and $z=-d$ to $z=+d$, as shown in Fig. 2(a),

$$I_{e,o}=\left(\frac{y_2-y_1}{b}\right)\left[\frac{x_2-x_1}{a}-\frac{1}{2\pi}\sin\left(\frac{2\pi x_2}{a}\right)+\frac{1}{2\pi}\sin\left(\frac{2\pi x_1}{a}\right)\right]Q^{+,-}. \tag{6a}$$

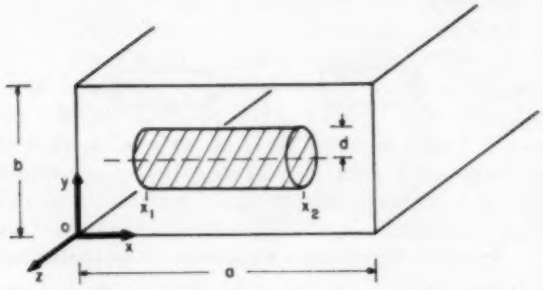

FIG. 2(b). A dielectric obstacle in a rectangular waveguide, in the form of a right circular cylinder of radius d parallel to the x axis.

(b) A right circular cylinder parallel to the x axis, extending from x_1 to x_2 and with radius d, as shown in Fig. 2(b). The integrals do not depend upon the y coordinate of the axis of the cylinder,

$$I_{e,o}=\frac{\pi d}{2b}\left[\frac{x_2-x_1}{a}-\frac{1}{2\pi}\sin\left(\frac{2\pi x_2}{a}\right)+\frac{1}{2\pi}\sin\left(\frac{2\pi x_1}{a}\right)\right]\times\left[1\pm\frac{J_1(2Kd)}{Kd}\right], \tag{6b}$$

where J_1 is a Bessel function.

(c) A right circular cylinder parallel to the y axis extending from y_1 to y_2, with radius d, and with the axis of the cylinder at $x=x_0$, as shown in Fig. 2(c),

$$I_{e,o}=\frac{\pi d(y_2-y_1)}{2ab}\left\{1\pm\frac{J_1(2Kd)}{Kd}-\cos\left(\frac{2\pi x_0}{a}\right)\left[\frac{J_1(2\pi d/a)}{\pi d/a}\pm\frac{J_1(2[(Kd)^2+(\pi d/c)^2]^{\frac{1}{2}})}{[(Kd)^2+(\pi d/c)^2]^{\frac{1}{2}}}\right]\right\}. \tag{6c}$$

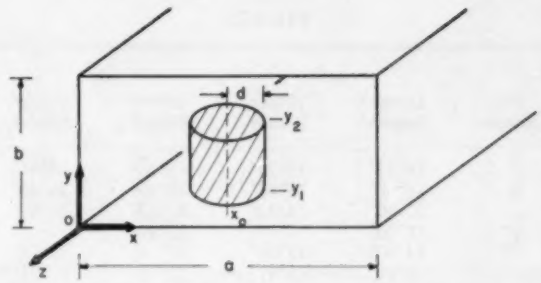

FIG. 2(c). A dielectric obstacle in a rectangular waveguide, in the form of a right circular cylinder of radius d parallel to the y axis.

(d) A right circular cylinder parallel to the z axis extending from $z=-d$ to $z=+d$ with radius R and with axis at x_0, as shown in Fig. 2(d). The integrals are independent of the y coordinate of the axis of the cylinder,

$$I_{e,o}=\frac{\pi R^2}{ab}Q^{+,-}\left[1-\left(\cos\frac{2\pi x_0}{a}\right)\frac{J_1(2\pi R/a)}{\pi R/a}\right]. \tag{6d}$$

On the basis of the above results, we can readily evaluate the necessary integrals for the case of hollow, composite, and multiple obstacles composed of simple shapes like those described above. Terms of the form $f(R)I$ are simply replaced by $\Sigma_n f(R_n)I_n$, where the index n refers to a constituent obstacle. The set of obstacles must still be symmetrical about $z=0$, and must not extend in the z direction more than the shortest half wavelength in the dielectric.

3. NUMERICAL EXAMPLES FOR DIELECTRIC OBSTACLES

In this section, numerical examples are presented for each of the obstacle geometries discussed in the preceding section: a rectangular parallelopiped, and right circular cylinders parallel to the x, y, and z axes, which will be referred to hereafter as geometries A, B, C, and D, respectively. The following parameters have been chosen arbitrarily for convenience,

$$\omega^2 a^2/c^2=2\pi^2 \tag{7a}$$

$$b/a=\tfrac{1}{2} \tag{7b}$$

$$d/a=\tfrac{1}{4} \tag{7c}$$

$$\epsilon=2\epsilon_0, \tag{7d}$$

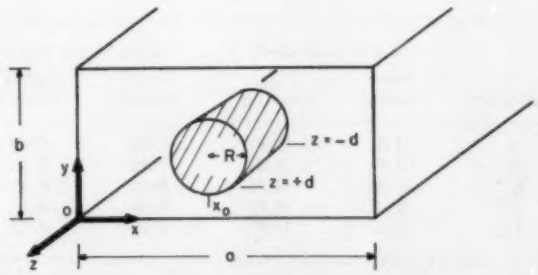

FIG. 2(d). A dielectric obstacle in a rectangular waveguide, in the form of a right circular cylinder of radius R parallel to the z axis.

TABLE I.[a]

Geometry	η_0 Lower bound	η_0 Upper bound	η_e Lower bound	η_e Upper bound
A	18°42′	19°24′	34°20′	34°55′
B	13° 0′	13°47′	35°49′	36°46′
C	11°19′	12°12′	33°13′	33°50′
*C**	11°25′	—	32°19′	—
*D*1	14°30′	15°30′	31° 8′	32°18′
*D*2	3°19′	3°47′	12° 6′	13°25′

[a] Upper and lower bounds on the even and odd phase shifts were calculated with the simple trial function with the exception of *C**, which was calculated for geometry *C* using the trial function which generates the Schwinger integral variational principle.

where ϵ_0 is the permittivity of free space. Note that with this choice of the parameters only the dominant mode propagates, since

$$k_n=\left[\frac{\omega^2}{c^2}-\frac{n^2\pi^2}{a^2}\right]^{\frac{1}{2}}$$

is real only for $n=1$. Also, a half guide wavelength in the dielectric is $a/3^{\frac{1}{2}}$ which exceeds $2d=\frac{1}{2}a$ by the factor $2/3^{\frac{1}{2}}$. In addition, the following dimensions have been selected for the particular geometries:

Geometry (A): $x_1=\frac{1}{2}a-d$, $x_2=\frac{1}{2}a+d$, $y_1=0$, $y_2=b$

Geometry (B): $x_1=0$, $x_2=a$.

Geometry (C): $x_0=\frac{1}{2}a$, $y_1=0$, $y_2=b$

Geometry (D): $x_0=\frac{1}{2}a$. Two cases are calculated, (1) $R=\frac{1}{4}a$ and (2) $R=\frac{1}{8}a$.

The parameter Kd/π might be expected to yield the closest bounds for some value between $\frac{1}{4}$ and $3^{\frac{1}{2}}/4$, corresponding to no obstacle and to a dielectric slab with the same permittivity as the obstacle, respectively. Calculations were carried out for $Kd/\pi=0.25$, 0.30, 0.35, 0.40, and 0.45. The best of the upper and lower bounds on η_0 and η_e for each geometry are listed in Table I. The corresponding values for Kd/π are listed in Table II. Bounds on $\cot(\eta-\theta)$ are actually calculated, so that in general bounds on η are determined only to within an integral multiple of π. However, in all of the examples considered we have required that the obstacle be such that $-\pi<\eta-\theta<0$ in order to obtain lower bounds on α_θ and β_θ. In addition, it follows from the monotonicity theorem that $0<\eta$ since the permittivity is positive in all examples considered. As a consequence, bounds can be determined on η directly as well as on $\cot(\eta-\theta)$. It is more conventional to present the data in terms of the elements of the equivalent circuit shown in Fig. 3.[3,4] The reactances X_1 and X_2 are relative to the characteristic impedance of the waveguide, and are related to the phase shifts η_0 and η_e by

$$X_1=\tan\eta_0 \tag{11a}$$

$$X_2=\tfrac{1}{2}(\cot\eta_e+\tan\eta_0). \tag{11b}$$

The upper and lower bounds on X_1 and X_2 for each of the geometries are listed in Table III.

Geometries *A*, *C*, and *D*1 correspond to obstacles of comparable volume, whereas the volume of *D*2 is one-quarter that of *D*1, resulting in a smaller series reactance and larger shunt reactance. Obstacle *B* has twice the volume of *C* and *D*1, but the additional material is in a region of low field and makes relatively little contribution.

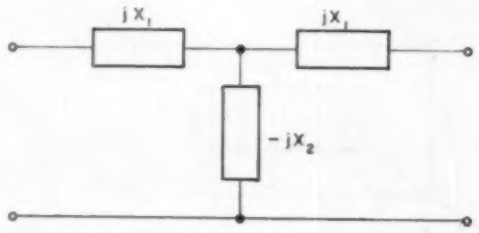

FIG. 3. Equivalent *T* network for describing the far field effects of scattering by dielectric obstacles in waveguides.

The upper and lower bounds on the even and odd phase shifts for geometry *D*1, corresponding to all five values of the variation parameter Kd/π, are listed in Table IV. The best bounds were obtained with $Kd/\pi=0.40$, except for the upper bound on η_0, which was obtained with $Kd/\pi=0.35$. The best bounds with geometry *D*2 were all obtained with $Kd/\pi=0.30$. The same range of values of Kd was employed in calculating both geometries (*D*1) and (*D*2), since then only the integrals I_e and I_0 of Eq. (6d), which are independent of Kd, were different for the two cases. However, the above result suggests that better bounds might have been obtained for geometry (*D*2) if a smaller range of values of Kd close to $\pi/4$ had been selected.

If the "potential" of the slab is taken as the average of the actual "potential" contained within the slab,

TABLE II.[a]

Geometry	Kd/π (odd case) Lower bound	Kd/π (odd case) Upper bound	Kd/π (even case) Lower bound	Kd/π (even case) Upper bound
A	0.40	0.40	0.40	0.40
B	0.40	0.30	0.40	0.40
C	0.40	0.30	0.40	0.40
*D*1	0.40	0.35	0.40	0.40
*D*2	0.30	0.30	0.30	0.30

[a] Bounds on the phase shifts were calculated with the simple trial function using five values of the variation parameter Kd/π: 0.25, 0.30, 0.35, 0.40, and 0.45. The best of the five bounds in each case is listed in Table I; in this table are listed the corresponding values of Kd/π (note that these are not bounds on Kd/π).

[3] Nathan Marcuvitz, *Waveguide Handbook* (McGraw-Hill Book Company, Inc., New York, 1951), Massachusetts Institute Technology Radiation Laboratory Series, Vol. 10.

[4] C. G. Montgomery, R. H. Dicke, and E. M. Purcell, *Principles of Microwave Circuits* (McGraw-Hill Book Company, Inc., New York, 1948), Massachusetts Institute Technology Radiation Laboratory Series, Vol. 8.

TABLE III.[a]

Geometry	X_1 Lower bound	X_1 Upper bound	X_2 Lower bound	X_2 Upper bound
A	0.3348	0.3522	0.8833	0.9082
B	0.2309	0.2453	0.7846	0.8155
C	0.2001	0.2162	0.8460	0.8717
*D*1	0.2586	0.2773	0.9202	0.9664
*D*2	0.05795	0.06613	2.125	2.365

[a] Upper and lower bounds on the reactances of the equivalent T network shown in Fig. 3, for the geometries described in the text.

TABLE IV.[a]

Kd/π	η_0 Lower bound	η_0 Upper bound	η_e Lower bound	η_e Upper bound
0.25	13°27′	15°59′	24°56′	90° 9′
0.30	14° 0′	15°41′	27°42′	48° 6′
0.35	14°26′	15°30′	30° 9′	33°37′
0.40	14°30′	15°31′	31° 8′	32°18′
0.45	13°54′	15°52′	0°	34°16′

[a] The upper and lower bounds on the even and odd phase shifts for geometry *D*1 are listed for all five values of the variation parameter Kd/π.

weighted with the square of the trial field, it is evident that the first order correction term vanishes in Eq. (14) of Part I. As a consequence, the trial phase shift is itself a variational approximation to the actual phase shift, and when $\beta_0=\infty$ it is a lower bound. It seems likely that the potential which provides the best bounds is not very different from the average potential. A rough estimate of the average potential might provide a criterion for selecting the range of values of Kd in a particular problem. It would also follow that Kd should be close to $\pi/4$ for small obstacles.

Approximate values of η_0 and η_e were calculated for the example of geometry (3) by using the Schwinger integral variational principle and trial function described in another paper[5] and are listed in Table I. If we take $\rho=W$ in Eq. (27) of Part I, and if we have $W>0$ and $\eta<\pi$, then $\beta_0=1$ as shown in Part I. We can combine Eqs. (14) and (27) of Part I to obtain an upper bound on $\cot\eta$. It can be shown that the Schwinger variational principle provides a lower bound on $\cot\eta$ by substituting in this inequality the trial function,

$$\mathbf{u}_t=\frac{\mathbf{j}}{(ab)^{\frac{1}{2}}}\left[2\cot\eta\psi(\mathbf{r})+a\int_v G(\mathbf{r},\mathbf{r}')W(\mathbf{r}')\phi(\mathbf{r}')d\tau'\right], \quad (12)$$

where $\psi(\mathbf{r})$ is the field that would exist in the absence of the obstacle, $\phi(\mathbf{r})$ is the trial function used in the Schwinger variational principle, and $G(\mathbf{r},\mathbf{r}')$ is the appropriate Green's function defined in footnote (5). (This result was previously proved by Kato[2]). The Schwinger result provides a better lower bound on η_0 and a worse lower bound on η_e than the simple trial function; however, the comparison between the two trial functions is not altogether fair because the trial function for the Schwinger case was chosen to provide accurate results only for small obstacles.

We have seen that relatively close bounds can be obtained with a rather crude trial function and only five values of the variational parameter. Closer bounds might be obtained with the same trial function by varying θ, or by considering other values of Kd; the most natural way to choose another value of Kd would probably be to plot the bound on $\cot(\eta-\theta)$ vs Kd for the values of Kd originally considered, to guess from the curve the best value of Kd, and then to do the calculation for that value of Kd. It is of course also possible to introduce a more sophisticated trial function with more variational parameters, but this procedure will probably result in considerably more labor.

[5] David S. Saxon, "Notes on lectures by Julian Schwinger: Discontinuities in waveguides" (unpublished, 1945).

Stacking Faults in Zinc

A. FOURDEUX AND A. BERGHEZAN
European Research Associates, Brussels, Belgium

AND

W. W. WEBB
Union Carbide Metals Company, Niagara Falls, New York

(Received January 18, 1960.)

Configurations of individual dislocations in zinc have been studied by electron transmission microscopy and by x-ray diffraction microscopy. Loops of sessile dislocation have been observed surrounding stacking faults lying on (0001) planes. These loops were evidently formed by condensation of point defects. Changes in loop size with climb of the surrounding dislocation have been observed occurring in the electron microscope. Separation of glissile dislocations into partial dislocations separated by stacking faults on (0001) planes have also been observed. Various interactions among the several types of dislocations occur.

STACKING faults and the associated partial dislocations have been observed in numerous face centered cubic metals using electron transmission microscopy techniques.[1–7] Predictions of stacking faults energies based on theoretical considerations[8] have not been entirely confirmed by experimental measurements.[9,10] Early theoretical calculations predicted that zinc, a hexagonal close packed metal, would have a high stacking fault energy. In spite of this, we have observed stacking faults in zinc both by transmission electron microscopy and by x-ray diffraction microscopy. In this metal, with a hexagonal crystal lattice, the two methods complement each other, since combination of results permits positive identification of stacking faults and both partial and total dislocations.

For electron transmission microscopy experiments 99.999% pure zinc obtained from Consolidated Mining and Smelting Company of Canada was rolled to a foil about 0.002 cm thick. These foils were then polished electrolytically to the necessary 1500–2000 A thickness. Essentially standard electron transmission techniques were used employing a Philips electron microscope.

Individual dislocations were readily observed in these foils and a variety of phenomena involving interactions of dislocations, grain boundaries, etc. were observed. However, our detailed work on these phenomena will be discussed in a later paper, since our present topic is stacking faults.

Partial glissile dislocations separated by stacking faults were occasionally observed. Figure 1 shows a collection of these defects lying on (0001) planes of the hexagonal zinc crystal. They could only be observed in the very infrequent cases where the (0001) planes lay at a substantial angle to the plane of the foil.

Circular discs of stacking faults surrounded by sessile dislocations were often observed and are shown in Fig. 2.[11] The appearance of distinct interference fringes within the loops on tilting the foil in the electron beam is shown in the insert of Fig. 2. This clearly demonstrates the presence of stacking faults within the loop. Some of these loops were as large as 5 microns in diameter. In some fields the loops appear darker, in others lighter, and in still others at the same intensity as the surrounding material depending on the crystal-

FIG. 1. Transmission electron micrograph showing stacking fault ribbons in a zinc foil formed by the splitting of glissile dislocations into partials which move apart distances of several microns.

[1] W. Bollmann, *Electron Microscopy Proceedings of the Stockholm Conference* (1956), edited by F. S. Sjöstrand and J. Rhodin (Almquist and Viskell, Stockholm, 1957), p. 316.
[2] M. J. Whelan, P. B. Hirsch, and W. Bollmann, Proc. Roy. Soc. (London) **A 240**, 524 (1957).
[3] M. J. Whelan and P. B. Hirsch, Phil. Mag. **2**, 1121 and 1303 (1957).
[4] H. Murphy Tomlinson, Phil. Mag. **2**, 867 (1958).
[5] E. Votava and A. Fourdeux, Proc. 1958 Berlin Electron Microscopy Conf. (to be published, 1959).
[6] H. Wilsdorf, Proc. 1958 Berlin Electron Microscopy Conf. (to be published, 1959).
[7] A. Berghezan and A. Fourdeux, J. Appl. Phys. **30**, 1913 (1959).
[8] A. Seeger, "Stacking faults in close-packed lattices" in *Report of a Conference on Defects in Crystalline Solids* (Physical Society, London, 1954), p. 328.
[9] M. J. Whelan, Proc. Roy. Soc. (London) **A 249**, 114 (1958).
[10] A. Seeger, R. Berner, and H. Wolf, Z. Physik **155**, 247 (1959).
[11] A. N. Brown and M. J. Whelan also independently observed some dislocation loops in zinc by electron transmission microscopy. We have benefited by interesting discussions of this work with M. J. Whelan and P. B. Hirsch.

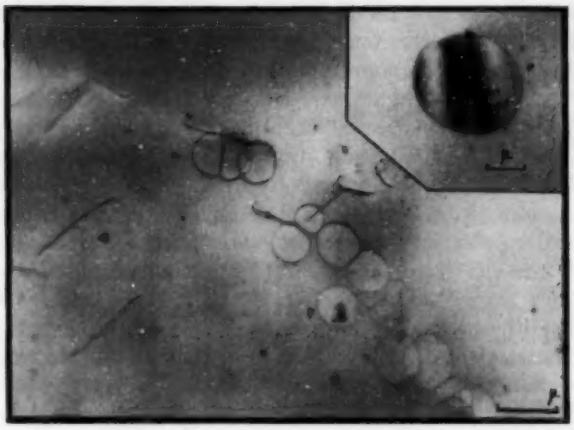

FIG. 2. Transmission electron micrograph showing dislocation loops in a zinc foil surrounding stacking fault regions, which appear with differing contrasts depending on the orientation of the sample with respect to the electron beam. This contrast may appear either darker or lighter (as in this photograph) than the surrounding areas. Interference fringes also appear in certain orientations as shown in the small inserted photograph.

lographic orientation with respect to the electron beam. It was not always possible to tilt the foil sufficiently to produce interference fringes within the loops, so it is not known whether all of these dislocation loops have stacking faults within them.

Crystals of zinc grown by deposition from the vapor in an inert gas atmosphere were examined by x-ray diffraction microscopy using techniques based on methods due to Lang[12] with variations for application to small crystals described in detail by Webb.[13] This method has proven capable of resolving individual dislocations in crystals and determining the slip vector directions. Figure 3 shows typical diffraction microscopy patterns obtained on a crystal 5 to 10 μ thick and 1 mm wide using copper $K\alpha$ radiation. Individual dislocations with various Burgers vectors lying in the basal planes are shown in these pictures.

The large hexagonal area in each pattern corresponds to a plateau on the crystal surface where the crystal is about 10 μ thick. The dark lines within the hexagonal plateau are dislocation lines lying nearly in the basal plane. Since dislocations will only be revealed in this technique if the Burgers vector has a component parallel with the diffraction vector (that is perpendicular to the diffracting planes) it is possible to determine the approximate Burgers vector direction of all dislocations lying near (0001) planes. By studying diffraction micrographs taken with several different sets of diffracting planes, it was determined that the Burgers vectors are, as expected, in the $\langle 11\bar{2}0\rangle$ type directions. A few dislocations appear to have separated slightly into two partials lying in $\langle 1\bar{1}00\rangle$ type directions, but this cannot be established with certainty since the method cannot conveniently distinguish between closely spaced partials and closely spaced total dislocations with different permutations of the $h\,k\,i$ indices. These dislocations are mobile at room temperature and dislocations introduced by plastic deformation annealed out at room temperature.

Figures 3(a) and 3(b) were obtained using $(1\bar{1}00)$ type diffracting planes. Figure 3(c) was obtained using $(\bar{2}110)$ planes. The significant point in Fig. 3(c) is the absence of the two large nearly round dark areas that appear near the center of Figs. 3(a) and 3(b). The dark discs invariably appeared in all diffraction micrographs taken from $(1\bar{1}00)$ type planes in all permutations of the h, k, and i indices, but do not appear in diffraction micrographs taken from $(11\bar{2}0)$ type planes in any permutation of h, k, and i indices. A stacking fault on the basal plane of a hexagonal crystal produces no perturbation of the phase of diffraction from $(11\bar{2}0)$ type planes but does perturb $(1\bar{1}00)$ type planes.[14] Thus, it appears that these discs are actually due to stacking faults. There may be more than one fault present in the dark circles of the crystal studied by diffraction x-ray microscopy.

It is possible to form stacking fault loops in a hexagonal lattice with the Burgers vectors of the bounding dislocation either perpendicular to the plane of the loop or at an angle with the basal plane so the trace on it is $\frac{2}{3}$ a $\langle 1\bar{1}00\rangle$ with all permutations of the h, k, and i indices permitted. Since there is apparently no line of contrast around the stacking fault area in any of the $(11\bar{2}0)$ type diffraction patterns, it appears likely that the dislocation bounding the stacking faults in the vapor grown crystal has a Burgers vector in the $\langle 0001\rangle$ direction. It is similarly possible in principle to work out the Burgers vectors of the dislocation loops in the thin foils.

The loops of stacking fault observed in electron transmission microscopy are probably formed by condensation of point defects although this is not necessarily true for those in the vapor grown crystal studied by x rays. In many cases growth and shrinkage of the

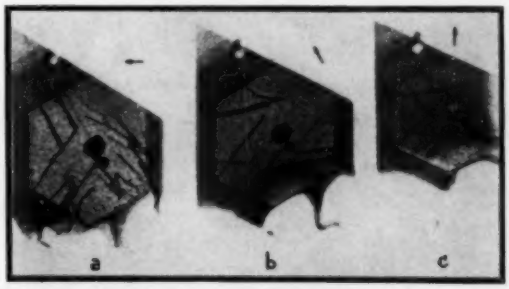

FIG. 3. X-ray diffraction micrographs of zinc single crystal platelet. Hexagonal region corresponds to a plateau about 10 μ thick. Magnification about 15×. Arrows indicate directions of diffraction vectors (perpendicular to the diffracting planes). Figures 3(a) and 3(b) were made by diffraction from $(1\bar{1}00)$ type planes and Fig. 3(c) was made by diffraction from $(\bar{1}\bar{2}10)$ type planes. The dark circles near the center of the hexagon are due to stacking faults.

[12] A. R. Lang, J. Appl. Phys. **29**, 597 (1958).
[13] W. W. Webb, J. Appl. Phys. **31**, 194 (1960).
[14] M. S. Paterson, J. Appl. Phys. **23**, 805 (1952).

loops in the foils by addition or subtraction of point defects resulting in climb of the bounding dislocations in the basal plane was observed. It was also observed that sometimes large loops expanded at the expense of neighboring small loops as expected. Although it is possible that some of the loops observed in the electron transmission patterns may be formed by the condensation of two layers of point defects so that they contain no stacking fault, this is not true of the loops observed in the x-ray diffraction samples, since in that case the contrast would not then be observed.

Servi, Stern, and Webb[15] have observed small circular precipitate particles of lead in high-purity zinc. However, these particles are substantially smaller than the loops observed here, which reach diameters as large as $5\,\mu$ in the foils and $50\,\mu$ in the vapor grown crystal. Lead precipitate particles would not yield the various diffraction characteristics observed in the x-ray diffraction micrographs.

Some of the other phenomena observed in zinc may be mentioned although they are not discussed in detail in this paper. Pinning of glissile dislocations by pile-up against sessile loops has been observed and there is evidence for climb of the glissile dislocations over the loops. There are also the expected elastic interactions between the sessile dislocations forming the edges of the loops as can be seen in Fig. 2. One example of this can be seen where two loops are overlapped. The fact that dislocation lines of the glissile dislocations do not stay exactly in the basal planes is demonstrated by various observations with both electron microscopy and x-ray diffraction microscopy.

The size of the dislocation loops in the thin foils sometimes changed during observation in the electron microscope. Occasionally, the smaller loops shrank and the larger loops simultaneously enlarged as would be expected. Somewhat more surprising was the observation that all of the visible dislocation loops frequently appeared to enlarge simultaneously. This implies either that a supersaturation of point defects is present within the foil which becomes mobile on electron irradiation or that a supersaturation of point defects is generated by the electron irradiation. The first possibility is unlikely since annealing occurs at room temperature. On the other hand, there is a plausible mechanism for generation of point defects at the surface during electron irradiation in the moderate vacuum of the electron microscope. Irradiation during the formation of thin oxide films on zinc at room temperature has been observed to increase the oxidation rate substantially. Oxidation of zinc involves transfer of zinc atoms from the zinc lattice to the coherent zinc oxide lattice. Therefore, oxidation can provide an ample source of point defects in the lattice originating at the zinc-zinc oxide interface that would yield the observed climb of dislocations within the foil through condensation of these point defects.[16]

ACKNOWLEDGMENT

The authors acknowledge with pleasure the support of this work by Union Carbide Corporation and in particular the opportunity afforded them to meet in Brussels and in Niagara Falls to combine their independent results to reach the conclusions presented in this paper.

[15] I. S. Servi, M. Stern, and W. W. Webb, Trans. AIME **212**, 361 (1958).

[16] The authors are indebted to S. Amelinckx for suggesting this mechanism by which the surface can act as a source for point defects. It may be also of importance in electron microscopy studies on other metals.

Evolution of Gases and Ions from Different Anodes Under Electron Bombardment

J. R. YOUNG
General Electric Research Laboratory, Schenectady, New York
(Received November 30, 1959)

With the aid of a bakeable mass spectrometer a study has been made of the material evolved from Ag, Cu, Ni, Mo, Ta, Ti, and W anodes exposed to oxide cathodes. Chlorine was found to be evolved from all the anodes during the first period of bombardment. No evidence of the dissociation of the thin films of BaO or SrO on the anodes was obtained, suggesting it does not play a significant role in oxide cathode poisoning. It is believed that the Cl evolution may be responsible for the early slump in emission commonly observed at low anode voltages from oxide cathodes. Evolution of O^+ ions was observed from oxidized Cu, Ni, Mo, Ta, and Ti with efficiencies up to approximately 10^{-6} ions/electron for electron energies of 90 ev and current densities of 10 ma/cm². This O^+ evolution reduced considerably the dc emission capabilities of the oxide cathodes. It was found that heating the anodes from 700° to 1000°C for long periods of time does not always eliminate all evolution products caused by electron bombardment. Hydrogen was observed to be evolved from Ti and O^+ ions were observed from formerly oxidized Cu, Ni, Mo, and Ta immediately after outgassing at temperatures less than 1000°C.

INTRODUCTION

MANY workers have reported on oxide cathode poisoning which they believed was due to material evolved from the anode under electron bombardment.[1–14] Since BaO and SrO are evaporated during normal cathode operation the dissociation of BaO and SrO under electron bombardment has been suspected of producing poisoning. Results obtained on the dissociation rate of BaO and SrO[15–21] indicate the liberation of oxygen could account for some types of emission decay. Evidence has also been reported indicating different anode materials produce different amounts of poisoning to oxide cathodes.[12,21] However, the reason for this difference has not been clearly established.

In this study the materials evolved from different anodes under electron bombardment were determined. The dependence of this evolution upon anode heat treatment, oxidation, and exposure to oxide cathodes was investigated.

EXPERIMENTAL PROCEDURE

The anode materials studied were mounted separately in a mass spectrometer opposite two cylindrical oxide coated cathodes as shown schematically in Fig. 1. A fraction of the material evolved from the anode under electron bombardment entered the ion chamber of the mass spectrometer and contributed components to the observed mass spectrum which were characteristic of the evolution products. Also, positive ions evolved from the anode were accelerated into the analyzer portion of the mass spectrometer. These ions appeared at different positions in the spectrum than the same mass ion produced in the ion chamber because they had more energy upon entering the magnetic analyzer. The sensitivity for detecting ions liberated from the anode was greater than for the detection of neutral atoms because of the inefficiency of ionizing neutrals on one pass through the ionization chamber and the reduced solid angle for neutrals entering the ionization chamber. It was estimated that the sensitivity for the detection of positive ions from the anode was between 10^3 and 10^4 times greater than for neutral atom evolution.

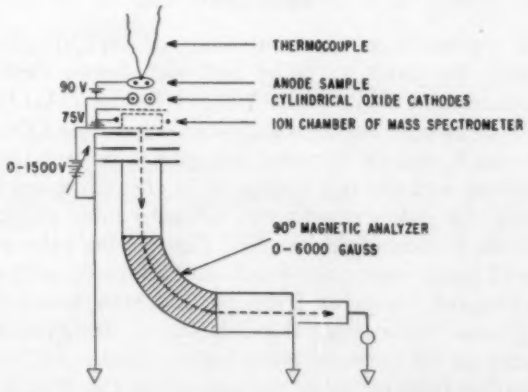

FIG. 1. Schematic drawing of mass spectrometer showing arrangement for bombarding anodes exposed to oxide cathodes.

[1] L. B. Headrick and E. A. Lederer, Phys. Rev. **50**, 1094 (1936).
[2] H. Jacobs, J. Appl. Phys. **17**, 596 (1946).
[3] L. Jacob, Nature **157**, 586 (1946).
[4] Hamaker, Bruining, and Aten, Philips Research Repts. **2**, 171 (1947).
[5] G. R. Feaster, J. Appl. Phys. **20**, 415 (1949).
[6] G. H. Metson, Proc. Phys. Soc. (London) **B62**, 589 (1949).
[7] J. Woods and D. A. Wright, British J. Appl. Phys. **4**, 56 (1953).
[8] K. Amakasu and T. Imai, J. Appl. Phys. **24**, 107 (1953).
[9] D. A. Wright and J. Woods, Proc. Phys. Soc. (London) **B66**, 1073 (1953).
[10] T. Imai, J. Phys. Soc. (Japan) **9**, 28 (1954).
[11] D. A. Wright, British J. Appl. Phys. **5**, 108 (1954).
[12] T. Imai, LeVide **10**, 384 (1955).
[13] L. Jacob, Proc. Phys. Soc. (London) **B70**, 235 (1957).
[14] L. Jacob, J. Elec. and Control **3**, 339 (1957).
[15] Yoshida, Shibata, Igarashi, and Arata, J. Phys. Soc. (Japan) **9**, 640 (1954).
[16] G. E. Moore and W. T. Huges, Phys. Rev. **99**, 1643 (1955).
[17] G. E. Moore, Phys. Rev. **100**, 1794 (1955).
[18] Yoshida, Shibata, Igarashi, and Arata, J. Appl. Phys. **27**, 497 (1956).
[19] P. Wargo and W. G. Shepherd, Phys. Rev. **106**, 694 (1957).
[20] G. E. Moore, J. Appl. Phys. **30**, 1086 (1959).
[21] R. H. Plumlee and L. P. Smith, J. Appl. Phys. **21**, 811 (1950).

The mass spectrometer was a direction focusing, 2 in. radius, 90° sector magnetic analyzer type, constructed of glass and metal, without demountable joints.[20,22] It was possible to bake the mass spectrometer to temperatures up to 400°C. After bakeout pressures in the 10^{-10} mm of Hg region were obtainable. The sensitivity was sufficient to measure partial pressures down to about 10^{-11} mm of Hg and masses up to 50 could be resolved. The system was evacuated with a single Hg diffusion pump and a trap cooled with liquid N_2 was located between the diffusion pump and the mass spectrometer. At the lowest pressures and throughout most of the operation CO was the most abundant component present. After bakeout water peaks were usually absent. During the outgassing of the cathodes and anodes CO and CO_2 were usually the main components although hydrogen was a major component when Ti was outgassed. These results are in agreement with those reported by Wagner and Marth.[23]

Anode materials investigated were Ag, Cu, Ni (499), Mo, Ta, Ti, and W. These anodes were prepared of 0.005-in. sheet in the form indicated in Fig. 1, having outside dimensions of $\frac{1}{2}\times\frac{3}{16}\times\frac{1}{16}$ in. A heater was placed inside the anodes for outgassing and maintaining the anodes at different temperatures during measurements. A Pt-Pt 10% Rh thermocouple was attached to the top of the anodes for temperature determination. The cathodes were prepared by spraying a mixture of 57.3% $BaCO_3$, 41.4% $SrCO_3$ and 1.3% $CaCO_3$ suspended in amyl acetate onto $\frac{1}{8}$-in. diam 220 Ni sleeves.

The procedure followed after bakeout was to outgas the anode target material at 1000°C for 20 min, except for Ag and Cu, which were only heated to 700°C. After anode outgassing, the cathodes were heated slowly to a temperature up to approximately 1000°C. During the outgassing of the cathode, the anode material was not heated and usually remained at a temperature less than 250°C. After the pressure had dropped to about 10^{-8} mm of Hg with the oxide cathodes hot, the anode voltage was applied and changes in the mass spectrum were noted.

RESULTS

A typical mass spectrum observed just after outgassing the oxide cathodes and just before electron bombardment of the anode is shown in Fig. 2(A). Here the only components of significance other than CO and CO_2 are F and Cl. Fluorine was always present in the spectrum and did not change in intensity appreciably during the entire experiment. There is some evidence that the F comes from the 7052 glass during bakeout.[20] The Cl peaks were quite small until the oxide cathodes were heated. Hamaker, Bruining, and Aten[4] found that HCl could come from the bakeout of the glass and deposit on the cathode. No definite evidence of Cl or F evolution resulting from the bakeout of the 7052 glass

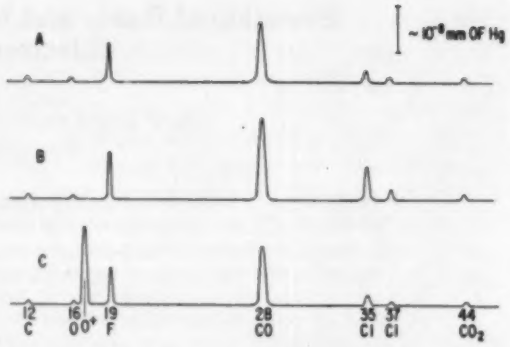

FIG. 2(A) Typical spectrum observed after outgassing oxide cathodes and before anode voltage applied. Note absence of water peaks. (B) Spectrum observed upon drawing current to W anode covered with evaporation products from oxide cathode outgassing, $V_a=90$ v, $I_a=0.3$ ma. Note increase in Cl peaks; others have not changed appreciably. (C) Spectrum observed when oxidized Mo anode bombarded with 90 ev electrons 5 ma. Note O^+ ions from anode.

employed here was found. However, the $(BaSrCa)CO_3$ analysis indicated a chloride impurity of 17 ppm. This may be sufficient to account for the Cl observed. Small H_1 and H_2 peaks were usually observed, but masses greater than 44 were rarely found.

Figure 2(B) shows the spectrum observed when current was drawn to a W anode coated with evaporation products from the outgassing of the oxide cathodes. The characteristic dc electron emission slump was observed when the anode voltage was applied. All peaks increased slightly upon the application of anode voltage, but the Cl peaks more than doubled in height. In some cases Cl^+ ions were observed to come from the anode. It is believed that the Cl evolution may account for the emission slump observed at low anode voltages since the Cl peaks were observed to increase upon the application of anode voltages as low as 6 v. Also, when the anodes were outgassed after outgassing the cathodes, the Cl peaks did not increase when current was drawn to the anode and emission poisoning was usually absent. The increase in the CO and CO_2 peaks when current was drawn to the anode could also be responsible for emission decay. However, upon increasing the CO and CO_2 pressure an order of magnitude, the cathode emission was not significantly changed. No indication of oxygen evolution was ever observed upon bombarding an anode just after outgassing the oxide cathodes or after prolonged exposure of the anode to hot oxide cathodes. Therefore, it does not seem likely that the dissociation of the thin film of BaO and SrO on the anode can account for appreciable emission decay.

Occasionally, upon heating Mo and Ta anodes to about 1000°C, after outgassing the cathodes, O^+ ions were observed to be liberated under electron bombardment, Fig. 2(C). The O^+ evolution continued, but at a lower rate when the anode temperature was reduced to near room temperature. It was at first thought that the heating at 1000°C had allowed small crystallites

[22] Homer D. Hagstrom, Rev. Sci. Instr. **24**, 1122 (1953).
[23] J. S. Wagner and P. T. Marth, J. Appl. Phys. **28**, 1027 (1957).

of BaO and SrO to grow,[24] and that the dissociation rate of these crystallites was much greater than the former thin amorphous layer. However, when these metals were outgassed thoroughly and O^+ ions could not be detected, they did not reappear when material from the cathodes was again evaporated onto the anodes and the anodes were again heated to 1000°C. When these well outgassed anodes were heated for a short time in oxygen at a pressure of 10^{-6} mm of Hg, O^+ evolution was present under electron bombardment. Efficiencies of O^+ evolution as high as approximately 10^{-5}+ions/electron with 90 ev electrons at 10 ma/cm² were observed. This O^+ evolution significantly reduced the dc emission capabilities of the oxide cathodes. Detectable decay in the oxide cathode thermionic emission was observed for efficiencies as low as 10^{-9}+ions/electron. This is a very small quantity of +ions to affect the electron emission appreciably. However, if the number of donors/cm² at the surface is estimated and if the diffusion of oxygen or oxygen vacancies is rapid, the quantities involved would significantly change the donor concentration at the surface and consequently the electron emission. The O^+ evolution rate usually increased with anode temperature and under constant bombarding energy and current the O^+ decay rate was greater at the higher temperatures. Similar O^+ evolution was observed for oxidized Cu, Ni, and W anodes, while no O^+ evolution was observed from Ag even after considerable heating and cooling in an oxygen atmosphere. In the case of Cu and Ni after oxidation, it was not possible to heat them hot enough to eliminate the O^+ evolution. Also, many hours of heating at temperatures greater than 1000°C were required to eliminate the O^+ evolution from Mo, Ta, and W.

Titanium was quite different than the other anode materials studied. During the early electron bombardment, Cl was evolved to about the same degree as for the other anodes, but hydrogen was also evolved. Upon heating the Ti after outgassing, the cathodes Ba and Sr were observed to be evolved at a Ti temperature of about 500°C. This Ba and Sr evolution coincided with a considerable electron emission increase of the oxide cathodes, as would be expected.[25] It is believed that the BaO and SrO, which had evaporated onto the anode reacted with the hot Ti, the Ti taking up the oxygen and evolving the Ba and Sr.[26] The oxygen apparently diffuses into the bulk of the Ti since O^+ ions could not be observed under electron bombardment. However, when the Ti was oxidized at 400°C and then bombarded with electrons, large O^+ ion peaks were observed. The dc electron emission decayed in an identical manner to the previously mentioned oxidized anodes. Upon heating the Ti above 500°C the O^+ peak disappeared. By heating the Ti for several hours in an oxygenpressure of 10^{-6} mm of Hg, it became increasingly difficult to reduce the O^+ peak by heating the Ti above 500°C. Therefore, excessively oxidized Ti was a poor anode material.

It was not possible to completely eliminate the evolution of hydrogen from the Ti by heating to 1000°C. At Ti temperatures less than 500°C, much of the evolution appeared to be atomic hydrogen, while at higher temperatures molecular hydrogen was predominant. This hydrogen evolution was increased by electron bombardment. There was a definite indication that the hydrogen increased the emission capabilities of the oxide cathodes, although not to the extent observed when Ba and Sr were evolved.

[24] P. N. Russell and A. S. Eisenstein, J. Appl. Phys. **25**, 954 (1954).
[25] L. S. Nergaard, RCA Rev. **13**, 523 (1952).
[26] V. L. Stout (private communications).

SUMMARY

From the results obtained, it would appear that the anode material and method of anode processing plays a significant role in the electron emission capabilities of oxide cathodes. No definite evidence was obtained to indicate that dissociation of BaO or SrO on the anode contributed to the decay of emission from oxide cathodes. However, O^+ ions were obtained from oxidized Cu, Ni, Mo, Ti, and W anodes with efficiencies up to 10^{-5} ions/electron with 90 ev electrons. The O^+ ion intensity could be reduced to a small value by outgassing at high temperatures. Both Cl positive ions and Cl neutral atoms were observed upon electron bombardment of all anodes just after outgassing the oxide cathodes. However, these peaks decayed after a few hours or upon further anode outgassing. It is believed that this Cl evolution may be responsible for the initial emission decay observed so frequently from oxide cathodes.

ACKNOWLEDGMENTS

The writer wishes to express his appreciation to V. L. Stout, A. B. Laponsky, and N. R. Whetten for many helpful suggestions and discussions.

Energy Distribution and Cooling Effect of Electrons Emitted from an Arc Cathode

T. H. Lee
General Electric Company, Philadelphia, Pennsylvania
(Received February 20, 1959)

The energy distribution and the average cooling effect of electrons emitted by the *T-F* process are calculated over a wide range of temperatures and electric fields for several values of work functions. It is shown that at low temperatures, the average cooling effect approaches zero and at high temperatures, it is approximately equal to the reduced work function. The limitation of the validity of reduced work function can be easily seen.

INTRODUCTION

THE importance of the cooling effect of electron emission in the study of energy balance at the arc cathode is well known. VonEngel and Steenbeck[1] calculated the limiting ratio of positive ion current to electron current in the cathode drop region by assuming that the positive ions give to the cathode all the energy gained in the cathode drop and that this energy input is balanced by the cooling effect of electrons emitted thermionically from refractory cathodes. For thermionic emission, the average cooling effect is in general assumed to be equal to the work function of the cathode material. Compton[2] in treating the energy balance at the mercury cathode, used effective work function ϕ_- as the average cooling effect per electron. Such an effective work function, given by (1), is calculated from the field enhanced thermionic emission first studied by Schottky,[3]

$$\phi_-=\phi-(eE)^{\frac{1}{2}}, \tag{1}$$

where ϕ is the work function of the material, E is the electric field at the cathode and e is the electronic charge. As pointed out by Compton, ϕ_- can be anywhere between zero and the work function of the material. For the case of pure field emission, ϕ_- is usually set to zero.

The use of Eq. (1) for strong fields and relatively low temperatures is questionable. Murphy and Good[4] recently showed that the entire emission phenomenon can be divided into three regions: The high-temperature region where Schottky's equation applies, the high-field region where Fowler-Nordheim's[5] equation applies, and an intermediate region where emission is strongly dependent on both temperature and electric field. The emission in the intermediate region was first studied by Dolan and Dyke,[6] who designated the process of emission in the presence of both high-field and high-temperature "*T-F* emission." It is now quite obvious that one should limit the use of Eq. (1) to the high-temperature region only. For arcs where the emission from the cathode is strongly dependent on both temperature and electric field,[7] the average cooling effect of electrons requires more careful consideration.

In this paper the cooling effect is studied from a general point of view. The results are given as functions of temperature, electric field and work function. The manner in which the cooling effect approaches zero for the field emission case and the effective work function for the thermionic emission case is shown.

AVERAGE ENERGY OF EMITTED ELECTRONS

The basic assumptions involved are the Fermi-Dirac distribution for the free electrons and the classical image force barrier at the surface. For this model, the number of electrons with momenta in the range p_x, p_y,

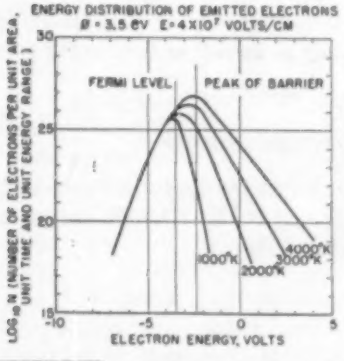
ENERGY DISTRIBUTION OF EMITTED ELECTRONS
ϕ = 3.5 eV E = 4 X 10⁷ VOLTS/CM
FERMI LEVEL
PEAK OF BARRIER
1000°K
2000°K
3000°K
4000°K
LOG₁₀ N (NUMBER OF ELECTRONS PER UNIT AREA, UNIT TIME AND UNIT ENERGY RANGE)
ELECTRON ENERGY, VOLTS

FIG. 1. Distribution of the energy associated with the motion of electrons normal to the potential barrier for electrons emitted from a surface with $\phi=3.5$ ev and $E=4\times10^7$ v/cm.

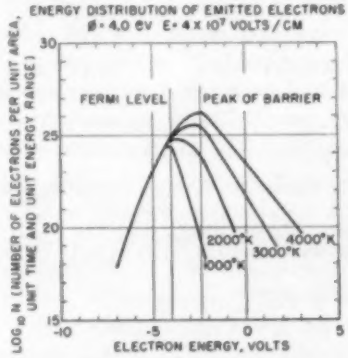
ENERGY DISTRIBUTION OF EMITTED ELECTRONS
ϕ = 4.0 eV E = 4 X 10⁷ VOLTS/CM
FERMI LEVEL
PEAK OF BARRIER
1000°K
2000°K
3000°K
4000°K
LOG₁₀ N (NUMBER OF ELECTRONS PER UNIT AREA, UNIT TIME AND UNIT ENERGY RANGE)
ELECTRON ENERGY, VOLTS

FIG. 2. Distribution of the energy associated with the motion of electrons normal to the potential barrier for electrons emitted from a surface with $\phi=4.0$ ev and $E=4\times10^7$ v/cm.

[1] A. VonEngel and M. Steenbeck, Elek. Gasentladungen, ihre Physik U. Tech. **2**, 133.
[2] K. T. Compton, Phys. Rev. **37**, 1077 (1931).
[3] W. Schottky, Ann. Physik **44**, 1011 (1914).
[4] E. L. Murphy and R. H. Good, Jr., Phys. Rev. **102**, 6, 1464 (1956).
[5] R. H. Fowler and L. Nordheim, Proc. Roy. Soc. (London) **A119** (1928).
[6] W. W. Dolan and W. P. Dyke, Phys. Rev. **95**, 2, 327 (1954).
[7] T. H. Lee, J. Appl. Phys. **28**, 920 (1957); T. H. Lee, J. Appl. Phys. **29**, 734 (1958).

p_z, and p_x+dp_x, p_y+dp_y, p_z+dp_z, penetrating a unit area of the barrier in unit time is[8]

$$\frac{2p_zD(E,W_x)dp_xdp_ydp_z}{mh^3\{\exp\{[(p_x^2+p_y^2+p_z^2/2m)-\epsilon_0]/kT\}+1\}},$$

where ϵ_0 is the Fermi energy, h is Planck's constant, m is the electronic mass, k is Boltzmann's constant, T is the temperature, E is the external applied electric field, W_x is the kinetic energy of the electron associated with its motion in the x direction, and $D(E,W_x)$ is the transmission coefficient.

The total energy carried away by the electrons from a unit area in a unit time is then equal to

$$W=\int_{p_x=-\infty}^{\infty}\int_{p_y=-\infty}^{\infty}\int_{p_z=-\infty}^{\infty}\frac{p_z(p_x^2+p_y^2+p_z^2)D(E,W_x)dp_xdp_ydp_z}{m^2h^3\{\exp\{[(p_x^2+p_y^2+p_z^2/2m)-\epsilon_0]/kT\}+1\}}. \tag{2}$$

By substituting

$$W_x=\frac{p_x^2}{2m} \tag{3}$$

$$p_y=\rho\cos\theta \tag{4}$$

$$p_z=\rho\sin\theta \tag{5}$$

one obtains,

$$W=\frac{2}{h^3}\int_{p_x=0}^{\infty}\int_{\rho=0}^{\infty}\int_{\theta=0}^{2\pi}\frac{W_xD(E,W_x)\rho d\rho d\theta dW_x}{\exp\{[W_x-\epsilon_0+(\rho^2/2m)]/kT\}+1}$$
$$+\frac{2}{h^3}\int_{p_x=0}^{\infty}\int_{\rho=0}^{\infty}\int_{\theta=0}^{2\pi}\frac{\rho^3D(E,W_x)d\rho d\theta dW_x}{2m\{\exp([W_x-\epsilon_0+(\rho^2/2m)]/kT)+1\}}. \tag{6}$$

The first integral in (6) is simply equal to

$$W_1=\int W_xN(W_x)D(E,W_x)dW_x, \tag{7}$$

where $N(W_x)$ is the so called supply function.[8] This term undoubtedly represents the major portion of the energy carried away by the electrons. The distribution of W_x, which is given by the product of $N(W_x)$ and $D(E,W_x)$ has been calculated for several work functions, electric fields and temperatures and shown in Figs. 1–9. The transmission coefficients used were those given by Murphy and Good.[4] These curves were obtained in the process of calculating the current density as a function of electric field and temperature on a digital computer.[9]

Figures 1–3 show clearly the shift of the peak of the distribution curve from the Fermi level to the peak of the barrier as the temperature is increased from 1000 to 4000°K with an electric field of 4×10^7 v/cm. With a field of 2×10^7 v/cm, the shift takes place between 1000 and 2000°K, while with a field of 1×10^7 v/cm, the shift takes place under 1000°K.

The second integral in (6) can be written in two parts:

$$W_2=\frac{4\pi m}{h^3}\int_0^{\epsilon_0}D(E,W_x)\left[\int_0^{\infty}\frac{W_{yz}dW_{yz}}{A\exp(W_{yz}/kT)+1}\right]dW_x$$
$$+\frac{4\pi m}{h^3}\int_{\epsilon_0}^{\infty}D(E,W_x)$$
$$\times\left[\int_0^{\infty}\frac{W_{yz}dW_{yz}}{A\exp(W_{yz}/kT)+1}\right]dW_x, \tag{8}$$

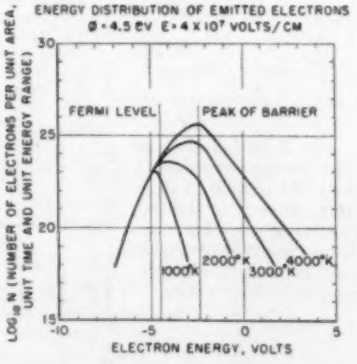

FIG. 3. Distribution of the energy associated with the motion of electrons normal to the potential barrier for electrons emitted from a surface with $\phi=4.5$ ev and $E=4\times10^7$ v/cm.[8]

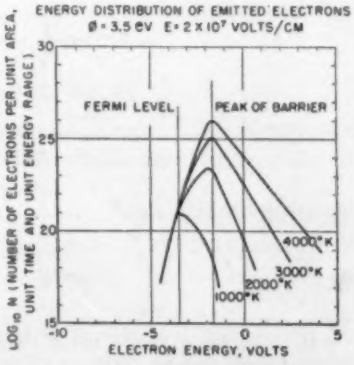

FIG. 4. Distribution of the energy associated with the motion of electrons normal to the potential barrier for electrons emitted from a surface with $\phi=3.5$ ev and $E=2\times10^7$ v/cm.

[8] *Handbuch der Physik* (Springer-Verlag, Berlin, Germany, 1956), Vol. XXI, p. 187.
[9] T. H. Lee, J. Appl. Phys. **30**, 166 (1959).

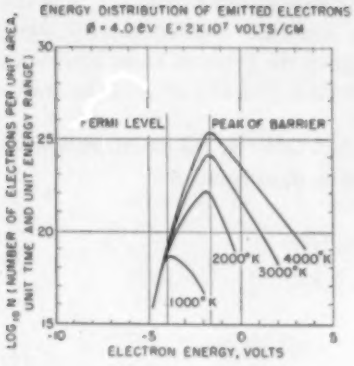
ENERGY DISTRIBUTION OF EMITTED ELECTRONS
ϕ = 4.0 ev E = 2 x 10⁷ VOLTS/CM
FERMI LEVEL
PEAK OF BARRIER
2000°K
4000°K
3000°K
1000°K
LOG₁₀ N (NUMBER OF ELECTRONS PER UNIT AREA, UNIT TIME AND UNIT ENERGY RANGE)
ELECTRON ENERGY, VOLTS

FIG. 5. Distribution of the energy associated with the motion of electrons normal to the potential barrier for electrons emitted from a surface with $\phi=4.0$ ev and $E=2\times10^7$ v/cm.

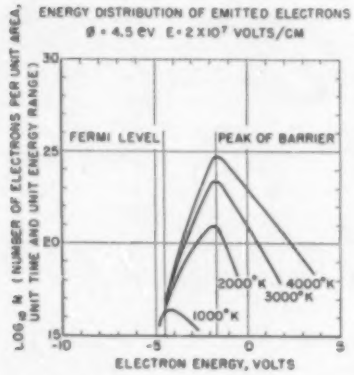
ENERGY DISTRIBUTION OF EMITTED ELECTRONS
ϕ = 4.5 ev E = 2 x 10⁷ VOLTS/CM
FERMI LEVEL
PEAK OF BARRIER
2000°K
4000°K
3000°K
1000°K
LOG₁₀ N (NUMBER OF ELECTRONS PER UNIT AREA, UNIT TIME AND UNIT ENERGY RANGE)
ELECTRON ENERGY, VOLTS

FIG. 6. Distribution of the energy associated with the motion of electrons normal to the potential barrier for electrons emitted from a surface with $\phi=4.5$ ev and $E=2\times10^7$ v/cm.

where

$$W_{yz}=p^2/2m \tag{9}$$

$$A=\exp[(W_x-\epsilon_0)/kT]. \tag{10}$$

For $W_x>\epsilon_0$, the integral in the bracket of (8) can be evaluated in the following manner:

$$\int_0^\infty \frac{W_{yz}dW_{yz}}{A\exp(W_{yz}/kT)+1}$$

$$=\frac{1}{A}\int_0^\infty W_{yz}\exp\left(-\frac{W_{yz}}{kT}\right)\left[1-A^{-1}\exp\left(-\frac{W_{yz}}{kT}\right)\right.$$

$$+A^{-2}\exp\left(-\frac{2W_{yz}}{kT}\right)$$

$$\left.-A^{-3}\exp\left(-\frac{3W_{yz}}{kT}\right)+\cdots\right]dW_{yz}$$

$$=(kT)^2\left[\frac{1}{A}-\frac{1}{2^2A^2}+\frac{1}{3^2A^3}-\frac{1}{4^2A^4}+\cdots\right] \tag{11}$$

by using the relation,[10]

$$\int_0^\infty x^ne^{-ax}dx=\frac{n!}{a^{n+1}}. \tag{12}$$

[10] B. O. Pierce, *A Short Table of Integrals* (Ginn and Company, Boston, Massachusetts, 1929), p. 63, 493.

For large A, (11) can be approximated by

$$(kT)^2\ln[1+(1/A)].$$

The second integral in (8) is therefore approximately equal to

$$(kT)\int_{\epsilon_0}^\infty \frac{4\pi mkT}{h^3}\ln\left(1+\frac{1}{A}\right)D(E,W_x)dW_x, \tag{13}$$

but (13) is equal to[8]

$$(kT)\int_{\epsilon_0}^\infty D(E,W_x)N(W_x)dW_x. \tag{14}$$

Consequently, for W_x much greater than ϵ_0, the average energy carried by an electron due to its motion normal to the electric field is equal to kT. At $W_x=\epsilon_0$, $A=1$. Equation (11) is equal to

$$(kT)^2\left(1-\frac{1}{2^2}+\frac{1}{3^2}-\frac{1}{4^2}+\cdots\right)=0.82(kT)^2. \tag{15}$$

This was approximated by $0.69(kT)^2$ in (13).

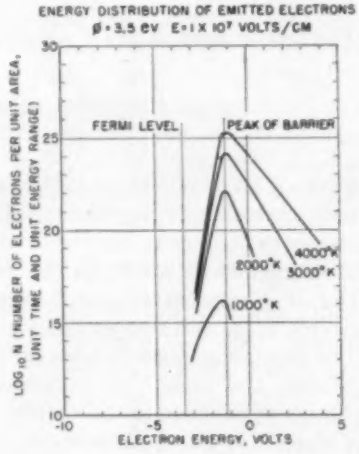
ENERGY DISTRIBUTION OF EMITTED ELECTRONS
ϕ = 3.5 ev E = 1 X 10⁷ VOLTS/CM
FERMI LEVEL
PEAK OF BARRIER
2000°K
4000°K
3000°K
1000°K
LOG₁₀ N (NUMBER OF ELECTRONS PER UNIT AREA, UNIT TIME AND UNIT ENERGY RANGE)
ELECTRON ENERGY, VOLTS

FIG. 7. Distribution of the energy associated with the motion of electrons normal to the potential barrier for electrons emitted from a surface with $\phi=3.5$ ev and $E=1\times10^7$ v/cm.

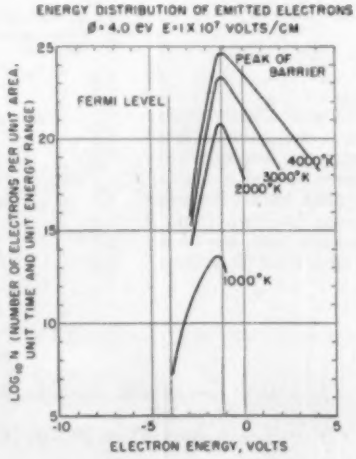
ENERGY DISTRIBUTION OF EMITTED ELECTRONS
ϕ = 4.0 ev E = 1 X 10⁷ VOLTS/CM
PEAK OF BARRIER
FERMI LEVEL
4000°K
3000°K
2000°K
1000°K
LOG₁₀ N (NUMBER OF ELECTRONS PER UNIT AREA, UNIT TIME AND UNIT ENERGY RANGE)
ELECTRON ENERGY, VOLTS

FIG. 8. Distribution of the energy associated with the motion of electrons normal to the potential barrier for electrons emitted from a surface with $\phi=4.0$ ev and $E=1\times10^7$ v/cm.

For $W_x<\epsilon_0$, the left hand side of (11) can be evaluated by breaking up the integral into two parts with limits from 0 to ϵ_0-W_x for one and ϵ_0-W_x to ∞ for the other. These two integrals can then be separately evaluated. The sum of the two parts gives

$$\frac{(\epsilon_0-W_x)^2}{2}+\frac{\pi^2}{6}(kT)^2-(kT)^2 \times\left(A-\frac{A^2}{4}+\frac{A^3}{9}-\frac{A^4}{16}+\cdots\right). \quad (16)$$

The first integral in (8) is then equal to

$$\frac{4\pi m}{h^3}\int_0^{\epsilon_0}\left\{\frac{(\epsilon_0-W_x)^2}{2}+(kT)^2\frac{\pi^2}{6}-(kT)^2 \times\left(A-\frac{A^2}{4}+\frac{A^3}{9}\cdots\right)\right\}D(E,W_x)dW_x. \quad (17)$$

The above expression was evaluated numerically. In many cases, it can be neglected. The average energy $\bar{W}$ per electron is obtained by dividing the number of electrons into W, or

$$\bar{W}=\frac{W_1+W_2}{\int_0^\infty N(W_x)D(E,W_x)dW_x}. \quad (18)$$

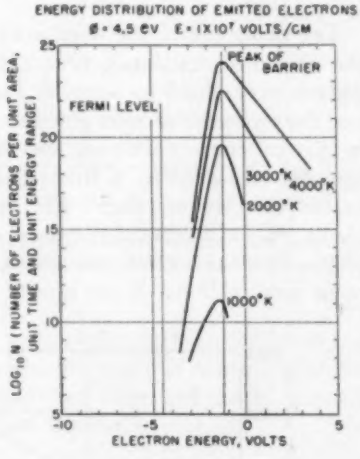

FIG. 9. Distribution of the energy associated with the motion of electrons normal to the potential barrier for electrons emitted from a surface with $\phi=4.5$ ev and $E=1\times10^7$ v/cm.

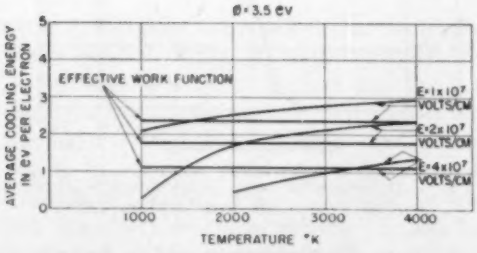

FIG. 10. Average cooling effect of emitted electrons for $\phi=3.5$ ev.

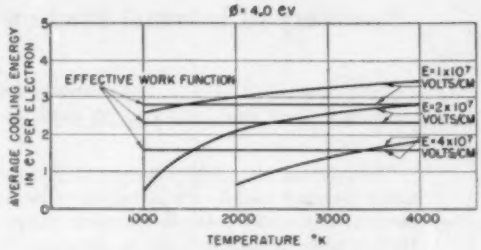

FIG. 11. Average cooling effect of emitted electrons for $\phi=4.0$ ev.

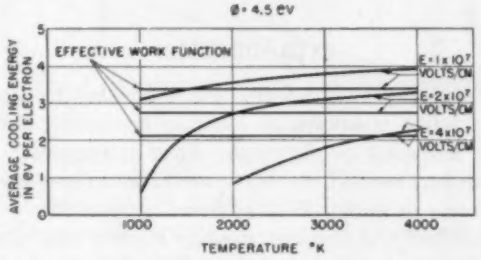

FIG. 12. Average cooling effect of emitted electrons for $\phi=4.5$ ev.

COOLING EFFECT OF ELECTRONS

For every electron emitted from the cathode, an electron flows from the circuit behind as a replacement. To consider the cooling effect of electron emission, one must make certain assumptions about the energy of the replacement electron. For a metal in equilibrium at low temperature, the conduction electrons can be considered to have Fermi energy. The replacement electrons will also be assumed to have this energy because although the temperature at the cathode spot is very high, the temperature gradient is such that within a very short distance from the surface of the cathode, the temperature is only slightly higher than room temperature. The effect of the temperature gradient will partly be taken care of in the consideration of heat flow.

The average cooling effect per electron is then given by

$$\Delta W=\bar{W}-\epsilon_0, \quad (19)$$

where ΔW has been calculated numerically for several values of electric field, temperature, and work function. The results are shown in Figs. 10–12. These curves should be used in the study of energy balance at the cathode spot of an arc.

CONCLUSIONS

1. The use of effective work function as the average cooling effect of an electron should only be used in the thermionic emission region.

2. The error resulting from using the effective work function can be quite high, even if the temperature is higher than 2000°K, as long as the electric field is sufficiently high.

3. The curves presented in Figs. 10–12 should be used in the study of energy balance at the arc cathode.

Recovery of Internal Friction in Aluminum after Plastic Deformation

IVAR HOLWECH
Department of Physics, University of Oslo, Norway

(Received July 20, 1959; revised manuscript received January 15, 1960)

The internal friction in polycrystalline, super purity aluminum has been measured during and after creep under constant load by the ultrasonic pulse method. The increase of internal friction was found to be independent of frequency in the measured range (2.5 to 12 Mc). The room temperature recovery of internal friction after unloading could be described by the formula: $\Delta\alpha = C_1/(t+C_2)^{C_3}$. Typical values of the constants C_2 and C_3 are 10 sec. and 0.6, respectively. The experimental results are discussed in terms of the Weertman-Salkovitz theory of low-amplitude internal friction.

INTRODUCTION

DURING plastic deformation of a metal the internal friction is known to increase markedly, and the elastic modulus to decrease. After deformation, the internal friction and the elastic modulus recovers almost completely in about 20 hr at room temperature.

This effect was first observed by Förster and Köster.[1] It has since been observed in brass,[2–4] iron,[5] aluminium,[6–10] zinc,[11] copper,[12] Ni-Cr alloy,[13] and platinum.[14] The experiments of Alers[11] and other evidence[14] seem to prove that the effect is caused by dislocation motion. The fact that the effect has been observed in so many different materials suggests that it is caused by fundamental properties of dislocation movement. The present knowledge of the effect is, however, very incomplete, as the dependence on such parameters as dislocation density, impurity concentration and frequency of measurement has not been systematically investigated.

Up till now two mechanisms of mechanical damping resulting from dislocations has been proposed. One which has been worked out in detail by Lücke and Granato[15] leads to a dynamical hysteresis type of loss for small strain amplitudes, while the theory by Weertman and Salkovitz[16] gives a loss of the static hysteresis type.

The main aim of this work has been to investigate the frequency dependence of the effect in order to decide which of the two types of dislocation damping is the most important one.

EXPERIMENTAL METHOD

The specimens were machined from a single rod of super purity (99.995%) polycrystalline aluminium. The mean diameter of the grains was about 0.5 mm. The diameter of the rod was 2 in. Two pairs of parallel faces were machined along the length of the rod, and then the rod was cut into 5-cm long specimens. The end faces and the two pairs of side faces were mutually parallel within 10^{-3} rad. The area of the end faces was 17 cm². Before the experiment, the specimen was annealed for 24 hr at 400° C and slowly cooled.

The test specimens were deformed by compression in a constant load creep machine. The load being obtained by a mechanical and hydraulic force multiplication from a weight which could be moved along a lever by a motor-driven trolley. The loads used in this work were of the order of 3000 kg corresponding to about 180 kg/cm².

The deformation was measured by strain gauges of the electrical resistance type. The two active strain gauges were glued to opposite faces on the specimen, and the two passive were glued to a piece of aluminium in thermal contact with the specimen. The bridge voltage was measured by a Brüel & Kjær apparatus calibrated directly in strain. The relative accuracy was about 1% for strains of the order of 10^{-3}.

The internal friction was measured by the ultrasonic pulse method.[17] An X-cut quartz crystal was glued to

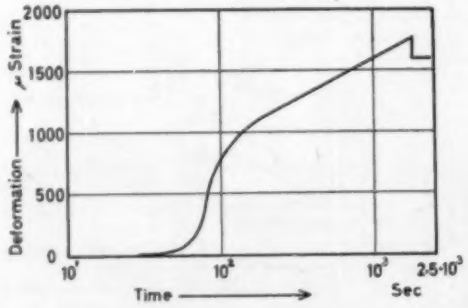

FIG. 1. Deformation curve for specimen 19 showing loading, logarithmic creep, and unloading.

[1] F. Förster and W. Köster, Z. Metallk. **29**, 116 (1937).
[2] W. Köster and K. Rosenthal, Z. Metallk. **30**, 345 (1938).
[3] H. I. Fusfeld, Phys. Rev. **82**, 769 (1953).
[4] W. Köster and E. Stolte, Z. Metallk. **45**, 356 (1954).
[5] W. Köster, Arch. Eisenhüttenw. **14**, 271 (1940).
[6] W. Köster, Z. Metallk. **32**, 282 (1940).
[7] G. B. Brook and A. H. Sully, Acta Met. **3**, 460 (1955).
[8] R. Truell, A. Hikata, A. Granato, B. Chick, and K. Lücke, J. Appl. Phys. **27**, 396 (1956).
[9] R. Truell and A. Hikata, J. Appl. Phys. **28**, 522 (1957).
[10] R. Truell and R. Bayer, Phys. Rev. **110**, 1206 (1958).
[11] G. A. Alers, Phys. Rev. **97**, 863 (1955).
[12] A. D. N. Smith, Phil. Mag. **44**, 453 (1953).
[13] C. Boulanger, Compt. rend. **226**, 1170 (1948).
[14] A. S. Nowick, Acta Met. **3**, 312 (1955).
[15] K. Lücke and A. Granato, J. Appl. Phys. **27**, 583 (1956).
[16] J. Weertman and E. I. Salkovitz, Acta Met. **3**,1 (1955).
[17] W. P. Mason, *Physical Acoustics and the Properties of Solids* (D. Van Nostrand Company, Inc., Princeton, New Jersey, 1958).

one of the side faces of the specimen. The same crystal being used both as transmitter and receiver. The high-frequency pulses were supplied by a pulsed oscillator type pulse generator. The pulse amplitude was 100 v peak to peak, pulse length about 4 μsec and pulse repetition frequency 400 cps. The frequency of the oscillator could be switched between two predetermined values so that one could make measurements on two different frequencies on the same specimen. The reflected pulses were amplified by an untuned wide band amplifier and displayed on an oscilloscope. During measurements the pulse train was photographed, and the pulse amplitudes were measured from the film. In this way, one was able to make accurate measurements even when the internal friction was changing rapidly.

The amplitudes of the pulse train is to a good approximation given by

$$A = A_0 e^{-\alpha x}, \tag{1}$$

where x is the sound path in cm and α the attenuation in nepers per cm.

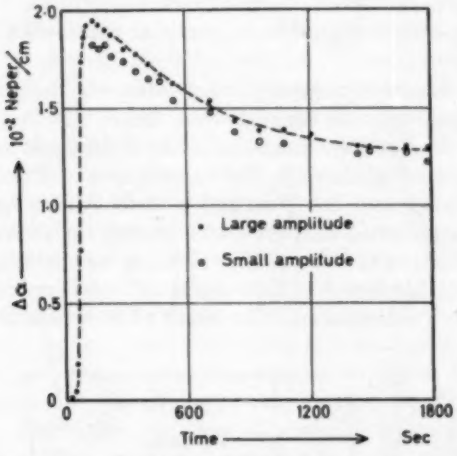

FIG. 2. Increase of attenuation during loading and logarithmic creep for specimen 19 measured simultaneously with two different amplitudes at 10 Mc.

If the amplitude of a certain pulse in the pulse train is A_1 before the experiment, and if it at some later time during the experiment has decreased to A_2, then the increase in attenuation is given by

$$\Delta\alpha = 1/x \ln(A_1/A_2). \tag{2}$$

In practice, the pulse train will depart somewhat from the simple relation of Eq. (1) resulting from diffraction effects and also because of the fact that the reflecting faces and the crystal are not exactly parallel. When the specimen is deformed these "humps" on the pulse train will move. In our case, most of the deformation takes place during the loading and unloading of the specimen, so that the effect of these moving "humps" on our measurements will be to shift all the measured values upwards or downwards by a certain amount. In order

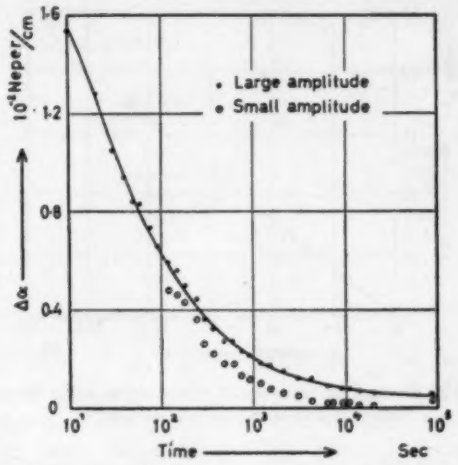

FIG. 3. Recovery of attenuation after unloading for specimen 19 measured simultaneously with two different amplitudes at 10 Mc. The solid curve represents the formula

$$\Delta\alpha = [10/(t+13.2)^{0.60} + 0.04] \cdot 10^{-2} \text{ Neper/cm}$$

to minimize this effect we measured the amplitudes of several pulses, usually the 5, 6, 7 and 8 reflected pulse, and computed the mean value of $\Delta\alpha$. Even then, the error due to this effect was sometimes as large as 10% of the maximum value of $\Delta\alpha$. Fortunately, this does not affect the slope of the recovery curve or the total amount of recovery. The other important source of inaccuracy was frequency and amplitude drift in the pulse generator. This was specially important during the later part of the recovery when the change in attenuation is very slow.

The experimental procedure was as follows: Before starting the experiment the pulse train was photographed. Then the load was applied to the specimen. The specimen was allowed to creep under constant load for 30 min, when the load was taken off. The time of unloading was about 3 sec. The pulse train was photographed and strain measurements taken with suitable intervals during creep, and for about 24 hr after unloading. By then the recovery of the internal friction was essentially complete.

EXPERIMENTAL RESULTS

A typical deformation curve is shown in Fig. 1. The curve is drawn with logarithmic time scale to demonstrate that the strain is proportional to log t during the constant load creep. All experiments gave this type of creep, as one would expect at the values of load and temperature chosen. In no case was there any measurable recovery of strain after unloading was complete.

Figures 2 and 3 show typical curves of the time variation of attenuation during creep and during recovery. The curves on Figs. 1–3 are all from the same experiment. As can be seen from Fig. 2, the attenuation reaches a maximum when the loading is complete and decreases slowly during creep under constant load. When the load is taken off, the attenuation increases

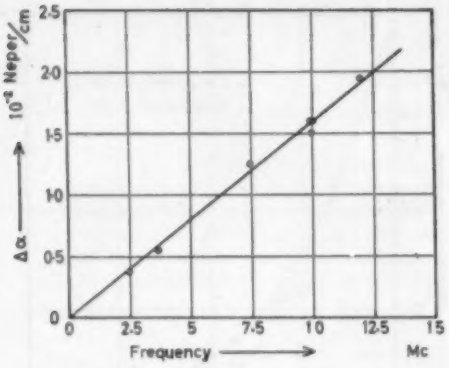

FIG. 4. The amount of recovery of attenuation after 10 sec after unloading as a function of frequency.

instantaneously and then falls rapidly towards the initial value. The attenuation just after unloading was found to be independent of the shape of the attenuation curve during creep.

In order to check the amplitude dependence of the attenuation, some measurements with about half amplitude were made in the experiment shown in Figs. 2 and 3. These points can be seen to lie parallel to, but somewhat below the points taken with normal amplitude. The fact that the curves are parallel also during the last part of the recovery make us believe that the small displacement may be due to a small frequency shift in the oscillator. As the Q of the pulse generator output circuit is higher in the "large amplitude" than in the "small amplitude" position, such a frequency shift would give just the observed result. One may therefore conclude that the amplitude dependence, if any, is small.

In Fig. 4 is plotted the amount of recovery of attenuation in the time interval from 10 sec after unloading to 24 hr after unloading for a number of experiments. In all the experiments the maximum deformation was about 0.19%. The amount of recovery of attenuation can be seen to be proportional to frequency, which means that the recoverable part of the internal friction is independent of frequency. In order to determine whether the internal friction is independent of frequency also during creep, an experiment was done where the attenuation was measured simultaneously on two frequencies. The result can be seen on Fig. 5. The numbers between the two curves are the ratio between the high-frequency and the low-frequency attenuation. As the ratio between the two frequencies (7.2 and 2.5 Mc) is 2.88, one can see that the attenuation is proportional to frequency also during creep.

The recovery curve was found to be fitted by an expression of the type

$$\Delta\alpha = C_1/(t+C_2)^{C_3} \qquad (3)$$

as shown in Fig. 3. Here t is the time after unloading. Table I gives the values of the constants C_2 and C_3 for some experiments where the measurements were complete enough to allow their determination. The values for the low-frequency measurements are rather uncertain due to the larger relative uncertainty in these measurements.

DISCUSSION

The Lücke-Granato theory[15] seems to be unable to explain our experimental results for the following reasons.

1. The assumption of a velocity dependent dislocation damping leads to a frequency dependent internal friction, while our experiments show that the increase of internal friction is independent of frequency.

2. Lücke and Granato have proposed[15] that the recovery of internal friction after plastic deformation is caused by pinning of the vibrating dislocation loops by impurity atoms. Cottrell and Bilby predict[19] that the number of impurity atoms per cm of dislocation line will be proportional to $t^{\frac{1}{3}}$, which means that the free dislocation length L will be inversely proportional to $t^{\frac{1}{3}}$. As the Lücke-Granato theory for small amplitudes gives $Q^{-1} \propto L^4$, one should expect $Q^{-1} \propto t^{-8/3}$, while the experiments give exponents between -0.42 and -0.63.

The observed frequency independence of the increase of internal friction suggests that the energy loss may be due to some mechanism involving dislocation motion across potential barriers. The calculations of Weertman and Salkovitz are based on such a model.[16] They assume that the potential barriers are caused by the stress field around impurity atoms. The mean wavelength of the potential barriers λ is then equal to $c^{\frac{1}{3}}$, where c is the impurity concentration. The result of their calculations

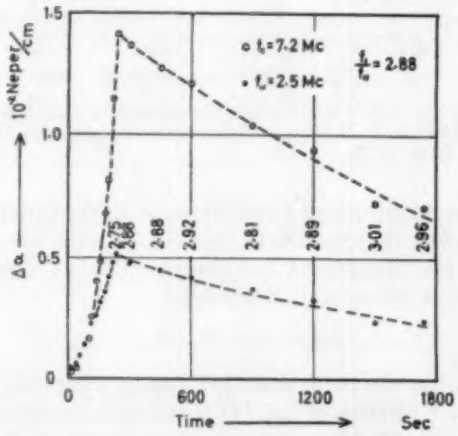

FIG. 5. The increase of attenuation during loading and logarithmic creep measured simultaneously at two frequencies. The numbers between the curves are the ratios between the observed attenuation values.

[18] *Dislocations and mechanical properties of crystals*, Lake Placid Conference, Sept. 6–8, 1956 (John Wiley & Sons Inc., New York, 1957), pp. 449, 450.

[19] A. H. Cottrell, *Dislocations and Plastic Flow in Crystals* (Clarendon Press, Oxford, England, 1956), pp. 147–150.

is

$$Q^{-1}=BNb\lambda\cdot 1/\sigma_M, \tag{4}$$

where B is a constant, N is the dislocation density, b is Burgers vector, and σ_M is the Mott-Nabarro critical stress, which is nearly proportional to the impurity concentration near the dislocation core. We will therefore assume that σ_M is proportional to the number of impurities per cm of dislocation line $n(t)$. Thus, we can rewrite Eq. (4) for the recovery as

$$Q^{-1}=K\lambda/n(t), \tag{5}$$

where K is a constant, since the dislocation density probably does not change much after unloading of the specimen; $n(t)$ is given by[19]

$$n(t)=n(0)+at^{\frac{1}{3}}, \tag{6}$$

where $n(0)$ is the number of impurity atoms per cm of dislocation line at the beginning of the recovery, and a is a constant.

The model then gives the following picture of recovery of internal friction after deformation: The energy loss from the sound field is caused by motion of long dislocation lengths from one position of equilibrium to another. The short lengths will not contribute as they will not be able to reach the nearest equilibrium position under the weak stress of the sound field. During unloading of the specimen after creep, the dislocations will tear away from their atmospheres of impurity atoms, thereby reducing σ_M and increasing the internal friction. When the dislocations has come to rest, the impurities will diffuse towards them again, thus giving rise to the slow recovery of internal friction.

The behavior to be expected of λ in Eq. (5) depends upon whether the distance to the nearest equilibrium position is determined by the number of impurities on the dislocation line or not. If the nearest equilibrium position lies within the cloud of impurity atoms on the dislocation line, we would expect λ to be proportional to $n(t)^{-\frac{1}{3}}$. If the nearest equilibrium position is outside the impurity cloud, λ is determined by the impurity concentration outside the dislocation line, which, according to Cottrell and Bilby, is constant. Thus, we are led to the following two expressions for the time dependence of internal friction depending upon whether we assume λ to be constant, or proportional to $n(t)^{-\frac{1}{3}}$

$$Q^{-1}=K'\frac{1}{n(0/a+t^{\frac{1}{3}})} \tag{7}$$

$$Q^{-1}=K''\frac{1}{(n(0)/a+t^{\frac{1}{3}})^{\frac{1}{3}}}. \tag{8}$$

For large values of t we get the internal friction proportional to $t^{-0.66}$ and $t^{-0.89}$, respectively, while the experiments give exponents from -0.42 to -0.63.

TABLE I. Experimental values of the constants C_2 and C_3 in the empirical formula $\Delta\alpha=C_1/(t+C_2)^{C_3}$ for the recovery of attenuation after plastic deformation.

Frequency Mc	Max def microstrain	C_2 sec	C_3
3.1	700	3	0.44
5.5	5000	3	0.42
6.25	700	16	0.57
7.2	1780	7	0.63
10	2400	11	0.55
10	1769	13	0.60
12	1900	9	0.58

In order to have agreement with the experimental results for small values of t, $n(0)/a$ must have a numerical value of about 5. The constant a is given approximately by[19]

$$a=3c\left(\frac{4\mu b\epsilon r^3 D_0\exp(-U/kT)}{kT}\right)^{\frac{1}{3}}, \tag{9}$$

where c is the impurity concentration outside the dislocations, r is the atomic radius, $D_0\exp(-U/kT)$ is the diffusion constant, ϵ is the factor of misfit for the impurity atoms, and μ is the elastic modulus. By putting $n(0)/a=5$, $n(0)=10^5$ per cm, $c=10^{19}$ per cm^3, $\epsilon=0.1$ and $D_0=1$ the activation energy for diffusion U comes out as 0.95 ev. This is a rather low value compared to the results of Bückle[20]; Mg/Al 1.13 ev, Si/Al 1.39 ev, Cu/Al 1.82 ev, Mn/Al 3.46 ev. But when the approximate nature of Eq. (9) and the uncertainty both in the numerical values put into it and in the values of the diffusion constants at room temperature is taken into account, the result is not unreasonable.

CONCLUSION

Our experiments indicates that the increase of internal friction during plastic deformation is probably caused by a static hysteresis type of loss mechanism. The rough model for the recovery of internal friction proposed here seem to be able to give some of the main features of the phenomenon, such as frequency independence, amplitude independence and also an approximately correct time dependence.

ACKNOWLEDGMENTS

The author wishes to thank T. Olsen and J. Lothe for their help and encouragement, without which this paper would probably not have been written. He would also like to thank Dr. J. Weertman for reading the manuscript and making some valuable suggestions.

[20] H. Bückle, Z. Elektrochem. 49, 238 (1943).

Effect of Atomic Interaction Potential on Defect Production in Metals*

E. Brown and G. H. Goedecke
Rensselaer Polytechnic Institute, Troy, New York
(Received December 10, 1959)

The cascade of displaced atoms in metals, induced by high energy radiation, has been investigated, with the assumption of a screened coulomb interaction between atoms. The problem was treated stochastically on an IBM 650 electronic computer for several different models. The comparison of our results with those for which a hard sphere interaction has been used shows only a slight decrease in the expected number of atomic displacements.

I. INTRODUCTION

THE number of displaced atoms produced by high energy radiation in metals has been calculated for several different models.[1–6] By and large the calculations were based on a hard sphere interaction between colliding atoms in the crystal. In the present paper we are concerned with the sensitivity of the results of these calculations to this aspect of the model and have chosen a screened Coulomb potential for comparison.

The problem can generally be separated into two parts, (1) the creation of a primary knock-on, an atom of the crystal which receives sufficient energy from the incident radiation to be displaced from its normal site, and (2) the creation of secondaries from subsequent collisions. The first part depends on the nature of the incident radiation and must be treated differently for each case. We consider only the process after a primary has been created.

This problem can be treated stochastically if a number of simplifying approximations are made. In essence, the usual stochastic model neglects the fact that the atoms are arranged in an orderly array and treats a succession of collisions as a sequence of independent events.

We are concerned here with the number of interstitials produced as a function of the energy of the primary and not with the geometrical distribution of damage. It is only necessary, then, to study a sequence of collisions with regard to the probable energy transfer from an incident atom to an atom in its normal site. The fact that an atom is bound to its site is accounted for by the assumption of an escape probability which is a function of the energy transfer. The multiplication of secondaries by such collisions is handled by a Monte Carlo method, programmed for an electronic computer. The cascade is followed until the energy in each displaced atom is degraded to the point where no further damage can take place. It is assumed that no recombination of interstitials takes place with vacancy sites during irradiation so that a count of displaced atoms is all that is necessary.

II. THE INTERACTION POTENTIAL

The stochastic model which has been outlined is characterized by two probability functions, one for the energy transfer in a collision, the second for the escape of an atom from its site. The former is determined by the interaction potential between colliding atoms. In dealing with high energy primaries, it may be expected that the nature of the cascade will be sensitive to the manner in which the energy divides in a collision. For discussion purposes we call an interaction hard if there is likely a transfer of a large fraction of the energy of an incident atom in a collision. Qualitatively, a hard cascade would result in rapid energy degradation and relatively few collisions. This is the type of cascade characteristic of a hard sphere interaction. For this interaction all transfer energies are equally likely up to the incident energy. The hard sphere interaction has the virtue that it can be handled analytically for the case of simple escape probability functions.

A screened coulomb interaction was chosen for the present determination of defect production. This is a physically reasonable choice. The choice was also based on the fact that scattering calculations are available from which to determine the energy transfer function[7] and because it leads to a soft cascade.

The interaction potential energy between two atoms was taken to be

$$V=(Z^2e^2/r)\exp(-r/a),$$

where $a=a_0/(2)^{\frac{1}{2}}Z^{\frac{1}{3}}$. Here a_0 is the Bohr radius. Z was chosen as 29, the value appropriate for copper.

As the collisions are presumed to be elastic, the energy transferred is a simple function of the scattering angle. The energy transfer probabillty is shown in Fig. 1 with that of a hard sphere interaction for comparison.

* This research was supported by the U. S. Atomic Energy Commission.

[1] W. S. Snyder and J. Neufeld, Phys. Rev. **97**, 1636 (1955); **99**, 1326 (1955); **103**, 862 (1956).

[2] W. A. Harrison and F. Seitz, Phys. Rev. **98**, 1530 (1955).

[3] J. B. Sampson, H. Hurwitz, Jr., and E. F. Clancy, Phys. Rev. **99**, 1657 (1955).

[4] C. A. Bruch, W. E. McHugh, and R. W. Hockenbury, J. Metals **8**, 1362 (1956).

[5] G. H. Kinchin and R. S. Pease, Rept. Progr. in Phys. **18**, 1 (1955).

[6] For a summary of much of this work see G. J. Dienes and G. H. Vineyard, *Radiation Effects in Solids* (Interscience Publishers, Inc., New York, 1957) p. 17.

[7] E. Everhart, G. Stone, and R. J. Carbone, Phys. Rev. **99**, 1287 (1955).

III. CALCULATIONS AND RESULTS

The stochastic calculation requires a model governing the escape mechanism of an atom from its site. We have investigated several different models for which hard sphere calculations have been made. The model of Kinchin and Pease[5] is that of a simple threshold at an energy E_d. The probability of escape is zero for energies less than E_d, and unity for energies above this. The escaping atom loses no energy in leaving its site. In addition, replacement collisions are allowed in which the incident atom replaces the struck atom when the incident atom is left with energy less than E_d. The model of Seitz and Harrison[2] is similar, except that replacement collisions are not considered and an energy of amount E_d is lost when an atom is displaced. We have also considered the case where the above models are each altered slightly by having an escape probability of 0.8 for energies above E_d. These latter models take slight account of the fact that there are directions of motion of the struck atom for which it has little likelihood of escape regardless of energy. The altered Kinchin and Pease model has been treated for hard spheres by G. H. Vineyard.[8] In this case the average number of displacements is not a linear function of the primary energy E_p, being given by $\langle \nu \rangle = (E_p/2E_d)^{0.8}$.

The number of displacements was calculated as a function of primary energy by a Monte Carlo method by using an IBM 650 electronic computer. A cascade was followed until the energy of all the knock-ons was degraded to the point where no further displacements were possible. The calculations were repeated one hundred times for each primary energy considered so as to get reliable statistics. E_d was chosen as 25 ev. The results are plotted in Figs. 2 and 3. The hard sphere results are included for comparison. Curve (A) is based on the Kinchin and Pease model; curve (B) is based on the altered model of 0.8 probability of escape beyond threshold; curve (C) is based on the Harrison and Seitz model; curve (D) is based on the altered model of Harrison and Seitz. No calculations are available for the hard sphere interaction with the latter model. It is seen that the differences brought about by the interaction are small compared to the other uncertainties in the model.

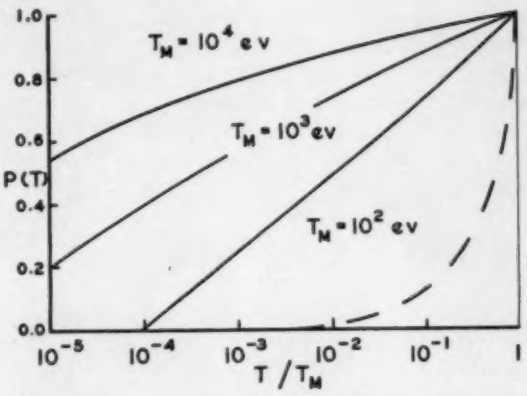

FIG. 1. Integrated probability for transferring energy T as a function of T/T_m. T_m is the energy of the incident atom. The solid curves are based on a screened coulomb interaction between atoms. The dashed curve is based on a hard sphere interaction and is independent of T_m.

IV. DISCUSSION AND CONCLUSIONS

It is possible to make a qualitative argument based on the Kinchin and Pease model, which suggests that the number of displacements is insensitive to a wide choice of interaction potentials. We fix our attention on cascades resulting from a single primary energy and

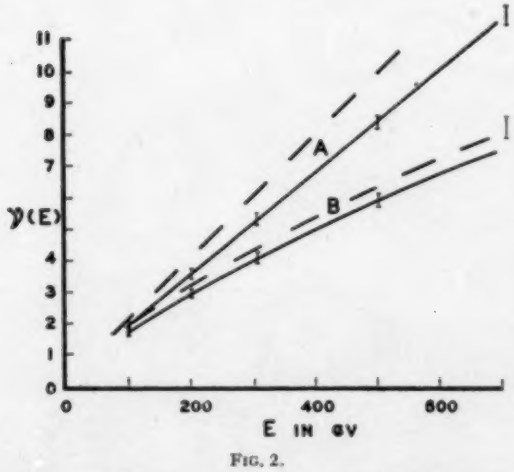

FIG. 2.

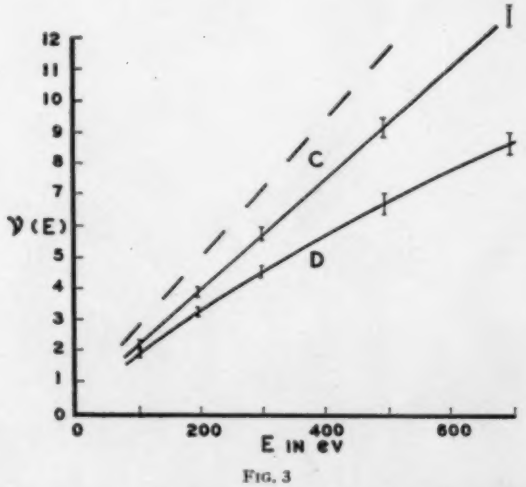

FIG. 3

FIGS. 2 AND 3. Average number of displaced atoms as a function of the energy of the primary knock-on. The threshold energy of escape is taken as 25 ev. Solid curves are based on a screened coulomb interaction. Dashed curves are based on a hard sphere interaction.

[8] G. H. Vineyard (unpublished).

consider the distribution of energies among the atoms which have finished their histories. In this model, these are the atoms whose energies are less than $2E_d$[5,6]. Denoting the distribution function by $f(E)$ (the dependence on the primary energy of $f(E)$ is not explicitly included) we get for the average number of displacements

$$\langle \nu \rangle = \left[\int_{E_d}^{2E_d} f(E)dE \right] \left[E_p \Big/ \int_0^{2E_d} Ef(E)dE \right],$$

where E_p is the primary energy. The first factor is the probable fraction of atoms ending up as displacements in a given cascade. The second factor is the average number of atoms involved in a cascade.

The determination of $f(E)$ requires a detailed analysis for each postulated interaction. However, it is possible to suggest its form by using crude arguments. There are two contributions to $f(E)$: the first coming from those knock-ons which receive an energy less than $2E_d$ and the second coming from higher energy knock-ons which subsequently degrade their energy in collisions. The first contribution is of the form E^{-2} for a coulomb interaction.[9] The effect of screening may be approximated by reducing the magnitude of the exponent. To the extent that the logarithmic plots of Fig. 1 may be approximated by straight lines, the appropriate value of the exponent for the present calculation is -1. A hard sphere interaction yields the exponent zero.

[9] As it stands, this function cannot be normalized to unity. The problem may be avoided by assuming the function is valid only for energies above a cutoff value which is much smaller than E_d. This corresponds to the physical assumption of a minimum energy transfer per collision.

We temporarily neglect the second contribution and assume $f(E) \propto E^{-\alpha}$. The average number of displacements is then $\langle \nu \rangle = \beta E_p / 2E_d$, where $\beta = (1-2^{\alpha-1}) \times (2-\alpha)/(1-\alpha)$. Although the coeff. β approaches zero for pure coulomb scattering, it is relatively insentitive to α over a large part of the range. For example, for $0 \leqslant \alpha \leq 1$, $1 \geq \beta \geq ln2 = 0.693$. The insensitivity is caused by the competition of the two terms in the expression for $\langle \nu \rangle$.

The second contribution to $f(E)$ will tend to compensate the first. If low energy transfers are very likely, the knock-ons which degrade from high energy have a higher probability of ending their histories in the upper part of the energy range. These considerations indicate that a much weaker screening than has been used for the present calculation would be necessary to get a significant departure from the results of the hard sphere model.

Our results indicate that the number of displacements produced by primaries of energy well above threshold is insensitive to the interaction potential between atoms, provided a stochastic treatment is valid. However, the nature of the cascade is dependent on the interaction in that many more collisions take place for soft interactions with most secondaries produced with low energies. These considerations would be pertinent to the geometrical distribution of displaced atoms and play a role in the annealing of radiation damage.

ACKNOWLEDGMENTS

We would like to thank Dr. H. B. Huntington for suggesting this problem and for taking active interest in its progress. Thanks are also due Dr. George H. Vineyard for helpful comments.

Letters to the Editor

"Foldover" Effects Caused by Spin Wave Interactions in Ferromagnetic Resonance

H. SUHL
Bell Telephone Laboratories, Inc., Murray Hill, New Jersey
(Received January 5, 1960)

TWO distinct high-power effects in ferromagnetic resonance have been familiar for some time: spin wave instability effects[1] and foldover effects of the response curve.[2] The former are caused by coupling between spin waves via the uniform precession. The latter have been understood (up to now) only for nonspherical samples with sufficient shape anisotropy, or for samples with correspondingly high crystalline anisotropy. Yet bistabilities characteristic of foldover have been observed in spherical samples with small anisotropy also.[3]

In this note we suggest that the spin wave interactions likewise lead to foldover. Thereby we can explain why the dissipative part of the susceptibility χ'', after following a reasonably well understood decline when the power exceeds a certain "first threshold" value[4,5] suddenly begins to show multivalued behavior when the power is further increased above a " second threshold."

The foldover occurs as follows: The current theory of χ'' [4,5] assumes that in the experiment under consideration, the biasing field or the signal frequency is always adjusted so that χ', the real part of the susceptibility, is zero. For infinitesimal powers this occurs exactly at the usual resonance. When the power is substantially increased, this zero phase condition is no longer even approximately fulfilled at the same value of field or frequency, and no effort is usually made to retune the system so that $\chi'=0$. Hence it becomes necessary to examine the whole response curve. When this is done, the foldover phenomenon becomes apparent at once.

The direction of the foldover depends on the sign of p, which according to the simplest theory for the nonlinear spin wave coupling is unequivocally positive. Weiss,[3] however, reports opposite directions of foldover for yttrium iron garnet, and manganese ferrite. We have no explanation for this difference. It may be that the nonlinear spin wave theory requires improvements taking into account anisotropy and spin wave scattering effects, or it may be that the explanation of Weiss[3] in terms of a spin temperature dependent g factor also plays an important role.

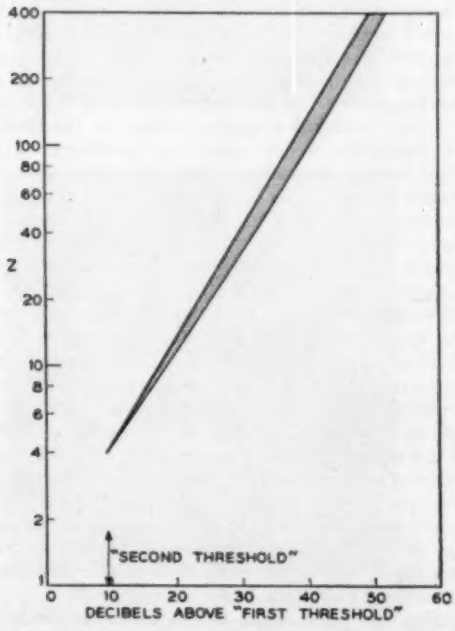

FIG. 1. Region of bistability in the y-s plane.

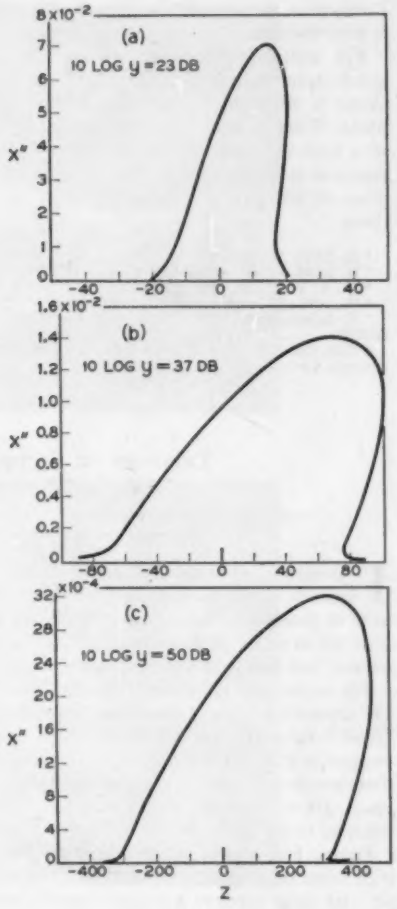

FIG. 2. (a) (b) (c) Shapes of the response curves at three different power levels.

In the notation of footnote 4, the uniform precession amplitude when the phase shift is not tuned out is given by[6]

$$B_0=h_s\left[\left\{S(\omega_s-\omega_0)+\sum\frac{|v_{0k}|^2\{\omega_s-\omega_k+p_k|B_0|^2\}}{(\omega_s-\omega_k)^2+\eta_k^2-p_k^2|B_0|^4}\right\}+i\left\{S\eta_0+\sum\frac{|v_{0k}|^2\eta_k}{(\omega_s-\omega_k)^2+\eta_k^2-p_k^2|B_0|^4}\right\}\right]^{-1},$$

where h_s is the signal field in frequency units and ω_s the signal frequency.

The sums are now evaluated with the same approximations as in footnote 4, and squares of absolute values are taken on both sides of this equation. It is then convenient to solve for the frequency deviation in terms of $|B_0|^2$. In reduced notation the result is

$$z=-\frac{x}{(1-x^2)^{\frac{1}{2}}}\pm\left\{\frac{y}{x}\left(1+\frac{\eta_0}{\eta_{sp}}\right)^2-\left[\frac{1}{(1-x^2)^{\frac{1}{2}}}+\frac{\eta_0}{\eta_{sp}}\right]\right\}^{\frac{1}{2}},$$

where $z=(\omega_s-\omega_0)/\eta_{sp}$ is the frequency deviation measured in units of the frequency linewidth resulting from spin wave scattering alone, $x=|B_0|^2/|B_0|_{crit}^2$ is the square of the ratio of the uniform precession angle to the critical angle and $y=P/P_C$ is the ratio of applied power to critical power. The two branches of the z-x curve join smoothly with a vertical tangent. The reader will readily verify that for infinitesimal x it becomes the usual

Lorentzian curve (laid on its side since the frequency deviation is here the ordinate).

For simplicity, we now confine the discussion to the case $\eta_0=0$ (spin wave scattering only). As y increases, the Lorentzian shape is distorted so that more of the area is in the lower half plane. When y reaches 10, the distortion begins to take the form of a foldover (see Fig. 1) so that over a certain range of z the response is triple valued. Figure 2 shows the region in the z-y plane in which this occurs, so that bistability may be expected there.

[1] H. Suhl, J. Phys. Chem. Solids 1, 209 (1957).
[2] H. Suhl, Proc. Inst. Radio Engrs. 44, 1270 (1956) (Introduction).
[3] M. T. Weiss, J. Appl. Phys. 30, 2014 (1959).
[4] H. Suhl, J. Appl. Phys. 30, 1961 (1959).
[5] E. Schlömann, J. J. Green, and U. Milano, J. Appl. Phys. 31, 385S (1960).
[6] This formula was derived independently by P. Gottlieb of Hughes Aircraft Company.

Terraces on Etchpits

J. J. Gilman
General Electric Research Laboratory, Schenectady, New York
(Received January 25, 1960)

It is often observed that the side faces of etchpits do not have smooth surfaces, but are terraced. It is the purpose of this note to present evidence for a simple cause of such terraces that may act in many cases. No doubt there are several other possible causes, but they will not be considered here.

For some time it has been known that "aged"[1] dislocations in LiF crystals tend to produce etchpits with terraced sides, whereas "fresh" dislocations do not.[1] It has been suspected that segregated impurities that form nonuniform threads along the aged dislocations are responsible for the phenomenon, but there has been no proof. Direct evidence that discontinuous precipitates can form terraced etchpits is presented here.

Figure 1(a) shows an etchpit with very high terraces along with some other pits with smaller terraces. At the center of the pit with large terraces a string of small dots may be seen. These dots are caused by small particles which lie on the surface of the crystal. As the etching proceeded, each time a new terrace was observed, a new particle was also observed at the center of the pit. Figure 1(b) shows the etchpit of Fig. 1(a) after it had been etched additionally. The photograph was made just after a new terrace with its associated precipitate particle appeared. During the 4 min etching interval between the two pictures, the number of particles increased from 7 to 10; but the total number of terraces did not increase by the same number, because the terraces are not stable. They gradually become rounded off and disappear. The particles are 2–4000 A in diam, and the terraces have approximately this height when they first form.

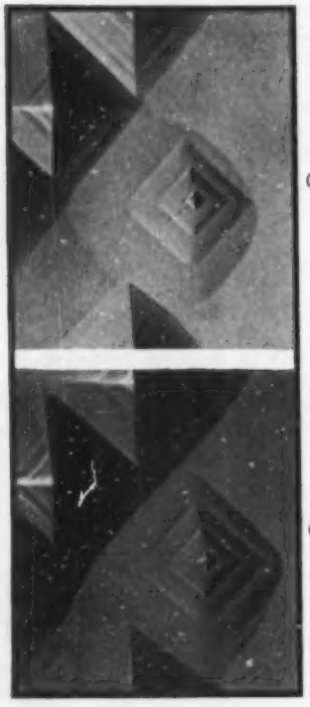

(a)

(b)

Fig. 1. Deeply terraced etchpit with an associated stringer of precipitate particles. The LiF crystal was etched in Etch *A* in 30 sec increments (Etch *A* =1 pt HF, 1 pt glacial HA_c, and 2×10^{-6} pt FeF_3). (a) 7 min etch; (b) 11 min etch. 1000X.

The terraces in the case of Fig. 1 were caused by rapid development of the etchpit at a precipitate particle followed by slow etching between particles. In other cases, the rapid and slow stages might be reversed, because of different chemical factors, but the resulting terracing would look the same.

In Fig. 1, the precipitate particles are not located along a dislocation line. This may be deduced because the etchant (Etch *A*) is known to attack dislocations at a more rapid rate than was observed here. However, when dislocations *are* present together with precipitates, two sequences seem to operate which lead to terraced pits. In the first sequence, the rate of attack is most rapid at the parts of a dislocation that have precipitates, and is slower between precipitates where only the dislocation line is present. In the second sequence, the relative rates are reversed.

[1] "Aged" means dislocations that have been slowly cooled from the melting temperature or from a temperature above about 250°C. "Fresh" means dislocations introduced at room temperature and not allowed to stand more than several weeks.

Effect of Nuclear Polarization on the Behavior of Solid State Masers*

G. Makhov, L. G. Cross, R. W. Terhune, and J. Lambe†
Willow Run Laboratories, The University of Michigan, Ann Arbor, Michigan
(Received January 15, 1960)

Cowen, Schafer, and Spence[1] have shown that the saturation of the electron spin transitions of the Cr^{+++} ions in ruby produces significant polarization of the Al_{27} nuclei. Other investigators[2,3] have detected a similar effect in a variety of paramagnetic materials. Recently, we have observed what amounts to the inverse of this effect, i.e., that the application of rf power at or near frequency of the quadrupole resonance of the aluminum nuclei in ruby produced a marked change in the electron-spin resonant absorption under saturation conditions.[4] This communication deals with the effect of this interaction on the behavior of solid-state maser.

In the basic experiment, a two-turn coil was wound about a ruby sample containing nominally 0.1% chromium. This assembly was placed in a doubly resonant microwave cavity and located in the dc magnetic field in such a manner that the axis of the coil was perpendicular to the direction of the field, and the polar angle was approximately 60°. With the system cooled to 4.2°K, a *K*-band microwave pump was used to saturate the 1–3 transition, and stimulated emission at *X*-band frequency was obtained in the 3–2 transition. Subsequent application of rf power at 4.5 Mc produced an increase in the gain of the maser amplifier, and resulted in a change of mode of operation of the maser oscillator. The effect was most pronounced at the resonant frequency of the free aluminum nuclei; however, at higher levels of rf power substantial interaction was obtained over a band extending from 500 kc to 20 Mc. Typically, power levels required to produce a detectable effect were of the order of 10 mw on resonance, and about an order of magnitude higher off resonance.

Comparing the performance of the maser amplifier with rf power on and off, as shown in Figs. 1(a) and 1(b), respectively,

we may calculate the change in the magnetic Q due to the change in polarization of aluminum nuclei. The dependence of gain of the maser amplifier on the magnetic Q is given by

$$G=\left(\frac{1}{Q_c}-\frac{1}{Q_L}+\frac{1}{|Q_m|}\right)^2\Big/\left(\frac{1}{Q_c}+\frac{1}{Q_L}-\frac{1}{|Q_m|}\right)^2,$$

where Q_c is the coupling Q, Q_L is the loss Q, and Q_m is the negative magnetic Q. In our setup, Q_c and Q_L are typically 10^3. By using this value, we compute the decrease in Q_m caused by the application of rf to be approximately 20%. This change in magnetic Q was observed under conditions of partial saturation of the pumping transition.

The effect of decreased nuclear polarization on the behavior of the maser oscillator is shown in Fig. 2. The application of rf power tended to make the transient of the cw mode of the oscillator [Fig. 2(a)] less damped, and led eventually to the relaxation mode of operation [Fig. 2(b)]. The use of high rf power levels tended to diminish, or even reverse the effect.

It should be noted that the transient form of the interaction can be observed without the use of rf power. When maser action is initiated by bringing the dc magnetic field rapidly to the appropriate value, there results a transient during which the amplifier gain rises quickly to a high value, then decays slowly to a lower steady-state value. The time constant of the transient is of the order of seconds. The existence of the transient cannot be ascribed to spin-lattice relaxation, since T_1 for cooled ruby is of the order of 0.1 sec. Rather, it appears to result from the relaxation of polarization of aluminum nuclei.

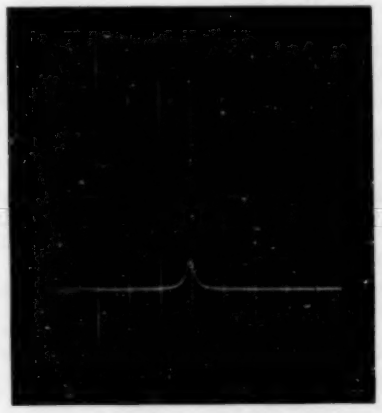

(a)

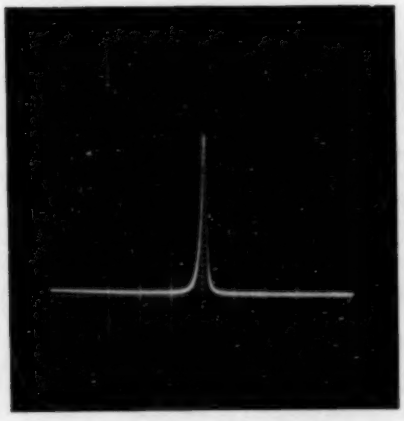

(b)

FIG. 1. Effect of change of nuclear polarization on maser amplifier gain. (a) rf off; power gain—15 db; (b) rf on; power gain—35 db.

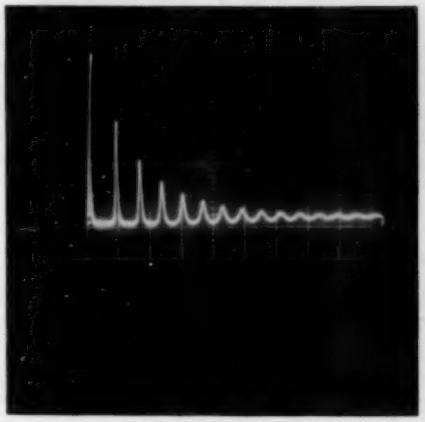

(a)

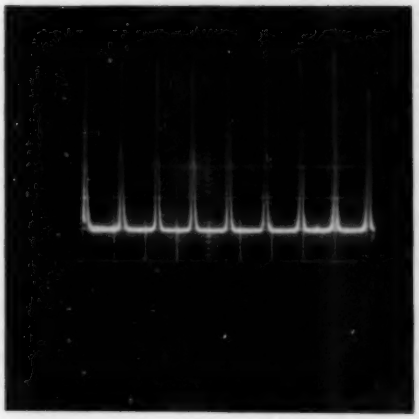

(b)

FIG. 2. Effect of change of nuclear polarization on the behavior of maser oscillator. (a) rf off; cw mode of operation; (b) rf on; relaxation mode of operation.

Subsequent experiments have indicated that the application of rf power does not affect thermal relaxation processes to any perceptible degree. Rather, it can be thought of as added pumping, resulting in an increase in the magnetic Q. The degree of enhancement of the punping process is of the order of change in the degree of nuclear polarization, estimated to be about 1% under our experimental conditions.[4] Under conditions of marginal saturation of the pumping transition, this may lead to substantial decrease in magnetic Q, as noted in the foregoing.

These considerations suggest that the recovery of a solid-state maser device from saturation, or from fluctuations in pumping power, is characterized in general by two time constants. There is rapid recovery, of the order of 0.1 sec, determined by spin-lattice relaxation; and slow recovery, of the order of seconds, determined by nuclear-electronic relaxation. These effects have been observed experimentally. The latter effect, of course, becomes significant only when the on-period of the saturating signal, or variations in the degree of saturation of the pumping transition, are on a time scale comparable to that of nuclear relaxation.

In conclusion, we would like to conjecture that the observed increase in gain of the maser amplifier resulting from the application of rf power may be used to advantage in detecting weak nuclear resonances as well as in studies of ENDOR-type effects. In essence, the effect on the electron system produced by resonant pumping of the nuclear system, is amplified by the practically noiseless maser amplifier. When a high degree of regeneration is used, a small change in the magnetic Q results in a very con-

siderable change in gain, or output, as attested by Figs. 1(a) and 1(b), and the corresponding calculation. A disadvantage of this method is, when using ruby, that maser action cannot be obtained in the vicinity of $\theta=0°$, whereas nuclear resonance effects are conveniently observed at that orientation. Presumably, this can be remedied by using a paramagnetic material, such as iron-doped sapphire, which permits maser action at the above orientation.

We are grateful to Professor C. Kikuchi and Professor G. Hok for many valuable discussions and helpful suggestions. We are appreciative of competent technical assistance rendered by A. Birko.

* This work was conducted by Project MICHIGAN under Department of the Army Contract administered by the U. S. Army Signal Corps.

† Now with the Scientific Laboratories, Ford Motor Company, Dearborn, Michigan.

[1] J. A. Cowen, W. R. Schafer, and R. D. Spence, Phys. Rev. Letters 3, 13 (1959).
[2] Erb, Montchane, and Überfeld, Compt. rend. 246, 2121 and 3051 (1958).
[3] M. Abraham, M. A. H. McCausland, and F. N. H. Robinson, Phys. Rev. Letters 2, 449 (1959).
[4] R. W. Terhune, J. Lambe, G. Makhov, and L. G. Cross, Phys. Rev. Letters (to be published).

Microwave Measurement of Semiconductor Carrier Lifetimes

H. A. Atwater
Department of Electrical Engineering, Pennsylvania State University, University Park, Pennsylvania

(Received January 5, 1960; revised manuscript received January 28, 1960)

In a recent communication, Ramsa, Jacobs, and Brand[1] have described a microwave technique for the measurement of carrier lifetime in semiconductors. In this technique, a pulse of minority carriers is injected into a slab of semiconductor placed transversely across a waveguide. The carrier lifetime is deduced from observation of the resulting transient variation of microwave attenuation by the sample. The authors find, from an analysis of the attenuation time decay curve shape, that the relative carrier injection level must be kept small in order that the increment of attenuation shall decay exponentially with the same time constant as the surplus carrier density. It may also be shown that the conditions under which this attenuation decay has the same time constant as the surplus carrier decay may be derived from an analysis wave propagation problem. We treat here the propagation of dominant mode waves in a waveguide containing an imperfect dielectric medium in which the conductivity is a function of time.

On assuming charge neutrality for the medium, as must be the case macroscopically, for example, with optical injection of carriers, the electric field must satisfy a wave equation of the form

$$\nabla^2 E_y=\mu\sigma(\partial E_y/\partial t)+\mu\epsilon(\partial^2 E_y/\partial t^2). \tag{1}$$

Here, σ is the conductivity and μ and ϵ the magnetic permeability and dielectric constant of the medium, respectively. The dominant mode solution of Eq. (1) is

$$E_y=\sin(\pi x/b)e^{-\gamma z}e^{j\omega t}, \tag{2}$$

in which b is the waveguide width, ω is the angular frequency of the waves, and γ is a complex propagation constant defined as

$$\gamma=\alpha+j\beta. \tag{3}$$

From Eqs. (1) and (2) the propagation constant is

$$\gamma=\pm[(\pi/b)^2-\mu\epsilon\omega^2+j\mu\sigma\omega]^{\frac{1}{2}}. \tag{4}$$

If the waveguide is operating far from its cutoff frequency, $(\pi/b)^2$ in Eq. (4) may be neglected in comparison with $\mu\epsilon\omega^2$. If it is further assumed that $(\sigma/\omega\epsilon)<1$, and expanding to second order in $(\sigma/\omega\epsilon)$, Eq. (4) becomes approximately

$$\gamma\approx(\sigma/2)(\mu/\epsilon)^{\frac{1}{2}}+j\omega(\mu\epsilon)^{\frac{1}{2}}[1+\sigma^2/(8\omega^2\epsilon^2)]. \tag{5}$$

If the second term in the square brackets of Eq. (5) is not negligible with respect to unity, the wave propagation constant β will depend on σ. The resulting change in the impedance of the sample may cause a change in reflected power, and hence an incorrect deduction of transmitted power. It may also be shown that a similar result can occur if $(\sigma/\omega\epsilon)>1$. The condition assumed to hold in the reference of footnote 1, namely that only the absorbed power varies with the excess conductivity, requires that $(\sigma/\omega\epsilon)\ll 1$. By using $\epsilon=16\epsilon_0$, for germanium, this condition would limit the usable conductivity, for X-band measurements, to about 10 (ohm-m)$^{-1}$, or for K-band operation, to about 30 (ohm-m)$^{-1}$. If the restriction of small $(\sigma/\omega\epsilon)$ is retained, the behavior of the microwave power attenuation by the sample may be deduced as follows. The power propagated along the waveguide is

$$P=\frac{1}{2}\int \mathbf{E}\times\mathbf{H}^*\cdot d\mathbf{S}=j[(ab)/(4\mu\omega)]\gamma^* e^{-2\alpha z}, \tag{6}$$

where a is the height of the waveguide, and the factor j is a phase factor. On using Eq. (3), Eq. (6) is of the form,

$$P=A\alpha e^{-2\alpha z}+Be^{-2\alpha z}, \tag{7}$$

in which A and B are constants not dependent on time.

It is known that the decay of a surplus minority carrier concentration in a semiconductor can be described under certain restrictive conditions of low surplus carrier concentration in terms of a lifetime τ associated with an exponential time decay.[2-4] For very large surplus carrier densities the decay is no longer of exponential form. However, the concept of carrier lifetime is sufficiently useful to justify its retention as an approximate description of the surplus carrier density decay. Consequently, the conductivity-dependent attenuation constant α is assumed to have the time dependence,

$$\alpha=\alpha_0[1+c\exp(-t/\tau)], \tag{8}$$

in which c is a measure of the initial surplus carrier concentration, and τ is the carrier lifetime. On using Eq. (8), Eq. (7) has the form

$$P=A\alpha_0[1+c\exp(-t/\tau)]\exp\{-2z\alpha_0[1+c\exp(-t/\tau)]\}+B\exp\{-2z\alpha_0[1+c\exp(-t/\tau)]\}. \tag{9}$$

In general, $c<1$ and if the sample thickness z is made very small, Eq. (9) becomes

$$P=A\alpha_0[1+c\exp(-t/\tau)]+B \tag{9a}$$

and the time dependence of the transmitted power is exponential with a time constant equal to the carrier lifetime τ.

However, a very small sample thickness is not practically desirable and it also increases the relative importance of surface recombination, leading to an incorrect result for bulk lifetime. An alternative experimental restriction is that of low initial surplus carrier density; $c\ll 1$. In this approximation, the exponential factors in Eq. (9) may be expanded. On neglecting terms in c^2, the transmitted power then has the form,

$$P=F+cG\exp(-t/\tau), \tag{9b}$$

where F and G are constants. Hence it is seen that with the restriction of low carrier injection level, the transmitted microwave power decays exponentially with time constant τ.

The transmitted power Eq. (9) may be expressed in a third alternative form if with the values of material constants σ and ϵ cited above, α in Eq. (3) is approximately an order of magnitude smaller than β. The logarithm of power in Eq. (6) has the form,

$$\ln P=\ln K+\ln\gamma^*-2\alpha z, \tag{10}$$

where K is a constant. After expanding the $\ln\gamma^*$ term,

$$\ln P=\ln[(K\beta)/j]-\alpha(2z+j/\beta). \tag{11}$$

Therefore, when α/β is small, the logarithm of the transmitted power exhibits a transient variation similar in character to that of the attenuation constant α, and hence to that of the conductivity of the semiconductor medium.

In summary, it has been shown that the time constant of the microwave power attenuation transient curve can furnish a

direct evaluation of surplus carrier lifetime, when the latter is assumed to follow a simple exponential behavior, under the conditions of (a) small sample thickness, (b) low carrier injection level, or (c) use of the logarithm of the transmitted power decay curve when the ratio of attenuation constant to propagation constant is small.

[1] A. P. Ramsa, H. Jacobs, and F. A. Brand, J. Appl. Phys. **30**, 1054 (1959).
[2] R. N. Hall, Phys. Rev. **87**, 387 (1952).
[3] W. Shockley and W. T. Read, Phys. Rev. **87**, 835 (1952).
[4] G. K. Wertheim, Phys. Rev. **109**, 1086 (1958).

High-Temperature Hall Coefficient in GaAs*

L. W. Aukerman and R. K. Willardson
Battelle Memorial Institute, Columbus, Ohio
(Received January 18, 1960)

INFRARED absorption of n-type GaAs suggest that there is a conduction band minimum a few tenths of an ev above the lowest conduction band minimum[1] in accordance with the conduction band structure proposed by Callaway.[2] Gray and Ehrenreich[3] have also suggested this conduction band structure as an explanation of the maximum in Hall coefficient of n-type GaAs at high temperatures.[4,5]

The separation of the two conduction band minima was estimated by Spitzer and Whelan[1] to be about 0.25 ev; however, this was done by estimating the threshold of the free carrier absorption, which is rather difficult to do accurately. It should be possible to estimate the separation of the minima from the temperature dependence of Hall coefficient.

Let η_1 and η_2 be, respectively, the concentration of electrons in the lower minimum (Band 1) and the upper minimum (Band 2), and let the ratio of the mobilities be $\mu_1/\mu_2=b$. Then the Hall coefficient R at weak magnetic fields is

$$R=(r/e)(\eta_1 b^2+\eta_2)/(\eta_1 b+\eta_2)^2, \tag{1}$$

where r depends on the scattering processes and the band structure and is not expected to change appreciably in the temperature range of interest here. For nondegenerate statistics, which should apply in the temperature range at which the Hall coefficient starts to increase (about 500°K), we can write

$$\frac{\eta_1}{\eta_2}=\left(\frac{m_1}{m_2}\right)^{\frac{3}{2}}e^{\Delta E/kT}, \tag{2}$$

where m_1 and m_2 are the effective density-of-states masses of electrons in Band 1 and Band 2, and ΔE is the separation between the two conduction band minima. Furthermore, if the donors are completely ionized,

$$n_1+n_2=N_D-N_A=r/eR_0, \tag{3}$$

where N_D-N_A is the net donor concentration and R_0 is the Hall coefficient at exhaustion, but at a temperature well below 500°K, where $n_2\approx 0$. If we neglect the small differences in r between Eqs. (1) and (3) and combine Eqs. (1), (2), and (3) we obtain

$$\frac{R-R_0}{R_0}=\frac{(b-1)^2(m_1/m_2)^{\frac{3}{2}}\exp(\Delta E/kT)}{[1+b(m_1/m_2)^{\frac{3}{2}}\exp(\Delta E/kT)]^2}$$

Thus, the quantity $(R-R_0)/R_0$ should be nearly independent of the total carrier concentration. Furthermore, when the percentage change in Hall coefficient is small, the exponential in the denominator predominates and one has, approximately,

$$(R-R_0)/R_0\approx(b-1)^2[b^2(m_1/m_2)^{\frac{3}{2}}\exp(\Delta E/kT)]^{-1}. \tag{5}$$

Figure 1 is a plot of the percentage change in Hall coefficient against the reciprocal of temperature in the temperature range where the increase becomes noticeable for three n-type GaAs specimens of widely different carrier concentrations.

The room temperature Hall coefficient remained constant to within 2% after samples were heated to as high as 640°C (corresponding to the highest temperature plotted in Fig. 1). However, when one of the specimens was heated to 850°C it was p-type when cooled to room temperature.

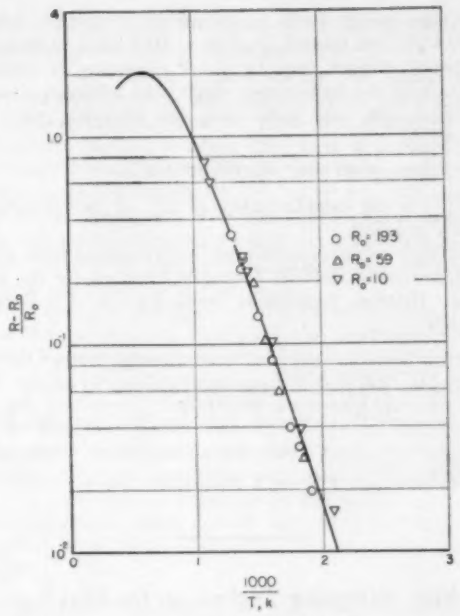

FIG. 1. The fractional increase in Hall coefficient of three n-type specimens of GaAs as a function of the reciprocal of temperature. The solid curve is a plot of Eq. (4), where $\Delta E=0.38$ ev, $b=10$, and $m_1/m_2=0.04$. R_0 is the Hall coefficient near room temperature.

On assuming b is constant, the slope of the straight portion of the curve of Fig. 1 yields an activation energy, $\Delta E=0.38\pm0.02$ ev. The curve is calculated from Eq. (4) by using $b=10$, $(m_1/m_2)=0.04$ and no temperature dependence of ΔE. From the curves of Folberth and Weiss,[6] it is concluded that $b\geq 10$. The value for the effective mass ratio would not be appreciably altered by assuming a larger value for b, but might be affected if ΔE depends strongly on temperature.

For example, if the temperature coefficient α of ΔE is -1×10^{-4} ev/°C, then m_1/m_2 would be 0.07. Although the temperature dependence of phonon interactions and other absorption mechanisms makes it difficult to obtain a good value for α, the value used above is not inconsistent with the data of Spitzer and Whelan.

The discrepancy between $\Delta E=0.38$ ev obtained here and the value of 0.25 ev obtained by Spitzer and Whelan can hardly be ascribed to experimental error. Again it suggests a temperature dependence of ΔE, since the 0.38 ev value corresponds to the separation of minima at $T=0$.

For the three GaAs samples shown in Fig. 1, the increase in resistivity with increasing temperature is consistent with the expected temperature dependence of the decrease in mobility of the light mass electrons and the reduced mobility of the electrons excited to the upper minimum. The effect of interband scattering on the mobility of the light mass electrons in the lower minimum does not appear to be significant. This is in contrast to the case where pressure is used to change the positions of the minima so that they approach each other and give a minimum average mobility when the minima are at equal energy.[6]

The two-carrier effect may have to be taken into consideration in the application of GaAs for devices which must operate at temperatures above 300°C. Since the mobility ratio is large, the Hall mobility ($R\sigma$) is essentially that of the lighter electron. This fact is born out experimentally, since the mobility trend appears to be at most only slightly affected as the temperature is increased above 500°K.

When deep energy levels which are not completely ionized at 500°K or above are present, analysis of Hall effect vs temperature in the usual manner may be either confusing or misleading. However, since the two carrier effect is an intrinsic property of the material, one need only apply the following, very simple correction:

$$n_1+n_2=(r/eR)[1+F(T)],$$

where $F(T)$ is the right-hand side of Eq. (4) and is determined empirically in Fig. 1.

The authors wish to acknowledge the Compound Semiconductor Research Group of Battelle Memorial Institute for the samples of GaAs. Helpful suggestions from Dr. A. C. Beer were appreciated.

* This research was supported by the Aeronautical Research Laboratory, Wright Air Development Center.

[1] W. G. Spitzer and J. M. Whelan, Phys. Rev. **114**, 59 (1959).
[2] J. Callaway, J. Electronics **2**, 330 (1957).
[3] P. V. Gray and H. Ehrenreich, Bull. Am. Phys. Soc. Ser. II, **3**, 225 (1958).
[4] Edmond, Broom, and Cunnell, *Rugby Semiconductor Conference*, Phys. Soc. (London) (1956).
[5] O. G. Folberth and H. Weiss, Z. Naturforsch. **10a**, 615 (1955).

Film Stripping Technique for Making Thin Silica Windows

E. TANNENBAUM
Bell Telephone Laboratories, Inc., Murray Hill, New Jersey
(Received December 21, 1959)

TRANSPARENT silica windows can be made in a range of thicknesses from 1000 to 100 000 A with areas as large as 1 cm² by selective gaseous etching of the silicon substrate. The technique is based on the well-known reaction between silicon and chlorine at elevated temperatures to form silicon tetrachloride.[1,2] SiO_2 is not attacked by chlorine so that the silicon can be selectively etched away leaving behind the SiO_2.

An amorphous SiO_2 layer is grown on a slice of silicon by thermal oxidation to the desired thickness. Both the silicon slice and the oxidation furnace must be clean to obtain uniformly thick SiO_2 layers free of imperfections and crystallites. The SiO_2 is removed from the desired area on one side of the oxidized slice by masking with scotch tape or wax and exposing to HF vapor. After removing the masking material, the slice is placed in the hot Cl_2 gas, etching away the exposed silicon leaving a "window" of SiO_2 in the supporting silicon frame.

The chlorination system consists of a forepump, quartz reaction tube, furnace, and a series of traps for distilling the chlorine gas on the line. The chlorine is twice sublimed from liquid nitrogen to remove traces of H_2O. The system is then backfilled with argon to prevent oxidation of the exposed silicon in the process of placing it in the furnace. The reaction proceeds at an appreciable but still controllable rate in the temperature range 700–1100°C. The Cl_2 pressure is similarly not critical. Under typical operating conditions, $T=800$°C, $P_{Cl_2}=200$ mm Hg, the etching rate is approximately 0.001 in. per min. It is essential that O_2 and H_2O be removed from the system because chlorides of silicon will hydrolyze and Si oxidize in the presence of O_2 and H_2O producing powdery SiO_2 on the reacting surface.

FIG. 1. 3000 A SiO_2 stripped films in silicon frame.

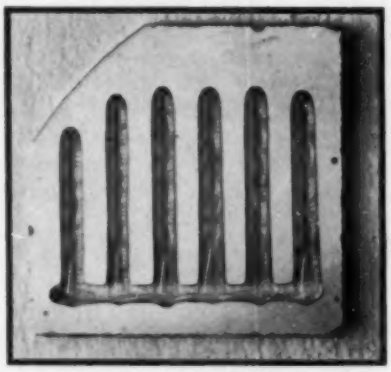

FIG. 2. Etch pattern in silicon made by diamond scribing through the oxide and chlorine etching.

A typical sample produced in this way is shown in Fig. 1. The oxide film is 3000 A thick and each of the four windows is approximately 0.5 cm×0.5 cm. The oxide tends to buckle in the silicon frame possibly because the SiO_2 film is grown at about 1000°C and the difference in the coefficient of expansion of Si and SiO_2 causes the SiO_2 to be under compressive strain when attached to the silicon substrate at room temperature. The lattice mismatch at the Si/SiO_2 interface would tend to produce the same result.

Although the films are naturally quite fragile, films as thin as 1000 A are sturdy enough for some experimental purposes. For example, such films are currently being used in studies of the mechanism of silicon oxidation[3] and in studies of the optical constants of SiO_2 from infrared transmission and reflection measurements.[4]

The technique is also useful for cutting silicon into shapes too intricate for mechanical machining or conventional liquid etching. This is done by scribing the desired outline of the pattern through the grown oxide layer with a diamond point. The chlorine then attacks the silicon at the scribe, etching through to give the desired shape. For example, see Fig. 2. The slice is ½ in. on a side. The scribe line can be seen through the overhanging oxide. The etching is a smooth clean line, and when care is taken to eliminate H_2O and O_2, mirror smooth silicon etched surfaces can be obtained.

The technique has also been used to study imperfections in oxidized surfaces.[5]

[1] Gatterman and Weinlig, Ber. **27**, 1943 (1894).
[2] Martin, J. Chem. Soc. **105**, 2036 (1914).
[3] J. R. Ligenza and W. G. Spitzer, J. Phys. and Chem. Solids (to be published).
[4] W. G. Spitzer and D. A. Kleinman (to be published).
[5] Atalla, Tannenbaum, and Scheibner, Bell System Tech. J. **38**, 749 (1959).

Influence of Negative Ions on Ambipolar Diffusion of Electrons*

HENDRIK J. OSKAM AND VERLYN R. MITTLESTADT
Electrical Engineering Department, University of Minnesota, Minnesota
(Received January 8, 1960)

THE free electrons produced in a gaseous discharge plasma can disappear by one of the following loss processes or by a combination of them: diffusion towards the discharge boundaries, recombination with positive ions in the volume, and attachment to electronegative gas particles. The disappearance of the electrons by diffusion in general is space-charge limited caused by the large difference between the free diffusion coefficients of electrons and positive ions. The diffusion coefficient, taking into account the influence of the produced space-charge field on the electron loss, is called the ambipolar diffusion co-

efficient, the value of which depends on the type of charge carriers present in the plasma.

For a plasma consisting of electrons and one type of positive ion, the ambipolar diffusion coefficient of electrons is found to be independent of time; for electrons and several types of positive ion, this coefficient decreases with time and approaches the value corresponding to the situation of electron loss in the presence of the slowest type of positive ion.[1-3] By assuming certain initial conditions, Oskam calculated the ambipolar diffusion coefficient of electrons in a plasma consisting of positive ions and negative ions (one type of either) and electrons.[3] It was found that this coefficient increases with increasing ratio of the negative ion and electron densities. Moreover, it was shown that the diffusion loss of negative ions from the plasma is small compared with that of the electrons. Therefore, in this type of plasma, the ambipolar diffusion coefficient of electrons increases with time. Oskam calculated, for a few special cases, the curves representing the electron density as a function of time during the afterglow period for an electron disappearance by a combination of ambipolar diffusion and attachment.

When measuring the afterglow properties of plasmas produced in neon-argon mixtures, we obtained curves which resembled very closely the calculated curves. The measurements were carried out with the aid of microwave equipment (working at a frequency of about 9000 Mc/sec) analogous to that developed by Brown and Biondi.[4,5] The quartz vessel, containing the neon-argon mixture, was vacuum processed in the usual way and sealed off. In contrast with the containers used in previous measurements, the quartz vessel did not contain getter material for gas purification.[6] Moreover, the measurements were carried out more than one year after preparing the vessel. Therefore, it can be expected that at least a small amount of impurity is present in the gas container.

The measurements of the electron density as a function of time during the afterglow period are presented in Fig. 1. In the range of the measurements, the electron density is proportional to the shift in resonance frequency of the microwave cavity.[6,7] Curve 1 was obtained when using a low-excitation energy for producing the plasma. The increase of the ambipolar diffusion coefficient is apparent only for the lowest measured electron densities. The positive ions present during the afterglow period can be assumed to be Ar^+ ions resulting from the large efficiency of the Penning effect in neon-argon mixtures.[8] The mobility of the Ar^+ ions in neon calculated from the slope of the straight part of curve 1 is found to be 7.9 cm/sec per v/cm and is in good agreement with previous measurements.[6]

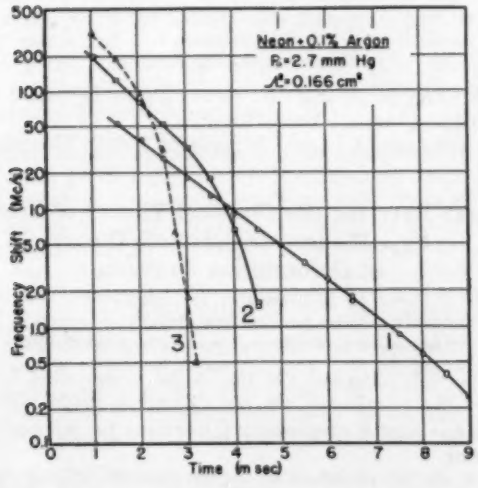

FIG. 1. The afterglow in contaminated neon with 0.1% A. The microwave cavity, in which the discharge was contained, resonated in the TM_{010} mode. An energy pulse length for exciting the discharge of 0.5 msec was used. Room temperature is about 27°C.

When increasing the excitation energy for producing the plasma, the increase of the ambipolar diffusion coefficient with time is much stronger (curve 2). Moreover, the slope of the straight part of curve 2 is larger than that of curve 1, which indicates a larger production of negative ions during the afterglow period than in the previous case.[3]

Curve 3 was measured; after that, an intense, continuous discharge was produced in the gas container. This was expected to increase the amount of impurities available; the effect of this procedure on the decay curve is obvious.

The dependence of the shape of the afterglow curves on the excitation energy used for producing the discharge pulse for fixed pulse lengths strongly indicates that the impurities are attached to the walls of the quartz container and are released during each discharge pulse. The amount of impurity present during the afterglow period was also found to increase with decreasing pulse length and/or repetition frequency. This leads us to assume that the impurities are released from the walls mainly during the build-up period of the discharge.

The measurements were carried out using a TM_{010} mode cavity as well as a TE_{011} mode cavity. Both cavities gave the same results.

* Supported by Air Force Office of Scientific Research (ARDC) under an Air Force contract.

[1] W. Schottky, Physik Z. **25**, 342–348 (1924).
[2] A. V. Phelps and S. C. Brown, Phys. Rev. **86**, 102–105 (1952).
[3] H. J. Oskam, Philips Research Repts. **13**, 335–400 (1958).
[4] D. J. Rose and S. C. Brown, J. Appl. Phys. **23**, 711–718 (1952).
[5] M. A. Biondi, Rev. Sci. Instr. **22**, 500–502 (1951).
[6] H. J. Oskam, Philips Research Repts. **13**, 401–457 (1958).
[7] K. B. Persson, Phys. Rev. **106**, 191–195 (1957).
[8] A. A. Kruithof and F. M. Penning, Physica **4**, 430–463 (1937).

Proposed Molecular Amplifier and Coherent Generator for Millimeter and Submillimeter Waves*

WALTER GORDY AND MONROE COWAN†
Department of Physics, Duke University, Durham, North Carolina
(Received February 4, 1960)

IN an attempt to construct a coherent quantum mechanical submillimeter wave generator or amplifier through stimulated emission of molecules in molecular beams, as in the ammonia maser,[1,2] practical difficulties arise in the design for an effective state selector for securing the needed excess population in the upper, emitting state. These difficulties result partly from the increasing number of sublevels (as J increases) but primarily from the decreasing sensitivity of molecules to field gradients with an increase in rotational frequency. Upon first thought it seems that one should be able to overcome the latter difficulty by using $K=0$, $M=0$ levels of symmetric-top molecules which have first-order Stark effects and are sensitive to deflection by inhomogeneous electric fields up to very high frequencies. For molecules without nuclear coupling, the first-order energy is

$$E_{JKM}=\frac{-\mu\mathcal{E}MK}{J(J+1)},$$

and in a field gradient $(\partial\mathcal{E}/\partial x)$ the molecules would experience a deflecting force

$$f_x=\frac{-E_{JKM}}{\partial x}=\frac{\mu KM}{J(J+1)}\left(\frac{\partial\mathcal{E}}{\partial x}\right).$$

By choosing molecules such as CH_3F or PH_3 which have rotational states of low J that give rise to submillimeter wave lines, one can keep the denominator of this expression relatively small and the deflecting force effective up to very high submillimeter wave

frequencies, of the order of 3×10^{12} cps (wavelength 0.1 mm). However, one encounters the difficulty that the lower as well as the upper J levels are deflected in the same direction for the sublevels with the same sign of M. This not only decreases the angular separation achieved but also imposes the difficulty that one must focus into the emission cavity molecules which are deflected by the inhomogeneous field in the same direction as those rejected.

It has occurrred to us how one can avoid the above difficulties by employing as the stimulated emitters states of symmetric-top molecules with $M=0$ but $K\neq0$. The states have no first-order Stark effect and are, relative to the $M\neq0$, $K\neq0$ states, essentially insensitive to field gradients. Thus by passing a collimated beam of symmetric-top molecules through an electric field gradient one can scatter out of the beam the $M\neq0$ states while leaving the $M=0$ states relatively well focused into the cavity. The upper state, $J+1$, K, $M=0$, however, will not have greater population in the cavity than the lower state, J, K, $M=0$. Hence, one will not achieve maser action by this state selection alone. If, however, a homogeneous Stark or Zeeman field is applied on the molecules in the microwave emission cell so as to lift the M degeneracy with the direction of the field arranged relative to the mode lines (or the microwave radiation field) in such a way that the $\Delta M=\pm1$ transitions are stimulated, it is apparent that stimulated emission will occur between the upper $J+1$, K, $M=0$ to the lower, J, K, $M=\pm1$ levels (which by the preselection are depleted in population). The counter absorption, J, K, $M=0$ to $J+1$, K, $M=\pm1$ can also occur; but because of the marked difference in the splitting of the $M=\pm1$ levels for different J values for first-order, Stark, or Zeeman effect [in each case the splitting varies inversely as $J(J+1)$], the latter absorption will occur at a different frequency and will not cancel the emission. Also, the $\Delta M=0$ transitions will be separated in frequency from the desired emission lines.

Thus by a combination of an inhomogeneous field outside the radiation cell and an homogeneous (Stark or Zeeman) field inside the cell, amplification of submillimeter waves can be achieved through stimulated $J+1\rightarrow J$, $K\rightarrow K$, $M\rightarrow M\pm1$ transitions where $K\neq0$ and $M\neq0$. An energy level diagram indicating these transitions with a selected case is given in Fig. 1.

We are attempting to construct millimeter and submillimeter amplifiers and generators based upon the above principle, one type employing the Stark and the other the Zeeman splitting. In this laboratory, cells for observing $\Delta M=\pm1$ components of rotational transitions in absorption have already been designed and successfully applied for both Stark[3] and Zeeman[4] effects. We shall first employ a parallel plate cell for Stark effect and a cylindrical, high Q cavity for the Zeeman cell.

Although the quantum mechanical amplifier proposed here may perhaps be applied most simply with symmetric-top molecules, it is by no means limited to them. The principle of applying a homogeneous field in combination with an inhomogeneous one for state separation in masers is applicable to quantum mechanical systems of other types. Certain asymmetric-top molecules are also usable. Furthermore this amplifier is not limited to millimeter or submillimeter wavelengths but can be used for lower frequencies as well. Because the second-order effect is superimposed on the first-order effect, the spacing of the Stark sublevels for a given J and K are not exactly equal, and the transition $\Delta J=0$, $\Delta K=0$, $M=0\rightarrow+1$ can similarly be employed for low-frequency maser action after the $M\neq0$ states are removed. Unlike the zero-field maser, the one proposed here is tunable over a limited range, and yet with easily obtainable field homogeneities it can be made highly monochromatic.

An early maser proposed by Weber[5] employing stimulated emission between Stark levels of particular rotational states of symmetric-top molecules is entirely different from the one described here. Weber proposed a pulsed Stark field to obtain the excess population in upper states somewhat as Purcell and Pound achieved excess population of upper states in a nuclear resonance experiment to accomplish the first observation of stimulated emission.[6]

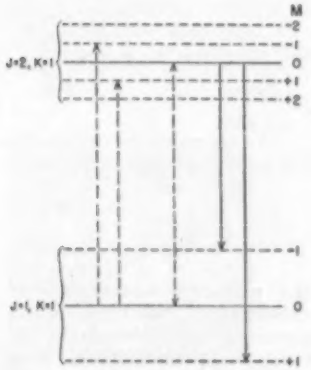

FIG. 1. Energy level diagram for $J=1$, $K=1$ and $J=2$, $K=1$ levels showing populated $M=0$ substates in solid lines and the depleted $M\neq0$ states in broken horizontal lines. The solid vertical lines pointing downward indicate the transitions employed for the maser action.

* This research was supported by the United States Air Force through the Air Force Office of Scientific Research of the Air Research and Development Command.

† National Science Foundation Postdoctoral Fellow.

[1] J. P. Gordon, H. J. Zeiger, and C. H. Townes, Phys. Rev. **95**, 282 (1954); **99**, 1264 (1955).

[2] N. G. Bassov and A. M. Prokhorov, J. Exptl. Theoret. Phys. **28**, 249 (1955).

[3] Bhattacharya, Gordy, and Fujii, Bull. Am. Phys. Soc. Ser. II, **2**, 213 (1957).

[4] J. T. Cox and W. Gordy, Phys. Rev. **101**, 1298 (1956).

[5] J. Weber, I.R.E. Trans. on Electron Devices ED-**3**, 1 (1953).

[6] E. M. Purcell and R. V. Pound, Phys. Rev. **81**, 279 (1951).

Erratum: Magnetization of the Compound TiFe

[J. Appl. Phys. **31**, 155 (1960)]

M. V. NEVITT
Argonne National Laboratory, Lemont, Illinois

THE fourth sentence of the fifth paragraph on page 156 is not stated correctly. It should read: "Below the region of saturation the slopes decrease linearly with increasing temperature in the range from 9° to 79°K inclusive."

Errata: Alternative Forms of Some Exponential and Power Functions for Graphical Representation

[J. Appl. Phys. **31**, 215 (1960)]

C. C. HARRIS
The University, Leeds, England

EQUATIONS (7) and (9): To avoid printing double superscripts Q was substituted for q^n.

Line 2 and footnote 1: For "Mengelsdorf" read "Mangelsdorf."

Errata: Reviving the Classical Theory of Friction by a Modern Dislocation Theory of Deformation Revision

[J. Appl. Phys. **31**, 221 (1960)]

JOHN H. DISMANT
University of North Dakota, Grand Forks, North Dakota

IN the fifth paragraph the size of the copper wires actually used was 4.0 mils, 6.0 mils, and 10.0 mils so that as published, the decimal point is misplaced and especially the last number is misleading.

Again in the list of footnotes, the one marked "5" includes the number 3 which should be a 2; thus this reference should read—"Reference 2, p. 157."

The underlined numbers are the correct ones.

Books Reviewed

Prompt, noncritical reviews appear in this column. Critical reviews of many of the books described here will appear in Physics Today, The Review of Scientific Instruments, *or* American Journal of Physics.

Annual Review of Nuclear Science, Vol. 9. E. SEGRE AND L. SCHIFF, EDITORS. Pp. 592. Annual Reviews, Inc., Stanford, California, 1959.

The latest volume of this well-known series contains fifteen reviews of diverse topics from the field of nuclear physics and its applications. The topics include nuclear photodisintegration, application of dispersion relations to pion physics, strange particles, beta decay, nuclear fission, plasma research, fast reactors, and several topics from the fields of radiochemistry and radiobiology. Each review includes an extensive bibliography.

High-Resolution Nuclear Magnetic Resonance. J. A. POPLE, W. G. SCHNEIDER, AND H. J. BERNSTEIN, EDITORS. Pp. 465+xxii. McGraw-Hill Book Company, Inc., New York, 1959. Price $13.50.

A survey of principles and techniques in the application of nuclear resonance techniques to chemical problems.

An Introduction to Plasticity. WILLIAM PRAGER. Pp. 148. Addison-Wesley Publishing Company, Inc., Reading, Massachusetts, 1959. Price $9.50.

The book is a translation of a volume based on a series of lectures given by the author at the Federal Polytechnic Institute in Zurich, Switzerland. It treats the basic theory and selected examples of the ideal perfectly plastic solid. Each chapter is followed by a well chosen group of problems and appropriate historical and contemporary references. The mechanical behavior of plastic solids under combined loading is used to introduce the generalized plastic potential. The second chapter treats the mechanical behavior of elastic, perfectly plastic structures with consideration of the extremum principles, load carrying capacity, and shake down. Chapter three gives the methods of limit analysis which determine the load carrying capacity of rigid, perfectly plastic continua. The fundamental theorems are followed by applications to frames, rings, plates, cylindrical shells, and a discussion of problems of limit design. The last chapter investigates problems of plane plastic flow which are characterized by finite plastic deformations. Steady plastic flow is illustrated by the problem of sheet extrusion; pseudosteady plastic flow is illustrated by the problems of the indentation of a plastic half space by a rigid wedge and the compression of a slab between parallel rigid plates. The notched tension specimen is discussed and the problem of tube drawing is used as an example of linearization in finite plastic deformation.

Electron Impact Phenomena and the Properties of Gaseous Ions. F. H. FIELD AND J. L. FRANKLIN. Pp. 317+xxxii. Academic Press, Inc., New York, 1957. Price $8.50.

This volume gives a critical and comprehensive compilation of electron impact phenomena with particular emphasis on the chemical physics of the various systems studied. It opens with a chapter on instrumentation in general and mass spectrometry in particular. It then gives a theoretical treatment of the impact processes, discusses energetics, and describes the various types of ions formed including their chemical properties. The book closes with an exhaustive compilation of all the critical potentials of positive and negative ions published in the period 1930 to 1955 inclusive.

Physikalische Kernchemie. ULRICH SCHINDEWOLF. Pp. 194. Friedrich Vieweg and Sohn, Braunschwieg, Germany, 1959. Price 19.80 D. M.

This is a concise, easily understood introduction to nuclear physics. It is directed primarily at the chemist and assumes minimal background in theoretical physics and mathematics. The essential ideas of nuclear systematics, models, and reactions are reviewed together with their chemical applications. An excellent wall chart of the nuclide properties comes tucked in the back cover.

Physics of the Earth's Interior. BENO GUTENBERG. Pp. 221 +vi. Academic Press, Inc., New York, 1959. Price $8.50.

This fairly small first volume of a projected International Geophysics Series summarizes available evidence on the earth's interior as garnered by gravity studies, terrestrial magnetism, tectonic processes and the earth's history. Seismological investigations are to be covered in another volume and are only considered wherever they bear on the earth structure and interior. Complete references are given after each chapter. These are listed as Fundamental Problems and Fundamental Data; Structure of the Earth; The Earth's Crust; The Mantle of the Earth; The Core, Temperature and Thermal Processes in the Earth; Density, Pressure Gravity and Flattening in the Earth. It is for the most part descriptive and summary in nature such that it is of interest to the nonspecialist in the field as well as serving as a review for those working in the field.

Atomic Energy in the Communist Bloc. G. A. MODELSKI. Pp. 215+iv. Cambridge University Press, New York, 1959. Price $5.50.

Although this is primarily a study of the growth of the nuclear industry in the Soviet bloc, there is also included an account of the Soviet program of nuclear and high energy research. Both administrative and technical aspects are discussed. The book gives one an outline of the basic facts that are needed to estimate the present level of activity in applied atomic energy in the Communist world and to assess its future. No attempt is made to discuss the military phase of the program.

The Special Theory of Relativity. J. AHARONI, EDITOR. Pp. 285+xvi. Oxford University Press, Oxford, 1959. Price $7.50.

The choice of topics in this text is somewhat different from that in most previous treatments of Special Relativity: Besides the usual topics, there are chapters on General Field Theory, Relativistic Hydrodynamics, and Spinors. The relationship between tensor-analysis and group theory is stressed without requiring much preknowledge of either. Although quantum mechanics is not actually dealt with, the book is intended as a preparation for relativistic quantum mechanics and especially for quantum field theory.

High Speed Aerodynamics and Jet Propulsion. Vol. V. Turbulent Flows and Heat Transfer. C. C. LIN, EDITOR. Pp. 549. Princeton University Press, Princeton, New Jersey, 1959. $15.00.

This is the ninth to appear of twelve volumes which have been planned by a committee at Princeton under the chairmanship of Dr. von Karman during the past decade. The aim has been to provide an authoritative survey of progress to date in aeronautical engineering and its related branches of pure and applied science, with sections written by leading workers in each field.

The first three sections of the present volume deal with the more fundamental aspects of the vast and confusing subject of turbulence, and each amounts to a monograph in its own right:

A. Transition from laminar to turbulent flow, by H. L. Dryden.

B. Turbulent flow by G. B. Schubauer and C. M. Tchen.

C. Statistical theories of turbulence by C. C. Lin.

The remaining sections, dealing with applications, may be more briefly listed:

D. Conduction of heat by M. Yachter and E. Mayer.

E. 1. Convective heat transfer and friction in flow of liquids by R. G. Deissler.

2. Survey of problems in boiling heat transfer by R. H. Sabersky.

F. Convective heat transfer in gases by E. R. van Driest.

G. Cooling by protective fluid films by S. W. Yuan.

H. Physical basis of thermal radiation by S. S. Penner.

I. Engineering calculations of radiant heat exchange by H. C. Hottel.

Proceedings of the Sixth Midwestern Conference on Fluid Mechanics. Pp. 465. The University of Texas, Austin, Texas, September 9–11, 1959. Price $12.50.

These are thirty papers in a wide range of fluid mechanics, including such diverse subjects as rarefied-gas dynamics, ablation, theory of lubrication, magnetohydrodynamics, undersea explosions, meteorology, sonic flow, and two-phase flow in pipes, but not ignoring the more familiar problems of heat transfer, secondary flows, turbulence, and skin friction. There are both theoretical studies and purely experimental observations. The volume appears to present a reliable picture of what is understood and what is not, and what fluid mechanicists are concerned with, at the end of 1959. The quality of the research reported here is generally impressively high.

Encyclopedic Dictionary of Electronics and Nuclear Engineering. ROBERT I. SARBACHER. Pp. 1417. Prentice-Hall, Inc., Englewood Cliffs, New Jersey, 1959. Price $35.00.

This immense $35.00 investment of 1400 pages with perhaps an average of eight to ten entries per page covers everything in the jargon in any way related to Electronics and Nuclear Engineering. One begins to be impressed by the generally logical terminology used in science, which make the terms almost self explanatory to one having some acquaintance in the fields, but for those completely ignorant of the fields, it is questionable how valuable this book will prove to be.

Kinetics of High Temperature Processes. W. D. KINGERY, EDITOR. Pp. 326. The Technology Press of Massachusetts Institute of Technology and John Wiley & Sons, Inc., New York, 1959. Price $13.50.

The publication consists of the proceedings and discussion of a conference on the kinetics of high-temperature processes held at the Massachusetts Institute of Technology, June 23–27, 1958. Specific research on the mechanisms and theory relating to physical and chemical processes occurring mainly in nonmetallic refractory materials in the condensed state at elevated temperatures are covered. Arbitrary distinctions based on traditional fields of study are avoided and specific phenomena are analyzed from general principles as much as possible. Simple as well as complex systems are considered which recommends this book to both the technologist and the scientist interested in recent advances in this field.

Books Received

Engineering Mechanics. D. F. GUNDER AND D. A. STUART. Pp. 380+vi. John Wiley & Sons, Inc., New York, 1959. Price $7.75.

Lehrbuch der Hockspannungstechnik. LESCH AND BAUMANN, EDITORS. Pp. 420+xvi. Springer-Verlag, Berlin, Germany, 1959. 39.60 marks.

An Introduction to the Mechanics of Solids. S. H. CRANDALL AND N. C. DAHL, EDITORS. Pp. 432+iv. McGraw-Hill Book Company, Inc., New York, 1959. Price $8.50.

Radiation Counters and Detectors. C. C. H. WASHTELL, EDITOR. Pp. 108+ii. Philosophical Library, Inc., New York, 1960. Price $7.50.

Nomography. A. S. LRVENS, EDITOR. Pp. 212+lxvi. John Wiley & Sons, Inc., New York, 1959. Price $8.50.

Fundamentals of Electronics. F. H. MITCHELL. Pp. 251 + ii. Addison-Wesley Publishing Company, Inc., Reading, Massachusetts, 1959. Price $6.50.

Tables of the Bevariate Normal Distribution Function and Related Functions. Pp. 258. National Bureau of Standards, Washington, D. C. Price $3.25.

Der Raman-Effekt. F. MATOSSI. Pp. 78. Friedrich Vieweg and Sohn, Brauscheneig, Germany.

Close Binary Systems. Z. KOPAL, EDITOR. Pp. 548. John Wiley & Sons, Inc., New York, 1959. Price $16.75.

La Menace Radioactive. A. PIRIE, EDITOR. Pp. 128. Dunod, Paris, France, 1959. Price 950 fr.

Source Book of Industrial Solvents. I. MELLAN. Pp. 266 + vi. Reinhold Publishing Corporation, New York, 1959. Price $10.00.

The Cathode Ray Tube and its Applications. G. PARR AND O. H. DAVIE. Pp. 422. Reinhold Publishing Corporation, New York, 1959. Price $9.50.

Guide de Thermometrie. CLAUDE GOUX. Pp. 229 + iii. Gauthiers-Villars, Paris, France, 1959. Price 2760 fr.

Open-Channel Hydraulics. VEN TE CHOW. Pp. 621 + xxxv. McGraw-Hill Book Company, Inc., New York, 1959. Price $17.00.

Fonctions Spheriques de Legendre et Fonctions Spheroidales. LOUIS ROBIN. Pp. 279. Gauthiers-Villars, Paris, France, 1959.

Fluid Dynamics. D. E. RUTHERFORD. Pp. 221+iii. Interscience Publishers, Inc., New York, 1959. Price $1.95.

German-English Science Dictionary. 3rd. ed. LOUIS DEVRIES. Pp. 531+lix. McGraw-Hill Book Company, Inc., New York, 1959. Price $7.00.

Modern Electronic Components. G. W. A. DUMMER. Pp. 467. Philosophical Library, Inc., New York. Price $15.00.

Properties of Matter. F. C. CHAMPION AND N. DAVY. Pp. 310+xiv. Philosophical Library, Inc., New York, 1959. Price $10.00.

Method Generales D'essai et de Controle en Laboratoire Livre I: Mesures Geometriques et Mecaniques. Pp. 698+xvii. R. L'HERMITE. Editions Eyrolles, Paris, 1959. Price 9965 fr.

Flat Rolled Products: Rolling and Treatment. Vol. I (Metallurgical Society Conference) T. E. DANCY AND E. L. ROBINSON. Pp. 128. Interscience Publishers, Inc., New York, 1959. Price $3.75.

Analog Methods Computation and Simulation. 2nd. ed. W. J. KARPLUS AND W. W. SOROKA. Pp. 426+xlviii. McGraw-Hill Book Company, Inc., New York, 1959. Price $12.50.

University Mathematics. 2nd. ed. JOSEPH BLAKELY. Pp. 556+xxi. Philosophical Library, Inc., New York, 1959. Price $10.00.

Foundations of Aerodynamics. 2nd. ed. A. M. KUETHE AND J. D. SCHETZER. Pp. 326+cviii. John Wiley & Sons, Inc., New York, 1959. Price $11.75.

Hydrodynamics. D. H. WILSON. Pp. 139+iv. Edward Arnold and Company, London, England, 1959. Price $5.50.

Theoretical Elasticity and Plasticity for Engineers. D. E. R. GODFREY. Pp. 263+xliii. Thames and Hudson, London, 1959.

Quality Requirements of Super-Duty Steels. Vol. 3. R. W. LINDSAY, EDITOR. Pp. 301+vii. (Metallurgical Society Conferences.) Interscience Publishers, Inc., New York, 1959. Price $8.50.

Reactive Metals. Vol. 2. W. R. CLOUGH, EDITOR. Pp. 602 +viii. (Metallurgical Society Conferences.) Interscience Publishers, Inc., New York, 1959. Price $15.00.

Physical Metallurgy of Stress Corrosion Fracture. Vol. 4. T. RHODIN. Pp. 378+vii. (Metallurgical Society Conferences.) Interscience Publishers, Inc., New York, 1959. Price $13.00.

A History of Science Technology and Philosophy in the 16th and 17th Centuries. Vol. I. A. WOLF. Pp. 349. Harper and Brothers, New York, 1959. Price $1.95.

A History of Science Technology and Philosophy in the 16t and 17th Centuries. Vol. II. A. WOLF. Pp. 675. Harp and Brothers, New York, 1959. Price $1.95.

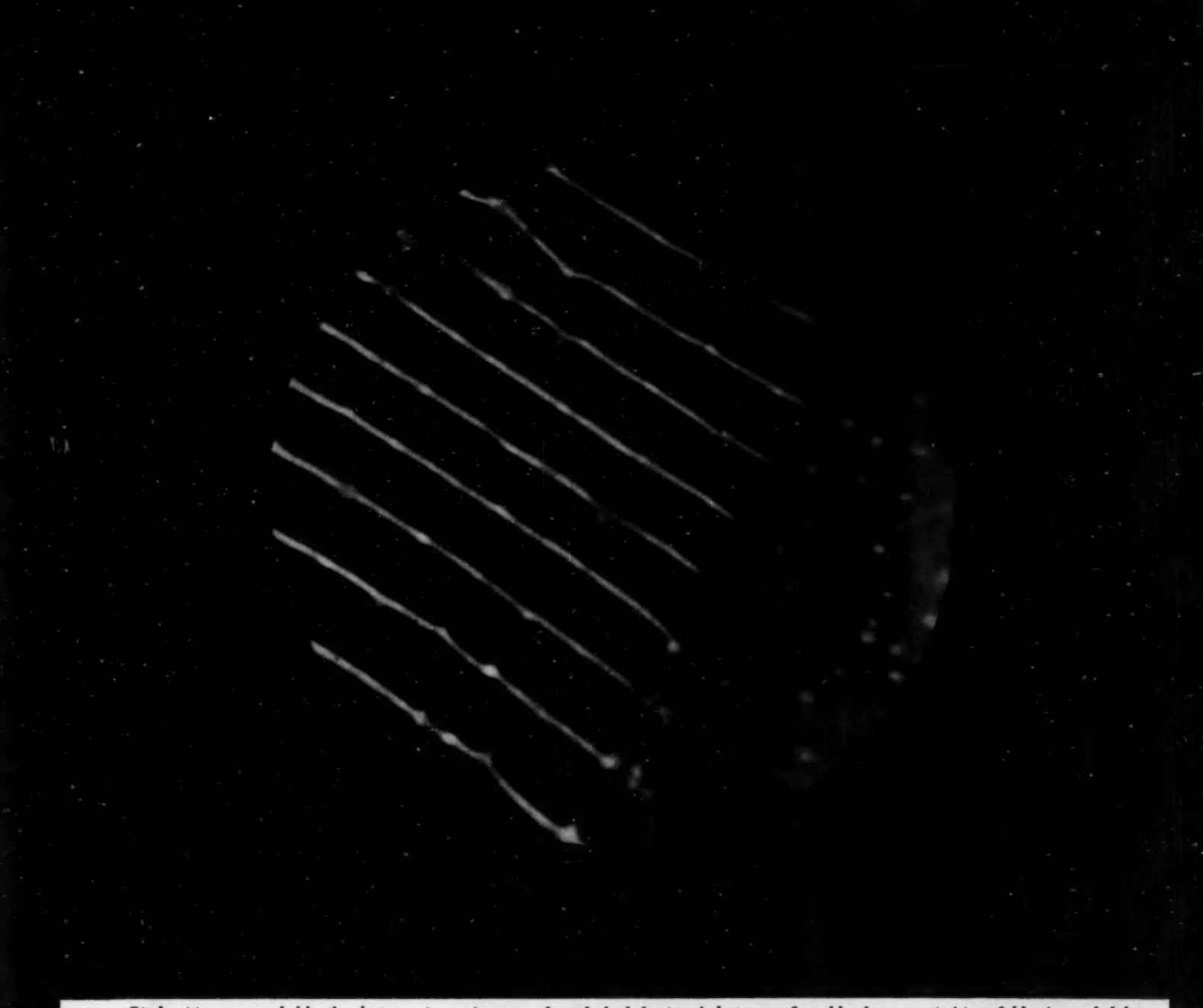

Bit densities are revealed by the electron mirror microscope through the behavior of electrons reflected by the magnetic fringe fields of recorded data.

Reflections from an Electron Mirror

The photograph is a representation of the magnetic fringe fields above a small portion of a recording surface. Behind these magnified tracks of recorded data is the story of a device now decades old in principle, but which has only recently been applied to the study of high-density magnetic information storage.

The electron mirror microscope was constructed by IBM scientists as a laboratory instrument. Based on the excellent resolution capabilities of an electron beam, the electron mirror principle has its primary application in the observation of tiny magnetic fringe fields.

In the operation of an electron mirror microscope, an electron beam is accelerated down a tube toward a specimen mounted on a conductive plate with a negative potential relative to the cathode. At the zero equipotential surface in the tube, the electrons traveling toward the specimen change their directions and are reflected in somewhat the same way light rays are reflected by a mirror. By controlling the potentials of the cathode and the conductive plate, the "mirror" can be placed at any height above the magnetic surface. When the mirror is set close enough to the surface to be in the fringe fields of recorded information, these fields distort the return paths of electrons in the beam. Passing the return beam through a magnetic lens results in a magnified representation on a phosphor viewing plate, capable of resolving bit densities far greater than those in use in present systems.

It is well known that the "writing" abilities of present magnetic recording transducers exceed their "reading" abilities. The mirror microscope produces accurate evidence of all-but-undetectable recorded information. Thus the magnetic recording process is no longer limited to verification by velocity-dependent readback capabilities. By the same token, the mirror microscope serves both as the spur to, and the measure of progress toward further refinements in the art of magnetic recording.

IBM.RESEARCH

Investigate the many career opportunities available in exciting new fields at IBM.
International Business Machines Corporation, Dept. 579Q, 590 Madison Avenue, New York 22, New York.

unequalled for **SELECTIVITY**

RANGE 0.2 TO 35 MICRONS

A highly versatile instrument which can be used for the ultraviolet, visible and infrared regions simply by interchanging prisms, cams and λ scales. High spectral purity, isolation of narrow wave-lengths, highest resolution and negligible scattered radiation are inherent characteristics. Available for automatic or manual operation.

Farrand Double

SPECTROMETER· MONOCHROMATOR

Technical data available on request
Specify Bulletin No. 806AP

FARRAND OPTICAL CO., INC.
BRONX BLVD. AND EAST 238th STREET • NEW YORK 70, N. Y.
Engineering Research, Development, Design and Manufacture of Precision Optical, Electronic and Scientific Instruments

NEWS from the NRC Vacuum MICRONICLE*

ULTRA HIGH VACUUM GAGE AIDS STUDIES

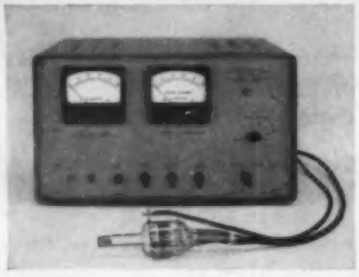

It has been hard to measure the pressures in ultra high vacuum systems used for space chamber testing, thermonuclear power research, micromolecular circuit development and solid state studies. The new Nottingham Ionization Gage gives direct measurements of 10^{-10} mm mercury and indirect estimates of pressures to 10^{-12}. The Gage is linear, stable and repetitive.

***FREE NRC Vacuum Micronicle**

A periodical containing news about improving products with NRC high vacuum equipment. Write on your firm letterhead.

NRC EQUIPMENT CORPORATION
A Subsidiary of National Research Corporation

DEPT. P-5, 160 Charlemont St., Newton 61, Mass.

TADANAC BRAND
High Purity
SILVER

Approximately 99.9999% pure, this specially refined silver has only cadmium and lead as significant impurities, both in the range of 0.1 to 0.2 ppm. There are three standard forms: 25 troy oz. bars, 10 troy oz. rods and shot.

Other high purity TADANAC Brand metals or compounds include: Special Research Grade antimony, indium and tin. High Purity Grade bismuth, cadmium, indium, lead, tin, zinc and indium antimonide. Send for our brochure—TADANAC Brand High Purity Metals.

COMINCO

THE CONSOLIDATED MINING AND SMELTING COMPANY OF CANADA LIMITED
215 ST. JAMES ST. W., MONTREAL 1, QUEBEC, CANADA • PHONE AVenue 8-3103
0163

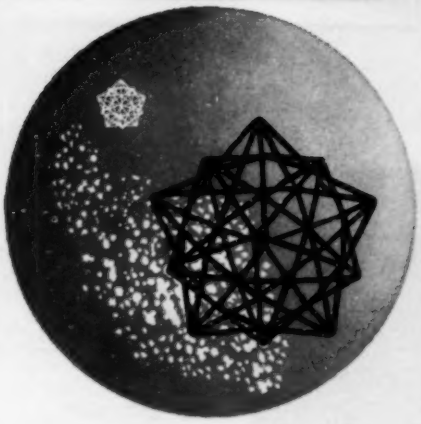

ENGINEERS
SCIENTISTS

FUTURISM in contemporary R&D

Radical departures from traditional forms of scientific investigation are the keynote of Republic Aviation's forward-looking programs in space exploration and upper atmosphere flight. In an environment that regards with skepticism the seeming validity of conventional conclusions, engineers and scientists seek below-the-surface solutions of problems... bypassing the superficial.

Expanding the scope and depth of present programs is Republic's recently completed $14 million Research and Development Center. Extensive facilities here are an invitation to professional men to realize the future by solving today's most perplexing problems.

• • • • • • • • • • • • • • • • • • •

SENIOR LEVEL OPENINGS EXIST IN THESE IMPORTANT AREAS:

Navigation & Guidance Systems / Radar Systems / Information Theory / Radio Astronomy / Solid State & Thermionic Devices / Microwave Circuitry & Components / Countermeasures / Digital Computer Development / Radome & Antenna Design / Receiver & Transmitter Design / Miniaturization-Transistorization / Radiation & Propagation *(RF, IR, UV)* / Telemetry-SSB Technique

Please forward resumes to:
Mr. George R. Hickman
Technical Employment Manager,
Department 17E

REPUBLIC AVIATION

Farmingdale
Long Island, New York

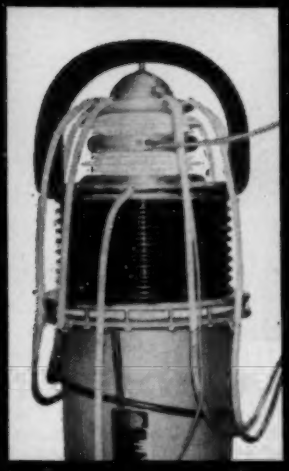

600,000 amperes help harness H-power

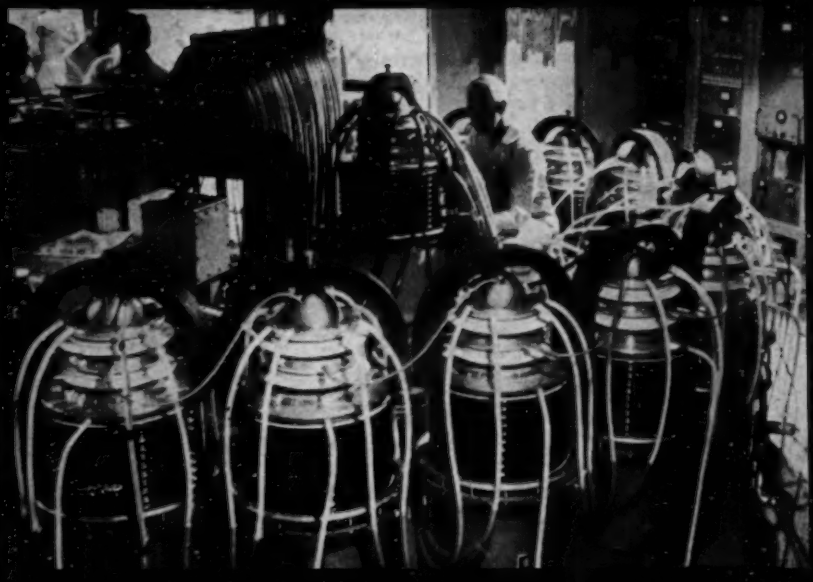

At the historic Geneva Atoms-For-Peace Conference, Los Alamos scientists unveiled **Scylla**—a fusion device used to heat a plasma of ionized heavy hydrogen particles millions of degrees by blasting it with a 600,000-ampere thunderbolt.
Surrounding the heart of this thermonuclear machine is a bank of low-inductance, energy-storage capacitors...each rated at 100,000 volts, each capable of a 20,000 megawatt peak surge.
This unique installation, like others of its type, is the result of long experience in capacitor specialization. If adherence to rigid specifications is a 'must' on your project—call us in to help with creative engineering. We invite inquiries for a single energy-storage capacitor or a complete energy-storage system including capacitors, racks, interconnecting lines, protective devices and charging power supply.

For further technical information, write for Bulletin No. 191 to Cornell-Dubilier Electric Corporation, New Bedford, Mass.

CDE **CORNELL-DUBILIER ELECTRIC CORPORATION**
AFFILIATED WITH FEDERAL PACIFIC ELECTRIC COMPANY

A Superior Detector for Infra-Red Spectroscopy

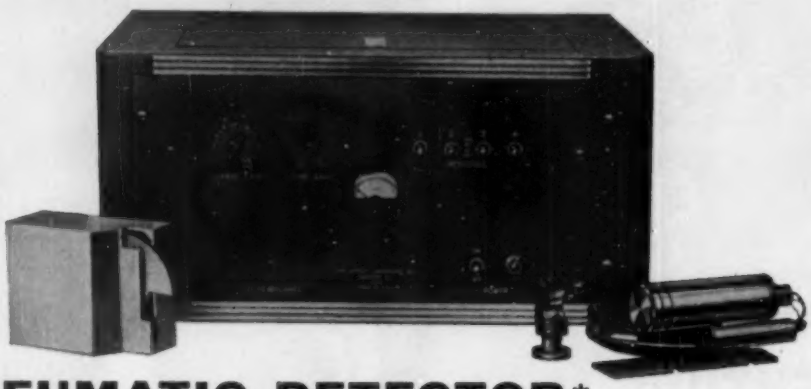

GOLAY PNEUMATIC DETECTOR*

Among the characteristics that render the Golay Detector superior to other types of detectors for use in infra-red spectroscopy are:

1. **An effective sensitive area 3/32" in diameter.**
2. **Sensitivity of 6 x 10^{-11} watts RMS-ENI when used with "chopped beam" method and with recording time constant of 1.6 second.**
3. **Uniform sensitivity from the ultra-violet through the visible and the entire infra-red, and up to the micro-wave region.**
4. **Improved, drift-free, A. C. operated amplifier with step gain controls and four response periods.**

Write for EPLAB Bulletin No. 10

*Fundamental and experimental aspects of this detector are discussed in the following publications: Rev. Sci. Inst. *18*, 347 and 357 ('47); Ibid. *20*, 816 ('49); Proc. IRE *40*, 1161 ('52).

278-8

THE EPPLEY LABORATORY, INC.
SCIENTIFIC INSTRUMENTS
6 Sheffield Ave. • Newport • Rhode Island • U.S.A.

SCIENTISTS
ENGINEERS
CALIFORNIA
offers you and your family

- A world center of the electronics-missile-space industries for CAREER ADVANCEMENT
- The High Sierra and the Pacific Ocean for RECREATION
- And for your children some of the nation's FINEST PUBLIC SCHOOLS
- World Famous Universities for ADVANCED STUDY
- MAJOR CULTURAL CENTERS

while living in such places as
Exciting San Francisco
Fabulous Southern California
Cultural Palo Alto

Companies pay interview, relocation and agency expenses

Submit resume in confidence to:
PROFESSIONAL and TECHNICAL RECRUITING ASSOCIATES
(a Division of the Permanent Employment Agency)
Suite A
825 San Antonio Road
Palo Alto, Calif.

PHYSICIST

ADVANCE DEVELOPMENT OF SEMICONDUCTOR DEVICES

PHD, MS or equivalent with a background in solid state physics or electronics to analyze the operation of high frequency devices leading to the development of new device structures.

WRITE:
M. D. Chilcote, Div. AP-5
Semiconductor Products Dept.
Electronics Park, Syracuse, New York

GENERAL ELECTRIC

OPPORTUNITIES
IN
IBM
RESEARCH

MECHANICS

The IBM Research Center in Westchester County, New York, has two excellent career openings for qualified senior mechanical engineers.

Heat transfer and thermodynamics:

This work—to originate new ways of cooling electronic equipment—requires a high degree of creativity and a strong grasp of experimental methods. The work deals with both fundamental and applied problems. The assignment is to discover how to dissipate maximum heat in minimum space and in an economical fashion. Problems may include encapsulation of components or the application of boundary-layer flow techniques in an effort to improve heat dissipation.

Fluid mechanics:

A senior engineer with experience in the classical and modern areas of fluid mechanics is being sought. The assignment involves formulating a program which will provide a basis for the study of fluid mechanics. Several different areas of fluid flow will be involved: boundary-layer, turbulence, pulse propagation, and flutter.

QUALIFICATIONS:

Advanced degree in Engineering or Physics and considerable related experience.

For details, please write, outlining your background and interests, to:

Mr. K. J. Turner
Dept. 579Q1
IBM Corporation
Box 218
Yorktown Heights, New York

IBM.
INTERNATIONAL BUSINESS
MACHINES CORPORATION

Senior
Research Scientists
& Engineers

to help solve an important communications problem

The problem... to define the parameters and establish feasibility of a long-range, ECM-proof, single or multiple path communications system capable of negligible degradation and an ultra-high degree of reliability while operating in a constantly changing environment.

The solution, at present, is difficult... all known techniques, individually or multi-plexed, would provide only marginal performance.

Research Scientists and Engineers with advanced degrees who feel they can contribute new insight, new concepts, and the application of new techniques to the establishment of this vitally important system are invited to forward their confidential inquiry to:

Dr. R. L. San Soucie.

Amherst Laboratory / SYLVANIA ELECTRONIC SYSTEMS
A Division of
SYLVANIA
Subsidiary of GENERAL TELEPHONE & ELECTRONICS
1145 Wehrle Drive—Williamsville 21, New York

ACF ELECTRONICS DIVISION

ELECTRO-PHYSICS LABORATORIES

Responsible assignments in furthering the state-of-the-art of Ionospheric Physics, combining competitive salaries and unusual growth potential, are offered to men who can contribute. Our present needs are for:

Physicists

FOR RESEARCH PROGRAMS IN

IONOSPHERIC PROPAGATION & HF COMMUNICATIONS

SENIOR IONOSPHERIC PHYSICISTS

Ph.D. preferred, with several years' experience in the study of Ionospheric phenomena. Should be familiar with present knowledge of upper atmosphere physics and possess an understanding of current programs using rockets and satellites for studies in F-region and beyond. Qualified individuals with supervisory abilities will have an exceptional opportunity to assume project leadership duties on HF projects already under way involving F-layer propagation studies backed by a substantial experimental program.

The Electro-Physics Laboratories are located in the suburban Washington, D.C. area, where post-graduate study is available in several nearby universities. Housing is plentiful in attractive, well-established neighborhoods. Our relocation allowance is liberal.

All inquiries will be held in strictest confidence and answered promptly.

Please send resume to:

ROBERT REID, PROFESSIONAL EMPLOYMENT SUPERVISOR

ACF ELECTRONICS DIVISION

acf

Industries, Incorporated

Riverdale, Maryland **WArfield 7-4444**

SILICA SPRINGS

(FUSED QUARTZ)

for mass sorption measurements

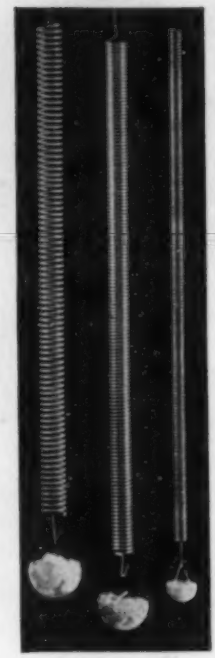

Loads from
10 milligrams to 100 grams

Extensions
to 1000 millimeters

Supplied with end hooks, with reference pointers if desired.

Fused Quartz Pans, hemispherical, with bails, are available in diameters from 5 to 50 millimeters and in weights from 15 to 200 milligrams.

•

An engineering experimental kit containing 5 springs, having extensions from 50 to 100 millimeters and maximum loads from 50 milligrams to 5 grams is available at $25.00.

•

Designers and manufacturers of special quartz measuring systems, all-quartz fused microbalances for very precise weight measurements in evacuated systems, and laboratory apparatus in quartz and Vycor.

WORDEN LABORATORY

695 Rocky River Road Houston 27, Texas

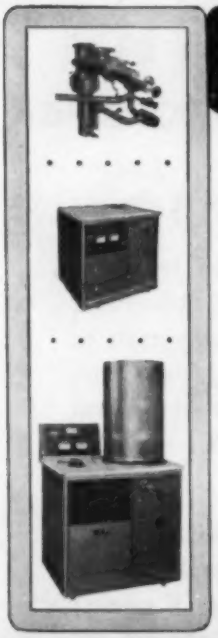

You're guaranteed
10 $^{-9}$ mm Hg *fast* with . . .

THE MODULAR "400" SERIES 4" VACUUM SYSTEMS & EVAPORATORS

GUARANTEED PERFORMANCE:

5×10^{-6} in 45 sec. Less than 5×10^{-7} ultimate (blanked port)

5×10^{-6} in 4 min. Less than 10^{-6} ultimate (18" x 30" Bell Jar)

MODULAR CONSTRUCTION:

Buy exactly what you need, from basic plumbing to complete Evaporators and Bakeout Systems. Incorporate additional equipment as your requirements grow.

TROUBLE-FREE PERFORMANCE:

Each VE-400 System undergoes a full week (168 hrs.) of test run and inspection before shipment.

FREE "400" SERIES BROCHURE contains complete performance data and design specifications on the 4" building block components and modular systems. Write Department A-1436.

Veeco **VEECO VACUUM CORP.**

86 J Denton Avenue, New Hyde Park
Long Island, New York

HIGH VACUUM & LEAK DETECTION EQUIPMENT

WANTED!

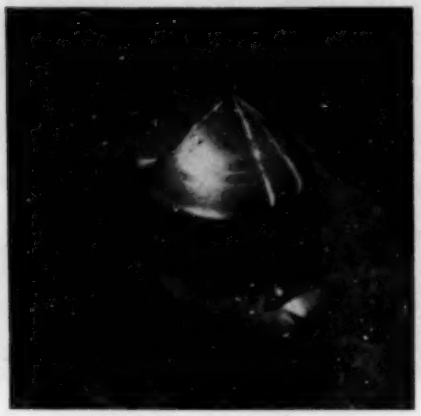

BRAIN

to direct these hands

CRYSTAL GROWING: physicist or physical chemist for senior position in currently growing research and development activity in solid-state materials with present emphasis on scintillation crystals. Require experience in crystal-growing techniques and materials-purification and some knowledge of scintillation spectroscopy. Desire leadership, initiative, and imagination in generating and carrying out new programs to expand present activities.

Combined with the opportunity to assume high-level responsibilities are the advantages of a full program of health benefits, life insurance, and participation in a profit-sharing plan.

Plant is located in Stanford Industrial Park, Palo Alto, in an outstanding center of science and technology. The climate is one of the most favorable in the world. The area offers the best in housing, recreation, and technical stimulation.

For more information, telephone DAvenport 6-1640 or write today, including your resume, to Dr. Elliott C. Levinthal at:

LEVINTHAL ELECTRONIC PRODUCTS

STANFORD INDUSTRIAL PARK · PALO ALTO 3, CALIFORNIA

SUBSIDIARY OF

RADIATION INCORPORATED

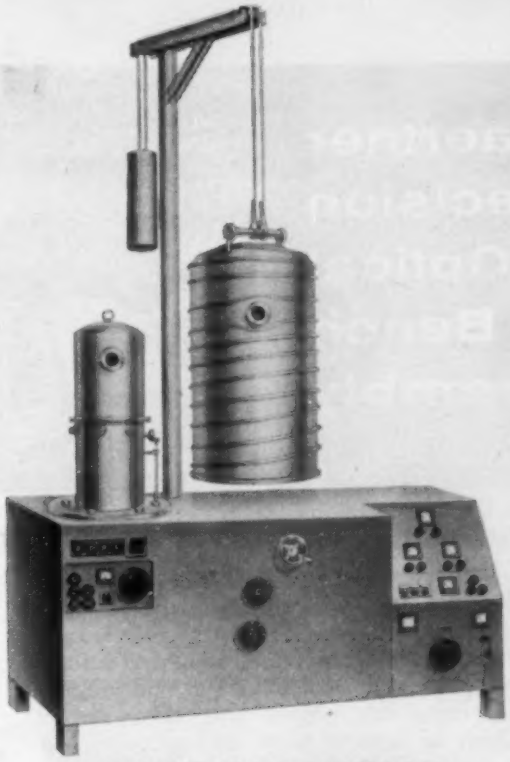

WHAT HAPPENS AT 1,200,000 FEET UP?

You can have the answer NOW . . . and leave theory and the educated guess to others. KINNEY offers fully developed working tools which provide pressures of better than 1×10^{-9} mm Hg . . . ready to work in areas heretofore closed to physicist and researcher.

Kinney®

TWO NEW DEVELOPMENTS IN ULTRA HIGH VACUUM

The KINNEY UH-9A Ultra High Vacuum System, (illustrated above) employing the principle of differential pumping, consistently produces Vacuum in the order of 1×10^{-9} mm Hg in the work chamber. KINNEY also offers a new Ionic High Vacuum System which develops pressures even lower than the $^{-9}$ scale. This system features the Ultek® Ion Pump for which KINNEY is exclusive distributor.

The facts about these significant developments in Vacuum technology are yours for the asking. **Write for KINNEY bulletins 4150, 4160 and 4450 today!**

KINNEY VACUUM DIVISION

THE NEW YORK AIR BRAKE COMPANY

3556E WASHINGTON STREET · BOSTON 30 · MASS.

Please send me copies of Bulletins 4150, 4160 and 4450 describing KINNEY Ultra High Vacuum Systems.

Name_____

Company_____

Address_____

City_____ Zone____ State_____

Gaertner Precision Optical Bench Assembly

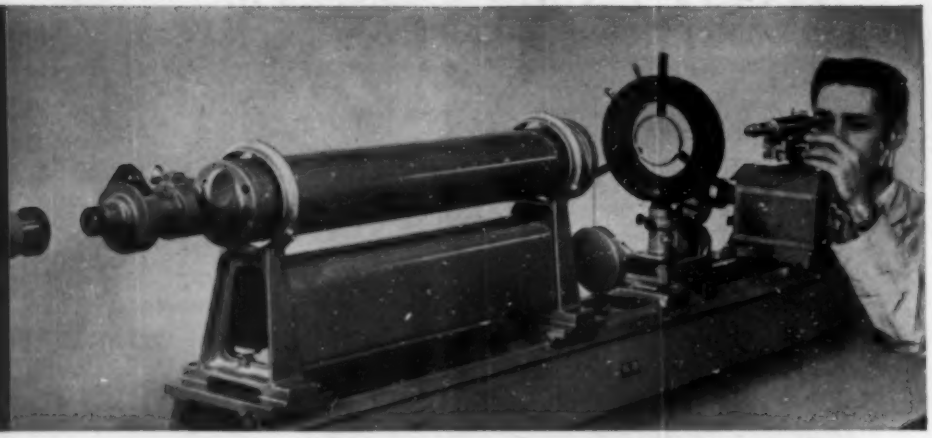

Useful in checking optics and for experimental instrumentation setups

The Precision Optical Bench is a versatile measuring instrument consisting of a lathe-bed-type base, light source, collimator with interchangeable filters and targets, nodal slide and microscope with three-dimensional adjustment. Focal lengths, resolving power and the various aberrations of optical parts and systems can be measured.

The several components can be used independently for special test setups, mock-ups and experimental instrumentation—providing linear and angular motions and measurements, alignment and stable support.

Double and single rod benches and a large selection of carriages, holders and supports provide a complete selection from which to choose.

Gaertner offers a wide range of optical and measuring instruments, including special modifications, design and manufacture of special instruments and optical systems, and manufacture of subassemblies and instruments from customer sketches and drawings.

Send for bulletin 156-59

Designed and manufactured in the U.S.A. by

Gaertner
SCIENTIFIC CORPORATION
1246 Wrightwood Ave., Chicago 14, Illinois • BU 1-5335

PHYSICIST or PHYSICAL CHEMIST

for Basic Research on Electrical Contacts and Brushes

One of the country's oldest and largest manufacturers of carbon, graphite, & metal powder products has opportunity for topranking scientist in a fundamental field where professional activities and technical papers are encouraged.

Work involves surface phenomena and the fundamental physical processes associated with friction and commutation. Work will be done in association with Dr. Ragnar Holm, a leading authority on contacts, in fully-equipped, new labs.

Company offers the usual fringe benefits and enjoyable living in the mountains of Pennsylvania. School and hospital facilities are excellent. Any age or degree of experience will be considered and salary will be in proportion. All replies held in strictest confidence. Send resumes to:

Dr. E. I. Shobert, II, Mgr. of Research
STACKPOLE CARBON COMPANY
St. Marys, Pa.

To demonstrate transistor functions . . .

NEW CENCO TRANSISTOR ANALYZER

Graphically demonstrates three basic transistor configurations—common emitter, base and collector. May also be used for simple circuit experiments and plotting response curves. Utilizes any general purpose transistor. Mounted on "Lucite".

No. 80390
$37.50

Ask for Booklet 311

cenco
Serving education since 1899.

CENTRAL SCIENTIFIC CO.
A Subsidiary of Cenco Instruments Corporation
1718-A Irving Park Road • Chicago 13, Illinois
Branches and Warehouses—Mountainside, N. J.
Boston • Birmingham • Santa Clara • Los Angeles • Tulsa
Houston • Toronto • Montreal • Vancouver • Ottawa

KOPPERS COMPANY INC.
RESEARCH DEPARTMENT

has an immediate position available for a Ph.D. physical chemist or physicist, to conduct Research Program in the fields of high polymers or condensed ring systems, to determine structure, elastic constants and other mechanical properties, by the use of techniques such as those employing X-rays, ultrasonic waves, etc.

Excellent opportunity, liberal salary, and other benefits available.

Please send a complete resume of experience and qualifications to:

KOPPERS COMPANY, INC.
Personnel Section
Room 230 Koppers Bldg.
Pittsburgh 19, Pa.

All replies will be held in strict confidence.

NOW!
Easy Demonstration of basic Gas Laws

CENCO Kinetic Theory Apparatus

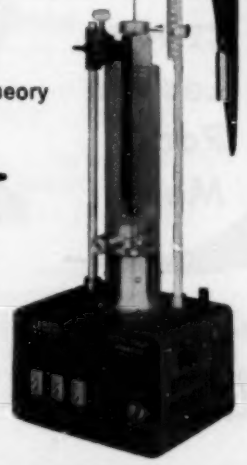

Permits quantitative determination of the most fundamental principles of gas mechanics. Adapted from a design by H.F Meiners of Rensselaer Polytechnic Institute. Plot p-V and p-T curves-measure molecular diameters, verify the fundamental gas laws and Van der Waals Corrections.

No. 77722 without stroboscope, **$295.00**

cenco®

CENTRAL SCIENTIFIC CO.
A Subsidiary of Cenco Instruments Corporation
1718-A Irving Park Road • Chicago 13, Illinois
Branches and Warehouses—Mountainside, N. J
Boston • Birmingham • Santa Clara • Los Angeles • Tulsa
Houston • Toronto • Montreal • Vancouver • Ottawa

HIGH IN RESOLVING POWER, EASIER TO MAINTAIN THAN ANY OTHER ELECTRON MICROSCOPE

BENDIX TRONSCOPE TRS-50 E1

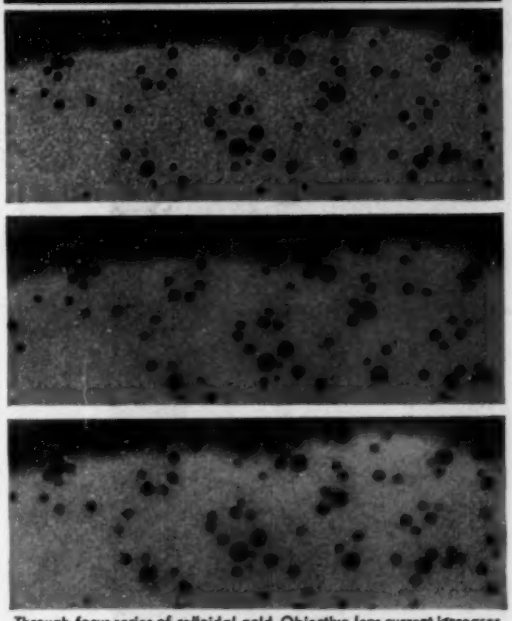

Through focus series of colloidal gold. Objective lens current increases from top to bottom.

BENDIX TRONSCOPE
demonstrates 20Å resolving power with no adjustments.

BENDIX TRONSCOPE
is first electron microscope with absolutely no decrease in resolving power from adjustments.

BENDIX TRONSCOPE
is the most trouble-free electron microscope in the world.

BENDIX TRONSCOPE,
including electron tubes, is *warranted unconditionally* for one year against defects in materials and workmanship. Service is available after warranty period on either a contract or a transportation, per diem, parts basis.

FULL DETAILS
can be obtained by writing Dept. EMS5.

Cincinnati Division
3310 Wasson Road • Cincinnati, Ohio
Bendix

Export Sales & Service:
Bendix International, 205 E. 42nd St., New York 17, N. Y.
Canada:
Computing Devices of Canada, Ltd., Box 508, Ottawa 4, Ont.

a vacuum pump as compact as a . . .

Yes, designed for compactness . . . and with no costly extras to buy. Saves up to 50% of your valuable floor space. But these are just a few of the revolutionary features of the new Stokes Series H Microvac pump.

Find out why Stokes offers you *more pumping performance per dollar*. Just write: Vacuum Equipment Division, P. J. STOKES CORPORATION, 5500 TABOR RD., PHILA. 20, PA.

STOKES

SEND TODAY for your free Vacuum Slide Calculator!

ARE YOU PLANNING A NEW PHYSICS BUILDING?

SELECTED REPRINTS OF ARTICLES ON PHYSICS BUILDINGS

A 182 page republication of some of the most interesting and significant articles from architectural magazines and from the American Journal of Physics. This book assists those now faced with immediate problems in programming and planning for new building facilities for physics teaching and research.

PROJECT ON DESIGN OF PHYSICS BUILDINGS

Checks for two dollars per copy should accompany orders to the

AMERICAN INSTITUTE OF PHYSICS
335 East 45th Street, New York 17, N.Y.

LONG RANGE VISIBILITY

The NEW CENCO Lecture Room Meter

Now—a combination galvanometer, four-range voltmeter and four-range ammeter with figures and graduations on a large 17" scale that is plainly seen from both sides over any distance in the classroom. An accurate, versatile lecture meter with a modern, shielded movement. All parts and circuits clearly visible.

Cenco No. 82140 complete with shunts and multipliers $260.00

cenco®
Serving education since 1889.

CENTRAL SCIENTIFIC CO.
A Subsidiary of Cenco Instruments Corporation
1718-A Irving Park Road • Chicago 13, Illinois
Branches and Warehouses—Mountainside, N. J. Boston • Birmingham • Santa Clara • Los Angeles • Tulsa Houston • Toronto • Montreal • Vancouver • Ottawa

POSITION OPEN

JUNIOR TECHNICAL PERSONNEL

Bachelor Degree in Electrical Engineering, Physics, or Chemistry, with high class and grade standing for work in solid state physics. Send resume to

M. Korenich
Industrial Relations—Dept. 567-L
WESTINGHOUSE RESEARCH LABORATORIES
Beulah Road, Churchill Borough
Pittsburgh 35, Pennsylvania

POSITION OPEN

WANTED

Assistant or Associate Professor of Physics

Attractive position combining light teaching load with direction of graduate research program in Solid State Physics. Good salary to right person. Excellent group of graduate students. Good possibilities for expansion of research program. Fine atmosphere and working conditions. Contact: D. A. Wells, Head, Department of Physics, University of Cincinnati, Cincinnati 21, Ohio.

POSITIONS OPEN

Graduate Research Assistants with Opportunities Working Toward M.S. and Ph.D.

Theoretical and experimental work in the following areas during regular academic year and summer:

1. **Wave Propagation**
2. **Viscoelasticity**
3. **Physics and Mechanics of Solids**
4. **Irradiation Effects on Strength of Solids**
5. **Time Dependent Fracture Phenomena**
6. **Deformation Dependent Mechanical Breakdown Phenomena**
7. **Molecular Orientation Studies of High Polymers**

Send resumé to:

Room 113, Aero-Engineering
University of Minnesota
Minneapolis 14, Minnesota

Scientists or engineers of other countries are also invited to apply.

PHYSICISTS

You are invited to investigate career opportunities with the Roy C. Ingersoll Research Center, Borg-Warner Corporation. Known for its diversification and proprietary product lines, Borg-Warner has a substantial interest in long range basic and applied research.

Physicists at all degree levels and with experience in one or more of the following areas:

PLASMA PHYSICS
MAGNETOHYDRODYNAMICS
SEMI-CONDUCTOR MATERIALS
OPTICAL PROPERTIES OF SOLIDS
MAGNETIC RESONANCE
MICROWAVE PHYSICS
ELECTRONIC PHYSICS

will find challenging problems and an opportunity to do original work in their areas of interest. Progressive management policies strongly encourage professional growth.

The Roy C. Ingersoll Research Center is located in pleasant, attractive northwest suburban Chicago. Liberal benefits, including a tuition reimbursement plan, are provided for the Research Center staff, along with personal recognition and opportunity for undirected research in corporate-supported R & D programs.

Contact in strict confidence:

Dr. L. V. Sloma, Associate Director—
Physics & Electronics

ROY C. INGERSOLL RESEARCH CENTER

Borg-Warner Corporation, Des Plaines, Ill.

INDEX TO ADVERTISERS

Name	*Page*
ACF INDUSTRIES, INC.	xxvi
APPLIED PHYSICS CORP.	xii
ARNOLD ENGINEERING CO.	iii
BELL TELEPHONE LABS.	v
BENDIX AVIATION CORP. CINCINNATI DIV.	xxix
BORG–WARNER CORP. INGERSOLL RESEARCH CENTER	xxxi
CENTRAL SCIENTIFIC CO.	xxviii, xxix, xxx
CONSOLIDATED MINING & SMELTING CO.	xxii
CORNELL–DUBILIER ELECTRIC CORP.	xxiii
EASTMAN KODAK CO.	ix
EPPLEY LAB., INC.	xxiv
ERIE RESISTOR CORP.	x
FARRAND OPTICAL CO.	xxii
GAERTNER SCIENTIFIC CO.	xxviii
GENERAL ELECTRIC CO. SEMICONDUCTOR PRODUCTS DEPT.	xxiv
GENERAL ELECTRIC CO. MISSILES & SPACE VEHICLE DEPT.	xv
GENERAL RADIO CO.	Cover 4
HARSHAW CHEMICAL CO.	Cover 2
HUGHES AIRCRAFT CO.	iv
IBM CORPORATION	xi, xxi, xxv
KEITHLEY INSTRUMENTS, INC.	vii
KINNEY VACUUM DIVISION N. Y. AIR BRAKE CO.	xxvii
KOPPERS CO., INC.	xxix
LEVINTHAL ELECTRONIC PRODUCTS	xxvii
LOS ALAMOS SCIENTIFIC LAB.	viii
McGRAW–HILL BOOK CO., INC.	vi
NRC EQUIPMENT CORP.	xxii
PERMANENT EMPLOYMENT AGENCY	xxiv
RADIO CORP. OF AMERICA	xiii
REPUBLIC AVIATION	xxiii
SPACE TECHNOLOGY LABS.	Cover 3
STACKPOLE CARBON CO.	xxviii
STOKES CORP., F. J.	xxx
SYLVANIA ELECTRONIC SYSTEMS	xvii, xxv
VARIAN ASSOCIATES	xviii, xix
VEECO VACUUM CORP.	xxvi
WELCH SCIENTIFIC CO., W. M.	xx
WILEY & SONS, INC., JOHN	xvi
WORDEN LABORATORY	xxvi

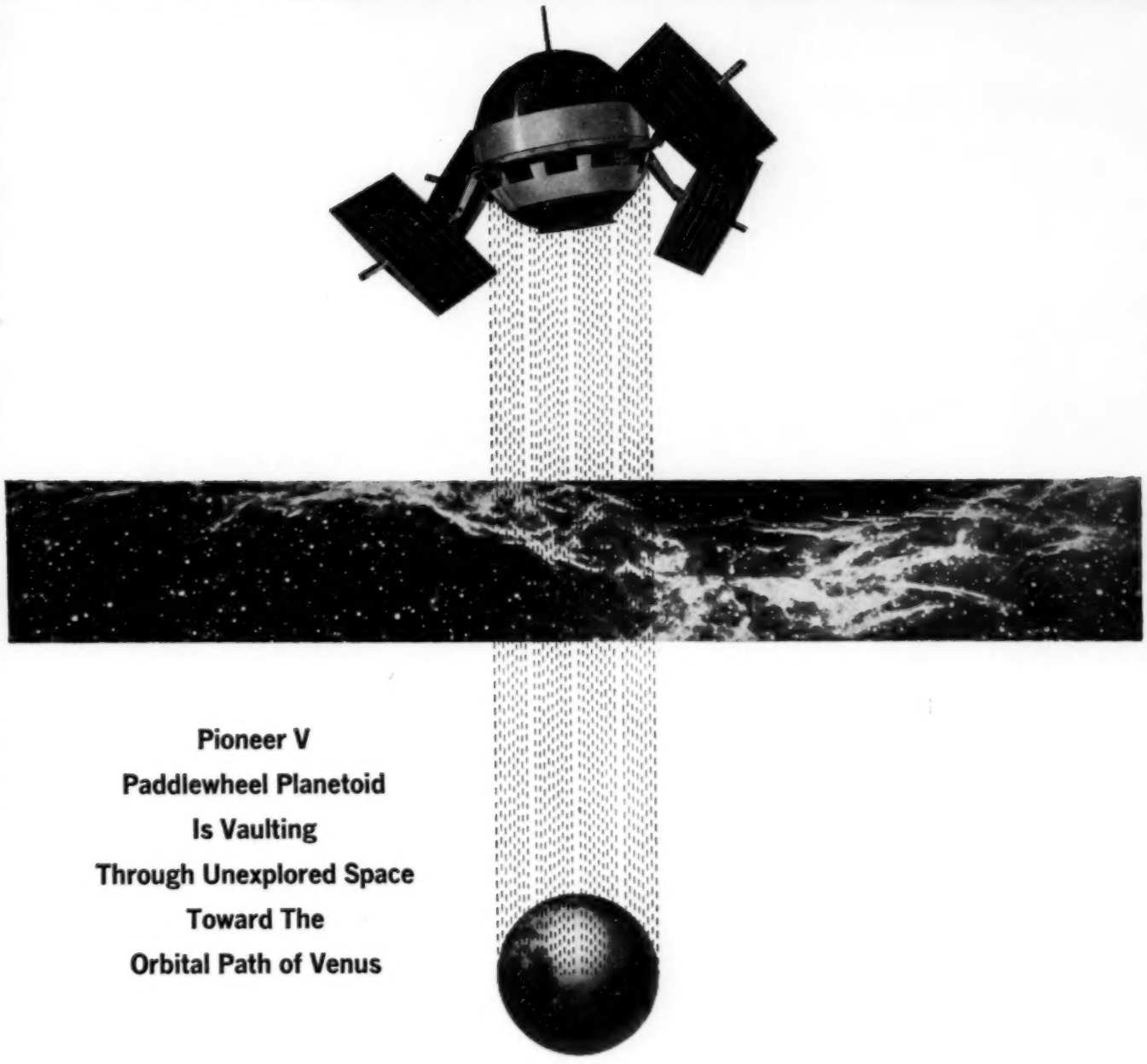

Pioneer V
Paddlewheel Planetoid
Is Vaulting
Through Unexplored Space
Toward The
Orbital Path of Venus

At this moment Pioneer V, one of the most advanced space probe vehicles ever launched, is on a course toward the path of Venus—26 million miles from earth. Blasted aloft March 11 by a Thor Able-4 rocket booster, this miniature space laboratory will reach its destination in about 130 days.

The project, carried out by Space Technology Laboratories for the National Aeronautics and Space Administration under the direction of the Air Force Ballistic Missile Division, may confirm or disprove long-standing theories of the fundamental nature of the solar system and space itself.

Energy from the sun—captured by almost 5,000 cells mounted in the four paddles—is used to supply all of the electrical power to operate the sophisticated array of instrumentation packed into the 94-pound spacecraft which measures only 26" in diameter.

By combining a phenomenal digital electronic brain (telebit) with a powerful radio transmitter inside the satellite, STL scientists and engineers expect to receive communications from Pioneer V at their command over interplanetary distances up to 50 million miles.

STL's technical staff brings to this space research the same talents which have provided over-all systems engineering and technical direction since 1954 to the Air Force missile programs including Atlas, Thor, Titan, Minuteman, and related space programs.

Important positions in connection with these activities are now available for scientists and engineers with outstanding capabilities. Inquiries and resumes are invited.

SPACE TECHNOLOGY LABORATORIES, INC.

Los Angeles • Santa Maria • Edwards Rocket Base • Cheyenne
Cape Canaveral • Manchester, England • Singapore • Hawaii

P. O. Box 95004, Los Angeles 45, California

INSTRUMENTS FOR DIELECTRIC MEASUREMENTS

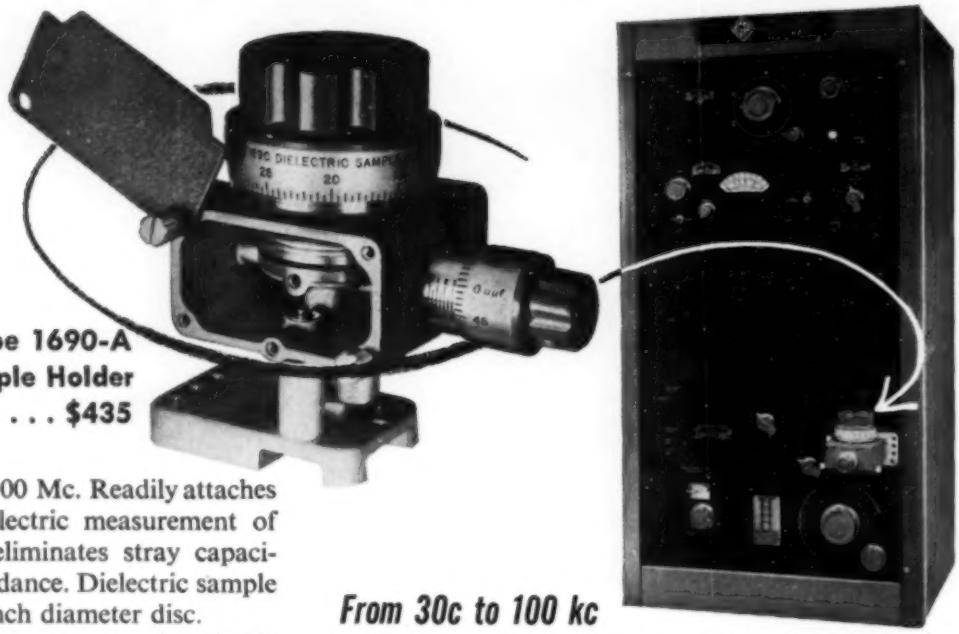

Type 1690-A
Dielectric Sample Holder
. . . $435

Useful to better than 100 Mc. Readily attaches to bridges for precise dielectric measurement of solid materials; virtually eliminates stray capacitance effects and lead impedance. Dielectric sample size is standard ASTM 2-inch diameter disc.

The Holder's electrodes are ground optically flat and are circular. One electrode is fixed, and the other is driven by a precision micrometer screw for accurate determination of electrode spacing. The drive automatically disengages when the electrodes come in contact with the specimen, thus providing the same contact pressure in all cases and preventing accidental damage. A micrometer-driven vernier capacitor with a range of 5 $\mu\mu$f provides accurate increments of capacitance for measurements by ASTM resonant-circuit methods.

From 30c to 100 kc

Type 1610-A2 Capacitance Measuring Assembly...$1875

A complete system for measuring capacitance from 100 $\mu\mu$f to 1.15 μf at 1 kc; to 1150 $\mu\mu$f at frequencies to 100 kc. Will measure capacitance as small as 0.1 $\mu\mu$f using substitution methods. Accuracy, $\pm 0.1\%$ using direct method, $\pm 0.2\%$ for substitution method. Dissipation-factor range, 0.00002 to 0.56; accuracy, $\pm 2\%$. Assembly may also be used with liquid-dielectric cells.

At 1 Mc

Type 1610-AH Capacitance Measuring Assembly...$1035

Can be used from 0.1 to 5 Mc with external generators. Range: direct method, 100 to 1150 $\mu\mu$f; substitution method, 0.1 to 1050 $\mu\mu$f. Accuracy and D range same as 1610-A2.

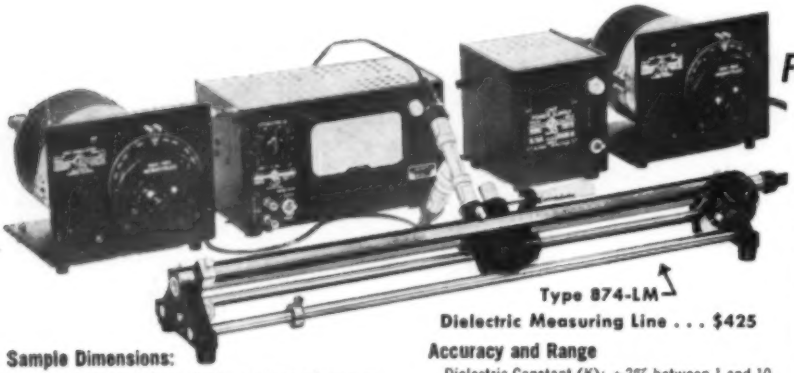

Type 874-LM
Dielectric Measuring Line . . . $425

For Measurements From 200 to 5000 Mc

The Type 874-LM Dielectric Measuring Line . . .

An air-dielectric, coaxial line whose field is sampled by an electrostatic probe mounted on a movable carriage. Also shown is a driving oscillator (right), and a Type DNT Detector assembly that is made up of an oscillator, mixer-rectifier, and combination i-f amplifier and null detector (left).

Sample Dimensions:

Length dependent upon K and frequency.

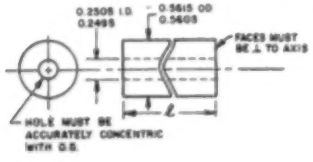

Accuracy and Range

Dielectric Constant (K): ±2% between 1 and 10
Dissipation Factor (D): ±(5% + 0.0001) between 0 and 0.05

Frequency Range:

Maximum: 5000 Mc or $\frac{9000}{\sqrt{K}}$ whichever is smaller

Minimum: $\frac{200}{\sqrt{K}}$ Mc

Operation is simple . . .

A cylindrical dielectric specimen is fitted into the open end of the line. The frequency of the signal source driving the line is adjusted until a voltage minimum is detected with the probe about a centimeter away from the sample. Dielectric constant and dissipation factor are then quickly calculated from two simple algebraic expressions.

Write For Complete Information

GENERAL RADIO COMPANY

WEST CONCORD, MASSACHUSETTS

NEW YORK, WOrth 4-2722 District Office in Ridgefield, N. J. WHitney 3-3140	CHICAGO Oak Park Village 8-9400	PHILADELPHIA Abington HAncock 4-7419	WASHINGTON, D.C. Silver Spring JUniper 5-1088	SAN FRANCISCO Los Altos WHitecliff 8-8233	LOS ANGELES Los Angeles HOllywood 9-6201	IN CANADA Toronto CHerry 6-2171

JOURNAL
OF
APPLIED PHYSICS

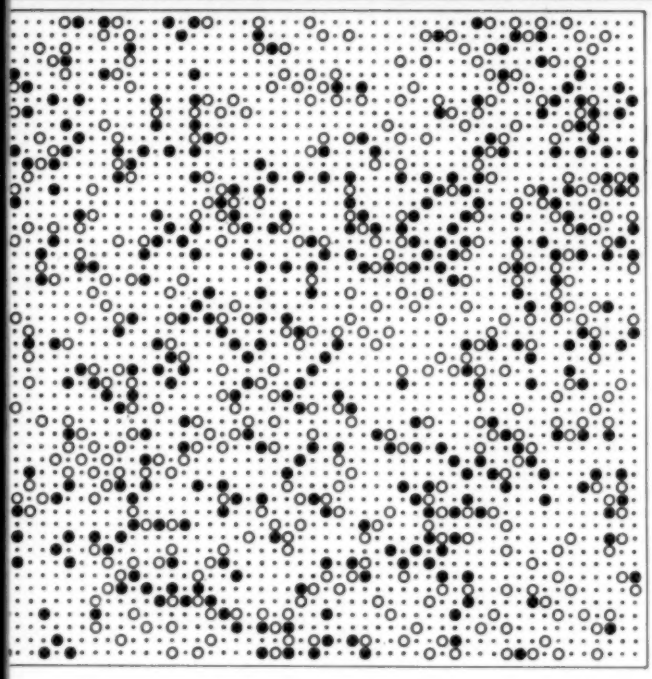

Square Lattice Representation of Disordered Alloy of 30 Percent Manganese (Circles) in Copper or Silver (Dots). Closed and Open Circles Indicate Manganese Atomic Moments in Plus and Minus Directions, Respectively.

See Page 142S.

May
1960

Supplement
to
Vol. 31 No. 5

Above: Lowest Magnetic Energy State Configuration.

Right: Configuration for the System Cooled in Large Field in Plus Direction.

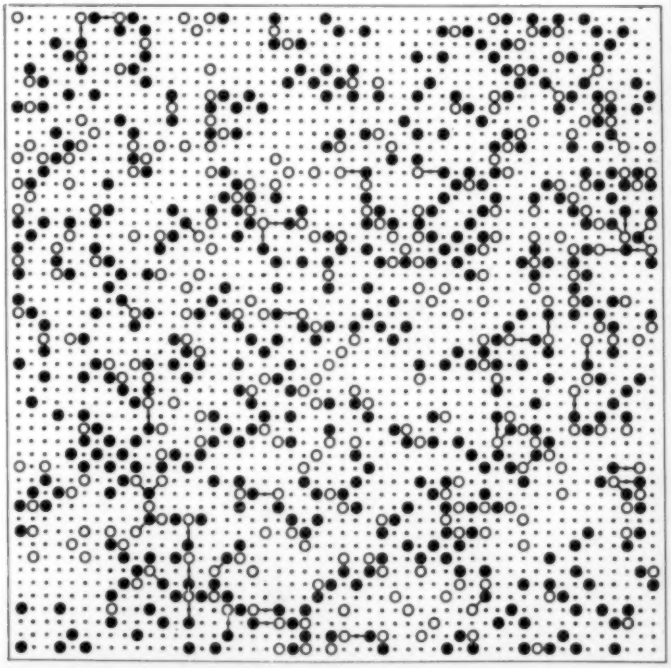

JOURNAL OF APPLIED PHYSICS

A journal of general physics and its applications to other sciences and to industry

Published by the

American Institute of Physics

GOVERNING BOARD

Ralph A. Sawyer, *Chairman*

J. G. Baker
R. H. Bolt
W. R. Brode
Harvey Brooks
Dirk Brouwer
J. W. Buchta
Vernet E. Eaton
J. H. Elliott
Herbert A. Erf
S. A. Goudsmit
W. W. Havens, Jr.
Winston E. Kock
R. Bruce Lindsay
H. V. Neher
C. J. Overbeck
G. E. Pake
Ray Pepinsky
R. A. Sawyer
F. W. Sears
Frederick Seitz
John Strong
G. E. Uhlenbeck
M. E. Warga
V. F. Weisskopf
W. R. Willets

ADMINISTRATION

Elmer Hutchisson
Director

Henry A. Barton
Associate Director

Wallace Waterfall
Secretary and Treasurer

Ruth F. Bryans
Publication Manager

W. C. Kelly
Director of Education Projects

Eugene H. Kone
Director of Public Relations

Alice Mastropietro
Circulation Manager

Kathryn Setze
Assistant Treasurer

Edward Tober
Manager, Production and Distribution

Theodore Vorburger
Advertising Manager

Emily Wolf
Office Manager

Editor
James A. Krumhansl

Assistant Editor
Ethel McMillan

Editorial Board

J. H. Crawford
Arthur Kantrowitz
A. F. Kip
J. E. Goldman
J. L. Tuck
C. A. Wert
Herman A. Haus
C. Lester Hogan
R. S. Rivlin

THE JOURNAL OF APPLIED PHYSICS is devoted to general physics and its applications to other sciences, to engineering, and to industry. Previous to 1937, this journal was called PHYSICS.

The JOURNAL OF APPLIED PHYSICS welcomes articles of two distinct kinds: (1) Descriptions of new results in experimental or theoretical physics which are of general interest to physicists. The author should explain his contribution in such a way that a physicist or engineer in another field of specialization can appreciate its objectives and essential features. (2) Critical reviews of particular areas of physics or surveys of extensive investigations at a single laboratory. Authors contemplating writing such should correspond with the Editor before they begin writing.

The JOURNAL OF APPLIED PHYSICS welcomes letters to the editor which describe in a few words the content of laboratory reports and theses and which tell readers how they may obtain copies of such reports.

Manuscripts should be submitted to the Editor, James A. Krumhansl, Rockefeller Hall, Cornell University, Ithaca, New York. Authors should read the "Information for Contributors," facing page 1 of the January issue, before writing articles or letters. The *Style Manual* of the American Institute of Physics is also helpful to writers preparing manuscripts for journals published by the American Institute of Physics. It can be obtained for $1.00 from the American Institute of Physics, 335 East 45 Street, New York 17, New York.

Corrected proofs and all correspondence concerning papers in the process of publication should be addressed to the Publication Manager, American Institute of Physics, 335 East 45 Street, New York 17, New York.

Subscriptions, renewals, and orders for back numbers should be addressed to the American Institute of Physics, 335 East 45 Street, New York 17, New York.

Subscription Price	U.S. and Canada	Elsewhere
To members of member organizations of the American Institute of Physics and Affiliated Societies ..	$12.00	$13.00
To all others	14.00	16.00

Back Number Prices

Yearly back number rate when complete year is available: $17.00.
Single copies: $1.75 each (exception: March, 1958—$3.00 each).

Changes of address should be sent to the American Institute of Physics.

Advertising rates supplied on request. Orders, advertising copy, and cuts should be sent to the American Institute of Physics.

The Journal of Applied Physics is published monthly at Prince and Lemon Streets, Lancaster, Pennsylvania.

Second-class postage paid at Lancaster, Pa.

PROCEEDINGS OF THE FIFTH SYMPOSIUM ON MAGNETISM AND MAGNETIC MATERIALS

Supplement to the
Journal of Applied Physics
Vol. 31, 1960

November 16–19, 1959
Detroit, Michigan

CONFERENCE ON MAGNETISM AND MAGNETIC MATERIALS

Papers presented at the Conference on Magnetism and Magnetic Materials, Detroit, Michigan, November 16–19, 1959

Sponsored by the American Institute of Electrical Engineers

Cooperating Societies:

American Physical Society

The Institute of Radio Engineers

The Metallurgical Society of the A. I. M. E.

Office of Naval Research

May, 1960

American Institute of Electrical Engineers Headquarters

33 West 39th Street, New York 18, New York

JOURNAL OF APPLIED PHYSICS

Supplement to Vol. 31, No. 5 MAY, 1960

In This Issue

Preface 1S

Magnetism, General and Theory

State of *d* Electrons in Transition Metals . . . . . Conyers Herring 3S
Microwave Resonance in Rare Earth Iron Garnets . . . . . C. Kittel 11S
Crystal Distortion in Magnetic Compounds . . . . . Junjiro Kanamori 14S
Relations between Superconductors and Ferromagnets . . . . . Bernd Matthias 23S
On the Laws of Magnetization of Ferromagnetic Single Crystals and Polycrystals. Application to Uniaxial Compounds . . . . . L. Néel, R. Pauthenet, G. Rimet, and V. S. Giron 27S

Garnets

Magnetic Interactions and Distribution of Ions in the Garnets . . . . . S. Geller 30S
Resonance Experiments with Single Crystal Yttrium Iron Garnets in Pulsed Magnetic Fields . . . . . Martin R. Stiglitz and Frederic R. Morgenthaler 37S
Absorption and Reflectivity Measurements on Some Rare Earth Iron Garnets and α-Fe_2O_3 . P. C. Bailey 39S
Instability of Magnetic Resonance in Single Crystal Spheres of Yttrium Iron Garnet . Joseph I. Masters 41S
Ferrimagnetic Resonance in Impurity Doped Yttrium Iron Garnet (YIG) . . . . . J. F. Dillon, Jr., and J. W. Nielsen 43S
Samarium Substitutions in Yttrium Iron Garnet . . J. Richard Cunningham, Jr., and Elmer E. Anderson 45S
Initial Permeability Characteristics of Mixed Yttrium-Gadolinium Iron Garnets . . . . . G. E. McDuffie, Jr., J. R. Cunningham, Jr., and E. E. Anderson 47S
Specific Heat of Some Rare Earth Iron Garnets and YIG at Low Temperatures . . . . . Horst Meyer and A. B. Harris 49S
Improved Method for the Growth of Yttrium-Iron and Yttrium-Gallium Garnets . . . . J. W. Nielsen 51S
Paramagnetic Resonance of Yb^{+++} in Aluminum and Gallium Garnets . . . . . John W. Carson and Robert L. White 53S
Magnetostriction of Gadolinium Iron Garnets . . . . . K. P. Belov and A. V. Pedko 55S

Permanent Magnets

On the Remanence of Ferromagnetic Powders . . . . . S. Shtrikman and D. Treves 58S
Angular Variation of the Magnetic Properties of Elongated Single-Domain Iron Particles . . . . . F. E. Luborsky and T. O. Paine 66S
Coercive Force and Remanence of 25-A to 2000-A Diameter Cobalt, Iron, and Iron-Cobalt Alloy . . . . . F. E. Luborsky and T. O. Paine 68S
Comparison of the Critical Single-Domain Size for Fe_3O_4 and γ-Fe_2O_3 . L. A. K. Watt and A. H. Morrish 71S
On the Resolution of Brown's Paradox . . . . . S. Shtrikman and D. Treves 72S
Precipitation of Dispersed Fine-Particle Magnetite . . . . . Lynore E. Slaten 74S
New Material for Permanent Magnets on a Base of Mn and Al . . . . . A. J. J. Koch, P. Hokkeling, M. G. v. d. Steeg, and K. J. de Vos 75S
"Interaction Anisotropy" Model of the Structure of Alnico Magnet Alloys . T. O. Paine and F. E. Luborsky 78S
Transmission Electron Diffraction of Alnico V . . . . . K. J. Kronenberg 80S
Long-Term Magnetic Stability of Alnico and Barium Ferrite Magnets . . . . . K. J. Kronenberg and M. A. Bohlmann 82S
Hot Working of Alnico 5 Alloys . . . . . C. L. Kolbe and D. L. Martin 84S

(*continued on page ivS*)

Spin Waves and Magnetostatic Modes

Use of Magnetostatic Modes as a Research Tool . . . . . Robert L. White 86S
Electron Spin Relaxation in Ferromagnetic Insulators* . R. C. LeCraw, R. C. Fletcher, and E. G. Spencer 95S
Survey of Ferromagnetic Resonance in Small Ferrimagnetic Ellipsoids . . . . Frederic R. Morgenthaler 95S
Harmonic Generation in a Ferrimagnetic Disk . . . . . Glenn E. Bennett 97S
Theory and Application of Dipolar Ferrite Modes . . . . . William H. Steier and Paul D. Coleman 99S
Magnetic Anisotropy from the Magnetostatic Modes . . . . . I. H. Solt, Jr., and P. C. Fletcher 100S
Ferrimagnetic Resonance at High Power . . . . . M. T. Weiss 103S
Magnetostatic Modes of a Ferromagnetic Slab . . . . . R. W. Damon and J. R. Eshbach 104S
Finite Amplitude Electromagnetic Waves in Gyromagnetic Media . . . . . B. A. Auld 106S
Spin Waves in Complex Exchange-Coupled Lattices and Neutron Scattering . . . . . A. W. Sáenz 108S

Computers and Switching

Flux Reversal in Soft Ferromagnetics . . . . . E. M. Gyorgy 110S
Development of High-Speed Coincident Current Memory Cores . . . . . Barlane R. Eichbaum 117S
Operation of Magnetic Film Parametrons in the 100- to 500-Mc Regions . . . . . A. V. Pohm, A. A. Read, R. M. Stewart, Jr., and R. F. Schauer 119S
Ferrite Films—New Logic and Storage Devices . . J. M. Brownlow, W. L. Shevel, Jr., and O. A. Gutwin 121S
Electrodeposited Memory Elements for a Nondestructive Memory . . . . . T. R. Long 123S
New Approach to High-Speed Storage—Low Flux Density Materials . . W. L. Shevel, Jr., and H. Chang 125S
Miniature Memory Planes for Extreme Environmental Conditions . . . . . R. Straley, A. Heuer, B. Kane, and G. Tkach 126S
New Multi-Aperture Magnetic Logic Element . . . . . David R. Bennion 129S
Fast Switching by Domain Walls in Ferrites . . . . . Walter Wiechec and Clinton M. Kelley 131S
Effect of Previous History on Switching Rate in Ferrites . . . . . R. W. McKay and K. C. Smith 133S
Elastic Switching Properties of Some Square Loop Materials in Toroidal Structures . . . . . W. C. Seelbach and J. R. Kiseda 135S

Anisotropy

Anisotropy Properties of Hexagonal Ferrimagnetic Oxides . . . . J. Smit, F. K. Lotgering, and U. Enz 137S
Exchange Anisotropy in Cu-Mn and Ag-Mn Alloys . . . . . J. S. Kouvel 142S
Internal Structure of Bloch Walls . . . . . S. Shtrikman and D. Treves 147S
Anisotropic Magnetization . . . . . Earl R. Callen 149S
Temperature Dependence of Anisotropy and Saturation Magnetization in Iron and Iron-Silicon Alloys . . . . . C. D. Graham, Jr. 150S
Temperature Dependence of the Saturation Magnetization of Nickel Films of Thickness Less Than 100A . . . . . C. A. Neugebauer 152S
Internal Friction Anomalies in Ferromagnets and Antiferromagnets near the Curie Point . . . . . K. P. Belov, G. I. Katayev, and R. Z. Levitin 153S
Magnetic Anisotropy and Magnetostriction of Ordered and Disordered Cobalt-Iron Alloys . . R. C. Hall 157S
Roll Magnetic Anisotropy of Iron-Aluminum Crystals . . . . . Soshin Chikazumi 158S
Magnetic Anisotropy in Ferrimagnetic Crystals . . . . . R. F. Pearson 160S

Techniques and Devices

Exchange Anisotropy in the System $Mn_{(1-x)}Cr_xSb$ . . . . . R. H. Pry, J. S. Kouvel, and E. S. Miksch 162S
Exchange Anisotropy in Rock Magnetism . . . . . W. H. Meikeljohn and R. E. Carter 164S
Influence of Ionic Order on the Magnetocrystalline Anisotropy and Crystalline Field Parameters in Lithium Ferrite Monocrystals . . . . . V. J. Folen 166S
Tetrahedral Junction . . . . . Jerald A. Weiss 168S
High-Speed Ferrite Rotating Half-Wave Plate . . . . . Franklin S. Coale 170S
Double Pump Degenerate Ferrite Amplifier . . . . . Peter Gottlieb 172S
Broadband Reciprocal Ferrite Phase Shifters . . . . . T. D. Geiszler and R. A. Henschke 174S

* Abstract only.

(*continued on page vS*)

Multimode Propagation in Gyromagnetic Rods and Its Application to Traveling-Wave Devices . . . . . J. E. Tompkins, F. Reggia, and L. Joseph 176S
Ferromagnetic Powders in Waveguides at Elevated Temperatures* . . A. D. Krall and E. T. Hooper, Jr. 178S
Instrumentation Applications of Inverse-Wiedemann Effect . . . . . J. A. Granath 178S
Practical Hysteresigraph . . . . . R. R. Bockemuehl and W. E. Sargeant 180S
Rictometer System for Calibrating Transmitters of Remote Indicating Compasses . . . L. I. Mendelsohn 183S
Simple Recording Torque Magnetometer . . . . . P. W. Neurath 184S
Magnetic Field Measurement Using Ultrasonics . . . . . R. J. Radus 186S
Permanent Magnet Leakage Permeance Evaluation Based on Polar Radiation Analogy . . . . . J. E. Foy and R. J. Parker 188S
Effect of Geometry on Thick Film Toroids . . . . . J. C. Sagnis, Jr., M. Teig, and R. L. Ward 190S
Experimental Flux Pattern Determination in Magnetic Cores . . . . . Robert L. Ward 192S
Method for Measuring Iron Losses in Elliptically Pollarized Magnetic Fields . . . . . F. J. Young and H. L. Schenk 194S
Localized Field Permanent Magnet Arrays . . . . . H. L. Stadler 196S

Resonance

Interaction of Magnetic Crystals with Radiation in the Range 10^{4}–10^{5} cm^{-1} . . . . . A. M. Clogston 198S
Nuclear Resonance in Ferromagnetic Cobalt . . . . . A. M. Portis and A. C. Gossard 205S
Initial-Permeability Spectra of Microscopic Iron-Oxide Particles . . . . . W. F. Brown, Jr., J. P. Hanton, and A. H. Morrish 214S
Galvanomagnetic Effects in Ferromagnetic Resonance . . . . . M. H. Seavey, Jr. 216S
Initial Susceptibility Spectra of Permalloy Films . . . . . R. F. Soohoo 218S
Volume Dependence of Ferrimagnetic Resonance Properties in $Ni_{1-x}Co_xFe_2O_4$ . . . . . I. P. Kaminow 220S
Effects of Surface Irregularities on Single Crystal Resonance Parameters . . . . . C. R. Buffler 222S
Saturation Effects in Ferrimagnetic Resonance . . . . . P. E. Seiden and H. J. Shaw 225S
Resonance Line Widths of Sintered Nickel Ferrites Having Low Porosities . . . . . L. G. Van Uitert, R. R. Soden, and F. W. Swanekamp 226S

Soft Magnetic Materials

A Necessary Factor for Heat Treatment of the Permalloys in a Magnetic Field . . . . . E. A. Nesbitt, R. D. Heidenreich, and A. J. Williams 228S
Effects of Directional Ordering on the Damping of Zone-Melted Iron . . . . . R. E. Maringer 229S
Study of Heat Treatments for Low Coercive Force 14 to 17% Aluminum Iron Alloys . . . . . D. Pavlovic and K. Foster 231S
Effect of Directional Orientation on the Magnetic Properties of Cube-Oriented Magnetic Sheets . . . . . K. Foster and J. J. Kramer 233S
Secondary Recrystallization in Vacuum Annealed Silicon Iron . . . . G. Baer, D. Ganz, and H. Thomas 235S
Characteristics of Supermendur at 500°C . . . . . M. Lauriente and G. E. Lynn 237S
Effects of Hydrostatic Pressure on the Properties of Magnetic Materials . R. E. Alley, Jr., and V. E. Legg 239S
Magnetic Contribution to the Ultrasonic Attenuation in Annealed and Deformed Steel (SAE 1020) . . . . . W. J. Bratina, U. M. Martius, and D. Mills 241S
Direct-Current Measurements on Tape-Wound Cores . . . . . R. C. Barker and R. M. Brownell 243S
Effect of Applying a Magnetic Field During Neutron Irradiation on the Magnetic Properties of Fe-Ni Alloys . . . . . A. I. Schindler and E. I. Salkovitz 245S
Rigorous Solution of Eddy Current Losses in Rectangular Bar for Single Plane Domain Wall Model . . . . . Paul D. Agarwal and L. Rabins 246S
Effect of Eddy Currents on Domain Wall Behavior Configurations, Wall Motion, and Loss for a Domain Model of Cube-On-Edge Material . . . . . P. D. Agarwal and D. C. Graham 249S

Ferrites and Oxides

Role of Cation Vacancy in Magnetic Annealing of Iron-Cobalt Ferrites . . . . . Shūichi Iida 251S
Intrinsic and Anneal-Induced Anisotropy in Cobalt-Substituted *W*-Type Hexagonal Oxides . . . . . L. R. Bickford, Jr. 259S
Valence and Distribution of Manganese Ions in Ferrospinels . . . . . Arthur Miller 261S

(*continued on page viS*)

High Field Magnetization Study of Ferrimagnetic Arrangements in Chromite Spinels* . . . I. S. Jacobs 263S
$GaFeO_3$: A Ferromagnetic-Piezoelectric Compound . . . . . J. P. Remeika 263S
High-Temperature Susceptibility of Ferrimagnetic Spinels . . . . . Peter J. Wojtowicz 265S
Time Decrease of Initial Permeability in $Mn_xFe_{3-x}O_{4+y}$ . . . . . W. A. Crapo 267S
Square Loop Properties of Copper-Manganese Ferrites . . . . . R. S. Weisz and D. L. Brown 269S
Temperature Dependence of the Saturation Magnetization of Ferrites with Magnetoplumbite Structure . . . . . G. Heimke 271S
Magnetic Behavior in the Transition Region of a Hematite Single Crystal . . . . . S. T. Lin 273S
Metamagnetic Behavior of Manganese Arsenide . . . . . D. S. Rodbell and P. E. Lawrence 275S
Magnetic Properties of the $Li_xMn_{1-x}Se$ System . . . . . Thomas R. McGuire and Robert R. Heikes 276S
Ferroelectric and Ferrimagnetic Properties of $(Ba_{6-2x}R_{2x})$ $(Nb_{9-x}Fe_{1+x})O_{30}$ . . P. H. Fang and R. S. Roth 278S

Magnetic Films

Some Physical Properties of Thin Magnetic Films . . . . . A. C. Moore and A. S. Young 279S
Millimicrosecond Magnetization Reversal in Thin Magnetic Films . . . W. Dietrich and W. E. Proebster 281S
Flux Reversal by Noncoherent Rotation in Magnetic Films . . . . . K. J. Harte 283S
Magnetization Reversal in Uniaxial Films near to the Preferred Direction . E. M. Bradley and M. Prutton 285S
Influence of Nearby Conductors on Thin Film Switching . . . . . J. S. Eggenberger 287S
Preferred Orientation and Ordering in Evaporated Films of Fe, Ni, and Fe-Ni . . . . . R. F. Adamsky 289S
Investigations into the Origin of Anisotropy in Oblique-Incidence Films . . . . . M. S. Cohen, E. E. Huber, Jr., G. P. Weiss, and D. O. Smith 291S
Magnetic Anisotropy in Evaporated Iron Films . E. W. Pugh, J. Matisoo, D. E. Speliotis, and E. L. Boyd 293S
Anisotropy and Inversion in Permalloy Films . . . . . D. O. Smith, E. E. Huber, Jr., M. S. Cohen, and G. P. Weiss 295S
Microcalorimetric Technique for the Study of Damping and Hysteresis in Ferromagnetic Films . . . . . J. R. Mayfield 298S
Domain Wall Velocities in Thin Iron-Nickel Films . . . . . N. C. Ford, Jr. 300S
Domain Walls in Thin Magnetic Ni-Fe Films . . . . . S. Methfessel, S. Middelhoek, and H. Thomas 302S
Annular Uniaxially Magnetized Domains in Thin Ni-Fe Films . . . . . O. W. Muckenhirn, A. E. LaBonte, and P. J. Besser 304S
Cross-Tie Walls in Thin Films . . . . . Harvey Rubinstein and Robert J. Spain 306S
Static and Dynamic Studies of Magnetization Distribution in Thin Films by Electron Microscopy . . . . . Harrison W. Fuller and Murray E. Hale 308S

Metals and Alloys

Magnetic Properties of Manganese Copper Alloys . . . . . R. Street 310S
Mechanism of Antiferromagnetism in Dilute Alloys* . . . . . A. W. Overhauser 317S
Long-Range Magnetic Interactions via Conduction Electrons . . . . . Arthur Paskin 318S
Hyperfine Interactions in Magnetic Materials by γ-γ Angular Correlation Measurements . . . . . M. E. Caspari, S. Frankel, and M. A. Gilleo 320S
Magnetic Properties of Ferromagnetic Superconductors . . . . . R. M. Bozorth and D. D. Davis 321S
Strong Field Magnetization at Low Temperatures and Approach to Absolute Saturation of Thulium Metal . . . . . Warren E. Henry 323S
Magnetic Behavior of Polycrystalline Neodymium, Holmium, and Erbium from 300 to 1500°K . . . . . Sigurds Arajs and D. S. Miller 325S
Analysis of Magnetic Interactions in Alloys of Platinum with Iron Group Transition Elements . . . . . Hiroshi Sato 327S
Effect of Impurities on the Low-Temperature Spontaneous Magnetization of Cubic Ferromagnetic Crystals . . . . . A. A. Maradudin and P. A. Dixon 329S
Antiferromagnetism of Iron in Face-Centered Crystalline Lattice and the Causes of Anomalies in Invar Physical Properties . . . . . E. I. Kondorsky and V. L. Sedov 331S

Magnetic Salts

Paramagnetic Resonance Absorption of Nickel in Sapphire . . . . . S. A. Marshall and A. R. Reinberg 336S
Magnetic Susceptibilities of Single Crystal $NiCl_2 \cdot 6H_2O$ and $CoCl_2 \cdot 6H_2O$ at Low Temperatures . . . . . R. B. Flippen and S. A. Friedberg 338S

(*continued on page viiS*)

Properties of Manganese Ferrites Prepared at Various Oxygen Pressures* . . . . Aleksander Bragiński 339S
Effect of Potassium Ions on the Reaction and Final Properties of Mn-Zn Ferrite* . . Stefan Makolagwa 339S
Magnetic Properties of Uranium Digermanide . . . . . Clayton E. Olsen 340S
Interpretation of the Magnetic and Crystallographic Properties of Several Iron, Nickel, and Iron-Nickel Nitrides . . . . . J. B. Goodenough, A. Wold, and R. J. Arnott 342S
Magnetic Transitions in Ti_2O_3 and V_2O_3 . . . . . P. H. Carr and S. Foner 344S
Low-Temperature X-Ray Diffraction Studies on Vanadium Sesquioxide . . . . . E. P. Warekois 346S
Ionic Ordering Effects in the Ferromagnetic Resonance of Lithium Ferrite Monocrystals . . . . . A. D. Schnitzler, V. J. Folen, and G. T. Rado 348S

Magnetic Compounds and Neutron Diffractions

Precise Measurement of Magnetic-Form Factors . . . . . Robert Nathans 350S
Antiferromagnetic Structure and Domains in Single Crystal NiO . . . Walter L. Roth and Glen A. Slack 352S
Neutron Diffraction Investigation of the Magnetic Structure of Nickel Oxide . . . . . H. A. Alperin 354S
Neutron Diffraction Investigation of the $Fe_{1-\delta}S$ System . . . . . J. T. Sparks, W. Mead, A. J. Kirschbaum, and W. Marshall 356S
Neutron Diffraction Investigations of the Magnetic Ordering in Rare Earth Nitrides . . . . . M. K. Wilkinson, H. R. Child, J. W. Cable, E. O. Wollan, and W. C. Koehler 358S
Direct Cation-Cation Interactions in Primarily Ionic Solids . . . . . John B. Goodenough 359S
Theory of the Low Lying States of Some Rare Earth Compounds . . . . . G. T. Trammell 362S
Classical Theory of Spin Configurations in the Cubic Spinel . . . . . T. A. Kaplan 364S
Magneto Structural Studies on Gadolinium-Iron Alloys . . . . . R. C. Vickery, W. C. Sexton, V. Novy, and E. V. Kleber 366S
Magnetic Moments of Alloys of Gadolinium with Some of the Transition Elements . . . . . W. M. Hubbard, E. Adams, and J. V. Gilfrich 368S
Ferromagnetic-Alloy Phases Near the Compositions Ni_2MnIn, Ni_2MnGa, Co_2MnGa, Pd_2MnSb, and PdMnSb . . . . . F. A. Hames 370S
Magnetic-Form Factor of Fe_3Al . . . . . S. J. Pickart and R. Nathans 372S
Effect of Crystalline Fields on Magnetic-Form Factors . . . . . A. J. Freeman and R. E. Watson 374S

Ferrimagnetic Resonance Effects and Miscellaneous

Resonance Measurements in Magnetic Garnets . . . . . G. P. Rodrigue, H. Meyer, and R. V. Jones 376S
Growing Spin Waves in Ferrites in Unstable Equilibrium . . . . . Tor Schaug-Pettersen 382S
Nucleation Experiments on Thin Magnetic MnBi Films . . . . . Ludwig Mayer 384S
Recent Developments in Ferromagnetic Resonance at High Power Levels . . . . . E. Schlömann, J. J. Green, and U. Milano 386S
Transfer Function and Error Probability of a Digital Magnetic Tape Recording System . . . . . John Wenchung Hung 396S
Particle Interaction in Magnetic Recording Tapes* . . . . . J. G. Woodward and E. Della Torre 398S
Switching Behavior of Low Remanence Ferrite . . . . . F. B. Hagedorn and E. M. Gyorgy 398S
Pulsed Ferrimagnetic Microwave Generator . . . . . B. J. Elliott, T. Schaug-Pettersen, and H. J. Shaw 400S
Analysis of a Practical Perpendicular Head for Digital Purposes . . . . . George J. Y. Fan 402S
Magnetism in Medicine . . . . . M. W. Freeman, A. Arrott, and J. H. L. Watson 404S
Blood Flow Measurements Using Dynamical Paramagnetic Relaxation Times and Paramagnetic Tracer Techniques . . . . . J. R. Singer 406S
Promotion of Cubic Grain Growth in 3% Silicon Iron by Control of Annealing Atmosphere Composition . . . . . Dale Kohler 408S
Author Index 410S
Subject Index 414S

Journal
of
Applied Physics

Supplement to Volume 31, Number 5 May, 1960

Preface

"When Columbus, to his immortal honour, had newly perfected his Discovery of the West Indies, the Spaniards went up and down in Clubbs and Cabals, vilifying the Action, and Derogating from the Glory of the Work. They saw nothing in the Business, they said, but another body might have done it as well as He. . . . Columbus had the hap to be Incognito at one of these Meetings, and when he had set still a while, as a Person not at all concerned in the Discourse, he called for a Hens Egg, which was immediately brought him. He took it; and after viewing and turning of it one way and t'other, Gentlemen, says he, I would gladly see any Man here set this Egg upright now upon the Table. They fell to Whispering and Fleerings one upon another, and after several Tryals, concluded the Thing was not to be done. Pardon me, says Columbus, there's nothing easier in Nature: and so he took the Egg, Crack'd it, and set it up-an-end. The Company, upon Second Thoughts, took the Hint as he intended it." *Fables and Storyes Moralized*, Sir Roger L'Estrange, London, 1699.

THIS is the fifth Conference on Magnetism and Magnetic Materials, and as with all the young we are still counting our birthdays. Such anniversaries are also a proper time to look about a little to see where we have been and where we might be going. The story above perhaps is appropriate as it is taken from a worn book written for the purpose of instructing the young. Each reader will probably see something different in this tale. It serves to remind this observer that it was the contributions of *individuals* with talent and points of view that made this conference and proceedings possible. For no conference *organization* possesses any special talent except that of reproducing itself. The many people who contributed to the meeting and the Proceedings cared about whether they were well done, and acted as responsible members of the scientific community to see that they were done.

The major scientific news from this conference was the important advances being made in understanding phenomena in magnetic materials. While these are fundamental in nature, they have most important implications for practical applications later. Many useful applications can be made of phenomena by harnessing the interactions between macroscopic parameters of materials without truly understanding the *why* and *how* of these. Those new device concepts which are revolutionary in nature, however, issue increasingly from an incisive comprehension of the physical nature of phenomena. Hence, it is important that in ferromagnetic materials means were demonstrated for measuring the field at the nucleus of the surrounding electrons and hence their magnetic state; also, the understanding of spin wave phenomena in ferrimagnetic materials as a function of composition, structure, and perfection—particularly at elevated power levels. There were a number of elegant papers on these and other subjects which should whet the readers' appetite for more new things to come. It does seem that the field of magnetism may be about to experience the rapid theoretical development and practical exploitation seen in the field of semiconductors.

Workers doing research and/or development of materials and devices sometimes feel that they are not appreciated by those scientists doing the more glamorous fundamental work. The former can reasonably point to the fact that it is after all the transformer iron that helps make experimental power supplies go, the computers that make it possible to do theoretical calculations. And those who have visited countries without a well-developed technology, know how much more difficult it is to carry on research without a ready supply of materials and devices to use in their work. The fact of the matter is that all the fields of technology and research are separated by semipermeable information membranes. If conditions can be adjusted so that there is flow of knowledge both ways, both will benefit. It is our hope that we can continue to attract workers in all aspects of magnetism to these meetings so as to provide the mutual stimulation necessary for the health of the entire scientific body.

Particular acknowledgment is made here of the

Copyright © 1960 by the American Institute of Physics.

contribution made by those busy scientists who took the time to write tutorial and summary papers for the benefit of their colleagues. Also special mention should be made of the nearly 70 referees who frequently interrupted their own work to act with great dispatch on the papers sent them. It would probably surprise them to know of the many comments sent to the editor thanking the referee for the errors pointed out or the pertinent questions asked.

Each year the method of editing and publishing the Proceedings has been set up as an experiment (hopefully) designed to do a better job than the year before. The suggestions and comments of readers have been very helpful, and are always considered carefully. This year all papers were refereed just before the conference, then returned to the authors before the conference or made available at the conference. Members of the Publications Committee then made themselves available at the conference to try to give on-the-spot answers to the many questions posed by the authors or the referees. In the main, this scheme worked very well. It not only made the corrected manuscripts available for publication much sooner, but it was found that the authors immediately took advantage of the situation to incorporate corrections and additions at the conference resulting from discussions or relevant papers.

Lastly, I should like to mention that it was my good fortune to have *working* colleagues on the Publications Committee: H. Brooks, J. Goldman, L. Hogan, and J. Krumhansl. Their suggestions drawn fron a considerable experience, and their ready assistance, were essential to the method of preparing this year's Proceedings.

J. A. Osborn
Editor

JOURNAL OF APPLIED PHYSICS SUPPLEMENT TO VOL. 31, NO. 5 MAY, 1960

Magnetism, General and Theory

The State of *d* Electrons in Transition Metals

CONYERS HERRING
Bell Telephone Laboratories, Murray Hill, New Jersey

This paper gives a brief critique, in elementary language, of the principal types of theoretical pictures which have been advanced concerning the electronic states of transition metals, especially those of the iron group. It also calls attention to the possibility that some of the properties of these metals can be correlated by the use of concepts which have an exact, not just approximate, meaning for a many-electron system. The Fermi surface is probably a concept of this type. Major conclusions are that in the iron group metals the 3*d* electrons ought not to differ radically from those in the free atoms either in number or in spatial distribution, and that in most, though perhaps not all, of these metals the 3*d* electrons, magnetic or nonmagnetic, have an itinerant behavior.

INTRODUCTION

IN the last quarter century, a wide variety of pictures of the electronic structures of transition metals have been proposed and elaborated. Some of these are still flourishing; some have died. The diversity of viewpoints is much wider for these materials than for, say, monovalent metals or nonmetals. The reason for this diversity is that, of the two main approaches to the electron theory of solids—the free-electron idea and the idea of electrons bound to particular atoms—neither seems adequate to describe a metal made from atoms with incomplete *d* shells. Each school of thought has therefore been driven to use its own combination of crude approximations, and usually the concepts of one school have no clear-cut meaning in the framework of another school.

In this paper, I shall begin by enumerating briefly the principal types of theories and indicating which approaches appear to me to be wrong or unproductive. The latter part of this first section will be devoted to a description of some conclusions which have emerged from one of these approximate approaches (the self-consistent field method), and to adding some words of caution about its limitations. Finally, I shall try to show that at least a partial picture of the state of electrons in transition metals can be constructed using concepts which are not approximate, but which have an exact meaning for a many-electron metal. The main object of this paper, in fact, will be a plea for more experimental and theoretical work aimed in this direction.

For simplicity, the discussion will be limited throughout to pure elements of the iron group.

1. SURVEY OF PAST AND PRESENT THEORIES

Blending of Basic Ideas

In surveying the various theories one is struck with the fact that there are just a few basic ideas which enter into all the theories, and that the divergences of viewpoint are due merely to their employing these ideas in different relative proportions. It is like mixing a few liquors in various proportions to get a variety of different cocktails. Table I lists these main ideas, liquors, at the top, and the main categories of theories, cocktails, in the first column.

(i) The first of the ideas is that of electronic energy bands made up of states of an electron in which it moves freely through the crystal. Such a state of motion resembles that of an electron in free space in being described by a traveling wave; however, this wave in a crystal, called a Bloch wave, differs from that of a free particle in being not of pure sinusoidal form, but rather a sine wave periodically modulated by the interaction of the electron with the fields of the atoms.

TABLE I. Approximate compositions of the major types of theories of transition-metal electrons. The symbols X, x, denote respectively a major and a subordinate use of the idea of a given column; the subscripts a, b, c, refer to different aspects of ideas (ii) or (iii), as enumerated in the text.

Liquors → Cocktails ↓	(i) Bands	(ii) Correlation	(iii) Coupled atoms	(iv) Valence bonds
Itinerant	X	x_a	0	0
Minimum polarity	x	X_b	$X_{a,c}$	0
s-d models	X	x_a	$X_{a,b,c}$	0
Valence	X	X_b	$X_{a,b,c}$	X

(ii) The second idea, related to this, has to do with the modification of the motion of itinerant electrons by their mutual electrostatic repulsion. Two approaches to this modified motion may be distinguished: (a) The application of a "correlation" correction to the theory of noninteracting electrons in Bloch states.[1] (b) The conception of the state of a metal as a resonant superposition of states corresponding to various distributions of neutral atoms and positive and negative ions.[2,3]

[1] E. Wigner, Phys. Rev. **46**, 1002 (1934); Trans. Faraday Soc. **34**, 678 (1938); D. Pines, in *Solid State Physics* edited by F. Seitz and D. Turnbull (Academic Press, Inc., New York, 1955), Vol. 1, p. 367; J. G. Fletcher and D. C. Larson, Phys. Rev. **111**, 455 (1958).

[2] J. C. Slater, Phys. Rev. **35**, 509 (1930).

[3] S. Schubin and S. Wonsowsky, Proc. Roy. Soc. (London) **A145**, 159 (1934), Physik. Z. Sowjetunion **7**, 292 (1935); **10**, 348 (1936).

(iii) The third idea is the conception of electrons bound in a specific configuration on a single atom. This leads to three further conceptions which are sometimes important in solid-state theories: (a) Intra-atomic coupling of electrons (Hund's rule, etc.). (b) Crystal-field splitting (i.e., the development of a difference in energy between states which in the free atom would have the same energy, differing only in orientation). (c) The ferro- or antiferromagnetic coupling of the total spin of one atom to the total spin of a neighbor.

(iv) The last idea is that of directed valence bonds, in which an electron on one atom joins with an electron on a neighboring atom, these two becoming paired into a singlet state and losing any coupling they may have had to other electrons of their own atoms.

The theoretical schools have been grouped into four main types, although within each type there may still be quite a diversity (no two men mix a given cocktail in quite the same way):

The first category, itinerant theories, is based mainly on the idea of electrons moving freely through the crystal (hence the capital X in the first column) with rough corrections for the mutual repulsions of the electrons sometimes grafted on as an afterthought (hence the small x in the second column). Theories of this type, giving interpretations of magnetic and other properties of transition metals, have been variously developed by Slater,[4,5] by Stoner[6] and Wohlfarth,[7] by Friedel,[8] and by many others.[9] The various *a priori* calculations of the electronic energy band structures which underlie such theories have been summarized in a review by Callaway[10]; more recent work by Stern[11] and Wood[12] may also be cited.

The next group of theories, for which I use Van Vleck's name "minimum-polarity," has as its central feature the idea of fluctuating ionic states, the transitions between these being crudely allowed for using the band-theory concepts of the first column. While the basic idea goes back to some old papers of Slater[2] and of Schubin and Vonsovski,[3] in the thirties, the most detailed application to iron-group metals is that of Hurwitz and Van Vleck,[13] reported at the 1952 magnetism conference.

The third group, *s-d* models, assumes that the 4*s* electrons (the ones that have large orbits in the isolated atom) become free electrons in the metal, but that the 3*d* electrons (those in incompletely filled shells of more compact orbits) remain bound to the individual atoms. To this group belong, among others, the theories of Vonsovski,[14] Zener,[15] Mott and Stevens,[16] and Lomer and Marshall.[17]

The fourth group, valence-bond theories, is associated mainly with the name of Pauling.[18] It borrows ideas from all columns, but relies mainly on the concept of valence bonds formed from hybrid mixtures of *s*, *p* and *d* states.

Divergent Opinions

As illustrations of the divergencies between the viewpoints of the different schools, one may list some of the answers which different theorists have given to four important questions pertaining to metals of the iron group:

(1) *How many electrons per atom are in states with the angular momentum and charge distribution characteristic of 3d electrons?* Most of the theories have assumed this number to be the same as in the free atom or (more often) about one more, the number being nonintegral in the itinerant theories, integral in some of the *s-d* theories. Pauling[18] has suggested, however, that 6 electrons per atom are in conduction states formed from hybridized orbitals differing widely from atomic *d* states; this leaves correspondingly fewer electrons with the compact 3*d* distribution.

(2) *Are these electrons in general, and ferromagnetic 3d electrons in particular, bound or itinerant?* In the itinerant theories they are all itinerant. In some of the *s-d* theories they are all bound. According to the minimum-polarity model,[13] there should be some itinerant behavior of magnetic electrons for cases like Ni, where the average number of 3*d* electrons per atom is nonintegral, but very little when it is integral. According to Griffith[19] and to Mott and Stevens,[16] there are two classes of 3*d* electrons, one of which (symmetry t_g) is itinerant, the other (symmetry e_g) bound if of integral occupation. The latter carry most of the magnetic moment in Fe, but not in Ni. Pauling's[18] view seems similar to this.

(3) *What is the origin of the exchange forces which align the spins in the ferromagnetic metals?* According to most of the itinerant models,[4] it is the intra-atomic exchange responsible for Hund's rule in the free atom: electrons flitting from atom to atom find that their

[4] J. C. Slater, Phys. Rev. **49**, 537, 931 (1936).
[5] J. C. Slater, Revs. Modern Phys. **25**, 199 (1959).
[6] E. C. Stoner, Phys. Soc. Repts. Progress Phys. **11**, 43 (1948); J. phys. radium **12**, 372 (1951).
[7] E. P. Wohlfarth, Revs. Modern Phys. **25**, 211 (1953).
[8] J. Friedel, J. phys. radium **16**, 829 (1955); **19**, 573 (1958).
[9] A. B. Lidiard, Proc. Phys. Soc. (London) **A65**, 885 (1952); G. S. Krinchik, Izvest. Akad. Nauk S.S.S.R. Ser. Fiz. **21**, 869 (1957); Bader, Ganzhorn, and Dehlinger, Z. Physik **137**, 190 (1954).
[10] J. Callaway, in *Solid State Physics*, edited by F. Seitz and D. Turnbull (Academic Press, Inc., New York, 1958) Vol. 7, p. 99.
[11] F. Stern, Thesis, Princeton University (1955); Phys. Rev. (in press).
[12] J. H. Wood, *Quarterly Progress Report, Solid-State and Molecular Theory Group* (Massachusetts Institute of Technology, October 15, 1959), p. 4.
[13] J. H. Van Vleck, Revs. Modern Phys. **25**, 220 (1953).
[14] S. Vonsovsky, J. Phys. (U.S.S.R.) **10**, 468 (1946); S. V. Vonovski and E. A. Turov, J. Exptl. Theoret. Phys. (U.S.S.R.) **24**, 419 (1953). For a brief review see S. V. Vonsovski, Izvest. Akad. Nauk. S.S.S.R. Ser. Fiz. **21**, 854 (1957) [translation: Bull. Acad. Sci. U.S.S.R. (Columbia Technical Translations, White Plains, New York), **21**, 854 (1957)].
[15] C. Zener, Phys. Rev. **81**, 440 (1951); **83**, 299 (1951); see also C. Zener and R. R. Heikes, Revs. Modern Phys. **25**, 191 (1953).
[16] N. F. Mott and K. W. H. Stevens, Phil. Mag. **2**, 1364 (1957).
[17] W. M. Lomer and W. Marshall, Phil. Mag. **3**, 185 (1958).
[18] L. Pauling, Phys. Rev. **54**, 899 (1938), Proc. Natl. Acad. Sci. **39**, 551 (1953).
[19] J. S. Griffith, J. Inorg. & Nuclear Chem. **3**, 15 (1956).

interaction energy with other electrons momentarily on the same atom is lower if their spins are parallel. In Van Vleck's discussion of the minimum-polarity model,[13] he suggests that although it is only rarely that an electron belonging on one magnetic atom gets onto another magnetic atom, these occasional events may still suffice to give the necessary exchange coupling. In the *s-d* theories, the coupling of the free conduction electrons to the bound *d* electrons affects both the energy and the moment. In some theories,[14,15] these effects are taken to be small, and the principal coupling is taken to be the inter-atomic effect (iii) (c) above arising from the slight overlap of *d* orbitals on neighboring atoms. Zener's theory,[15] on the other hand, pictures the inter-atomic coupling as always antiferromagnetic, and the coupling of the conduction electrons to the *d* electrons as being so strongly in favor of parallel spin alignment as to overbalance the former in the ferromagnetic metals. An interesting speculation, diametrically opposed to this, has been made by Vonsovski and Vlasov,[20] by Mott and Stevens,[16] and by Anderson.[21] This is that it is energetically more favorable for a conduction electron to align itself antiparallel to the 3*d* electrons, because in the antiparallel orientation it can lower its energy by hybridizing with unfilled 3*d* orbitals; i.e., it doesn't have to work so hard to keep away from the 3*d* electrons to the extent required by the exclusion principle. If this effect is large it can increase the effective ferromagnetic coupling of the 3*d* cores with each other, just as in Zener's theory, and at the same time will lower the saturation moment.

(4) *What is the origin of the large binding energies of the iron-group metals?* Although it has been argued[15] that the *d* shells in these metals have a purely repulsive interaction, the prevailing view is that in some way they contribute a large part of the binding energy. The itinerant and valence theories (though using rather different concepts) both picture this as arising from the hybridization of *s-p* conduction states with *d* states, to form bands of lower energy, or more effective valence bonds. A further suggestion has been made by Friedel and by Mott,[22] namely, that because of the small energy separation of the 3*d* and conduction states in the metal, the van der Waals interaction of the 3*d* shells can become quite large.

In all these matters, the views of the different schools are hard to compare and evaluate because each school works with an admittedly approximate picture ("good" to its adherents, "crude" to its rivals) and because the picture, sharp in its simplest version, becomes increasingly fuzzy when one tries to graft improvements onto it.

[20] S. V. Vonsovski and K. B. Vlasov, J. Exptl. Theoret. Phys. **25**, 327 (1953).
[21] P. W. Anderson (unpublished).
[22] J. Friedel, Proc. Phys. Soc. (London) **B45**, 769 (1952); N. F. Mott, Phil. Mag. **44**, 187 (1953).

Critique of the Not-Fully-Itinerant Theories

Now let me indicate some preferences. The valence theories, as they have been formulated so far, are not of the type that theoretical physicists like to use, in that there is almost no mathematical superstructure, and the adjustable parameters are almost simple transliterations of the experimental data. Thus, in spite of a qualitative appeal of some of their ideas, these theories have provided no framework for correlating the more complex phenomena. Van Vleck's[13] version of the minimum-polarity theory goes further in the direction of calculating things from first principles, but still does not provide a set of basic concepts adequate for a fully quantitative theory. As for the *s-d* theories, most of them in the past have made assumptions which can now be shown to be incorrect. For example, much of this work has ignored the fact that at least some of the 3*d* electrons *can* move from atom to atom, a fact I shall try to demonstrate later on. Other work has assumed an antiferromagnetic coupling of the spins of neighboring atoms, even in some ferromagnetic metals, an assumption inconsistent with recent neutron diffraction data. However, these theories have made a notable contribution to the theory of ferromagnetism, in that they have called attention to the fact that it is possible for the spins of bound electrons to be aligned via the spin polarization which a magnetic ion can induce in the sea of conduction electrons in which it is bathed. This "indirect exchange" coupling is now believed to be the dominant coupling mechanism in the rare earth metals, though of less importance in the iron group.

The two most recent theories of the *s-d* group, those of Mott and Stevens[16] and of Lomer and Marshall,[17] have adopted the idea, suggested long ago by Pauling[18] and revived in recent controversies[23] over x-ray determinations of electron density, that in some transition metals the number of electrons which have the compact orbits characteristic of 3*d* electrons in a free atom is much less than the number in the free atom. But there are other types of experimental evidence against this view, and it will be argued presently that it is most unreasonable on purely theoretical grounds. So this feature of these theories must be rejected. The most carefully thought-out of these theories, that of Mott and Stevens,[16] has another feature which seems dubious to me, but which is hard to reject definitively. This is the assumption that the anisotropy of the electrostatic field around an atom in a metal splits the 3*d* states into a high-energy and a low-energy group, the former being itinerant, the latter bound. My own opinion is that it is very doubtful that the crystal-field anisotropy is large enough to make a clear separation of this sort.

[23] R. J. Weiss and J. J. DeMarco, Revs. Modern Phys. 30,59 (1958); Phys. Rev. Letters **2**, 148 (1959); B. W. Batterman Phys. Rev. Letters **2**, 47 (1959); Komura, Tomiie, and Nathans, Phys. Rev. Letters **3**, 268 (1959).

Yardstick for Itinerant Theories

Only the itinerant theories are left to discuss. These are the theories which have gone farthest in the direction of setting up a quantitative description of the states of the electrons. However, none of these theories takes adequate account of the correlations in the positions of the electrons due to their electrostatic repulsion. This being the case, it is natural to gauge the adequacy of all these theories by comparing them with the best theory one can construct neglecting these correlations. The "best" such theory (by the criterion of having the lowest energy, and probably by most other criteria as well) is that obtained by solving the self-consistent field equations for electrons in a metal. This means that one determines the motion of each electron in the field produced by the nuclei and the average distribution of all the other electrons. Several efforts at calculations of this sort for iron group metals have been made, the most ambitious being the current one of Wood.[12] A study of such calculations makes clear several points:

The first point has to do with the concept of a *d* band, states in which an electron hops from atom to atom, being in a 3*d* level on each atom as it does so. Some of the simpler itinerant theories picture such a band of states as existing side by side with a normal *s-p* or conduction band, overlapping it in its energy range, but otherwise independent. They also picture holes in this *d* band as acting just like ordinary free particles, except for having a heavier effective mass. There are two things wrong with this picture. One, which has a crucial bearing on the occurrence of ferromagnetism,[24] is that there are different

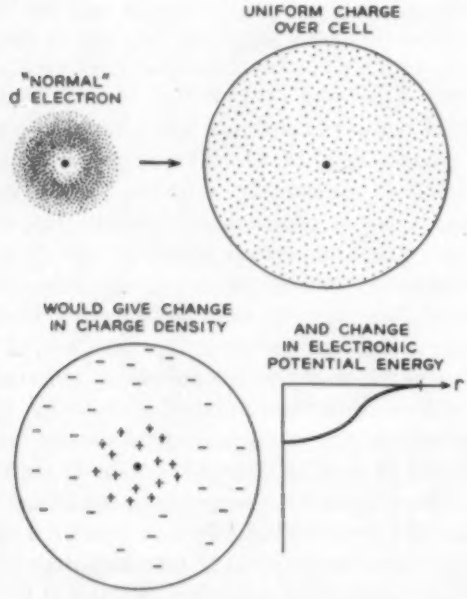
UNIFORM CHARGE OVER CELL
"NORMAL" d ELECTRON
WOULD GIVE CHANGE IN CHARGE DENSITY
AND CHANGE IN ELECTRONIC POTENTIAL ENERGY
r

FIG. 1. Change of charge density and potential energy produced by transferring an electron from a compact *d* state to a state with a uniform distribution over an atomic cell.

[24] Slater, Statz, and Koster, Phys. Rev. **91**, 1323 (1953).

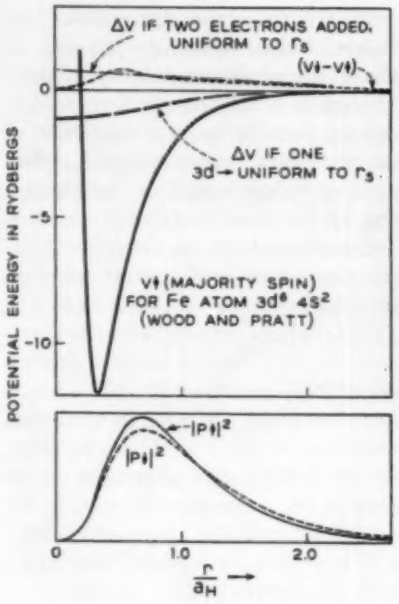

FIG. 2. Top, full curve: sum of the Coulomb, exchange, and centrifugal potentials for a majority-spin *d* electron in atomic iron, from the self-consistent field calculations of Wood and Pratt. Top, other curves: changes in the potential due to various hypothetical redistributions. Bottom: charge per unit radius for majority- and minority-spin 3*d* electrons.

kinds of 3*d* states, differing in the orientation of the electron's orbit around the nucleus. Thus, for a given wavelength and direction of motion of an electron wave formed from such states, there will be not just one quantum state, as for a free particle, but several. For certain values of the wave number, these states even have the same energy; in this case, one speaks of a "degenerate" band. The other defect of the simplified theory is that it turns out not to be possible to separate a band formed from the 3*d* atomic states from a band formed from states with larger orbits—the 4*s* and 4*p*; the actual states of electrons in a metal are usually a little of both.

Charge Distribution

Another conclusion which has come out of self-consistent field studies, is that in a metal such as iron neither the number of 3*d* electrons nor their spatial distribution differs very radically from that in the free atom. As recent x-ray studies[23] have made this a much talked about question, it may be worthwhile to elaborate a little on the reason, which is basically one of pure electrostatics. Figure 1 shows, in the upper left, the rather compact charge distribution of a *d* shell electron in iron, spherically averaged. Suppose we were to remove an electron from this compact state and distribute its charge uniformly over the much larger atomic cell, as shown at the upper right. This would alter the charge distribution in the atom by the amount shown at the lower left. The corresponding alteration in the potential energy of an electron would therefore be, as a function of radius, as shown in the curve at the lower right. In other words, each *d* electron that we place in a spread-out state changes the potential in such a way as to make the compact state more stable.

Now, there are two influences which might con-

ceivably act to spread out the 3*d* electrons in the metal. One, which by itself would surely not suffice to produce a major redistribution, is the altered boundary conditions which the wave function must satisfy. The other is the electrostatic effect of compressing the valence electrons of the atom into the smaller atomic volume of the metal. The upper part of Fig. 2 shows, in the full curve, the sum of the electrostatic potential and the effective potential of the centrifugal force arising from the angular momentum of a *d* electron, for a majority-spin *d* electron in atomic iron. The dot-dash curve shows the amount by which this potential would be changed if the renormalization of the valence distribution amounted to simply adding two electrons with a uniform distribution out to the radius r_s of the cell. The dashed curve is the one drawn schematically in Fig. 1, namely, the change in potential resulting from shift of a single *d* electron to a uniform distribution. Notice that such a shift would more than compensate the effect of valence-electron renormalization. The shifting of a number of *d* electrons to a uniform distribution clearly would be energetically unfavorable. To give an idea of the sensitivity of the 3*d* charge distribution to such changes in the potential, the dotted curve shows the difference of the effective potentials for majority and minority spin electrons, the corresponding charge distributions being drawn in at the bottom.

The conclusion from these simple arguments, which is given quantitative form by the recent band calculations of Wood,[12] is that the 3*d* electrons should be a little more spread out in the metal than in the free atom, but that neither their number nor their distribution will be radically changed. Correlation effects, which tend to make the *d* shell more compact, only reinforce this conclusion.

To justify this last statement I must take up another major topic, namely, the shortcomings of the self-consistent field approach and the direction in which one should correct it to take account of the fact that the electrons do not move as independently as this approach assumes, but correlate their motions to stay out of each other's way. Being able to do this, the several electrons which form the 3*d* shell of an atom will be less reluctant to occupy this central region of the atom than they would be if they moved independently. Therefore, they will huddle a little closer to the nucleus than self-consistent field theory predicts, and as the size of the 3*d* distribution is known to be fairly sensitive to the form of the potential energy function, we may expect this contraction to be appreciable.

TABLE II. Principal conclusions of Sec. 1.

Charge distribution of *d*-like electrons:
Only slightly different from that of free atom
Slightly expanded, but not as much so as self-consistent field calculations predict.
If itinerant picture is adopted, *d* band is:
Degenerate
Not fully separable from *s-p* band.
Correlation correction to itinerant picture:
Serious, but fluctuations in the number of *d* electrons on an atom are encouraged by compensating fluctuations of *s-p* electrons.

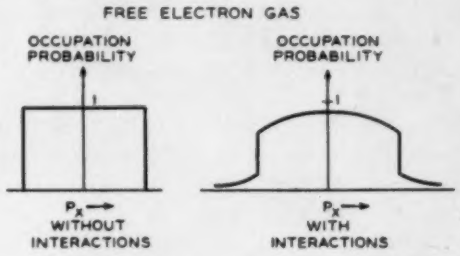

FIG. 3. Occupation of momentum states for a Fermi gas, with and without interactions between the particles.

Itinerancy vs Correlation

A more fundamental aspect of the correlation correction has to do with an objection sometimes raised by opponents of itinerant theories, who argue that since it costs quite a bit of energy to remove an electron from one isolated atom and put it on another isolated atom, the self-consistent field solution cannot be very near the truth, because it allows the wrong number of 3*d* electrons to be on an atom for much of the time. This objection has some validity, but I think not as much as its extreme proponents claim, because the electrostatic effects of having too many or too few 3*d* electrons on a given atom in a metal can be largely compensated by redistribution of the charge of the conduction electrons, which latter are surely quite mobile.

Table II summarizes the conclusions of this section.

2. FERMI SURFACE OF AN ASSEMBLY OF INTERACTING ELECTRONS

The remainder of this paper will be devoted to the thesis that many properties of pure transition metals can be understood and correlated using concepts which have an *exact* meaning for a system of interacting electrons, and to a plea for more theoretical and experimental work oriented in this direction. Although there are several such concepts, I shall discuss only the most important one, that of the Fermi surface.

Definition and Properties of the Fermi Surface

Consider first the lowest energy state of a gas of completely free electrons having no interactions with each other. Since the exclusion principle says that no more than one electron of each spin can occupy each momentum state, the distribution in momentum will have the familiar form shown at the left of Fig. 3, with all states below a certain limiting momentum occupied, all states above it empty. The occupation probability thus drops from one to zero as we cross the boundary of a sphere in momentum space, and this boundary is called the Fermi surface.

If the electrons repel each other, as real electrons do, it will no longer be possible for each electron to continue permanently in a state of a particular momentum; it will suffer accelerations, and may sometimes go faster than it ever would in the noninteracting case. Therefore, the occupation probability of the momentum states will no longer be one below the Fermi surface, but rather less than one, and it will no longer be zero in the region outside. One might suppose that the Fermi surface would be washed out completely, but according to current many-body theories[25] this is not the case. Instead, as shown on the right, there apparently remains, in the exact true state of affairs, a discontinuity in the momentum distribution at the Fermi surface.

A closely related property is that even in the presence of interactions there still seem to exist excited states of the many-electron system which can, in a certain abstruse but nevertheless exact sense, be described as having holes in certain states just below the Fermi surface and excited electrons in states just above it.[25,26] This analogy of states of the coupled many-electron system to states of a noninteracting assembly only holds for states very near the Fermi surface, not for all states. The reason for this is discussed in the appendix: if we try to construct a state of the interacting-electron system having an electron or hole far from the Fermi surface, electron-electron collisions will shift the electron or hole to other momentum states so rapidly that the initial state can by no means be described as stationary; however, if the electron or hole is placed very close to the Fermi surface, these collisions become very rare, and the initial state departs very little from stationarity.

These and similar arguments, put forward in embryonic form many years ago by Skinner[27] and more recently stressed by Mott,[28] are believed by many to apply as well to electrons in the crystal field of a metal as to the free-electron gas. This view is beginning to receive sophisticated theoretical attention from several angles.[29] If it is correct, then in the space of momentum or wave-number vectors for an electron there exists a surface across which the occupation probabilities of the possible one-electron states are discontinuous, and in the neighborhood of which there can exist quasi-particles, electron-like or hole-like, which can carry a current, be accelerated, etc. The surface so defined may be called the Fermi surface; such a surface exists in metals and does not exist in insulators.

In addition to these speculations, which if true are exactly true, one can make other speculations about the extent of the admittedly only approximate correspondence between the true states of interacting metallic electrons and the states of the itinerant theories which ignore interactions. For example, in the latter theories the volume of momentum space enclosed by the Fermi surface is exactly proportional to the number of electrons per unit volume. On the basis of what we know about the free-electron gas, it is plausible to speculate that in the many-electron theory of a metal this relation is still either exact or very nearly correct. [*Note added in proof.*—J. M. Luttinger (personal communication) has recently shown that the relation in question is exact for any model of interacting electrons for which perturbation series converge.] Another plausible speculation is that there exists a set of one-electron states of the traveling-wave type for which the occupation probability is comparable with unity inside the Fermi surface, small outside it. In other words, it is reasonable to hope that the discontinuity in occupation on crossing the Fermi surface is a major fraction of unity in real metals. This hope is supported by the smallness of the departure from unity for the high-density free-electron gas, by the modest magnitude of correlation energies for an electron gas of typical metallic density, by the comparative ideality of the momentum distribution found for alkali metals in positron-annihilation experiments, etc.; however, there is little evidence bearing on its reasonableness for transition metals.

Fermi Surfaces of Transition Metals

If the shape and location of the Fermi surface can be determined (and I shall argue presently that there is a reasonable chance this can be done), then a precise meaning can be attached to certain statements which the itinerant and *s-d* theorists often argue about. Figure 4 shows some typical examples of possible situations in a ferromagnetic metal. The top row, showing Fermi surfaces for up-spin and down-spin electrons which are both of rather simple form and not very different from each other, corresponds to the picture of all the 3*d* electrons being bound (or in filled bands), only a single band of weakly polarized conduction electrons being itinerant. The second row, with both Fermi surfaces of complex form but only slightly different, corresponds to the conception of itinerant 3*d* electrons which carry very little of the magnetization, so that the magnetization must be attributed mainly to bound electrons. The third row, with a complex Fermi surface for the minority spin direction and a simple one for the majority spin direction, corresponds to the picture of

[25] V. M. Galitski and A. B. Migdal, J. Exptl. Theoret. Phys. U.S.S.R. **34**, 159 (1958) (translation: Soviet Phys.—JETP **7**, 96 (1958)). Most of the current theories of the many-Fermion problem, e.g., those of footnote 26, imply the existence of this sort of discontinuity of occupation numbers, though they do not point it out explicitly. However, none of the treatments yet has full mathematical rigor.

[26] L. D. Landau, J. Exptl. Theoret. Phys. **30**, 1058 (1956); M. Gell-Mann, Phys. Rev. **106**, 368 (1957); N. M. Hugenholtz, Physica **23**, 481, 533 (1957); N. M. Hugenholtz and L. Van Hove, Physica **24**, 363 (1958).

[27] H. W. B. Skinner, Trans. Roy. Soc. (London) **239**, 95 (1940).

[28] N. F. Mott, Nature **178**, 1205 (1956).

[29] P. Nozieres and D. Pines, Phys. Rev. **109**, 1062 (1958); V. P. Silin, J. Exptl. Theoret. Phys. (U.S.S.R.) **33**, 495 (1957); W. Kohn and J. M. Luttinger, Phys. Rev. (in press). It is noteworthy, also, that for dilute electrons or holes in a semiconductor the many-body analysis can be carried through with much greater rigor than for the metal or the Fermi gas: W. Kohn, Phys. Rev. **105**, 509 (1957); A. Klein, Phys. Rev. **115**, 1136 (1959).

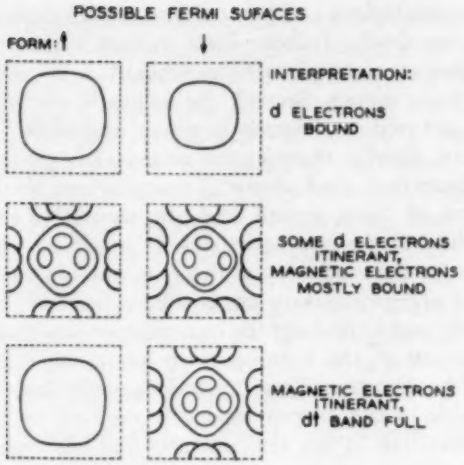

FIG. 4. Some possible forms of the Fermi surface in a ferromagnetic metal.

overlapping 3*d* and conduction bands, with the up spin 3*d* band full; this is a picture with the magnetic electrons itinerant.

We come now to the question: how can one determine the characteristics of the Fermi surface experimentally? Since most sources of information are indirect, it may be worthwhile to start by discussing an experiment which in principle could give the desired information directly, although in practice its accuracy does not suffice for this. When a positron is shot into a metal, it soon comes to rest and subsequently combines with an electron with emission of two gamma-ray quanta, which go off in nearly opposite directions in order to conserve momentum. The small but usually finite momentum of the combining electron is transmitted to the gamma rays, which then go off at an angle slightly different from 180°. Measurement of the angular distribution of gamma rays thus amounts to a measurement of the momentum distribution of the electrons of the metal.[30] Since this momentum distribution is discontinuous across the Fermi surface, the location and shape of the Fermi surface could in principle be determined. In practice, it turns out that the directly measured yield curves[31] for the practical type of slit geometry only have discontinuities of slope at the Fermi surface, and small fluctuations in the data can easily wash them out, as can the averaging over crystallographic directions in a polycrystalline sample.

There are other techniques of mapping out Fermi surfaces which have been used successfully in other materials, though they will be difficult to apply successfully to the iron group. These are methods based on the use of high magnetic fields and low temperatures, with material of sufficient purity to make the mean free path of the metallic electrons rather larger than the size of their cyclotron orbits in the magnetic field. Under these conditions, cyclotron resonance,[32] anomalous skin effect,[33] Hall effect,[34,35] magnetoresistance,[35] etc., can be made to yield information about the Fermi surface.

Although such detailed information is much to be desired, we do not have it now for transition metals. We do have, however, some information about certain properties which can be expressed as averages over the Fermi surface, and it should be possible to obtain still more information of this kind in the near future. A very well-known and very useful property of this sort is the contribution which the electrons make to the specific heat at low temperatures. This measures the number of quantum states per unit energy for the quasi-particles—electrons and holes near the Fermi surface. This in turn depends on the area of the Fermi surface and on the rate of variation of energy normal to it. The high values observed[36] for the electronic specific heats of all the iron group metals, except chromium, almost certainly mean that Fermi surfaces of the simple form shown in the top row of Fig. 4 do not occur for these metals. This conclusion is confirmed by less direct information from other sources. Of these, I shall mention only one, the electrical resistivity, whose high value in the iron group metals is, according to Mott,[37] to be interpreted as due to the availability of a large number of 3*d*-like states at the Fermi surface into which the conduction electrons—or quasi-electrons—can be scattered. Here again, chromium seems exceptional in showing little or none of this extra scattering. In the ferromagnetic and antiferromagnetic metals, there is, of course, an additional mechanism of scattering, namely scattering by the exchange fields of the thermally disordered spins.[38] This is responsible for the rapid rise of resistivity as the Curie point is approached from below. But at room temperature the spin ordering in iron, cobalt, and nickel is so complete that this is a very minor effect. Collisions of high-mobility conduction electrons with itinerant 3*d*-like electrons can also introduce extra resistivity,[39] but these too are probably unimportant near room temperature.

If we grant from all this that at least some of the 3*d*

[30] For a more complete discussion of the theory of positron annihilation, including the effects of Coulomb interactions and zero-point momentum of the positron, see R. B. Ferrell, Revs. Modern Phys. **28**, 308 (1956). The latter effects, though they have some important consequences, do not round off the discontinuity at the Fermi momentum.

[31] S. Berko and F. L. Hereford, Revs. Modern Phys. **28**, 299 (1956).

[32] See for example the detailed application to bismuth by Galt, Yager, Merritt, Cetlin, and Brailsford, Phys. Rev. **114**, 1396 (1959).

[33] See, for example, the application to copper by A. B. Pippard, Trans. Roy. Soc. (London) **250**, 325 (1957).

[34] J. A. Swanson, Phys. Rev. **99**, 1799 (1955).

[35] See, for example, E. S. Borovik, Izvest. Akad. Nauk S.S.S.R. Ser Fiz. **19**, 429 (1955) [translation: Bull. Acad. Sci. U.S.S.R. (Columbia Technical Translations, White Plains, New York) **19**, 383 (1955)].

[36] J. G. Daunt, in *Progress in Low-Temperature Physics*, edited by C. J. Gorter (Interscience Publishers, Inc., New York, 1955), Vol. 1, p. 202.

[37] N. F. Mott, Proc. Phys. Soc. (London) **47**, 571 (1935), Proc. Roy. Soc. (London) **A153**, 699 (1936); **156**, 368 (1936).

[38] T. Kasuya, Progr. Theoret. Phys. (Kyoto) **16**, 58 (1956); P. G. de Gennes and J. Friedel, J. Phys. Chem. Solids **4**, 71 (1958).

[39] W. G. Baber, Proc. Roy. Soc. (London) **A158**, 383 (1937).

electrons must be pictured as itinerant, we may still ask whether the bulk of the magnetic electrons of the ferromagnetic metals are itinerant. In other words, do the Fermi surfaces of up and down spin electrons differ by enough to account for the magnetic moment? There are again many possible sources of information, few of them conclusive at present. I shall only mention some arguments which have been unduly neglected. One is that if the 3*d* electrons are bound to specific atoms and yet have an average magnetic moment per atom different from that of a free atom with a partially filled 3*d* shell, then at low temperatures a superlattice of spins should form. If this does not show up in neutron diffraction, then one should picture the magnetic electrons as itinerant. Another related argument is that the presence of bound 3*d* electrons, of a number insufficient to exactly fill one of the subshells (e_g or t_{2g}) into which the 3*d* levels might be split by an environment of cubic symmetry in a crystal, must entail a departure of an atomic cell from full cubic symmetry, and either a superlattice or a noncubic nature for the crystal as a whole.[40] No indications of such structures are known, except in manganese. Finally, at least some of the possible models with bound 3*d* electrons would lead to an unquenched orbital magnetic moment in a cubic environment, hence to a g factor departing seriously from the spin-only value 2, contrary to observation.[40] Arguments of this type indicate that the magnetic electrons are itinerant in cobalt and nickel, but leave open the question whether they are in iron.

Concluding Remarks

Before closing, I would like to call attention to a group of experiments which, though only indirectly related to the Fermi surface, hold great promise for giving information about the states of magnetic electrons, at least in some materials. These are experiments which measure the magnetic fields $H(0)$, which the ferromagnetic electrons produce at the position of an atomic nucleus. This field, due to orbital moments, polarization of conduction electrons, and polarization of inner-shell electrons by the 3*d* electrons, can be measured by its orienting effect on the nucleus, via nuclear resonance,[41] gamma-ray correlations,[42] or nuclear specific heat.[43] Of the various contributions to $H(0)$, one can reasonably hope to estimate the orbital and inner-shell terms by a combination of theory and hyperfine-structure data from nonmetals. The empirical value of the remaining contribution, due to spin density of the magnetic and conduction electrons at the position of the nucleus, should give considerable insight into the extent to which *s* and *d* states get mixed in the metal, and the extent to which the Fermi surfaces of the two spins differ.

[40] P. W. Anderson (personal communication).
[41] A. C. Gossard and A. M. Portis, Phys. Rev. Letters **3**, 164 (1959); A. M. Portis and A. C. Gossard, J. Appl. Phys. **31**, 205 (1960).
[42] N. Kurti, J. phys. radium **20**, 141 (1959).
[43] V. Arp, N. Kurti, and R. Petersen, Bull. Am. Phys. Soc. Ser. II, **2**, 388 (1957).

The conclusions and admonitions of this section may be summarized as follows: First, at least some of the 3*d* electrons are to be pictured as itinerant in all or nearly all of these metals. Second, the magnetic electrons are to be pictured as itinerant in cobalt and nickel; iron is in doubt. Finally, there is great promise in experimental and theoretical work aimed at mapping out the Fermi surfaces of these metals and the associated inertial properties of the quasi-particles. It would be very desirable for the fundamental theorists to place the existence of a Fermi surface on as solid a basis of logic as possible, and to find out the quantitative significance of the volume of the Fermi surface for metals with far-from-free electrons. Experimentalists might find it very profitable to concentrate especially on work with very pure materials at low temperatures and high magnetic fields.

ACKNOWLEDGMENTS

I am much indebted to Dr. W. Kohn and Dr. J. M. Luttinger for some very illuminating discussions of many-electron theory, and to Dr. P. W. Anderson for a number of suggestions regarding electrons in transition metals.

APPENDIX: ASYMPTOTIC STATIONARITY OF QUASI-PARTICLE STATES

For noninteracting electrons the low-lying excited states consist, of course, of states with one or a number of electrons removed from states just inside the Fermi surface and placed in states just outside it. If one introduces a small electron-electron interaction into the theory, the Hamiltonian will acquire matrix elements connecting these states with other, mostly higher, states. The matrix elements from one of these low-lying states α to states of considerably higher energy will lower the energy E_α of the state in question, and change its wave function, but in a continuous and orderly manner, which will not introduce any confusion regarding which unperturbed state it originated from. The matrix elements connecting two states α, α' of nearly the same energy, on the other hand, will cause the perturbed stationary states to be such complicated linear combinations of the unperturbed ones as to make any one-to-one correspondence of the former with the latter rather meaningless. This is just another way of saying that the state α will be scattered into states α' with approximate conservation of the unperturbed energy. The quantitative effect of this part of the perturbation can be measured by the lifetime τ_α of the state α with respect to this sort of scattering, or by the associated natural width $\hbar/\tau_\alpha$. Now the density of states per unit excitation energy E_α above the ground state goes to zero as $E_\alpha \to 0$, so in this limit $\hbar/\tau_\alpha \to 0$ also. In fact, since an electron of a given excitation energy ϵ can only create holes within this same energy interval ϵ below the Fermi energy ϵ_f, and since only a fraction of order ϵ/ϵ_f of these hole states can be created without putting a scattered electron either in-

side the Fermi surface or at an energy $>\epsilon$ outside it, it is easy to see that $\hbar/\tau_\alpha$ must be of order ϵ^2 as $\epsilon<0$.[44] Therefore, for all sufficiently low-lying excited states $\hbar/\tau_\alpha \ll E_\alpha$. This means that one can define "asymptotically stationary states" α with the properties: they are in one-to-one correspondence with the unperturbed stationary states (electron-hole distributions); they are derived from the unperturbed states by continuous perturbation, using only the high-frequency matrix elements of the interaction; though not true stationary states of the perturbed system, their level width s get$\ll$ their excitation energies as the latter become small.

The picture given by the rather intuitive reasoning of the preceding paragraph has been verified in more careful studies of the general interacting-fermion or free-electron gas.[26] Although special difficulties have plagued attempts to make calculations of comparable rigor for electrons in the periodic field of a crystal, it is very reasonable to suppose that adjoining the ground state of a metal there exist asymptotically stationary states compounded out of "elementary excitations" identifiable as electrons or holes, each electron or hole having a wave vector in the neighborhood of a certain surface in the Brillouin zone. The surface thus defined may be called the Fermi surface; it is clear that its size and shape, and the normal derivative of the energy of an elementary excitation near it, enter into electronic specific heat and other properties in much the same way as in the theory for noninteracting electrons.

[44] V. L. Ginzburg and V. P. Silin, J. Exptl. Theoret. Phys. **29**, 64 (1955); see also footnotes 27 and 39 above.

JOURNAL OF APPLIED PHYSICS SUPPLEMENT TO VOL. 31, NO. 5 MAY, 1960

Microwave Resonance in Rare Earth Iron Garnets*

C. KITTEL
Miller Institute for Basic Research in Science, University of California, Berkeley 4, California

This paper gives an elementary discussion of the theory of g values and line widths in ferromagnetic resonance in certain rare earth garnets. The experimental facts are reviewed briefly.

IN three recent papers, de Gennes, Portis, and the present author have considered the theory of several aspects of microwave resonance in the rare earth iron garnets and also in yttrium iron garnet containing rare earth ions as impurities. The papers are concerned successively with g values,[1] line widths,[2] and giant anisotropy peaks.[3] The purpose of the present note is to make available the central results relating to g values and line widths in a brief and simple form.

The exchange interactions in the rare earth iron garnets may be characterized, according to the analysis of Pauthenet,[4] by two strong features: (1) a strong exchange interaction among the ferric ions, as demonstrated by the approximate equality of the Curie temperatures of YIG and the several rare earth iron garnets; (2) much weaker exchange interactions between the ferric and rare earth ions and also between the rare earth ions themselves.

The relaxation time of the ferric ions alone is quite long; this follows because the intrinsic line width in pure YIG is very narrow, less than 1 oe. The relaxation times of the trivalent rare earth ions of Sm, Tb, Dy, Ho, Er, Tm and Yb are probably quite short (by virtue of their strong orbital components) and above 100–200°K may be the dominant aspect of the problem. Our belief in the shortness of the relaxation times is based on the line widths of rare earth ions in dilute paramagnetic salts measured by Bleaney and coworkers at Oxford.

We may readily derive a relation for the g value in the limit of infinitely rapid relaxation of the rare earth ions. Denoting by M_A the magnetization of the ferric ions and by M_B the magnetization of the rare earth ions, we have, for the equation of motion of M_A,

$$d\mathbf{M}_A/dt=\gamma_A\mathbf{M}_A\times(\mathbf{H}+\lambda\mathbf{M}_B), \tag{1}$$

where $\lambda\mathbf{M}_B$ is the exchange field on A from B. If the relaxation frequency of the B ions is taken to be infinitely fast, then $\mathbf{M}_B$ must at every instant point exactly in the direction of the total effective field $\mathbf{H}+\lambda\mathbf{M}_A$ acting on the B ions. We must therefore have

$$\mathbf{M}_B=(\mathbf{H}+\lambda\mathbf{M}_A)/|\mathbf{H}+\lambda\mathbf{M}_A| \cong(\mathbf{H}+\lambda\mathbf{M}_A)M_B/\lambda M_A. \tag{2}$$

On substituting (2) in (1), and noting that $\mathbf{M}_A\times\mathbf{M}_A=0$, we have

$$d\mathbf{M}_A/dt=\gamma_A[1+(M_B/M_A)]\mathbf{M}_A\times\mathbf{H}, \tag{3}$$

so that

$$g_{\rm eff}=g_A[(M_A+M_B)/M_A]. \tag{4}$$

The correction to (4) occasioned by a finite relaxation frequency is considered in references 1 and 2. Generally

* Supported in part by the National Science Foundation.

[1] C. Kittel, Phys. Rev. **115**, 1587 (1959).

[2] P.-G. de Gennes, C. Kittel, and A. M. Portis, Phys. Rev. **116**, 323 (1959).

[3] C. Kittel, Phys. Rev. Letters **3**, 169 (1959); a more complete account has been submitted to Phys. Rev.

[4] R. Pauthenet, Ann. phys. **3**, 424 (1958).

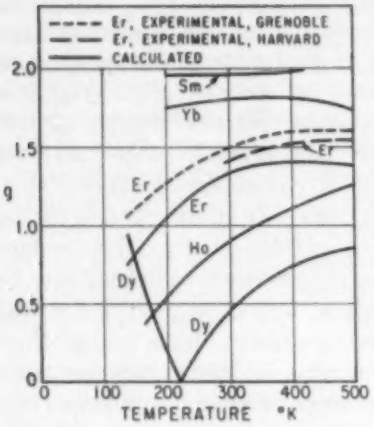

FIG. 1. Theoretical g factors as a function of temperature, as calculated from Eq. (4); also shown are experimental results for ErIG. Present uncertainties in the experimental magnetizations and g values should be borne in mind in comparing the calculated and experimental curves.

speaking, the relation (4) gives a fair account of the available experimental data from room temperature to the neighborhood of the Curie temperature, for the ions commonly supposed to relax rapidly. In Fig. 1 we give several calculated curves of g *vs* temperature, together with experimental data for ErIG from the Harvard[5] and Grenoble[6] groups. Not shown are experimental curves from Harvard for HoIG, SmIG, and YbIG. The calculated curves are not in bad agreement with the experimental results, if we exclude data taken below 200°K, where the relaxation is apparently not always sufficiently rapid for our theory to be applicable.

The measure of success of our model applied to g values encourages the discussion of line widths on the same model. The line width, however, will vanish if the rare earth relaxation frequency is infinite. In the temperature range in which the g value theory is applicable, we can obtain an expression for the line width by considering together with Eq. (1), the equation of motion of the B lattice, including a damping term of the Landau-Lifshitz form. This is a special case of a problem considered by Wangsness.[7] In reference 1 we find the result

$$\Delta H/H \cong \gamma_A \lambda M_B \tau, \tag{5}$$

where τ is the relaxation time of the rare earth ions. The derivation of (5) is slightly tedious, and it is more interesting to go into a physical analysis of the line width, using the concept of motional narrowing familiar in nuclear resonance from the classic work of Bloembergen, Pound, and Purcell. The result (5) holds in the temperature region in which the rare earth ions may be treated as relaxing rapidly, but not over the Curie temperature. We note that the shorter the relaxation time τ of the rare earth ions, the narrower the width ΔH of the resonance line.

We consider first the situation above the Curie temperature. Here, the ferric spin lattice is disordered, and we have to deal with the problem of a single ferric ion coupled by a random exchange field $H_{AB}=\omega_{AB}/\gamma_A$ to a rare earth ion supposed to have a radically different g value from the ferric ion. The line width is controlled by the fraction of the noise spectrum falling within the *static* line width ω_{AB}. If τ_c is the correlation time of the random process, then $\omega_{AB}\tau_c$ is the effective fraction of the power spectrum. Thus, the final width for $T>T_c$ is

$$\Delta\omega \approx (N_B/N_A)\omega_{AB}^2\tau_c; \tag{6}$$

this is an exchange-narrowed width or a motionally-narrowed width according to whether the correlation time ω_{AA}^{-1} of the AA exchange interaction or the correlation time τ of the relaxation of the rare earth ions is the shorter time, respectively. The N's denote the concentration of A and B ions.

Below the Curie temperature the ferric spin lattice is ordered, and we have to deal only with the relaxation time τ. The dominant part of the transition rate is then

$$W \approx (N_B/N_A)\omega_{AB}^2\tau, \tag{7}$$

in the temperature region intermediate between the Curie temperature down to a temperature such that the B-ion relaxation frequency is no longer high in comparison with the AB exchange frequency.

In many of the spin equilibrium problems encountered in electron and nuclear resonance the relaxation frequency is simply $2W$. The usual requirement that this be true is that the over-all energy splitting of the individual system be $\ll kT$. In our problem, the strong AA exchange interaction means that we must treat the A spin lattice as a whole as the system, so that the total Zeeman splitting is $\gg kT$ and the usual result fails for the relaxation frequency. It is found instead that the relaxation frequency is reduced below (7) by a factor $\hbar\omega/kT$, where T is the temperature of the phonon heat bath and ω is the frequency of the uniform precession mode. We can understand this factor qualitatively by comparison with a two-level system, where a single quantum transition will relax the system. In our system, with $\sim 10^{22}$ excited states having zero wave vector, the

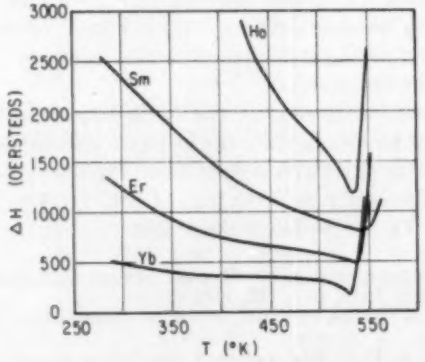

FIG. 2. Line width vs temperature in polycrystalline rare earth garnets at 9200 mc/sec, according to Rodrigue et al.[5]

[5] Rodrigue, Pippin, Wolf, and Hogan, Inst. Radio Engrs. Trans. on Microwave Theory Tech. MTT **6**, 83 (1958); G. P. Rodrigue, H. Meyer, and R. V. Jones, J. Appl. Phys. **31**, 376 (1960).
[6] B. Dreyfus, Compt. rend. (Paris) **241**, 552 (1955).
[7] R. K. Wangsness, Phys. Rev. **111**, 813 (1958).

system relaxes from the nth excited state by diffusion in n space. We consider one-phonon relaxation. The spin system gradually settles down to equilibrium because the rate of downward transitions is proportional to $\bar{p}+1$ and the rate of upward transitions is proportional to $\bar{p}$; here, $\bar{p}$ is the thermal average quantum number of the phonons of frequency ω in the heat bath. A net downward flow results from the fraction

$$\frac{(\bar{p}+1)-\bar{p}}{(\bar{p}+1)+\bar{p}} \approx \frac{1}{2\bar{p}} \approx \frac{\hbar\omega}{2kT} \tag{8}$$

of the transitions. On combining (7) and (8), we have

$$\Delta\omega \approx (N_B/N_A)\omega_{AB}^2\tau(\hbar\omega/kT) \tag{9}$$

for the coherent part of the relaxation in the intermediate temperature range. This result is just the line width given in Eq. (5). If we let $M_B \approx N_B\mu_B^2(\lambda M_A)/kT$, according to the Curie law for field λM_A, (5) becomes

$$\begin{aligned}\Delta\omega &\approx (N_B/N_A)(\gamma\lambda M_A)^2\tau(\mu_B/\gamma)(\omega/kT) \\ &\approx (N_B/N_A)\omega_{AB}^2\tau(\hbar\omega/kT),\end{aligned} \tag{10}$$

in agreement with (9). Rigorous calculation shows that the coherent part of the line width calculated by the microscopic and macroscopic methods are exactly identical. The line width in the intermediate temperature region decreases as the temperature is increased, partly because of the $1/T$ factor in (10) and partly because τ may be expected to decrease as the temperature is increased. This result is in accord with the experimental observations of Fig. 2.

At low temperatures, such that $\omega_{AB}\tau \gg 1$, the resonance line intercepts only the high-frequency tail of the noise spectrum. Here a calculation shows that, roughly,

$$\Delta\omega/\omega \approx M_B/\omega_{AB}\tau M_A, \tag{11}$$

so that the line width is directly proportional to the relaxation frequency $1/\tau$ of the B ions; the width is, as in the other temperature regions, directly proportional to the concentration of rare earth ions on the B sites.

We have then the over-all temperature dependence of the line width shown in Fig. 3. Starting from 0°K, the width increases as the rare earth relaxation frequency increases with temperature. The width goes through a maximum near $\omega_{AB}\tau \approx 1$; the position of the maximum is not expected to depend markedly upon the rare earth ion concentration, but the height of the whole curve may be directly proportional to the concentration of rare earth ions. At still higher temperatures the motional-narrowing effect sets in and the width decreases. Near the Curie temperature there is a sharp rise to a high plateau above T_c; the rise has been observed experimentally, but no work in the plateau region has been reported. The plateau is not necessarily horizontal.

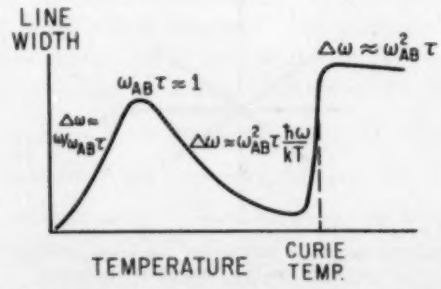

FIG. 3. Schematic indication of the line width vs temperature. The factor N_B/N_A, giving the fraction of rare earth ions, has been omitted from the right-hand side of each expression for $\Delta\omega$.

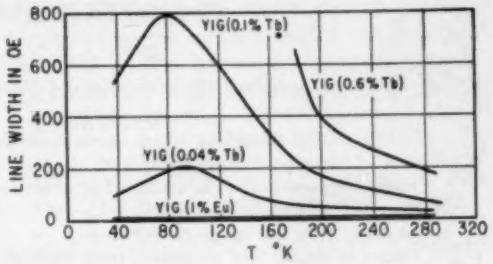

FIG. 4. Line width vs temperature in YIG containing small amounts of Tb, after Dillon and Nielsen. The Eu^{+++} ion in the lower curve is probably in a $J=0$ state and does not contribute to relaxation processes.

In all temperature regions the contribution of the rare earth ions to the line width is expected to be directly proportional to the concentration of rare earth ions, according to (6), (9), and (11). In this connection, Sirvetz and Zneimer[8] have reported at room temperature Sm substitution for Y in YIG produces an approximately linear increase in line width with Sm content. At 10 kMc/sec and room temperature, they report $\Delta H \approx 22$ oe/at. % Sm, in satisfactory agreement with the observed $\Delta H \approx 2000$ to 2400 oe in SmIG. In Fig. 4, further evidence is presented on the effect of rare earth contaminants in YIG, from the work of Dillon and Nielsen.[9] Thus the maximum in the line width of YIG at low temperatures, as reported in the early experimental work, can now be attributed with some confidence to rare earth impurities or, as suggested by R. L. White,[10] to rapidly relaxing impurities of the first transition element group, such as ferrous ion.

Line width and relaxation in pure YIG are considered theoretically by Sparks and Kittel,[11] and R. London.[12]

ACKNOWLEDGMENTS

I am indebted to P.-G. de Gennes and A. M. Portis for their invaluable collaboration on this problem. Thanks are due R. L. White for his initial stimulus to undertaker the problem. Part of the work was undertaken in connection with consultation at the Hughes Research Laboratories.

[8] M. H. Sirvetz and J. E. Zneimer, J. Appl. Phys. **29**, 431 (1958).
[9] J. F. Dillon, Jr., and J. W. Nielsen, Phys. Rev. Letters **3**, 30 (1959).
[10] R. L. White, Phys. Rev. Letters **2**, 465 (1959).
[11] M. Sparks and C. Kittel, Phys. Rev. Letters (to be published).
[12] R. London (to be published).

Crystal Distortion in Magnetic Compounds

JUNJIRO KANAMORI*
Institute for the Study of Metals, University of Chicago, Chicago 37, Illinois

The crystal distortion which arises from the Jahn-Teller effect is discussed in several examples. In the case of compounds containing Cu^{2+} or Mn^{3+} at octahedral sites, the lowest orbital level of these ions is doubly degenerate in the undistorted structure, and there is no spin-orbit coupling in this level. It is shown that, introducing a fictitious spin to specify the degenerate orbital states, we can discuss the problem by analogy with the magnetic problems. The "ferromagnetic" and "antiferromagnetic" distortions are discussed in detail. The transition from the distorted to the undistorted structure is of the first kind for the former and of the second kind for the latter. Higher approximations are discussed briefly. In compounds like FeO, CoO, and $CuCr_2O_4$, the lowest orbital level is triply degenerate, and the spin-orbit coupling is present in this level. In this case the distortion is dependent on the magnitude of the spin-orbit coupling relative to the strength of the Jahn-Teller effect term. The distortion at absolute zero temperature and its temperature dependence are discussed.

A. INTRODUCTION

THE spontaneous crystal distortion is observed in various magnetic compounds. Generally it is a cooperative phenomenon, and the crystal is of high (either cubic or trigonal) symmetry above the transition temperature and of lower symmetry below the transition temperature. Since the mechanism of the distortion and its statistical-mechanical aspect depend on the species of the ions involved, we concentrate in this paper on the cases in which the electronic orbital level of the magnetic ion is degenerate in the undistorted crystal structure. As has been discussed by Goodenough and Loeb,[1] Goodenough,[2] Dunitz and Orgel,[3] such cases present interesting examples of the Jahn-Teller[4] effect in the crystal. In this paper we discuss the microscopic and statistical-mechanical aspects of this effect in several representative crystals.

Many spinel-type crystals containing Cu^{2+} or Mn^{3+} at octhahedral sites such as $CuFe_2O_4$ and Mn_3O_4 deform from cubic to tetragonal symmetry ($c/a>1$). The transition temperature is 360°C for $CuFe_2O_4$[5] and 1170°C for Mn_3O_4.[6] $(c-a)/a$ is about 6% for the former and about 15% for the latter. The distortion in these substances is attributed by the authors mentioned above to the Jahn-Teller effect, which can be stated as follows: when the electronic level of a molecule is degenerate at a structure of high symmetry, this structure is generally unstable and the molecule will have a sturcture of lower symmetry. In the case of the spinel-type substances, the lowest electronic orbital level of Cu^{2+} or Mn^{3+} is doubly degenerate when the crystal is undistorted and is split into two levels when the crystal is distorted. The energy of the two orbital states changes linearly with the tetragonal distortion as illustrated in Fig. 1 where the abscissa is proportional to the tetragonal distortion. Therefore the structure of cubic symmetry cannot be stable at the absolute zero of temperature. At sufficiently high temperature, however, we can expect that the cubic structure is stable because more entropy will be available in the undistorted structure than in the distorted structure. The phenomenon is cooperative because the distortion around one magnetic ion will influence neighboring magnetic ions. Finch, Sinha, and Sinha[7] presented a treatment of this collective Jahn-Teller effect which will be referred to in later sections. We discuss in this paper the problem from a different point of view and try to construct a theory based on the microscopic Hamiltonian. We confine ourselves in this paper mostly to the first approximation, which is correct in the strong coupling limit at absolute zero. Further details will be published in another paper.

In the substances mentioned above, the transition temperature of the crystal structure does not coincide with the magnetic transition temperature at which the spin ordering begins. This is because the spin-orbit coupling vanishes in the first order in the degenerate orbital level, and thus the spin system is independent of the orbital level scheme. However, antiferromagnetic monoxides of the iron-group elements such as Mn, Fe,

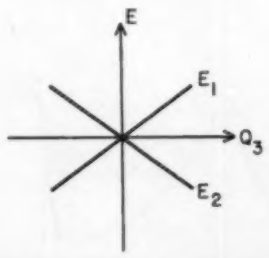

FIG. 1. Dependence of the energies of the lowest orbital states of Cu^{2+} or Mn^{3+} on the tetragonal distortion.

* On leave from Department of Physics, Osaka University, Osaka, Japan.

[1] J. B. Goodenough and A. L. Loeb, Phys. Rev. **98**, 391 (1955).

[2] J. B. Goodenough, Phys. Rev. **100**, 564 (1955).

[3] J. D. Dunitz and L. E. Orgel, J. Chem. Phys. Solids **3**, 20 (1957).

[4] H. A. Jahn and E. Teller, Proc. Roy. Soc. (London) **A161**, 220 (1937).

[5] H. Ohnishi, T. Teranishi, and S. Miyahara, J. Phys. Soc. Japan **14**, 106 (1959).

[6] H. F. McMurdie, B. M. Sullivan, and F. A. Mauer, J. Research Natl. Bur. Standards **45**, 35 (1950).

[7] G. I. Finch, A. P. B. Sinha, and K. P. Sinha, Proc. Rov. Soc. (London) **A242**, 28 (1957).

Co, and Ni show characteristic distortion at their Néel temperature.[8] Above the Néel temperature they have the rock-salt type crystal structure. Below the Néel temperature the crystal of MnO and NiO contracts slightly along one of the {111} directions and becomes rhombohedral. The crystal of FeO becomes also rhombohedral, but it elongates along a body-diagonal. The crystal of CoO becomes tetragonal. The distortion in FeO and CoO is of the order of 10^{-2}, while it is of the order of 10^{-3} for MnO and NiO. The present author discussed these substances previously,[9] but we shall discuss the cases of FeO and CoO briefly, because they present examples of the Jahn-Teller effect in the presence of the spin-orbit coupling. The lowest electronic orbital level of Fe^{2+} and Co^{2+} in the undistorted crystal is triply degenerate and the spin-orbit coupling is present in this level. Generally speaking, the spin-orbit coupling is incompatible with Jahn-Teller effect because the latter effect discriminates one orbital state with a real wave function from other states, and the spin-orbit coupling vanishes in such a state. When the directions of the spins are at random, degenerate orbital states are equally occupied. Below the Néel temperature, however, the direction of the spins, which are subject to a strong exchange field, is fixed and consequently the orbital states, which are coupled with the spin, are no longer equally occupied, or in other words, the shape of the electronic cloud has no longer cubic symmetry. Thus the crystal distortion which produces the maximum energy lowering of an orbital state will be favored.[10] The result of the detailed calculation shows that the magnitude of the spin-orbit coupling relative to the Jahn-Teller effect is actually strong enough to support the above picture and the calculated distortion agrees well with the experimental data.

$CuCr_2O_4$ shows the tetragonal distortion with $c/a<1$ above the magnetic transition temperature.[11] In this substance, Cu^{2+} is situated at tetrahedral sites and the lowest orbital level is triply degenerate like Fe^{2+} in FeO. As pointed out by Dunitz and Orgel,[3] the strength of the Jahn-Teller effect is strong enough to overcome the spin-orbit coupling. Some discussions will be given on the statistical mechanical treatment of this case.

In Secs. B and C, the case of Cu^{2+} or Mn^{3+} at octahedral sites will be discussed. In Sec. D the crystal structure of MnF_3 will be discussed. The characteristic distortion of this crystal as compared with FeF_3 and CoF_3 can be explained as a manifestation of the collective Jahn-Teller effect. In Sec. E we discuss some unsatisfactory points in the discussions of the preceding sections and the higher approximation. Section F deals with the cases of the Jahn-Teller effect in the presence of the spin-orbit coupling.

B. THE JAHN-TELLER EFFECT ARISING FROM Cu^{2+} OR Mn^{3+} AT OCTAHEDRAL SITES

The orbital states of $Cu^{2+}(d^9)$ can be specified by the orbital which is occupied by the hole in the d shell. In the case of $Mn^{3+}(d^4)$, the spins of four d electrons are parallel to each other according to the Hund rule, and therefore the orbital states can be specified by the orbital occupied by the hole in the half d shell. The d level of a free ion is split in the crystalline field of cubic symmetry into two sublevels, the triply degenerate $d\epsilon$ level and the doubly degenerate $d\gamma$ level. Since at octahedral sites the $d\gamma$ level lies higher than the $d\epsilon$ level, the lowest orbital states of both ions are such that one of the $d\gamma$ orbitals is occupied by the hole. We specify by φ_1 the wave function of the state in which the $d\gamma$ orbital given by $d(x^2-y^2)$ is occupied by the hole, and by φ_2 the wave function of the state in which the other $d\gamma$ orbital given by $d(2z^2-x^2-y^2)$ is occupied by the hole, where (x^2-y^2) and $(2z^2-x^2-y^2)$ denote the angular part of the d orbitals, the coordinates being referred to the cubic axes. It is convenient for the following discussion to introduce the Pauli spin matrix σ which operates in the two dimensional space spanned by φ_1 and φ_2 as follows:

$$\sigma_z\varphi_1=\varphi_1, \quad \sigma_z\varphi_2=-\varphi_2, \quad \sigma_x\varphi_1=\varphi_2 \quad \text{and} \quad \sigma_x\varphi_2=\varphi_1. \quad (1)$$

First we discuss briefly the case of a molecule consisting of a Cu^{2+} or Mn^{3+} and six octahedrally surrounding negative ions. Van Vleck[12] showed that the normal coordinates of the vibration whose associated crystalline field splits the degenerate orbital level in such a way as shown in Fig. 1 are given by

$$Q_2=(1/\sqrt{2})(X_1-X_4-Y_2+Y_5)$$

and

$$Q_3=(1/\sqrt{6})(2Z_3-2Z_6-X_1+X_4-Y_2+Y_5), \quad (2)$$

where X, Y, and Z are the coordinates of the surrounding negative ions, the suffix denoting the ion involved in the motion. Figure 2 illustrates the normal modes given by Q_2 and Q_3 and the numbering of the negative ions. The effective Hamiltonian of the interaction between Q's and φ's can be expressed as

$$H_1=-g\sqrt{C}(\sigma_z Q_3+\sigma_x Q_2), \quad (3)$$

where g is the coupling constant which has the dimension of the square root of the energy and can be calculated from the knowledge of C and the crystalline field produced by Q's; C is defined as the coefficient of the

[8] T. Nagamiya, K. Yosida, and R. Kubo, Advances in Phys. 4, 1 (1955).
[9] J. Kanamori, Progr. Theoret. Phys. (Kyoto) 17, 177 and 197 (1957).
[10] Correctly speaking, the exchange energy has no preference in determining the direction of the spins. Therefore the energy of the distortion which is dependent on the direction of the spins will make an important contribution to the determination of the direction.[9]
[11] S. Miyahara and H. Ohnishi, J. Phys. Soc. Japan 12, 1296 (1956).
[12] J. H. Van Vleck, J. Chem. Phys. 7, 472 (1939).

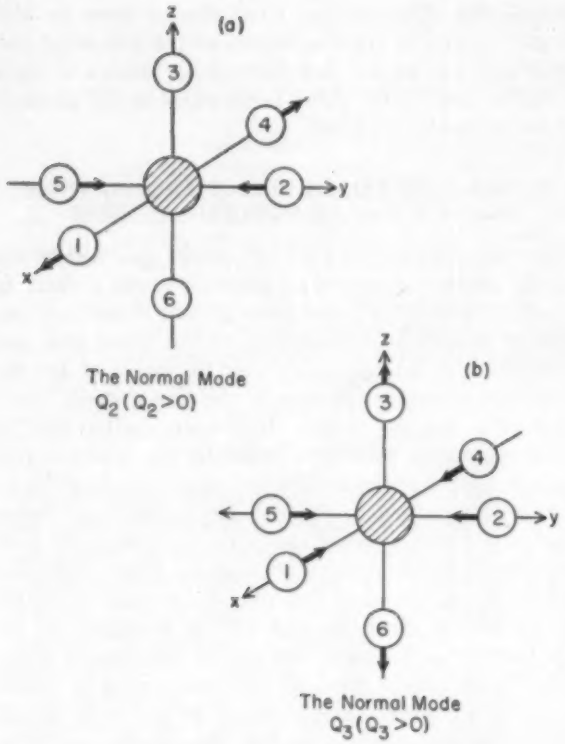

FIG. 2. (a) The normal mode Q_2 ($Q_2>0$).
(b) The normal mode Q_3 ($Q_3>0$).

potential energy associated with Q's which is given by

$$H_2=(C/2)(Q_2^2+Q_3^2). \tag{4}$$

The Hamiltonian (3) is determined, except for the constant $g\sqrt{C}$, from the requirement of invariance under the transformation of the cubic group.[13]

The distortion at absolute zero is obtained by minimizing the eigenvalue of $H=H_1+H_2$ with respect to Q_2 and Q_3. The result is

$$Q_{20}=(g/\sqrt{C})\sin\theta \quad \text{and} \quad Q_{30}=(g/\sqrt{C})\cos\theta \tag{5}$$

with arbitrary θ. The electronic state is such that the average of σ's with respect to this state is

$$\bar{\sigma}_z=\cos\theta \quad \text{and} \quad \bar{\sigma}_x=\sin\theta. \tag{6}$$

The total energy is given by $-g^2/2$. Thus the lowest state cannot be determined uniquely with the Hamiltonian, (3) and (4), except that the distortion corresponds to a point on the circle with a radius $\delta=g/\sqrt{C}$ in the Q_3Q_2 plane. Correspondingly the electronic state is specified only by the condition that the average value of the vector operator $\boldsymbol{\sigma}$ lies in the $\sigma_x\sigma_z$ plane, or in other words, the wave function is the eigenfunction of $\sigma_z\cos\theta+\sigma_x\sin\theta$ with arbitrary (real) θ (see Fig. 3). The point in the direction of $\theta=0$ in the

[13] Q_2,Q_3 and φ_1,φ_2 are respectively the bases of the two-dimensional representation of the cubic group. It can be shown that σ_x and σ_z transform in the same way as Q_3 and Q_2.

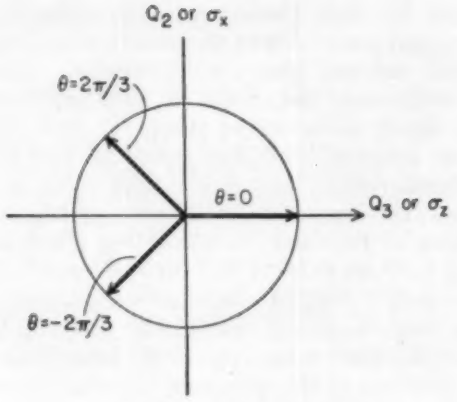

FIG. 3. The Q_3Q_2 and $\sigma_x\sigma_z$ plane.

Q_3Q_2 plane corresponds to the tetragonal distortion along the z axis (the ions on the z axis go away from the magnetic ion and the ions on the x and y axis come nearer to the ion, since $Q_3>0$). From (2) and (5) it is easily shown that the points with $\theta=+2\pi/3$ and $-2\pi/3$ correspond to the tetragonal distortions along the x axis and the y axis, respectively. As will be inferred from this fact, the cubic symmetry requires only the threefold symmetry in the Q_3Q_2 or $\sigma_x\sigma_z$ plane. Therefore we can expect that an anisotropic energy whose angular dependence is $\cos 3n\theta (n=1, 2, \cdots)$ will be produced from the higher order terms which are neglected so far.

Öpik and Pryce[14] pointed out that the anharmonic terms of the potential energy associated with Q_2 and Q_3 give rise to such an anisotropy energy. The lowest order term of the anharmonic terms is given by

$$-A_3(Q_3^3-3Q_3Q_2^2). \tag{7}$$

Inserting (5) into (7), we obtain the first-order contribution of (7) to the energy as

$$-A_3\delta^3\cos 3\theta. \tag{8}$$

Öpik and Pryce showed that the sign of A_3 is generally positive. This leads to the conclusion that $\theta=0$ or $\pm 2\pi/3$ gives the minimum energy, or in other words, the tetragonal distortion with the elongated tetragonal axis is the stable structure. This result is in accord with the experiments except in a few cases. On the other hand, Liehr and Ballhausen[15] showed that the higher order coupling between Q's and σ's given by

$$B_3[(Q_3^2-Q_2^2)\sigma_z-2Q_2Q_3\sigma_x] \tag{9}$$

contributes to the anisotropy energy. Inserting (5) and (6) into (9), we can see that this term also gives to the energy proportional to $\cos 3\theta$ given by

$$B_3\delta^2\cos 3\theta. \tag{10}$$

[14] U. Öpik and M. H. L. Pryce, Proc. Roy. Soc. (London) **A238**, 425 (1957).
[15] A. D. Liehr and C. J. Ballhausen, Ann. Phys. (N. Y.) **3**, 304 (1958).

They showed, however, that B_3 is calculated to be positive when the surrounding negative ions are assumed to be point charges. Therefore the effect of (10) is opposite to that of (8). However, if the covalent effect has a tendency to favor the square bond formation of Cu^{2+} (or Mn^{3+}), it will give rise to the term similar to (9) with negative B_3. One of the exceptional cases in which the interaction (9) with positive B_3 seems to be the most effective is the crystal of K_2CuF_4.[16] However, in the isomorphous crystal K_2NiF_4, the octahedron made of six F^- is also contracted along the tetragonal axis.[17] Since Ni^{2+} will not cause the Jahn-Teller effect, Cu^{2+} in K_2CuF_4 is considered to be subject to the tetragonal field even in the absence of the Jahn-Teller effect. In the present author's opinion we cannot conclude that the interaction (9) with positive B_3 is the decisive factor in determining the distortion specified by $Q_3<0$ in K_2CuF_4.

We now proceed to the discussion of the Jahn-Teller effect in the crystal. For simplicity we consider in the following a crystal in which every ion is at center of symmetry and whose unit cell contains one Cu^{2+} or Mn^{3+} at a site of cubic symmetry. The ideal perovskite or ReO_3 type crystals satisfy these conditions. The discussion can be extended to more complicated crystals without difficulty.

When the periodic boundary condition is assumed, the normal modes of the vibration in the crystal are plane waves with the normal coordinate $q_{\mathbf{k}s}$, where $\mathbf{k}$ is the propagation vector and s specifies one of the modes belonging to the same $\mathbf{k}$. With the periodic boundary condition, however, we need some parameters which describe the bulk deformation of the crystal. For this purpose, we use the strain components, $e_{ij}(i,j=x,y,$ and $z)$, which are defined with reference to the undistorted cubic crystal. The normal coordinates $q_{\mathbf{k}s}$ are referred to the lattice which is uniformly deformed from the cubic as described by e_{ij}.[18]

As for the interaction between e_{ij} and σ of each ion, we can see from the discussion of the single molecule case that in the first order only the Q_2- and Q_3-like bulk deformation can produce the crystalline field which lifts the degeneracy of the orbital level. For $q_{\mathbf{k}s}$ the interaction with the $\mathbf{j}$th ion will be different from the interaction with the zeroth ion by the phase factor, $e^{i\mathbf{k}\cdot\mathbf{j}}$, where $\mathbf{j}$ is the position vector of the $\mathbf{j}$th ion measured from the zeroth ion in the unit of the lattice constants. The magnitude of the interaction between $q_{\mathbf{k}s}$ and σ_j will be specified by the coupling constant $g_{\mathbf{k}s,z}$ or $g_{\mathbf{k}s,x}$ which has the same dimension as g in the single molecule case. Thus we write the total Hamiltonian as follows:

$$
\begin{aligned}
H=&\Omega(c_{11}-c_{12})(u_z^2+u_x^2)/2\\
&-g_0[\Omega(c_{11}-c_{12})/N]^{\frac{1}{2}}(u_z\textstyle\sum_j\sigma_{zj}+u_x\sum_j\sigma_{xj})\\
&+\textstyle\sum_{\mathbf{k},s}(\hbar\omega_{\mathbf{k}s}/2)(p_{\mathbf{k}s}^*p_{\mathbf{k}s}+q_{\mathbf{k}s}^*q_{\mathbf{k}s})\\
&-\textstyle\sum_{\mathbf{k},s}[g_{\mathbf{k}s,z}(\hbar\omega_{\mathbf{k}s})^{\frac{1}{2}}/(N)^{\frac{1}{2}}]q_{\mathbf{k}s}\sum_j e^{i\mathbf{k}\cdot\mathbf{j}}\sigma_{zj}\\
&-\textstyle\sum_{\mathbf{k},s}[g_{\mathbf{k}s,x}(\hbar\omega_{\mathbf{k}s})^{\frac{1}{2}}/(N)^{\frac{1}{2}}]q_{\mathbf{k}s}\sum_j e^{i\mathbf{k}\cdot\mathbf{j}}\sigma_{xj},\\
u_z=&(1/\sqrt{6})(2e_{zz}-e_{xx}-e_{yy}),\\
u_x=&(1/\sqrt{2})(e_{xx}-e_{yy}),
\end{aligned}
\tag{11}
$$

where Ω is the volume of the system; c_{11} and c_{12} are the elastic constants[19] in the absence of the Jahn-Teller effect; g_0 is the coupling constant for the interaction between u's and σ's; $g_{\mathbf{k}s}$ vanishes for $k=0$ in the crystal defined above; $p_{\mathbf{k}s}$ is the momentum associated with $q_{\mathbf{k}s}$ and satisfies the commutation relation given by $[q_{\mathbf{k}s},p_{\mathbf{k}'s'}]=i\delta_{\mathbf{k}'\mathbf{k}}\delta_{s's}$; $\omega_{\mathbf{k}s}$ is the frequency of the normal mode; N is the number of the unit cells. Here the terms which correspond to the anisotropy energy are not included.

First we discuss the distortion at absolute zero. We assume that the wave function of the j-th magnetic ion is given by $\cos(\theta_j/2)\varphi_1+\sin(\theta_j/2)\varphi_2$, or in other words, the average value of σ_{zj} and σ_{xj} is given by

$$\bar{\sigma}_{zj}=\cos\theta_j \quad \text{and} \quad \bar{\sigma}_{xj}=\sin\theta_j. \tag{12}$$

Replacing the operators by their average values in (11) and minimizing the energy with respect to u's and q's, we can easily find that the energy is given by

$$
\begin{aligned}
E=&-(g_0^2/2N)[(\textstyle\sum_j\cos\theta_j)^2+(\sum_j\sin\theta_j)^2]\\
&-(1/2N)[\textstyle\sum_{k,s}g_{\mathbf{k}s,x}^*g_{\mathbf{k}s,z}(\sum_j e^{i\mathbf{k}\cdot\mathbf{j}}\cos\theta_j)\\
&\times(\textstyle\sum_j e^{-i\mathbf{k}\cdot\mathbf{j}}\cos\theta_j)+\sum_{k,s}g_{\mathbf{k}s,x}^*g_{\mathbf{k}s,x}\\
&\times(\textstyle\sum_j e^{i\mathbf{k}\cdot\mathbf{j}}\sin\theta_j)(\sum_j e^{-i\mathbf{k}\cdot\mathbf{j}}\sin\theta_j)\\
&+\textstyle\sum_{k,s}g_{\mathbf{k}s,z}^*g_{\mathbf{k}s,x}(\sum_j e^{i\mathbf{k}\cdot\mathbf{j}}\sin\theta_j)\\
&\times(\textstyle\sum_j e^{-i\mathbf{k}\cdot\mathbf{j}}\cos\theta_j)+\sum_{k,s}g_{\mathbf{k}s,x}^*g_{\mathbf{k}s,z}\\
&\times(\textstyle\sum_j e^{i\mathbf{k}\cdot\mathbf{j}}\cos\theta_j)(\sum_j e^{-i\mathbf{k}\cdot\mathbf{j}}\sin\theta_j)],
\end{aligned}
\tag{13}
$$

where we omitted the zero point energy of the vibration. It is convenient to treat σ's as if they were the spins in the magnetic problem. Since $\cos\theta_j$ and $\sin\theta_j$ correspond to the z and x component of the spin, respectively, to minimize (13) with respect to θ_j corresponds to finding the lowest state of the spin system with the interaction which can be obtained from (13) by rewriting the expression. We do not go into the detailed discussion of this interaction in this paper. Rather we assume the "ferromagnetic" and "antiferromagnetic" solutions and discuss their nature in the following sections, since only these solutions seem to correspond to the actual distortions observed so far. The necessary condition

[16] K. Knox, J. Chem. Phys. **30**, 991 (1959).
[17] D. Balz and K. Plieth, Z. Elecktrochem. **59**, 545 (1955).
[18] When the relative displacements of ions are accompanied by the elastic strain, we define that the zero points of $q_{\mathbf{k}s}$ are those which would be realized under the strain in the absence of the Jahn-Teller effect.
[19] Strictly speaking, the first term of (11) represents the change of the potential energy associated with u_z and u_x, while the usual elastic energy includes the change of the vibrational free energy. However, we shall discuss this point in another paper. The following calculation does not depend on this point.

for the realization of the ferromagnetic state is $g_0^2 > \sum_s |g_{\mathbf{k}x,s \text{ or } x}|^2$ for all $\mathbf{k}$.

C. THE "FERROMAGNETIC" CASE (THE TETRAGONAL DISTORTION)

When all $\boldsymbol{\sigma}$'s are parallel to each other, we obtain $\sum_j e^{i\mathbf{k}\cdot\mathbf{j}} \cos\theta_j = \sum_j e^{i\mathbf{k}\cdot\mathbf{j}} \sin\theta_j = 0$ for $k \neq 0$. Since $g_{\mathbf{k}s}$ is equal to zero for $\mathbf{k}=0$ in such a crystal as specified before, the distortion is described only by u_z and u_x which are given by

$$u_z = \delta \cos\theta \quad \text{and} \quad u_x = \delta \sin\theta$$
$$\text{with} \quad \delta = \{g_0 N^{\frac{1}{2}} / [\Omega(c_{11}-c_{12})]^{\frac{1}{2}}\}, \quad (14)$$

where θ specifies the direction of the total magnetization. The total energy is given by $E = -Ng_0^2/2$. So far the energies which correspond to the anisotropy energy like (7) and (9) in the single molecule case is not considered. From arguments similar to those in the single molecule case we can show that the anharmonicity of the potential energy is expressed as

$$-NK_1(u_z^3 - 3u_z u_x^2) \quad (15)$$

and also the higher order coupling between u's and $\boldsymbol{\sigma}$'s is given by

$$-K_2[(u_z^2 - u_x^2)\sum_j \sigma_{zj} - 2u_x u_z \sum_j \sigma_{xj}]. \quad (16)$$

The first-order contribution of these terms is given by inserting (14) into (15) and (16). The result is

$$-N(K_1\delta^3 + K_2\delta^2)\cos 3\theta. \quad (17)$$

Thus if $(K_1\delta^3 + K_2\delta^2)$ is positive, the crystal will be distorted tetragonally with the elongated c axis. The magnitude of the anisotropy energy will be generally smaller than the first-order energy, $Ng_0^2/2$, by the ratio of the displacement to the interionic distance, that is, u_z, which is about 0.1 experimentally.

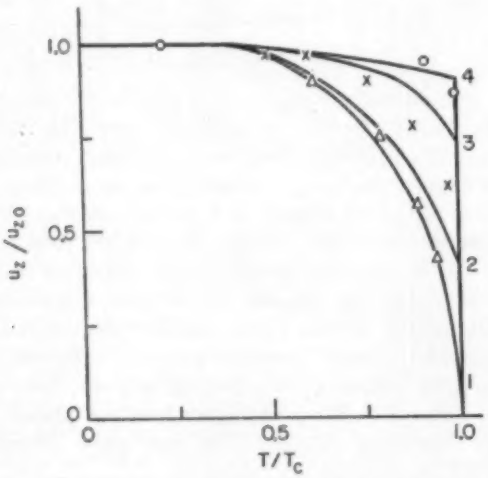

FIG. 4. The u_z/u_{z0} vs T/T_c curves and the experimental data. Curve 1: $k_1 = k_2 = 0$; curve 2: $k_1 = 0.25$, $k_2 = 0$; curve 3: $k_1 = 0$, $k_2 = 0.175$; curve 4: $k_1 = 0$, $k_2 = 0.263$. ○ : 95% Mn_3O_4 + 5% Fe_3O_4[6]; × : $CuFe_2O_4$[5]; △: $CuFe_{1.7}Cr_{0.3}O_4$.

The temperature dependence of the distortion will be obtained in the first approximation by the following procedure. We assume that the distortion is determined by the thermal averages of $\boldsymbol{\sigma}$'s and correspondingly the electronic state is determined by the thermal averaged positions of the ions. Neglecting the anisotropy energy for a while, we replace in (11) $\boldsymbol{\sigma}$'s by their thermal averages and minimize the free energy with respect to u and q. Since the thermal average of σ_j does not depend on j in the ferromagnetic state, the interaction term involving $q_{\mathbf{k}s}$ vanishes, and the distortion is given by

$$u_z = u_{z0}\bar{\sigma}_z, \quad (18)$$

where u_{z0} is the distortion at absolute zero. Correspondingly $\bar{\sigma}_z$ depends only on u_z, since the thermal averages of $q_{\mathbf{k}s}$ vanishes. Thus we obtain

$$\bar{\sigma}_z = u_z/u_{z0} = \tanh g_0^2 u_z/(u_{z0}kT), \quad (19)$$

where we used the relation, $u_{z0} = \delta = g_0[N/\Omega(c_{11}-c_{12})]^{\frac{1}{2}}$. From (19) we can see that the transition temperature is given by $kT_c = g_0^2$ and the transition is of the second kind. The temperature dependence of u_z is the same as the magnetization in ferromagnets of spin of 1/2.

The anisotropy terms can be taken into account straightforwardly. Applying the same argument as before, we can show that u_z is determined by minimizing

$$F = \Omega(c_{11}-c_{12})u_z^2/2 - g_0[N\Omega(c_{11}-c_{12})]^{\frac{1}{2}}\bar{\sigma}_z u_z$$
$$-NK_1 u_z^3 - NK_2\bar{\sigma}_z u_z^2 + (NkT/2)\{(1+\bar{\sigma}_z)$$
$$\times \ln[(1+\bar{\sigma}_z)/2] + (1-\bar{\sigma}_z)\ln[(1-\bar{\sigma}_z)/2]\}, \quad (20)$$

and $\bar{\sigma}_z$ is given by

$$\bar{\sigma}_z = \tanh\{g_0[\Omega(c_{11}-c_{12})/N]^{\frac{1}{2}}u_z + K_2 u_z^2\}/kT. \quad (21)$$

If we use the following reduced unit,

$$u_z/\delta = x, \quad kT/g_0^2 = t, \quad 3K_1\delta^3/g_0^2 = k_1$$
$$\text{and} \quad K_2\delta^2/g_0^2 = k_2, \quad (22)$$

then the temperature dependence of x is given by

$$x + k_1 x^2 = (1 + 2k_2 x)\tanh(x + k_2 x^2)/t. \quad (23)$$

The transition is no longer of the second kind in the presence of the anisotropy energy. This is because the free energy contains now the odd powers of the long-range order parameter, x, as seen from (20). In Fig. 4 the T/T_c vs u_z/u_{z0} curves for several values of k_1 and k_2 are shown with some experimental points, where u_{z0} is the distortion at absolute zero and is different from δ in the presence of the anisotropy energy.

Experimentally it is not clear yet whether the transition is of the first kind or of the second kind. However, when some portion of Cu^{2+} or Mn^{3+} is substituted by other ions, the crystal separates into two phases, the tetragonal and the cubic, near the transition temperature in several cases.[6,20] This is an indirect evidence of a transition of the first kind.

[20] T. Teranishi (private communication).

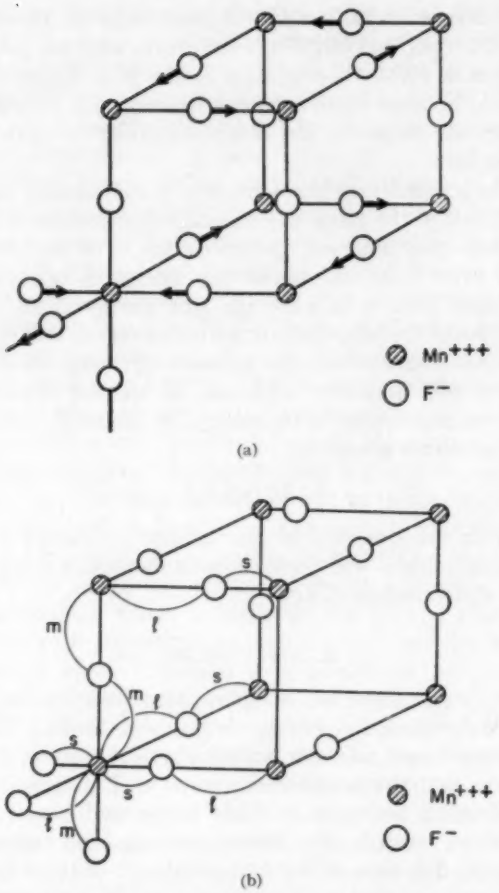

FIG. 5. (a) The idealized undistorted crystal structure of MnF_3. The arrows denote the Q_2-like mode with $k=(\pi,\pi,\pi)$. (b) The idealized distorted structure of MnF_3.

D. THE "ANTIFERROMAGNETIC" STRUCTURE (THE CRYSTAL STRUCTURE OF MnF_3)

Before going into the theoretical discussion, we describe briefly the crystal structure of MnF_3[21] which seems to be a typical example of this case. FeF_3 and CoF_3[22] have the crystal structure which can be understood as a deformed ReO_3-type structure. In these crystals the point symmetry at the metal ion site is trigonal and the surrounding fluorine ions form an octahedron deformed along its trigonal axis. In MnF_3, the octahedron is distorted further such that the distances between the magnetic ion and the fluorine ion along the x, y, and z axis become different from each other. Since the orbital level of Mn^{3+} is degenerate in the trigonal field, the distortion seems to be the result of the Jahn-Teller effect. For simplicity we assume that the crystal structure in the absence of the Jahn-Teller effect is the ideal ReO_3 type cubic structure [see Fig. 5(a)]. The distorted structure with three different Mn-F distances is approximately given by the structure in which the Mn-F distance along the z axis (m) is equal for all Mn-F, but those along the x and y axis are given alternately by l and s [see Fig. 5(b)]. Since $l>m>s$ and m is shorter than $(l+s)/2$, the bulk symmetry is tetragonal with $c/a<1$. In the actual crystal $l=2.09$ A, $m=1.91$ A and $s=1.79$ A.

From Fig. 5(b) it is clear that two kinds of the distortion occur alternately along the x, y, and z axis. This suggests that the lattice of the magnetic ions is divided into two sublattices, and the arrangement of σ's is just like that in antiferromagnetics. Thus returning to (13), we assume that the lowest state is specified by

$$\sum_j e^{i\mathbf{k}\cdot\mathbf{j}}\cos\theta_j=0 \text{ and } \sum_j e^{i\mathbf{k}\cdot\mathbf{j}}\sin\theta_j=0 \quad \text{except for } \mathbf{k}=(\pi,\pi,\pi) \text{ and } \mathbf{k}=(0,0,0) \tag{24}$$

and we define M_+ and M_- as

$$M_{+z}=\sum_+\cos\theta_j,\ M_{+x}=\sum_+\sin\theta_j,\ M_{-z}=\sum_-\cos\theta_j$$

and

$$M_{-x}=\sum_-\sin\theta_j, \tag{25}$$

where $\sum_+$ means the sum over one sublattice and $\sum_-$ the sum over another sublattice.

From group-theoretical arguments we can show that the normal modes with $\mathbf{k}=(\pi,\pi,\pi)$ which interact with σ are just Q_2-like and Q_3-like [see Figs. 5(a), 6]. They are the basis of the two-dimensional representation of the cubic group and one interacts with σ_z and another with σ_x. Therefore the cross terms between $\sin\theta_j$ and $\cos\theta_j$ vanish in (13). Writing $g_{\mathbf{k}s}$ for these modes as g_x, we obtain the energy in terms of M_+ and M_- as

$$E=-(g_0^2/2N)[(M_{+z}+M_{-z})^2+(M_{+x}+M_{-x})^2] -(g_x^2/2N)[(M_{+z}-M_{-z})^2+(M_{+x}-M_{-x})^2]. \tag{26}$$

Thus if $g_x^2>g_0^2$, the lowest state is the "antiferromagnetic" state with $M_{+z}=-M_{-z}$ and $M_{+x}=-M_{-x}$.

The role of the anisotropy energy in this case is a little different from that in the "ferromagnetic" case. As discussed in the previous sections, we can assume that the directions given by $\theta=0$ and $\theta=\pm 2\pi/3$ in

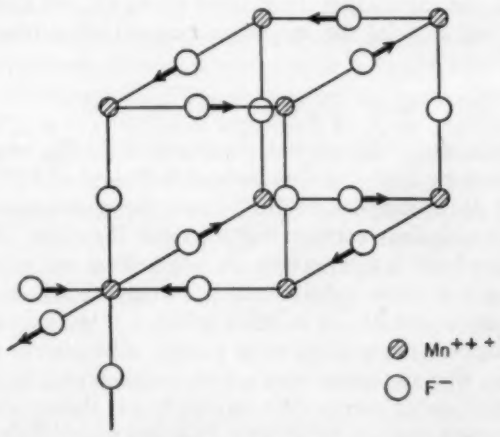

FIG. 6. The Q_2-like mode with $k=(\pi,\pi,\pi)$.

[21] M. A. Hepworth and K. H. Jack, Acta Cryst. **10**, 345 (1957).
[22] M. A. Hepworth, K. H. Jack, R. D. Peacock, and G. J. Westland, Acta Cryst. **10**, 63 (1957).

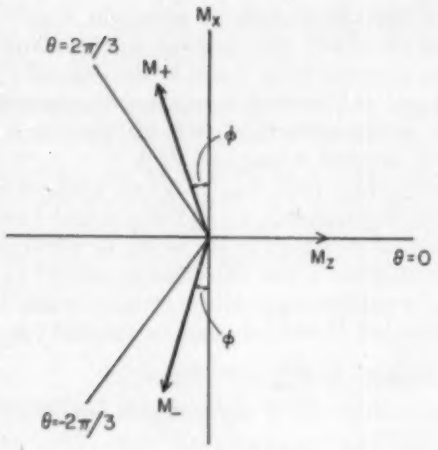

FIG. 7. The "antiferromagnetic" state.

the $\sigma_x\sigma_z$ or M_xM_z plane are the easy axes for the sublattice magnetizations. Then the lowest state will be such that the two sublattice magnetizations are almost antiparallel to each other along the x axis, but both are slightly inclined toward the directions given by $\theta=\pm 2\pi/3$, or in other words, toward the negative z axis (see Fig. 7). This situation is similar to that in the case of NiF_2 discussed by Moriya[23] in which the two sublattice magnetizations (in this case these are true magnetizations) are canted to each other by the anisotropy energy and a small ferromagnetism is produced.

The theoretical prediction discussed above agrees well with the crystal structure of MnF_3. We expect from the theory that either positive or negative Q_2-type distortion and small negative Q_3-type distortion occur in each octahedron around the magnetic ion. The distortion can be expressed as a vector in the Q_3Q_2 plane which points to the same direction as the sublattice magnetization in the M_xM_z plane. Q_2 and Q_3 are expressed by l, m, s defined before as

$$Q_2=\pm(2/\sqrt{2})(l-s) \text{ and } Q_3=(2/\sqrt{6})(2m-l-s). \quad (27)$$

Inserting the experimental values for l, m and s into (27) and calculating the ratio of Q_3 vs Q_2, we find the canting angle of the sublattice magnetization from the x axis to be

$$\tan\phi=(Q_3/Q_2)=0.115,\ \phi=6°35'.$$

Previously the crystal structure of MnF_3 was explained by applying Goodenough's theory[2] of $LaMnO_3$ to it. He assumed that Mn^{3+} forms the square covalent bond with four surrounding ions and the plane of the square bond is alternately the zx plane or the yz plane along the three cubic axes. This corresponds in our picture to $\phi=30°$, or in other words, to the case of the extremely strong anisotropy energy. The above result shows that the anisotropy energy is much smaller than the first-order energy. We can apply our theory also to $LaMnO_3$ which has a similar crystal structure. However, as Gilleo pointed out,[24] it is uncertain whether the distortion in $LaMnO_3$ originates in the Jahn-Teller effect or not, because there are some isomorphous crystals in which the magnetic ion is not supposed to cause the distortion.

The temperature dependence of the distortion can be discussed in the same way as in the ferromagnetic case. In this case, however, the transition is of the second kind even when the anisotropy energy is taken into account. This is because the free energy is an even function of the long-range order parameter as will be understood from the fact that we can interchange the direction of one sublattice with that of another sublattice without any change of the energy. It can be shown that the transition occurs at

$$kT_c=g_x^2 \quad (28)$$

even in the presence of the anisotropy energy. The canting angle ϕ will decrease with increasing temperature and vanishes at kT_c.

E. DISCUSSION

To begin with, we compare our theory with the model adopted by Finch, Sinha, and Sinha.[7] Their theory is based on the following physical picture. They assume that the octahedron around each magnetic ion is distorted tetragonally both below and above the transition temperature. Above the transition temperature, the direction of the tetragonal axes of the octahedrons are at random, and thus no bulk distortion is observed. Below the transition temperature the tetragonal axes are aligned along one direction, being accompanied by the resultant bulk distortion. They allowed two directions, the right and the wrong, for the tetragonal axes in the calculation of the entropy, and the interaction energy between the octahedrons are assumed to be proportional to the long-range order parameter. The result for the temperature dependence of the distortion is the same as given by (19). However, an obvious logical inconsistency in their theory is that there are three directions for the tetragonal axis, that is, the x, y, and z axis, while they count only two directions. If we assume that there are one right direction and two wrong directions for the tetragonal axis, the transition becomes of the first kind as will be shown in the next section.[25]

Returning to our theory, we can see that our discussion on the temperature dependence of the distortion does not take into account the local distortion around each magnetic ion. If we neglect the anisotropy energy, the local distortion will be expressed as a circle in the Q_3Q_2 plane. The contribution of this local distortion to the free energy arises from both the energy lowering

[23] T. Moriya, Phys. Rev. (to be published).

[24] M. A. Gilleo, Acta Cryst. **10**, 161 (1957).

[25] Recently, P. J. Wojtowicz developed a theory of this line [Phys. Rev. (to be published); J. Appl. Phys. **30**, 30S (1959)].

due to the distortion and the reorientation of the distortion. The latter part will be expressed as the modification of the vibrational free energy. Since the local distortion will be at any point on the circle in the Q_3Q_2 plane, the reorientation will not be described properly as the reorientation of the tetragonal axis of the octahedron. Finch, Sinha, and Sinha's theory in the modified form in which three directions are allowed for the tetragonal axis corresponds, therefore, to the case of the strong local anisotropy energy, that is, the case in which the anisotropy energy is larger than the transition temperature. In the present author's opinion this is not true in actual examples, especially, the compounds containing Mn^{3+} or Cu^{2+} in high concentration. The anisotropy energy in the single molecule will be the order of several hundred degrees. However, if the magnetic ions share the surrounding negative ions with each other, the local distortion will be much smaller than in the single molecule case, and since the anisotropy energy depends strongly on the magnitude of the distortion, the anisotropy energy will be even smaller.

Our method, which is based on the general Hamiltonian, can be improved to take into account the local distortion which is present even above the transition temperature. We discuss briefly the refinement in the following. We neglect the anisotropy energy and assume the "ferromagnetic" case. We first transform the Hamiltonian (11) by a canonical transformation which associates the distortion with the electronic states. The canonical transformation is simply to shift the equilibrium points of the oscillators to eliminate the interaction terms in which σ_{zj} is involved. This transformation results in an effective interaction between σ_{zj} as well as the self-energy, $-(1/2)\langle\sum_s|g_{\mathbf{k}s,s}|^2\rangle_{\mathrm{av}}$ where the average is taken over all $\mathbf{k}$. The interaction part is the interaction between the local distortions, and the self-energy represents the energy lowering due to the local distortion. The transformed interaction terms, in which σ_{zj} is involved, represent the energy of the reorientation. Treating the reorientational energy as a perturbation in the calculation of the density matrix, we can show that this energy does not affect the transition temperature much. If we neglect its contribution, the temperature dependence of the distortion has the same form as (19) except that the transition temperature is now given by $g_0^2-\langle\sum_s|g_{\mathbf{k}s,s}|^2\rangle_{\mathrm{av}}$. This modification of the transition temperature implies that we must subtract the contribution from the local distortion from the total interaction energy in determining the transition temperature, because the local distortion is present both below and above the transition temperature. If the local anisotropy energy is small, the discussion on the temperature dependence in the presence of the anisotropy energy is also approximately correct. Therefore the discussion given in previous sections has a sound basis on the more refined theory, and its phenomenological aspect will not be affected much in the higher approximation.

Another point which we have not discussed yet is the dependence of the distortion on the concentration of Mn^{3+} or Cu^{2+}. Experimentally the transition temperature decreases more rapidly than linearly with the concentration. The transition vanishes at about 60% in the spinel-type compounds[26] containing Mn^{3+} and at about 20% for Cu-ferrite-chromite series[5]. When we extend our theory in a simple fashion to the less-than-100% cases, we obtain an approximately linear dependence of the transition temperature on the concentration, though the effect of the reorientational energy makes the dependence a little stronger.

Two effects which are not taken into account in our theory are conceivable. One is the local crystalline field of lower symmetry which is produced by the introduction of ions of different size and valence. The directions of this crystalline field will be at random. Therefore if the strength of this crystalline field becomes larger than of the crystalline field produced by the bulk distortion, we cannot expect to observe a bulk distortion, because the local crystalline field will fix the electronic states such that the directions of σ's are at random. Another effect is the change of the vibrational mode. When the concentration becomes small enough, some normal modes will be localized around Mn^{3+} or Cu^{2+}. This will make the local distortion larger and the transition temperature lower. To extend the theory to include these effects has not yet been done.

F. THE JAHN-TELLER EFFECT IN THE PRESENCE OF THE SPIN-ORBIT COUPLING

The lowest electronic orbital states of $Fe^{2+}(d^6)$ in the octahedral cubic field are such that one of the three $d\epsilon$ orbitals is doubly occupied and other orbitals are singly occupied. In the case of $Co^{2+}(d^7)$, the lowest orbital states are approximately given by the configurations that two of the $d\epsilon$ orbitals are doubly occupied, though the Coulomb interaction between the electrons mixes in these configurations the configurations that one of the $d\epsilon$ orbitals and one of the $d\gamma$ orbitals are doubly occupied. Thus the lowest orbital level in Fe^{2+} and Co^{2+} is triply degenerate. Corresponding to $\boldsymbol{\sigma}$ in the previous sections, the angular momentum $\boldsymbol{l}$ of magnitude of one, is convenient to specify these three orbital states. The orbital angular momentum, L, of the magnetic ion is expressed as $\rho\boldsymbol{l}$ with $\rho=-1$ for Fe^{2+} and $\rho=-3/2$ for Co^{2+} within these three states. The wave function of the state specified by $l_z=0$ corresponds to either the configuration that $d(xy)$ is doubly occupied (Fe^{2+}) or the configuration that $d(zx)$ and $d(yz)$ are doubly occupied (Co^{2+}) (in other words, $d(xy)$ is singly occupied). The state $l_z=\pm1$ is such that $d(yz)\pm id(zx)$ is doubly occupied (Fe^{2+}) or the same orbital is singly occupied (Co^{2+}). The electronic orbital states of Cu^{2+} at tetrahedral sites

[26] D. G. Wickham and W. J. Croft, J. Phys. Chem. Solids **7**, 351 (1958).

resemble those of Fe^{2+} at octahedral sites, since in this case the $d\epsilon$ level has higher energy than the $d\gamma$ level and consequently the hole will occupy one of the $d\epsilon$ orbitals.

We discuss first the distortion in FeO and CoO at absolute zero. The interaction between the electronic states and the bulk deformation is given by

$$H=b_1[e_{xx}l_x^2+e_{yy}l_y^2+e_{zz}l_z^2-(2/3)(e_{xx}+e_{yy}+e_{zz})] +(b_2/2)[e_{xy}(l_xl_y+l_yl_x)+e_{yz}(l_yl_z+l_zl_y) +e_{zx}(l_zl_x+l_xl_z)]. \quad (29)$$

At absolute zero the spins align along one of the {111} directions in FeO and approximately along one of the {100} directions in CoO. Therefore the orbital angular momentum is subject to a strong effective magnetic field through the spin-orbit coupling. The lowest state is roughly either $l_f=-1(S_f=S)$ or $+1(S_f=-S)$, where l_f and S_f are the components along the easy axis. If we average (29) over this orbital state, the interaction does not vanish and causes the crystal distortion. Following this line, the present author calculated the distortion previously. The result is $e_{xy}=e_{yz}=e_{zx}=-1.1$ percent for FeO and $(a-c)/a=1.2\%$ for CoO.[27] The experimental values are, respectively, -0.7% and 1.2%.

The characteristic feature of this distortion is that the distortion occurs in the way opposite to that which would occur in the absence of the spin-orbit coupling. If we assume the tetragonal distortion, then the average of (29) over the electronic state is given by

$$(b_1/2)(2e_{zz}-e_{xx}-ee_{yy})[\langle l_z^2\rangle_{av}-(2/3)]. \quad (30)$$

From (30) it is evident that the absolute magnitude of the interaction for the state of $\langle l_z^2\rangle_{av}=0$ is twice as large as for the states of $\langle l_z^2\rangle_{av}=1$, and the sign of the interaction, and consequently, the sign of the distortion is different between both cases. For the state of $\langle l_z^2\rangle_{av}=0$ the spin-orbit coupling vanishes in the first order and for $\langle l_z^2\rangle_{av}=1$, the energy lowering due to the distortion is one-fourth of that for $\langle l_z^2\rangle_{av}=0$. In FeO the rough estimate shows that the energy lowering in the absence of the spin-orbit coupling is about 100 cm^{-1} per ion and the spin-orbit coupling in the state of $l_z=\pm1$ is about 200 cm^{-1}. Therefore it is understandable that the spin-orbit coupling plays the primary role in determining the sign of the distortion. In CoO the spin-orbit coupling is even larger.

However there is an example of the opposite case. The spinel-type compound, $CuCr_2O_4$, in which Cu^{2+} are situated at tetrahedral sites is distorted tetragonally $(c/a<1)$ at 600°C, far above the Curie temperature. As discussed by Dunitz and Orgel,[3] the sign of the distortion is understandable if the Jahn-Teller effect is assumed.[28] In this case, b_1 or b_2 in (29) is expected to be much larger than in FeO, since the $d\epsilon$ orbitals have a larger overlap with the surrounding ions at tetrahedral sites than at octahedral sites. Though the exact treatment is difficult, a simple approximate theory can be worked out if the spin-orbit coupling is neglected. At tetrahedral sites, the magnetic ions do not share the surrounding negative ions with each other. Therefore the local distortion will be larger than in the case of the octahedral sites. In contrast with the octahedral case, the number of the stable distortion of the tetrahedron is three if the tetragonal distortion has the lowest energy or four if the trigonal distortion is favored.[14] Even when the local distortion is very small, the number of the electronic orbital levels are three. Therefore the statistical treatment is exactly the same in both extreme cases. We formulate the theory in the following, assuming the strong local distortion case. The state in which the tetrahedron is distorted along the z axis is assumed to have the energy $-2W$ in the presence of the bulk distortion along the z axis. Then the other states in which the tetrahedron is distorted along either the x or y axis will have the energy $+W$. The bulk distortion is proportional to the difference between the occupation numer of the state with distortion along the z axis and that along either the x or the y axis. Therefore we obtain

$$u_z=u_{z0}[\exp(2W/kT)-\exp(-W/kT)]/[\exp(2W/kT)+2\exp(-W/kT)]. \quad (31)$$

Assuming W is proportional to u_z, we can calculate the temperature dependence of u_z. In this case the transition is of the first kind and occurs at $u_z=(1/2)u_{z0}$. The relation between u_z/u_{z0} and T/T_c is shown in Fig. 8 with some experimental points for $CuCr_2O_4$.

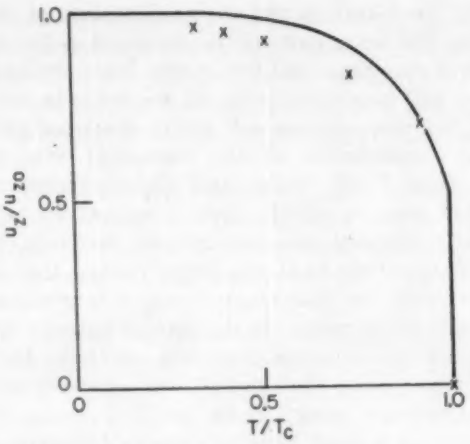

FIG. 8. The theoretical u_z/u_{z0} vs T/T_c curve for the compounds which contain Cu^{2+} at tetrahedral sites. X's are the experimental points taken from the data on $CuCr_2O_4$.[11,28]

[27] These values are different for those previously reported.[9] Here the Hartree wave function is used in the calculation, whereas the Slater function was used there.

[28] The state $l_z=0$ corresponds to the occupation of $d(xy)$ by the hole. Since this orbital is flat in the xy plane, the tetrahedron of the surrounding negative ions is contracted along the z axis.

ACKNOWLEDGMENTS

The author is indebted to Professor J. W. Stout for valuable discussions and helpful comments on the manuscript and to Dr. T. Teranishi for sending the unpublished data. This research was supported in part by the Office of Naval Research.

Note added in proof. Recently the crystal structure of KMF_3 with M = Cr, Mn, Fe, Co, Ni, and Cu has been determined at both room temperature and low temperature (78°K and 4.2°K). [A. Okazaki, Y. Suemune, and T. Fuchikami, J. Phys. Soc. Japan **14**, 1823 (1959); V. Scatturin, L. Corliss, N. Elliott, and J. Hastings (unpublished).] The distortion observed in $KFeF_3$ and $KCoF_3$ seems to correspond to that in FeO and CoO discussed in the text, respectively. To the crystal structure of $KCuF_3$ and $KCrF_3$ the discussion on MnF_3 will be applicable.

JOURNAL OF APPLIED PHYSICS SUPPLEMENT TO VOL. 31, NO. 5 MAY, 1960

Relations between Superconductors and Ferromagnets

BERND MATTHIAS
Bell Telephone Laboratories, Inc., Murray Hill, New Jersey

Ferromagnetic interactions of the rare earth elements in dilute solutions or in compounds with nonmagnetic elements have been discovered and will be described. The Curie points are essentially proportional to the spin while the saturation moment follows the value for the effective moment. This ferromagnetic interaction, known to take place via the conduction electrons, follows criteria resembling closely those for the occurrence of superconductivity.

It is shown that by suitable combination of similar superconductors and ferromagnets both phenomena can happen simultaneously in the same crystal.

THE occurrence of superconductivity in elements, solid solutions, alloys or intermetallic compounds is determined by very simple rules. If the average number of valence electrons per atom is between 2 and 8, then superconductivity will be present and the transition temperature will be generally an oscillatory function of the electron concentration. Among the exceptions are manganese, iron, and some systems containing these or any of the other magnetic elements such as chromium, cobalt, or nickel. It has been assumed for quite some time that ferromagnetism and superconductivity were mutually exclusive. Some isolated cases showing a depression of the superconducting transition upon introduction of 'ferromagnetic impurities' seemed to strengthen this viewpoint and the nonsuperconductivity of the magnetic rare earths (with the exception of lanthanum) was considered a further case in point.

In the following paragraphs, I would like to show that both these conclusions are rather erroneous.[1]

Superconductors containing ferromagnetic elements have been known in increasing number during the last fifteen years. Some of them are listed in Table I.

These compounds illustrate that systems containing elements which were ferromagnetic by themselves could still become superconducting. However, in these compounds, since they are quite different from the constituent elements, drastic changes in the electronic configuration of the individual elements might have taken place and thus account for the lack of any appreciable magnetism. The next step was, therefore, a systematic study of these magnetic elements in dilute solution.

Some years ago, we had already observed that the superconducting transition temperature of zirconium is raised by dissolving 10 at% of iron, cobalt or nickel in it.[2]

From an atomic diameter viewpoint, these combinations were far from ideal as zirconium was rather large to dissolve most elements of the first transition period. We, therefore, investigated the corresponding solid solutions in titanium and found in this case that all the magnetic elements from chromium to nickel raised the superconducting transition temperature up to more than ten times its original value.[3] The diagrams in Figs. 1–4 will illustrate this behavior.

They show that not only do the magnetic transition elements *not* depress superconductivity, but instead they raise it by *more* than the amount attributable to variation of the number of valence electrons. This is demonstrated by comparison with the corresponding

TABLE I. Superconducting compounds containing ferromagnetic elements.

NiBi[a]	U_6Mn[b]	$CoTi_2$
$NiBi_3$[a]	U_6Fe[b]	$CoZr_2$
$NiZr_2$	U_6Co[b]	$CoSi_2$
$NiPdAs_2$	UCo[b]	$CoTh_2$
		$FeTi_2$

[a] Alekseyevsky, Brandt, and Kostina, J. Exptl. Theoret. Phys. (U.S.S.R.) **21**, 951 (1951).
[b] Chandrasekhar and Hulm, J. Phys. Chem. Solids **7**, 259 (1958).

[1] An exception is the simultaneous condensation of ferromagnetic and superconducting elements in thin films at liquid helium temperatures, done in Hilsch's laboratory. Here, ferromagnetic elements lower the transition temperature of superconductors. This is however not an equilibrium state as the metals are insoluble in each other and the phenomenon disappears irreversibly upon heating. See N. Barth, Z. Physik **142**, 58 (1955).

[2] Matthias and Corenzwit, Phys. Rev. **100**, 626 (1955).
[3] B. Matthias, U. B. Compton, H. Suhl, and E. Corenzwit, Phys. Rev. **115**, 1597 (1959).

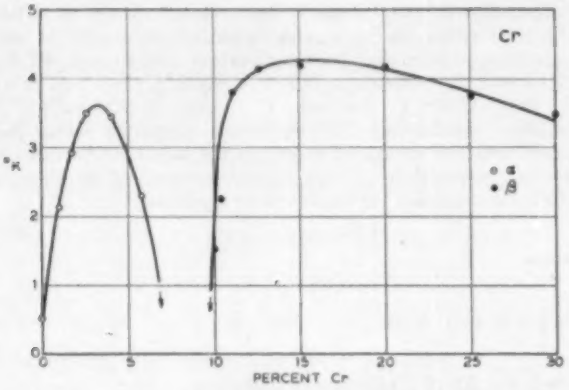

FIG. 1. Superconducting transition temperatures of solid solutions in titanium. Percentage of Cr.

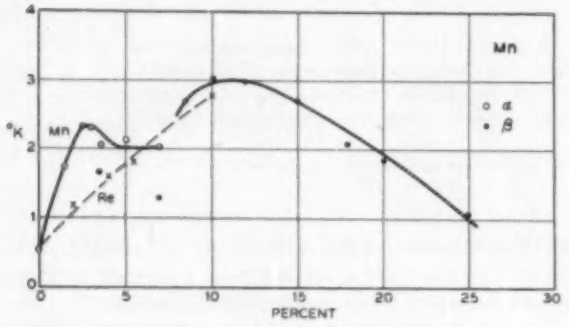

FIG. 2. Superconducting transition temperatures of solid solutions in titanium. Percentage of Mn.

solid solutions to those elements of the second row of the transition elements which contribute the same number of valence electrons without, however, a magnetic moment. One can even carry this one step further. Instead of using pure titanium as a solvent, one might do the same with an alloy of 60% titanium and 40% vanadium, the transition temperature of which has already passed the maximum temperature located between 4 and 5 electrons. An increase of valence electrons will now lower the transition temperature and again as shown in Fig. 5 due to its magnetic moment, iron will lower it less than the same amount of ruthenium.

Although the meaning of this will be discussed at the end, it becomes already abundantly clear that ferromagnetic transition element solutes and superconductivity are certainly compatible with each other as long as no actual ferromagnetism results.

However, an entirely different situation exists when the rare earths enter the picture, that is, when $4f$ spins are involved. Those rare earths which are without $4f$ electrons are either superconducting as in the case of lanthanum or form many superconducting compouuds that range from those with scandium to those with lutetium. Table II gives a small sampling of superconducting compounds in which the similarity of Y, Sc, and Lu to La becomes apparent. If, however, instead of Sc, Y, La, or Lu, similar compounds are formed using rare earth atoms that have a partly filled $4f$ shell, then these compounds will invariably be ferromagnetic. This is also true for $5f$ elements as will be shown by C. E. Olsen[4]; and there is until now only one superconducting compound in which $4f$ electrons may be present, namely $CeRu_2$, which becomes superconducting at 5°K. The Curie temperatures of these compounds are roughly a function of the spin of the rare earth atom of the form of $J(J+1)(g-1)^2$,[5,6] while the saturation polarization is given essentially by the effective moment. To be more precise the Curie temperatures are proportional to the projection of the spin on the J vector. To return to the ferromagnetic *and* superconducting rare earth compounds one observes for one given rare earth element a variation of the Curie point also with the variation of the inert element. A further examination shows that Curie points and superconducting transition temperatures have a similar dependence upon the average num-

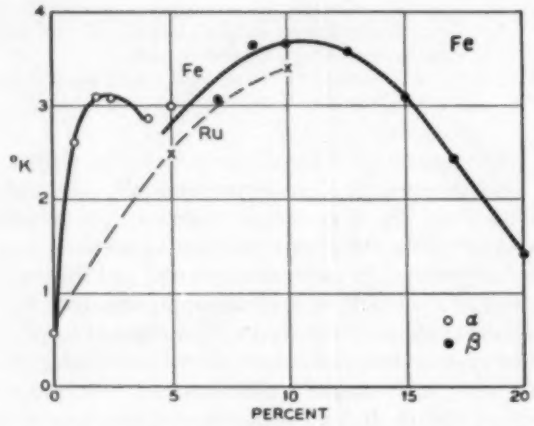

FIG. 3. Superconducting transition temperatures of solid solutions in titanium. Percentage of Fe.

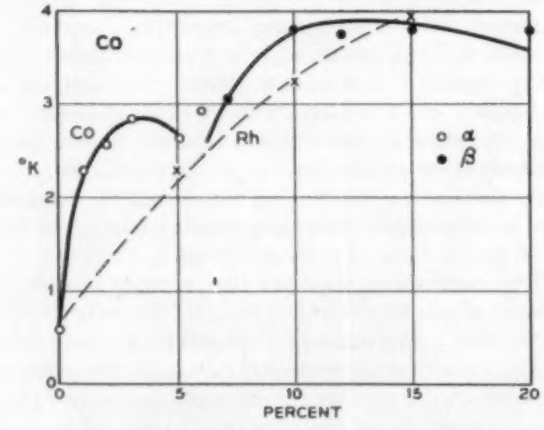

FIG. 4. Superconducting transition temperatures of solid solutions in titanium. Percentage of Co.

[4] C. E. Olsen, J. Appl. Phys. **31**, 340S (1960), this issue.
[5] R. M. Bozorth, B. T. Matthias, H. Suhl, D. D. Davis, and E. Corenzwit, Phys. Rev. **115**, 1595 (1959).
[6] That formula was independently arrived at by P. G. de Gennes, Compt. rend. **247**, 1836 (1958).

ber of valence electrons per atom. Here now is a connection between electron concentration and Curie points that until now could not be found among the transition elements. (Fig. 6).

The very same *spin* dependence that controlled the Curie point has also been observed for the lowering of the superconducting transition temperature of lanthanum upon dissolving rare earths in it. While this lowering is increased with increasing spin of the impurity rare earth, the effective moment in turn does not lower but actually raise the superconducting transition temperature.[7] This is shown by comparing the drop of the superconducting transition in La-Nd solid solution, to those in La-Er solid solutions. While Nd and Er both have the same spin, the effective moment of Er is much larger than that of Nd (Fig. 7).

At the same time, another phenomenon appeared that also does not seem to exist among the transition elements, namely the occurrence of very dilute ferromagnetism. When dissolving a rare earth element such as Gd in lanthanum, ferromagnetism appears already at very small concentrations and the saturation moment corresponds to the theoretical value of 7 bohr magnetons per Gd atom. This existence of dilute ferromagnetism indicated the way to look for ferromagnetic superconductors. Extrapolation in La-Gd solid solutions and subsequent results by Hein et al.[8] indicated simultaneous occurrence of superconductivity and ferromagnetism at temperatures near 0.5°K and 1 at% Gd.

In the hope of raising this intersection to higher temperatures, we returned to compounds. As pointed out before, the comparison between superconducting and ferromagnetic rare earth compounds shows strikingly similar variation with the valence electron concentration. This comparison is made possible by varying the noble metal. By forming now mixed crystals between these corresponding superconducting and ferromagnetic compounds in which only the relative proportions of the rare earth elements were different, we obtained systems

TABLE II. Superconducting rare earth compounds.[a]

$ScGe_2$	YGe_2		$LaGe_2$
$ScRu_2$	YRu_2		$LaRu_2$
$ScOs_2$	YOs_2	$LuOs_2$	$LaOs_2$
$ScIr_2$	YIr_2		$LaIr_2$
	YPt_2		

[a] Matthias, Corenzwit, and Zachariasen, Phys. Rev. 112, 89 (1958); Compton and Matthias, Acta Cryst. 12, 651 (1959).

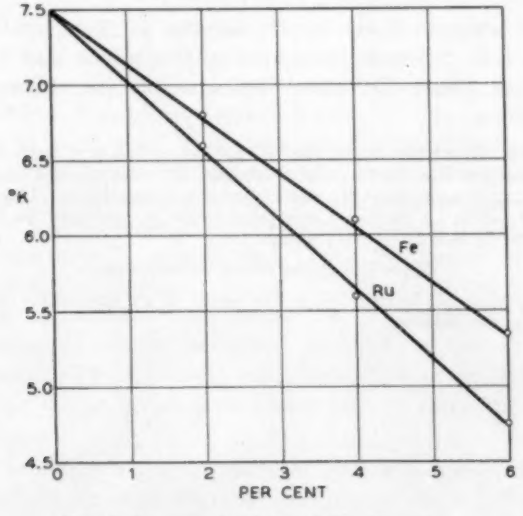

FIG. 5. Superconductivity of $Ti_{0.6}V_{0.4}$ alloys with iron or ruthenium.

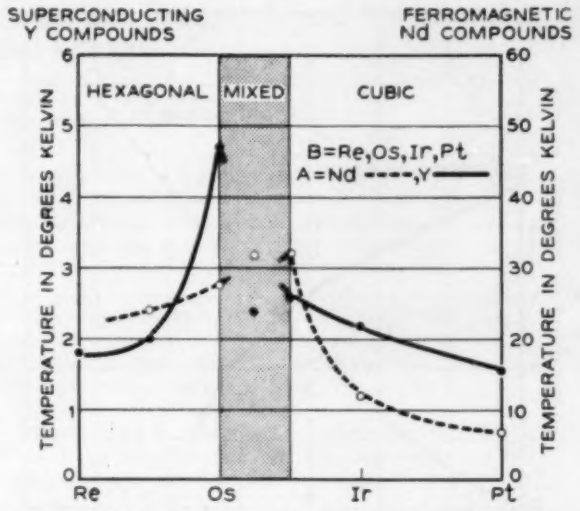

FIG. 6. Variation of superconducting and ferromagnetic transition temperature with average number of valence electrons per atom in AB_2 Compounds.

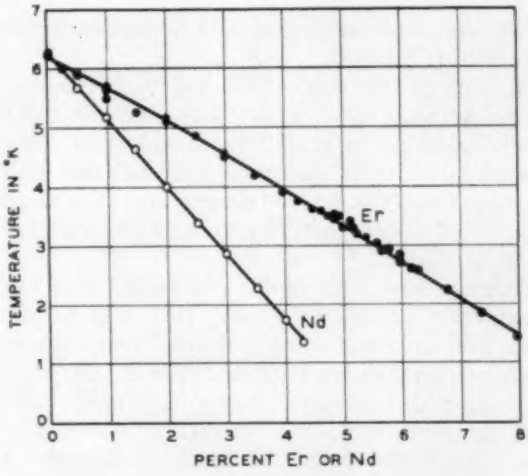

FIG. 7. Superconducting transition temperatures of Nd and Er solid solutions in lanthanum.

[7] Matthias, Suhl, and Corenzwit, Phys. Rev. Letters 1, 92 (1958); J. Phys. Chem. Solids (to be published).

[8] Hein, Falge, Jr., Matthias, and Corenzwit, Phys. Rev. Letters 2, 500 (1959).

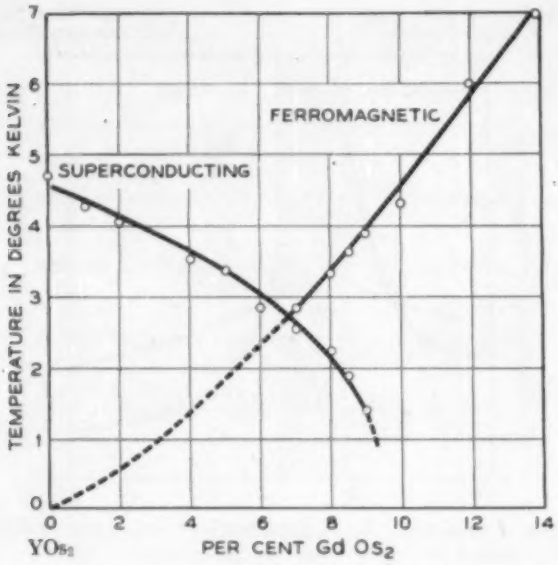

FIG. 8. Ferromagnetic superconductors of (Y, Gd)Os_2.

which were superconducting and ferromagnetic simultaneously (Figs. 8–9).

According to the concentration of the 4*f* element, the crystal becomes either at first ferromagnetic and then superconducting, or at first superconducting and then ferromagnetic, or at the proper concentration, both at the same time. The detailed description of the magnetic behavior of ferromagnetic superconductors will be given by R. M. Bozorth.[9]

Here are now some of the conclusions that can be drawn from all this. Of course, they may be wrong. Since the superconducting transition temperatures of the transition elements are raised upon the introduction of atoms with a magnetic moment, it seems possible that the electron-electron interaction responsible for superconductivity among the transition elements is to a large extent a magnetic one. The superconductivity is not adversely affected by these magnetic moments. Whereas *s-f* interactions always lead to a simple long range, indirect *f-f* interaction, and ferromagnetism, *s-d* interactions are not in evidence at all. At least, they do not announce their presence through any resultant ferromagnetism.

At the same time that *s-f* interactions always seem

[9] R. M. Bozorth, J. Appl. Phys. **31**, 321S (1960), this issue.

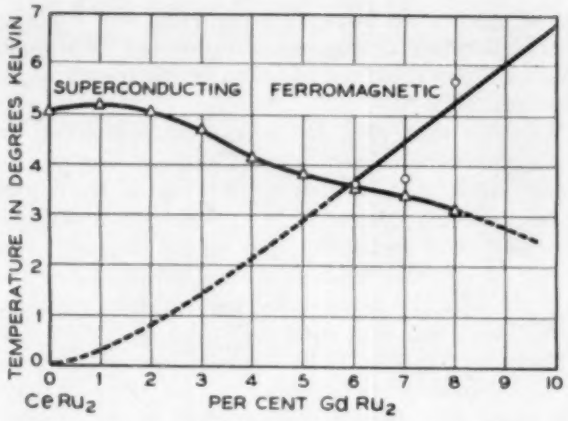

FIG. 9. Ferromagnetic superconductors of (Ce, Gd)Ru_2.

to cause ferromagnetism,[10] they invariably lower the superconducting transition temperature in a manner proportional to this magnetic interaction. Yet the reduction is not so drastic as to prevent overlap of the two phases for a wide range of materials. Thus, superconducting ferromagnets or ferromagnetic superconductors have so far been possible only with *s-f* interactions, and the *s-d* analog usually leads to superconductivity alone. In the case of the ferromagnetism in transition elements, which according to experimental evidence can be due to *d-d* interactions only, the simultaneous occurrence of ferromagnetism and superconductivity has thus far not been observed. The reason for this seems to be the apparent impotence of the conduction electrons to establish ferromagnetic order by *s-d* exchange, and the apparent need for *d-d* nearest neighbor-type interaction (impossible in dilute cases) in establishing spin order in the magnetic transiton elements.

ACKNOWLEDGMENTS

I want to thank T. H. Geballe, H. Suhl, and T. K. Galt for many enlightening discussions and Professor Brout for many welcome private communications.

[10] R. Brout has shown that if this interaction is of long range character, the Curie point variation vs concentration should adhere more to linearity the higher the concentration. The fact that Gd in La shows a Curie point linear in concentration from 0.5 at % to 8 at % only, where

$$8\% = (1/\text{number of nearest neighbors})$$

may then be interpreted as the onset of an alternative short range mechanism.

JOURNAL OF APPLIED PHYSICS SUPPLEMENT TO VOL. 31, NO. 5 MAY, 1960

On the Laws of Magnetization of Ferromagnetic Single Crystals and Polycrystals. Application to Uniaxial Compounds

L. NÉEL, R. PAUTHENET, G. RIMET, AND V. S. GIRON*
University of Grenoble, France

One of the authors (L.N.) describes the mechanism of magnetization of a ferromagnetic single crystal: the elementary domains can be classified in several groups, called "phases" each having a certain direction of the spontaneous magnetization. The variation of the total magnetization takes place in various "modes," corresponding to the number of coexisting phases in a given field. The calculation of the magnetization curve in these various modes explains the experimental results for single crystals of iron, pyrrhotine and magnetoplumbite.

The results of measurements at room temperature on this latter compound, $6Fe_2O_3-PbO$, are treated in greater detail. The crystal is uniaxial; for different angles of the external field with the c axis, the magnetization first increases proportionally to the field, followed by a gradual approach to saturation (except for the angles 0 and 90°). The anisotropy constant K_1 is first determined (K_2 is negligible). The two parts of the curve can be interpreted by two "modes," with respectively, two and one "phases."

The variation of the magnetization of polycrystalline $6Fe_2O_3-BaO$ samples can be explained by the rotation mechanism only; the crystallites are too small in size to be divided into phases. The experimental curves can be explained by taking into account the interactions between crystallites in calculating the law of approach to saturation.

BY introducing the concept of "phase",[1] it is possible to clarify the magnetization mechanism of perfect ferromagnets from zero magnetization to saturation. By "perfect ferromagnet" we mean an ideal ferromagnetic crystal, of large dimensions, and ellipsoidal shape, with no faults, internal stress or inclusions, placed in a homogeneous magnetic field. Such a body should show no hysteresis. In the state of perfect equilibrium the internal magnetic field is equal to the sum of the applied and the demagnetizing field, and has the same value throughout the body, except perhaps in a surface layer or within the domain walls.

In these conditions, if we neglect the surface closure domains that occupy only a small fraction of the total volume, the elementary domains can be grouped in a *finite* number of families, called phases, such that the magnetizations of all domains of a phase are parallel.

In the state of zero magnetization, the number of phases equals twice the number of directions of easy magnetization, that is to say 8 for nickel (ternary axes), 6 for iron (quaternal axes), 2 for cobalt. The internal field is then zero. This field remains zero, and the number of phases remains constant, if we apply an external field of such magnitude that the vector representing the total magnetization remains within a certain volume that is symmetrical about the origin (this volume can degenerate into a plane figure or line segment for uniaxial substances). For higher fields, the number of phases decreases, and an internal field appears. Finally, for very large fields, the magnetization of the body becomes uniform; only a single phase subsists.

For iron, when we increase the applied magnetic field in a fixed direction, we thus pass through the initial six-phase stage, then a three-phase in which the internal field is along a ternary axis, followed by a two-phase stage with an internal field in a binary plane of symmetry, and finally a 1-phase stage, in which the internal field has no simple relation to the crystal axes. Obviously, in equilibrium, all phases existing have the same thermodynamic potential. This explains why the field must have these directions of symmetry in the intermediate stages. This theory has been well verified for iron.[1]

In uniaxial substances, where the axis is the easy direction, the theory is much simpler, and has been treated in a recent article for the case of pyrrhotine.[2] In the initial stage, there are only two phases with an internal field perpendicular to the axis, followed at once by the final single phase stage.

The study of the magnetization processes of a $6Fe_2O_3-PbO$ single crystal also illustrates these mechanisms. The compound is isomorphous to natural magnetoplumbite $Pb(Fe, Mn)_{12}O_{19}$[3]; and crystallises in the hexagonal system. The parameters are $a=5.877$ A and $c=23.02$ A. At room temperature, the c axis is the easy direction,[4,5] and the basal plane can be considered to be isotropic with respect to the large field, about 1000 oe, used in our experiments. A spherical sample of 5.5 mm diameter was prepared. Let us call (Fig. 1) φ and θ respectively the angles of the external field H_e and the spontaneous magnetization J_s with the c axis, OX the (hard) axis in the basal plane, parallel to the projection of the external field on this plane, $n=4\pi/3$ the demagnetizing factor of the sample. We represent the magnetocrystalline energy by an expression of the form $K_1 \sin^2\theta + K_2 \cdot \sin^4\theta$. It is probable and in agreement with the first experimental results,[6] that the domains in the

* Now at the Institute of Iron and Steel, Madrid, Spain.

[1] L. Néel, J. phys. radium **5**, 241, 265 (1944).

[2] L. Néel, Colloque National de Magnétisme, July 8–10, 1957 (Centre National de la Recherche Scientifique, Paris, 1958).

[3] V. Adelsköd, Arkiv för Kemi, **A12**, n°29, (1938), 1.

[4] G. Villers, Compt. rend. **248**, 2973 (1959).

[5] R. Pauthenet and G. Rimet, Compt. rend. **249**, 656 (1959).

[6] Unpublished results.

crystal, supposed free of stress, are parallel to the c axis. In zero field, the spontaneous magnetizations of adjacent domains are along the c axis, but in opposite directions. The domains thus form two "phases." The volumes of the two phases are equal; their relative proportions λ and μ, both have the value 1/2. When the field is applied, the magnetization will start in a two-phase stage.

First of all consider the special case in which the field H_e is perpendicular to the c axis ($\varphi=\pi/2$). The magnetization J_H along the field has been measured between 2.3 and 748°K, in field up to about 30 000 oe. Each isotherm (Fig. 2) has 2 regions: up to the fields of the order of 14 000 oe, J_H increases proportionally to H_e; for higher fields J_H remains constant. This form of variation is characteristic of a uniaxial substance, for a field perpendicular to the easy axis, when K_2 is small with respect to K_1. In the first part of the curve, the spontaneous magnetization of each domain turns through the same angle θ. The magnetization J_H equals $J_s\cdot\sin\theta$. Above a certain field H_s, all domains are aligned parallel to H_e, and only the variations of the spontaneous magnetization with the field remain. The determination of the two constants K_1 and K_2 has been made by the following method, used earlier by W. Sucksmith and J. E. Thompson.[7] The equilibrium condition for the spontaneous magnetization leads to the condition:

$$\frac{2K_1}{J_s^2}+n+\frac{4K_2}{J_s^4}\cdot J_H^2=\frac{H_e}{J_H}. \tag{1}$$

The graph of H_e/J_H against J_H^2 should be linear, the ordinate at the origin equals $2K_1/J_s^2+n$, and the slope is $4K_2/J_s^4$. K_1 and K_2 have thus been determined with errors of 2% and 15% respectively. Their variations are represented in Fig. 3. Both are always positive, with K_2 at the most equal to $K_1/50$. In the following, we all suppose that the magnetocrystalline energy is sufficiently well represented by the energy term $K_1\cdot\sin^2\theta$. Its influence is equivalent to a demagnetizing field, parallel to OX, proportional to J_x, the projection on OX of the total magnetization of the sample, and with demagnetizing coefficient $2K_1/J_s^2$.

In the general case, when the field makes an angle φ with the c axis that is not equal to $\pi/2$ (Fig. 1), the total magnetization J will be such that the internal field $\mathbf{H}_i$, equal to $\mathbf{H}_e-n\,\mathbf{J}$, is along the OX axis in the 2-phase stage. The spontaneous magnetizations of the two phases are then symmetrical with respect to OX, and have the same projection J_s on this axis. The relative ratios λ and μ of these phases varies by the wall displacement mechanism. The equilibrium conditions for the magnetization[2] shows that for fields H_e smaller than

$$H_s=J_s\cdot\left(\frac{\cos^2\varphi}{n^2}+\frac{\sin^2\varphi}{(n+N)^2}\right)^{-\frac{1}{2}}, \tag{2}$$

the two phases coexist. The magnetization J makes a constant angle ψ with the c axis, given by $tg\psi=ntg\varphi/(N+n)$; J_H the magnetization parallel to the field H_e is proportional to H_e. We then define a susceptibility $\chi=(n+N\cos^2\varphi)/n(n+N)$, and obtain the relative abondances λ and μ of the phases:

$$\frac{1}{2}\pm\frac{1}{2}\left[\frac{n^2J_s^2}{\cos^2\varphi}\cdot\left(\frac{1}{H_e^2}-\frac{1}{H_s^2}\right)+1\right]^{-\frac{1}{2}} \tag{3}$$

When H_e increases, the phase whose spontaneous magnetization make the smaller angle with the direction of H_e gains relatively to the other. When H_e is equal to or larger than H_s the domains form one single phase only, the variation of the magnetization J_H is then only due to rotations of the spontaneous magnetization and can be found from the relations:

$$\sin2\theta=(H_eJ_s/K_1)\cdot\sin(\varphi-\theta) \quad\text{and}\quad J_H=J_s\cdot\cos(\varphi-\theta).$$

In Fig. 1, we have represented the experimental values of the reduced magnetization $i=J_H/J_s$ as a function of the reduced field $h=H_e/(2K_1/J_s)$; the curves in heavy line are those calculated by the methods given

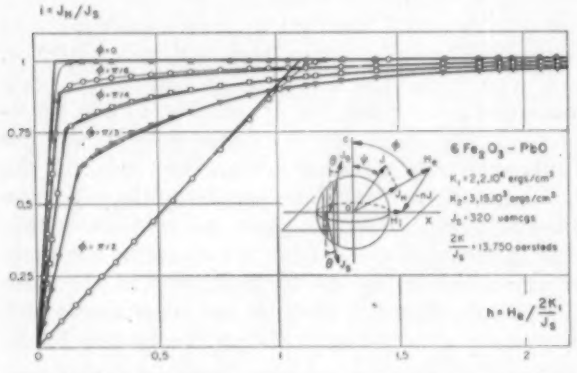

FIG. 1. Theoretical and experimental dependence of reduced magnetization $i=J_H/J_s$ on reduced field $h=He/(2K_1/J_s)$ for a $6Fe_2O_3-PbO$ crystal.

[7] W. Sucksmith and J. E. Thompson, Proc. Roy. Soc. (London) **225**, 362 (1954).

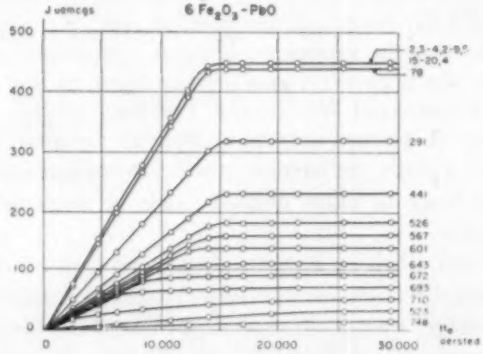

FIG. 2. Isotherms of J_H vs H_e for perpendicular to the c axis in a $6Fe_2O_3-PbO$ crystal.

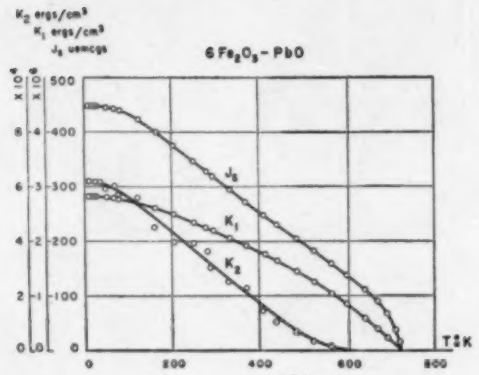

FIG. 3. Anisotropy constants K_1 and K_2, and spontaneous magnetization J_s as functions of temperature.

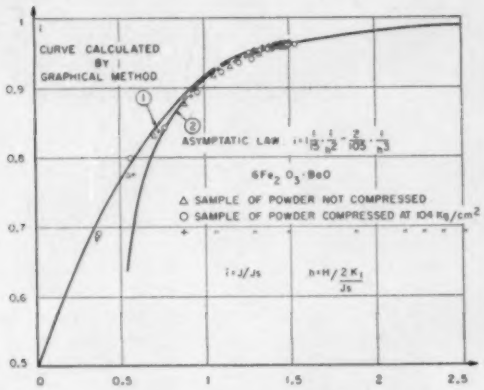

FIG. 4. Magnetization of a polycrystal. Theoretical curves: 1 calculated graphically, and 2, the asymptotic form Eq. (4).

above; the differences between the two curves is smaller than 4%.

We now consider polycrystalline samples of magnetoplumbite; we will refer to measurements made on polycrystalline ferroxdure or barium ferrite $6Fe_2O_3-BaO$, which only differs from the preceding compound in one non-magnetic ion Pb being replaced by an other non-magnetic ion Ba. The magnetic properties of the single crystal[8] are analogous to those described above. The experiments show (Fig. 4) that in a polycrystal the remanent magnetization is within 2% equal to half the saturation magnetization[9] and that the approach to saturation follows a $1/H_e^2$ law. These results show that the variations of the magnetization are due to rotations only. The grains are single domain grains; their size is too small to allow two phases to appear. This investigation on the polycrystal has allowed us to express the law of approach to saturation when K_2 is negligible. This law can be written

$$i=1-\frac{1}{15}\cdot\frac{1}{h^2}-\frac{2}{105}\cdot\frac{1}{h^3} \qquad (4)$$

the coefficient of the $1/h^4$ term is zero.

[8] U. Enz, J. F. Fast, and H. P. J. Wijn, J. phys. radium **20**, 300 (1959).

[9] V. S. Giron and R. Pauthenet, Compt. rend. **248**, 368 (1959).

JOURNAL OF APPLIED PHYSICS SUPPLEMENT TO VOL. 31, NO. 5 MAY, 1960

Garnets

Magnetic Interactions and Distribution of Ions in the Garnets

S. GELLER
Bell Telephone Laboratories, Inc., Murray Hill, New Jersey

Since the discovery of the magnetic yttrium and rare earth iron garnets, a systematic investigation has been made of interactions of magnetic ions and the distribution of both magnetic and nonmagnetic ions in the garnets. The results of substitution of the tetravalent tin for Fe^{3+} ion in yttrium-iron garnet (balanced by substitution of Ca^{2+} for Y^{3+} ions) have led to the development by Gilleo of a statistical interaction theory which accounts well for the spontaneous magnetizations and Curie temperatures of the system. This theory has been further strengthened by results from zirconium substituted yttrium-iron garnets and by its successful extension to substituted rare earth iron garnets.

In the course of our investigations, many new garnets have been discovered. Several of these have enabled us to observe *directly* interactions between magnetic ions in dodecahedral and octahedral sites, dodecahedral and tetrahedral sites, octahedral sites only and tetrahedral sites only. The work on the garnets has also already been adequately extensive to lead to the establishment of some rather simple rules pertaining to site preference of ions entering the garnets.

INTRODUCTION

SINCE the discovery[1,2] of the ferrimagnetic garnets. the interest in these materials has spread rapidly, Investigations of a variety of types are being carried out. These have not been restricted to the magnetic properties alone. However, ultimately all of these investigations can only lead to a better fundamental understanding of the interactions of the magnetic ions in these crystals if not also in many others.

For some years, there has been great interest in the ferrospinels, and although there is yet much to understand about these, microcrystalline ferrospinels have become very important technologically. (Of course, much of the present effort on the garnets is in this direction, with presumably not always the same applications in mind.) The interest in the ferrospinels has led to widespread studies of the crystal chemistry and interaction of magnetic ions in these crystals. These have shown that the crystal chemistry of the spinels is rather complex, perhaps particularly because of the existence in any crystal containing transition metal ions, of more than one valence state of that ion.

It is outside the purpose of this paper to discuss the spinels at any length. However, because they are so different from the garnets, it is worthwhile pointing out some of these differences to be sure that the reader less acquainted with the garnets is able to thwart the tendency to extrapolate from the spinels to the garnets.

The original spinel has the formula $MgAl_2O_4$.[3] The structure[4] belongs to space group $Fd3m-O_h^7$, with eight formula units in a cubic unit cell. The ions are in the following special space group positions: 8 Mg in *a*, 16 Al in *d* and 32 O in *e*. The metal ions are therefore in highly specialized positions; the oxygens have one degree of freedom. The oxygen parameter, of course, depends very much on what ions are in the *a* and *d* positions. Also the crystal fields of some of these ions affect the structures in such ways as to tend to distort them to lower symmetry.[5]

In the spinel structure, each Mg^{2+} or *a* ion is surrounded by a tetrahedron and each Al^{3+} or *d* ion by an octahedron of oxygens. Each oxygen is at the corner of three octahedra and one tetrahedron. Thus a tetrahedral magnetic ion may interact with twelve octahedral magnetic ions.

A typical mineral garnet grossularite,[6,7] $Ca_3Al_2Si_3O_{12}$[8] belongs to space group $Ia3d-O_h^{10}$ with 8 formula units in the cubic unit cell. All metal ions are in highly special positions: 24 Ca in *c*, 16 Al in *a* and 24 Si in *d*, and the 96 oxygen ions are in the general positions *h*, that is with 3 deg of freedom. Each oxygen is at the corner of four polyhedra: one tetrahedron surrounding the Si^{4+} or *d* ion, one octahedron surrounding the Al^{3+} or *a* ion and two dodecahedra surrounding Ca^{2+} or *c* ions. Here again, the distortions of the oxygen polyhedra depend on the metal ions in the structure and can change rather radically from one formula to another. However, as far as is known to date, there is no "distorted garnet" as in the cases of spinels and perovskites. Experience tells us that the latter are structurally more stable, forming with a tremendous variety of ions, whereas the garnet structure appears to be quite selective. That is, the forces tending to hold the spinels and perovskites together are great enough to allow distortion to lower symmetry, whereas the garnet structure is not as efficiently packed. In fact,

[1] F. Bertaut and F. Forrat, C. R. Acad. Sci. (Paris) **242**, 382 (1956).
[2] S. Geller and M. A. Gilleo, Acta Cryst. **10**, 239 (1957).
[3] However, magnetic Fe_2O_4, was the first crystal shown to have this structure (see reference 4).
[4] W. H. Bragg, Phil. Mag. **30**, 305 (1915); S. Nishikawa, Proc. Tokyo Math. Phys. Soc. **8**, 199 (1915).
[5] D. S. McClure, J. Phys. Chem. Solids **3**, 311 (1957) (see also other pertinent references in this paper).
[6] G. Menzer, Z. Krist. **69**, 300 (1929).
[7] S. C. Abrahams and S. Geller, Acta Cryst. **11**, 437 (1958).
[8] Mineral garnets are usually impure, but all of them have now been synthesized in the pure state.

most garnets appear to melt incongruently and when quenched from above the melting point give ABO_3 and Me_2O_3 mixtures. (Several garnets, however, have been found to melt congruently.)

Now, the prototype of the magnetic garnets is $\{Y_3\}[Fe_2](Fe_3)O_{12}$.[9] In this formula, the Y^{3+} ion is replaceable by most of the rare earths. The rare earth ions Nd^{3+}, Pr^{3+}, and La^{3+} appear to be too large, but will enter if mixed with proper amounts of the smaller ions. Thus, unlike the ferrospinels, the unsubstituted magnetic garnets contain all trivalent ions. Therefore, they are inherently high-resistivity materials which as a result of their nature preclude the possibility of valency interaction. Apparently also, these particular garnets prefer to be properly stoichiometric, so that the problem of preparing microcrystalline and large crystal specimens is not nearly as difficult as in the case of the transition metal oxide spinels.

In yttrium-iron garnet, there are five iron ions out of twenty in the formula unit. This ratio, of course, is not as favorable as that in the ferrospinel. For example, in $MnFe_2O_4$ there are three magnetic ions out of seven in the formula unit. The moment per gram of $MnFe_2O_4$ is considerably greater than that of yttrium-iron garnet. Also the Curie temperature is greater for $MnFe_2O_4$ as a consequence of the larger number of magnetic interactions per magnetic ion.[9a] Interaction distances and angles are similar in the two structures.[10]

There are now several structures which are favorable to ferrimagnetism yielding substantial net moments, but only two of these are "essentially cubic," these are of the garnet and spinel types.

The ferrimagnetic garnets were the first crystals in which it was clearly established that the magnetic rare earth ions substituted for Y^{3+} ions are involved in superexchange interaction with the Fe^{3+} ions.[11]

The purpose of the remainder of this paper is to show that crystal chemical and magnetic studies have led to a relatively good understanding of these aspects. Theoretical, ferrimagnetic resonance, and optical studies being carried out in various laboratories are adding greatly to the understanding of the garnets; these subjects are, however, outside the scope of the present paper.

SURVEY OF THE IONS WHICH ENTER GARNETS

In this section, we consider the site preference of those ions known to enter the garnet structure. A possibly effective way of doing this is to go through the periodic table, note which ions go into which sites and to give only a limited number of examples[12]:

Group IA

1. Li^+—enters *d* sites only:

   $\{Na_3\}[Al_2](Li_3)F_{12}$ (cryolithionite, the only garnet known to contain substantial amounts of Li^+ ion).

2. Na^+—being a large ion probably enters only dodecahedral or *c* sites:

   $\{NaCa_2\}[Mn_2](As_3)O_{12}$ (berzeliite)
   See also 1.

Group IB

3. Cu^{2+}—enters *c* sites:

   $\{CuGd_2\}[Mn_2](Ge_3)O_{12}$.[13]

Group IIA

4. Mg^{2+}—enters *c* or *a* sites:

   $\{Mg_3\}[Al_2](Si_3)O_{12}$.[14]
   $\{Gd_3\}[Mg_2](GaGe_2)O_{12}$.[13]
   $\{MgGd_2\}[Mg_2](Ge_3)O_{12}$.[13]

5. Ca^{2+}—a large ion which probably enters only *c* sites:

   $\{Ca_3\}[Fe_2](Si_3)O_{12}$ (andradite).

6. Sr^{2+}—enters *c* sites but there is no known garnet in which Sr^{2+} ions *fill* the *c* sites:

   $\{SrY_2\}[SnFe](Fe_3)O_{12}$.[15]

7. Ba^{2+}—small amounts are known to enter *c* sites.[15]

Group IIB

8. Zn^{2+}—enters *a* sites:

   $\{Gd_3\}[Zn_2](GaGe_2)O_{12}$.[13]
   Zn^{2+} ions will probably enter *c* sites also if the sizes of other cations present permit.

9. Cd^{2+}—enters *c* sites:

   $\{CdGd_2\}[Mn_2](Ge_3)O_{12}$.[13]

Group IIIA

10. Al^{3+}—enters *a* or *d* sites:

    $\{Ca_3\}[Al_2](Si_3)O_{12}$.[6,7]

    $\{Y_3\}[Al_2](Al_3)O_{12}$.[16]

11. Sc^{3+}—enters *a* sites only:

    $\{Y_3\}[Sc_{1.5}Fe_{0.5}](Fe_3)O_{12}$.[17]

---

[9] Where the brackets { } indicate a *c* or dodecahedral site, [ ] an *a* or octahedral site, and ( ) a *d* or tetrahedral site.

[9a] M. A. Gilleo, Phys. Rev. **109**, 777 (1958).

[10] S. Geller and M. A. Gilleo, J. Phys. Chem. Solids **3**, 30 (1957).

[11] R. Pauthenet, C. R. Acad. Sci. (Paris) **243**, 1499 (1956); **243**, 1737 (1956).

[12] The references given will often contain several more.

[13] S. Geller and C. E. Miller, Acta Cryst. (in press).

[14] L. Coes, J. Am. Ceram. Soc. **38**, 298 (1955).

[15] S. Geller, R. M. Bozorth, M. A. Gilleo, and C. E. Miller, J. Phys. Chem. Solids (in press).

[16] H. S. Yoder and M. L. Keith, Am. Mineral. **36**, 519 (1951).

[17] M. A. Gilleo and S. Geller, Phys. Rev. **110**, 73 (1958).

12. Y^{3+}—probably enters only *c* sites, see other examples in this list.

13. Rare earths—almost all trivalent rare earth ions enter the *c* sites.[11,18] Pm being very rare has not been tried. Ce^{3+} garnets have not been made. La^{3+}, Pr^{3+} and Nd^{3+} appear to be too large to fill the *c* sites in an iron garnet, but these may be mixed with smaller ions: For example, the garnets $\{La_{1.5}Y_{1.5}\}[Fe_2](Fe_3)O_{12}$[19] and $\{Nd_{1.5}Y_{1.5}\}[Fe_2](Fe_3)O_{12}$[18] exist. The garnet $\{Nd_3\}[Ga_2](Ga_3)O_{12}$ has also been made,[18,20] and $\{Pr_3\}[Ga_2](Ga_3)O_{12}$ has been reported.[18]

Group IIIB

14. Ga^{3+}—enters *c* and *d* sites:

$\{Y_3\}[Ga_2](Ga_3)O_{12}$.[17,21]
See also examples 4 and 8.

15. In^{3+}—enters *a* sites only:

$\{Y_3\}[In_{0.5}Fe_{1.5}](Fe_3)O_{12}$.[17]

Group IVB

16. Ti^{4+}—probably prefers *a* sites but will enter *d* sites:

$\{Ca_3\}[TiNi](Ge_3)O_{12}$.[13,21a]

17. Zr^{4+}—enters *a* sites only:

$\{Ca_2Y\}[Zr_2](Fe_3)O_{12}$.[22]

18. Hf^{4+}—enters *a* sites only:

$\{Ca_2Y\}[Hf_2](Fe_3)O_{12}$.[22]

Group IVA

19. Si^{4+}—greatly prefers *d* sites, but there is some indication that small amounts may enter *a* sites.[23]
See examples 4 and 5. An article by Coes[14] lists many silicate garnets made at high pressures and temperatures, some of which do not exist naturally.

20. Ge^{4+}—prefers *d* sites, but will enter *a* sites to an extent depending on the sizes of other cations present.[24] In $\{CaY_2\}Fe_4GeO_{12}$, the ion distribution is

$\{CaY_2\}[Fe_{1.85}Ge_{0.15}](Fe_{2.15}Ge_{0.85})O_{12}$.[23]

In examples 3, 4, 9 and 16, the Ge^{4+} ions are probably all in *d* sites.

21. Sn^{4+}—prefers *a*, but enters *d* sites;

probable distribution in $Ca_3Fe_2Sn_3O_{12}$ is

$\{Ca_3\}[Sn_{1.8}Fe_{0.2}](Fe_{1.8}Sn_{1.2})O_{12}$.[15]
(See example 6).

Group VB

22. V^{5+}—probably enters only *d* sites.

23. Nb^{5+}—probably enters *a* sites:

$\{Mn_3\}[NbZn](FeGe_2)O_{12}$.[13]
Ta^{5+} having very nearly the same size as Nb^{5+} could probably be substituted for Nb^{5+} in this compound, but it has not been tried.

Group VA

24. P^{5+}—enters only *d* sites:

$\{NaCa_2\}[Mg_2](P_3)O_{12}$.[25]

25. As^{5+}—see example 2.

26. Bi^{3+}—enters *c* sites to a limited extent.[19]

Group VIB

27. Cr^{3+}—enters only *a* sites:

$\{Ca_3\}[Cr_2](Si_3)O_{12}$. (uvarovite)[6,26]
$\{Mn_3\}[Cr_2](Ge_3)O_{12}$.[13,27]
$\{Y_3\}[Cr_{0.25}Fe_{1.75}](Fe_3)O_{12}$.[17]

Group VIIB

28. Mn^{2+}—enters *c* or *a* sites:

$\{Mn_3\}[Al_2](Si_3)O_{12}$ (spessartite).
$\{Gd_3\}[Mn_2](GaGe_2)O_{12}$.[13,28]
$\{MnY_2\}[Mn_2](Ge_3)O_{12}$.[13,28]
See also examples 2, 3, 9.

Group VIII

29a. Fe^{2+}—enters *a* or *d* sites:

$\{Y_3\}[Fe_2](Fe_3)O_{12}$.
See other examples in this list.

b. Fe^{2+}—enters *a* sites:

$\{Fe_3\}[Al_2](Si_3)O_{12}$ (almandite).

---

[18] F. Bertaut and F. Forrat, C. R. Acad. Sci. (Paris) **243**, 1219 (1956).
[19] M. A. Gilleo (unpublished work).
[20] S. Geller (unpublished work).
[21] M. L. Keith and R. Roy, Am. Mineral. **39**, 1 (1954).
[21a] A. Durif, International Conference on Physics of the Solid State and Application to Electronics and Telecommunications, Brussels, Belgium, June (1958).
[22] S. Geller, R. M. Bozorth, C. E. Miller, and D. D. Davis, J. Phys. Chem. Solids (in press).
[23] R. M. Bozorth and S. Geller, J. Phys. Chem. Solids **11**, 263 (1959).
[24] S. Geller, J. Phys. Chem. Solids (in press).
[25] E. Thilo, Naturwiss. **29**, 239 (1941).
[26] S. Geller and C. E. Miller, Am. Mineral. **44**, 445 (1959).
[27] A. Tauber, E. Banks, and H. H. Kedesdy, J. Appl. Phys. **29**, 385 (1958).
[28] M. A. Gilleo and S. Geller, J. Phys. Chem. Solids **10**, 187 (1959); See also J. Appl. Phys. **30**, 297S (1959).

30. Co^{2+}—enters *c* or *a* sites:

$\{Gd_3\}[Co_2](GaGe_2)O_{12}$.[13]

$\{CoGd_2\}[Co_2](Ge_3)O_{12}$.[13]

31. Ni^{2+}—enters *a* sites:

$\{Gd_3\}[Ni_2](GaGe_2)O_{12}$.[13]

See also example 16.

SUBSTITUTED YTTRIUM-IRON GARNETS

The preceding section will already have produced ideas about the effects on magnetic properties of yttrium-iron garnet of substituting other ions for the Fe^{3+} ion. Actually, many of the developments indicated in that section resulted from studies to be reviewed in this and subsequent sections.

As in the case of the ferrospinels, it is important to know what effects substitutions of other ions have on the magnetic properties of the garnets. It will be seen that a systematic study of this kind indicates that the garnets are easier to understand than the ferrospinels, probably because the garnet structure is more restrictive than the spinel structure.

Now it is obvious that substitution of any nonmagnetic or 3*d* transition metal ion for Fe^{3+} in a *d* site and not having a $3d^5$[29] electronic configuration will reduce the 0°K saturation magnetization, whereas any such ion substituted in at least small amounts for *a* site Fe^{3+} ions should raise this moment. Thus, it seemed logical to examine first the trivalent nonmagnetic ions.

Now, on the basis of steric considerations, one might think that an ion with a rare gas configuration would show preference for a site which is in accord with its size. Furthermore, one might suspect that the relative sizes of ions in the perovskite-like structures might be a clue to their relative sizes in the garnets. All known sets of radii indicate the Al^{3+} ion to be considerably smaller than that of the Fe^{3+} ion, and the Al^{3+} ion does indeed show a great preference for the *d* sites on substitution for Fe^{3+} ion in YIG.[17] Eventually, an yttrium-aluminum garnet is formed as indicated earlier.

Pauling's radii indicate the Ga^{3+} ion to be larger than that of Fe^{3+}, whereas Goldschmidt's radii indicate Fe^{3+} to be larger than Ga^{3+}. There is little doubt that Fe^{3+} *is* larger than Ga^{3+} in both the perovskites[30,31] and the garnets.[17,32] Thus, Ga^{3+} also shows a great preference (though not quite as great as Al^{3+}) for the tetrahedral sites.[17]

Now, both the Pauling and Goldschmidt radii indicate the Sc^{3+} and In^{3+} ions to be considerably larger than Fe^{3+} ion. The radii derived from the perovskites[31] however, indicate that substitution in the garnets should be possible as indeed, it is. Both of these ions prefer the octahedral sites. The In^{3+} ion, which is larger than Sc^{3+} cannot replace as much of the Fe^{3+} ion as the latter.[17] It is probable that very little of either of these ions enter the *d* sites. Thus, already it is seen that size plays a most important role in site preference. This is not quite so clear for the spinel structure.

Although exhaustive experiments have not been carried out, it does appear that only three *trivalent* 3*d*-transition metal ions enter the garnets in an *appreciable* amount. These are the Sc^{3+}, Cr^{3+}, and Fe^{3+} ions. It is also noteworthy that at the time of this writing, as far as is known, the Fe^{3+} ion is the only magnetic ion which enters the tetrahedral sites in appreciable amount. Now, both the Pauling and Goldschmidt radii put the Cr^{3+} ion as larger than Fe^{3+}. Here again, this is contrary to observation in several structures and particularly in the perovskites[31] and garnets.[17,26] Although Cr^{3+} is actually smaller than Fe^{3+}, it will replace an Fe^{3+} ion only in an octahedral site in the iron garnets. This is explained by the effect on the *d*-orbital splitting of the octahedral and tetrahedral fields; i.e., in the octahedral field, the filling of the lower energy *d*-orbitals gives a pseudospherical electronic configuration to the Cr^{3+} ion. Thus, we begin to see that in the garnets, the octahedral and tetrahedral sites show a preference for ions with spherical or pseudospherical electronic configurations. (See note added in proof.)

Because the Cr^{3+} ion is, however, smaller than Fe^{3+}, its substitution for Fe^{3+} is very limited,[17] or in other words, the garnet structure puts a lower limit on the ratio of the octahedral to tetrahedral metal-oxygen distance.[22] Thus, in uvarovite, $\{Ca_3\}[Cr_2](Si_3)O_{12}$, the *a* sites are filled with Cr^{3+} ions; this is probably also the case for $\{Ca_3\}[Cr_2](Ge_3)O_{12}$[27] and $\{Mn_3\}[Cr_2](Ge_3)O_{12}$.[13,27]

The tetravalent nonmagnetic ions behave in a manner similar to that of the trivalent ones. (In the case of substitution of tetravalent ions for Fe^{3+}, it is of course also necessary to substitute charge compensating divalent ions for an equal number of other trivalent ions in YIG.) The smaller ions Si^{4+} and Ge^{4+} show a great preference for the tetrahedral sites[28]; the large ones such as Sn^{4+}, Zr^{4+}, and Hf^{4+} greatly prefer octahedral sites.[15,22,23] The Ti^{4+} ion also appears to prefer the octahedral sites; however, work on this ion has not as yet been adequate to be definitive.

It would be interesting to study the properties of garnets such as $\{R_3\}[M^{2+}M^{4+}](Fe_3)O_{12}$, in which R is a rare earth or yttrium and M^{2+} a divalent magnetic ion. Attempts to make a number of these have not proved successful.

MAGNETIC INTERACTION STATISTICS OF THE Fe^{3+} IONS IN SUBSTITUTED YTTRIUM-IRON GARNETS

Our early work on the magnetic interactions in trivalent ion substituted yttrium-iron garnet was limited to small substitution. The discovery of the tin garnet

[29] For 4*d* and 5*d* transition metal ions, the situation may, of course, be different.

[30] S. Geller, Acta Cryst. **10**, 243 (1957).

[31] S. Geller, Acta Cryst. **10**, 248 (1957).

[32] This is also the case in other structures such as Fe_2O_3 vs Ga_2O_3 and FeF_3 vs GaF_3.

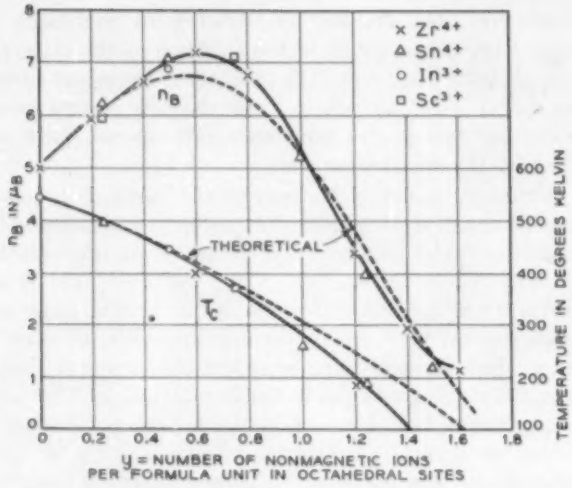

FIG. 1. Theoretical and experimental variation of magnetic moment (at 0°K) and of Curie temperature with composition for garnets $\{Y_{3-y}Ca_y\}[M_y'Fe_{2-y}](Fe_3)O_{12}$, M′=Sn, Zr and $\{Y_3\}[M_y''Fe_{2-y}](Fe_3)O_{12}$, M″=Sc, In.

$Ca_3Fe_2Sn_3O_{12}$ and the existence of a complete solid solution range between it and YIG have led to a significant improvement in the understanding of the general statistics of the magnetic interactions in the substituted yttrium-iron garnet. It was noted (Fig. 1) that on initial substitution of Sn^{4+} for Fe^{3+} the 0°K saturation magnetization ($n_B(\infty,0)$) rose. On continued substitution a maximum is reached for $x=0.6$ in the formula $\{Y_{3-x}Ca_x\}Sn_xFe_{5-x}O_{12}$. (We write the formula in this fashion to indicate that either we do not yet know or do not yet wish to indicate the ion distribution over the octahedral and tetrahedral sites.) Then there is a rather rapid decrease of $n_B(\infty,0)$ for further substitution.

The x-ray scattering factor for Sn is fortunately appreciably different from that of Fe, and therefore, quantitative x-ray measurements permitted us to ascertain that even when $x=2$ the number of Sn^{4+} ions per formula unit going into octahedral sites, $y=1.8$.[15] Thus, it could be seen that the original formula[17] expressing the interaction statistics was only a first approximation and held only for small substitution. These results led to a reconsideration of the problem by M. A. Gilleo, with the consequence that the interaction statistics of substituted yttrium-iron garnets are quite well understood. A paper by Dr. Gilleo[33] on the subject is in press, but he has kindly permitted me to outline his results.

One asks which Fe^{3+} ions are removed from interaction or do not contribute to the spontaneous magnetization as a result of the substitution of nonmagnetic for Fe^{3+} ions. In the Gilleo-Geller paper,[17] the formula there derived excludes those Fe^{3+} ions which are linked only to nonmagnetic ions through oxygens. The ferrimagnetic crystal must be considered as of semi-infinite extent. A broken network of $-Fe^{3+}-O^{2-}-Fe^{3+}-$ interactions results in the loss to the spontaneous magnetization of the contribution from the Fe^{3+} at the ends of the chains. That is to say, to participate in the ferrimagnetism, the Fe^{3+} ion must be linked to *at least two* other Fe^{3+} ions through oxygens.

The following development of the saturation magnetization at 0°K[34] is taken from Gilleo's paper.[33] Consider the formula unit of a substituted garnet:

$$\{Y_{3-y-z}Me_{y+z}\}[Fe_{2-y}M_y']\left(Fe_{3-z}M_z''\right)O_{12},$$

where it must be remembered that charge balance must be maintained. The ions Me, M′ and M″ are nonmagnetic. For simplicity, let $k_o=(y/2)$ and $k_t=(z/3)$. Now, the probability $p_n(m)$ that an ion of coordination n be linked with m ions each of probability $(1-k)$ is

$$p_n(m)=\binom{n}{m}k^{n-m}(1-k)^m,$$

from which it follows that the probability E that an ion is linked with at most one magnetic ion is

$$E=\sum_{m=0}^{1}p_n(m)=nk^{n-1}-(n-1)k^n. \qquad (1)$$

Thus, if the fraction, E, of magnetic ions in a specified site is excluded from contribution to the spontaneous magnetization, the portion $(1-E)(1-k)$ does contribute.

The total moments from each of the magnetic sublattices in the substituted yttrium-iron garnet are then given by

$$n_B^{(o)}=10(1-k_o)[1-E_o(k_t)],$$
$$n_B^{(t)}=15(1-k_t)[1-E_t(k_o)],$$

where from (1)

$$E_o(k_t)=6k_t^5-5k_t^6,$$
$$E_t(k_o)=4k_o^3-3k_o^4.$$

Then

$$n_B(k_o,k_t)=n_B^{(t)}-n_B^{(o)}$$
$$=5\{3(1-k_t)[1-E_t(k_o)]$$
$$-2(1-k_o)[1-E_o(k_t)]\}\mu_B. \qquad (2)$$

For substitution of nonmagnetic ions in the tetrahedral sites in the range previously studied,[17] that is $z\leq 1$, Eq. (2) does not change things much from the first order approximation given in the Gilleo-Geller paper.[17] In fact, results in this range are not much different from those obtained from the simplest approximation, namely $n_B(\infty,0)=5(1+y-z)\mu_B$. However, for octahedral substitution, very significant differences are obtained which, in fact, led us to modify[22,33] some former conclusions[17] with regard to Sc^{3+} and In^{3+} substitution.

For the cases in which substituted nonmagnetic ions

[33] M. A. Gilleo, J. Phys. Chem. Solids (in press).

[34] See the Gilleo paper and references 15 and 22 for qualification.

go only into octahedral sites (2) reduces to:

$$n_B(k_o,0)=5[3(4k_o^3-3k_o^4)-2(1-k_o)]\mu_B$$
$$=5\{3[1-4(y/2)^3+3(y/2)^4]-2(1-y/2)\}\mu_B.$$

This function is plotted in Fig. 1 together with the curve derived by plotting all 0°K saturation magnetizations obtained from a number of systems. (The actual calculated and observed n_B values are collected in another paper.[22]) It is seen that the theoretical and experimental curves are in very good agreement. Also, it is necessary to conclude that since the Sn^{4+} [35] and Zr^{4+} ions are all located in octahedral positions, the In^{3+} and Sc^{3+} must also be so situated.

The Gilleo paper also shows how one may estimate the Curie temperatures of the substituted yttrium-iron garnets. For the octahedrally substituted garnets agreement between theoretical and observed Curie temperatures for $y\leq 0.8$ is excellent. Thereafter, the observed values drop away somewhat from the theoretical curve (Fig. 1). Agreement however, is generally still good and attests to the validity of Gilleo's ideas.

INTERACTIONS IN SUBSTITUTED RARE EARTH IRON GARNETS

We have considered at some length the effects of substitution of nonmagnetic ions for the Fe^{3+} ions in YIG. We now ask about the effects of substituting a magnetic rare earth ion for yttrium. It is now well known that in such a garnet, the rare earth ion magnetic sublattice has little effect on the Curie temperature. Consider a substituted YIG such as $\{Gd_{3-w}Y_w\}[Fe_2](Fe_3)O_{12}$. Apparently ,it is possible to obtain the magnetization, $n_B(T,w)$, as follows

$$n_B(T,w)=[(3-w)/3]n_{B(Gd)}(T)-n_{B(YIG)}(T),^{24,36}$$

where $n_{B(Gd)}$ and $n_{B(YIG)}$ are the Gd^{3+} ion sublattice and YIG magnetizations, respectively. This treatment gives an excellent estimate of the compensation points, if any, in such systems. Furthermore, compensation points and magnetizations may be determined in a similar fashion when a mixture of magnetic ions fill the c sites.[36,37]

This result again demonstrates the importance to the magnetization of the continuous linkage of the magnetic ions. It is obvious that as long as the a and d sites are filled with Fe^{3+} ions, the magnetic ions in c sites will always be actively linked in a chain of antiferromagnetically interacting ions. In such a situation, every magnetic ion in a c site is in a favorable situation for superexchange interaction. Also it is seen that the magnetizations of the Fe^{3+} ion sublattices are not significantly affected by the amounts of magnetic rare earth ions in the c sites.

TABLE I. Fraction of Al^{3+} ions in tetrahedral sites, f_t, in $\{Gd_3\}[Al_yFe_{2-y}](Al_zFe_{3-z})O_{12}$ as deduced from data of Villers et al.[10]

$x=y+z$	n_B(obs)	f_t
0.5	17.7	0.92
1.0	18.1	0.84
1.5	17.6	0.72
2.0	15.8	0.64
3.0	10.2	0.62

The considerations of interaction statistics have now been extended to more complicated systems and despite the scarcity of data, there appears to be adequate evidence of the validity of the assumptions made. If we examine the yttrium-iron garnet structure,[10] we see that if we substitute a magnetic rare earth, R, for yttrium, the R−O−Fe(a) angles would probably not be favorable to superexchange interaction. Also, only half of the R−O−Fe(d) angles *would* be favorable to such interaction. Thus, for a garnet $\{R_3\}[M_yFe_{2-y}](M_zFe_{3-z})O_{12}$, since the moment $n_B^{(D)}$[38] of the dodecahedral sublattice would be[24]

$$n_B^{(D)}=3M_D[1-E_D(k_t)],$$

where $E_D(k_t)=4k_t^3-3k_t^4$, we would get for the total magnetization:

$$n_B=n_B^{(D)}-n_B^{(t)}+n_B^{(o)}=3M_D[1-E_D(k_t)]$$
$$-\{15(1-k_t)[1-E_t(k_o)]$$
$$-10(1-k_o)[1-E_o(k_t)]\}\mu_B$$
$$=3M_D(1-4k_t^3+3k_t^4)-\{15(1-k_t)(1-4k_o^3+3k_o^4)$$
$$-10(1-k_o)(1-6k_t^5+5k_t^6)\}\mu_B.$$

Data for several systems have been reported by Villers et al.,[39,40] the most extensive being for that in which R=Gd, M=Al. The $n_B(0)$ value for $x=y+z=1.0$ obtained by Villers et al. appears to be much too low in comparison with their other points and therefore the curve they draw is probably off. The points we have taken modify this curve, i.e., raise it somewhat in the region $0<x<2$. The values of $n_B(0)$ thereby deduced and the values of f_t, the fraction of Al^{3+} ions in tetrahedral sites,[41] obtained by use of the above expression are given in Table I. In the calculations, each active Gd^{3+} ion is considered to contribute $7\mu_B$ to the magnetization despite the fact that this does not appear to be the case for the specimens measured by Villers et al.[39] This may imply the presence of impurity ions in their samples. Nevertheless, the results demonstrate the ap-

[35] For Sn^{4+}, this occurs for $x(=y+z)$ less than or equal to approximately 1.5.

[36] Villers, Loriers, and Claudel, C. R. Acad. Sci. (Paris) **247**, 710 (1958).

[37] G. Villers and J. Loriers, C. R. Acad. Sci. (Paris) **247**, 1101 (1958).

[38] A capital D is used here to avoid confusion with d sites. The other designations are consistent with those in the Gilleo paper. (see reference 33).

[39] Villers, Pauthenet, and Loriers, J. phys. radium **20**, 382 (1959).

[40] The moments reported are obtained by extrapolation to H=0, T=0°K.

[41] That is, $f_t=z/x$.

plicability of the statistical theory and appear to account especially well for the low magnetizations for high x. It is seen that the f_i values for this system appear quite reasonable when compared with those of the $\{Y_3\}[Al_yFe_{2-y}](Al_zFe_{3-z})O_{12}$ system.[17]

One further interesting example may be given. If we have a system such as

$$\{R_{3-w}Me_w\}[M_yFe_{2-y}](M_zFe_{3-z})O_{12},$$

where Me and M are nonmagnetic ions, the contribution from the dodecahedral sublattice will then be

$$n_B=3M_D(1-k_D)[1-F_D(k_i)].$$

Magnetic data have been reported for the solid solutions $\frac{1}{3}Ca_3Al_2Si_3O_{12}-\frac{2}{3}R_3Fe_2Fe_3O_{12}$. It was concluded in that paper[23] that the distributions of ions were as follows:

$\{Y_{2.4}Ca_{0.6}\}[Fe_{1.86}Al_{0.14}](Fe_{2.14}Al_{0.26}Si_{0.6})O_{12}$ $1.4\mu_B$,

$\{Gd_{2.4}Ca_{0.6}\}[Fe_{1.74}Al_{0.26}](Fe_{2.26}Al_{0.14}Si_{0.6})O_{12}$ $14.2\mu_B$.

However, the behavior of the Gd specimen appeared to be anomalous. Now, the distribution of ions in the Y specimen is not affected by the new treatment, but that of the Gd specimen is. In fact, if we allow the ionic distribution in that specimen to be exactly the same as in the Y specimen, we now obtain the $14.2\,\mu_B$ 0°K moment. Presumably, the ionic distributions are *not* exactly the same, but the new result is certainly an improvement on that obtained by applying the simplest interaction model idea.

Application is made to other systems and further details of the statistical theory are given in other papers.[24,33]

DIRECT OBSERVATION OF OTHER THAN OCTAHEDRAL-TETRAHEDRAL ION MAGNETIC INTERACTION IN THE GARNETS

Much of the work on synthetic garnets, some of which was exemplified in earlier sections, was an outgrowth of the desire to observe *directly* interactions between magnetic ions in other than the octahedral (a) and tetrahedral (d) sites. As mentioned earlier, the refinement of the structure of YIG indicated that if yttrium (c sites) were replaced by a magnetic ion, the c-d would be stronger than the c-a interaction. However, because it appeared simpler, we tried to make garnets containing magnetic ions only in the c and a sites. We began by attempting[42] to make $Mn_3Fe_2Si_3O_{12}$. The anticipation of the possibility of obtaining a ferrimagnetic silicate, even with a low Curie temperature, was somewhat exciting. We did not obtain such a garnet with the technique of direct dry synthesis, but we learned that Coes had done so with a high pressure hydrothermal synthesis.[14] Magnetic measurements on a specimen kindly supplied by Mr. Coes were disappointing showing a 0°K spontaneous magnetization of only 0.1 μ_B.[23]

[42] S. Geller and C. E. Miller, Am. Mineral. 44, 666 (1959).

Meanwhile a number of germanium garnets were discovered by Tauber et al.[27] including $Mn_3Fe_2Ge_3O_{12}$. We found this garnet to be one of the few congruently melting ones and were able to isolate a mass of pure material which was measured. This garnet was found to be only antiferromagnetic at low temperatures indicating mainly a-a interactions among the Fe^{3+} ions as borne out by measurements on $Ca_3Fe_2Ge_3O_{12}$ also.[23]

The garnets $\{M^{2+}Gd_2\}[Mn_2](Ge_3)O_{12}$, M = Mn and Ca were indeed found to be ferrimagnetic at 6°K or lower.[28] More definitive measurements were however carried out on $\{Gd_3\}[Mn_2](GaGe_2)O_{12}$, which was found to have a Curie temperature of 8°K and a 0°K saturation magnetization of $9.6\,\mu_B$ (theoretical = $11\,\mu_B$).[28] This is especially interesting because from the simplest considerations one would expect Mn−O−Fe interactions to be stronger than Gd−O−Mn interactions. The answer might be found in a consideration of structure: We know from experiment that the geometrical arrangement of ions in the garnets is quite sensitive to the sizes of the ions present. It is also probable that when the interactions are very weak, this geometry plays a more important role. Thus, it is probable that the geometry (angles and distances) is more favorable for interaction in the $\{Gd_3\}[Mn_2](GaGe_2)O_{12}$ case than in that of $Mn_3Fe_2Si_3O_{12}$, for example.

It is noteworthy that a-a antiferromagnetic interaction exists in $[MnY_2][Mn_2](Ge_3)O_{12}$. Also, $\{Gd_3\}(Ni_2)[GaGe_2]O_{12}$ and $\{Gd_3\}[Co_2](GaGe_2)O_{12}$ show only a very small tendency toward antiferromagnetism.[23] Antiferromagnetic interaction among tetrahedral Fe^{3+} ions has been observed in $\{YCa_2\}[Zr_2](Fe_3)O_{12}$.[22]

We have recently succeeded in making the garnet $\{Gd_3\}[Sc_{1.75}Fe_{0.25}](Fe_3)O_{12}$. In this case, magnetic measurements indicate that this garnet is ferrimagnetic with a 0°K moment less than 6 μ_B and a Curie temperature of about 26°K. Thus, the c-d interactions are the strong ones in this case.

Note added in proof. The rules for ionic site preference in the garnets may be summarized as follows:

1. The octahedral and tetrahedral sites appear to prefer exclusively ions with spherical or pseudospherical electronic configuration. The dodecahedral sites are not selective in this regard.

2. Site preferences depend on relative ionic sizes: (a) If an ion has a spherical electronic configuration in both octahedral and tetrahedral crystal fields, the larger the ion, the greater will be its preference for the octahedral site. The dodecahedral sites are usually occupied by the largest metal ions present. (b) The substitution of one ion for another in a particular garnet is limited by the relative sizes of all of the ions involved.

The Co^{3+} ion with $3d^7$ configuration prefers the octahedral site and would appear to be an exception to the first rule. However, it has been pointed out to me by Dr. A. D. Liehr that for a Co^{3+} ion in an octahedral field, the spin-orbit coupling is large enough to produce a Γ_7 or pseudospherical electronic ground state.[43] A Co^{3+} ion would also have a pseudospherical electronic configura-

[43] A. D. Liehr, Symposium on Synthesis and Properties of Inorganic Compounds, 137th National Meeting of the American Chemical Society, Cleveland, Ohio, April (1960).

tion in a tetrahedral crystal field, but then in accord with Rule 2, it would be expected to prefer the octahedral site.

CONCLUSION

I have tried in this paper to summarize the results of our work on the interactions of magnetic ions in and crystal chemistry of the garnets. Despite the great length of the paper, some of the points discussed must of necessity be of insufficient detail and may therefore lead to some erroneous impressions. It is hoped that the interested reader will find it worthwhile to look at some of this detail given in the references.

ACKNOWLEDGMENTS

I should like to mention that, as shown by the references, much of the work described herein was done jointly with Dr. M. A. Gilleo and/or Dr. R. M. Bozorth and the assistance of C. E. Miller, D. W. Mitchell and D. D. Davis.

JOURNAL OF APPLIED PHYSICS SUPPLEMENT TO VOL. 31, NO. 5 MAY, 1960

Resonance Experiments with Single Crystal Yttrium Iron Garnets in Pulsed Magnetic Fields

MARTIN R. STIGLITZ AND FREDERIC R. MORGENTHALER
Air Force Cambridge Research Center, Cambridge, Massachusetts

A crystal sphere of YIG was placed in either a doubly resonant transmission type coaxial cavity or into a nonresonant transmission line device and biased with a dc magnetic field. A low power microwave signal in the S band frequency range (cw or pulsed) was used to excite resonance. Current pulses of approximately 1 μsec duration and low duty cycle were sent through a low impedance coil that was wound around the cavity or transmission line respectively. These pulses induced pulsed magnetic fields of the order of 1000 gauss, which (vectorially) added to the existing dc field.

A microwave receiver, attached to the cavity output, detected weak oscillations at higher or lower frequencies. Shifts of 280 Mc have been obtained with the cavity, and shifts of 1280 Mc above and 530 Mc below the driving frequency have been obtained with the transmission type device.

The detected signal is associated with either the rise of the current pulse, or the decay, or two signals may appear simultaneously corresponding respectively to the rise and decay. This depends upon the angular relation of the dc field with respect to the cavity or transmission line.

1. INTRODUCTION

THE prospect of obtaining microwave radiation from ferrimagnetically coupled electrons has been of interest ever since it was discovered that single crystals of yttrium iron garnet $3Y_2O_3 5Fe_2O_3$ are characterized by relatively long relaxation times. Certain theoretical aspects of the behavior of the magnetization in such a medium, when it is subjected to transient magnetic fields have previously been treated by the coauthor of this paper, and various schemes have been proposed.[1–3] The physics in its simplest form involves the assumption that a single crystal of YIG, which has been given some initial magnetic energy and is subjected to a rapidly established pulsed magnetic field, will be raised to a new energy level corresponding to a higher resonance frequency, and under suitable conditions will be free to radiate this energy at the higher frequency. The initial energy might come from conventional ferromagnetic resonance at a lower frequency or through a pulsed magnetic field. The former method has been the subject of this experimental study. It appears from the preliminary results that several effects are being observed.

2. EXPERIMENT

A transmission type device (resonant or nonresonant) was placed between the pole pieces of an electromagnet. The garnet of 1.5 mm diam was placed within the device such that it could be oriented in two planes. The line width was not measured because of the large crystal size. Small crystals from the same source (Microwave Chemical) have lines of typically a few oersteds, measured at X-band. A low impedance coil was wound around the device and was connected to a modulator which was capable of delivering up to 1200 gauss pulses at a rise time of 0.1 μsec and a pulse duration from 1 to 2 μsec. Microwave energy at 3000 Mc and of 240 mw cw power was fed into the device (Fig. 1). The electromagnet was adjusted to bias value for 3000 Mc (approximately 1100 gauss). The output of the cavity led to a microwave receiver and the output of the receiver

---

[1] F. R. Morgenthaler, "New developments in microwave applications of ferromagnetic and ferroelectric materials," Proc. conf. International Congres Ultra High Frequency Circuits and Antennas (Paris, France, October 21–26, 1957).

[2] F. R. Morgenthaler, Inst. Radio Engrs. Trans. MTT-7 No. 1, 6–11 (January, 1959).

[3] F. R. Morgenthaler, "Microwave radiation from coupled electrons in transient magnetic fields," presented orally at the Congres International sur la Physique de l'etat Solide et ses Applications a l'Electronique et aux Telecommunications (Bruxelles, Belgium, June, 1958).

to a dual trace oscilloscope. When the modulator delivered pulses of approximately 100 gauss within the cavity, frequency shifts of 280 Mc were measured by the receiver at a power level of 10 dbm peak and 0.25 μsec duration. The current pulse wave form was observed simultaneously on a dual trace scope and time relation between the current pulse and the rf pulse was measured. A graph of cw incident power at 3000 Mc versus peak pulse output power at 3280 Mc is shown on Fig. 2. The rapid change of the slope of the curve at the incident power level of 110 mw is of considerable interest. At frequencies of 50 Mc above and below the incident frequency clusters of oscillations occurred, lasting from 4 to 6 μsec. These appear to be correlated with low amplitude ripples in the pulsing current following the main pulse. With the nonresonant device, oscillations were observed at a frequency shift of 1300 Mc with induced pulses of approximately 500 gauss at peak power levels of 20 dbm. The rf pulse wave form had sharp peaks, especially at the higher frequencies. When the magnetic field was pulsed in line with the dc magnetic field the generated rf pulses appeared during the rise of the magnetic pulse. When the pulsed magnetic field opposed the dc field, the rf pulse was observed to correspond to the decay portion of the current pulse. When the dc field was rotated about the device at an angle $0 \cdot < \alpha < 90$; both rf pulses were observed simultaneously at a combined power level approximately equal to a single pulse.

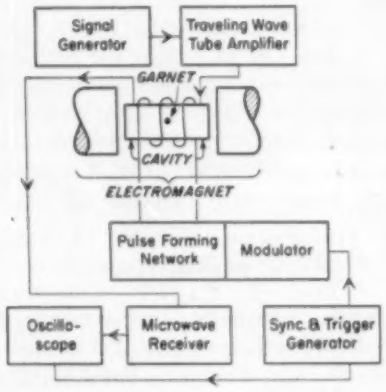

FIG. 1. Block diagram of experimental setup.

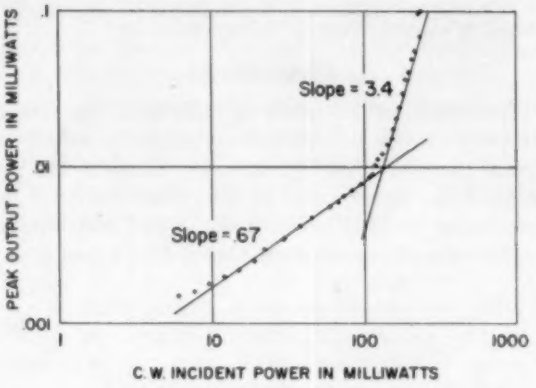

FIG. 2. cw incident power vs peak output power.

3. SUMMARY

Pulsed rf fields have been generated by pulsing garnets with magnetic fields from resonance to a higher energy level. Experiments involving the nonresonant structure indicated that the YIG crystal gave up its energy continuously throughout the allowed frequency spectrum. The highest frequency of this spectrum appeared to be linearly related to the magnitude of the pulsed field by the simple Larmor relation. A reduction of the pulsed field of 100 gauss reduced the high frequency limit of the spectrum approximately 300 Mc. This point tentatively agrees with the theory. In addition signals were received, which clustered on either side of the main resonance. It is reasonable to assume that these are magnetostatic modes, and efforts are continuing to correlate these results with the assumption. The signals which correspond to the decay portion of the current pulse are not completely understood at the present time. This work will be continued and extended to higher powers and higher frequencies. The possibility of generating pulsed millimeter waves by this method is being investigated.

A complete report of the experiment will be published in the near future.

ACKNOWLEDGMENT

The authors are indebted to James R. Littler of the Air Force Cambridge Research Center who fabricated the necessary cavities and auxiliary equipment.

Absorption and Reflectivity Measurements on Some Rare Earth Iron Garnets and α-Fe_2O_3*

P. C. Bailey
Magnetic Materials Development Section, Materials Engineering Departments, Westinghouse Electric Corporation, East Pittsburgh, Pennsylvania

Measurements of the absorption coefficient of (111) crystal sections of α-Fe_2O_3 were made in the visible and near infrared. Absorption peaks were observed centered at energies of about 12 000 cm^{-1} and 16 000 cm^{-1}. Reflectivity measurements on the α-Fe_2O_3 crystals were carried out in the 30 000 cm^{-1} to 400 cm^{-1} range. Broad reflectivity peaks are found in the near ultraviolet at 24 500 cm^{-1} and 26 000 cm^{-1}, respectively. Very strong reflection peaks resulting from the lattice vibrations are present at energies smaller than 700 cm^{-1}.

Several quite sharp peaks are found in the absorption spectra of the rare-earth iron garnets of Dy, Ho, Er and Yb in the 10 000 cm^{-1}–13 000 cm^{-1} energy range. The circular dichroism of ytterbium iron garnet is displayed by means of absorption curves for the two senses of circularly polarized light.

INTRODUCTION

INTEREST in the optical properties of magnetic oxides has been stimulated by the observations of Dillon[1,2] of the optical absorption and rotations in the rare earth iron garnets.[3] This note reports on the absorption of several of these, and on the absorption and the reflectivity of α-Fe_2O_3.[4]

The garnet crystals were grown by the lead oxide flux technique of Nielsen.[5] For their absorption measurements, sections were ground and carefully polished to a thickness of about 0.0015 in. The α-Fe_2O_3 crystals used were natural or grown from fluxes of sodium metaborate and sodium tetraborate. Some of these appeared in the form of (111) platelets which were thin enough (~0.00025 in.) to use directly for absorption measurements. The as-grown (111) faces of other, thicker samples were used for the reflectivity measurements to avoid back surface reflections. The absorption and reflectivity measurement techniques used were fairly standard for the single beam spectrophotometers available and so will not be described further.

RESULTS

α-Fe_2O_3 Absorption

The linear absorption coefficient α of α-Fe_2O_3 for room and liquid nitrogen temperatures is illustrated in Fig. 1. The room temperature curve is also shown corrected for the considerable losses due to reflectivity.

The absorption peak near 12 000 cm^{-1} shows signs of structure which is somewhat obscured by the band width (~100A) of the spectrophotometer available to us for the 10 000–20 000 cm^{-1} region. A second absorption peak at 16 000 cm^{-1} becomes quite pronounced at liquid nitrogen temperatures. The general shape of these curves resembles those for YIG; i.e., the peaks at 16 000 cm^{-1} and 12 000 cm^{-1} in Fig. 1 correspond to those of this garnet at 16 500 cm^{-1} and 11 000 cm^{-1}. Since all the Fe^{3+} ions in the α-Fe_2O_3 possess 6-fold oxygen coordination, this indicates that these garnet absorptions are associated with transitions between energy levels of Fe^{3+} ions in octahedral positions. The absorption present in the garnet spectrum at about 14 000 cm^{-1} is not observed in the α-Fe_2O_3.

α-Fe_2O_3 Reflectivity

We can but mention here the results of the α-Fe_2O_3 reflectivity measurements, some of which were used to correct the absorption coefficient curves of Fig. 1. Space precludes mention of similar measurements made on YIG. For α-Fe_2O_3, a broad ultraviolet reflection peak is centered at 24 500 cm^{-1} with a maximum reflection coefficient of 0.34. Broad, weaker peaks appear at 18 250 cm^{-1} and 12 000 cm^{-1}. The ultraviolet peak is presumably associated with the strong absorption in this region.

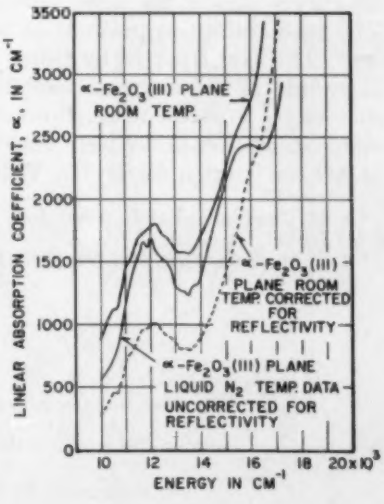

FIG. 1. The visible and near infrared apparent linear absorption coefficients of a (111) section of α-Fe_2O_3 vs energy at room and liquid nitrogen temperatures. The room temperature absorption coefficient is also given after correction for reflectivity.

* This work was supported in part by the Electronics Research Directorate of the Air Force Cambridge Research Center, Air Research and Development Command.

[1] J. F. Dillon, Jr., J. Appl. Phys. **29**, 539 (1958).

[2] J. F. Dillon, Jr., J. phys. radium **20**, No. 2–3, 374 (1959).

[3] The rare earth iron garnets will be designated hereafter as YIG for yttrium iron garnet, DyIG for dysprosium iron garnet, etc.

[4] F. J. Morin [Phys. Rev. **93**, 1195 (1954)] has reported the percent transmission of a sintered film of α-Fe_2O_3 in the 0.5 to 1.9-ev region.

[5] J. W. Nielsen, J. Appl. Phys. **29**, 390 (1958).

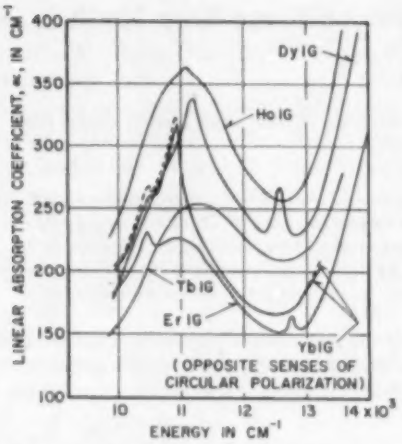

FIG. 2. The room temperature absorption coefficients of the rare earth iron garnets TbIG, DyIG, HoIG, ErIG, and YbIG vs energy in the range 10 000–14 000 cm^{-1}. The coefficients are uncorrected for reflectivity. The circular dichroism of a sample of YbIG magnetized to saturation parallel to the light path is also shown.

Clogsten and Wood[6] suggest that this arises from transitions of Fe^{3+} $3d$ electrons to the $4p$ shell, or from a process involving a charge transfer of an electron from an oxygen ion to a ferric ion. In the visible, the reflection coefficient R is quite large; e.g., 0.26 at 14 900 cm^{-1}. The corresponding index of refraction for the ordinary ray is 3.06. In the infrared, there are two uniform high peaks ($R>0.8$) centered at 560 cm^{-1} and 460 cm^{-1} believed to be associated with fundamental lattice vibrations. Similar strong reflection bands have been reported for some of the ferrites.[7]

Rare Earth Iron Garnet Absorption

Dillon first reported[1,2] sharp absorption lines in ErIG near 6525A and 5206A. Room temperature measurements of the absorption spectra of a series of the garnets therefore were made in the 10 000 cm^{-1} to 18 000 cm^{-1} region. The linear absorption coefficients of several of these, uncorrected for reflectivity, are shown in Fig. 2. All curves possess the same general form as that for YIG with absorption peaks at 16 500 cm^{-1} and 11 000 cm^{-1}. The lines reported by Dillon were not observed, likely due to the marginal resolution of the spectrophotometer available to us. However, additional quite sharp absorption peaks were resolved in the 10 000–13 000 cm^{-1} region for DyIG, YbIG, ErIG and, to a lesser extent, HoIG. In the absorption spectra of TbIG and LuIG (not shown in Fig. 2), these peaks were not seen. Table I lists the positions of the peaks which were observed in our measurements.

TABLE I. Energies of absorption lines in some garnets.

Crystal	Energies of absorption peaks in cm^{-1}	
DyIG	11 200	12 580
HoIG	11 070	
ErIG	10 450	12 760
YbIG	10 500	10 900

These sharp absorption lines in materials containing rare earth ions are generally interpreted as arising from transitions between various levels of the $4f$ electron configurations of the rare earth ion. Gobrecht[8] has assigned a number of infrared absorption lines in the rare earths to such transitions. Several appear to be the same as those reported in Table I; others do not so correlate.

When thin sections of the foregoing garnets are viewed with a polarizing microscope, they display not only Faraday rotation but also dichroism. That is, a difference in the absorption of right and left hand circularly polarized light. Measurements are usually made with a fixed source of circularly polarized light; the sense of the polarization with respect to the specimen moment is changed by magnetically saturing the specimen parallel and anti-parallel to the light direction. Dillon,[1] who first pointed out these effects in the garnets, has reported on the absorption of GdIG for the two senses of rotation.[2] Figure 2 illustrates that for YbIG.

ACKNOWLEDGMENTS

The author would like to express his thanks to W. Palmer for preparation of the very thin samples used, and to E. F. Kelly for assistance with the measurements. The cooperation of J. H. Lady of the Westinghouse Research Laboratories in carrying out the infrared reflectivity measurements is also appreciated.

Note. Because the author has been absent from this country, it has not been possible to consult with him regarding the revision of this paper. Rather than omit the paper, his colleague, J. A. Osborn, has attempted to revise and shorten the Conference paper in accordance with the referee's suggestions, while trying to adhere closely to the sense of the author's original paper.

[6] A. M. Clogston and D. L. Wood, Bull. Am. Phys. Soc. Ser. II 4, 241 (1959).
[7] R. D. Waldron, Phys. Rev. **99**, 1727 (1955).
[8] H. Gobrecht, Ann. Physik **3**, 755 (1938). Several references also to other work on absorptions of rare earth salts and salt solutions.

JOURNAL OF APPLIED PHYSICS SUPPLEMENT TO VOL. 31, NO. 5 MAY, 1960

Instability of Magnetic Resonance in Single Crystal Spheres of Yttrium Iron Garnet

JOSEPH I. MASTERS
Electronic Material Sciences Laboratory, Electronics Research Directorate, Air Force Cambridge Research Center, Air Research and Development Command, L. G. Hanscom Field, Bedford, Massachusetts

Instabilities in YIG spheres that exist above certain threshold power values of cw microwave field are studied using samples of about $\frac{1}{4}$–$\frac{1}{2}$ mm diam, that have low power line widths of 1 oe or less. Whereas the characteristic behavior such as asymmetrical line shape, "jump" effect etc. is somewhat similar to that reported for disks, the phenomenon is generally different.

It has been determined that this instability, which can occur at cw power levels below the threshold for significant spin wave growth, is due entirely to the heating effect of resonance absorption upon the anisotropy energy of the crystal lattice. As a result, the instability is characterized by a threshold curve that follows both the extrema and symmetry of the anisotropy curve for a given orientation. A straightforward theoretical explanation based on familiar relationships is outlined which fits the instability threshold *vs* orientation curve. The temperature instability provides a technique for measuring the "g" factor that is believed to be more direct than previous methods.

ALTHOUGH a quantitative explanation has previously been given only for resonance instability in ferromagnetic disks, in general such an instability can occur if any power dependent effect of the resonance can produce a sufficiently large shift in the resonant frequency and if this shift is somehow properly compensated for in the experiment. The characteristic symptoms of resonance instability have been described in some detail previously.[1–3]

Conditions for a particular type of instability observed here in spherical samples of YIG are as shown in Fig. 1. The threshold curve is typical of those obtained from YIG spheres of about 0.020 in. in diam, and about 1 oe in line width, orientated for rotation of the dc magnetic field in the crystallographic (110) plane. All measurements were taken by observation of the perturbation of the reflected wave from a shorted wave guide in which the sample was placed. Resonance conditions were established with a stable cw 9000-Mc source and slow manual variation of the dc magnetic field.

The fact that extrema of the threshold curve are coincident with principle axes and that the direction of fold-over or frequency shift (indicated in Fig. 1 schematically by the unstable asymmetric absorption line) varies with rotation angle both indicate a strong dependence upon anisotropy energy. On the other hand, the observed threshold of rf field for degenerate spin wave growth (broken horizontal line), is nearly independent of rotation angle and from its position we can conclude that the instability is not directly related to abnormal spin wave activity. Certain findings lead to the conclusion that the instability phenomenon in question is actually due to self heating of the sample, namely: the relaxation time of the magnetization vector in the unstable region is too long for anything but thermal relaxation, and more conclusively, precautions such as air cooling raise the level of the instability threshold. Because of the long thermal time constant, this instability is not generally observed under transient conditions where a "swept" klystron source or pulse technique is used. In these cases, only a frequency drift of the magnetic resonance may be seen, if the duty cycle is too high for the lattice to completely cool between sweeps or pulses.

For samples that are perfect spheres the uniform precession frequency reduces effectively to

$$\omega_r^2=\gamma^2\{H_0^2+H_0[f(\theta)K_1(T)/M+g(\theta)K_2(T)/M]\}, \quad (1)$$

where f and g are the appropriate coefficients for various rotation angles, and only the first-order anisotropy constant, K_1, need be considered for YIG. Two possibilities exist for producing a power dependent frequency shift over and above the familiar power independent anisotropy shift due to $f(\theta)$ alone. These are the "g" factor, contained in γ, or the quantity K_1/M. The former case[4] allows, at least from the 1st order phenomenological aspect of Eq. (1), a fold over in only one direction and is therefore rejected as a principle cause of this instability. However, since the direction of fold over, illustrated in Fig. 1, is consistant with the

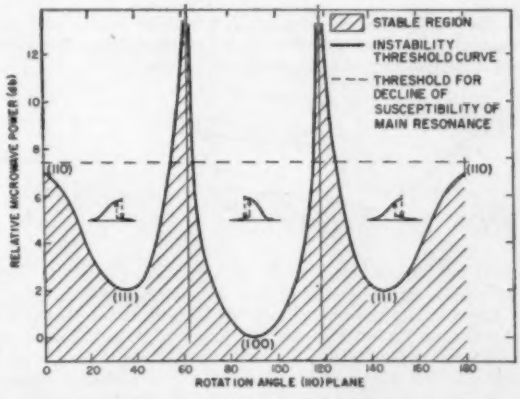

FIG. 1. Threshold curves YIG sphere.

[1] P. W. Anderson and H. Suhl, Phys. Rev. **100**, 1788 (1955).
[2] H. Suhl, Proc. Inst. Radio Engrs. **44**, 1270 (1956).
[3] M. T. Weiss, J. Appl. Phys. **30**, 146S (1959).
[4] M. T. Weiss (private communication).

sign of $f(\theta)$, the dependence of K_1/M on resonance absorption is accounted for as a dependence on sample temperature, T.

An expression for the threshold of the instability results from an examination of the absorptive component of susceptibility, χ'', for the anisotropic sphere. For convenience, a simplified form introducing negligible error is stated here for the case of plane wave excitation.

$$\chi''=\gamma M\gamma\Delta H/\{4[\omega-\omega_r(\chi'')]^2+[\gamma\Delta H]^2\}. \quad (2)$$

ω_r is established as a function of χ'' in the following manner. Absorbed power per unit volume is given by $\chi''h^2\omega/2$. Furthermore, in any steady-state heat transfer situation temperature is proportional to input power.[5] For a small temperature rise above ambient, a linear relation may be assumed for K_1/M vs T so that K_1/M is of the form $K_1/M=a\chi''h^2\omega+b$, and thus $\omega_r=\omega_r(\chi'')$ via Eq. (1). As reported previously for the case of M_z in disks[1] the criterion for instability in χ'' is that the ratio of differentials with respect to χ'' in Eq. (2) must exceed unity. It is apparent from the algebra that independent of the origin of instability, the least threshold will occur when the value of H_0 is about one third of the line width away from the unstable side of resonance. The resulting threshold for the temperature instability is

$$h^2_{\text{crit}}=\frac{1}{A}\cdot\frac{(\Delta H)^2}{\gamma MH_0|f(\theta)|}, \quad (3)$$

where $f=4-5\sin^2\theta-(15\sin^2 2\theta)/4$ for rotation in the (110) plane. Within the undetermined constant A, which includes the product of the slope of the K_1/M *vs* T curve and the reciprocal of a heat transfer coefficient for the garnet sample, Eq. (3) gives a qualitative fit to the threshold curve of Fig. 1. For a 1 oe YIG sphere a least threshold of the order of about 1 moe is observed if no cooling precautions are taken.

It is important to restate that the existence of the temperature instability results because the anisotropy energy is power dependent near resonance and not because of a dependence on ambient temperature. Thus it was found that threshold curves, taken at 77° and 300°K for a given sample, were very similar.

Of particular interest are the two cusps which occur experimentally at about 62° and 118° in good agreement with Eq. (3) for $|f(\theta)|=0$. At these angles, characterized by no fold over and hence no instability with increasing cw power, it is found directly that the anisotropy torque on M is essentially zero. Thus, within the assumptions made, the resulting cusp angles experimentally determine a direction for which, excepting lack of sphericity, the internal and external magnetic fields are effectively equal. Therefore, for a check on sphericity, the same dc field for resonance must be observed at each of the four cusps that occur in the 360° excursion. Furthermore, if the sample is a sphere, γ can be measured using the reduced form of Eq. (1), $\omega_r=\gamma H_0$ with an accuracy of about 1 part in 10^4 in accordance with the current uncertainty in measuring H_0 and ω_r. It can be shown that this procedure depends on the assumption that ambient temperatures are chosen such that the anisotropy energy consists of terms that are either temperature dependent or negligible. As a result, a more direct measurement of γ may be made than in previous resonance techniques where an arbitrary form for the anisotropy energy is assumed.

It is clear that the temperature instability phenomenon, as well as the stability angles, may be observed under far less restrictive conditions of material, sample shape, and orientation than those stated for convenience above. Furthermore, the advent of commercially available higher power stable cw microwave generators and amplifiers imposes less of a restriction on the line width, ΔH, in Eq. (3).

[5] In the particular case of a small, uniformly self-heated sphere of assumed poor heat transfer to its surroundings, the internal temperature gradient can be shown to be negligible.

ACKNOWLEDGMENTS

It is a pleasure to acknowledge the efforts of Benjamin R. Capone, who first pointed out the phenomenon that led to this paper and who shared in the experimental work. The author also wishes to thank Dr. M. T. Weiss of Hughes Research Laboratory for his comments and interest in the problem.

Ferrimagnetic Resonance in Impurity Doped Yttrium Iron Garnet (YIG)

J. F. Dillon, Jr., and J. W. Nielsen
Bell Telephone Laboratories, Inc., Murray Hill, New Jersey

A research program aimed at understanding our earlier line width and anisotropy measurements on YIG has led to a study of ferrimagnetic resonance in doped crystals. YIG crystals have been grown containing appropriate concentrations (~.01 to 5.0 atomic percent) of various impurities, including the 4*f* rare earth elements, members of the iron transition group, and several non-magnetic elements. This paper gives new results for the variation of the field for resonance with crystal direction at several temperatures in the liquid hydrogen and liquid helium range. In the case of holmium, sharp peaks in the H_{res} vs angle curve are seen which vary rapidly with temperature. The corresponding curves for the dysprosium containing sample do not show such sharp variations in (110), and at least in part do not vary with temperature below about 4°K. Though Kittel's recent theoretical results should apparently apply to the peaks in the holmium case, his results for the temperature dependence of the anomaly height and width do not correspond with our data.

INTRODUCTION

WORK on the resonance properties of YIG intentionally doped with small percentages of various ions was originally undertaken in order to clarify experimentally the interesting low-temperature data reported on the first YIG crystals studied.[1] The results reported earlier covered the cases of YIG with terbium and europium impurities.[2] These made it clear that small numbers of rare earth ions in the garnet lattice could indeed produce huge changes in the anisotropy as represented by the field for resonance. We also found that the maximum below 100°K in the line width vs temperature plot was at least in large part tied to the presence of rare earth impurities. This was also demonstrated by concurrent experiments[3] on YIG prepared with specially purified yttrium oxide. Our program includes the study of YIG containing separately each of the rare earth ions except gadolinium and lutecium. We have chosen in this short paper to give some field for resonance results for holmium and dysprosium doped YIG.

The crystal growing prodecure was that described in a separate paper.[4] The samples were highly polished 0.016 in. diam spheres made by the two-pipe technique.[5] Frequencies were near 20 kmc. Further experimental particulars will be given in later papers.

HOLMIUM

The starting material from which these crystals were grown contained 0.2 atomic percent of holmium.[6] Analyses of the crystals themselves are not yet available. Figure 1 shows H_{res} in (110) for these doped crystals at a number of temperatures as well as a 1.5°K curve of the purest YIG we have yet measured. For the holmium samples there are sharp peaks at [100] and [110]. This is quite different from the behavior previously reported for YIG(Tb).[2] In that case there was a good deal more structure including a number of peaks along nonsymmetry directions. Note that the peak height falls off rapidly with increasing temperature, and does, in fact, change considerably between the lowest temperatures studied.

DYSPROSIUM

Here also the intended dilution of the rare earth ion was 0.2 atomic percent,[6] but an analysis is not yet available. The plot of H_{res} in (110) at several temperatures is given in Fig. 2. The field for resonance is topologically similar to that shown in reference 1. On comparing data with the H_{res} curves corresponding to each of the rare earths, as an impurity in YIG, it is quite clear that the principal impurity in that original crystal was dysprosium.

The feature of the Fig. 2 curves, which we wish to stress, is the contrast between the temperature variation here and that associated with the sharp spikes in the

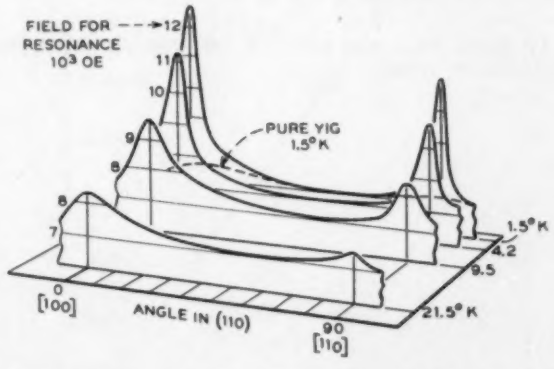

FIG. 1. The variation of H_{res} with angle in (110) for YIG(0.2% Ho) at several temperatures. The measuring frequencies are near 20 kmc. To clarify the comparison the curves have been adjusted vertically so the minima all appear to be at the same field. The dashed curve at 1.5° applies to pure YIG. Note the rapid decrease in the height of both peaks starting with the lowest temperatures. In terms of Kittel's explanation these sharp peaks as well as those in YIG(Tb) presumably correspond to cases in which the two lowest components of the ground state actually cross or approach within $k\times$ (a few degrees) of each other.

[1] J. F. Dillon, Phys. Rev. **111**, 1476–1478 (1958).
[2] J. F. Dillon and J. W. Nielsen, Phys. Rev. Letters **3**, 30–31 (1959).
[3] R. G. Spencer, R. C. LeCraw, and A. M. Clogston, Phys. Rev. Letters **3**, 32 (1959).
[4] J. W. Nielsen, J. Appl. Phys. **31**, 000 (1960).
[5] W. L. Bond, Rev. Sci. Instr. **25**, 401 (1954).
[6] The doping percentages used in this paper represent the atomic fraction Ho/(Ho+Y) or Dy/(Dy+Y) as appropriate.

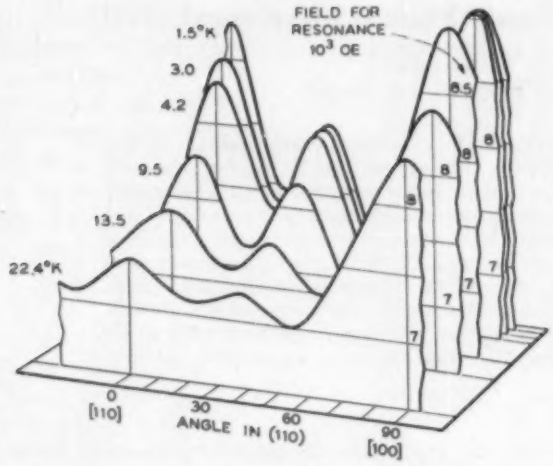

FIG. 2. H_{res} in (110) for YIG(0.2% Dy) at several temperatures. The frequencies were near 20 kmc. Here too, the curves have been justified vertically so that the lower minimum in each curve lies at the same apparent field. Though the peak at [110] seems to be changing in height at the lowest temperatures, those at [111] and [100] do not seem to change at all below 4.2°. These may represent cases where the lowest components of the ground state only approach within say $k\times$(10 or 15 degrees) of each other.

terbium and holmium cases. The height of the peaks at [111] and [100] essentially does not change between 1.5° and 4.2°K. They do no compare in sharpness with the spikes seen in the other two cases. The peak at [110] is varying fairly rapidly with temperature.

DISCUSSION

The unusual behavior of the anisotropy has its origin in the complicated splitting of the ground manifold of the rare earth ions in the crystalline and exchange fields, which are here of comparable magnitude. Kittel[7] has suggested that if there are near crossings of the lowest pair levels, they will give rise to sharp peaks in the field of resonance. Walker[8] has shown that for terbium such near crossings exist.

TABLE I. Height and width of the peak at 100 in YIG(0.2% Ho) at several temperatures.

T (°K)	H_a (oe)	$\Delta\theta_{\frac{1}{2}}$ (°)	$H_a(\Delta\theta_{\frac{1}{2}})^2$ (oe×deg²×10⁵)
1.5	5440	6	1.95
4.2	3980	7.8	2.42
9.5	2180	10.0	2.18
13.5	1645	11.5	2.17
21.5	930	14.2	1.89
22.5	1000	14.5	2.10

It is of interest to attempt a comparison of our results with Kittel's. For a case in which $kT\gg$ closest approach of the levels, the central consequence of his treatment is that $-H_a(\Delta\theta_{\frac{1}{2}})^2=2\xi kTN'/M$. In this, H_a is the anisotropy field, $\Delta\theta_{\frac{1}{2}}$ the angular width of the peak, N' the concentration of rare earth ions involved. ξ is a constant of order one, M is the total magnetization.

In the symmetry direction [100], H_a is merely the height of the peak, presumably corrected by subtracting the corresponding peak height measured for pure YIG. Table I below gives the corrected height and measured width of the peak at [100] in YIG(0.2%Ho) at a number of temperatures. The quantity $H_a(\Delta\theta_{\frac{1}{2}})^2$ in Kittel's theory should vary directly with temperature in a region where M is constant. It will be seen in the last column of Table I that the measured $H_a(\Delta\theta_{\frac{1}{2}})^2$ remains a constant though the temperature changes by a factor of fifteen.

ACKNOWLEDGMENTS

The authors are pleased to acknowledge discussions with A. M. Clogston and with L. R. Walker. V. Jaccarino suggested the three-dimensional presentation of the data used in the figures. H. E. Earl has provided valuable technical assistance.

[7] C. Kittel, Phys. Rev. Letters **3**, 169 (1959); C. Kittel, Phys. Rev. **117**, 681 (1960).

[8] L. R. Walker (to be published).

Samarium Substitutions in Yttrium Iron Garnet

J. RICHARD CUNNINGHAM, JR., AND ELMER E. ANDERSON
U. S. Naval Ordnance Laboratory, White Oak, Silver Spring, Maryland

Polycrystalline garnets of the form $(3-x)Y_2O_3 \cdot xSm_2O_3 \cdot 5Fe_2O_3$ have been prepared where x was varied from 0 to 3 in six steps. Lattice constants were found to vary linearly from 12.374±0.005 A for yttrium iron garnet ($x=0$) to 12.533±0.005 A for samarium iron garnet ($x=3$). The theoretical x-ray densities were calculated and vary from 5.17 gms/cc for $x=0$ to 6.22 gms/cc for $x=3$. Magnetic moments were measured from 77° to 600°K. No magnetic compensation points were observed. The Curie temperature for these garnets is 570±10°K. Thermal magnetization curves for this series indicate that samarium substitution for yttrium produces very little change in the magnetization. The relative complex initial permeability was measured from dc to 2 kMc for several temperatures. The results of these measurements are discussed briefly.

INTRODUCTION

SAMARIUM iron garnet, whose crystallographic properties were first reported by Bertaut and Forrat,[1] is of considerable interest for its potential use as a broadband material in microwave applications. Previous work has been done in the X band region on polycrystalline samarium iron garnet by Rodrigue and his co-workers at Harvard,[2] and on a few of the mixed yttrium-samarium garnets by Sirvetz and Zneimer.[3] This present paper is concerned with powder data and permeability spectra below 2 kMc for a series of polycrystalline yttrium-samarium garnets.

PREPARATION OF MATERIALS

Polycrystalline garnets of the form $(3-x)Y_2O_3 \cdot xSm_2O_3 \cdot 5Fe_2O_3$ were prepared where x was varied from 0 (yttrium iron garnet) to 3 (samarium iron garnet) in six half-integer steps. These materials were prepared using techniques described elsewhere.[4,5] The resulting toroids had a density which was 95.3±1.6% of the theoretical x-ray density. The experimental densities were determined from weight and dimension considerations.

LATTICE CONSTANTS AND X-RAY DENSITIES

X-ray powder diffraction patterns were taken using a Norelco high-angle goniometer spectrometer employing unfiltered Cr radiation. The intensity vs 2θ curves were scanned at a rate of $\frac{1}{4}$° per minute. The x-ray analysis showed that only the garnet phase is present after the final sintering of the powders. The calculated lattice constants are shown in Fig. 1 with the values ranging from 12.374±0.005 A for $x=0$ (YIG) to 12.533±0.005 A for $x=3$ (SmIG). The increase in the unit cell size with samarium addition is due to the larger radius of the Sm ion (1.13 A vs 0.95 A). The linear variation of the lattice constant with x has been found for other garnet series by various investigators.[6,7] The value for samarium iron garnet found here is in good agreement with previous values: 12.530,[3] 12.52[1] and 12.505±0.005 A.[2] From the unit cell edge and the weight per unit cell, the theoretical x-ray densities were calculated and also found to exhibit a linear variation with x. These densities vary from 5.17 g/cc for $x=0$ to 6.22 g/cc for $x=3$.

MAGNETIC MEASUREMENTS

Magnetic moments were measured from 77° to 600°K by E. Wenzel of this Laboratory using a modified Gouy method.[8] No magnetic compensation points were observed. Thermal magnetization curves for this series indicate that samarium substitution for yttrium produces little change in the magnetization. This is to be expected from the fact that Y^{3+} is diamagnetic and

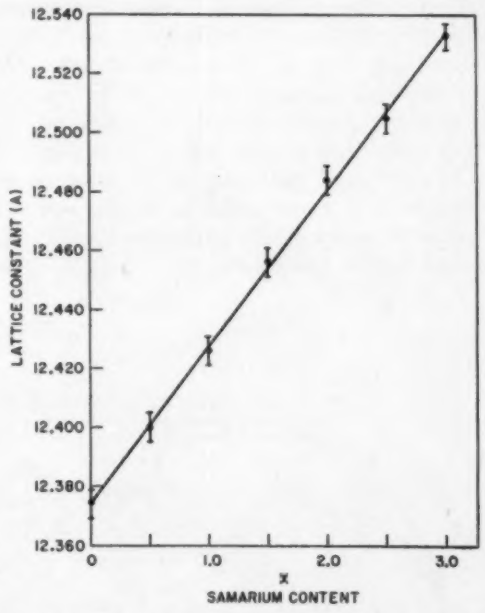

FIG. 1. Lattice constant vs x for $(3-x)Y_2O_3 \cdot xSm_2O_3 \cdot 5Fe_2O_3$.

[1] F. Bertaut and F. Forrat, Comp. rend. **242**, 382 (1956).
[2] Rodrigue, Pippin, Wolf, and Hogan, Sci. Rept. **11**, Gordon McKay Laboratory, Harvard (1957).
[3] M. H. Sirvetz and J. E. Zneimer, J. Appl. Phys. **29**, 431 (1958).
[4] Elmer E. Anderson, J. Appl. Phys. **30**, 299S (1959).
[5] E. E. Anderson, J. R. Cunningham, G. E. McDuffie and Ayers, NAVORD Rept. 6741.
[6] E. E. Anderson, J. R. Cunningham, and G. E. McDuffie, Phys. Rev. **116**, 624 (1959).
[7] M. A. Gilleo and S. Geller, Phys. Rev. **110**, 73 (1958).
[8] T. R. McGuire and C. T. Lane, Rev. Sci. Instr. **20**, 489 (1949).

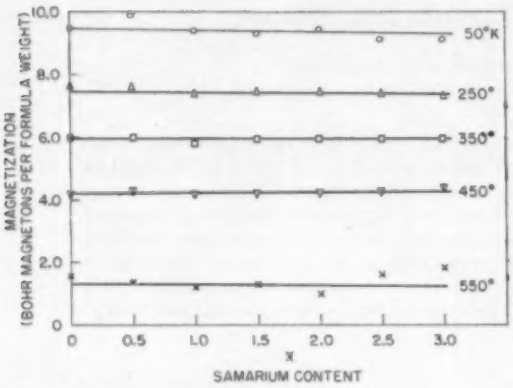

FIG. 2. Magnetic moments vs x at several temperatures for $(3-x)Y_2O_3 \cdot xSm_2O_3 \cdot 5Fe_2O_3$.

Sm^{3+} is only slightly paramagnetic. The plot of the magnetic moment vs samarium content for several temperatures shown in Fig. 2 bears this out.

PERMEABILITY SPECTRA

Measurements of the relative complex initial permeability, $\mu^* = \mu' - j\mu''$, have been made over a frequency range from 1 kc to 2 kMc using various ac bridges and slotted lines.[9] The substitution of samarium resulted in a decrease in μ_0', the low-frequency value of μ', at $T = 23°C$. The lowering of the temperature to $-78°C$ and $-196°C$ also reduced μ_0'. These data are given in Table I. The general shape of the spectra is similar to that shown by McDuffie *et al.* in their paper on gadolinium substitutions.[10] The case of samarium, unlike that of gadolinium, is not complicated by the presence of compensation temperatures. Recently, Pippin[11] published the permeability spectrum of a samarium iron garnet having a relatively low density; however, the spectrum does not differ appreciably with the data presented here. Although the low temperature measurements are not complete at this time, it is evident from the data available that there is no significant frequency shift in the radio-frequency loss peak in these garnets.

TABLE I. Low frequency initial permeability.

Composition	$T = 23°C$ μ_0'	$T = -78°C$ μ_0'	$T = -196°C$ μ_0'
YIG	112	60	35
0.5 Sm_2O_3	94	45	15
1.0 Sm_2O_3	63	28	6
1.5 Sm_2O_3	46	20	3
2.0 Sm_2O_3	41	16	~2.5
2.5 Sm_2O_3	30	14	~2.5
SmIG	28	15	~2.5

ACKNOWLEDGMENTS

The authors wish to thank E. Wenzel for the magnetic moment data, W. E. Ayers for his preparation of the materials and help in the measurements and G. E. McDuffie, Jr. and D. Schacker for their assistance in the permeability measurements.

[9] G. E. McDuffie, Jr., and J. Richard Cunningham, Jr., NAVORD Rept. 6742.

[10] G. E. McDuffie, J. R. Cunningham, and E. E. Anderson, J. Appl. Phys. **31**, 47S (1960), this issue.

[11] J. E. Pippin and C. L. Hogan, Sci. Rept. **1**, Gordon McKay Laboratory, Harvard (1959).

Initial Permeability Characteristics of Mixed Yttrium-Gadolinium Iron Garnets

G. E. McDuffie, Jr., J. R. Cunningham, Jr., and E. E. Anderson
U. S. Naval Ordnance Laboratory, White Oak, Silver Spring, Maryland

Complex initial permeability measurements have been made on polycrystalline garnet toroids of the form $(3-x)Y_2O_3 \cdot xGd_2O_3 \cdot 5Fe_2O_3$ where x ranged from zero (yttrium iron garnet) to three (gadolinium iron garnet). Both the real initial permeability μ' and the imaginary initial permeability μ'' were measured at 23°C, −78°C and −196°C over a frequency range of 1 kc to 2000 Mc. At room temperature, the low frequency value of μ' was found to decrease with increasing gadolinium content. At lower temperatures the low frequency value of μ' exhibits a minimum in x caused by the temperature dependent behavior of the two different magnetic sublattices. The frequency at which the maximum value of μ'' occurs was found to increase with the addition of gadolinium. No thermal relaxation was observed in these garnets, but rather the peaks in the curves shifted to slightly higher frequencies with decreasing temperature.

INTRODUCTION

As a continuation of the study of mixed yttrium-gadolinium iron garnets previously reported,[1,2] magnetic measurements have been made on ceramic toroids of these garnets. The mixed garnets may be represented by the formula $(3-x)Y_2O_3 \cdot xGd_2O_3 \cdot 5Fe_2O_3$, where x may be varied from 0 for yttrium iron garnet to 3 for gadolinium iron garnet. Toroids were prepared for the following values of x: 0, 0.5, 1.0, 1.5, and 3.0. The method of preparation has been described elsewhere.[3,4] The measurements given in this paper are for toroids having a density of 94.4±1% of the theoretical x-ray density.

The relative complex initial permeability, $\mu^* = \mu' - j\mu''$ was measured from 1 kc to 2 kMc. In the lower frequency range (10^3 cps to 15 Mc), measurements were made by placing windings on the toroid and using normal inductance measuring techniques. In the higher frequency range (20 Mc to 2 kMc), a transmission lins technique was used. Various bridges and slotted linee were used for the actual measurements.[5]

PERMEABILITY DISPERSION

The permeability dispersion curve with x as a parameter is shown in Fig. 1 for $T = 23$°C. No curve is shown for $x = 3$ because near this temperature a compensation point occurs and μ' is approximately unity. Examination of Fig. 1 shows several obvious facts. First, both μ' and μ'' decrease with increasing x and the frequency at which the maximum in the loss curve occurs increases with increasing x. Secondly, no clear separation of the low and high frequency dispersions occurs. Dispersion curves of the permeability for $T = -78$°C and $T = -196$°C are similar in form to the curves of Fig. 1. However, the curves at these lower temperatures show slightly more detail at the higher frequencies, and the order of the curves in x is altered because of the shift of the compensation temperature.

LOW FREQUENCY PERMEABILITY

Measured values of low frequency (1000 cps) permeability, μ_0', are shown in Table I, with the corresponding values of the saturation magnetization M_s calculated from powder data.[2] These values indicate that at room temperature μ_0' decreases with x, while at $T = -78$°C and $T = -196$°C it exhibits a minimum in x. These results are consistent with the temperature dependency of M_s, which in turn is dependent on the competing effects of the gadolinium and iron sublattices. If $\ln(\mu_0' - 1)$ is plotted as a function of $\ln M_s$ with T as a parameter, the curves for $T = 23$°C and −78°C can be interpreted as being linear with slopes of approximately 2, indicating that the contribution to the initial permeability for domain wall motion and domain

Table I. Low frequency initial permeability.

Temperature (°C)	$x=0$		$x=0.5$		$x=1.0$		$x=1.5$		$x=3.0$	
	μ_0'	M_s	μ_0'	M_s	μ_0'	M_s	μ_0'	M_s	μ_0'	M_s
23	112	130	80	109	44	88	25	68	2	6.3
−78	60	157	49	124	22	90	9	57	12	58
−196	35	178	20	100	2.5	25	9	53	58	286

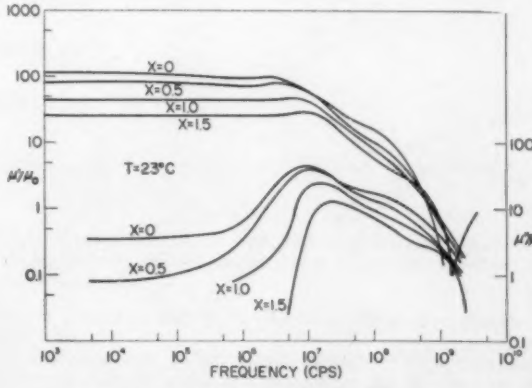

Fig. 1. Initial permeability spectrum for yttrium-gadolinium garnets.

[1] Villers, Loriers and Claudel, Compt. rend. **247**, 710 (1958).
[2] E. E. Anderson, J. R. Cunningham, and G. E. McDuffie, Bull. Am. Phys. Soc. **II, 4**, 241 (1959); Phys. Rev. **116**, 624 (1959).
[3] Elmer E. Anderson, J. Appl. Phys. **30**, 299S (1959).
[4] Anderson, Cunningham, McDuffie, and Ayers, NAVORD Rept. 6741.
[5] G. E. McDuffie, Jr., and J. Richard Cunningham, Jr., NAVORD Rept. 6742.

TABLE II. Dispersion frequencies (Mc).

Temperature (°C)	$x=0$		$x=0.5$		$x=1.0$		$x=1.5$		$x=3.0$	
	f_1	f_2	f_1	f_2	f_1	f_2	f_1	f_2	f_1	f_2
23	8.5	...	10.5	400	17	600	24.5	...	...	...
−78	10	350	17.5	410	30	510	50	740	...	...
−196	...	620	50	1400	...	...	60	...	27	700

rotation add linearly and vary as M_s^2. At $T=-196°C$ the curve deviates somewhat from a straight line and the slope is considerably less than 2 indicating a more complicated relation between $\mu_0'-1$ and M_s.

DISPERSION FREQUENCIES

The frequency at which the loss part of the initial permeability is maximum will be referred to as the dispersion frequency. The curves shown in Fig. 1 indicate the existence of at least two dispersion frequencies, f_1 and f_2, one in the radio-frequency range and one in the microwave range. It is fairly well accepted that these two dispersions are due to domain wall motion and domain rotation, respectively. Table II shows the dispersion frequencies taken from the measured permeability curves. The dispersion frequencies in the radio-frequency range may be determined from the μ'' curves but those in the microwave range are at best only an estimate since the two dispersion ranges overlap and radio-frequency dispersion predominates. If the effective anisotropy constant, K_{eff}, is calculated from Snoek's formula[6] using the microwave dispersion frequencies at $T=23°C$ and $-78°C$, values are found to vary between 1.1×10^3 and 1.5×10^3. This large spread is attributed to the high degree of inaccuracy encountered in determining the microwave dispersion frequencies. However, the mean value of K_{eff} is in agreement with the value of $K_{eff}=2|K_1|$ found by other authors.[7] At $T=-196°C$, the limited data available allow no conclusions on the value of the effective anisotropy constant.

Epstein and Frackiewicz[8] have shown a temperature dependent relaxation in the radio-frequency range for selected yttrium iron garnet toroids, and have related this to the electron diffusion occurring between the Fe^{2+} and Fe^{3+} ions of the lattice. Their argument is supported by a frequency dispersion of the complex dielectric constant in the radio-frequency range. Our samples do not show a similar temperature dependent shift of the radio-frequency dispersion as shown in Table II, nor do the room temperature measurements of complex dielectric constant show a frequency dispersion in the radio-frequency range. The low frequency resistivities of our samples are also approximately an order of magnitude higher than those used by Epstein and Frackiewicz. These results indicate that the radio-frequency dispersion reported in this paper is not controlled by an electron diffusion mechanism.

ACKNOWLEDGMENT

The authors wish to acknowledge the able assistance of W. E. Ayers in obtaining the experimental data presented in this paper.

[6] J. L. Snoek, Physica **14**, 207 (1948).

[7] Kriessman, Harrison, and Belson, J. Appl. Phys. **29**, 452 (1958).

[8] D. J. Epstein and B. Frackiewicz, M.I.T. Technical Rept. 135 (1959).

Specific Heat of Some Rare Earth Iron Garnets and YIG at Low Temperatures*

HORST MEYER† AND A. B. HARRIS
Gordon McKay Laboratory, Harvard University, Cambridge, Massachusetts

Heat capacity measurements of the iron garnets of Y, Gd, Er, Ho, and Yb between 1.4° and 20°K are presented. Below 5°K, the specific heat of YIG can be represented by the sum of a lattice term proportional to T^3 and the spin-wave contribution $2.15\times10^{-3}T^{\frac{3}{2}}$ joules/mole-deg. This last term agrees satisfactorily with that calculated from a spin-wave analysis, in which the exchange interaction coefficients were those derived from Pauthenet's magnetization data. The results of the magnetic specific heat of the rare earth ions could be interpreted in terms of a Weiss molecular field acting on these ions. For Gd^{3+} and Yb^{3+}, this field was found to be, respectively, about 3.0×10^5 and 1.5×10^5 oe below 20°K, in satisfactory agreement with that derived from Pauthenet's data.

IN the past few years, the rare earth iron garnets (formula $5\ Fe_2O_3\cdot3\ M_2O_3$, where M is a rare earth or yttrium) have been the subject of numerous experimental investigations both by resonance and by magnetization measurements. Pauthenet[1,2] was able to interpret the magnetization results of several garnets by applying the Weiss molecular field theory to the following ferrimagnetic model; between the ions Fe^{3+}, situated on the octahedral sites 16*a* and tetrahedral sites 24*d*, there exists a strong interaction which aligns their moments in an antiparallel way and determines the Curie point of these garnets. The ions M of the sites 24*c* are magnetized principally by the molecular field produced by the resultant magnetization of the Fe^{3+} ions. Their magnetization tends to compensate that of the Fe^{3+} sublattices. There is, in addition, a smaller interaction between the ions M. For zero external applied field, the effective molecular field H_{eff} acting on the ions M is the difference of the fields from these two interactions. From Pauthenet's data, H_{eff} is of the order 10^5 oe, which corresponds to energy level splittings Δ of about 10–30 cm^{-1}, and one would expect to observe these splittings by an anomaly in the specific heat at sufficiently low temperatures. We therefore measured the specific heat of the iron garnets of Gd, Yb, Er, and Ho between 1.4° and 20°K in zero external magnetic field. We also investigated very pure (99.99%) yttrium iron garnet (YIG), where only the interactions between the Fe^{3+} ions are present. As these interactions are very strong and correspond, below 50°K, to a Weiss molecular field of the order of 4×10^6 oe, no such anomaly in the specific heat was expected.

The experimental results are presented in Fig. 1. For yttrium iron garnet, our results between 1.4° and 4°K could be represented to a good approximation by the expression,

$$C=2.15\times10^{-3}T^{\frac{3}{2}}+0.36\times10^{-3}T^3 \text{ joules/mole.}$$

The specific heat is appreciably smaller than that found by Edmonds and Petersen,[3] possibly because of some rare earth or orthoferrite impurities in their sample.[4] As the specific heat of the other rare earth garnets is much larger, the amount of impurities here is very critical. The lattice contribution in T^3 agreed satisfactorily with that calculated from velocity of sound measurements by McSkimin,[5] taking $V_t=3.87\times10^5$ cm/sec, and $V_l=7.17\times10^5$ cm/sec as transverse and longitudinal velocities, respectively. The term in $T^{\frac{3}{2}}$, which is the magnetic contribution to the specific heat, will be discussed below.

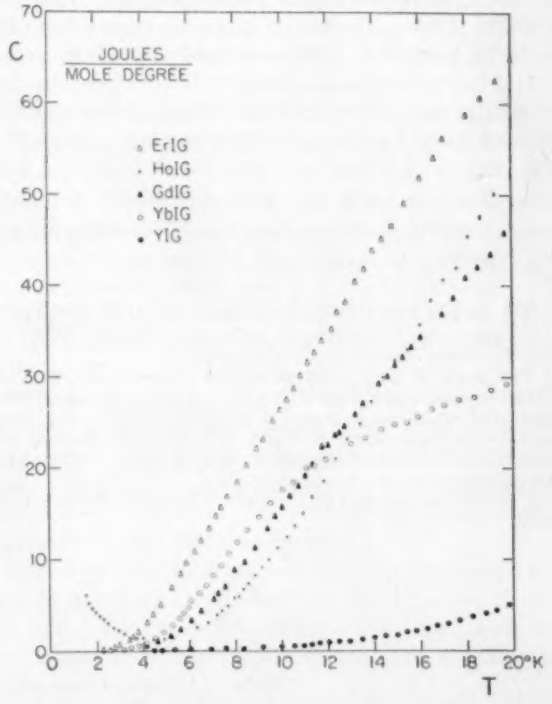

FIG. 1. Specific heat of the iron garnets of yttrium, gadolinium, holmium, erbium, and ytterbium. Most of the points below 5°K have been omitted.

* Research jointly sponsored by Air Force and Office of Naval Research contracts.

† Now at the department of Physics, Duke University, Durham, North Carolina.

[1] R. Pauthenet, Ann. phys. **3**, 424 1958.

[2] R. Pauthenet, J. phys. radium **20**, 388 1959.

[3] D. T. Edmonds and R. G. Petersen, Phys. Rev. Letters **2**, p. 499 1959.

[4] Measurements on a YIG sample with about 10% orthoferrite impurity have shown a marked increase of the specific heat over that of the pure YIG sample.

[5] H. J. McSkimin (private communication).

For the other rare earth iron garnets, we have assumed that, in first approximation, the specific heat can be written as $C_L+C_{RE}+C_{Fe}$, where C_L is the lattice contribution, C_{RE} is the magnetic specific heat of the rare earth "c" sublattice and C_{Fe} is that of the "a" and "d" iron sublattices. (C_L+C_{Fe}) was assumed to be about the same for all the rare earths except for YIG, where the lattice contribution should be somewhat smaller because of the smaller molecular weight. From our results, we have determined by successive approximations C_{RE} and (C_L+C_{Fe}) for gadolinium iron garnet, where the energy level disposition of Gd^{3+} is particularly simple. We then subtracted this value of (C_L+C_{Fe}) from the total specific heat of the other garnets, in order to find C_{RE} in each case.

For $Gd^{3+}(S=\frac{7}{2})$ which is in an S state, one finds that at these low temperatures each level is separated from the next one by the energy 28 cm^{-1} corresponding to an effective magnetic field $H_{eff}=3.00\times10^5$ oe. This is in satisfactory agreement with the value of 2.66×10^5 oe obtained from Pauthenet's results at 20°K.[1]

For Yb^{3+} $(J=\frac{7}{2}, S=\frac{1}{2})$, the crystalline field theories by White and Andelin[6] and by Ayant and Thomas[7] show that at low temperatures only two levels are populated. The splitting between them was found to be about 24.4 cm^{-1}, corresponding to an effective field $H_{eff}=1.55\times10^5$ oe, if one assumes the magnetic moment of these levels to be $M_z=1.7$ Bohr magnetons.[7] This experimental value is to be compared to 10 cm^{-1}, as estimated by White and Andelin.[8,*] The value of the splitting, deduced from Pauthenet's data, is about 26 cm^{-1} at 15°K.

For the rare earth ions Er^{3+} and Ho^{3+}, the energy level scheme is more involved,[6] and the interpretation of the results is being undertaken presently. The specific heat anomaly for Ho^{3+} near 1°K probably is due to the interaction between the electronic and the nuclear spins.

At low enough temperatures, when nearly all the magnetic ions are in their lowest energy state, the spin-wave theory should be followed rather than the molecular field approach. Calorimetric measurements can confirm this point because these theories give a very different temperature dependence of the specific heat (respectively, T^3 and $(\Delta/kT)^2e^{-\Delta/kT}$). Below 20°K, the spins in yttrium iron garnet almost have reached their zero-point alignment and a spin-wave calculation by one of us (A. B. H.) gives the energy-*versus*-k relation for the lowest acoustical mode as

$$\hbar\omega=1/16\{40J_{aa}-25J_{ad}+15J_{dd}\}a^2k^2,$$

where $J_{aa}-5.75$ cm^{-1}, $J_{ad}-24.2$ cm^{-1}, $J_{dd}-10.3$ cm^{-1} are the interaction coefficients derived by Pauthenet from his magnetization measurements,[1] $a=12$ A is the lattice constant for the garnet, and k is the usual wave vector. The spin-wave specific heat then is found to be $2.6\times10^{-3}T^3$ joules/mole in reasonable agreement with our experimental value. As one can see from this equation, small changes of the J's will affect drastically the energy spectrum and, hence, the spin-wave specific heat. The discrepancy with the experiment is, therefore, not astonishing. For Gd^{3+}, the specific heat below 3°K is systematically larger than that expected from the Weiss molecular field theory. This excess of specific heat probably is due partly to dipole-dipole interaction, although for an unmagnetized sample, the theoretical situation is unclear. The observed specific heat in this temperature range is about twice as large as predicted from a spin-wave analysis.

In conclusion, the specific heat results offer a valuable comparison with those obtained from magnetization measurements. At least for Yb^{3+} and Gd^{3+}, the Weiss molecular field theory is confirmed well by the experiments above about 3°K. Measurements on other garnets are in progress, and soon we will extend our experiments to lower and higher temperature ranges.

ACKNOWLEDGMENTS

The authors are very indebted to Professor R. V. Jones for stimulating discussions.

[6] R. L. White and J. P. Andelin, Phys. Rev. **115**, 1435 (1959).
[7] Y. Ayant and J. Thomas, Comptes rend. **248**, 387 1959.
[8] R. L. White (private communication).
[*] *Note added in proof.*—Recent optical measurements on YbIG by Wickersheim and White[9] showed the existence of inequivalent sites of the ytterbium ions with 2 different splittings of the two lowest levels, respectively 17.1 and 31.7 cm^{-1}. The specific heat calculated from these splittings still does not agree quantitatively with our data.
[9] K. A. Wickerman and R. L. White, Phys. Rev. Letters **4**, 123 (1960).

Improved Method for the Growth of Yttrium-Iron and Yttrium-Gallium Garnets

J. W. NIELSEN
Bell Telephone Laboratories, Incorporated, Murray Hill, New Jersey

Large single crystals of yttrium and rare earth iron garnets, and yttrium and rare earth gallium garnets, have been grown from molten solutions of lead oxide and lead fluoride. The crystals are grown by slowly cooling melts from about 1260°C to near 950°C. Sample compositions are: for YIG, 8 mole % Y_2O_3, 22 mole % Fe_2O_3, 30 mole % PbO and 40 mole % PbF_2; for YGaG, 5.8 mole % Y_2O_3, 14 mole % Ga_2O_3, 39.4 mole % PbO and 40.8 mole % PbF_2.

This method provides crystals both large in size and of superior quality. Best results are obtained when the containing crucible is hotter near its top than at its base since nucleation is thereby reduced.

INTRODUCTION

THE use of lead oxide as a solvent from which yttrium-iron-garnet (YIG) can be crystallized was reported almost two years ago.[1] Experience since that time has revealed that while the method is satisfactory for the preparation of small amounts of small YIG crystals, it has several serious drawbacks. First, the temperatures required to dissolve the components in PbO in a reasonable time are high, thus shortening crucible life. Second, the temperature-composition range over which YIG can be crystallized is narrow, hence crystal yields are small. Third, the large quantities of magneto-plumbite ($PbFe_{12}O_{19}$), which form with YIG, enhance YIG nucleation so that crystal sizes are usually small, and crystal sizes are only slightly increased by using melts of large mass. Finally, the melts are quite viscous. This leads to poor stirring of the melt and irregular transport of components to the YIG crystal faces. The result is crystals which are highly flawed.

It thus became obvious that the addition of another component to the system would be advantageous even though it would complicate it considerably from the standpoint of phase equilibrium. If properly chosen, the added component should lower the temperature of crystallization of YIG and at the same time reduce the viscosity of the melt. It also must not be incorporated into the YIG crystals. An examination of the published phase diagrams with lead monoxide as a component suggested that lead fluoride might be a beneficial additive to use. It has been reported[2] to form a simple, nearly ideal eutectic system with PbO. Furthermore, the use of pure PbF_2 as a solvent for other oxides had revealed its low viscosity and high stability. Although the phase diagram which supported the selection of PbF_2 has been found to be incorrect, the use of PbO-PbF_2 melts has greatly improved the yield and soundness of YIG crystals.

[1] J. W. Nielsen, J. Appl. Phys. **29**, 390 (1958).
[2] C. Sandonnini, Atti reale accad. sci. Torino **22**, (I), 959 (1914); see E. M. Levin, H. F. McMurdie, and F. P. Hall, *Phase Diagrams for Ceramists* (American Ceramic Society, Inc., Columbus, Ohio, 1956), p. 235.

EXPERIMENTAL PART

A description of the materials and the crystal growing furnaces used in this work has been reported.[3] The preparation and conditions of the crystal growth runs were similar to those of reference 3 with several important exceptions which are given below.

All but a few runs were held at 1250–1260°C for times varying from 4 hrs for 100 ml crucibles to 20 hrs for 800 ml crucibles. This time was sufficient to reduce the crucible contents to a single liquid phase.

Compositions of runs varied considerably, but high yields of YIG were obtained by using initial PbF_2/PbO molar ratios varying from 0.67 to 3.0 and initial Fe_2O_3/Y_2O_3 molar ratios varying from 5.60 to 1.77. In all of these runs the Y^{3+}/Pb^{2+} atom ratio remained less than 0.28.

The initial composition which will give the highest yield starting from 1250°C is not known precisely since losses by volatilization will usually differ for each run, and the yield also depends on rate of cooling. An example of a reliable composition and set of conditions, which will give a high yield of YIG is as follows: Place in a platinum crucible 8 mole % Y_2O_3, 22 mole % Fe_2O_3, 30 mole % PbO, 40 mole % PbF_2; hold for 4 to 20 hrs at 1250°C, depending on melt size, and cool at from 0.5° to 5° per hr.

Yttrium gallium garnets can be grown under nearly the same conditions as YIG. A good yield of YGaG can be obtained from a melt made up as follows: 5.8 mole % Y_2O_3, 14 mole % Ga_2O_3, 39.4 mole % PbO and 40.8 mole % PbF_2. The same growth conditions as those recommended for YIG can be used.

Solid solutions of YIG and YGaG, rare earth iron garnets made with Sm, Eu, Gd, Tb, Dy, Ho, Er and Yb, and YGaG doped with transition metals or rare earths have also been prepared with little modification of the conditions listed above.

Large garnets weighing up to 19 g each (see Fig. 1) were prepared in 800 ml crucibles with the top of the crucible 8–10° hotter than the bottom. The total melt mass was about 2 kg; the cooling rate was 0.5° per hr.

The large runs and many of the smaller ones were

[3] J. W. Nielsen and E. F. Dearborn, J. Phys. Chem. Solids **5**, 3, 202 (1958).

FIG. 1. Single crystals of yttrium iron garnet grown from 2 kg PbO-PbF_2 melt (scale in cm).

poured at temperatures between 900° and 1000°C to remove the liquid from the crystals. This saves much time in separating the crystals from the melt. A solution of 1 part acetic and 1 part nitric acid to 3 parts water was used to either clean the crystals after pouring the melt or to separate them if the melt had been allowed to solidify.

RESULTS AND DISCUSSION

The immediately obvious advantages provided by the PbO-PbF_2 solvent are the dramatic increase in size and quality of the crystals and the increased yields. Crystals weighing 5 g each are commonly formed in 100 ml crucibles. In large melts of 2 kg it is possible to form a half dozen crystals weighing from 10 to nearly 20 g each, and the total yield of crystals will weigh over 200 g. This increase in size and yield is accompanied by an improvement in crystal quality. Crystals weighing over 10 g usually are about 70% sound. This is a great improvement over the crystals obtained with the earlier technique. In fact, cracks caused by thermal shock remain the greatest problem in preparing samples whose dimensions are over 1 cm.

A complete analysis of the system discussed here from the standpoint of phase equilibria would be an impossibly lengthy task. In lieu of this, an empirical approach must determine the optimum conditions for garnet growth. Even this is quite complicated and will be the subject of a separate paper. However, a few words about the chemistry of the system may aid those who use it to provide garnet crystals.

First, it has been observed that the main component in quenched melts containing flouride equivalent to 30 mole % PbF_2 is Pb_2OF_2. This compound has been reported by Bystrom[4] who determined its structure. It apparently melts congruently and its existence was overlooked by Sandonnini[2] who studied the system PbO-PbF_2.

The composition suggested above for the growth of YIG will yield only YIG between 1250°C and 950°C under most conditions of cooling and volatilization loss. However, it is possible to crystallize large quantities of magneto-plumbite from iron-rich melts and yttrium oxyflouride, YOF, from melts containing larger quantities of Y_2O_3 and PbF_2.

Detailed analyses, which will be reported elsewhere, show that the major component lost by evaporation is PbF_2. Most of this is lost early in the run and losses from ordinary 100 ml crucibles with crimped lids average 15%.

Finally, if the top of the crucible is kept hotter than the bottom during the run, nucleation on the surface of the melt is prevented, and a great increase in both size and quality of the crystals results.

ACKNOWLEDGMENTS

The experimental work of E. F. Dearborn and x-ray diffraction photographs taken by Miss A. D. Mills were an indispensable aid to this work.

[4] A. Bystrom, Arkiv. Kemi, Mineral. Geol. **24A**, No. 33, 18 (1947).

Paramagnetic Resonance of Yb^{+++} in Aluminum and Gallium Garnets

JOHN W. CARSON AND ROBERT L. WHITE
Hughes Research Laboratories, Culver City, California

The paramagnetic resonance spectrum of Yb^{+++} in gallium and aluminum garnets has been observed at liquid nitrogen and helium temperatures. The components of the principal g tensor are 2.85, 3.60, and 3.74 in gallium garnet, and 2.47, 3.78, and 3.87 in aluminum garnet. In aluminum garnet, for a range of Yb concentrations (relative to Y) of from 2% to .1%, the line width varies linearly from 98 gauss to 20 gauss. The longitudinal relaxation time T_1, for the same Yb variation, increases from 0.001 sec to 0.02 sec.

IT has become increasingly apparent in recent years that an understanding of the magnetic properties of the ferrites and garnets must rest upon knowledge of the individual ion energy levels. In the rare earth iron garnets (5 $Fe_2O_3 \cdot 3\ M_2O_3$, where M is a trivalent rare earth ion), considerable evidence is available concerning the exchange fields acting upon the individual ions. Very little information exists, however, on the crystalline Stark fields and how they perturb the free ion energy levels. We have commenced a program of microwave, infrared, and optical experiments in the nonmagnetic rare earth garnets to obtain this information. This paper reports some results of the microwave paramagnetic resonance studies, specifically on yttrium gallium garnet and yttrium aluminum garnet doped with various concentrations of Yb^{+++}.

X-ray oriented single crystals were observed in an 8 mm spectrometer at 77°K, 4.2°K, and 1.8°K. The spectrometer is of conventional design, using the signal transmitted through a TE_{011} circular cylindrical cavity. Magnetic field modulation and a phase sensitive detector were used in the usual derivative method. The usual technique of Pound stabilizing the source klystron to the sample cavity was not used for two reaons: (1) helium in the cavity-waveguide system seriously degraded the stabilizer performance through microwave phase shifts as the helium bubbled or the helium level dropped, (2) it was necessary to operate at exceedingly low level microwave power densities in the cavity to avoid saturation of lines under observation. A free-running EMI type R-5146 klystron was found to be sufficiently stable for the experiments.

For the gallium garnet crystals reported on here the crystal 16*a* and 24*d* sites are occupied by Ga ions. The 24*c* sites are occupied with a controlled mixture of Yb and Y ions. The nonmagnetic yttrium ions are used to dilute the Yb concentration sufficiently to permit observation of a resolved spectrum. Figure 1 shows the absorption spectrum at 4.2°K and 34.2 kMc for a ½% Yb concentration. Only the major lines are plotted; subsidiary nuclear hyperfine lines are omitted for simplicity.

For a general orientation of the magnetic field 6 separate major absorptions are observed. For the dc magnetic field confined to the (110) plane only 4 lines are observed. This result is consistent with the crystal structure which shows that the rare earth ions are located on six inequivalent sites, with [100] directions of the local oxygen coordination cube occurring along each of the six unit cell ⟨110⟩ directions. Examination of the crystal structure also reveals that crystal [100] and [110] directions coincide with the major axes of the local g tensor for some of the ions. Consequently, the principal axes of the g tensor can be computed from the high field line in the [100] direction (cf Fig. 1) and from the two low field lines of the [110] direction absorption spectrum. The values obtained are $g_1=3.60$, $g_2=2.85$, and $g_3=3.74$. By using these values, the resonant magnetic fields as a function of crystal orientation were computed, as shown in Fig. 1.

Similar measurements on the same ion were made simultaneously and independently by a group at Oxford University[1] at 9.7 kMc. Their reported g values are 3.71, 2.91, and 3.85, all about 3% higher than those reported here. They also obtained a somewhat better detailed fit for the resonance field as a function of orientation. We believe the difference to result from the fact that the larger magnetic fields used in the 34.2 kMc experiment caused higher order terms in H to become

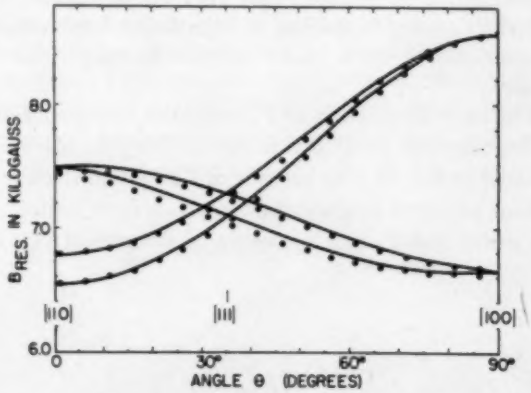

FIG. 1. Paramagnetic resonance spectrum of Yb^{+++} in Y Yb Ga garnet (½% Yb conc.) at 34.2 kMc and 4.2°K. The magnetic field resonance (B_{ext}) is plotted as a function of the angle θ between B_{ext} and the crystal [110] direction. The magnetic field was confined to the (110) plane. Points are experimental; solid lines were computed from the measured principal g tensor components.

[1] Boakes, Garton, Ryan, and Wolf, Proc. Phys. Soc. (London) (to be published). We are indebted to W. Wolf for making available to us a preprint of this paper.

significant in the Zeeman energy. Under these circumstances detailed fit to a simple g tensor is not possible.

Note added in proof. The authors of footnote 1 have informed us that recalibration of their equipment has led to revised g values identical to ours. Conversely, we have discovered errors in our calculations which led to the poorer detailed fit of resonance field as of function of orientation. Higher order terms in H need not be invoked to obtain an excellent fit to all data.

The lowest lying levels of the Yb^{3+} ion in a pure cubic field are a Kramers doublet with an isotropic g factor of 3.42. The actual oxygen coordination cube is twisted and squashed from the pure cubic configuration, introducing an asymmetry in the observed g. If one assumes that the dominant crystalline potential is of the form $V_4[x^4+y^4+z^4-(\frac{3}{5})r^4]$ and that perturbing potentials $V_2(3z^2-r^2)$ and $V_2^2(xy)$ are acting (corresponding respectively to the twisting and squashing of the coordination cube) one can fit the g tensor with $\langle r^2\rangle_{av}V_2^0/\langle r^4\rangle_{av}V_4^0=2.26\times10^{-2}$ and $\langle r^2\rangle_{av}V_2^2/\langle r^4\rangle_{av}V_4^0=2.04\times10^{-1}$. The average of the principal g values should in this approximation remain 3.42; our measured g values average 3.40, suggesting that the assumption of a dominant cubic potential is probably essentially correct. It should be pointed out that the choice of perturbing potentials is not uniquely determined by the data.

The spectrum was also examined at 1.8°K and 77°K. The unsaturated line widths were essentially the same at 1.8° as at 4.2°, about 25 gauss. At 77°K the line width was approximately 200 gauss.

A remarkable and suprising property of the Yb^{+++} ion in this lattice is the long relaxation time, T_1. For the $\frac{1}{2}\%$ Y Yb Ga garnet, T_1 was found to be about 0.01 sec at 4.2°K. T_1 was obtained from measurements on line width as a function of microwave power, interpreted using the standard susceptibility expressions for line width. This method is not very satisfactory, so the T_1 values quoted here must be regarded as approximate. Measurements by a more reliable technique are in progress.

The surprising value of T_1 indicated the desirability of determining T_1 as a function of Yb concentration. Because of the relative expense of Ga_2O_3 and the length of time required to grow these crystals from a flux, the line width and T_1 measurements on samples of varying Yb concentration were made on aluminum garnets grown by the flame fusion (Verneuil) process. The g values of the Yb^{3+} in the aluminum garnet were slightly more anisotropic than for the gallium garnet. The measured g values were $g_1=3.78$, $g_2=2.47$, $g_z=3.87$. Aside from this difference, the absorption spectrum in the aluminum garnet was quite similar to that in the gallium garnet.

TABLE I. Data at 4.2°K on line width and T_1 in aluminum garnet as a function of Yb^{+++} concentration. Data taken on absorption corresponding to the 6800 gauss line in [110] direction of Fig. 1.

Yb^{+++} concentration (%)	Line width (gauss)	T_1 (sec)
2	98	0.001
1	61	0.005
0.75	43	0.006
0.5	32	0.01
0.25	30	0.01
0.1	20	0.02

The data at 4.2°K on line width and T_1 in the aluminum garnet as a function of Yb^{3+} concentration are given in Table I. The line width is roughly linear in the Yb^{3+} concentration, with an extrapolated line width at zero concentration of some 17 or 18 gauss. The scatter in the data is sufficient to preclude an accurate determination of the exact form of the concentration dependence. The longitudinal relaxation time also increased an order of magnitude as the concentration was decreased from 2% to 0.01%. T_1 at 1.8°K was from 2 to 4 times longer than at 4.2°K. No theory for longitudinal relaxation times appropriate to the rare earth ions currently exists; the formulation of such a theory is being attempted.

ACKNOWLEDGMENTS

We wish to express our thanks to R. A. Lefever and his coworkers for their untiring efforts in growing the garnet crystals. J. W. Carson takes this opportunity to thank I. H. Solt, Jr., whose advice, assistance, and constant encouragement in the experimental aspects of this work have been invaluable. We also wish to thank E. H. Gregory for his expert x-ray orientation of the samples involved.

On Magnetostriction of Gadolinium Iron Garnets

K. P. Belov and A. V. Pedko
Moscow State University, Moscow, U.S.S.R.

The temperature dependence of magnetostriction in the gadolinium ferrite having structure of a garnet has been measured within the temperature range from liquid nitrogen up to the Curie point. At temperatures above the compensation point of sublattices, θ_k, the magnetostriction isotherms are of the same kind as for ferromagnetics (λ_{II} and $\lambda_\perp$ have opposite signs and the λ vs H curves exhibit saturation). In cooling below, θ_k there is an effect of superposition of large volume magnetostriction of paraprocess on the "ordinary" magnetostriction, which results in the distortion of the magnetostriction isotherms (λ_{II} and $\lambda_\perp$ are of the same sign and without saturation). It is shown that the "ordinary" magnetostriction is caused by the interaction of Fe^{3+} ions in sublattices a and d, while the volume magnetostriction of the paraprocess is caused by the interaction of Gd^{3+} and Fe^{3+} ions.

IN this report, we would like to point out the peculiar magnetostrictive properties of gadolinium iron garnets, which we found out in the temperature range from liquid nitrogen up to the Curie point.

The magnetic properties of these interesting substances are known to have been studied by Pauthenet,[1] Gilleo and Geller.[2] They have thrown light upon the character of the interaction of the magnetic sublattices in iron garnets. Here we intend to show that the investigation of the magnetostriction in the gadolinium iron garnets enables one to obtain the necessary data for finding out the details of the interaction of the sublattices in this material.

To study magnetostriction, we prepared by the ordinary ceramic techniques several samples of gadolinium ferrites. They were sufficiently large and had the following contents:

$$3Gd_2O_3 \cdot 5Fe_2O_3,$$
$$3Gd_2O_3 \cdot 0.2Gd_2O_3 \cdot 4.8Fe_2O_3,$$
$$3Gd_2O_3 \cdot 0.2Y_2O_3 \cdot 4.8Fe_2O_3.$$

It was desirable for us to know the influence of a small change of composition on the magnetostriction.

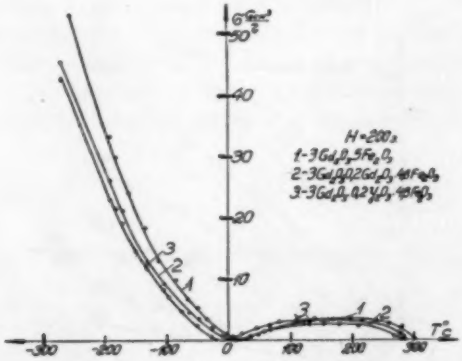

FIG. 1. The dependence of the spontaneous magnetization on temperature in gadolinium iron garnets: (1) $3Gd_2O_3 \cdot 5Fe_2O_3$; (2) $3Gd_2O_3 \cdot 0.2Gd_2O_3 \cdot 4.8Fe_2O_3$; (3) $3Gd_2O_3 \cdot 0.2Y_2O_3 \cdot 4.8Fe_2O_3$.

[1] R. Pauthenet, Compt. Rend. **242**, 1859 (1956); **243**, 1737 (1956).
[2] S. Geller and M. Gilleo, Acta Cryst. **10**, r3, 239 (1957).

By x-ray analysis, it was ascertained that all ferrites had the structure of a garnet.

Figure 1 shows the dependence of σ on T. The values of the Curie points θ and the compensation points θ_k are close to the values observed by Pauthenet.[1] The magnetization isotherms $\sigma(H)$ above θ_k and below θ_k are of entirely different character. Figure 2 presents the magnetic hysteresis loops taken at the boiling points of N and He. Although hysteresis is completed in relatively weak fields, there is no saturation of magnetization on Fig. 2.

To show with certainty that here we deal with paraprocess and not with the rotation of magnetization in domains, we measured the temperature dependence of magnetostriction. The magnitude of magnetostriction in the gadolinium ferrite is not large; we measured it with the aid of wire tensometers by using a photoelectric amplifier (FEOU-15). It was found that at the temperatures above the compensation point ($T > \theta_k$), the curves of longitudinal λ_{II} and transverse $\lambda_\perp$ magnetostriction are of the same kind as for the ordinary ferromagnetics (Fig. 3); λ_{II} and $\lambda_\perp$ have opposite signs and there is a saturation on the curves $\lambda(H)$. Below the compensation point ($T < \theta_k$), at the liquid nitrogen temperature, for instance, the shape of these curves changes sharply. In weak fields, one can see the signs of "ordinary" magnetostriction (opposite signs of λ_{II} and $\lambda_\perp$); in stronger fields, however, λ_{II} and $\lambda_\perp$ have the

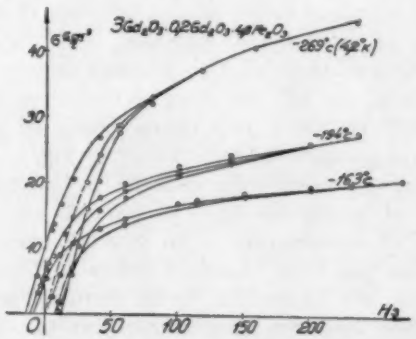

FIG. 2. Hysteresis loops of the gadolinium iron garnet at low temperatures.

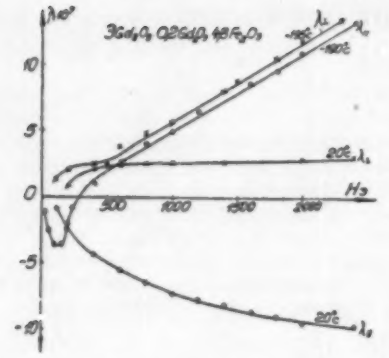

FIG. 3. Transversal and longitudinal magnetostriction for the ferrite, $3Gd_2O_3 \cdot 0.2Gd_2O_3 \cdot 4.8Fe_2O_3$ at the room temperature and the liquid nitrogen temperature.

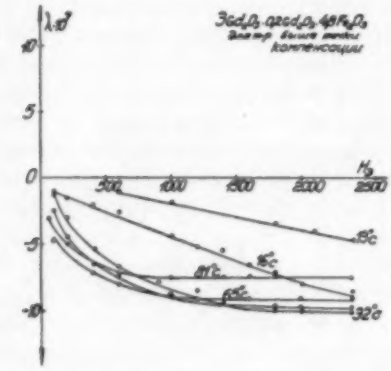

FIG. 4. Isotherms of the longitudinal magnetostriction of the ferrite, $3Gd_2O_3 \cdot 0.2Gd_2O_3 \cdot 4.8Fe_2O_3$ above the compensation point.

same positive signs without any tendency to saturation. It is clear that in the temperature range below θ_k, we have an effect of superposition of large volume magnetostriction of paraprocess on the "ordinary" magnetostriction.

Figures 4–6 show isotherms of longitudinal magnetostriction, taken for various samples of gadolinium iron garnet with different contents. One can see that in the temperature region above θ_k, the longitudinal striction is negative and saturation takes place; when the temperature decreases below θ_k, the influence of magnetostriction of paraprocess increases, and the sign of longitudinal magnetostriction becomes positive.

The value $\Delta\lambda/\Delta H$, the slope of the curve in strong fields, may be taken as a characteristic of magnetostriction of paraprocess. One can see on Fig. 7 that with decreasing temperature the value $\Delta\lambda/\Delta H$ increases. The increase of magnetostriction of paraprocess with the decrease of temperature is an unusual phenomenon, which has not been observed before in other ferromagnetics. We know that in all ferromagnetics, the paraprocess and the magnetostriction of the paraprocess augment with increasing temperature, and the value $\Delta\lambda/\Delta H$ reaches its maximum near the Curie point. In gadolinium ferrites, the increase of $\Delta\lambda/\Delta H$ near the Curie point also takes place, but the value of $\Delta\lambda/\Delta H$ is small in comparison with the value of $\Delta\lambda/\Delta H$ below the compensation point, θ_k.

To understand the observed phenomenon, we shall proceed from Néel's model for iron garnets. According to this model, iron garnets have 3 magnetic sublattices: **c**, **d** and **a**.[3] The sublattice **c** is formed by Gd^{3+} ions, while the sublattices **d** and **a** are formed by Fe^{3+} ions. All three sublattices interact antiferromagnetically, and according to the measured values of magnetic momenta the resultant magnetization of these sublattices can be presented in the following way,

$$\underset{\mathbf{c}}{Gd^{3+}} \longrightarrow \quad \longleftarrow \underset{\mathbf{d}}{Fe^{3+}} \quad \longrightarrow \underset{\mathbf{a}}{Fe^{3+}}.$$

Our experiments in magnetostriction make us suppose that there is something like two ferromagnetic states in the gadolinium iron garnet. One of them is determined by the interaction of sublattices **d** and **a** (Fe^{3+} ions take part in this interaction), and the other is determined

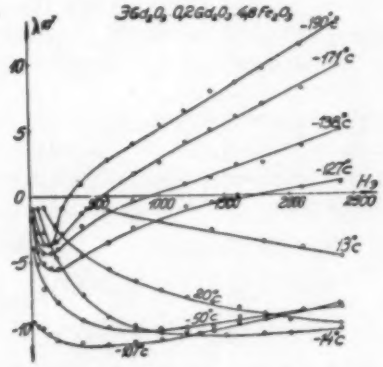

FIG. 5. Isotherms of the longitudinal magnetostriction of the ferrite, $3Gd_2O_3 \cdot 0.2Gd_2O_3 \cdot 4.8Fe_2O_3$ below and above the compensation point.

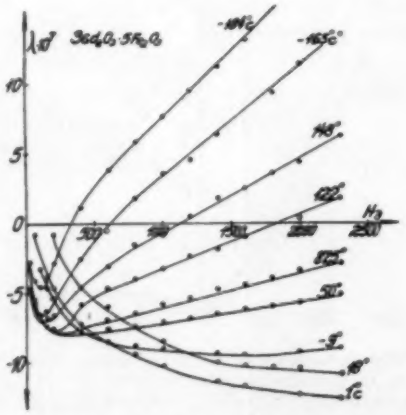

FIG. 6. Isotherms similar to those in Fig. 5, only for the ferrite $3Gd_2O_3 \cdot 5Fe_2O_3$.

[3] L. Néel, Compt. Rend. **239**, 8 (1954).

by the interaction of the sublattice **c** with the sublattices **d** and **a** (the interaction of the Gd^{3+} ions with Fe^{3+}). Both these interactions originate magnetostrictions of different types. The interaction **d**—**a** (we mean magnetic dipole coupling) results in "ordinary" magnetostriction. One can provide an indirect proof of this fact by measuring magnetostriction in the yttrium iron garnet ($3Y_2O_3 \cdot 5Fe_2O_3$). If we substitute nonmagnetic Y^{3+} ions for the Gd^{3+} ions in the sublattice **c**, only the interaction **d**—**a** will take place. The measurements of magnetostriction in the sample $3Y_2O_3 \cdot 5Fe_2O_3$ have shown that it belongs to the usual type.

We attribute the large volume magnetostriction of the paraprocess at the temperatures below θ_k to the interaction of the Gd^{3+} ions with the Fe^{3+} ions. In other words, this magnetostriction is caused by the interaction of the sublattices **c** and **d**—**a**. The exchange interaction of the Gd^{3+} ions with the Fe^{3+} ions is small, which originates the large paraprocess. The greater are the atomic magnetic moments and the smaller is the exchange interaction, the greater is the paraprocess. Under these conditions, the external field will "disturb" the magnetic spin moments inside the domains with greater ease. At the same time, the thermal motion will destroy the spontaneous magnetization faster. It will cause the broadening of spontaneous magnetization curves in such materials (curve 1 on Fig. 8), as it takes place in Invar alloy Ni, 30%, Fe, 70%. On the contrary, in the case of sublattices **a**—**d**, the interaction is strong and the resultant magnetic moment is small; therefore, the $\sigma_S(T)$ curve will be steeper (curve 2 on Fig. 8). By taking into consideration the character of the temperature behavior of the curves, we can qualitatively explain the appearance of the compensation point θ_k in the gadolinium iron garnet. On subtracting graphically the curve 2 from the curve 1, we shall have the curve $\sigma_S(T)$ with the compensation point (curve 3, Fig. 8).

In this way, the measuring of magnetostriction in the gadolinium iron garnet makes it possible to estimate qualitatively the character and the magnitude of the interaction of Gd^{3+} and Fe^{3+} ions, and to understand the type of the dependence of the spontaneous magnetization upon the temperature in iron garnets. Because of

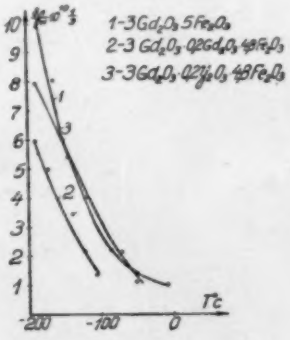

FIG. 7. The dependence of the value $(\Delta\lambda/\Delta H)$ on temperature for: (1) $3Gd_2O_3 \cdot 5Fe_2O_3$; (2) $3Gd_2O_3 \cdot 0.2Gd_2O_3 \cdot 4.8Fe_2O_3$; (3) $3Gd_2O_3 \cdot 0.2Y_2O_3 \cdot 4.8Fe_2O_3$.

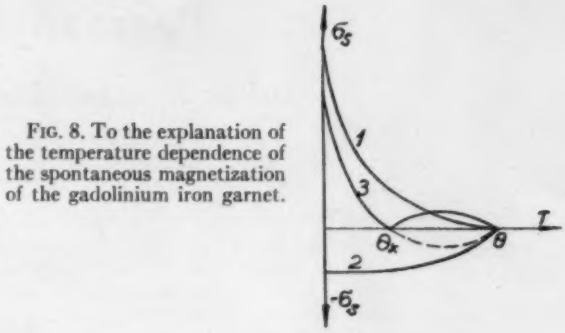

FIG. 8. To the explanation of the temperature dependence of the spontaneous magnetization of the gadolinium iron garnet.

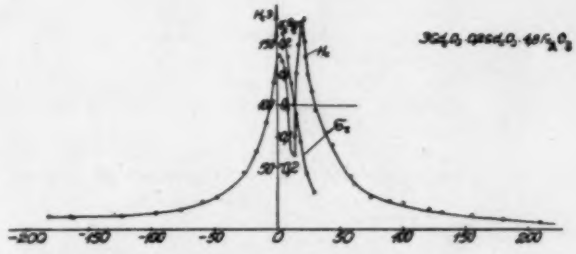

FIG. 9. The temperature dependence of the coercive force in the ferrite $3Gd_2O_3 \cdot 0.2Gd_2O_3 \cdot 4.8Fe_2O_3$.

the large magnetostriction of paraprocess in the gadolinium iron garnet below θ_k, we are to expect great influence of pressure on the magnitude of spontaneous magnetization. This means that the dependence of exchange interaction on the interatomic distances between the Gd^{3+} and Fe^{3+} ions is greater than the same dependence between the Fe^{3+} and Fe^{3+} ions.

The gadolinium iron garnets have some other peculiar features in their magnetic behavior. Thus, for example, the coercive force greatly increases when temperature approaches θ_k, and reaches its maximum at θ_k. At first, we explained the existence of this maximum H_c in a very simple way. We assumed that some structural inhomogeneities in polycrystalline ferrites manifested themselves in the vicinity of θ_k. Because of this inhomogeneity, we can consider our sample near θ_k to consist of a weak magnetic medium and stronger ferromagnetic areas with slightly different compensation points. This causes the appearance of monodomain structure, the processes of remagnetization are hindered, and H_c increases. Our further measurements of temperature dependence of H_c showed, however, that actually more complex maxima (double maxima—Fig. 9) are to be found in the neighborhood of θ_k in most cases. Both maxima are situated close to each other, but on the opposite sides of θ_k. So far, we cannot offer an exhaustive interpretation of the observed phenomenon. It is possible that the two above mentioned ferromagnetic states (the interaction of the ions Gd^{3+}—Fe^{3+} and Fe^{3+}—Fe^{3+}) are responsible for the appearance of the double maxima.

Permanent Magnets

On the Remanence of Ferromagnetic Powders

S. SHTRIKMAN AND D. TREVES*
The Weizmann Institute of Science, Department of Electronics, Rehovot, Israel

The angular dependence of the maximum remanence parallel to the applied field, I_p, and perpendicular to it, I_t, when the specimen is rotated through an angle β about an axis perpendicular to the field direction, is considered theoretically. For a rather wide range of materials the relation $I_t = (dI_p/d\beta)$ should hold. For an assembly of noninteracting uniaxial single domains, it is shown that the distribution of the easy axes can be calculated from $I_p(\beta)$ or $I_t(\beta)$ and that $2\int_0^{\pi/2} I_p \sin\beta d\beta = I_s$, where I_s is the saturation magnetization. The above method yields a Legendre series for the distribution; it is deficient in that the high terms are quite sensitive to small changes in the remanences. Measurements of I_p and I_t with a vibrating-sample magnetometer were carried out on commercially oriented Ferroxdure, on magnetically oriented Ferroxdure powder, on oriented elongated single-domain iron particles and on anisotropic Alnico. For the first three materials I_t was a few percent lower, for the last up to 20% higher, than the value theoretically expected from the relation between I_p and I_t. For Ferroxdure this small discrepancy is attributed to the reduction of I_t by splitting into domains; for the elongated single-domain sample it is attributed to particle agglomeration. In order to furnish further magnetic evidence for the agglomeration of particles in magnetic powders, remanence curves are considered. Relations between remanences obtained by different methods are derived for the interacting-pair model. These relations differ from Wohlfarth's relations, which hold for an assembly of noninteracting single-domain particles. Comparison with experiment favors the pair model.

I. INTRODUCTION

IN discussing the remanent magnetization of ferromagnets, it is perhaps best to consider the maximum or saturation remanence and the various remanence curves separately.[1] The maximum remanence of random assemblies of particles[2] with various anisotropies was calculated by Gans,[3] Wohlfarth,[4] and Wohlfarth and Tonge.[5,6] The main assumption in these calculations is that on removal of the field after saturation, the magnetization comes to that preferred crystal direction which includes the smallest angle with the previously applied field. This assumption is correct only if the magnetostatic interactions between the different particles as well as the possibility of nucleation of domains of reverse magnetization[7,8] are neglected. However, it is not yet clear how these assumptions can be justified, since very little progress[9,10] has been made in the study of the effect of interparticle interactions on the remanence. Furthermore, the nucleation of domains of reverse magnetization is far from being understood,[11,12] at least quantitatively.[13]

Notwithstanding its drawbacks, it is proposed in this paper to use the above assumption in order to study the maximum remanence of assemblies of aligned particles. Some work along these lines has already been done by Bozorth[14] and by Wohlfarth.[15] However, only the maximum remanence parallel and perpendicular to the direction of alignment has been considered by these authors.

In this paper the maximum remanence in any direction will be discussed and a relation between its parallel and transverse components derived (in Sec. II). The special case of a rotationally symmetric assembly of uniaxial particles is treated in Sec. III, and formulas[16] are derived which enable the calculation of the distribution of the easy axes of the particles from the angular dependence of the maximum remanence. Measurements of the maximum remanence are described in Sec. IV. These measurements are discussed in Sec. V with special attention to effects which may cause deviations from the assumptions mentioned above.

Theoretical study of the various remanence curves[17] is much more difficult than that of the maximum remanence. In the first case knowledge of the critical

* Present address: Pomona College, Department of Physics, Claremont, California.

[1] E. P. Wohlfarth, J. phys. radium **20**, 231 (1959).

[2] Here and in the following, each particle will be assumed to be a single crystal; the words *particle* and *crystallite* will therefore be interchanged freely.

[3] R. Gans, Ann. Physik **15**, 28 (1932).

[4] E. P. Wohlfarth, Phil. Mag. **46**, 1155 (1955).

[5] E. P. Wohlfarth and D. G. Tonge, Phil. Mag. **2**, 1333 (1957).

[6] D. G. Tonge and E. P. Wohlfarth, Phil. Mag. **3**, 535 (1958).

[7] R. M. Bozorth, Z. Physik **124**, 519 (1948).

[8] R. M. Bozorth, *Ferromagnetism* (D. Van Nostrand Company, Inc., Princeton, New Jersey, 1951), pp. 505–506.

[9] L. Néel, Ann. Univ. Grénoble Sec. Sci.-Méd. **22**, 299 (1947); see p. 325.

[10] E. P. Wohlfarth, Proc. Roy. Soc. (London) **A232**, 208 (1955).

[11] W. F. Brown, Jr., Revs. Modern Phys. **17**, 15 (1945).

[12] L. Néel, J. phys. radium **17**, 15 (1956).

[13] For an attempt to take into account the effect of splitting into domains on the maximum remanence, in a phenomenological way, see L. Néel, Advances in Phys. **4**, 191 (1955), pp. 222–223.

[14] See reference 8, pp. 504–505.

[15] E. P. Wohlfarth, Advances in Phys. **8**, 87 (1959); see p. 104.

[16] E. H. Frei, S. Shtrikman, and D. Treves, J. Appl. Phys. **30**, 443 (1959).

[17] Here only the isothermal remanent magnetization will be discussed.

fields at which the magnetization changes irreversibly is essential, at least in studies of the explicit field dependence of the remanence, while in the second case it is not. Thus, for example, different remanence curves result for a random assembly of infinite cylinders whether rotation in unison[18] or curling[19] is assumed, the maximum remanence being the same. Study of the remanence curves can therefore be of invaluable, albeit indirect, importance for the investigation of the mechanism of magnetization reversal. Unfortunately only very little work has been done in this field. This work, which has mostly been done recently,[20–23] will be discussed in Sec. VI, where relations between remanences acquired by different modes of magnetizing are derived.

II. RELATION BETWEEN PARALLEL AND PERPENDICULAR MAXIMUM REMANENT MAGNETIZATIONS

Consider the following experiment. A ferromagnetic sample is saturated by an external magnetic field. The maximum remanence, in the direction of the applied field I_p, and in some direction perpendicular to it, I_t, are then measured. The sample is then rotated by an angle β in the plane defined by these two directions; it is saturated again, and I_p and I_t are measured as before. It will be shown in the following that for an assembly of noninteracting uniaxial single-domain particles,[24] I_p and I_t are related by

$$I_t(\beta)=\frac{dI_p(\beta)}{d\beta}. \tag{1}$$

To prove this relation a single uniaxial domain is first considered. Let a spherical coordinate system be defined whose axis coincides with the axis of rotation of the sample, and in which the saturating field takes the direction $(\pi/2,\pi/2)$. If initially the axis of the particle pointed in the direction (φ_0,θ_0), then after rotation by an angle β, I_p and I_t will be given by

$$I_p=I_s\sin\theta_0\sin(\varphi_0+\beta), \tag{2a}$$

$$I_t=I_s\sin\theta_0\cos(\varphi_0+\beta), \tag{2b}$$

satisfying relation (1).

As on removal of the field after saturation, the magnetization returns to the easy direction which includes the smallest angle with the previously applied field, the above equations will hold only for

$$0<\varphi_0+\beta<\pi \tag{2c}$$

and will be replaced by

$$I_p=-I_s\sin\theta_0\sin(\varphi_0+\beta) \tag{3a}$$

$$I_t=-I_s\sin\theta_0\cos(\varphi_0+\beta) \tag{3b}$$

for

$$\pi<\varphi_0+\beta<2\pi; \tag{3c}$$

(3a) and (3b) also satisfy relation (1). Finally, I_p remains continuous through the transition from Eq. (2) to Eq. (3) so that (1) is also satisfied in this region.

The remanence of an assembly of noninteracting particles is obtained simply by superposition. It follows therefore, once (1) has been proved for a single uniaxial single-domain particle, that I_p and I_t of a noninteracting assembly of such particles, irrespective of difference in their sizes, anisotropy energies or magnetizations, will also be related by (1). It is interesting to note that relation (1) is not confined to uniaxial particles alone. It is evident from the above considerations that this relation will also hold for a single-domain particle[25] with any type of anisotropy as long as $I_p(\beta)$ remains continuous. On the other hand when I_p is not continuous, this relation will not be satisfied even for a uniaxial particle. This can happen in the case of some special anisotropy energies.

III. DETERMINATION OF THE DISTRIBUTION OF THE EASY AXES FROM REMANENCE MEASUREMENTS

Relation (1), which was derived in the previous section, holds for a rather wide range of different assemblies of ferromagnetic particles. In this part, on the other hand, the discussion is limited to an assembly of noninteracting uniaxial single-domain particles (not necessarily identical) which has rotational symmetry. Referring to the experiment described in Sec. II, a spherical coordinate system $(\theta;\varphi)$ is chosen, whose axis coincides with the direction of the applied field. It is assumed that the sample is mounted so that the symmetry axis of the assembly is perpendicular to the axis of rotation. The parallel remanence will then be given by

$$I_p=\frac{I_s}{2\pi}\int_0^{2\pi}\int_0^{\pi/2}f(\alpha)\cos\theta\sin\theta d\theta d\varphi, \tag{4}$$

where the distribution function $f(\alpha)$ is defined so that $f(\alpha)\sin\alpha d\alpha$ gives the probability of finding the axis[26] of the particle between α and $\alpha+d\alpha$ and is normalized by

$$\int_0^{\pi/2}f(\alpha)\sin\alpha d\alpha=1. \tag{5}$$

[18] E. P. Wohlfarth, Research **8**, S42 (1955).
[19] A. Aharoni, J. Appl. Phys. **30**, 705 (1959).
[20] C. Johnson and W. F. Brown, Jr., J. Appl. Phys. **29**, 313 (1958).
[21] C. E. Johnson, Jr., amd W. F. Brown, Jr., J. Appl. Phys. **29**, 1699 (1958).
[22] C. E. Johnson, Jr., and W. F. Brown, Jr., J. Appl. Phys. **30**, 136S (1959).
[23] E. P. Wohlfarth, J. Appl. Phys. **29**, 595 (1958).
[24] A single-domain particle is defined here and in the following as one whose magnetization is uniform in the absence of an external field.
[25] It should be noted that single-domainness is not an essential requirement for the above relation. For example, an elongated ellipsoidal particle whose magnetization has curled a little at remanence will also fulfill this relation, although its magnetization is not uniform at remanence.
[26] This definition refers only to identical particles. When this is not the case, the probability should be referred to a given magnetization.

Here α is the angle from the axis of symmetry and I_s the saturation magnetization. Let β denote the angle between the applied field and the symmetry axis of the assembly. Expanding $f(\alpha)$ and $I_p(\beta)$ in a series of Legendre polynomials,

$$f(\alpha)=\sum_{n=0}^{\infty} A_{2n}P_{2n}(\cos\alpha), \tag{6}$$

$$I_p(\beta)=\sum_{n=0}^{\infty} B_{2n}P_{2n}(\cos\beta), \tag{7a}$$

$$B_{2n}=(4n+1)\int_0^{\pi/2} I_p(\beta)P_{2n}(\cos\beta)\sin\beta d\beta, \tag{7b}$$

and using the addition theorem for Legendre polynomials,[27] one gets from (4)

$$B_{2n}=I_sA_{2n}\int_0^{\pi/2}\cos\alpha P_{2n}(\cos\alpha)d\alpha. \tag{8}$$

From (6), (7), and (8) and the relation[28]

$$\int_0^{\pi/2}\cos\alpha P_{2n}(\cos\alpha)\sin\alpha d\alpha = \frac{(-1)^n(-1)\times1\times3\cdots(2n-3)}{2^{n+1}(n+1)} \tag{9}$$

one obtains the distribution function expressed in terms of the angular dependence of the maximum parallel remanence,

$$f(\alpha)=2\int_0^{\pi/2}\frac{I_p(\beta)\sin\beta d\beta}{I_s} + \sum_{n=1}^{\infty}(4n+1)\frac{(-2)^{n+1}(n+1)!}{(-1)\times1\times3\cdots(2n-3)}P_{2n}(\cos\alpha) \times\int_0^{\pi/2}\frac{I_p(\beta)}{I_s}P_{2n}(\cos\beta)\sin\beta d\beta. \tag{10}$$

In a similar way one can derive the distribution function from the perpendicular remanence I_t,

$$I_t(\beta)=\frac{I_s}{2\pi}\int_0^{2\pi}\int_0^{\pi/2} f(\alpha)\sin^2\theta\cos\varphi d\theta d\varphi. \tag{11}$$

Expanding I_t into a Legendre series,

$$I_t(\beta)=\sum_{n=1}^{\infty} C_{2n}P_{2n}{}^1(\cos\beta), \tag{12b}$$

$$C_{2n}=\frac{4n+1}{2n(2n+1)}\int_0^{\pi/2} I_t(\beta)P_{2n}{}'(\cos\beta)\sin\beta d\beta, \tag{12b}$$

and using the addition theorem for Legendre polynomials, one gets from (6), (11), and (12a) after integrating with respect to φ

$$C_{2n}=I_sA_{2n}\frac{1}{2n(2n+1)}\int_0^{\pi/2}\sin^2\alpha P_{2n}{}'(\cos\alpha)d\alpha. \tag{13}$$

By integration by parts and use of (9) and[29]

$$P_{2n}(0)=(-1)^n\frac{1\cdot3\cdot5\cdots(2n-1)}{2\cdot4\cdot6\cdots2n}$$

it can be shown that

$$\int_0^{\pi/2}\sin^2\alpha P_{2n}{}'(\cos\alpha)d\alpha=-\int_0^{\pi/2}\sin^2\alpha d(P_{2n}\cos\alpha) =2n(2n+1)\int_0^{\pi/2}\cos\alpha P_{2n}(\cos\alpha)\sin\alpha d\alpha. \tag{14}$$

Finally from (5), (6), (9), (12), (13), and (15) one gets

$$f(\alpha)=1-\sum_{n=1}^{\infty}\frac{4n+1}{2n(2n+1)}\frac{(-2)^{n+1}(n+1)!}{(-1)\cdot1\cdot3\cdots(2n-3)} \times\int_0^{\pi/2}\frac{I_t(\beta)}{I_s}P_{2n}{}'(\cos\beta)\sin\beta d\beta. \tag{15}$$

By comparing (15) and (10) one can see that relation (1) is fulfilled and that

$$2\int_0^{\pi/2} I_p(\beta)\sin\beta d\beta=I_s. \tag{16}$$

It is seen that apart from (1) (which, as has already been noted, holds quite generally) one also has a relation specific to uniaxial single domains. This can be seen, for example, by considering an assembly of particles with cubic anisotropy; for it the r.h.s. of (16) is much higher than I_s. Thus relation (1) and, to a greater degree, relation (16) provide some kind of check of the validity of the proposed model in attempts to determine the distribution of axes in real oriented ferromagnets, such as anisotropic Ferroxdure or Alnico, by the method suggested. This will be further discussed in Sec. V.

IV. MEASUREMENTS OF THE ANGULAR DEPENDENCE OF THE REMANENCE IN ANISOTROPIC FERROMAGNETICS

In this section, measurements will be described which were carried out primarily in order to check relations (1) and (16) in uniaxial ferromagnets, but also in an attempt to determine the distribution of easy axes in these materials.

The measurements were made with a vibrating-

[27] H. Margenau and G. M. Murphy, *The Mathematics of Physics and Chemistry* (D. Van Nostrand Company, Inc., Princeton, New Jersey, 1956), second edition, p. 112, Eqs. (3)–(60) and (3)–(61).
[28] E. W. Hobson, *The Theory of Spherical and Ellipsoidal Harmonics* (Cambridge University Press, New York, 1955), p. 39.
[29] E. Jahnke and F. Emde, *Table of Functions* (Dover Publications, New York), fourth edition, p. 114.

TABLE I. Geometry, saturation magnetization, and coercive force of the samples whose angular dependence of the remanence is given in Figs. 1–4. The integral G defined by Eq. (17), which should theoretically equal 1.0, and the first coefficients of the expansion of the distribution function into a Legendre series [Eq. (6)] are also given.

Sample	Shape	Thickness (mm)	Diameter or width (mm)	Saturation Magnetization ($4\pi I_s$) (gauss)	Coercive force (oe)	G	A_2 from I_p	A_2 from I_t	A_4 from I_t	A_6 from I_t
a. Alnico	square prism	4.0	5.2	12 500	650	0.25	...	...	...	...
b. Commercial Ferroxdure	disc	3.8	9.7	4000	2200	1.02	3.6	3.4	3.3	2
c. Ferroxdure Powder	disc	4.8	11.0	900	1300	0.96	4.4	4.3	6.5	8
d. E.S.D. iron (156A G.E. designation)	disc	2.6	12.7	6800	1100	0.87	2.6	2.6	1.9	1

sample magnetometer (VSM) of the Foner[30] type, mounted on a Varian 4-in. magnet with 1-in. tapered conical polecaps at an airgap of approximately 2 cm. To save space only one pair of coils (5500 turns each), with the axes parallel to the axis of vibration and lying in a plane perpendicular to the applied field, was used to measure both I_p and I_t. The procedure of measuring the remanences was therefore as follows. The magnetometer, which could be rotated around its direction of vibration, was adjusted to a certain angle. Maximum field was switched on and off. The voltage on the pickup coils, which is proportional to I_t, was noted down. The magnetometer was rotated by 90°, and the voltage on the pickup coils (which is now proportional to I_p) was noted. There were some difficulties in centering the sample between the coils. Following Foner's method[30] for every angle was found to be impractical, and, instead, the coils and sample were moved until exactly the same voltage, but with opposite sign, was obtained upon rotation of the sample by 180°. This procedure was carried out at a few different angles. A final test was made by magnetizing the sample *once* along its axis of symmetry and measuring the angle dependence of the voltage picked up by the coils. The curves obtained were generally within 0.5% of the expected sine curve. It should be noted that the reproducibility of all the remanence measurements carried out on this magnetometer was within 0.1%. The angle of rotation could be read to an accuracy of ±0.1%.

Several materials for which the model described in Sec. III was believed to be at least a rough approximation were chosen to be studied. These materials were (a) anisotropic Alnico (unfortunately it is not known what type of Alnico this was); (b) commercial oriented Ferroxdure; (c) magnetically oriented Ferroxdure powder in wax matrix; (d) oriented elongated single-domain (ESD) iron particles.[31] The geometry of the samples measured and their important magnetic characteristics are given in Table I. The remanences measured are plotted in Figs. 1–4 in terms of the saturation magnetization, which was measured with a lever type VSM, shown in Fig. 5.

The saturation magnetization was measured with this type of VSM in order to enable the gap of the electromagnet to be kept small so as to reach fields large enough to saturate the samples.[32] Image effects, however, prevented accurate measurements at fields above approximately 14 000 oersteds. The accuracy of the saturation measurements, which determines only the absolute accuracy of Figs. 1–4, is thus limited to about ±2% by the need to extrapolate to infinite field.

V. DISCUSSION

From the comparison of I_t and $dI_p/d\beta$ (Figs. 1–4) it can be seen that except for the Alnico sample, relation (1) agrees fairly well with the experimental results. On the other hand, the measured values for G

$$G=2\int_0^{\pi/2}\frac{I_p(\beta)}{I_s}\sin\beta d\beta \qquad (17)$$

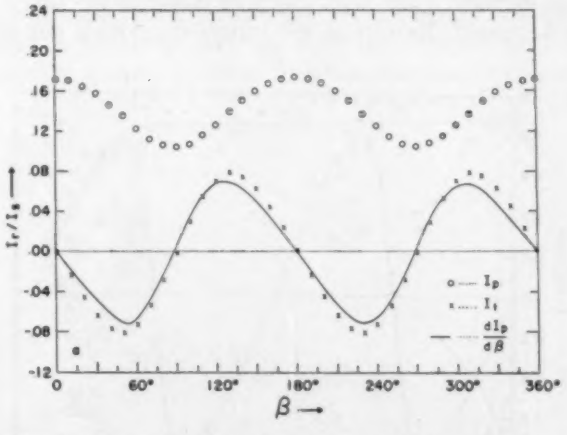

FIG. 1. Measured angular dependence of the maximum remanence parallel to the applied field, I_p, and perpendicular to it, I_t, for the Alnico sample. To facilitate the comparision of the measurements with relation (1), the derivative of I_p with respect to the angle β is also plotted.

[30] S. Foner, Rev. Sci. Instr. **27**, 548 (1956) and a private communication, which is gratefully acknowledged.

[31] The authors wish to thank Dr. I. S. Jacobs for supplying them with this sample.

[32] This was impossible to achieve with the arrangements used to measure the remanences.

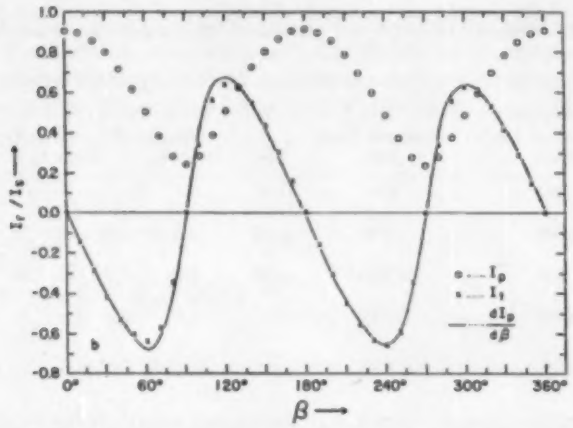

FIG. 2. Measured angular dependence of the maximum remanence parallel to the applied field, I_p, and perpendicular to it, I_t, for commercial Ferroxdure. To facilitate the comparison of the measurements with relation (1), the derivative of I_p with respect to the angle β is also plotted.

given in Table I are close to 1.0, the theoretical value given by Eq. (16), only for the Ferroxdure samples. The experimental results will be discussed in the following for each sample in detail.

(1) Alnico Sample

As shown in Table I, G is much lower than is theoretically expected by Eq. (16). This discrepancy is most probably due to the fact that, because of experimental difficulties, the remanence was measured in zero external field, not in zero internal field as was assumed in the derivation of (16). Since for this sample the demagnetizing field is not small compared with the coercive force, the remanence and therefore G will be reduced by the demagnetizing field. It is thus expected that G will increase if the demagnetizing factor of the sample is decreased. Results of measurements carried out on Ticonal G confirm this and show (Fig. 6) that when the demagnetizing factor is small enough, G reaches the value 1.0 as is theoretically expected. The disagreement between relation (1) and the experimental results for this sample might also be due to neglect of the demagnetizing field. However, no detailed study of this was made.

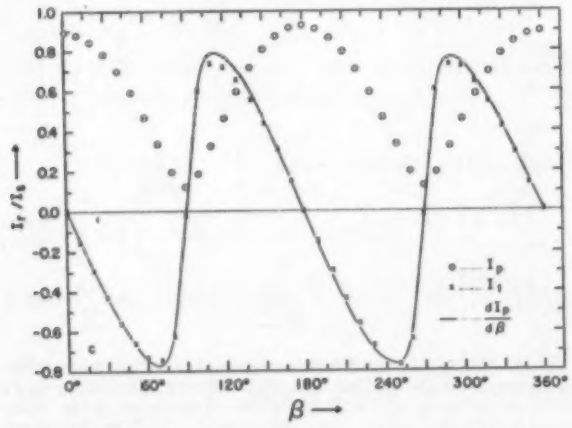

FIG. 3. Measured angular dependence of the maximum remanence parallel to the applied field, I_p, and perpendicular to it, I_t, for oriented Ferroxdure powder. To facilitate the comparison of the measurements with relation (1), the derivative of I_p with respect to the angle β is also plotted.

(2) Ferroxdure

For this case the anisotropy field is large compared with the demagnetizing field, and, as is theoretically expected, the measured values of G (Table I) are close to 1.0.

Figures 2 and 3 show that I_t compares favorably with $dI_p/d\beta$ but is generally a few percent lower. The reason for this discrepancy might be incorrectness of the assumption that a uniaxial particle has only two possible states at remanence. To show this, consider, for example, a ferromagnetic sphere having a magnetocrystalline anisotropy energy in the form $K\sin^2\alpha$. If the external field is applied parallel to the easy direction, then on removal of the field, the sphere will remain a single domain. Here $2K/I_s > 4\pi/3I_s$ is assumed. If, however, the field is applied perpendicular to the easy direction, then on removal of the field, the magnetization will buckle, and the particle will divide into domains, thus leaving a lower transverse remanence than if this were not the case. Here it is assumed that the size of the sphere is large compared with the characteristic radius[33] of the material. The case of the field perpendicular to the easy axis is the easiest to understand intuitively. A detailed calculation shows, however, that the same effect will exist over a finite range of angles dependent on K/I_s^2. This dependence is shown

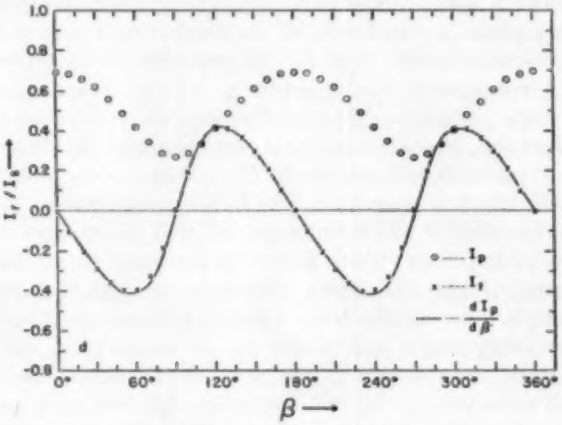

FIG. 4. Measured angular dependence of the maximum remanence parallel to the applied field, I_p, and perpendicular to it, I_t, for elongated single-domain iron powder. To facilitate the comparison of the measurements with relation (1), the derivative of I_p with respect to the angle β is also plotted.

[33] E. H. Frei, S. Shtrikman, and D. Treves, Phys. Rev. **106**, 446 (1957).

in Fig. 7 for a sphere whose radius is very large compared with the characteristic radius. The effects described above will of course be more marked for an oblate spheroid, which should be a better approximation to Ferroxdure crystallites.[34] Further support for this effect in Ferroxdure is given by permeability measurements. It has been found that the permeability of the Ferroxdure samples parallel to their axis of symmetry is much higher after saturation perpendicular to this axis than after saturation parallel to it. This suggests[35] the appearance in the first case of Bloch walls which are wiped out in the second.

(3) Elongated Single-Domain Sample

In this sample the measured value of G is somewhat lower than that expected, and the explanation given in the case of the Alnico probably holds here also. As can be seen from Fig. 4, the measured I_t is gain a little lower than $dI_p/d\beta$. Here some reason other than that invoked in the case of Ferroxdure causes this reduction of I_t, as the particles are too small to split into domains. A possible reason, in this case, might be interparticle interactions. Thus, for example, a pair of elongated particles lying side by side will lose their remanence after saturation perpendicular to their long axis. The reduction of I_t in this case, however, should not be accompanied by an increase of the susceptibility, in agreement with the observations made on the ESD sample. Interparticle interactions will be further discussed in Sec. VI, where remanence curves are considered, as these curves should be particularly sensitive to interparticle interactions.

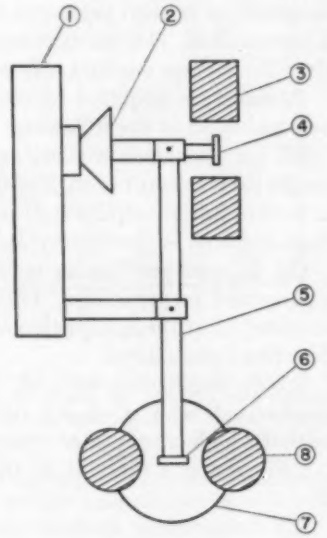

FIG. 5. Lever type vibrating sample magnetometer used for saturation magnetization measurements. 1, base; 2, actuating speaker; 3, reference coils; 4, reference magnet; 5, lever; 6, sample; 7, magnet pole piece; 8, pickup coils.

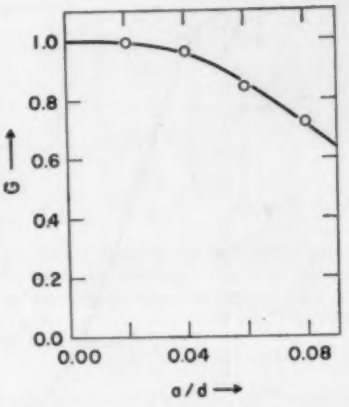

FIG. 6. Measured shape dependence of G for Ticonal G disks. Here "a" is the thickness of the disk and d its diameter. G is defined by Eq. (17).

Concerning the calculation of the distribution of the easy axes in the samples measured, the following should be noted. As can be seen from the formulas developed in Sec. III, the remanences, in particular the parallel one, are rather insensitive to the high polynomials in the Legendre expansion of the distribution function. This means that even small deviations from the theoretical relations, caused by changes in the remanences due to the effects discussed above, which were not taken into account in Sec. III, might indicate that the calculated distribution is actually far from the true distribution. Furthermore even small experimental inaccuracies can cause large errors in the determination of the high terms of the distribution function. Actual numerical calculation confirmed this consideration and showed that only the first few terms of the distribution function, could be determined with reasonable accuracy. (These terms are given in Table I.) The method suggested in Sec. III is therefore of value only in cases where only the first few terms of the expansion of the distribution function into a Legendre series are of importance, as for example in materials which are not highly oriented. This is probably the case with the commercial Ferroxdure sample, whose distribution function, calculated

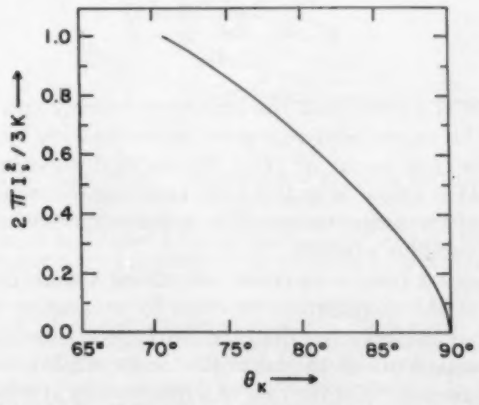

FIG. 7. Theoretical dependence of θ_K, the maximum angle between the easy axis and the applied field for which a sphere remains a single domain after saturation, on K/I_s^2. Here K is the magneto-crystalline anisotropy constant, and I_s the saturation magnetization.

[34] K. J. Sixtus, K. J. Kronenberg, and R. K. Tenzer, J. Appl. Phys. **27**, 1051 (1956).

[35] Compare G. W. Rathenau, Revs. Modern Phys. **25**, 297 (1953).

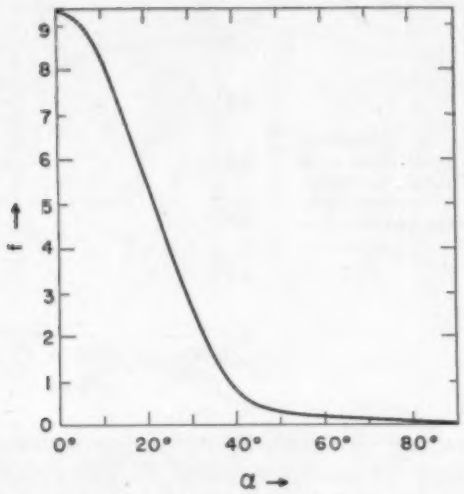

FIG. 8. Distribution of the easy axes in the commercial Ferroxdure sample as determined from the transverse remanence using Eq. (15), with $n<4$. The distribution functions $f(\alpha)$ is defined so that $f(\alpha)\sin\alpha d\alpha$ gives the probability of finding the axis of a particle between α and $\alpha+d\alpha$. The angle α is measured from the preferred axis.

from the transverse remanence by using the results given in Table I, is plotted in Fig. 8. Another example of the feasibility of such cases is described below.

Consider the magnetocrystalline energy of a uniaxial crystal expressed as a series of Legendre polynomials,

$$E_K=\sum_{n=1}^{\infty} K_{2n}P_{2n}(\theta). \tag{18}$$

If the anisotropy energy of an oriented assembly with a distribution function given by (6) is described by

$$\bar{E}_K=\sum_{n=0} \bar{K}_{2n}P_{2n}(\cos\beta), \tag{19}$$

then by using the Legendre polynomials addition theorem, one can show that

$$K_{2n}=\frac{(2n+1)\bar{K}_{2n}}{A_{2n}}. \tag{20}$$

As it is known that the anisotropy energy can generally be represented to a good approximation by only the first few terms of (18), the method described in Sec. III is valuable in this case, enabling the measurement of the magnetocrystalline anisotropy on oriented polycrystalline samples.

Finally a note is in order concerning the determination of the distribution function by measuring magnetic parameters other than the remanence, for example the components of the reversible susceptibility tensor at remanence.[36] For the case of a rotationally symmetric assembly of identical uniaxial single domains the distribution function can be calculated from the angular dependence of these components by methods similar to those used in Sec. III. It should be noted, however, that small deviations from the model assumed, such as different anisotropies for different particles, or in particular deviation from single-domainness, may result in serious changes in the susceptibility, making this method impractical for real materials.

VI. RELATIONS BETWEEN THE DIFFERENT MODES OF ACQUISITION OF THE REMANENT MAGNETIZATION

In the study of the remanence curves, either of two methods has been followed. In the first method the remanence curves were calculated[18,19] by making assumptions which enable the evaluation of the spectrum of critical fields for irreversible magnetization changes. In the second,[23] only the relations between the various remanence curves were studied. Knowledge of the spectrum of critical fields can be dispensed with in the latter method. This method is therefore more attractive than the former one and will be adopted here.

Remanences acquired by four different methods will be considered in the following.

(a) ac demagnetization method. The sample is magnetized to saturation, and then a slowly diminishing ac field of initial amplitude H is applied. The remanence thus acquired is denoted by $I_D'(H)$.

(b) dc demagnetization method. The sample is first magnetized to saturation. Then the remanence $I_D(H)$ obtained after the application of a field H in the reverse direction is measured.

(c) dc remanence method. The sample is first demagnetized with a slowly decreasing ac field of an initially high amplitude. Then the remanence $I_R(H)$ is measured as a function of an increasing applied field H.

(d) Anhysteretic method. On a dc field, H, a slowly decreasing ac field of an intially high amplitude is superposed. The remanence $I_A(H)$ is measured as a function of H.

For an assembly of noninteracting single domain particles, Wohlfarth[23] has proved the following relations between the remanences considered above:

$$I_D'(H)=I_R(\infty)-I_R(H) \tag{21}$$

and

$$I_D'(H)=\tfrac{1}{2}I_R(\infty)+\tfrac{1}{2}I_D(H). \tag{22}$$

Johnson and Brown,[21] who measured the above remanence curves for fine γ-F_2O_3 particles in an attempt to determine their shape distribution, observed, as is shown in Fig. 9, marked deviations from formulas (21) and (22). Wohlfarth's relations should be obeyed by any model whose remanence curves are constructed from an assembly of elementary systems, each possessing only two remanence values $\pm I_r$ and a symmetrical hysteresis loop. It follows that allowing

[36] E. H. Frei and S. Shtrikman, *Proceeding of the Conference on Magnetism and Magnetic Materials, Boston, 1956* (American Institute of Electrical Engineers, New York, 1957), AIEE Spec. Publ. T-91, p. 504.

reversal of magnetization by curling instead of by rotation in unison will not remove the above disagreement, nor will this be done by assuming each particle to consist of a Jacobs and Bean[37] chain of spheres, an assumption which was made by Wohlfarth[38] in order to account for the difference found by Johnson and Brown between the magnetically determined and directly observed axial ratios of the particles in their samples.

As the simple "two zero-field states" model is in disagreement with the results of the experiments by Johnson and Brown, a more elaborate model has to be adopted. Perhaps the least elaborate one is to assume a third remanence value, equal to zero, in addition to the two remanence values $\pm I_r$ assumed by Wohlfarth. The hysteresis curve for this case, shown[39] in Fig. 10(e), is characterized by two critical fields, $|H_1|>|H_2|$; H_1

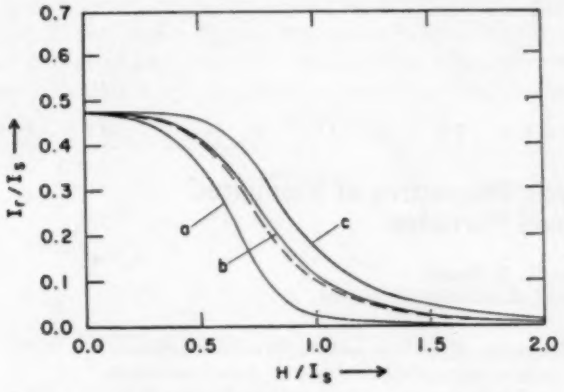

FIG. 9. Solid lines: The remanence I_r versus the field H of randomly oriented $\gamma-F_2O_3$, measured by Johnson and Brown[21] by three methods. Curve *a* by ac demagnetization, curve *b* by dc demagnetization and curve *c* by dc remanence. For comparison all curves are plotted in terms of ac demagnetization method. The broken line is the average of the curves *a* and *c* in the remanence direction; according to relation (23) it should coincide with curve *b*.

is associated with the transition from the demagnetized state to that with the maximum remanence, H_2 with the opposite transition. The various remanences considered in the beginning of this section are easily derived from the hysteresis curve and are shown in Figs. 10(a)–(d). It is readily seen that these curves obey the relations

$$I_D'(H)=I_D(H)+I_R(H) \tag{23}$$

and

$$2H_A(I)=H_R(I)-H_D'(I), \tag{24}$$

which are also obeyed by the particles assumed by

[37] I. S. Jacobs and C. P. Bean, Phys. Rev. **100**, 1060 (1955).
[38] E. P. Wohlfarth, submitted to J. Appl. Phys.
[39] Here the reversible part of the magnetization curve is neglected, as this does not influence the conclusions to be reached on the remanence curves.

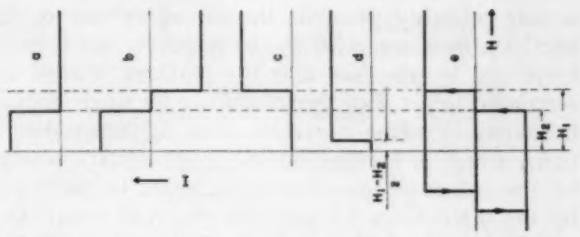

FIG. 10. Remanence, I, versus the field H for the "three zero-field states" model by four different methods. Curve *a* by dc demagnetization, curve *b* by dc demagnetization, curve *c* by dc remanence and curve *d* by anhysteretic magnetization. Curve *e* shows the hysteresis loop for this model.

Wohlfarth, with only two remanence values $\pm I_r$ and a single critical field.[40]

Relation (21) is compared in Fig. 9 with the measurements made by Brown and Johnson on γ-F_2O_3 powder. Following these authors, all results are given after having been converted by Eqs. (21) and (22) into $I_D'(H)$. Relation (23) then means that curve *b* should be equal to the average in the remanence direction of the *a* and *c* curves. This, as is shown in Fig. 9, is in rather good agreement with the experiment.

Up to now the treatment given was rather formal. Néel[41] has already noted that hysteresis curves like that shown in Fig. 10(e) are found for pairs of magnetostatically interacting particles, the special case treated in this paper being that of a pair of equal particles interacting negatively. Magnetization reversal in such

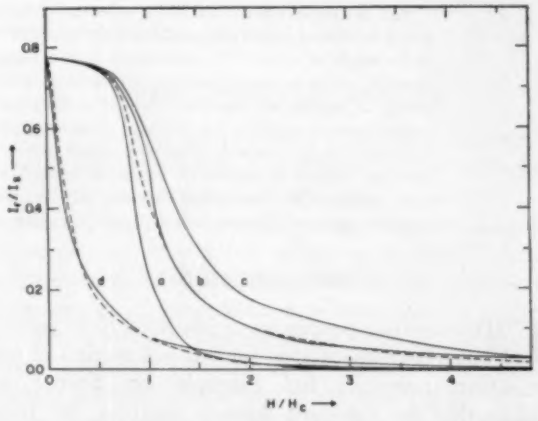

FIG. 11. Solid curves: The remanence I_r versus the field H of a Ferramic *C* ring by four different methods. Curve *a* by ac demagnetization, curve *b* by dc demagnetization, curve *c* by dc remanence and curve *d* by the anhysteretic method. For comparison all curves are plotted in terms of the ac demagnetization method. Dashed curves: The one close to curve *b* is the average of curves *a* and *c* in the remanence direction, and according to relation (23) should coincide with curve *b*. The one close to curve *d* is half the difference between curves *c* and *a* in the field direction, and according to relation (24) should coincide with curve *d*. The saturation magnetization I_s and the coercive force H_c for this sample are 4260 gauss and 2.1 oe respectively.

[40] These relations follow also from the formal model assumed by G. Biorci and D. Pescetti, Nuovo cimento **1**, 829 (1958).
[41] L. Néel, Compt. rend. acad. sci. **246**, 2313 (1958).

a pair probably proceeds by curling of one of the particles, as is suggested by the relatively low coercive force and by the fact that the particles studied are somewhat larger than the critical size for single-domain behavior. It seems, therefore, that agglomeration in pairs, which is favored by the magnetostatic energy for the case of elongated particles, might be the reason for the discrepancy between the observed remanences and Wohlfarth's relations. It should be noted that this conclusion is not in disagreement with the fact that the above discrepancy remains after diluting the powder,[21] as there is no serious reason to believe that dilution reduces the agglomeration appreciably.

Finally, it is interesting to note that relations (23) and (24) were found, as is shown in Fig. 11, to be in quite good agreement with the remanences measured on a Ferramic *C* Ferrite.[42] Here again, the remanences are plotted in terms of the ac demagnetization method. Relation (24) then means that curve *d* should be equal to half the difference of the *c* and *a* curves in the *H* direction. Preliminary measurements[42] made on a Supermalloy ring and a square loop ferrite also agree better with relations (23) and (24) than with Wohlfarth's relations.

ACKNOWLEDGMENTS

The authors wish to thank Dr. E. H. Frei, under whom the work reported here has been carried out, for continuous interest and encouragement, and J. Lipkin for helping in the construction of the electronic circuitry. They are especially indebted to A. Neeman for carrying out most of the measurements and many of the calculations.

[42] The authors wish to thank Miss J. Bartfeld from the Institut Fourier, Grenoble, who carried out these measurements during her stay in the Weizmann Institute of Science, for allowing them to quote her results.

JOURNAL OF APPLIED PHYSICS SUPPLEMENT TO VOL. 31, NO. 5 MAY, 1960

Angular Variation of the Magnetic Properties of Elongated Single-Domain Iron Particles

F. E. Luborsky and T. O. Paine
General Electric Research Laboratory, Schenectady, New York

The demagnetization curves of oriented elongated single-domain (ESD) iron particles have been measured as a function of angle and packing fraction. The reduced coercive forces of dilute compacts show a maximum at an angle of about 50° associated with a buckling magnetization reversal. As the packing fraction is increased, particle magnetostatic interaction lowers the coercive force and suppresses the 50° max. The residual to saturation ratio appears as a distorted cosine function, which the simple single-domain particle model cannot account for without assuming particle orientations inconsistent with electron micrographs. A more realistic model is proposed which accounts for the experimental results by considering the effect on particle domain structure of dendritic branches and cross-links to adjacent particles. The new model has been analyzed by measuring the magnetic properties of arrays of pivoted magnets, which simulate the proposed domain configurations at various angles and packing fractions.

INTRODUCTION

THE magnetic properties of idealized ESD particles have been calculated for various models of magnetization reversal; for example by Stoner and Wohlfarth[1,2] for coherent domain rotation, by Jacobs and Bean[3] for noncoherent "fanning," and by Brown[4] and Frei[5] et al. for the more general cases of "curling" and "buckling." Any of these reversal mechanisms may occur, depending on particle geometry. Noncoherent buckling accounts best for the various observed properties of ESD iron particles: the value of coercive force, the existence of a packing effect, the unique angular variation of coercive force, and the rotational hysteresis behavior.[2,6–8] The additional contribution of crystal anisotropy and the influence of distributions of alignment and coercive force have also been discussed[2,9–12] but the significance of particle shape irregularities and specific particle interactions have not been considered in any detail. This paper briefly describes the observed angular dependence of the magnetic properties of ESD

[1] E. C. Stoner and E. P. Wohlfarth, Trans. Roy. Soc. (London) **A240**, 599 (1948).
[2] E. P. Wohlfarth, J. Appl. Phys. **30**, 117S (1959).
[3] I. S. Jacobs and C. P. Bean, Phys. Rev. **100**, 1060 (1955).
[4] W. F. Brown, Phys. Rev. **105**, 1479 (1957).
[5] E. H. Frei, S. Shtrikman, and D. Treves, Phys. Rev. **106**, 446 (1957).
[6] T. O. Paine, L. I. Mendelsohn, and F. E. Luborsky, Phys. Rev. **100**, 1055 (1955).
[7] I. S. Jacobs and F. E. Luborsky, J. Appl. Phys. **28**, 467 (1957).
[8] F. E. Luborsky, L. I. Mendelsohn, and T. O. Paine, J. Appl. Phys. **28**, 344 (1957).
[9] C. E. Johnson and W. F. Brown, J. Appl. Phys. **30**, 320S (1959).
[10] F. E. Luborsky, E. F. Fullam, and D. S. Hallgren, J. Appl. Phys. **29**, 989 (1958).
[11] W. F. Brown, J. Appl. Phys. **30**, 62S (1959).
[12] A. Aharoni, J. Appl. Phys. **30**, 70S (1959).

iron particles at various packing fractions, and relates this to proposed local variations in the domain structures of dendritic particles.

ESD IRON PARTICLES

The ESD particles used in this study were prepared by electrodeposition into mercury followed by thermal growth and metal treatment to develop a particle geometry with optimum magnetic properties as previously described.[13] Complete hysteresis loops were obtained with the recording hysteresigraph on dispersions of these particles aligned by a magnetic field at various packing fractions and angles to the direction of measurement.

The more pertinent results of these measurements are presented in Fig. 1 as a function of the angle of measurement, θ, and the packing fraction of the particles, p. The packing fraction was calculated as the ratio of the saturation magnetization of the sample, B_{is}, to that of pure iron: 21 500 gauss. B_{is} was determined for each sample by a $1/H$ extrapolation to infinite field. The coercive force showed a roughly linear dependence on packing fraction which extrapolated to zero at $p \sim 0.75$ for all angles.

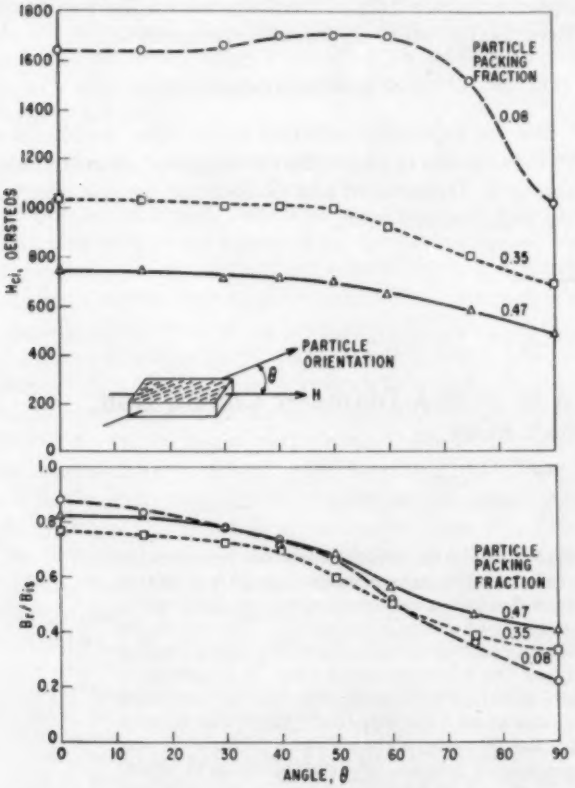

FIG. 1. Effect of particle packing fraction and orientation on the intrinsic coercive force and residual to saturation ratio of ESD iron particles. Saturation induction obtained by $1/H$ extrapolations to infinite field. Sample at 0.08 particle packing measured at −197°C, others at room temperature.

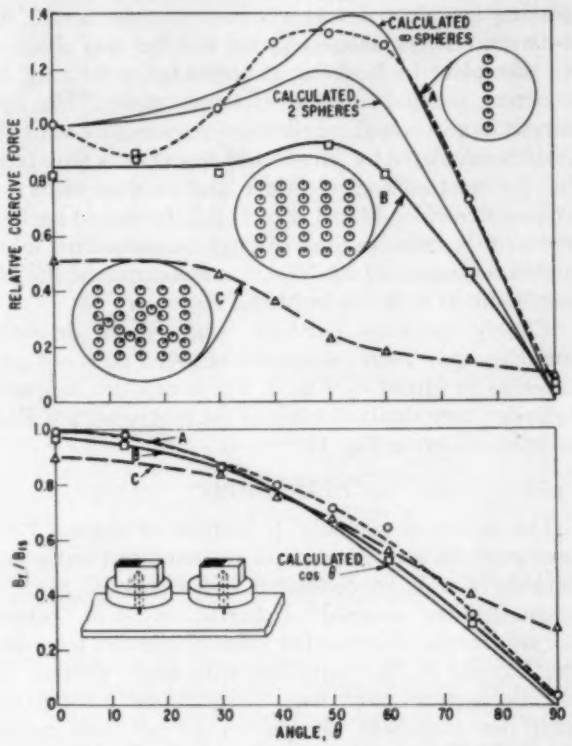

FIG. 2. Measurements of magnetic models illustrating the effects of particle packing and orientation on the coercive force and residual to saturation ratio of six magnet chains-of-spheres: A. Isolated Chain, B. Packed Chains, C. Packed chains with cross links. Calculated values for isolated chain from Jacobs and Bean.[3]

DOMAIN STRUCTURE MODELS

Physical models of proposed domain structures of hypothetical particles and assemblies of particles were made from unoriented barium ferrite magnets $\frac{7}{16}$ in. diam and $\frac{1}{4}$ in. thick magnetized across their diameter and supported on a pivot as shown in Fig. 2. Actual hysteresis loops of various magnetostatically interacting planar arrays of these disks were measured by the hysteresigraph using a large Helmholtz coil for the applied field and suitably placed B and $-H$ coils. The applied field was a negligible fraction of the coercive force of the barium ferrite magnets. Each magnet in an assembly represents the magnetization vector of a single domain segment of a particle, thus affording visual observation of the relation between reversal modes and magnetic properties. (This work is reminiscent of Ewing's early use of pivoted magnetic arrays in his attempts to relate ferromagnetism to magnetostatic interactions between atomic magnetic moments.[14])

Model A, Fig. 2 shows the simplest model: a buckling cylindrical particle with an axial ratio of 6:1 made by

[13] F. E. Luborsky, T. O. Paine, and L. I. Mendelsohn, Powder Metallurgy 4, 57 (1959).

[14] J. A. Ewing, *Magnetic Induction in Iron and Other Metals* (D. Van Nostrand Company, Inc., Princeton, New Jersey, 1900), p. 348, 352.

placing six pivoted magnets in a straight row 2 cm. between centers. Magnetization reversal was observed to take place by buckling at angles up to 60°, and by coherent parallel rotation at larger angles. The hysteresis loops showed excellent correspondence with the results calculated by Jacobs and Bean,[2] as is illustrated by the reduced coercive force and residual induction curves shown for Model *A* in Fig. 2. Increased packing reduced the coercive force through magnetostatic interaction as suggested by Néel,[15] and suppressed the H_{ci} maximum as is shown in Model *B*.

Closely packing particles with short dendritic branches may form cross links between adjacent particles as in Model *C*, Fig. 2. These produce magnetic behavior very similar to that of the highly packed ESD samples shown in Fig. 1.

DISCUSSION

The observed magnetic properties of aligned ESD iron particles as a function of measurement angle and packing fraction are consistent with a buckling mode of magnetization reversal. Coherent rotation cannot account for the observed low value of coercive force and the H_{ci} and B_r/B_{is} variations with angle without invoking particle alignment distributions inconsistent with the alignment determined by electron micrographs.[8,16] These show that 95% of the particles lie with their axes within 20° of the alignment direction, while the simple shape anisotropy model requires that a large fraction be oriented between 20° and 90°. Curling does not seem appropriate for these highly irregularly-shaped particles, and does not account for the observed magnetostatic particle interaction effect on coercive force.

The effect of packing is to reduce coercive force due to magnetostatic particle interactions as discussed by Néel,[15] and to suppress the maximum in the H_{ci} *vs* θ curve, as illustrated by Model *B*, Fig. 2. In addition ot the purely magnetostatic particle interaction effect of Model *B*, packing may bring about cross-links between adjacent particles which will radically alter their behavior. Model *C* in Fig. 2 illustrates the drastic effect on magnetic properties of a few cross-links between adjacent particles. This situation is particularly likely to occur when dendritic particles are compacted. The increase of B_r/B_{is} at 90° when ESD iron particles are compacted can be attributed to this effect. The properties of ESD particles as a function of angle and packing are thus best understood by extending the previous simple single-domain particle models to take into account longitudinal variations in domain structure brought about by irregularities in particle shape and cross links between particles. A few of these domain imperfections acting as buckling nucleation points can have a large effect on magnetic properties.

ACKNOWLEDGMENTS

We are especially indebted to the able assistance of P. Frischmann in setting up the magnetic measurements and to B. Drummond and G. Stebbins for their part in the experimental work.

[15] L. Néel, Compt. rend. **224**, 1550 (1947).
[16] L. I. Mendelsohn, F. E. Luborsky, and T. O. Paine, J. Appl. Phys. **26**, 1274 (1955).

JOURNAL OF APPLIED PHYSICS SUPPLEMENT TO VOL. 31, NO. 5 MAY, 1960

Coercive Force and Remanence of 25-A to 2000-A Diameter Cobalt, Iron, and Iron-Cobalt Alloy

F. E. LUBORSKY AND T. O. PAINE
General Electric Research Laboratory, Schenectady, New York

This paper reports an experimental study of the size dependence of the coercive force and remanence of essentially spherical cobalt, iron, and iron-cobalt alloy particles over the diameter range from 25 A to 2000 A. The particles were prepared by low-temperature electrodeposition into a mercury capillary jet, followed by thermal growth; size and shape distributions were determined by electron microscopy. The maximum coercive force at 76°K was 1330 oe for cobalt, 890 oe for iron, and 1380 oe for iron-cobalt alloy; these maxima occurred at a diameter of 30 A for cobalt, 130 A for iron, and 240 A for iron-cobalt alloy. At a sufficiently small diameter superparamagnetism reduced the remanence and coercive force to zero. This occurred at a particle diameter below 25 A for cobalt, at 50 A for iron, and at 40 A for iron-cobalt alloy. The coercive force, remanence, and their temperature coefficients are discussed in terms of the approach to single-domain behavior, the anisotropy constants which determine single-domain rotation, and the transition to superparamagnetic behavior. Crystal anisotropy predominates in the cobalt particles, a combination of shape and crystal in the iron particles, and shape anisotropy in the iron-cobalt alloy particles.

INTRODUCTION

As the particle diameter of a magnetic material is decreased the intrinsic coercive force, H_{ci}, and remanence ratio, B_r/B_{is}, increase rapidly as single-domain particle size is approached. This phenomenon has been generally discussed by Kittel,[1,2] Néel,[3]

[1] C. Kittel, Phys. Rev. **70**, 965 (1946).
[2] C. Kittel, Revs. Modern Phys. **21**, 541 (1949).
[3] L. Néel, Compt. rend. **224**, 1488 (1947).

Meiklejohn,[4] Brown,[5] Aharoni,[6] and Frei *et al.*[7] Shur[8] and co-workers have concluded from domain observations of MnBi particles that this increase is associated with the progressive removal of domain boundaries and domain reversal nuclei. Although these studies have more clearly defined the problem, the precise relationship between particle diameter and magnetic properties in this size range is still not clearly understood. Wohlfarth[9] has recently reviewed this situation.

When a sufficiently small diameter has been reached, particles may become single-domain; their coercive force can then be understood in terms of the resistance to domain rotation imposed by magnetic anisotropy forces as discussed by Néel,[10] Kittel,[1,2] and Stoner and Wohlfarth.[11] The criterions for single-domain behavior have been discussed by the above authors.

As the particle size is futher reduced a critical diameter is reached below which thermally activated magnetization reversal occurs causing H_{ci} and B_r/B_{is} to decrease to zero. This phenomenon, called superparamagnetism, has been discussed by Néel[12] and Bean and Livingston.[13]

This paper reports an experimental investigation of H_{ci}, B_r/B_{is} and the temperature coefficients of H_{ci} and B_r/B_{is} for cobalt, iron, and iron-cobalt alloy particles over the diameter range from 25 A to 2000 A, which covers the region from superparamagnetic to polydomain behavior.

EXPERIMENTAL

Particles of cobalt, iron, and iron-cobalt alloy in the 20 A size range were prepared by electrodeposition into a capillary jet of mercury at −30°C from a chloride salt in a water-alcohol electrolyte. The mercury was immediately frozen and stored at −197°C. The particles were magnetically concentrated below 0°C to about 1% metal in mercury, and subsequently thermally aged for 20 minutes at temperatures from 0°C to 350°C to obtain larger particle sizes. The H_{ci}, B_r/B_{is} and magnetization curves[14] were measured at 76°K and 207°K by removing the sample from a sensing coil connected to a fluxmeter in a controlled magnetic field. The remanence values were corrected for the demagnetizing factor of the sample. The saturation induction was obtained by extrapolation to infinite field.[14]

Samples for particle size and shape determination were obtained by two methods. In the first method the metals dispersed in mercury were oxidized by placing the dispersion under hydrogen peroxide. The oxidized particles expelled from the mercury were removed as a relatively mercury-free powder, and mounted on carbon films for direct viewing in the electron microscope by conventional techniques. In the alternative method collodion films were cast directly on a clean surface of the mercury-metal mixture. The films and adhering particles were then transferred to a mounting screen for direct viewing in the electron microscope. Both methods gave the same results.

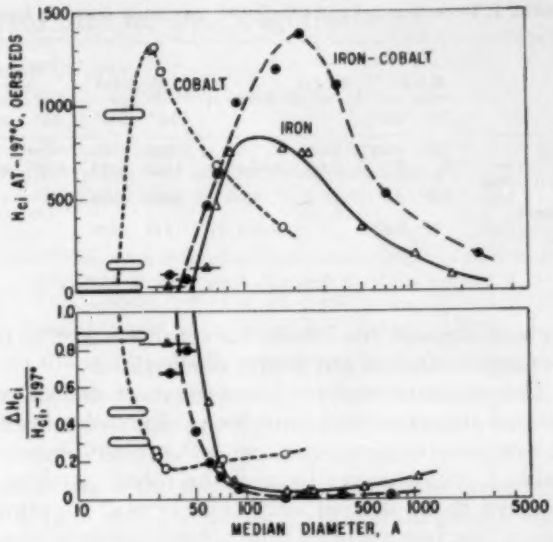

FIG. 1. The variation with particle diameter of intrinsic coercive force, H_{ci}, and temperature coefficient of H_{ci} from 207°K to 76°K, for cobalt, iron, and 44% iron–56% cobalt alloy.

Figure 1 summarizes the measurements of H_{ci} as a function of particle diameter. The iron-cobalt alloy had a composition of 44% Fe-56% Co as determined by chemical analysis. Another sample with 36.5% Fe had similar properties; the peak H_{ci} at 76°K reached with this alloy was 1310 oe rather than 1380 oe.

DISCUSSION

It has previously been found[9] in many materials that as single-domain size is approached H_{ci} varies as $1/d$. In this study the iron and iron-cobalt alloy exhibited this behavior at both 76° and 207°K. The H_{ci} of the cobalt particles, however, exhibit a $1/d^{\frac{1}{2}}$ dependence. No correlation with I_s, exchange constant, or K is apparent, nor is this result in accord with the curling hypothesis of Frei, Shtrikman and Treves,[7] which leads to a $1/d^2$ relationship.

Particle size and shape measurements show that the iron and iron-cobalt particles have a median length to diameter ratio of 1.35 independent of particle size. The diameter distributions were normal Gaussian with a width of one $\sigma = \pm 21\%$ of the diameter at all diameters

[4] W. H. Meiklejohn, Revs. Modern Phys. **25**, 302 (1953).
[5] W. F. Brown, Phys. Rev. **105**, 1479 (1957).
[6] A. Aharoni, J. Appl. Phys. **30**, 70*S* (1959).
[7] Frei, Shtrikman, and Treves, Phys. Rev. **106**, 446 (1957).
[8] Ia. S. Shur, Akad. Nauk. SSSR, Trudii Inst. Fiz. Metal. **20**, 111, (1958).
[9] E. P. Wohlfarth, Advances in Phys. **8**, 88 (1959).
[10] L. Néel, Compt. rend. **224**, 1550 (1947).
[11] E. C. Stoner and E. P. Wohlfarth, Phil. Trans. Roy. Soc. London **A 240**, 599 (1948).
[12] L. Néel, Compt. rend. **228**, 664 (1949).
[13] C. P. Bean and J. D. Livingston, J. Appl. Phys. **30**, 120*S*, (1959).
[14] To be published.

TABLE I. Experimental and calculated maximum coercive forces.

	$K\times10^{-6}$ ergs/cm³		ΔN for $1/d=1.35$	Relation	Calculated H_{ci}, oe		Observed max H_{ci}, oe	
	76°	207°			76°	207°	76°	207°
Iron	0.52	0.49	1.42	[a]	880	890	890	860
37% iron-63% cobalt	0	0	1.42	$0.47\Delta NI_s$	1270	1260	1310	1260
Cobalt hex	8.0	6.4	0	K/I_s	5600	4500	1330	1060
Cobalt fcc	1.17	1.05		$0.64K/I_s$	520	470		

[a] C. E. Johnson and W. F. Brown, J. Appl. Phys. **30**, 320S (1959).

TABLE II. Experimental and calculated critical particle diameters for superparamagnetic and single domain behavior.

	Superparamagnetic transition				Experimental median diam at max H_{ci}, A	
	Calculated $KV=25kt$, A		Experimental $H_{ci}=0$, A			
	76°K	207°K	76°K	207°K	76°K	207°K
Iron	45	63	50±10[a]	55±10	130±50[a]	140±50
44% iron-56% cobalt	40	56	40±10	45±10	240±50	250±50
Cobalt	40(hex.)	60	25	25	30±10	35±10

[a] Estimated uncertainty in absolute value.

for both iron and iron-cobalt. For cobalt $\sigma=\pm38\%$, but no particles showed any degree of elongation.

The maximum coercive forces for single-domain particles of these materials have been calculated using the known anisotropy constants with the results shown in Table I. The coercive force of the cobalt particles is assumed to be derived only from crystal anisotropy energy, the iron particles from a combination of shape and crystal anisotropy, and the iron-cobalt alloy particles from only shape anisotropy. In the case of the iron-cobalt alloy the crystal anisotropy constant, K_1, becomes zero at 55% Fe at room temperature. With no low-temperature anisotropy data as a guide we infer that K_1 is negligible because the particle properties were found to be insensitive to variation in composition over the range from 36 to 44% iron. The coherent rotation magnetization reversal mode used in these calculations is consistent with previous results[15] and with the small degree of elongation.

The smaller H_{ci} for the iron particles is explained in terms of a negative crystal anisotropy energy contribution as previously deduced for highly elongated iron particles where the elongated axis of the particles was found to lie in the [111] crystallographic direction.[16] The H_{ci} shown in Table I was obtained on the basis of the detailed calculations of Johnson and Brown for this model where the ratio of the crystal to the shape anisotropy contributions is 0.12. Reasonable agreement with experiment is obtained.

The change in H_{ci} from 207°K to 76°K as a function of particle size shown in Fig. 1 is consistent with the above views. The B_r/B_{is} curves were also determined and were found to parallel the H_{ci} curves reaching a peak of about 0.5 in each case as expected for random orientation of particles with uniaxial anisotropy. The rapid change in properties with temperature below the size corresponding to the peak H_{ci} and B_r/B_{is} indicates the onset of superparamagnetic behavior.

It thus appears that essentially spherical iron and iron-cobalt particles attain the maximum H_{ci} predicted for single-domain behavior before the critical diameter for superparamagnetic behavior is reached. The cobalt particles on the other hand become superparamagnetic before reaching the H_{ci} calculated for hcp cobalt.

The particle diameters calculated for the onset of superparamagnetic behavior are shown in Table II. The same anisotropy contributions used for the H_{ci} calculations were assumed. For comparison the diameter at which H_{ci} reaches zero is also tabulated. This corresponds to the diameter at which half of the sample volume is superparamagnetic. Again results for cobalt appear somewhat anomolous.

The decrease in H_{ci} for the iron-cobalt particles in the superparamagnetic region appears to follow the relation $H_{ci}=2K[1-5(kt/KV)^{\frac{1}{2}}]/I_s$ derived by Bean and Livingston.[13] The precision of the cobalt and iron data in this region are insufficient to test this relation.

The particle diameters determined for iron are consistent with previous results,[4] but the cobalt particle diameters are considerably smaller. Improved electron microscope resolution is believed to account for this difference.

ACKNOWLEDGMENTS

The able experimental assistance of Betty Drummond, and stimulating discussions with I. S. Jacobs and C. P. Bean are greatly appreciated. The careful electron microscope work of E. F. Koch of this laboratory and E. F. Fullam of E. F. Fullam, Inc., is also acknowledged.

[15] I. S. Jacobs and C. P. Bean, Phys. Rev. **100**, 1060 (1955).
[16] F. E. Luborsky, E. F. Fullam, and D. S. Hallgren, J. Appl. Phys. **29**, 989 (1958).

Comparison of the Critical Single-Domain Size for Fe_3O_4 and γ-Fe_2O_3*

L. A. K. WATT† AND A. H. MORRISH
University of Minnesota, Minneapolis 14, Minnesota

On theoretical grounds the critical single-domain size for $\gamma-Fe_2O_3$ is expected to be somewhat larger than for Fe_3O_4. Measurements of the variation of coercive force with temperature and with compression for a single iron-oxide powder in both the Fe_3O_4 and $\gamma-Fe_2O_3$ forms yield strong evidence in support of this conclusion.

MORRISH and Yu[1] have calculated the critical single-domain size for both Fe_3O_4 and $\gamma-Fe_2O_3$ as a function of particle shape. They assumed that the particles were prolate ellipsoids and neglected crystalline anisotropy. They found that the critical single-domain size for $\gamma-Fe_2O_3$ was somewhat larger than for Fe_3O_4. Hence, a single-domain particle of $\gamma-Fe_2O_3$ close to the critical size would behave as a multidomain particle when reduced to Fe_3O_4. This paper describes experimental evidence in support of this conclusion.

A single iron-oxide powder containing acicular particles has been studied in the form of both Fe_3O_4 and $\gamma-Fe_2O_3$. The variation of coercive force with temperature from 77° to 300°K was studied by a method described previously.[2] The results are shown in Fig. 1 for both Fe_3O_4 and $\gamma-Fe_2O_3$. In both cases, curve 1 shows the data obtained for the powder under study, curve 2 gives the results which were found for powders which were known to contain mostly single-domain particles, while curve 3 indicates the behavior found for a powder known to contain mostly multidomain particles.[2] A comparison of the three curves in each case shows that in the form of Fe_3O_4 the powder behaves as though most of the particles are multidomain whereas, when converted to $\gamma-Fe_2O_3$, it behaves as though most of the particles are single domains.

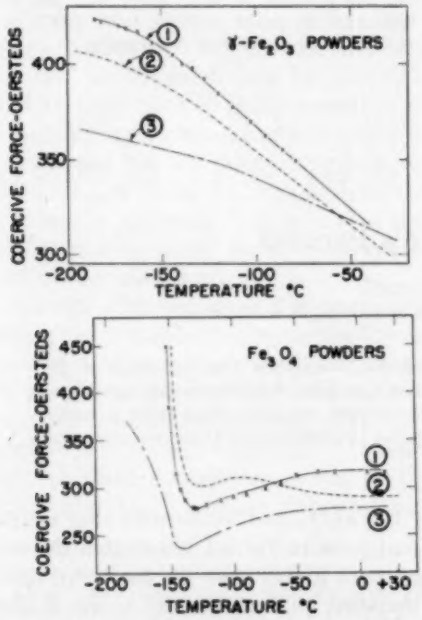

FIG. 1. Variation of coercive force with temperature for both the magnetite and $\gamma-Fe_2O_3$ forms of the powder.

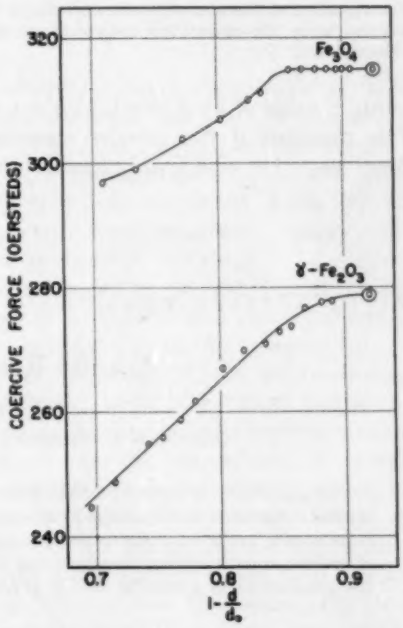

FIG. 2. Variation of coercive force with compression for both the magnetite and $\gamma-Fe_2O_3$ forms of the powder.

Measurements were also made of the variation of coercive force with compression for both forms of the powder. The results are shown in Fig. 2. The coercive force has been plotted as a function of $1-d/do$ where d is the powder density and d_0 is the density of the bulk material. The circled points at greatest dilution were obtained by immersing the powder in paraffin; the other points by compressing the powder in a die. For the Fe_3O_4 powder, the coercive force shows no variation with com-

* This work was supported by the Mines Experiment Station of the University of Minnesota.

† Present address: Department of Electrical Engineering, University of Washington, Seattle 5, Washington.

[1] A. H. Morrish and S. P. Yu, J. Appl. Phys. **26**, 1049 (1955).

[2] A. H. Morrish and L. A. K. Watt, J. Appl. Phys. **29**, 1029 (1958).

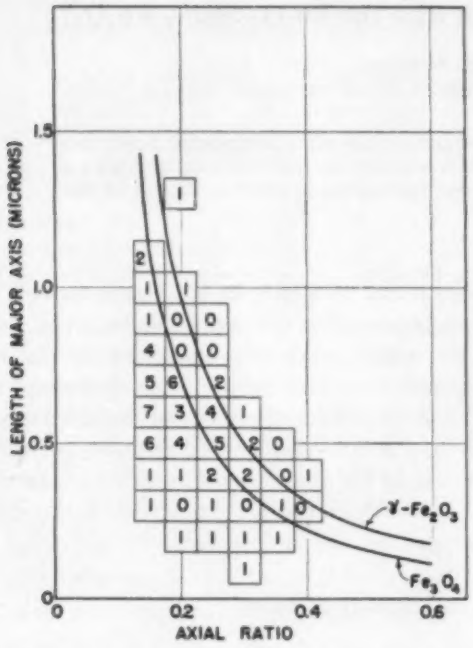

FIG. 3. Comparison of the observed size and shape distribution of the particles with the calculated critical single-domain size curves of Morrish and Yu.

pression until a value of $1-d/do=0.85$ is reached. This behavior is expected if the powder contains mostly multidomain particles which are close to the critical single-domain size.[3] For the $\gamma-Fe_2O_3$ form of the powder, the coercive force varies with $1-d/do$ in the manner which would be expected if the powder contained mostly single-domain particles.[3,4] These results are therefore in agreement with those found in the low temperature experiment.

The actual size and shape distribution of the particles in the powder was determined by means of an electron microscope. In Fig. 3, this distribution has been superimposed on a portion of the theoretical curves of Morrish and Yu.[1] The number in each square represents the number of particles whose axial ratio and major axis length lie within the boundaries of the square. About 50% of the particles have values of length and axial ratio lying between the two theoretical curves. Only two particles lie on the multidomain side of the $\gamma-Fe_2O_3$ curve, the remainder falling on the single-domain side of the Fe_3O_4 curve. In view of the fact that a number of assumptions have been made in the theory, which are not satisfied by the particles studied, this agreement between the actual distribution and the theoretical sizes is probably somewhat fortuitous. However, the results lead to the conclusion that the critical single-domain size for particles of $\gamma-Fe_2O_3$ is somewhat larger than for particles of Fe_3O_4.

[3] A. H. Morrish and L. A. K. Watt, Phys. Rev. **105**, 1476 (1957).
[4] E. P. Wohlfarth, Advances in Phys. **8**, 88 (1959); see p. 95 for a discussion of the validity of this relationship.

JOURNAL OF APPLIED PHYSICS SUPPLEMENT TO VOL. 31, NO. 5 MAY, 1960

On the Resolution of Brown's Paradox

S. SHTRIKMAN AND D. TREVES*
Department of Electronics, The Weizmann Institute of Science, Rehovot, Israel

The possibility is examined that Brown's paradox results from the assumption that the shape of the crystal considered is ellipsoidal. It is argued that the large local demagnetizing fields developed near sharp corners of a uniformly magnetized crystal cause the appearance of closure domains, which serve as nuclei of reverse magnetization, thus lowering the coercive force. A tentative development of these domains upon the application of a reverse field is given.

BROWN[1] showed in 1945 that for an ideal ellipsoidal ferromagnetic crystal, whose long axis coincides with the easy direction of magnetization and the external applied field, no nucleation, that is deviation from saturation, can occur until this field has reached a negative value larger than $2K/I_s-NI_s$. Here, K is the magnetocrystalline anisotropy constant, I_s the saturation magnetization and N the demagnetizing factor in the field direction. Comparison of the measured coercive force[2] for $BaFe_{12}O_{19}$ and MnBi with that estimated by Brown,[1] and given in Table I, shows that the theoretical values are much higher than the measured ones, and it is clear therefore that the model assumed above is a poor approximation for the particles which constitute these powders.

A much more realistic picture for a small ferromagnetic particle, and one which will be adopted here, is that of a single crystal with sharp corners. In this case, a completely different situation occurs because the de-

* Present address: Pomona College, Department of Physics, Claremont, California.
[1] W. F. Brown, Jr., Revs. Modern Phys. **17**, 15 (1945).
[2] K. J. Sixtus, K. J. Kronenberg, and R. K. Tenzer, J. Appl. Phys. **27**, 1051 (1956).

TABLE I. Comparison of the magnetocrystalline anisotropy field, $2K/I_s$, and the demagnetizing field for a sphere, $4\pi I_s/3$. [The values for iron and MnBi are computed from data given by Bozorth, *Ferromagnetism* (D. Van Nostrand, Company, Inc., Princeton, New Jersey, 1951). Those for $BaFe_{12}O_{19}$ are taken from reference 9.]

Material	$BaFe_{12}O_{19}$	MnBi
$2K/I_s$(oe)	16 000	38 000
$4\pi I_s/3$(oe)	1600	2600

magnetizing field of the uniformly magnetized crystal is no longer uniform. This results in the possibility of finding, in uniformly magnetized particles, demagnetizing fields much higher than $4\pi I_s$, the maximum value for an ellipsoidal particle. What is most important to note is that near a sharp corner these fields reach infinitely large values.[3] It can, therefore, be expected that neglect of the demagnetizing effects for particles having such corners will lead to results which disagree with experiment, even for cases where $K \gg I_s^2$. Moreover, it might be that taking them into account will resolve Brown's paradox. The measurements made by Deblois and Bean,[4] in which they find a coercive force of approximately $2K/I_s$ in the middle of an iron whisker, decreasing considerably near its tip, support these ideas to some extent. There is, thus, hope that for the purpose of calculating its magnetization curve, a small particle may be approximated by a homogeneous single crystal, the boundary of which is not necessarily ellipsoidal but still a singly connected surface. A definite conclusion, it seems, can be obtained only by solving Brown's equations[5] for a crystal with sharp corners. This, as has already been noted,[5] involves formidable mathematical computations and has not been attempted yet by the authors. Still it is believed that this problem can be discussed profitably, although in a somewhat speculative way, without making use of Brown's equations. This is attempted in the following.

It is assumed that the huge demagnetization fields associated with a uniformly magnetized corner cause the formation of closure domains. These then serve as nuclei of reverse magnetization,[6] whose existence has already been postulated in the study of the dependence of the coercive force on particle size.[7–9] A tentative development of these domains is shown in Fig. 1. At remanence [Fig. 1(a)], closure domains will already

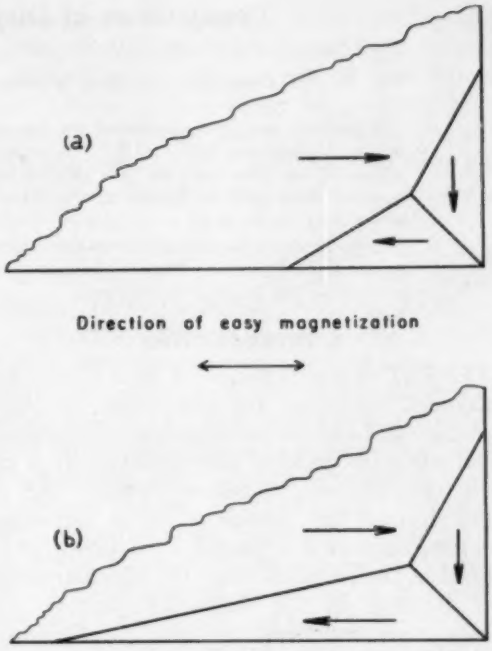

FIG. 1. Possible domain configuration at a sharp corner: (a) at remanence; (b) upon application of a small reverse field.

exist. Upon application of a reverse field, the domain of reverse magnetization will start to increase its length reversibly [Fig. 1(b)], until it reaches the full length of the crystal. Magnetization reversal will then proceed easily by irreversible movement of the 180° Bloch wall that has been formed because its energy will be independent of position at this stage.

In conclusion, it can be said that there are at least some grounds to believe that sharp corners can cause considerable reduction of the coercive force and thus resolve Brown's paradox. From this conclusion, if true, it follows that in order to get high magnetic strength, it is necessary to avoid sharp corners, analogously to what is known for the electric case. It would be very interesting to test this conclusion by trying to produce crystallites having no sharp corners. Also, a rigorous calculation of the magnetization curve of an ideal crystal with sharp corners would help considerably in clearing up this problem. This admittedly requires very elaborate mathematical computation which can be carried out only with the help of modern automatic computers. However, it seems worthwhile because of its basic as well as applied importance.

ACKNOWLEDGMENT

The authors are much indebted to Dr. E. H. Frei, under whom the study reported here has been carried out, for continuous interest and encouragement.

[3] As can easily be seen by calculating the field caused by a square surface charge, this is a logarithmic infinity.
[4] R. W. Deblois and C. P. Bean, J. Appl. Phys. **30**, 2258 (1959).
[5] W. F. Brown, Jr., Phys. Rev. **105**, 1479 (1957).
[6] Studies of the domain configuration at the tips of whiskers, in an attempt to clarify these points, are being carried on by one of the authors (D.T).
[7] L. Néel, J. phys. radium **17**, 250 (1956).
[8] C. Kittel and K. Galt, Adv. Solid State Phys. **3**, 437 (1956).
[9] G. W. Rathenau, J. Smit, and A. L. Stuijts, Z. Physik **133**, 250 (1952).

Precipitation of Dispersed Fine-Particle Magnetite

LYNORE E. SLATEN
International Business Machines Research Laboratory, Poughkeepsie, New York

A method has been developed for preparing well-dispersed fine-particle magnetite by precipitation *in situ*. A solution of Fe^{++} and Fe^{+++} is formed into a sol by the addition of agar-agar and polyvinyl alcohol; magnetite particles are then precipitated by diffusing NaOH into the resulting semi-rigid gel. The size range of these particles is from 40 A to 800 A. Typical magnetite films exhibit a coercivity of about 50 oe, with a B_r/B_s ratio of 0.4.

A study of the precipitation reaction has shown that the properties of the resulting magnetic particles appear to be limited by factors intrinsic in the mechanism of the reaction rather than by the limitations imposed by the gel-resin system used.

I. INTRODUCTION

INTEREST in fine particles for such applications as magnetic recording and permanent magnets has placed an emphasis on investigating the behavior of single-domain fine-particle micropowders. It is known that as particle size decreases through the single-domain region, the coercivity of a ferromagnetic powder increases until it reaches a maximum, and then decreases as the particles enter the superparamagnetic range. Because of the difficulties intrinsic in the breaking and dispersing of small agglomerates of magnetic particles, no system of truly isolated single-domain magnetite particles has been prepared for study. This paper describes an investigation into a method of precipitation *in situ* in which iron ions are held dispersed within a gel, then precipitated as dispersed magnetite by diffusing hydroxide ions into the matrix.

II. EXPERIMENTAL PROCEDURE

The salts $FeCl_2 \cdot 4H_2O$ and $FeCl_3 \cdot 6H_2O$ in a 1:2 mole ratio were dissolved at room temperature in a known volume of a 10% polyvinyl alcohol ("72-60 Elvanol") solution. The resulting volume was doubled by addition of a hot (about 85°C) 4% agar-agar solution. After thorough mechanical mixing, the resulting homogeneous sol was spread on a substrate, usually a glass slide, or poured into a petri dish to a depth of about 1 cm. A semi-rigid gel was produced after standing at room temperature for ½–1 hr. Magnetite was precipitated by covering the gel with a solution of $2.5f$ NaOH (where f is the number of formula weights per liter of solution). When the reaction was complete (after 1–2 hr), the sample was washed in a running-water bath until both gel and rinse-water appeared neutral to *p*H paper (about 2 hr), then air-dried on its substrate for at least 15 hr.

It was assumed that the reaction

$$Fe^{++} + 2Fe^{+++} \xrightarrow{OH^-} Fe_3O_4$$

went to completion. Since each sample was made up in a known concentration of reactants, the theoretical amount of product could easily be calculated.

The values of the coercivity, H_c, and the ratio of residual induction to saturation induction, B_r/B_s, were measured for each sample from *B-H* loops made on a 60-cycle *B-H* loop tracer. Maximum drive field of the instrument was about 800 oe. At that drive field several of the films remained unsaturated. Electron microscopy was used to estimate particle size, shape, and state of agglomeration *in situ*.

III. RESULTS AND DISCUSSION

The resulting films exhibited *B-H* loops of the type shown in Fig. 1. All coercivities obtained were far lower than might be expected for a dispersed assemblage of fine single-domain Fe_3O_4 particles.

From the electron micrographs (see Fig. 2) it is difficult to judge accurately the physical configuration of these particles. Corresponding to the ultimate resolution of the microscope, the smallest particles visible are about 40 A in diameter; the largest are about 800 A. However, the latter may principally be agglomerates of smaller particles. Particles were seen to agglomerate under the beam of the electron microscope, probably as a result of the gel softening. Since hysteresis is observed, some of the particles present must be above the superparamagnetic range. No acicular particles were observed in any of the samples.

X-ray powder patterns confirmed the presence of Fe_3O_4 and hydrated α-Fe_2O_3 with no indication of metallic Fe or other iron salts.

Wet chemical analyses indicated a tendency for the occurrence of reduction in these systems. In samples made up in initial Fe^{+++}:Fe^{++} ratios of 2:1 and 3:1, the precipitated products yielded ratios of 0.4:1 and 1:1, respectively.

Samples were subjected to variation of several reaction parameters, and no trend toward orientation, larger particle size, higher coercivity, or improved

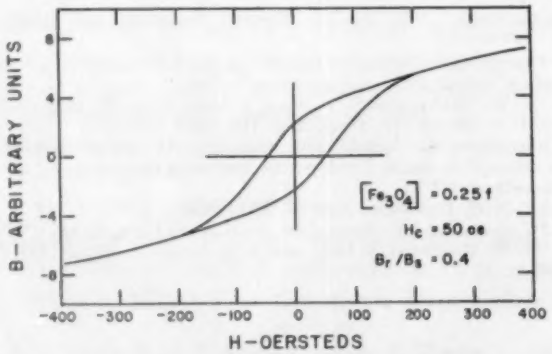

FIG. 1. *B-H* loop of dispersed fine-particle Fe_3O_4 precipitated in polyvinylalcohol-agar-agar.

FIG. 2. Electron micrograph of Fe_3O_4 particles precipitated in polyvinylalcohol-agar-agar. $[Fe_3O_4]=0.25f$.

B-H-loop squareness was observed. Time of precipitation ranged from 30 sec to 24 hr. Concentration of NaOH was lowered from $2.5f$ to $0.002f$. Theoretical Fe_3O_4 concentration was varied from $0.05f$ to $1f$. Gels were precipitated in the presence of a 10 000 gauss field, and through a temperature range of 0°C to 70°C. The ratio of $Fe^{+++}:Fe^{++}$ was changed from 2:1 to 3:1. Precipitation and oxidation were made to occur simultaneously in a sample containing only ferrous ions, with $NaNO_2$ added as oxidant to the NaOH.

In the course of investigating the effects of varying these parameters, it was found that some conditions were totally unfavorable for producing Fe_3O_4, while some were simply unfavorable for producing particles larger than superparamagnetic size.

A further investigation into the precipitation reaction in water, methanol, and ethanol solvents, using NH_4OH, NH_3-vapor, and both aqueous and alcoholic NaOH as precipitants, seemed to confirm that the reaction itself is the limiting factor. Precipitation occurred instantaneously upon the contact of OH^- with iron ions. Attempts to slow it down and to produce larger particles resulted either in a nonmagnetic product or in a mixture of iron oxides.

Direct precipitation *in situ* appears unsatisfactory as a method for producing, for study, samples of dispersed Fe_3O_4 particles in which the particle size and shape can be varied through the single-domain region. However, the present investigation has indicated that the method may be adaptable to the preparation of dispersed superparamagnetic particles.

ACKNOWLEDGMENTS

The author is sincerely grateful to C. F. Aliotta for his work in preparing all the electron micrographs and and to J. A. Morrow for his assistance in the laboratory.

JOURNAL OF APPLIED PHYSICS SUPPLEMENT TO VOL. 31, NO. 5 MAY, 1960

New Material for Permanent Magnets on a Base of Mn and Al

A. J. J. KOCH, P. HOKKELING, M. G. v. D. STEEG, AND K. J. DE VOS
Metallurgical Laboratory, N. V. Philips' Gloeilampenfabrieken, Eindhoven, The Netherlands

During an investigation of the Mn-Al system from 40–100% Mn, a new metastable phase was found, which has a tetragonal structure with lattice constants $a=2.77$ A and $c=3.57$ A and lattice positions 000 and $\frac{1}{2}\frac{1}{2}\frac{1}{2}$ with a preference of the Mn atoms for one of these positions. This τ phase, which has the approximate composition $Mn_{1.11}Al_{0.89}$, can only be obtained by special heat treatment. It possesses remarkable magnetic properites. From the approach to saturation an anisotropy constant of about 10^7 ergs/cm^3 can be calculated, while the extrapolated value σ_∞ amounts to 96 erg/oe g; the latter corresponds to a $4\pi I_s$ of 6200 *G*.

Particles obtained by grinding the bulk material possess an ${}_iHc$ value of up to 6000 oe. No fixed correlation exists between particle size and the value of ${}_iHc$; the latter is strongly dependent on the method of pulverization, and the authors are inclined to think that ${}_iHc$ is largely determined by the extent of deformation.

The increase of ${}_iHc$ caused by grinding is accompanied by a decrease of the magnetic moment. This decrease can be partially reversed by aging. The observed decrease in the magnetic moment on pulverizing agrees with the value calculated from X-ray and neutron diffraction data. The current fine-particle theory is unable to give an adequate explanation of the ${}_iHc$.

An anisotropic permanent magnet was obtained by swaging cast bars, with the following properties in the preferred direction: $B_r=4280$ *G*, ${}_iHc=4600$ oe, ${}_BHc=2750$ oe, $BH_{max}=3.5\times10^6$ G oe.

INTRODUCTION

MATERIALS having a high uniaxial magnetic anisotropy can be used successfully for permanent magnets. Such anisotropy can be expected, for instance, in materials with a tetragonal or hexagonal crystal structure. Well-known examples are barium-

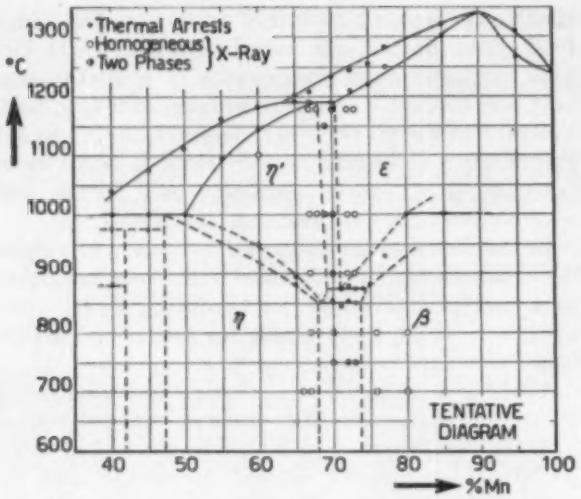

FIG. 1. Mn-Al system from 40–100% Mn.

ferrite and the intermetallic compound MnBi. Although MnBi possesses excellent permanent magnetic properties, its industrial use is limited by its low corrosion resistance, large temperature coefficient, and by the fairly high price of bismuth. For these reasons, there was a search for other ferromagnetic compounds of manganese without these disadvantages. One of the systems investigated was Mn-Al, both components being nonstrategic and cheap materials.

Mn-Al SYSTEM FROM 40–100% Mn[1]

This part of the system has been investigated among others by Ishiwara[2] and Köster.[3] Unlike Köster, we found the compound MnAl (67.0% Mn) to be paramagnetic. X-ray diffraction patterns of this phase can be interpreted as belonging to a hexagonal structure with parameters $a=7.20$ A and $c=22.95$ A. As appears from Fig. 1 this phase η can dissolve a large amount of Aluminium, but the solubility for Mn is very small. By differential thermal analysis it was shown that at higher temperatures this phase η transforms to a high-temperature modification η', whose structure is up to now unknown. No change in volume can be observed during transformation from η to η'. Microscopical investigations showed a highly twinned structure for the η phase, the appearance of which might be connected with the isochoric transformation.

From about 68% Mn to 74% Mn and below 850°C, this phase is in equilibrium with a β phase, a solid solution of Al in β-Mn. At 850°C and 870°C, respectively, the following eutectoidic reactions occur:

$$\beta+\eta \leftrightarrows \eta' \quad \text{and} \quad \beta+\eta' \leftrightarrows \epsilon.$$

The ϵ phase has a hexagonal structure with lattice constants $a=2.68$ A, $c=4.34$ A. This ϵ phase can be supercooled, while the degree of supercooling depends greatly on cooling rate and composition. Cooling an alloy of about 72% Mn from the ϵ state at a rate of 30°C/sec, the ϵ phase does not decompose into the equilibrium phases, but at about 700°C it transforms into a tetragonal structure with lattice parameters $a=2.77$ A and $c=3.57$ A and lattice positions 000 and $\frac{1}{2}\frac{1}{2}\frac{1}{2}$ with a strong preference of the Mn atoms for one of these positions. This τ phase possesses remarkable magnetic properties.

MAGNETIC PROPERTIES OF THE METASTABLE τ-PHASE

To measure the magnetic properties of the τ phase, cast specimens containing 72.3% Mn were homogenized for 1 hr at 1150°C and subsequently cooled, at an average rate of 30°C/sec in the temperature region of 825°C–600°C.

σ-T curves of these specimens showed a normal ferromagnetic behavior and a Curie-temperature of 380°C.

From the approach to saturation, an estimation can be made of the anisotropy constant, which amounts to about 10^7 ergs/cm³ at room temperature. Extrapolation to infinite field yields a magnetic moment $\sigma_\infty=96$ erg/oe g, corresponding to a $4\pi I_s$ of 6200 G.

From the high magnetic anisotropy, an increase of the intrinsic coercive force ${}_IH_C$, which varies from about 500–1000 oe for the bulk material, might be expected by pulverizing. After pulverizing the material in a mortar, it was found that particles of about 200–300 μ had an ${}_IH_C$ value of 2600 oe, which is remarkably high for such a coarse powder. A sieve fraction of 60–80 μ possessed an ${}_IH_C$ of 3550 oe, while at powder <40 μ an ${}_IH_C$ of 3750 oe was measured. When the particle fraction of 177–200 μ (${}_IH_C$=2750 oe) was ground for several hours in a ball mill, the coercivity increased to a nearly constant value of 4100 oe for all particle fractions. This means that no firm correlation exists between particle size and ${}_IH_C$; obviously the latter depends greatly on the pulverizing method.

It appears that the rise of ${}_IH_C$ is accompanied by a decrease of the magnetic moment. By measuring the σ of the particle fraction 37–44 μ up to a field strength of 27 500 oe, an extrapolated value σ_∞ of about 71 erg/oe g was found.

By aging the powders, the magnetic moment can be raised again, but then the coercivity tends to decrease. For instance, another powder fraction <40 μ of the same casting was aged 2 hrs at 400°C and by this the σ measured at 10 000 oe rose from 42.4 erg/oe g to 51.2 erg/oe g, while the ${}_IH_C$ decreased from 4350 oe to 3840 oe.

From all this, we are inclined to think that the material does not have a normal fine particle character, but rather that the deformation of the material causes the increase in ${}_IH_C$.

[1] Hiroshi Kono, J. Phys. Soc. (Japan) **13**, 1444–1451 (1958). (During these investigations, Kono, J. Phys Soc. (1958) came to our attention.)

[2] T. Ishiwara, Sci. Rep. Tôhoku Imp. Univ. **19**, 500–504 (1930).

[3] W. Köster and W. Bechthold, Z. Metallkunde **30**, 294–296 (1938).

As deformation by pulverizing can hardly be determined, cast bars were deformed by other methods, e.g., by swaging. As the material is fairly brittle, special precautions have to be taken. The coercive force of the massive bar does indeed increase by deformation, which moreover gives rise to an anisotropic material with a preferred direction parallel to the axis of the bar. The magnetic properties in the preferred direction are: $B_r = 4280$ G, ${}_IH_C = 4600$ oe, ${}_BH_C = 2750$ oe, $BH_{max} = 3.5 \times 10^6$ G oe.

RELATION BETWEEN MAGNETIC PROPERTIES AND STRUCTURE

By X-ray diffraction it was shown that in the τ phase the lattice positions 000 (A) and $\frac{1}{2}\frac{1}{2}\frac{1}{2}$ (B) are occupied, with a strong preference of the Mn atoms for either of these positions. It was further proved by neutron diffraction that the Mn atoms have their spins aligned parallel to the c axis, while those of the Mn atoms on B positions are directed antiparallel to those on A positions. Finally, the degree of order in the low coercive bulk material was found to differ from that in the powder with high coercive force.[4]

On the base of this information, an explanation of the decrease of the magnetic moment after pulverizing is possible. The tetragonal configuration occurs at the composition $Mn_{1.11}Al_{0.89}$, with a narrow existence region. Let there be x Al and $(1-x)$ Mn atoms on the A position; then, the number of Al and Mn atoms on B position should be $(0.89-x)$ and $(0.11+x)$, respectively. By neutron diffraction a value of $x=0.03$ was found for the bulk material (${}_IH_C = 600$ oe) and by X-ray patterns a value of the order of 0.13 for the powder (${}_IH_C = 4100$ oe). This means that, for $x=0.03$, the net moment per unit cell is 0.83 of the magnetic moment per Mn atom (assuming that the Mn atoms on A and B sites have the same electron configuration), while for $x=0.13$ it is 0.63 of the magnetic moment per Mn atom. As measured on the bulk material, σ_∞ amounts to 96 erg/oe g; therefore, the powdered material must have a value $\sigma_\infty = (0.63/0.83) \times 96 = 73$ erg/oe g, which is in good agreement with the measured value of 71 erg/oe g.

[4] P. B. Braun and J. A. Goedkoop (to be published).

An explanation of the cause of the ${}_IH_C$ is difficult. On assuming that by deformation disordered cells are concentrated in the neighborhood of slip planes or perhaps twin boundaries, we can imagine that the material is built up of highly anisotropic ferromagnetic regions, separated by antiferromagnetic layers of low order. By electron-microscopic investigations, regions, with a smallest dimension of 0.2–1 μ, are revealed in the highly twinned structure. These regions are of the appropriate order of magnitude for single-domain behavior in a material with such a high magnetic anisotropy. The number of these single-domain regions increases by deformation, which results in a higher ${}_IH_C$, but lowers the σ.

This explanation is somewhat unsettled by an experiment, in which a very fine powder ($<1\ \mu$) was made from bulk material by electrolytic anodic corrosion. Although a very high coercive force would be expected, the powder possessed an ${}_IH_C$ nearly equal to that of the bulk material (500–1000 oe). After subsequent deformation, these very fine powders likewise raise their coercive force to about 3000 oe.

A relation might be found between the coercivity and the presence of the disordered antiferromagnetic regions, as only when these exist in juxtaposition with the ferromagnetic ordered material, high coercivities are observed. A ferromagnetic-antiferromagnetic interaction analogous to the Meiklejohn effect,[5] observed in the system Co-CoO, might occur here, though no displaced hysteresis loops could be found. Rotational hysteresis[6] appeared considerable up to 30 koe, but there was no indication that it would retain a finite value at infinite field.

Experiments will be continued to investigate this subject.

ACKNOWLEDGMENTS

The valuable discussions with J. Smit and H. Zijlstra are greatly appreciated.

[5] W. H. Meiklejohn and C. P. Bean, *Proceedings of the Conference on Magnetism and Magnetic Materials, Boston*, 1956, (American Institute of Electrical Engineers, New York, 1957), AIEE Spec. Publ. T-91, pp. 16–33.

[6] H. Zijlstra (to be published).

"Interaction Anisotropy" Model of the Structure of Alnico Magnet Alloys

T. O. PAINE AND F. E. LUBORSKY
General Electric Research Laboratory, Schenectady, New York

The permanent magnet properties of Alnico alloys have been attributed to the shape anisotropy of an elongated single-domain magnetic precipitate oriented by cooling in a field. This paper reports measurements of the angular variation of the magnetic properties of highly directional crystal-oriented Alnico 5 DG, Columax, and Ticonal XX which are inconsistent with the simple shape anisotropy model. A domain "interaction anisotropy" model is proposed which treats the structure as a complex interconnected single-domain network. The interaction between single-domain elements within this structure minimizes magnetostatic and exchange energy by introducing local variations in particle domain configuration; these nucleate buckling magnetization reversal at particle irregularities and cross-links. In its simplest form this structure can be visualized as a series of *H*-shaped single-domain size units. The rather complex behavior of such a structure has been analyzed by measuring the magnetic properties of analogous physical models consisting of arrays of pivoted magnets. This analysis suggests that the progressive increase in maximum energy product from 6 million gauss-oersteds for Alnico 5 DG and 8 million gauss-oersteds for Columax to twelve million gauss-oersteds for Ticonal XX is associated with the suppression of buckling through the reduction of particle irregularities and cross-links. Electron micrographs of the structures of these materials and their observed angular variation of magnetic properties are consistent with this new model.

INTRODUCTION

NÉEL[1] and Stoner and Wohlfarth[2] first proposed that the shape anisotropy of an ESD (elongated single-domain) particle should lead to a substantial coercive force, and that the properties of Alnico permanent magnets might be derived from the shape anisotropy of an elongated single-domain magnetic precipitate. The presence in Alnico of a structure of the required size, shape, and orientation was subsequently established through magnetic analysis and electron microscope studies by Nesbitt, Heidenreich, Williams, and Bozorth,[3–5] and others. Paine, Mendelsohn, and Luborsky[6,7] experimentally demonstrated the existence of a strong shape-anisotropy effect, and showed that it was of sufficient magnitude to account for the properties of Alnico by reproducing the properties of eight Alnico alloys with ESD iron and iron-cobalt particles. Jacobs and Bean[8] noted that the properties of ESD particles were not consistent with Stoner and Wohlfarth's coherent magnetization rotation model, and proposed a "chain-of-spheres" model in better agreement with the observed properties. A general treatment of magnetization reversal processes for ideal infinite cylinders was subsequently given by Frei, Shtrikman, and Treves,[9] and Aharoni,[10] who predicted the specific conditions under which magnetization reversal would occur by curling, buckling, or coherent rotation. A recent comprehensive review of magnetization processes in high

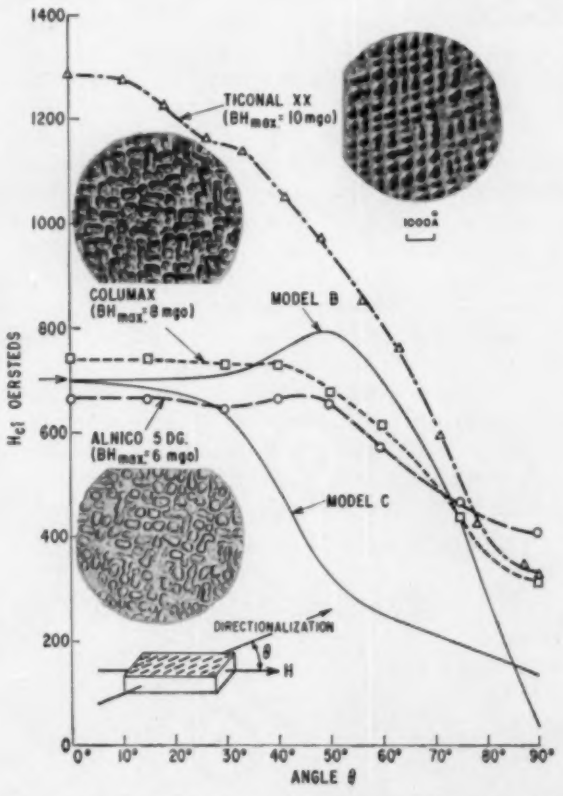

FIG. 1. The intrinsic coercive force as a function of angle for Alnico 5 DG, Columax and Ticonal XX, compared to the results from Model B and Model C normalized to 700 oe at $\theta = 0$. Model B consists of 5 parallel chains of 6 interacting elements in a straight chain; Model C contains one interconnecting element between each chain. Electron micrographs showing a section perpendicular to the directionalization axis of each alloy were prepared from shadowed carbon replicas of the etched surfaces.

[1] L. Néel, Compt. rend. **224**, 1550 (1947).
[2] E. C. Stoner and E. P. Wolfarth, Phil. Trans. Roy. Soc. London **A240**, 599 (1948).
[3] E. A. Nesbitt and R. D. Heidenreich, J. Appl. Phys. **23**, 352 (1952).
[4] E. A. Nesbitt, H. J. Williams, and R. M. Bozorth, J. Appl. Phys. **25**, 1014 (1954).
[5] E. A. Nesbitt and H. J. Williams, J. Appl. Phys. **26**, 1217 (1955).
[6] T. O. Paine, L. I. Mendelsohn, and F. E. Luborsky, Phys. Rev. **100**, 1055 (1955).
[7] F. E. Luborsky, L. I. Mendelsohn, and T. O. Paine, J. Appl. Phys. **28**, 344 (1957).
[8] I. S. Jacobs and C. P. Bean, Phys. Rev. **100**, 1060 (1955).
[9] E. H. Frei, S. Shtrikman, and D. Treves, Phys. Rev. **106**, 446 (1957).
[10] A. Aharoni, J. Appl. Phys. **30**, 70*S* (1959).

TABLE I.

Material	Composition, %(bal. Fe) Co	Ni	Al	Ti	Cu	Nb	B_{is} gauss	B_r gauss	B_r/B_{is}	H_{ci} oe	BH_{max} m.g.o.
Alnico 5 DG	24.0	14.0	7.9	0	2.8	0	14 000	13 100	0.94	665	5.8
Columax	25.0	13.3	7.5	0	3.0	0.8	14 450	14 000	0.97	740	8.3
Ticonal XX[a]	34.0	14.5	7.0	5.0	4.0	0	12 100	11 800	0.97	1340	11.0

[a] A. J. J. Koch, M. G. van der Steeg and K. J. de Vos, Proc. Am. Inst. Elec. Engrs. Conference on Magnetism, AIEE Tech. Pub. T-91, (1956) p. 173.

coercive force materials has been published by Wohlfarth.[11]

In an accompanying paper[12] it is pointed out that magnetization buckling best accounts for the angular variation of the properties of ESD particles, and that dendritic branches and particles in contact with one another at high-packing densities provide buckling nucleation points. In this paper similar measurements for highly-directional crystal-oriented Alnico 5 DG, Columax, and Ticonal XX magnets are presented, and the results briefly discussed in terms of a model-based upon interactions between interconnected single-domain elements.

EXPERIMENTAL

The compositions and magnetic properties of the materials studied are given in Table I. Complete demagnetization curves for samples cut at various angles were obtained with a magnetic permeameter;[13] the results are summarized in Figs. 1 and 2. The Ticonal XX specimen was too small for measurements of complete demagnetization curves, but the intrinsic coercive force was determined at a number of angles.

Physical models of the proposed interacting single-domain element configurations were constructed by arranging pivoted permanent magnet discs in various arrays and measuring the demagnetization curves with a recording hysteresigraph while visually observing the magnetization reversal modes. Model A was a simple ESD particle model with six interacting domain elements in a straight line; it exhibited the general magnetic properties and transition from buckling to coherent magnetization reversal at an angle of 45° predicted by Jacobs and Bean.[8] Model B was constructed by placing two additional six-element particles on either side of Model A to measure the magnetostatic reduction in coercive force proposed by Néel,[14] while Model C was made by adding one connecting magnet between each particle to measure the buckling nucleation effect of a crosslink. These models are discussed in greater detail in an accompanying paper.[12] Their properties are shown in Figs. 1 and 2, with the coercive forces normalized to 700 oe.

[11] E. P. Wohlfarth, Advances in Phys. **8**, 88 (1959).
[12] F. E. Luborsky and T. O. Paine, J. Appl. Phys. **31**, 66S (1960).
[13] T. O. Paine, *Berichte der Arbeitsgemeinschaft Ferromagnetismus* (Riederer Verlag, Stuttgart, 1959).
[14] L. Néel, Compt. rend. **224**, 1550 (1947).

DISCUSSION

The variation in coercive force with measurement angle shown for each material in Fig. 1 indicates that Alnico 5 DG and Columax do not exhibit the decrease in coercivity with increasing angle expected of a highly oriented shape anisotropy magnet reversing by coherent domain rotation. Instead they display the constant coercive force out to an angle of 45° associated with a magnetization buckling reversal process. It does not appear reasonable to attribute this behavior to simple single-domain particle misalignments in view of the carefully directionalized crystal structures, the well-oriented precipitate observed in electron micrographs,[13,15] and the high B_r/B_{is} at 0° as shown in Fig. 2.

As an alternative hypothesis it is suggested that the particle irregularities and crosslinks revealed in electron micrographs of these materials nucleate buckling magnetization reversal at the intersections of single-domain elements as illustrated in the schematic domain con-

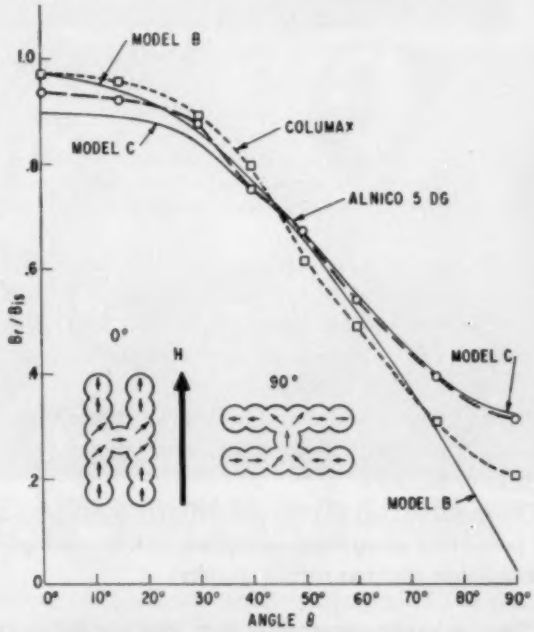

FIG. 2. The ratio of residual to saturation induction as a function of angle for Alnico 5 DG and Columax compared to the results from Model B and Model C. The magnetic structure of the *H*-shaped elements is shown in zero field after magnetization at 0° and 90°.

[15] J. J. de Jong, J. M. G. Smeets, and H. B. Haanstra, J. Appl. Phys. **29**, 297 (1958).

figurations sketched in Fig. 2. The basic H-shaped unit drawn here would also account for the substantial B_r/B_{i_0} and coercive force observed at 90°.

The magnetic structure of Alnico is thus visualized as an interconnected single-domain network, and the magnetic properties are attributed to complex interactions between single-domain elements within the structure. These interactions minimize magnetostatic and exchange energies by introducing local variations in domain configuration which provide nucleation points for magnetization buckling.

The behavior of the Alnico 5 DG and Columax magnets lies between the behavior of the two models, indicating that fewer crosslinks than the one-per-particle of Model C provide the best fit. The B_r/B_{i_0} values of the models shown in Fig. 2 are also in reasonable agreement with the observed properties of the Alnico 5 DG and Columax magnets. In striking contrast to the properties of these two materials is the high coercive force of Ticonal XX which decreases sharply with increasing-measurement angle as shown in Fig. 1. This behavior approaches that predicted for single-domain particles reversing their magnetization by coherent domain rotation.[2] It is significant that electron micrographs[15] of this material show fewer particle irregularities and crosslinks; the packing as revealed in cross-section appears much more uniform than that of Alnico 5 DG and Columax. The increase in coercive force from 665 oe for Alnico 5 DG and 740 oe for Columax to 1285 oe for Ticonal XX[16] is consistent with the proposed model which predicts that fewer particle irregularities and crosslinks should minimize buckling nucleation and thus lead to the higher coercive force associated with coherent magnetization rotation.

ACKNOWLEDGMENTS

The authors wish to thank R. J. Studders of General Electric's Metallurgical Products Department, J. E. Gould and M. McCaig of the Permanent Magnet Association Research Laboratory at Sheffield, and K. J. deVos of the Philips Metallurgical Laboratory at Eindhoven for making available samples of Alnico 5 DG, Columax, and Ticonal XX for these studies. The assistance of P. G. Frischmann with the domain model measurements is gratefully acknowledged.

[16] A. J. J. Koch, M. G. van der Steeg, and K. J. de Vos, *Berichte der Arbeitsgemeinschaft Ferromagnetismus* (Riederer Verlag, Stuttgart, 1959).

JOURNAL OF APPLIED PHYSICS SUPPLEMENT TO VOL. 31, NO. 5 MAY, 1960

Transmission Electron Diffraction of Alnico V*

K. J. KRONENBERG
The Indiana Steel Products Company, Valparaiso, Indiana

By grinding, polishing, and etching it is possible to render Alnico V thin enough for transmission electron metallography. 80-kv electrons penetrated Alnico V metal confirming the two-phase structure found earlier with replica techniques. Transmission diffraction on Alnico V samples reveal the crystal structures of both phases. The development of one phase out of the other was studied on samples from Alnico V at various states of the usual heat treatment.

ELECTRON metallography has been successful in the investigation of the complex structure of Alnico V and related materials.[1–4] However, on the account of the brittleness of these materials, it was believed up to now that one had to resort solely to surface investigations. Electron diffraction was done only by reflection, electron micrographs were all made from replicas of surfaces.

The shortcomings of reflected diffraction patterns and the possibility of artifacts in replicas can be avoided by transmission electron metallography.

EXPERIMENTAL PROCEDURE

A slice of 0.2 to 0.1 mm is cut off an Alnico rod, is imbedded in epoxy, and polished until the edges warp and fringe out. After being removed from the epoxy, the slice is placed into cold concentrated nitric acid for several days. If contamination is carefully avoided, the etching proceeds extremely slowly, thinning the metallic sliver evenly. When holes appear in the sliver, it is rinsed and mounted on the object carrier of the electron microscope. At many places close to the outer edge of the sliver and around holes the material is transparent enough for 80-kv electrons to allow image formation and diffraction by transmission [Fig. 1(a)]. The sliver has to be thin over its entire area, otherwise the strong permanent magnet material in the electron beam causes too much distortion of the picture. The etching procedure proved to be just selective enough to reveal the phase structure of Alnico V after it was fully heat

* Research was supported by the U. S. Air Force under a contract monitored by the Aeronautical Research Laboratory, Wright Air Development Center.

[1] R. D. Heidenreich and E. A. Nesbitt, J. Appl. Phys. **23**, 352–265 (1952).
[2] K. J. Kronenberg, Z. Metallk. **45**, 440–447 (1954).
[3] H. Fahlenbrach, Tech. Mitt. Krupp, **12**, 1954, 177–184
[4] K. J. Kronenberg and R. K. Tenzer, J. Appl. Phys. **29**, 299–301 (1958).

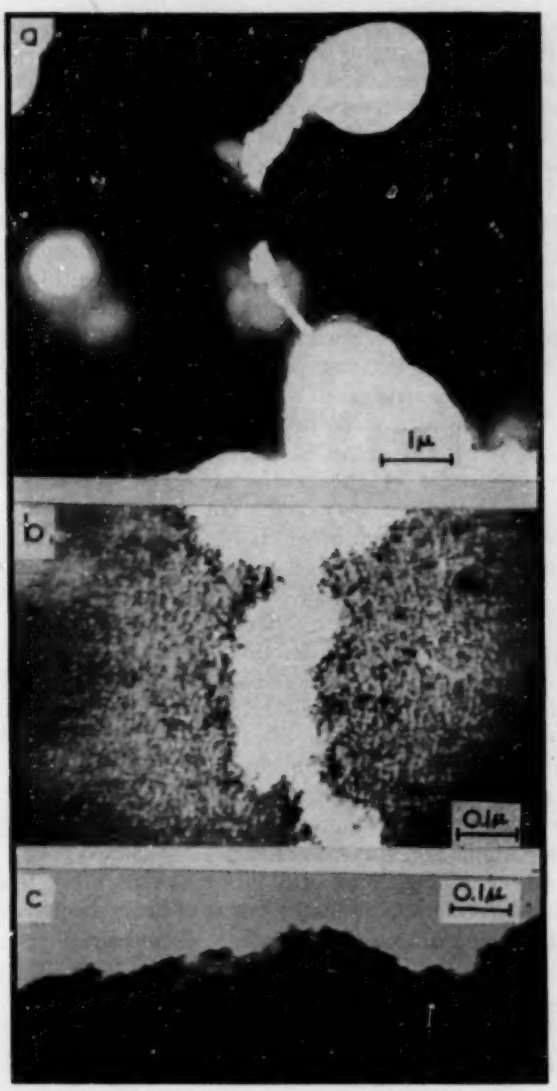

FIG. 1. Transmission electron micrographs of Alnico V. (a) Thin edge of Alnico V sliver cut perpendicular to magnetic axis. (b) Closeup of center of (a). (c) Edge of Alnico V sliver cut parallel to magnetic axis.

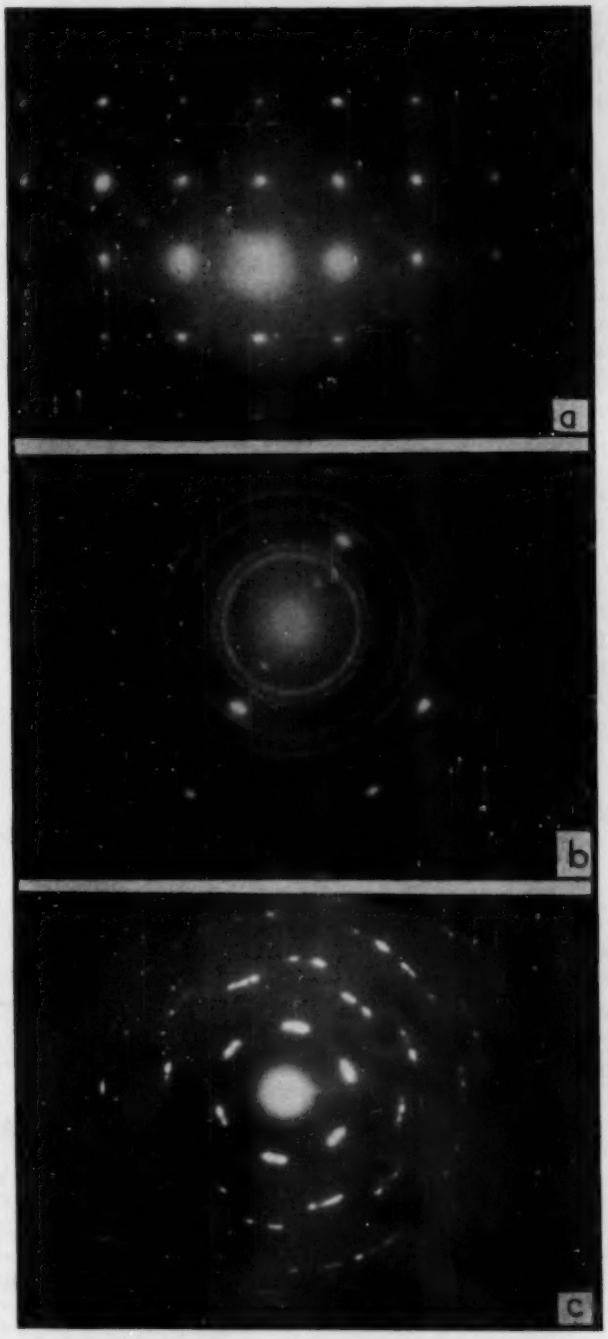

FIG. 2. Transmission electron diffraction of Alnico V. (a) Alnico V air cooled after casting. (b) Alnico V after controlled field cooling. (c) Alnico V after complete heat treatment.

treated [Fig. 1(b) and (c)]. Only very little oxidation occurred, as the diffraction patterns showed.

Samples were prepared from a rod of Alnico V which was cooled in air after casting. The same rod was then heated to 960°C, cooled in a field to 700°C in three minutes, and air cooled to room temperature. After we took samples of the rod in this condition, the rod was reheated to 630°C for one hour and 550°C for six hours. The rod was measured after each treatment and had the magnetic qualities of commercial Alnico V after the final treatment. Electron micrographs and diffraction patterns have been made at numerous locations of many samples.

Areas of 1 micron square have been selected for the diffraction. It was easy to determine where in the selected area the diffraction dots were originating. While reducing continuously the magnification of the picture from 30 000 to zero, one observes on the screen of the microscope, beside the center picture of the direct electron beam, an increasing number of pictures produced by those electrons which are diffracted by the crystal lattice of the sample. These dark-field illumination pictures shrink to form the dots of the diffraction pattern of the crystal when the magnetization is reduced

to zero. Only these diffraction patterns, the dots of which originated over extended areas of the sample, represent the crystal lattice and were used for the structural study.

RESULTS

Many earlier findings based on different experiments have been confirmed.

1. Samples of Alnico V, air cooled after casting, produced exclusively the diffraction patterns of a body-centered cubic lattice, which was found by Héidenreich and Nesbitt with reflection diffraction.[1] [See Fig. 2(a)]. It represents the crystal lattice of the matrix. Electron micrgraphs of transparent areas of the material show a milky cloudiness without structure.

2. After cooling in a field the material exhibits almost everywhere a completely new diffraction system in addition to the one found without field cooling. Figure 2(b) shows a ring pattern superimposed on the former spot pattern. The rings indicate a face-centered cubic lattice which has no correlation to the matrix lattice. The rings are granulated but otherwise exhibit a uniform intensity all around. They must originate from a great multitude of very small crystals which have little correlation to one another. A precipitation has obviously started with very many nuclei. The dots of the matrix patterns are still intense. But they have grown less sharp and have changed their distance. While the precipitate grew, the matrix changed composition and lost a bit of its former degree of order. Electron micrographs look cloudy with dark granules of irregular arrangement.

3. After the final heat treatment, the diffraction pattern of Alnico V has changed into a dot pattern representing a highly ordered crystal structure. The dots are the remainders of the rings found after field cooling. Almost everywhere in the sample the matrix pattern has vanished to faint traces. Like in Fig. 2(c), the dots are often double or triple if they originate from a transparent sample area which extends over about a square micron. The dots have almost the same distance as the rings had before the final heat treatment. We find areas of the sample where the rings are still intact but heavily emphasized at places where the final dots would be expected. Such areas may have been delayed in precipitating and represent an intermediate situation of incomplete structure.

The growing concentration of the intensity of the rings at certain angles is the consequence of the increasing order of the precipitate. This proceeds in Alnico V to form very sharp dot patterns indicating perfect single crystal order. It has to be assumed that the precipitate particles grow together and recrystallize to produce a sort of single crystal network. The matrix becomes subdivided into separated particles producing only faint and diffuse diffractions.

4. The fact that an area of one square micron usually produces double or triple dots confirms an earlier assumption concluded from electron micrographs of the Alnico V structure.[4] The precipitated network of Alnico V is subdivided by dislocation lines into a mosaic type structure with 2 to 5 areas of slightly differing crystal orientations per square micron.

Diffraction patterns of alnico materials other than Alnico V differ mainly in the degree of order the precipitate is achieving.

JOURNAL OF APPLIED PHYSICS SUPPLEMENT TO VOL. 31, NO. 5 MAY, 1960

Long Term Magnetic Stability of Alnico and Barium Ferrite Magnets*

K. J. KRONENBERG AND M. A. BOHLMANN
The Indiana Steel Products Company, Valparaiso, Indiana

Alnico and barium ferrite materials do not age at room temperature. The decreases in remanence, occurring with time, are adjustments by the magnet to its environment. Remanence adjustment proceeds with the logarithm of time and amounts to 2% or less one year after magnetization. Remanences in magnets with $H_{ci} > 2200$ oe show no changes. Also, the smaller the irreversible susceptibility at the operating point, the more stable is remance. Remanences can be stabilized completely by preadjustment.

Alnico V magnets are more stable than similar Alnico III magnets, even when the Alnico V magnets operate at a higher susceptibility. Néel's theory suggests that the oriented material is more stable than the isotropic material because larger volumes are involved in each magnetization reversal. To explain relatively large domain-like regions of reversal, we have to assume that magnetic regions cooperate during the magnetization reversal.

THE permanent magnet materials, Alnico and barium ferrite, do not change in time at room temperatures. Figure 1 compares the aging of a quench-hardened steel to the stability of remanence B_d of the Alnicos. The decrease of remanence of the stable materials is not a permanent one. Remagnetization to saturation restores the original remanence value exactly. Since the remanence behavior is not related to the age

* Research was supported by the USAF under contract, monitored by the Aero. Res. Lab., WADC.

TABLE I. Natural stability of remanence.

Material	H_{ci} oe	L/D	Relative remanence 10 000 hr after magnetization (percent)	Measuring tolerance
Indox I	4000	0.9	100.0	±0.1
Indox V	2030	0.8	99.6	±0.1
Alnico III	580	3.5	98.10	±0.04
		2.2	97.04	±0.05
Alnico VII	1200	3.5	99.32	±0.04
		2.2	98.96	±0.06
Alnico V	630	8.0	99.95	±0.01
		4.3	99.23	±0.02
		3.5	98.84	±0.04
		2.2	98.3	±0.07

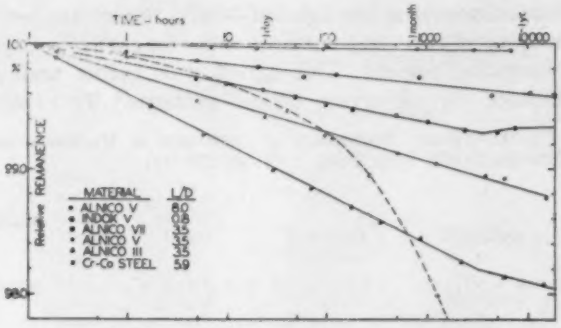

FIG. 1. Aging of steel compared to natural stability of alnicos and barium ferrite.

of these materials, one should not describe it as "aging." This word should be reserved for materials which do change with age.

The decrease of remanence with time in the non-aging materials could be described best as remanence self adjustment. The arrangement of magnetic domains or regions is disturbed constantly by randomly distributed influences from within and without. They provoke rearrangements to lower-energy configurations which result, generally, in a decrease of remanence. The amount depends on many parameters concerning the magnet as well as its environment. For quantitative details of our experiments, see references 1–3 and Table I. Here we can only qualitatively summarize the measured relations.

(1) Remanence adjustment proceeds with the logarithm of time after magnetization. In our measurements, we chose an hourly scale. Starting with 0.1 hr after magnetization, the first year contains 5 decades and 10 years contains 6 decades.

(2) The higher the coercive force, the more stable is remanence. Magnets with $H_{ci} > 2200$ oe (isotropic barium ferrite) had unchanging remanences during the first year.

(3) The remanence adjustment in magnets of $H_{ci} < 2200$ oe (alnicos and oriented barium ferrites) amounts to values from fractions of a percent to a few percent during the first year. But, these remanences too can be stabilized completely by preadjusting the remanence. Partial demagnetizing after magnetization to saturation leads to a somewhat smaller, but stable, remanence. However, excessive or rather sudden demagnetization results in erratic behavior. The proper knockdown for a magnet depends on individual circumstances, but generally is about 5–15%.

(4) Incompletely magnetized magnets have a more stable remanence than fully magnetized magnets. However, they are not as stable as those which are fully magnetized and properly stabilized.

(5) Magnets of different shapes show different rates of remanence adjustment. The smaller the irreversible susceptibility at the operating point, the more stable is the remanence. Thus, a longer magnet shape has the advantage over a shorter one.

(6) Effect of orientation. It might seem from (5) that highly oriented materials may have poor stability if one cannot avoid unfavorable shapes or operating conditions which may bring the operating point into the steep part of the demagnetization curve. This is not the case. Generally, oriented material has the advantage over isotropic material in spite of higher susceptibility. A glance at the theory may help to understand this.

Néel calculated quantitative relations of the problem, which we have verified experimentally.[4] The basic idea of his theory is the assumption that, for each disturbance influencing the magnetic situation at a certain location in a magnet, one can assign a magnetic field. These fictitious local fields can represent mechanical shocks, effects of external fields, rotations in the earth field, influences of temperature, or thermal fluctuations inherent in every material above absolute zero. Under constant environmental conditions in storage or usage, the latter fictitious fields occur randomly with the passing of time. Each occurrence provokes an adjustment—stabilizing against all ensuing occurrences of equal or smaller sizes. Only a larger one initiates a new adjustment. The effect of these fields on magnetization is directly proportional to field strength and susceptibility.

But, Néel's theory considers also the importance of the volume of material involved in Barkhausen jumps. The smaller the regions of simultaneous reversal are, the more likely are occurrences of disturbances extensive enough to initiate reversals, and *vice versa*. This offers an explanation of the surprisingly high stability of Alnico V magnets operating in the steep part of the demagnetization curve. The stability of such Alnico V magnets is many times better than one would expect from the susceptibility. To explain this, we assume that volumes involved in reversals must be several hundred times larger in the oriented material. The stability

[1] K. J. Kronenberg, Archiv. Eisenhuttenw. **24**, 441 (1953).
[2] K. J. Kronenberg, Z. Angew. Phys. **5**, 321 (1953).
[3] K. J. Kronenberg and M. A. Bohlmann, WADC TR 58-535 ASTIA Document No. AD 203387, O.T.S.-PB151716, (1958).
[4] L. Néel, J. phys. radium **11**, 49 1950; **12**, 339 (1951).

measurements in the light of Néel's theory suggest a grouping of reversing portions of the magnet into larger cooperating regions. This agrees with earlier findings obtained by observing colloid patterns.[5] To explain relatively large domain-like regions of reversal, we had to assume that magnetic regions cooperated during the magnetization reversal. The stability behavior of oriented barium ferrite suggests similar conditions and tends to confirm our assumptions of domain groups reversing cooperatively.

[5] R. K. Tenzer, *Proceedings of Conference on Magnetism and Materials*, AIEE Spec. Publ. T-91, pp. 203–211.

JOURNAL OF APPLIED PHYSICS SUPPLEMENT TO VOL. 31, NO. 5 MAY, 1960

Hot Working of Alnico 5 Alloys

C. L. Kolbe and D. L. Martin
General Electric Research Laboratory, Schenectady, New York

Alnico permanent magnet alloys have been successfully shaped into rod, wire and strip by hot working at elevated temperature. It has been found that by careful processing, certain Alnico alloys can be fabricated by extrusion, swaging, and rolling. The wrought Alnico after heat treatment was found to have comparable permanent magnet properties and improved mechanical properties compared to cast specimens of the same alloy.

INTRODUCTION

ALNICO magnets are made commercially by casting molten metals or by pressing and sintering of powders. The brittleness of these alloys, which makes them unworkable at room temperature, and moderately high temperatures, is associated with a two-phase microstructure.

At a high temperature the Alnico alloys usually transform into a ductile body-centered cubic phase. This transformation is the basis of the successful hot fabrication of Alnico. In practice, the solution to the hot shaping problem is more involved because of the effect of alloying elements on the phase fields, and the effect of impurities, segregation, etc. on the workability.

Alnico-type alloys have been successfully hot deformed before. Bieber[1] added 2% titanium to a 25 Ni, 9 Al, 64 Fe alloy and hot forged to ½-in. flats. He also added titanium to Fe-Ni-Al-Co alloys[2] and hot rolled to ⅛-in. strip. Finch and White[3] hot forged Fe-Ni-Al-Co-Cu alloys containing 4.8% vanadium. Hansen[4] describes successful 180° hot bend tests on alloys to which titanium and zirconium had been added. The alloys covered in these three investigations were of the Alnico 1–4 types with energy product values under 2 million gauss-oersteds in contrast to values of 4–5 million gauss-oersteds reported in the present investigation.

Earlier studies by R. Ahles, W. Reich and R. McKechnie[5] in General Electric had established the workability of Alnico 5 alloys. This present study is an extension of their work and includes several of the alloys melted by R. McKechnie.

EXPERIMENTAL

More than forty compositions were prepared and evaluated for their hot fabrication characteristics. In this paper only a general summary of results is given. The twelve alloys listed in Table I to illustrate our observations are divided into four groups: The first, Nos. 1–3, second, Nos. 4–8, and fourth, Nos. 11–12, groups are vacuum melted. Groups two and three, Nos. 4–10, contain zirconium additions, and the fourth group has high cobalt-titanium Alnico 10 modifications (Ticonal X).

Extrusion

In the early experiments it was found that the alloys containing zirconium successfully extruded at low temperatures in the range of 1050–1100°C. Sounder bars with fewer surface cracks were obtained than with the straight Alnico 5 composition.

An improved surface condition of the extruded bars was obtained by encasing the billet in a steel jacket. In one case (Alloy 9) the surface cracked badly when the alloy was extruded bare, but had a crackfree surface when re-extruded within a steel jacket. A heavy steel jacket is not necessary. A wall thickness of ⅛ in. was found satisfactory.

Extrusion was a method of preconditioning prior to further working by swaging or rolling. Extrusion, however, is not a prerequisite for satisfactory swaging and rolling results. Cast bars of several alloys were swaged without prior extrusion (Alloys 5 and 11).

While acceptable extrusions were obtained with air-melted as well as with vacuum-melted alloys, provided

[1] C. G. Bieber, Permanent Magnet, U. S. Patent 2,285,406 (1942).
[2] C. G. Bieber, Alloy for Permanent Magnet, U. S. Patent 2,384,450 (1945).
[3] O. J. Finch and J. H. White, Permanent Magnet Material, U. S. Patents 2,347, 817 and 2,349, 857 (1944).
[4] J. R. Hansen, Permanent Magnet and Magnets Therefor, U. S. Patent 2,499,862 (1950).
[5] R. Ahles, W. Reich, and R. McKechnie (private communications).

TABLE I. Chemical analyses and summary of fabrication results. The evaluation of fabrication is based on surface condition and soundness of the bar.

Alloy no.	Chemical analysis[a] Al	Ni	Co	Cu	Zr	Ti	Type of melt	Evaluation of results[b] Extrusion	Swaging	Rolling
1	7.9	14.9	23.5	1.1	nil	nil	vac.		Poor	
2	8.1	14.3	25.9	3.0	nil	nil	vac.		Fair	
3	8.9	14.1	24.0	2.1	nil	nil	vac.	Fair		
4	6.9	14.3	24.6	3.0	0.36	nil	vac.	Good[c]	Excellent	Excellent
5	7.4	14.5	24.0	2.7	0.24	nil	vac.		Excellent	
6	7.6	14.3	23.6	2.3	0.25	nil	vac.	Fair	Excellent	
7	7.8	14.4	23.7	2.7	0.26	nil	vac.	Good[c]	Excellent	Excellent
8	9.3	13.6	23.4	3.1	0.29	nil	vac.	Fair[c]	Poor	
9	7.6	13.8	24.2	2.7	0.22	nil	air	Good[c]	Good[c]	
10	8.1	14.3	23.9	3.5	0.33	nil	air	Poor	Poor	
11	6.7	14.8	34.4	4.0	nil	5.0	vac.		Excellent	Fair
12	6.7	15.1	33.7	4.1	nil	5.1	vac.	Good[c]	Good[c]	

[a] Balance of alloy is mainly iron.
[b] A vacant space indicates no tests made.
[c] Specimen was encased in steel jacket.

the billets were jacketed, the best results in regard to all types of deformation were obtained on vacuum-melted material.

Swaging

The swaging tests were conducted on cast and extruded samples. In general, the extruded bars swaged much better than the cast bars. Alloys 5 and 11 were two outstanding exceptions. These cast bars had excellent working characteristics and swaged to wire without cracking. Alloys 8 and 10 extruded very well, but could not be swaged without serious cracking. The smallest wire swaged was 0.040-in. diameter. Below that size the wire lost heat too rapidly for successful swaging.

Rolling

Only a few attempts were made to roll Alnico. Those alloys which swaged well, such as Nos. 7 and 11, could also be hot rolled. Alloy 4 strip was hot rolled at 1050°C from ½-in. diameter rod to 0.090-in. thick. It was possible to make 0.005-in. strip of Alloy 7 by pack rolling.

TABLE II. Comparison of peak permanent magnet properties of cast and swaged specimens.

Alloy	Cast Br kg	Hc oe	(BH)m×10⁶ goe	Swaged Br kg	Hc oe	(BH)m×10⁶ goe
1	12.8	585	4.8	12.3	585	4.5
7	12.6	580	4.7	12.5	590	5.1
11	8.5	1310	4.6	8.7	1260	4.4
12	8.5	1310	4.7	7.9	1240	3.5

Discussion of Hot Working

Vacuum melting alloys were found to work better than air-melted alloys. The beneficial effect of zirconium and titanium may be related to their high reactivity with oxygen, sulfur, and other elements that could cause hot shortness; or perhaps these two elements cause a shift in the alpha-gamma phase boundary.

Encasing the billets in a steel jacket prevents a serious drop in the billets surface temperature and at the same time introduces a surface easier to lubricate.

Hot working refines the grain structure. The finer grained extruded bars were in general easier to swage. Wrought alloys ground to an improved surface smoothness, and had increased strength and toughness.

The results indicate that the alloys with aluminum higher than 8% did not work as well. This effect may be related to the generally poor workability of the high alloy binary iron-aluminum and nickel-aluminum alloys.

Magnetic Studies

Only a few of the wrought alloys were heat treated and tested for their magnetic properties. These are listed in Table II together with the peak properties obtained on the cast specimens of the same alloy. The results show comparable permanent magnet properties for the swaged bars.

ACKNOWLEDGMENTS

We would like to acknowledge the assistance of the following during the course of this program: R. McKechnie, Miss Eleanor Freeman, T. Doig, D. Wilkins and L. Hibbs.

Spin Waves and Magnetostatic Modes

Use of Magnetostatic Modes as a Research Tool

ROBERT L. WHITE
Hughes Research Laboratories, Culver City, California

The use of ferrimagnetic resonance and in particular of the magnetostatic modes of spheres to obtain information on basic physical magnetic parameters is discussed. The effects of random and systematic deviations of the experimental situation from the theoretical upon the determination of $4\pi M$, γ, and the magnetic anisotropy constants are treated. A summary is also given of the use of line width and rf power saturation measurements on the magnetostatic modes to obtain information on the spin-wave spectrum of the material.

INTRODUCTION

THE strong and active interest shown by many laboratories in recent years in the phenomenon of ferrimagnetic resonance has two main sources: (1) the potential of resonance techniques for investigation of basic magnetic properties, and (2) the great utility in microwave devices of the gyrotropic propagation characteristics associated with ferrimagnetic resonance. This paper will be concerned exclusively with the former aspect, ferrimagnetic resonance as a research tool, and will in particular stress those situations where observations made on the higher order magnetostatic modes either yield information not available from observations of the uniform precession only or yield information more accurate or more conveniently than is possible using the uniform precession alone. The paper is intended to be a review of the current situation and tutorial in tone, and therefore contains little data not already available in the literature.

BACKGROUND

A single magnetic dipole placed in an orienting static magnetic field H_0 will have but one resonant precessional frequency, given by $\omega_0=\gamma H_0$ where γ is the gyromechanical ratio of the dipole. An array of N coupled dipoles placed in the same field will sustain N precessional modes, having various geometric distributions of relative precessional phase and spread over a frequency range determined by the inter-dipole coupling strength. Considered as an array of coupled dipoles, an ordinary piece of magnetic material constitutes a formidably complicated dynamical system. The 10^{22} dipoles per cubic centimeter involved are coupled to one another by exchange and by magnetic dipole fields, and to the crystal lattice through spin-orbit effects. The analytic solution of the total problem is, as usual, an essentially hopeless task. There do, however, exist certain limiting cases which are both analytically tractable and experimentally attainable. In these instances we can turn the complications of the problem to good usage by extracting information about the magnetic material from the very multiplicity of the precession phenomenon.

The limiting case which we will discuss here is that of the long wavelength precessional disturbance of "small" samples. By a long wavelength disturbance we mean one for which $\nabla^2 M$ is small: specifically we wish $H_{ex}l^2k^2 \ll H_0$, where H_{ex} is the equivalent exchange field, l is the magnetic lattice constant, and k is the propagation number of the disturbance. If the inequality above is satisfied, the torques arising from exchange energies will be negligible compared to those arising from dipolar and applied external magnetic fields. By a small sample we mean one whose maximum dimension is considerably less than a free space wavelength of electromagnetic radiation at the frequency involved. If this condition is met one can ignore propagation effects and use static potentials to derive the electromagnetic fields. Hence the name magnetostatic modes for these disturbances.

The calculation of the magnetostatic modes of an insulating spheroid was first successfully undertaken by L. R. Walker.[1] We will lean heavily on his results, but not present his calculations in any detail. The reader is referred to the original article for this information. For present purposes it is sufficient to note that the calculation consists of the simultaneous solution of the gyromagnetic or torque equation,

$$dM/\gamma dt = M \times H, \tag{1}$$

and of Maxwell's equations (static case) subject to the appropriate boundary conditions. A solution is found in which all the spins of the sample precess in the same phase and amplitude (the uniform precession) with the resonance condition,

$$\omega = \gamma[H-(N_z-N_t)M], \tag{2}$$

in agreement with Kittel's[2] expression derived when only a uniform mode was contemplated. N_z and N_t are the classical demagnetization factors of the ellipsoid in the direction of the applied static field (N_z) and transverse to the applied field (N_t). Additional solutions are also found corresponding to spatially nonuniform distributions of transverse magnetization. The resonant

[1] L. R. Walker, Phys. Rev. **105**, 390 (1957); J. Appl. Phys. **29**, 318 (1958).
[2] C. Kittel, Phys. Rev. **73**, 155 (1948).

fields for the various modes are spread, at fixed frequency, over a range of magnetic field equal to $2\pi M$, or half the saturation magnetization of the sample.

In addition to magnetic field for resonance each absorption can also be characterized by a line width. The line widths which have been observed in actual experiments range from a fraction of a gauss to thousands of gauss, depending primarily upon the material under observation, but there are also variations with temperature and frequency and from magnetostatic mode to magnetostatic mode for any one sample. Formally a line width can be introduced into the resonance expressions by the insertion of a phenomenological loss term into the gyromagnetic equation (1). Such an approach does not lead to a physical understanding of the loss processes involved, and, in fact, the common forms of the phenomenological loss terms do not lead to correct predictions concerning the variation of line width with mode. We will return later to the subject of line widths and their origin considered from a more fundamental point of view.

For a number of reasons, both experimental and theoretical, spherical samples have been most commonly used in ferrimagnetic resonance experiments. We will need, subsequently in this article, to call in some detail upon our knowledge of the magnetostatic modes of a sphere. Hence we pause here to delineate the characteristics of these solutions.

MAGNETOSTATIC MODES OF A SPHERE

What one requires of a theory of magnetostatic modes is predictions concerning magnetic fields for resonance of the various modes and concerning the spatial distribution of the rf magnetization and magnetic field for each mode. Walker's original paper contains this information implicitly for all modes and explicitly for a few low-order modes. Subsequently Fletcher, Solt, and Bell[3,4] have derived explicit expressions for the quantities of interest for a sizeable number of modes of the sphere, and checked the theory in detail against the experimental results. Many of their conclusions are very pertinent to the measurement of physical properties from the magnetostatic modes. We present these results in outline here and in more detail later as they become pertinent to the measurement at hand.

Each magnetostatic mode is most conveniently identified by a three-digit index: *nmr*. The first two digits are the indices of a spherical harmonic P_n^m associated with the magnetic potential; the third index distinguishes between roots of a secular equation from which the magnetic field for resonance of each mode must be obtained. Figure 1 gives in graphical form the resonant magnetic fields for all the modes of $n \leqslant 5$. Figure 1 also contains two nearly vertical traversal lines indicating how the

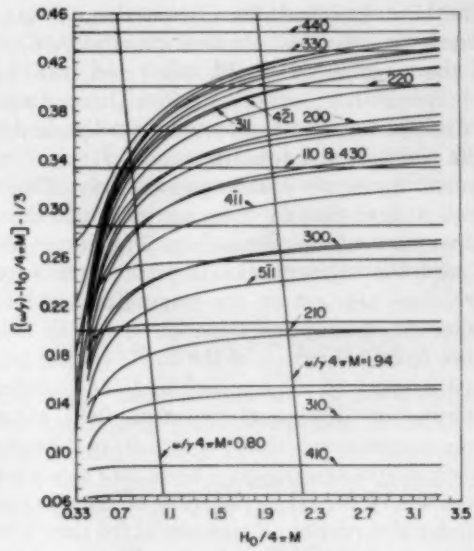

FIG. 1. Plot of $H_0/4\pi M$ versus $[(\omega/\gamma)-H_0]/4\pi M+\frac{1}{3}$ for ferrimagnetic sphere.

mode pattern is traversed as H is varied in a typical magnetic resonance experiment. One traversal line is drawn for $\omega/\gamma 4\pi M = 1.94$, corresponding, for instance, to an X-band experiment on Yttrium Iron Garnet (YIG). A second traversal line is drawn for $\omega/\gamma 4\pi M = 0.80$, corresponding to an X-band experiment on MnZn ferrite or an S-band experiment on YIG.

The resonant fields are seen to be dependent in general on the frequency, ω; the gyromagnetic ratio, γ; and the saturation magnetization of the sample, $4\pi M$. The uniform precession, the 110 mode, appears as a horizontal line at an ordinate value of 0.333. This and the 430 mode are the only resonances whose position in field, at fixed frequency, are not a function of saturation magnetization. All other modes will vary in their spacing and absolute position as $4\pi M$ is changed, as it can be, for instance, by varying the temperature of the sample. There exist many instances where modes will cross one another as the temperature is changed. In the pure magnetostatic case for a perfectly spherical sample these modes will be orthogonal and non-interacting.

The solutions are computed in a small signal approximation, that is, subject to the assumption that the transverse rf magnetization is always small compared to the component of the magnetization which lies along the applied field and is approximately equal to the saturation magnetization of the material. At large signal amplitudes the linearized form of the equations no longer hold and the conditions for resonance will be changed.

MAGNETIC PARAMETERS ACCESSIBLE THROUGH THE MODES

Since the magnetic fields for resonance of the various modes depend on ω, γ, and $4\pi M$, it is obvious that from resonance experiments at some known frequency γ and

[3] P. C. Fletcher and R. O. Bell, J. Appl. Phys. **30**, 687 (1959).
[4] P. C. Fletcher, I. H. Solt, Jr., and R. O. Bell, Phys. Rev. **114**, 739 (1959).

$4\pi M$ can be determined. Were these the only physical parameters measurable through ferrimagnetic resonance, the phenomena would still be of considerable interest; fortunately, still other information on material properties and magnetic interactions can also be derived from the resonant absorptions.

Magnetic materials usually possess crystalline magnetic anisotropy; that is, there are easy and there are hard directions of magnetization. The same torques which cause the magnetization to prefer certain crystalline directions also act on the magnetization during a precession experiment and cause the magnetic field for resonance to be a function of the single crystal orientation with respect to the applied field. The analysis of this orientation dependent resonant field excursion yields the magnetic anisotropy constants of the material.

The line widths observed in a resonance measurement are a measure of the relaxation time of the precessional mode under observation; a measure of the time it would take this precession to die out if its driving fields were removed. These decay times are often very short, e.g., 10^{-8} sec, preventing direct observation of the decay, and forcing us to rely on line widths for our information. The processes by which this decay occurs are incompletely understood. Though the mechanism is known for some materials, it is not known in any detail or with any degree of certainty for may others. The decay in many cases is believed to occur in two stages, the first of which is the breaking up of the long wavelength precession into disturbances of very much shorter wavelength, known as spin waves. The spectrum of the spin waves is quite different from that of the magnetostatic modes since exchange effects play a dominant role in determining their frequencies. The spin waves are very difficult to observe directly, so the magnetostatic modes, through their relaxation interaction with the spin waves, constitute a valuable set of windows into the spin wave spectrum.

The magnetostatic modes act as probes of the spin wave spectrum in a second way; through their saturation behavior at high rf powers. This saturation occurs at rf power levels much less than one would expect if only a failure in the linearized form of the gyromagnetic equation were involved. The saturation results from the coupling of energy from the magnetostatic mode into certain spin waves which can be caused to "run away" when the energy input exceeds the natural losses of the spin wave involved. Information on the relaxation processes of the spin waves can therefore also be obtained through the magnetostatic modes.

Before passing on to a detailed discussion of the above areas we should like to point out that the magnetostatic modes are ideally suited for observing transient or periodic fluctuations in material properties. Variations in any parameter significantly affecting the resonance field of a mode can be detected so long as they occur more slowly than the relaxation rate of that mode. This is not a severe limitation. Relaxation times are typically in the range of 10^{-6} to 10^{-8} seconds, and the transient variations in M or the crystalline anisotropy of as short a duration as a few microseconds can be readily observed.

MEASUREMENT OF γ, $4\pi M$, AND MAGNETIC ANISOTROPY CONSTANTS

The determination of the gyromagnetic ratio γ, the saturation magnetization $4\pi M$, and the magnetic anisotropy constants from the raw data on resonance fields proceeds as follows: The resonance fields are measured for the various modes in several crystal directions. From the variation of resonance field with crystal orientation magnetic anisotropy constants are obtained, and the magnetic anisotropy shifts subtracted out to give undisplaced resonance fields. Corrections for propagation effects are now made to these resonance fields. The resulting absorption spectrum can be compared to the theoretical magnetostatic mode solutions and the parameters γ and $4\pi M$ determined.

The procedure described in the foregoing assumes that the maximum obtainable accuracy in measuring the various parameters is sought. If only approximate values are required the smaller corrections can be omitted. Let us discuss now the accuracy obtainable in the material property determinations and the factors limiting this accuracy.

The parameters we are now discussing are all inferred from the measurement of the magnetic field corresponding to the maximum of a resonant absorption, and the accuracy of the parameters deduced is limited ultimately by the precision with which this maximum can be located. This precision is, in turn, limited primarily by the line width of the absorption involved. The center of a 1 gauss wide absorption can obviously be located with greater absolute precision then the center of a 500 gauss wide line. A fair rule of thumb is that the maximum can be located to a precision approximately 1/20 the line width. For a YIG sphere of less than a gauss line width the measurement of the resonant field at X-band (around 3500 gauss) will be accomplished with a precision of roughly one part in 10^5.

The accuracy of the parameters deduced from the data is reduced below the ultimate accuracy implied by the precision of setting by two kinds of effects; (1) fluctuation in experimental parameters such as frequency or temperature which introduce random errors into the data (2) systematic deviations of the experimental situation from the idealized case treated by the theory with resultant systematic errors introduced into the interpretation of the data.

The first type difficulty is by far the simpler to bring under control. In an experiment in which the resonant field at fixed frequency is measured for several modes the frequency must be held "fixed" with a stability exceeding γ times the precision of field setting if frequency fluctuations are not to degrade the measurement. For a narrow line material like YIG this requires a frequency stability of roughly $\gamma \times$ (0.1 gauss), or 250

kc. At the microwave frequencies commonly used for spectroscopy this can readily be obtained. For wider line materials the requirement on frequency stability is even less stringent. Temperature fluctuations of the sample will change some of the material constants influencing the line position, such as $4\pi M$, and perturb the setting accuracy. The saturation magnetization of YIG is changing at the rare of about 3 gauss/°C at room temperature; that of MnZn ferrite at about twice the above rate. To hold fluctuations in absorption position to within the precision of setting requires temperature control to between 0.1 and 0.01 C°. This also is attainable with a moderate amount of care and instrumentation. One must in particular avoid the sample becoming heated significantly by the rf energy it absorbs during the magnetic resonance. It should also be pointed out that one seldom wishes to realize the full accuracy of one part in 10^4 or 10^5 in determining, say, $4\pi M$. For most purposes a great deal less accuracy is required and very nominal precautions on frequency and temperature stability are more than adequate. At very low temperatures, where a very accurate measurement of $4\pi M$ is of considerable physical interest, the experimental difficulty is alleviated by the reduced temperature variation coefficients of most physical parameters.

The systematic deviations of the experimental situation from the theoretical are a far more serious difficulty. The sources of systematic errors we will discuss are sample shape perturbations, the effects of propagation (ignored in the magnetostatic theory), and errors in the interpretation of the influence of magnetic anisotropy on the resonances.

The magnetic sample should ideally be a perfect (and smooth) sphere. The spherical samples used in resonance work are most often shaped by tumbling in an abrasive chamber. Though this method produces very nearly spherical samples, Dillon[5] has shown that there is also differential abrading in the various crystalline directions due to anisotropy in crystal hardness. The sample therefore develops systematic deviations from sphericity which shift the resonance field as a function of crystal orientation in a manner not readily separable from magnetic anisotropy shifts. Truly spherical samples can be produced, as Dillon pointed out, by a grinding and polishing technique utilizing counter-rotating tubes of small diameter. At present, this technique is convenient only for spheres greater than 0.5 mm in diameter, so one is constrained to use a sphere for which propagation effects are significant if one wishes to avoid asphericity problems.

Propagation effects appear in two forms. One is a systematic shift of all modes toward higher resonance fields. The second is a lifting of the orthogonality of the magnetostatic modes, which results in a scrambling of normal coordinates when two coupling modes have the same resonance field. The coordinate scrambling manifests itself experimentally as anomalous intensity and line position behavior near mode degeneracy points. Let us first consider the shifts of mode position due to propagation.

It has long been known that there were "size effects" in ferrimagnetic resonance[6] and that the field for resonance of the uniform precession was dependent on the diameter of the sphere used. The amount of field shift resulting from propagation effects has been calculated by Hurd[7] and by Mercereau[8] for the uniform precession and can be written

$$\Delta H = 4\pi M(2/9)[1+(\epsilon/5)](kR_0)^2, \tag{3}$$

where ϵ is the dielectric constant of the material, k is the free space propagation number ω/c, and R_0 is the (spherical) sample radius. The shift has not been calculated for the higher order modes but appears experimentally to be of the same form:

$$\Delta H_{nmr} = C_{nmr} \cdot 4\pi M(kR_0)^2. \tag{4}$$

Some data on this effect is given in Fig. 2. It can be seen that the C_{nmr} tend to diminish with increasing n; the uniform mode is the most seriously perturbed by propagation effects. On putting some typical numbers into (3) we find that the uniform mode of a YIG sphere 1 mm in diameter is shifted roughly 20 gauss in a room temperature X-band experiment. This systematic shift is well over a hundred times larger than the precision of measurement of the resonance field. For a MnZn ferrite sphere of the same radius the field shift will be 50 gauss, a truly significant perturbation of the resonance absorption spectrum, and one large enough to cause misidentification of other modes if the importance of the propagation shift is not appreciated.

The second effect of propagation is to remove the orthogonality of the magnetostatic modes in some cases.

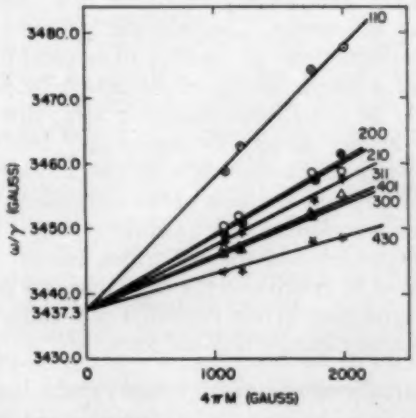

FIG. 2. ω/γ versus $4\pi M$ for a few of the magnetostatic modes. The data are for a 1.3 mm diam YIG sphere at 9688 Mc/sec. The dependence of ω/γ on $4\pi M$ is due to propagation effects.

[5] J. F. Dillon, Jr., Phys. Rev. **112**, 59 (1958).

[6] J. O. Artman, J. Appl. Phys. **28**, 92 (1957).

[7] R. A. Hurd, Can. J. Phys. **36**, 1072 (1958).

[8] J. E. Mercereau, J. Appl. Phys. **30**, 184S (1959).

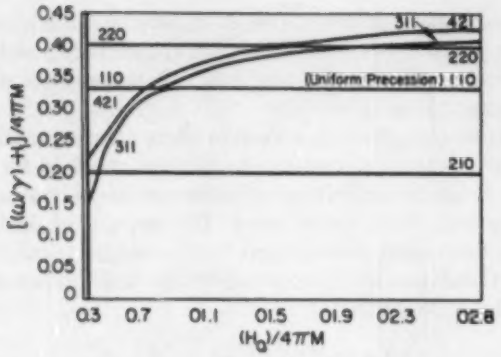

FIG. 3. Simplified magnetostatic mode diagram showing propagation-induced mode couplings.

For instance the uniform precession is no longer truly uniform but will contain components of magnetic field of proper symmetry to drive some of the higher order modes. If these modes are such that they can become degenerate in field with the uniform mode (their mode lines cross the 110 mode line in Fig. 1) the nonorthogonality will cause a coupling of the two magnetostatic modes and a doubling of the absorption into two resonances whose separation is determined by the strength of the coupling. This phenomenon has been studied by Solt, Fletcher, Mercereau, and White[9] and empirical selection rules for the coupling, supported by quasi-theoretical arguments, established. The selection rule derived is that propagation will couple modes for which $\Delta n=2, 4, 6, \cdots 2p$, $\Delta m=0$, $\Delta r=0, 1, 2, \cdots$. A mode diagram showing the effect of coupling is shown in Fig. 3. The 311–110 and 220–421 interaction are shown as well as some non-interacting cross-overs like the 421–110 and 311–220. Deviations from sphericity of the sample produce additional mode interactions, for instance, a 110–3$\bar{1}$1 interaction.

The shift of the resonances by magnetic anisotropy is fortunately quite readily calculable in a wide class of materials of interest. The principal requirement for a simple analytic form of the shift to be valid is that the direction of magnetization of the sample be dominated primarily by the applied magnetic field; that the anisotropy energy density be appreciably less than the $M\cdot H$ energy of interaction with the applied H. This condition prevails for most of the ferrospinels and garnets over a considerable temperature range. The form of the dependence of the anisotropy energy upon the direction of M relative to the crystal axes is prescribed by the symmetry of the crystal. For a cubic material the anisotropy energy is of the form

$$E=K_1(\alpha_1^2\alpha_2^2+\alpha_2^2\alpha_3^2+\alpha_3^2\alpha_1^2)+K_2\alpha_1^2\alpha_2^2\alpha_3^2 +\text{higher order terms}, \quad (5)$$

where α_1, α_2, α_3 are the direction cosines of the magnetization with respect to the crystal ⟨100⟩ directions and K_1 and K_2 are the first and second anisotropy constants. The torques on the magnetization due to magnetic anisotropy are obtained by taking derivatives of the energy with respect to the appropriate angular displacements of the magnetization. These torques are added into the gyromagnetic equation (1), often in the form of "effective demagnetizing factors." The magnetostatic mode problem now becomes very difficult to solve rigorously, except for the uniform mode. Fortunately the shift can be shown for many cases of interest to be essentially the same for all modes. A subsequent paper in this same session, that by Solt and Fletcher.[10] examines carefully the problem of variation from mode to mode of the resonant field excursion, and the extraction of accurate anisotropy constants from the data. The anisotropy excursion for all modes turns out to be the same to order K_1/M and commences to differ when $(K_1/M)^2/(\omega/\gamma)$ becomes appreciable.

The magnetic anisotropy constants are extracted from data obtained by measuring the resonance fields in several major directions. The anisotropy constants thus obtained can be used to calculate the field shifts for the magnetic field in any orientation with respect to the crystal axes, and a set of "undisplaced" line positions obtained from the data.

The systematic deviation of the sample from sphericity as a result of anisotropic grinding of the single crystal in the tumbling process can produce substantial errors in K_1 and K_2. The shape anisotropy adds to the intrinsic magnetic anisotropy to produce additional resonance field excursion of essentially the same analytic form. Shape anisotropy can often be detected from the fact that it affects the various modes very differently, and produces large differences in apparent magnetic anisotropy among the modes. Errors of some 10% can be introduced into K_1 by shape anisotropy, of even more for K_2. This source of error can be essentially eliminated using the Dillon two-pipe grinding technique (and the larger spheres it implies).

We are now ready to obtain the saturation magnetization and the gyromagnetic ratio from the modes. A best fit of several absorptions, corrected for propagation, to the two parametes $4\pi M$ and γ yields these parameters to maximum accuracy. Actually $4\pi M$ can usually be obtained fairly accurately from the raw data because the mode spacings for many modes is a particularly simple function of the magnetization. Figure 3 shows an idealized absorption pattern and indicates that the spacings between three of the most accessible and simplest modes, the 220, 210, and 110, are linear in M. Reference to Fig. 2 shows that the propagation shift for the 110 mode is significantly larger than for the $2mr$ modes, but that the 210 and 200 modes have nearly the same propagation shift. The 220 mode, not shown in Fig. 2, also has very nearly

[9] I. H. Solt, Jr., R. L. White, and J. E. Mercereau, J. Appl. Phys. **29**, 324 (1958); P. C. Fletcher and I. H. Solt, Jr., J. Appl. Phys. **30**, 181S (1959).

[10] I. H. Solt, Jr. and P. C. Fletcher, J. Appl. Phys. **31**, 100S (1960).

the same propagation shift as the 210 and 200 modes, so $4\pi M$ can be obtained to fairly high accuracy by simply measuring the 210–220 mode interval. If accuracy approaching the precision of setting is required, propagation shift differences can be corrected by measuring the C_{nmr} coefficients involved, and differences in the anisotropy shifts of the two lines can be computed using the theory of Solt and Fletcher.[10]

The uniform mode alone is often used to measure the gyromagnetic ratio, since the resonance field for a sphere is given, in the magnetostatic limit, by $\omega=\gamma H$ for this mode. The result at X-band on g-factor measurements as a function of temperature for MnZn ferrite spheres of various radii using only the uniform mode are given in Fig. 5, which illustrates some of the hazards of this procedure. The g-factor is related to the gyromagnetic ratio by $g=(2\,mc/e)\gamma$. Since small deviations of g from the free spin value of 2.002 are of physical interest it is desirable to know this quantity with a high degree of accuracy. Figure 5 shows the systematic shift of the apparent g-factor of the uniform mode caused by propagation effects as the sphere radius is increased. Figure 5 also shows the anomalies in g-factor which occur when a propagation-coupled mode crosses the uniform mode. The anomaly near room temperature is caused by the crossing of the 311 mode; the anomaly at $-25°$ by the crossing of the 512 mode. One is forced to the conclusion that if only the 110 mode is to be used the measurement should be performed on very small spheres, and indeed the reliable measurements of g-factors in the literature have been measured on such small spheres.

It is often desirable to measure g, $4\pi M$, K_1, and K_2 on the same sample which is being used for line width measurements, or to compare these material properties with one another as a function of temperature or frequency using the same sample. Shape anisotropy problems may then force one to use a moderately large sphere, and the perturbations of the spectrum by propagation effects must be explicitly considered. In this case reference to the higher order modes is invaluable.

To summarize this fairly lengthy section, our knowledge of the anatomy of the magnetostatic modes allows us to obtain material constants from the resonance spectrum with an accuracy limited primarily by the precision of setting on the resonance maxima. If conclusions of lesser accuracy are satisfactory, the constants can be obtained from the data with fairly simple calculations. The saturation magnetization can be measured to roughly 1%, the g-factor to about 0.1% and the first anisotropy constant K_1 to about 1% with relative ease for many materials using the magnetostatic modes and a simple first order interpretation.

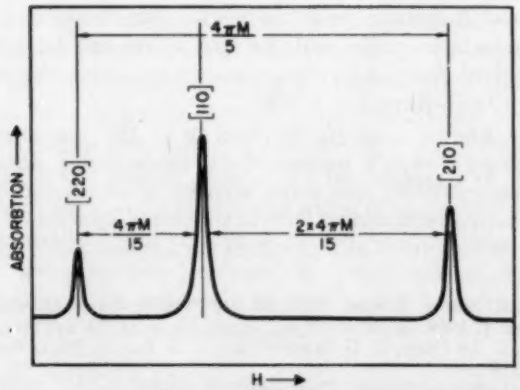

FIG. 4. Idealized magnetic absorption pattern of sphere showing certain lower order mode spacings.

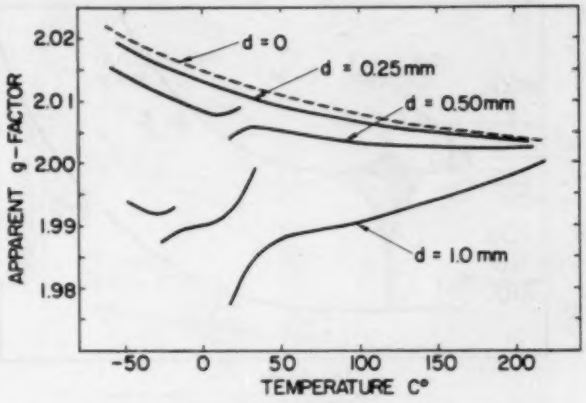

FIG. 5. Idealized plot of apparent g-factor versus temperature as deduced from uniform precession of MnZn ferrite spheres of various diameters.

MAGNETIC RELAXATION TIMES

Despite recent major strides forward in the understanding of magnetic relaxation times and resonance line widths, it is a safe statement that some of the most perplexing problems in magnetism still lie in this area. In this section we shall see how the magnetostatic modes can be used as an investigative tool to help identify the relaxation processes active in specific materials and under specific circumstances.

The relaxation processes occurring in a microwave resonance can be divided into two major categories: (1) those in which rece. .onal energy is communicated directly to the lattice (2) those in which the long wavelength precession is first scattered into shorter wavelength disturbances[11] (spin waves), with the spin waves subsequently coupling the magnetic energy to the lattice. In the language of the trade, the first process is one for which a magnon of precessional energy is destroyed and a phonon of lattice energy is created directly, with no change in state of the other magnetic modes; the second process is one in which a magnon of a long wavelength precessional mode ($k\approx 0$) is first scattered into one or more magnons of $k\gg 0$, which are subsequently converted into phonons of lattice energy.

For certain materials, for instance the rare earth garnets above 50°K, the direct communication of energy

[11] Clogston, Suhl, Walker, and Anderson, J. Phys. Chem. Solids 1, 129 (1956).

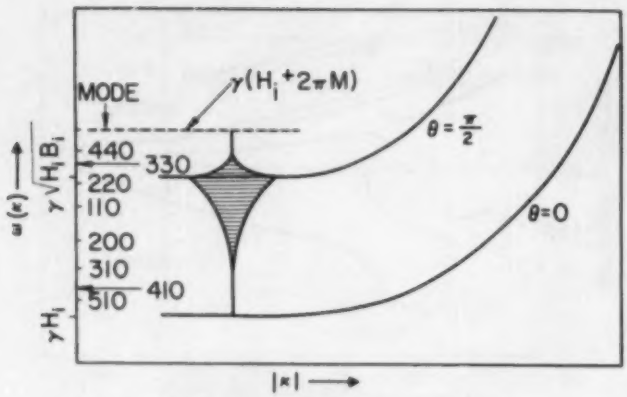

FIG. 6. Spin-wave spectrum of sphere, showing also magnetostatic modes.

to the lattice without benefit of intermediary spin waves is almost certainly the dominant loss mechanism, as discussed by C. Kittel in the opening session of this conference[12] and elsewhere.[13] For other materials, for instance the ferrites, the dominant loss processes are not clearly established. In these ambiguous cases, some light can be shed on the subject by observation of line widths of some of the modes as a function of temperature or frequency, or by measurement of the line widths for several modes at the same temperature.

Just how such observations can be useful can be clarified by reference to Fig. 6. We see here the envelope of the spin-wave spectrum as derived by Clogston, Suhl, Anderson, and Walker[11] and an indication in the region $k \rightarrow 0$ of the relative positions of the magnetostatic modes on the same ordinate. The magnetostatic modes extend from γH_i to $\gamma(H_i+2\pi M)$, while the spin-wave limits as $k \rightarrow 0$ confine the spin waves of modest k between γH_i and $\gamma(H_iB_i)^{\frac{1}{2}}$. The shaded area is intended to indicate the density of spin-wave states, which is greatest just below the upper spin-wave limit and tapers to zero at the lower spin-wave limit. The pertinent point for present purposes is that there exist magnetostatic modes above the upper spin-wave limit, for which no energy conserving scattering into spin waves of modest k can occur. Further, the spin-wave upper limit is shifted relative to the magnetostatic modes by changing M, i.e., changing the temperature. Hence we can, by changing temperature, cause a magnetostatic mode to move from inside the spin-wave manifold to outside the spin-wave manifold. If scattering to spin waves is an important relaxation process, the density of terminal states available must strongly influence the line width. If, further, it is the spin waves of modest k which are involved in the scattering, the available terminal states will be maximum just inside the spin-wave manifold and sharply decreased just outside the spin-wave manifold. Experiments have been done, notably by Buffler,[14] in which a given mode is passed through the spin-wave limit, with the results indicated in Fig. 7. The data indicate clearly that for polycrystalline samples the scattering from micro-crystal grain boundaries to spin waves of comparable wavelength is indeed an important relaxation process, whereas there is little comparable scattering of this nature in the polished single crystal of the same material.

Whence, then, the line width of the single crystal? Either from relaxation processes not involving the spin-wave spectrum or from scattering processes which favor high k spin waves, where the spin-wave spectrum (cf. Fig. 6) has again curved upward to provide terminal stages degenerate with the driven precession. Probably both kinds of relaxation are active with relative importance determined by the sample at hand. That the second process, scattering to short k spin waves, is important is demonstrated by the dependence of single crystal line width upon degree of surface polish of the spherical sample.[15] Still further evidence for such a scattering process is the data on line width as a function of mode[16] at fixed temperature for MnZn ferrite and YIG spheres. The line widths show no maximum inside the spin wave limit, indeed show a pronounced minimum in this region but do show an increase as one moves to an increased density of high k terminal states.

The interpretation of the line width data cited above is still tentative, and is used as an illustration of the manner in which the magnetostatic modes can be used to help parse and clarify a difficult problem. Hopefully further and more definitive experiments will be devised in which the various magnetostatic modes, acting as so many windows into the spin-wave spectrum, can be used to pin down specific relaxation processes.

rf POWER SATURATION EFFECTS

In the previous section we have seen how a fairly well-known characteristic of the spin waves, their frequency dispersion, can be used to draw inferences concerning the nature of certain energy scattering processes important in magnetic relaxation. In this section we will see how a known coupling mechanism between the magnetostatic modes and the spin waves can be used to yield information on a lesser known spin-wave characteristic, spin-wave line width.

The known coupling mechanism is the non-linear coupling between a magnetostatic mode and a simultaneously existing spin wave, a coupling introduced by the essentially nonlinear form of the equations of motion which is important at high signal amplitudes. Suhl[17] has

[12] C. Kittel, J. Appl. Phys. **31**, 11S (1960).
[13] C. Kittel, Phys. Rev. **115**, 1587 (1959). P. G. de Gennes, C. Kittel, and A. M. Portis, Phys. Rev. **116**, 323 (1959).
[14] C. R. Buffler, J. Appl. Phys. **30**, 172S (1959); thesis, Harvard University, 1959 (unpublished); J. Appl. Phys. **31**, 222S (1960).
[15] R. C. Le Craw, E. G. Spencer, and C. S. Porter, Phys. Rev. **110**, 1311 (1958).
[16] R. L. White, J. Appl. Phys. **30**, 182S (1959).
[17] H. Suhl, Proc. Inst. Radio Engrs. **44**, 1270 (1956); J. Phys. Chem. Solids **1**, 209 (1957).

shown how this non-linear coupling can feed energy from a driven uniform precession into certain spin waves, and how in fact this energy fed to the spin wave can exceed the spin wave's natural losses, whereupon the spin wave commences to grow exponentially and the uniform precession commences to show saturation. We will not develop here Suhl's theory of the saturation threshold but will only quote here some of his results to show the nature of the information obtainable. A particularly illustrative result is Suhl's expression for the critical value of rf magnetic field, h_{crit}, required to produce unstable spin waves of the same frequency,

$$h_{crit}=\Delta H[\Delta H_k/4\pi M]^{\frac{1}{2}}, \qquad (6)$$

where ΔH is the line width of the uniform precession (directly observable) and ΔH_k is the line width of the unstable (z directed) spin wave. Equation (6) is not the most general expression, but suffices to illustrate that by measurement of h_{crit} and ΔH, certain information otherwise inaccessible to direct observation, namely, ΔH_k, can be obtained. Other expressions parallel to expression (6) but representing different experimental situations can be derived to specify ΔH_k for other spin waves, notably those of frequency $\omega/2$, and give further information on spin-wave intrinsic loss parameters. The spin-wave line widths ΔH_k appear to be independent of sample surface treatment[18] and constitute a material parameter probably more fundamental than the line widths of the uniform mode. A generous fraction of current activity in ferrimagnetic resonance is directed toward rf power saturation effects and the characteristics of the excited spin waves.

Calculations have also been made for the rf power saturation threshold of magnetostatic modes other than the uniform.[19] Experimental results indicate that unstable spin waves are generated as soon as the point of maximum precessional amplitude of these nonuniform distributions exceeds the amplitude at which a uniform precession would have saturated. Some information concerning the way spin waves are propagated away from the hot spots where they are being generated may be obtained from the rf saturation curves of these nonuniform precessions above the saturation threshold.

The coupling between long-wavelength precessions and the spin waves can also be used in principle to generate spin waves of large amplitude at one point for detection and examination elsewhere. For instance, high rf power driving one end of a ferrimagnetic rod will produce spin waves at this end which it might be possible to detect at the far end of the rod, yielding information on spin-wave propagation characteristics. Such experiments are indeed under way, as will be described more fully in the next section.

[18] R. C. LeCraw and E. G. Spencer, J. Appl. Phys. **30**, 185S (1959).
[19] P. C. Fletcher (private communication).

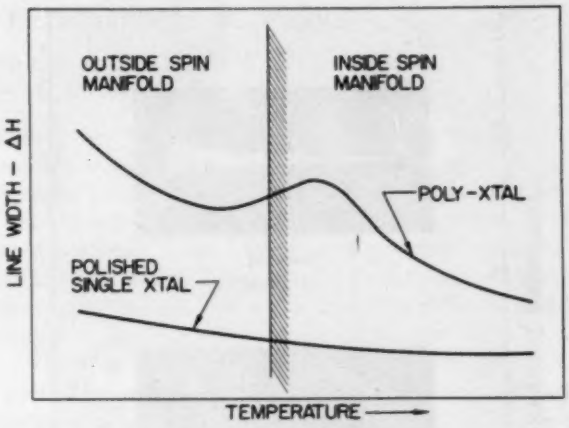

FIG. 7. Resonance line width as a function of temperature for a magnetostatic mode crossing the spin-wave limit (after Buffler).

THE OBSERVATION OF TRANSIENT MAGNETIC PHENOMENA

We now pass on to an as yet little exploited use of the magnetostatic modes; the detection of transient magnetic phenomena, such as the passage of spin-wave packets or acoustic disturbances.

Consider the following experiment. A long ferrite rod is passed through a waveguide, and the waveguide and rod are placed in a magnetic field of such magnitude that one is operating half-way up the side of the absorption due to some magnetostatic mode of the rod. Now we imagine a spin-wave packet generated at one end of the rod and propagating along the rod. This spin-wave packet comprises a local hot spot in the spin system, with a locally reduced saturation magnetization. As this hot spot propagates through the part of the rod in the waveguide the change in M will cause a shift of the magnetostatic mode and a change in the absorption by the rod of the microwaves coming down the waveguide. If the packet is long lived and bounces back and forth in the rod we

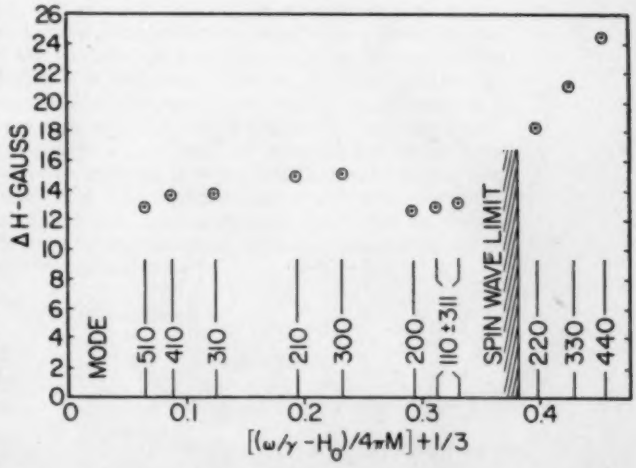

FIG. 8. Resonance line width as a function of magnetostatic mode for a MnZn ferrite sphere at 9600 Mc.

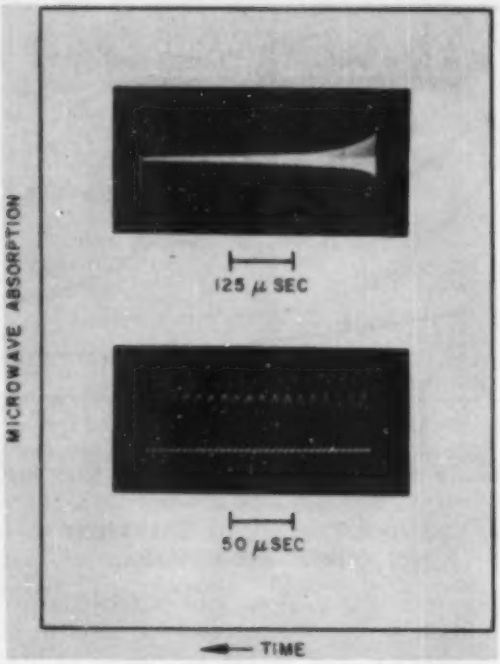

FIG. 9. Oscilloscope trace showing variation in magnetic absorption of ferrite rod caused by presence of acoustic disturbance. Decay of the acoustic wave can be seen.

will get a dip (or increase, depending on which way the mode moves with decreasing M) in transmitted power each time the spin-wave packet passes.

Or let us consider a different kind of transient. Suppose we subject the end of the rod to an acoustic shock. As the acoustic disturbance propagates it will produce, through magnetostriction, a local change in the magnetic anisotropy. As the acoustic pulse passes through the waveguide the magnetostatic mode will again shift and produce a fluctuation in transmitted power. Figure 9 shows photographs of an oscilloscope trace displaying the results of just such an experiment. The decay of the acoustic pulse as it bounces back and forth in the rod can be seen, and the acoustic Q of the rod measured. In this experiment the rod was rather short, so the successive pulses give an almost sinusoidal variation of the absorption. The indicated time scale shows that rather rapid transients can indeed be observed by such a technique.

To the best of the author's knowledge no use is being made of the magnetostatic modes to monitor transient changes in magnetic parameters other than the experiments described above, which are being done by P. C. Fletcher, and the experiments of M. T. Weiss[20] on long relaxation times for certain classes of spin waves. It seems likely that greater use of this potential is inevitable in the near future.

ACKNOWLEDGMENTS

The material reviewed here has been drawn from the integrated output of many laboratories. The references cited have, on the other hand, been representative rather than comprehensive, and where similar work has been carried on in several laboratories the author has tended to refer to the work most familiar to him. No editorializing as to quality or significance was intended. In view of these circumstances perhaps the most appropriate acknowledgement for this paper is to the scores of workers not explicitly referenced whose investigations form the body of fact and interpretation upon which this review is based.

[20] M. T. Weiss (private communication).

Electron Spin Relaxation in Ferromagnetic Insulators

R. C. LeCraw, R. C. Fletcher, and E. G. Spencer
Bell Telephone Laboratories, Incorporated, Murray Hill, New Jersey

A REVIEW is presented[1] of the various approaches in the literature to describe electron spin relaxation in ferromagnetic insulators. Emphasis is placed on recent developments involving scattering into spin waves due to inhomogeneities in the magnetization,[2,3] particularly as it pertains to relaxation in narrow line width materials.

A new treatment of ferromagnetic relaxation is described[1] together with experimental data which demonstrate the adequacy of the approach. The equation of motion of the magnetization involves T_{10}, the relaxation time of the uniform precession to the lattice; T_{2k}, the relaxation time of the uniform precession to the kth spin wave; and T_{1k}, the relaxation time of the kth spin wave to the lattice. For the special case $T_{10}=T_{1k}$, the equation of motion is shown to reduce to the Bloch equation.

Measurements have been made at 6200 Mc/sec on a single crystal sphere of yttrium iron garnet (YIG) with the above relaxation times determined as a function of controlled amounts of scattering into spin waves, obtained by varying the surface roughness. The same sample is used throughout, with only the surface being varied. To make the measurements at rf power levels below the first evidence of saturation effects required the development of a nonpulsed frequency modulation method, in place of the usual pulsed decay scheme for measuring spin-lattice relaxation times. The principal features of this new technique are discussed.[1]

The theory provides an excellent fit to the experimental data. The theory, together with the modulation technique, permits the bulk property, T_{1k}, to be determined experimentally in the presence of large surface scattering (unpolished spheres with $\Delta H=3.56$ oe). The other bulk property, T_{10}, is obtained by applying the theory to data for the smoothest surface ($\Delta H=0.47$ oe). The relevance of these bulk properties for studying fundamental relaxation mechanisms is discussed.[1] In particular, with respect to the high-purity YIG samples now available,[4] it is believed that T_{10} and T_{1k} are of considerably more theoretical value than ΔH, because of the strong dependence of the latter on both volume and surface inhomogeneities.

[1] R. C. Fletcher, R. C. LeCraw, and E. G. Spencer, Phys. Rev. **117**, 955 (1960).
[2] A. M. Clogston, H. Suhl, L. R. Walker, and P. W. Anderson, J. Phys. Chem. Solids **1**, 129 (1956).
[3] R. C. LeCraw, E. G. Spencer, and C. S. Porter, Phys. Rev. **110**, 1311 (1958).
[4] E. G. Spencer, R. C. LeCraw, and A. M. Clogston, Phys. Rev. Letters **3**, 32 (1959).

Survey of Ferromagnetic Resonance in Small Ferrimagnetic Ellipsoids*

Frederic R. Morgenthaler
Department of Electrical Engineering, Research Laboratory of Electronics, Massachusetts Institute of Technology, Cambridge, Massachusetts

This paper discusses the response of the magnetization in a small ferrimagnetic ellipsoid, magnetized in an arbitrary direction and excited by spatially uniform microwave magnetic fields, when a typical spin wave is present. The generalized Kittel frequency is given, and possible frequency generation processes appropriate to the ellipsoidal geometry are treated. If the ellipsoid is magnetized at an angle to a principal axis, time-varying components of demagnetizing field at the fundamental frequency occur in the longitudinal direction, as well as transverse components varying at this frequency. Previous analyses have not included such a possibility and certain interesting solutions have, therefore, been missed. In particular, it is found that subharmonics as well as harmonics may be created when the driving field exceeds a certain threshold power. The particular case of the half-frequency resonance is considered and the conditions for the minimum threshold are given. The generalized Suhl spin-wave spectrum is found, together with the coupling relations between the uniform precession and the spin wave. The Suhl first and second order instability thresholds, for the general ellipsoid, are formulated, and a zero order coupling is established for certain transient states of the magnetization. In addition, direct parametric coupling between a longitudinal pumping field and both the uniform precession and the spin waves is discussed.

INTRODUCTION[1-3]

A FERRIMAGNETIC ellipsoid is assumed to have its principal axes along coordinates x, y, and z. Primed coordinates x', y', and z' are defined by the transformation

$$\begin{aligned} x' &= x\sin\beta - y\cos\beta \\ y' &= x\cos\alpha\cos\beta + y\cos\alpha\sin\beta - z\sin\alpha \\ z' &= x\sin\alpha\cos\beta + y\sin\alpha\sin\beta + z\cos\alpha, \end{aligned} \tag{1}$$

* This work was supported in part by the U. S. Army (Signal Corps), the U. S. Air Force (Office of Scientific Research, Air Research and Development Command), and the U. S. Navy (Office of Naval Research).

[1-3] F. R. Morgenthaler, "On the theory of ferromagnetic resonance in small ferrimagnetic ellipsoids": Part I, The uniform precession; Part II, The spin wave spectrum; Part III, The transient magnetization [J. Appl. Phys. (to be published), treat this material in detail].

where α is the angle between $+z'$ and $+z$ and β is the angle between the $+x$ axis and the projection of $+z'$ onto the xy plane. By definition, the z' axis is in the direction of the total internal *dc* magnetizing field, so that in the absence of any excitation the magnetization vector $\mathbf{M}$ of the material is along $+z'$.

Demagnetizing factors N_x, N_y, and N_z (whose sum is unity) for the principal directions, can be calculated from the physical shape of the ellipsoid in the usual manner, and are assumed known.

The externally applied dc magnetic field must, in general, be non-parallel to the magnetization. In fact, the applied field will be of the form,

$$\mathbf{H}=\mathbf{i}'\frac{N_x-N_y}{2}M_{z'}\sin\alpha\sin2\beta+\mathbf{j}'\frac{N_x\cos^2\beta+N_y\sin^2\beta-N_z}{2}M_{z'}\sin2\alpha+\mathbf{k}'H_0, \quad (2)$$

where $\mathbf{i}'$, $\mathbf{j}'$, and $\mathbf{k}'$ are unit vectors in the primed coordinate system, $M_{z'}$ is the dc component of $\mathbf{M}$ along z', and H_0 is any value of magnetic field sufficient to magnetize the sample.

GENERALIZED RESONANCE FREQUENCY

It may be shown that the generalized Kittel frequency for small amplitude excitation is[1] (in mks units)

$$\omega_0^2=\gamma^2\mu_0^2\{[H_0-(Z-X)M]\times[H_0-(Z-Y)M]-W^2M^2\}, \quad (3)$$

where

$$X=N_x\sin^2\beta+N_y\cos^2\beta$$
$$Y=(N_x\cos^2\beta+N_y\sin^2\beta)\cos^2\alpha+N_z\sin^2\alpha$$
$$Z=(N_x\cos^2\beta+N_y\sin^2\beta)\sin^2\alpha+N_z\cos^2\alpha$$
$$W=\frac{N_x-N_y}{2}\cos\alpha\sin2\beta.$$

SUBHARMONIC RESONANCE

If a transverse circularly polarized driving field is present at frequency ω_1 and the sample is magnetically biased to ω, one can show[1] that a resonance is possible provided that $\omega=(\omega_1/1+k)$ $k=0,1,2,\cdots$.[4-5] Feedback is present because the precession cone angle θ, is determined by the strength of the internal z' modulating field, which in turn is proportional to θ. Because of this, the subharmonic resonances exist only above certain thresholds.

For $k=1$ the half-frequency subharmonic is obtained. Calculation shows that above the threshold the cone angle is given approximately by

$$\theta=\frac{h^c}{\Delta H_0}\left[\tfrac{1}{2}\left(1-\frac{h^c}{h}\right)\right]^{\frac{1}{2}} \quad (4)$$

where

$$h^c=\frac{\omega_1\Delta H_0}{(-\gamma\mu_0M)[W^2+(Y-N_z)^2]^{\frac{1}{2}}\tan\alpha} \quad (5)$$

and $2\Delta H_0$ is the resonance line width. It can be shown that the minimum threshold is obtained when the ellipsoid is a thin disk magnetized 45° to the plane, e.g., $N_z=1$, $\alpha=45°$.

SPIN WAVES

The generalized Suhl spin-wave spectrum is[2]

$$\omega_k^2=\gamma^2\mu_0^2(H_0-ZM\cos\theta+\lambda k^2M\cos\theta)\times(H_0-ZM\cos\theta+\lambda k^2M\cos\theta+\sin^2\psi M\cos\theta) \quad (6)$$

if $|\cos\theta|\simeq1$,

where λ is an exchange parameter, ψ the cone angle the spin-wave vector makes with the z' axis, k the spin wave number, and Z the effective demagnetizing factor. When $\theta\approx0$, except for the replacement of Z for N_z, this is identical to the small amplitude Suhl spectrum.[6]

The spin-wave amplitude SM is given approximately by[2]

$$\delta\dot{M}=-\gamma\mu_0\left[\frac{\sin^2\psi}{2}\sin2(\varphi_k-\xi)-\frac{\theta}{2}\sin2\psi\sin(2\varphi_k-\varphi_0-\xi)+\frac{\theta^2}{2}\left(\lambda k^2+\cos^2\psi-\frac{X+Y}{2}\right)\times\sin2(\varphi_k-\varphi_0)-\frac{\Delta H_k}{M}\right]M\delta M. \quad (7)$$

It is apparent by inspection of Eq. (7) that the spin wave loss ΔH_k may be overcome by at least two different mechanisms. The first occurs when $\varphi_k\simeq(\varphi_0/2)\simeq\omega_0t$ and is a first order coupling in θ. The second occurs when $\varphi_k\simeq\varphi_0$ and is a second order coupling. It will be important only when the former mechanism is not possible, that is when the frequency $(\omega_0/2)$ lies below the spin-wave manifold.

It may be shown that the threshold cone angle for the first order process is[2]

$$\theta\simeq\frac{2\Delta H_k/M}{[\{W^2+(Y-N_z)^2\}/\omega_0]^{\frac{1}{2}}\tan\alpha(-\gamma\mu_0M)\sin^2\psi\pm\sin2\psi[J_0(2\delta_k)J_0(\delta_0)-(-\gamma\mu_0M)/2\omega_0\sin^2\psi]}, \quad (8)$$

[4] R. L. Jepsen, "Harmonic generation and frequency mixing in ferromagnetic insulators," Scientific Report No. 15, AFCRC-TN-150, Gordon McKay Laboratory, Harvard University, Cambridge, Massachusetts (1958).
[5] F. R. Morgenthaler, J. Appl. Phys. **30**, 4, 157S (1959).
[6] H. Suhl, Proc. Inst. Radio Engrs. **44**, 1270 (1956).

where the + or − is chosen to minimize θ,

$$\delta_0 \simeq [(X-Y)^2/4+W^2]^{\frac{1}{4}}(-\gamma\mu_0 M/2\omega_0)J_0(2\delta_0),$$

$$\delta_k \simeq (-\gamma\mu_0 M/2\omega_0)\sin^2\psi J_0(2\delta_k),$$

and J_0 is a Bessel function of order zero.

The second-order process threshold angle occurs when $\omega_k=\omega_0$ and has been given by Suhl.[6] It should be noted that the internal modulating fields will add correction terms to this threshold also, but that they will not be very important except at low frequencies and then the first order process will be the important one.

The first term in Eq. (7) could overcome the spin-wave loss very easily if φ_k were constant and of the proper phase. This "zero order" coupling is normally impossible, but it has been shown by the author[3,7,8] as well as by Schaug-Petterson[9] that if, during a transient, the magnetization is completely inverted, i.e., $\theta \simeq \pi$ there will occur a range of spin-wave numbers with cut off frequencies [corresponding to negative values of ω_k^2 from Eq. (6)]. It is apparent that the maximum coupling will occur for $\psi=\pi/2$ and $\varphi_k-\xi=\pi/4$. The latter phase condition is satisfied when $k^2=H_0+(Z-\frac{1}{2}M)/\lambda M$. Then, initially,

$$\delta M=\delta M_0 \exp\left[-\gamma\mu_0\left(\frac{M}{2}-\Delta H_k\right)t\right] \simeq \delta M_0 \exp\left[-\gamma\mu_0\frac{M}{2}t\right] \quad (9)$$

and a very rapid buildup of δM ensues. This should be of considerable importance in determining ferrite switching times for certain geometries.

The quasi-static behavior of the spin-wave spectrum for any θ has been derived by the author, as well as several other topics involving the transient magnetization,[3,8] but cannot be included in this short paper.

DIRECT PARAMETRIC COUPLING

A longitudinal microwave driving field (h_z) of frequency 2ω can be shown to parametrically couple, in a direct manner,[1,8] to the uniform precession present at frequency ω, and also to spin waves of frequency ω.[2,8] The effective line widths for the uniform precession and a typical spin wave are (for $z=z'$)

$$\Delta H_0{}^{\text{eff}}=\Delta H_0\left[1-\frac{N_x-N_y}{4\omega}M\frac{(-\gamma\mu_0 h_z)}{\Delta H_0}\sin\beta_0\right] \quad (10)$$

and

$$\Delta H_k{}^{\text{eff}}=\Delta H_k\left[1-\frac{\sin^2\psi}{4\omega}M\frac{(-\gamma\mu_0 h_z)}{\Delta H_k}\sin\beta_k\right], \quad (11)$$

where $\beta_{0,k}$ are the appropriate phase angles.

It should be noted that these couplings are independent of the uniform precession amplitude. The former coupling is due to the transverse demagnetizing field and is maximized when N_x or $N_y=1$. The latter coupling is due to the transverse volume dipolar field and is maximized for transverse ($\psi=\pi/2$) spin waves. This latter coupling has also been independently discovered and experimentally verified by Schlömann et al.[10]

[7] F. R. Morgenthaler, "Microwave radiation from coupled electrons in transient magnetic fields," presented orally at the Congrès International sur la Physique de l'Etat Solide et ses Applications à l'Electronique et aux Télécommunications, Bruxelles, Belgium (June, 1958).

[8] F. R. Morgenthaler, Doctoral Thesis Proposal, MIT, Dept. of E.E. (May, 1959).

[9] T. Schaug-Petterson, J. Appl. Phys. **31**, 382S (1960), this issue.

[10] E. Schlömann, M. Green, and U. Milano, J. Appl. Phys. **31**, 385S (1960), this issue.

JOURNAL OF APPLIED PHYSICS SUPPLEMENT TO VOL. 31, NO. 5 MAY, 1960

Harmonic Generation in a Ferrimagnetic Disk

GLENN E. BENNETT
Electromagnetic Radiation Laboratory, Electronics Research Directorate, Air Force Cambridge Research Center, Air Research and Development Command, United States Air Force, Bedford, Massachusetts

A small ferrimagnetic ellipsoid biased to resonance with an arbitrarily directed dc magnetic field will, in general, produce second harmonic components of the magnetization vector in both longitudinal and transverse planes—defined relative to the internal dc field. For an ellipsoid of revolution this paper reports the theoretical dependence upon the direction of magnetization of these and higher harmonic components.

S-band doubling experiments performed on a thin polycrystalline YIG disk mounted in rectangular waveguide confirm the theoretical dependence of the two doubling processes and the expected linear dependence of conversion efficiency on input power. Transverse third and fourth harmonics which were respectively cubic and quartic functions of the input power have also been detected.

I. INTRODUCTION

THE analysis of ferrimagnetic resonance in small ellipsoidal samples has recently been extended by Morgenthaler[1] to include situations in which the internal dc magnetic field is not directed along an ellipsoid axis. In this general case, time-varying demagnetizing fields modulate the uniform precession to produce harmonic components of the magnetization vector in directions both parallel to the internal dc field and in the plane transverse to it. Hereafter, these components will be re-

[1] F. R. Morgenthaler, J. Appl. Phys. **31**, 95S (1960), this issue.

ferred to as longitudinal or transverse, respectively. This paper outlines the theory which predicts these harmonics and reports experimental results for comparison.

II. ANALYSIS

Assume a small ferrimagnetic ellipsoid excited by a positively circularly polarized rf magnetic field in the plane transverse to the internal dc field, and biased to the normal resonance with this dc field. Defining the Z axis colinear with the internal dc field, the equations of motion for the magnetization vector may be written in conventional spherical coordinates[1]:

$$\dot{\phi}=A+B\cos\theta\cos 2\phi+C\sin\theta\cos\phi+D\sin\theta\sin\phi \quad (1)$$

$$\dot{\theta}=B\sin\theta\sin 2\phi, \quad (2)$$

when the driving term is neglected. The literal coefficients are functions of the material, sample shape, and direction of magnetization. The C and D coefficients in the first equation are present only when the sample is biased away from an ellipsoid axis, and it is these terms which lead to transverse frequency doubling. An approximate solution may be obtained in an iterative manner by assuming that ϕ and θ each contain a zero order term plus a sum of small amplitude harmonics of the driving frequency ω, and then determining the amplitude of these terms. Longitudinal and transverse harmonic components of the magnetization vector may then be computed. For an ellipsoid of revolution, the coefficients which result are as follows:

Transverse:

$$|M|_{2\omega}=\delta\theta_0^2\sin 2\alpha,$$

$$|M|_{3\omega}=(\delta^2/2)\theta_0^3[\sin^2 2\alpha\pm(\cos^4\alpha)/4];$$

Longitudinal:

$$|M|_{2\omega}=\delta\theta_0^2\cos^2\alpha,$$

$$|M|_{3\omega}=(4/3)\delta^2\theta_0^3\cos^2\alpha\sin 2\alpha,$$

where the internal field angle α is defined in Fig. 2. This solution assumes $\delta=-\gamma\mu_0 M_S|N_X-N_T|/4\omega_0\ll 1$, and terms of order δ^3 and greater have not been included.

III. EXPERIMENTAL GEOMETRY

A thin disk of polycrystalline YIG (0.05 in. by 0.75 in., $4\pi M_S=1800$ oe, $\Delta H=80$ oe, $g=2.01$) was mounted in S-band waveguide as indicated in Fig. 1, the disk's axis

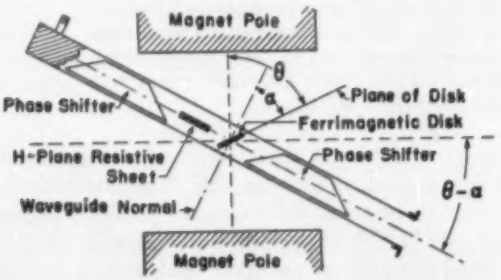

FIG. 1. Schematic diagram of harmonic generator.

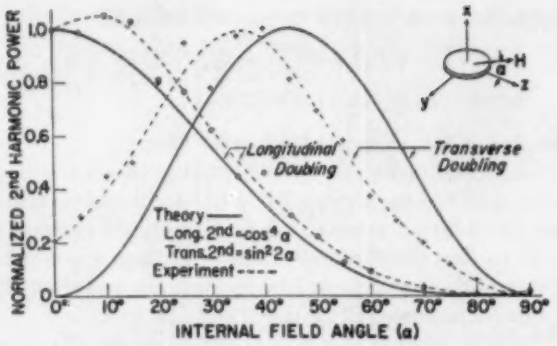

FIG. 2. Normalized 2nd harmonic power generated in a ferrimagnetic disk via longitudinal and transverse processes as a function of dc magnetic field orientation.

of rotation being perpendicular to the narrow wall of the guide. The orientation of the external dc field with respect to the plane of the disk is indicated by θ and for disk-like shapes $\theta\geq\alpha$. Varying both the orientation of the waveguide axis with respect to the external dc field and the plane of the disk with respect to this axis enables one to bias the disk at any angle to its plane, simultaneously constraining the longitudinal and transverse directions within the sample to correspond respectively to the E and H planes of the waveguide. The two doubling processes then excite waveguides modes with orthogonal E field vectors, and proper use of waveguide transitions and cutoff sections allows independent detection of either process.

The phase shifter adjacent to the coaxial input, indicated in Fig. 1, tunes transverse harmonic energy reflected from the input to add in phase with transverse harmonic energy traveling from the disk toward the output. Longitudinal harmonic energy traveling toward the input is absorbed by an H-plane resistive sheet.[2] The second phase shifter tunes S-band reflections from the output for maximum coupling to the sample.

IV. RESULTS

Using relations given in reference 1, a computer has been programed to yield the external vector dc magnetic field required for resonance in an ellipsoidal sample in terms of the internal field orientation and other relevant parameters. For the garnet disk, a single frequency measurement of the external resonance field as a function of disk orientation agreed well with the computed curve, indicating that satisfactory control of the apparatus geometry existed.

The results of second harmonic power measurements are displayed in Fig. 2. The deviations from the theoretical curves can be assigned in part to mode conversion within the waveguide due to the presence of various discontinuities. In addition, the sample diameter was $\lambda/5$ (free space wavelength) at the fundamental frequency and the parameter δ, assumed much less than one in the

[2] J. L. Melchor, W. P. Ayres, and P. H. Vartanian, Proc. Inst. Radio Engrs. 45, 643 (1957).

theoretical calculations, was approximately 0.4. These last circumstances place the experiment only marginally within the purview of the theory.

Transverse third and fourth harmonics were also detected with this device. Measurement of higher longitudinal harmonics was not attempted.

Normalized to one kilowatt of peak pulsed power absorbed by the sample (requiring roughly five kilowatts incident on the device), harmonics were detected at approximately the following levels: longitudinal second, −50 db; transverse second, −45 db; third, −75 db; fourth, −95 db. Conversion efficiencies of the doubling, tripling, and quadrupling processes were measured to be linear, quadratic, and cubic functions respectively of the power absorbed by the sample.

In conclusion, data has been presented supporting the theoretical prediction of two shape-dependent, frequency-doubling processes in an arbitrarily magnetized ferrimagnetic ellipsoid. An optimized doubling device would benefit by simultaneous use of both processes.

ACKNOWLEDGMENTS

The author is grateful to F. R. Morgenthaler for suggestions and discussions and to Miss S. J. Naumann who prepared the computer program.

JOURNAL OF APPLIED PHYSICS SUPPLEMENT TO VOL. 31, NO. 5 MAY, 1960

Theory and Application of Dipolar Ferrite Modes*

WILLIAM H. STEIER AND PAUL D. COLEMAN
Ultramicrowave Group, Department of Electrical Engineering, University of Illinois, Urbana, Illinois

Experimental verification at X and K band of theoretical calculations on the magnetodynamic resonant modes of a ferrite rod between parallel conducting sheets is reported. Critically coupled mode Q's as high as 1100 have been measured.

The characteristic equation includes propagation effects and dipolar coupling between electron spins. Mode charts for the symmetric modes are displayed for biasing fields from 3 to 20 koe and for frequencies from 4 to 50 kMc for both Ferramic R-1 and polycrystalline YIG.

The modes have been experimentally observed in the ranges of 10 and 20 kMc. Comparison of theoretical and experimental data is made in these bands for both R-1 and YIG. The variation of the observed loaded Q with biasing magnetic field is described.

The advantages that these modes possess over the magnetostatic modes for microwave engineering applications are pointed out. These include: (a) relatively high Q, (b) ability to critically couple, and (c) sample size is comparable to the wavelength.

I. INTRODUCTION

A FERRITE rod between two parallel conducting sheets has been shown to exhibit high Q magnetodynamic resonances into which energy can be efficiently coupled.[1] Contrasted to the magnetostatic modes, these dipolar modes must include propagation effects. This means the ferrite sample is large compared to the wavelength. The properties of high Q, ability to critically couple, and large sample size make these modes attractive for microwave ferrimagnetic engineering applications.

II. THEORY

The characteristic equation as derived earlier[1] includes dipolar coupling between electron spins and propagation effects. The solution assumes the rod to approximate an ellipsoid and hence that the permeability tensor is not a function of the spatial coordinates.

Unlike the magnetostatic modes, the dipolar modes are not limited to a frequency band determined by the biasing H field.[2] However, there is a high frequency cutoff determined by the dimensions. The cutoff wavelength is $\lambda_{co}=2l/m$, where $m=$ No. of axial variations and $l=$ length of the rod. At this frequency, the modified Bessel function $K_n(k_0r)$, which describes the fields outside the rod, reverts to a Hankel function and the modes are no longer trapped.

In Figs. 1–3 are shown the calculated mode charts for the symmetric (0, 1, m) modes for three values of l/m. It should be noted that for each value of the radius r_0 there is a branch both above and below the $\mu=0$ line (μ is the diagonal component of the permeability tensor).

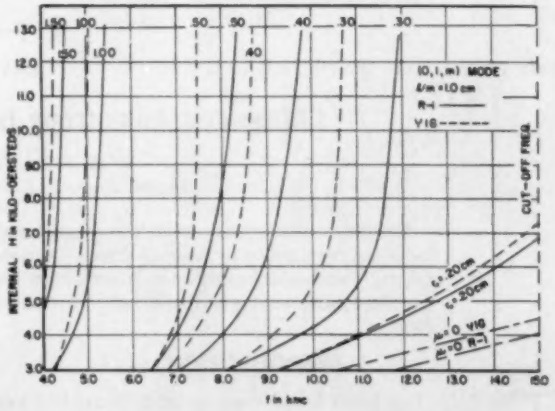

FIG. 1. Mode chart for $l/m=1.00$ cm.

* This research was supported by the U. S. Air Force through the Physics Division of the Office of Scientific Research of the Air Research and Development Command, under an Air Force contract.

[1] W. H. Steier, P. D. Coleman, J. Appl. Phys. **30**, 1454 (1959).
[2] L. R. Walker, Phys. Rev. **105**, 390 (1957).

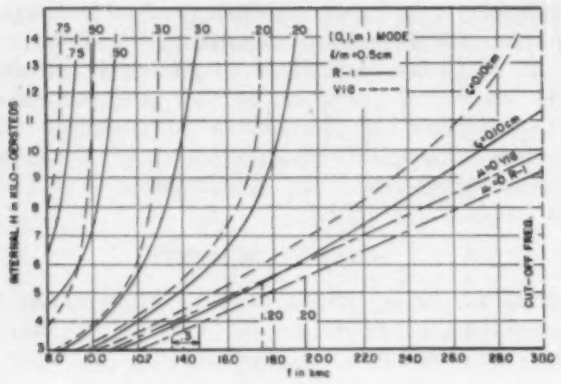

FIG. 2. Mode chart for $l/m=0.50$ cm.

III. EXPERIMENT

These modes have been observed at X and K band in both Ferramic R-1 and polycrystalline YIG. In all cases, the experimental results are in good agreement with those predicted by the theory.

In Fig. 4, comparisons are shown between the experiment and theory in both frequency bands for R-1 and YIG. The value of the relative dielectric constant necessary to bring the experimental and calculated curves into coincidence is also shown.

The X band R-1 resonator from which the data of Fig. 4 was taken had a critically matched loaded Q varying from 1100 to 550 over the band of biasing fields considered. The X band YIG resonator's Q_L varied from 300 to 100. At K band, the R-1 resonator had a Q_L of from 120 to 50, while the YIG resonator's Q_L went from 60 to 30. In all cases, the Q_L decreased as the Kittel resonance point of the rod was approached.

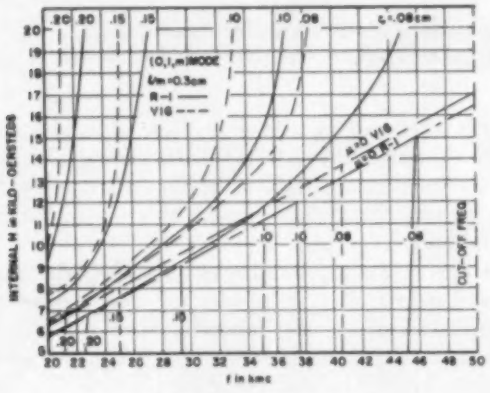

FIG. 3. Mode chart for $l/m=0.30$ cm.

IV. CONCLUSIONS

The theory of these dipolar magnetodynamic modes has been substantiated at X and K band. It has been shown that the characteristic equation will accurately predict the experimental results.

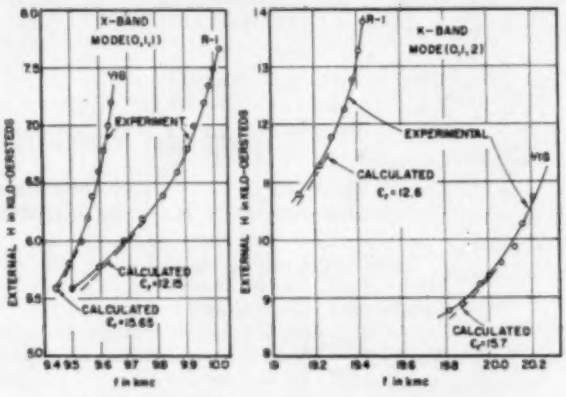

FIG. 4. Comparison of theory and experiment.

Since the polycrystalline YIG with its lower line width but higher dielectric loss produced lower Q resonators, it appears that the dielectric losses and not the magnetic losses are predominant in these modes. Therefore, if ferrite materials could be found with very low dielectric loss tangents (<0.001), it appears possible to increase still further the dipolar mode Q's and extend their application to higher frequencies.

The characteristic equation is sensitive to small changes in the relative dielectric constant of the ferrite. This suggests the use of these modes to measure the dielectric constant at microwave frequencies.

With further work the advantages inherent in the dipolar modes will quite possibly find application in many engineering devices.

JOURNAL OF APPLIED PHYSICS SUPPLEMENT TO VOL. 31, NO. 5 MAY, 1960

Magnetic Anisotropy from the Magnetostatic Modes

I. H. SOLT, JR., AND P. C. FLETCHER
Hughes Research Laboratories, Culver City, California

The differential equations for the magnetostatic modes in ferrimagnetic resonance have been rederived including the anisotropy torques. Exact solutions have been obtained for four of the low order modes of a sphere. These solutions differ in general from those for the differential equations not including anisotropy. Excellent agreement was found between measured resonance fields and those predicted by the modified theory.

I. INTRODUCTION

THERE has been some controversy in recent years as to whether the spacings of the magnetostatic modes of a single crystal sphere are independent of the crystal orientation. That is, does the effective magnetocrystalline anisotropy vary from mode to mode, and if so, from which mode does one infer the intrinsic anisotropy constants? In the early observations of the

modes,[1] large variations in mode separation were measured. These variations were later apparently explained[2] as arising entirely from the nonsphericity of the samples. However, even for "good" spheres there still appeared to be some differences. In order to clarify this situation, the differential equation for the modes has been modified to include the anisotropy and new solutions have been obtained for several of the low order modes.

II. THEORETICAL DISCUSSION

Walker[3] obtained the solutions for the magnetostatic modes by combining the static approximation of Maxwell's equations with the dynamical equation of motion for a magnetization vector in an external magnetic field. There resulted the differential equation,

$$(1+\kappa)[(\partial^2\psi/\partial x^2)+(\partial^2\psi/\partial y^2)]+\frac{\partial^2\psi}{\partial z^2}=0, \qquad (1)$$

where ψ is the scalar magnetic potential and κ is a position independent function of the frequency ω, the gyromagnetic ratio γ the external applied field H_0, and the saturation magnetization $4\pi M$. Equation (1) was solved exactly by Walker for a spheroid in terms of oblate spheroidal coordinates. In order to see what effect the anisotropy will have on the solutions of Eq. (1) the torques due to the anisotropy must be introduced into the dynamical equations.

In their linearized form they become

$$\begin{aligned}\partial m_x/\gamma\partial t&=H_i m_y-Mh_y+T_x m_y,\\ \partial m_y/\gamma\partial t&=-H_i m_x+Mh_x+T_y m_x,\\ \partial m_z/\gamma\partial t&=0,\end{aligned} \qquad (2)$$

where $H_i=H_0-N_zM$ is the internal field and M is assumed to be parallel to H_0.

$$\begin{aligned}T_x&=(K_1/M)(2-\sin^2\theta-3\sin^2 2\theta)+(K_2/2M)\\ &\quad\times\sin^2\theta(6\cos^4\theta-11\sin^2\theta\cos^2\theta+\sin^4\theta),\\ T_y&=-(2K_1/M)(1-2\sin^2\theta-\tfrac{3}{8}\sin^2 2\theta)+(K_2/2M)\\ &\quad\times\sin^2\theta\cos^2\theta(3\sin^2\theta+2),\end{aligned} \qquad (3)$$

are the well known torque constants[4] for a cubic crystal with H_0 lying in a [110] plane, θ being the angle between H_0 and the [100] direction in this plane. When Eqs. (2) are solved for $m_{x,y}$ and combined with Maxwell's equations, there results:

$$(1+\kappa')\left(\frac{\partial^2\psi}{\partial x^2}+\frac{\partial^2\psi}{\partial y^2}\right)+\frac{\partial^2\psi}{\partial z^2}+\epsilon_x\frac{\partial^2\psi}{\partial x^2}-\epsilon_y\frac{\partial^2\psi}{\partial y^2}=0, \qquad (4)$$

where

$$\kappa'=4\pi MH_i/\delta,\ \epsilon_x=T_x/\delta,\ \epsilon_y=T_y/\delta,$$

and

$$\delta=H_i^2-(\omega/\gamma)^2+(T_x-T_y)H_i-T_xT_y.$$

The effect of the anisotropy has thus been two fold: (1) the form of the differential equation has been altered, and (2) the boundary conditions at the surface of the sphere have been changed. Equation (4) can be solved exactly. The general solutions involve ellipsoidal harmonics which are rather difficult to handle and have not been considered at present. However, one can see a very important feature of all solutions from just the differential equation. That is, namely, when $\epsilon_x=-\epsilon_y$, Eq. (4) is of the identical form of Eq. (1), and the solutions for the modes will be the same as Walker's except that all of the modes are displaced by some constant amount which is related to the first and second order anisotropy constants. By using Eqs. (3) and setting $T_x=-T_y$ one obtains nontrivial solutions for the [100] and [111] crystal directions, but for all other angles, $T_x\neq-T_y$. Thus, for only these two crystal directions will the spacings of the modes be those given by Walker's solutions.

Because of the mathematical difficulty of obtaining a general solution for all modes, solutions have been obtained for only the four lowest order modes (110, 200, 210, 220), in a spherical sample. A trial ψ-function was used involving spatial coordinates to the second order only, since it was expected that the form of the solutions would be similar to those of Eq. (1). Matching the boundary conditions, the following solutions for the resonant frequencies were obtained.

$$110\quad[H_0+T_x][H_0-T_y]=(\omega/\gamma)^2$$

$$210\quad\left[H_0-\frac{8\pi M}{15}+T_x\right]\left[H_0-\frac{8\pi M}{15}-T_y\right]=(\omega/\gamma)^2$$

$$220\quad\left[H_0+\frac{4\pi M}{15}+T_x\right]\left[H_0+\frac{4\pi M}{15}-T_y\right]$$
$$=(\omega/\gamma)^2+\frac{2}{25}(4\pi M)^2\left\{1-\left[1+25\left(\frac{T_x+T_y}{8\pi M}\right)^2\right]^{\frac{1}{2}}\right\} \qquad (5)$$

$$200\quad\left[H_0+\frac{28\pi M}{15}+\frac{T_x-T_y}{2}\right]\left[H_0-\frac{4\pi M}{3}+\frac{T_x-T_y}{2}\right]$$
$$=(\omega/\gamma)^2+\left(\frac{T_x+T_y}{2}\right)^2-\frac{2}{25}(4\pi M)^2\left\{1-\left[1+25\left(\frac{T_x+T_y}{8\pi M}\right)^2\right]^{\frac{1}{2}}\right\}.$$

[1] R. L. White and I. H. Solt, Jr., Bull. Am. Phys. Soc., Ser. II 2, 22 (1957).
[2] J. F. Dillon, Jr., Phys. Rev. **112**, 59 (1958).
[3] L. R. Walker, Phys. Rev. **105**, 390 (1957).
[4] L. R. Bickford, Tech. Rept. **XXIII**, Lab. Insulation Research MIT (October, 1949); also see, D. W. Healy, Jr., Phys. Rev. **86**, 1009 (1952).

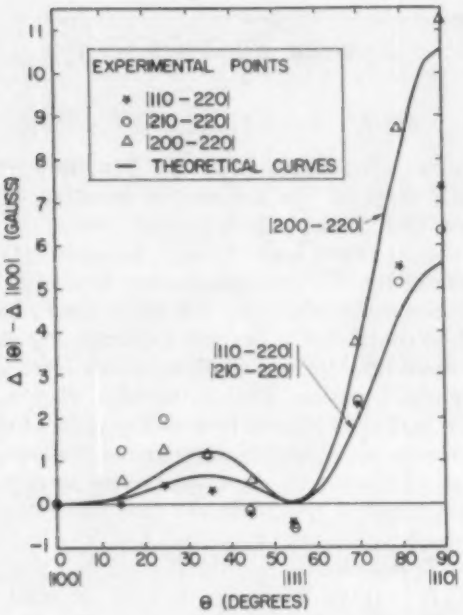

FIG. 1. Variation in mode spacing for a single crystal YIG sphere at 8300 Mc and 77°K. H_0 is in a [110] plane and θ is the angle between H_0 and the [100] direction. $\Delta[\theta]=H_{nmr}[\theta]-H_{220}[\theta]$ is the separation between the nmr mode and the 220 mode at some angle, θ, and $\Delta[100]$ is the same separation in the [100] direction.

III. COMPARISON WITH EXPERIMENT

One can see that the resonant frequencies for the 110 and 210 lines are just what one would have obtained using the original Kittel formula[5] for the resonant frequencies with the anisotropy introduced as an effective demagnetizing factor. The 200 and 220 solutions, though, have added correction factors. These correction factors are of order of magnitude of the ratio of the square of the anisotropy constant to the resonant magnetic field. By using Eqs. (5), one can determine the variation in spacing as a function of angle for the four modes considered. For Yttrium Iron Garnet (YIG) single crystals at room temperature, this variation will be the order of one gauss at 9000 Mc. At lower temperatures, K_1/M is about 3 times larger, making the correction quite appreciable. In Fig. 1, we have plotted this variation as a function of angle at 77°K and 8300 Mc. Here, $\Delta[\theta]$ is the spacing between the 220 mode and one of the other three modes. Since this separation is several hundred gauss, we have subtracted out the separation for the [100] crystal direction ($\Delta[100]$). Hence, we have plotted the difference in mode separation at some angle θ from that in the [100] direction. The theoretical curves were obtained from Eqs. (5) together with the experimentally determined values of K_1/M and K_2/M. One can see that the separations are nearly equal in the [100] and [111] directions as predicted, but can be quite different in the other directions. We have shown in general that the variation in the [110] direction is larger than for any other cubic crystal direction. Thus, if this correction were not taken into account, the apparent measured value of K_2/M would be much larger.

[5] C. Kittel, Phys. Rev. **73**, 155 (1948).

TABLE I.

Mode	Without anisotropy correction K_1/M	Without anisotropy correction K_2/M	With anisotropy correction K_1/M	With anisotropy correction K_2/M
110	−124.50	− 2.52	−124.50	−2.52
210	−125.14	− 4.67	−125.14	−4.67
220	−126.54	+ 6.55	−125.20	−3.49
200	−123.92	−11.96	−125.10	−3.07

Table I shows the excellent agreement between the values of K_1/M and K_2/M as determined from the experimental data using Eqs. (5). The absolute errors of these measurements have not been evaluated yet and hence are not included. They will be discussed at a later time. However, the relative precision of the measurements is quite good, as evidence by the excellent agreement between modes.

IV. CONCLUSION

In conclusion, it has been shown both theoretically and experimentally that the separations of the magnetostatic modes are not independent of the crystal orientation. This variation is the order of

$$\frac{(T_x+T_y/2)^2}{\omega/\gamma},$$

which becomes quite appreciable below room temperature for many materials like YIG and Mn ferrites. For cubic crystals, the solutions of Walker are only valid for H_0 in the [100] and [111] directions for which these corrections vanish.

V. ACKNOWLEDGMENTS

The authors wish to acknowledge many helpful discussions with R. L. White concerning the theory and the technical assistance of E. H. Gregory and other members of the Solid State and Cryogenics Section.

Ferrimagnetic Resonance at High Power

M. T. WEISS*
Microwave Laboratory, Hughes Aircraft Company, Culver City, California

Ferrimagnetic resonance experiments have been performed on single-crystal manganese ferrite at high microwave powers. The variation of susceptibility with power level is in good agreement with Suhl's recent theoretical treatment of the saturation process in which scattering of the uniform precession at impurities and imperfections is taken into account. Our results show that the ratio of intrinsic to scattering decay constants is close to zero, so that χ'' decreases gradually at power levels substantially below the theoretical critical signal level. At very high power levels various anomalous effects appear such as bistabilities, line asymmetries, and flat topped absorption lines.

THE early onset of saturation of ferrimagnetic resonance lines has previously been explained by Suhl[1] as being due to a nonlinear coupling between the uniform precession and the degenerate spin waves. When the signal level exceeds a certain critical value, this coupling increases so that the amplitudes of the degenerate spin waves increase exponentially with time. More recently, this theory has been extended by Schlomann[2] and by Suhl[3] by taking into account the scattering of the uniform precession at impurities and imperfections in the material. Thus, if the scattering decay constant becomes appreciable compared to the intrinsic decay constant, then saturation effects at the main resonance can occur at rf field levels below the theorectical critical value calculated in reference 1 where it is assumed that there is no scattering process. Theoretical curves of susceptibility as a function of rf power are given by Suhl[3] for various values of the ratio of intrinsic to scattering decay constants.

In order to check on the foregoing theory and to study the high power behavior of ferrimagnetic resonance, cavity experiments at 9300 Mc were performed on a single crystal sphere of manganese ferrite of 0.022 inch diameter kindly supplied by J. F. Dillon, Jr. The results for three crystalline orientations are shown in Fig. 1 which gives a plot of μ''/μ_0'' as a function of P/P_c where P_c is a "critical" power level and was chosen so as to give a best fit with a Suhl type saturation curve. The solid curve of Fig. 1 is Suhl's theoretical curve for a ratio of intrinsic to scattering decay constants of zero. The agreement between the experimental points and the theoretical curve is remarkable for all three orientations of the crystal. The P_c values for the three orientations are different with h_c^2 being 5.9 oe^2 for the [100] direction, 9 oe^2 for [111] direction and 10 oe^2 for the [110] direction. No explanation is as yet available for the variation of P_c with orientation.

Another interesting effect was observed in these experiments. For all crystalline orientations there is a general tendency for the dc magnetic field required for resonance (defined as the field at which μ'' is a maximum) to increase with increasing power level. This effect and the resulting asymmetry in line shape has been tentatively explained in a previous publication[4] as due to a variation in g-factor with spin temperature. At still higher power levels, with an h^2 of 33 oe^2 and higher,

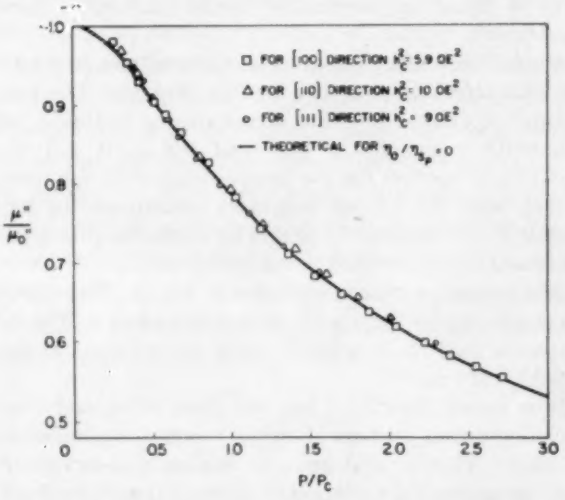

FIG. 1. The variation of susceptibility with power level for three crystalline orientations of a single crystal manganese ferrite sphere (diam = 0.022 in.).

an unstable situation arises with a pronounced jitter and bistability in the resonance curves becoming evident. Furthermore, the resonance absorption curve as a function of dc field becomes flat topped and has no resemblance to the usual low power Lorentzian line shape.

The author wishes to thank H. Suhl and J. F. Dillon, Jr. for many helpful discussions.

* This paper is based on data obtained while the author was at Bell Telephone Laboratories, Holmdel, New Jersey.

[1] H. Suhl, Proc. Inst. Radio Engrs. 44, 1271 (1956).
[2] E. Schlomann, Bull. Am. Phys. Soc. Ser. II, 4, 53 (1959).
[3] H. Suhl, J. Appl. Phys. 30, 1961 (1959).
[4] M. T. Weiss, J. Appl. Phys. 30, 2014 (1959).

Magnetostatic Modes of a Ferromagnetic Slab

R. W. DAMON AND J. R. ESHBACH
General Electric Research Laboratory, Schenectady, New York

The characteristic modes of a thin slab magnetized in its plane are obtained in the magnetostatic limit, and the mode spectrum and configuration are discussed. The wavelength dependence of magnetostatic mode density is determined and utilized to establish a connection to the modes obtained in the spin-wave approximation. In this geometry the modes lying above the spin-wave band are surface waves, decaying toward the interior of the slab, while volume modes occur in the same frequency range as the long-wavelength limit of the spin-wave band of an infinite medium. The mode density exhibits poles at the upper and lower frequency limits of the surface mode spectrum. The surface modes become statistically less important at shorter wavelengths because the ratio of surface mode density to volume mode density varies approximately as $1/|k|$.

THE resonant modes of ferromagnetic samples have been previously calculated in the magnetostatic limit for spheres[1] and for spheroids magnetized along the axis of revolution.[2] Since the characteristic modes of a thin slab magnetized in its plane permit fairly straightforward solution, we have examined this geometry in some detail. Many properties of the modes of this system are similar to those of the spheroidal case, and the simpler form of the results is of considerable assistance in obtaining an intuitive understanding of these modes.

We follow Walker's approach and notations to obtain the characteristic equation for this problem. The procedure amounts to the simultaneous solution of Maxwell's equations in the limit $\nabla \times H = 0$ and the equation of motion for the sample magnetization, consistent with the proper boundary conditions. In rectangular coordinates the magnetic potential ψ is separable and can be written $\psi = X(x)Y(y)Z(z)$.

The geometry chosen is shown in Fig. 1. The slab is perpendicular to the x axis, and of thickness s. The dc magnetic field H_0 is applied along the z axis, and the rf fields vary as $e^{i\omega t}$.

It is found that $Y(y)$ has the form $e^{ik_y y}$, and thus traveling waves, and not standing waves, are admissible solutions. This is analogous to Walker's observation[3] that the azimuthal variation in spheroidal samples must be $e^{im\varphi}$. Standing waves of the form $\sin(k_z z)$ or $\cos(k_z z)$ provide suitable solutions for $Z(z)$. Inside the slab, the form of $X(x)$ depends on the sign of the diagonal element of the permeability tensor, $(1+\kappa)$. This is because the equation for the potential obtained from Poisson's equation

$$(1+\kappa)\left[\frac{\partial^2\psi}{\partial x^2}+\frac{\partial^2\psi}{\partial y^2}\right]+\frac{\partial^2\psi}{\partial z^2}=0$$

changes from hyperbolic to elliptic form when $(1+\kappa)$ changes sign. Since $Y(y)$ and $Z(z)$ cannot be exponential functions in an infinite slab, the internal wave-vector component k_x[4] must change from real to imaginary, and $X(x)$ changes from a sinusoidal function extending throughout the sample for $(1+\kappa)<0$, to an exponential function having significant amplitude only near the surface for $(1+\kappa)>0$. The clear distinction between volume and surface modes results from the plane-wave nature of the solutions in this geometry.

The boundary conditions further determine the mode configuration and spectrum. The limits of the complete mode spectrum are the same as for the spheroid, namely, $\Omega_H \leq \Omega \leq (\Omega_H + 1/2)$, where Ω is the reduced angular frequency $\omega/4\pi\gamma M$, Ω_H is the reduced internal magnetic field $H_i/4\pi M$, and $H_i = H_0 - N_z \cdot 4\pi M$. In the geometry chosen $N_z = 0$ and $H_i = H_0$.

Since there are no boundaries in the y and z directions of the slab, k_y and k_z have continuous characteristic values. Discrete characteristic values are thus determined only by the boundary conditions at the surfaces,

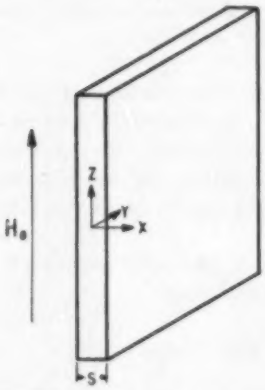

FIG. 1. Orientation of magnetic field and coordinate system.

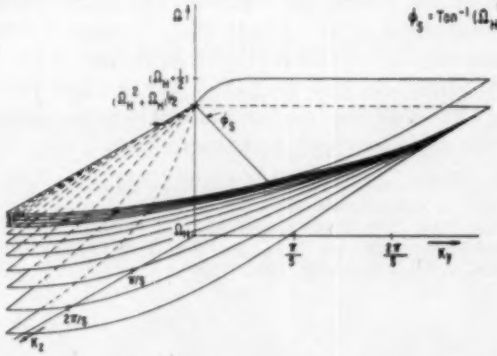

FIG. 2. Magnetostatic mode spectrum of a ferromagnetic slab.

[1] J. Mercereau and R. P. Feynman, Phys. Rev. **104**, 63 (1956).
[2] L. R. Walker, Phys. Rev. **105**, 390 (1957).
[3] L. R. Walker, J. Appl. Phys. **29**, 318S (1958).

for which x is constant. In $k_y-k_z-\Omega$ space, characteristic surfaces are obtained as shown in Fig. 2 for one octant of this coordinate system.

In the range $\Omega_H \leq \Omega \leq (\Omega_H^2+\Omega_H)^{\frac{1}{2}}$, all wave vector components are real since $(1+\kappa)<0$. Successive sheets with increasing Ω correspond to an increased number of nodes in the x direction. The complete range of frequencies in which $(1+\kappa)<0$ is available only to modes with $k_y=0$, and modes near the bottom of the band are longitudinal waves, $k_z^2 \gg (k_x^i)^2+k_y^2$, analogous to spin-waves with $\theta=0$. For volume modes propagating at a surface angle ϕ, corresponding to $\tan\phi=k_y/k_z$, the minimum characteristic frequency is $\Omega^2=\Omega_H(\Omega_H+\sin^2\phi)$. Near the k_y axis, where $(k_x^i)^2+k_y^2 \gg k_z^2$, the modes are transverse waves at $\Omega=(\Omega_H^2+\Omega_H)^{\frac{1}{2}}$, similar to $\theta=\pi/2$ spin waves.

At frequencies for which $(1+\kappa)>0$, k_x^i is imaginary and the mode configuration is that of a surface wave. Only a single characteristic surface is obtained, bounded in frequency by $(\Omega^2{}_H+\Omega_H)^{\frac{1}{2}}<\Omega<(\Omega_H+1/2)$. Propagation of these surface modes tends to be transverse to the applied field, since the characteristic surface exists only at angles for which $\tan\phi \geq \Omega_H^{\frac{1}{2}}$.

In the volume mode region, the mode density approaches the spin-wave value as $|k|$ increases. The spin-wave density is readily calculated to be $dN_v(k,\Omega) = C_v \cdot 2\pi k^2 dk \cdot \rho_v(\Omega) d\Omega$, where C_v is the uniform density of modes in k space and $\rho_v(\Omega)=\Omega[\Omega_H(\Omega_H^2+\Omega_H-\Omega^2)]^{-\frac{1}{2}}$. The function $\rho_v(\Omega)$ is shown in Fig. 3(a). In the surface mode region, we assume that the mode distribution is uniform in k_y and k_z, with C_s modes per unit area. Writing the surface wave number $k_s^2=k_y^2+k_z^2$, the surface mode density also has a product form, $dN_s = C_s k_s dk_s \rho_s(\Omega) d\Omega$, where

$$\rho_s(\Omega)=\Omega_H\{\Omega^2-\Omega_H^2-\Omega_H\}^{-\frac{1}{2}} \times\{2(\Omega^2-\Omega_H^2)-\Omega_H-2\Omega[\Omega^2-\Omega_H^2-\Omega_H]^{\frac{1}{2}}\}^{-\frac{1}{2}}.$$

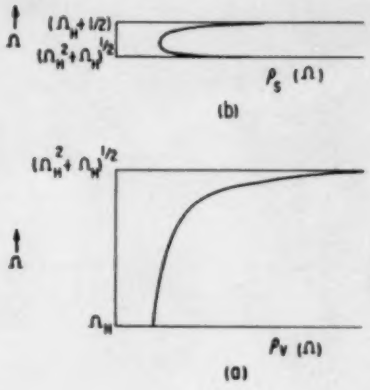

FIG. 3. Surface mode and volume mode densities.

The function $\rho_s(\Omega)$ is shown in Fig. 3(b). The two factors in $\rho_s(\Omega)$ give poles at $\Omega=(\Omega_H^2+\Omega_H)^{\frac{1}{2}}$ and at $\Omega=(\Omega_H+1/2)$. This latter pole has not been recognized previously, and may contribute to the resonance line width and other relaxation effects for modes in this frequency range. Closer examination may reveal a similar pole for other sample shapes, but the specific function $\rho_s(\Omega)$ probably depends on sample geometry.

At sufficiently short wavelength, the surface mode density becomes small compared to the volume mode density because of the differing dependence on wave-vector magnitude. Thus although surface modes exist for arbitrarily short wavelength, their effects become less important as the wavelength decreases. The magnetostatic volume modes merge smoothly into the spin-wave modes of an infinite medium, bounded by the same limits in frequency and with substantially the same spectral distribution.

Finite Amplitude Electromagnetic Waves in Gyromagnetic Media*

B. A. AULD
Microwave Laboratory, W. W. Hansen Laboratories of Physics, Stanford University, Stanford California

A perturbation method is developed for obtaining forced steady-state solutions to Maxwell's equations and the torque equation subject to the usual boundary condition. This procedure is applied to the scattering of a normally incident plane wave from a semi-infinite gyromagnetic slab and numerical results are presented.

THE usual treatment of propagation in a gyromagnetic medium, which neglects nonlinear terms in the torque equation, is strictly valid only for waves of infinitesimal amplitude. For waves of finite amplitude the nonlinearity of the medium leads to generation of harmonic frequencies and progressive distortion of the wave fronts, as in the analogous case of finite amplitude sound waves.

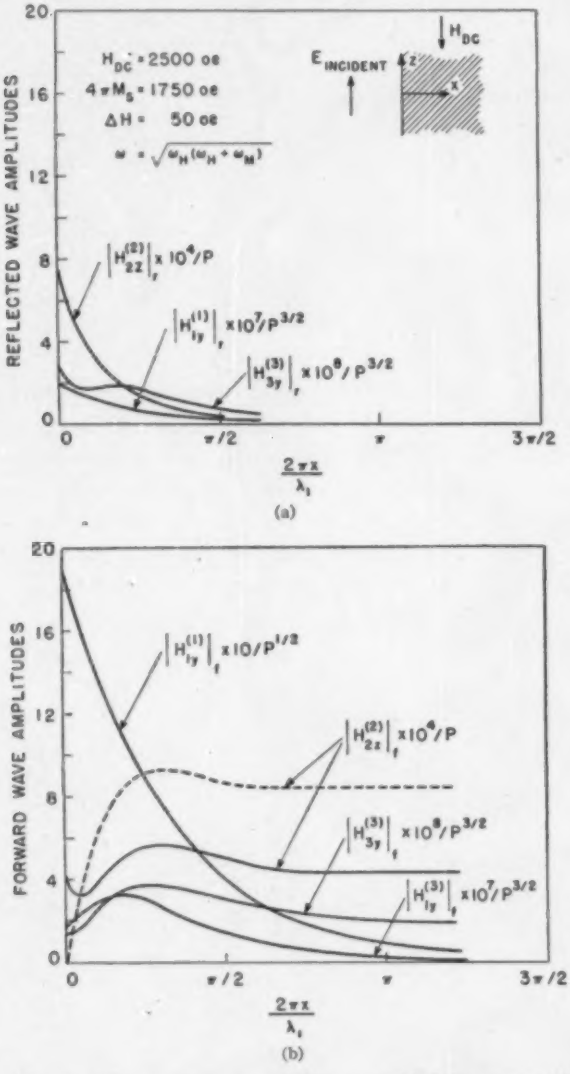

FIG. 1. Component waves within a semi-infinite garnet slab illuminated by a normally incident plane wave. The dotted curve shows the effect of matching the interface at the second harmonic frequency. P = incident power density, $kw/m^2\lambda_1 1$ = fundamental wavelength in the medium. (a) Reflected wave amplitude. (b) Forward wave amplitude.

The general problem considered here is the excitation of finite amplitude waves in a semi-infinite uniform gyromagnetic waveguide by an incident wave of frequency ω and amplitude a. At every point within the waveguide the fields satisfy Maxwell's equations,

$$\nabla\times\mathbf{E}+\mu_0(\partial/\partial t)(\mathbf{H}+\mathbf{M})=0\ \nabla\cdot\epsilon\mathbf{E}=0$$
$$\nabla\times\mathbf{H}-\sigma\mathbf{E}-\epsilon(\partial\mathbf{E}/\partial t)=0\ \nabla\cdot(\mathbf{H}+\mathbf{M})=0. \tag{1}$$

(It is necessary to use *both* the divergence and curl relations because of zero-frequency terms resulting from the nonlinearity of the gyromagnetic medium.) The magnetization is specified by the torque equation,

$$\frac{\partial\mathbf{M}}{\partial t}=\mu_0\gamma(\mathbf{M}\times\mathbf{H})+\frac{\alpha}{|M|}\left(\mathbf{M}\times\frac{\partial\mathbf{M}}{\partial t}\right). \tag{2}$$

($\gamma=-1.74\times10^{11}$ coulomb kg^{-1}) inside the medium, and is zero outside. At surfaces of discontinuity the tangential components of $\mathbf{E}$, $\mathbf{H}$ and the normal components of $\epsilon\mathbf{E}$, $(\mathbf{H}+\mathbf{M})$ are continuous, and at infinity the usual conditions of regularity and outward radiation are required. A solution to (1) and (2) is sought in the form of a power series in the amplitude a of the incident wave and, since we are concerned with steady-state conditions, this solution is represented as a Fourier time series having the same period as the excitation. Thus,

$$\mathbf{H}(\mathbf{r},t)=\sum_{k=-\infty}^{\infty}\sum_{q=0}^{\infty}\mathbf{H}_k^{(p)}(\mathbf{r})a^p e^{jk\omega t} \tag{3}$$

with similar expressions for $\mathbf{M}$ and $\mathbf{E}$. The zero-order terms in these expansions are, of course, $\mathbf{H}_0^{(0)}=\mathbf{z}H_{DC\,\mathrm{int}}$ and $\mathbf{M}_0^{(0)}=\mathbf{z}M_s$.

The problem is reduced to a set of linear boundary-value problems by substituting the expansions (3) into (1), (2) and the boundary conditions, and equating corresponding terms. From the transverse components of the kth harmonic pth order term in (2),

$$(\mathbf{M}_k^{(p)})_t=\chi_s(k\omega)(\mathbf{H}_k^{(p)})_t+\mathbf{N}_k^{(p)}, \tag{4}$$

* The research reported in this paper has been sponsored by the Electronics Research Directorate of the Air Force Cambridge Research Center, Air Research and Development Command under an Air Force contract.

where χ_s is the Polder susceptibility tensor and

$$\mathbf{N}_k^{(p)}=\mu_0\gamma\begin{pmatrix} jk\omega & \omega_0+j(k\omega/\omega_0 T) \\ -\omega_0-j(k\omega/\omega_0 T) & jk\omega \end{pmatrix}^{-1} \times\sum_{q=1}^{p-1}\sum_{l=-\infty}^{\infty}\left[\mathbf{M}_{k-l}^{(p-q)} \times\left\{\mathbf{H}_l^{(q)}-j\frac{l\omega}{\omega_0\omega_m T}\mathbf{M}_l^{(q)}\right\}\right]_t,$$

where

$$T=1/\alpha|\omega_0|,\quad \omega_0=-\mu_0\gamma H_0^{(0)},\quad \omega_m=-\mu_0\gamma M_0^{(0)}.$$

The z component of $\mathbf{M}_k^{(p)}$ is obtained by demanding that $|M|$ be conserved up to terms of order p. Thus,

$$M_{kz}^{(p)}=-\sum_{q=1}^{p-1}\sum_{l=-\infty}^{\infty}\frac{\mathbf{M}_{k-l}^{(p-q)}\cdot\mathbf{M}_l^{(q)}}{2M_0^{(0)}}. \tag{5}$$

Substitution of (4) and (5) into the kth harmonic pth order term in (1) leads to the following equations for the fields within the medium,

$k\neq 0$

$$\nabla\times\mathbf{E}_k^{(p)}+jk\omega\mu_0\boldsymbol{\mu}_s(k\omega)\mathbf{H}_k^{(p)} =-jk\omega\mu_0[\mathbf{N}_k^{(p)}+\mathbf{z}M_{kz}^{(p)}] \tag{6}$$

$$\nabla\times\mathbf{H}_k^{(p)}-(\sigma+jk\omega\epsilon)\mathbf{E}_k^{(p)}=0$$

$k=0$

$$\mathbf{H}_0^{(p)}=\nabla\psi_0^{(p)}\quad \mathbf{E}_0^{(p)}=0$$
$$\nabla\cdot\boldsymbol{\mu}(0)\nabla\psi_0^{(p)}=-\nabla\cdot(\mathbf{N}_0^{(p)}+\mathbf{z}M_{0z}^{(p)}), \tag{7}$$

where $\boldsymbol{\mu}(k\omega)$ is the Polder permeability tensor. Outside the medium, it is required that the linear field equations be satisfied, subject to the usual boundary conditions at discontinuity surfaces and at infinity. The terms on the right-hand sides of (6) and (7) may be regarded as fictitious magnetic source densities driving the kth harmonic pth order fields. Solutions for the problem of a gyromagnetic waveguide with distributed sources have been discussed by Bresler.[1] Since the expressions for the pth order source densities contain only terms of order less than p, the coefficients in (3) may be obtained by a step-by-step procedure.

As an example, the analysis has been applied to the problem of a plane wave normally incident upon a semi-infinite slab. It has been assumed that only magnetic losses are present. Figure 1 shows the magnitudes of the expansion coefficients up to the 3rd harmonic third-order term. In the higher order terms it is seen that reflected waves occur *within* the body of the slab. These appear in the analysis as backward radiation from the distributed sources. The irregularity in the curve $|h_{2z}^{(2)}|_f$ is due to interference between the forward radiated wave (dotted) and that part of the backward radiated wave, which is reflected at the interface.

[1] A. D. Bresler, Inst. Radio Engrs. Trans. **MTT-7**, 282–287 (1959).

Spin Waves in Complex Exchange-Coupled Lattices and Neutron Scattering

A. W. SÁENZ
U. S. Naval Research Laboratory, Washington, D. C.

A spin-wave theory of Holstein-Primakoff type is developed for exchange-coupled lattices with an arbitrary number n of magnetic ions per primitive magnetic unit cell. This theory is used to obtain a cross-section formula for the one-magnon zero-phonon scattering of arbitrarily polarized neutrons by such lattices for the case of complete orbital quenching of the magnetic ions thereof. For $n>1$, this equation can be reduced to a simple approximate form in a limiting case, of interest fror certain ferrimagnets, which involves only the scattering of "acoustic" magnons of sufficiently large wavelengths. The parallelism between this last result and the specialization of the above cross section formula for simple ferromagnets ($n=1$) is pointed out.

RECENT experiments on the scattering of unpolarized[1] and polarized neutrons[2] by spin waves in Fe_3O_4 and possible extensions of this work to similar complex spin lattices indicate the need for two theoretical developments. The first is a spin-wave theory applicable to exchange-coupled lattices with an arbitrary number of magnetic ions per primitive magnetic unit cell for temperatures $T\ll T_c$, where T_c is the transition temperature. The second is the derivation of cross-section formulas for the spin-wave scattering of neutrons of arbitrary polarization by such lattices. In this study we treat these two questions by means of a formalism parallel to that of Holstein and Primakoff.[3]

We designate the primitive magnetic unit cells by $i, j, k=1, \cdots, N$, and the magnetic ions in one of these cells by $\alpha, \beta, \gamma=1, \cdots, n$. The equilibrium position of the αth ion in the ith magnetic cell is $\mathbf{X}_{i,\alpha}\equiv\mathbf{X}_i+\boldsymbol{\varrho}_\alpha$, where $\mathbf{X}_i$ specifies a fixed point in this cell, and the resultant electronic spin quantum number and spin vector operator of this ion are denoted by S_α and $\mathbf{S}_{i,\alpha}$, respectively.

The Hamiltonian of the magnetic ions is taken to be

$$H\equiv-\sum_{i,j,\alpha,\beta}J_{i\alpha,j\beta}(\mathbf{S}_{i,\alpha}\cdot\mathbf{S}_{j,\beta})-\sum_{i,\alpha}K_\alpha S_{i,\alpha}{}^{(z)}; \quad (1)$$

where $J_{i\alpha,j\beta}$ depends solely on α, β, and $|\mathbf{X}_{i,\alpha}-\mathbf{X}_{j,\beta}|$, where this last dependence is of the usual short-range variety; and K_α is linear in an external magnetic field and a hypothetical anisotropy field of conventional type acting on the αth ion in a unit cell, the only nonzero components of these fields being along the axis of spin alignment, called the z axis.

In the spirit of Holstein and Primakoff,[3] we approximate the cartesian components of $\mathbf{S}_{i,\alpha}$ as follows:

$$S_{i,\alpha}{}^{(x)}\pm iS_{i,\alpha}{}^{(y)}=S_\alpha{}^{\frac{1}{2}}\{q_{i,\alpha}\pm i\sigma_\alpha p_{i,\alpha}\};$$
$$S_{i,\alpha}{}^{(z)}=\sigma_\alpha\{S_\alpha-\tfrac{1}{2}[p_{i,\alpha}{}^2+q_{i,\alpha}{}^2-1]\}; \quad (2)$$

where $\sigma_\alpha\equiv\pm1$, depending on whether the thermal average of $\mathbf{S}_{i,\alpha}$ for $T\ll T_c$ is almost parallel or antiparallel to z, respectively; and where $[p_{i,\alpha},q_{j,\beta}]=(1/i)\delta_{ij}\delta_{\alpha\beta}$, the other pairs of operators commuting. We shall disregard here the restriction that the maximum eigenvalue of $\frac{1}{2}[p_{i,\alpha}{}^2+q_{i,\alpha}{}^2-1]$ is $2S_\alpha$.

From now on, unless stated otherwise, we shall understand by $\boldsymbol{\kappa}$ a vector which can roam continuously throughout the fundamental zone of the reciprocal lattice of the $\mathbf{X}_i$ lattice. We shall suppose invariably that the matrix with elements

$$R_{\kappa,\alpha\beta}\equiv 2\sigma_\alpha[\sum_{k,\gamma}J_{k\alpha,0\gamma}\sigma_\gamma S_\gamma+\tfrac{1}{2}K_\alpha]\delta_{\alpha\beta}$$
$$-2(S_\alpha S_\beta)^{\frac{1}{2}}\sum_k J_{k\alpha,0\beta}\exp[i\boldsymbol{\kappa}\cdot\mathbf{X}_k], \quad (3)$$

is positive semidefinite when $K_\alpha=0$ for $\alpha\geq1$, which implies that $(R_{\kappa,\alpha\beta})$ is positive definite if and only if $\sigma_\alpha K_\alpha>0$ for $\alpha\geq1$. From this positive-definiteness, there follows the existence of nonsingular matrices $(T_{\kappa,\alpha\beta})$, such that, making familiar spin-wave approximations consistent with (2),

$$H=C+\tfrac{1}{2}\sum_{\kappa,\alpha}\epsilon_{\kappa,\alpha}\{\pi_{-\kappa,\alpha}\pi_{\kappa,\alpha}+\xi_{-\kappa,\alpha}\xi_{\kappa,\alpha}\};$$
$$\pi_{\kappa,\alpha}\equiv N^{-\frac{1}{2}}\sum_{j,\beta}\exp[-i\boldsymbol{\kappa}\cdot\mathbf{X}_j]T_{\kappa,\alpha\beta}{}^{-1}p_{j,\beta}; \quad (4)$$
$$\xi_{\kappa,\alpha}\equiv N^{-\frac{1}{2}}\sum_{j,\beta}\exp[i\boldsymbol{\kappa}\cdot\mathbf{X}_j]T_{\kappa,\beta\alpha}q_{j,\beta};$$

where the $\boldsymbol{\kappa}$ summation extends over the usual set of N points of the above fundamental zone; C is a c number; and the superscript -1 denotes matrix inversion. For fixed $\boldsymbol{\kappa}$, the possible energies $\epsilon_{\kappa,\alpha}$ are given by the absolute values of the eigenvalues of $(\sigma_\beta R_{\kappa,\beta\gamma})$. By suitable permutations, $\epsilon_{\kappa,\alpha}$ and $T_{\kappa,\alpha\beta}$ can be chosen to be continuous in the components of $\boldsymbol{\kappa}$ for fixed α and β, and such that $\epsilon_{-\kappa,\alpha}=\epsilon_{\kappa,\alpha}$ and $T_{-\kappa,\alpha\beta}=T_{\kappa,\alpha\beta}{}^*$. We shall assume in the future that these properties hold.

Let $K_\alpha\to0$ for $\alpha\geq1$. We then deduce, with the aid of (3), the existence of at least one "acoustic" spin-wave branch of this spectrum, i.e., of a set of energies $\epsilon_{\kappa,\beta}{}^{(0)}\equiv\lim_{K_\alpha\to0}\epsilon_{\kappa,\beta}$ for some fixed β and for $\boldsymbol{\kappa}$ varying over the foregoing continuous domain, such that $\epsilon_{\kappa,\beta}{}^{(0)}\to\epsilon_{0,\beta}{}^{(0)}$

[1] B. N. Brockhouse, Phys. Rev. **106**, 859 (1957) and **111**, 1273 (1958); T. Riste, K. Blinowski, and J. Janik, J. Phys. Chem. Solids **9**, 153 (1959).

[2] These experiments are being carried out by Mr. G. A. Ferguson at the Naval Research Laboratory.

[3] T. Holstein and H. Primakoff, Phys. Rev. **58**, 1098 (1940). From the work of F. J. Dyson, Phys. Rev. **102**, 1217, 1230 (1956), one expects the spin-wave theory of the present paper (based on a formalism of the Holstein-Primakoff type) to be satisfactory for $T\ll T_c$, when applied to the neutron scattering phenomena dealt with here.

$=0$ as $\varkappa\to\mathbf{0}$, where the last limit involving K_α is taken over all α.

Let a neutron, with wave-number $\mathbf{k}$ and polarization f parallel to a unit vector $\boldsymbol{\lambda}$, be scattered by a spin lattice of type (1) into a state with wave-number vector $\mathbf{k}'\equiv\mathbf{k}+\mathbf{q}$ inside $d\Omega$, differing in energy by ϵ from the initial state. We assume that the magnetic ions are orbitally quenched and that the magnetic electrons move rigidly with the corresponding nuclei, and we make other familiar hypotheses listed by Van Hove.[4] We restrict ourselves to magnetic scattering phenomena involving all possible transitions in which there is a difference of ±1 between the initial and final occupation numbers of one and only one energy level $\epsilon_{\varkappa,\alpha}$ of (4), and in which the initial and final vibrational states are identical (one-magnon zero-phonon processes). By employing the foregoing spin-wave theory and the approach of Van Hove,[4] making spin-wave approximations of the type alluded to previously, and replacing the pertinent $\varkappa$ summations by integrations, we find when $\sigma_\alpha K_\alpha>0$ for $\alpha\gtrless1$ that the corresponding cross section summed over the final neutron spin states, per unit-energy range and per magnetic unit cell, is given by[5]

$$(d^2\sigma_{01}/d\epsilon d\Omega)=[1+(\mathbf{e}\cdot\boldsymbol{\mu})^2]A_+(\epsilon)+2f(\mathbf{e}\cdot\boldsymbol{\lambda})(\mathbf{e}\cdot\boldsymbol{\mu})A_-(\epsilon);$$

$$A_\pm(\epsilon)\equiv\tfrac{1}{2}(k'/k)\sum_\tau\sum_{\eta=\pm1}\int d\varkappa\delta(\mathbf{q}-\varkappa-2\pi\boldsymbol{\tau})\cdot\sum_\alpha \mathcal{S}_{\varkappa,\alpha}{}^{\pm}[\langle n_{\varkappa,\alpha}\rangle\pm\tfrac{1}{2}(1+\eta)]\delta(\epsilon+\eta\epsilon_{\varkappa,\alpha});\tag{5}$$

$$\mathcal{S}_{\varkappa,\alpha}{}^{+}\pm\mathcal{S}_{\varkappa,\alpha}{}^{-}\equiv\tfrac{1}{2}\Big|\sum_\beta S_\beta{}^{\frac{1}{2}}f_\beta\exp[i\mathbf{q}\cdot\boldsymbol{\varrho}_\beta]\cdot[T_{\varkappa,\alpha\beta}{}^{-1}\pm\sigma_\beta T^*{}_{\varkappa,\beta\alpha}]\Big|^2;$$

where the $\varkappa$ integration runs over the above fundamental zone; $\mathbf{e}\equiv|\mathbf{q}|^{-1}\mathbf{q}$; $\boldsymbol{\mu}$ is a unit vector parallel to z; $2\pi\boldsymbol{\tau}$ is a vector of the reciprocal lattice of the $\mathbf{X}_i$; $\langle n_{\varkappa,\alpha}\rangle\equiv\{\exp[\epsilon_{\varkappa,\alpha}/k_BT]-1\}^{-1}$, where k_B is Boltzmann's constant; and $f_\alpha S_\alpha$ is the coherent magnetic scattering amplitude of the αth ion in a unit cell times the Debye-Waller exponential $\exp[-W_\alpha]$.

For $n>1$ and in the case when $K_\alpha\to0$ for $\alpha\gtrless1$, let there be exactly one acoustic spin-wave branch with energies $\epsilon_{\varkappa,1}{}^{(0)}$, which implies $\sum_\beta\sigma_\beta S_\beta\neq0$, and let the zero of $\epsilon_{\varkappa,1}{}^{(0)}$ for $\varkappa=\mathbf{0}$ be isolated in the continuous $\varkappa$ space considered here. Imposing, in addition, the stability condition $\sum_\beta\sigma_\beta S_\beta>0$, one finds

$$\lim_{\varkappa\to0}\lim_{\sigma_\alpha K_\alpha\to0+}\mathcal{S}_{\varkappa,1}{}^{\pm}=\frac{|\sum_\beta\sigma_\beta S_\beta f_\beta{}^{\tau}\exp[2\pi i\boldsymbol{\tau}\cdot\boldsymbol{\varrho}_\beta]|^2}{\sum_\gamma\sigma_\gamma S_\gamma},\tag{6}$$

where $\lim_{\sigma_\alpha K_\alpha\to0+}$ means that this limit is to be taken for all α; $f_\alpha{}^{\tau}\equiv f_\alpha$ for $\mathbf{q}=2\pi\boldsymbol{\tau}$; and the subscript 1 denotes the acoustic branch.

Let us now consider the situation when $n>1$ and $\sigma_\alpha K_\alpha\to0+$ for $\alpha\gtrless1$, supposing that the requirements of the last paragraph are satisfied and that the only scattering processes contributing significantly to $\lim_{\sigma_\alpha K_\alpha\to0+}(d^2\sigma_{01}/d\epsilon d\Omega)$ are those for which $|\epsilon|=\epsilon_{\varkappa,1}{}^{(0)}$ (one-magnon processes involving solely the acoustic branch). In this case, taking $\lim_{\sigma_\alpha K_\alpha\to0+}$ inside the integral sign in (5) and assuming that the values of $|\varkappa|$ contributing to the cross section of interest are so small that $\lim_{\sigma_\alpha K_\alpha\to0+}\mathcal{S}_{\varkappa,1}{}^{\pm}$ can be replaced by the right-hand side of (6) in the pertinent limiting form of the integrand of (5), we are led to an approximate formula for $\lim_{\sigma_\alpha K_\alpha\to0+}(d^2\sigma_{01}/d\epsilon d\Omega)$ with the same structure as the corresponding, formally exact one obtained from (5) for $n=1$ and $\sigma_1=1$, i.e., for simple ferromagnets, where, $\mathcal{S}_{\varkappa,1}{}^{\pm}=S_1(f_1{}^{\tau})^2$. This approximate formula should be of interest for certain ferrimagnets, such as Fe_3O_4.

We shall give detailed derivations of the results of this paper in a future publication, where we shall also discuss some of the experimental implications of the present work.

[4] L. Van Hove, Phys. Rev. **95**, 1375 (1954).

[5] For brevity, we omit the corresponding cross section formula for scattering into a given final neutron spin state.

Computers and Switching

Flux Reversal in Soft Ferromagnetics

E. M. GYORGY
Bell Telephone Laboratories, Incorporated, Murray Hill, New Jersey

Many aspects of flux reversal in soft ferromagnetic materials may be interpreted in terms of three types of flux reversal processes. These three types are domain wall motion, nonuniform rotation, and uniform rotation. It has been shown that in general wall motion is the predominant mechanism for values of the applied magnetic field slightly in excess of the coercive field, that nonuniform rotation predominates for intermediate magnetic fields, and that uniform rotation predominates for large fields. The salient features of these three types of flux reversal are discussed and compared with experimental findings. Special emphasis is given to polycrystalline, square-looped ferrites, and thin Permalloy films. The importance of geometric effects is illustrated in a review of detailed models for the uniform and nonuniform rotational processes. Specific limitations of the existing models are discussed, and possibilities for future advances are briefly outlined.

INTRODUCTION

THE mechanism of rapid flux reversal has recently received considerable attention. At present it is possible to interpret many aspects of flux reversal in terms of three types of reversal processes. These three types are wall motion, nonuniform rotation, and uniform rotation. However, for given experimental conditions, it is not possible at present to determine the relative importance and the detailed behavior of these three types of processes from basic principles. Rather it is necessary to make some rather arbitrary assumptions. This necessity arises at least in part from the fact that it has not been possible to specify the magnetic properties of the material and its imperfections completely. Various calculations of quasi-static reversal have shown that small imperfections play a vital role in the reversal process.[1] Furthermore, even if the material could be completely specified, severe computational difficulties would be encountered in a general solution of the reversal process. In spite of the limitations enumerated, models developed to describe the three flux reversal mechanisms have been quite successful in explaining the switching properties of soft square loop magnetic materials, since for these materials each of the flux reversal mechanisms can be made to predominate under suitable experimental conditions.

For an applied magnetic field slightly in excess of the coercive force, domain wall motion will, in general, be the predominant reversal mechanism. In this case the flux change is accomplished by the motion of Bloch walls which separate the domains of differently oriented magnetization. For suitably oriented single crystals of ferrite, a very simple domain configuration may be achieved which makes it possible to obtain information on the behavior of a moving domain wall.[1,2] However, in extending the domain wall motion concept to polycrystalline materials, Menyuk and Goodenough[3] found it necessary to make certain arbitrary assumptions since the actual domain configuration is not known. To derive the actual domain configuration in a polycrystalline sample would be exceedingly difficult since domain wall nucleation depends critically on imperfections in the material.

For higher values of the applied field a nonuniform rotational model has been proposed.[4–6] This model assumes that the magnetization rotates in such a way that the demagnetizing effects may be neglected. A specific flux configuration has been analyzed to justify neglecting demagnetizing fields.[5] If it is assumed that such a flux configuration actually exists during the reversal process and if the damping constant is arbitrarily treated as a parameter, the nonuniform rotational model is in quite good agreement with the experimental observations made at intermediate values of the applied field.

For still higher values of the applied field the uniform rotational model has been proposed first for thin ferromagnetic films[7–9] and later for ferrite toroids.[10–12] In the case of thin films this model assumes that the magnetization can be represented by a single vector which rotates during reversal. As a result demagnetizing effects cannot be neglected; rather, they play an important part in the switching process. With assumptions similar to the assumptions of the nonuniform rotational model, the

[1] *Solid State Physics*, edited by F. Seitz and D. Turnbull (Academic Press, Inc., New York, 1956), Vol. 3, p. 439.
[2] J. F. Dillon, Jr., and H. E. Earl, Jr., J. Appl. Phys. **30**, 202 (1959).
[3] N. Menyuk and J. B. Goodenough, J. Appl. Phys. **26**, 8 (1955).
[4] E. M. Gyorgy, J. Appl. Phys. **28**, 1011 (1957).
[5] E. M. Gyorgy, J. Appl. Phys. **29**, 1709 (1958).
[6] F. B. Humphrey and E. M. Gyorgy, J. Appl. Phys. **30**, 935 (1959).
[7] R. L. Conger and F. C. Essig, Phys. Rev. **104**, 915 (1956).
[8] C. D. Olson and A. V. Pohm, J. Appl. Phys. **29**, 274 (1958).
[9] D. O. Smith, J. Appl. Phys. **29**, 264 (1958).
[10] W. Lee Shevel, Jr., J. Appl. Phys. **30**, 47S (1959).
[11] E. M. Gyorgy and F. B. Hagedorn, J. Appl. Phys. **30**, 308S (1959).
[12] E. M. Gyorgy and F. B. Hagedorn, J. Appl. Phys. **30**, 1368 (1959).

uniform rotational model describes reasonably well experimental observations made with large applied fields.

Experimentally, the relative importance of the three flux reversal mechanisms is most easily shown by plotting the reciprocal of the switching time as a function of the applied field. To obtain curves of this type the material is first placed in a reproducible remanent point by a large pulse of magnetic field. The flux is then reversed by a second pulse. During this reversal the switching time is measured. Typical results both for thin Permalloy films[6,8] and for ferrite toroids[10–12] are shown in Fig. 1.[13] Experimental plots similar to Fig. 1(b) were first reported by Olson and Pohm[8] who made a systematic study of rapid flux reversal in thin films. It can be seen in Fig. 1 that there are three regions separated by definite breaks in the curve. It is possible to ascribe a reversal mechanism to each region. In the following sections we will describe in detail the specific models proposed for these reversal mechanisms.

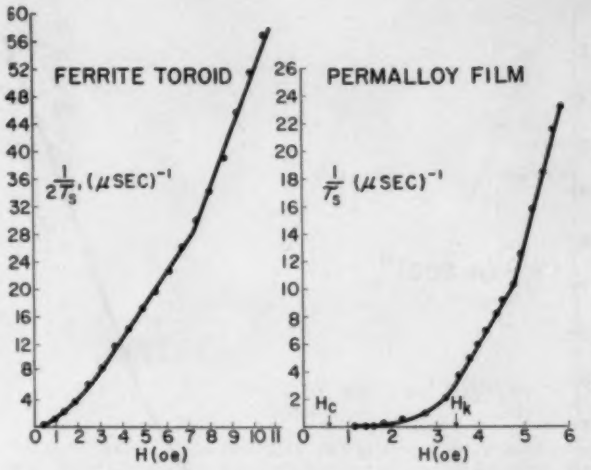

FIG. 1. Inverse of the switching time as a function of the applied field for a ferrite toroid and a 3500 A Permalloy film. The thin film data were taken with a transverse field of 0.2 oe. The definition of the switching time for the toroid data is not the usual one and is discussed in the text.

WALL MOTION

In the domain wall motion region the magnetization is reversed by the motion of many 180° walls. The reversal time is then equal to the reciprocal of the wall velocity times the average distance a wall must move before colliding with a neighboring wall. The distance a wall must move depends of course on the number of walls nucleated. Since walls nucleate at lattice imperfections which are very difficult to specify for a given material, it is in general not possible to determine *a priori* the distance a wall will move. Consequently, the switching time and its dependence on the applied field cannot be predicted. When Menyuk and Goodenough[3] applied the domain wall motion concept to flux reversal in polycrystalline ferrites, they assumed that the number of walls nucleated was independent of the applied field once the field was above the threshold for wall motion. Theoretical studies[1] and experiments performed with single crystals of ferrite[1,2] have shown that the wall velocity depends linearly on the applied magnetic field. As a result, the assumptions of Menyuk and Goodenough lead to a linear relation between the applied field and the reciprocal of the switching time. However, since the actual domain configuration is not known, the details of the reversal process cannot be predicted. Haynes[14] extended the concept of Menyuk and Goodenough by assuming a spatially random distribution of nucleating centers. With this added assumption it is then possible to calculate the rate of change of magnetization predicted by this model with the number of walls nucleated per unit volume and the wall velocity as parameters still to be determined.

The two preceding domain wall motion models lead to a linear relationship between the reciprocal of the switching time and the applied field. This linear relation is often observed experimentally.[3,10] However in some cases, especially in the case of thin Permalloy films, a linear relation is not observed. To account for this nonlinearity the domain wall motion model must be modified. Conger and Essig[15] suggested that the number of walls nucleated is a function of the applied field. However, we will indicate later that at least in the case of Permalloy films their particular formulation assumes more walls than are energetically possible.

As an example to illustrate some of the aspects of the domain wall motion models discussed, we will consider the low speed reversal of a thin Permalloy film. Thin magnetic films have the advantage that the Kerr magneto-optic effect makes it possible to observe the actual domain configuration.[1] Actually, only the static domain structure can be observed, but in the domain wall motion models it is implicitly assumed that the static and dynamic domain configurations are similar. A plot of the inverse reversal time as a function of the applied field is shown in Fig. 2.[16] The region between H_c, the threshold for wall motion, and H_k, the threshold for rotation, is the region of interest here. It may be seen that the relationship between the reciprocal of the switching time and the applied field is not linear in this case, implying that the number of walls nucleated is a function of the applied field. That this is indeed the case is shown in Fig. 3.[16] Figure 3 shows the domain structure of the film obtained when the applied field is terminated after half the flux has been reversed. We may see that as the applied field is increased the number of domain walls in the half-switched configuration is increased. At

[13] In the third region the switching waveforms of the ferrite toroid indicated that the reversal occurred by means of two competing processes.[11,12] In order to measure primarily the faster process the switching time was taken as twice the time required for the reversed flux to increase from 10% to 50% of the total flux switched.

[14] M. K. Haynes, J. Appl. Phys. **29**, 472 (1958).

[15] R. L. Conger and F. C. Essig, J. Appl. Phys. **28**, 855 (1957).

[16] F. B. Hagedorn (unpublished).

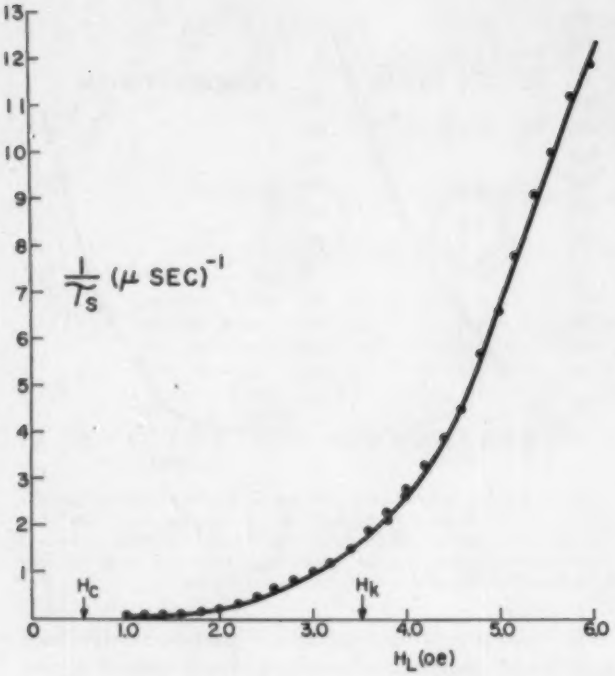

FIG. 2. Inverse of the switching time as a function of the applied field for a 3500 A Permalloy film. Only the slow speed regions are shown. The transverse field was zero.

an applied field of 1.0 oe we have about 6 walls and at 2.6 oe we have about 15 walls. Using this information we may deduce an approximate value of the domain wall velocity. The value we obtain this way is 8×10^3 cm/sec oe with a threshold field for wall motion of 0.4 oe. The coercive force of 0.65 oe is then determined by the field required to nucleate a domain wall and not by the critical field for irreversible wall motion. This is a condition given by Goodenough for obtaining the square hysteresis loop observed.[17]

As we stated earlier, implicit in the domain wall motion models is the assumption that the static and dynamic domain configurations are similar. This implies that the switching process may be interrupted without affecting the flux reversal process when another pulse is applied to complete the switching. Partial switching experiments with tape cores[3] and thin Permalloy films[18] have shown that for applied fields slightly in excess of the coercive force, this prediction of the domain wall motion model is verified by experiment. In Fig. 4 we show the partial switching results in the domain wall motion region for the ferrite toroid discussed in connection with Fig. 1. The first pulse was terminated after reversing approximately half the available flux. The amplitude of both pulses was 0.46 oe. From Fig. 4 it may be seen that the two partial waveforms reproduce the complete waveform fairly well.

We may conclude our discussion of the domain-wall motion models by noting that for fields slightly in excess of threshold, these models fit many of the experimental observations obtained with ferrite toroids and thin films. However, since in general neither the actual domain configuration nor its dependence on the applied field is known, these models do not permit us to make detailed predictions of the flux reversal in a specific material.

NONUNIFORM ROTATION

As has been shown in Figs. 1 and 2, as the applied field is increased region II appears. In this region the relationship between the reciprocal of the switching time and the applied field is linear. For the case of

(a)

(b)

FIG. 3. A photograph of the domain configuration of the thin film discussed in connection with Fig. 2. The applied magnetic field pulses of 1.0 oe and 2.6 oe respectively were terminated when half the flux was reversed. The film is 0.187 in. by 0.400 in.

[17] J. B. Goodenough, Phys. Rev. **95**, 917 (1954).
[18] F. B. Hagedorn, J. Appl. Phys. **30**, 254S (1959).

Permalloy films this region cannot be explained by assuming, as was suggested by Conger and Essig,[15] that the number of walls nucleated has increased to the point where the whole film is effectively filled by domain walls. In fact by calculating the energy required to form a domain wall,[19] it can be shown easily that for an applied field of 3 oe only about 0.1% of the area of a 2000 A film can be in walls at once. The relatively high-domain wall energies calculated are the result of the demagnetizing effects at the surfaces of the film, which make no significant contribution to the energy of a wall in bulk material.

That the flux reversal mechanism in this region differs from the wall motion mechanism predominant in the lower region is also shown by the partial switching experiments. If the switching process in a thin film is interrupted, the partial switching waveforms reproduce the complete waveform in the domain wall motion region but not in the higher drive region being considered in this section.[18] Similar experiments have been performed with ferrite toroids.[20] As an example, in Fig. 5 we show the results obtained with the same toroid discussed in connection with Figs. 1 and 4. The applied field was 3.1 oe which is well in the second region shown in Fig. 1. The first pulse again reversed half the available flux. It is easily seen that the rate of change of magnetization after the interruption is slower than would be predicted from the uninterrupted waveform.

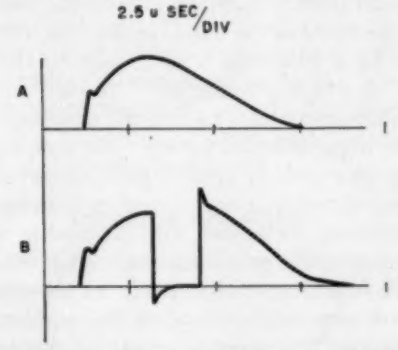

FIG. 4. The complete and partial waveforms for the ferrite toroid discussed in connection with Fig. 1. The applied field was 0.46 oe. The instrument response time was 0.03 μsec.

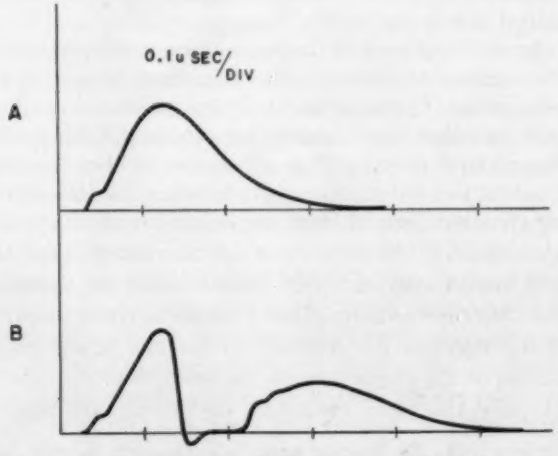

FIG. 5. The complete and partial waveforms for the ferrite toroid discussed in connection with Fig. 1. The applied field was 3.10 oe. The instrument response time was 0.01 μsec.

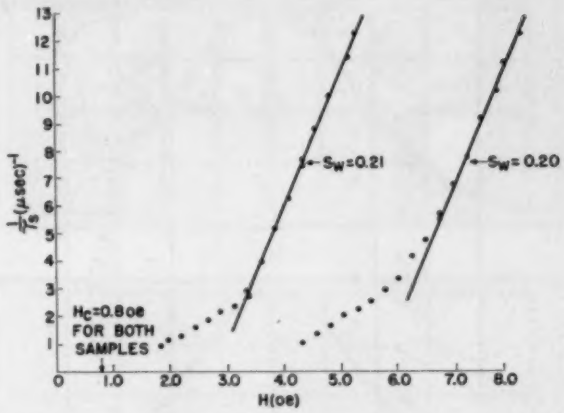

FIG. 6. Inverse of the switching time as a function of the applied field for two Permalloy films evaporated at normal incidence and at 30° incidence respectively. Both films were 2400 A thick. The anisotropy fields were 3.0 and 6.2 oe, respectively. The transverse field was zero.

One of the important experimental observations concerning the second region is that the inverse slope, or switching coefficient, of the plot of the reciprocal of the switching time as a function of the applied field is relatively independent of the material under consideration. Ferrites of a wide selection of chemical compositions and a large variation in grain size, garnets, Permalloy tape, and thin Permalloy films of different compositions and thicknesses in most cases[21] have switching coefficients of about 0.2 oe μsec.[4,6,10] To illustrate this fact here the switching time measurements of two Permalloy films evaporated at different angles of incidence are shown in Fig. 6.[16] As has been shown by Smith[22] larger angles of incidence during the evaporation lead to higher values of the uniaxial anisotropy. The switching coefficient is

[19] L. Néel, Compt. rend. **241**, 533 (1956).

[20] E. M. Gyorgy and J. L. Rogers, *Proceedings of the Conference on Magnetism and Magnetic Materials, Boston, 1956* (American Institute of Electrical Engineers, New York, 1957), AIEE Spec. Publ. T-91, p. 637.

[21] In the cases reported where the switching coefficient is significantly larger than 0.2 oe μsec the measurements may not have been taken at sufficiently large applied fields to make certain that nonuniform rotation rather than wall motion was the predominant mechanism. It should also be noted that the thin film measurements referred to here were taken with zero transverse field. The measured thin film switching coefficients in reference 8 decrease more rapidly with the application of a transverse field than is predicted by the dependence of the nonuniform rotational switching coefficient on the initial angle. This discrepancy may be resolved by noting that the flux reversal process in region II is no longer pure nonuniform rotation as the transverse field is increased. F. B. Humphrey, J. Appl. Phys. **29**, 284 (1958) has pointed out that the reversal process in region II with nonzero transverse field is best described as a mixture of uniform and nonuniform rotation.

[22] D. O. Smith, J. Appl. Phys. **30**, 264S (1959).

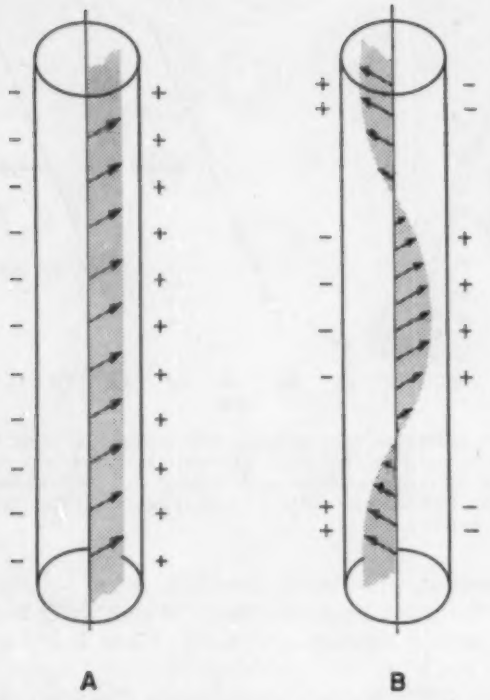

FIG. 7. A schematic representation of the simple uniform and spiral mode in a magnetic cylinder.

seen, however, to be unchanged and equal to approximately 0.2 oe μsec for both films. This general invariance of the switching coefficient can be accounted for in terms of the nonuniform rotational model, the fundamentals of which we will review next. Since a specific configuration has been developed for ferrite toroids,[5] we will limit ourselves to that case.

The nonuniform rotational model assumes that the magnetization rotates simultaneously but in such a way that demagnetizing effects arising from the boundary can be neglected. If the magnetization rotated uniformly as shown in Fig. 7(a), the surface poles arising from the discontinuity at the boundary would give rise to large demagnetizing effects. In fact, the threshold field for this type of rotation is about 10^3 oe, three orders of magnitude higher than the threshold field usually encountered experimentally. For simplicity we have approximated the toroid by an infinite cylinder. However, if we postulate a spiral flux configuration as is shown schematically in Fig. 7(b), the discontinuity at the boundary leads to poles of alternating signs. If the period of the surface poles is much smaller than the diameter of the cylinder, the magnetic field due to these poles will be negligible throughout most of the volume of the cylinder. This observation has been verified by a detailed calculation of the spiral model.[5] Hence we may treat the rotation in this region as occurring in the applied field only The crystalline anisotropy fields have been neglected. If the magnetization is rotating under the influence of the applied field only, the solution to the equation of motion of the magnetization vector is relatively simple.

The equation of motion we use to describe the flux reversal is the Gilbert[23] modification of the Landau-Lifshitz equation. The Gilbert equation assumes that the damping force resulting from the loss of energy of the magnetization to the lattice is proportional to the "velocity" of the magnetization. As a result the motion of the magnetization vector can be described as a precession about the applied field in a viscous medium. The viscous medium or energy loss is specified by one damping constant. Without any calculations we may deduce some of the effects of the energy loss on the motion of the magnetization. If there is no energy loss, that is, if the damping constant is zero, the magnetization will just precess about the applied field at the initial angle. In this case the reversal time would be infinite. If the damping constant increased to infinity, or the medium became infinitely viscous, all motion of the magnetization would cease. In this case too, the reversal time would be infinite. Since the reversal time is infinite for zero and infinite damping constants, there must be at least one value of the damping for which the reversal time will be a minimum with respect to the damping constant. A simple calculation[5,24] verifies the existence of the minimum and shows that the equation of motion leads to a linear relation between the reciprocal of the switching time and the applied field. Consequently, the minimum reversal time corresponds to a minimum value of the switching coefficient. The calculation also allows us to evaluate the minimum switching coefficient in terms of a function which depends on the exact definition of switching time used and on the initial angle of the magnetization. The dependence of this function on the initial angle is relatively insensitive, so we may obtain an approximate value of the minimum switching coefficient. This value is about 0.2 oe μsec which is in favorable agreement with the experimental values obtained in this region.[4,10]

In the framework of the nonuniform rotational model, the agreement between the minimum switching coefficient and the experimentally measured value allows us to calculate the damping constant applicable to this flux reversal process. This calculation yields a damping constant two orders of magnitude larger than the damping constant derived from low power microwave measurements. This observation is not unexpected, since the spin wave theory of Suhl[25] indicates that the apparent damping constant is in general not an intrinsic property of the material but depends rather on the modes of motion of the magnetization. However, why the experimentally measured switching coefficients are usually

[23] T. L. Gilbert and J. M. Kelly, *Proceedings of the Conference on Magnetism and Magnetic Materials, Pittsburgh, 1955* (American Institute of Electrical Engineers, New York, 1955), AIEE Spec. Publ. T-78, p. 253.
[24] R. Kikuchi, J. Appl. Phys. **27**, 1352 (1956).
[25] H. Suhl, Proc. Inst. Radio Engrs. **44**, 1270 (1956).

near the minimum value cannot be understood at present.

The nonuniform rotational model also yields an expression for the shape of the switching transient. The calculated shape agrees fairly well with the observed shape obtained with square-loop material.[4] In Fig. 8 the observed shape is shown in comparison with the calculated shape. The data was taken with a MgMn ferrite and with applied fields ranging from 2.5 oe [Fig. 8(a)] to 5.0 oe [Fig. 8(c)]. The switching time varied from 0.64 μsec to 0.10 μsec. The agreement is good except for the initial part of the pulse. This initial deviation can be attributed to another mechanism which switches a small fraction of the total flux. It has been observed that for less square materials the contribution of the second mechanism is larger.[26] Perhaps the poor agreement with the calculated pulse shapes reported by Shevel[10] can be attributed to this fact.

We may summarize our discussion of nonuniform rotation by noting that if we assume that a flux configuration such as the spiral mode actually exists and that the appropriate damping constant has a value which yields the minimum switching time, the results of this model are in quite good agreement with experiment. However, the threshold fields for nonuniform rotation cannot be predicted correctly. This discrepancy is presumably the result of neglecting the crystalline anisotropy of the individual grains.

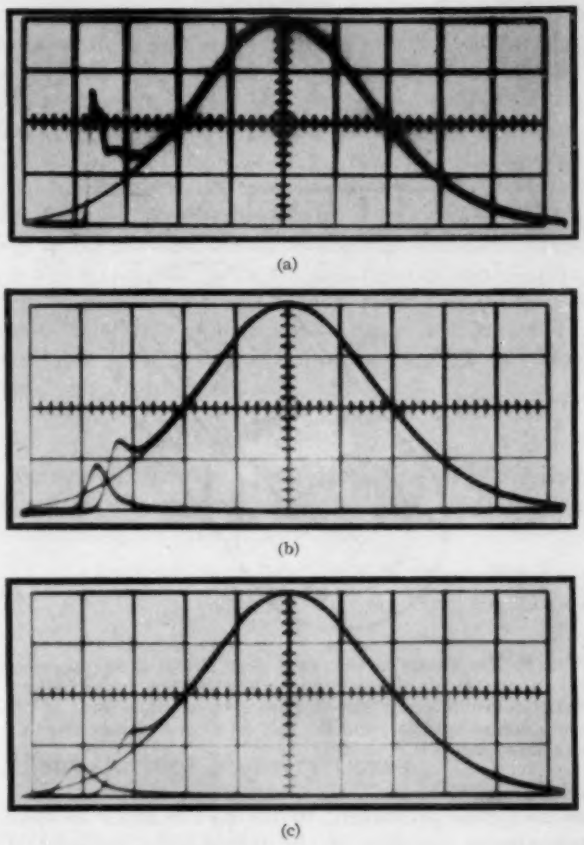

FIG. 8. Photographs of the observed and calculated pulse shapes for a thin-walled ferrite toroid. The calculated shape is inscribed on the oscilloscope graticule. The applied fields were 2.5, 4.2, and 5.0 oe, respectively.

UNIFORM ROTATION

The effect of the demagnetizing fields has been assumed negligible in the nonuniform rotational modes. It is evident that for many flux configurations the demagnetizing fields cannot be neglected. In fact, it can be shown that for some configurations the interaction of the demagnetizing fields and the magnetization leads to flux reversal times shorter than would be possible in the absence of demagnetizing effects. This type of interaction has been suggested as the reason that region III in Fig. 1 has a switching coefficient less than the minimum predicted by the nonuniform rotational model. An illustration of this interaction between the magnetization and the demagnetizing field is the uniform rotational reversal of a thin film which was first discussed by Conger.[7]

In this model the magnetization, which is uniform over the film and initially in the plane of the film, tends to precess about the applied field. This precession gives rise to a small component of the magnetization which is normal to the plane of the film. The discontinuity of this normal component at the surfaces of the film leads to a demagnetizing field perpendicular to the plane of the film. Energy considerations permit an estimate of the demagnetizing field. For an applied field of 2 oe and an isotropic thin film, the demagnetizing field could be of the order of 100 oe in Permalloy films. The fast reversal process may therefore be interpreted physically as a precession of the magnetization in the plane of the film around this demagnetizing field in a half-period (for small damping) of 2×10^{-9} sec. In contrast to the nonuniform mode, the uniform reversal mechanism does not depend directly on the presence of damping. If the damping constant is small, flux reversal will take place quite rapidly but the magnetization will oscillate about its equilibrium value.

The qualitative observations of the preceding paragraph are verified by the calculations of Kikuchi[24] and Smith.[9] Since the precession about the applied field and the precession about the demagnetizing field actually occur simultaneously, the solution of the equation of motion is relatively complicated and requires the aid of a computer. From Kikuchi's results it is possible to estimate that for most materials currently under investigation the minimum value of the switching coefficient is approximately 10^{-3} oe μsec. This is in close agreement with the value obtained from the semiquantative approach outlined above.

A reversal mode analogous to the uniform mode in thin films has been suggested for ferrite toroids.[10–12] As

[26] F. B. Hagedorn and E. M. Gyorgy, J. Appl. Phys. 31, 398S (1960).

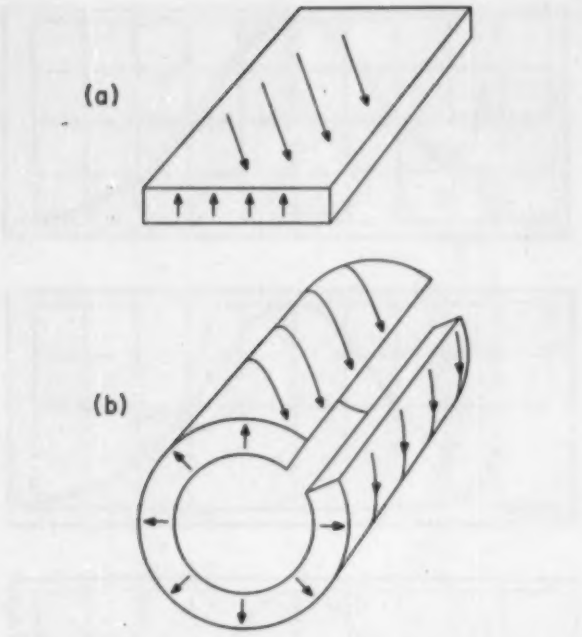

FIG. 9. The arrows in the plane sheet shown in (a) represent the two components of magnetization in a thin film during uniform rotational flux reversal. The film has been wrapped up in (b) to form a hollow cylinder, and the flux lines become helical with a radial component.

has been done previously, to discuss this mode we shall approximate the case of the toroid by a cylinder of infinite length. The flux configuration proposed is helical with a small radial component. The relationship of this mode to uniform rotation in films can be seen in Fig. 9. In Fig. 9(a) we have represented the thin film at an intermediate state of the uniform rotational process. The arrows represent the two components of the magnetization in the film. In Fig. 9(b) we show the film wrapped up to form a hollow cylinder, and the flux lines have now become helical with a small radial component. We then superpose many such hollow cylinders of decreasing radii in order to obtain a solid cylinder. Analysis of this model to a very good approximation leads to results identical with those obtained from isotropic thin films.[12]

The uniformity suggested by this mode is not essential to the model, since as has been pointed out by Shevel,[10] the magnetization in each hollow cylinder is independent of the magnetization in the other cylinders. Hence the mode could consist equally well of layers of right- and left-handed helices. However, exchange effects which were tacitly neglected by Shevel will in very small samples tend to favor the more uniform configuration.

The uniform rotational model gives a relatively satisfactory explanation for the existence of the high speed or third region shown in Fig. 1. The model, however, does not correctly predict the threshold for uniform rotation.[6,12] Considering that the model neglects the detailed structure of the magnetic material, this discrepancy is not surprising. For thin films the uniform rotational model predicts that during the switching process the total magnetization will appear perpendicular to the applied field. This transverse switching transient is indeed observed and is verification of the general features of the model.[8] However, detailed agreement between the theoretical and observed switching wave forms is rather poor. The lack of agreement can be attributed to a number of causes. Neither the actual structure of the magnetic material nor the damping constant applicable to this process are known. The difficulties of measuring the very rapid flux reversal in this region introduces some uncertainty in the experimental results. Finally, in many cases the flux reversal does not appear to take place by only one mechanism. A fraction of the flux seems to reverse by a slower mechanism. The presence of two competing processes has been especially apparent in ferrites.[12]

CONCLUSION

As has been indicated in the preceding discussion, the domain wall motion, nonuniform rotational and uniform rotational models make it possible to interpret most features of the flux reversal process except for threshold fields. However, these models contain a number of arbitrary assumptions. To conclude, we will examine some of the possibilities of eliminating these assumptions. In the nonuniform and uniform rotational models it was postulated that these flux configurations actually existed during reversal. This assumption could be eliminated if the problem could be attacked by the methods of micromagnetics outlined by Brown.[27] By requiring that the variation of the total energy be zero for small displacements of the magnetization, Brown obtains an equation describing the possible static reversal modes. In order to obtain a solution the equation must be linearized, thereby making the solution only valid for small angles. Using this approach, Aharoni and Shtrikman[28] have obtained modes for the quasi-static flux reversal of a cylinder which are very similar to the rotational modes discussed here for the dynamic flux reversal. If, as has been suggested by Brown, the methods of micromagnetics were extended to the dynamic reversal, a systematic theoretical study of reversal modes would be possible. However, a calculation of Aharoni[29] shows that the behavior of these modes is very sensitive to imperfections in the material. Since it is difficult to specify the imperfections present in a sample, the reversal modes obtained by the foregoing analysis would be primarily applicable to experiments performed with nearly perfect single crystals.

Most of the experiments concerning flux reversal have been carried out with polycrystals. The effect of the crystalline anisotropy of the individual crystallites of

[27] W. F. Brown, Jr., J. Appl. Phys. **30**, 62S (1959).
[28] A. Aharoni and S. Shtrikman, Phys. Rev. **109**, 1522 (1958).
[29] A. Aharoni, J. Appl. Phys. **30**, 70S (1959).

ferrite has been included in the two rotational models only by the *ad hoc* introduction of a threshold field for rotation. At present the value of this threshold field cannot be predicted from the magnetic properties of the ferrite material. The success of the rotational models seems to indicate that it should be possible to treat the effect of the individual grains by a simple average, but no progress in this direction has been reported. In the case of thin films the effect of the crystalline structure is presumably smaller, and Olson and Pohm[6] have found good agreement between the threshold predicted from the uniaxial anisotropy and the threshold for nonuniform rotation. However, according to the model used by Olson and Pohm, this also should have been the threshold for uniform rotation. Actually the threshold for uniform rotation is higher, and this discrepancy has not been satisfactorily explained.[6]

In the treatment of rotational flux reversal the damping constant was treated as an adjustable parameter. A number of experiments which indicate that the damping constant is not an intrinsic property of the material but rather depends on the modes of motion of the magnetization give a qualitative justification for this assumption. For example, the spin waves induced by high microwave power[25] or the surface roughness of the sample[30] give rise to large apparent damping constants. The increase of the apparent microwave damping constant has been treated theoretically by Suhl.[25] So far it has not been possible to extend a calculation of this type to the problem of flux reversal. In summary, then, it may be said that while the flux reversal models give a quite satisfactory explanation of the experimental results, relatively sophisticated methods will have to be employed to put the assumptions implicit in these models on a firm theoretical basis.

ACKNOWLEDGMENTS

I would like to thank F. B. Hagedorn for permission to use his unpublished data and J. K. Galt for his critical reading of the manuscript.

[30] R. C. Le Craw, E. G. Spencer, and C. S. Porter, Phys. Rev. **110**, 1311 (1959).

JOURNAL OF APPLIED PHYSICS SUPPLEMENT TO VOL. 31, NO. 5 MAY, 1960

Development of High-Speed Coincident Current Memory Cores

BARLANE R. EICHBAUM
Aeronutronic Division of Ford Motor Company, Newport Beach, California

In present day large computers the memory cycle is on the order of 8 μsec requiring memory cores to switch in 1.5 μsec with a full select drive of approximately 0.7 amp. Memory cores used in such a computer can be fabricated from a $MgO \cdot MnO \cdot Fe_2O_3$ ferrite material. Using the same ferrite material, memory cores have been developed which have a switching speed of 0.4 μsec with a full select drive of approximately 1.0 amp. The procedure used to develop these high-speed coincident current memory elements is described. The drive current is reduced to approximately 0.7 amp when partial substitutions of CaO and Cr_2O_3 are made for MgO and Fe_2O_3, respectively, in the $MgO \cdot MnO \cdot Fe_2O_3$ core composition.

A FEW years ago large high-speed computers had a memory cycle of 8–10 μsec. The memory in these computers consists of ferrite cores 50 mils i.d. by 80 mils o.d. which switch in 1.5 μsec when operating under 10% marginal conditions (670/410 ma, 200 mμsec rise time pulses).[1] The object of the research being described was to develop a coincident current memory core having a switching time of approximately 0.4 μsec with a full select drive of approximately 1 amp so that the computer memory cycle could be reduced by a factor of four to approximately 2 μsec.

A typical ferrite composition which can be used to fabricate the 50–80 memory cores (for the large high-speed computer) by the carbonate decomposition method[2] consists of 37.5 $MgO \cdot 22.5$ $MnO \cdot 40$ Fe_2O_3 (MMF). Such memory cores have the characteristics shown for Run No. 1 in Table I. The switching coefficient of 0.95 oe-μsec was determined using Goodenough and Menyuk's equation,[3]

$$S_w = T_s(H - H_0),$$

where S_w is the switching coefficient, T_s is the switching time, H is the applied magnetic field, and H_0 is the operating threshold field.

The first step in an attempt to increase the speed of the MMF 50–80 toroids was to increase the coercivity to between 3.5 and 4.0 oe and still retain square loop characteristics.[1] This was accomplished through process alterations. Since the switching coefficient remained at 0.95 oe μsec, a switching speed of 0.5 μsec was obtained with a full select drive of 1.9 amp. This result is plotted as Run No. 2 and compared with the plot of Run No. 1 in Fig. 1.

By using cores similar to those used in Run No. 2,

[1] W. W. Lawrence, Jr., *Proceedings of the eastern joint computer conference* (American Institute of Electrical Engineers, New York, 1957), Spec. Publ. T-92, pp. 1–3.
[2] G. Economos, J. Am. Ceram. Soc. **38**, 353 (1955).
[3] N. Menyuk and J. Goodenough, J. Appl. Phys. **26**, 8 (1955).

TABLE I. Ferrite core characteristics tested under coincident current conditions[a]

Run No.	Composition	Core size i.d./o.d. (mils)	H_c (oe) 60 cycle	Pulse rise time (mμsec)	Drive[d] current (ma)	Switching time (μsec)	S_w (oe-μsec)
1	MMF[b]	50–80	1.2	200	670/410	1.5	0.95
2	MMF	50–80	3.5	200	1900/1160	0.5	0.95
3	MMF	50–80	3.5	100	1800/1100	0.46	0.82
4	MMF	30–50	3.5	100	1050/640	0.4	0.60
5	MMF-2C[c]	30–50	2.8	100	735/445	0.42	0.50

[a] Evaluations at 40°C.
[b] MMF (37.5 MgO·22.5 MnO·40 Fe_2O_3).
[c] MMF-2C (5 CaO·32.5 MgO·22.5 MnO·35 Fe_2O_3·5 Cr_2O_3).
[d] 10% Marginal drive currents.

the drive current rise time was increased from 200 to 100 mμsec with the result that T_s was reduced to 0.46 μsec with a decreased drive requirement of 1.8 amp full select as shown for Run No. 3. The switching coefficient value decreased with this faster rise time to 0.82 from 0.95 oe-μsec.[4–6]

In order to further reduce the drive requirements the MMF material was used to fabricate 30-mil i.d.–50-mil o.d. toroids to have an H_c of 3.5 oe. By reducing the core radius, the field per unit current for the smaller core is increased, and the drive requirements are decreased. This was the case as can be seen in Table I for Run No. 4. These toroids require 1.05 amp full select to switch in 0.4 μsec. The performance of these cores satisfied the original objectives of this research. After this investigation with MMF material, at least four other compositions were found to perform in a similar manner. It should be noted that the rV_1 to wV_s ratio (which is essentially a signal-to-noise ratio since rV_1 is a disturbed "one" output and wV_s is a disturbed "zero" output) is of the order of 3.3 to 1. A reasonable signal-to-noise ratio is also a requirement of these memory cores. The switching coefficient was reduced to 0.60 oe μsec.

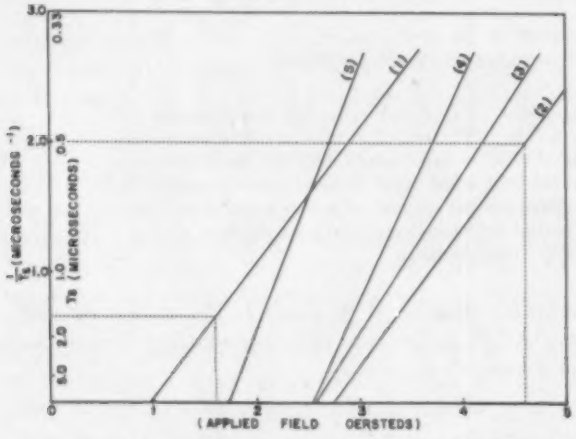

FIG. 1. Switching coefficient curves (H vs $1/T_s$) of MMF and MMF-2C (numbers correspond to Run No. in Table I).

In order to further reduce the drive requirements with no additional changes in geometry it was necessary to alter the chemical composition. One such improvement was made by substituting 5% CaO for MgO and 5% Cr_2O_3 for Fe_2O_3 so as to have a chemical composition (MMF-2C) of 5 CaO· 32.5 MgO·22.5 MnO 35 Fe_2O_3·5 Cr_2O_3. Toroids (30–50) were processed to have a square loop and H_c of 2.8 oe. These toroids switched in 0.42 μsec with a 735/445 amp-drive as shown for Run No. 5. Such toroids have a S_w of 0.5 oe-μsec. Their drive requirement is approaching those of the original Run No. 1 toroids yet they switch almost four times as fast (1.5 vs 0.4 μsec).

In general, high speeds have been obtained with coincident current memory cores through the procedure of increasing H_c, increasing the pulse rise time speed, decreasing the core size, and altering the ferrite chemical composition.

ACKNOWLEDGMENTS

The author would like to acknowledge P. Haddon, R. Booth, and R. Johnson for their assistance and suggestions during the course of this research.

[4] B. R. Eichbaum, J. Appl. Phys. Suppl 30, 49S–52S (1959).
[5] R. Lamy and K. Strong (private communications in 1957).
[6] W. L. Shevel, Jr., J. Appl. Phys. Suppl 30, 47S–48S (1959).

Operation of Magnetic Film Parametrons in the 100- to 500-Mc Regions*

A. V. Pohm, A. A. Read, R. M. Stewart, Jr., and R. F. Schauer
Electrical Engineering Department and Engineering Experiment Station, Iowa State University of Science and Technology, Ames, Iowa

An analysis of the behavior of thin magnetic films of Permalloy when used as time variable inductors has been made in terms of a modified Landau-Lifshitz equation. These results show that parametrons using time variable magnetic film inductors can be made to operate at reasonable power levels with large grains per cycle at oscillating frequencies in the 100- to 500-Mc region.

A way of fabricating magnetic film parametrons with strip line techniques is shown. Calculations indicate that units with dissipations in the 10 mw range are feasible with existing techniques for operation in the 100- to 500-Mc region.

Ways of advantageously using capacitive coupling between parametron units is indicated in which the two new subharmonic states of a magnetic film parametron created by a bias reversel are used.

I. INTRODUCTION

THE authors[1] recently reported on the experimental operation of magnetic film parametrons with oscillating frequencies ranging from about 3 to 15 Mc. The results of this investigation showed that magnetic film parametrons are capable of operating at low power levels with large gains per cycle, that they possess logical flexibility, are reliable, and are amenable to simple fabrication techniques. Because of equipment limitations, measurements were made only up to oscillating frequencies of 15 Mc.

It is the intent of this paper to show analytically that with suitable Permalloy films and proper fabrication techniques, high performance, low-power consumption magnetic-film parametrons can be constructed for operation in the 100- to 500-Mc oscillating frequency range.

II. ANALYSIS

Let one consider a single domain, thin magnetic film with a very small uniaxial anisotropy axis in the plane of the film with an easy or rest direction $\phi=0$, $\psi=0$, where ϕ represent rotation of the magnetization M (gauss) away from its rest position in the plane of the film and ψ represents the rotation of the magnetization out of the plane of the film. Consider a pump field Hp (oe) from a pump winding applied along the rest direction with a constant component Ho and a time varying component $hp(t)$ such that $(hp)\leqslant Ho$. Also consider a signal field $hs(t)$ (oe) applied perpendicular to the rest direction in the plane of the film due to a signal current $i_s(t)$ in a signal winding. Under the assumptions that $\cos\psi\approx 1$, $\sin\psi\approx\psi$, $4\pi M\gg Hp$, Hs, and that Ho is much larger than the anistropy field, the dynamic magnetic behavior in the plane of the film as described by a modified Landau-Lifshitz equation[2] is given by

$$\frac{(1+\alpha^2)^2}{(\nu M)^2}\frac{d^2\phi}{dt^2}+\frac{\alpha 4\pi(1+\alpha^2)}{(\nu M)}\frac{d\phi}{dt}+\frac{4\pi(1+\alpha^2)}{M}[(Ho+hp)\sin\phi-hs\cos\phi)]+\frac{(1+\alpha^2)}{(\nu M)}\frac{\alpha}{M}\frac{d}{dt}[(Ho+hp)\sin\phi-hs\cos\phi]=0, \quad (1)$$

where ν is the gyromagnetic ratio (1.76×10^7 per oe sec) and α is the phenomenological damping constant. For 80–20 Permalloy, α has a value of about 0.015[3] and $4\pi M$ a value of about 10 000 gauss.[3]

Consequently, for frequencies less than 10 Kmc, the last term of (1) may be neglected. By making the substitutions $hs=K_1 i_s$, and $\lambda=\lambda_M\sin\phi$ (flux linkages due to the magnetic material) (1) reduces to

$$\frac{1}{4\pi\nu^2 M}\left\{\frac{\ddot{\lambda}}{\lambda m[1+(\lambda^2/\lambda m^2)]}+\frac{\lambda\dot{\lambda}^2}{\lambda^3 m[1+(\lambda^2/\lambda m^2)]^2}\right\}+\frac{\alpha}{\nu}\frac{\dot{\lambda}}{\lambda m[1+(\lambda^2/\lambda m^2)]}+\frac{(Ho+hp)}{(1-\lambda^2/\lambda m^2)^{\frac{1}{2}}}\frac{\lambda}{\lambda m}=K_1 i_s. \quad (2)$$

Consider that the signal winding is shunted by a capacitor C and a resistance R_L. If L_a is the air inductance of the signal winding, the nodal current equation becomes

$$i_s+\frac{1}{R_L}(\dot{\lambda}-L_a\dot{i}_s)+C(\ddot{\lambda}-L_a\ddot{i}_s)=0. \quad (3)$$

For simplicity, assume that the air inductance is small in comparison to the inductance due to the material $L_0=\lambda K_1/Ho\gg L_a$. Also choose C so that the resonant frequency is less than $\frac{1}{2}$ the frequency of the low-level

* The research reported in this paper was supported by a National Science Foundation Grant.

[1] A. V. Pohm, A. A. Read, R. M. Stewart, Jr., and R. F. Schauer, Proc. Natl. Electronics Conf. (October, 1959) (to be published).

[2] P. R. Gillette and K. Oshima, J. Appl. Phys. **29**, 529 (1958).

[3] D. O. Smith, J. Appl. Phys. **29**, 264 (1958).

magnetic resonance

$$4\pi\nu^2 MH_0 \geq \frac{4}{[L_a+(\lambda mK_1/H_0)]C}.$$

Equations (2) and (3) then simplify to the following neglecting the nonlinearities in the higher order terms and expanding the $1/(1-\lambda^2/\lambda m^2)$ factor of the $(Ho+hp)/(1-\lambda^2/\lambda m^2)^{\frac{1}{2}}(\lambda/\lambda m)$ term:

$$C\ddot{\lambda}+(1/R_e)\dot{\lambda}(+1/L_0)(1+hp/Ho)(\lambda+\lambda^3/2\lambda_m^2)=0, \quad (4)$$

where $1/R_e=1/R_L+(\alpha/\nu LoHo)$. Let $W_0=1/(LoC)^{\frac{1}{2}}$, $Qe=Re/W_0L_0$ and $G=(hpm/2Ho)Qe$, where the time varying pump field is given by $hp(t)=hpm\sin 2\omega t$.

If we assume an exponentially increasing form for $\lambda(t)$ at low amplitudes of λ, where the cubic term can be neglected,

$$\lambda(t)=Ae^{+\sigma wt/2\pi}\cos(wt+\theta), \quad (5)$$

and on substituting into (4) and equating $\sin wt$ and $\cos wt$ terms while neglecting higher harmonics, one obtains[1]

$$g\approx\pi[(hpm/2Ho)-(1/Qe)], \quad \theta\approx 0. \quad (6)$$

One notes if $hpm=Ho$, the pump field introduces a "negative Q" equal to two. If no losses or air inductance were present the maximum gain in voltage amplitude per cycle would be over 4.5. Notice that the Q of material itself (Qm) for operation at w_0 is given by

$$Qm=\nu L_0H_0/\alpha W_0L_0. \quad (7)$$

By using the value $\alpha=0.015$ for permalloy, one finds the necessary bias field to maintain a certain material Qm as a function of frequency is given by

$$Ho=0.53Qmf \text{ (in 100 Mc)}. \quad (8)$$

For a $Qm\geq 6$, the value of Ho given by (8) is adequate in the 100–500 Mc range to maintain the magnetic resonance frequency above the pump frequency. Note that for a Qm of 7.5, fields strengths (Ho) ranging from 4 oersteds to 20 are required as the oscillating frequency changes from 100 to 500 Mc.

III. PARAMETRON DESIGN

Consider the exploded view of Fig. 1 of a way in which a magnetic film parametron can be constructed using a pair of films around etched wiring in a three wire strip line technique for operation at 500 Mc.

The calculated low-level inductance from the "tapered" pair of magnetic films in the sandwich as indicated in Fig. 1(B) for the dimensions shown is about 1×10^{-9} h with an "air inductance" of about 0.5×10^{-9}. For operation at 500 Mc with the insulation thicknesses shown, capacitive tabs of about 0.8 cm² are required.

For a maximum pump field $hpm=Ho=20$ oe, and an assumed over-all Qe of 5, the continuous-operation power consumption was calculated to be about 20 mw for the pump frequency equal to $2\omega o$. Calculation of eddy current and magnetic losses indicates the assumed $Qe=5$ is conservative. The power consumption was calculated by solving (4) for a steady-state solution for the value of pump field and frequency assumed. One finds signal saturation occurs at a value of the magnetic flux linkage (λ) equal to about $0.7\lambda m$. This agrees with the results measured for lower frequency operation.[1] Since the harmonic terms are small, a straight forward ac circuit calculation yields the power dissipation.

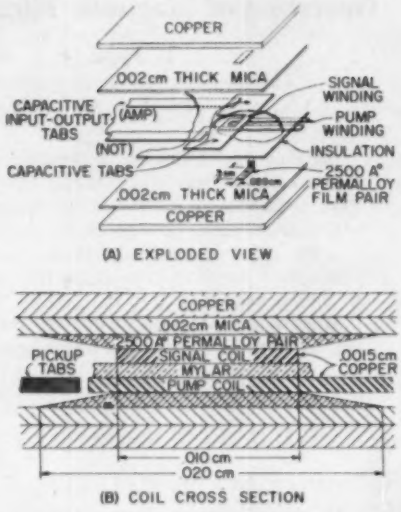

FIG. 1. Film pair, etched wire strip line parametron.

One can note from Fig. 1 that the etched circuit lends itself to capacitive coupling between elements rather than necessitating resistive coupling with solder or other joints. This type of coupling can be used because a reversal of the bias on a film gives rise to subharmonic states shifted 90° from those obtained without bias reversal.[1] Thus the near 90° phase shift introduced by the small capacitive coupling is just right to couple into a parametron with its bias reversed. Notice that by coupling to one tab or the other an amplifying or complementing function can be achieved.

IV. CONCLUSIONS

Calculations indicate that by using the favorable geometry of thin Permalloy films in a strip line arrangement, it is possible to construct high-performance magnetic-film parametrons for operation in the 100 to 500 Mc oscillating frequency region with present techniques. Power dissipations in the 10- to 20-mw range for continuous operation are feasible.

By using the two additional subharmonic phase states obtained by a bias reversal, capacitive coupling without the necessity of connections can be easily achieved.

Because operating characteristics of the Permalloy material are primarily determined by the geometry and bias field, the material should be easy to make. Because of the large hysteresis region,[1] three state operation should also be possible.

JOURNAL OF APPLIED PHYSICS SUPPLEMENT TO VOL. 31, NO. 5 MAY, 1960

Ferrite Films—New Logic and Storage Devices

J. M. Brownlow, W. L. Shevel, Jr., and O. A. Gutwin
IBM *Research Laboratory, Poughkeepsie, New York*

Magnetic devices for storage and switching applications in digital computers have been fabricated in the form of open flux path elements. The geometry employed is that of a planar film with thicknesses in the range of 5 to 50 μ and other dimensions in the fractional inch range. These elements have the advantages of a ferrite composition and of open flux paths without many of the disadvantages present in similar metallic devices. For use in storage systems, these devices possess excellent squareness characteristics and have coincident selection times comparable with ferrite-toroidal devices. Properties of these devices are given in terms of switching curves, low-frequency hysteresis loops, and one to zero-signal ratios. Other aspects that are discussed include disturb sensitivity of storage elements, heating effects due to high pulse repetition frequency, and mechanical properties. For each of these, comparison is made with other types of magnetic elements such as toroids and metallic films. Applications are discussed in terms of drive requirements, packing densities, and switching times.

INTRODUCTION

ADVANTAGES of thin magnetic films as computer elements have been described in the literature.[1] However, efforts to achieve practical devices have thus far been unrewarding. Although matrices of thin films have been fabricated that are operable in very small memories,[2] it is questioned whether the difficulties associated with obtaining film arrays for practical storage systems may be overcome. These difficulties are manifested in problems such as reproducibility, uniformity of easy axis alignment and switching threshold, and transmission effects. The transmission or drive and sense line problem, although more subtle, is perhaps the more serious.[3] In addition, detrimental effects exist in films such as stress sensitivity, disturb sensitivity, and aging effects.

Until recently, thin magnetic films for computer components were composed only of metals. This paper reports the successful fabrication of ferrite films. The objective is not to simply replace metallic films by ferrite; rather, the objective is to exploit an advanced materials technology to obtain the advantages of open flux path elements while circumventing some problems encountered by metallic films. A further objective is to take advantage of some ferrite device characteristics that are superior to those of metallic devices. The virtual elimination of detrimental effects of stress, disturb sensitivity, and aging has been achieved for some time for many ferrite toroidal devices.

MAGNETIC PROPERTIES OF FERRITE FILMS

The ferrite elements studied were planar structures with thicknesses of about 10 μ and other dimensions in the fractional inch range. The compositions employed are the same as those of ferrite toroids for conventional storage applications. The element is a sintered product made from calcined ferrite formed in the desired geometry. The use of a ferrite (with $B_s = 2000$ gauss compared to 10 000 gauss for a nickel iron material) allows a proportionately greater thickness for a given demagnetizing field and sample dimensions. For circular elements of 10 μ thickness and a quarter inch diameter, a demagnetizing field of about 0.1 oe is found.

By studying a number of ferrites, it is found that the squareness characteristics of ferrite films are very similar to characteristics of the ferrite in a bulk toroidal geometry. From 60 cps hysteresis loop measurements, squareness ratios of 0.95 and loop shear of 0.2 oe are found to be typical of many ferrite samples. Coercive forces for these elements are in the range of 1–10 oe.

A switching curve, plot of inverse of switching time versus amplitude of applied field pulse, is shown in Fig. 1. The sample described by this curve has dimensions of 8 μ by 0.1 in. by 0.3 in. Note that the switching time for an applied field equal to twice the wall motion threshold field is 0.25 μsec. For this curve the exciting fields were applied parallel to the easy axis of magnetization. This axis was determined by shape anisotropy. Results of a study of the influence of transverse fields on switching curves are not conclusive enough for a report at this time. A comparison of the switching curves of materials in bulk and in film structures shows the

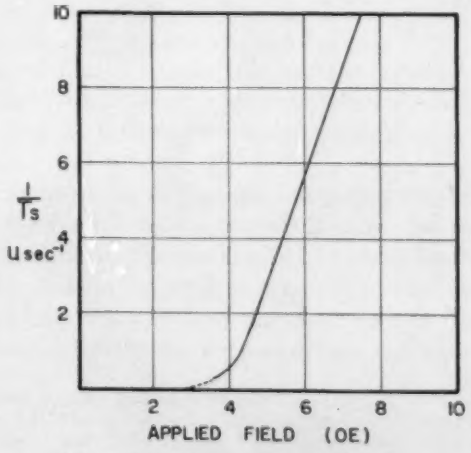

FIG. 1. Switching curve for ferrite film.

[1] D. O. Smith, Electronics **32**, 26 (1959).
[2] J. I. Raffel, J. Appl. Phys. **30**, 4 (1959).
[3] J. S. Eggenberger, J. Appl. Phys. **31**, 287S (1960), this issue.

following similarities. Over the range of switching times, $T_s > 0.1$ μsec, there are two linear regions of the switching curve. The slopes for these regions are nearly the same for the two cases of film and bulk samples. The lower field region is ascribed to a domain wall motion process, and the higher field region (>4 oe in Fig. 1) to a rotational process. A difference between the curves for film and bulk materials is observed, such that for the film samples, the region of the switching curve attributed to a wall motion process is smaller than for bulk material. It is apparent from Fig. 1 that the application of fields of amplitude twice the threshold field is sufficient for the flux reversal process to be dominated by the higher speed mechanism.

The switching threshold is well defined for the film samples fabricated of ferrite materials. If the threshold field is measured as the amplitude of a succession of ten 1 μ sec pulses required to switch an arbitrarily small percentage of the magnetic flux (say 5%) then this value so measured agrees with that measured using dc current. This characteristic differs from the threshold behavior of many nickel-iron films; it is common to find a significant difference between the threshold values[4] measured using dc, and using a series of pulses. Such a condition leads to problems of disturb sensitivity in multidimensional selection of storage devices.

Because of the favorable geometry of a thin film, heating effects due to pulse repetition frequencies of at least a few megacycles are negligible. It is expected that ohmic losses in selection lines would account for most of the energy dissipation in a storage array.

As mentioned earlier, the lower magnetization of ferrite allows a greater thickness of material when other dimensions and the demagnetizing field are not changed. This results in an element of greater mechanical strength. In fact, handling of unsupported elements does not ordinarily harm the device properties.

Ferrite bodies are chemically stable. The problem of aging or of reaction with normal atmospheres is as negligible with ferrite films as with ferrite toroids. The aging effects observed with square loop metallic films are nonexistent in ferrite structures. (For electroplated metallic films and for vacuum deposited thin films on substrates at room temperature, measurements in our laboratory indicate a typical change in the anisotropy field H_k of 15%, and in the wall motion coercive field H_c of 10% with an associated time constant of a few weeks.)

[4] N. F. Lockhart, IBM Research Laboratory (private communication).

APPLICATIONS

For storage applications, a mode of operation similar to that employed with toroidal cores may be used. Only fields parallel to the easy axis are applied and the resultant response is typified by Fig. 1. Since selection ratios as low as 1.5 have been obtained, the elements are capable of three dimensions of selection as in a bit-organized memory. In a 2-*D* system, the use of bias allows selection times of less than 0.1 μsec for full switching. Another reduction in switching time results when employing the technique of partial switching.

The effects of transverse fields are currently being studied. Modes of operation similar to those proposed for metallic film devices are expected to result from these investigations.

The samples employed up to the present time have dimensions of about 0.1 in. to 0.4 in. A resultant bit density using these elements would be smaller than for some toroidal core arrays. However, it is expected that a decrease in sample size would result in information density as great as with core or metallic film arrays. Such a decrease eases the drive problem in some respects but at the expense of the available information signal from a storage location.

ACKNOWLEDGMENTS

The authors wish to thank R. A. Hill for the use of his unpublished data concerning thin film aging. The assistance of K. R. Grebe in the fabrication of samples is gratefully acknowledged. N. J. Mazzeo was most helpful with measurements for device evaluation.

JOURNAL OF APPLIED PHYSICS SUPPLEMENT TO VOL. 31, NO. 5 MAY, 1960

Electrodeposited Memory Elements for a Nondestructive Memory

T. R. Long
Bell Telephone Laboratories, Incorporated, Murray Hill, New Jersey

Nickel-iron films are being electrodeposited on to a wire substrate to form memory elements for a fast, nondestructive memory. By plating in the presence of a directed magnetic field, an anisotropy favoring circumferential orientation is established. Axial interrogation fields cause reversible rotations of less than 90° and produce output signals across the ends of the wire. The apparatus and techniques used to make this wire are discussed together with the rationale back of the design. The choice of alloy composition and the plating conditions strongly affect the results. The amount of stress in the deposit, the residual stress in the substrate, the control of precleaning of the substrate, the use of a suitable wetting agent, and the degree of stirring in the electrolyte appear as the vital factors in obtaining consistent results. Moderate fields (~30 oersteds) applied during plating produce a preferred circumferential orientation with high anisotropy ($H_K/H_0=3.0$). Squareness ratio in the easy direction is 0.99. Output signals appear during the rise time of the interrogation pulse with an amplitude inversely related to the rise time and directly proportional to the length interrogated. Very fast switching with unusually high output signals per unit length are possible. Selective write in is possible with current margins of 3:1. Preliminary investigations indicate that it would be feasible to make plated wire on a production basis with properties suitable for memory applications.

INTRODUCTION

THE use of easy directions of magnetization in magnetic wires to form an attractive nondestructive readout memory was originally proposed by Gianola.[1] In the operation of this memory element, a strong anisotropy favoring circumferential orientation is established in a wire-like material. Axial interrogation fields cause the magnetization vector to rotate reversibly through an angle of less than 90° thereby causing the circumferential component of magnetization to decrease by an amount $\Delta\varphi_c$. This change of circumferential flux induces an emf in the wire which translates into output signals observable across the ends of the wire. Since the rotation is reversible, the magnetization vector returns to its original orientation upon removal of the axial field thereby producing a nondestructive readout. The reversibility of this process relies on the existence of a high anisotropy in the material. It can be appreciated that if the original circumferential magnetization is in a positive sense, the $\Delta\varphi_c$ will be negative, and vice versa.

At the time of proposal of this memory device, solid wires with a stress induced anisotropy were contemplated. Solid wires, however, have a poor device geometry because it is not possible in them to obtain a uniform switching field at all radii. A tubular geometry is called for, but it is almost impossible to draw a tube of the desired wall thickness. One way to fabricate a satisfactory tube is to deposit a thin magnetic plating on a nonmagnetic wire. Anisotropy can be obtained by the application of a controlled stress, by magnetic annealing, or by the imposition of a directed magnetic field during deposition. The latter method is the one used here.

The choice of plate thickness is determined by a number of factors: It should be thick enough to provide a useful amount of flux yet not so thick as to impair the high-speed switching characteristics. A thickness greater than the skin depth utilized by a fast pulse would be unused. A plating thickness of 1.2 μ appears to be a reasonable compromise to such arguments. Unfortunately, such a thin plate imposes severe requirements on the surface roughness of the substrate. A particularly smooth OFHC Cu wire is chosen as the substrate material.[2]

PLATING CONSIDERATIONS

The electrolyte used for plating is a mixture of nickel and ferrous sulfamate in acid solution. The choice of electrolyte was determined by the reputed ability of the commerical nickel sulfamate bath[3] to give high quality, low-stress deposits. Also, a stress reducing additive is available and since tensions in the deposit will have an adverse effect on anisotropy and coercivity, the ability to minimize the stress is important.

A five mil copper wire is used as the cathode of the electrodeposition cell while the anode material found to be most successful is Rolled, Depolarized Nickel.[4] This material does not suffer from passivity when used in the sulfamate bath. In this particular operation, the plated material is derived from the electrolyte rather than from the anode material. The electrolyte contains approximately 5% ferrous ions but because of the small volume of deposit, simple iron content titrations with subsequent additions of ferrous sulfamate are adequate for holding the bath concentrations within good working limits.

The composition of the nickel iron alloy deposited is affected primarily by the current density, the electrolyte temperature, the percentage of ferrous ions in the solution, and the degree of stirring. The nickel content of the plate increases with increased current density, decreased temperature, decreased iron concentration,

[1] U. F. Gianola, J. Appl. Phys. **29**, 849 (1958).

[2] Obtained from the Phelps Dodge Corporation.

[3] Barett Chemical Products Company, Shelton, Connecticut.

[4] A type of nickel produced by INCO containing 0.18% oxygen plus traces of Fe and Cu.

and less agitation. Representative values required to obtain a nonmagnetostrictive plate (81% Ni-19% Fe) are 40 amp/dm², 150°F, *p*H of 4.0, and a high degree of circulation.

One other electrolyte constituent which markedly affects the magnetic quality of the deposit is the presence of suitable and sufficient wetting agent. Many wetting agents can enter into detrimental side reactions with one or more of the bath constituents. Maprofix 563[5] a sodium lauryl sulfate especially free of inorganic salts appear to be free of these deficiencies.

EXPERIMENTAL DETAILS

A continuous processing system was chosen as the only feasible way of maintaining control of the many parameters involved. Wire from a supply spool extends the full length of the apparatus, about 12 ft, and is kept under small controlled tension by a constant-torque motor acting on the supply spool. Each of the stages in the process is designed to minimize bending and drag as the wire passes through them. At the far end, a constant-speed drive mechanism is designed to keep from introducing a twist in the wire. The fact that the wire is annealed and straightened in a hydrogen reduction furnace makes these tasks simpler. An electrical connection is made to the wire on the supply spool for the field current. This current passes down the wire, past the plating chamber, to the common ground and thus supplies the circumferential magnetic field during deposition which establishes the magnetic anisotropy.

In order to obtain consistent results with uniform adherence, stress, and magnetic characteristics, it is necessary to plate on a meticulously clean substrate. The cleaning procedure utilized removes vegetable and mineral oils in a hot, ultrasonically agitated detergent bath. A hot peroxide bath oxidizes the animal fats. Animal-fat residue plus physical contaminants are then removed in an ultrasonically agitated deionized water bath. The remaining copper oxide is removed in a hydrogen furnace from which it passes directly under the surface of the electrolyte and is plated. Following the cleaning procedure sketched above, there is less than 0.1 monomolecular layer of hydrophobic surface contamination.

The plating chamber is made of $\frac{7}{8}$ in. i.d. Pyrex tubing with an active plating region 1 inch long. The wire enters and leaves without bending via self-stabilizing meniscus seals in flared capillary tubing. The anode is a cylindrical cage concentric with the wire. A thermocouple is located adjacent to the wire and it is used to hold the temperature to ±0.3°F. Electrolyte is recirculated through this chamber from a separate reservoir at rates as high as 3 liters/min.

After rinsing the plated wire, it is passed through a mercury ground contact and then through small testing coils. These coils provide axial fields similar to those experienced in a memory module and allow a continuous monitor of the nondestructive readout signal. In addition, the symmetry of this signal and the coincident field switching characteristics can be measured. Following this section, the wire passes through an additional set of coils by which the axial or hard direction *B-H* loop is monitored and displayed on a CRT. Subsequent comparison of this loop with a similar one measured in the circumferential or easy direction provides a measure of the anisotropy energy obtained.

From the testing section, the wire is pulled through four feet of glass tubing and thence to the drive mechanism. The glass tubing allows the wire to be removed and transported for subsequent evaluation with a minimum of handling.

RESULTS AND CONCLUSIONS

The plating process described above yields material which is extremely uniform and reproducible by conventional plating standards. However, for this memory, a uniformity of 1% in magnetic characteristics is desired. The uniformity of the present process is 3% and indications are that with additional refinements the desired uniformity will be reached.

Moderate fields (~30 oe) applied during plating are capable of producing an anisotropy (H_k/H_c) of approximately 3.9 with a coercive field (H_c) of 1.7 oe. If an identical material is prepared without the presence of a circumferential magnetic field, the anisotropy obtained is 1.00 to an accuracy of 2%. Squareness ratios of 0.99 have been obtained in the easy direction.

Output signals occur during the rise time of the interrogating pulse with an amplitude proportional to the bit length. A representative signal from a 60 mil length is 50 mv into a 50 Ω load in 0.15 μsec. Output signals have been obtained in 25 mμsec with correspondingly higher peak amplitudes. Selective write-in margins of 3:1 are available. In short, the switching characteristics are similar to those obtained in vapor deposited films on a flat substrate but the geometry has been changed to obtain very tight coupling to external circuitry since this coupling is provided by the magnetic wire itself.

ACKNOWLEDGMENTS

The author wishes to express his appreciation to J. E. Schwenker and Dr. C. D. Green for many helpful discussions. My thanks also to R. R. Johnson for able assistance in carrying out the many tests and experiments involved.

[5] A product of Onyx Oil and Chemical Company, Jersey City, New Jersey.

JOURNAL OF APPLIED PHYSICS SUPPLEMENT TO VOL. 31, NO. 5 MAY, 1960

New Approach to High-Speed Storage—Low Flux Density Materials

W. L. Shevel, Jr., and H. Chang
IBM Research Laboratory, Poughkeepsie, New York

This paper presents a new approach toward overcoming the factors currently limiting the frequencies at which storage devices may be switched from one information state to another. Ferrite elements for random access storage have been developed which require a fraction of a microsecond for a cycle. Thus the ferrite switching time establishes a maximum switching rate given by the inverse of the total switching time in a cycle. However, operation of elements such as these in a large capacity memory at rates limited only by switching times is usually prevented by: deterioration of magnetic properties due to heating effects, increase in selection line impedance, and long transmission delays.

A series of ferrimagnetic oxides have been developed with properties such that the limits on minimum cycle time are appreciably extended. The most important of these properties is the saturation flux density. Over a range of composition, flux densities have been obtained which extend from 100–500 gauss. The lower flux density results in an appreciably lower energy dissipation in the magnetic structure and consequently in higher switching rates for a given temperature rise within the magnetic material. In addition, temperature dependence of those magnetic properties which determine storage applicability is more favorable than with the better known ferrites.

Toroids have been fabricated with these materials which are suitable for random access memories. These elements have been operated successfully in free air at repetition frequencies in excess of 2 Mc.

The improvements in array characteristics that result are discussed in terms of impedances and transmission delays.

A REQUIREMENT of future computing machines is for random access memories whose storage elements may be switched between information states at megacycle frequencies. A three-dimensional storage system employing multi-apertured ferrite cores has been described that is capable of a read-write cycle within a half μsec.[1] At a read-write frequency of 2 Mc, the power being dissipated in the storage elements is great enough to require liquid coolants. A two-dimensional system employing toroids and the partial switching technique has been described whose cycle time is a half μsec.[2] For this case, the mode of operation is such that air cooling may be sufficient. However, it is apparent that as higher information rates become necessary, the power dissipated in the magnetic structure will be a limiting factor on frequency.

Another limiting factor arises when magnetic devices of a given geometry and composition are switched faster in order to shorten a memory cycle. The faster switching causes the core to offer a higher impedance to the selection currents. For storage arrays of large capacity, the impedance due to storage element switching can be prohibitively great.

When memory elements are switched in times of a μsec, transmission delays are not excessive, even in large capacity systems. But an array whose elements require less than a tenth μsec for switching may be limited in capacity by transmission delays. An appreciable part of the transmission delay is due to the loading caused by a multiplicity of magnetic elements on the selection line. If the loading per magnetic element were lessened, the delays would be shortened.

The foreground factors currently limit the read-write frequency capability in random access memories. This paper presents a new approach to overcoming these difficulties. A series of materials have been developed with properties that allow the current limits on minimum cycle time to be appreciably extended. These materials have a garnet structure and have the following formula:

$$Y_{3-y}Gd_yFe_{5-z}Al_zO_{12}.$$

The substitution of aluminum serves to lower the saturation magnetization of the garnet. With this series, flux densities are obtained in the range 100 to 500 gauss. Although the flux density is decreased by an order of magnitude compared to conventional ferrite materials, the other magnetic properties important in storage application are preserved.

The effect on the heating problem of using these low flux density materials is seen by noting that the energy dissipated in an element for a given amplitude of drive field is nearly proportional to the amount of flux that is switched. With the new materials described here, a typical storage core would have, for example, a half line of saturation flux compared to five lines for an element used in the IBM 704 memory. Of course, a reduction in flux can be accomplished by simply making the elements smaller; but this has the attendant disadvantage of lowering the heat dissipative ability to the medium surrounding the material. The partial switching technique in effectively reducing core flux is limited since a minimum fraction of saturation flux must be switched.

Figure 1(a) shows the temperature dependence of the saturation flux for two garnet samples. The dependence of the AlYIG sample is similar to that of spinel ferrites. The dependence of the AlYGdIG sample departs from that of substituted garnets as well as spinel ferrites. In particular, the slight temperature dependence at room temperature is very desirable for memory components. For the samples described in Fig. 1(a), the Curie temperatures for AlYIG and for AlYGdIG are respectively 120°C and 280°C.

With switching times of about 0.1 μsec, AlYIG samples have been cycled at frequencies as high as 2 mc with only air cooling. An apparent temperature rise of about 10°C has been observed under these con-

[1] W. W. Lawrence, Proc. Eastern Joint Computer Conf., Am. Inst. Elec. Engrs. (Special Publication, T-92).
[2] R. E. McMahon, 1959 Solid State Circuits Conf., Philadelphia, Pennsylvania (February 12, 1959).

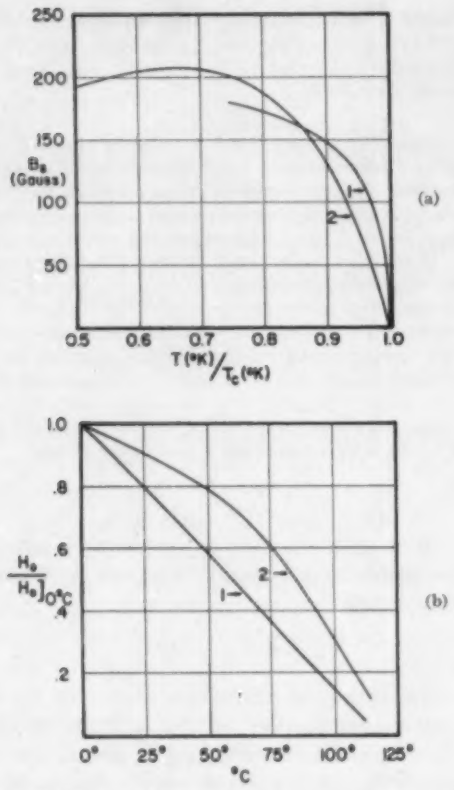

FIG. 1. (a) Plot of flux density vs normalized temperature: (1) AlYIG sample, (2) AlYGdIG. (b) Plot of the switching thresholds of: CdMn Ferrite, (2) AlYIG.

ditions. This rise is too small to cause a deterioration of magnetic properties for storage applications.

The transmission line loading problem using these materials is eased. The magnetic loading is less because of the low magnetization of the materials. The impedance offered by a switching element is less, since a smaller amount of flux is switched.

Reducing core flux does reduce the available information signal from the core. For the high-frequency applications considered here, however, the faster switching results in a larger signal. In fact, as the required frequency is increased, the flux may be proportionately lowered; this leaves the sense signals approximately unchanged in amplitude.

Figure 1(b) shows a comparison of the switching thresholds of AlYIG material and a CdMn ferrite. These materials have approximately the same Curie temperature The dependence of the garnet is more desirable for a storage element. At lower temperatures than those shown in Fig. 1(b), the threshold field of the garnet is even less temperature sensitive.

CONCLUSIONS

Low flux density materials offer a new approach toward extending the information rates of random access memories. The heating problem has been successfully attacked. Advantages attendant to low flux elements are apparent in terms of selection line impedance and transmission delays.

ACKNOWLEDGMENTS

The authors are indebted to Dr. B. A. Calhoun who was responsible for suggesting this approach and for the garnet materials research. The assistance of N. J. Mazzeo in measurements is gratefully acknowledged.

JOURNAL OF APPLIED PHYSICS SUPPLEMENT TO VOL. 31, NO. 5 MAY, 1960

Miniature Memory Planes for Extreme Environmental Conditions

R. STRALEY, A. HEUER, B. KANE, AND G. TKACH
General Ceramics Division of Indiana General Corporation, Keasbey, New Jersey

Two serious limitations of present memory systems by using ferrite cores have been their relative bulk and narrow operating temperature range.

A marked reduction in size has been achieved by use of a "continuous wire" method of inserting drive lines through memory planes and then folding the planes. This method eliminates the conventional frames and all solder connections between planes. By greatly reducing the number of solder connections, the new method increases reliability and facilitates assembly of stacked memory planes. A typical folded stack of memory planes occupies as little as 2% of the volume of its conventional counterpart. The new miniature memory stacks perform as well as conventional units.

The development of ferrite memory cores operable at ambients as high as 85°C, 100°C, and 125°C (together with the greatly reduced volume of the memory stack) allows operation under extreme environmental conditions with a minimum of space and power requirements. The folded memory planes are packaged with a heating element and control circuit which maintain the temperature of the cores at the maximum ambient. A tested prototype of twelve (12) 16×16 memory planes, along with the heating element and control circuit, measures 2 in.×2½ in.×2½ in. and has been successfully operated in the temperature range −55° to +125°C.

Ferrite cores have been perfected of both the "fast" relatively high drive and relatively "slow" lower drive type. They are Mg-Mn ferrites with possible minor additions of other bivalent oxides.

IF memory systems using ferrite cores could be made smaller and their operating temperature range extended, their usefulness would be vastly increased. These limitations have prompted investigations of other

approaches to memory systems, such as ferrite plates,[1] twistors,[2] etc.

By eliminating the need for frames and terminals generally used to support each individual array of cores and by means of a folding process which will be described below, some of these problems have been greatly minimized. We shall for convenience refer to these new ferrite core memories as microstacks.[3]

We shall first compare space requirements and packing density of microstacks with conventional memory stacks. Ten 16×16 memory planes wired in a conventional stack occupy 60 cu in., thereby affording a packing density of approximately 75 000 bits/cubic ft. This stack requires 1236 solder joints in and between planes. A microstack of the same ten planes occupies only 3 cu in.; core densities are approximately 1 530 000 bits/cu ft; the unit requires only 84 solder joints. Similar calculations for 64×64 memory planes stacked twelve high show a volume of 330 cu in., a density of 270 000 bits/cu ft, and a total of approximately 5900 solder joints. The corresponding microstack occupies 22.7 cu in., has a core density of 3 740 000 bits/cu ft, and needs only 280 solder joints. The foregoing volume and capacity comparisons represent present production models. Engineering prototypes have, however, been constructed with extreme space limitation in mind; the volume reduction in these units has been better than fifty to one.

Most of the space savings in the microstacks is accomplished by the elimination of frames and terminals for supporting the individual arrays of cores. This has been achieved by folding mats of cores strung on continuous wires. For purposes of demonstration we shall describe a very small memory employing 4 mats of 16 cores each.

The mats are arranged side by side as in Fig. 1(a) and spaced about $\frac{1}{8}$ in. to $\frac{3}{16}$ in. apart. The "X" and "Y" drive lines are then threaded through all of the mats. The "X" lines are threaded directly through the mats in a horizontal plane. The No. 1 "Y" wire runs down through the first row of cores in the first mat, up through the last row of cores in the second mat, down through the first row in the third mat and up through the last row in the fourth mat. The rest of the "Y" lines follow similar paths as in Fig. 1(a). The sense and inhibit lines are then inserted in each mat. Each mat may then be covered with a suitable insulation which cushions the cores against damage or pressure. The sense and inhibit lines are not shown in the diagram.

The planes are then folded one upon the other, as in Fig 1(b). The folded memory stack is then placed in a housing and the leads are brought out to a terminal board or a connector.

A further refinement has been the temperature control

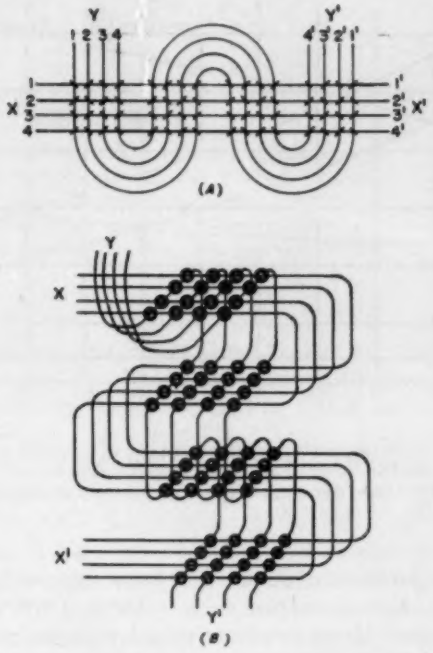

FIG. 1. (A) Stringing operation prior to folding. (B) Method of folding arrays of cores.

of these microstacks. The very large reduction in volume has greatly reduced the power needed to maintain a constant temperature over a large ambient temperature range. Besides the reduction in power, the compactness of the microstack minimizes the problem of temperature control for airborne applications, where the rarefied air becomes an excellent, but unwanted, thermal insulator. The volume of a 16×16 twelve-plane temperature-controlled microstack is 12.5 cu in. as compared with 3 cu in. for the standard, while in the 64×64 twelve-plane microstack, the size is increased from 22.7 to 62.5 cu in. in making the unit temperature controlled.

Temperature controlled folded memories are achieved by heating the planes to the maximum ambient temperature and maintaining that temperature through the entire ambient range. Two thermistors are placed in the folded memory and the folded memory is covered on all six sides by a heating pad. The thermistors are designed to unbalance a bridge circuit, which causes a transistor to conduct and therefore supply current to the heating pad when the ambient temperature falls below the maximum.

The folded memory encased in its heater pad is then insulated with pads of polyurethane and placed in a suitable housing.

The microstack schematically is the same as a conventional wired coincident current system. For worst noise conditions, when all the half selected core outputs are additive, the minimum "one" and the maximum "zero" voltages are at least as good as in a conventional memory stack.

[1] J. A. Rajchman, Proc. Eastern Joint Computer Conference (December, 1956), p. 107.
[2] A. H. Bobeck, Bell System Tech. J. **36**, 1319 (1957).
[3] Trade Name—General Ceramics; patents pending on all phases of the microstack.

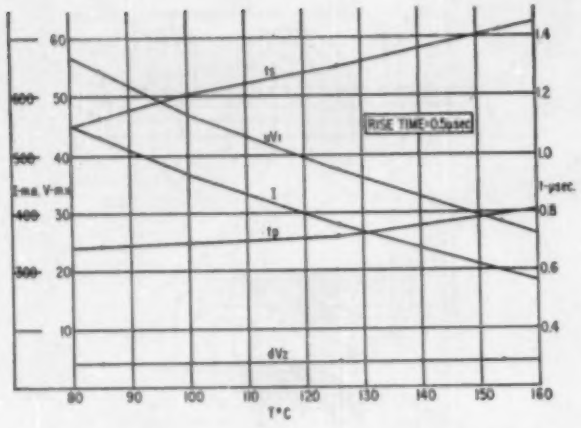

FIG. 2. Core parameters vs temperature, of a typical high temperature memory core. The half select currents are 61% of the full select current; signal-noise ratio is maximum at each temperature and full select current.

An experimental model has been constructed and tested in the temperature range −55° to +125°C. This unit consists of twelve 16×16 memory planes; the total volume including heaters and temperature control circuits occupies 12.5 cu in. (2½ in.×2½ in.×2 in.). The ferrite cores used were similar to those described below. Any individual plane in the stack had for "worst case" conditions, a signal-noise ratio of at least 3:1 at nominal currents, and also at ±10% variation from nominal current. This compares quite favorably with conventional memory stacks tested in a similar manner at room temperature. Ten watts of power is required for the heater circuit. When the unit is subjected to an ambient temperature of −55°C, a maximum of ten minutes warm up time is required to insure reliable operation. Temperature variation in the package itself was within ±2°C, of the maximum ambient (125°C) at any point in the package.

The development of temperature controlled microstacks has been made possible by the development of memory cores, which function quite well at much higher temperatures than has heretofore been the case. We have concentrated our development on the temperature range −55° to +125°C, as this is a standard military specification. Ferrite memory cores have been made with switching times varying from 2.6 μsec to 0.5 μsec. The drive currents vary from 200 ma to 800 ma. These cores are Mg-Mn ferrites with compositions close to the apex of maximum squareness in the system. It is felt that the usefulness at high ambient temperatures is associated with a uniform grain size, which causes the coercive field to have a low distribution from grain to grain. This grain size and distribution can be controlled by preparation techniques and minor addition of other oxides. The microstacks that have been built were intended for 125°C operation although test of the cores proved that they can be used effectively at 155°C, the highest available test temperature.

Figure 2 shows a typical plot of core parameters vs ambient temperature in the temperature range 80–160°C. In all cases, the half-select current was 61% of the full select current. This type of testing guarantees a considerable safety margin; half or full select drive currents may vary ±10% without any deterioration or errors in the memory.

The points plotted are those with the greatest signal to noise ratio at each temperature. For a core operable at a 125°C typical values are as follows: full select current 380 ma, the minimum undisturbed one voltage is 38 mv, maximum disturbed zero voltage is 5 mv; peaking time 0.72 μsec and switching time 1.3 μsec.

The trend in the observed data can be explained by a decrease in both saturation magnetization and coercive force with increased ambient temperatures. The lower magnetization and increased switching time causes a decrease in the output voltage. The longer switching time is a result of the lower coercive force, which permits the use of lower drive currents.

JOURNAL OF APPLIED PHYSICS SUPPLEMENT TO VOL. 31, NO. 5 MAY, 1960

New Multi-Aperture Magnetic Logic Element*

DAVID R. BENNION
Stanford Research Institute, Menlo Park, California

A new magnetic multi-aperture device (MAD) having general logic capability has been designed, constructed, and tested. This device can be used for either direct or complementary transfer of binary information, depending only on a simple change in wiring. *And* and *or* logic functions can be performed in the interconnecting circuitry, which consists only of conducting wire. Significant operating tolerances have been exhibited by the new element, which is simpler in structure and associated wiring than previous MADs having the same logic capability.

INTRODUCTION

A SYSTEM has been described by Crane[1] for performing digital logic using magnetic multi-aperture devices (MADs) and connecting wire only. Two basic elements in this system are *positive* and *negation* MADs, simplified shapes of which are shown in Figs. 1(a) and 1(b). Compatibility and handling problems would be reduced if a MAD of one shape could be used for either positive or negative transfers of information, depending only upon the method of wiring it into the circuit. Several different structures have been devised for MADs of this type, which we will refer to as *plus-minus* elements.[2-4] A particularly simple one and some of the logical and operational design principles leading to it are described below.

LOGICAL DESIGN

Figure 1(a) shows a *positive* MAD in its cleared or binary *zero* state. Because of the parallel flux condition by the output aperture, I_{drive} cannot switch flux locally, and hence, no output current will be induced. On the other hand, if the element had previously been set to its binary *one* state by a large input current, there would be an antiparallel flux condition by the output aperture, and hence, I_{drive} could cause local switching of flux. This would produce an output current which could be used for setting a succeeding element.

For a *negation* element, the input-output relations should be exactly reversed from those given in the foregoing. That is, there should be an antiparallel flux condition by the output aperture when the element is in a cleared state. This requirement is satisfied by the structure shown in Fig. 1(b), provided the central leg is held in the state shown by a steady current, I_{hold}.

Various methods have been used for evolving combination *plus-minus* elements from the structures of Fig. 1(a) and (b).[2,3] A particularly direct approach can be achieved by careful consideration of the essential aspects of the *positive* MAD. Consider the transition from Fig. 1(a) to 1(c). Let us abandon the "parallel or antiparallel" interpretation and note that the inner leg by the output aperture of Fig. 1(a) serves for information storage in the sense that it will be saturated downward or upward for storage of *zero* or *one* states, respectively. This information leg is retained without alteration in Fig. 1(c). Now note that a positive drive current tends to reverse flux in the output leg of Fig. 1(a), but that a negative drive current could do nothing since it would push on the output leg in the saturated direction. Let this leg be doubled in size and left in a demagnetized state (on the average), represented by a downward arrow balanced by an upward arrow in Fig.

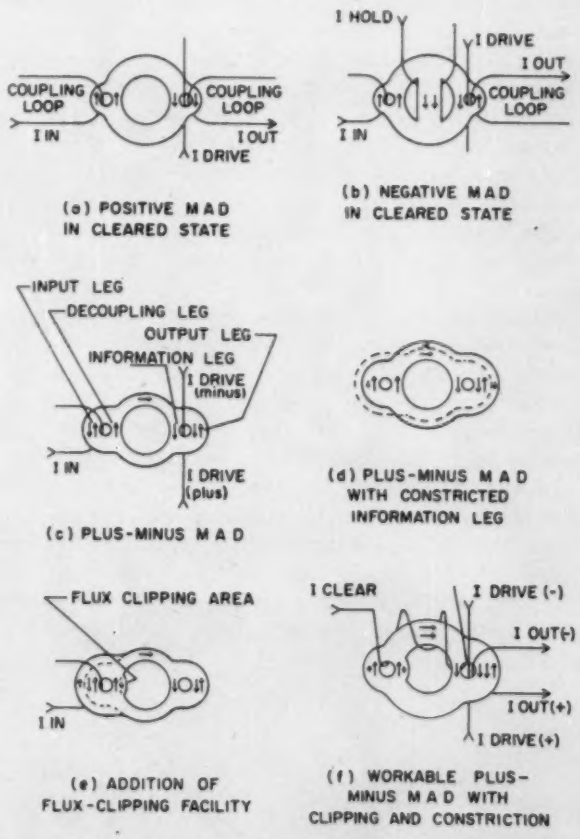

FIG. 1. Evolution of a workable plus-minus multi-aperture logic element.

* Part of this work was sponsored by the Information Systems Branch, Office of Naval Research, and part by the Burroughs Corporation.

[1] H. D. Crane, Proc. Inst. Radio Engrs. 47, 63 (1959).
[2] H. D. Crane (unpublished notes, Stanford Research Institute).
[3] D. C. Engelbart (unpublished notes, Stanford Research Institute).
[4] E. K. Van De Riet (unpublished notes, Stanford Research Institute).

1(c). Now flux in the output leg *can* be switched by either an upward or downward drive current. The inner leg by the input aperture must be retained as in Fig. 1(a) in order to allow decoupling of the input once setting has occurred. The sizes of the main leg about the central aperture and the input leg are governed by flux closure requirements. Logically speaking, the structure arrived at in Fig. 1(c)[3] will operate like that of Fig. 1(a) if an upward drive current is used, or like that of Fig. 1(b) if a downward drive current is used.

The foregoing development provides one logical design, though not a unique one, for a *plus-minus* logic element. Various modifications can be made to improve operation, for example, in terms of increased tolerances on drive current levels. In general, these changes will result in a loss of simplicity, an increase in wiring complexity, or an increase in the amount of driving energy required. Fortunately, a number of modifications can be made that are fairly simple, yet helpful.

OPERATIONAL DESIGN

Three design principles that have evolved from experience and theory are described below:

(1) When an element is in its cleared state, as much as possible of the material in the element should be saturated, to provide a good threshold to block reception of flux during binary *zero* inputs. For example, additional apertures could be placed in the centers of the input and output legs of the structure of Fig. 1(c) so that a current could be applied to wind flux around the new apertures, thus reducing the amount of demagnetized material.

(2) It is also desirable for a *negation* element to be well saturated at the time of transmitting a *zero*, primarily in the information leg and, secondarily, the rest of the way around the main aperture. For perfectly square loop material, the structure of Fig. 1(c) would be quite adequate in this respect. However, it has been found that with practical materials, the available input current is not great enough to provide hard reverse saturation all the way around the central aperture. Hence, a compromise of the type illustrated in Fig. 1(d) must be made. The unmodified structure is shown overlaid with a dotted line. The net effect of this change is to make the information leg appear constricted relative to the cross section of the main leg around the central aperture. As a result, the input current can cause harder saturation of the information leg at the expense of poorer saturation of the remaining material about the central aperture.

(3) The manner in which flux clipping (the subtraction of a constant amount of flux from the transferred level) aids operation has been known for some time.[3,5] One of several means for obtaining this effect is shown in Fig. 1(e), compared with Fig. 1(c). Now, when flux switches in the input leg, a small amount is subtracted out in the decoupling leg, with only the remainder going on to the information leg. Unfortunately, it is impossible to clear this structure to the flux state shown. Either an additional aperture must be added, or the design must be further modified so that the input leg can be completely saturated by the clearing current. Figure 1(f)[4] shows how the latter modification can be made, along with the winding arrangement for clearing. This structure is a close approximation to the new *plus-minus* logic element that has been developed at SRI under ONR sponsorship. It incorporates the variation of Fig. 1(d) to a high degree and hence does not satisfy the second design principle in an optimum way, but because of the incorporation of the third principle, it exhibits good operational properties while retaining a high degree of simplicity.

EXPERIMENTAL RESULTS

A pair of the new logic elements were connected in closed loop fashion in the three possible modes. First, both were connected as *plus* elements, second, both as *minus* elements and third, one as a *plus* and one as a *minus* element. Advance currents could be simultaneously varied over ranges of approximately 15%, 30%, and 25%, respectively, for these three connections.

DISCUSSION

It is possible to realize general digital logic with an array of the elements described and connecting wire only. However, increased logic capability would be gained by addition of more input and output apertures. Achievement of a practical design with additional apertures may require tightening up on the first and second operational design principles, and in particular, in choosing a design that results in an output leg that takes up a smaller portion of the periphery of the element.

ACKNOWLEDGMENT

H. D. Crane, D. C. Engelbart, C. H. Heckler, Jr., and E. K. Van De Riet all contributed substantially to the developments reported here.

[5] D. R. Bennion and H. D. Crane, Proc. Western Joint Computer Conf. **21**, (1959).

Fast Switching by Domain Walls in Ferrites

WALTER WIECHEC AND CLINTON M. KELLEY
Stanford Research Institute, Menlo Park, California

Experimental evidence indicates that small grain size is associated with faster domain wall switching in ferrite cores. It has been shown by H. Amar that small grain size contributed an additional energy to the wall energy density σ_w. Incorporation of this energy into the power equation $H\cdot(dM/dt)=\lambda H_e^2$ reveals that the loss coefficient decreases more than σ_w increases, and, therefore, faster switching results.

A qualitative explanation is given for faster switching by domain walls in magnetic materials. The significant variables in the switching coefficient equation are "d," T_c, K, and α. Experimental data show that the switching coefficient is lowered by decreasing values of the first three variables. Considerably faster switching is predicted when similar cores with grain sizes less than 1 μ are made.

BASED on the Galt, Andrus, and Hopper treatment[1] of the motion of domain walls, Menyuk and Goodenough[2] define a switching coefficient

$$S_w=(H_{app}-H_c)\tau=\frac{\beta_r d}{2I_s\langle\cos\theta\rangle}+S_{we}. \tag{1}$$

When S_{we} is negligible, as in ferrites, and with the approximation $\lambda\ll 1$ one obtains

$$S_w=\frac{\alpha}{\gamma}\frac{d}{\langle\cos\theta\rangle}\left[\frac{a(K+\lambda_i\sigma)}{kT_c}\right]^{\frac{1}{2}}, \tag{2}$$

where λ is replaced by $\alpha\gamma I_s$, α is the loss coefficient, d is the distance a domain wall moves, and the term in brackets is proportional to the domain wall energy σ_w. The significant variables for this discussion are α, d, K, and T_c.

Henri Amar,[3] following Neel's discussion of an additional magnetostatic field affecting the domain wall energy, finds that the domain wall increases in energy and decreases in width for very small particles, containing domain walls of limited length. Introduction of the additional energy term yields

$$\sigma_w=4[A(K+\lambda_i\sigma+2NI^2)]^{\frac{1}{2}}, \tag{3}$$

with N as a coefficient dependent upon wall dimensions. Kittel's[4] $g(\theta)$, thus increased, is by minimization

$$g(\theta)=A(d\theta/dz)^2. \tag{4}$$

The power dissipation equation[1]

$$H\cdot(dM/dt)=\lambda H_e^2 \tag{5}$$

involves the Becker field[5]

$$H_e=-(\omega/\gamma)(d\theta/dz), \tag{6}$$

associated with the motion of the domain wall, where ω is the precessional angular velocity of the spins and θ is the rotational angle of the spins in a 180° wall. This shows that the power dissipation is proportional to $\lambda g(\theta)/A$. H. Amar's work shows that $g(\theta)/A$ increases with decreasing particle size, whereas empirical results indicate no increase in power dissipation. It must be concluded that λ decreases proportionately. Integration of (5) over z for the power dissipated for unit wall area allows an evaluation of wall velocity,

$$v=(2I_s\gamma^2A^{\frac{1}{2}}H_{app})\Big/\left(\lambda\int_0^{\pi}[g(\theta)]^{\frac{1}{2}}d\theta\right), \tag{7}$$

directly proportional to the applied field. The relation between λ and $g(\theta)/A$ predicts an increase in v at constant H_{app} with decrease in particle size.

Henri Amar shows that if grains are small, a demagnetizing field arises between the ends of a domain wall, Fig. 1. The smaller the length of the wall, the stronger the field. If one considers the $\oint H\cdot dl=0$, due to pole formation at the ends of the domain wall, then in addition to the demagnetizing field, closing fields may occur on both sides of the wall. A transverse field effect is obtained—one side accelerating the unreversed magnetization, the other side damping the reversed precession about the applied field. This action would serve to take care of the faster switching and lowered loss coefficient. In fact, this explanation may be the reason for the faster switching now noticed at high fields.[6] Be-

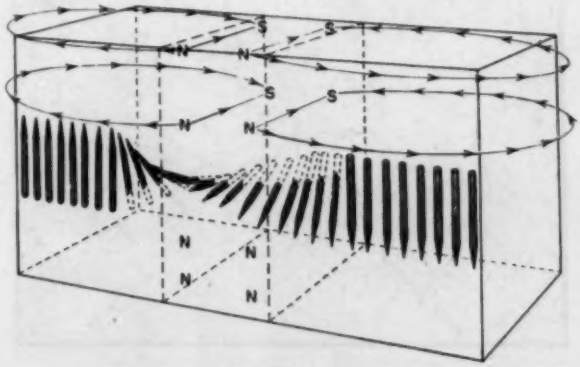

FIG. 1. Bloch wall indicating some demagnetizing and closure field lines.

[1] Galt, Andrus, and Hopper, Revs. Modern Phys. **25**, 93 1953)).
[2] N. Menyuk and J. Goodenough, J. Appl. Phys. **26**, 8 (1955).
[3] H. Amar, J. Appl. Phys. **28**, 732 (1957).
[4] C. Kittel, Revs. Modern Phys. **21**, 541 (1950).
[5] R. Becker, J. phys. radium, **12**, 332 (1951).
[6] E. M. Gyorgy, J. Appl. Phys. **28**, 1011 (1957).

cause of the high fields, many reverse domains are nucleated at defects within grains. The increased number of walls forces the walls to remain small.

A study of the grain structure of ferrite cores reveals that in nearly every instance of faster switching at low fields, the grains are small. A grain structure study of two different industrial low-drive square loop cores, Fig. 2, shows a grain size difference between their largest grains to be about 180 μ. The switching coefficient for the small grained core is $S_w=0.53$ and for the other $S_w=0.71$ oe-μ sec. The driving fields were from coercive field to three times this field.

Published values of S_w and grain size appear to be unreliable. Pulse rise time corrections and ringing on the pulse fall affect switching measurements. Measurement of S_w by pulse width techniques gives values which are too low. Current calibration is a constant source of trouble. Because of the numerous difficulties encountered, it would seem proper that some standard S_w's would be established and these referred to. Industry has a number of reproducible cores which could be used as a standard of reference. Grain size measurements consider an average size on a two-dimensional scale, but not percent volume distribution. Therefore, it would seem more reasonable to take as the grain size the largest grains since these take up the biggest part of the volume.

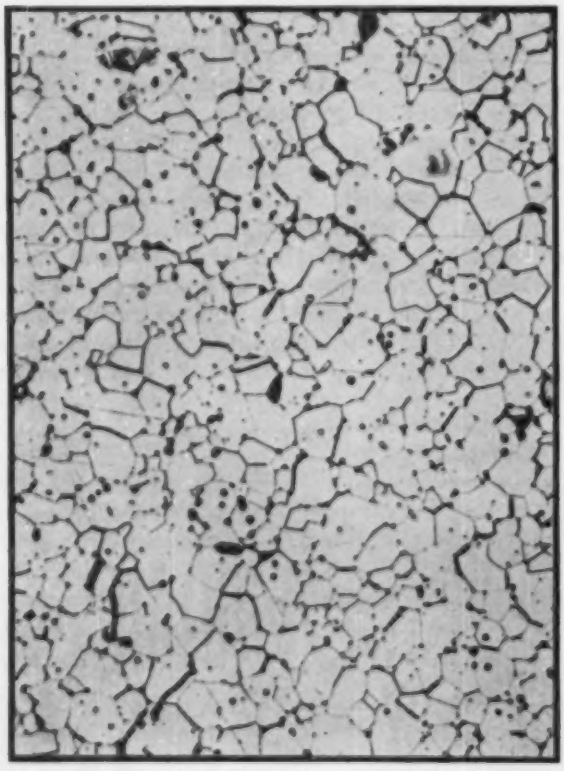

(a)

(b)

FIG. 2. A grain size comparison of two different industrial low-drive cores. (a) largest grain 20 μ, (b) 200 μ

The domain-wall equation appears to have more validity than other equations, since it is related more to the material characteristics. In addition to d, the other significant variables are K, T_c, and α. Very low switching coefficients have been reported for low Curie temperature cores.[7] Here the Curie temperatures appear to be tied in with the anisotropy K which is also lowered. It is well known that zinc and cadmium lower both. As a result of improved processing and the lowering of the Curie temperature, industry has been able to offer increasingly lower drive cores. This fact substantiates the power dissipation argument.

An attempt has been made to show that it is not necessary to assume different modes of remagnetization for high and low applied fields, but that both may be domain wall motion; that a relationship exists between the distance a domain wall moves and the loss coefficient. Since values of S_w, now being obtained at low fields, are approaching the high-field limit of $S_w=0.2$ oe-μ sec, then domain-wall motion must be the mechanism of remagnetization.

[7] See in addition published data on magnetic cores by RCA, Needham, Massachusetts.

Effect of Previous History on Switching Rate in Ferrites*

R. W. McKay and K. C. Smith
Department of Physics, University of Toronto, Canada

Existing theories of switching of square-loop ferrites indicate that the rate of switching is a function of the present state of magnetization and of the applied field. Experiments are described which show that the switching rate is also dependent on previous history.

Two cases have been studied. In the first case, the ferrite was partially switched to a predetermined extent by a pulse of variable amplitude and then the switching cycle was completed by a pulse of fixed amplitude. In the second, the ferrite was brought to the remanent state by a pulse of variable amplitude before the switching cycle. Changes as great as two to one in switching rate were produced by variations of previous treatment.

INTRODUCTION

THE theories of Haynes[1] and Gyorgi[2] both lead to equations which express the rate of change of magnetization of a square-loop ferrite as functions of the magnetization and the applied field. Haynes assumes motion of 180° domain walls from randomly scattered nucleating centers as the mechanism for low applied fields. At higher fields, incoherent rotation is postulated by Gyorgi. Both equations fit experimental switching curves for complete switching by constant applied fields, provided certain undertermined parameters are adjusted. To what extent these mechanisms overlap at intermediate fields is unknown.

Some effects are described in this paper which cannot be adequately explained by either theory. Considerable differences are found for the rate of change of magnetization with the same applied field for samples, which have been brought to a given state of magnetization in different ways. The same state of magnetization for a macroscopic sample may occur with quite different detailed arrangement of the domains. The differences between possible arrangements of domains apparently are of greater importance than has been previously thought.

Since the thickness of the walls of commercially available cores is such that the field changes appreciably with radius, affecting the results in some experiments, cores were prepared by grinding, which had thin walls. Those used in most of the experiments below had inside and outside diameters 0.060 in. and 0.050 in., respectively, and were prepared from General Ceramics S4 cores.

INTERRUPTED SWITCHING

Experiments on interrupted switching by Gyorgi and Rogers[3] in 1956 appeared to show that the rate of magnetization was dependent on previous treatment as well as on the present state of magnetization and the applied field. However, Haynes[1] states that a careful study of interrupted wave forms shows no serious discrepancies. We have carried out experiments on interrupted switching in an attempt to resolve this contradiction.

Cores in the remanent state were switched by two pulses of equal amplitude, the first of which was of insufficient duration to switch the core completely. The interrupted switching curve produced by these two pulses was compared with the complete switching curve produced by a longer pulse of the same amplitude.

The curves shown in Fig. 1A are for conditions such that 50% of the flux change was produced by the first pulse. As may be seen the response produced during the completion of the switching by the second pulse very nearly coincides with the corresponding part of the complete switching curve. Similar results were obtained when the interruption in switching occurred earlier or later, and for various amplitudes of the switching pulse. These results agree with the statement of Haynes.

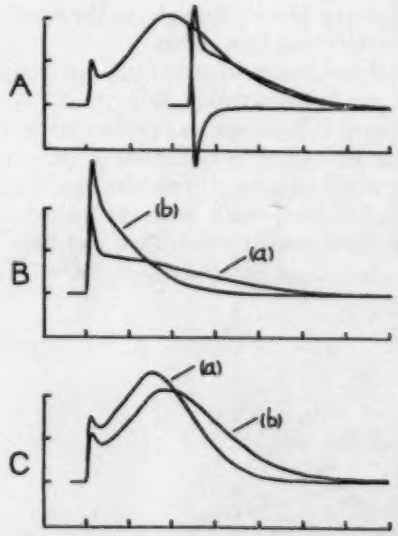

FIG. 1. Tracings of response curves. Vertical scale 0.1 v/division. Horizontal scale 0.2 μsec/division. Excitation 800 ma turns. A. Interrupted switching. B. Second half of curves when initial pulse was (a) 680 ma-t. (b) 1200 ma-t. C. Switching curves when core was previously reset by (a) 800 ma-t. (b) 1600 ma-t.

* The research for this paper was supported (in part) by the Defence Research Board of Canada.

[1] M. K. Haynes, J. Appl. Phys. **29**, 472 (1958).
[2] F. M. Gyorgi, J. Appl. Phys. **29**, 283 (1958).
[3] F. M. Gyorgi and R. Rogers, Conference on Magnetism, Boston (1956), p. 637.

SWITCHING BY TWO PULSES OF DIFFERENT AMPLITUDE

The main difference in conditions between this experiment and the one described in the previous section was that the two pulses used to switch the core were not of the same amplitude. A minor difference in technique used in this and succeeding experiments was the use of a series of three large pulses, of alternating polarity, in place of a single reset pulse. Some small effects due to previous treatment were removed by this procedure and the standard state of the core at the remanent point was made more reproducible.

In Fig. 1B an example is given showing the response produced by the second switching pulse of 800 ma turns. In both cases the duration of the first pulse had been adjusted to produce a flux change equal to 50% of that for complete switching. The difference in condition of the core at the beginning of the second pulse results from the difference in amplitude of the first pulse, 1200 maturn and 680 turns as indicated.

Many measurements have been made of curves such as the above. In all cases, significant dependence of switching rate on the value of the current which had been used to bring the core to the given state of partial magnetization was found. The greatest change in switching rate found due to this cause was approximately two to one.

EFFECT OF VARIATION OF RESET PULSE

A similar, although less marked, dependence of switching rate on previous history was found when the amplitude of the reset pulse preceding the switching cycle was varied. In Fig. 1C the two curves show the response for an 800 ma turn switching pulse when the core had been previously brought to the remanent state by 800 and 1600 ma turn pulses.

The greatest change in switching rate found due to this cause was approximately 50%.

A subsidiary experiment was performed to determine whether the difference in condition of the cores at the beginning of the switching cycle was due to the rate at which they had been reset, or to the maximum field in the reverse direction to which they had been exposed. The rectangular reset pulse was replaced by a triangular ramp with constant rate of rise of current but variable duration and maximum current. Resetting the core always occurred at a constant rate during the earlier part of this pulse. Comparatively little variation of the following cycle was found in this experiment. This appears to indicate that the effect shown in Fig. 1C was mainly caused by variation in the rate at which the core was reset.

EFFECT OF A TRANSVERSE FIELD

If a strong transverse field (i.e., a field perpendicular to the plane of the toroid) is applied and then removed the core is left in a state where the tangential magnetization is very small. The core can then be magnetized to saturation by a switching pulse in a winding through the core. The flux change during this operation has been found to be approximately 50% of that for complete switching, which is what might be expected. The form of the switching curve under these conditions has been compared with curves for completion of switching of half-switched cores as shown in Fig. 1B. It has been noted that the response after half-switching becomes more and more similar to the response after transverse field as the amplitude of the initial half-switching pulse is increased.

It has been previously shown[4] that the reversible or elastic component of magnetization varies approximately 3:1 between the remanent state and the demagnetized state. It is of interest to note that when the core is demagnetized by transverse field, the elastic response is approximately three times that at remanence also.

DISCUSSION

We are unable yet to give any theoretical explanation of the effects described. There is, however, some evidence that 180° domain wall motion is not the only mechanism even at low fields. The measurements of reversible magnetization appear to indicate that some domains are magnetized in a direction perpendicular to the toroid circumference in demagnetized samples. The resemblance between cores demagnetized by transverse field and cores demagnetized by partial switching strengthens this view.

[4] R. W. McKay, J. Appl. Phys. **30**, 565–575 (1959).

Elastic Switching Properties of Some Square Loop Materials in Toroidal Structures

W. C. SEELBACH AND J. R. KISEDA
IBM Research Laboratory, Yorktown Heights, New York

Elastic switching properties of some square loop materials are presented and the concept of an elastic switching constant $S_{w(r)}$ is introduced. The plot of applied "turn over" field strength vs the inverse of the drive width indicates that the inelastic switching constant for a given material is four to five times greater than the elastic switching constant $S_{w(r)}$. The "turn over" field strength is defined to be that value of field strength at which inelastic switching just starts and therefore is considered to be the upper limiting field strength for elastic switching. To a first-order approximation, the ratio of $S_{w(r)}$ to S_w is shown to be equal to the percentage of the total flux capacity of the core that can be switched in an elastic mode of operation. $S_{w(r)}$ values for Molybdenum Permalloy ranged from 0.0374 oe-μsec for $\frac{1}{4}$-mil tapes to 0.0913 oe-μsec for $\frac{1}{2}$-mil tape.

INTRODUCTION

THE inelastic switching curve[1] for full flux reversal with slope S_w and the elastic switching curve for zero-net flux reversal with slope $S_{w(r)}$ are limit curves. Between these limit curves lies a family of curves where the percentage of inelastic flux switched is the parameter. To the authors' knowledge, the concept of an elastic switching constant is new; it affords a new means for material evaluation in elastic or quasi-elastic switching modes.[2]

Bobbin cores made[3] of $\frac{1}{8}$, $\frac{1}{4}$, and $\frac{1}{2}$ mil Molybdenum-Permalloy tape prepared from the same heat were driven in the set direction by current pulses with fast rise and fall times ($\sim$8 mμsec) over a range of pulse widths from 40 mμsec to 1 μsec. The magnitude and rate of change of induction relative to a reproducible reset state was observed for elastic and inelastic switching modes as a function of applied field.

MEASUREMENT TECHNIQUE

The techniques used for obtaining inelastic switching curves were similar to those described by Shevel.[4] Elastic switching curve data was obtained by first premagnetizing the sample to the reset state and then subjecting it to unipolar drive pulses in the opposite direction. For each drive pulse width, the field strength was increased to the point where inelastic switching just started. For the tape materials investigated, this "turn over" point is relatively sharp and easily detected.

EXPERIMENTAL RESULTS

In a plot of applied field strength as a function of inverse switching time, where the latter is adjusted to equal the inverse drive pulse width, S_w is a linear function of tape thickness squared. This linear relationship was predicted and experimentally verified by Menyuk and Goodenough,[1,5] Our experimental values were somewhat smaller than those obtained by Menyuk, probably because of differences in test techniques and materials. The elastic and inelastic switching curves for $\frac{1}{8}$, $\frac{1}{4}$, and $\frac{1}{2}$ mil samples are shown in Fig. 1, wherein the plot shows $S_w/S_{w(r)}$ ratios ranging between four and five. Other samples not reported here showed ratios of approximately ten indicating an appreciable variance of the ratio of inelastic to elastic switching coefficients can be expected for Molybdenum-Permalloy.

The elastic switching coefficient $S_{w(r)}$ as a function of tape thickness, as shown in Fig. 2, was found to be linear. Because of this linear dependence, one might postulate that the elastic switching properties are dependent on microscopic eddy currents, and spin relaxation damping mechanisms, as shown by Friedlaender,[6] where wall motion is limited to the surface of the tape.

The maximum rate of change of inelastic induction as a function of applied field for the samples of Fig. 1

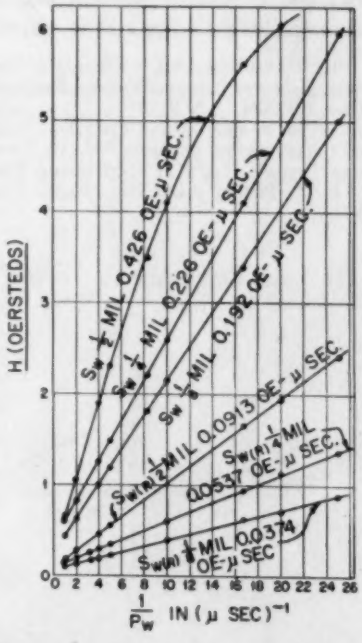
H (OERSTEDS)
$\frac{1}{P_w}$ IN (μ SEC)$^{-1}$
S_w $\frac{1}{2}$ MIL 0.426 OE-μ SEC.
S_w $\frac{1}{4}$ MIL 0.228 OE-μ SEC.
S_w $\frac{1}{8}$ MIL 0.192 OE-μ SEC.
$S_{w(r)}$ $\frac{1}{2}$ MIL 0.0913 OE-μ SEC.
$S_{w(r)}$ $\frac{1}{4}$ MIL 0.0537 OE-μ SEC.
$S_{w(r)}$ $\frac{1}{8}$ MIL 0.0374 OE-μ SEC

FIG. 1. Elastic and inelastic switching curves for 4–79 Mo-Permalloy bobbin cores.

[1] N. Menyuk and J. B. Goodenough, J. Appl. Phys. **26**, 8 (1955).
[2] V. L. Newhouse, Proc. Inst. Radio Engrs., **45**, 1484 (November, 1957).
[3] Obtained from Magnetics, Inc.
[4] W. Lee Shevel, Jr., J. Appl. Phys. **30**, 475S (April, 1959).
[5] N. Menyuk, J. Appl. Phys. **26**, 692 (1955).
[6] F. J. Friedlaender, Trans. Am. Inst. Elec. Engrs. **75**, Pt. I, 268 (July, 1956).

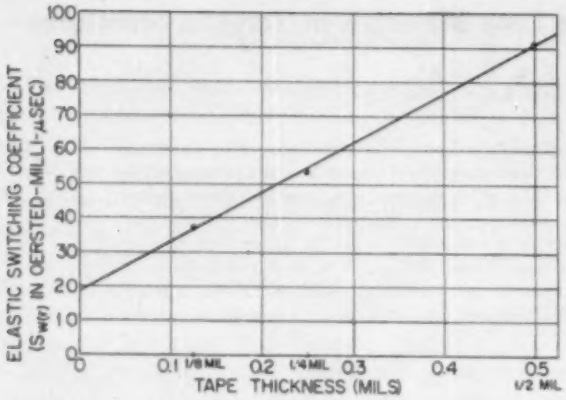

FIG. 2. Variation of the elastic switching coefficient as a function of tape thickness.

were plotted. The slopes of these curves in the linear region have been defined as the switching resistance, R_0,[7,8] and can be shown to be approximately equal to the ratio of the total flux capacity of the core to the product of the switching coefficients S_w and the mean magnetic path length[9]

$$R_0 \cong \bar{R}_0 = \Delta\phi_1 / S_w l_m. \tag{1}$$

The maximum rate of change of elastic induction at the "turn over" points vs applied field (mmf) for cores of different tape thicknesses was also plotted. These curves are the loci of the "turn over" points and their slopes are equal to the slopes of the curves traced for elastic peak volts per turn vs F (mmf) with pulse width as a parameter.

From the plots R_0, the inelastic switching resistance for a core of given tape thickness, is approximately equal in magnitude to the elastic switching resistance $R_{0(r)}$. Van Sant[10] has shown, in terms of viscosity coefficients, that elastic to inelastic switching resistance ranges between one and three experimentally. It is postulated that the elastic switching resistance can be represented by the equation

$$\bar{R}_{0(r)} \cong \Delta\phi_{1(r)} / S_{w(r)} l_m, \tag{2}$$

where $\Delta\phi_{1(r)}$ is the elastic flux changed, $S_{w(r)}$ is the elastic switching constant and l_m is the mean magnetic path length. Since it was shown that

$$R_{0(r)} \cong R_0, \tag{3}$$

then it can be seen that

$$\Delta\phi_{1(r)} / \Delta\phi_1 \cong S_{w(r)} / S_w. \tag{4}$$

Stated simply, the percentage of flux capacity equal to the elastic flux output at the "turn over" can be approximated by the ratio of $S_{w(r)}$ to S_w.

Experimental validity of Eq. (4) was established to be within the degree of approximation as postulated. For the cores tested, Eq. (4) becomes more accurate as the set pulse width is decreased. At set pulse widths of 100 mμsec and less $\Delta\phi_{1(r)}$ approaches its limit value.

In the course of investigation, 1 mil Deltamax[11] samples and some ferrite materials were tested. The ratios of the slope of the elastic and inelastic switching curves of Deltamax were comparable to Molybdenum-Permalloy, but the absolute magnitude of the slopes were numerically larger by approximately an order of magnitude. Ferrite materials, in general, showed much smaller ratios of $S_{w(r)}/S_w$ relative to what was seen in Molybdenum-Permalloy and Deltamax.

ACKNOWLEDGMENTS

The authors express their thanks to J. N. Cole and V. A. Ranieri for their contributions in instrumentation and measurements and to P. E. Stuckert for his stimulating and enlightening discussions.

[7] L. S. Onyshkevych, "Analysis of circuits with multiple-hole magnetic cores," Massachusetts Institute of Technology, Tech. Rept. No. 329 (July 9, 1957).

[8] W. G. Breckenridge, "Electronic realization of linear sequential binary coding networks," S. M. Thesis, Department of Electrical Engineering, MIT (September, 1956).

[9] E. A. Sands, Proc. Inst. Radio Engrs. **40**, 1246 (October, 1952).

[10] O. J. Van Sant, J. Appl. Phys. **28**, 486 (1957).

[11] Obtained from Arnold Engineering.

Anisotropy

Anisotropy Properties of Hexagonal Ferrimagnetic Oxides

J. SMIT, F. K. LOTGERING, AND U. ENZ
Philips Research Laboratories, N. V. Philips' Gloeilampenfabrieken, Eindhoven-Netherlands

The effects of the incomplete alignment of all magnetic moments of a sample in an applied field on the torque curves are discussed. Examples are given of torque curves determined for cobalt-substituted hexagonal compounds of the ferroxdure type with low anisotropy. It is shown that the characteristic details of these curves can be interpreted in terms of this incomplete alignment, both on a microscopic and an atomic scale.

I. INTRODUCTION

CONSIDER a ferromagnetic crystal having an uniaxial anisotropy energy $K\sin^2\theta$ equivalent to an anisotropy field $H^A=2K/M$. In a strong external field making an angle α with the easy axis the magnetization is practically parallel to the field. If the field is in the direction perpendicular to the easy direction, exact colinearity exists for $H\gtrsim H^A$ and the torque is zero. The torque curve as a function of α is essentially sinusoidal. If however, $H<H^A$ and $\alpha=90°$, the magnetization cannot be aligned along H, but takes up an intermediate angle θ_0 given by

$$\sin\theta_0=H/H^A. \tag{1}$$

In this position, the torque is not zero but is given by

$$T_0=HM\cos\theta_0=\pm HM[1-(H/H^A)^2]^{\frac{1}{2}}. \tag{2}$$

If α is slightly less than 90°, $\theta_0<90°$ and the torque is positive. If α is increased to a value greater than 90°, the equilibrium angle θ_0 changes abruptly to $180-\theta_0$, and the torque is thus reversed. A torque curve of the type given in Fig. 1 results. In crystals this sudden change will occur by wall motion and may be accompanied by hysteresis. The aim of this paper is to show that similar behavior can occur on a microscopic, and even on an atomic scale, giving rise to peculiar anisotropy properties of the material.

II. MICROSCOPIC MAGNETICALLY HARD INCLUSIONS

Let us assume that we have a magnetic crystal in which there is a cluster formation or an inclusion of a relatively hard ferromagnetic material with an anisotropy field H^A. One may expect therefore that a field smaller than H^A but larger than the bulk anisotropy field will not be able to rotate all the magnetic moments into the perpendicular direction. This will not occur even if there is exchange coupling between the moments of the precipitate or cluster ions and those of the matrix. Let us consider a spherical particle, with radius R small enough to assure essential parallelism of the spins inside it. The particle is coupled by exchange energy with the surrounding matrix so that the total energy outside the particle is given by

$$E=4\pi\int_R^\infty r^2\left[\frac{1}{2}AM^2\left(\frac{d\varphi}{dr}\right)^2-HM\cos\varphi\right]dr, \tag{3}$$

in which $\varphi(r)$ is the angle of the spin with the applied field. The dipolar energy is neglected. This gives for the equilibrium orientation at any point

$$AM^2\left(\frac{d^2\varphi}{dr^2}+\frac{2}{r}\frac{d\varphi}{dr}\right)-HM\sin\varphi=0. \tag{4}$$

For $\varphi<90°$ we approximate $\sin\varphi$ by φ, and obtain then

$$\varphi=Ce^{-qr}/r\,|\,(r\gtrsim R), \tag{5}$$

where C is a constant and

$$q=\left(\frac{H}{AM}\right)^{\frac{1}{2}}=\frac{1}{a}\left(\frac{H}{H^E}\right)^{\frac{1}{2}}, \tag{6}$$

since $AM=a^2H^E$, where a is the atomic spacing and H^E the exchange field. This configuration may be considered a three-dimensional Bloch wall. At $r=R$, the total surface exchange torque must be equal to the torque exerted on the particle by the crystal anisotropy defined by $K=\frac{1}{2}H^AM$ and by the field

$$-4\pi R^2AM^2\left(\frac{d\varphi}{dr}\right)_{r=R}=\frac{4\pi}{3}R^3[K\sin2(\alpha-\varphi)-HM\sin\varphi]_{r=R}. \tag{7}$$

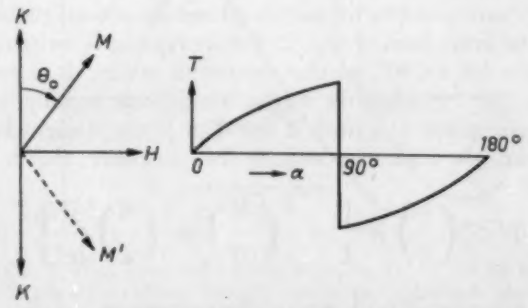

FIG. 1. Torque curves for an uniaxial ferromagnetic crystal. The applied field H is smaller than the anisotropy field H^A.

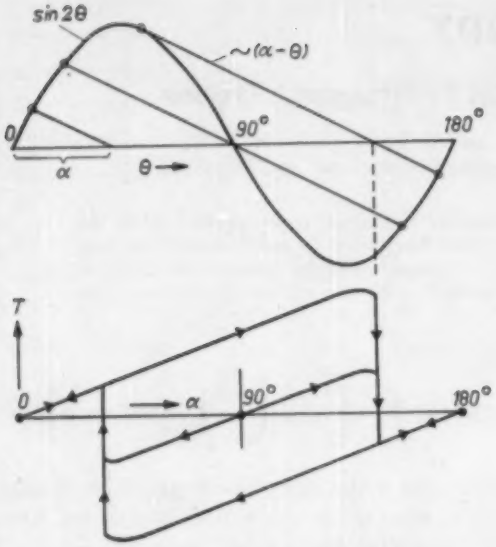

FIG. 2. In the upper curve the anisotropy torque and the exchange torque are plotted for a hard magnetic sphere in a soft magnetic matrix, whereas in the lower curve is shown the resulting torque as function of the orientation of the applied field.

If the angle that the particle magnetization makes with the easy axis is $\theta=\alpha-\varphi_{r=R}$, then, according to Eq. (5) and replacing the sine by its argument in the last term in Eq. (7):

$$\sin 2\theta=6\left(\frac{a}{R}\right)^2\frac{H^E}{H^A}\times\left[1+\frac{R}{a}\left(\frac{H}{H^E}\right)^{\frac{1}{2}}+\frac{1}{3}\left(\frac{R}{a}\right)^2\frac{H}{H^E}\right](\alpha-\theta). \quad (8)$$

The left and the right hand side of Eq. (8) have been plotted as a function of θ in Fig. 2 for different values of α. For small values of α, there is only one point of intersection, corresponding to one stable value of θ. For increasing values of α, there may occur three points of intersection, of which the upper one corresponds to the state with the lowest energy for $\alpha\leqslant 90°$. For $\alpha=90°$ the two extreme crossing points are stable, but there is no easy way of switching. This has to wait until the straight line has become a tangent of the sine function. The corresponding torques as a function of α are plotted in the lower part of Fig. 2. For decreasing α, switching occurs for $\alpha<90°$, so that hysteresis occurs. It is seen that the hysteresis is absent when there is only one crossing point at a time, if the slope of the straight line exceeds the maximum slope of the sine curve; that is, if

$$H^A<3\left(\frac{a}{R}\right)^2 H^E\left[1+\frac{R}{a}\left(\frac{H}{H^E}\right)^{\frac{1}{2}}+\frac{1}{3}\left(\frac{R}{a}\right)^2\frac{H}{H^E}\right], \quad (9)$$

which for small fields essentially reduces to

$$H^A<3(a/R)^2H^E, \quad (10)$$

and for strong fields to

$$H^A<H. \quad (11)$$

If one starts the measurements at $\alpha=90°$, which is thought to be the difficult direction, then as many domains point up as downwards, i.e., are in the upper as in the lower point of intersection of Fig. 2. The torque curve between the switching points is then the average of the two, whereas beyond the switching points, the original curves are followed. This torque curve, therefore, has the remarkable property that it has a positive slope at $\alpha=90°$, indicating the existence of a preferential direction. This is only true if the value of θ at $\alpha=90°$ is smaller than 45°.

This behavior may also be demonstrated in Fig. 3. Two preferential directions for the particles, pointing in arbitrary directions are indicated. When, after demagnetization, the applied field is along the bisector, the magnetizations point along M_1 and M_2. Because of symmetry there is no torque. If the field is rotated through a small angle, the magnetization vectors rotate in the sense indicated, because the exchange "spring" of M_1 is released and the other is stretched. It is seen that for large anisotropies the resulting torque tends to restore the crystal axis in the original orientation with respect to H, as is the case for an easy direction of magnetization.

Such phenomena as hysteresis and the occurrence of an easy direction in an intrinsically abhorred direction are observed in compounds with the hexagonal magnetoplumbite structure and the general chemical formula $BaFe_{12-2x}Co_xTi_xO_{19}$. It is known[1] that the substitution of iron by cobalt reduces the crystalline anisotropy constant K_1, and that K_1 becomes negative at low temperatures for $x>\approx 1$. Torque measurements

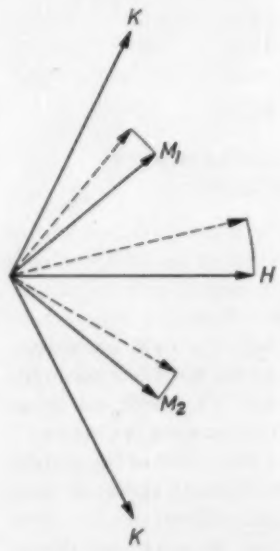

FIG. 3. Schematical representation of the orientation of the magnetic vectors of two types of hard magnetic particles in a field.

[1] E. W. Gorter, see H. B. G. Casimir et al., Proc. Magnetism Conference, Grenoble, France, July 1958, p. 303.

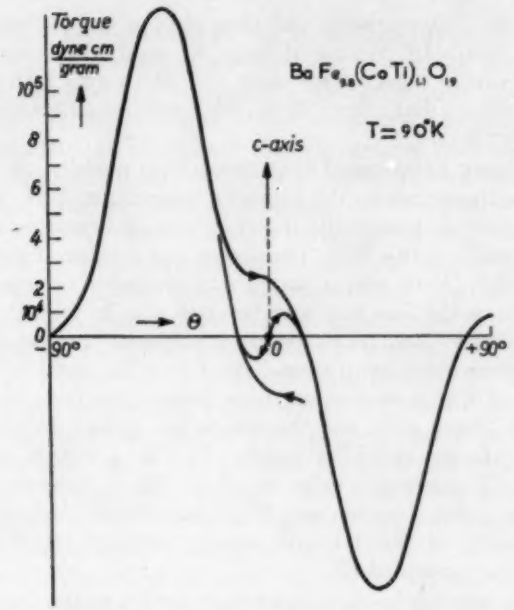

FIG. 4. Torque curves for $BaFe_{9.8}Co_{1.1}Ti_{1.1}O_{19}$ in a field of 32 000 oe at $T=90°K$ for rotations in the basal plane. The samples were heated to room temperature before each series of measurement.

were carried out (Fig. 4) on polycrystalline samples with compositions near the compensation point for K_1. The c axes of the crystals of the samples were oriented by the so-called topotactical reaction.[2] This method is essential for these low anisotropy materials because direct orientation of the crystals in a field is not effective. Figure 4 gives the torque curve for $x=1.1$ at $T=90°K$ in fields of 32 000 oe.

Cobalt-rich clusters presumably play the role of the hard magnetic particles here. The anisotropy of Co is very high. (This is discussed in the next section.) When the measurements were started with the field along the c axis, this direction proved to be an easy direction for small deviations. The slope of the torque curve at $\theta=0$ is, however, much larger than that of the torque curves obtained when starting with the field in the basal plane. At room temperature no anomalous properties were observed. It may be expected that condition (10) then applies because the anisotropy of cobalt is strongly temperature dependent. Apparently at $T=90°K$ the applied field of 32 000 oe is smaller than that given by (11).

It will be shown in the next section that although the resultant anisotropy of all cobalt ions is negative, each Co ion is not isotropic in the basal plane. Most of them have one easy direction near to the basal plane. The anisotropy in the basal plane is then to a first approximation cancelled out by the combined action of all ions. If cluster formation takes place, however, it may also be expected that clusters occur with specific preferential orientations in the basal plane again giving rise to hysteresis (in this case, rotational hysteresis). This was only observed in relatively small fields, in which the material was not saturated (<3000 oe). At strong fields (32 000 oe), however, torque curves of the type of Fig. 5 were observed; that is, a more or less normal torque curve with 180° symmetry was found, with the direction in which the field was first applied as easy axis. Two such curves are shown, obtained at 90°K after heating the specimen to room temperature. The material always remembers the axis of the first field to which it has been exposed after demagnetization. It possesses, as it were, an absolute memory.

A tentative explanation of this behavior is the following. Let us assume that the clusters with different easy axes in the basal plane are not too far apart, so that the exchange interaction tends to align them parallel. If a strong field is applied, an equilibrium configuration will be established in which the total energy (consisting of field energy, anisotropy energy, and exchange energy) is minimum with respect to the slight rotations of the field, as has been discussed (Fig. 3). This means that the magnetization of any individual cluster is not freely rotatable. If the field is rotated and passes the direction perpendicular to the cluster, which originally made the largest angle with the field, this cluster will not now reverse its magnetization because it is fixed to the neighboring clusters. The configuration can only rotate as a whole, maintaining the mutual orientations of the clusters, when the perpendicular orientation of an appreciable part of all clusters is passed. In this way one, obtains an anisotropy with 180° symmetry. The observed torques are of the same order of magnitude as the amplitude of the hysteresis in Fig. 4.

III. ANOMALOUS TORQUE CURVES ON AN ATOMIC SCALE

The theory of the crystalline anisotropy energy for the Co^{II} ion in an octahedral site in the spinel lattice has been worked out by Slonczewski.[3] It was shown

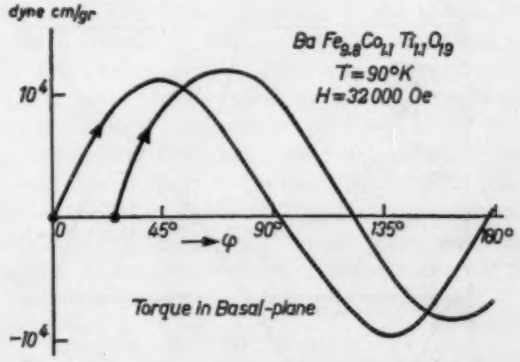

FIG. 5. Torque curve for $BaFe_{9.8}Co_{1.1}Ti_{1.1}O_{19}$ at T=90° in the bacal plane for different orientations of the field which has been first applied after demagnetization.

[2] F. K. Lotgering, J. Inorg. Nuclear Chem. **9**, 113 (1959).

[3] J. C. Slonczweski, Phys. Rev. **110**, 1341 (1958).

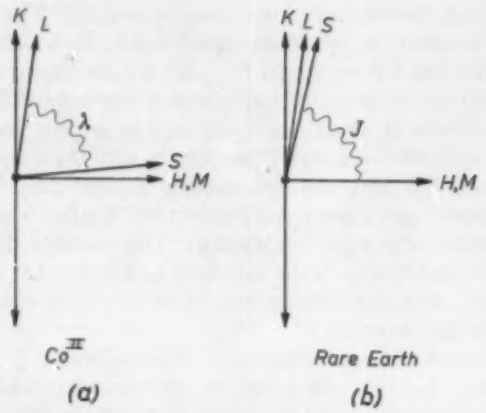

FIG. 6. Schematic representation of the orientation of the spin and orbital angular momentum vectors with respect to the axis of an uniaxial potential in an applied field for the Co^{II} ion and an typical rare earth ion.

there that the ion in its lowest state has an orbital angular momentum, which is quantized as if it were in a P state. Due to the action of a trigonal electrostatic field, the orbital momentum is strongly bound to one of the [111] axes of the crystal. The torque exerted by the field on the crystal is then caused by the coupling of the spin to the orbit given by $\lambda\mathbf{LS}$ and by the coupling of the spin to the field. If we consider only one Co ion in a matrix, the coupling with the magnetization of the matrix (which is aligned along the field) by means of the exchange energy J is more important than the action of the field itself on the Co ion. In a series of springs the force for a certain deformation is determined by the weakest spring. In this case this is the spin-orbit energy λ, which is about ten times as small as the other interactions. Schematically one then obtains the picture of Fig. 6(a). In passing it may be said that similar behavior is expected for some rare earth ions with the difference that then J is the smallest interaction [Fig. 6(b)].

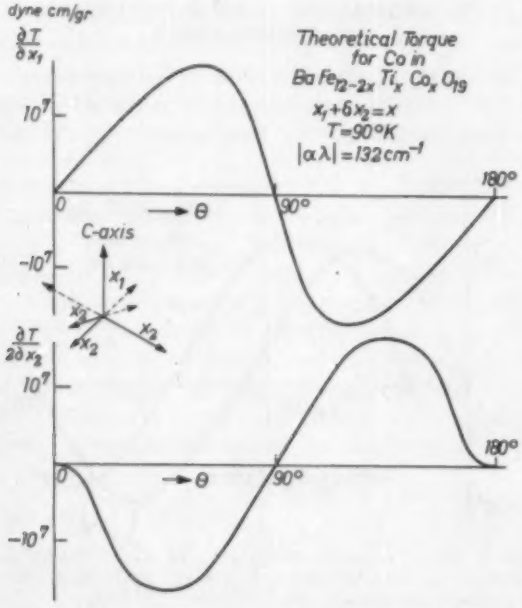

FIG. 7. Theoretical torque curves at $T=90°$K for Co ions in different sites in hexagonal compounds.

It may be assumed that the orbital moment of the Co-ion switches to the opposite orientation if H, and therefore S, passes the direction perpendicular to the trigonal axis ($\theta=90°$). The torque has a value of about $\frac{3}{2}\alpha\lambda\sin\theta$ ($S=\frac{3}{2}$ and a factor α is included because λ refers to the free ion) and reverses sign at $\theta=90°$. In the atomic case, no hysteresis is involved because of a quantum mechanical tunnel effect (not discussed here). Actually, at finite temperatures the ion is not completely in its lowest state and the torque has to be multiplied by a factor $\tanh\frac{3}{2}|\alpha\lambda|(\cos\theta)/kT$. For $T=90°$K and using Slonczewski's value of $|\alpha\lambda|=132$ cm^{-1} the upper curve of Fig. 7 is obtained. The characteristic feature of the curve of Fig. 1 is still present although the sharp edges are rounded off.

We now apply these theoretical results to the torque curves of some cobalt substituted ferroxdure samples of the type discussed in Section 2. For the composition $BaFe_{12-2x}Co_xTi_xO_{19}$ torque curves, averaged for clock-wise and contour clock-wise rotation, are given in Fig. 8 for $x=0.9$, 1.0, 1.1 lying in the compensation region, and for $x=1.5$. The influence of the Co ions on the torque curves is particularly strong near $\theta=30°$. For $x=1.0$ there is both a preferential direction (c axis) and a preferential cone. Expansion in a Fourier series would give terms up to at least $\sin12\theta$ and is therefore not very appropriate. In order to understand these curves we have to consider the atomic structure of these compounds.[4] Like the spinels, they are composed of a close-packed structure of oxygen ions, some of the interstices being occupied by the metal ions. In some layers a fraction of the oxygen ions is replaced by Ba ions, rendering the structure hexagonal. The layers in between have the spinel structure, with one of the [111] axes parallel to the c axis. The position of the octahedral ions is indicated in Fig. 9. The trigonal axis of the central ion is parallel to the c axis and those of the others make angles of about 71° or 109° with the c axis. The latter metal ions do not find themselves in a field of purely trigonal symmetry around their appropriate [111] axes because one octahedral ion is missing in the environment of each octahedral ion but a Ba ion is present at a greater distance. We shall neglect this difference since Ti ions and other Co ions also distort the crystalline fields. A similar situation is present in disordered inverse spinels and there the effect of Co on the anisotropy is of the same type as in magnetite, though somewhat weaker. The central octahedral ion together with the three-upper ions of Fig. 9 would give no uniaxial anisotropy. Therefore, for equal occupation

[4] J. J. Went, G. W. Rathenau, E. W. Gorter, and G. W. van Oosterhout, Philips Tech. Rev. 13, 194 (1952).

number, the influence of the noncentral ions on the uniaxial anisotropy is predominant. Since the central ions give rise to a positive K_1, we can already understand why the overall effect of Cobalt on the anisotropy is negative. It is assumed that the greater part of the Co ions goes into the spinel layers, as one should expect from electroneutrality reasons. We shall show that also the more detailed structure of the torque curves can be understood on this basis, by summing the the torque curves of the individual ions. That of the central ions is already given in the upper curve of Fig. 7. For an ion having an axis making an angle of 109° with the c axis a torque reversal will occur at $\theta=19°$. This is a very characteristic effect and is still found in the torque curve obtained by averaging over all azimuthal angles and taking into account the finite temperature (Fig. 7, lower curve). We have now to superimpose both curves and this is done in Fig. 9 for different ratios of the two occupation numbers for $x=1$. It is satisfying that the right type of curve is found for approximately equal values of x_1 and x_2. Of course the positive $\sin 2\theta$ curve of the iron ions has still to be added. The calculated effect of the Co ions is about 2–3 times too large to explain the experimental results. This may be compared with the reduction factor 4 in nickel ferrite with respect to magnetite in which Co ions are substituted.[5]

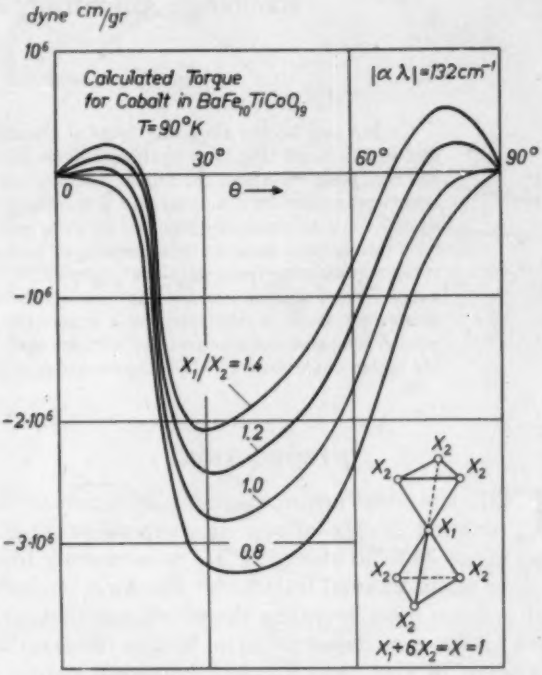

FIG. 9. Theoretical torque curves at $T=90°K$ for Co ions in $BaFe_{10}CoTiO_{19}$ for various distributions over the octahedral sites in the spinel layers.

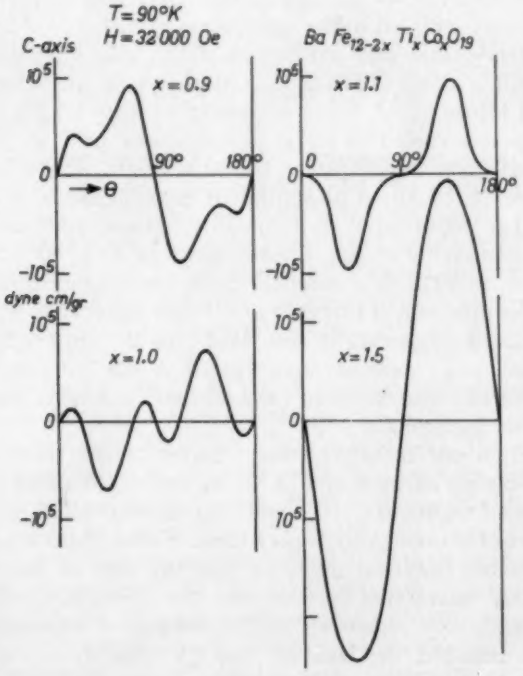

FIG. 8. Torque curves for compounds $BaFe_{12-2x}Co_xTi_xO_{19}$ for $x=0.9$, 1, 1.1 and 1.5 at $T=90°K$ and $H=32\,000$ oe.

[5] C. M. van der Burgt, Philips Research Repts. **12**, 97 (1957).

In conclusion we can say that the large negative slope near $\theta=90°$, giving rise to a preferential cone in some cases, is due to the central octahedral ions, whereas the small or positive slope near $\theta=0°$ and the large dip around $\theta=20$ or 30° is due to Co ions on the other sites. On the basis of this model one should not expect a preferential cone to occur at small angles ($\theta<20°$).

Finally, we will briefly consider the dynamic behavior of our simple model. If we apply a static field at right angles to the easy axis and a superimposed transverse microwave field, the orbital angular momentum of the Co ions will change sign periodically and, with it, the sign of the large torque. In the first approximation we already have this large amplitude of the torque for a very small alternating field, as if a very large opposing static field were present. This can in principle be identified with the so-called giant anisotropy fields found by Dillon[6] and explained by Kittel.[7] For a purely uniaxial field the situation is as simple as treated here, and should apply to Co ions in octahedral sites in spinels or similar compounds. For the rare earth ions in garnets, the crystalline fields do not have this simple symmetry. Consequently more orbital states are stable, and switching at intermediate angles may occur.

[6] J. F. Dillon, Phys. Rev. **105**, 759 (1957).

[7] C. Kittel, Phys. Rev. Letters **3**, 169 (1959); J. Appl. Phys. **31**, 11S (1960), this issue.

Exchange Anisotropy in Cu-Mn and Ag-Mn Alloys

J. S. KOUVEL
General Electric Research Laboratory, Schenectady, New York

Cu-Mn and Ag-Mn alloy specimens of about 25 atomic % Mn were cooled to 4.2°K in a magnetic field, and it was found that their hysteresis loops measured parallel to this field were displaced from their symmetrical positions about the origin. The displacement of the loops decreases monotonically with increasing temperature, and its disappearance is accompanied by large hysteresis losses. These unusual properties are similar to those previously reported for disordered Ni-Mn alloys and are also attributed to exchange anisotropy interactions between small regions of ferromangetic and antiferromagnetic order. It is proposed that these regions arise from statistical composition fluctuations in the alloys and the existence of both ferromagnetic and antiferromagnetic interactions between Mn atoms. The essence of this microscopic exchange anisotropy model is illustrated for a square lattice representation of these alloys. The magnetic transformation temperatures are identified with anomalies in the $1/\chi$ vs T curves; these temperatures are considerably higher than those at which the exchange anisotropy effects disappear.

INTRODUCTION

THE low-temperature magnetic behavior of disordered Ni-Mn alloys, of composition ranging from about 20 to 30 atomic % Mn, was recently found to have many unusual features.[1–4] The most intriguing and perhaps most revealing discovery was that when these alloys were cooled to liquid helium temperatures in a magnetic field, their magnetic hysteresis loops were displaced from their symmetrical positions about the origin, i.e., the alloys could be magnetized more easily in the direction of the field applied during cooling than in the opposite direction. Subsequent torque measurements confirmed this unidirectional anisotropy and also revealed a rotational hysteresis that did not vanish at high fields. All these properties and their variation with temperature were readily though very qualitatively interpreted in terms of the exchange anisotropy model originally conceived for the ferromagnetic Co-antiferromagnetic CoO system.[5] Moreover, the anomalous field and temperature dependences of magnetization for these alloys cooled in zero field were also shown to be consistent with this model.

It was therefore concluded that there are regions of ferromagnetic and antiferromagnetic spin alignment in these disordered Ni-Mn alloys. Furthermore, the results of neutron diffraction and magnetic measurements indicated that these regions, if present, must be very small.[4] The origin of this magnetic inhomogeneity of the Ni-Mn alloys could be attributed to small ferromagnetic regions of ordered Ni_3Mn phase in an atomically disordered and presumably antiferromagnetic matrix. More recently, however, it was found that Co-Mn alloys (25 to 35 atomic % Mn) also exhibit exchange anisotropy properties,[6] and there is no reported tendency for long-range atomic ordering in these alloys. Hence, it is now believed that the statistical composition fluctuations inherent in a disordered alloy and the presence of competing magnetic interactions (antiferromagnetic for Mn-Mn nearest neighbor atoms and possibly for Co-Mn pairs, and ferromagnetic for Ni-Ni, Ni-Mn, and Co-Co pairs) are together responsible for small regions of ferromagnetic and antiferromagnetic order in these alloy systems.

Low-temperature measurements of magnetic susceptibility, spin resonance, and electrical resistivity have recently led to the speculation that there are both ferromagnetic and antiferromagnetic spin alignments in dilute alloys of Mn in Cu.[7] Moreover, in the Schmitt and Jacobs paper, it is mentioned that when a 1.8% Mn alloy was cooled to 4.2°K in a magnetic field, its hysteresis loop was displaced from the origin. This effect, however, could not be attributed unambiguously to exchange anisotropy. Subsequently, Street and Smith found that by cooling Cu-Mn alloys of 40 to 50% Mn down to 80°K in a magnetic field, the magnetizations in the direction of this field were much larger than those obtained by cooling in zero field.[8] Since complete hysteresis loops were not investigated, it was not possible to identify the observed behavior with a specific interaction mechanism.

From our tentative interpretation of the exchange anisotropy effects found in Ni-Mn and Co-Mn alloys, it seemed reasonable to expect that disordered alloys of Mn in Cu would also display these effects. There is considerable empirical evidence that the sign of the exchange interaction between two Mn atoms in an alloy depends very sensitively on the distance of separation. For example, the Heusler alloy,[9] Cu_2MnAl, in which the shortest distance between Mn atoms is 4.20A, is ferromagnetic, whereas in both the Mn-rich Cu-Mn

[1] J. S. Kouvel, C. D. Graham, Jr., and J. J. Becker, J. Appl. Phys. **29**, 518 (1958).
[2] J. S. Kouvel, C. D. Graham, Jr., and I. S. Jacobs, J. phys. radium **20**, 198 (1959).
[3] J. S. Kouvel and C. D. Graham, Jr., J. Appl. Phys. **30**, 312S (1959).
[4] J. S. Kouvel and C. D. Graham, Jr., J. Phys. Chem. Solids **11**, 220 (1959).
[5] W. H. Meiklejohn and C. P. Bean, Phys. Rev. **102**, 1413 (1956); and Phys. Rev. **105**, 904 (1957).
[6] J. S. Kouvel, J. Phys. Chem. Solids (to be published).
[7] Owen, Browne, Arp, and Kip, J. Phys. Chem. Solids **2**, 85 (1957); R. W. Schmitt and I. S. Jacobs, J. Phys. Chem. Solids **3**, 324 (1957).
[8] R. Street and J. H. Smith, J. phys. radium **20**, 18 (1959).
[9] O. Heusler, Ann. physik (5) **19**, 155 (1934).

alloys[10] and the ordered alloy[11] NiMn the distance between nearest-neighbor Mn atoms is about 2.62A and the moments of these atoms are coupled antiferromagnetically. Undoubtedly, the crossover separation distance varies with the particular system, but it can nevertheless be speculated that in a disordered fcc Cu-Mn alloy of 25% Mn the interaction between nearest-neighbor Mn atoms, separated by[12] 2.62A, is antiferromagnetic while the interaction between next-nearest-neighbor Mn atoms, separated by[12] 3.70A, is ferromagnetic. The possible coexistence of ferromagnetic and antiferromagnetic spin alignments in Cu-Mn alloys and the provocative experimental results cited above suggested the present investigation of exchange anisotropy in this alloy system. We also decided on a similar study of fcc Ag-Mn alloys, whose atomic separations are about 10% greater[13] than those of the Cu-Mn alloys.

EXPERIMENTAL RESULTS AND DISCUSSION

For this preliminary study, Cu-Mn and Ag-Mn alloys of about 25% Mn were prepared by induction-melting in an argon atmosphere. Chemical analysis of the ingots gave 24.1 and 23.7 atomic % Mn for the Cu-Mn and Ag-Mn alloys, respectively, with about 0.01 atomic % Fe in each. Cylindrical specimens 0.5 in. long by 0.25 in. diam, machined out of the ingots, were annealed 15 hrs at 800°C (Cu-Mn) or 900°C (Ag-Mn) and then quenched into water. X-ray diffraction examination of filings given the same heat treatment showed up only fcc structures for the two alloys; the lattice parameters obtained were 3.697A (Cu-Mn) and 4.083A (Ag-Mn), which compare closely with published values.[12,13]

Between liquid helium and room temperatures, hysteresis loops were obtained for these specimens in the apparatus described previously[1]; magnetizations were measured while the applied field was slowly cycled between ±10 koe. For all the data presented, the applied fields have been corrected for demagnetizing fields estimated from the magnetizations and over-all shapes of the specimens.

The curves shown in Fig. 1 represent the measurements made for increasing temperature after the specimens had been cooled to 4.2°K in zero field. The most obvious feature of these curves, which are very similar for the two alloys, is the maximum in the magnetization measured in a given field. It is particularly noteworthy that the remanent magnetizations have their maximum values at about 60°K (for the Cu-Mn alloy) and 40°K (Ag-Mn). At these temperatures, the hysteresis losses of the alloys are maximum. Moreover, it is clear that these losses disappear at liquid helium temperatures and, with increasing temperature, at about 100°K (Cu-Mn)

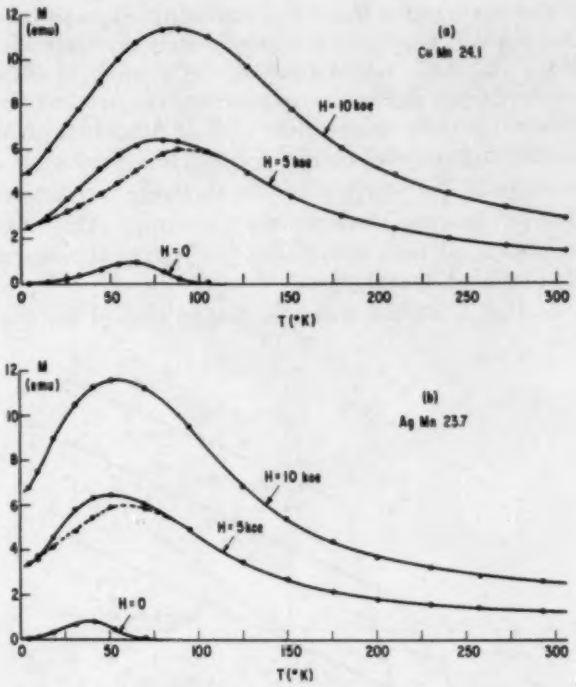

FIG. 1. Magnetization vs temperature curves for various fields for the alloys (a) CuMn 24.1 and (b) AgMn 23.7. For $H=5$ koe, the solid and dashed curves represent the descending and ascending branches of the hysteresis loops, respectively.

and 80°K (Ag-Mn). This behavior strongly resembles that of the Ni-Mn alloys previously reported,[2] particularly the 31.1% Mn composition, where the similarity is even quantitative. Hence, in the following experiments, the Cu-Mn and Ag-Mn specimens were cooled down to 4.2°K from 300°K in a 5 koe field applied in the direction of magnetization measurement; hysteresis loops were measured at 4.2°K and at higher temperatures. These experiments were then repeated with a 10 koe field applied during cooling. The loops measured at 4.2°K, including those obtained for zero field during cooling, are shown as solid curves in Fig. 2. It is very clear from this figure that the fields applied during cooling result in hysteresis loops that are drastically displaced from symmetrical positions about the origin. The corresponding curves for the two alloys are strikingly similar in every respect. It should be noted that the loops for a 10 koe field during cooling give equal and opposite magnetizations for $H=\pm 10$ koe. Hence, since the magnetizations are completely reversed in sufficiently high reverse fields, the displaced hysteresis loops are proof of an exchange anisotropy mechanism. It is also evident from Fig. 2 that the mean remanent magnetization varies almost linearly with the field applied during cooling, $H_{cl\theta}$. The mean coercive field, however, decreases as $H_{cl\theta}$ increases from 5 to 10 koe. In fact, since for each alloy the slopes of the curves at positive fields are essentially independent of $H_{cl\theta}$, it is probably more meaningful to consider the fields at which the curves for $H_{cl\theta}=5$ and 10 koe

[10] Bacon, Dunmur, Smith, and Street, Proc. Roy. Soc. (London) **A241**, 223 (1957).
[11] J. S. Kasper and J. S. Kouvel, J. Phys. Chem. Solids **11**, 231 (1959).
[12] S. Valentiner and G. Becker, Z. Physik **80**, 735 (1933).
[13] E. Raub and A. Engel, Z. Metallk. **37**, 62 (1946).

cross the curve for $H_{clg}=0$. These adjusted mean coercive fields, it is seen, vary approximately inversely with H_{clg}. Therefore, for each alloy, the product of these coercive fields and the corresponding remanent magnetizations is fairly independent of H_{clg}. According to the simple exchange anisotropy model,[5] this product is a measure of the strength of the exchange interactions that produce the unidirectional anisotropy. The value we obtain for both alloys over this restricted range of H_{clg} is about 30 000 erg/cc.

In Fig. 2, we also show (as dashed curves) the hysteresis loops for the two alloy specimens cooled to 4.2°K in a 5 koe field applied perpendicular to the axis of measurement. It is clear that the magnetizations for these loops at any given field are higher than those for the $H_{clg}=0$ loops. The same result was previously obtained for Ni-Mn alloys and was shown to be difficult to explain in terms of the simple exchange anisotropy model.[4]

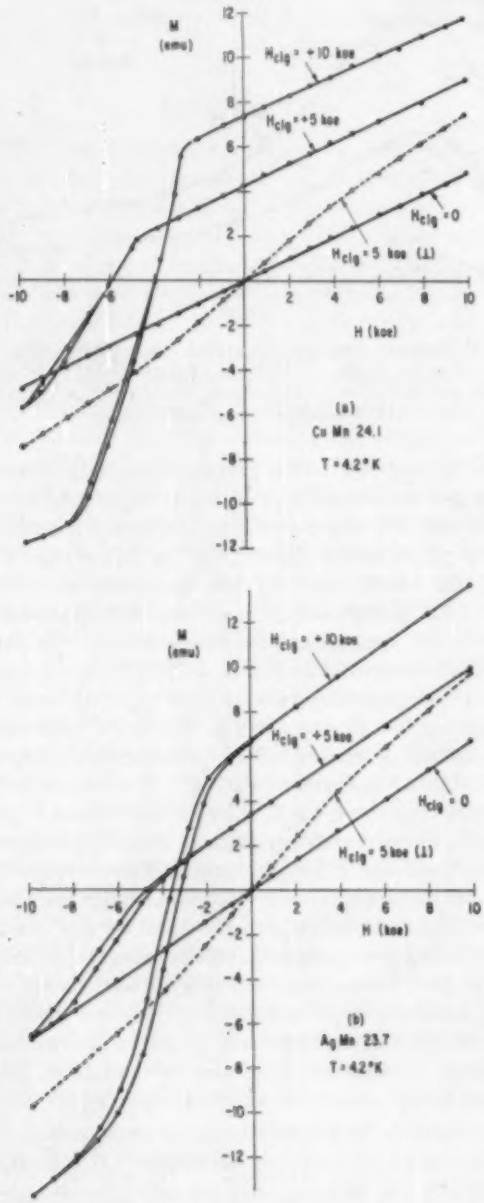

FIG. 2. Hysteresis loops measured at 4.2°K for the alloys (a) CuMn 24.1 and (b) AgMn 23.7 cooled in +5 koe or +10 koe field applied parallel to measurement axis, or in zero field, or in 5 koe field perpendicular to measurement axis.

Upon warm up, after the specimens were cooled to 4.2°K in a 5 koe field applied in the direction of measurement, it was found that the shift of the hysteresis loops decreased monotonically, disappearing at about 80° and 60°K for the Cu-Mn and Ag-Mn alloys, respectively. The hysteresis losses (as determined from the area of the loops), however, rose from essentially zero at 4.2°K to a maximum value at about 60°K (Cu-Mn) and 40°K (Ag-Mn) and then vanished at about 100°K (Cu-Mn) and 80°K (Ag-Mn). This is the same temperature dependence as that of the hysteresis losses for the specimens cooled in zero field, as described above. The accompaniment of the disappearance of the hysteresis loop shift by increased hysteresis losses was also previously observed for Ni-Mn alloys and, within the context of the simple exchange anisotropy model, was explained in terms of discontinuous rotations of antiferromagnetically aligned moments.[4]

The exchange anisotropy effects reported here for the Cu-Mn and Ag-Mn alloys strongly suggest there are both ferromagnetic and antiferromagnetic alignments of Mn moments in these alloys. Moreover, since no long range atomic ordering has been detected in either system,[14,15] the basis for this magnetic inhomogeneity is presumably the statistical atomic inhomogeneity inherent in disordered alloys, combined with a strong dependence of the exchange coupling on the separation distance between Mn atoms. We have been studying the possibilities of this model, and our initial findings are fairly promising. In Fig. 3 there are two identical 50×50 square-lattice representations of a disordered Cu-Mn (or Ag-Mn) alloy of 30 atomic % Mn. The positions of the Mn atoms were chosen by means of a table of random digits.[16] By restricting the magnetic problem to that of an Ising model, we then invoked a strong antiferromagnetic coupling between nearest-neighbor Mn moments. This immediately fixed the relative moment directions within each Mn group (composed of Mn atoms having at least one nearest-neighbor Mn). The absolute directions of these moments were determined under two different conditions. In Fig. 3(a) we assumed that next-nearest-neighbor Mn moments are coupled ferromagnetically and that longer range interactions are also ferromagnetic but progressively weaker. The system was then allowed to seek its lowest magnetic energy state. This resulted in the configuration of

[14] D. Meneghetti and S. S. Sidhu, Phys. Rev. **105**, 130 (1957).
[15] D. P. Morris and I. Williams, Proc. Phys. Soc. (London) **73**, 422 (1959).
[16] *A Million Random Digits with 100 000 Normal Deviates*, The Rand Corporation (The Free Press, Glencoe, Illinois, 1955).

moment directions shown in this figure. It is found that of the 721 Mn atoms in this picture 331 have moments in the plus direction and 390 in the negative direction; hence, there are 59 uncompensated moments. The fact that in Fig. 3(a) the number of uncompensated moments is small (ideally zero in a sufficiently large lattice sample) arises from the small or zero net moment of each Mn group (defined above) and from the alignment of these net moments such that they cancel out. Moreover, in this configuration of moment directions, every ferromagnetic bond between second and third-nearest-neighbors as well as every antiferromagnetic bond between nearest-neighbors is obeyed. In Fig. 3(b), we made the same assumption of ferromagnetic next-nearest-neighbor and longer range interactions between Mn moments. However, in this case, we considered the system cooled in a magnetic field in the plus direction, which is large enough to align the net moment (if any) of each Mn group. We then supposed that all the atomic moments within each Mn group are frozen in place by a large magnetocrystalline anisotropy, so that when the field is removed only the Mn moments having no nearest-neighbor Mn can relax to their lowest energy directions. In the resulting configuration, shown in Fig. 3(b), 446 of the Mn atoms have plus moments and 275 have minus moments. The number of uncompensated moments is therefore 171; this represents a net gain of 230 over the number of uncompensated moments (in the plus direction) in Fig. 3(a). The price paid for this magnetization is the number of ferromagnetic bonds that are disobeyed by the atomic moments. These are indicated by the solid lines in Fig. 3(b) for the bonds between second- and third-nearest-neighbors, and there are 43 of them.

The configuration of Fig. 3(a) indicates that when such a system is allowed to reach its lowest energy state its remanent magnetization will be zero. However, if this system is subjected to a magnetic field at a temperature where the effective magnetocrystalline anisotropy of each group of antiferromagnetically aligned Mn moments is small, the resulting configuration will be that of Fig. 3(b). If, subsequently, the system is cooled in this field and the effective magnetocrystalline anisotropy increases rapidly, it may become large enough to prevent the configuration from relaxing back to that Fig. 3(a) when the field is removed. Thus, the remanent magnetization will not be zero. Furthermore, the reversal of magnetization will be accomplished only when the reverse field is large enough to turn some of the Mn moments against their antiferromagnetic coupling with their neighbors, that are held by the anisotropy; hence, when the reverse field is removed, the magnetization will revert back to its original polarity.

A qualitative similarity therefore exists between some of the predicted properties of this microscopic exchange anisotropy model and the behavior of our disordered Cu-Mn and Ag-Mn alloy specimens indicated by some of the curves in Fig. 2. Quantitatively,

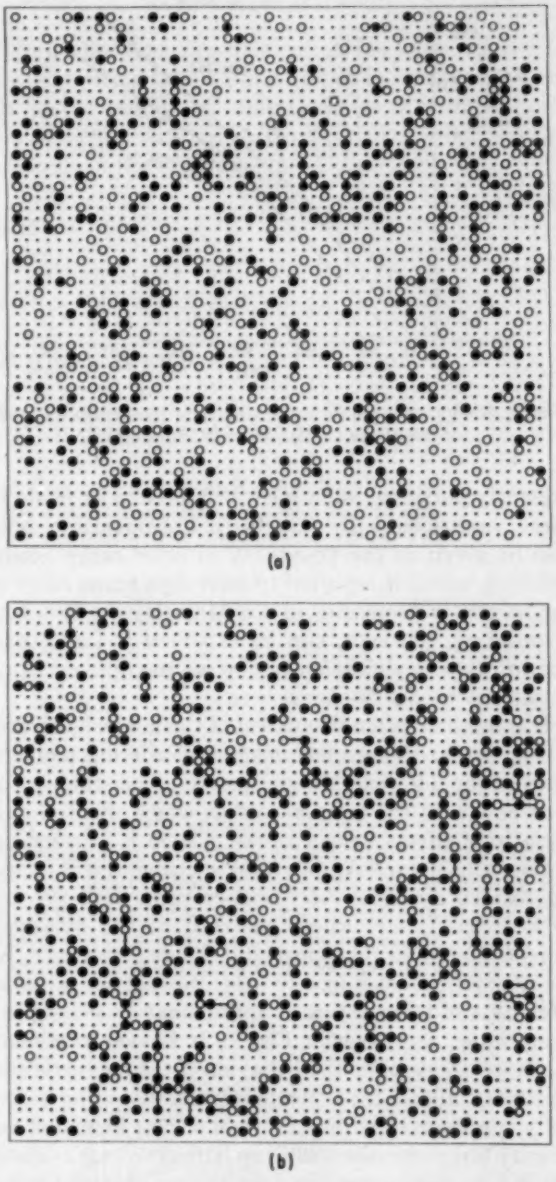

FIG. 3. Square lattice representation of disordered alloy of 30 atomic % Mn (circles) in Cu or Ag (dots). Closed and open circles indicate Mn atomic moments in plus and minus directions, respectively. (a) lowest magnetic energy state configuration. (b) configuration for the system cooled in large field in plus direction.

of course, the properties of such a model will depend on the particular structure studied. For example, simple configurations like those of Fig. 3, in which all the antiferromagnetic bonds between nearest-neighbors are obeyed, would be impossible for a triangular net or a face-centered cubic crystal, which have nearest-neighbor atoms mutually sharing nearest-neighbors. Moreover, for a given composition, the probability that a Mn atom will have a given number of nearest-neighbor Mn atoms will vary from structure to structure. Hence, in a more complete investigation of this model, which we are

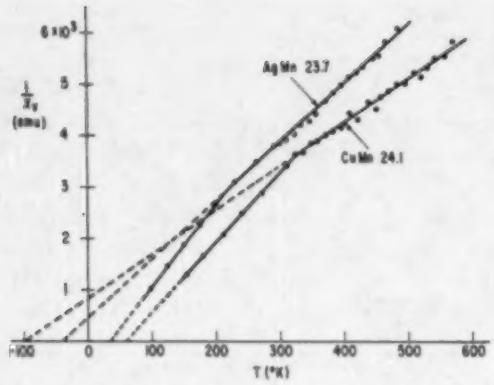

FIG. 4. Reciprocal volume susceptibility *vs* temperature curves for the alloys CuMn 24.1 and AgMn 23.7.

presently pursuing, allowances will have to be made for these variations with structure. Consideration must also be given to the possibility of short-range atomic ordering, which is reported to have significant effect on the magnetic properites of Cu-Mn alloys.[17] This type of ordering, however, can be expected to cause only quantitative modification of the microscopic exchange anisotropy model discussed here.

It is implicit in our discussion of the model illustrated in Fig. 3 that the antiferromagnetic ordering temperatures of the different Mn groups are higher than (or at least equal to) the temperature at which the exchange anisotropy effects vanish as the system is warmed up. For our Cu-Mn and Ag-Mn alloy specimens, it is tempting to identify these Néel temperatures with 80° and 60°K, respectively, where the shift of the hysteresis loops is found to disappear and where, moreover, for the specimens cooled in zero field, the magnetization as a function of temperature is approximately at its maximum value, as shown in Fig. 1. It is very pertinent, therefore, to examine the behavior of the magnetic susceptibility above these temperatures. By using essentially the same experimental method, we extended our magnetization measurements on both alloys up to about 500°K; the results combined with those obtained below room temperature are shown in Fig. 4 as a plot of inverse volume susceptibility *vs* temperature. Despite considerable scatter of our data above room temperature, it is clear from this figure that a simple Curie-Weiss relation (i.e., $1/\chi_v=(T-\theta)/C_v$) is not obeyed by either alloy. Instead, the data for each of the alloys seems to be very well represented by two such relations operating over different temperature ranges. The values of the constants θ and C_v for the different linear portions of the curves are given in Table I, and it should be noted that the positive θ values obtained from the lower temperature portions correspond very closely to the temperatures at which the hysteresis losses in the alloys are

TABLE 1.

Specimen	Temp. range	θ	C_v	μ_{eff}	gS
CuMn 24.1	150–320°K	60°K	0.071	4.2	3.3
CuMn 24.1	>320°K	−100°K	0.117	5.4	4.5
AgMn 23.7	100–220°K	35°K	0.062	4.6	3.7
AgMn 23.7	>220°K	−40°K	0.088	5.5	4.6

maximum. According to our microscopic exchange anisotropy model, maximum losses occur at the temperature at which the moments within each Mn group rotate discontinuously against magnetocrystalline anisotropy forces in response to a field. Moreover, if all the moments within each Mn group rotate together, keeping their antiferromagnetic alignment intact, then each Mn group with its small net moment will be equivalent to an elementary magnet of a superparamagnetic system. Hence, we can consider the positive θ of the lower temperature portion of each of the curves in Fig. 4 to be a measure of the forces trying to stabilize the net moments of the different Mn groups against their thermal motion. Furthermore, the negative θ obtained from the higher temperature portion of each curve suggests that at the temperature where the curve changes slope the antiferromagnetic alignments within the different Mn groups break down. The Néel temperatures are therefore identified with the kinks in the curves of Fig. 4, and only at higher temperatures are the alloys truly paramagnetic. In view of this hypothesis, we became especially interested in computing the average Mn moments from the Curie constants for the different portions of the curves in Fig. 4. First, we made use of the definition: $C_v=N_v g^2\mu_B^2 S(S+1)/3k$, where N_v is the number of Mn atoms per unit volume, and computed the effective paramagnetic moment per Mn atom, $\mu_{eff}=g\{S(S+1)\}^{\frac{1}{2}}$. The actual Mn atomic moment is characterized better by gS, which we evaluated from μ_{eff} by assuming that $g=2$. The computed values for μ_{eff} and gS are shown in Table I. Comparison with previously published results[18] indicate good agreement between our values taken from the higher temperature portions of the $1/\chi_v$ *vs* T curves and earlier results for alloys much more dilute in Mn. Our values for μ_{eff} and gS obtained from the lower temperature portions of the curves, however, indicate a decline of the Mn moment with increasing Mn concentration that is as steep as that predicted from earlier work on lower Mn concentrations. Since it is very likely that only the higher temperature portions of the curves in Fig. 4 represent truly paramagnetic states, our results would suggest that the average atomic moment of Mn in Cu-Mn and Ag-Mn alloys is fairly constant over a wide composition range and that any decrease of Mn moment with increasing Mn concentration previously

[17] E. Scheil and E. Wachtel, Z. Metallk. **48**, 571 (1957).

[18] E. Kronquist and A. Giansoldati, Arkiv Fysik **7**, 343 (1953); H. P. Myers, Canad. J. Phys. **34**, 527 (1956).

noted for these alloys is partly due to an unrecognized intrusion of a superparamagnetic state at lower temperatures.

The experimental as well as the theoretical aspects of this work are being investigated at present more extensively.

ACKNOWLEDGMENTS

The author is particularly grateful to G. W. Rathenau for his inspiring interest and advice in this problem, to I. S. Jacobs and W. H. Meiklejohn for their many helpful comments, and to H. N. Treaftis for his capable assistance in the experiments.

JOURNAL OF APPLIED PHYSICS SUPPLEMENT TO VOL. 31, NO. 5 MAY, 1960

Internal Structure of Bloch Walls

S. SHTRIKMAN AND D. TREVES*
Department of Electronics, The Weizmann Institute of Science, Rehovot, Israel

The subdivision of a Bloch wall into a periodic structure of right- and left-hand walls observed by Williams and Goertz and by DeBlois and Graham is shown to be caused by the self-magnetostatic energy of the wall. The period of this structure is calculated by an approximate minimization of the energies involved. The results compare favorably with experimental evidence.

THE self-magnetostatic energy of a Bloch wall, which is due to the free poles at the intersection of the wall with the surface of the crystal,[1] will cause the wall to divide into domains. It will be assumed in the following that the domain structure of the thermodynamic equilibrium of the wall will be similar to that of a film whose thickness equals the width δ of the wall and whose length equals the thickness L of the sample. The period T of this fine structure, which is actually composed of right- and left-hand walls divided by Bloch lines[2] is calculated by the usual method of energy minimization.[3]

The geometry of the configuration assumed is shown in Fig. 1. The total energy per unit area of the wall for a ferromagnetic with uniaxial anisotropy is

$$E=E_m+KD+\pi^2A/2D+\gamma_l/T, \qquad (1)$$

where E_m is the magnetostatic energy of the Bloch wall, A the exchange constant, D the wall thickness, γ_l the energy of the Bloch line per unit length, and $2T$ the period of the wall domains.

The magnetostatic energy is

$$E_m=3I_s^2D^2\ln(0.7T/D) \quad \text{for} \quad L\gg T\gg D, \qquad (2)$$

where I_s denotes the saturation magnetization. This energy is calculated assuming that $T\ll L$ so that one can neglect the energy of interaction between the two edges of the wall. Each edge is further approximated by a cylinder of diameter D covered with a surface charge which is a square wave with period $2T$ and amplitude I_s/π.

The Bloch line energy is given by

$$\gamma_l=XD\cdot 2\pi\frac{X}{D}I_s^2+\frac{\pi^2}{2}\frac{A}{X^2}XD, \qquad (3)$$

where X is the thickness of the line.

Here the first term is the magnetostatic energy of the line calculated, following Néel,[1] by approximating the line to an elliptic cylinder, and is valid for $X\ll D$. The second term is the part of the exchange energy associated with the gradient of the magnetization in the

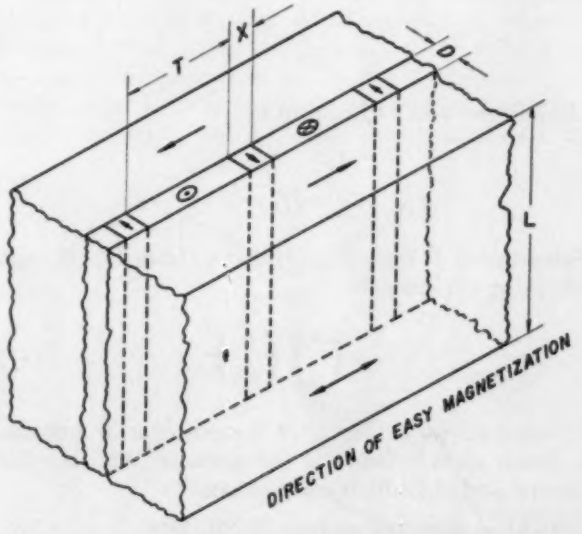

FIG. 1. Diagram of the suggested internal structure of a 180° Bloch wall, in a uniaxially anisotropic single crystal. The thickness of the wall is denoted by D, half the period of the wall domains by T and the width of the Bloch line by X.

---

* Present address: Pomona College, Department of Physics, Claremont, California.

[1] The effect of this energy on the width of the wall was studied by L. Néel, Compt. rend. **241**, 533 (1955), and J. Kaczer, Czechoslov. J. Phys. **6**, 310 (1956).

[2] R. W. DeBlois and C. D. Graham, Jr. J. Appl. Phys. **29**, 932 (1958).

[3] A similar model was proposed by E. E. Huber, Jr., D. O. Smith, and J. B. Goodenough, J. Appl. Phys. **29**, 294 (1958).

easy direction, while the part associated with the gradient in the hard direction has been included in the third term of Eq. (1). The magnetocrystalline anisotropy energy does not contribute to the energy of the line as the magnetization rotates in a plane perpendicular to the direction of easy magnetization. Its contribution to the total energy has been included in the second term of Eq. (1).

The width of the wall will be calculated by minimizing the energy

$$\frac{\partial E}{\partial D}=\frac{\partial E_m}{\partial D}+\frac{1}{T}\frac{\partial \gamma_l}{\partial D}+K-\frac{\pi^2 A}{2D}. \tag{4}$$

The first two terms are small compared to the last two for $L\gg D$; neglecting them in the calculation of D is equivalent to stating that the magnetostatic energy of the wall has little effect on the thickness of the latter for $L\gg D$ as Néel[1] has already shown. For these approximations one gets a domain-wall thickness equal to that calculated by Kittel,[4] δ

$$D=\delta=(\pi^2 A/2K)^{\frac{1}{2}}. \tag{5}$$

The width of the Bloch line will be given by

$$\frac{\partial E}{\partial X}=\frac{1}{T}\frac{\partial \gamma_l}{\partial X}=0. \tag{6}$$

Using Eqs. (4) and (5) one gets from (6)

$$X^3=\frac{\pi AD}{8I_s^2}=\frac{\pi^2 A^{\frac{1}{2}}}{8\sqrt{2}I_s^2K^{\frac{1}{2}}} \tag{7}$$

and

$$\gamma_l=\tfrac{3}{2}\pi^{5/3}(ADI_s)^{\frac{1}{3}}. \tag{8}$$

Finally from

$$\frac{\partial E}{\partial T}=0 \tag{9}$$

the half-period T is found to be

$$\frac{T}{L}=\frac{\gamma_l}{3D^2I_s^2}. \tag{10}$$

Substituting D from Eq. (5) and γ_l from Eq. (8) and using Eq. (5) one gets

$$\frac{T}{L}=\left(\frac{\pi}{2}\right)^{\frac{1}{2}}\left(\frac{K}{I_s^2}\right)^{\frac{1}{2}}. \tag{11}$$

Experimental evidence for the existence of domains in Bloch walls is found in the works of Williams and Goertz[5] and of DeBlois and Graham.[2]

The beautiful experimental work of DeBlois and Graham[2] on domain configurations in iron whiskers, which also reveals the domain structure of Bloch walls, provides rough experimental check of the theory.[6]

For iron one finds from Eq. (11), $T/L=0.3$ which compares favorably with the lowest observed values.[2] See for example reference 2, Fig. 11.

Using Eqs. (5) and (7) one gets

$$D=3\times10^{-6}\text{ cm}\quad X=0.7\times10^{-6}\text{ cm}\quad \gamma_l\approx3\times10^{-5}\frac{\text{erg}}{\text{cm}}$$

so that one is within the limitation $X\ll D$.

The observed values of T/L deduced from data kindly made available by DeBlois and Graham[7] varied over a large range. However, the smallest values were in fair agreement with the calculated one, while the largest ones were more than an order of magnitude off. One might perhaps expect this as the value T/L given by Eq. (11) yields the state of lowest energy. The actual state might be any minimum energy state probably with a higher value of T/L as there is an energy barrier for creation of Bloch lines.

The calculation above, being based on the similarity between the domain structure of a wall and that of a thin film, should be directly applicable to the domain structure of the latter. By taking D to be the thickness of the film, L its width and $\gamma_l=\gamma D$, formula (11) will given the domain width of the open flux domain configuration in films whose direction of easy magnetization lies in their surface.[8] This is of interest for many iron nickel films which have recently been studied most intensively in connection with the possibility of their being used as memory elements.

It is interesting to note that the conception of Bloch lines generated by alternate direction of magnetization in the Bloch wall, cannot be pushed further to Bloch points generated by alternate direction of magnetization in the Bloch line. This is because the magnetization in these points will be antiparallel to that in one of the adjacent main domains, thus greatly raising the exchange energy.

ACKNOWLEDGMENTS

The authors are indebted to R. W. DeBlois, C. D. Graham, and H. J. Williams for providing them with some of their unpublished data, to S. Methfessel for a most stimulating conversation and to E. H. Frei, under whom this work has been carried out, for continuous interest and encouragement.

[4] C. Kittel, Revs. Modern Phys. **21**, 551 (1949).
[5] H. J. Williams and M. Goertz, J. Appl. Phys. **23**, 316 (1952).
[6] Although throughout the paper, uniaxial anisotropy was assumed, it is believed that the results will not be considerably changed for cubic anisotropy.
[7] R. W. DeBlois and C. D. Graham (private communication).
[8] The only other domain configuration that was analyzed in film is for films whose easy direction is perpendicular to their surface. See for example Z. Malek and V. Kambersky, Czechoslov. J. Phys. **8**, 416 (1958).

JOURNAL OF APPLIED PHYSICS SUPPLEMENT TO VOL. 31, NO. 5 MAY, 1960

Anisotropic Magnetization

EARL R. CALLEN
U. S. Naval Ordnance Laboratory, White Oak, Silver Spring, Maryland

In the presence of magnetocrystalline anisotropy the magnetization of a ferromagnet depends upon its orientation as well as upon the temperature. The temperature dependences of the anisotropic parts of the magnetization have been worked out, both classically and quantum-mechanically, for all symmetries and for ferro- and ferrimagnets in the internal field approximation. The nonspherical terms are small at all temperatures in iron and nickel but are appreciable in some uniaxial materials, and very large in many crystals of low Curie point and large anisotropy. In these materials the magnetization will be very unlike a Brillouin function.

BECAUSE of the magnetocrystalline anisotropy, the magnetization **M** of a ferromagnet in an aligning external field has a magnitude which depends upon its crystallographic orientation. Thus

$$M(T,\boldsymbol{\alpha})=M_0(T)+\sum_l M_l(T)g_l(\boldsymbol{\alpha}), \tag{1}$$

where $\boldsymbol{\alpha}$ is a unit vector along the magnetization, and the $g_l(\boldsymbol{\alpha})$ are linear combinations of spherical harmonics of degree l, with the crystal point group symmetry. It is the purpose of this work to determine the $M_l(T)$. The magnetocrystalline anisotropy free energy can also be expanded in these harmonics, in a series analogous to Eq. (1), but with the $M_l(T)$ replaced by anisotropy coefficients $\kappa_l(T)$, which are linear combinations of the conventional $K_i(T)$.

Assume a perturbation $v(\mathbf{v})$ with the crystal symmetry, where $\mathbf{v}$ is a unit vector along an individual spin. If μ is the ionic dipole moment and γ the molecular field constant, the energy of an ion is

$$\epsilon=-\mu\gamma M(T,\boldsymbol{\alpha})(\mathbf{v}\cdot\boldsymbol{\alpha})+v(\mathbf{v}). \tag{2}$$

By calculating the expectation value of $(\mathbf{v}\cdot\boldsymbol{\alpha})$ and expanding to first order in βv, the ratio of anisotropy to thermal energy, one finds for the reduced anisotropic components

$$m_l(T)\equiv\frac{M_l(T)}{M_0(O)}=\frac{-\kappa_l^0}{2n^2\Gamma}\,\frac{\hat{I}_{l+\frac{1}{2}}+\hat{I}_{l-\frac{1}{2}}-\hat{I}_{l+\frac{1}{2}}\left(2m_0+\dfrac{1}{n\Gamma\beta m_0}\right)}{3/n\Gamma\beta-(1-m_0^2)}, \tag{3}$$

where $\hat{I}_s(n\Gamma\beta m_0)$ is defined as the ratio of the hyperbolic Bessel function of order s to that of order one-half, Γ equals $\gamma\mu^2$, and m_0 is the Langevin function. In particular,

$$m_2(T)=\frac{-\kappa_2^0}{n^2\Gamma}\,\frac{3}{n\Gamma\beta m_0(T)}. \tag{4}$$

m_2 rises from zero rather linearly with temperature, but Eq. (4) no longer represents the uniaxial component above about three quarters of the Curie temperature; the closed form expressions nevertheless indicate that all m_l return to zero at T_C. We corroborate the general behavior of m_2 by a quantum-mechanical internal field calculation, for arbitrary spin in uniaxial symmetry, and with a nearest-neighbor pseudo-dipolar perturbation. A result qualitatively very similar to Eq. (4) occurs.

m_4 and m_6 have relatively low and broad maxima at lower temperatures.

This theory is closely related to the Akulov geometrical explanation of the temperature dependence of the $\kappa_l(T)$ and is illustrated in Fig. 1. At $T=0°K$ all the spins are rigidly aligned, $|\kappa_l|$ is a maximum, and all m_l vanish. As the temperature increases, the spin cone widens, decreasing $\kappa_l(T)$ by an averaging process. The perturbation now tends to narrow the spin cone in easy directions and broaden it in hard ones, giving M an angular dependence as well.

In ferrimagnets we find that in a case in which one sublattice has a thermally reduced isotropic magnetization while another sublattice is still moderately aligned, the latter sublattice has an enhanced anisotropic magnetization. If this happens to occur near a compensation point, the net magnetization will be quite anisotropic, and the compensation temperature will be slightly orientation dependent.

Because of the ratio of perturbation to exchange energy in Eq. (3), m_4 and m_6 are negligible at all temperatures in iron and nickel. In a uniaxial material with the magnetic parameters of Co the maximum in m_2 would occur at a rather high temperature; actually, cobalt transforms to the cubic phase. However, in

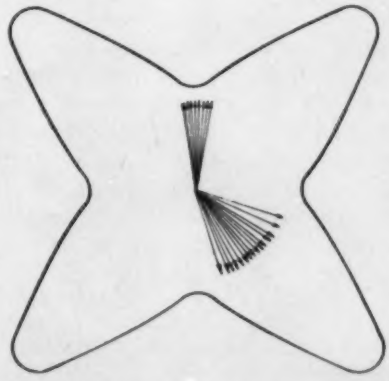

FIG. 1. Angular width of spin cone in easy and hard magnetization directions in a ferromagnet with cubic anisotropy.

MnBi, m_2 should be marginally measurable even at room temperature.

The anisotropy of the magnetization will be particularly large in materials of large anisotropy and low exchange energy, of which there are many. For example, ludlamite[1] has a Curie temperature of 20°K and a uniaxial anisotropy field greater than 12 500 oe. In this case the magnetization will be quite unlike the Brillouin or spin wave prediction. Similarly, in cobalt ferrite the anisotropy energy of a cobalt ion is comparable to its exchange coupling, and the anisotropic sublattice magnetization will be large. The deviation of the magnetization of the cobalt sublattice from a Brillouin function will produce a deviation of the total magnetization from the Néel curves.

This work has been written up in detail by the present author and H. B. Callen for publication elsewhere.

[1] R. M. Bozorth and Vivian Kramer, J. Phys. radium **20**, 393 (1959).

JOURNAL OF APPLIED PHYSICS SUPPLEMENT TO VOL. 31, NO. 5 MAY, 1960

Temperature Dependence of Anisotropy and Saturation Magnetization in Iron and Iron-Silicon Alloys

C. D. Graham, Jr.
General Electric Research Laboratory, Schenectady, New York

The temperature dependence of the magnetocrystalline anisotropy constant K_1 and of the saturation magnetization have been measured from 77 to 575°K on single-crystal samples of iron, 3.2% silicon-iron, and 5.1% silicon-iron. For iron and 3.2% Si-Fe, the anisotropy decreases as the third or fourth power of the magnetization at low temperatures; this increases to approximately the ninth power at high temperatures. The anisotropy of 5.1% Si-Fe decreases as the seventh or eighth power of the magnetization at low temperatures, and as the ninth power at high temperature.

THE temperature dependence of the magnetocrystalline anisotropy constant K_1 and of the saturation magnetization σ have been measured over the temperature range from liquid nitrogen to 300°C on single-crystal samples of iron and two iron-silicon alloys. The data are used to check the theoretical prediction that the anisotropy should decrease as the tenth power of the magnetization as the temperature is increased from absolute zero,[1] i.e., $K/K_0=(\sigma/\sigma_0)^{10}$, where K and σ are the anisotropy constant and saturation moment at a given temperature, and subscript zero means 0°K.

The iron samples were crystals of Armco iron obtained from the Virginia Institute for Scientific Research, containing about 0.2% total impurities. Anisotropy was also measured on a crystal of Ferrovac E iron containing less than 0.1% impurity. This crystal had a few small included grains and so could not be used to obtain absolute values of the anisotropy; however, it was used to follow the temperature dependence of the anisotropy. The measurements listed as made on 3.2% silicon-iron were made on two crystals, one containing 3.1±0.1% silicon and less than 0.1% impurity and the other containing 3.25±0.05% silicon and about 0.2% impurity. The 5.1% silicon alloy contained 0.1% vanadium and less than 0.1% of other impurities. Since neither the magnetization nor the anisotropy is greatly influenced by small amounts of impurity, these general purity levels are satisfactory for the purpose of the experiment.

The magnetic properties of the silicon alloys may be affected by ordering. The samples were slowly cooled from well above the ordering temperature, and were therefore at least partly ordered. However, these compositions are at the low end of the ordering range, and there is other evidence that ordering has little effect on the magnetic properties of iron-silicon alloys.[2]

The anisotropy constants were determined from torque measurements on single-crystal disks, as described previously.[3] Disks cut in a {100} plane gave more consistent results than those cut in a {110} plane, presumably because the second anisotropy constant K_2 affects the torque in a {110} plane. The error in the absolute values of the anisotropy constants is estimated as about $\pm 10\times 10^3$ erg/cm³ at room temperature and below, and about $\pm 20\times 10^3$ erg/cm³ at the higher temperatures. The percent uncertainty therefore ranges from 2% at the lowest temperature to as much as 15% at the highest temperature.

Saturation magnetization was measured by a slight

[1] C. Zener, Phys. Rev. **96**, 1335 (1954); W. J. Carr, Jr., J. Appl. Phys. **29**, 436 (1958); Phys. Rev. **109**, 1971 (1958); J. H. Van Vleck, "Conference on Magnetism and Magnetic Materials, Boston, 1957," Proc. Am. Inst. Elec. Engrs., p. 6; T. Kasuya, J. Phys. Soc. (Japan) **11**, 1217 (1956); F. Keffer and T. Oguchi, Bull. Am. Phys. Soc. Ser. II, **4**, 177 (1959).

[2] R. C. Hall, WADC Technical Note 58-127, ASTIA No. AD 155519, Westinghouse Electric Corporation (April, 1958), p. 20-25.

[3] C. D. Graham, Jr., Phys. Rev. **112**, 1117 (1958); J. Appl. Phys. **30**, 391 (1959).

TABLE I.[a]

	Fe				3.2% Si-Fe				5.1% Si-Fe			
T, °K	T/Tc	K_1	K/K_0	σ/σ_0	T/Tc	K_1	K/K_0	σ/σ_0	T/Tc	K_1	K/K_0	σ/σ_0
0	0	(523)	1.0	1.0	0	(427)	1.0	1.0	0	(358)	1.0	1.0
77	0.074	520	0.995	0.999	0.076	425	0.995	0.999	0.078	355	0.991	0.999
195	0.187	505	0.965	0.990	0.192	405	0.948	0.985	0.197	325	0.908	0.987
300	0.288	480	0.919	0.979	0.296	365	0.855	0.969	0.304	285	0.795	0.970
425	0.407	400	0.765	0.956	0.418	280	0.655	0.941	0.428	215	0.600	0.942
575	0.550	265	0.507	0.916	0.565	195	0.456	0.900	0.580	140	0.392	0.900

[a] Tc = Curie temperature; K_1 in 10^6 erg/cm³.

modification of the isthmus method of Ewing and Low.[4] Samples about 2 cm long and of the order of 0.01 cm² in cross section were cut from portions of the same crystals used to make the anisotropy samples. The long axes of the strip samples were ⟨100⟩ easy directions. Each strip was closely wound with a few turns of insulated wire, and the integrated voltage signal from this coil was measured as the sample was quickly turned end for end in a strong magnetic field. By repeating this measurement over a range of applied fields (500 to 15 000 oe), it is possible to correct for the part of the signal due to the applied field. The remaining signal is proportional to the magnetization of the sample. The absolute magnetization could be determined in this way within 2 or 3%; the room-temperature values obtained agreed (within this error) with the values plotted by Bozorth.[5] The relative magnetization of a single sample over a range of temperatures could be measured to 0.3%.

Measurements of K_1 and of σ were made in liquid nitrogen (77±1°K), in dry ice and acetone (195±3°K), at room temperature (300±5°K), and in a silicone oil bath at 150 and 300°C (425±5°K and 575±10°K). The anisotropy samples were weighed, and the anisotropy constants converted to ergs/cm³ on the basis of the following assumed densities: Fe, 7.87 g/cm³; 3.2% Si-Fe, 7.66; 5.1% Si-Fe, 7.55. No correction was applied for the change in density with temperature.

The data are summarized in Table I. The values at 0°K had to be obtained by extrapolation, which makes the ratios K/K_0 and σ/σ_0 somewhat uncertain at the lowest temperatures. The values of K_1 at room temperature and below have been published previously.[3,6] The figures for iron agree well with a recent summary by Bozorth in the American Institute of Physics Handbook.[7] The room-temperature values for K_1 in the iron-silicon alloys agree with recent measurements by Hall,[2]

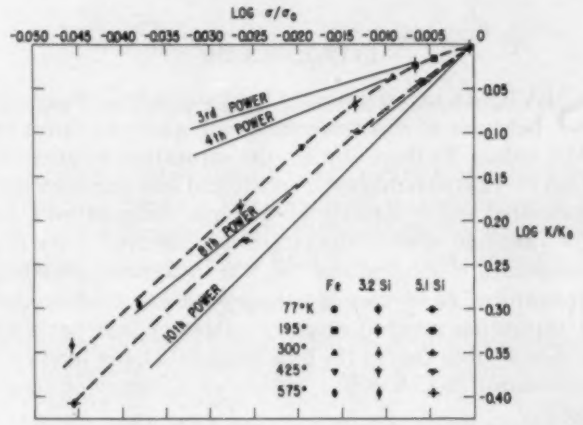

FIG. 1. Log K/K_0 vs log σ/σ_0 for iron and two Fe-Si alloys.

as well as with earlier work summarized by Bozorth[8]; there are apparently no previous measurements above or below room temperature. The σ/σ_0 values for the alloys are nearly identical, which is surprising in view of Fallot's report that there is a regular change in σ/σ_0 with increasing silicon content.[9] The numerical values of σ/σ_0 disagree with Fallot's for iron as well as for the two alloys.

A test of the tenth-power law is made in Fig. 1, where log K/K_0 is plotted against log σ/σ_0 for all three materials. The data for iron and 3.2% Si-Fe superpose, and indicate a third- or fourth-power dependence at low temperatures, changing gradually to a ninth-power law at high temperatures. The 5.1% Si-Fe alloy follows a seventh- or eighth-power law at low temperatures, changing to a ninth-power law at high temperatures. The disagreement with theory is especially marked since all the various theoretical treatments are low-temperature approximations which should have decreasing validity at high temperatures.

Note added in proof. W. J. Carr, Jr. has recently shown [J. Appl. Phys. **31**, 69 (1960)] that taking account of the effect of thermal expansion on anisotropy can lead to deviations from the tenth-power law at low temperatures.

[4] J. A. Ewing and W. Low, Phil. Trans. Roy. Soc. (London) **180A**, 221 (1889); J. A. Ewing, *Magnetic Induction in Iron and Other Metals*, (The Electrician Printing and Publishing Company, Ltd., London, 1900), Third edition, p. 138 ff.

[5] R. M. Bozorth, *Ferromagnetism* (D. Van Nostrand Company, Inc., Princeton, New Jersey, 1951), p. 77.

[6] C. D. Graham, Jr., J. Appl. Phys. **30**, 317S (1959).

[7] R. M. Bozorth, *American Institute of Physics Handbook* (McGraw-Hill Book Company, Inc., New York, 1957), Sec. 5, pp. 208, 211.

[8] See p. 572 of footnote 5.

[9] M. Fallot, Ann. phys. **6**, 305 (1936).

Temperature Dependence of the Saturation Magnetization of Nickel Films of Thickness Less Than 100A

C. A. NEUGEBAUER
General Electric Research Laboratory, Schenectady, New York

Nickel films varying in thickness from 300 to 15A were prepared by evaporation on glass substrates in a vacuum sufficiently high to prevent gas adsorption on the film during preparation and measurement. Their magnetization was measured as a function of field up to 10 000 oe using a vacuum torsion magnetometer. The saturation magnetization of these films was determined as a function of their thickness at various temperatures. No decrease in saturation magnetization from that of bulk nickel has been observed for films of thickness down to 20A, at room temperature. The Curie temperature of a 30A film was found to coincide with that of bulk nickel.

INTRODUCTION

SEVERAL investigators[1–4] have studied the magnetic behavior of small, ferromagnetic particles down to 51A radius. In these studies, the saturation magnetization of superparamagnetic cobalt and iron particles was measured either directly at different temperatures, or its variation with temperature was inferred from the temperature dependence of the magnetocrystalline anisotropy. In no case has there been any evidence for a saturation magnetization of cobalt or iron particles different from that of the bulk material at any temperature down to 15A radius, within an accuracy of about 10%.

In sharp contrast to this striking independence of the saturation magnetization with particle size, even at room temperature, are the results of various workers on thin films.[5–13] According to this work, the saturation magnetization of films thinner than about 100A decreases much more rapidly with temperature than that of the bulk material. Such a dependence of saturation magnetization on temperature and film thickness has been predicted by a theory of Klein and Smith,[14] who used the Bloch spin wave approach.

In this work the temperature dependence of the saturation magnetization of thin films of nickel in the thickness range less than 100A was again investigated.

TECHNIQUES USED

The experimental method used in the preparation of films and the measurement of their magnetic properties has been described in detail elsewhere,[15] and will only be outlined here. The films of nickel were prepared by evaporation from 99.99% pure Ni filaments in an ultra-high vacuum system at pressures of the order of 10^{-9} mm of Hg, or less. The films were kept in this vacuum during the measurement. This vacuum is sufficiently high to insure that, within the period of measurement, the film remained essentially free from adsorbed gases. Film thickness was measured by X-ray emission spectrography (X-ray fluorescence analysis). The maximum error in the method is estimated as 10% of the measured film thickness.

The substrate and film is suspended on a calibrated torsion wire and while still in vacuum can be placed in a variable magnetic field between the pole pieces of an electromagnet. When the film is positioned at an angle of 45° to the field direction, the torque which must be applied to the torsion wire to keep the film at this angle with increasing field, at saturation, is given by

$$L = M_S V H \sin\theta, \tag{1}$$

where L is the torque, M_S the saturation magnetization, V the volume of the material, H the field, and θ is the angle between the magnetization vector and the field direction. At low fields this equation becomes

$$\frac{L}{H} = -\left[\frac{M_S^2 V}{4(2\pi M_S^2 + K)}\right] H + \left(\frac{1}{2}\right)\sqrt{2} M_S V, \tag{2}$$

where K is an anisotropy constant inserted to accommodate a possible easy or hard direction of magnetization perpendicular to the plane of the film. The intercept of a L/H vs H plot yields $(L/H)_0 = 0.707\ M_S V$. From the experimentally measured value of this intercept, the known area of the film, the torque constant of the torsion wire and the thickness of the film as obtained from the X-ray measurement, the saturation magnetization of the film can be easily calculated. Also, the intercept $(L/H)_0$ varies directly with the saturation magnetization as a function of temperature. The temperature of the film was varied by inserting the part of the vacuum system containing the film in a furnace

[1] C. P. Bean, J. D. Livingston, and D. S. Rodbell, J. phys. radium **20**, 298 (1959).
[2] C. P. Bean and I. S. Jacobs, J. Appl. Phys. **27**, 1448 (1956).
[3] F. Luborsky, Phys. Rev. **109**, 40 (1958).
[4] J. J. Becker, Trans. Am. Inst. Mining Engrs. **209**, 59 (1957).
[5] A. Drigo, Nuovo cimento **8**, 498 (1951).
[6] E. C. Crittenden, Jr., and R. W. Hoffman, Revs. Modern Phys. **25**, 310 (1953).
[7] L. Reimer, Z. Naturforschung **12a**, 550 (1957).
[8] W. Ruske, Ann. Physik, **2**, 274 (1958).
[9] H. J. Bauer, Z. Physik **153**, 484 (1959).
[10] A. Colombani, G. Goureaux, and P. Huet, J. phys. radium **20**, 303 (1959).
[11] W. Hellenthal, Z. Naturforschung **13a**, 566 (1958).
[12] W. Reincke, Z. Physik **137**, 169 (1954).
[13] M. H. Seavey, Jr., and P. E. Tannenwald, J. Appl. Phys. **29**, 292 (1958).
[14] M. J. Klein and R. S. Smith, Phys. Rev. **81**, 378 (1951).
[15] C. A. Neugebauer, *Structure and Properties of Thin Films* (John Wiley & Sons, Inc., New York, 1959), pp. 358.

TABLE I. Saturation magnetization of nickel films as a function of thickness at room temperature.

Thickness of film, A	$\frac{M_S(\text{film})}{M_S(\text{bulk Ni})}$
171	1.14
91	1.07
86	1.02
42	1.05
34	1.09
32	1.00
30	1.10
27	1.00
25	0.93
24	1.12
21	0.95
21	1.05
16	0.91
15	0.87

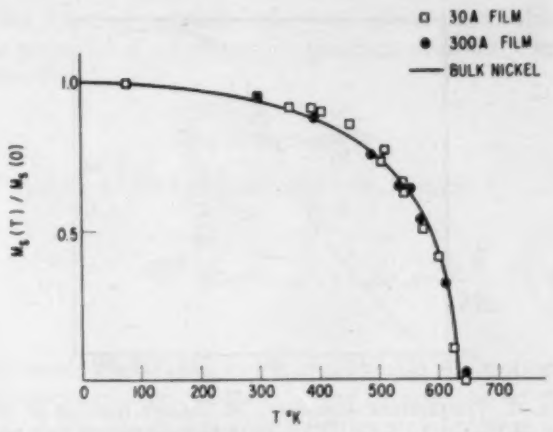

FIG. 1. The saturation magnetization of a 30 and 300A nickel film as a function of temperature.

(or Dewar flask for lower temperatures), and letting the system attain thermal equilibrium. The furnace temperature was taken as the temperature of the film. Fields up to 10 K oe were utilized.

Table I summarizes the results obtained on the dependence of the saturation magnetization on thickness for thin films between 171 and 15A. The ratio M_S (film)/M_S (bulk nickel) applies to 300°K. Within experimental error (~10%), this ratio can be seen to be unity for each film.

A 30A film was prepared, and its saturation magnetization was determined by the method outlined above at fourteen different temperatures between 77° and 650°K. The results are plotted in Fig. 1 (open squares). Some of the values for M_S were obtained when the temperature was increased in successive steps and others when it was decreased.

This measurement was repeated under identical experimental conditions with a 300A film, and the results are given by the full circles in Fig. 1. The full line in this graph is a plot of the experimental values of the saturation magnetization of bulk nickel as obtained by Weiss and Forrer.[16] The saturation magnetization of a 30A nickel film is seen to have identically the same temperature dependence as a 300A film, or even bulk nickel.

CONCLUSIONS

A. The saturation magnetization of thin, evaporated nickel films in the 100 to 20A range is the same as that of bulk nickel, at room temperature.

B. The saturation magnetization of nickel films does not vary abnormally as a function of temperature down to a thickness of 30A.

C. Thin films less than 100A thick have a Curie temperature equal to that of bulk nickel, at least down to a thickness of 30A.

ACKNOWLEDGMENTS

The author is indebted to G. Ehrlich, C. P. Bean, J. D. Livingston, I. S. Jacobs, and D. S. Rodbell for many valuable discussions.

[16] P. Weiss and R. Forrer, Ann. Physik **5**, 153 (1926).

JOURNAL OF APPLIED PHYSICS SUPPLEMENT TO VOL. 31, NO. 5 MAY, 1960

Internal Friction Anomalies in Ferromagnets and Antiferromagnets near the Curie Point

K. P. BELOV, G. I. KATAYEV, AND R. Z. LEVITIN
Lomonosov State University, U.S.S.R.

Measurements of the temperature dependence of internal friction in a number of ferromagnets and antiferromagnets were carried out. In ferromagnetic alloys (Invars) and antiferromagnets (MnO etc.), which have a large spontaneous deformation of the crystalline lattice near the Curie point, sharp peaks of the internal friction were found. The thermodynamical theory of second order phase transitions is used to interpret this phenomenon.

INTERNAL friction anomalies in ferromagnets caused by the domain structure dynamics have been studied rather thoroughly and their nature essentially ascertained.[1] This report deals with the discussion of internal friction anomalies of a different kind. These anomalies are caused by the redistribution of spins within the domains under the action of elastic stresses. As our experiments have determined, such internal friction anomalies, which do not disappear under application of a magnetic field, are observed near the Curie

[1] R. M. Bozorth, *Ferromagnetism* (D. Van Nostrand Company, Inc., Princeton, New Jersey, 1951).

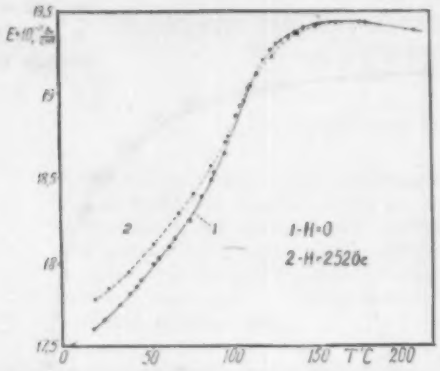

FIG. 1. Temperature dependence of Young's modulus of the alloy 53.5% Co, 8.7% Cr, 37.8% Fe in a demagnetized state and in the field of 252 oe.

point in ferromagnets and antiferromagnets possessing a large spontaneous deformation of the lattice.

Measurements of the temperature dependence of internal friction (elastic modulus as well) have been taken with different fields and frequencies (1 kc/sec, 50–150 kc/sec and 5 Mc/sec); with the help of an astable circuit generating flexural oscillations of the specimen[2]; the "composite oscillator" method[3] and the impulse method[4] using longitudinal oscillations. To determine the frequency of the oscillations of a specimen, we used decade scalers and a quartz clock that made it possible to obtain the magnitude of modulus with a 0.004% precision, and the magnitude of a logarithmic damping decrement within 1–5%. The measurements were taken on invar-type alloys (Fe-Ni, Fe-Pt, Fe-Ni-Cr, Fe-Co-Cr) on the one hand, and the antiferromagnets (MnO, CoO, NiO) and on Ni, Ni-Zn ferrite and antiferromagnetic Cr_2O_3, which have small spontaneous deformation of the lattice near the Curie point, on the other hand.

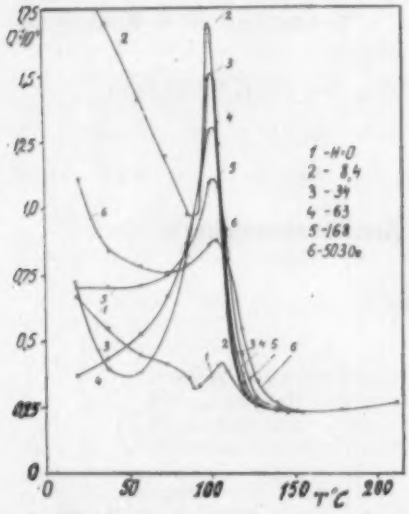

FIG. 2. The temperature dependence of the internal friction of the same alloy with the frequency of 1 kc/sec of flexural oscillations in different magnetic fields.

In Figs. 1 and 2, the curves of the temperature dependence of the elastic modulus and the internal friction for an invar alloy, 53.5% Co, 8.7% Cr, 37.8% Fe, are given. They have been obtained with the frequency of 1-kc/sec of flexural oscillations. Analogous curves have been obtained for other alloys of the same type as well. We can see that, in the region of the Curie point (111°C), the elastic modulus and the internal friction have sharp anomalies which do not disappear under application of the field of "technical" saturation. The magnetic field, however, somewhat reduces the magnitude of the peak of the internal friction and moves it nearer to the Curie point like the maximum of susceptibility of the paraprocess[5] in the region of the Curie point.[6] If the frequency of oscillation rises to 100 kc/sec,

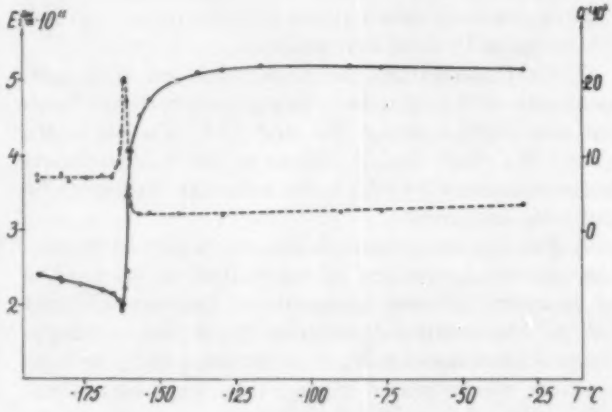

FIG. 3. The temperature dependence of Young's modulus and the internal friction of antiferromagnetic MnO with the frequency of 140 kc/sec of longitudinal oscillations.

the maximum of internal friction moves in the direction of lower temperatures. With the frequency of 5 Mc/sec, it was impossible to find such a maximum in the interval 20°–150°C; apparently, it moved to lower temperatures.

Figure 3 shows the temperature dependences of Young's modulus and the internal friction for the antiferromagnetic MnO. It can be seen that the elastic modulus and the internal friction near the Curie point have anomalies analogous to those of invar alloys. Similar behavior has been obtained for NiO and CoO by us and other authors.[7]

On the other hand, measurements on pure nickel and nickel-zinc ferrite show the absence of anomalies in the elastic modulus and internal friction near the Curie point. In the case of the antiferromagnetic Cr_2O_3, such anomalies are very small.

[2] R. Becker and W. Döring, *Ferromagnetismus* (Berlin, 1939), C. V. Vonsovsky and Y. S. Shur, *Ferromagnetism* (Gostechizdat, 1948); G. I. Kataev, Zavodskaya Laboratory **24**, 1258 (1953).

[3] I. R. Zacharias, Phys. Rev. **44**, 116 (1933).

[4] W. P. Mason, Piezoelectric crystals and their application to ultrasonics, N. Y., 1950.

[5] We call "paraprocess" the change of intrinsic or "true" magnetization.

[6] K. I. Belov, Uspechi Fizichesnich Nauk **65**, 207 (1959).

[7] M. E. Fine, Phys. Rev. **87**, 1143 (1952); R. Street and B. Lewis, Nature **168**, 1036 (1951).

The results given may be interpreted on the basis of the thermodynamical theory of second-order phase transition with the relaxation.[8] The specific thermodynamic potential of an isotropic substance near the Curie point in the absence of the field may be represented as follows[9]:

Ferromagnets	Antiferromagnets
$\phi=\phi_0+\frac{\alpha}{2}\sigma^2+\frac{\beta}{4}\sigma^4+\frac{\gamma}{2}\sigma^2 p-\frac{p^2}{2E_0\rho}$	$\phi'=\phi_0'+\frac{\alpha_1}{2}(\sigma_A^2+\sigma_B^2)+\alpha_2\sigma_A\sigma_B+\frac{\beta'}{4}(\sigma_A^4+\sigma_B^4)+\frac{\gamma_1}{2}p(\sigma_A^2+\sigma_B^2)+\gamma_2 p\sigma_A\sigma_B-\frac{p^2}{2E_0\rho};$ (1)

Here $\alpha(T)$, $\beta(T)$, $\alpha_1(T)$, $\alpha_2(T)$, and $\beta'(T)$ are the thermodynamic coefficients which characterize the isotropic exchange interaction and $\gamma(T)$, $\gamma_1(T)$, and $\gamma_2(T)$ are the magnetostrictive constants of the paraprocess for the ferromagnets and the antiferromagnets; ρ is the density; E_0 is the Young's modulus (without considering the magnetic interaction); P is the unidirectional stress; σ is the specific magnetization of the ferromagnets; σ_A and σ_B are the specific magnetizations of the sublattices of the antiferromagnets when $\sigma_A=-\sigma_B$.

From the conditions of equilibrium, we can find the equilibrium specific spontaneous magnetization (if $P=0$):

$\sigma_S^2=-\frac{\alpha}{\beta}=\frac{\alpha_\theta(\theta-T)}{\beta}$ $(T\leqslant\theta)$	$\sigma_S'^2=\sigma_A^2=(-\sigma_B)^2=-\frac{\alpha_1-\alpha_2}{\beta}=\frac{\alpha_\theta'(\theta-T)}{\beta}$ $(T\leqslant\theta)$ (2)
$\sigma_S=0$ $(T\geqslant\theta)$	$\sigma_S'=\sigma_A=-\sigma_B=0$ $(T\geqslant\theta).$

Let us investigate the behavior of the part of internal friction that is caused by the interaction between the crystalline lattice and the spin-system near the Curie point. It follows, from the thermodynamics of nonequilibrium process, that the establishment of equilibrium in magnets is determined by the kinetic conditions[8]

$\frac{d\sigma}{dt}=-k\frac{\partial\phi}{\partial\sigma}$	$\frac{d\sigma_A}{dt}=-k\frac{\partial\phi'}{\partial\sigma_A};\ \frac{d\sigma_B}{dt}=-k\frac{\partial\phi'}{\partial\sigma_B}.$ (3)

With the application of an alternative mechanical stress P of frequency ω, there appears an alternating component of magnetization $\sigma_P(\ll\sigma_S)$ caused by the change of the exchange interaction.

If $\sigma_P\sim e^{i\omega t}$, then from (3), considering Eq. (1), we get

$-\rho\frac{\partial^2\phi}{\partial P^2}=\frac{1}{E_{\text{compl}}}=\frac{1}{E_0}+\frac{k^2\gamma^2\sigma_S^2\rho}{2k\beta\sigma_S^2+i\omega}$ $(T\leqslant\theta)$	$-\rho\frac{\partial^2\phi}{\partial P^2}=\frac{1}{E_{\text{compl}}}=\frac{1}{E_0}+\frac{2k^2(\gamma_1-\gamma_2)^2\sigma_S'^2\rho}{2k\beta'\sigma_S'^2+i\omega}$ $(T\leqslant\theta)$ (4)
$-\rho\frac{\partial^2\phi}{\partial P^2}=\frac{1}{E_{\text{compl}}}=\frac{1}{E_0}$ $(T\geqslant\theta)$	$-\rho\frac{\partial^2\phi}{\partial P^2}=\frac{1}{E_{\text{compl}}}=\frac{1}{E_0}$ $(T\geqslant\theta).$

By separating the real and the imaginary parts, we get expressions for the dynamic elastic modulus and the logarithmical decrement of damping which characterizes the internal friction,

$$E=E_0\left(1-\frac{\Delta_E}{1+\omega^2\tau^2}\right) \tag{5}$$

$$\delta=\pi\Delta_E\frac{\omega\tau}{1+\omega^2\tau^2}, \tag{6}$$

---

[8] L. D. Landau and E. M. Lifshitz, *Statistical Physics* (Gostechizdat, 1951); L. D. Landau, I. M. Kalatnikov, Doklady Akad. Nauk. SSSR, **94**, 469 (1954); V. T. Shmatov, Fiz. Metal. i Metalloved. Akad. Nauk. S.S.S.R., Ural. Filial **6**, 570, 934 (1958).

[9] K. I. Belov, Fiz. Metal. i Metalloved, Akad. Nauk. S.S.S.R., Ural. Filial **2**, 447 (1956); K. I. Belov, P. Z. Levitin, Vestnik Moskov. Univ. Ser. Fiz-Mat. i Estestven. Nauk. No. 3 (1959).

where the time of relaxation τ and the degree of relaxation of modulus Δ_E are expressed as follows:

$$\tau=-\frac{1}{2k\alpha}=\frac{1}{2k\alpha_\theta(\theta-T)} \quad (T\leqslant\theta)$$
$$\tau=\infty \quad (T\geqslant\theta)$$
$$\Delta_E=\frac{E_0\gamma^2\rho}{2\beta} \quad (T\leqslant\theta)$$
$$\Delta_E=0 \quad (T\geqslant\theta)$$

$$\tau=-\frac{1}{2k(\alpha_1-\alpha_2)}=\frac{1}{2k\alpha_\theta'(\theta-T)} \quad (T\leqslant\theta) \qquad (7)$$
$$\tau=\infty \quad (T\geqslant\theta)$$
$$\Delta_E=\frac{E_0(\gamma_1-\gamma_2)^2\rho}{\beta} \quad (T\leqslant\theta) \qquad (8)$$
$$\Delta_E=0 \quad (T\geqslant\theta).$$

From Eq. (6) it follows that several things must be observed below Curie point: (a) a Young's modulus anomaly, and (b) anomalous internal friction, resulting from the appearance of magnetic order. Under the condition $\omega\tau=1$, the internal friction reaches a maximum which equals

$$\pi\Delta_E/2. \qquad (9)$$

The temperature of the maximum is defined from (7) by

$$\theta-T_{\max}=(\omega/2k\alpha_\theta); \qquad (10)$$

In Eq. (8) we see that the magnitude of the anomaly of the elastic modulus and the internal friction must be large in a substance which has a large magnetostrictive constant of paraprocess γ which specifies a spontaneous deformation of the crystalline lattice in the ferromagnetic state.

A more detailed theory for ferromagnets in which an external magnetic field is taken into consideration, is given by the present authors.[10] From this theory, it follows that, near the Curie point, the application of the field widen the temperature range of the anomaly in Young's modulus. It also decreases as well as widens the maximum of damping and makes the maximum approach the Curie point.

So, the thermodynamical theory qualitatively agrees with the experimental data for both elastic and nonelastic properties of magnets near the Curie point. This shows, that the observed anomalies, in fact, are explained by the redistribution of spins inside the domain as the effect of elastic stresses. For the ferromagnets, the above statement is confirmed by the fact that the anomalies do not vanish under the application of a magnetic field large enough to make the specimen a "single domain." The similarity between the behavior of elastic properties of ferromagnetic and antiferromagnetic substances near the Curie point shows that, evidently, the anomalies of the internal friction and the Young's modulus in this region of temperature are caused by the same effects, and are not associated with the redistribution of domains as assumed by R. Street and B. Lewis.[7,11]

It appears, however, that (according to the magnetic data) theoretically calculated magnitudes of the maximums of the internal friction for the ferromagnets are greater than those observed (with the frequency of 1 kc/sec) by one or two orders of magnitude. This difference may be accounted for by the fact that the theory given is only true for an isotropic single-domain specimen under homogeneous mechanical stresses. All these conditions could not be completely met in our experiments, especially for demagnetized specimens; this fact probably explains the smaller height of the maximum in these experiments.

Equation (10) and the value of $T_{\max}$ obtained from the experiment enable us to evaluate kinetic coefficient k. It can be done only for alloys for which we have measured the thermodynamical coefficients. For instance, we obtained $k=35$ (cm³/g-sec) for the alloy 53.5% Co, 8.7% Cr, 37.8% Fe.

Equation (11) enables us to evaluate the time of relaxation for the investigated ferromagnetic and antiferromagnetic substances near the Curie point: $\tau=10^{-4}-10^{-5}$ sec. At present, it is difficult to say whether this time of relaxation is defined either by spin-lattice or by spin-spin interaction.

[10] K. I. Belov, G. I. Kataev, and P. Z. Levitin, Zhurnal Exptl. Teoret. Fizik **37**, 10 (1959).

[11] R. Street and B. Lewis, Phil. Mag. **1**, 663 (1956); R. Street, "The Proceedings of the Grenauble conference."

Magnetic Anisotropy and Magnetostriction of Ordered and Disordered Cobalt-Iron Alloys

R. C. HALL*
Magnetic Material Development Section, Westinghouse Electric Corporation, East Pittsburgh, Pennsylvania

The magnetic anisotropy and magnetostriction of single crystals of alloys between 25 weight % and 59 weight % cobalt in iron have been determined in the disordered and ordered states. The magnetostriction is large and positive for all alloys in both states of order (up to 150×10^{-6} for λ_{100} and 40×10^{-6} for λ_{111}). The magnetic anisotropy becomes zero near 41% Co for the disordered state. Ordering shifts the zero-anisotropy composition to about 50% Co.

COBALT-IRON alloys have for many years been of interest as magnetic materials because they have unusually high magnetic saturation values. This interest was increased recently by the discovery of Supermendur.[1] Supermendur is an alloy of 49 wt % Co-49 wt % Fe-2 wt % *V*, which was found by suitable purification and heat treatments, including a magnetic anneal, to possess excellent soft magnetic properties. Two factors which are important in determining the magnetic hysteresis properties are the basic magnetic properties of magnetostriction and anisotropy. Since very meagre data are available in the literature on the single crystal anisotropy and magnetostriction of the Co-Fe alloys, the present program was undertaken to determine these two properties in the disordered and ordered states.

Ingots of the Co-Fe alloys containing from 25% to 50% Co in iron were slowly cooled through their transformation temperatures for the growth of large grains. From these grains, single crystal disks were fabricated with either the (110) or (100) plane parallel to the faces of the disk. The crystals were heat treated to produce either the ordered state by cooling at a rate of 20°C per hr from 850°C or the disordered state by water quenching from 850°C. The spontaneous saturation magnetostriction was measured by the strain gauge technique and the anisotropy from torque curves.

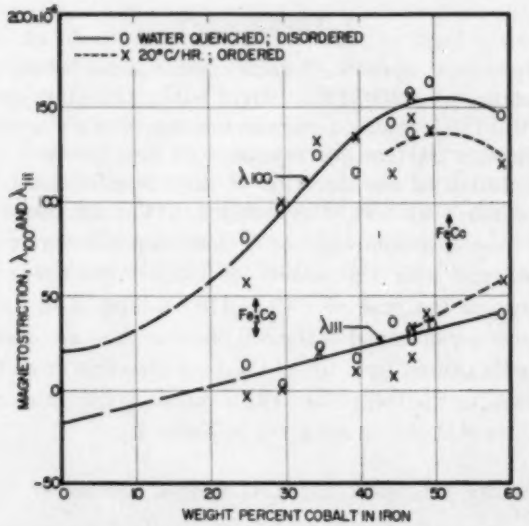

FIG. 1. The saturation magnetostriction (λ) in the [100] and [111] crystallographic directions for the Co-Fe alloys.

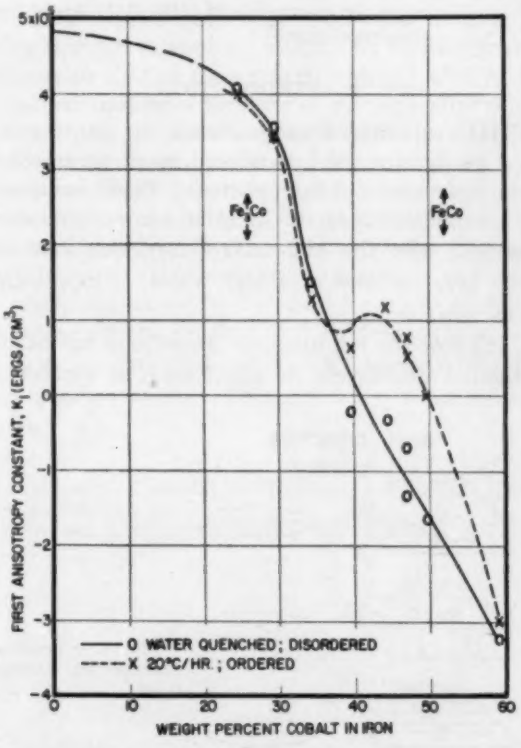

FIG. 2. The first anisotropy constant for the Co-Fe alloys.

The magnetostriction, shown in Fig. 1, in the [100] and [111] directions (λ_{100} and λ_{111}, respectively) became large positive values as cobalt was added to iron. Values of λ_{100} reached 150×10^{-6} and λ_{111} reached 30×10^{-6} at equal percentages of iron and cobalt. Near the FeCo composition, λ_{100} was lowered and λ_{111} was raised as the degree of order was increased. Magnetostriction strains

* Now with Research and Development Laboratory, Universal-Cyclops Steel Corporation, Bridgeville, Pennsylvania. Complete paper submitted to the American Institute of Mining and Metallurgical Engineers.

[1] H. L. B. Gould and D. H. Wenny, *Conference on Magnetism and Magnetic Materials* (American Institute of Electrical Engineers, February, 1957), AIEE Spec. Publ. T-91, p. 675.

normally associated with the movement of 90° domain boundaries are reduced in commercial alloys by employing a magnetic anneal.

Figure 2 illustrates the first anisotropy constant K_1. For the disordered state, K_1 was lowered slightly with the addition of cobalt up to 30%. From 30% to 59% Co, K_1 dropped precipitously to large negative values. The easy direction of magnetization changed from the [100] to the [111] near 41% Co. Ordering shifted the zero-anisotropy composition to about 50% Co. From 37% to 59% Co, K_1 changed toward larger positive values with increased order. These data indicate that the excellent magnetic properties of Supermendur are associated not only with its high purity and the magnetic anneal, but with the zero anisotropy in the ordered state near equal percentages of Fe and Co.

JOURNAL OF APPLIED PHYSICS SUPPLEMENT TO VOL. 31, NO. 5 MAY, 1960

Roll Magnetic Anisotropy of Iron-Aluminum Crystals

SOSHIN CHIKAZUMI*
Institute for Solid State Physics, University of Tokyo, Komaba, Meguroku, Tokyo, Japan

Magnetic anisotropy measurements and domain pattern observations were made on the rolled Fe_3Al single crystals. Rolling parallel to [001] on a (110) plane induced a uniaxial anisotropy as large as 7.1×10^5 erg/cc at 12% roll-reduction. The direction of easy magnetization was parallel to the roll direction. Calculations were made on the roll magnetic anisotropy in terms of the "slip-induced directional order model," under the assumption of (110) ⟨111⟩ slip system. (110) [1$\bar{1}$0], (001) [010], and (001) [110] rollings were also investigated.

1. INTRODUCTION

THIS experiment was made for the purpose of investigating the roll-induced magnetic anisotropy of the body-centered cubic material. Fe_3Al was selected as a specimen because this alloy has a low crystal anisotropy and also the high magnetostriction constants, which give promise of a high value of dipole-dipole interaction.

Until now the roll magnetic anisotropy has been investigated exclusively on alloys such as Fe-Ni[1,2] and Fe-Ni-Cu[3–5] which have a face-centered cubic lattice. Although several interpretations[6] have been proposed concerning the mechanism of roll magnetic anisotropy, the experiments on Fe-Ni alloys seemed to be explained reasonably well in terms of "slip-induced directional order".[7,8]

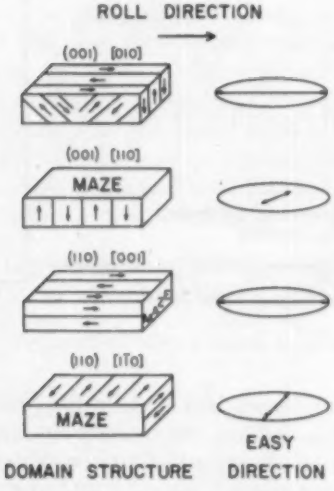

FIG. 1. Schematic of experimental configurations.

2. EXPERIMENT

Specimens were Fe_3Al single crystal plates having the orientations (001) [010], (001) [110], (110) [001], and (110) [1$\bar{1}$0]. Figure 1 summarizes experimental results of domain pattern observation, and also indicates the orientation of the direction of easy magnetization as determined by torque measurement. The directions of the magnetization observed in domain pattern were all consistent with the results of torque measurement, except in the case of (001) [110] rolling. The finite anisotropy observed in the roll plane in this case is supposedly caused by a tilt of the easy direction from the normal to the roll plane. The anisotropy constants for each case of rolling are given in Table I.

---

* Temporarily staying at IBM Research Center in Poughkeepsie.

[1] H. W. Conradt, O. Dahl, and K. J. Sixtus, Z. Metallk. **32**, 231 (1940).

[2] G. W. Rathenau and J. L. Snoek, Physica **8**, 555 (1941).

[3] W. Six, J. L. Snoek, and W. G. Burgess, Ingenieur **49**, E195 (1934).

[4] A. Kussmann, B. Scharnors, and W. Steinhaus, *Heraeus Vacuumschmelze*, (Albertis, Hanau, 1933), pp. 310–338.

[5] M. Kersten, Wiss, Veröffentl. Siemens-Konzern **13** (3), 1–9 (1934).

[6] L. Néel, Compt. Rend. **238**, 305 (1954); J. phys. radium **15**, 225 (1954); S. Taniguchi and M. Yamamoto, Sci. Repts. Research Inst. Tohoku University **A6**, 330 (1954).

[7] H. J. Bunge and H. G. Müller, Wiss. Z. Hochschule Verk Dresden **5**, 327 (1957); H. J. Bunge, Z. Metallk. **49**, 40 (1958).

[8] S. Chikazumi and K. Suzuki, Phys. Rev. **98**, 1130 (1955); S. Chikazumi, K. Suzuki, and H. Iwata, J. Phys. Soc. (Japan) **12**, 1259 (1957); S. Chikazumi, J. Appl. Phys. **29**, 346 (1958).

TABLE I. Roll magnetic anisotropy of Fe_3Al single crystals.

Roll plane and direction	Roll reduction in %	Torque measurement K_u in 10^5 erg/cc	Easy direction	Calculation $\frac{K_u}{p\sigma Nl_2}$	Value of $p\sigma Nl_2$ in 10^5 erg/cc
(001) [010]	10.3	3.70	[010]	−1/32	−1.15
(001) [110]	10	1.76	27° from r.d.	0	—
(110) [001]	12	7.06	[001]	−1/64	−3.76
(110) [1$\bar{1}$0]	8.7	4.34	[001]	−3/256	−4.25

3. INTERPRETATION OF THE EXPERIMENTAL RESULTS

It is reported that the slip systems in body-centered cubic metals are {110} ⟨111⟩, {112} ⟨111⟩, and {123} ⟨111⟩. Observation of the slip bands on the rolled specimens confirmed our initial assumption that the slips in the present case belong exclusively to the class {110} ⟨111⟩.

The concept of slip-induced directional order is based upon the assumption that when the slip takes place in a somewhat ordered crystal some disordering should be induced in the atom pairs, which connect both sides of the slipped plane. It should be expected, however, that the atom pairs which connect nearest neighbors would not contribute to the anisotropy in the case of the present crystal, where the effective slip planes occur in intersecting perpendicular pairs. The directions of the second-neighbor pairs are three ⟨100⟩, one of which is lying in the slip plane, while the other two are out of the slip plane. When, therefore, the slip takes place in one of the slip systems, the ⟨100⟩ atom pairs which are lying in the slip plane become lacking in *B-B* pairs as compared to the other two ⟨100⟩ directions. Since the directions of *B-B* pairs means the easy direction for Fe-Al alloy, the induced anisotropy has a hard direction parallel to the ⟨100⟩, which is lying in the slip plane.

Now in the case of (001) [010] rolling, (011) and (01$\bar{1}$) must be effective as the slip planes, so the induced anisotropy should have a hard direction parallel to [100]: in other words, (100) should be the plane of easy magnetization. In the case of (001) [110] rolling, (011), (01$\bar{1}$), (101), and (10$\bar{1}$) must be effective as the slip planes, so [100] and [010] will become hard directions, which means the easy direction being parallel to [001]. In the cases of (110) [001] and (110) [1$\bar{1}$0] rolling, the effective slip planes are the same as the case of (001) [110] rolling, though the sense and the direction of the slip in each plane must be different. The easy direction, therefore, is also parallel to [001]. This means that the easy direction is parallel to the roll direction for (110) [001] rolling, while it is perpendicular to roll direction and parallel to the roll plane for (110) [1$\bar{1}$0] rolling. These results are in good agreement with the experiments.

The results of exact calculations[9] are given in Table I. We obtained almost the same values of $p\sigma Nl_2$ for (110) [001] and (110) [1$\bar{1}$0] rollings, but a slightly different value for (001) [010]. The value of $Nl_2=N(l_{AA}+l_{BB}-2l_{AB})$, which means the coefficient of dipole-dipole interaction per unit volume, can be calculated to be -30.1×10^5 erg/cc from magnetostriction data by assuming that the ratio of the interaction between nearest neighbors to that of second neighbors is 1.35:1 as has been determined from the data of magnetic annealing.[10] Since p, the probability for one dislocation to produce the disordered plane, and σ, the degree of short range order, should both have values lying between 0.1 and 1, the obtained values of $p\sigma Nl_2$ may be reasonable. It is, however, interesting to note that the value of $p\sigma$ obtained from the experiment of roll magnetic anisotropy was much smaller for Ni_3Fe[8] than for Fe_3Al. This fact may supposedly be assigned to the difference in the ease of producing the stacking disorder between the two cases of face-centered cubic and body-centered cubic crystals.

[9] S. Chikazumi, K. Suzuki, and H. Iwata, J. Phys. Soc. (Japan) (to be published).
[10] K. Suzuki, J. Phys. Soc. (Japan) 13, 756 (1958).

Magnetic Anisotropy in Ferrimagnetic Crystals

R. F. PEARSON
Mullard Research Laboratories, Salfords, Redhill, England

Absolute values of K_1, the first-order anisotropy constant, have been determined at different temperatures from torque measurements on single crystals of the following compositions:

$Mn_xFe_{3-x}O_4$, where $0.7 \leqslant x \leqslant 1.0$;
$Co_x Mn_{1-x}Fe_2O_4$, where $0 \leqslant x \leqslant 0.25$;
$Co_{0.04}Mn_{x-0.04}Fe_{3-x}O_4$, where $0.70 \leqslant x \leqslant 0.91$;
$Ga_xFe_{3-x}O_4$, where $0 \leqslant x \leqslant 0.8$;
$Sm_3Fe_5O_{12}$
$Gd_3Fe_5O_{12}$.

The magnetocrystalline anisotropy of manganese ferrous ferrite was found to vary considerably with the concentration of ferrous ions (Fe^{2+}), some compositions even possessing a positive value of K_1 at room temperature, as previously found by Penoyer (1959). In these cases, K_1 becomes negative at low temperatures in contrast with the behavior of cobalt-substituted crystals which are found to have rapidly increasing positive values of K_1 as the temperature is reduced. The anisotropy contribution of cobalt ions (Co^{2+}) substituted in manganese ferrous ferrite varies with crystals of different compositions.

The experimental values of K_1 are compared wherever possible with present theories of magnetic anisotropy. In particular, the recent theory proposed by Slonczewski (1958) to explain the anisotropy of cobalt ions substituted in magnetite (Fe_3O_4) is found to be unsuccessful in the case of Co^{2+} ions in manganese ferrite ($MnFe_2O_4$).

Measurements at low temperatures on the gallium-substituted magnetite crystals reveal an additional interesting effect. For certain crystals, the torque curves at 80°K exhibit considerable rotational hysteresis in fields above 10 000 oe, when the material should certainly be saturated. This hysteresis is shown to be related to the ordering of the ferrous (Fe^{2+}) and ferric (Fe^{3+}) ions which takes place on the octahedral sites at low temperatures.

INTRODUCTION

NOW that most ferrimagnetic compounds can be prepared in single crystal form, it is possible to investigate in detail the variation of magnetocrystalline anisotropy with composition in order to eventually identify and determine the mechanisms which produce such a large variation of anisotropy in these materials. In this paper, the results of measurements on a wide range of materials will be presented in a shortened form and briefly discussed.

EXPERIMENTAL DETAILS

Single crystals of substituted manganese ferrite, substituted magnetite, and certain rare earth garnets were grown by the flame fusion method, the Bridgman method, and from a lead oxide solution, respectively, by J. L. Page and R. Crumpton of these laboratories. A survey of these methods of crystal growing has recently been given by Harrison.[1] The crystals were shaped into the form of spheres about 1.5 mm diam and oriented by x-ray methods. Torque curves [in either a (110) plane or a (100) plane] were measured in a field of 12 000 oe using an automatic recording torque magnetometer similar to that described by Penoyer[2] and previously referred to by the author.[3] Values of K_1, the first-order anisotropy constant, were deduced either from the peak heights of the (100) curves or from a Fourier analysis of the (110) curves. A summary of the experimental values of K_1 is given in Table I.

DISCUSSION OF RESULTS

The results for cobalt substituted manganese ferrite ($Co_xMn_{1-x}Fe_2O_4$) show that the cobalt ions give an additive contribution to the anisotropy, which increases linearly with composition up to at least 25% substitution compared to a limit of 10% found for cobalt substitution in Fe_3O_4 by Bickford.[4] The value of K_1 obtained on extrapolating the cobalt concentration up to 100% ($x=1$) is 0.8×10^6 erg cm^{-3} at 290°K compared to 3×10^6 erg cm^{-3} for cobalt ferrite and $K_1=1.5\times10^7$ erg cm^{-3} for cobalt substitutions in magnetite. The anisotropy contribution of the Co^{2+} ions is thus smaller for substitution in $MnFe_2O_4$ than in Fe_3O_4, but varies much faster with temperature, as shown in Fig. 1. Although the theory recently proposed by Slonczewski[5] to explain the anisotropy of cobalt ions in magnetite does not satisfactorily produce the temperature variation of the anisotropy found for substitutions in man-

TABLE I. Anisotropy constants of certain ferrites.

Nominal composition	Chemical analysis	Value of K_1 erg cm$^{-3}\times10^{-3}$ $T=290$°K	$T=200$°K
$MnFe_2O_4$	$Mn_{0.95}Fe_{1.99}O_4$	−40.7	−105.3
$Co_{0.01}Mn_{0.99}Fe_2O_4$	$Co_{0.009}Mn_{0.99}Fe_{1.98}O_4$	−31.2	−46.8
$Co_{0.02}Mn_{0.98}Fe_2O_4$	$Co_{0.019}Mn_{1.03}Fe_{1.94}O_4$	−22.2	+10.0
$Co_{0.04}Mn_{0.96}Fe_2O_4$	$Co_{0.038}Mn_{0.96}Fe_{1.97}O_4$	−7.0	+112.2
$Co_{0.06}Mn_{0.94}Fe_2O_4$	$Co_{0.056}Mn_{0.96}Fe_{1.97}O_4$	+6.3	+210.0
$Co_{0.08}Mn_{0.92}Fe_2O_4$	$Co_{0.077}Mn_{0.92}Fe_{1.99}O_4$	+29.1	—
$Co_{0.10}Mn_{0.9}Fe_2O_4$	$Co_{0.094}Mn_{0.91}Fe_{1.97}O_4$	+37.3	+407.5
$Co_{0.24}Mn_{0.72}Fe_2O_4$	$Co_{0.244}Mn_{0.747}Fe_{1.99}O_4$	+171.0	—
$Mn_{0.91}Fe_{2.09}O_4$	$Mn_{0.891}Fe_{2.093}O_4$	−16.8	−48.5
$Co_{0.04}Mn_{0.87}Fe_{2.09}O_4$	$Co_{0.041}Mn_{0.878}Fe_{2.088}O_4$	+15.9	+172.9
$Mn_{0.87}Fe_{2.13}O_4$	$Mn_{0.818}Fe_{2.134}O_4$	−9.6	−35.5
$Co_{0.04}Mn_{0.83}Fe_{2.13}O_4$	$Co_{0.0358}Mn_{0.838}Fe_{2.131}O_4$	+44.3	+224.0
$Mn_{0.74}Fe_{2.26}O_4$	$Mn_{0.747}Fe_{2.241}O_4$	+4.9	−8.1
$Co_{0.04}Mn_{0.72}Fe_{2.26}O_4$	$Co_{0.0371}Mn_{0.722}Fe_{2.234}O_4$	+93.6	+328.8
$Mn_{0.70}Fe_{2.3}O_4$	$Mn_{0.697}Fe_{2.291}O_4$	+0.6	−17.2
$Co_{0.04}Mn_{0.66}Fe_{2.3}O_4$	$Co_{0.0372}Mn_{0.647}Fe_{2.31}O_4$	+118.1	—
$Ga_{0.4}Fe_{2.6}O_4$	$Fe_{0.938}^{3+}Fe_{1.062}^{3+}Ga_{0.443}O_4$	−80.9	−121.8
$Ga_{0.7}Fe_{2.3}O_4$	$Fe_{0.985}^{3+}Fe_{1.015}^{3+}Ga_{0.625}O_4$	−49.7	−97.8
$Ga_{0.8}Fe_{2.2}O_4$	$Fe_{0.945}^{3+}Fe_{1.055}^{3+}Ga_{0.767}O_4$	−36.9	−75.7
$Gd_3Fe_5O_{12}$	...	−6.7	−15.2
$Sm_3Fe_5O_{12}$	...	−19.8	−82.5

[1] F. W. Harrison, Research (1959) (to be published).
[2] R. F. Penoyer, Rev. Sci. Instr. **30**, 711 (1959).
[3] R. F. Pearson, J. phys. radium **20**, 409 (1959).
[4] L. R. Bickford, M. S. Brownlow, and R. F. Penoyer, Proc. Inst. Elec. Engrs. (London) 104B, Suppl., p. 238 (1957).
[5] J. C. Slonczewski, Phys. Rev. **110**, 341 (1958).

ganese ferrite, a more comprehensive treatment[6] using the same mechanism seems capable of giving better agreement with the present results. We have also investigated the effect of cobalt on the anisotropy of crystals of composition between magnetite and manganese ferrite, i.e., manganese ferrous ferrite. The anisotropy contribution for cobalt substituted in a particular composition $Mn_{0.7}Fe_{2.3}O_4$ is also plotted in Fig. 1. Finally, it is of interest to report a difference in the value of K_1 obtained from these torque measurements and microwave resonance measurements of R. W. Teale[7] for a certain composition of cobalt substituted manganese ferrite. K_1 (resonance) for $Co_{0.25}Mn_{0.75}Fe_2O_4$ is 116 000 erg cm^{-3} at 291°K, whereas K_1 (torque) = 164 000 erg cm^{-3}.

The intrinsic anisotropy of manganese ferrous ferrite ($Mn_{1-x}Fe_{2+x}O_4$) is of great interest mainly because the values of K_1 for certain compositions ($x=0.70$, 0.76) are found to be positive at room temperature. This was also recently reported by Shafer and Penoyer[8] from measurements made independently on crystals grown by the Bridgman method, thus confirming that these rather anomalous values of K_1 are an intrinsic property of these compositions. The temperature variation of K_1 for $Mn_{0.7}Fe_{2.3}O_4$ is quite different from $MnFe_2O_4$, changing to a negative value at low temperatures, but remaining quite small (less than 20 000 erg cm^{-3}) down to 120°K. These results may be qualitatively explained by assigning a positive contribution to the substituted Fe^{2+} ions.

Analysis of the anisotropy constants of gallium and aluminium-substituted magnetite crystals is still continuing,[3] but it is of interest here to describe an effect discovered at low temperatures (82°K) in these samples. The torque curves at 82°K exhibited considerable rotational hysteresis in a high field (approximately 12 000 oe), which is much larger than the calculated anisotropy field of 5000 oe assuming a value for K_1 of 1.2×10^6 ergs cm^{-3}. As this phenomenon only appeared in samples in which the Fe^{2+} and Fe^{3+} ions on the octahedral lattice sites were tending to form an ordered arrangement, we assume the losses are related to the ordering process. Further analysis of the results has shown that hysteresis

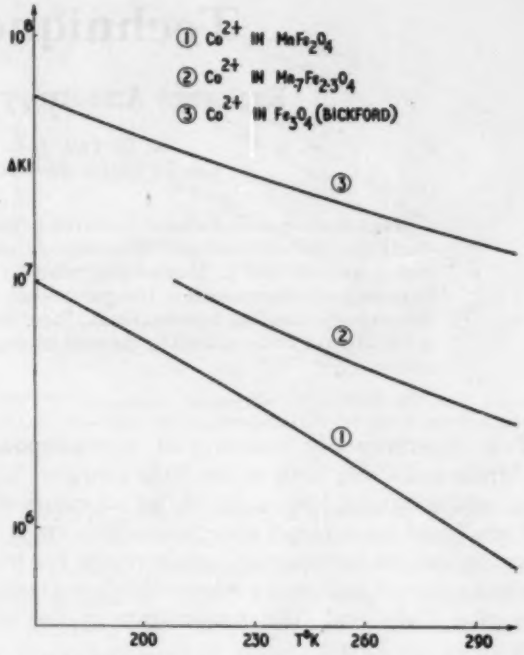

FIG. 1. Anisotropy contribution of Co^{2+} ion (extrapolated to 100% substitution) plotted on a logarithmic scale as a function of temperature.

of this type can be produced by the mechanism of "axis switching" previously reported for Fe_3O_4 below the transition point.[9]

The values of K_1 measured for gadolinium and samarium garnet agree well with the values reported by Rodrigue[10] from microwave resonance measurements. The anisotropy of SmIG was found to increase more rapidly than GdIG at low temperatures.

ACKNOWLEDGMENTS

The author wishes particularly to thank R. Cooper for making the torque measurements, E. J. Millett and J. Roberts for the chemical analysis, and all my colleagues in the Magnetics Group for their advice and encouragement. This work is published by kind permission of P. E. Trier, director of the Mullard Research Laboratories.

[6] J. C. Slonczewski (private communication).
[7] R. W. Teale and R. F. Pearson (submitted to the Physical Society).
[8] R. F. Penoyer and M. W. Shafer, J. Appl. Phys. 30(S), 315 (1959).
[9] B. A. Calhoun, Phys. Rev. 94, 1577 (1954).
[10] G. P. Rodrigue, R. V. Jones, and W. P. Wolf, J. Appl. Phys. 29, 434 (1958).

Techniques and Devices

Exchange Anisotropy in the System $Mn_{(1-x)}Cr_xSb$

R. H. Pry, J. S. Kouvel, and E. S. Miksch
General Electric Research Laboratory, Schenectady, New York

Magnetization and rotational hysteresis measurements have been made on some alloys of $Mn_{(1-x)}Cr_xSb$. For $0.5 \leq x \leq 0.7$ the rotational hysteresis continuously increases with applied magnetic field in the temperature range of 80–300°K. This behavior supports the hypothesis that there is a coexistence of ferro-and antiferro-magnetic components in this composition range and that there exists an exchange anisotropy due to the magnetic coupling between them. These magnetic components probably arise from local fluctuations in the Mn to Cr ratio caused by the near random distribution of these ions on the magnetic ion sites in this system.

IT is experimentally known that the compounds MnSb and CrSb, both of the NiAs structure type, form solid solutions, $Mn_{(1-x)}Cr_xSb$, for all values of x. For small and large values of x these alloys are ferromagnetic and antiferromagnetic respectively. For intermediate values of x there is evidence indicating coexistence of a Curie and Néel temperature in the same alloy.[1,2]

Since only a small tendency toward ordering has been reported[3] between the Mn and Cr ions in this system, a question arises as to whether the existence of the macroscopic ferro-antiferromagnetic behavior of these alloys originates from the properties of a uniform homogeneous alloy or from the coexistence of microscopic antiferromagnetic and ferromagnetic regions, brought about by the normal heterogeneous distribution of the magnetic ions in a random, or near random, solid solution.

Some recent experiments[4] on disordered Ni_3Mn have demonstrated that microscopically both ferro- and antiferromagnetic regions can exist in disordered alloys and that an exchange anisotropy can exist between them.

The demonstration of the coexistence of these components and an interaction energy between them rests on two experimental results: (1) When the material is cooled from a high temperature in a magnetic field: (a) the low temperature hysteresis loop is shifted along the H axis, and (b) a $\sin\theta$ component is seen in the torque exerted by the sample when it is rotated in a strong magnetic field. (2) At low temperatures, the rotational hysteresis measured on the sample does not vanish at high fields.

Magnetization and torque measurements have been made by a method previously described[5] on a series of samples in the $Mn_{(1-x)}Cr_xSb$ system in order to determine whether the system could be characterized in this manner by the coexistence at low temperatures of ferro- and antiferromagnetic components. Sample powders were prepared in a manner similar to that described in footnote 2, for $x=0$, 0.5, 0.6, 0.7, and pressed into cylindrical samples approximately $\frac{1}{4}$ in. in diam and $\frac{1}{2}$ in. long.

Each of these samples was cooled from room temperature to 4.2°K in a magnetic field of approximately 5000 oe. Magnetization measurements were then made in fields up to 9000 oe at 4.2°K and upon subsequent heating of the sample, at several intermediate temperatures up to room temperature. Torque magnetometer measurements were made in a similar way, except that the samples were cooled in a 5000 oe field to 78°K only.

Although none of the samples tested exhibited either a shifted hysteresis loop or a $\sin\theta$ component of torque when rotated in a magnetic field, a rotational hysteresis was observed between room temperature and 78°K in fields up to 9000 oe.

The absence of a shifted hysteresis loop and a $\sin\theta$ component of torque could be caused either by the fact that the antiferromagnetic alignment occurs at a higher temperature than the ferromagnetic alignment in every part of these materials, or that the magnetocrystalline anisotropy of the antiferromagnetic component is small enough to allow it to rotate with the ferromagnetic component when the direction of the applied field is changed. In either case, the suggestion of the existence of two magnetic components in this system rests, in the present study, upon the interpretation of the rotational hysteresis measurements.

Figure 1 shows the rotational hysteresis and magnetization measurements for the three alloy samples tested at 80°K. The rotational hysteresis is seen to increase rapidly at low fields and then increase more gradually up to 9000 oe. The shape of the rotational hysteresis curve was the same for these samples between 80 and 300°K. Figure 2 shows the magnitude of the rotational hysteresis at 4000 oe and the magnetization at 9000 oe for these samples as a function of temperature in this temperature range.

The observed rotational hysteresis could have its

[1] T. Hirone, S. Maeda, I. Isubokawa, and N. Ysuya, J. Phys. Soc. Japan **11**, 1083 (1956).
[2] F. K. Lotgering and E. W. Gorter, J. Phys. Chem. Solids **3**, 238 (1957).
[3] S. J. Pickart and R. Nathans, J. Appl. Phys. **30**, 280S (1959).
[4] J. S. Kouvel and C. D. Graham, J. Appl. Phys. **30**, 312S (1959).
[5] J. S. Kouvel, C. D. Graham, and J. J. Becker, J. Appl. Phys. **29**, 518 (1958).

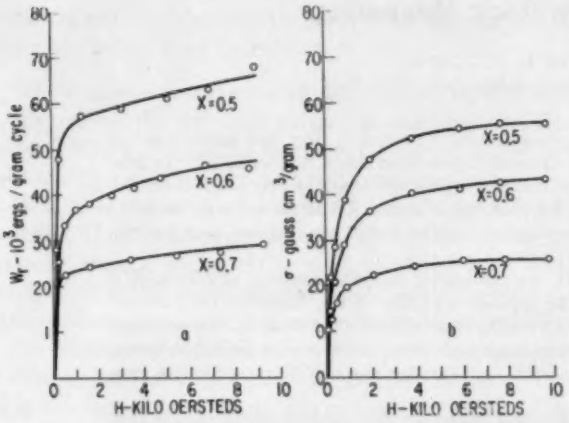

FIG. 1. Rotational hysteresis, curve *a*, and magnetic moment, curve *b*, vs applied magnetic field for three compositions of $Mn_{(1-x)}Cr_xSb$ at 80°K.

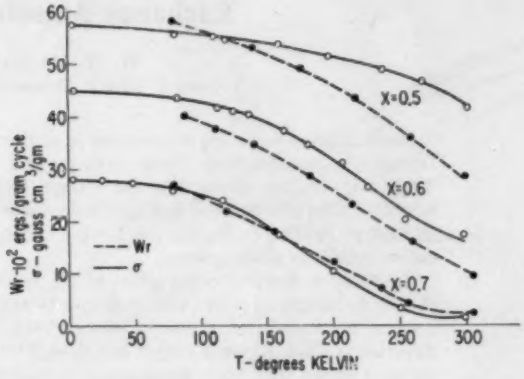

FIG. 2. Rotational hysteresis ($H=4000$ oe) and magnetic moment ($H=9000$ oe) vs temperature for three compositions of $Mn_{(1-x)}Cr_xSb$.

origin in either the magnetocrystalline anisotropy of the ferromagnetic component or the exchange anisotropy between coexisting ferromagnetic and antiferromagnetic components. However, it is difficult to attribute the rotational hysteresis observed to the magnetocrystalline anisotropy effects of an ordinary ferromagnetic system. If this were the origin of the energy loss then one would expect the hysteresis to begin decreasing with increasing field for field strengths of the order of ½ the maximum field strength used, since, according to the magnetization measurements of Fig. 1(b) and previous work at higher fields[2] these alloys are quite close to saturation at a field of 9000 oe.

It is possible that the observed hysteresis has as its origin an exchange anisotropy but that the antiferromagnetic component is an antiferromagnetic impurity in the system. Of the possible oxide impurities only Cr_2O_3 has a Néel temperature above 120°K, and so could contribute to the measured hysteresis above this temperature. Both the quantity of oxide present and the crystal structure of the oxide make this origin doubtful. The most likely impurity which could lead to the observed result is a stoichiometric excess of either Cr or Mn. Both of these elements, if present in excess, would dissolve in interstitial lattice sites and might be expected to be antiferromagnetically coupled to the neighboring atoms. A "pure" MnSb sample, prepared in a way identical with the alloys, had a field independent rotational hysteresis of about 1500 ergs/g cycle, from 2000 to 9000 oe when measured at 80°K. Thus, this explanation of the effect cannot be ruled out and requires a closer examination than has been made to date. Since the rotational hysteresis of the MnSb sample had a value considerably lower than the alloys, it is reasonable to assume that the entire effect in the alloys is not of this origin.

It therefore is tentatively suggested that the existence of a nonvanishing rotational hysteresis at high fields found in the solid solution alloys of MnSb and CrSb arises from the coexistence at low temperatures of a ferromagnetic and an antiferromagnetic component, the ferromagnetic component being regions rich in MnSb, the antiferromagnetic components rich in CrSb. It is supposed that these regions are a result of local fluctuations in the Mn-Cr ratio resulting from a near random distribution of these ions on the magnetic ion sites.

Exchange Anisotropy in Rock Magnetism

W. H. MEIKLEJOHN AND R. E. CARTER
General Electric Research Laboratory, Schenectady, New York

Some igneous rocks are magnetized in a direction opposite to that expected, if they had been cooled in the earth's magnetic field. These rocks are said to have a reverse thermo-remanent magnetization (reverse TRM). Uyeda has shown that the reverse TRM of the Haruna deposit in Japan is due to an ilmenite-hematite solid solution and has synthesized a solid solution that has a reverse TRM when cooled in fields as high as 16 000 oe. He has put forth a theory which contains a mechanism similar to that found in the cobalt-cobaltous oxide system.

Based upon Uyeda's explanation of the reverse TRM, we postulated that the material should have a shifted hysteresis loop and that it should be shifted in the opposite direction to that found in the Co-CoO system. We found that the solid solution—0.6 $FeTiO_3$ 0.4 Fe_2O_3—was shifted by 350 oe in the opposite direction to Co-CoO when cooled in a field. The loop was symmetrical when cooled in zero field. Moreover, we have shown that when the material is cooled in a magnetic field through the Morin transition the loop is shifted in the same direction as Co-CoO.

These results confirm the general features of Uyeda'a model, although the detailed mechanism is still being studied.

We believe that Uyeda's work definitely establishes the reverse TRM of the Haruna deposit as due to a magnetic phenomenon and not due to the reversal of the earth's magnetic field. We believe that the type of magnetic investigation reported in this paper may be applied to other deposits that have a reverse TRM to establish if they are also due to a magnetic phenomenon.

INTRODUCTION

VARIATION in the direction of the earth's magnetic field,[1] shifts in continental land masses[2] and theories of the origin of the earth's magnetic field have all been postulated from studies of the direction of the residual magnetization of rocks. A magnetic phenomenon which influences the direction of the residual magnetization will obviously modify or invalidate the above ideas.

The Haruna pumice in Japan shows a reverse thermoremanent magnetization (reverse TRM) to that expected if it had cooled in the earth's magnetic field. Nagata, Akimoto and Uyeda have cooled the Haruna pumice from above its magnetic transformation temperatures in a magnetic field and developed reverse TRM. Uyeda[3] has also synthesized the ilmenite-hematite solid solution found in the Haruna rock and developed in it a reverse TRM. Uyeda has explained this result by an exchange interaction similar to that in the Co-CoO system.[4]

EXCHANGE INTERACTION MODEL

If Uyeda's model is correct, an ilmenite-hematite solid solution having a reverse TRM should have a hysteresis loop displaced in the opposite direction to that of Co-CoO. In Uyeda's model an antiferromagnetic Fe_2O_3 rich phase having a parasitic ferromagnetism, phase *A*, is coupled to a ferrimagnetic $FeTiO_3$ rich phase *B*. During cooling in a magnetic field, the parasitic ferromagnetism of phase *A* is aligned by the applied field and is locked in this direction when the antiferromagnetic spins order. On further cooling, the larger spins of the ferrimagnetic phase *B* are locked through an exchange interaction antiparallel to the parasitic ferromagnetism. Because the magnetization of phase *B* is greater than the magnetization of the parasitic ferromagnetism, the material has a reverse TRM. This model develops a uniaxial anisotropy as does the Co-CoO model; but because the net magnetization is locked antiparallel to the external field, the hysteresis loop should be shifted in the opposite direction to that of Co-CoO. We indeed found such a shifted loop.

SPECIMEN PREPARATION

The ilmenite-hematite solid solutions which show a reverse TRM appear to be dependent upon the method of synthesis as well as upon composition. Uyeda[3] has reported that material showing reverse TRM lies between 50 and 65 mole % $FeTiO_3$ except for special heat treated samples. Uyeda prepared his material by reacting purified natural ilmenite with synthetic Fe_2O_3 in an evacuated fused silica ampule at 1200°C and air quenching. This method was retained here in order to duplicate Uyeda's work as closely as possible, but the starting materials were varied. Mechanical mixtures were made from each of the following.

I. Synthesized FeO, chemical grade TiO_2 (rutile or anatase), and chemical grade Fe_2O_3.

II. Synthesized ilmenite and chemical grade Fe_2O_3. The ilmenite had been previously synthesized by reacting FeO and TiO_2 at 1000°C in a H_2O/H_2 ratio of 0.89 which will maintain FeO as the stable phase in the Fe-O system. This synthetic ilmenite gave a Debye-

[1] J. G. Koenigsberger, Terrestrial Magnetism and Atmospheric Elec. **43**, 119, 299 (1938); E. Thellier, Ann. inst. phys. globe, Univ. Paris bur. central magnétisme terrestre **16**, 157 (1938).
[2] S. K. Runcorn, Advances in Phys. **4**, 244 (1955); P. M. S. Blackett, Lectures on Rock Magnetism, Jerusalem (1956).
[3] S. Uyeda, Japan J. Geophys. **2**, (1958).
[4] W. H. Meiklejohn and C. P. Bean, Phys. Rev. **105**, 904 (1957).

Scherrer pattern identical to the ASTM pattern and no impurity peaks were found.

The ilmenite-hematite solid solutions so formed were analyzed by the unit cell volume vs composition.[5] Reverse TRM was found in samples containing 36, 58, and 64 mole % $FeTiO_3$ which had been prepared by method I. A sample containing 48 mole % $FeTiO_3$ prepared by method II did not show reverse TRM. Reverse TRM appears over a wider range than reported by Uyeda, while within this range reverse TRM is not found when specimens are prepared from different starting materials.

In ceramic fabrication it is well known that complete reaction, uniform composition, is not obtained in a single firing. Fluctuations in composition which differ from those in Uyeda's specimens may account both for our finding reverse TRM outside Uyeda's range, and for not finding reverse TRM in the specimen prepared by method II.

In contrast to Uyeda's findings, we were never able to make single phase ilmenite-hematite. In every case pseudobrookite was found in both Debye-Scherrer patterns and in polished sections.

RESULTS

A $FeTiO_3$-Fe_2O_3 solid solution containing 64 mole percent $FeTiO_3$ was magnetically annealed from 500°C to room temperature in air in a field of 10 000 oersteds. The room temperature hysteresis loop was shifted by 350 oe in the direction of the cooling field, a direction opposite to that found for Co-CoO.[6]

Since the antiferromagnetic phase *A* is almost pure Fe_2O_3, it should have a Morin[7] transition; the antiferromagnetic spins should lie in the basal plane above −20°C and be perpendicular to the basal plane below −20°C.

We performed the following experiment to show the presence of this transition, indicating that phase *A* is as proposed by Uyeda. A cylindrical specimen was cooled from 500°C to room temperature with a 10 000 oe field perpendicular to the axis of the cylinder. The room temperature hysteresis loop along the axis of the cylinder, Fig. 1, curve a, is symmetrical, as expected, since the magnetization has been locked perpendicular to the axis of the cylinder. The specimen was then cooled to 77°K with the magnetic field along the cylinder axis. The ferrimagnetic uncompensated spins and the parasitic ferromagnetic spins aligned along the axis by the field are now locked in this orientation by the antiferromagnetic spins which reorder parallel to the trigonal crystallographic axis. The hysteresis loop along the cylinder axis, Fig. 1, curve b, is now shifted in the same direction as in Co-CoO.

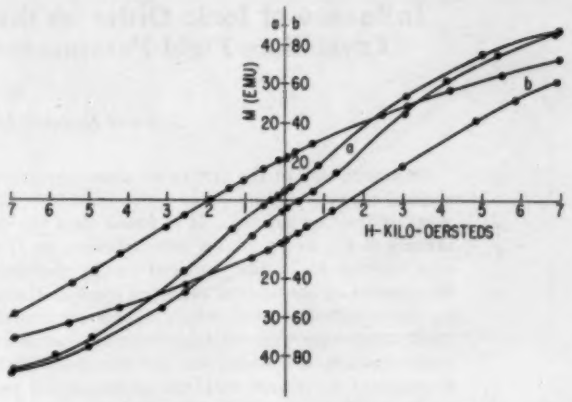

FIG. 1. Hysteresis loop "*a*" measured along axis of rod sample at 300°K after cooling from 800°K in magnetic field (2000 oersteds) perpendicular to axis. Hysteresis loop "*b*" measured at 77°K along axis of the same rod sample after cooling from 300°K in magnetic field (2000 oersteds) along axis. Although the data above 7000 oersteds is not shown, the measurements extend to 12 000 oersteds.

DISCUSSION

These results corroborate Uyeda's model of the magnetic interactions in the Haruna pumice. The inability to develop in the laboratory a reverse TRM in rocks which show a reverse TRM in their geological formation does not prove that the earth's field has reversed. A deposit which had a reverse TRM may undergo chemical change and some of the Fe_2O_3 react to form a ferromagnetic compound. When this rock is magnetically annealed the ferromagnetic phase masks the reverse TRM. Indeed, the Fe_3O_4 in some samples of ilmenite-hematite must be leached out to observe a laboratory induced reverse TRM.[3] The hysteresis loop, however, would show the reverse TRM in such a rock. The difference of the coercivity in each direction may be small due to the masking by the ferromagnetic impurity but in principle there will be a difference.

[5] Y. Ishikawa and S. Akimoto, J. Phys. Soc. (Japan) **13**, 10, 1110–1118 (1958).
[6] W. H. Meiklejohn and R. E. Carter, J. Appl. Phys. **30**, 2020 (1959).
[7] F. J. Morin, Phys. Rev. **78**, 819 (1950).

Influence of Ionic Order on the Magnetocrystalline Anisotropy and Crystalline Field Parameters in Lithium Ferrite Monocrystals

V. J. FOLEN
U. S. Naval Research Laboratory, Washington, 25 D. C.

Measurements of the first order anisotropy constant (K_1), utilizing the torque method, are reported for various degrees of long range order (LRO) in lithium ferrite. The LRO parameters were determined by x-ray diffraction analysis. It is found that the degree of cation "order" in the octahedral sites strongly influences K_1. For example, measurements at 77°K yield the values -127×10^3 ergs/cm³ and -162×10^3 ergs/cm³ for K_1 in the "ordered" and "disordered" states, respectively. The experimental results were interpreted on the basis of the ferric ion spin Hamiltonian. Certain parameters (a_B' for octahedral sites and a_A' for tetrahedral sites) which include the contributions of the cubic term and the quartic axial term to cubic anisotropy were deduced from measurements of the temperature dependences of K_1 and saturation magnetization. It is found that in "disordered" lithium ferrite, $a_B' = +0.0242$ cm^{-1} and $a_A' = -0.0118$ cm^{-1}, in excellent agreement with the corresponding parameters determined by Folen and Rado in magnesium ferrite which is also a "disordered" ferrite. In the "ordered" lithium ferrite, it is found that $a_B' = +0.0104$ cm^{-1} and $a_A' = +0.0034$ cm^{-1}. The experimental temperature dependences of K_1 in both the "ordered" and "disordered" states are in quantitative agreement with that obtained from the Yosida-Tachiki theory. The changes in the magnitudes and signs of the observed a'-values resulting from the "order-disorder" transition are consistent with alterations of the quartic axial term.

THE x-ray work of Braun[1] has shown that a 3 to 1 long range "ordering" of the cations occurs on octahedral sites in lithium ferrite. In this paper a study is made of the influence of this cation "ordering" on the first order magnetocrystalline anisotropy constant (K_1). The results of the K_1 measurements are analyzed on the basis of the "one-ion" anisotropy model.[2-6] Lithium ferrite is particularly suitable for this type of analysis as it contains only one type of magnetic ion, namely Fe^{+++}, and the crystalline structure changes that occur as a result of the "order-disorder" transition may provide information on the parameters entering in the spin Hamiltonian which is used to quantitatively explain the temperature dependence of K_1. One of the problems arising from the application of the spin Hamiltonian to ferrimagnetic anisotropy is the sign of the cubic crystalline field splitting parameters (a). In magnesium ferrite[6,7] the sign of a is observed to be positive for octahedrally situated ferric ions, while the sign is found to be negative for tetrahedrally situated ferric ions. However, results of a calculation by Watanabe[8] indicate that the a is always positive. Also, Geschwind[9] has obtained positive values of a for tetrahedrally and octahedrally situated ferric ions from paramagnetic resonance measurements in garnet materials.

Measurements of the temperature dependence of K_1, utilizing the torque method, are reported for various states of cation "order" in spherical x-ray oriented lithium ferrite monocrystals. Saturation magnetization (M_s) measurements were made with a torsion magnetometer method which consists of measuring the force exerted on a crystal by a constant gradient magnetic field. In the M_s measurements, the crystals were oriented with their easy directions along the applied magnetic field. The long range "order" parameter (S) was determined by x-ray diffraction analysis of powdered lithium ferrite subjected to the same thermal treatments as the monocrystals used in the K_1 and M_s measurements. The monocrystals used in all the measurements were grown in a PbO flux, and chemical analysis showed that the PbO content was less than 0.2 weight percent. Also, chemical analysis for cations in the monocrystals yielded the formula $Li_{0.55}Fe_{2.45}O_4$.

The results of the anisotropy measurements are shown in Fig. 1. The open circles correspond to K_1 measurements on a completely "ordered" ($S=1$) monocyrstal, and the closed circles correspond to measurements of K_1 on an almost completely disordered monocrystal ($S\approx0.1$). Anisotropy measurements on a sample in an intermediate state of long range "order" yielded values of K_1, which at a given temperature are between those shown in Fig. 1, indicating that the change in K_1 associated with the "order-disorder" transition is a gradual process. The state ($S=1$) was produced by slow-cooling the sample from 700°C to 300°C. The state ($S\approx0.1$) was obtained as a result of quenching the sample in H_2O from 950°C.[1] After the completion of one of the lithium ferrite single crystal runs, the crucible was removed from the furnace at 875°C and subsequently cooled in air. This latter heat treatment resulted in the intermediate state of long range order. Figure 1 also shows that the degree of cation "order" in the octahedral sites strongly influences K_1 and that the "disordered" state possesses the higher absolute magnitude of K_1 in the temperature range between 77° to 300°K.

[1] P. B. Braun, Nature **170**, 1123 (1952).
[2] G. T. Rado, V. J. Folen, and W. H. Emerson, Proc. Inst. Elec. Engrs. (London) **104B**, Suppl. No. 5, 198 (1957).
[3] G. T. Rado and V. J. Folen, Bull. Am. Phys. Soc. **1**, 132 (1956).
[4] K. Yosida and M. Tachiki, Progr. Theoret. Phys. (Kyoto) **17**, 331 (1957).
[5] W. P. Wolf, Phys. Rev. **108**, 1152 (1957).
[6] V. J. Folen and G. T. Rado, J. Appl. Phys. **29**, 438 (1958).
[7] H. S. Belson and C. J. Kriessman, J. Appl. Phys. **30**, 170S (1959).
[8] H. Watanabe, Progr. Theoret. Phys. (Kyoto) **18**, 405 (1957).
[9] S. Geschwind, Phys. Rev. Letters **3**, 207 (1959).

The temperature dependence of K_1 was interpreted on the basis of the ferric ion spin Hamiltonian,[4,5]

$$H=g\beta\mathbf{H}\cdot\mathbf{S}+(a/6)[S_x^4+S_y^4+S_z^4] +D'S_\zeta^2+(35/180)FS_\zeta^4, \quad (1)$$

where a is the coefficient of the cubic term and D' and F are the coefficients of the quadratic and quartic axial terms, respectively. Wolf[5] showed that in addition to the cubic term, the quadratic and quartic terms can contribute to cubic anisotropy. The temperature dependence of K_1 for the cubic term in the spin Hamiltonian is given by the relation[4]

$$K_1=-(5/48)N[\mu a_B W(v)+\lambda a_A W(u)], \quad (2)$$

where the subscripts A and B refer to tetrahedral and octahedral sites, respectively, N is the number of molecules/cm^3, λ and μ are the number of ferric ions per molecule on A and B sites, respectively, and W is a function[4] of u or v, the arguments of the Brillouin functions which give the sublattice magnetizations in the Néel theory.[10] We find that K_1 for the quartic axial term is given by

$$K_1=[35N/(24)^2][\mu(\gamma F)_B W(v)+\lambda(\gamma F)_A W(u)], \quad (3)$$

where W is the same function as in Eq. (2) and γ is the coefficient of the direction cosine term $(\alpha_1^2\alpha_2^2+\alpha_1^2\alpha_3^2+\alpha_2^2\alpha_3^2)$, obtained as a result of averaging $\cos^4\theta$ over a particular set of distortion axes in the unit cell. Here, θ is the angle between the magnetization and a distortion axis, and α_1, α_2, α_3 are the direction cosines of the magnetization referred to the cubic axes. The coeff. γ is $-2/3$, $4/9$ and $1/6$ for the distortion axis along the [100], [111], and [110] directions, respectively. When more than one set of distortion axes occurs on each of the sublattices, the right hand side of Eq. (3) should be summed over all these sets. If the cubic term and the quartic axial terms contribute to the cubic anisotropy simultaneously, then we can replace a by a' in Eq. (2), where we have $a_A'=a_A-(7/12)(\gamma F)_A$ and $a_B'=a_B-(7/12)(\gamma F)_B$. Values for a_A' and a_B' were deduced from our measurements of $K_1(T)$ and $M_s(T)$ with the aid of Eq. (2). For the purpose of calculating the sublattice magnetization from the M_s measurements, use was made of an analytical method[11] for the determination of the molecular field coefficients. The crystalline field parameters in "disordered" lithium ferrite are, respectively, $a_B'=+0.0242$ cm^{-1} and $a_A'=-0.0118$ cm^{-1}, in excellent agreement with the corresponding parameters determined previously in magnesium ferrite,[6] which is also a "disordered" ferrite. For "ordered" lithium ferrite, we find that $a_B'=+0.0104$ cm^{-1} and $a_A'=+0.0034$ cm^{-1}. It should be noted that in the "ordered" state a_B' is considerably smaller that that obtained for the "disordered" state, and the a_A' is opposite in sign to the a_A' obtained for the "disordered" state. As shown in Fig. 1, the experimental temperature dependence of K_1 in both the "ordered" and "disordered" states are in good agreement with that obtained from Eq. (2). Since the temperature dependence arising from the D' term[5] is different from that arising from the a' term, this agreement between the experimental and theoretical temperature dependences indicates that the contribution of the D' term to K_1 is negligible compared to the a' terms.

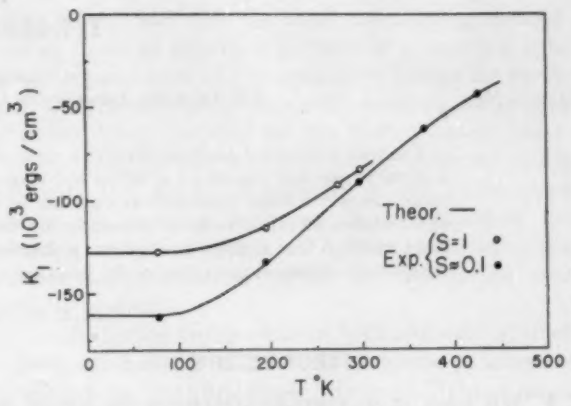

FIG. 1. Temperature dependence of K_1 in $Li_{0.55}Fe_{2.45}O_4$ in "ordered" ($S=1$) and "disordered" ($S\approx0.1$) states. The theoretical curves are calculated from the Yosida-Tachiki theory.

In principle, one can attribute the order-induced changes in the magnitudes and signs of the experimentally determined a'-values to alterations in the crystalline fields. As indicated by the observed crystal structures for the "ordered" and "disordered" states, the changes in the cubic crystalline fields due to the nearest neighbor oxygen ions seem to be insufficient to account for the changes in the a' values, particularly the change in the sign of a_A'. However, the axial distortions are altered as a result of the "order-disorder" transition, and therefore the F term might account for the observed changes in the signs and magnitudes of the a' values. On this basis, one would deduce values for the F parameter comparable in magnitude to the a parameter.

A more detailed account of this work is in preparation.

[10] L. Néel, Ann. phys. **3**, 137 (1948).
[11] G. T. Rado and V. J. Folen, J. Appl. Phys. **31**, 62 (1960).

Tetrahedral Junction

JERALD A. WEISS
Bell Telephone Laboratories, Incorporated, Murray Hill, New Jersey

The term *tetrahedral junction* refers to a class of waveguide junctions having the symmetry properties of a tetrahedron, and loaded by a ferrite rod magnetized axially. The structure possesses a combination of properties which make it suitable as a gyrator or switch and, with appropriate modifications, as an isolator or circulator. It exhibits characteristically low dissipative loss, high mechanical symmetry, and moderate band width. A first attempt to construct a simple theoretical model has yielded a correlation with the most conspicuous observed properties of the junction.

INTRODUCTION

THE class of waveguide structures for which the term *tetrahedral junction*[1] is proposed is a ferrite-loaded transition connecting two transmission lines, such as rectangular waveguide, whose principle axes are mutually crossed, and having the symmetry properties of a tetrahedron. The simplest example is a butt joint of the two guides. A somewhat more elaborate one is a taper composed of planes joining the corresponding edges of the two guides, as shown in Fig. 1(a). Coupling from one guide to the other is produced by a ferrite element, such as a rod, mounted on the common axis of the two and magnetized longitudinally.

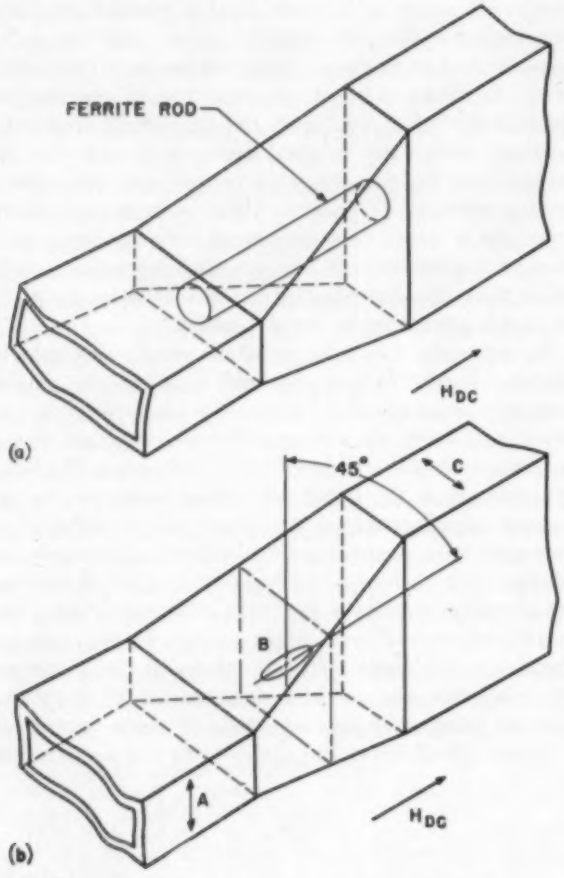

FIG. 1. Basic structure and polarization characteristics of the tetrahedral junction.

OBSERVATIONS

By experimenting with the ferrite and taper geometry and the magnetizing field in the structure of Fig. 1, it is possible to produce transmission with exceptionally low insertion loss: less than 0.1 db over a considerable band (at least 5%). On the other hand, the taper lends itself to precise machining and by its propagation characteristics permits the connecting guides to be accurately decoupled from one another. Thus, extremely high insertion loss values, as high as 60 db, are observed when the ferrite is demagnetized. This combination of high and low transmission loss is useful in difficult switching applications, such as in the protection of masers, where the low loss of the device in the transmitting state leads to only a small thermal noise contribution, and its high loss in the nontransmitting (reflecting) state protects the active maser material (e.g., ruby) from saturation effects. This switching mechanism has the additional advantage of requiring relatively small magnetizing fields applied over a small volume, which, together with the longitudinal orientation of the field, suggests the possibility of switching at high speeds with relatively little energy.

A further characteristic of the junction in its transmitting state is that the polarization of the wave at the center plane is in general elliptical with major axes oriented at 45° with respect to the symmetry planes of the structure [Fig. 1(b)]; under certain conditions the ellipse is observed to degenerate into linear polarization. This state of polarization persists over a wide range of magnetizing fields. From the symmetry of the junction and the gyromagnetic property of the ferrite, it is apparent that the device is a gyrator, and that whether the wave is polarized at plus or minus 45° depends on the direction of propagation, or alternatively, on the direction of the magnetizing field. This additional property of the junction suggests a variety of applications to nonreciprocal devices such as switchable isolators and circulators. For example, a film of dissipative material placed in the vicinity of the center plane and oriented

[1] J. A. Weiss, "The Tetrahedral Junction as a Waveguide Switch," to be published in IRE Trans. PGMTT 8 (January, 1960).

at 45° makes the device into an isolator which, in principle at least, ought to combine the desirable properties of low forward loss, high reverse loss, insensitivity to variations in applied field, and, perhaps, bandwidth of the same order as that of the switch. Some caution is called for here because exhaustive studies of the rather complicated effects of the taper and ferrite on scattering and polarization have not yet been carried out. A still more difficult design problem, namely the addition of a third, and perhaps a fourth, port at the center plane, offers the possibility of yielding a compact circulator possessing values of isolation, "forward" loss, and bandwidth similar to those quoted above for the switch. The following additional observations on the experimental device are significant: (i) its transmission characteristics (i.e., transmission as a function of frequency and magnetizing field) are quite insensitive to the position and length of the ferrite rod, indicating that the coupling between the two guides takes place almost entirely at the center plane; (ii) the transmission is not dependent in any essential way on the length of the taper, but presents the same basic appearance over the range from zero to several wavelengths; (iii) the useful range of ferrite rod diameters extends below the minimum amount of loading required to permit Faraday rotation to occur in rectangular guide.

ANALYSIS

A simple scattering problem which represents schematically the situation at the tetrahedral junction can be set up on the basis of the resemblance between the ferrite-waveguide configuration in this structure and that of the Reggia-Spencer phase shifter.[2,3] As discussed in reference 3, a longitudinally magnetized ferrite rod on the axis of rectangular guide supports a single, elliptically polarized mode which is experimentally observed to be readily matched to the dominant mode in empty rectangular guide. There exists a second mode, also in general elliptically polarized, which is, however, in cutoff under the operating conditions of the phase shifter, and makes no significant contribution to its observed properties. In the present structure, on the other hand, this nonpropagating mode is strongly excited at the discontinuity between the two coupled guides. The model uses the same simplifying assumptions as those of reference 3, namely to make a conceptual replacement of the composite ferrite-air-waveguide structure by a homogeneous medium possessing the permeability specified by the Polder tensor, and a phenomenological anisotropic dielectric constant which represents the elliptic symmetry of the guide cross section. The problem is then that of computing the scattering coefficients for plane waves at the interface between two such media having their anisotropy axes mutually crossed.

The calculation yields some rather involved formulas for the coefficients in terms of the magnetic parameters of the medium, the anisotropic "dielectric" parameters, and the propagation constants for the two types of modes. They contain, among other things, two special cases in which the junction transmits with no reflection. Of these, one is that of circular symmetry with Faraday rotation, in the usual sense, through 90°. The other case occurs under conditions quite different from those ordinarily associated with the Faraday effect: the symmetry of the guide is far from circular, in the sense discussed in reference 3, and the condition of match requires the presence of the evanescent modes referred to above. This latter case seems to correspond to the observation mentioned earlier that the scattering occurs in a small region close to the center plane. A further result of the model in this case is that the state of polarization at the center plane is, as observed, elliptically polarized at 45°, and under special assumptions, linear.

REMARKS

The correspondence between the device and the theory is not complete. Particularly in the case of the tapered junction, the observed properties have features (e.g., inteference effects[4]) which might be described as intermediate between the extremes of scattering at a single plane, on the one hand, and Faraday rotation on the other. The theory contains some doubtful features, particularly relating to the states of polarization of the modes, which may stem from the schematic character of the model. The principle is altogether a complicated one, and yet, in view of its unusual and useful properties, worthy of considerable further investigation.

[2] F. Reggia and E. G. Spencer, Proc. Inst. Radio Engrs. **45**, 1510–1517 (1957).

[3] J. A. Weiss, Proc. Inst. Radio Engrs. **47**, 1130–1137 (1959).

[4] J. A. Weiss, "An interference effect associated with Faraday rotation···" *Proceedings of the Conference on Magnetism and Magnetic Materials, Boston, 1956* (American Institute of Electrical Engineers, New York, 1957), AIEE Spec. Publ. T-91, pp. 580–585.

High-Speed Ferrite Rotating Half-Wave Plate*

FRANKLIN S. COALE
Melabs, Palo Alto, California

A novel approach for constructing a ferrite rotating half-wave plate for use as a frequency translator or an amplitude modulated single sideband modulator is presented. This is accomplished through the use of a four-wire balanced transmission line for generating both the rotating microwave fields and the rotating low frequency magnetizing fields. The principles of operation of this type modulator should allow modulation frequencies in excess of 10 Mc/sec.

Eddy current losses, which usually limit the high frequency modulation of ferrite single sideband modulators are minimized by passing high currents down the wires of the four-wire transmission line to generate the magnetizing field at the modulation frequency. The magnetic fields which are developed are sufficient to cause 180° relative phase shift between the orthogonal microwave components. The magnetizing fields are phased in quadrature so that a rotating magnetic field is developed whose speed of rotation is determined by the frequency of the magnetizing field. The resultant microwave frequency shift is twice the frequency of the magnetizing field due to the inherent action of the half-wave plate.

If the amplitude of the magnetizing field is varied, then the relative phase shift produced by magnetic birefringence is no longer 180° but may be some value between 0° and 180°. This in effect produces a frequency translated signal whose amplitude varies with the magnitude of the magnetizing field.

1. INTRODUCTION

THERE are several methods for linearly increasing the phase of a microwave signal.[1-3] The most common method is probably that of a rotating half-wave plate. By mechanically rotating a half-wave plate, the input frequency is translated by twice the rotational frequency. For most applications, frequencies of mechanical rotation are considerably below the frequencies required for communication. Therefore, it is evident that some electrical scheme must be employed to rotate a half-wave plate.

A half-wave plate will cause one linear component to be delayed by 180° compared to the orthogonal component. Thus, it may be used to convert right circular polarization to left circular polarization. Weiss and Fox[4] have shown that a ferrite magnetized transverse to the direction of microwave propagation exhibits different permeabilities for microwave polarizations normal to and parallel to the magnetizing field, i.e., the ferrite is birefringent since the propagation constant is proportional to the square root of the permeability. Thus, for a sufficient length of this ferrite a phase difference of 180° can be obtained between two orthogonal polarizations. If the magnetic field causing birefringence is rotated about an axis in the direction of propagation the ferrite half-wave plate will rotate. A right circularly polarized wave will undergo a phase shift as a function of time when transformed from the laboratory reference frame to the rotating half-wave plate frame. As the signal emerges at the other end of the half-wave plate, it will be left circularly polarized and the transformation to the laboratory reference frame will add another phase shift as a function of time. These two phase shifts cause a frequency translation of twice the rotational frequency of the half-wave plate, i.e., the input frequency has been shifted to a new frequency, $f_0 \pm 2f_m$, where f_m is the frequency of rotation of the constant amplitude applied magnetic field.

In a manner similar to the mechanically rotating half-wave plate used as a phase shifter, a ferrite half-wave plate may be placed in a circular waveguide which is excited by a circularly polarized TE_{11} mode. In obtaining large f_m values, eddy current losses in the circular waveguide walls become a problem. Various means of reducing such losses have been suggested in articles on high speed microwave switching in ferrites. For low microwave frequencies, the size of the circular waveguide becomes large and the difficulty of obtaining large frequencies f_m of the magnetic field increases.

There are other means of exciting circular polarization in the plane perpendicular to the direction of propagation. Circular polarization may be excited in the center of a three-wire or four-wire balanced TEM line—if the phases of the signal on each line differ by 120° or 90°, respectively. Also, the magnetic field of frequency f_m may be produced by passing currents down the transmission lines in such a phase as to produce a rotating magnetic field of constant amplitude. The transverse dimensions are not frequency dependent. The maximum frequency, $f_{m(max)}$ is only dependent upon the driving source since the only eddy currents set up are in the ferrite itself which is a good insulator.

The ferrite geometry is an important factor in determining the amplitude of the bias currents. Initially, a ferrite rod was employed which was tapered at both ends for matching purposes. The demagnetizing factors were large for this configuration making it difficult to achieve an internal field of the required value. The geometry of the four-wire line allows a ferrite with a cross-shaped cross section to be placed in between the wires. The ferrite cruciform and the four-wire line may be enclosed in a soft magnetic material which completes the magnetic circuit. By this means, the demagnetizing factors are reduced to a minimum.

* This work was supported by the U. S. Army Signal Corps.

[1] A. G. Fox, Proc. Inst. Radio Engrs. **35**, 1489–1498 (1947).
[2] J. C. Cacheris, Proc. Inst. Radio Engrs. **42**, 1242–1247 (1954).
[3] H. I. Glass, Inst. Radio. Engrs. Trans. **MTT-7**, 295 (1959).
[4] M. T. Weiss, A. G. Fox, Phys. Rev. **88**, 146–147 (1952).

An excitation system for the four-wire line may be constructed from stripline components. The input signal may be passed through a balun which is connected to a balanced transmission line 3-db directional coupler producing a total of four balanced transmission lines in phase quadrature. The principles of operation of this type of modulator should allow modulation frequencies in excess of 10 Mc/sec.

2. ANALYSIS OF OUTPUT SPECTRUM

It is well known that various forms of modulation of a sinusoidal signal generate sidebands around the carrier frequency. There is a superficial resemblance between the spectrum of a single-sideband-modulated signal and the spectrum of a frequency translated signal. In some reports, the two modulation schemes have both been called single sideband modulators. This, however, is not actually the case. Single sideband modulation refers to amplitude modulation, while frequency translation is similar to frequency modulation in that the amplitude is a constant. It is desirable in any application of modulators to ascertain in detail the effect of modulation on the frequency spectrum of the output signal. In the rotating half-wave plate frequency translators, the effect is to add a phase term (which may be a function of time) to the frequency of the input signal.

Let us examine the effect of a plate which has an arbitrary phase difference between orthogonal components rather than 180°. This will convert a right circularly polarized input to a mixture of left and right circular waves. The output circuit may be constructed to accept only left circular waves and absorb right circular waves. By varying the amplitude of the magnetizing field, thus departing from perfect half-wave plate action, an amplitude modulation is obtained. With zero magnetic field or a large field to produce 360° phase difference the output wave amplitude is reduced to zero.

A change in output frequency may be obtained by varying the frequency of the magnetizing field. If the amplitude of the magnetizing field is changed a variation in output level is produced. A combination of these effects is sufficient to create a single sideband modulated signal whose average power is 3 db below the unmodulated carrier. Ordinarily the average power in a sideband of a 100% modulated A-M signal is 6 db below the unmodulated carrier.

The results of an analysis of the device show that when neglecting multiple reflections there are three spectral components produced by this modulating scheme. If the direction of rotation of the magnetizing field is the same as the rotation of the input microwave magnetic field, the desired component will be at f_0+2f_m. On assuming perfect quarter-wave plate action (perfect excitation by the strip-line system), the amplitude of the spectral components at f_0 and f_0-2f_m is zero. The amplitude of the output is proportional to the cosine of one half the angle of departure of the half-wave plate from 180°. For values of magnetic field less than that required for saturation, one may assume that the magnetization is a function of H_0. If one assumes hysteresis is small then the functional dependence will be just that of the magnetization curve of the ferrite. Rather than operate between 0° and 180°, it might be advantageous insofar as low field losses are concerned to operate between 180° and 360°. This requires a change of orientation of one of the quarter-wave plates so that maximum output occurs at 360° rather than 180°. The only difficulty with such a scheme is that larger bias fields will be necessary.

3. APPLICATIONS

This type of device may find application in microwave frequency translators, Doppler simulators, single sideband modulators, FM modulators, and phase shifters. For use as a phase shifter this device is insensitive to nonlinearities found in conventional phase shifters; the phase being determined only by direction of the magnetizing field. An analysis of temperature dependence shows that the resultant phase shift is not dependent on temperature. However, a small insertion loss will exist due to imperfect operation of the half-wave plate.

ACKNOWLEDGMENT

The author wishes to express his appreciation to Dr. W. P. Ayres and Dr. P. H. Vartanian for their helpful discussions during the course of this work.

Double Pump Degenerate Ferrite Amplifier

PETER GOTTLIEB
Microwave Laboratory, Hughes Aircraft Company, Culver City, California

A theoretical discussion of the possibilities for the design of a parametric amplifier using a pump frequency lower than the signal frequency (but higher than one half the signal frequency) is given. In particular, a detailed mechanism for the operation of a ferrite amplifier with such properties is described. The amplifier operation is similar to that used by Bloom and Chang for a diode amplifier with cubic nonlinearity. Hogan, Jepsen, and Vartanian have proposed a ferrite device to serve the same purpose as the present amplifier; however, their scheme is quite different, and a detailed comparison is given in this paper.

The main feature of the present amplifier is a doubling of the pump frequency to obtain an effective pump frequency which is larger than the signal frequency. The whole amplifier requires four resonances: the pump frequency, twice the pump frequency, the signal frequency, and twice pump minus signal (idle). The most efficient assignment of the modes uses cavity resonances for the signal and pump, and then uses either cavity or ferrite resonances for the other frequencies.

Since the pump doubling is a result of nonlinear mixing, the efficiency of doubling will be greater for larger pump fields. This is limited in practice by the onset of saturation in the ferrite. For pump fields close to saturation the required pump field is calculated to be five to ten times larger than that required to produce the same gain in an ordinary three resonance amplifier.

INTRODUCTION

THEORETICAL proposals for a parametric amplifier with a pump frequency lower than the signal frequency have been made by several writers. Bloom and Chang[1] have discussed an amplifier using a cubic (rather than the usual quadratic) nonlinear element. The cubic element mixes three frequencies at a time, so that two pump frequencies mixed with a signal or an idle will have the same effect as a pump with its frequency equal to the sum of the two pump frequencies mixed with signal or idle in an ordinary quadratically nonlinear parametric amplifier. If the two pump frequencies are made equal, this device requires only three resonances, and cubic nonlinearity is necessary to make an amplifier with pump frequency lower than signal frequency, when only three resonances are used.

If a quadratic nonlinear element (such as a ferrite) is used, it is necessary to have four resonant frequencies. In a scheme of this type suggested by Hogan, Jepsen, and Vartanian,[2] the signal and the pump fields are mixed to produce a new signal with frequency lower than the pump frequency. (The pump frequency must, of course, be greater than half the original signal frequency.) This scheme, as originally proposed, used three ferrites in separate cavities (one ordinary amplifier and two frequency mixers). The efficiency would be increased if all the operations were performed in one piece of ferrite in one cavity. The difficulty is that three of the resonant circuits (the pump, the signal, and the difference frequency) will form an ordinary converter circuit with pump frequency lower than signal frequency, and will consequently attenuate the signal. Thus, there will be competition between a three-frequency attenuator and a four-frequency amplifier, and the filling factors must be adjusted so that the latter is dominant.

The present paper also proposes a four-frequency ferrite amplifier, but no three of the four frequencies can form a three-frequency amplifier which can attenuate the signal.

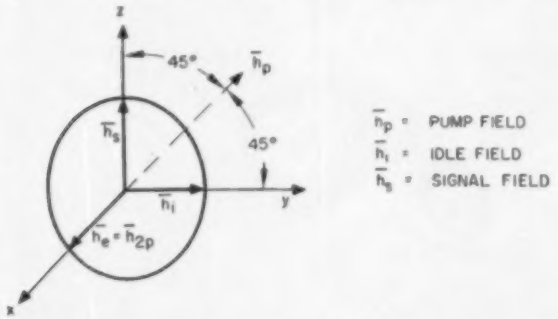

FIG. 1. Field orientations at a ferrite sample symmetric about the z axis. The angle between $\mathbf{h}_e$ and the z axis has been set at 45° only so that $h_{pz}=h_{ps}$ in a spherical sample.

DISCUSSION OF METHOD

The essence of the present method is to combine a frequency doubler with an ordinary ferrite amplifier in one piece of ferrite placed in one cavity. The amplification process is straightforward. The fields involved are illustrated in Fig. 1. The incident pump field $\mathbf{h}_p$ can be resolved into components degenerate in frequency along the y and z axis. These components interact with each other to give a doubled frequency component in the x direction. (This is not a frequency doubler of the conventional type, for it requires that the frequency to be doubled be resolved into the two indicated components, and it is therefore a mixer. This type of doubler has been discussed by Jepsen.[3]) This doubled frequency component now acts as the pump field for an ordinary ferrite amplifier. This requires four resonances which are at pump frequency ω_p, twice pump frequency $2\omega_p=\omega_e$, signal frequency ω_s, and idle frequency $\omega_i=\omega_e-\omega_s$. (A

[1] S. Bloom and K. K. N. Chang, J. Appl. Phys. **29**, 594 (1958).
[2] C. L. Hogan, R. L. Jepsen, and P. H. Vartanian, J. Appl. Phys. **29**, 422 (1958).
[3] R. L. Jepsen, AFCRC-TN-58-150 (1958).

TABLE I.[a]

Case	1	2	3	4
Pump	TE_{011} TM_{110}	TM_{010}	TM_{110}	TM_{012}
Signal	TM_{120}	TM_{120}	TM_{120}	TM_{120}
Double pump	Ferrite resonance	Ferrite resonance	TE_{012}	TE_{012}
Idle	Ferrite resonance	TE_{011}	Ferrite resonance	TM_{110}
A	$(\omega_M^2/\lambda^3\omega^3)$	$(\omega_M{}^b/\lambda\omega^2)^2Q_iF_i$	$(\omega_M{}^3/\lambda\omega^6)(Q_eF_e)^2$	$(\omega_M{}^4/\omega^8)(Q_eF_e)^2Q_iF_i$

[a] The mode configurations are only approximate since the cavity must be distorted to tune to more than two frequencies. For Cases 1 and 2 the ferrite is placed in the center of the cavity, while for Cases 3 and 4 it is on the axis but at $\frac{1}{4}$ the distance between top and bottom.
[b] $\omega_M=\gamma M_s$, and for simplicity we have set $\omega_s=\omega_i=\omega_p=\omega_e=\omega$.

similar analysis can also be made for the nondegenerate case where the frequencies of h_{py} and h_{pz} are unequal.) This is all done in one piece of ferrite and the efficiency achieved with all four components resonant makes operation feasible.

If the amplifier of Hogan et al. is made in one cavity, it will differ from the present amplifier by having the fourth resonant frequency $\omega_s-\omega_p$ instead of $2\omega_p$ as in the present case. In the Hogan amplifier, this extra frequency forms an attenuating three-frequency converter with ω_p and ω_s. In the present case, no such combination of frequencies can be formed.

There are many possible cavity and ferrite resonances, which can be combined to satisfy the frequency conditions required for the present amplifier. The most convenient methods use cavity resonances for the pump and signal since these fields must be coupled into the cavity from the waveguide. We can summarize the analysis for each particular case in terms of the extrinsic imaginary susceptibility, χ'', (in place of the usual negative resistance) of the signal field.[4] We are interested in the part of the signal magnetization m_s which is 90° out of phase with the driving field h_s and is given by $\chi''h_s$. For the main ferrite resonance at ω_e, and a cavity resonance at ω_i, the susceptibility can be written in the simple form,

$$\chi''=-\frac{\pi\gamma^6M_s^2Q_iF_i}{2\lambda^2\omega_s^2\omega_e^2}h_0^4, \tag{1}$$

where F_i is the combination form and filling factor $F_i=vg_i/V$, v=ferrite volume, V=cavity volume, $g_i=\langle h_i^2\rangle_{\text{ferrite}}/\langle h_i^2\rangle_{\text{cavity}}$; γ is the usual gyromagnetic ratio; M_s is the dc magnetization; $\lambda=\gamma\Delta H$ is the damping constant with ΔH the line width; and $h_0=h_{py}=h_p$, in this spherical, degenerate example. If we define Q_s to be the loaded Q of the cavity at the signal frequency, taking into account the wall and dielectric losses and the loading of input and output ports, then in analogy with the analysis in reference 4, we can write the condition for spontaneous oscillation as

$$(1/Q_s)+4\pi F_s\chi''=0. \tag{2}$$

[4] A. D. Berk, L. Kleinman, and C. E. Nelson, Wescon Convention Record (1958).

The exact values of χ'' have been calculated for various types of resonances in addition to those used for Eq. (1), but they are much more complicated than Eq. (1). These values of susceptibility can be simplified if all four frequencies are set equal to ω in the solution for χ'' and the numerical factor of order 1 is neglected. This assumes that all resonance frequencies are the same order of magnitude, and the approximation will merely indicate the dependence of χ'' on operating frequency. It is then convenient to write the approximation,

$$\chi''\approx -A(\gamma h_0)^4. \tag{3}$$

Approximate values for the factor A for the various cases are given in Table I. (The particular example used for Eq. (1) corresponds to Case 2 in Table I.)

To get an approximate idea of the pump field needed for oscillation in Case 2 (Table I), we can take all the Q's equal to 4000, $M_s=2000$ gauss, $\Delta H=10$ oe, $V/v=250$, $g=10$, $\omega_s=2\pi\times10^{10}$, $\omega_e=3\pi\times10^{10}$. With these parameters, the threshold field is found [by substitution of Eq. (1) in Eq. (2)] to be $h_0=23$ oe. For these parameters, the other cases of Table I require a threshold field of the same order of magnitude.

Care must be taken to assure that operation of this device does not require magnetic fields which are beyond the saturation of the ferrite sample.[5] In the example above, $h_0=23$ oe is permissible in itself since the pump is not at the ferrite resonance frequency. However, when calculating this example in detail we find $m_e=15$ oe, which is much too large since ω_e is the ferrite resonance. A glance at Eq. (1) shows that we would have to use lower frequencies to achieve oscillation in this case. For the cases which do not have a ferrite resonance at ω_e, this problem does not arise, and oscillation should be possible at high frequencies.

ACKNOWLEDGMENTS

The author wishes to thank Dr. A. D. Berk for suggesting this amplifier scheme, and for many helpful discussions concerning the development. He also wishes to thank Dr. M. T. Weiss for his comments and suggestions.

[5] H. Suhl, Proc. Inst. Radio Engrs. 44, 1270–1284 (1956).

Broadband Reciprocal Ferrite Phase Shifters*

T. D. Geiszler and R. A. Henschke
Melabs, Palo Alto, California

Broadband ferrite phase shifters were constructed in X band waveguide by locating wide ferrite slabs along the center line of the broad waveguide wall and applying a longitudinal magnetic field. The bandwidth of these phase shifters was optimized through proper selection of ferrite dimensions and the amount of dielectric loading or by an appropriate choice of guiding structure. The relative phase shift obtained from broadband configurations was found to vary in an almost linear fashion with the applied field when the ferrite was magnetically saturated.

PUBLISHED information on the broadbanding of ferrite phase shifters is unknown to the authors. The present paper describes a study of ferrite phase shifters in X band waveguide structures for the frequency range from 8.2–12.4 kmc. The development of broadband devices was considered to be of particular importance.

Investigations were carried out at X band for various ferrite geometries, using transverse and longitudinal fields. The reciprocal characteristics of transverse field devices have been discussed briefly by Rowen[1] and by Fox, Miller, and Weiss,[2] however bandwidth information was not given. Measurements of transverse field configurations indicated that the phase shift was quite frequency dependent. Longitudinal field devices of the Reggia-Spencer[3] type were also found to be frequency sensitive, although they provided large phase shifts for a small applied field. Longitudinally magnetized ferrite slabs of rectangular cross section, centrally mounted on the broad wall of the waveguide, were found to have a smaller frequency dependence. The phase shift, θ, for these configurations was found to increase with frequency. With the ferrite saturated, the change in phase shift with field, $d\theta/dH$, was relatively independent of both field and frequency.

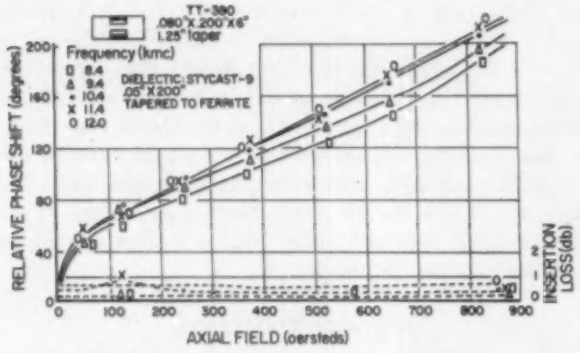

FIG. 1. Relative phase shift and insertion loss as a function of longitudinal field for broadband rectangular guide phase shifter.

Measurements were made to determine the effect of ferrite slab dimensions on the bandwidth and magnitude of phase shift. Trans-Tech. TT-390 ferrite material was used with longitudinal fields varying from 0 to 900 oe. Data were obtained for slabs having a height of 0.060 in., but variable width. It was found that narrow slabs provided better bandwidth, but wider slabs gave greater phase shift for a given applied field. Widths of 0.200 to 0.300 in. appeared to provide a reasonable compromise between bandwidth and magnitude of phase shift. Data obtained for slabs having a constant width of 0.200 in., but variable height indicated that a reasonable compromise between phase shift and bandwidth could be obtained if slab heights between 0.060 and 0.080 in. were used. Further increase in the height resulted in a large increase in phase shift but a decrease in bandwidth. The increase in phase shift was apparently caused by energy concentration in the slab when a critical height was reached at a given frequency. It was found, empirically, that the critical height is directly proportional to wavelength.

A study was also made of configurations constructed from a pair of ferrite slabs mounted on opposite broad walls of the waveguide. The slab heights could be chosen such that the bandwidth and phase shift obtained from a slab pair were considerably better than those obtained from only one of the slabs. The insertion loss increased by less than a factor of two.

Most slab configurations yield constant frequency curves of relative phase shift as a function of applied field, which resemble curves computed from Polder's[4] expression for the scalar propagation constant of a positive circularly polarized wave in an infinite medium. The resemblance, of course, holds only in the saturated region. In this region, the propagation constant of the negative polarized wave does not change appreciably with the applied field. The frequency dependence of the relative phase shift at a given field, calculated from Polder's expression, is opposite to that measured for waveguide devices. The discrepancy may be explained if it is recalled that the effects of waveguide dispersion and of microwave energy concentration in the ferrite slabs cause the phase shift to increase with frequency. The latter effects mask the frequency dependence of the ferrite phase constant. Waveguide dispersion and energy

* This work was supported by the U. S. Army Signal Corps under contract.

[1] J. H. Rowen, Bell System Tech. J. **32**, No. 6, 1333 (November, 1953).

[2] A. G. Fox, S. E. Miller, and M. T. Weiss, Bell System Tech. J. **34**, No. 1, 5 (1955).

[3] F. Reggia and E. G. Spencer, Proc. Inst. Radio Engrs. **45**, 11, 1510, (November, 1957).

[4] D. Polder, Phil. Mag. **40**, 99 (1949).

concentration effects can be reduced by loading the waveguide with material of high dielectric constant in the vicinity of the ferrite. A degree of broadbanding can be achieved by adjusting the loading until the waveguide dispersion counter-balances the opposite frequency dependence of the ferrite phase constant. Characteristics of a phase shifter constructed in this fashion are shown in Fig. 1.

Ferrite slabs were also mounted in singly ridged guide which exhibited small dispersion in the frequency range of interest. Through proper choice of ridged guide and ferrite dimensions, it was possible to construct a phase shifter having characteristics similar to those obtained for the rectangular guide configuration of Fig. 1. The ridged guide structure gave equivalent phase shifts but slightly higher insertion losses for shorter lengths of ferrite and the same range of applied field. When the space between the ridge and the broad wall of the waveguide was filled with ferrite, providing an additional reduction of the waveguide dispersion because of dielectric loading by the ferrite, a frequency dependence similar to that predicted by Polder's expression was noted. Measured and computed curves for this case are shown in Fig. 2.

Temperature measurements, made at 10.4 kMc on a phase shifter constructed in rectangular guide, showed a phase variation of roughly 20% at 500 oe for temperatures ranging from 22° to 80°C. The variation in phase shift was somewhat larger at 8.4 kMc for the same field setting. The reduction in temperature sensitivity with increasing frequency may be predicted in a qualitative way from Polder's expression. It was noted that at the higher frequency the slope, $d\theta/dH$, was insensitive to temperature changes when the ferrite was magnetically saturated. Similar results were obtained with a ridged guide phase shifter.

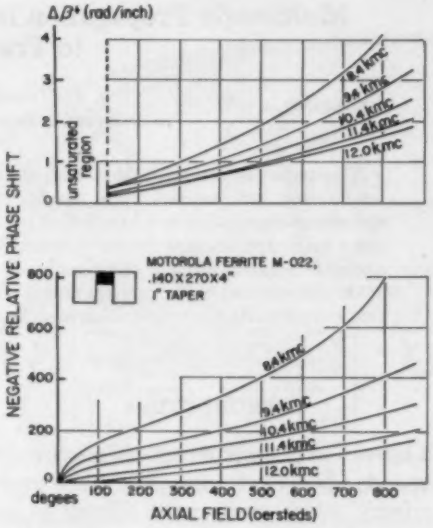

FIG. 2. Upper set of curves are phase shifts as calculated from Polder's infinite medium expression. Lower set of curves are measured phase shifts for the geometry indicated.

ACKNOWLEDGMENT

The authors wish to express their thanks to Dr. W. P. Ayres for his many valuable contributions during the course of this work.

Multimode Propagation in Gyromagnetic Rods and Its Application to Traveling-Wave Devices

J. E. Tompkins, F. Reggia, and L. Joseph
The Diamond Ordnance Fuze Laboratories, Washington 25, D. C.

This paper summarizes the results of exact calculations of the propagation constants in longitudinally-magnetized gyromagnetic rods. Specifically described are: (a) the mode behavior for a lossless rod in cylindrical waveguide as a function of rod diameter in the low-field region, (b) a comparison of the calculations with experimental results obtained with a magnetized ferrite rod in rectangular waveguide showing probable negative circular polarization of the field when concentrated within the rod, (c) a brief summary of the calculations of the propagation in rods at high dc fields, and (d) a new broadband microwave absorption switch having constant electrical characteristics over a bandwidth of 3000 Mc at *X* band.

INTRODUCTION

THE operation of a gyromagnetic microwave device depends upon electromagnetic wave propagation characteristics, which are usually difficult to analyze if the gyromagnetic element has dimensions large compared with the wavelength in the material. Since the initial investigation of microwave ferrites, much attention has been given to this problem.[1] Exact numerical solutions to the problem of a lossless longitudinally-magnetized rod were obtained from an electronic digital computer at these laboratories.[2] These solutions yield quantitative data on the behavior of the fundamental and higher-order modes.

In cylindrical coordinates (r,θ,z) the propagation in the rod is assumed to be $\exp[j(\omega t+n\theta)+\Gamma z]$. We consider the case $n=+1$ and $n=-1$, representing respectively normal rotating modes in the antiLarmor and Larmor sense. Solution of the boundary value problem gives a characteristic equation,[1,2] which contains complicated functions of the geometry, frequency-dielectric constant and tensor permeability of the rod material.

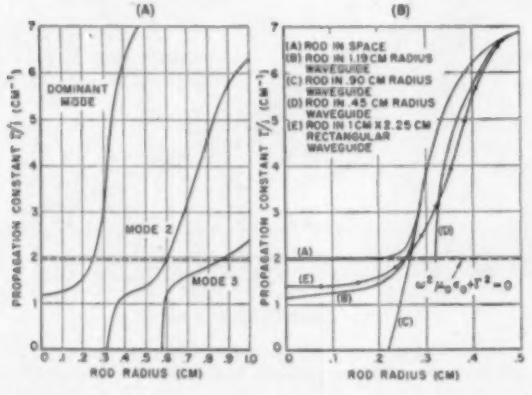

FIG. 1. Propagation constant at $f=9375$ Mc and dc field of 35 oe.

LOW-FIELD BEHAVIOR: NEW-TYPE FERRITE SWITCH

Figure 1a shows the calculated propagation characteristics in an infinite-length MgMn ferrite rod in cylindrical waveguide for the antiLarmor sense excitation. Experimental values of the tensor components used for the calculations were obtained at these laboratories and correspond to a dc field of 35 oe.[3] A more complete treatment of this and Larmor sense excitation under these conditions is given in reference (2). Dr. P. J. B. Clarricoats has obtained similar solutions using perturbation techniques.[4]

The dotted line shown in Fig. 1 represents the value of Γ/j above which the microwaves are primarily guided by the rod itself, and the microwave energy is increasingly concentrated in the rod, i.e., the metal guide wall has decreasing effect upon propagation characteristics. In Fig. 1b, computed data for the dominant antiLarmor mode are shown for several cases along with experimental data (curve *E*) for the rectangular waveguide reciprocal phase shifter.[5,6] The similarity of the propagation constant curves for large Γ/j indicates the possibility that the internal fields along the axis of the rod in the phase shifter may be circularly polarized in the antiLarmor sense.[2,7]

Experimental results shown in Fig. 2 indicate this conclusion is probably correct. Here, an indirect method is used for sampling the rf electric field inside the rod as a function of the applied magnetic field. A very thin resistive film is placed between the two sections of a split ferrite rod which is rotated about its axis. When the ferrite rod is magnetically saturated, the insertion loss of the system is seen to be the same for all orientations of the resistive film, thus indicating a rotating wave inside the magnetized rod.

The data of Fig. 2 also reveal characteristics desirable in a microwave switch. By improving the technique

[1] M. L. Kales, J. Appl. Phys. **24**, 604 (1953); also A. A. Th.M. van Trier, Appl. Sci. Research, **3B**, 305 (1953).
[2] J. E. Tompkins, Brussels Conference on Solid State Physics in Electronics and Telecommunications, June, 1958 (to be published).
[3] R. C. LeCraw and E. G. Spencer, Inst. Radio Engrs. Convention Record, Pt. **5**, 66 (1956).
[4] P. J. B. Clarricoats, Proc. Inst. Elec. Engrs. **106**, 335 (1959).
[5] F. Reggia and E. G. Spencer, Proc. Inst. Radio Engrs. **45**, 1510 (1957).
[6] J. Weiss, J. Appl. Phys. **30**, 153S (1959).
[7] P. A. Rizzi and B. Gatlin, Proc. Inst. Radio Engrs. **47**, 446 (1959).

used to obtain the resistive film and by adjusting the geometry of the ferrite rod, we have developed a very broadband electrically controlled ferrite switch with high isolation in the OFF state and low insertion loss in the ON state. This switch has the following electrical characteristics which are nearly constant over a 3000-Mc frequency range at X-band: a zero-field insertion loss of approximately 0.5 db, an isolation of greater than 40 db in the OFF state which is nearly independent of the magnetic control field, an input VSWR of less than 1.20 for all values of the applied magnetic field, and capability of switching several watts of microwave power in a time of less than 1 μsec.

RESONANCE BEHAVIOR

Propagation in extended bodies at fields near ferrimagnetic resonance is generally quite complicated. It is difficult to describe resonance when numerous propagation modes may exist. Such multiple modes are important in the study of traveling-wave parametric devices. We have calculated the propagation characteristics for Larmor and antiLarmor sense excitation with large applied magnetic fields, obtaining solutions of the characteristic equation for rods of a gyromagnetic material assumed to be lossless. Briefly, it is found that a multimode condition of propagation exists just above the value of magnetic field for which $\mu=0$ in the lossless microwave permeability tensor

$$\begin{pmatrix} \mu & jk \\ -jk & \mu \end{pmatrix},$$

where μ and k are real quantities. This multimode condition continues for values of magnetic field up to several hundred oersteds above this value, depending upon rod diameter. The number of modes, however, increases rapidly in the vicinity of $\mu=0$ as one approaches

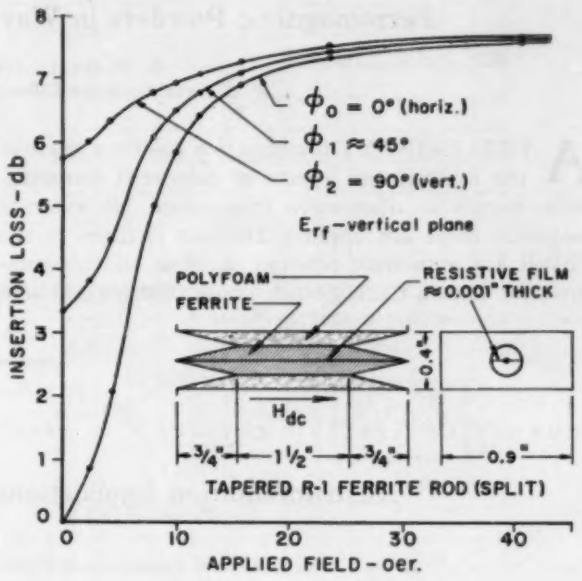

FIG. 2. Technique for sampling internal rf field.

from the high-field side. Such behavior is not particularly surprising, for the point $\mu=0$ is a singularity of the wave equations for the gyromagnetic medium.[1,2] On the low-field side of $\mu=0$, the propagation characteristics are much simpler. At $\mu+k=-1$, rods of a very small diameter exhibit propagation behavior interpreted as the Kittel resonance, which undergoes a slight shift to higher values of the dc field as the rod radius increases. However, the multimode condition near $\mu=0$, not predicted by perturbation theory, also begins to appear in calculations for very small diameters. Calculations made for the antiLarmor excitation reveal a similar multimode condition just above $\mu=0$. The above results and the details of the ferrite switch will be described more fully at a later date.

Ferromagnetic Powders in Waveguides at Elevated Temperatures

A. D. KRALL AND E. T. HOOPER, JR.
U. S. Naval Ordnance Laboratory, Silver Spring, Maryland

A PRELIMINARY investigation has been made of the temperature effects of powdered ferromagnetic metals at microwave frequencies. No external magnetic fields are applied. Distinct changes in the VSWR and minimum position occur at the temperatures for known Curie points, phase changes and zero anisotropy. Powder metallurgy changes such as sintering and outgassing have been observed.

The simplicity of equipment necessary to reach extremely high temperatures should provide a valuable tool in studying and understanding changes occurring in high temperature alloy systems.

Instrumentation Applications of Inverse-Wiedemann Effect

J. A. GRANATH
Armour Research Foundation of Illinois Institute of Technology, Chicago, Illinois

The principle of the magnetostrictive rod and coil assembly which provides an ac voltage output at fundamental excitation frequency, with amplitude proportional to applied torque and phase-reversible with torque direction is reviewed.

The literature on applications of torsional magnetostriction and inverse-Weidemann effect is limited and widely scattered. A brief summary of some of the literature on instrumentation applications for measurement of torque, force, and other physical quantities is presented. Examples include measurement of torque in rotating shafts, dynamometers, accelerometers, flowmeters, and force balance sensors.

For use as a guide in transducer design, a simplified mathematical representation of the torque-signal relationship for one mode of operation is developed from the equations of mechanical strain and applied magnetic field energy. Shape of the torque-signal curve is linear in the vicinity of zero torque, curving off to asymptotes at the extremes. Means for extending the results of tests on standard samples to design guides on rod diameter, coil turns, and excitation frequency are suggested.

INTRODUCTION

THE inverse-Wiedemann effect in a ferromagnetic rod or tube is the shift in direction of induced magnetization with respect to applied magnetic field that occurs when torque is applied. While the phenomenon has been known for many years,[1] there recently has been renewed interest. Among the recent applications are use of the device in computer memory application,[2,3] and electromechanical filters.[4,5] Another area of application is force or torque measurement for instrumentation purposes.

A simple configuration is to pass alternating current along a ferromagnetic rod to establish a circumferential field. Application of torque to the magnetostrictive rod produces a shift in the direction of the flux to a helical path. A solenoid coil over the rod will have induced in it a voltage, due to the axial component of the skewed flux, which is at the fundamental excitation current frequency, is proportional in amplitude to applied torque over a useful range, and which is phase-reversible with the direction of the torque.

Among the alternate modes of operation are use of the solenoid coil for excitation, taking the signal from the ends of the rod; use of a ferromagnetic tube with multiple turns wound normal to the direction of winding of the solenoid coil; use of an external magnetic structure containing an airgap for the magnetic source, for the magnetic sensor, or both, with the rod in proximity to the gaps to control flux direction.[6-8] If a dc current or permanent magnet field excitation is used, the output of the device will be proportional to rate of change of torque.

APPLICATIONS

One of the earliest applications found in the literature is due to Kobayosi[9] who, in 1929, used the inverse-Wiedemann effect for measurement of instantaneous torque in the crankshaft of an internal combustion engine. A magnetostrictive rod was inserted as a shaft coupling, excitation current was supplied to the rotating

[1] G. Wiedemann, Electrizitat **3**, 519 (1881).
[2] A. H. Bobeck, Bell System Tech. J. **36**, 6, 1319 (1957).
[3] A. H. Bobeck and R. F. Fischer, J. Appl. Phys. **30**, 435 (1959).
[4] V. F. Gianola, J. Appl. Phys. **26**, 9, 1152 (1955).
[5] A. P. Thiele, Electronics **32**, 25, 72–74 (1959).
[6] R. A. Beth and W. W. Meeks, Rev. Sci. Instru. **25**, 6, 603 (1954).
[7] C. M. Rifenbergh, D. S. Schover, and E. H. Schulz, Proc. Natl. Electronics Conf. **3**, (1947).
[8] O. Dahle, Proc. Instrument Society of America 14th Annual Conference, Paper No. 74–59 (1959).
[9] T. Kobayosi, Repts. of the Aeronautical Institute of Tokyo University **52**, (1929).

rod by brushes, and a fixed solenoid coil was used as the sensing element. Many of the developments found in the more recent literature are also for measurement of torque in a rotating shaft.[10,11]

For more general instrumentation use, the applications shown by Roters[12] are of interest. Among these are dynamometer applications in which cradle reaction torque is measured, a force-balance pressure measuring system, an accelerometer consisting of a seismic mass attached to a torque sensor, and gyro torque pick-off mechanisms without bearings. Uses of the sensor in loudspeaker, microphone, and phonograph pickup are also shown.

Another instrumentation application is use of the torque sensor for measurement of dynamic friction in ball and roller bearings. The inner race of a ball bearing is restrained by means of the magnetostriction torsion spring while the outer race is rotated. The average level of friction torque and variations in instantaneous torque can be recorded and interpreted in terms of bearing quality.[13]

The technique can be used in a variety of torque or force ranges and in various device sizes. The mechanism used by Dahle for measurement of torque in rotating shafts is most suitable for shaft diameters of four inches and up, and has been used on fourteen-inch shafts in steel mill rolls. J. N. Van Scoyoc at Armour Research Foundation constructed an air flow (drag) sensor using 0.014 in. diam iron alloy wire as the torsional magnetostriction element and a vane of 0.002 in. brass shim stock $\frac{3}{16}$ by $\frac{3}{8}$ in. in area. Among the advantages of the magnetostriction torque sensor is the ability to obtain useful signal levels with very small displacements or deflections (of the order of seconds of a degree of arc). Repeatability and linearity of 0.1% of full scale have been obtained with some designs tested at ARF.

DESIGN GUIDE ANALYSIS

The mechanism of operation can be considered in terms of the orientation of domains due to applied mechanical stress and orientation due to an applied magnetic field. Bozorth[14] gives energy equations that provide such a description for the general case. These are

$$E=\tfrac{3}{2}\lambda_s\sigma\sin^2\theta, \tag{1}$$

and

$$E_H=-HI_s\cos\alpha=-HI_s\cos(\theta_0-\theta), \tag{2}$$

since $\alpha=\theta_0-\theta$ and where E_σ = magnetic strain energy; λ_s = the magnetostriction expansion occurring between the demagnetized state and saturation (increase in length per unit length); σ = the tensile stress; θ = the angle between the directions of σ and H; E_H = energy due to an applied magnetic field; H = the magnetic field strength; I_s = saturation intensity of magnetization; and α = the angle between the directions of H and I.

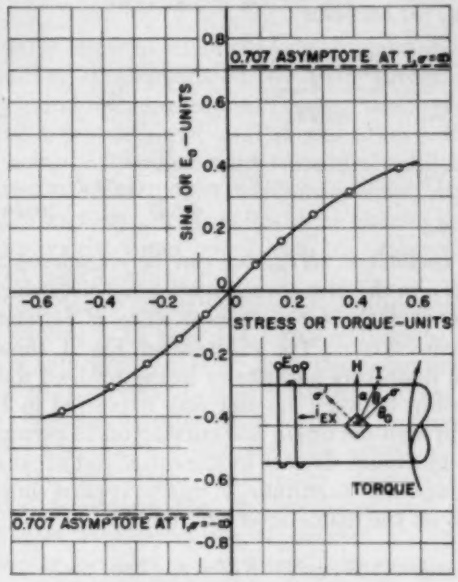

FIG. 1. Calculated transfer characteristic for torqued rod with axial current.

From Eqs. (1) and (2), expressions may be developed for the special case of a ferromagnetic rod in torsion with applied circumferential field. The analysis given is not rigorous, but may be useful as a guide for predicting the effects of changing parameters. To simplify the analysis the assumptions will be made that the material is isotropic, that the magnetization and magnetostriction curves are ideal, linear, and single valued. In practice, an anisotropic material will show a hysteresis in the torque-signal characteristic; nonlinearity in the magnetic material characteristics appears as waveform distortion in the output voltage. Also λ_m and I_m, maximum values for given operating conditions, will be used in place of λ_s and I_s.

By using the hypothesis that the total energy in the rod will be a minimum[15] when magnetomechanical and electromagnetic transients have decayed to negligible values, a relationship between θ and σ is obtained. At minimum energy:

$$(dE_\sigma/d\theta)+(dE_H/d\theta)=0,$$

$$\sigma=(-2HI_m/3\lambda_m)(\sin(\theta_0-\theta)/\sin2\theta). \tag{3}$$

For the case of a torqued rod, the direction of σ, the applied stress, is at an angle of 45 deg with respect to the axis of the shaft and with respect to a circumferential field. Thus, the angle θ_0 for this special case is 45 deg

[10] See references 6, 8.

[11] M. J. O'Neill, "A dynamic torquemeter utilizing the reciprocal Wiedemann effects in torque measurement," Thesis for Master of Science Degree, Massachusetts Institute of Technology (1956).

[12] H. C. Roters, U. S. Pat. 2,511,178 (1950).

[13] S. Sajiki and S. Aoki, J. Mechanical Laboratories **5**, 8, 353–356, December (1951) (in Japanese, English abstract).

[14] R. M. Bozorth, "Ferromagnetism" (D. Van Nostrand Company, Inc., Princeton, New Jersey, 1951), p. 482.

[15] L. F. Bates, *Modern Magnetism* (Cambridge University Press, Cambridge, England, 1951), third edition, p. 408.

and Eq. (3) becomes

$$\sigma_{45}=\frac{-2HI_m}{3\lambda_m}\frac{\sin(\pi/4-\theta)}{\sin 2\theta}$$

$$=K_1\frac{\sin(\pi/4-\theta)}{\sin 2\theta}=K_1\frac{\sin\alpha}{\cos 2\alpha}. \quad (4)$$

The coefficient $2HI_m/3\lambda_m$ can be considered a constant, K_1, in the first approximation for given operating conditions of the torque sensor since H is related to excitation current. The diagram of Fig. 1 shows the directed quantities and angles in the torqued rod. The relationship between σ_{45} and $\sin\alpha$ is plotted in Fig. 1, linear through the origin and curving off to asymptotes.

The maximum stresses in a torqued rod occur at the surface and the magnitude, σ, due to applied torque, T, depends on the diameter of the rod.

$$\sigma_{45}=(16T/\pi d^3)=K_2T=K_1(\sin\alpha/\cos 2\alpha), \quad (5)$$

or

$$T=(K_1/K_2)(\sin\alpha/\cos 2\alpha), \quad (6)$$

and the constant K_2 becomes another linear scale factor applied to the abscissa of Fig. 1 to obtain a relationship between applied torque and magnetization angle.

The voltage induced in the coil, using the elementary transformer equation for sinusoidal operation and the fact that the component of I that links the turns of the coil is $I_{mL}=I_m\sin\alpha$, is

$$E_0=K_3\sin\alpha, \quad (7)$$

where $K_3=4.44fNI_mA$ and f=frequency of excitation, N=number of turns on solenoid coil, A=cross sectional area of solid rod. K_3 becomes a linear scale factor applied to the ordinate of Fig. 1 to obtain the torque-voltage characteristic.

Simple tests may be made in a standard manner on rod samples of various materials to obtain the coefficients K_1, K_2, and K_3. Rod diameter, excitation frequency, or coil turns may then be adjusted, using knowledge of the factors included in the coefficients, to obtain an open-circuit torque-to-signal relationship with the scale desired for a given application.

ACKNOWLEDGMENT

Acknowledgment is made to J. N. Van Scoyoc, Engineering Advisor, for his guidance and suggestions.

JOURNAL OF APPLIED PHYSICS — SUPPLEMENT TO VOL. 31, NO. 5 — MAY, 1960

Practical Hysteresigraph

R. R. Bockemuehl and W. E. Sargeant
General Motors Research Laboratories, Warren, Michigan

A relatively low-cost hysteresigraph has been developed which is suitable for both laboratory and industrial application. The instrument utilizes standard component parts and employs mutual inductance feedback to perform the necessary integrating operation. The instrument is reasonably insensitive to environment and permits direct recordings of hysteresis loops and magnetization curves to be made in less than one minute. Both theoretical and practical considerations of the instrument are presented.

INTRODUCTION

ONE of the more important problems involved in the study of magnetic materials is the determination of the B-H characteristics. One method of doing this is to slowly increase the H field, and to sense changes in the B field by noting the voltage induced in a pickup coil. Integration of the induced signal is necessary to produce a signal which is analogous to the flux in the sample. We have developed a hysteresigraph which does this reliably and accurately and which possesses the ruggedness, portability, low cost, and ease of operation required in a practical, general purpose instrument.

Point by point determination of flux with ballistic galvanometers has been used for this purpose for many years. However the delicate equipment and long measurement time inherent in this method essentially limited its use to laboratory applications. Continuous integrators[1,2] have been used successfully for several years by some laboratories. Although the continuous method reduces measuring time to a practical value, previously reported designs were unsatisfactory for industrial use because of sensitivity to environment, critical adjustments and high costs. The continuous integrating technique which is used is basically the same as those described by Edgar[1] and Cioffi.[2] However, further development, stressing simple design and the use of commercially available components and subassemblies, has yielded a more practical instrument for less cost with little, if any, sacrifice in accuracy.

[1] R. F. Edgar, Trans. Am. Inst. Elec. Engrs. **56**, 805–809 (1937).
[2] P. P. Cioffi, Rev. Sci. Instr. **21**, 624 (1950).

INTEGRATING PRINCIPLE

The voltage induced in a coil of (N) turns wound on a sample in which the flux (ϕ) is changing is equal to $Nd\phi/dt\times10^{-8}$ volt. This voltage is applied to the input terminals of a circuit which consists of an amplifier with a mutual transconductance (G_m) and a feedback loop with a mutual inductance (M). The feedback voltage is equal to $-MdI/dt$ where (I) is the amplifier output current. The amplifier output current is equal to the mutual transconductance times the sum of the coil voltage plus the feedback voltage. This relationship can be arranged in the following form:

$$M(dI/dt)=N(d\phi/dt)\times10^{-8}-I/G_m.$$

As G_m approaches infinity, $MdI/dt=Nd\phi/dt\times10^{-8}$ and the total change in output current during any time interval is directly proportional to the total change of flux during that time interval. The effect of a finite G_m is to introduce an integrating time constant $T=MG_m$. Thus the amplifier gain has negligible influence on output current if the period of the measurement is considerably less than T.

SYSTEM REQUIREMENTS

The finite integrating time constant imposes a compromise between recording time and accuracy. The time required to record a complete hysteresis loop is typically 10 seconds and seldom, if ever, exceeds 1 minute. A 10^4 second time constant introduces an error of less than 0.01% of the maximum measured flux for every second of the recording interval. This time constant is adequate for all industrial applications and for almost all research investigations.

Low rates of flux change can produce sensing coil voltages much less than one microvolt. Therefore the amplifier must have very low equivalent input noise. The magnitude of the recorded noise determines the minimum sample cross section and number of turns in the sensing coil required to produce a good signal to noise ratio. A recorded noise level equivalent to 2.5 maxwell-turns permits a practical number of turns on most samples to yield signal to noise ratios greater than 40 db.

Thermal potentials in the input circuit are integrated and produce a drift in the output current. These potentials must be kept constant during a measurement so that their effect can be effectively canceled.

In addition, the practical objectives of the development required that the number of components be minimized and that these components be commercially available "stock" items. Furthermore, any costly refinement which reduces the error due to one particular effect by an order of magnitude below the total error is unjustified and may even increase effective error by reducing reliability.

PRACTICAL SOLUTION

The large required value of G_m is obtained through a combination of amplification by both galvanometer-photocell and vacuum tube methods. Consideration of the relative proportion of total amplification performed by each method is important from the standpoint of noise. Mutual transconductance is more simply achieved with vacuum tube amplifiers but these circuits generate more equivalent input noise than do galvanometer-photocell amplifiers.

The function of the galvanometer-photocell amplifier in this system is to raise the signal voltage to a level which is sufficiently greater than the noise and drift levels of the first vacuum tube amplifier. Increasing the gain by adding vacuum tube stages is relatively inexpensive and does not increase noise appreciably over that of the first stage. This design philosophy automatically minimizes the galvanometer and optical system gain requirements and permits an optimum compromise between integrating time constant, recorded noise level and cost.

The design illustrated in Fig. 1 is based on the previously discussed considerations. The 50 mh mutual inductance combined with the mutual transconductance of 2×10^5 mhos yields an integrating time constant of 10^4 seconds. The gain obtained with a triode voltage amplifier (6C4) neon coupled to a current amplifier (6BL7) and with gas phototubes (921) in the photocell bridge permits use of a relatively low sensitivity (180 mm/μa) but rugged galvanometer. Additional gain could be realized through use of positive feedback. However, this imposes a constant open loop gain requirement on the amplifier which is difficult to meet with simple circuitry in an industrial environment.

Noise generated in a galvanometer-photocell amplifier results primarily from vibration of the galvanometer. The galvanometer is an internally oil damped unit which is mounted with its associated optical system on a heavy iron block. The block is supported by four damped-spring shock mounts at the bottom of a four foot high instrument cabinet which houses the entire integrator assembly. The resulting noise level in a moderate vibration environment is equivalent to a flux linkage change of 2.5 maxwell turns and is even less in an ideal laboratory environment.

Thermal voltages are bucked out by an adjustable voltage in the galvanometer circuit. All connections in the low-level circuit are made on large mica-insulated copper blocks which have a long thermal time constant so that thermal junction temperatures cannot change appreciably during a curve determination.

There are several important design details in the vacuum tube amplifier. The neon coupling network simplifies the power supply requirements so that a commercial regulated power supply can be used. A simple series potentiometer-capacitor network permits optimum adjustment of high-frequency attenuation for

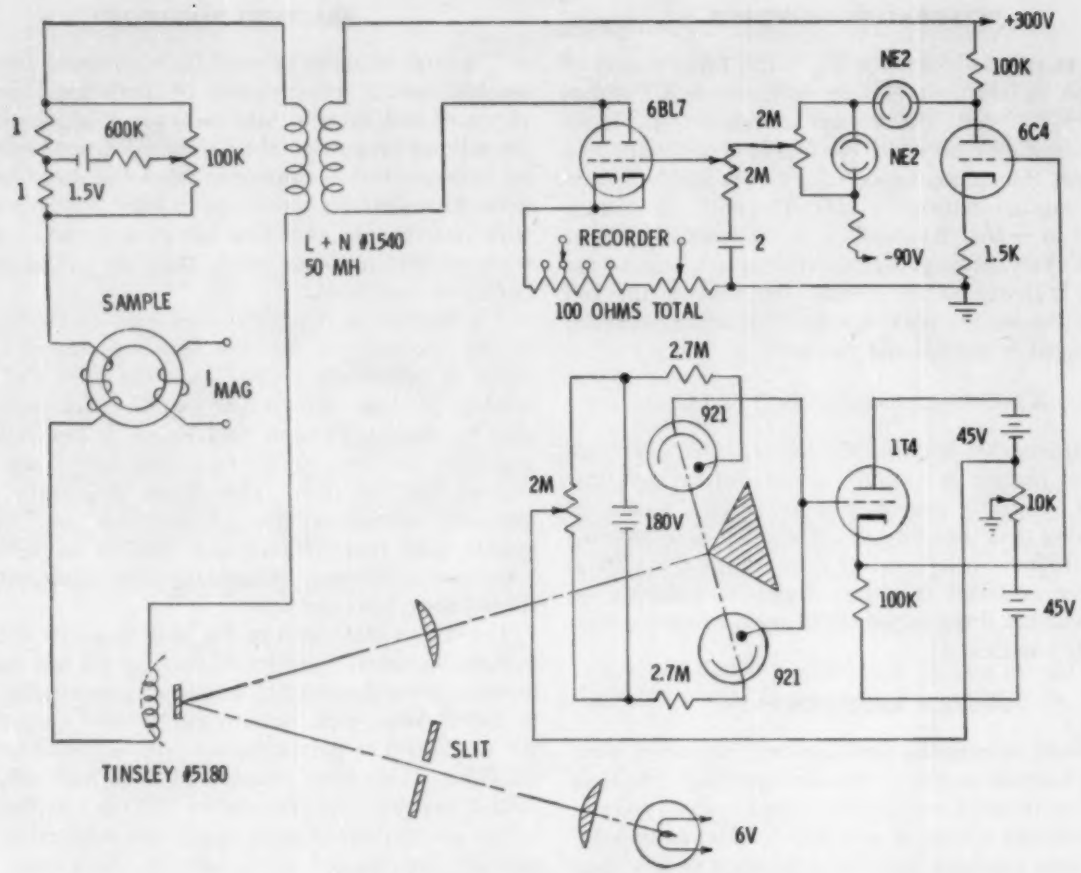

FIG. 1. Schematic diagram of the hysteresigraph.

system stability. The current amplifier is a cathode follower in which the plate circuit is effectively a constant current source for the mutual inductance primary. A decade resistance and helical potentiometer comprise the cathode resistance and permit accurate calibration of recorded voltage in terms of flux density after consideration of sample dimensions.

Reproducibility of design has been proven by construction of three units with identical characteristics without custom tailoring of components.

APPLICATION

Major and minor hysteresis loops and magnetization curves of ring samples can be plotted directly by recording the integrator output versus magnetization current on a commercial X-Y recorder. Records of these curves for a bar sample can be obtained with two integrators. The integrator also serves as a direct reading fluxmeter when a milliammeter measures the output current.

This type of integrator requires that a smoothly variable magnetization current source be used. Simple current controllers[3] employing power transistors are ideal for this application.

This hysteresigraph has proved to be satisfactory for accurate laboratory measurements and its reliability, simplicity and low cost make it suitable for plant applications.

[3] R. R. Bockemuehl, Electronics **32**, 25, 76 (1959).

Rictometer System for Calibrating Transmitters of Remote Indicating Compasses

L. I. MENDELSOHN
Instrument Department, General Electric Company, West Lynn, Massachusetts

Calibration of the sensor (transmitter), of a remote indicating compass system, must be carried out in a magnetic field whose magnitude and direction simulate closely those of the earth at a specified point. Major disturbances of the earth's magnetic field by electrical equipment occur in most laboratories. Where conventional Helmholtz calibrating schemes are used, accuracy can be achieved only by lengthy averaging of repeated measurements and exercising extreme care. This paper describes a measurement system called a rictometer, which permits precise transmitter calibration with much greater ease than previously.

The rictometer consists of a system of shields which reduces the earth's horizontal field component from 200 milligauss to about $\frac{1}{4}$ of a milligauss. Two pairs of Helmholtz coils within the shielding system restore the horizontal component of the earth's field. By proper selection of currents in each of these pairs of coils, this horizontal component can be rotated in discrete steps through 360° for calibration purposes. The rictometer allows the experimenter to calibrate a compass transmitter readily with a precision of plus or minus 0.1 deg in normal laboratory fields. Deliberate immersion of the rictometer in a 50 gauss field causes a maximum transmitter calibration change of plus or minus 0.15°. Thus, the system should prove valuable for reliable sensor calibration under most adverse field conditions.

INTRODUCTION

In most aircraft, the direction sensor for the magnetic compass system is located in the wing tip, or tail structure, away from the disturbing influences of the electrical equipment and of the engines. Remote indication, then, is mandatory since information on heading must be transmitted to the cockpit for visual indication, as well as for automatic control.

One of the problems associated with remote indicating compass systems is the calibration of the transmitter or sensor. One way to calibrate a transmitter would be simply to rotate it through measured angles in the earth's field. Unfortunately, in most laboratories, this field is subject to variations stemming from electrical equipment as well as from the random movement of such large magnetic masses, as elevators and nearby cars. To compensate for these variations, a pair of Helmholtz coils may be mounted so that it can be rotated to restore the horizontal field component. With magnetometers continually monitoring the original field in magnitude and direction, any variation of this horizontal field component is compensated by rotation of the Helmholtz-pair and simultaneous adjustment of the current through it. The earth's vertical component is similarly monitored, and its magnitude is adjusted by a fixed Helmholtz-pair. The compass transmitter can then be calibrated by rotating it through specified angles in this uniform constant reference field.

Under laboratory conditions, calibration errors can be minimized by exercising great care and averaging many readings. The Helmholtz compensating system outlined above is a satisfactory primary reference standard for laboratory-type work. For maintenance or production testing, a measurements system which can perform reliably with a maximum ease of operation under even the most adverse field variations is highly desirable. These requirements demand that the final calibrating equipment be a shielded system.

RICTOMETER DESIGN

The main objectives of the rictometer system were as follows: First, to achieve as good shielding as possible against the horizontal component of the earth's field, $\|H_E$; second, to reproduce this field within the shielded region and by means of a suitable coil system rotate $\|H_E$ through specified angles; third, to make the calibration region as readily accessible as possible.

Figure 1 shows the shields and coil system used to achieve these objectives. The case and cover arrangement provides good accessibility. Two sets of Helmholtz coils fastened vertically to the four faces of a supporting block reproduce $\|H_E$ and allow it to be rotated. The horizontally mounted set of coils provides the vertical component $\perp H_E$. The base and cover each consists of four concentric members. The two shields M of both base and cover are high-permeability material (mu-metal or hymu-80), while the inner and outer members are structural and serve mainly to protect these strain-sensitive shields. The overlapping of the case and cover assemblies in closure provides a low reluctance path for $\|H_E$ and yields good shielding against this horizontal field.

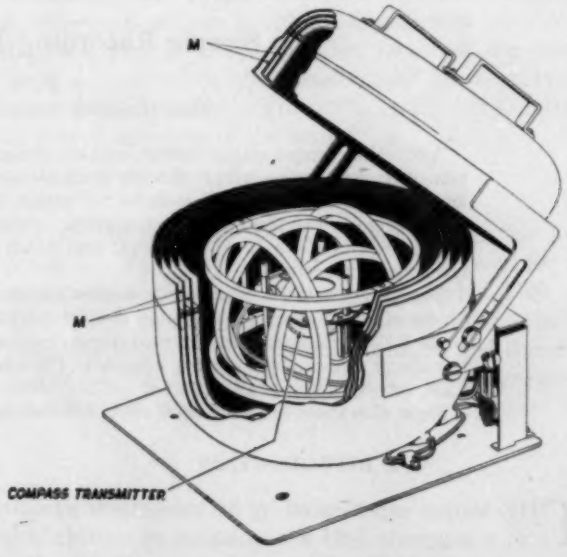

FIG. 1. The rictometer shielding system.

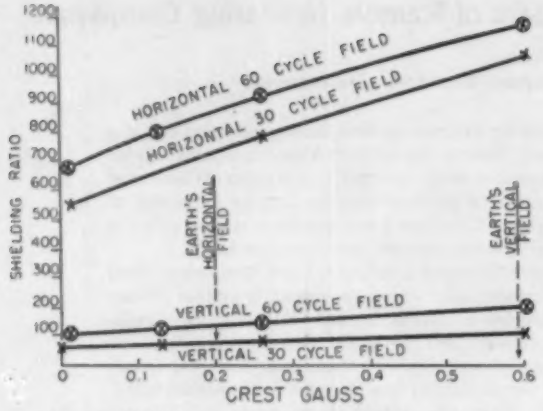

FIG. 2. Shielding ratios of the rictometer system.

SHIELDING RATIO DETERMINATION

A four-foot diam Helmholtz pair produced a uniform field H_0 over the region to be occupied by the rictometer. The latter was then centrally located in the field coils and the field H_i inside the shielding system measured. The ratio H_0/H_i is defined as the shielding ratio. Sixty and thirty cycle field excitation allowed the induced emf in a search coil to serve as a measure of the field. To increase coil sensitivity this 4800-turn coil was wound around twenty 0.020 in.$\times\frac{1}{2}$ in.$\times$7 in. mumetal laminations. Errors caused by wave shape were minimized by taking final readings on a rectifying type voltmeter. Crest flux density of a cyclic wave is proportional to the average value of the voltage wave and is independent of wave shape. A rectifying type voltmeter will read this average value.

The field measurement system was calibrated during the H_0 determination, since absolute values of H_0 could be calculated from the current value and Helmholtz-coil dimensions. The measurement of H_i was made with this same calibrated system; field disturbance caused by the mumetal core was present during both H_0 and H_i measurements. Thus, the ratio H_0/H_i is essentially free of errors caused by field redistribution due to the probe. Shielding ratios for both the horizontal and vertical components were determined and are plotted in Fig. 2.

DISCUSSION AND CONCLUSION

The shielding ratio corresponding to each H_E component can be plotted as a function of frequency and extrapolated to zero. Since the sensor is pendulously mounted, $\perp H_E$ produces a second order effect. For the 200 milligauss horizontal component $\|H_E$, the dc shielding ratio is estimated to be 620. Thus, the field inside the rictometer ($\|H_i$) is 0.32 milligauss. If this field is added vectorially at 90° to $\|H_E$, we can anticipate an error of $\pm 0.086°$ or $\pm 5.2'$. Actual measurement of transmitter calibration shift due to rotation of the rictometer in the earth's field gave a change of ± 0.10 or $\pm 6'$. It must be remembered that at best the repeatability of the transmitter calibration measurement is $\pm 2'$. A 50 gauss dc field impressed on the system caused a maximum transmitter calibration change of $\pm 0.15°$. Thus, we conclude that even under the most adverse field conditions, the rictometer provides a rapid, reliable, and stable means of calibrating remote indicating compass transmitters to a precision of plus or minus 0.1 deg.

ACKNOWLEDGMENTS

The writer wishes to acknowledge the many valuable discussions with H. S. Whitehead and R. A. Pfuntner during the progress of this work.

JOURNAL OF APPLIED PHYSICS SUPPLEMENT TO VOL. 31, NO. 5 MAY, 1960

Simple Recording Torque Magnetometer

P. W. NEURATH
General Electric Company, Pittsfield, Massachusetts

A recording torque magnetometer has been designed and constructed, using commercially available components in conjunction with commonly available laboratory equipment. It appears to be much simpler than any described heretofore and needs no calibration. The sample disk is mounted at the end of a shaft which is supported in two fixed radial nonmagnetic precision ball bearings of low starting torque. The other end of the shaft carries a 10-cm long lever arm which exerts a force on a Statham Instruments, Inc., 0.3 oz transducer (Model G7A).

The relative rotation of sample to magnet is converted to an electrical signal of any convenient magnitude by use of a 360° continuous rotation Helipot potentiometer. Both torque and rotation signals are recorded on an XY-mv recorder. The electrical circuits consist only of batteries and resistors and the factory supplied transducer calibration is entirely adequate. The assembly can be rotated manually. At $\pm 40\times 10^3$ ergs full scale, corresponding to an output of ± 5 mv, errors are about 1%.

Slight alterations in the design to cover full scale ranges from 10×10^3 to 100×10^3 ergs or more are possible.

I. INTRODUCTION

THE torque experienced by an anisotropic sample in a magnetic field is a quantity of considerable interest in magnetics. Often an automatic recording method becomes very desirable and a variety of such instruments have been designed.[1,2]

[1] W. S. Byrnes and R. G. Crawford, J. Appl. Phys. **29**, 493 (1958).

[2] R. F. Penoyer, AIEE Spec. Publ. T-91, p. 365 (February, 1957).

It was found possible to build such a device in a simpler way and at low cost using commercially available parts together with standard laboratory equipment. The resulting instrument, described below, has ample sensitivity and accuracy for anisotropic samples weighing about one gram.

II. DESCRIPTION OF INSTRUMENT

Its essential features shown in Fig. 1 are the following:

1. A holder, *H*, for a disc sample which is easily removed from the instrument to insert the disc.

2. A $\frac{1}{8}$ in. shaft is supported by two simple radial nonmagnetic miniature precision ball bearings. Their nominal starting torque is less than 1500 d-cm. Actual operation, which allows for a slight angular motion reduces the resulting uncertainty to less than 1000 d-cm for all the frictional forces involved in the whole assembly.

3. A Statham G7A Transducer which has a force range of ± 8.4 g for a displacement of ± 0.04 cm, with an output of about 0.35 μv/v per dyne.

4. A lever arm, of 10 cm length, slotted and clamped to the shaft, transmits the force due to the magnetic torque to the transducer. For a 1.5 g sample having a maximum torque of 200 000 ergs per cm^3 the output of the transducer will be about ± 5 mv at a transducer supply voltage of about 3.5 v. These voltages are both convenient; ± 5 mv being a most common laboratory recorder full scale sensitivity and 3.5 v (at about 10 ma) being available from dry cells. The sensitivity can be increased proportionately to the transducer supply voltage, which may be raised up to 9 v.

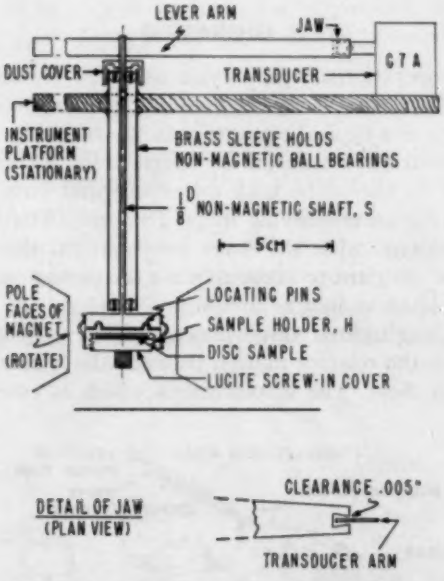

FIG. 1. Schematic view of the torque magnetometer assembly.

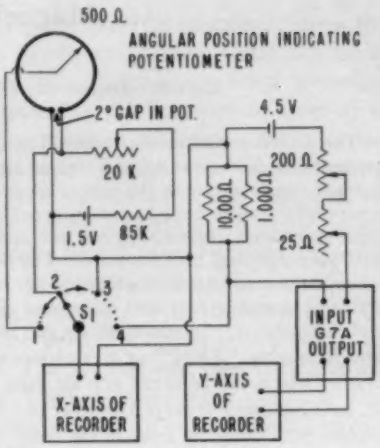

FIG. 2. Circuit diagram of the recording torque magnetometer. Resistance values are adjusted to go with a full scale recorder voltage of 4.545 mv. On switch *S*, the functions of the various positions are as follows: (1) read angle, (2) calibrate angle, (3) set recorder zero, (4) calibrate torque.

5. Finally, the whole assembly is mounted with the disc at the center of the gap of a rotating electromagnet. If only a stationary magnet is available, the platform holding the transducer and ball bearings may be rotated instead of the magnet.

6. The angular position of the magnet (or the transducer assembly) is converted to an electrical signal by the use of a precision 360° continuous rotation Helipot potentiometer. The error in the angular position signal due to the slack in the lever jaw and the deflection of the transducer and the $\frac{1}{8}$ in. shaft is about 1°.

7. The outputs form the Statham transducer and from the angular position indicating potentiometer are fed to the *Y* and *X* axis of any *XY* recorder of suitable sensitivity; then, as the electromagnet is rotated with respect to the sample, the complete torque curve of the sample can be traced by the recorder in about 1 or 2 min.

8. The electrical parameters of the currents can be calibrated with simple resistance networks using the recorder as a voltage standard, as shown in the circuit diagram, Fig. 2. The calibration factor of the transducer as supplied by the manufacturef has been found to be perfectly reliable within the $\pm 1\%$ limit claimed as overall accuracy of the transducer.

III. CONCLUSIONS

A simple recording torque magnetometer has been described. The materials and direct labor costs for the construction of this equipment were under $500, excluding the cost of the magnet and recorder. The instrument is easy to operate and maintain and therefore makes possible the use of such apparatus in a magnetic laboratory of moderate size.

Magnetic Field Measurement Using Ultrasonics

R. J. RADUS
Materials Engineering Departments, Westinghouse Electric Corporation, East Pittsburgh, Pennsylvania

The detection and measurement of magnetic field intensity for purposes of field plotting and uniformity studies is a most important consideration in the field of magnetics. Field plotting and uniformity studies have been conducted on certain sizes of magnetic geometries with rotating coil instruments and Hall generators and quartz crystal magnetometer.[1] The obvious limit of such devices is their minimum resolving power which can be defined in terms of sampling area and mimimum air gap. For the rotating coil instruments, the minimum air gap is $\frac{1}{4}$ in. and the sampling area is roughly 1.2×10^{-2} sq in. Commercially available Hall generators which can be fitted into air gaps of approximately 0.011 in. have sampling areas in the order of 3.2×10^{-3} sq in. Hall generators with sampling areas in the order of 10^{-7} sq in. have been reported in the literature. Minimum thickness[2] of this type device is presumably less than 0.01 in. The more recent work[3] with the vibrating quartz crystal magnetometer has been used to measure flux density normal to the surface of permanent magnets. The sampling area of this type of equipment is 0.56×10^{-6} sq in. The minimum thickness of this equipment has not yet been reported in the literature.

The flux-measuring equipment being described in this paper has a sampling area of approximately 6.25×10^{-6} sq in. and a sensitivity of approximately 0.01×10^{-3} v/gauss. The probe consists of a single turn inductor of length $\frac{1}{16}$ in. which vibrates ±0.00005 in. The inductor is fastened to a probe of 0.01 in. thickness and the 0.0001 in. motion is perpendicular to this 0.01 in. probe thickness. The physical geometry and size of this probe permits measurements in a variety of positions relative to the magnetic circuit. This type of probe is applicable for measuring flux density in air gaps as small as 0.017 in.

The driving device for this equipment is a 60 Kcps magnetostrictive transducer. The complete probe consists of the transducer reactor, a coupling bar of nonmagnetic stainless steel and the thin strip of the nonmagnetic stainless to which the inductor is fastened. The geometry and size of this thin strip can be changed to accommodate variations in both inductor length and displacement.

I. INTRODUCTION

General

A VARIETY of magnetic field measuring equipments have been developed and are being used. For many applications, these equipments are entirely adequate—for others they are inadequate. The prime limitations to the use of these equipments are sensitivity of measurement, size of sampling volume, accuracy, and availability. Sampling volume is defined as that volume within a magnetic field which is used to interrogate the field strength. Of these limitations, the size of the sampling volume is one of the most important. Hence, the practicability of this equipment exists because the sampling volume of this new equipment permits micromeasurement in relatively small air gaps.

Specific

The geometry of commercially available sensing elements determines their resolution of measuring. For the rotating coil equipments, the sampling area is approximately 1.2×10^{-2} sq in. The minimum air gap into which this sensing element can be fitted is approximately $\frac{1}{4}$ in. For the Hall generator, the sampling area is approximately 3.2×10^{-3} sq in. The minimum air gap for these sensing elements can be as small as 0.011 in. The sampling area of the vibrating quartz equipment is 0.56×10^{-6} sq in. The minimum thickness of this equipment has not yet been reported in the literature.

The sampling area of the sensing element of the equipment described in this paper is approximately 6.25×10^{-6} sq in. The minimum air gap into which the probe of this equipment can be fitted is approximately 0.017 in. The probe consists of a single turn inductor with length of approximately $\frac{1}{16}$ in. This single turn is vibrated approximately ±0.00005 in. at a frequency of 56.24 Kcps. Thus the magnetic field which is being analyzed can be resolved in a given direction into increments as small as 0.0001 in. The effective area is 0.0625 in.$\times$0.0001 in. or 6.25×10^{-6} sq in.

II. OPERATION

The operation of the device uses the technique of vibrating a straight wire or inductor in a magnetic field. A sketch of a typical equipment is shown in Fig. 1. The magnetostrictive transducer designed for 60 Kcps, is coupled to the probe with an exponential horn which also acts as an amplifying stage. The probe length must be consistent with the wave propogation, the width must be sufficient to accommodate the pickup turn and the thickness should be minimum.

The longitudinal displacement of the pickup wire produces the relative motion between the wire and the magnetic field. The displacement which is essentially

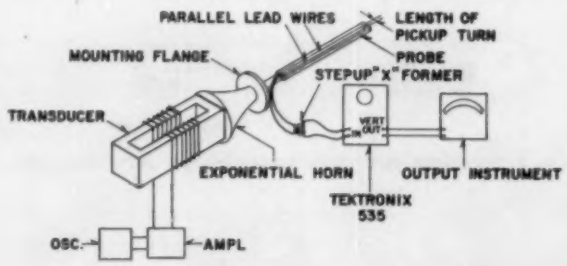

FIG. 1. Sketch of complete equipment.

[1] D. M. Chapin, Rev. Sci. Instr. **20**, 945–946 (1949).
[2] B. Kostyshyn and D. Roshon, Proc. Inst. Radio Engrs. **47**, 451 (1959).
[3] L. I. Mendelsohn, J. Appl. Phys. **29**, 407–408 (1958).

sinusoidal originates in the transducer. The voltage induced into the pickup wire and the leads is essentially sinusoidal since it is directly related to the periodic displacement. The practical use of this induced voltage requires that the net output voltage be only that voltage which is induced into the relatively short length defined as the pickup turn.

The approach to this ideal condition relies exclusively on the complete cancellation of the voltages induced in the parallel lead wires. Ideally, the voltage induced into the pickup turn is not subjected to a canceling voltage because the diametrically opposite side of the pickup turn is effectively out of the field being measured. The cancellation in the lead wires occurs on a point by point basis if the wires are symmetrical about a longitudinal axis and if there is not a field gradient between the wires.

Another condition to the practical use of this equipment is a constancy or stability of both of the frequency and amplitude of the longitudinal displacement of the pickup wire.

III. EXPERIMENTAL PROCEDURE

Equipment

The transducer was assembled from available 60 Kcps laminations. To the combination of transducer and amplifying stage, the probe is fastened. In the laboratory equipment, the probe is $1\frac{7}{8}$ in. long, $\frac{5}{16}$ in. wide and 0.01 in. thick. The single turn pickup, a No. 34 copper wire, with its lead wires is fastened with cement to the $1\frac{7}{8}$ in.$\times\frac{5}{16}$ in. surface. The single turn, approximately $\frac{1}{16}$ in. long, is positioned at the free end of the probe.

Application

As in the application of any basic sensing device, the accuracy is determined by the stability of the equipment and the method with which it is applied. The voltage and frequency of the drive power for this equipment must be constant at the resonant frequency of the transducer. A further condition of stability requires the pickup turn be fastened securely to the probe. This fastening of the wire to the probe is effectively done by reducing the power to the transducer until available cements would maintain a satisfactory bond between the wire and the probe. At this low-power level of 6 watts the total displacement of the wire is in the order of 0.0001 in. The sensitivity with this displacement, based on a 50 mv peak output at a field strength of 5000 gauss, is 0.01 mv/gauss. This ratio can be increased appreciably by making a better bond between the wire and probe to permit the use of higher power level to increase the total displacement. With the sensitivity of 0.01 mv/gauss, a noise level of 0.2 mv, is equivalent to a field of 20 gausses. The accuracy of measurement for these relatively low fields is very poor because the normal variations in noise show up as appreciable variations in the total output.

In a field of 5000 gausses, a signal-to-noise ratio of approximately 250 to 1 contributes 0.4% error. The error which results from calibration would be the accuracy of the reference or standard used in the calibration. This part of the gross error is selected at $\pm 3\%$. If an additional $\pm 1.6\%$ is included to account for variations in supply frequency and voltage then the total error is $\pm 5\%$. This is a somewhat conservative estimate of accuracy offered in lieu of actual accuracies.

A measuring accuracy of $\pm 5\%$ is not particularly attractive for the majority of applications. However, since this equipment can resolve distance in increments of 0.0001 in., it is ideally suited for determining the gradient through extremely small distances. For those applications in which a knowledge of the uniformity is more significant than knowledge of the absolute value, the accuracy can be in the order of $\pm 2\%$ for a full scale value of 5000 gausses. If the drive frequency and voltage can be held constant the accuracy of the probe output can be of the order of $\pm 0.5\%$.

Both the peak value and the rms value of the pickup voltage are linearly related to the magnetic field being measured. Thus, either type of instrument could be calibrated against a reference field. The direct reading fluxmeter thus produced has an accuracy of approximately $\pm 5\%$. The utility of this equipment exists because of the small sampling area, $\frac{1}{16}$ in.$\times$0.0001 in., and the small probe thickness, 0.017 in.

Permanent Magnet Leakage Permeance Evaluation Based on Polar Radiation Analogy

J. E. Foy and R. J. Parker
General Electric Company, Edmore, Michigan

This paper is based on the premise that the permanent magnet can be considered as an equipotential body and hence electrostatic analogies can be used to advantage in evaluating permanent magnet leakage. The spherical pole formula, which is based on the substitution of a sphere having dimensions, which will make it the equivalent of the actual magnet limb in leakage effect, is described and its application to permanent magnet limb geometry is discussed. Evershed used this approach extensively with his work on the early steel permanent magnet. The authors review this work and explore the conditions affecting the use of this technique in modern permanent magnet materials.

Reversible permeability and limb magnet area to cross section area ratios are found to be influential in the location of the center of the effective polar regions. Today's high coercive force permanent magnet with shorter limb lengths is found to be particularly well-suited to this polar radiation analogy, since the departure from the spherical shape is less extreme than was the case with the earliest low coercive steel magnets. Calculation of demagnetization factors for rods, rings, "*U*" and "*C*" shaped magnets are convenient and accurate arrived at by this approach. A geometric criterion is developed which allows magnet configurations to be considered either (a) open circuit (permeance due to limb radiation), or (b) closed circuit magnets where the proximity of the polar regions is such as to increase the free polar radiation. In closed circuit magnet arrangements, the free polar radiation occurs for at least half the magnet limb area so that the spherical pole formula represents a very useful technique in the evaluation of any permanent magnet configuration.

To demonstrate the breadth of usage possible with the spherical pole formula a tubular-shaped magnet used as a magnetron field supply is analyzed to show the utility of this approach in estimating the shape of the axial field characteristic and its relationship to geometry and permanent magnet unit properties.

INTRODUCTION

ACCURATELY estimating magnetic leakage permeance is of great importance in any magnetic circuit problem. This paper describes useful techniques for estimating permeance based on the use of an analogy which treats a magnetic member as an equipotential body and allows rather simple expressions for estimating leakage permeance.

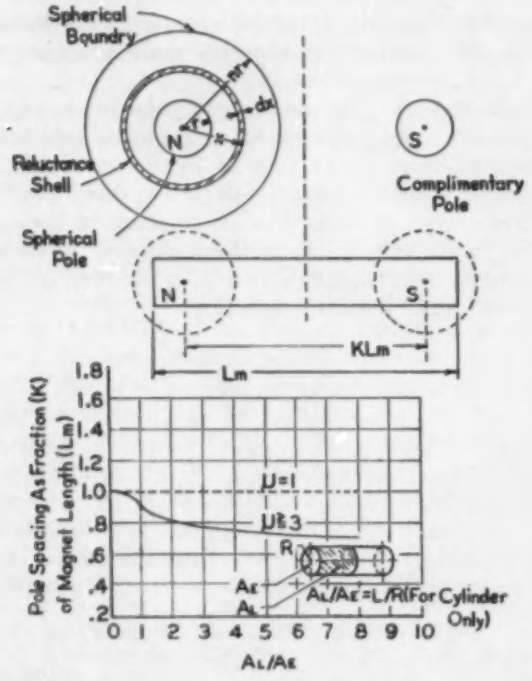

FIG. 1. Spherical pole formula application to bar magnet.

SPHERICAL POLE FORMULA

Consider the spherical pole (N) in Fig. 1. Evershed[1] has shown that reluctance from such a pole to a distant boundary of $n(r)$ is given by the expression $\frac{1}{4}\pi r$. The reluctance from pole to pole would be $\frac{1}{2}\pi r$ and the permeance $2\pi r$. By expressing radius (r) in terms of surface area (S) the pole to pole permeance can be expressed as $P=1.77(s)^{\frac{1}{2}}$. Real magnet limbs to a large extent approximate the conditions of free polar radiation. To apply this formula to permanent magnet configurations whose permeance is due entirely to the permeance from limb to limb one need only substitute a sphere having the same area as the real magnet limb and calculate the permeance from the expression $P=1.77(s)^{\frac{1}{2}}$.

LIMITATIONS AND SUPPLEMENTAL DATA REQUIREMENTS

Evershed used the free pole formula extensively in his work on early low coercive force permanent magnets. The extremely long limbs were a serious departure from the spherical pole and some error resulted. Today's high coercive force permanent magnets rarely are used in length to area ratios greater than ten; the free pole formula closely estimates the permeance for such configurations. The spacing of the effective polar regions is of great importance in using this formula. In early low coercive force magnets, the poles were about 0.7 of the full magnet length apart. For very low values of magnet length to area, the end leakage outweighs the leakage from the periphery of the limb and the pole spacing then becomes the full length of the magnet.

The premise that the magnet is an equipotential body

[1] Evershed, J. Inst. Elec. Engrs. 58, 780–837 (1920).

is based on the assumption that the reversible permeability of the magnet is much greater than that of air. For some permanent magnets the permeability approaches that of air (Ferrites 1.1). In practice, measured data suggests that for permeabilities of three and greater the analogy with respect to an equipotential body is preserved to a satisfactory degree; but for permeabilities of one the effective polar regions move to the ends of the magnet. Figure 1 shows the variation of pole spacing as influenced by geometry and permeability. Pole regions move toward the end of a magnet due to low permeability and due to a low length to area ratio.

APPLICATION OF THE FORMULA

The basic equation relating flux (ϕ), magnetomotive force (F) and permeance (P) is $\phi = FP$ or $BmAm = HmLmP$, where Bm = flux density of magnet Hm = unit magnetomotive force, Am = magnet area and Lm = magnet length. Rearranging and substituting $1.77(s)^{\frac{1}{2}}$ for P gives $Bm/Hm = (Lm/Am)K[1.77(s)^{\frac{1}{2}}]$ where K is a fraction of (Lm) denoting effective pole spacing. Bm/Hm is the slope of the load line and for magnet bars, rods, rings, and in general, open circuit magnets, the load line, and total leakage permeance can be determined

To demonstrate the extremes to which this formula can be used consider Fig. 2 where a tubular magnet configuration used as a field supply for magnetron type tubes is shown. Permanent magnet properties are explored to find a critical field strength and axial uniformity. The free pole formula was used to select outside magnet diameters to allow a common value of field strength (Hi) to be obtained from Alnico 6, Alnico 7, and barium ferrite. It is interesting to note the influence of pole spacing and geometry on the axial field uniformity. The areas above and below the horizontal axis

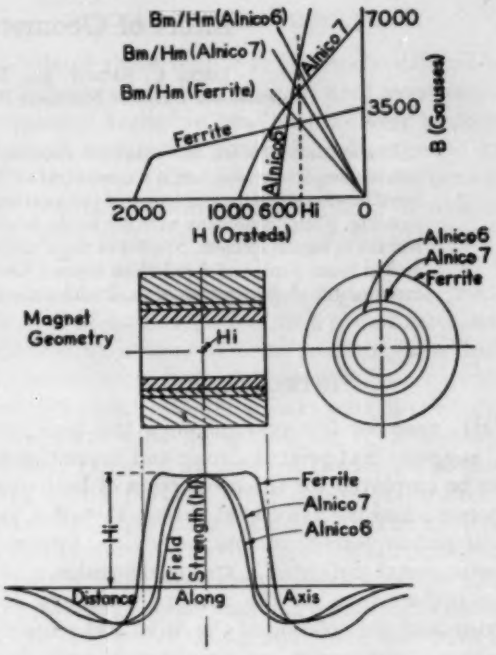

FIG. 2. Analysis of tubular-shape magnet field distribution.

are equal to satisfy the line integral thereof. Both magnet permeability and area to length ratios influence the area below the horizontal axis.

CONCLUSION

The permanent magnet can be treated as an eqiupotential body without serious error and the free pole permeance formula with proper supplementation constitutes a useful technique for evaluating leakage permeance and magnet circuit configurations.

Effect of Geometry on Thick Film* Toroids

JAMES C. SAGNIS, JR., MICHAEL TEIG, AND ROBERT L. WARD
International Business Machines Research Laboratory, Yorktown Heights, New York

In the study of thick-film magnetic circuits, it has been found that thick film cores of certain sizes could not be completely switched if a concentrated drive winding was used. In addition, the induced voltages differed in waveshape as a function of the location of the sense windings with respect to the concentrated drive winding. Both phenomena were obviously detrimental to the "normal" operation of the device as a magnetic storage or logical element. Studies of these phenomena were conducted using planar thick film toroids, photo-etched from ¼-mil and ½-mil thick Square Loop Hy-Mu 80. From the results of these studies, qualitative explanation of the aforementioned phenomena is offered in the form of a three part flux pattern model.

INTRODUCTION

THE need for low cost memory and logic arrays suggests that printed circuit and deposition techniques be employed for the production of both storage components and the associated wiring. However, initial tests of planar toroids of low coercivity, square loop magnetic metal indicated a strong dependence of the device performance on the relative geometry of the structure and the position of the drive and sense windings. As a consequence, an experimental investigation was undertaken to determine the nature and magnitude of these effects.

EXPERIMENTAL PROCEDURE

The material chosen for this experiment was Square-Loop Hy-Mu 80,† because of its availability and known characteristics. Thirty test samples of various sizes were prepared by photo-etching techniques from ¼ and ½ mil rolled sheets and were mounted on plastic test jigs. Two types of drive windings were provided: (1) a symmetric winding consisting of a long centrally located wire perpendicular to the plane of the core and having a remote return path, (2) an asymmetric winding consisting of a single, tightly wrapped concentrated turn, linking the core. In addition, three concentrated sense windings were placed around the core at 0°, 90°, and 180° positions relative to the asymmetric winding. To eliminate any effects due to external magnetic fields, the samples were tested in a field free region provided in the center of three mutually orthogonal Helmholtz coils.

Two sequences of square wave current pulses were employed. The first consisted of a variable amplitude set pulse and a fixed amplitude reset pulse applied alternately to the symmetric drive winding. The second was similar, except that the set pulse was applied to the asymmetric drive winding. In each case, the reset pulse was sufficient to saturate the core and the width of the set pulse was longer than any of the observed switching times. Finally, the voltages induced in the sense windings were integrated electronically to provide the major portion of the recorded data.

* 1–20 microns.
† Magnetics Inc., Butler, Pennsylvania.

RESULTS

The specimens tested were duplicate sets of ½ and ¼ mil cores ranging in i.d. from 0.125 to 1.500 in. and in o.d. from 0.250 to 2.000 in. The test for each core consisted of obtaining the "S" curve (final relaxed flux state *vs* set current amplitude) for each of the sense winding positions with the set pulse applied to the asymmetric winding. A typical family of these "S" curves is shown in Fig. 1 along with the normal "S" curve obtained by applying the set pulse to the symmetric winding. These curves illustrate the principal effect of asymmetric excitation of thick film structures in excess of a certain size, namely; the percentage of total flux that can be switched irreversibly is less than 100% and decreases monotonically from the 0° to the 180° sense position.

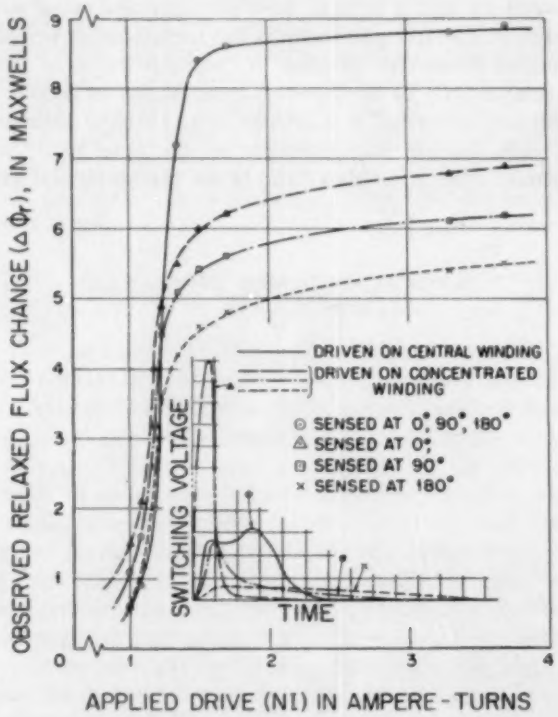

FIG. 1. "S"-curves and switching voltages for a thick film planar toroid showing the effects of geometry on switching properties. The dimensions of this core are i.d. = 1.5 in., o.d. = 2.0 in., 0.5 mil thick.

In addition, there is a similar disparity among the switching times (insert, Fig. 1).

Additional tests, under the above conditions, have indicated the existence of a critical i.d. for a given material and thickness in excess of which 100% irreversible flux change can never be attained, regardless of the o.d. On the other hand, for an i.d. below this critical value, there exists an o.d. for which 100% irreversible flux can be switched, although there may be a slight variation in switching times around the core. Tests of both ½ and ¼ mil cores show the critical i.d. to be greater for the thicker gauge. Extrapolation indicates these critical i.d.'s to be approximately 0.3 and 0.2 in. for the ½ and ¼ mil material, respectively.

Figure 2 illustrates the dependence of the percentage irreversible flux switched for asymmetric drive, on either i.d., o.d. or thickness, provided the remaining two dimensions are held constant. In addition, it shows that the rate of percentage flux decrease, as a function of o.d., is greater for the thinner material.

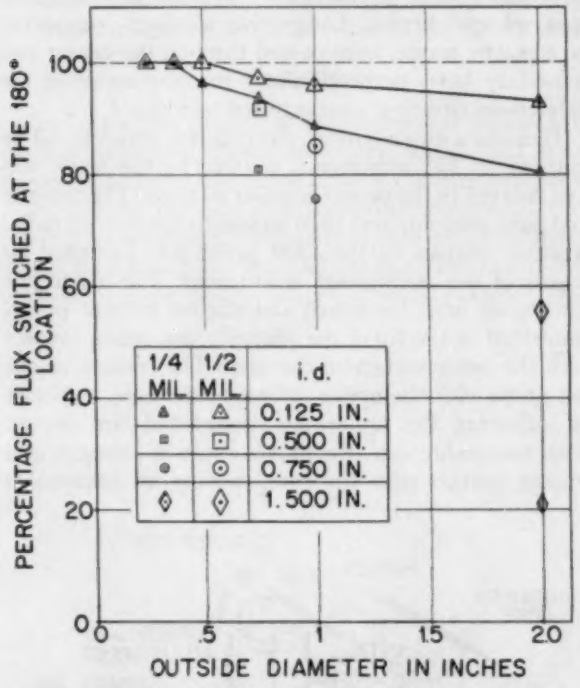

FIG. 2. The percentage of total flux irreversibly switched at the 180° sense location using asymmetric drive, as a function of o.d., for various i.d.'s and thicknesses. The flux was evaluated at a value of set current sufficient to switch 95% of the total flux in a core with a centrally applied set pulse.

DISCUSSION AND CONCLUSION

Analysis of these results is extremely difficult since the planar nature of the specimens used invalidates the assumption of negligible "end effects" basic to previous analyses of asymmetric excitation of magnetic cylinders.[1,2] However, the underlying phenomenological model[3] of surface polarity proved useful in arriving at a qualitative explanation of the remagnetization state in planar structures.

On the basis of experimental evidence, a proposed model of the final flux state of such planar cores may be represented by a three-part flux pattern: (a) a "hub"—consisting of that flux which links all the sense windings, (b) air flux—that flux which links part of the core and finds its return path through the air, (c) a "decoupled" or "kidney shaped" pattern[2]—a circulation of flux extending over a portion of the core with closures contained completely within the material. The existence of the "hub" was confirmed by applying alternate set and reset pulses to the asymmetric drive windings and observing the flux change common to all the sense windings. The existence of the air flux can be seen from Fig. 1 by noting the difference between $\Delta\Phi$ (0°) and $\Delta\Phi$ (180°). This flux must complete its path through air in order to satisfy the flux continuity condition. The existence of the "decoupled" pattern was demonstrated by the inability to reset a portion of the flux with an asymmetric drive which was previously set utilizing the same winding. This flux could only be reset by a current applied to the symmetric winding. Hence, there is decoupling from the asymmetric winding.

Further aspects of this investigation are being pursued, to arrive at a more detailed explanation of the model, the mechanisms involved, and further effects of geometry on asymmetrically driven thick films.

ACKNOWLEDGMENTS

The authors wish to thank J. N. Cole, V. A. Ranieri, and S. LaBare for their aid in the preparation and testing of the samples. The assistance of H. T. Lee in making available his analytic study of the leakage flux in thick films is particularly appreciated.

[1] P. Hammond, J. Inst. Elec. Engrs. (London) **102C**, 198 (1955).
[2] S. Abbas, "Method of Analysis of Flux Patterns in Ferrite Multiple Core," Thesis; Carnegie Institute of Technology (June, 1958).
[3] E. B. Moullin, *The Principles of Electromagnetism* (University Press, Oxford, England, 1955), 3rd ed., pp. 164–168.

Experimental Flux Pattern Determination in Magnetic Cores

ROBERT L. WARD
International Business Machines Research Laboratory, Yorktown Heights, New York

The difficulties in determining the quiescent flux patterns in nonlinear magnetic structures is considered and two techniques are briefly described for measuring these patterns in magnetic cores etched from sub-mil thicknesses of 4–79 Molybdenum Permalloy. Both methods utilize a sensing loop formed by moveable surface probes and a part of the core itself, which conductively completes the sense circuit. A detailed description of the measuring apparatus and the testing technique is given, and the graphical procedure for plotting the flux configuration, of a two aperture multi-path core is outlined. Finally, additional applications are enumerated.

INTRODUCTION

WITH the advent of the multi-path magnetic core as a component for the logic and memory functions[1,2] in digital computers, speculation arose as to the internal flux patterns existing at various stages of the device's operation. Analysis[3] of this problem proved very difficult, despite the introduction of many simplifying assumptions. Similarly, the experimental method of drilling holes through strategic portions of the core structure and measuring the flux changes induced in linking sense windings was tedious and, moreover, rudimentary, since more than a limited number of holes destroyed the inherent characteristics of the element. To circumvent these deficiences, a surface probing technique, based upon the conductivity of square-loop magnetic metals, was developed.

EXPERIMENTAL PROCEDURE

Initially, two preliminary experiments were performed. In the first, two small metallic probes were brought gently into contact with a magnetic core etched from a sheet of ultra-thin gauge metal. The probes were placed in the same planar position but on opposite sides of the core. Upon switching the core, the voltage induced in the closed circuit (consisting of the detector leads, the probes, and the portion of the core between the points of contact) was identical to that induced in a sense winding linking the core through a small hole adjacent to the point of contact. In the second, with a similar core supported on a rigid nonconducting substrate, the probes were again brought into contact with the core at two planar positions sufficiently separated (greater than 20 times the material thickness) on the same side of the core. This time, the induced voltage was one half the amplitude, but otherwise identical to that induced in a comparison sense winding, linking the portion of the core between the contact points. The equivalence of the probe circuit to a well defined sense loop was established in each case.

The first result suggested the more elaborate experiment performed with the test jig shown in Fig. 1. The magnetic core, photo-etched from a ½-mil sheet of square-loop 4–79 Molybdenum Permalloy, was a representative multipath with an i.d. of ½ in., an o.d. of 1 in., and a 10-mil peripheral hole midway between the inner and outer radii. The core was centered on the face of the serrated capstan and held in place with a layer of glycerine. To insure the insulation of the specimen, the face of the silver plated brass capstan was first lightly sprayed with krylon. Long drive windings, supported on a plastic frame, were passed through the center and secondary holes perpendicularly in order to avoid the deleterious effects of concentrated windings.[4]

To make a measurement, the capstan, which could be indexed in 15° increments relative to the base, was first rotated to the proper angular position. The capstan and base assembly was then moved to the desired radial position relative to the fixed probe-jaw assembly by means of the micrometer adjustment. The lower jaw was raised until the honed and aligned bottom probe, embedded in the tip of the phenolic jaw, made contact with the lower surface of the core. The contact of the top probe with the upper surface of the core, achieved by adjusting the upper jaw, completed the circuit. With reasonable care, the probes could be brought into grazing contact with the core, causing no discernable

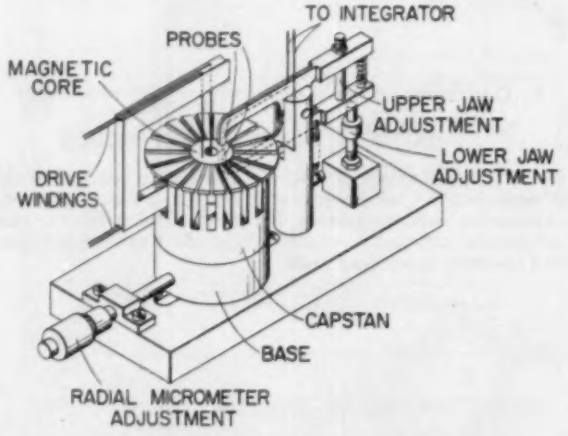

FIG. 1. Test jig for flux probing experiment.

[1] J. A. Rajchman and A. W. Lo, R.C.A. Rev. **16**, 303 (1955).
[2] L. P. Hunter and E. W. Bauer, J. Appl. Phys. **27**, 1257 (1956).
[3] S. A. Abbas, "Methods of analysis of flux patterns in ferrite multipath cores," Thesis, Carnegie Institute of Technology, Pittsburgh, Pennsylvania (1958).
[4] J. C. Sagnis, Jr., M. Teig, and R. L. Ward, J. Appl. Phys. **31**, 190S (1960), this issue.

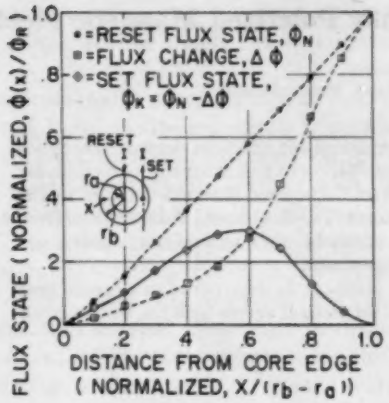

FIG. 2. Flux state for the 180° position from the peripheral winding for a set pulse applied to that winding. Set current was sufficient to reverse half of the total flux and the flux was measured inward from outer core edge.

distortion of the switching voltage waveform as monitored on a separate sense winding. Indeed, from resistance measurements, a rough calculation indicated an effective diameter of contact area of less than 0.2 mil.

RESULTS

Since only the change of flux states was measurable by this technique, a reference state, $\phi_N(x)$, had to be chosen in order to determine other static flux configurations. Current pulses of alternate polarity applied to the *center* drive winding cycled the core between its remnant states, ϕ_N and ϕ_S, and the resulting flux difference measurement, $\phi_M(x) = \phi_N(x) - \phi_S(x)$, was made as a function of the distance from the outer core edge. If we assume that $\phi_S(x) = -\phi_N(x)$, which was reasonable since it was tantamount to saying the hysteresis loop of the material was symmetric, $\phi_N(x) = \frac{1}{2}\phi_M(x)$. The normalized result is plotted in Fig. 2.

Next a set pulse, sufficient to reverse half of the total remnant flux, ϕ_R, was applied to the peripheral winding and the flux change, $\Delta\phi(x)$, was measured at reset time. Finally, the flux state, ϕ_K, resulting from the set pulse was constructed, Fig. 2. (Note that the derivative of $\phi_K(x)$ would yield the normal component of average flux density, $\langle B(x)\rangle_{Av}$ as a function of x.)

A family of such curves could be plotted with the angular separation from the set winding as a parameter. Then, by marking off equi-flux levels with lines parallel to the normalized x axis, the loci of equivalent "flux tubes" could be determined and the complete flux pattern constructed on polar coordinate paper.

CONCLUSION

Future plans call for the application of this technique to the study of the dynamics of remagnetization and to the leakage flux problem in thick films. In addition, the single side probing, briefly described in the Procedure, will be applied to thin film investigations.

ACKNOWLEDGMENTS

The author wishes to thank J. C. Sagnis, Jr. and V. A. Ranieri for their assistance in the preparation of the samples and the instrumentation of the experiment.

Method for Measuring Iron Losses in Elliptically Polarized Magnetic Fields

F. J. Young and H. L. Schenk
Westinghouse Research Laboratories, Pittsburgh, Pennsylvania

A method for measuring iron losses in elliptically polarized magnetic fields has been devised. The fields are produced in a laminated one-inch cubic specimen by the superposition of two mutually perpendicular magnetic fields whose magnitudes and time phase angles can be varied. Orthogonal fields are obtained by the use of two "C" cores with air gaps large enough to contain the specimen. The flux density is ascertained from the voltages induced in two coils wound on the specimen with axes parallel to the two field components. The iron loss is determined by measuring the heating transient in the specimen.

In addition, the anisotropy in losses due to alternating magnetic fields can be determined as a special case of elliptically polarized field excitation. The loss data obtained by this method agrees with the results given by the standard Epstein test to within 15%.

INTRODUCTION

THE magnetic fields in many iron core devices such as turbogenerators, railway motors and single phase synchronous motors are elliptically polarized.[1] The hysteresis losses due to elliptical rotating fields were investigated by Baily[2] and Radt[3] many years ago.

It is the purpose of this paper to describe a method for measuring the total losses caused by elliptically polarized magnetic fields in a small (one cubic inch) sample of ferromagnetic material.

TWO-CORE MAGNETIC TESTER

Elliptically polarized magnetic fields can be produced by the super-position of two mutually perpendicular magnetic fields.[1] By varying the magnitudes and time-phase angles of these two fields, all possible cases of elliptical polarization can be obtained. Ordinary alternating magnetic fields having various magnitudes and directions are included as special cases.

To obtain these orthogonal fields, two HIPERSIL C-cores having adjustable air gaps are placed mutually perpendicular to each other. The air gaps in the core are approximately one inch in length and accomodate the specimen and some thermal insulation. The thermal insulation between the pole faces and the specimen minimizes heat flow between the cores and the specimen and aids in making the flux density more uniform in the specimen.

THE SPECIMENS

The specimens consist of a stack of one inch square laminations with the same orientation. In case the laminations have been strain-annealed after the machining operations, it is necessary to electrically insulate the laminations from one another with thin (2-mil) paper. The bundle is held together by one layer of 2.5-mil cellophane tape which also provides added thermal insulation. The stack of laminations is inserted into the air gap in such a way that the field rotates in the plane of each lamination. The specimen is separated from the pole faces by cardboard strips whose thickness (9-mil) was adjusted by trial to minimize the heat transfer between the specimen and the cores without allowing the mmf drop across the gap to become too large.

FIELDS IN THE SPECIMEN

The precise calculation of the fields in the specimen, air gaps and two-core tester would be an undertaking of considerable difficulty. Consideration of a two-dimensional Laplacian field map of the specimen and the region around it indicated that the field in the specimen could be made almost uniform providing the specimen was surrounded by an air gap and was not too badly saturated. Measurements of the flux density near the specimen indicate that the field densities in the specimen are uniform to within $\pm 5\%$ of the average field density indicated by the pick-up coil wrapped around the specimen.

THE CIRCUITRY

One core of the 2-core tester is excited by a variable auto transformer which is connected directly to the mains and the other by a variable auto transformer fed by a 3-phase induction motor excited by the mains and which is used as a phase shifter.

Two mutually perpendicular one turn pick-up coils are wound around the specimen to measure the two components of flux density. Earlier in the investigation coils having as many as 20 turns had been used but were abandoned because of the limited space in the air gap and their tendency to eventually become shorted out. Because of the small area enclosed by the coil, it is necessary to amplify the coil voltage at least by twenty times. The amplified voltages are applied to a flux voltmeter commonly used to measure the peak induction in the Epstein test. This reading can be compared to one taken by an rms meter to ascertain the waveform distortion. The outputs of the pick-up coils are also amplified by two identical direct-coupled amplifiers and integrated by two identical integrating circuits. The integrated voltages are applied to a phase angle meter.

[1] J. Ben Uri, Bull. schweiz. elektrotech. Ver. 41, 604–607 (1950).
[2] F. Baily, Phil. Trans. Roy. Soc. London 187, 715–746 (1896).
[3] M. Radt, Arbeiten aus dem Elektrotechnischen Institut der Grossherzoglichen Technischen Fridericiana zu Karlsruhe 2, 249–296 (1910).

From the various signals so obtained, it is possible to view the ellipse within which the flux density vector rotates.

A copper-constantin thermocouple is held in a grove in a piece of 9-mil cardboard which is sandwiched between two laminations at the center of the specimen. The thermocouple comes into contact with the laminations which are adjacent to the cardboard. Another identical copper-constantin junction is embedded in a similar specimen which is placed in the vicinity of the two-core tester. The two junctions are connected in series opposition so that variations in output due to room temperature fluctuations are cancelled. The remaining voltage is amplified by a dc microvolt amplifier which supplies the amplified signal to a recording potentiometer. Depending upon the magnitude of the iron loss being measured, amplifications of 5 to 200 times are required to give suitable deflection on the recording potentiometer. This apparatus is capable of measuring temperature differences down to 0.001°C.

MEASUREMENT OF POWER LOSS

The power dissipated in the specimen is calculated from the transient heating which occurs when the magnetic fields are turned on. It can be shown that the power dissipated at any point in the medium is equal to the product of the specific heat, density, and the time derivative of temperature at that point, provided the whole medium is at the same temperature. This condition is satisfied when the specimen has no applied field and is at room temperature or when the specimen is subjected to a magnetic field until it has reached an equilibrium temperature. It was found most convenient to use the initial slope of the transient heating curve for power measurement because it did not require as much experimental time as the "load dump" method.

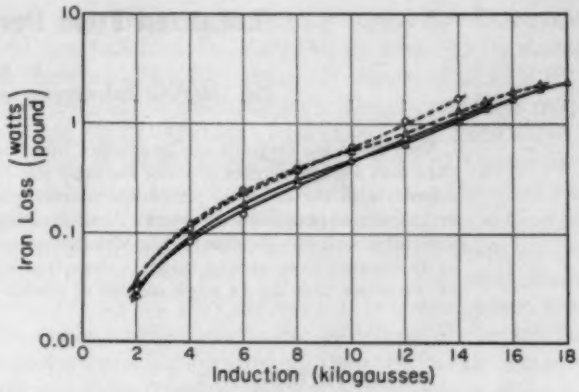

FIG. 1. 60-cps alternating magnetic field iron loss vs induction for an M-14 steel specimen. Solid curves are the losses in the rolling direction and dashed curves are the losses in the cross-rolling direction. The 2-core tester data is represented by the circles and the Epstein test data is represented by the triangles.

COMPARISON WITH EPSTEIN TEST DATA

By applying voltages which have the same time phase to both cores, it is possible to measure loss versus angle-of-magnetization for a given induction. This is advantageous because the "loss anisotropy" measurement can be made on one particular specimen rather than many different specimens required by the Epstein test.

By exciting one core at a time, it is possible to compare the losses measured by this apparatus to those obtained by the standard Epstein test. The comparison with Epstein losses is shown in Fig. 1. The two methods yield results which agree to within 15% when distortion is not present in the flux density waveform.

Localized Field Permanent Magnet Arrays

H. L. STADLER
Bell Telephone Laboratories, Incorporated, Murray Hill, New Jersey

Very short bar magnets can be grouped into linear arrays in such a way as to give a more localized field than does a single magnet of about the same size. Shaping the field from small magnet arrays is particularly important in the design of permanent magnet memories where the information is stored by the presence or absence of permanent magnets. To achieve high information density it is necessary to design magnet structures with very localized fields. Measurements of the response of a memory sensing element as a function of its distance from various magnets show that a linear array has a much stronger effect when very close to the sensor than does a single magnet of similar size and dipole moment.

INTRODUCTION

IN the Permanent Magnet Twistor Memory[1] the presence of permanent magnets is sensed by their effect on the switching of a short length of soft magnetic wire, or sensor, in a pulsed solenoid. The magnet, when used as in Fig. 1, must affect its own sensor strongly but have a negligible effect on neighboring sensors which may be quite close. If a single bar magnet strong enough to stop the switching of its own sensor is used, the nearest neighbor must be at least the magnet's length away to make the interaction negligible. A chain of shorter bar magnets, however, has a more localized field, permitting a considerable increase in the memory's information density.

The magnetic field at any point on the plane perpendicularly bisecting a bar magnet is given by

$$H = md/(r^2+d^2/4)^1,$$

where m is the magnetic pole strength, d is the length of the magnet, and r is the distance from the magnet axis to the observation point. In order to reduce H for large values of r while keeping H large for small values of r, it is necessary to reduce d. This suggests that a chain of short magnets will have a more localized field than a single magnet as long as the chain. The effect of such a magnet chain on a sensor at various distances has been measured and compared to the effect of a single long magnet.

EXPERIMENTAL

The sensing element used in the experiment was a piece of flat Permalloy wire ($B_s = 9000$ gauss) with a cross-sectional area of 1.2×10^{-6} sq in., wrapped around a 0.003-in. diameter copper wire to form a "Twistor." The sensor was centered within a strip solenoid 0.063-in. long (in the sensing wire direction) which applied an axial field at the sensor. The field was calculated to be

$$H(z_0) = 2.54i\left[\tan^{-1}\frac{0.031\text{ in.}-z_0}{0.005\text{ in.}}+\tan^{-1}\frac{0.031\text{ in.}+z_0}{0.005\text{ in.}}\right]\text{oe},$$

where i is the current in amperes and z_0 is the distance from the observation point to the center of the solenoid. The solenoid was driven by a sequence of two square pulses, a positive pulse 5.6 amp high followed by a nega-

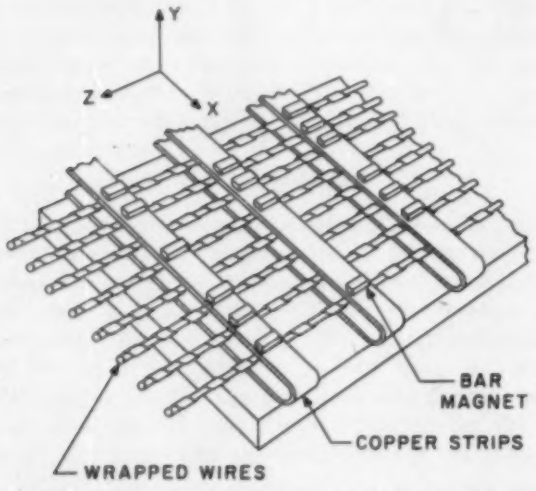

FIG. 1. A section of a Permanent Magnet Twistor Memory frame.

[1] D. H. Looney, Proceedings of the Western Joint Computer Conference, San Francisco, March 3, 1959, p. 36.

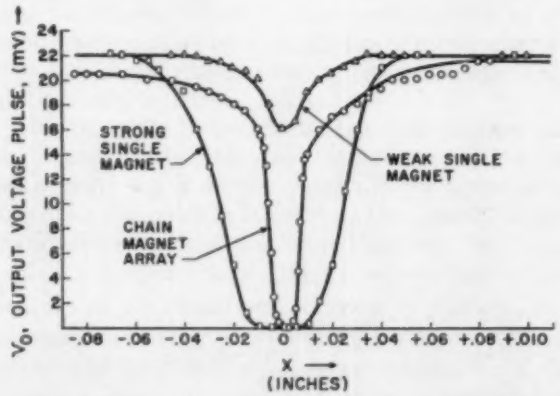

FIG. 2. Variation of output voltage of a sensing wire bit as various permanent magnet arrays are moved in the x direction. The magnet arrays were centered over the bit in the z direction and were 0.006 in. center to center from the bit in the y direction. Directions are as shown in Fig. 1. The chain array consists of four magnets, each 0.013 in. long and spaced 0.013 in. apart in a line with a total dipole moment of 3.1×10^{-3} gauss cu in. The "weak" and "strong" single magnets are each 0.063 in. long with dipole moments of 2.1×10^{-3} and 1.8×10^{-2} gauss cu in., respectively.

tive pulse 5.6 amp high. Both pulses were 5 μsec wide and had rise times of 1.0 μsec. The output signals induced on the center copper wire of the sensing element were measured just at the end of the rise time of the positive pulse. The axial magnetization of the sensing wire outside the solenoid was opposite in direction to the field applied by the positive drive pulse. This implied that any demagnetizing fields of the sensing wire tended to slow its switching.

The chain of magnets was cut from a single piece of Ferroxdure ceramic (B_r=2250 gauss, H_c=1500 oe). There were four square magnets, each 0.013 in. long $\times$0.013 in. wide$\times$0.0025 in. high, in a line with 0.013-in. spaces between each pair, making a chain 0.091 in. long by 0.013 in. wide. The ceramic was magnetized along the 0.091 in. axis of the chain (the z direction). The demagnetizing factor $N/4\pi$ for an oblate ellipsoid circumscribed by one of the square magnets is 0.15.[2] Assuming a uniform demagnetizing factor of 0.15 for the magnet itself, the flux density is 1850$\pm$150 gauss.

The magnet chain was placed with its long axis (the z axis) along the sensing wire axis and with the square magnet faces parallel to the x-z plane of Fig. 1. The distance in the y direction from the axis of the magnet chain to the axis of the sensor was 0.006 in.

RESULTS

The voltage output of the sensing bit is plotted against x in Fig. 2. For comparison two different single 0.063-in. long Vicalloy magnets were measured in exactly the same way. The weak single magnet had B_r=3300 gauss and was 0.001 in. thick$\times$0.010 in. wide, so its dipole moment was 2.1×10^{-3} gauss in.^{3} compared to 3.1×10^{-3} gauss in.^{3} for the chain magnet. The strong single magnet had B_r=9300 gauss and was 0.002 in. thick$\times$0.015 in. wide, so its dipole moment was 1.8×10^{-2} gauss in.^{3}. It can be seen from Fig. 2 that the "weak" magnet has slightly less effect on the sensing wire's switching at distances $|x|\geqq0.015$ in. than the magnet chain has, as would be expected from the fact that their total dipole moments are not very different. It can also be seen that the chain magnet affects the switching of the sensing wire very much more strongly than the "weak" magnet does for $|x|<0.006$ in. With available pulsers the solenoid magnetic field could not be made high enough to compare the effects of the chain and the "strong" magnet very close to the sensing bit.

DISCUSSION

The simple experiments show clearly that the chain magnet has a much more localized effect on the sensing bit than does a single larger magnet. The present chain magnet is too strong to allow an exact measurement of the localization that has been achieved. For any practical memory the chain magnets must be made considerably weaker than the present one.

ACKNOWLEDGMENTS

It is a pleasure to thank George Ellis and Edward Collyer for help with the experiment.

[2] J. A. Osborn, Phys. Rev. **67**, 351 (1945).

Resonance

Interaction of Magnetic Crystals with Radiation in the Range 10^4–10^5 cm^{-1}

A. M. Clogston
Bell Telephone Laboratories, Murray Hill, New Jersey

The optical absorption spectrum of magnetic crystals containing ferric iron in the range 10^4 to 10^5 cm^{-1} consists of a series of sharp peaks superimposed on a strong absorption band. The absorption band is associated with a large Faraday rotation of the transmitted light. The sharp peaks are identified as transitions within the configuration ($3d^5$). The broad band can arise either from an internal transition to ($3d^4 4p$) or to a charge transfer process. Both mechanisms are able to account for the observed intensity and rotation within a factor of two. Because of the Faraday rotation, the charge transfer must be associated with *d* levels of symmetry Γ_5. The rotation has the opposite sign for the two cases and could be used to distinguish between them.

I. INTRODUCTION

THE optical absorption spectra of compounds of the first row transition metals have been for a long time a matter of chemical and physical importance. Until lately, the bulk of the experimental work has been done on ionic complexes in solution, and on dilute paramagnetic salts. In recent years, however, the increasing availability of large single crystals of optical quality has made possible detailed observations on the absorption spectrum of compounds such as nickel oxide,[1] manganese and cobalt oxides,[2] manganese fluoride[3] and yttrium iron garnet.[4] The site symmetries that are found for the magnetic ions in these crystals are similar to those found in the ionic complexes and in the dilute salts. Consequently, there is a correspondence of the spectra in the various cases and much of the theory developed earlier has been successfully applied to the ferromagnetic and antiferromagnetic crystals. New features of great interest, however, are introduced by the magnetic ordering.

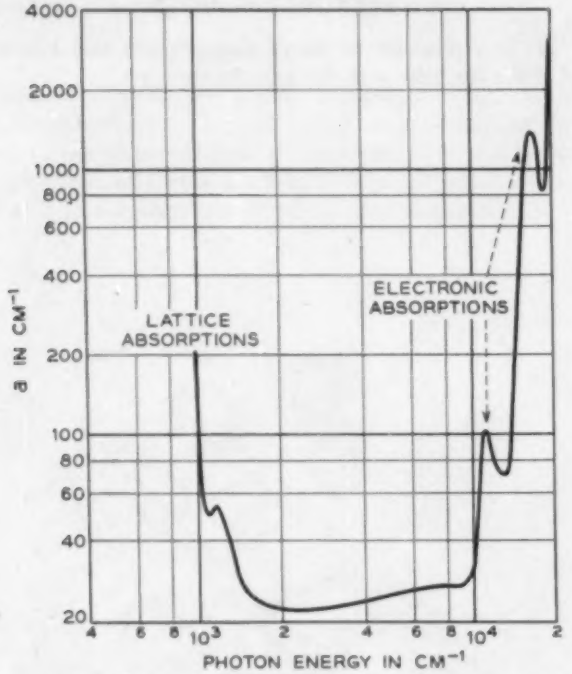

FIG. 1. Absorption coefficient of yttrium iron garnet as a function of photon energy in cm^{-1} measured by J. F. Dillon.

Our present knowledge of magnetic compounds has been largely derived from measurements made in three frequency ranges as shown in Table I. The development of power sources in the short microwave and far infrared regions from 1 to 100 wave numbers is certainly going to lead to much new information in the future. We have, however, already at hand the ability to explore the high frequency range between 10 thousand and 100 thousand wave numbers.

There are at least four processes which can be expected to contribute to the absorptions in this energy range. These are: (a) a change in the spin multiplicity of the metallic ion as, for example, from a sextuplet to a quartet state; (b) a transition between the split components of the free ion ground state due to crystalline Stark effect; (c) a transition internal to the metallic ion of an electron from a 3*d* orbit to a higher energy orbit such as 4*p*; and (d) a transfer of an electron from anion to cation as, for instance, from O^{2-} to Fe^{3+}. It is clear that the observation of optical resonances is important to a basic understanding of the electronic state of magnetic crystals.

TABLE I. Energy ranges of magnetic measurements.

Frequency in mc/sec	Wave number cm^{-1}	Measurements
0–3		Magnetization, anisotropy, specific heat, domain walls
3–300	10^{-4}–10^{-2}	Nuclear resonance
300–30 000	10^{-2}–1	Ferromagnetic resonance, spin waves
	1–100	Antiferromagnetic resonance
	1–1000	Lattice vibrations
	10^4–10^5	Electronic interactions

[1] R. Newman and R. M. Chrenko, Phys. Rev. **114**, 1507 (1959).
[2] G. W. Pratt and R. Coelho, Lincoln Laboratory Rept., (June 3, 1959).
[3] J. W. Stout, J. Chem. Phys. **31**, 709 (1959).
[4] J. F. Dillon, J. phys. radium **20**, 374 (1959).

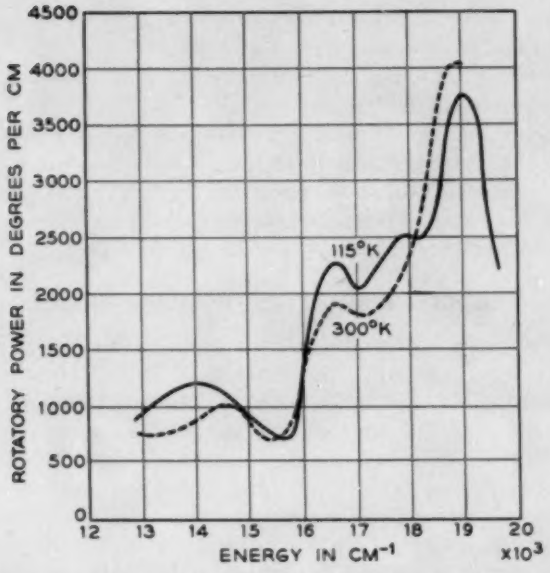

FIG. 2. Faraday rotation in yttrium iron garnet as a function of photon energy in cm^{-1} measured by J. F. Dillon.

Of particular interest is the study of optical absorption in the ferromagnetic ionic crystals such as yttrium iron garnet and the various ferrites. It is interesting that most of these crystals are based upon trivalent iron, and this fact is responsible for certain characteristic features of their absorption spectrum. In this paper, we shall attempt to interpret this spectrum by bringing together a variety of experimental facts.

II. ABSORPTION SPECTRUM OF Fe^{3+}

The initial observations of optical absorption in yttrium iron garnet were made by Dillon[4] and are reproduced in Fig. 1. The outstanding features of this curve are two fairly sharp absorption lines at 11 000 and 16 000 cm^{-1} that lie on the edge of an absorption band whose intensity is rising rapidly between 10 000 and 20 000 cm^{-1}. Beyond 20 000 cm^{-1}, the absorption is so great that no measurements have been possible on the thinnest crystals prepared to date. Measurements made on other crystals such as magnesium ferrite[5] and α-Fe_2O_3[6] show similar characteristics. It seems evident that the sharp lines and rapid increase of absorption towards 20 000 cm^{-1} are characteristic of the ferric ion in oxide crystals.

In yttrium iron garnet, the optical absorption is accompanied by a strong Faraday rotation of the plane of polarization of the transmitted light as is shown in Fig. 2, also observed by Dillon.[4] This curve has a rather involved shape, but close inspection shows that it consists of a steady rise in the Faraday rotation with superimposed dispersion shaped variations associated with the various absorption peaks. A theory of this effect has been given by Clogston.[7] The decrease in the curve towards 20 000 cm^{-1} is undoubtedly anticipatory of further absorption peaks that we shall see lie in this region. The steady rise in the Faraday rotation curve is associated with the rapidly increasing intensity of the absorption band, and will be an important help in identifying the source of the band.

In order to obtain more information about the band, the measurements need to be pushed toward higher frequencies. It is clearly impractical to attempt to prepare thinner sections of yttrium iron garnet in order to make these measurements. At the rate at which the absorption is increasing at 20 000 cm^{-1}, a tenfold decrease in thickness would only allow the measurements to be extended to 25 000 cm^{-1}. We may, however, accomplish much the same end by reducing the concentration of iron in the lattice. For example, crystals of yttrium gallium garnet can be grown with any desired concentration of iron. Such crystals will not, of course, be magnetic in the low concentrations, but we shall assume that this has a minor effect upon the nature of the absorption band. To this end, crystals of yttrium gallium garnet have been grown by Nielsen with varying concentrations of iron and absorption measurements have been made by Wood, some of whose curves are shown in Fig. 3. It is seen that progressive dilution has allowed the observations to be pressed further into the ultraviolet. More absorption

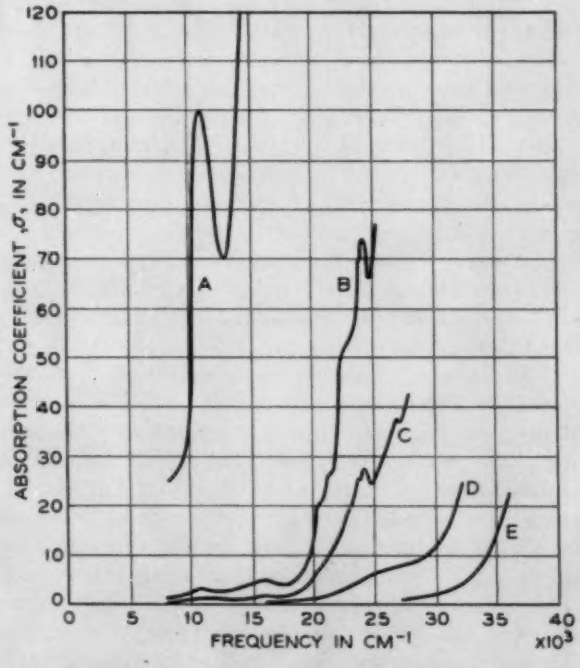

FIG. 3. Absorption coefficient as a function of frequency in cm^{-1} measured by D. L. Wood. (A) yttrium iron garnet; (B) yttrium gallium garnet plus 7 atomic % iron; (C) yttrium gallium garnet plus 3 atomic % iron; (D) yttrium gallium garnet plus residual iron; (E) aluminum oxide plus 0.005 atomic % iron.

[5] R. C. Sherwood, J. P. Remeika, and H. J. Williams, J. Appl. Phys. **30**, 217 (1959).

[6] F. J. Morin, Phys. Rev. **93**, 1195 (1954).

[7] A. M. Clogston, J. phys. radium **20**, 151 (1959).

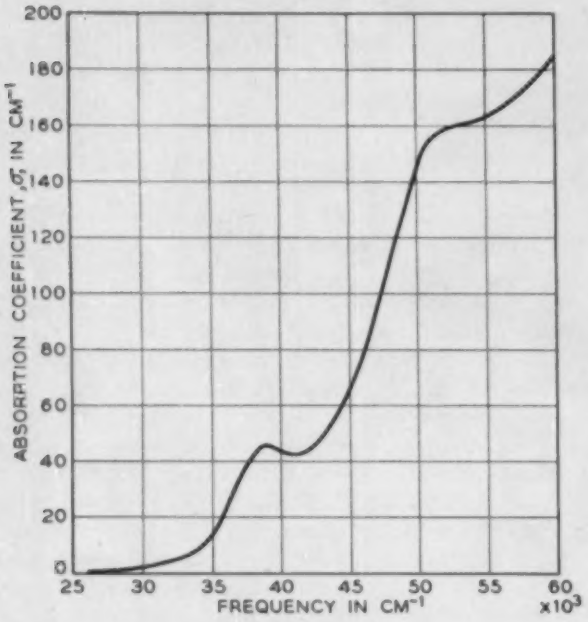

FIG. 4. Absorption coefficient as a function of frequency in cm^{-1} measured by D. L. Wood for aluminum oxide plus 0.005 atomic % iron.

peaks have been thereby revealed, but the absorption is still rising rapidly at the highest frequency indicating that the center of the absorption band is still remote.

At the time these crystals were prepared, it was not feasible to reduce the iron content still further. Some crystals of flux-grown aluminum oxide prepared by Remeika were available, however, with an iron concentration as determined by emission spectrographic analysis of 0.006% by weight. Other impurities were less than 0.001%. An absorption curve taken on these crystals by Wood is shown in Figs. 3 and 4. With the extremely low concentration of ferric iron present in the crystals, it has become possible to extend the measurements out to 60 000 cm^{-1}, and some structure has become apparent in the band. There appear to be two broad peaks located respectively at 39 000 cm^{-1} and 51 000 cm^{-1}, followed by a region of continuous absorption extending out to 60 000 cm^{-1}. The intensity of the peaks is very great. On assuming a Gaussian line shape for the peaks and taking account of the concentration of ferric ions, we may calculate an oscillator strength $f=0.9$ for the strongest transition and $f=0.1$ for the smaller peak. Bands of this intensity can only arise from an allowed electric dipole transition. While awaiting further measurements, we shall assume that the absorption band observed in yttrium iron garnet arises from the same physical mechanism as the band in iron-doped aluminum oxide and has a similar intensity. The progressive shift of the band edge with concentration seen in Figs. 3 and 4 make this assumption very plausible. Some uncertainty is introduced by the fact that the iron sites in yttrium iron garnet have both octahedral and tetrahedral symmetry, while only octahedral sites are present in Al_2O_3.

Wood has found that the curve in Fig. 4 is essentially independent of temperature down to 77°K. This is consistent with Dillon's observation between 10 000 and 20 000 cm^{-1}, where little change is noticed in the intensity of the absorption band with temperature although the sharp peaks narrow considerably between room temperature and liquid He temperature.

III. INTERPRETATION OF SHARP PEAKS

We turn now to the interpretation of the absorption spectrum of ferric iron, and shall discuss first the sharp peaks appearing in Fig. 1. The interpretation of these peaks is not difficult and is undoubtedly the following. Trivalent iron has the ground state electronic configuration $(3d^5)$. The states of this ion in a crystal field of octahedral (or tetrahedral) symmetry have been discussed at length by Orgel.[8] In Fig. 5 we show an energy level diagram similar to that given by Orgel for Mn^{2+} but calculated instead for Fe^{3+}. On the axis of ordinates are shown the states of the free ion, beginning with the ground state $(3d^5)^6S$. Next higher in energy are a set of quartet states such as $(3d^5)^4G$ arising from inverting one spin in the d shell. Above the quartet states are a series of doublet states also arising from $(3d^5)$, which will not concern us and are not shown. Much higher in energy is a set of states arising from $(3d^44s)$ and finally, a set coming from $(3d^44p)$. In the free ion, electric dipole transitions between the ground state ^6S and the quartet states are

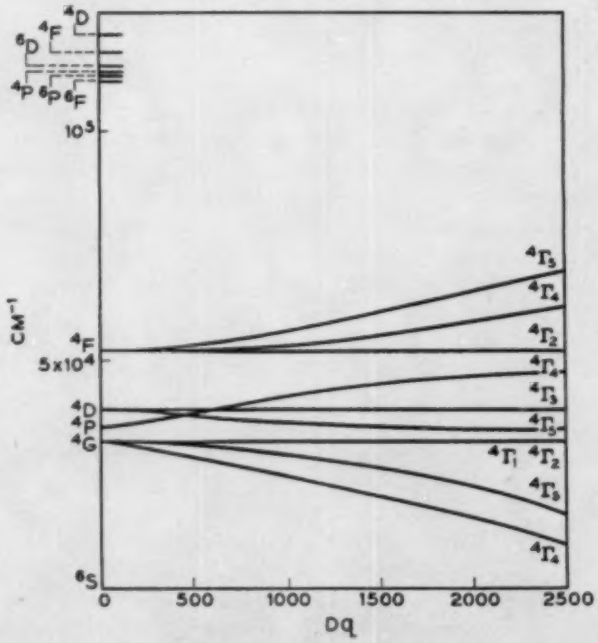

FIG. 5. Energy levels of Fe^{3+} in a cubic crystal field.

[8] L. E. Orgel, J. Chem. Phys. 23, 1004 (1955).

highly forbidden by parity and spin. The first electric dipole allowed transition is to $(3d^4 4p)^6P$.

In a crystalline electric field of octahedral symmetry whose strength is proportional to the parameter Dq, the quartet energy levels split into various representations of the octahedral group and move as shown. With a value of Dq equal to 2500, the two lowest energy levels are made to agree approximately with the positions of the sharp absorption peaks in Fig. 1, and we accordingly assign these peaks as transitions from ^6S to $^4\Gamma_4(^4G)$ and $^4\Gamma_5(^4G)$. The corresponding transitions for the tetrahedral sites will be at a considerably higher frequency since the crystal field will be weaker by a factor of about 4/9. As has been shown by Koide and Pryce[9] for hydrated manganous salts, these transitions have intensity because of the combined action of spin orbit coupling and lattice vibrations. The lattice vibrations overcome the parity selection rule by coupling the even parity states arising from $(3d^5)$ with odd parity states which are assumed by Koide and Pryce to be derived from $(3d^4 4p)$.[9]

In Fig. 5 we see that a variety of states exist at energies higher than $^4\Gamma_4(^4G)$ and $^4\Gamma_5(^4G)$. Transitions to these states are not seen in the concentrated iron crystals because of the strong absorption band, although indications of these transitions may be seen for the dilute crystals in Fig. 3. It is interesting to contrast this situation with that found for compounds of Mn^{2+}, which has the same ground state configuration as Fe^{3+}. In a recent paper, discussing the absorption spectrum of MnF_2,[3] Stout has been able to observe and identify all the states shown in Fig. 5. In this case also, a strong absorption band exists and has been found by Parkinson and Williams to peak at 62 000 cm^{-1}.[10] The band, however, does not extend to low enough energies to obscure the transitions to the quartet states.

IV. INTERPRETATION OF BROAD BAND

We turn now to the more ambiguous task of identifying the mechanism underlying the strong absorption band. There appear to be two possibilities which we may call internal transitions and charge transfer transitions. By an internal transition we mean a process in which an electron is transferred from the $3d$ shell of the metal ion into the ^4p shell. Such a process will be an electric dipole allowed transition and give rise to very strong absorptions. The absorption band found in MnF_2 was ascribed to this mechanism by Parkinson and Williams.[10] Virtual transitions to these levels have been used by Liehr and Ballhausen,[11] and by Koide and Price[9] to explain the intensities of the various parity forbidden transitions. The second possibility, the change transfer transition,[12] is a process in which an electron moves from an anion into the d-shell of the metal ion. This mechanism provides for electric dipole allowed transitions and can also account for strong absorption bands. It is clearly the same process which gives rise to exciton bands in alkali halide crystals.

TABLE II

Wave functions	Number	Representations
$3d$	5	$\Gamma_3^+ \Gamma_5^+$
$4s$	1	Γ_1^+
$4p$	3	Γ_4^-
p_σ	6	$\Gamma_1^+ \Gamma_3^+ \Gamma_4^-$
p_π	12	$\Gamma_4^+ \Gamma_5^+ \Gamma_4^- \Gamma_5^-$

In both of these cases, we shall discuss excited states of the crystal in which the excitation is localized at a particular metal ion. Such a state is, of course, degenerate with states where the excitation is localized on any other equivalent site, and interactions between these states spread the level into an exciton band. However, as indicated by Overhauser in discussing the alkali halides,[13] optical transitions take place only to exciton states with propagation vector k nearly equal to zero. The symmetry considerations we shall discuss below concern the states of a single metal ion surrounded by some configuration of anions. They apply, accordingly, not only to compounds but also to situations in which the metal ion appears as an impurity in a suitable host lattice. Because of the great strength of the absorption bands, the latter situation can be experimentally very advantageous in exploring their structure as we have seen.

Ground State Configuration

Let us now consider an ion of trivalent iron with the ground state configuration $(3d^5)^6S$ surrounded by an octahedral arrangement of oxygen ions. The six anions O^{2-} will each have a closed $2p$ shell configuration. The five electrons on the central ion half fill the $3d$ shell.

We can approach the symmetry analysis most usefully by considering the individual wave functions occupied by the electrons. On the central ion, we have five $3d$ wave functions, one $4s$ wave function and three $4p$ wave functions. The anions provide six $2s$ wave functions and six $2p$ wave functions oriented along the line joining anion to cation. These may be combined to form six wave functions, which are emphasized toward the central ion and are commonly called p_σ orbitals, and six others which are small near the central ion and may be ignored. The anions also provide twelve $2p$ wave functions that are oriented at right angles to the p_σ orbitals and are called p_π orbitals. In forming wave functions for the octahedral complex, we must first combine the various ligand orbitals to form representations of the octahedral group a slisted in Table II.[14,15] We then make

[9] S. Koide and M. H. L. Pryce, Phil. Mag. **3**, 607 (1958).
[10] W. W. Parkinson and F. E. Williams, J. Chem. Phys. **18**, 534 (1950).
[11] A. D. Liehr and C. J. Ballhausen, Phys. Rev. **106**, 1161 (1957).
[12] L. E. Orgel, Quarterly Revs. (London) **8**, 422 (1954).
[13] A. W. Overhauser, Phys. Rev. **101**, 1202 (1956).
[14] J. H. Van Vleck, J. Chem. Phys. **3**, 807 (1935).
[15] K. W. H. Stevens, Proc. Royal Soc. (London) **219**, 542 (1953).

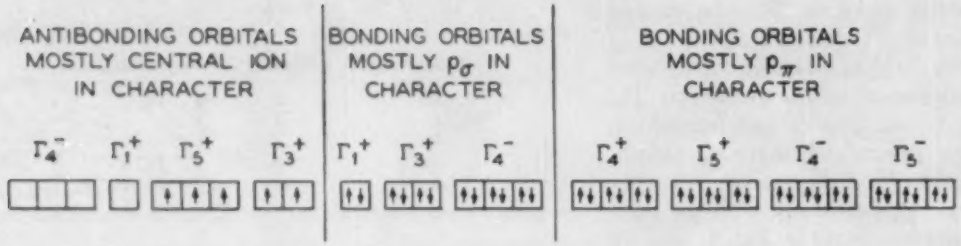
ANTIBONDING ORBITALS MOSTLY CENTRAL ION IN CHARACTER
BONDING ORBITALS MOSTLY p_σ IN CHARACTER
BONDING ORBITALS MOSTLY p_π IN CHARACTER
Γ_4^- Γ_1^+ Γ_5^+ Γ_3^+
Γ_1^+ Γ_3^+ Γ_4^-
Γ_4^+ Γ_5^+ Γ_4^- Γ_5^-

FIG. 6. Ground state configuration of Fe^{2+} octahedral complex.

linear combinations of the central ion and ligand wave functions belonging to the same representations. One set of such combinations, lying lower in energy, are known as bonding orbitals and will be filled with electrons. They will usually be predominantly ligand in character. The other set of combinations, lying higher in energy, are known as antibonding orbitals and will be only partially filled with electrons. These latter wave functions are usually predominantly central ion in character. The $3d$ wave functions of symmetry Γ_3^+ extend directly toward the anion positions, whereas those of symmetry Γ_5^+ are largest in directions lying between the anions. Similarly, wave functions made up from p_σ orbitals are larger near the central ion than wave functions made from p_π orbitals. The overlap and bonding of the states of symmetry Γ_3^+ are therefore comparitively large, while the bonding of states of symmetry Γ_5^+ is weaker. The antibonding orbital Γ_3^+ has a one electron energy higher than that of Γ_5^+, usually by about 10 000 cm^{-1}. The ground state configuration is illustrated in Fig. 6, where individual electron states are indicated by boxes, and the occupancy of the states by positive and negative spins by arrows.

Internal Transitions

Let us first consider transitions in which an electron shifts from the $3d$ shell of the ferric ion into the $4p$ shell. In terms of Fig. 6, a transition is made from the antibonding orbitals Γ_5^+ and Γ_3^+ into the antibonding orbital Γ_4^-. In octahedral symmetry, the electric dipole operator has symmetry Γ_4^-. Since $\Gamma_4^-\times\Gamma_5^+=\Gamma_2^-+\Gamma_3^-+\Gamma_4^-+\Gamma_5^-$, and $\Gamma_4^-\times\Gamma_3^+=\Gamma_4^-+\Gamma_5^-$, the two transitions are allowed by symmetry. This mechanism therefore predicts two strong lines in the absorption spectrum. The transition out of Γ_5^+ will have the higher energy by about 10 000 cm^{-1}. This same mechanism can be considered from a different point of view. The free ferric ion has the ground state $(3d^5)^6S$ and the excited states $(3d^44p)^6P^0$ and $(3d^44p)^6F^0$. For the free ion, a transition would be allowed only to the state $^6P^0$. In the crystal field, however, the states $^6P^0$ and $^6F^0$ will be mixed and two transitions of comparable strength will be allowed.

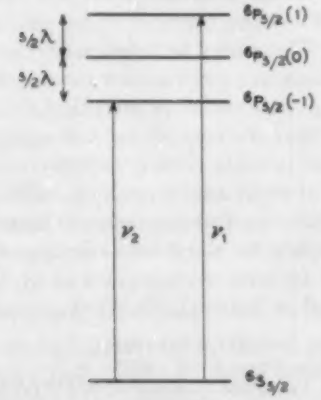

FIG. 7. Spin-orbit splitting of $(3d^44p)^6P_{\frac{5}{2}}$ in the exchange field.

The internal transitions will cause a Faraday rotation of the transmitted light in a ferromagnetic compound. This may be seen in the following way, considering for simplicity only the state $^6P^0$. The six-fold degeneracy of the ground state ^6S of the metal ion will be removed by the exchange field leaving the state $^6S_{\frac{5}{2}}$ lying lowest in energy. Similarly, the spin degeneracy of the excited state will be removed leaving a three-fold degenerate state $^6P_{\frac{7}{2}}^0$ lowest in energy. The remaining degeneracy will be lifted by the spin-orbit coupling energy $\lambda L\cdot S$ as shown in Fig. 7. Electric dipole transitions will occur between $^6S_{\frac{5}{2}}$ and the levels $^6P_{\frac{7}{2}}^0(m)$ with the matrix components

$$(^6P_{\frac{7}{2}}^0(1)|P_x|{}^6S_{\frac{5}{2}})=-M \qquad (^6P_{\frac{7}{2}}^0(1)|P_y|{}^6S_{\frac{5}{2}})=iM$$
$$(^6P_{\frac{7}{2}}(-1)|P_x|{}^6S_{\frac{5}{2}})=M \qquad (^6P_{\frac{7}{2}}^0(-1)|P_y|{}^6S_{\frac{5}{2}})=iM, \quad (1)$$

where m is the orbital quantum number of $^6P_{\frac{7}{2}}^0$, P_x and P_y are the components of the electric dipole operator, and M is the radial integral $(\frac{1}{5})^{\frac{1}{2}}(3d|er|4p)$. In terms of M, the f number of the transition is given by

$$f=(8\pi^2m\nu/hc^2)\sum_{\text{levels}}M^2. \quad (2)$$

It is easily seen that a right hand circularly polarized wave corresponding to the dipole operator P_x+iP_y will have matrix components only to the state $^6P_{\frac{7}{2}}^0(1)$, and a left hand wave only to $^6P_{\frac{7}{2}}^0(-1)$. Since these states are split, a Faraday rotation will be observed that is given in rad/cm by

$$R=\frac{4\pi^2(\epsilon)^{\frac{1}{2}}}{3hc}NM^2\frac{\nu\Delta\nu}{(\nu_1-\nu)(\nu_2-\nu)} \quad (3)$$

where ϵ is the dielectric constant of the material, N is the density of active ions, ν_1 and ν_2 are the frequencies of the upper and lower levels respectively, and $\Delta\nu$ is their difference. It will be most convenient to use (3) to express the splitting $\Delta\nu$ in terms of the experimentally

observed Faraday rotation and f number. We obtain

$$\Delta\nu=\frac{12}{\epsilon^{\frac{1}{2}}}\frac{mc}{e^2}\frac{\nu_0}{\nu}(\nu_0-\nu)^2\frac{R}{Nf}, \qquad (4)$$

where ν_0 is the average value of ν_1 and ν_2 and we have assumed $\nu-\nu_0\gg\Delta\nu$. Equation (4) has been derived in terms of the splitting of the states $(3d^4 4p)^6P_{\frac{9}{2}}^0(m)$. Actually, it applies generally to any situation where two orbital levels are split by spin-orbit interaction in the presence of a strong exchange field.

From Fig. 2 we may determine that $R=44$ rad/cm at 18 000 cm^{-1}. By taking account of the ferrimagnetic structure of yttrium iron garnet, the density of active ions is 4.22×10^{21} per cm^3. An appropriate value for $(\epsilon)^{\frac{1}{2}}$ is 2.5. By inserting the numbers and taking $\nu_0=51\,000$ cm^{-1}, we find for the experimentally determined value of $\Delta\nu$, expressed in wave numbers

$$\Delta\nu_{\text{exp}}=550/f \text{ cm}^{-1}. \qquad (5)$$

If we assume that the Faraday rotation in yttrium iron garnet is associated with an absorption having the intensity of the strongest peak in Fig. 4 we obtain $\Delta\nu_{\text{exp}}=610$ cm^{-1}. If the rotation were associated with the weaker peak, we have $\Delta\nu_{\text{exp}}=1700$, an impossibly large value. The transition which gives rise to the absorption band and Faraday rotation in the garnets must therefore have an oscillator strength close to unity and must involve an excited state split by several hundred wave numbers.

For the transition $(3d^5)^6S\rightarrow(3d^4 4p)^6P$ we may quite easily estimate from Eq. (2) that f is about 0.5.[11] The splitting $\Delta\nu$ may be estimated from the fine structure of the free ion state $(3d^4 4p)^6P$.[16] The effective spin-orbit coupling parameter λ is about 54 cm^{-1}, and the splitting will be 5λ or about 270 cm^{-1}.

We may say therefore the following: (1) the internal transitions have an oscillator strength and a splitting within a factor of about two of the experimental values. The theory also predicts two lines in the absorption spectrum as are observed in Fig. 4. It is not clear from this point of view, however, why the absorption peaks should be associated with a continuum unless by accident. The energy required for the transition $(3d^5)\rightarrow(3d^4 4p)$ should be much less than that required to ionize the $3d$ electron.

Charge Transfer Transitions

We next consider transitions in which an electron moves from a ligand orbital into a $3d$ wave function of the central ion. Referring to Fig. 6, these will be transitions in which an electron moves from a bonding orbital of p_σ or p_π character into the antibonding orbitals Γ_5^+ and Γ_3^+. The direct product of Γ_4^- with Γ_5^+ and Γ_3^+ shows that the electron can be transferred only from a wave function of symmetry Γ_4^- or Γ_5^- so that there will

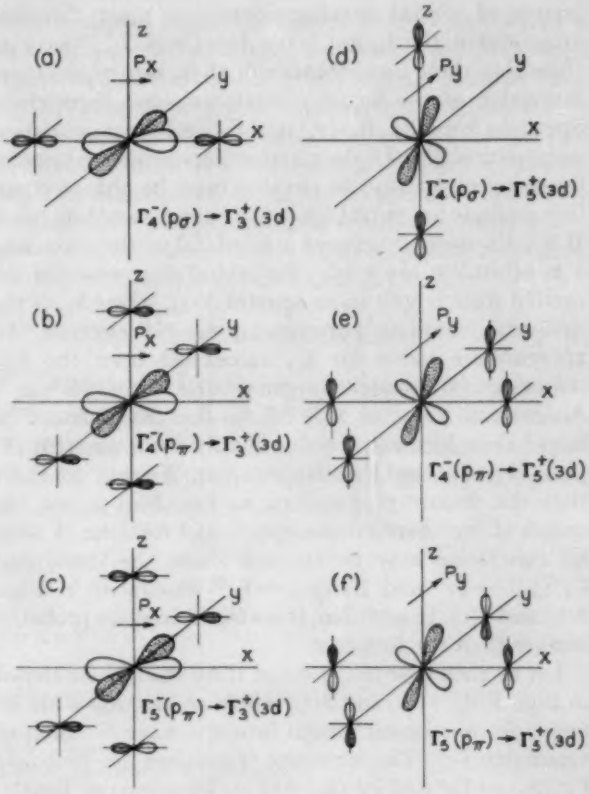

FIG. 8. Initial and final wave functions for charge transfer transitions.

be a total of six possible transitions. The six transitions are illustrated schematically in Fig. 8 where we show the initial and final wave functions of the transferring electron and the direction of the resultant dipole moment. The positive lobe of each wave function is marked by shading.

The strength of these various transitions will be determined by the overlap of the initial and final wave functions. It seems evident that the strongest transition will involve the transfer of an electron from $\Gamma_4^-(p_\sigma)$ to Γ_3^+ as in Fig. 8a. The strength may be estimated roughly from overlap integrals calculated by Tanabe and Sugano[17] and is about 0.4. The shift of an electron from Γ_4^- to Γ_3^+ creates excited states with symmetries $\Gamma_4^-\times\Gamma_3^+=\Gamma_4^-+\Gamma_5^-$, of which only Γ_4^- can be reached from the ground state. If we suppose the electron is shifted without spin change, the final state has a spin degeneracy of six and an orbital degeneracy of three. If we furthermore assume that exchange is still effective in this configuration, the spin degeneracy will be removed as before. If a Faraday rotation is to accompany the transition, we must also remove the orbital degeneracy by spin-orbit coupling. There are no matrix components of angular momentum within Γ_3^+ as we see from the product $\Gamma_3^+\times\Gamma_3^+=\Gamma_1^++\Gamma_2^++\Gamma_3^+$. Any matrix com-

[16] C. E. Moore, "Atomic energy levels," National Bureau of Standards circular 467 (1952), Vol. II.

[17] Y. Tanabe and S. Sugano, J. Phys. Soc. (Japan) 11, 864 (1956).

ponent of orbital angular momentum must therefore arise within the ligand wave functions. It is easy to show that these components will all be zero unless there is overlap of the ligand orbitals amongst themselves. Speaking formally, $\Gamma_4^-(p_\sigma)$ and $\Gamma_4^-(p_\pi)$ must overlap as suggested in Fig. 9 if the matrix components are to exist. Speaking physically, an electron must be able to circulate around the central ion in the ligand wave functions. If S is the overlap between a p_σ orbital on the x axis and a p_π orbital on the y axis, the orbital degeneracy of the excited state is split in an amount $S\lambda_{2p}$, where λ_{2p} is the spin-orbit coupling parameter for a $2p$ electron. An approximate value for λ_{2p} calculated from the fine structure of the neutral oxygen ground state is 150 cm^{-1}. An extreme value of S is 0.1, so that $S\lambda_{2p}$ cannot be larger than 15 cm^{-1}, a value totally inadequate to explain the observed Faraday rotation. We may conclude that the transition described in Fig. 8(a) is not the source of the observed absorption and rotation. A similar conclusion may be reached about the transitions $\Gamma_4^-(p_\pi) \rightarrow \Gamma_3^+$ and $\Gamma_5^-(p_\pi) \rightarrow \Gamma_3^+$ illustrated in Figs. 8(b) and 8(c). In addition, these transitions are probably weaker than the first case.

Let us turn now to the set of three transitions shown in Figs. 8(d), 8(e), and 8(f), where an electron is transferred from a ligand orbital into a d wave function of symmetry Γ_5^+. The strongest transitions are probably $\Gamma_4^-(p_\pi) \rightarrow \Gamma_5^+$ and $\Gamma_5^-(p_\pi) \rightarrow \Gamma_5^+$. By using the Tanabe and Sugano overlap integrals,[16] we have estimated the strength of these transitions to be $f=0.13$. The moving of an electron from an orbital of symmetry Γ_4^- to a wave function of symmetry Γ_5^+ creates excited states of symmetry $\Gamma_4^- \times \Gamma_5^+ = \Gamma_2^- + \Gamma_3^- + \Gamma_4^- + \Gamma_5^-$ of which again only Γ_4^- is available from the ground state. As before, any Faraday rotation must arise from the spin-orbit splitting of this state. In this case, however, matrix components of orbital angular momentum exist within Γ_5^+, and the splitting is easily calculated to be $\frac{1}{2}\lambda_{3d}$ where λ_{3d} is the spin-orbit coupling parameter for a $3d$ electron. The d wave functions of symmetry Γ_5^+ may be written $f(r)xy$, $f(r)yx$ and $f(r)zx$. The eigenfunctions of the spin-orbit interaction are $f(r)z(x \pm iy)$ and correspond to an electron circulating about the z axis. An appropriate value of λ_{3d} is 350 cm^{-1} as determined from the fine structure of the free ion state $(3d^4 4s)^6D$. The predicted splitting then is 175 cm^{-1}. If we now take account of all three transitions 8(d), 8(e), and 8(f), the effective f number of the process will be 0.4 and the effective splitting will be about 500. We must conclude therefore that charge transfer transitions into d orbitals of symmetry Γ_5^+ also come close to explaining the intensity and Faraday rotation of the absorption band.

It is interesting to note here that the electron transferred to $\Gamma_5^+(3d)$ must enter with spin reversed to the spin of the ferric ion. Consequently, the Faraday rotation produced will be opposite in sign to the rotation caused by the internal transitions to $(3d^4 4p)$. If the absolute sign of the rotation could be clearly established, and the sign conventions kept straight in the calculation it would be possible to distinguish with certainty between the two mechanisms.

One final aspect of the charge transfer transitions should be mentioned. These absorptions may be considered as involving the shift of a hole from the $3d$ shell of the central ion into the $2p$ shells of the surrounding anions. It is clear that somewhat more energy can ionize the hole completely into the s-p band of the oxygen ions. In that case, any absorption peaks resulting from charge transfer can be expected to be closely associated with a continuum of absorptions as appears to be the case in Fig. 4. The ionized hole should lead to photoconductivity.

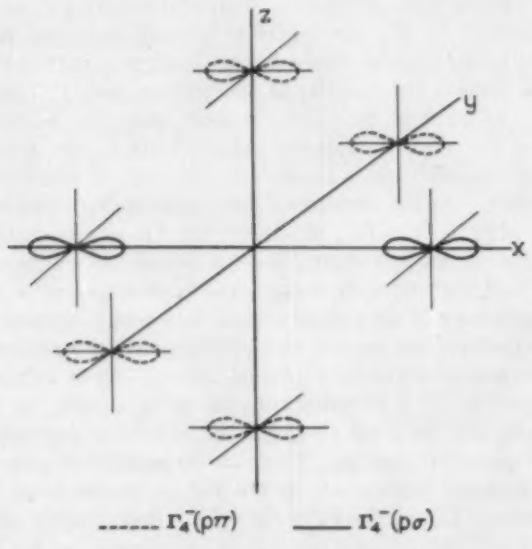

FIG. 9. Ligand wave functions of symmetry Γ_4^- formed from p_π and p_σ orbitals.

V. CONCLUSION

The absorption spectrum of the oxides containing ferric iron appears to consist of a series of sharp peaks lying near or in the visible region of the spectrum. In addition, there is a strong absorption band showing broad peaks at 39 000 cm^{-1} and 51 000 cm^{-1}. The sharp peaks are clearly identified as transitions confined to the $(3d^5)$ configuration. The absorption band is to be ascribed either to transitions to the configurations $(3d^4 4p)$ or to a charge transfer from ligand to central ion. The internal transition accounts within a factor of 2 for the strength of the band and the Faraday rotation, and the number of peaks, but fails to account for the association of the peaks with an absorption continuum. The charge transfer process also accounts for the intensity and Faraday rotation of the bands within a factor of two and gives a natural explanation of the continuum.

It does not seem at present possible to make a definite assignment of the origin of the absorption band. More experimental work should be done, and a number of

extremely interesting experiments suggest themselves. For example, a search could be made for photoconductivity in iron doped aluminum oxide and a determination made of the sign of the charge carriers. Hole conduction appearing upon irradiation in the neighborhood of 50 000 cm^{-1} would be strong evidence for the charge transfer process.

It would be particularly interesting to extend the studies of the optical properties of the ferrites begun by Sherwood, Remeika, and Williams.[5] Faraday rotation in the compounds $CoFe_2O_4$, $NiFe_2O_4$, and $CuFe_2O_4$ would be the result largely of the Co^{++}, Ni^{++}, and Cu^{++} ions since the iron ions are antiferromagnetically aligned. All of these ions have moderately strong absorptions in the visible resulting from Stark splitting of the ground state giving rise to spin allowed but parity forbidden transitions. A very strong Faraday effect such as seen in the garnets would, however, still require an allowed electric dipole transition due to charge transfer or a $3d \rightarrow 4p$ promotion. For these three ions, the charge transfer process could not lead to such a rotation since the Γ_5^+ orbitals would be filled in the excited state. A strong Faraday effect could therefore only be ascribed to internal transitions. These compounds are apparently not very transparent in the visible spectrum[5] probably because of the Stark transitions or lack of stoichiometry, and it would be necessary to make measurements below 10 000 cm^{-1}, or else obtain better crystals.

ACKNOWLEDGMENTS

The author would like to acknowledge many helpful discussions with D. L. Wood, J. F. Dillon, J. J. Hopfield, T. Moriya and A. D. Liehr. He is particularly indebted to D. L. Wood for permission to use some of his optical absorption curves prior to publication.

JOURNAL OF APPLIED PHYSICS SUPPLEMENT TO VOL. 31, NO. 5 MAY, 1960

Nuclear Resonance in Ferromagnetic Cobalt*

A. M. Portis and A. C. Gossard†
Department of Physics, University of California, Berkeley 4, California

The observation of nuclear magnetic resonance in ferromagnetic cobalt is reported. The resonance frequency for finely divided face-centered-cubic material has been measured in the intermediate temperature range. The frequency extrapolated to 0°K is 217.2 Mc/sec, and the temperature dependence in this range is in general agreement with that of the magnetization. This frequency implies a hyperfine field of 217 500 oe, which is in good agreement with the field deduced from specific heat measurements on hexagonal cobalt. The agreement in the two structures indicates that there is no dipolar contribution to the hyperfine field. The theoretical implications of this observation are discussed. The resonance line is inhomogeneously broadened with a half width of 400 kc/sec. A pattern of beats is observed at high passage rates which makes it possible to determine a spin-spin time of 25 μsec. By varying the modulation frequency under conditions of intermediate saturation the spin lattice relaxation time is measured to be 280 μsec. The resonance signal is remarkably intense, being 5×10^5 stronger than calculated for a dipole transition in the driving radio frequency field. It is shown from the saturation measurements that the rf field at the cobalt nucleus is 10^3 times stronger than the external driving field. These intensity and saturation measurements, as well as the observed line shape, establish that the resonance is driven by domain wall motion. Only those spins within the domain walls are affected. An external field reduces the intensity of the resonance but produces no shift in the resonance frequency. Both these effects are consistent with domain wall excitation. Spin-spin relaxation is interpreted as a spin wave coupling reduced in intensity by the broadening of the resonance spectrum. The spin-lattice relaxation is by spin diffusion away from the domain walls and ultimately to the lattice by coupling with the conduction electrons as suggested by the temperature dependence of the relaxation time.

INTRODUCTION

THE possibility of observing nuclear magnetic resonance in ferromagnetic materials has provided a new technique for the investigation of ferromagnetism. Each nucleus in a ferromagnet experiences a sizeable magnetic field, even in the absence of any externally applied field. Nuclear resonance in this internal field, which should be carefully distinguished from the familiar exchange field, has been observed in ferromagnetic cobalt.[1] This paper reports an experimental and theoretical study of this resonance. The value of the internal field may be obtained directly from the resonance frequency while the temperature dependence of the resonance frequency accurately yields the saturation magnetization temperature dependence. The observed nuclear resonance line width provides an upper limit on the inhomogeneity of the internal field. Further, comparison of the internal field in cubic and hexagonal phases of cobalt yields information on the dependence of the electronic configurations of cobalt on crystal structure. The resonance is found to be remarkably intense. We believe that those nuclei lying in the domain walls contribute the bulk of the resonance signal. This is because the wall motion in the radio frequency field produces a tremendous enhancement of the oscillating field seen by the nuclei. Studies of saturation effects, nuclear spin-spin relaxation, and line broadening, while all of interest in themselves,

* Supported by the U. S. Atomic Energy Commission.
† National Science Foundation Predoctoral Fellow.
[1] A. C. Gossard and A. M. Portis, Phys. Rev. Letters 3, 164 (1959).

TABLE I.

Temperature, °K	Frequency, Mc/sec
77.4	216.9
194.7	215.1
296.5	213.1

support this picture. Suhl's[2] theory of spin-spin coupling through spin waves is confirmed. Strong experimental support is found for spin-lattice coupling through interaction with conduction electrons, essentially as considered by Korringa.[3]

The initial work[1] was performed with one to five micron spherical particles,[4] prepared by hydrogen reduction of cobalt oxide[5] and predominantly cubic close-packed in structure. Subsequent investigations have been performed with five to 10 μ cobalt particles also produced by the oxide reduction process.[6] X-ray diffraction patterns confirmed that these particles as prepared are hexagonal close-packed. We searched for a resonance in this material without success. Since it is well known[7] that annealing above 430°C will convert material in this range of particle sizes to the cubic close-packed structure, the cobalt particles were then annealed. X-ray pictures established a 70% conversion to cubic, as well as a sharpening of the diffraction lines. A strong nuclear resonance having the same features as the resonance in the somewhat smaller hydrogen-reduced particles was then observed. The measurements described in this paper were made with the larger particles.

HYPERFINE FIELD

The resonance frequency of the cobalt nuclei in the face centered structure has been measured at a number of temperatures. These data are given in Table I. The frequency components in the excitation spectrum of the magnetization should lie well above the nuclear resonance frequency. The resonance frequency should then be proportional to the saturation magnetization apart from temperature dilation effects, which should be small. The resonance data shows the T^2 dependence which is usually found for the magnetization over this temperature range. We write[8]

$$\nu(T)=\nu(0)[1-(T/\theta)^2]^{\frac{1}{2}}.$$

The resonance data can be fitted reasonably well with $\nu(0)=217.2$ Mc/sec and $\theta=1400$°K, which is the observed ferromagnetic Curie temperature of cobalt.

At quite low temperatures, the excitations of the magnetization will be highly correlated and should be describable in the spin wave approximation. We should then expect the frequency to be given by the relation,

$$\nu(T)=\nu(0)[1-CT^{\frac{3}{2}}-\cdots].$$

One of the striking possibilities offered by nuclear resonance in ferromagnets is that of examining the low temperature variation in magnetization. With the present line widths, it should be possible to measure the magnetization to one part in 10^4 and this should be adequate to distinguish spin wave effects unambiguously.[9]

A theory of the nuclear hyperfine coupling in ferromagnets has been developed by Marshall.[10] We will first summarize Marshall's theory for cobalt and then compare it with the results of the nuclear resonance measurements. Marshall divides the hyperfine field into three contributions: (1) The local magnetic field, which is composed of the external plus demagnetizing fields and the Lorentz field; (2) the field from contact interaction with the 4*s* electrons, arising partly from polarization of the 4*s* electrons and partly from admixture of the functions into the 3*d* band; and (3) An atomic contribution from the core electrons surrounding the nucleus, which may be divided into a contact term from the inner 2*s* and 3*s* electrons, a contribution from the dipolar field of the 3*d* electrons, and an orbital contribution from the unquenched angular momentum of the 3*d* electrons. These contributions, with Marshall's estimates for hexagonal cobalt, are given in the first column of Table II.

TABLE II. Hyperfine field.

	Marshall	Corrected
Local magnetic fields		
External and demagnetizing field	...	...
Lorentz field	6 000	6 000
Conduction electrons		
Polarization	40 000	40 000
Admixture	(137 000)	(217 000)
Core electrons		
Contact	−128 000	−128 000
Dipolar	81 000	...
Orbital	83 000	83 000
Total	219 000	218 000

Marshall did not find it possible to calculate the admixture of 4*s* electron wave function into the 3*d* states. Instead he elected to determine the amount of *s* admixture from the experimental data. We have taken the more recent data of Arp, Edmonds, and

[2] H. Suhl, Phys. Rev. **109**, 606 (1958); J. Physique Rad. **20**, 333 (1959).
[3] J. Korringa, Physica **16**, 601 (1950).
[4] We are indebted to Mr. George Gordon for taking the electron micrograph.
[5] This sample was prepared by Murex, Ltd. and made available to us through the courtesy of Dr. J. Crangle.
[6] This material is available commercially through Matheson, Coleman, and Bell, Norwood, Ohio.
[7] H. Bibring and F. Sebilleau, Rev. Met, **52**, 569 (1955).
[8] E. C. Stoner, Proc. Roy. Soc. (London) **A165**, 372 (1938).
[9] V. Jaccarino has measured the temperature dependence of the nuclear resonance frequency between 1°K and 550°K, and finds confirmation of the $T^{\frac{3}{2}}$ spin wave prediction at low temperatures. V. Jaccarino, Bull. Am. Phys. Soc. Ser. II **4**, 461 (1959).
[10] W. Marshall, Phys. Rev. **110**, 1280 (1958).

Petersen[11] for the hyperfine field in hexagonal cobalt. The field resulting from the admixture is then 137 000 oe, implying an admixture of 3.9% 4*s* function, which is not unreasonable. This is based on the use of free atom values for the wave functions and for the *s-d* exchange and the use of the Van Vleck model[12] for the *d* orbitals.

Marshall also estimates the hyperfine field for cubic cobalt. The Lorentz fields for the hexagonal and cubic material are within 0.1% of each other and may be taken as the same. The contact fields from outer *s* electrons should be roughly comparable in hexagonal and cubic materials. Similarly, the contact interaction from the inner *s* electrons should be roughly the same, although there may be some difference in the orbital contribution. The principal difference is that the *d* orbitals must have cubic symmetry and therefore there can be no dipolar fields. By subtracting the dipolar contribution, we would expect a hyperfine field of 138 000 oe. Previous to the nuclear resonance work on pure cubic cobalt, the only data were from a measurement of the hyperfine field in a 60–40 cobalt-nickel alloy, which has the cubic close-packed structure. The effective field was found to be 161 000 oe, about 23 000 oe higher than was expected. Part of the discrepancy may arise from a difference in the orbital contribution although Marshall indicated that his treatment most likely overestimated the dipolar contribution in the hexagonal material because of the use of the Van Vleck model. Marshall hoped that a measurement of the hyperfine field in pure cubic cobalt would provide a real test of the validity of the Van Vleck model.

The nuclear resonance measurements indicate that the hyperfine field extrapolated to 0°K in pure cubic cobalt is 217 500 oe, only 1500 oe below the value given by Arp, Edmonds, and Petersen, and within their estimated error. There is evidently no significant difference between the hyperfine interaction in cubic and hexagonal cobalt. The most natural explanation of the absence of any difference between cubic and hexagonal material is that the *d* orbitals are insensitive to the uniaxial structure.[13] The condition that the *d* orbitals reflect the uniaxial structure is that their splitting in the crystal field be large compared with the width of the band. This is evidently the assumption made by Marshall. A study of crystal field effects in metals has recently been made by Leigh.[14] He finds that the effects on the *d* electrons from the crystalline field are small and that splittings are probably less than a few tenths of an electron volt. On the other hand recent calculations by J. H. Wood[15] indicate that the *d* configurations have widths of the order of volts. On this basis, it is understandable theoretically that the *d* electrons should have nearly spherical symmetry for both structures and that there is no contribution from dipolar fields. This result need not reflect on the Van Vleck model, which can as well be developed for bands widths large compared with the configuration splitting. Finally, if we accept Marshall's estimate for all but the dipolar contribution, we must expect that the contribution to the hyperfine field from admixture of 4*s* electrons into the 3*d* band is 217 000 oe, nearly equal to the net effective field. This implies an 8.4% admixture of these electrons.

LINE BROADENING AND SPIN-SPIN COUPLING

In the original measurements[1] the sample of cobalt with a paraffin binder was placed at the position of maximum rf magnetic field in the plate circuit of a marginal UHF oscillator. The oscillator was frequency modulated in the audio range. The grid voltage, established by self biasing, was amplified and then synchronously detected and finally recorded. With the observation of the tremendously enhanced resonance signal and the availability of increased amounts of sample, we adopted a very much simpler system for the studies of line broadening and spin-spin coupling. We simply insert a large sample of cobalt powder bound in paraffin in a section of 50 ohm coaxial line between a tunable radio frequency generator and a detector crystal. The dominant sample losses are magnetic in character, being produced by damping of domain wall motion. We insert sufficient sample, about 60 g of cobalt, to reduce the transmitted power to approximately 65% of its original value. Instead of finding a symmetrical dip in the transmitted power as is usual for an absorption process, we find a dispersion characteristic as is shown in Fig. 1. Our interpretation of the dispersion shape is as follows. The dominant sample losses are associated with the wall motion[16]

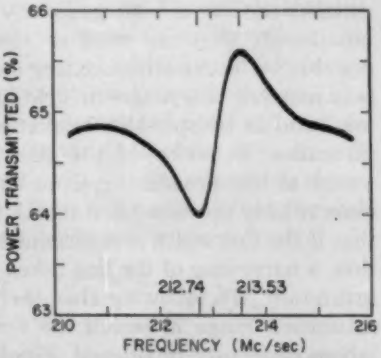

Fig. 1. Photograph of oscilloscope tracing of resonance line. The power transmitted off the resonance line is about 65%. The resonance signal produces nearly a 2% peak to peak change in transmitted power.

[11] Arp, Edmonds, and Petersen, Phys. Rev. Letters **3**, 212 (1959).

[12] J. H. Van Vleck, Revs. Modern Phys. **25**, 220 (1953).

[13] Recent polarized neutron diffraction studies of hexagonal and cubic cobalt by R. Nathans and A. J. Freeman also indicate that the *d* electrons have cubic symmetry in both structures; A. J. Freeman (private communication); Nathans, Shull, Shirane, and Andresen, J. Phys. Chem. Solids **10**, 138 (1959); R. J. Weiss and A. J. Freeman, J. Phys. Chem. Solids **10**, 147 (1959).

[14] R. S. Leigh, Proc. Phys. Soc. **71**, 33 (1958).

[15] J. H. Wood, Quarterly Progress Repts, Solid State and Molecular Theory Group, M. I. T.; see especially Rept. No. 34 (October 15, 1959).

[16] C. Kittel and J. K. Galt, "Ferromagnetic domain theory," in *Solid State Physics*, edited by Frederick Seitz and David Turnbull (Academic Press, Inc., New York, 1956), Vol. 3.

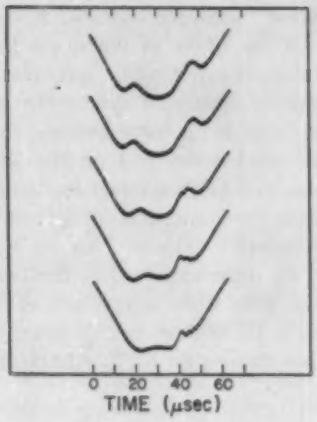

FIG. 2. Photograph of oscilloscope tracing of resonance line on repeated passage. A beat signal may be observed following the second passage when the time between passages is short. From this data the spin-spin relaxation time is determined to be 25 μsec.

and we look to a modulation of these losses by the cobalt nuclei. Although we normally neglect the nuclear contribution to the sample induction, the torque exerted by the nuclei back on the wall may not be neglected. As we shall see later, it is not unreasonable to expect that the nuclei make a contribution of several per cent to the wall losses. At frequencies far from the resonance frequency, the nuclei are unable to follow the wall motion and therefore make no contribution to the losses. Just below the resonance frequency, the nuclei make a contribution in phase with the magnetization in the wall. Exactly at their resonance frequency, they precess $\pi/2$ cut of phase and make no contribution. Just above their resonance frequency, they are π out of phase with the magnetization in the wall and act to reduce the wall losses. What we have described is just the usual dispersion characteristic. This situation is to be compared with the more usual one in metals where the nuclear resonance modulates the conduction electron losses. For this case, if the sample is large compared with a skin depth we observe the sum of absorption and dispersion characteristic. In the present case, we appear to observe just the dispersion.

We next take up the subject of line width and the broadening mechanism. We would hope to determine whether the line in homogeneously or inhomogeneously broadened; that is, whether the line is broadened possibly by lattice strains acting on the nuclear quadrupole moment or a magnetic field inhomogeneity on the one hand or by spin-spin relaxation on the other. The saturation behavior of the line should indicate the source of line broadening, even though we are able to observe only the dispersion signal. Redfield[17] has shown that if the line width is determined by spin-spin relaxation, a narrowing of the line takes place at the onset of saturation. By following this, there is an intermediate saturation range in which the line acts as if it were inhomogeneously broadened. Finally, when the rf field acting on the nuclei is comparable to the line width, a final stage of saturation sets in where the line begins to broaden and decrease in amplitude.

[17] A. G. Redfield, Phys. Rev. **98**, 1787 (1955).

Down to the lowest power levels at which we could detect a signal, we were unable to observe any of the effects which would indicate that the line width was produced by spin-spin coupling. That the line is in fact inhomogeneously broadened was established by the observation of a spin echo on rapid passage through the line. The resonance signal was sufficiently strong that with the UHF oscillator swept over several megacycles the signal could be displayed on the screen of an oscilloscope. It was observed that with the center frequency of the oscillator adjusted so that the resonance line fell just short of the maximum of the sweep a beat pattern could be observed on the resonance as it was traversed the second time. An effect of this kind was first reported by Gooden,[18] and has been explained by Gabillard.[19] One notices that if the center frequency is shifted so that the elasped time between repeated passages of the resonance is increased the beat signal decreases in amplitude. This effect is shown in Fig. 2 for various elapsed times. As interpreted by Gabillard the beats arise from nonadiabatic passage through the resonance line. The remarkable feature of the beat signal is that for an inhomogeneously broadened line it decays with the spin-spin relaxation rate rather than at a rate determined by the line width. As indicated in Fig. 2 the decay time is about 25 μsec. This estimate is supported by a more accurate measurement which involved varying the rate at which the rf is swept through the resonance. The time associated with the line width is only 0.6 μsec, very much shorter than the observed decay time. Measurements made at liquid nitrogen temperature give the same value for the relaxation time. We finally conclude that the over-all line width is determined by a static inhomogeneity; and that the observed time of 25 μsec is a spin-spin time rather than a spin-lattice time because of its temperature independence. This conclusion is supported by the direct measurement of spin-lattice relaxation.

SPIN-LATTICE RELAXATION

In his paper on nuclear resonance in metals, Redfield[17] traced the saturation behavior of the nuclei as a function of rf magnetic field intensity. He found that the response of the nuclei to the ratio frequency field was linear up to field intensities such that $\gamma^2 H_1^2 T_1 T_2 \sim 1$. This is the usual Bloch result. At higher intensities, he obtained the surprising result that the resonance line became narrow and the absorption signal saturated while the dispersion signal increased linearly with rf, as at low rf levels. We term this region intermediate saturation. The final stage of saturation is reached when the rf field becomes comparable with the line width. At rf fields greater than this the dispersion line

[18] J. S. Gooden, Nature (London) **165**, 1014 (1950).

[19] R. Gabillard, C. R. Acad. Sci. (Paris) **232**, 324 (1951). Also see the description of this effect in E. R. Andrew, *Nuclear Magnetic Resonance* (Cambridge University Press, Cambridge, England, 1956).

broadens and the signal saturates. Redfield discovered that if the signal response is measured as a function of modulation frequency in the intermediate saturation range, the signal decreases at high modulation frequencies. He found that the frequency at which the signal dropped to $1/\sqrt{2}$ of its low frequency value just corresponded to the spin-lattice relaxation rate. Redfield gives

$$(\partial\chi'/\partial\omega)_{\omega_m}=(1+i\omega_m T_1)^{-1}(\partial\chi'/\partial\omega)_0.$$

We have measured both the amplitude and phase of the signal as a function of modulation frequency[1] and obtain agreement with the expected frequency dependence. These measurements have been repeated for the present samples and we find that at room temperature and in zero external field $T_1=280$ μsec. At liquid nitrogen temperature and under the same conditions, we obtain $T_1=600$ μsec, nearly inversely proportional to the square root of the absolute temperature.

To summarize the relaxation measurements, we believe that the over-all line width arises from an inhomogeneity in nuclear resonance frequency. We are unable to determine whether the source of the inhomogeneity is quadrupole broadening or magnetic field broadening, although the latter seems more likely. Further, we cannot determine directly whether the inhomogeneity is on an atomic scale or varies only over much larger distances. Theoretical arguments, which we will discuss later, suggest that the inhomogeneity is on an atomic scale. Nuclear spins are not wholly decoupled from each other by the inhomogeneity, and spin-spin coupling is of importance. We measure a time for spin exchange of 25 μsec, independent of temperature. Finally, the rate at which spin energy is transferred to the lattice may be measured at intermediate saturation and is found to be 280 μsec at room temperature and longer at low temperatures.

SATURATION AND ENHANCEMENT

As was stated earlier, we attempted to detect the onset of intermediate saturation by looking for a change in either line width or line shape at low power levels. We were unable to observe any such change. This indicated (1) that the line was inhomogeneously broadened and (2) that the variation in sample losses is produced primarily by the real part of the susceptibility. As Redfield[17] has shown, the apparent spin-lattice relaxation time decreases as the sample drops out of intermediate saturation. We rather arbitrarily take it that the apparent relaxation time is 0.8 of the actual time when the saturation parameter $\gamma^2H_1^2T_1T_2$ is equal to unity. Our measurements of apparent spin-lattice relaxation time as a function of rf field are shown in Fig. 3. As may be seen from the figure, the relaxation time is 0.8 of the actual time at an rf field H_x approximately 0.002 oe. Now, if we calculate the saturation parameter assuming that $H_x=2H_1$, we obtain a saturation parameter equal to 0.3×10^{-6}, over six orders

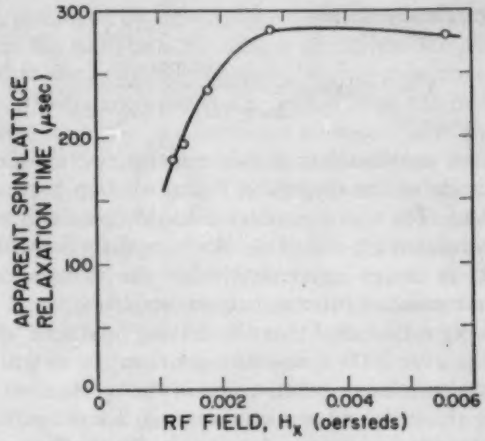

FIG. 3. Apparent spin-lattice relaxation time vs rf field. At high rf fields a spin-lattice time of 280 μsec is measured. As the rf field is reduced the apparent spin-lattice time shortens. The saturation parameter is taken to be unity for H_x about 0.002 oe.

smaller that we had expected. There are two possibilities: Either for some unexplained reason the relaxation times are very much longer than our measurements indicate, or the rf fields seen by the nuclei are very much larger than the external rf field. Let us suppose the latter and write

$$2H_1=\eta Hx.$$

The measurements of the onset of saturation would then indicate that $\eta\simeq1800$. We can check this interpretation by going to very high rf power. As Redfield has shown, the onset of final saturation occurs when H_1 is equal to the half width of the resonance line, in our case 400 oe. If we are correct in assuming that the driving field seen by the nuclei is enhanced by a factor of 2000 we should go into final saturation at an external rf field of about half an oersted. To produce an rf field of even this magnitude on a 50 ohm line requires a kilowatt of power at 200 Mc/sec. Since this amount of power was not available, we constructed a coaxial cavity resonant at the nuclear frequency. The cavity was a half wavelength long. Power was coupled in through a coupling loop so as to nearly match the cavity to the line. The level of excitation in the cavity was sampled with a second small coupling loop. The empty cavity had a Q of about 1000. Sufficient sample was introduced to reduce the Q to about 100. At a Q of 100 one might hope to saturate the dispersion signal with about 10 watts of power. We expect that the dispersion signal at high rf fields will be given by

$$\chi'(\omega)=\tfrac{1}{2}\chi_0\omega\int\frac{\omega-\omega'}{\gamma^2H_1^2+(\omega-\omega')^2}g(\omega')d\omega',$$

where $g(\omega')$ is the normalized line shape. If we take, for simplicity, that $g(\omega')$ is Lorentz;

$$g(\omega')=\frac{1/\pi\Delta\omega}{1+(\omega'-\omega_0)^2/\Delta\omega^2},$$

then we finally obtain

$$\chi'(\omega)=\tfrac{1}{2}\chi\omega\omega_0\frac{\omega_0-\omega}{(\Delta\omega+\gamma H_1)^2+(\omega_0-\omega)^2}.$$

From an examination of this relation, we expect the magnitude of the dispersion signal to drop to $\frac{1}{2}$ when $\gamma H_1=\Delta\omega$. The signal is observed to drop to this value at a calculated H_x of 0.61 oe. We compute $\eta=400/0.305=1300$ in rough agreement with the determination from the onset of intermediate saturation.

Having established that the driving field seen by the nuclei is over 1000 times stronger than the external rf field, we turn to an examination of the mechanism producing this tremendous enhancement. Even before the saturation measurements it was noted[1] that the present nuclear signal was very much stronger than would be expected in the external rf field. It was proposed that domain rotation might be exciting the nuclear resonance. A generous estimate of the expected enhancement put the rf field seen by the nuclei at 100 times stronger than the external rf field. This fails by at least a factor of ten to account for the observed enhancement. We can demonstrate that those nuclei lying in domain walls, however will be driven by rf fields sufficiently large to account for the observed enhancement.[20]

For simplicity, we consider a spherical particle with a single domain wall at its center. If we apply a field H_x in the plane of the wall, there will be a displacement of the wall to the left as shown in Fig. 4. The wall displacement will be limited by demagnetizing fields, and we expect the wall to be displaced a distance

$$\frac{z}{D}\simeq\frac{\mu-1}{4\pi+N(\mu-1)}\frac{H_x}{M_s}\simeq\frac{1}{N}\frac{H_x}{M_s},$$

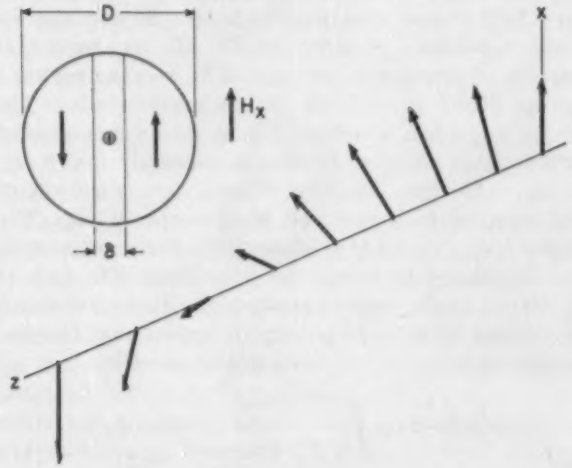

FIG. 4. Diagram of a particle with a single domain wall. A field H_x causes the wall to move to the left. The spins in the wall will all rotate slightly in the counter-clockwise direction, exciting the nuclear resonance.

[20] This possibility was first suggested by Dr. P. W. Anderson.

where μ is the permeability, assumed to arise from wall displacement only, D is the domain size, and N is a demagnetizing factor. Now, when the wall is displaced by a distance z, each moment on the line will rotate through an angle

$$\theta=\pi z/\delta.$$

If we denote the hyperfine field as H_n and H_x is an alternating field, the nuclei will experience a driving field

$$2H_1=\theta H_n=\frac{\pi}{N}\frac{H_n}{M_s}\frac{D}{\delta}H_x.$$

The enhancement factor is then

$$\eta=\frac{2H_1}{H_x}\simeq\frac{\pi}{N}\frac{D}{\delta}\frac{H_n}{M_s}.$$

If we take as reasonable values a domain wall thickness of 0.1 μ, and a domain diameter of 1 μ with $H_n=220\,000$ and $M_s=1400$, we obtain a value for η of 1200. Within the very considerable uncertainty in domain size, we consider that the mechanism of wall displacement can well account for the enhancement.

In order that the wall displacement mechanism produce a resonance at the static value of H_n, we require that the angle through which a given magnetization rotates be small or, what is equivalent, that the wall displacements produced by the radio frequency field be small compared with the wall thickness. The ratio of the displacement to the thickness is given by

$$(z/\delta)=(1/N)(D/\delta)(H_x/M_s).$$

The largest values of H_x, which we have used in these experiments, have been about one oersted. Under these circumstances, the fractional wall displacement is about 0.2%. We would expect a shift of the resonance to lower frequencies by less than one part in 10^5. This is too small a shift to be detectable with the present line widths.

Although we have accounted for the magnitude of the driving field at the cobalt nuclei, we have not as yet considered the mechanism of energy absorption. If we take the rate of energy absorption in the walls to be given by

$$dW/dt=2\omega\chi''H_1^2=\tfrac{1}{2}\omega\chi''(H_n/M)^2M_y^2,$$

we fail to account for the observed absorption. First, the above expression gives the wrong line shape and second it predicts a saturation of the observed signal which does not take place. More likely is that the principal resonance signal represents a modulation of the wall losses by the nuclear precession. As shown in Fig. 1 under conditions of 65% transmission of power through the sample, the nuclear signal represents a peak to peak change of 1.7%. Then the nuclei are producing approximately a 5% change in wall losses. We

will demonstrate from a phenomenological theory of precession of the wall magnetization that the observed change in absorption is quite reasonable and that a dispersion shape is to be expected.

We write an equation of motion for the magnetization in the wall as the sum of three terms:

$$\frac{d\mathbf{M}}{dt}=\gamma_e(\mathbf{M}\times\mathbf{H})+\gamma_e(H_n/M)\mathbf{M}\times\mathbf{m} -(\lambda/M^2)\mathbf{M}\times(\mathbf{M}\times\mathbf{H}).$$

The first term results from the field in the wall. The second term is the torque exerted by the nuclei back on the wall. Finally, the third term is a phenomenological damping term as introduced by Landau and Lifshitz. The rate at which work is done on the wall may be written as

$$\frac{dW}{dt}=\mathbf{H}\cdot\frac{d\mathbf{M}}{dt}=(\lambda/M^2)(\mathbf{H}\times\mathbf{M})^2+\gamma_e(H_n/M)\mathbf{m}\cdot\mathbf{H}\times\mathbf{M}.$$

The principal component of the alternating field is normal to the wall and results from demagnetizing fields. We take $H=H_z=-4\pi M_z$. Then the expression for the rate at which work is done becomes

$$\frac{dW}{dt}=\lambda H_z^2\left[1-\frac{\gamma_e H_n}{4\pi\lambda}\left(\frac{m_y}{M_z}-\frac{M_y}{M}\frac{m_z}{M_z}\right)\right].$$

As long as the wall displacements are small the contribution from m_z may be neglected. We write for the transverse component of nuclear magnetization,

$$m_y=(H_n/M)(\chi_{yy}M_y+\chi_{yz}M_z).$$

For a domain wall driven at a frequency below its relaxation frequency, the principal component of the magnetization will be in the plane of the wall. We expect from the equations of motion:

$$M_z\simeq-M_y(\lambda+i\omega)/4\pi\gamma_e M.$$

This puts M_z at about 1% of M_y and we may safely neglect it. The dominant wall losses may then be written as

$$\frac{dW}{dt}=\lambda H_z^2\left[1+\left(\frac{\gamma_e H_n}{\lambda}\right)^2\chi_{yy}\Big/\left(1+\frac{i\omega}{\lambda}\right)\right].$$

Observed losses are given by the real part of this expression. By dropping imaginary terms we obtain:

$$(dW/dt)=\lambda H_z^2\{1+(\gamma_e H_n/\lambda)^2[\chi'+(\omega/\lambda)\chi'']\}.$$

The above expression shows three contributions to the wall losses: (1) The usual wall losses present in the absence of nuclear coupling, (2) a modulation term from the torque exerted by the nuclei on the wall, and (3) the direct nuclear losses which must be fed by the wall. A complete treatment would also include the losses produced by driving the nuclei directly with the field in the wall, but this term is negligible. We observe first that the imaginary part of the susceptibility enters reduced by a coefficient ω/λ, which is of the order of 0.2. We would not expect to see an appreciable absorption signal even in the absence of saturation in agreement with experiment. The dominant nuclear signal then will have a dispersion characteristic. The real part of the susceptibility is positive below the resonance frequency and negative above. We then expect the losses to be larger on the low frequency side as is observed. We finally estimate the fractional change in wall losses resulting from the nuclear coupling.

With a sample of finely divided cobalt we observe that the transmitted power drops to $1/e$ of its initial value in about 25 cm of path or 0.2 wavelength. We expect then that the dissipation factor will be about five times the angular frequency or about 6×10^9. By taking χ' to be the Q of the line times the static nuclear susceptibility we obtain

$$(\gamma_e H_n/\lambda)^2(\omega/2\Delta\omega)\chi_0\sim.05.$$

This estimate is in good agreement with the observed signal. We conclude that a modulation of wall losses by the nuclei can well account for the observed signal.

EXTERNAL FIELD EFFECTS

If one examines the nuclear resonance in an external field, one naively expects that for a field sufficiently large to magnetize the particles the resonance frequency should be shifted by an amount γH. If one takes account of demagnetizing fields this should be reduced to

$$\Delta\omega=\gamma(H-NM).$$

One would expect that in a field of 1500 oe the resonance would be shifted 200 kc/sec or one part in 10^3. This is a detectable shift and should be observed. We find that the shift is less than one part in 10^4. The absence of any appreciable shift is understandable when one recognizes that only those spins within domain walls are observed. Domain walls move in such a way as to keep the local field below the coercive field. This means that at most the local field at the cobalt nuclei is increased by a fraction of an oersted. The shift produced by this magnitude of field is below the limits of observation under high field conditions.

A striking effect of an external magnetic field is the reduction that it produces in the observed signal. Above 1000 oe the signal drops off very rapidly and has dropped to one per cent of its value in a field of 5000 oe.[1] Under the same conditions, the sample losses decrease also, but not so spectacularly. Evidently, the decrease in signal results from the disappearance of domain walls as the sample is magnetized. One can compare the field dependence of the signal with that of the transverse permeability. One finds that the resonance signal drops off much more rapidly than does the permeability.

This is understandable in terms of the usual picture of magnetization processes. At low fields the predominant magnetization process is reversible wall motion. At somewhat higher fields we have irreversible wall processes. Finally, when the internal field exceeds the coercive field domain rotation processes are dominant. Now if the nuclear resonance is driven by wall motion exclusively, we would expect the resonance to be appreciably reduced by the time that domain rotation becomes important. This seems to be what is happening in the cobalt particles.

THEORY OF SPIN-SPIN AND SPIN-LATTICE RELAXATION

We finally discuss the processes that appear to be responsible for spin-spin and spin-lattice relaxation. The coupling of nuclear spins in ferromagnetic and antiferromagnetic media has been discussed by Suhl.[2] He finds that the usual dipolar coupling is dominated by a second order process involving virtual spin wave excitation in a way reminiscent of the Ruderman-Kittel[21] coupling through conduction electrons. The spin wave theory gives a second moment,

$$\langle\Delta\omega^2\rangle=[I(I+1)/24\pi S^2]\omega_0^2(\omega_0/\omega_{ex})^2(\omega_{ex}/\omega_{loc})^{\frac{1}{2}},$$

where ω_0 is the central nuclear resonance frequency, and ω_{loc} and ω_{ex} arise from writing the spin wave spectrum in quadratic form,

$$E(k)=\hbar(\omega_{loc}+\omega_{ex}a^2k^2).$$

When the resonance line is broadened the spin-spin relaxation time will be longer than what one would calculate from the second moment of the interaction. If the line broadening is purely static and the spins are completely uncorrelated we obtain by perturbation theory[22]

$$1/T_2=\langle\Delta\omega^2\rangle/\Delta\Omega,$$

where $\Delta\Omega$ is the half width of the distribution. If we take $\Delta\Omega$ to be associated with the observed absorption line we calculate

$$\tau_s=[\langle\Delta\omega^2\rangle]^{-1}=3.2\ \mu\text{sec}.$$

This relaxation time implies a local field in the Suhl theory

$$H_{loc}=\omega_{loc}/\gamma\sim 6\ \text{oe}.$$

If we were observing the interaction between nuclear spins in the bulk we would expect H_{loc} to be of the order of several hundred oersteds, the expected anisotropy field. It is not unreasonable that the local field within a domain wall may be very much smaller than this since the possibility of free wall motion should reduce the threshold of the excitation spectrum.

We next consider relaxation of the cobalt nuclear spins to the lattice. We expect that we will have to consider two kinds of processes. First, nuclear spins may relax directly to the lattice. The most effective relaxation mechanism appears to be through the conduction electrons. A theory for a ferromagnetic metal would differ from the Korringa theory[3] because of the strong exchange coupling of the conduction electrons to the core. The electron spin transitions would then be between eigenstates of conduction electron-core interaction. This amounts to a spin wave expansion of the conduction electron-nuclear interaction. If the Fermi energy of the conduction electrons is high compared with the exchange energy, we expect essentially the Korringa result. For a system of identical spins driven equally by the rf field direct relaxation to the lattice is all that need be considered. However, if only a small fraction of the spins are excited by the rf field as in the present problem, then magnetic energy may be carried away from the nuclei in the wall by spin diffusion. According to Suhl the interaction between a pair of spins separated by a distance r_{12} is

$$\mathcal{H}_{12}=-\frac{\hbar\omega_0^2}{8\pi S\omega_{ex}}\frac{a}{r_{12}}\exp\left[-\left(\frac{\omega_{loc}}{\omega_{ex}}\right)^{\frac{1}{2}}\frac{r_{12}}{a}\right]I_1^-I_2^+$$

From this expression, we compute a mean free path for diffusion

$$\Lambda=(\omega_{ex}/2\omega_{loc})^{\frac{1}{2}}a$$

We expect that the characteristic time for diffusion within the wall is just the spin-spin time T_2 which we measure. We assume that this time also applies for diffusion near the wall. We distinguish two diffusion constants, that for diffusion within the wall

$$D_1=\Lambda_1^2/3T_2$$

and that for diffusion outside the wall

$$D_2=\Lambda_2^2/3T_2,$$

where Λ_1 and Λ_2 are the mean free paths within the wall and within the domain volume, respectively.

Let S_1 be the density of the z component of nuclear spin within the wall. Let the transition probability in the rf field be w and let τ_ℓ be the relaxation time for direct coupling to the lattice. Under steady conditions we have:

$$(dS_1/dt)=wS_1-(S_1-S_0)/\tau_\ell+D_1(d^2S_1/dz^2)=0$$

The spin density outside the wall is represented by S_2. Since these spins are not driven by the rf field their equation of motion will be

$$(dS_2/dt)=-(S_2-S_0)/\tau_\ell+D_2(d^2S_2/dz^2)=0$$

We look for a solution such that both S and $D\,dS/dz$ are continuous at the boundary. We obtain within the wall

$$S_1=[S_0/(1+w\tau_\ell)][1+A\cosh K_1z],$$

[21] M. A. Ruderman and C. Kittel, Phys. Rev. **96**, 99 (1954).
[22] A. M. Portis, Phys. Rev. **104**, 584 (1956).

where

$$A=w\tau_\ell/[\cosh K_1\delta/2+(1+w\tau_\ell)(K_2/K_1)\sinh K_1\delta/2]$$

and

$$K_1=[(1+w\tau_\ell)/D_1\tau_\ell]^{\frac{1}{2}},\ K_2=[1/D_2\tau_\ell]^{\frac{1}{2}}.$$

A sketch of S both within and outside the wall is shown in Fig. 5. We define an effective relaxation time such that the average value of S_1 within the wall is given by

$$\langle S_1\rangle=S_0/(1+wT_1).$$

We obtain for the effective spin-lattice relaxation time at low rf levels:

$$T_1=\left[1-\frac{2}{K_1\delta}\frac{\sinh K_1\delta/2}{\cosh K_1\delta/2+(K_2/K_1)\sinh K_1\delta/2}\right]\tau_\ell.$$

The quantity $K_1\delta/2$ is small since the spin excitation diffuses easily within the wall. On expanding the bracketed expression, we obtain

$$T_1=[K_2\delta/(2+K_2\delta)]\tau_\ell.$$

On taking the usual expression for the width of a domain wall

$$\delta\sim\pi a(\omega_{ex}/\omega_{loc})^{\frac{1}{2}},$$

we finally obtain as the expression for the actual spin lattice relaxation time:

$$\tau_\ell=(T_1^2/6\pi^2T_2)[1+(1+6\pi^2T_2/T_1)^{\frac{1}{2}}]^2.$$

On taking the room temperature values of $T_1=280$ μsec and $T_2=25$ μsec, we calculate, for $T=300°$K:

$$\tau_\ell=0.6\text{msec}.$$

Based on the data taken at liquid nitrogen temperature we calculate $\tau_\ell=2.0$ msec for $T=77°$K. These times are inversely proportional to the absolute temperature to within the accuracy of the measurements. We have inserted reasonable values for cobalt into the Korringa expression[3] for relaxation through contact interaction with the conduction electrons. We calculate a room temperature relaxation time of 11.4 msec, over an order longer than the observed relaxation time. According to arguments of Mitchell,[23] in cases where the nuclear quadrupole moment is large and there is p or higher admixture into the conduction band, one may expect strong relaxation through quadrupolar interaction with the conduction electrons. This appears to be an attractive possibility in accounting for the rapid relaxation in metallic cobalt.

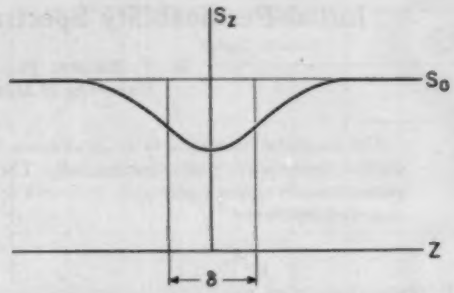

FIG. 5. Diagram of the z component of the spin as a function of position. Spin diffusion processes take the spin energy out of the wall where it finally goes to the lattice through contact with conduction electrons.

To summarize our views of the dominant relaxation processes we consider first that the observed line width results from static broadening. A first order variation in hyperfine coupling through the sample because of lattice strain is not unlikely. The observed transverse correlation time of the spins is much longer than what the line width would indicate, being 25 μsec. This observed spin-spin time is surprisingly short even on the basis of the Suhl theory. We feel that this is because we are observing the relaxation time of spins within the domain wall where the local magnetic field may be weaker than in the bulk. We find from the onset of saturation or better from the dependence of the resonance signal on modulation frequency that the spin lattice time is 280 μsec at room temperature and twice this at 77°K. This spin-lattice time is also quite short and has a $T^{-\frac{1}{2}}$ dependence rather than the expected T^{-1} dependence for interaction with conduction electrons. We feel that this altered temperature dependence results from spacial diffusion of the excitation away from the domain wall. No attempt has been made to study the details of spectral diffusion. From the fact that rapid passage effects could not be observed[1] it is believed that this diffusion is quite rapid.

ACKNOWLEDGMENTS

We would like to acknowledge helpful conversations with Dr. H. Suhl and Dr. P. W. Anderson. Professor C. Kittel has made a number of valuable suggestions regarding the interpretation of the present work.

[23] A. H. Mitchell, J. Chem. Phys. **26**, 1714 (1957).

Initial-Permeability Spectra of Microscopic Iron-Oxide Particles*

W. F. Brown, Jr., J. P. Hanton, and A. H. Morrish
University of Minnesota, Minneapolis 14, Minnesota

The magnetic resonance of single-domain ferromagnetic particles in zero applied steady magnetic field is studied theoretically and experimentally. The axial ratio of the powder particles deduced from the resonance measurements agrees reasonably well with optical data. This is strong evidence regarding the origin of the observed resonance.

THE phenomenon of magnetic resonance usually is observed by applying an alternating magnetic field perpendicular to a large steady magnetic field. However, whenever some strong orienting force is present, resonance may be observed at some experimentally convenient frequency without the application of an external steady field. This strong orienting force may be considered equivalent to an externally applied steady magnetic field; indeed it is often called the effective field. Such is the situation for single-domain ferromagnetic particles. The dipole-dipole interaction (or the free pole distribution) of such a particle produces a demagnetizing field; this is the effective field in this case. For our purposes a single-domain particle is defined as one that has uniform magnetization in zero applied field.

Consider a particle of spontaneous magnetization $\mathbf{M}$, having the shape of a prolate ellipsoid of revolution, with longitudinal demagnetization factor D_a, transverse demagnetization factor D_b, and negligible crystalline anisotropy. In zero applied field, the magnetization $\mathbf{M}$ will lie along the particle axis, called the z direction. Now, let an alternating field $\mathbf{H}_{ac}=\mathbf{H}_1\cos\omega t$, of small amplitude, be applied perpendicular to the particle axis, say along the x direction. Then, the equation of motion is given by

$$\frac{d\mathbf{M}}{dt}=\gamma\mathbf{M}\times\mathbf{H}_{eff}+\text{damping} \tag{1}$$

where $\mathbf{H}_{eff}=\mathbf{H}_{ac}-(\partial W/\partial\mathbf{M})$; W is the demagnetization energy, $W=\frac{1}{2}(D_b-D_a)M^2$, and γ is the ratio of the magnetic moment to the angular momentum. The damping is given by some appropriate expression, such as that proposed by Landau-Lifshitz, Gilbert, or Bloch. The solution to this equation to the first order of small quantities gives the alternating component of magnetization,

$$\mathbf{M}_{ac}=M(\alpha\mathbf{i}+\beta\mathbf{j}), \tag{2}$$

where α and β are direction cosines and $\mathbf{i}$ and $\mathbf{j}$ are unit vectors with respect to the x and y axes respectively.

Unfortunately the powders available today always consist of particles of various shapes. Let the volume fraction of particles with D_b-D_a between η and $\eta+d\eta(0\leqslant\eta\leqslant 2\pi)$ be $\phi(\eta)d\eta$, and let the volume fraction of total space occupied by the particles be p. Then this shape distribution is taken into account by multiplying the magnetization (2) by $p\phi(\eta)d\eta$ and integrating.

Usually one is concerned with a powder whose particles are oriented at random. Let the angle the equilibrium direction of $\mathbf{M}$ (the particle axis) makes with $\mathbf{H}_{ac}$ be θ for a particular particle. Then only the component $H_{ac}\sin\theta$ affects $\mathbf{M}_{ac}$. On averaging, assuming an isotropic distribution, one obtains an expression for the susceptibility of the powder, $\chi=(M\alpha/H_{ac})$. The quantity $M\beta$ averages to zero.

If the line width of an individual particle is small, at least as compared with the over-all width resulting from the particle size distribution, an approximate formula is obtained by letting the damping factor approach zero. The result is

$$\chi_1=(2/3)pM^2P\int_0^{2\pi}\phi(\eta)\frac{M^2\eta}{(M^2\eta)^2-(\omega\kappa)^2}d\eta$$

and (3)

$$\chi_2=\frac{\pi}{3}p\phi\left(\frac{\omega\kappa}{M^2}\right)$$

where $\chi=\chi_1-j\chi_2$, $\kappa=(M/\gamma$, and $P\int$ denotes the principal value of the integral. In this derivation the interaction between particles has been neglected. It is not clear at present how this local field can be treated.

Hence, provided the above approximation can be made, the value of χ_2 at any one frequency is determined by the fraction of particles with a certain D_b-D_a. This result permits a straightforward determination of the shape distribution for the powder. This distribution may then be compared with that obtained by optical methods. On the other hand there is a contribution to χ_1 at any one frequency from all the particles of the powder. Hence, the data analysis for the real part of the susceptibility is more difficult.

Experiments have been carried out with four powders of $\gamma-Fe_2O_3$. These powders differed in their particle size and shape distributions. These distributions as determined by an electron microscope have been published previously in connection with other experiments.[1] The particles are acicular in shape; the arithmetic mean axial ratios for the various powders are listed in Table I. It has been shown that the magnetic properties of similar acicular Fe_3O_4 particles are primarily determined

* This research was supported in part by the U. S. Air Force through the Air Force Office of Scientific Research (ARDC).

[1] A. H. Morrish and L. A. K. Watt, Phys. Rev. **105**, 1476 (1957).

TABLE I. Data on four γ-Fe_2O_3 powders.

Powder	Axial ratio from optical data	Resonance frequency (kmc/sec)	Axial ratio from resonance data
1	6.5	5.20	3.9
2	5.6	5.00	3.5
3	5.3	4.85	3.3
4*a*	3.5	4.45	2.9

$M=390$ at $T=300°K$

by shape anisotropy above the transition temperature.[2] While the evidence is less strong for the $\gamma-Fe_2O_3$ particles, it nevertheless is likely that neglect of the crystalline anisotropy is a good approximation here also. The powders were immobilized by suspension in paraffin with $p=0.15$. The initial permeability of these powder-paraffin mixtures has been determined over a wide range of frequencies, but in this paper we limit the range to 1–7.3 kilomegacycles per second. The measurements were made with coaxial lines, and the data were analyzed by utilizing standard transmission line theory.[3]

Typical results are shown in Fig. 1; the curves shown are for $\gamma-Fe_2O_3$ powders No. 1 and 4*a* in the notation of Table I. While there were slight differences in the shapes of the μ_1-1 curves, the frequency at which $\mu_1-1=0$ was nearly the same for the four powders ($f\approx 5.5$ kmc). The frequency at which μ_2 had its maximum value, together with the corresponding axial ratio calculated from Eq. (3), is listed in Table I. The optical axial ratio agrees with that obtained from the resonance data within a factor considerably less than two for each powder. This is much better agreement than is obtained from coercive force or remanence data.

Inclusion of the damping broadens and flattens the μ_2 curve, leading to an appreciable error in the location of the maximum. To first order the neglect of the damping does not change the position of the maximum; hence, it is at this frequency that one expects the best agreement with the optical data.

The following factors may explain the observed differences in axial ratios of Table I. First, particle interactions have been neglected; but since the volume density of the samples was only 15%, it may be that interactions are not of major importance. Second, the particles do not have exactly a prolate ellipsoidal shape. Finally, there is evidence from other experiments[1,2] that the least acicular particles (mainly powder 4*a*) are slightly larger than the critical single-domain size.

Magnetite (Fe_3O_4) powders produced by reducing the above four $\gamma-Fe_2O_3$ powders were also studied. Preliminary electron microscope data indicate that the Fe_3O_4 particle size and shape distributions remain almost the same as they were for the corresponding

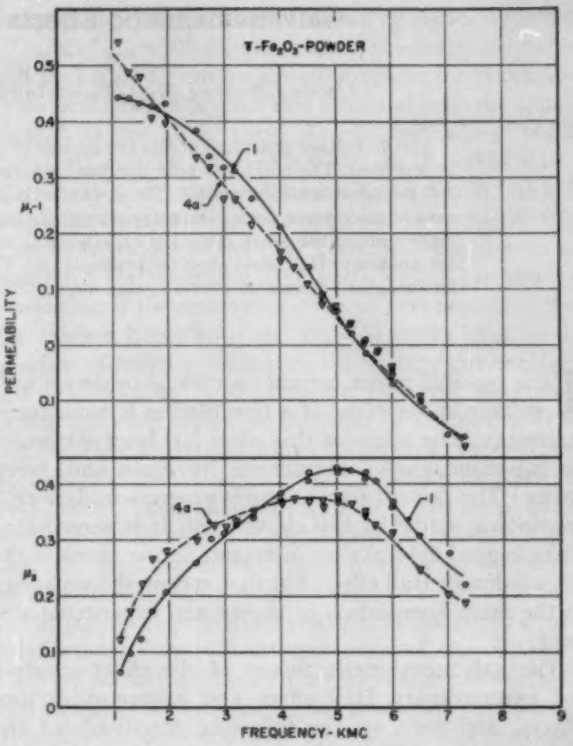

FIG. 1. Initial permeability spectrum for two γ-Fe_2O_3 powders, containing particles close to the single-domain size.

$\gamma-Fe_2O_3$ powders. The frequency at which $\mu_1-1=0$ is higher, being about 7 kMc/sec. The μ_2 curves have much flatter maximums, perhaps indicating that the natural line width of an individual Fe_3O_4 particle is considerably greater than for a $\gamma-Fe_2O_3$ particle. As a result the error in locating the maximum of μ_2 is very large; nevertheless the agreement between the optical and resonance axial ratios is of the same order of consistency as for the $\gamma-Fe_2O_3$ case.

The main conclusions are the following:

(1) The observed resonance is the result of the gyromagnetic behavior of the magnetization vector in the effective field. While it has been suspected that the resonance in sintered material had the same origin, the evidence was not as direct as in this experiment.[4]

(2) The axial ratio deduced from the resonance data is in much better agreement with the optical values than in experiments that involve magnetization reversal, such as measurements of the coercive force or remanence. In the latter experiments nonuniform reversal modes may be important[5]; they are not likely to be important in our experiment. Our results thus give indirect support for the existence of these reversal modes.

[2] A. H. Morrish and L. A. K. Watt, J. Appl. Phys. **29**, 1029 (1958); C. E. Johnson, Jr., and W. F. Brown, Jr., J. Appl. Phys. **30**, 1365 (1959).

[3] See for example, J. B. Birks, Proc. Phys. Soc. (London) **60**, 282 (1948); G. T. Rado, R. W. Wright, and W. H. Emerson, Phys. Rev. **80**, 273 (1950).

[4] G. T. Rado, V. J. Folen, and W. H. Emerson, Proc. Inst. Elec. Engrs. **104B**, Suppl. 5, 198 (1957); S. E. Harrison, C. J. Kriessman, and S. R. Pollack, Phys. Rev. **110**, 844 (1958).

[5] W. F. Brown, Jr., Phys. Rev. **105**, 1479 (1957); E. H. Frei, S. Shtrikman, and D. Treves, Phys. Rev. **106**, 446 (1957)

Galvanomagnetic Effects in Ferromagnetic Resonance*

M. H. Seavey, Jr.
Lincoln Laboratory, Massachusetts Institute of Technology, Lexington 73, Massachusetts

The dc voltage generated across the surface of a thin ferromagnetic film during ferromagnetic resonance is described. The effect has been analyzed in terms of the combined action of the extraordinary Hall effect and a magnetoresistance effect. The dc character arises from the dependence of the voltage on double products of microwave fields. Data are presented, and it is shown that the theory gives the proper order of magnitude of the effect. Also, the experimental voltage versus steady magnetic field curves show that the extraordinary Hall effect plays the principal role. The voltage provides a new and sensitive means of studying ferromagnetic resonance effects in thin films.

It is possible under certain conditions to detect a dc voltage in the plane of a thin film on ferromagnetic resonance. The origin of this effect has been attributed to galvanomagnetic interactions by Egan and Juretschke.[1] The present paper reports progress to date on a continuing study[2] of this dc voltage. It is shown that there is good evidence for interpretation in terms of the extraordinary Hall effect, but that certain discrepancies in the exact comparison of theory and experiment still exist.

The galvanomagnetic theory of the effect involves the extraordinary Hall effect and magnetoresistance effects, and rests on the following equation[3] for the electric field,

$$\mathbf{E}=\rho_\perp\mathbf{J}+(\rho_{11}-\rho_\perp)\frac{\mathbf{J}\cdot\mathbf{B}}{B^2}\mathbf{B}+R_0\mathbf{B}\times\mathbf{J}+4\pi R_0(\alpha-1)\mathbf{M}\times\mathbf{J}. \quad (1)$$

The first two terms on the right of Eq. (1) are magnetoresistance terms, the third is the ordinary Hall term and the last is the extraordinary Hall effect term. $\rho_\perp$ and ρ_{11} are the sample resistivities perpendicular and parallel to the magnetic induction $\mathbf{B}$, R_0 is the ordinary Hall coefficient, α is the extraordinary Hall "field parameter," $\mathbf{M}$ is the magnetization vector, and $\mathbf{J}$ is the current density. When, as in a resonance experiment, $\mathbf{B}$, $\mathbf{M}$, and $\mathbf{J}$ have microwave components, product terms appear which, in general, have nonzero average values. Thus a dc voltage is generated which exhibits a resonance behavior.

In the case of a thin film, the geometry can be arranged so that the dc voltage is developed in the film plane. In Fig. 1, we see that the usual condition for resonance is met and that the microwave eddy current is parallel to H. As the magnetization precesses a component of magnetization appears normal to the film (y direction). The product of this component with the current gives an extraordinary Hall voltage in the x direction in the film plane. The ordinary Hall term does not contribute since, caused by demagnetizing effects, the microwave magnetic induction normal to the film is zero. The dc components of the electric field in the film plane are from (1)

$$\bar{E}_x=\frac{\rho_{11}-\rho_\perp}{B}\langle Jb_x\rangle_{hr}+4\pi R_0(\alpha-1)\langle Jm_y\rangle_{hr}, \quad (2)$$

$$\bar{E}_z=0. \quad (3)$$

Thus, the voltage should be detected along the direction of microwave h, and is given by the average electric field through the film thickness d times the distance ℓ between probe contact points as follows,

$$V_{dc}=\ell\frac{\int_0^d\bar{E}_x dy}{d}, \quad (4)$$

When the steady magnetic field is perpendicular to the film, it can be shown from (1) that there are no dc contributions to the electric field in the film plane; thus, no dc voltage should be detected in the perpendicular case.

The quantities $\langle\overline{Jb_x}\rangle_{hr}$ and $\langle\overline{Jm_y}\rangle_{hr}$ as functions of magnetic field can be computed by suitable electromagnetic calculations. For a thick film (resonance skin depth less than thickness), we obtain

$$V=\ell\frac{c}{16\pi d}\left[\frac{\Delta\rho}{B}|\mu|\left(\frac{\mu_L}{\mu_R}\right)^{\frac{1}{2}}+4\pi R_0(\alpha-1)\left(\kappa'\left(\frac{\mu_L}{\mu_R}\right)^{\frac{1}{2}}+\kappa''\right)\right]h^2, \quad (5)$$

where $\mu_L(=-\mu''+|\mu|)$ and $\mu_R(=+\mu''+|\mu|)$ are the apparent permeabilities resulting from the skin effect, κ' and κ'' are the real and imaginary parts of the off-diagonal component of the tensor permeability. The magneto-resistance term contributes a dispersion-type curve through $|\mu|(\mu_L/\mu_R)^{\frac{1}{2}}$ while the Hall term contributes an absorption-type curve through $(\kappa'(\mu_L/\mu_R)^{\frac{1}{2}}$

* The work reported in this paper was performed at Lincoln Laboratory, a center for research operated by Massachusetts Institute of Technology with the joint support of the U. S. Army, Navy, and Air Force.

[1] W. G. Egan and H. J. Juretschke, Bull. Am. Phys. Soc. Ser. II 3, 194 (1958).

[2] Quarterly Progress Report on Solid State Research, Lincoln Laboratory, Mass. Inst. Technol. (May 1, 1958, August 1, 1958, and April 15, 1959), pp. 70, 54 and 37, respectively; P. E. Tannenwald and M. H. Seavey, Jr., J. phys. radium 20, 323 (1959).

[3] J. P. Jan, *Solid State Physics*, (Academic Press, Inc., New York, 1957), Vol. V, pp. 15, 75.

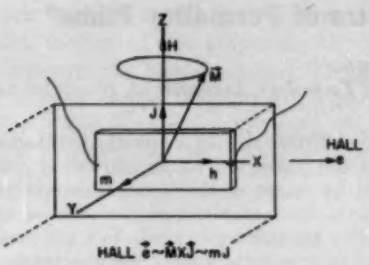

FIG. 1. Generation of dc hall voltage in FMR.

$+\kappa'')$. The observed voltage vs field curve is thus a weighted sum of the two curve types. If the direction of the magnetic field is reversed, the voltage curve changes shape since the Hall term changes sign while the magnetoresistance term does not. In the case of an ultra-thin film, we obtain

$$V=l\frac{c}{8\pi\delta}\left\{\frac{\Delta\rho}{B}\left(\frac{\sigma}{\sigma_0}\right)^{\frac{1}{2}}(\mu'-\mu'')+4\pi R_0(\alpha-1)\times\left[\left(\frac{\sigma}{\sigma_0}\right)^{\frac{1}{2}}(\kappa'+\kappa'')-\frac{d}{\delta}(\mu'\kappa'+\mu''\kappa'')\right]\right\}h^2, \quad (6)$$

where δ is film skin depth for unit permeability, σ is its conductivity, and σ_0 is the conductivity of the metal backing the film. The quantity $(\sigma/\sigma_0)^{\frac{1}{2}}$ is of order unity for a permalloy film backed by brass. Here, it is seen that both terms contribute in general dispersion-type curves.

Experimental voltage curves have been obtained for permalloy films at S, C, and X bands. The curve shape obtained is always intermediate between a dispersion-type and absorption-type, but merely changes polarity upon magnetic field reversal without changing shape. This implies that the magnetoresistance contribution is negligible since it is independent of magnetic field direction. By means of high microwave power experiments, it has been determined that for films less than about 1000 A thickness, the voltage is proportional to $(A\mu'+B\mu'')h^2$, where the weighting constants A and B are approximately equal, but have not been precisely determined. This would tend to confirm Eq. (6) with $\mu'\approx\kappa'$ and $\mu''\approx\kappa''$, except that the absorption-type term in $(\mu'\kappa'+\mu''\kappa'')$ makes a large contribution on resonance for even the thinnest films. This can be shown by letting $\mu''_{max}\approx\kappa''_{max}\approx 500$ (approximately the measured value) and $\delta=1.6\times10^{-4}$ cm for $\sigma=10^7$ mhos/m for permalloy. If we nevertheless neglect this term and take the experimental values at X band, $h^2=2.4$ oe^2, $\kappa''=\mu''=420$, $\kappa'=\mu'=0$, $l=0.69$ cm, $\delta=1.6\times10^{-4}$ cm, $R_0=0.61\times10^{-12}$ v cm/amp gauss and $\alpha=90$ for a 150 A film for nickel,[4] we obtain from (6) a voltage of 1.2 mv as compared with a measured value of 0.4 mv. Thus, it is possible to account for the measured voltage to within an order of magnitude if the absorption-type term is neglected. For the thicker films, however, Eq. (5) shows that in the absence of magnetoresistance the voltage curve clearly has an absorption-type character. However, agreement is still achieved to within an order of magnitude if we use Eq. (5) and the following experimental values taken at X band: $h^2=24$ oe^2, $\kappa''=\frac{1}{3}\kappa''_{max}\cong 140$, $l=0.60$ cm, $\delta=1.6\times10^{-4}$ cm, $R_0=0.61\times10^{-12}$ v cm/amp gauss, $\alpha=9$, the bulk value for nickel[4] and $d=3000$ A. Equation (5) predicts 1.1 mv, and a value of 0.8 mv is measured.

Perhaps the strongest evidence, although it is of a qualitative nature, for interpretation of the voltage in terms of the extraordinary Hall effect (and/or magnetoresistance) is to be found in the geometric dependence. It is always observed that the voltage is a maximum along the microwave h direction and zero along the steady H direction with H in the film plane; while with H normal to the film plane, no voltage can be detected. Further support for the galvanomagnetic theory would be obtained if a second harmonic voltage similar to the dc voltage term could be observed. Equation (1) predicts such a second harmonic (2ω) term. The fact that the dc voltage is easily detected in ultra-thin films ($\sim$50 A), where the resonance absorption is extremely small, and appears to be independent of film thickness in this range helps to confirm Eq. (6) (aside from the absorption-type term).

It has been shown that the dc voltage generation in a thin film provides a new and sensitive means of studying ferromagnetic resonance phenomena. The new effect has been analyzed in terms of a gyromagnetic-galvanomagnetic interaction, and there is good evidence that the extraordinary Hall effect plays a principal role.

[4] R. Coren and H. J. Juretschke, J. Appl. Phys. **28**, 806 (1957).

Initial Susceptibility Spectra of Permalloy Films*

R. F. Soohoo†
Lincoln Laboratory, Massachusetts Institute of Technology, Lexington 73, Massachusetts

The initial susceptibility of Permalloy films from 100 to 10 000 Mc/sec is investigated theoretically and experimentally. The exact boundary value problem of a film placed in a rectangular cavity is solved. This result is compared with the simpler solution obtained by means of the Bethe-Schwinger perturbation formula. As may be expected, the exact solution reduces to that obtained from perturbation theory when the film thickness and the value of the initial susceptibility are sufficiently small. In a self-consistent way, we show that exchange effects can sometimes be neglected as far as initial susceptibility values are concerned.

INTRODUCTION

THE initial susceptibility of a Permalloy film, being equal to the ratio of the rf magnetization **m** and rf field **h**, can be rigorously defined only when **m** and **h** have the same spatial dependence or are uniform throughout the medium. The direction of **M** may vary from point to point due to the presence of inhomogeneous magnetic fields or due to spin boundary conditions. In general, the spatial dependence of **M** can only be determined by a simultaneous solution of the equation of motion of the magnetization and Maxwell's equations. However, if we assume that $\nabla^2\mathbf{M}=0$, **M** would then be independent of position and the equation of motion of the magnetization can be solved independently of Maxwell's equations. If the frequency is low enough, or if a film is thin enough, there may be very little spatial variation of the magnetization direction in the film because the eddy current effects are then small. Thus, this simplification may be applicable to a variety of experimental circumstances.

In this paper, we shall neglect the exchange term in the equation of motion of the magnetization and solve the otherwise exact boundary value problem of a thin film in a rectangular cavity. Then the rf magnetic field distribution in the film is calculated to show that the assumption of $\nabla^2\mathbf{M}=0$ is justified. When the film is thin enough, we shall show that the exact solution reduces to the simpler one obtainable from perturbation theory.

BOUNDARY VALUE PROBLEM

Consider the case of a film of thickness δ placed against the back wall and filling the entire cross section of a TE_{10n} cavity of length d and cross-sectional wide and narrow dimensions a and b, respectively. The direction y is chosen to be normal to the film surface, and x and z are measured, respectively, in the wide and narrow dimensions of the cross section of the cavity.

The expressions for e_z, h_x, and b_y in the air-filled and film-filled portions of the cavity can be obtained from the solution of the equation of motion of the magnetization and Maxwell's equations as outlined above. By imposing the boundary conditions of the continuity of e_z and h_x at air-film boundary, and the conditions of $e_z=0$ at $y=0$ and at $y=d$ we obtain

$$\frac{\mu^2-K^2}{\mu}\left(\frac{i\gamma_a}{\gamma_f}\right)=\cot(-i\gamma_f\delta)\frac{e^{2\gamma_a\delta}-e^{2\gamma_a d}}{1+e^{2\gamma_a d}}, \tag{1}$$

where μ and K are components of the Polder permeability tensor[1] and γ_a^2 and γ_f^2 are given by

$$\begin{aligned}\gamma_a^2&=(-\omega^2/c^2)+(\pi/a)^2,\\ \gamma_f^2&=-\frac{\omega^2}{c^2}\left(\frac{\mu^2-K^2}{\mu}\right)\left(\frac{4\pi}{i\omega\rho}\right)+\left(\frac{\pi}{a}\right)^2,\end{aligned} \tag{2}$$

where ρ is the resistivity of the film.

If the ratio of the film thickness δ to the skin depth is sufficiently small (less than 0.4) Eq. (1) becomes

$$\begin{aligned}Re\left(\frac{\mu^2-K^2}{\mu}-1\right)&=-\left(\frac{\Delta\omega}{\omega}\right)\left(\frac{d}{\delta}\right)\left[1+\left(\frac{d}{na}\right)^2\right],\\ -Im\left(\frac{\mu^2-K^2}{\mu}-1\right)&=\Delta\left(\frac{1}{2Q}\right)\left(\frac{d}{\delta}\right)\left[1+\left(\frac{d}{na}\right)^2\right],\end{aligned} \tag{3}$$

where $\Delta\omega/\omega$ is the ratio of the change in the resonance frequency due to the presence of the film divided by the resonance frequency of the empty cavity and ΔQ is the corresponding change in the Q of the cavity. The error incurred in making the approximations above for a typical film at microwave frequencies should be less than 5%.

INITIAL SUSCEPTIBILITY

The permeability components μ and K are based upon internal fields. In the solution of the boundary value problem, no explicit account of the rf demagnetization factors are necessary. In actual measurements, it is convenient to define the susceptibility in terms of the external fields. Since the internal field is not known in general, it is also expedient to replace the term $\chi_{int}\cdot\mathbf{h}_{int}$ which occurs in the perturbation theory by $\chi_{ext}\cdot\mathbf{h}_{ext}$. This can be done in one of two ways. We can

* The work reported in this paper was performed by Lincoln Laboratory, a center for research operated by Massachusetts Institute of Technology with the joint support of the U. S. Army, Navy, and Air Force.

† Staff Member, Lincoln Laboratory, Massachusetts Institute of Technology, Lexington 73, Massachusetts.

[1] D. Polder, Phil. Mag. **40**, 99–115 (1949).

relate the internal fields to the external fields by means of the demagnetization factors of the ellipsoid. Alternatively, we may incorporate the demagnetizing torque into the equation of motion of the magnetization and solve the susceptibility in terms of external fields. The pertinent result of such a calculation when eddy current effects are neglected is[2,3]:

$$\chi_{xz}=\frac{m_x}{(h_x)_{ext}}=\frac{1}{1+(\omega_0/4\pi\lambda)^2[(\omega/\omega_0)-(\omega_0/\omega)]^2}\left[\frac{-\gamma^2M^2}{4\pi\lambda^2}\left(\frac{\omega_0}{\omega}\right)\left(\frac{\omega}{\omega_0}-\frac{\omega_0}{\omega}\right)-j\frac{\gamma^2M^2}{\omega\lambda}\right], \quad (4a)$$

$$\chi_{yz}=\frac{m_y}{(h_x)_{ext}}=\frac{1}{1+(\omega_0/4\pi\lambda)^2[(\omega/\omega_0)-(\omega_0/\omega)]^2}\times\left[\frac{\gamma M\omega_0}{(4\pi\lambda)^2}\left(\frac{\omega}{\omega_0}-\frac{\omega_0}{\omega}\right)+j\frac{\gamma M}{4\pi\lambda}\right], \quad (4b)$$

where $\omega_0=(4\pi MH_k)^{\frac{1}{2}}$ and H_k is the equivalent anisotropy field along the easy axis of the film (z). γ and λ are the gyromagnetic ratio and the damping parameter.

By noting that $4\pi\chi_{zz}$ is equal to $[(\mu^2-K^2/\mu)-1]$ of Eq. (3), we find that Eq. (3) is exactly the same as that obtained by use of the Bethe-Schwinger Perturbation formula,[4,5]

By using the expressions for $h_{x,y}$ we may calculate the y dependence of the rf magnetic field in the film. For example, if $\mu_i=10$, $\rho=21\times10^{-6}$ ohm-cm, $\delta=3900$ A and $f=9\times10^9$ cps, the ratio of h_x at the two surfaces of the film is 1.001. Thus, there is practically no magnetic field variation across the thickness of the film and therefore the neglect of eddy-current effects in the derivation of Eq. (4) is completely justified. In general, if the film thickness δ is less than the skin depth, the variation of $h_{x,y}$ within the film would be small.[6]

Because of the small variation in $\mathbf{h}$, exchange effects between adjacent spins due to inhomogeneous magnetic fields can be neglected. The microscopic boundary conditions on the spins due to surface anisotropy can also be ignored since no spin wave excitation has been observed in the experimental arrangement under consideration. Though $h_{x,y}$ has an x dependence, this variation is so slow on the microscopic scale that the exchange effects between adjacent spins in the x direction can again be ignored.

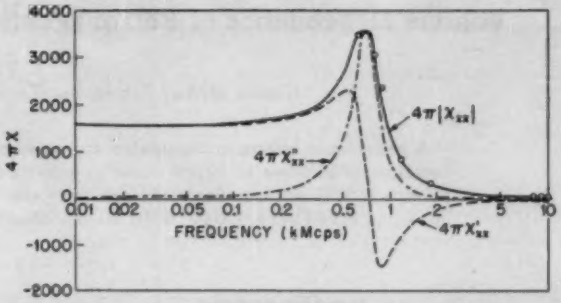

FIG. 1. Initial susceptibility of a typical Permalloy film vs frequency. The constants of the film are: $4\pi M=9875$ oe, $\gamma=2.91$ Mc/sec-oe, $\lambda=1.59\times10^8$ rad/sec, $H_k=6.3$ oe, $\rho=21\times10^{-6}$ ohm-cm, and $\delta=1200$ A. Note that circled points represent experimental values of $4\pi|\chi_{zz}|$.

EXPERIMENTAL RESULTS

The rectangular cavity enumerated above could in principle be used at all frequencies and our measurement of initial susceptibility at microwave frequencies have been carried out using it. At the lower frequencies (100–4000 Mc/sec), however, due to the lack of commercially available suitable waveguide and measuring equipment, we have found it more expedient to use a transmission method wherin the film is placed near the center conductor of a strip transmission line.[6] It can be shown[2,3] that the voltages induced in suitably oriented film encompassing loops are proportional to the components of the film susceptibility. In this case, only the magnitudes $|\chi_{zz}|$ and $|\chi_{yz}|$ can be measured. Experimental values of $4\pi|\chi_{zz}|$ of a typical Permalloy film is shown in Fig. 1 along with the theoretical prediction of Eq. (4). It is seen that the theoretical and experimental results agree reasonably well. To avoid the necessity of measuring absolute field intensities, the initial susceptibility values were obtained by comparing the voltage pickup by the loop at zero and at resonance external dc fields; the value of the susceptibility at resonance is seen to be simply $M/(\Delta H/2)$ from Eq. (4) and M and ΔH can be easily measured. Note that $\lambda=\gamma^2M(\Delta H)/2\omega$ where ΔH is the ferromagnetic resonance line width.

[2] D. O. Smith, J. Appl. Phys. **29**, 264 (1958).
[3] R. F. Soohoo, Solid State Research Quarterly Prog. Rept., Lincoln Laboratory, Mass. Inst. Technol. 104 (January, 1959).
[4] H. A. Bethe and J. Schwinger, "Perturbation theory of cavities," Cornell Univ. contract (March, 1943).
[5] R. F. Soohoo, Solid State Research Quarterly Progress Rept., Lincoln Laboratory, Mass. Inst. Technol. 97 (July, 1959).
[6] D. O. Smith, Phys. Rev. **104**, 1280 (1956).

Volume Dependence of Ferrimagnetic Resonance Properties in $Ni_{1-x}Co_xFe_2O_4$*

I. P. KAMINOW†
Gordon McKay Laboratory, Harvard University, Cambridge, Massachusetts

A microwave resonance apparatus for measuring K_1/M, K_2/M, g_{eff}, linewidth and magnetization as functions of pressure to 10 000 atmos is described. At this pressure the volume of nickel ferrite is reduced by only 0.68% but significant changes in magnetic properties are observed. The results of measurements on $Ni_{1-x}Co_xFe_2O_4$ ($x=0$, 0.05, 0.10) are discussed in terms of Slonczewski's anisotropy theory.

INTRODUCTION

THE properties of ferrimagnetic single crystals, and solids in general, are intimately related to the spacings between atoms. Hydrostatic pressure, since it is an isotropic stress, simply reduces the lattice constant of a cubic crystal without destroying the over-all symmetry (if no phase change occurs) and provides a means for studying the effects of atomic spacing.[1]

Slonczewski[2] has given a theory, for the anisotropy contributed by small percentages of Co^{2+} in magnetite, in which he assumes a one ion model and employs crystal field theory. If Co^{2+} ions are located on widely separated octahedral sites and no distinction is made between Fe^{2+} and Fe^{3+} ions, the crystal field is cubic with a small trigonal distortion along a [111] axis. In this situation, the ground state of Co^{2+} is an orbital doublet with effective angular momentum component α, where α lies in the range $1<\alpha<\frac{3}{2}$ and decreases with increasing cubic field V_C. The ground wave function, having trigonal symmetry, fits snugly into the trigonal surroundings, and the orbital angular momentum is constrained to lie along the trigonal axis. The fact that the orbital angular momentum is not quenched gives rise to large ferrimagnetic anisotropy. The anisotropy of the "locked in" orbital wave function is impressed upon the spin orientation (magnetization direction) via the spin-orbit interaction $\lambda\mathbf{L}\cdot\mathbf{S}$, where λ is the spin-orbit constant.

Slonczewski's expressions for the cobalt anisotropy constants K_1(Co) and K_2(Co) contain only one free parameter $\alpha\lambda$. Slonczewski obtains a good fit to temperature data[3] on the anisotropy of Co^{2+} in magnetite with $|\alpha\lambda|=132$ cm^{-1}. (From the experiment, $K_1(\text{Co})\sim 10^7$ erg/cc and $K_2(\text{Co})\sim -5\times 10^6$ erg/cc at 300°K). The fact that α does not fall within the prescribed range when λ is taken as the free ion value -176 cm^{-1} may be ascribed to (1) the neglect of higher levels[2,4] (taking the trigonal and exchange field splittings to be infinite), (2) the presence of nontrigonal distortions which lift the orbital degeneracy[2] and may be caused by differences in Fe^{2+} and Fe^{3+} on neighboring B sites or by clustering of Co^{2+} ions, or (3) the reduction of $|\lambda|$ in the crystal from the free ion value.[1,5]

APPARATUS

The high-pressure apparatus is shown schematically in Fig. 1. An x-band cylindrical TE_{011} cavity having aluminum walls and filled with alumina (Coors AD-99) dielectric is situated insde a cylindrical hardened beryllium copper vessel (2-in. o.d., $\frac{11}{16}$-in. i.d.). The bomb is filled with pentane (technical) through a flexible stainless steel tube to a maximum pressure 10^4 kg/cm^2 (approximately 10^4 atmos or 150 000 psi). The cavity is loop coupled to a tapered coaxial line, a pressure seal being provided by a small beryllium copper cone seated in a thin synthetic mica conical shell. The spherical sample (~0.02-in. diam) is mounted on a quartz rod [with a minimum of cement (Stycast 2662) to avoid nonhydrostatic stresses] so that a [110] axis coincides with both the cavity axis and the axis of a rotating magnet into which the assembly is placed. The pentane is free to circulate through the cavity and around the sample by way of holes in the wall and spaces between components. With this apparatus, K_1/M, K_2/M, g_{eff} and linewidth, ΔH can be determined from measurements in three principal directions. Magnetization can

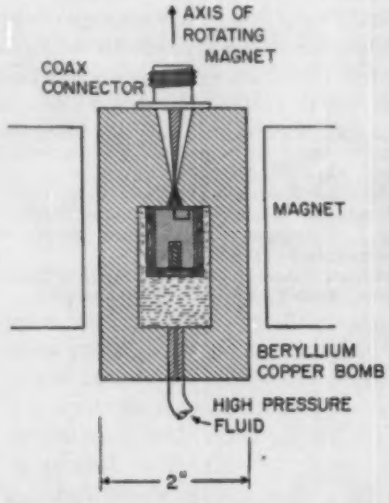

FIG. 1. Schematic drawing of the high-pressure apparatus. The spaces between components of the microwave cavity have been exaggerated in size for clarity.

* Research supported by contract with U. S. Air Force Cambridge Research Center.
† Bell Telephone Laboratories CDTP Fellow.
[1] W. M. Walsh, Jr., Phys. Rev. 114, 1473, 1485 (1959).
[2] J. C. Slonczewski, Phys. Rev. 110, 1341 (1958).
[3] Bickford, Brownlow, and Penoyer, Proc. Inst. Elec. Engrs. London 104B, Suppl. 5, 238 (1957).
[4] J. H. Van Vleck, Discussions Faraday Soc. 26, 96 (1958); J. H. Van Vleck, J. phys. radium 20, 124 (1959).
[5] J. Owen, Proc. Roy. Soc. (London) 227, 183 (1959); Bleaney, Bowers, and Pryce, *ibid.* 228, 166 (1955).

TABLE I. Parameters in linear least squares fit, $Y=A+BP$, for K_1/M, K_2/M and g_{eff} *vs* pressure, P(kg/cm²), in $Ni_{1-x}Co_xFe_2O_4$ at room temperature. The stated errors are the standard deviations found in the least squares procedure and include the effects of random temperature variations during a run.

Y	K_1/M (oe)		K_2/M (oe)		g_{eff}	
x	A	B	A	B	A	B
0	-236.6 ± 0.3	$-(1.06\pm0.05)10^{-3}$	~-28	~0	see text	
0.05	64.7 ± 0.9	$-(1.9\pm0.2)10^{-3}$	-323 ± 2	$(0.0\pm0.3)10^{-3}$	2.215 ± 0.001	$-(5\pm2)10^{-7}$
0.10	322 ± 2	$-(2.5\pm0.3)10^{-3}$	-528 ± 4	$-(1.8\pm0.7)10^{-3}$	2.26 ± 0.08	$(0\pm2)10^{-5}$

be measured by magnetostatic mode methods or by varying the sample shape.

RESULTS

Crystals of $Ni_{1-x}Co_xFe_2O_4$ were grown from the melt by C. Quadros using the proportions of oxides to give $x=0$, 0.05, 0.10. However, the Co^{2+} content was not analyzed in the crystals as grown. The isothermal compressibility of nickel ferrite[6] is 0.68 per cent in 10^4 kg/cm². From polycrystalline magnetization data[7], $M=257$, 273, 290 cgs for $x=0$, 0.5, 0.10, respectively.

The experimental results for K_1/M, K_2/M and g_{eff} are summarized in Table I. Linewidth measurements exhibited a large scatter. Nevertheless, a general increase in ΔH with pressure could be ascertained for $x=0$ and 0.05 (ΔH was not measured for $x=0.10$). The approximate increases from $P=0$ to 10^4kg/cm² for ΔH in the principal directions are for $x=0$: ΔH_{100}, 75 to 79 oe; ΔH_{111}, 55 to 55 oe; ΔH_{110} 77 to 86 oe; and for $x=0.05$: ΔH_{100}, 92 to 122 oe; ΔH_{111}, 58 to 79 oe; ΔH_{110}, 66 to 86 oe. The relatively large linewidths make it difficult to measure K_2/M and g_{eff} with sufficient precision to detect a pressure shift. The apparent behavior of g_{eff} for $x=0$ is anomalous in that g_{eff} increases from 2.209 at $P=0$ to 2.212 at 5×10^3kg/cm² and then decreases to 2.209 at 10^4 kg/cm².

DISCUSSION

If $K_1(x)=xK_1(\mathrm{Co})+(1-x)K_1(0)$ and $K_1(x)$ denotes the anisotropy constant in $Ni_{1-x}Co_xFe_2O_4$, then we calculate $K_1(\mathrm{Co})\sim1.6\times10^6$ erg/cc and $K_2(\mathrm{Co})\sim-1.6\times10^6$ erg/cc. Inserting these values into Slonczewski's expressions and making the rough approximation[8] $\partial\ln M/\partial P\sim-\partial\ln V/\partial P$, one obtains $|\alpha\lambda|\sim74$ cm^{-1} and $\partial\ln(\alpha\lambda)/\partial\ln V\sim1.1$, in which V denotes volume.

The large reductions in $|K_1(\mathrm{Co})|$ and $|K_2(\mathrm{Co})|$ for Co^{2+} in nickel ferrite compared to magnetite is very likely the result of nontrigonal distortions produced by the disordered distribution of Ni^{3+} and Fe^{3+} ions on neighboring B sites.[2] (Differences in Fe^{3+} and Fe^{2+} in magnetite are averaged out by electron transfer[2]). The Slonczewski theory, therefore, is probably not valid here. The insight it provides, however, indicates several explanations for the observed pressure dependence. We note that the anisotropy and $|\alpha\lambda|$ are reduced when (1) V_C is increased (α decreased), (2) the trigonal or exchange field is reduced (contribution from excited states increased), (3) the effect of nontrigonal distortions is increased, and (4) $|\lambda|$ is decreased. Any of these factors might vary with P in a direction to produce a reduction in anisotropy. The large effect of nontrigonal distortions noted in comparing nickel ferrite and magnetite, suggests that (3) may be the dominant factor.

ACKNOWLEDGMENT

It is a pleasure to acknowledge informative discussions with Professor R. V. Jones and the advice and assistance of Professor W. Paul on the construction and operation of the pressure apparatus.

[6] D. F. Gibbons, J. Appl. Phys. 28, 810 (1957).
[7] J. E. Pippin, Thesis, Harvard (1958).

[8] Unpublished magnetostatic mode-high pressure measurements on yttrium iron garnet and $MgFe_2O_4$ indicate that approximately 70% of the small change in M with pressure is due explicitly to the reduction in V. The ions involved, however, are in S states and may behave differently than Co^{2+}.

Effects of Surface Irregularities on Single Crystal Resonance Parameters*

C. R. BUFFLER†
Gordon McKay Laboratory, Division of Engineering and Applied Physics, Harvard University, Cambridge, Massachusetts

Measurements of ferromagnetic resonance line width, and anisotropy of line width of yttrium iron, garnet, and manganese zinc ferrite single crystals as a function of surface irregularities from 8 to 75 μ, and frequency from 2 to 16 kMc are presented. These measurements indicate that the frequency dependence of the line width and line width anisotropy in these materials for varying degrees of surface roughness can be interpreted with respect to spin wave scattering theories. In this case, the surface irregularities act as scattering centers for the uniform precession, causing a loss of energy into degenerate spin wave states with wavelengths corresponding to the size of the irregularities.

RECENTLY, a new mechanism for ferromagnetic relaxation has been proposed by Kittel[1] for materials containing fast relaxing rare earth ions on a sublattice separate from the magnetic ferric ions. This mechanism can be directly applied to explain the resonance behavior of the rare earth garnets. Dillon and Nielsen[2] have shown that the rare earth impurities in yttrium iron garnet can account for the intrinsic relaxation behavior of this material by means of the Kittel mechanism.

It has, however, been fairly well established that another primary mechanism in the ferromagnetic relaxation process is the scattering of the uniform precession or $k=0$ spin waves into higher k spin wave states with which they are degenerate. The scattering can take on several different forms depending on the scattering mechanism and the portion of the spin wave manifold which is involved. For example, Geschwind[3] and Schlömann[4] have proposed that the major portion of the line width in polycrystalline materials with small intrinsic lines arises from scattering into the portion of the manifold where exchange can be neglected, that is, into the so called medium k region. The scattering in this case arises from the granular structure of the polycrystalline material. In other words, the ordered properties of the magnetic sample are interrupted at the grain boundaries causing scattering into spin wave states with corresponding wavelengths. Striking confirmation of this proposal is exhibited by recent line width measurements on polycrystalline materials as a function of frequency and temperature.[5] These measurements show that the line width exhibits a sharp discontinuity as the uniform precession passes above the upper limit of the medium k portion of the manifold, thus eliminating these states from the relaxation process.

On the other hand Clogston et al.[6] have indicated a possible major contribution to the intrinsic line width of most ferrite materials is the energy loss to the very high k or "exchange" states due to the local fluctuation of the anisotropy fields of the randomly distributed magnetic ions. These fluctuations have mean separations on the order of several lattice constants so the scattering occurs to the states with k values corresponding to these dimensions. White[7] has recently proposed that any ferrous ions present in ferrite materials can contribute their fast relaxing property to the line width by means of the Kittel mechanism. Also, early works[8,9] have shown another contributor to single crystal line widths to be the surface finish of the material. These measurements show that the line width of yttrium iron garnet decreases directly with the grit size of the polishing compound. The intrinsic line of a fraction of an oersted is reached for grit sizes around 0.25μ. Early explanations of this behavior considered the rough surface as producing an inhomogeneous internal magnetic field, thus causing different spins to see different fields and producing a broadened line. The measurements presented here indicate that this view is not strictly applicable. Just as the inhomogeneous field due to the grain structure in polycrystals, or ionic distribution in single crystals, is narrowed by dipolar or exchange fields, respectively; the inhomogeneous field arising from surface irregularities is also affected by these latter fields. This point is illustrated by Fig. 1(a). From the classical point of view, a line width proportional to the number and size of the surface irregularities and independent of frequency should result. It is seen that this is not the case. The line width is proportional to the surface irregularities, expressed as the mean polishing grit size, but is not independent of frequency. The frequency dependent behavior can be explained as follows. The surface pits or irregularities can be considered as scattering centers exactly as the grains or pores were in the polycrystalline materials. The uniform precession will thus lose energy predominantly to the degenerate spin wave states that have k values corresponding to the dimensions of the surface irregularities. Curve A of Fig. 1(a) shows the

* This work was conducted under sponsorship of U. S. Air Force Cambridge Research Center contracts.
† Present address, Varian Associates, Palo Alto, California.
[1] C. Kittel, Phys. Rev. **117**, 681 (1960).
[2] J. F. Dillon and J. W. Nielsen, Phys. Rev. Letters **3**, 30 (1959).
[3] S. Geschwind and A. M. Clogston, Phys. Rev. **108**, 49 (1957).
[4] E. Schlömann, J. Phys. Chem. Solids **6**, 242 (1958).
[5] C. R. Buffler, J. Appl. Phys. **30**, 172s (1959).
[6] Clogston, Suhl, Walker, and Anderson, J. Phys. Chem. Solids **1**, 129 (1956).
[7] R. L. White, Phys. Rev. Letters **2**, 465 (1959).
[8] G. P. Rodrigue, Thesis, Harvard University.
[9] R. C. LeCraw, E. G. Spencer, and C. S. Porter, Phys. Rev. **110**, 1311 (1958).

line width versus frequency for an extremely well polished manganese zinc ferrite sphere. It can be seen that the line width is essentially independent of frequency. The slowly increasing tendency at high frequencies will be discussed later. The surface of this sample was carefully polished with 8-μ diamond dust so that no irregularities larger than this size existed. Resulting from the tumbling action of the sphere in the polishing wheel, the average irregularity size is probably considerably less. Scattering will therefore take place predominantly from the uniform precession to spin wave states with wavelengths corresponding to the average irregularity size, that is, sonewhat less than 8 μ. Spin waves with wavelengths of 8 μ are actually in the medium k, "no exchange" region of the spin wave manifold. It might be expected that a discontinuity in the line width curve should appear at the critical frequency $\omega_c=\gamma 2/3\ 4\pi M$ where the uniform precession passes out of the manifold for the medium k states so that these states can no longer enter into the relaxation process.[5] This peak does not occur for the 8 μ sample for the following reasons. As previously mentioned, the average irregularity size is probably well below the 8 μ polishing grit size thus causing a predominant scattering to occur not to the medium k but to the high k or "exchange" spin wave states. The state density of the high k spin wave modes is frequency wise continuous through the point ω_c. Thus, as the uniform precession passes above the top of the manifold, the line width does not exhibit the peak which is characteristic of the medium k states. Also, even if scattering does occur to the medium k region, it will be completely negligible compared to the intrinsic line width, since the volume of the surface shell containing the irregularities compared to the total volume becomes vanishingly small.

As the polishing grit size is increased, more scattering can occur to the medium k states. At first, the overall line does not increase appreciably. A peak, however, does appear at ω_c due to the uniform precession passing out of the manifold, indicating the increased role played by the medium k states. This peak is illustrated by curve B, Fig. 1(a) for a sphere polished with an effective grit of 20 μ. As the grit size is increased further, the over-all magnitude of the line width increases, but the size of the peak does not. This behavior is shown in Curve C. In other words, the line width of curve B has been increased by a constant value, independent of frequency. This behavior is explained by the fact that the predominant scattering now takes place into the low k or Walker mode region of the manifold. Walker[10] has pointed out that the spin wave analysis of ferromagnetic resonance is not valid for k values corresponding to wavelengths longer than approximately $\frac{1}{10}$ of the sample size. This value corresponds to about 55 μ for a sample 0.023 in. in diam. Thus, for grit sizes of this order or larger the spin wave scattering process is replaced by

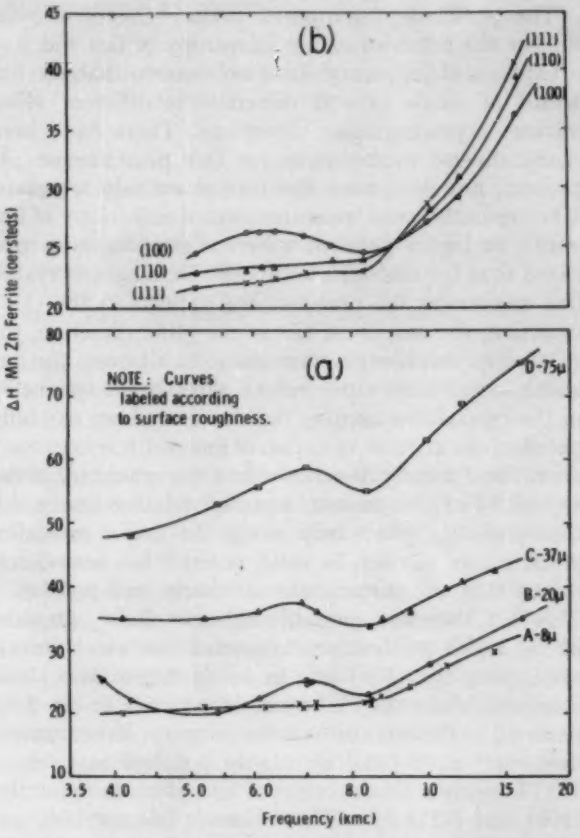

FIG. 1. (a) Line width of Mn Zn ferrite as a function of frequency and surface condition. (b). Line width anisotropy of Mn Zn ferrite as a function of frequency.

the excitation of Walker modes. It is known that the spectrum of magnetostatic modes extends above the top of the central or medium k region of the manifold. Therefore, when magnetostatic modes are predominantly excited, passing through the critical frequency ω_c, and thus rising above the top of the medium k manifold, does not cause a peak in the line width versus frequency curve. This behavior is associated with the slowly varying state density as a function of frequency in the vicinity of ω_c. This point is illustrated by curve D, Fig. 1(a) for a mean surface polish of 75 μ. The peak which first appears in curve A is still observable, but has not increased substantially in magnitude indicating that no further scattering is occuring to the medium k states. The overall line width, however, has tripled due to the essentially frequency independent excitation of the modes in the low k region of the manifold. The foregoing frequency independent contribution to the line width, when the surface irregularities become greater than approximately $\frac{1}{10}$ the sample size, can be considered analogous to the classical inhomogeneity broadening mentioned earlier. This analogy is true due to the fact that the mode excitation is directly proportional to the perturbing field set up by these irregularities as has been pointed out by Clogston.[3]

[10] L. R. Walker, Phys. Rev. **105**, 390 (1957).

The previously mentioned surface effects also influence the behavior of the anisotropy of line width as a function of frequency. It is well known that the line width of single crystal materials is different along various crystallographic directions. There have been many diverse explanations for this phenomenon. At present, however, none has proved entirely adequate. Until recently, most measurements of anisotropy of line width on highly polished spherical samples have indicated that for materials with negative magnetocrystalline anisotropy the broadest line appears in the (111) direction, the narrowest line in the (100) direction, the (110) direction being intermediate. In all cases, the line width versus angle curve reflects directly the symmetry of the crystal. On samples that have not been carefully polished the angular variation of line width is extremely erratic and usually does not reflect the symmetry of the crystal.[8] For this reason, reported relative line width measurements given only along the major crystallographic axes can not be valid, unless it has been determined that the surface was extremely well polished.[11] This fact, therefore, probably indicates the reason some of the earlier publications[12] reported line widths measured along the (100) axis as being larger than those measured along the (111) axis in contrast to the data reported in the literature to the contrary. Recent measurements[9] at S band on highly polished samples of YIG indicate a true reversal of line width between the (100) and (111) axes. This behavior has not been explained. In an attempt to learn more about this reversal in the anisotropy of line width, measurements were made as a function of frequency on a sample of Mn Zn ferrite. This material was chosen in preference to yttrium garnet because of the ease in sample preparation. Because of the narrow intrinsic line of yttrium garnet, it is extremely difficult to polish the surface so that the line width as a function of angle reflects the crystal symmetry. This problem is not as severe for the Mn Zn ferrite because of its slightly higher intrinsic line. A roughly polished sphere was first measured, and as expected the line width showed no symmety as a function of angle. The sample was polished with finer and finer abrasives until symmetry was observed at a grit size of 8 μ. The results of measurements made on this sample are shown in Fig. 1(b). At X band frequencies and higher the usual behavior is observed, that is, where the easy (111) axis is broader than the hard (100) axis. At approximately 9.5 kMc, a reversal of the line width occurs and the hard axis becomes broadest. A mechanism for this reversal is proposed as follows. Resulting from the 8 μ surface irregularities, scattering occurs predominantly into the medium k portion of the manifold. These spin-wave states have a density function, which has a singularity at the frequency corresponding to the top of the manifold, $\omega_e=\gamma 2/3\ 4\pi M$. For a given microwave frequency, measurements along each of the principle crystallographic axes will yield a situation where the uniform precession is degenerate with a different set of spin-wave modes. The difference arises simply from a relative shift in the spin-wave spectrum due to the different anisotropy field in each direction. As the frequency is decreased, a point is reached where the uniform precessional mode when measured along the easy (111) axis will be above the top of the manifold while the same mode measured along the other two axes will still be inside the manifold. This behavior occurs since the (111) axis has the lowest field for resonance. As the frequency is lowered further, the line width will decrease sharply since the medium k states can no longer play a part in the relaxation process. This initial decrease in the (111) line width is then responsible for the cross over observed. As the frequency is decreased still further, the uniform precession along the (110) and (100) axes will eventually also go out of the manifold, thus causing a similar decrease in line width for these axes. Below ω_e, therefore, the line widths should all decrease essentially parallel but in reversed order. If this scattering process is the mechanism responsible for the reversal of line widths, elimination of scattering to the medium k states would prevent the cross over from appearing. An attempt along this line was made by further polishing the sample with $\frac{1}{4}$ μ diamond dust. Unfortunately, this polishing had very little effect on the observed line width anisotropy because the cross over still existed. It is felt that this behavior was caused by inadequate elimination of the medium k states since the jump from 8 μ to $\frac{1}{4}$ μ grit size is much too large to give adequate polishing at the smaller grit size.[13] The final answer to the reversal in the line width will probably not be given until a satisfactory explanation for the anisotropy of line width, itself, is available.

[11] With YIG, for example, this usually means an average line width of less than 2 oe.

[12] M. H. Seavey, Jr., MIT Lincoln Laboratory Q.P.R. (November 7, 1, 1958).

[13] There is presently some question concerning the magnitude of the change in scattering due to the effective anisotropy field along each of the crystallographic directions. If the effect is small the proposed explanation cannot account for the cross over of the line width.

ACKNOWLEDGMENTS

In conclusion, I wish to express my appreciation to Professor R. V. Jones for his many suggestions and criticism and to C. Quadros, Mrs. L. Lin, and F. Molea for their technical assistance. I also wish to thank Dr. R. L. White, of the Hughes Research Laboratory for the use of several of his Mn Zn ferrite samples.

Saturation Effects in Ferrimagnetic Resonance*

P. E. SEIDEN
Lockheed Missiles and Space Division, Palo Alto, California and Microwave Laboratory, W. W. Hansen Laboratories of Physics, Stanford University, Stanford, California

AND

H. J. SHAW
Microwave Laboratory, W. W. Hansen Laboratories of Physics, Stanford University, Stanford, California

Saturation curves of susceptibility as a function of rf magnetic field have been measured for a number of samples of polycrystalline yttrium iron garnet of varying linewidth. The curves exhibit a region of susceptibility linear in $1/h_{rf}$ at high rf powers. The region of the initial decline in susceptibility is linear in h_{rf}^2, which is predicted both by a small signal relation derived from Callen's ferromagnetic dynamical equation and by a calculation of Schlömann which includes inhomogeneity interactions.

A new method of determining the critical field for spinwave build-up is discussed. This method takes account of the fact that the initial decline in susceptibility is not simply due to the Suhl mechanism for saturation in ferrites.

ACCORDING to the original Suhl[1] theory of the onset of saturation in ferrites, we would expect to find constant small signal susceptibility up to the Suhl critical rf magnetic field given by

$$h_c = \Delta H(\Delta H_k/4\pi M_s)^{\frac{1}{2}}, \tag{1}$$

where ΔH_k is the spinwave linewidth. At this point, the susceptibility will decrease proportional to $1/h_{rf}$. However, one finds that this is not the case.

What is experimentally observed is a slow decline in susceptibility that eventually becomes linear in $1/h$ and then deviates again from this behavior at higher power levels. A typical saturation curve of susceptibility as a function of inverse rf magnetic field for a sample of polycrystalline yttrium iron garnet is shown in Fig. 1.

Schlömann[2] has suggested that the initial decrease in susceptibility is due, not to the Suhl instability, but to inhomogeneity scattering in the material. That is, the inhomogeneities in the material preferentially scatter the uniform precession into spinwaves at all power levels. Therefore, the spinwave population at the Suhl threshold is much greater than the thermal level. Suhl[3] has recently recalculated the results of his theory with large spinwave driving terms, and he finds an initial decrease in susceptibility proportional to the fourth power of the rf magnetic field. Schlömann[2] has also calculated the saturation effect including the inhomogeneity interaction explicitly. He finds an initial decrease in susceptibility proportional to h_{rf}^2. We have derived a small signal relation for the initial decline in susceptibility from Callen's ferrimagnetic dynamical equation[4] and find

$$\frac{\chi''}{\chi_0''} = \frac{1}{1+(\pi\gamma^2/\omega\lambda_{kw})h_{rf}^2}, \tag{2}$$

where λ_{kw} is proportional to the transition probability for spinwave-lattice phonon transitions. The functional dependence on h_{rf} is essentially that predicted by Schlömann.

We have measured the saturation curves of a number of samples of polycrystalline yttrium iron garnet of varying yttrium to iron ratio whose linewidths ranged from 50 oe to 250 oe. The saturation curves in the region of the initial decline in susceptibility are shown in Fig. 2. The graph is a log-log plot with coordinates arranged such that Eq. (2) plots as a straight line with slope of -2. The complete Suhl curve[3] for the decline in susceptibility is also shown. It is seen that the data follow the square law quite well.

Since the inhomogeneity scattering obscures the sharp decline in susceptibility expected from the original Suhl theory, alternative methods[5] must be employed for evaluating h_c, which is to be used in Eq. (1). We assume that the linear region in Fig. 1 is due to the Suhl instability, so that if the inhomogeneity scattering were not present this linear region would then extend back to $\chi''/\chi_0''=1$. We then extend this line back as is shown in Fig. 1 and let h_c be the field at which this line inter-

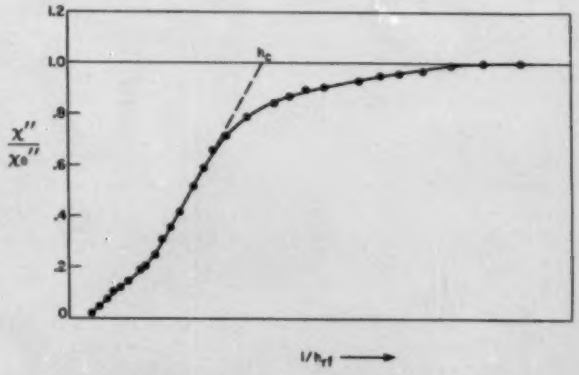

FIG. 1. Typical saturation curve of susceptibility as a function of inverse rf magnetic field.

* This research was supported in part by the U. S. Air Force under an Air Force contract, monitored by the Air Force Office of Scientific Research of the Air Research and Development Command, and in part by Lockheed Missiles and Sapce Division.

[1] H. Suhl, J. Phys. Chem. Solids 1, 209 (1957); Proc. Inst. Radio Engrs. 44, 1270 (1956).
[2] E. Schlömann, Bull. Am. Phys. Soc. Ser. II, 4, 53 (1959).
[3] H. Suhl, J. Appl. Phys. (to be published).
[4] H. B. Callen, J. Phys. Chem. Solids 4, 256 (1958).
[5] J. J. Green and E. Schlömann, High Power Ferromagnetic Resonance at X-Band in Polycrystalline Garnets and Ferrites, Tech. Mem. T-168, Raytheon Co. (1959).

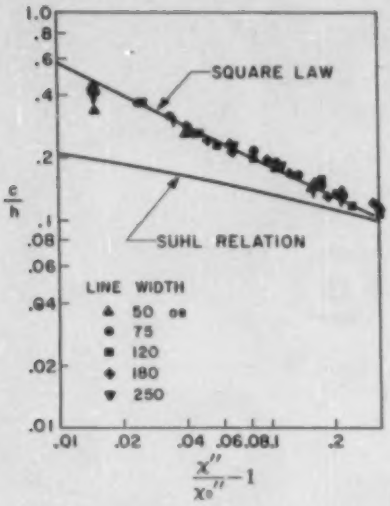

FIG. 2. Saturation curves for the region of the initial decline in susceptibility.

sects $\chi''/\chi_0''=1$. This means we are assuming that the susceptibility above the Suhl threshold has the follwing behavior:

$$\chi''/\chi_0''=(C_1/h_{rf})-C_2, \tag{3}$$

where C_1 and C_2 are constants. We may show that this form is plausible as follows:

$$\chi''=m/h=\theta M/h, \tag{4}$$

where m and M are the rf and total magnetizations, respectively, in the uniform mode. After the Suhl threshold, θ, the precession angle is approximately constant. Damon[6] and Bloembergen and Wang[7] have shown that the amount of magnetization going into spinwaves is proportional to h_{rf}. Therefore, as a first approximation, we may write

$$M=M_0-Kh_{rf}, \tag{5}$$

where K is a constant. Therefore, Eq. (4) becomes

$$\chi''=(\theta M_0/h)-\theta K, \tag{6}$$

which is just the form of Eq. (3).

ACKNOWLEDGMENTS

We are indebted to J. W. Katz of the Technical Ceramics Section of Lockheed Missiles and Space Division for preparing the samples and to M. Baldwin of the Solid State Physics Section for the $4\pi M_s$ measurements.

[6] R. W. Damon, Revs. Modern Phys. **25**, 239 (1953).
[7] N. Bloembergen and S. Wang, Phys. Rev. **93**, 72 (1954).

JOURNAL OF APPLIED PHYSICS SUPPLEMENT TO VOL. 31, NO. 4 APRIL, 1960

Resonance Line Widths of Sintered Nickel Ferrites Having Low Porosities

L. G. VAN UITERT, R. R. SODEN, AND F. W. SWANEKAMP
Bell Telephone Laboratories, Inc., Murray Hill, New Jersey

The evolution of gas during sintering can act as a source of line broadening in low porosity ferrites. When this occurs there are systematic dependencies of ΔH (line width) upon sintering conditions but not upon porosity. Nickel ferrites sintered under such nonideal conditions show minima in ΔH as a function of cobalt content. When the same materials are sintered under more ideal conditions, ΔH increases linearly with cobalt. ΔH varies as the reciprocal of saturation magnetization for modified nickel ferrites prepared under the most ideal conditions. The effects of anisotropy field and dipole narrowing on ΔH are evident.

THE ferrimagnetic resonance line width (ΔH) values of single crystal and a number of sintered nickel ferrites have been studied by previous investigators.[1–5] The compositions listed in Fig. 1 and their cobalt addition products, where Co=½, 1, 2, and 4% of the divalent metal ions present, prepared by sintering are discussed herein. ΔH values were measured using 15- to 20-mil spheres in a 16-kmc spectrometer. Comparison measurements were made on $Y_3Fe_5O_{12}$ and $Y_3AlFe_4O_{12}$ samples which were sintered 1475-5-O_2-300[6] and 1500-40-O_2-300, respectively. E. G. Spencer and R. C. LeCraw obtained $\Delta H=4.5$ oe for $Y_3Fe_5O_{12}$ and $\Delta H=7$ oe for $Y_3AlFe_4O_{12}$ on these materials at 3 kmc. These values apply at 16 kmc also.

DISCUSSION

Previous studies[6,7] of $NiFe_2O_4$ and $Y_3Fe_5O_{12}$ have shown a dependence of ΔH on porosity. This relation breaks down at high relative densities. However, ΔH and porosity show systematic dependencies on sintering conditions.[8] In the case of $Y_3Fe_5O_{12}$, both decrease as sintering temperature increases—up to a point. At higher temperatures, the trends reverse but with greater increases in ΔH due to porosity than at lower temperatures. The reversal is associated with gas generation, resulting from the reduction of trivalent iron in the low

[1] W. A. Yeager, J. K. Galt, F. R. Merrit, and J. Wood, Phys. Rev. **80**, 744 (1950).
[2] M. H. Sirvetz and J. H. Saunders, Phys. Rev. **102**, 366 (1956).
[3] J. E. Pippen and C. L. Hogan, Inst. Radio Engrs. Trans. M. T. T. **6**, 77 (1958).
[4] S. Geshwind and A. M. Clogston, Phys. Rev. **108**, 49 (1957).
[5] T. Okamura, Y. Torizuka, and Y. Kujima, Phys. Rev. **88**, 1425 (1952).
[6] Symbol groups indicate sintering conditions in the following order: sintering temperature in °C, time at temperature in hours, atmosphere, and the rate of approach to the sintering temperature above 1000°C.
[7] W. P. Wolf and G. P. Rodriguez, J. Appl. Phys. **29**, 105 (1958).
[8] L. G. Van Uitert, F. W. Swanekamp, and S. Preziosi, J. Am. Ceram. Soc. (to be published).

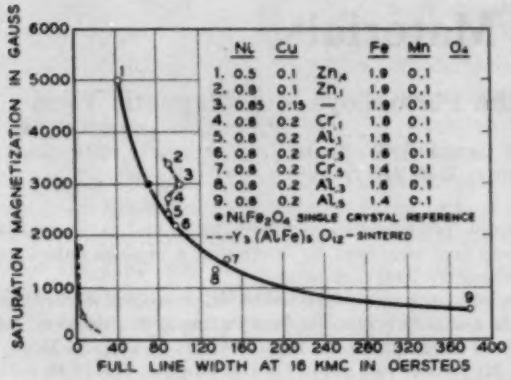
SATURATION MAGNETIZATION IN GAUSS
FULL LINE WIDTH AT 16 KMC IN OERSTEDS
Ni Cu Fe Mn O₄
1. 0.5 0.1 Zn₄ 1.9 0.1
2. 0.8 0.1 Zn₁ 1.9 0.1
3. 0.85 0.15 — 1.9 0.1
4. 0.8 0.2 Cr₁ 1.8 0.1
5. 0.8 0.2 Al₁ 1.8 0.1
6. 0.8 0.2 Cr₃ 1.8 0.1
7. 0.8 0.2 Cr₅ 1.4 0.1
8. 0.8 0.2 Al₃ 1.8 0.1
9. 0.8 0.2 Al₅ 1.4 0.1
• NiFe₂O₄ SINGLE CRYSTAL REFERENCE
---Y₃(AlFe)₅O₁₂ - SINTERED

FIG. 1. The dependence of line width upon saturation magnetization for a number of nickel ferrites. The solid line varies as reciprocal of magnetization and is based on the values for a single crystal of nickel ferrite. Comparison data for yttrium-aluminum-iron garnets are also given.

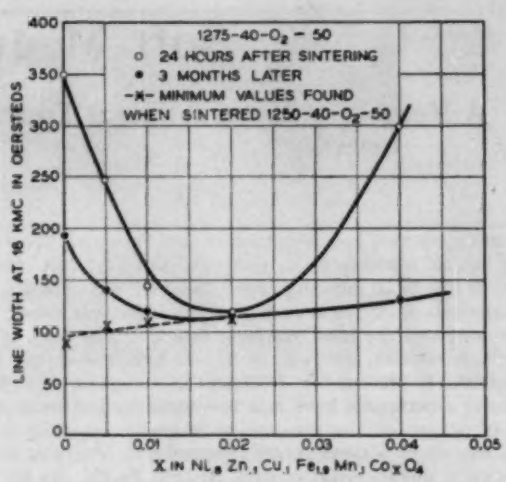
1275-40-O₂ - 50
○ 24 HOURS AFTER SINTERING
• 3 MONTHS LATER
-x- MINIMUM VALUES FOUND
WHEN SINTERED 1250-40-O₂-50
LINE WIDTH AT 16 KMC IN OERSTEDS
X IN Ni₀.₈ Zn₀.₁ Cu₀.₁ Fe₁.₉ Mn₀.₁ Co_X O₄

FIG. 2. Extremes in the dependencies of line width upon cobalt content for nearly similar sintering conditions, and the change in line width with time shown by the 1275–40-O_2 samples.

porosity materials at high temperatures. In the ferrites, nickel, cobalt, and manganese, which oxidize in part to the trivalent state upon cooling after calcination, also give up oxygen (so gained) during the sintering process.

Line broadening effects due to gas generation in the ferrites can be minimized by employing an optimum rate of approach to the sintering temperature. Factors of importance are: (1) equilibrium oxygen pressure increases with temperature; (2) time is required to reach equilibrium; and (3) the system should be at equilibrium prior to the time that sintering has reduced porosity to the point where the escape of gas becomes difficult.

Compositions such as 2, 3, and 4 of Fig. 1 show as much as a 3-fold variation in ΔH for samples of equal density (5.31±0.02 g/cc) depending upon the rate of approach to the sintering temperature. For 1275-40-O_2 conditions, a rate of approach of 100–150°/hr is optimum. For 1250-40-O_2 conditions, 50°/hr is optimum. It is probable that rates faster than optimum cause a too rapid densification, so that gas given up at the sintering temperature cannot freely escape. The slower heating rates may result in the samples being raised in temperature after densification has proceeded beyond the point of easy gas escape. This traps additional gas generated by the dissociation of the system.

The data in Fig. 2 show a dependence of ΔH on cobalt content similar to that found by Sirvetz and Saunders[2] for the samples sintered 1275-40-O_2-50 (upper curve) but not for those sintered 1250-40-O_2-50 (broken curve). Their densities fall within the range 5.31±0.02 g/cc. The spheres employed in the measurements were checked after a three month interval. It was found that, for the upper curve, the values away from the minimum greatly decreased, while the one at the minimum did not. The values for the broken curve did not change.

On considering that (1) under ideal sintering conditions ΔH increases linearly with cobalt content for all of the several series studied, (2) compositions in the range where minima occur are relatively insensitive to sintering conditions, and (3) ΔH values for materials prepared under nonideal conditions can diminish with time toward those for materials prepared under ideal conditions, it appears that there is an interaction between anisotropy dependent terms and strain which can increase ΔH. The above relationships do not indicate that K itself goes through a minimum with increasing cobalt content. Possibly, magnetostriction and strain interact to increase the number of areas of reverse magnetization occurring at high fields. These effects are most permanent in nickel ferrite, change slowly for composition 3 of Fig. 1, more rapidly for composition 2, and do not appear to be appreciable in the others. This trend parallels an increase in the variation of the sizes of the metal ions in the lattice, which probably facilitates movement of ions in the system and thus permits the escape of gas during sintering and the minimization of strain during cooling.

Figure 1 shows plots of ΔH for the indicated materials, when sintered 1275 or 1250-40-O_2-optimum rate, versus their saturation magnetizations ($4\pi M$). This observed ($\frac{1}{4}\pi M$) relationship is expected from theoretical considerations[3,4] when it is assumed that limited substitutions of zinc and aluminum for nickel and iron do not markedly affect K. The deviations of compositions 2 and 3 reflect their increased sensitivity to strain. The comparison data on sintered $Y_3Fe_5O_{12}$ and $Y_3AlFe_4O_{12}$ show that line broadening effects due to K are prominent in these ferrites. However, since ΔH for $NiFe_2O_4$ based on K alone would be about 200 oe,[3] the relatively small values measured show that dipole narrowing effects are also present.

ACKNOWLEDGMENTS

The authors wish to acknowledge helpful discussions with S. Geshwind, A. M. Clogston, and J. H. Scaff, and to thank E. G. Spencer and R. C. LeCraw for permission to cite their measurements on the sintered garnet samples.

Soft Magnetic Materials

A Necessary Factor for Heat Treatment of the Permalloys in a Magnetic Field

E. A. Nesbitt, R. D. Heidenreich, and A. J. Williams
Bell Telephone Laboratories, Inc., Murray Hill, New Jersey

Recently, we have been able to show that Perminvar (Ni-Fe-Co alloy) has an inhomogeneous structure[1] and that this inhomogeneity is due to an impurity fault.[2] Evidence was obtained that small amounts of oxygen as an impurity in Perminvar caused both the faulting and the heat treatment in a magnetic field. It was exceedingly difficult, however, to remove sufficient oxygen from this material to prevent heat treatment in a magnetic field. More conclusive experiments have now been done to demonstrate the effect of oxygen on the response to magnetic annealing in the nickel-iron alloys without cobalt (Permalloys). Magnetic torque curves on a single crystal of 63% Ni-35% Fe-2% Mo for two different heat treatments illustrate this point. When the crystal was purified in hydrogen and then was heat treated in a magnetic field, it did not respond. However, after a slightly oxidizing heat treatment (pot annealing at 1000°C for 16 hrs), it did respond to the field heat treatment by developing a uniaxial anisotropy of approximately 2000 ergs per cm³.

The intimate connection between the presence of impurity faults and the ability to respond to heat treatment in a magnetic field is shown by observations on single crystals of 68% Ni-31.9% Fe-0.1% Mg, which were grown for this purpose. The (100) surfaces of these crystals showed heavily and lightly faulted regions. The work on the Perminvars has shown that the heavily faulted areas contain more oxygen than the lightly faulted areas. The magnetic torque measurements on the 68% Ni alloy confirm this idea. The heavily faulted crystal had a uniaxial anisotropy of approximately 3000 ergs per cm³ while the lightly faulted crystal had a value of only 1000 ergs per cm³.

A MELT of high purity materials was made of 63% Ni-35% Fe and 2% Mo by K. M. Olsen of our Laboratories. Polycrystalline rings of this material were heat treated at 1000°C for 16 hr in dry H_2 and furnace cooled. The samples were then heated at 750°C for 1 hr and cooled in a magnetic field and the hysteresis loop obtained after this treatment indicated that the material responded to the magnetic field heat treatment. The oxygen content of these samples was 0.0057%. A single crystal was then grown in hydrogen from this material and a toroidal ring was cut from the (100) plane. The single crystal ring was heat treated at 1100°C for 16 hr in dry H_2 and furnace cooled. This was followed by a heat treatment at 750°C for 1 hr and cooled in a magnetic field. The hysteresis loop obtained after this treatment is shown in Fig. 1(a), and the sample obviously did not respond to the field heat treatment. The oxygen content of this ring was 0.0006%. The heat treatment on this ring was then repeated thermally except for the atmosphere which was made slightly oxidizing. The data obtained [Fig. 1(b)] shows a decided squaring of hysteresis loop as a result of the oxidizing atmosphere. Some recrystallization of the surface area occurred during this treatment. Removal of this surface area did not substantially change the shape of the hysteresis loop. The oxygen content of the ring after this oxidizing treatment was 0.0077%.

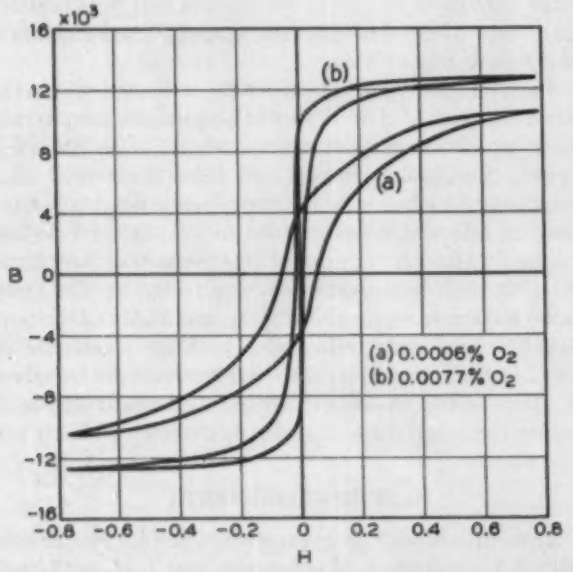

FIG. 1. Hysteresis loops on single crystal ring of 63% Ni-35% Fe-2% Mo showing the effect of annealing atmosphere (a) 1100°C-16 hr-F.C. in H_2 plus magnetic field heat treatment (b) same as (a) except for a slightly oxidizing atmosphere.

Similar experiments were made on this melt using disk specimens. A polycrystalline disk of this composition had a uniaxial anisotropy of 3100 ergs per cm³ after a magnetic field heat treatment. A single crystal disk (100) which was made from the same material did not respond to the magnetic anneal. However, after a slightly oxidizing anneal (pot anneal) at 1000°C for 16 hr followed by a magnetic anneal in a [011] direction, it did respond and yielded a uniaxial anisotropy of 2000 ergs per cm³. The behavior of these disks is similar to that of the toroidal rings discussed above.

In an attempt to reduce the oxygen content of the Permalloys, a melt was made of 68% Ni, 31.9% Fe with 0.1% Mg as a deoxidizer. A single crystal ingot was grown from this melt and a large cut across a (100) face was made. This large (100) face was then given a bromine etch and the results of this etch are shown on the left in Fig. 2 along with the results on a (100) single crystal of 63% Ni, 35% Fe and 2%Mo. The 68% Ni alloy exhibits dark and gray areas as a result of the bromine etch while the 63% Ni alloy shows only bright

areas. Electron diffraction results indicated the dark areas to be heavily faulted and the gray areas lightly faulted. The bright area of the crystal of 63% Ni showed an absence of faulting. Disks for torque measurements were cut from all three areas. Previous work on the Perminvar alloys showed that heavily faulted areas had higher oxygen contents than lightly faulted areas. The disk cut from the dark area after a magnetic anneal had a uniaxial anisotropy of 3000 ergs per cm³ while the disk cut from the gray area after a magnetic anneal had a uniaxial anisotropy of 1000 ergs per cm³. The disk cut from the bright area of the 63% Ni alloy did not show any uniaxial anisotropy.

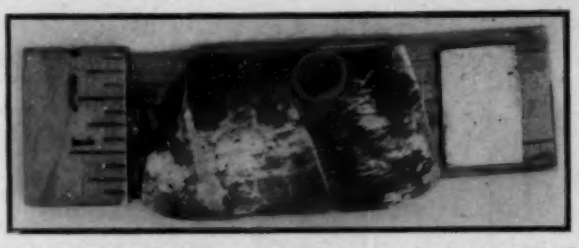

FIG. 2. Etched single crystal face (100) of 68% Ni-31.9 Fe-0.1% Mg (left) and of 63% Ni-35% Fe-2% Mo (right). Dark areas respond to magnetic annealing while bright areas do not.

CONCLUSIONS

Single crystals of 63% Ni, 35% Fe and 2% Mo were grown with sufficient purity (0.0006% O_2) so that they did not respond to heat treatment in a magnetic field. The introduction of an oxidizing atmosphere during the heat treatment caused the single crystals (0.0077% O_2) to respond to the magnetic field heat treatment. Substantiating experiments were also performed on single crystals of 68% Ni, 31.9% Fe and 0.1% Mg. As a result of these experiments we were able to conclude that oxygen is a necessary factor in the heat treatment of the Permalloys in a magnetic field. This corroborates the work recently published on the Perminvars.[1,2]

ACKNOWLEDGMENTS

This work was greatly aided by J. K. Galt and H. J. Williams. E. McDermott furnished able technical assistance by tracing many hysteresis loops using the Cioffi recording fluxmeter.

[1] E. A. Nesbitt and R. D. Heidenreich, J. Appl. Phys. **30**, 1000 (1959).
[2] R. D. Heidenreich, E. A. Nesbitt, and R. D. Burbank, J. Appl. Phys. **30**, 995 (1959).

JOURNAL OF APPLIED PHYSICS SUPPLEMENT TO VOL. 31, NO. 5 MAY, 1960

Effects of Directional Ordering on the Damping of Zone-Melted Iron*

R. E. MARINGER
Battelle Memorial Institute, Columbus, Ohio

Damping measurements (1–2 cps) have been made as a function of temperature and time on zone-melted high-purity iron, to which carbon or nitrogen have been added. Measurements were made with and without a magnetic field to isolate the magnetoelastic contribution to the damping. Two principal effects exist. These are a distortion of the Snoek peak and a time-dependent decrease in damping, which has been called the "magnetoelastic aftereffect." Magnetoelastic after-effect data for zone-melted iron, containing carbon, have been analyzed and shown to yield relaxation times in good agreement with those expected on the assumption that the effect is controlled by the interstitial diffusion of carbon.

THE well-known time dependence of permeability in alpha iron[1] has been explained by Néel[2] as the result of the directional ordering of solute interstitial atoms. The interstitials tend to inhibit the motion of ferromagnetic domain boundaries by assuming specific positions in the lattice relative to the magnetization vector.

Because of the magneto-mechanical coupling of magnetostriction, domain walls can be induced to oscillate by the application of an oscillating stress, as during a damping test. Since the motion of the domain walls is essentially an irreversible process, wall motion will absorb energy from a system in vibration, producing the magnetoelastic contribution to the damping. It is clear that, if directional ordering inhibits domain-wall motion, the inhibition should be observable by damping methods.

Damping measurements have been made on zone-melted iron containing less than 50 parts per million total impurities (other than interstitials), using a Kê-type torsional pendulum. Specimens were drawn wire, to which was added various amounts of either carbon or nitrogen. Damping tests were run at a frequency of about 1 to 2 cps over the temperature range of −60° to +130°C, using strain amplitudes of less than 5.5 $\times 10^{-6}$. The magnetoelastic contribution to the damping was identified by comparing data for a specimen tested in a 74-oe field to data for the same specimen tested in the absence of a field.

* This work is being carried out under the sponsorship of the Office of Naval Research.
[1] G. W. Rathenau, J. Appl. Phys. **29**, 239 (1958).
[2] L. Néel, J. Appl. Phys. **30**, 3S (1959).

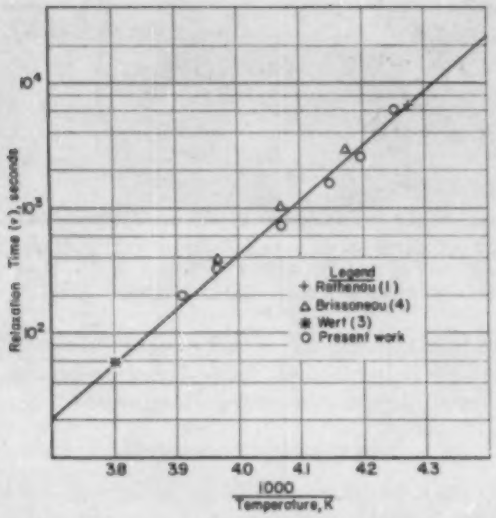

FIG. 1. Temperature dependence of the magnetoelastic aftereffect due to carbon in zone-melted iron.

Two general types of behavior were observed to result from the magnetoelastic contribution to the damping. These were (1) a distortion in the shape and size of the Snoek peaks, and a slight upward shift in their tempereatures, and (2) a time-dependent decrease in damping after the removal of a magnetic field.

The magnetoelastic contribution to the damping is low and roughly constant at temperatures below that of the Snoek peak, and is higher and roughly constant at temperatures above that of the Snoek peak. In the temperature range of the Snoek peak, the magnetoelastic damping increases in a sigmoidal fashion with increasing temperature. It is believed that this behavior is due to the increasing mobility of the interstitial atoms and a corresponding decrease in their ability to hinder domain-wall motion.

There appears also to exist in this temperature range a relaxation peak of magnetoelastic origin. This, together with the sigmoidal increase in damping, serves to distort the Snoek peak when measurements are made in the absence of a magnetic field. These data, however, are not sufficiently precise to allow an unambiguous interpretation; therefore, they cannot be discussed further at this time. The time-dependent decrease in damping, which we have called the magnetoelastic after effect, is apparently analogous to the time-dependent decrease in permeability, and the interpretation of the data is more straightforward.

To measure the magnetoelastic aftereffect, the specimen first is brought to temperature; then, the existing directional order is destroyed by the application of a small (5–20-oe) ac or dc field for a time long with respect to the relaxation time of the appropriate interstitial. The field then is removed, and the damping is measured as a function of time.

Curves of this type have been analyzed in a manner similar to that used by Rathenau[1] for the analysis of the after effect in magnetic permeability. The damping (Q^{-1}) can be expressed as

$$Q^{-1}=Q_0^{-1}+\sum Q_k^{-1}\exp(-t/\tau_k), \qquad (1)$$

where Q_0^{-1} is the background damping, t is the time since removal of the field, τ_k is a relaxation time, and Q_k^{-1} is the damping associated with τ_k at $t=0$. This relation assumes that the results of several different relaxation times are additive, and that, if they differ appreciably, they can be separated.

It should be pointed out that this type of test is particularly sensitive to vibration or to small temperature changes. These introduce discontinuous changes into the curve. A more serious experimental difficulty results from the fact that the damping is sensitive to the time elapsed since the previous reading was taken. When readings are spaced in a more or less logarithmic way, analyses according to Eq. (1) show the existence of a second and spurious relaxation time. This difficulty has been avoided by maintaining the specimens in oscillation at all times.

The significance of the rest-time effect is believed to be as follows. When a domain wall moves because of an oscillating stress, it sweeps out a certain volume. At rest, the wall occupies a smaller volume. Within the volume increment the interstitials tend to randomize, for they are first induced to order in one direction, and then in the other. Outside the swept-out volume, directional order is assumed as a function of time. As directional order occurs, it becomes more difficult for the domains to move, and the swept-out volume decreases. So long as readings are taken continuously, the swept-out volume should decrease uniformly. If, on the other hand, the oscillation is allowed to cease between readings, part of the swept-out volume tends to assume order which further inhibits the domain-wall motion, and the measured damping is lower than it otherwise would be.

The activation energy associated with the magnetoelastic aftereffect has been determined on a specimen of wet-hydrogen-purified, zone-melted iron which subsequently was carburized in CO and homogenized. The resulting solute carbon content, by internal-friction analysis, was about 3 parts per million.

Relaxation times obtained by analysis of the data in terms of Eq. (1) are shown in Fig. 1, along with several points measured by various means by Wert,[3] Brissoneau,[4] and Rathenau.[1] The line is drawn according to the equation $D=0.02\exp(-20\,100/RT)$, with $D=a^2/36\tau$, which Wert[3] determined for the diffusion of carbon in alpha iron. The agreement between magnetoelastic aftereffect relaxation times, and those of Wert leaves little doubt that the phenomenon is controlled by the diffusion of carbon. Nitrogen appears to behave in a qualitatively similar way. Experiments to verify this are in progress.

[3] C. Wert, *Modern Research Techniques in Physical Metallurgy* (American Society for Metals, Cleveland, Ohio, 1952), p. 225.
[4] P. Brissoneau, Compt. rend. **244**, 1341 (1957).

Study of Heat Treatments for Low Coercive Force 14 to 17% Aluminum Iron Alloys*

D. PAVLOVIC† AND K. FOSTER
Magnetic Materials Development Section, Materials Engineering Department, Westinghouse Electric Corp., East Pittsburgh, Pennsylvania

A study was made of the effects of atmosphere, temperature of initial annealing, and composition on the coercive force of 14 to 17% Al-Fe alloys. A combined effect of heat treatment atmosphere and temperature of initial annealing is shown to exist in this alloy region, and is discussed in terms of a possible influence of purification and atomic ordering. The unique feature of these alloys is that heat treatments in air at 900°C produce lower coercive force values than heat treatments in dry hydrogen at the same temperature. This factor would make the heat treatments of these alloys more economical than those of other standard high-permeability alloys. Observations made on the binary Al-Fe iron alloys apply to the heat treatment of Al-Fe alloys containing ternary additions. These observations also show that the heat treatment controls both the grain size and the distribution of the second phase in ternary alloys, which in turn affect the magnetic properties.

INTRODUCTION

THE unique combination of useful magnetic, physical, and mechanical properties of Al-Fe alloys in the composition range of 10 to 17 weight % Al has stimulated investigations of the problems connected with the processing and properties of these alloys. The investigations of magnetic properties of these alloys were centered largely on the studies of changes of both structure sensitive and structure insensitive magnetic properties with an ordering reaction taking place in the aluminum iron system between 10 and 20% Al.[1-3] It was found in the early stages of research on these alloys that a high temperature heat treatment followed by a quench from above the Fe_3Al ordered region is required to produce low coercive force materials in the alloys with 14 to 17% Al. Detailed investigations have been made in this laboratory to determine optimum heat treatment conditions for these alloys.[4] As a part of this program, the present study is concerned primarily with the effects of both different initial annealing temperatures and different heat treatment atmospheres on the coercive force of 14 to 17% Al-Fe alloys. Furthermore, the effect of the initial annealing temperature on the coercive force of 16% Al-Fe with small ternary additions was considered in this study.

EXPERIMENTAL PROCEDURES

The alloys used in this investigation were melted and poured in a vacuum melting furnace using electrolytic iron and high purity ingot aluminum as raw materials. The ingot analysis showed impurities such as C, S, P, N, and O, each to be on the order of 10–20 ppm or less. The alloys were hot rolled from the ingot directly to the final sheet thickness of 0.007 in. Ring laminations were punched from the rolled sheets for heat treatment and magnetic testing. The heat treatment consisted of initially heating the samples at 900 and 1200°C for 2 hrs, furnace cooling to 600°C and quenching in water after $\frac{1}{4}$ hr at the latter temperature. Two types of atmosphere were used in this program, dry hydrogen with a dew point of −70°C or better and still air. Coercive force values for all samples were measured from a field of 100 oe.

The alloys used in the major part of this work contained from 15 to approximately 17% Al. For the study of the effect of ternary additions, small amounts of boron, zirconium, and Lan-Cer Amp (a commercial mixture of rare earth elements) were added to a melt containing 16% Al, while 1% Si was added to a melt of 15% Al. The exact compositions of the ternary alloys are shown in Table I.

RESULTS AND DISCUSSION

The effect of initial annealing temperatures of 900 and 1200°C on the coercive force of aluminum iron alloys with 15 to 17% Al, heat treated in dry hydrogen, is

TABLE I. Effect of initial heat treatment temperatures on coercive force of Al-Fe alloys with additives.

Alloy Composition	Initial heat treatment temperature	Hc Oersteds
15.8% Al, No additive	900	0.035
	1200	0.021
15.5% Al, 0.24% B	900	0.081
	1200	0.028
15.6% Al, 0.09% Zr	900	0.110
	1200	0.031
15.8% Al, 0.014% Ce	900	0.037
	1200	0.037
15.0% Al, 1.0% Si	900	0.036
	1200	0.022

* This work was supported in part by the Aeronautical Research Laboratory, Wright Air Development Center, under a U. S. Air Force contract.

† Presently with Westinghouse Electric International Company, East Pittsburgh, Pennsylvania.

[1] H. Masumoto and H. Saito, Sci. Repts. Research Inst., Tohoku Univ. Ser. **A4**, 321 (1952).

[2] J. F. Nachman and W. J. Buehler, J. Appl. Phys. **25**, 307 (1954).

[3] R. C. Hall, J. Appl. Phys. **28**, 707 (1957).

[4] D. Pavlovic and K. Foster, *Proceedings of the Conference on Magnetism and Magnetic Materials, Boston*, 1956 (American Institute of Electrical Engineers, New York, 1957), AIEE Spec. Publ. T-91, p. 266.

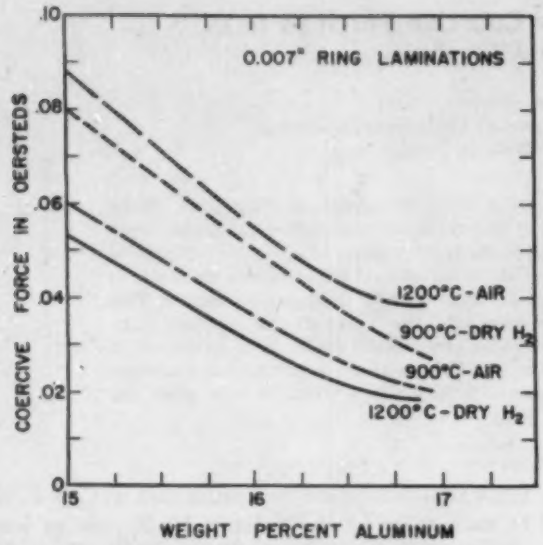

FIG. 1. Effect of atmosphere and initial heat treatment temperature on the coercive force of 15 to 17% Al Fe.

shown in Fig. 1 (second and fourth curve from the top). As can be seen, annealing at 1200°C prior to cooling to the temperature of quenching produces considerably lower coercive force values than annealing at 900°C. For both temperatures, the coercive force decreases with increasing aluminum content but the difference in the coercive force value decreases as the composition approaches 17% Al. The effect of the initial annealing temperatures between 900 and 1200°C was studied with a sample of 16% Al-Fe. The results (not shown in Fig. 1) showed that a fairly steep decrease in the coercive force value takes place between 1000 and 1100°C.

Variations in the annealing atmosphere showed some very interesting developments which can be of considerable economic advantage. Dry hydrogen (dew point −70°C or better) and still air were used with the initial annealing temperatures of 900 and 1200°C. The results shown in Fig. 1 demonstrate that a heat treatment at 900°C in still air produces considerably lower coercive force values than the similar treatment in dry hydrogen. At 1200°C, however, the situation is reversed. At this temperature, the coercive force values for the hydrogen heat treatment are the lowest for this series, while the corresponding values for air are the highest.

The combined effect of heat treatment atmosphere and initial annealing temperature on the coercive force of 14 to 17% Al-Fe alloys may be ascribed to a number of factors. The most logical ones to be considered are the effects of purification, oxidation, and atomic ordering, or rather an interplay of these. Although it is questionable whether the effect of atomic ordering may compete with the effect of oxidation and purification, it would be of interest to discuss the possible effect of atomic odering in more detail.

In this connection, the new phase diagram of the ordering region of the aluminum iron system should be considered.[5] This new phase diagram shows that at elevated temperatures (approximately 975 to 1075°C for 15 to 17% Al) the Fe-Al ordered structure transforms to a random structure; hence, the initial annealing at 900°C is expected to produce at least a partially Fe-Al ordered structure, whereas annealing at 1200°C results in a random distribution of aluminum in the bcc iron lattice. The oxidation of aluminum by annealing in air may be affected by the distribution of aluminum in the lattice, similar to a suggestion by Seybotl[6] that ordering effects the oxidation behavior of silicon in 3% silicon iron. At 900°C, the Al-Fe alloys under discussion are at least partially Fe-Al ordered; it can now be postulated that the aluminum is less available for oxidation since the activity of aluminum in solution in the ordered alloys is less than that of the disordered alloys.[7] Furthermore, with respect to impurities in these alloys, the reducing power of hydrogen at 900°C is relatively low, whereas air may be expected to partially remove carbon. At 1200°C, on the other hand, a random distribution of aluminum exists. The reducing power of hydrogen is high at this temperature as is the activity of aluminum making the aluminum available for oxidation.

The small ternary additions, shown in Table I, were used to change the microstructure and the mechanical characteristics of 16% Al-Fe. Additions of boron and zirconium were particularly effective, boron by increasing ductility and zirconium by raising the recrystallization temperature. However, both of these additives form a second phase in the alloy, resulting in relatively high coercive force values for the heat treatments with an initial annealing temperature of 900°C. Considerable improvements in the coercive force of these alloys resulted when the initial annealing was done at 1200°C. Microstructures of these alloys showed that the specimens heat treated at 900°C had fine, evenly dispersed inclusions, while the inclusions in the specimens initially heat treated at 1200°C were much larger and not so evenly dispersed. Hence, the changes in the distribution and size of the second phase were necessary to obtain the benefit of the initial anneal at 1200°C.

---

[5] A. Taylor and R. M. Jones, J. Phys. Chem. Solids **6**, 16 (1958).
[6] A. U. Seybolt, Trans. Met. Soc., Am. Inst. Met. Engrs. **215**, 757 (1959).
[7] In this connection, it is interesting to note that the initial anneal in air at 900°C increases the coercive force of 12% Al Fe as compared with the same treatment in hydrogen. This composition has a random structure at 900°C.

Effect of Directional Orientation on the Magnetic Properties of Cube-Oriented Magnetic Sheets

K. FOSTER AND J. J. KRAMER
Magnetic Materials Development Section, Materials Engineering Departments, Westinghouse Electric Corporation, East Pittsburgh, Pennsylvania

An investigation of the effect of directional orientation on the dc magnetic properties of cube-oriented ([001] (100) textured) 3% silicon iron sheets has been made. Induction values for a field of 10 oe (B_{10}) followed the relationship

$$B_{10}=B_s/(\cos\theta+\sin\theta),$$

where B_s is the saturation induction and θ is the average angular deviation of the ⟨100⟩ direction from the rolling direction. A plot of B_{10} values as a function of the percent of grains with a ⟨100⟩ direction within 10° of the rolling direction showed that very good directional orientation is required to obtain high B_{10} values.

INTRODUCTION

A PROCESS for obtaining cube-oriented magnetic sheets by secondary recrystallization has recently been reported.[1] When carried out properly, this process results in a very high degree of parallelism of the {100} plane with respect to the plane of the sheet. The orientation of the ⟨100⟩ direction with respect to the rolling direction, on the other hand, can vary considerably. The purpose of the present investigation has been to study the effect of this variation in directional orientation on the dc magnetic properties of thin silicon iron sheets having nearly 100% of their grains with the {100} plane closely parallel to the sheet surface. The results are correlated with calculations based on single crystal derivations.

EXPERIMENTAL PROCEDURE

Baby Epstein strips, 30 cm long by 3 cm wide were cut parallel to the rolling direction from a number of 3% silicon iron sheets which had been cold rolled to 0.004 in. These strips were heat treated to obtain essentially complete growth of cube-on-face grains (grains with a {100} plane in the plane of the sheet). Little variation in grain size was observed for different sheets; the average grain diameter was about 2 mm.

Orientation measurements were made using a domain pattern technique.[2] A colloidal magnetite (Elmore) solution[3] was applied to the as heat-treated sheets and allowed to dry. Domain patterns typical of the cube orientation could then be observed with a metallurgical microscope using bright field illumination. Deviations of the ⟨100⟩ direction from the rolling direction were measured for between 50 and 100 grains from each sample by measuring the angular deviation of 180° domain walls from the rolling direction for each grain. An angular deviation (θ) was calculated for each sample by taking a numerical average of the angular deviations of all the grains measured. The percent of grains having a ⟨100⟩ direction within 10° of the rolling direction was also calculated for each sample.

Dc magnetic tests were made using a 30-cm Epstein frame and an integrating fluxmeter. An automatic *B-H* loop tracer was used to obtain coercive force values and induction values (B_{10}) for a field of 10 oe. The coercive force values for these sheets ranged between 0.07 and 0.09 oe. No correlation between the coercive force and grain orientation of the sheets was made.

RESULTS AND DISCUSSION

The use of the induction value reached for a field of 10 oe (B_{10}) in the study of oriented magnetic sheets is based both on practical and theoretical considerations. A high B_{10} value is desirable in magnetic sheets in order to obtain high inductions for low exciting fields. The B_{10} value can also be taken as a good approximation of the magnetization value reached in a sheet when the initial stages of magnetization characterized by domain wall movement have taken place, but no domain rotation has occurred; this magnetization value is denoted as I_0. It can be shown[4,5] that little domain rotation can take place in 3% silicon iron for a field of 10 oe.

For a single crystal having no demagnetizing effects, the relation between I_0 and the saturation magnetization (I_s) is given as

$$I_0=I_s\cos\theta', \tag{1}$$

where θ' is the angle between the applied field and the easy direction of magnetization.[4] Since B_{10} is approximately equal to $4\pi I_0$,

$$B_{10}=B_s\cos\theta'. \tag{1a}$$

This function is plotted as a broken line in Fig. 1(a) for a saturation value (B_s) of 20 300 gauss.

Because of demagnetizing effects, Eq. (1) has been found not to hold for a single crystal rod, but

$$I_0=I_s/(\alpha_1+\alpha_2+\alpha_3) \tag{2}$$

[1] F. Assmus, et al., Z. Metallk. 48, 341–349 (1957).
[2] P. A. Albert, *Proceedings of the Conference on Magnetism and Magnetic Materials, Boston, 1956* (American Institute of Electrical Engineers, New York, 1957), AIEE Spec. Publ. T-91, p. 423.
[3] W. C. Elmore, Phys. Rev. 54, 1072 (1938).
[4] R. M. Bozorth, *Ferromagnetism* (D. Van Nostrand Company, Inc., Princeton, New Jersey, 1951).
[5] H. Lawton and K. H. Stewart, Proc. Roy. Soc. (London) A193, 72 (1948).

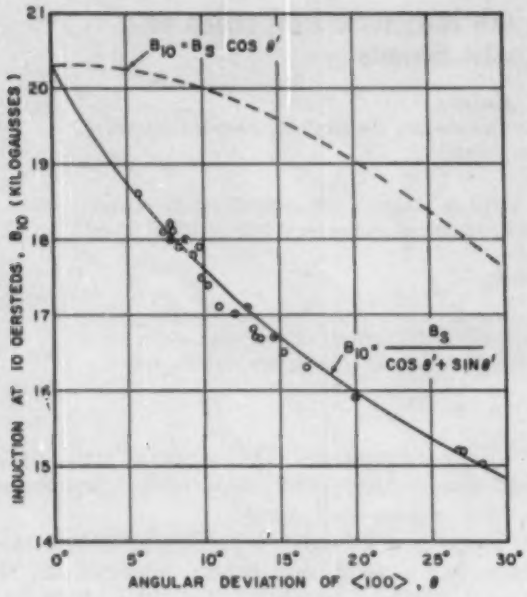

(a)

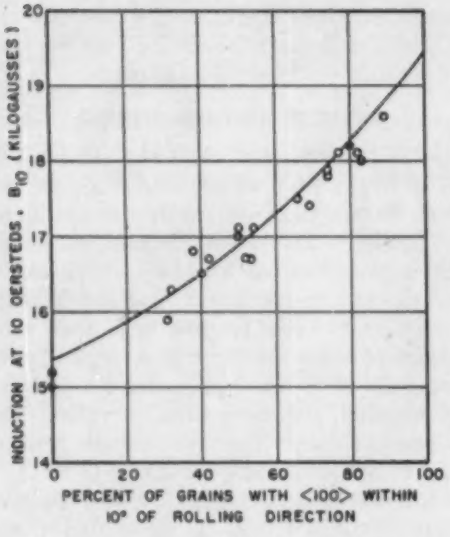

(b)

FIG. 1. Effect of directional orientation on B_{10} values of cube oriented sheets.

has been derived,[5] where α_1, α_2, and α_3 are the direction cosines between the easy directions of magnetization in the rod and the direction of the applied field. If a 3% silicon iron single crystal rod has a ⟨100⟩ direction normal to the direction of the field, then

$$B_{10}=B_s/(\cos\theta'+\sin\theta'), \qquad (2a)$$

where θ' is the angle between the nearest ⟨100⟩ direction and the direction of the applied field. Equation (2a) is plotted as a solid line in Fig. 1(a).

The experimental points in Fig. 1(a) represent measured B_{10} values as a function of the average angular deviation (θ) for each sheet. The smallest directional angular deviation (about 6°) observed in Fig. 1(a) corresponds to a distribution around the (100) [001] orientation. The largest deviation (about 27°) corresponds to a distribution around the (100) ⟨210⟩ orientation. Orientations closer to (100) [011], corresponding to the maximum directional angular deviation (45°) were not observed. The experimental data show a remarkably close fit with Eq. (2a). The results indicate that each grain in these cube-oriented silicon iron sheets behaves as a number of thin rods having a ⟨100⟩ direction normal to the rolling direction; i.e., there is essentially no deviation of the cube plane from the plane of the sheet. Thus, the demagnetizing effects are apparently similar and play an important role in the magnetization process. These results are in agreement with those of Lawton and Stewart[6] for polycrystalline silicon iron sheets with the Goss texture.

A convenient means for describing the directional orientation is the percent of grains having a ⟨100⟩ direction within 10° of the rolling direction.[1,7] A plot of the percent of grains having a ⟨100⟩ direction within 10° of the rolling direction (denoted by X) as a function of the average angular deviation (θ) approximated a straight line defined by

$$\theta=25.6-0.23X. \qquad (3)$$

Experimental values of the percent of grains with ⟨100⟩ within 10° of the rolling direction are plotted as a function of B_{10} in Fig. 1(b). The solid curve was calculated from Eqs. (2a) and (3). The best oriented sample in this experiment had approximately 90% of its grains with ⟨100⟩ within 10° of the rolling direction, resulting in a B_{10} value of 18 600 gauss.

Equation (3) is particularly dependent on the orientation distributions observed. For example, a sheet having 100% of its grains with ⟨100⟩ within 10° of the rolling direction would still have an average angular deviation (θ) of about 2.5°, and a maximum B_{10} value of 19 400 gauss would result. Thus, because of the demagnetization factors in thin sheets, extremely good directional orientations are required in cube-oriented 3% silicon iron sheets to obtain B_{10} values above 19 000 gauss.

[6] H. Lawton and K. H. Stewart, Proc. Phys. Soc. (London) **A63**, 848 (1959).
[7] G. Wiener et al., J. Appl. Phys. **29**, 366 (1958).

JOURNAL OF APPLIED PHYSICS SUPPLEMENT TO VOL. 31, NO. 5 MAY, 1960

Secondary Recrystallization in Vacuum Annealed Silicon Iron

G. Baer, D. Ganz, and H. Thomas
Laboratorium der Vacuumschmelze AG, Hanau, Germany

In 3% SiFe with high magnetocrystalline anisotropy, it is desirable to produce grain oriented material by secondary recrystallization. The size of the surface energy is an important reason for the selection of growing crystals during secondary grain growth. By studying the special crystal growth, it is essential to create well defined conditions on the surface of the sample. The surface is least disturbed if the sample is heated directly by an electric current. In such experiments, we found crystals growing either with a (110) or with a (100) orientation. The selection is influenced by the annealing temperature, by the conditions of evaporation, and by the surroundings of the sample. The growth of (110) plane grains rather than (100) grains can be understood from consideration of the surface energy.

INTRODUCTION

THE driving force for the selection of (110) or (100) grain growth is often interpreted in terms of the surface energy. Theoretically, in bcc lattices the close-packed crystal plane (110) should have the lowest surface energy.[1] Therefore, the growth of (110) is plausible as suggested by Walter and Dunn[2] for tertiary recrystallization. On the other hand growth of (100) grains is favored in thin tapes having a large ratio of surface to volume. Therefore, Detert,[3] Wiener,[4] and Walter[5] assume that the (100) growth is favored due to surface tension as the driving force. But the same mechanism can be responsible for the two different orientations, only if the surface state and the surface energy of the sample is changed by different conditions of thermal treatments.

For the study of the oriented crystal growth, defined surface conditions are very important. Experimentally, we were anxious to eliminate any influence of the environment during heat treating to secure conditions as pure as possible.

EXPERIMENTAL

The samples contained about 3% Si and were prepared by vacuum melting and processed to gauges between 2 and 12 mils. To get secondary recrystallization we annealed a set of samples in a tube of purest alumina inside a resistance furnace.

In other experiments, the sample was annealed by the passage of an electric current (direct heating). Thus, the specimen has the highest temperature in the assembly. In one arrangement the sample was freely suspended, surrounding walls were far away. In a second arrangement the sample was closely covered with purest alumina plates. The annealing atmosphere was high vacuum (pressure 0.1 μ or lower) or hydrogen at low pressure (1–100 μ). The crystal orientation was determined optically by etchpits. In this report, we only describe the crystal plane orientation neglecting the direction of cube edges.

RESULTS AND DISCUSSION

In alumina tube annealing, secondary recrystallization occurs with a (110) as well as with a (100) orientation. Occasionally, a zebra-like structure resulted with large (110) and (100) crystals side by side in the same strip. The annealing time seems unimportant. However, there is a remarkable temperature dependence. High annealing temperature favors (110) lower temperature (100) crystal growth.

The experiments with directly heated samples are better defined and more illuminating. At high temperatures (1200°C), with freely annealed samples, (110) crystals grow very rapidly so that in a short time the secondary recrystallization is completed. Surprisingly, this results for all thicknesses used. In contrast to other processes for the development of cube-on-edge texture, the (110) growth proceeds in thinner strips easier and quicker then in thicker ones. Our results are in best agreement with investigations of Albert and Foster.[6]

Because of the rapid (110) growth you can see the old primary grain boundaries still as steps and grooves in the completed (110) structure. There are also single small (100) crystals taken over by the rapid growing (110) grains.

The relations differ principally from the conditions previously reported by May and Turnbull.[7] There a dispersed second phase favors the grain growth of (110) in a lower temperature range.

In our experiments, the essential conditions for rapid growth of (110) grains are high annealing temperature, sample at the maximum temperature of the arrangement, and evaporation without restraints. These conditions confirm the surface tension being the driving force for selection of (110) growth. As expected for undisturbed surface conditions, the close-packed (110) crystal plane is preferred. If one lowers the annealing temperature under the same conditions, then also some

[1] I. Pfeiffer, Z. Angew. Phys. **11**, 477 (1959).
[2] J. L. Walter and C. G. Dunn, Trans. Am. Inst. Mining Engrs. **215**, 465 (1959).
[3] K. Detert, Acta Met. **7**, 589 (1959).
[4] G. Wiener (to be published).
[5] J. L. Walter, Acta Met. **7**, 424 (1959).
[6] P. A. Albert and K. Foster, Westinghouse Corporation (private communication).
[7] J. E. May and D. Turnbull, J. Appl. Phys. **30**, Suppl. 210 S (1959).

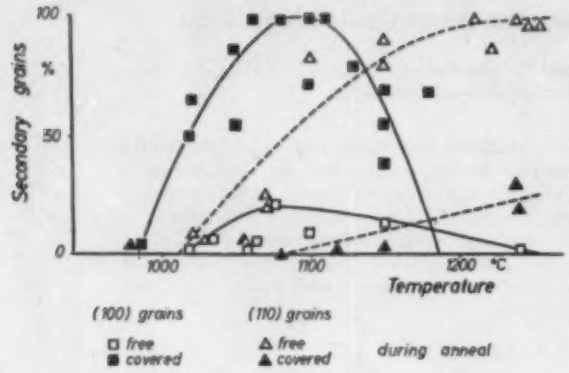

FIG. 1. Secondary recrystallization in 10 mil SiFe strips.

(100) crystals will grow. (110) growth is diminished. Complete secondary recrystallization with (100) orientation in directly heated samples was attained only by covering the sample during anneal, a practice often used in our laboratory. We covered the sample with purest alumina plates. The completion of cube grain growth requires a longer time than that of (110) growth. We found also a remarkable temperature dependence in good agreement with the results of tube furnace annealing (Fig. 1). Contrary to "free annealed" strips, the surface of "covered annealed" strips is smooth after heat treatment favoring (100) growth provided during the anneal the covering material is not remarkable colder than the sample. Without this precaution, no secondary recrystallization occurs but only coarsening of thermally etched grains with many orientations.

According to these results, we assume that a very important factor for (100) growth is the self vapor of the sample, which is reflected immediately or returns to the sample after temporary condensation on the covering material. By this returning vapor stream, the surface is continuously renewed, a process apparently promoting the cube grain growth. Neglecting an hypothetical temperature dependence of surface energy, two points of view may be considered. Firstly, there may be a change of the surface energy by a chemical reaction or an adsorption process. A reaction with the covering material can be excluded with a high certainty. Possibly, some substances volatilize out of the sample and form surface layers, perhaps as compounds due to the very small oxygen content of the annealing atmosphere, changing the surface energy levels of the crystal planes. Secondly, the reflected vapor of the sample may fill up the momentarily originated thermal grooves. That is just the spot, where grain boundary tension and surface tension should be in equilibrium. It may be imagined that the deposition of the returning metal atoms disturbs this equilibrium and grain boundary motion continues.

Further informations about grain growth can be attained studying "tertiary" recrystallization, a conception firstly used elsewhere.[3] Suitably prepared samples with (110) and (100) secondaries mixed in one strip contain a large amount of (110) tertiaries after a second anneal at high temperatures without covering, secondary (100) grains are almost consumed. By starting also with mixed orientation, but applying optimum (100) growth conditions, the sheet is transformed in (100) tertiaries completely. We found the transformation (100) → (110) in a macroscopic degree and further as well, the reversed process of transformation (110) → (100) by tertiary recrystallization. According to our experiments, it is an essential condition for a completed tertiary recrystallization that the later annealing temperature is higher than the preceding, which effected secondary grain growth. Therefore, it is generally more probable to get (110) final orientation, because high temperature favors always the growing of (110). But we could never force considerable tertiary (100) grain growth if the former annealing temperature was higher than the later temperature, which should be favorable for (100) growth.

Since even after a preanneal at higher temperature a difference in surface energy exists between different oriented crystals, we consequently suggest: Either the surface tension is of a type such that (110) crystals are favored to grow always, or we must assume that under certain conditions the surface tension can be of a type such that (100) growth is favored, but the amount of surface tension is too small to be effective unless the matrix is still an instable one containing sufficient strains, imperfections and dislocations.

Characteristics of Supermendur at 500°C

M. LAURIENTE AND G. E. LYNN
Westinghouse Electric Corporation, Air Arm Division, Baltimore, Maryland

An anomalous transient effect in Supermendur material is dramatically displayed when the magnetic properties of toroidal tape cores of the material are measured at temperatures between 500 and 600°C on a constant current flux reset tester. This test is designed to simulate the action of a half-wave self-saturating magnetic amplifier. Normally a steady-state cyclic flux change is achieved within one cycle of the applied alternating magnetizing field. A transient lasting several minutes (equivalent to several thousand cycles of alternating field) was observed instead for this alloy. When measured at room temperature after exposure to extreme temperatures the magnetic properties are observed to be degraded from the properties measured at room temperature before exposure. No direct evidence has been found to show that these two phenomena are related since specimens exposed to temperatures insufficient to cause the transient were observed to sustain some degradation in room temperature properties. The contributions of various mechanisms were investigated by environmental control. The most probable causes of the degradation of properties after high temperature exposure were concluded to be oxidation and relaxation of oriented domains.

INTRODUCTION

WHEN Supermendur material[1] was tested in air at temperatures in excess of 500°C using a 400 cps constant current flux reset core tester[2] unusual magnetic properties were found. This type of core tester normally establishes a steady-state cyclic flux condition in a core within one cycle of excitation frequency. It was found, however, that the Supermendur alloy required several hundred seconds to establish steady-state cyclic flux conditions at temperatures above 500°C. In addition to this transient, Supermendur suffers an irreversible change in magnetic properties at high temperatures.[3] From the known structure of Supermendur,[4] one may deduce that the instability at high temperatures may be a result of oxidation, order-disorder transformation, or relaxation of oriented domains. In this study an attempt was made to analyze the qualitative significance of these factors.

The cores were toroidally wound from 0.004-in. tape insulated by magnesium oxide which was first applied as magnesium methylate[5,6] and then thermally decomposed to the oxide. The wide spread in the original room temperature properties of the individual cores can be attributed to the fact that the samples used were randomly selected from a batch of experimental cores.

EXPERIMENTAL PROCEDURES

The tester, designed to AIEE Standard No. 432, excites the core through an asymmetrical minor dynamic hysteresis loop by means of a unidirectional half-sinusoid of current. The core is operated over a different minor loop by applying a dc mmf (usually called reset mmf), in opposition to the mmf produced by the excitation pulse. In general, tests are made at a series of values of reset mmf yielding the cyclic flux change achieved as a function of reset mmf.

There were three phases in the study. First considered was an experiment in which oxidation, ordering, and domain relaxation were presumed to be in action. This phase consisted of thermal cycling the core in air to 500°C. The core was first tested at room temperature; then brought up to temperature from a cold furnace, taking approximately one hour to arrive at 500°C. The core was then allowed ½ hour to reach equilibrium before testing again. Following furnace cooling, the core was tested again at room temperature. The second phase differed from the first by having the core in a dissociated ammonia atmosphere during the thermal cycle. It was assumed that oxidation would be prevented, allowing only ordering and relaxation of oriented domains. Elevated temperature tests could not be made in this phase because of the inadequacy of test equipment for testing

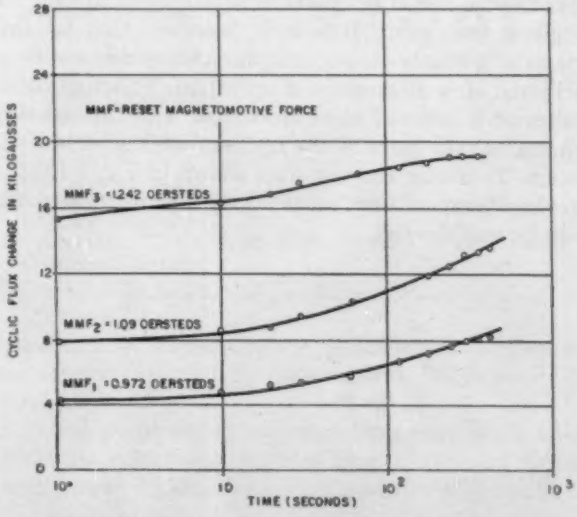

FIG. 1. 400-cps cyclic flux change characteristics produced as a function of reset mmf and time at 525°C.

[1] H. L. B. Gould and D. H. Wenny, Elec. Eng. (March, 1957).
[2] *Test Procedure for Toroidal Magnetic Amplifier Cores* (American Institute of Electrical Engineers, New York, 1959), AIEE Publ. No. 432.
[3] M. Pasnak and R. H. Lundsten, J. Appl. Phys. **30**, 4 (1959).
[4] W. C. Ellis and E. S. Greiner, Trans. Am. Soc. Metals **29**, 415 (1941).
[5] L. A. Suchoff, U. S. Patent No. 2,796,364, "Method of Forming Adherent Film of Magnesium Oxide," June 18, 1957.
[6] M. Lauriente, "Magnesium Oxide Films as Magnetic Tape Insulation," Insulation **5**, 11 (1959).

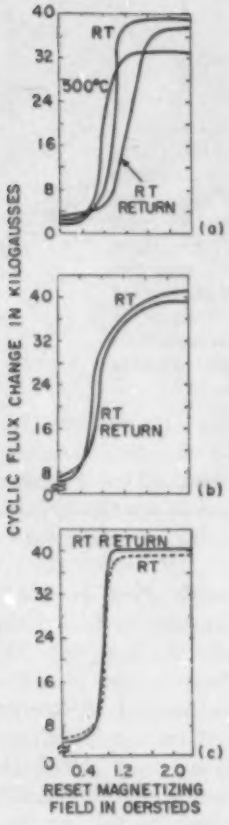

FIG. 2. 400-cps cyclic flux change characteristics during thermal cycle (a) in air; (b) in hydrogen atmosphere; and (c) in hydrogen atmosphere in the presence of a magnetic field.

in a controlled atmosphere furnace. The last phase was identical to the second except that a field of 24 oersteds was applied. This served to prevent relaxation of the oriented domains.

DISCUSSION

At the elevated temperature a transient condition, illustrated in Fig. 1, was found. Normally, the cyclic flux change would be constant with respect to time for a given reset mmf. It is seen, however, that for this material a steady-state cyclic flux change has not been achieved after 10 minutes of operation. This anomalous behavior is believed to be associated with the ordering known to take place in the temperature region investigated. To obtain the test data shown in Fig. 2 for the elevated temperatures, an arbitrary time interval of one minute was allowed.

In Fig. 2(a), the cyclic flux change for zero reset mmf (which corresponds to $B_m - B_r$) is seen to increase throughout the cycle, resulting in a loss in loop squareness. The loop width, measured from the midpoint of the curve, is seen to decrease with increasing temperature but is much wider after exposure. The peak cyclic flux change is analogous to magnetic saturation at small fields. This saturation is seen to decrease with increasing temperature, but does not quite return to the original value after the thermal cycle is complete.

These changes, which have just been described for the thermal cycle in air, are still present when the same experiment is conducted in a protective atmosphere, but to a considerably lesser degree, as shown in Fig. 2(b). When the material is heated in the presence of both a protective atmosphere and a magnetizing field, the curve after cycling is actually slightly improved, as may be seen in Fig. 2(c).

Comparison of Figs. 2(a) and (b) would seem to indicate that oxidation plays a major role in the degrading effects of thermal cycling. Comparison of Figs. 2(b) and (c), in turn, would indicate that relaxation of oriented domains makes a small contribution to the degradation observed in Fig. 2(a). Ordering effects, if the data of Fig. 2(c) are relied upon, would seem to improve properties rather than degrade them. This conclusion may not be justified, since the improvement observed might be a result of continuing domain orientation as a result of the applied field.

CONCLUSIONS

In conclusion, then, this paper would indicate that two important points must be considered when considering Supermendur for magnetic amplifiers at elevated temperatures:

(1) The transient phenomenon restricts the maximum allowed temperature to below 500°C.

(2) The permanent degradation of room temperature magnetic properties from thermal cycling is principally due to oxidation.

ACKNOWLEDGMENTS

The authors are indebted to F. W. Segel, W. Staewen, J. M. Kazaroff, and W. E. Pensmith for preparation of samples and various measurements.

Effects of Hydrostatic Pressure on the Properties of Magnetic Materials

R. E. Alley, Jr.,* and V. E. Legg
Bell Telephone Laboratories, Incorporated, Whippany, New Jersey

A review of the literature on hydrostatic pressure effects on magnetic materials showed a lack of information on technologically important properties such as initial permeability, and the hysteresis loop. Measurements of these properties up to 20 000 psi showed that most solid materials are only slightly affected. These include tape cores of supermalloy, supermendur, 4–79 Mo-permalloy and grain-oriented Si-steel, as well as S-5 ferrite memory cores, and compressed powder cores of 2–81 Mo-permalloy or of carbonyl iron. Some types of NiZn and MnZn ferrite show increase of coercive force and decrease of permeability with pressure. Measurements were made of permeability vs frequency of MnZn ferrite to find the relaxation frequency. At atmospheric pressure, the permeability shows a sharp decline above 0.85 Mc. At 20 000 psi the decline in permeability does not occur until 1.6 Mc.

THE recent practice of deep-sea submergence of apparatus has drawn attention to the possible effects on magnetic materials of hydrostatic pressures. It is well known that mechanical stresses such as bending, rolling or wire-drawing drastically reduce the initial permeability and increase the hysteresis loop area of high quality magnetic materials. Omni-directional stresses might be expected to have serious effects, also. Review of the literature on hydrostatic effects shows that interest in the past has been chiefly in magnetic theory, including data on Curie temperature,[1,2] and on saturation induction.[3] The present paper provides data on technologically important materials which may be useful in the design of components suitable for high pressure environment.

Pressure was applied to ring-shaped magnetic cores by enclosing them in an oil filled cylinder. All porous cores such as ferrite and compressed powder were vacuum impregnated with oil, before testing.

Temperature was maintained at approximately 25°C. Temperature sensitive materials such as ferrites showed transient changes immediately after increase of pressure, which were ascribed to temperature increase resulting from compression of the oil (G. E. 10 C insulating oil). Any such increase in temperature would disappear shortly by transfer of heat to the surrounding steel cylinder. Measurements on these materials were recorded after at least a 10 min wait, i.e., when it was ascertained that any drift of magnetic properties had ceased.

Dc hysteresis loops were observed using two windings on each ring, connected to a Cioffi recording fluxmeter. Coercive force and residual induction measurements were recorded for each pressure stage from zero to 20 000 lbs/sq in. and back to zero. No measurable changes in hysteresis loop characteristics were found on tape cores, as noted in Table I. Similarly, an S-5 ferrite memory core was unaffected. Gradual enlargement of the hysteresis loop with pressure was noted on MnZn and NiZn ferrite cores, reflected in an increase of coercive force. Correspondingly, a small increase of residual induction occurred, without appreciable change of saturation induction. These changes in hysteresis loop area of MnZn and NiZn ferrites under pressure were reversible, as were the accompanying decreases in initial permeability. This extends to MnZn ferrite the pressure sensitivity reported by Adams and Davis on NiZn ferrite.[4]

Table I. Effect of hydraulic pressures to 20 000 psi on magnetic materials.

	dc Loop			ac 1000 cps	
Core	B_r kgauss	H_c oe	H_c Change at 20 kpsi	μ_0	μ_0 Change at 20 kpsi
4–79 Mo-permalloy, 1 mil tape	5.40	0.015	0	9250	−1.5%
Supermalloy, 1 mil tape	4.20	0.009	0	52800	+0.4
Grain oriented Si-Steel, 4 mil tape	16.0	0.29	0	700	+3.0
Supermendur, 2 mil tape	22.5	0.285	0	...	...
2–81 Mo-permalloy Powder core	...	...	...	125	0
Carbonyl iron powder core	...	...	...	10	0
S-5 ferrite memory (General Ceramics)	1.80	0.65	0	60	+2.8
Ferramic Q_1 (General Ceramics)	...	...	...	145	+3.5
Ferramic Q_2 (General Ceramics)	...	...	...	43	+0.9
Ferramic O_2 (General Ceramics)	...	...	...	90	−5.7
Stanferrite S 4 (Std. Tel. & Tel.)	...	...	...	735	−24.4
NiZn ferrite (Western Electric)	0.60	0.02	+440%	5900	−64
Mn-Zn ferrite (Western Electric)	0.90	0.20	+320	2200	−54

Initial permeability measurements were made using 1000 cps inductance readings from a Maxwell bridge, with magnetic induction values less than 20 gauss. These

* Now with Texas Instruments, Inc.

[1] R. L. Steinberger, "Magnetic properties of Fe-Ni alloys under hydrostatic pressure," in *Physics* (1933), Vol. 4, p. 153.

[2] L. Patrick, Phys. Rev. **93**, 384 (1954).

[3] H. Ebert and A. Kussmann, Phys. Z. **38**, 347 (1937).

[4] C. Q. Adams and C. M. Davis, Jr., J. Appl. Phys. **29**, 372 (1958).

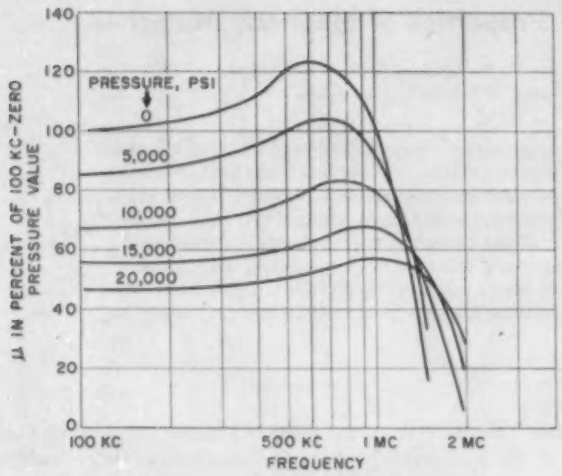

FIG. 1. Initial permeability, pressure, frequency curves for MnZn ferrite, "100%" permeability = 2440.

measurements tended to be more sensitive in response to pressure, than hysteresis loop measurements. Tape cores were practically unaffected, as noted in Table I. Powder cores were similarly immune to pressure effect. This behavior is in marked contrast to the effect of pressure on powder cores which are coated with an enamel protective finish. Such coated cores showed effects of pressure, due to unbalanced mechanical stresses. Sensitivity was removed when the enamel was stripped off, so as to admit hydrostatic fluid to surround the metallic powder particles uniformly. Ferrite cores showed varying amounts of sensitivity to hydrostatic pressure of 20 000 psi. Reduction of permeability was as much as 64% for NiZn ferrite having 5900 initial permeability, but lower reductions were observed for ferrites having lower permeabilities. Except for Ferramic O_2, the lowest permeability types of ferrites showed small increases of permeability with increase of pressure.

Measurements of inductance at higher frequencies give indications of wall motion relaxation, at somewhat less than 1000 kcs.[5] The relaxation frequency of MnZn ferrite increased as pressure was applied and the permeability decreased per Table I. At the same time, the frequency at which μ_0 reached a maximum increased almost linearly with pressure (see Fig. 1).

DISCUSSION

The general low sensitivity to pressure shown by solid metallic magnetic materials gives assurance that such materials may be used with reasonable stability over the range of pressures here employed. The sensitivity of enameled powder cores shows that uniaxial stresses must be avoided, to minimize magnetic impairments.

The response of ferrites to pressure presents problems more complex than posed by metallic materials. Memory cores (square loop), and low permeability ferrites show little effect of pressure. However, high permeability cores of MnZn and NiZn ferrite show drastic effects of pressure, but without noticeable pressure hysteresis. The behavior of these ferrites is quite similar to that recorded by Adams and Davis.[4] They found that with constant temperature the product $H_c\mu$ did not vary with pressure, on a NiZn ferrite sample. The variation of relaxation frequency with pressure (Fig. 1) in MnZn ferrite probably indicates variation in the domain wall stiffness or in the viscous damping of the domain walls in the ferrite.[5] However, because of the polycrystalline nature of the sample and the complicated domain structure, it is difficult to assign a definite mechanism for this effect.

[5] R. E. Alley, Jr., Bell System Tech. J. 32, 1152–1172 (1953).

Magnetic Contribution to the Ultrasonic Attenuation in Annealed and Deformed Steel (SAE 1020)

W. J. Bratina, U. M. Martius, and D. Mills
Ontario Research Foundation, Toronto, Ontario, Canada

The absorption of ultrasound of ~3 Mc/sec frequency was investigated in low carbon steel as a function of elastic strain applied in the presence of constant magnetic fields. The observed attenuation changes are interpreted in terms of magnetomechanical damping. The major part of the change appears to be accounted for by variation in the amplitude of the domain wall vibration, while the domain configuration changes appear to have relatively small effect. The maximum observed in the attenuation-strain curve for plastically deformed material is attributed to the presence of internal stresses.

INTRODUCTION AND EXPERIMENTAL METHOD

A STUDY of the changes in the attenuation of ultrasound caused by elastic tensile strain and/or external magnetic field in annealed and plastically deformed low carbon steel (SAE 1020) was made with a particular emphasis on the deformed material. Previously, little work has been reported in this particular field.[1–4]

Polycrystalline specimens in the form of rods 12 in. long and ½ in. diam were employed. The attenuation of ultrasonic waves, of ~3 Mc/sec frequency, sent longitudinally through the specimen was determined in db/μsec using the Sperry Ultrasonic Attenuation Comparator. External stresses and external magnetic fields were applied in the longitudinal direction of the specimen.

EXPERIMENTAL RESULTS AND ANALYSIS

Figure 1 shows the attenuation of ultrasound in a hydrogen annealed specimen as a function of external strain, which was applied in the presence of constant magnetic fields. A similar set of results for deformed material (1% permanent elongation) is seen in Fig. 2. The lack of space does not permit us to include the attenuation vs magnetic field strength curves obtained at constant stress levels.

The interpretation of the results is based on the assumption that the changes in attenuation caused by elastic strain or magnetic field are related to changes in magnetomechanical losses and that these are associated with micro-eddy currents induced by the vibration of the magnetic domain walls. Thus, the major factors determining the losses were concluded to be the effective[5] wall area, the amplitude of the wall vibration and the wall thickness. The approximate domain spacing at zero applied field was found, employing the magnetic powder technique on the specimen cross sections, to be ⅓ to $\frac{1}{10}$ of the average grain diameter.

[1] A. Hikata, Gov. Mech. Lab. Bulletin No. 1, Tokyo (1954).
[2] K. Winterton, Ontario Research Foundation (unpublished) (1955).
[3] A. Hikata and R. Truell, Rept. WAL, 143/14-51 Met. Research Lab., Brown University (1958).
[4] W. J. Bratina, Can. J. Phys. 37, 579 (1959).
[5] The effective wall area means the area of the domain wall actually affected by the ultrasonic wave.

Annealed Specimen (Fig. 1)

The application of external strain at zero field produces a pronounced decrease in attenuation. However, the contribution of the superimposed external strain on the attenuation becomes less and less pronounced as magnetic fields are increased.

The measured magnetization curve indicates that the main changes in the domain configuration occur at the fields below 20 oe. If the configuration changes would be a major contributing factor far larger differences would be expected between the attenuation curves at $H=0$ and at $H=10$ oe. It should, however, be remembered, that the changes in the configuration are not necessarily accompanied by equivalent changes in the effective wall area.

The further decrease in attenuation observed at zero

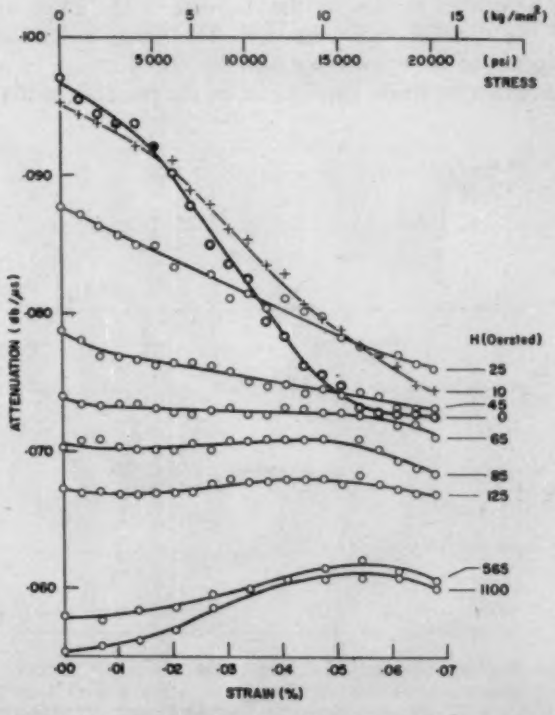

FIG. 1. Ultrasonic attenuation plotted vs strain at constant magnetic fields for annealed specimen.

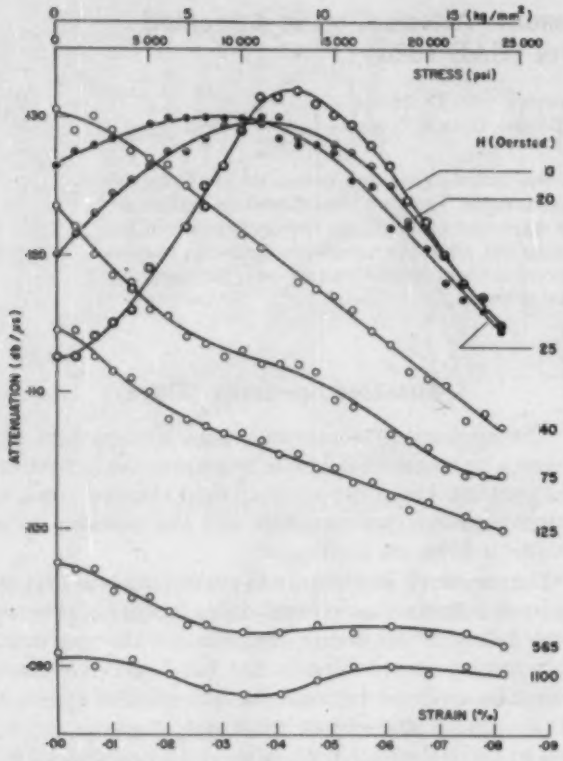

FIG. 2. Ultrasonic attenuation plotted vs strain at constant magnetic fields for plastically deformed specimen (1% permanent elongation).

strain at fields above ~20 oe appears in all probability to be caused mainly by the decrease in the amplitude of the domain wall vibration. The same mechanism appears to be responsible also for the decrease in attenuation on strain application, in the presence of magnetic fields of magnitude at which the changes in the domain configuration should be largely completed.

Only at very high fields, might a reduction in the domain wall thickness also become a contributing factor.[6]

Plastically Deformed Material

Plastically deformed material is characterized by a pronounced maximum in the attenuation vs strain curve (Fig. 2). In the presence of magnetic fields, the maximum moves towards the lower strain values. A corresponding maximum is observed if the attenuation is measured at constant stress levels against the magnetic field strength.

The fact that ultrasonic attenuation in a deformed specimen is found, on strain application, to increase at first can be explained by the assumption that internal microstresses are present within the deformed material. These are assumed to effect the domain configuration and to reduce the wall vibration amplitude. A certain level of externally applied stress or magnetic field is required before the effects of internal stress on the magnetic domain walls are overcome. From there on, the attenuation decreases in a manner similar to annealed material. However, much higher fields are required before the superimposed strain becomes ineffective.

ACKNOWLEDGMENTS

The work described formed part of a program of research in the Metal Physics Section of the Ontario Research Foundation. The authors wish to express their thanks to the Ontario Research Foundation for financial support of this program.

[6] L. Néel, J. Phys. Radium 5, 265 (1944).

Direct-Current Measurements on Tape-Wound Cores*

R. C. Barker and R. M. Brownell
Department of Electrical Engineering, Yale University, New Haven, Connecticut

This paper reports hysteresis-loop measurements made on tape-wound cores of commercial-grade grain-oriented 50Ni-50Fe material at very low domain wall velocities. The experimental equipment includes a low-output-impedance core driver, a low-drift electronic integrator, and a 30 in.×30 in. X-Y recorder. The duration of a complete flux reversal can be varied between 5 seconds and 30 minutes. The rate-of-change of flux during a reversal can be held constant within 1%, so that variations in the ease of domain wall motion (which appear as Barkhausen discontinuities in conventional measurements) are constrained to appear as variations of magnetomotive force. The coarse structure of these variations is repeatable on successive measurements; the fine structure, for the most part, is not.

In addition to showing these variations of mmf, the experimental arrangement displays minor loops in their correct locations with respect to the major loop. These measurements indicate that, under dc conditions, flux changes always begin at the inner circumference of the core, as predicted by a previously proposed model of flux change in polycrystalline tapes.[1] Many other aspects of these minor-loop measurements can be explained by this model, which is currently being further developed.

On the basis of the model, the recorded variations in mmf can easily be used to find the variations in the energy required to move domain walls in various portions of the core, under conditions of constant rate-of-change of flux. (Under such conditions, the product of wall velocity and wall area is a constant.) The repeatability of the coarse variations indicates their dependence on local metallurgical variations within the core. The nonrepeatability of the fine variations probably indicates a randomness in the configuration of the domain walls as they pass through the same region on successive measurements.

THE purpose of this paper is to indicate the sort of experimental results that can be expected of hysteresis loop measurements under conditions of constant induced voltage, and to report some of the preliminary inferences that have been drawn. The apparatus uses very-low-noise dc amplifiers. The core tested is a production quality Magnetics, Inc. 50026-2A, area about 5×10^{-5} (meter)^2, mean path length about 0.1 meter, with 115 wraps of two mil thick, 0.375 inch wide, grain-oriented 50-50 Ni-Fe alloy tape. The induced voltage is maintained constant by voltage feedback. As an example of signal levels encountered, a 5-min half-loop corresponds to 5 millivolts induced in a 10 000 turn feedback winding. The recorder does not resolve reversals of volumes smaller than 10^{-3} cm^3, but data taken by other means not subject to this limitation confirms the results shown here.

The conduct and interpretation of these experiments is based upon the postulate[1] that when the field applied to a toroidal core is reversed, the bulk of the flux reversal begins at the inner circumference of the core where the field intensity H is the highest, and that the domain walls move spirally outward along the length of the tape toward the outer circumference of the core. It is also assumed that the region containing moving domain walls extends through several wraps of tape. The flux reversal process would thus be describable macroscopically in terms of a cylindrical transition region several wraps thick whose radius expands as the flux reversal proceeds.

Since propagation of domain walls at any point along the tape takes place at roughly the same value of H, the initial part of the flux reversal at the inner circumference of the core would require less magnetomotive force F than the final part, which occurs at the outer circumference where the magnetic path is longer. The ratio of these two values of F should be equal to the ratio of the outer to inner diameters of the core. In Fig. 1, this comparison is made in terms of H. (In Figs. 1 and 2, H is calibrated at the mean path length of the core.)

The position and shape of the minor loop in Fig. 1 also substantiate the above postulate. The core is first brought from negative to positive saturation in 2.5 min. The excitation is reversed and the flux caused to change in the negative direction at the same rate. At the point

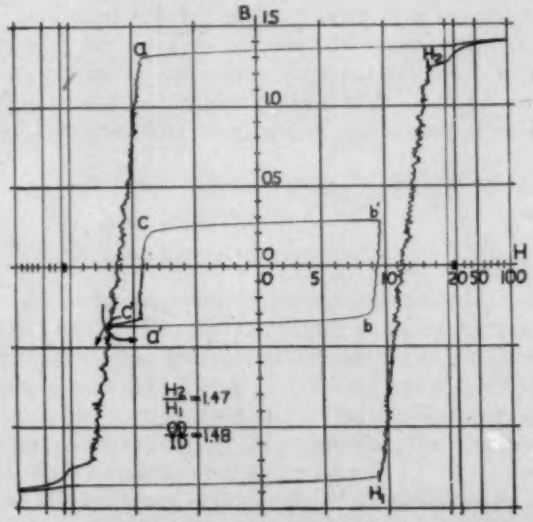

FIG. 1. Measured major hysteresis loop with enclosed minor loop. B is in webers/(meter)^2. H intervals are one ampere-turn/meter to 20, then 10 ampere-turns/meter to 100. ID and OD are the inner and outer diameters of the core.

* This work is part of a research project undertaken by the junior author in pursuit of the Doctor's degree in Electrical Engineering at Yale University. It has been supported in part by Magnetics, Inc., of Butler, Pennsylvania.

[1] R. C. Barker, *Proceedings, Conference on Nonlinear Magnetics and Magnetic Amplifiers, Los Angeles, 1958* (American Institute of Electrical Engineers, New York, 1958) (also to be published in AIEE Communications and Electronics).

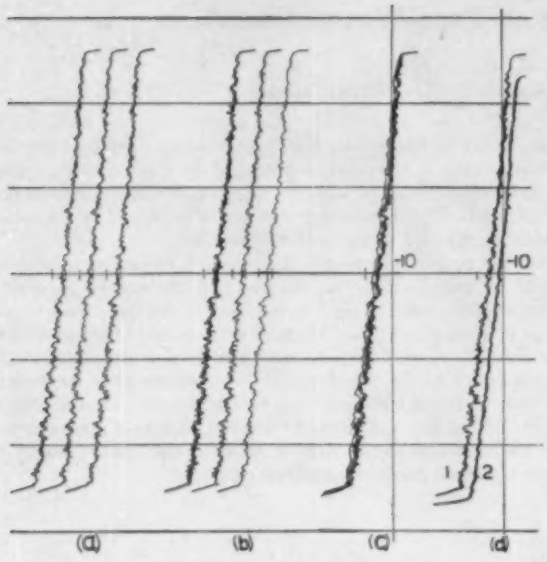

FIG. 2. Left-hand sides of several hysteresis loops of the same core. Vertical intervals are 0.5 webers/(meter)^2; horizontal, one ampere-turn/meter. Saturation levels, (a)–(c), 100 ampere-turns/meter. (a) Successive 2.5 minute loop sides, displaced two ampere-turns/meter, showing correlation of coarse but not fine detail. (b) Loop sides taken in 5, 2.5, and 1.25 minutes, displaced two ampere-turns/meter, showing variation in amount of fine detail. (c) Loop sides taken in 0.5 and 5 minutes, not displaced, showing slight loop widening. (d) 2.5 minute loop sides, not displaced, taken from 1, heavy saturation and 2, very light saturation, showing narrower loop and much less detail of 2.

a, domain walls are established at the inner circumference of the core. The change of flux down to the point a' corresponds to the movement of this transition region about three quarters of the way to the outer circumference. When the excitation is removed, the walls remain in place, separating an outer positively saturated region from an inner negatively saturated one. Reversing the field and changing the flux from b to b' is accounted for by the motion of a second transition region from the inner circumference outward into the core. When the field is again reversed, a third transition region is established at the inner circumference, point c, and moves outward toward the second, reversing the flux in the inner positively saturated region. When the point c' is reached, the walls in the third transition region meet those of the second, and both are annihilated. To produce a further negative flux change, F must increase to the value required at the location of the original transition region, which then moves further radially outward.

Close inspection of Fig. 2(a) shows that the coarse structure is generally repeatable, indicating variations along the tape in the metallurgical properties of the material. The fine structure is not repeatable, indicating a substantial degree of independence and therefore randomness in the motion and position of small elements of domain wall.

In Fig. 2(b) at the lower speeds, the domain walls move by small local movements of wall elements seeking out lowest energy configurations in a condition of nearly static equilibrium. At higher speeds, there is insufficient time for these small local movements.[1,2] Hence, much of the independence of motion of small segments is lost, and the average motion is smoother and more coherent, as indicated by the smaller variations of F. Figure 2(c) shows the extent of loop widening in the speed range of these loops.

Both loops in Fig. 2(d) start at -270 a-t/m (ampere-turns/meter). In 1, the core is taken to $+270$ a-t/m, the excitation is reversed, and loop 1 is recorded. In 2, the core is taken only to $+15$ a-t/m prior to recording loop 2. These loops confirm that the regions of the core hard to reverse, which produce the last 5% of the flux reversal at higher fields, remain negatively saturated throughout the positive-directed reversal and act as wall-growth centers during the subsequent return to negative saturation.

We are indebted to Magnetics, Inc., of Butler, Pennsylvania, and to Dr. Charles B. Wakeman of that company for providing many special samples of tape-wound cores.

[2] W. J. Carr, Jr., J. Appl. Phys. **30**, 90S (1959).

JOURNAL OF APPLIED PHYSICS SUPPLEMENT TO VOL. 31, NO. 5 MAY, 1960

Effect of Applying a Magnetic Field During Neutron Irradiation on the Magnetic Properties of Fe-Ni Alloys

A. I. SCHINDLER AND E. I. SALKOVITZ
Metallurgy Division, U. S. Naval Research Laboratory, Washington, D. C.

To test the similarity between thermally induced ordering and irradiation induced ordering, a series of commercial Fe-Ni samples have been irradiated in the presence of a saturating magnetic field. Square hysteresis loops were found for all the samples irradiated in this manner. Such results are consistent with the proposal that directional short range ordering and consequent uniaxial anisotropy has been created by the neutron irradiation.

L. NÉEL[1] and S. Taniguchi[2] have independently proposed an explanation for the uniaxial anisotropy that is created in a binary alloy annealed in a magnetic field. According to their model, directional diffusion takes place and local or short range anisotropic atomic configurations result. Such short range directional ordering can stabilize the magnetization in a direction related to the atomic anisotropy and this results in uniaxial magnetic anisotropy. Taniguchi[2] has further proposed that directional ordering effects can occur even if the alloy is heat treated in the absence of a magnetic field. In this case, the internal magnetic field of each domain will influence the directionality of diffusion. Now, however, this direction will change from domain to domain.

If the normal magnetic anisotropy is small, as in the case of permalloys, then any additional uniaxial anisotropy has a strong effect on the magnetization process. The direction of the uniaxial anisotropy that is created by annealing in a magnetic field will be the same for all of the domains and this will result in square hysteresis loop. Annealing in the absence of a magnetic field also causes uniaxial anisotropy, but the direction of the anisotropy will be different from domain to domain, and a constricted or kinked hysteresis loop will be obtained. An indirect method of examination of the growth of uniaxial anisotropy can then be made by a study of the magnetic hysteresis loop. However, for iron-nickel alloys there is also a tendency for long range superlattice formation, i.e., formation of Ni_3Fe. Long range ordering, on the other hand, impedes the formation of directional short range ordering. As the formation of the Ni_3Fe superlattice occurs, the short range directional ordering, and consequently, the uniaxial anisotropy decreases and the more normal hysteresis loop is obtained. The new hysteresis loop will of course have different values of coercive force and remanence consistent with the values of cubic anisotropy and magnetostrictive constants of the ordered alloy.

In previous reports,[3] the similarity between thermal directional ordering and radiation induced ordering has been demonstrated. Specifically, it was found that irradiated Ni-Fe samples previously disordered, resulted in hysteresis loops of the constricted type. This suggested that neutron irradiation caused short range ordering to take place. When the irradiated samples had been previously partially ordered by thermal means, the resulting hysteresis loops indicated that the thermal ordering and radiation induced ordering were additive. In addition, it was shown that long range ordering could occur when the samples were irradiated at higher temperatures.

To further test the similarity between thermal ordering and radiation induced ordering, another experiment has been carried out in which the samples have been irradiated in the presence of a saturating magnetic field. The samples used were commercially available toroids of mainly iron and nickel alloys of the following compositions:

1. 4% Mo-79% Ni-17% Fe (permalloy)
2. 5% Mo-79% Ni-16% Fe
3. 5% Cu-2% Cr-78% Ni-15% Fe (mumetal)
4. 48% Ni-52% Fe.

Two samples of each material were wound with appropriate B and H coils and installed on the same sample holder. Pre-irradiation 60 cycle hysteresis loop measurements were taken and the samples were then irradiated at the Brookhaven reactor for 2 weeks. This short irradiation time was chosen so that only short range ordering could occur. The total integrated flux for these samples were

$$\phi \text{ fast} = 1.25\times10^{16} \text{ to } 3.0\times10^{16} \text{ nvt}$$

$$\phi \text{ epi} = 2.6\times10^{17} \text{ nvt}$$

$$\phi \text{ thermal} = 5.9\times10^{18} \text{ nvt}$$

while the temperature during irradiation varied between 80° and 120°C. During irradiation a saturating magnetizing dc current was passed through the H coil of one sample of each pair. The field produced was of course in the same direction as the field applied during hysteresis loop measurements. After the irradiation, the hysteresis loops of each sample were again taken.

The allotted space only permits the discussion of two samples. In Fig. 1 is shown the pre- and post-irradiation hysteresis loops of permalloy and in Fig. 2 the loops for samples of mumetal. The pre-irradiation loops are marked a, while the post-irradiation loops are the curves marked b and c. Loop b is the hysteresis loop of the

[1] L. Néel, J. phys. radium 15, 225 (1954).
[2] S. Taniguchi, Sci. Rept. RITU A-7, 269 (1955); A-8, 173 (1956).
[3] A. I. Schindler, E. I. Salkovitz, and G. S. Ansell, J. Appl. Phys. 30, 282S (1959).

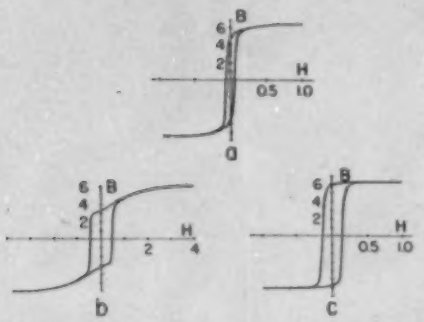

FIG. 1. The effect of neutron irradiation on the 60 cycle hysteresis loops of permalloy. a. Pre-irradiation hysteresis loop. b. Post-irradiation hysteresis loop (no field applied during irradiation). c. Post-irradiation loop (saturating magnetic field applied during irradiation). B in kilogauss, H in oersteds.

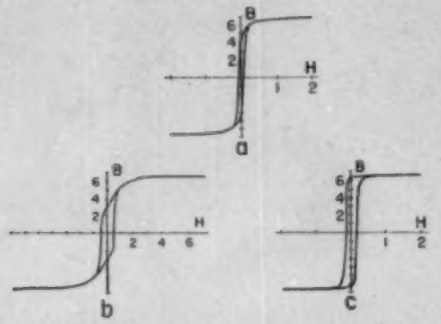

FIG. 2. The effect of neutron irradiation on the 60 cycle hysteresis loops of mumetal. a. Pre-irradiation hysteresis loop. b. Post-irradiation hysteresis loop (no field applied during irradiation). c. Post-irradiation loop (saturating magnetic field applied during irradiation). B in kilogauss, H in oersteds.

sample irradiated in the absence of a magnetic field, while loop *c* is that for the sample irradiated in the presence of a saturating magnetic field applied to the toroid. In both cases, loop *b* is similar to results previously observed, i.e., decreased remanence, increased coercive force and decreased permeability. (Note that to saturate the sample a field several times that of the pre-irradiation saturating field is required.) In loop *c*, a strikingly different effect was observed, namely square loop characteristics were obtained with both the coercive force and remanence increasing.

These results are consistent with the suggestions previously madt ehat neutron irradiation causes ordering in Ni-Fe alloys. The modified hysteresis loops reflect a change in the uniaxial anisotropy of the state of final order. In the case of samples irradiated for short times in the absence of an applied field, the resulting directional short range ordering causes constricted hysteresis loops, while for samples irradiated in a magnetic field the resulting directional ordering causes square hysteresis loops. It would also appear for the samples irradiated in the absence of a magnetic field that long term irradiation causes the formation of the Ni_3Fe superlattice. The directional short range ordering and resulting magnetic anisotropy then decreases and the normal hysteresis loop is obtained.

JOURNAL OF APPLIED PHYSICS SUPPLEMENT TO VOL. 31, NO. 5 MAY, 1960

Rigorous Solution of Eddy Current Losses in Rectangular Bar for Single Plane Domain Wall Model

PAUL D. AGARWAL*
Department of Electrical Engineering, University of Massachusetts, Amherst, Massachusetts
AND
L. RABINS
Power Transformer Department, General Electric Company, Pittsfield, Massachusetts

Williams, Shockley, and Kittel, and other authors have presented a simple domain model in which magnetization takes place by the movement of a single plane domain wall. The net flux is zero when the domain wall is in the middle of the cross section and the material is magnetized fully when the wall moves to the surface.

Maxwell's equations for the case of a rectangular bar are rigorously solved for any position of the wall and expressions are derived for the current stream function in both regions I and II. The stream function was calculated using an IBM 705 computer and is shown for various positions of the wall and for several ratios of the sides of the rectangle. The power loss for sinusoidal applied induction is calculated. The results show that the loss in the material increases as the distance traversed by the wall, i.e., the dimension of the rectangle at right angles to the domain wall increases.

This solution with some modification also applies to thin laminations; where the domain model, proposed by several authors, consists of domains of equal width alternately magnetized in opposite directions to give the unmagnetized state. The domain walls are perpendicular to the plane of the sheet and magnetization in the sheet plane takes place by lateral movement of these domain walls. For any given thickness of the laminations, a domain wall spacing can be determined to correlate the power loss with experimental values.

THE study of eddy current losses in materials whose magnetization is controlled largely by domain wall motion represents a departure from the classical study of such phenomena and accounts in part for the higher experimentally observed eddy losses. For a rectangular bar, a simple domain model has been presented by Williams, Shockley, and Kittel,[1] in which

* Also consultant to the General Electric Company.

[1] H. J. Williams, W. Shockley, and C. Kittel, Phys. Rev. 80, 6 (1950).

a single plane domain wall divides the material into two regions of uniform flux density $\pm B_s$ as shown in Fig. 1. The wall, which is parallel to the xz plane, moves from $x=0$ to $2d$ reversing the direction of magnetization.

In this model of a rectangular bar, the eddy-current pattern is determined by the position of the domain wall and the magnitude of the eddy currents is determined by the velocity of the wall. Maxwell's equations are applied to determine the resulting eddy-current flow. MKS units are used.

The position of the domain wall is

$$x_0=d(1-\cos\omega t),$$

corresponding to an applied flux

$$\phi=4dcB_s\cos\omega t.$$

The applicable Maxwell's equations are given in terms of the current density $\bar{i}$,

$$\nabla\times\bar{i}=0,$$
$$\nabla\cdot\bar{i}=0.$$

Thus, the components of i can be given by a stream function U, where

$$i_x=\partial U/\partial y \quad \text{and} \quad i_y=-\partial U/\partial x.$$

The rectangular bar must be considered as having two regions in order to solve for the stream functions. The boundary conditions are

$$i_{\text{norm}}=0 \text{ at all external boundaries,} \tag{1}$$
$$i_{x1}=i_{x2} \quad \text{at} \quad x=x_0, \tag{2}$$
$$i_{y1}-i_{y2}=2\sigma v_0 B_s \quad \text{at} \quad x=x_0. \tag{3}$$

σ is the conductivity of the bar, and $v_0=dx_0/dt$ is the domain wall velocity.

The solution for the stream function in the two regions is

$$U_1=16cv_0B_s\sigma\sum_{\substack{n=1,3,5\cdots\\ \text{odd}}}^{\infty}\frac{\sin(n\pi/2)}{n^2\pi^2\sinh(n\pi d/c)}\times\sinh\frac{n\pi(x_0-2d)}{2c}\sinh\frac{n\pi x}{2c}\cos\frac{n\pi y}{2c}$$

$$U_2=16cv_0B_s\sigma\sum_{\substack{n=1,3,5\cdots\\ \text{odd}}}^{\infty}\frac{\sin(n\pi/2)}{n^2\pi^2\sinh(n\pi d/c)}\times\sinh\frac{n\pi x_0}{2c}\sinh\frac{n\pi(x-2d)}{2c}\cos\frac{n\pi y}{2c}.$$

For several ratios of the sides of the rectangular bar and for various positions of the wall the stream functions were calculated using the IBM-705 computer[2] and several are shown in Fig. 3. The average power loss is found by summing the square of the current losses over the bar cross section and over a full time cycle. When

[2] The assistance of J. L. Oprisch in preparing the computer programs is gratefully acknowledged.

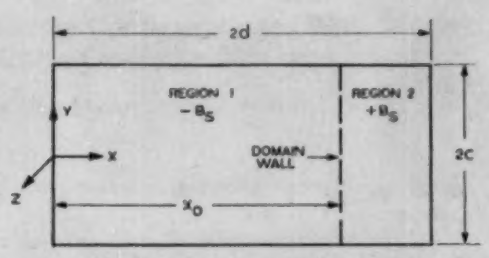

FIG. 1. Single domain wall model for a rectangular bar.

evaluated for the case of sinusoidal applied flux, the changing wall velocity v_0 and wall position x_0 must be taken into account. This results in an average power loss

$$W=\frac{16\omega^2dcB_s^2\sigma}{\pi^2}\sum_{\substack{n=1,3,5\cdots\\ \text{odd}}}^{\infty}\frac{1}{n^3}\left\{\tfrac{1}{2}\coth\frac{n\pi d}{c}-\frac{I_1(n\pi d/c)}{(n\pi d/c)\sinh(n\pi d/c)}\right\}\text{w/m}^3.$$

I_1 is the modified Bessel function of the first order.

A similar solution applies to thin laminations where the domain model consists of domains of equal width alternately magnetized in opposite directions to give the unmagnetized state. The domain walls are perpendicular to the plane of the laminations, Fig. 2, and magnetization takes place by lateral movement of all the walls. The eddy-current flow in each of the sections between the centerlines of two adjacent domain walls is identical. Such a section can be represented by the rectangle of Fig. 1. Thus, $2c$ is the thickness of the laminations and $2d$ is the domain wall spacing in this case. We may solve for this stream function by again considering Fig. 1 and changing only the boundary condition (i),

$$i_y=0 \quad \text{at} \quad x=0 \quad \text{and} \quad 2d.$$

This gives

$$U_1=16cv_0B_s\sigma\sum_{\substack{n=1,3,5\cdots\\ \text{odd}}}^{\infty}\frac{\sin(n\pi/2)}{n^2\pi^2\sinh(n\pi d/c)}\times\cosh\frac{n\pi(x_0-2d)}{2c}\cosh\frac{n\pi x}{2c}\cos\frac{n\pi y}{2c}$$

$$U_2=16cv_0B_s\sigma\sum_{\substack{n=1,3,5\cdots\\ \text{odd}}}^{\infty}\frac{\sin(n\pi/2)}{n^2\pi^2\sinh(n\pi d/c)}\times\cosh\frac{n\pi x_0}{2c}\cosh\frac{n\pi(x-2d)}{2c}\cos\frac{n\pi y}{2c}.$$

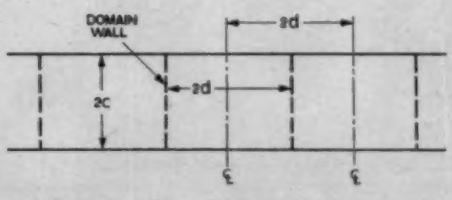

FIG. 2. Domain wall model for a thin magnetic sheet.

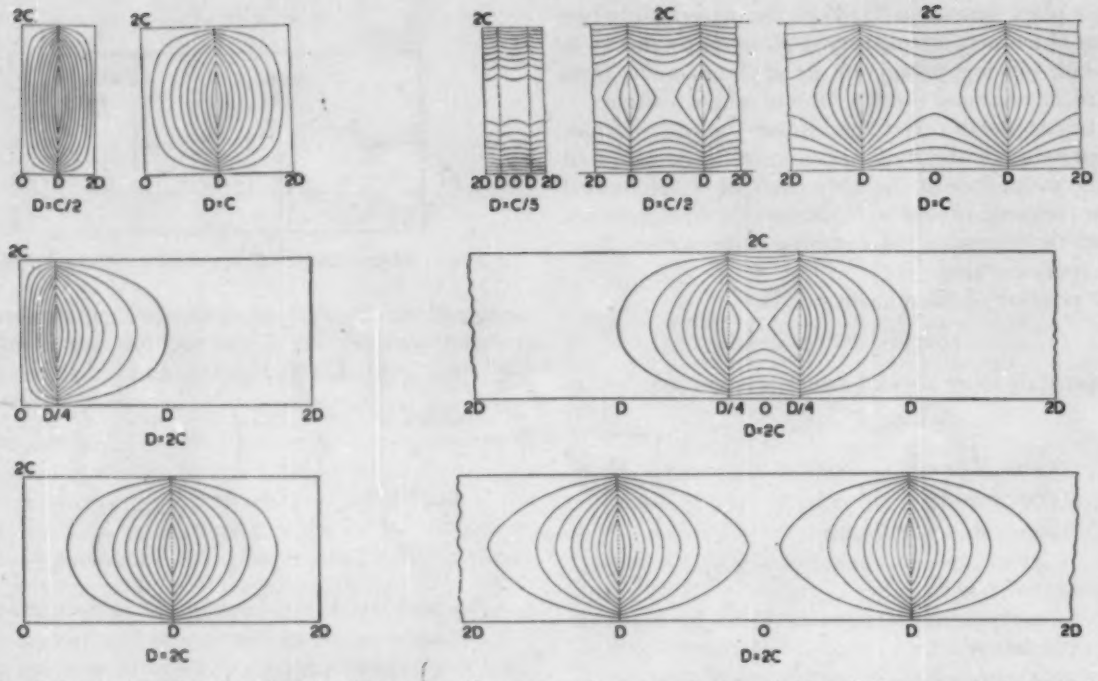

FIG. 3. Stream function plots showing eddy current flow patterns in rectangular bars (left) and thin magnetic sheets (right).

Plots of the stream function for various values of domain width to lamination thickness and wall position are also shown in Fig. 3. Brouwer[3] obtained an approximate solution of the eddy-current distribution problem by an electric circuit model and presented similar stream flow diagrams for symmetrical position of the domain walls only. We note that the current flow differs greatly from the classical straight line distribution which is approached as d/c approaches zero. The average power loss for sinusoidal induction is given by an expression similar to that for the rectangular bar except that the sign of the second term is positive. The same result was presented by Pry and Bean.[4] Calculated losses as a function of (domain spacing/sheet thickness) and correlation with experimentally observed losses provide information on the domain spacings.

[3] G. Brouwer, J. Appl. Phys. **26**, 1297 (1955).

[4] R. H. Pry and C. P. Bean, J. Appl. Phys. **29**, 532 (1958).

Effect of Eddy Currents on Domain Wall Behavior Configurations, Wall Motion, and Loss for a Domain Model of Cube-On-Edge Material

P. D. AGARWAL,* *Electrical Engineering, University of Massachusetts, Amherst, Massachusetts*

AND

D. C. GRAHAM, *General Electric Company, Power Transformer Department, Pittsfield, Massachusetts*

Domain wall motion in single crystals and polycrystalline material has been observed and studied by many physicists and metallurgists under different conditions of excitation. The field has been applied in the rolling direction and in the cross rolling direction and observations made on the surface of the domain wall motion. In these studies the rate of change of wall motion of necessity must be slow because of the limitations of the procedure for following and photographing the wall motion. It has been recognized that at higher frequencies, the wall tends to bow, but the actual motion has not been defined. The published data under dc excitation conditions, along with the required minimum energy relationship, establishes the boundary conditions that must be met by a domain model for polycrystalline cube-on-edge material. A domain model has been developed which appears to fit these boundary conditions under dc excitation.

Analysis of the induced voltage and resulting eddy currents was made on the assumption that the domain wall remain straight and that the velocity was such as to give sinusoidal flux change. The actual flow of eddy currents dictated that the wall must bow. By modifying the domain wall motion to fit the conditions as dictated by the eddy currents, the eddy current losses were calculated and compared with losses measured in present-day material. The variations of magnetizing force with time are also calculated and show reasonable agreement with expected excitation curves versus time.

I. INTRODUCTION

THE determination of the magnetic characteristics of any cube oriented material such as 3.25% silicon steel involves the complex relationship between the direction of stress, strain, excitation, magnetization, the crystal directions, the domain configurations, the anisotropy constants, and the elastic constants. If the domain models were related to the crystal directions in a reasonably simple manner, the calculations of the magnetic properties under somewhat ideal conditions would be greatly enhanced. The suggestion has some merit because studies to date show a tendency for the domains to align themselves in the easy direction of magnetization which are along the directions of the cube edges.

II. DOMAIN MODEL

A suitable domain model can be developed by selecting a cube and extending it in the rolling direction to form a rectangular parallelepiped with a square end. By splitting the parallelepiped along the diagonals of the square, we form a module in the form of a prism which can be used to make up a complete sheet of steel having a rectangular cross section and with the cubes on edge. The domain arrangement on the large surface of such a prism would consist of two main and two closure domains separated by 180° and 90° Bloch walls as shown by Williams, Bozorth, and Shockley[1] and given in Fig. 1(a). The shape of the closure domains could be best described by a quarter of a four-sided pyramid.

By taking four such modules we can recombine them to form the parallelepiped. In order to satisfy the condition of minimum energy, the modules must be arranged in such a fashion that like domains are adjacent. Under these conditions, the closure domains will have directions as shown in Fig. 1(a) in the (010) plane. By orienting the long dimension of the parallelepiped in the rolling direction [100] and the cube face diagonal perpendicular to the surface of the sheet of steel, we have the domain model related to the crystal directions for cube-on-edge oriented steel. Additional modules can be added to represent a sheet of oriented steel as shown in Fig. 1(b). The straight lines in the surface of the steel without closure domains are consistent with the observations made on the surface of oriented cube-on-edge silicon steel. The applying of a field in the [−100] direction will then produce a wall motion in the direction of the arrows shown in Fig. 1(b) (100) plane. A field applied in the [100] direction will produce a disappearance of the walls on the surface, and the rectangles shown in the (100) plane of Fig. 1(b) will ultimately collapse to zero initiating new walls as required.

The model possesses the necessary closure domains oriented along the easy directions of magnetization to satisfy the conditions of excitation in the [011] direction as described by Williams, Bozorth, and Shockley,[1]

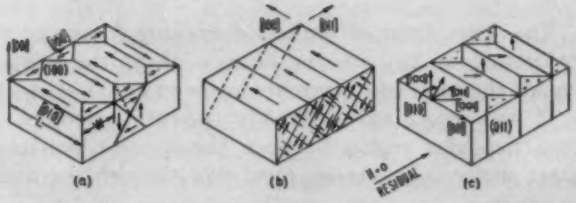

FIG. 1. (a) Domain structure of a single crystal (100) plane; (b) Composite domain structure of cube-on-edge crystal; (c) Domain structure of a single crystal (110) plane.

* Also consultant for the General Electric Company.

[1] H. J. Williams, R. M. Bozorth, and W. Shockley, Phys. Rev. 75, 155–178 (1949).

and shown in Fig. 1(c). It is obvious that the direction of some closure domains must change by 180° and additional walls must be added to eliminate free-poles. At the higher densities, free-poles cannot be avoided and rotation must take place. Just how this transition takes place is not completely understood.

One other boundary condition for the domain model is described by C. D. Graham, Jr.[2] Under these conditions, the domain wall is shown to be continuous from the top to the bottom surface of normal thin cube-on-edge oriented materials and at an angle nearly 30° rather than 90° or 45° to the surface. The model appears to be in slight violation of this boundary condition since the walls were chosen to be 45° to the surface.

III. EDDY CURRENT CALCULATIONS FOR SINUSOIDAL INDUCTION

The motion of the domain walls described previously causes a change of flux and the value of the induced electric field at the domain boundary is $E=2B_s v$, where v is the velocity of the wall which is determined by the condition that the total flux variation is sinusoidal, and B_s is saturation induction. It can be shown that there is no electric field in the region between $X=\zeta$ and $\sqrt{2}d$. The value of electric field in the region between $X=0$ and ζ is a function of domain wall configuration.

(i) For a cylindrical domain wall electric field intensity beyond the wall varies inversely with radius.
(ii) For domain walls parallel to the sheet surface the electric field will be constant between the domain wall and the surface.

In this particular model, at certain time intervals one or the other condition exists. The path of eddy currents as the domain walls move under excitation in the rolling direction is shown in Fig. 2 (a,b,c). On considering one unit length of the material in the rolling direction that is perpendicular to the paper:

di = element of current in thickness $dx=\gamma E dx$
dr = element of resistance $=l_{(x)}/\gamma dx$
dL = power loss in the elementary strip

$$=(di)^2 dr=\gamma E^2 l_{(x)} dx$$

L = average power loss in eddy currents

$$=(1/\pi)\int_0^{\sqrt{2}d}\gamma E^2 l_{(x)} dx.$$

The wave form of impressed exciting force can be calculated at any instant because H at the surface equals the total eddy currents in the material.

It was recognized that eddy currents generated in the triangular region between the domain wall and sheet surface of necessity must flow through the walls

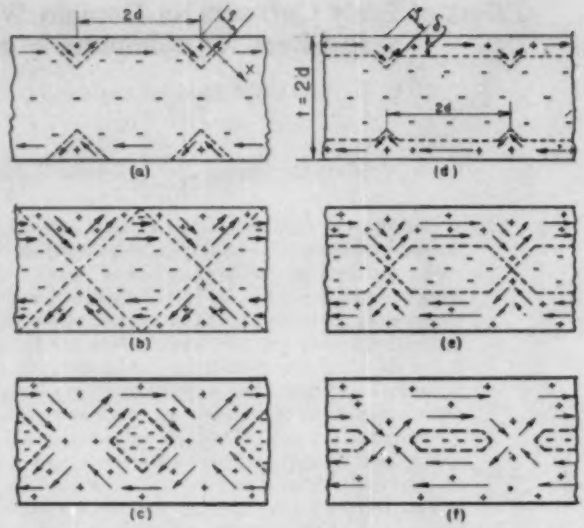

FIG. 2. (a,b,c) Sequence of domain wall motion and eddy current flow in initially assumed model. (d,e,f) Sequence of domain wall motion and eddy current flow in modified model.

as shown in Fig. 2 (a,b). It was initially assumed that the domain boundaries were unaffected by this current flow. Eddy current losses and time wave shape of impressed H were calculated for this case. The calculated wave had a discontinuity and differed materially from the known experimental wave shape for sinusoidal flux. This led us to reason that the flow of eddy currents in the δ region would produce an excitation, which would initiate a wall parallel to the surface thus modifying the domain wall configuration as shown in Fig. 2 (d,e,f).

For this modified domain wall model, it was assumed that the domain walls at ζ and δ moved with velocities v_1 and v_2 respectively such that the total current in the two regions is the same. This calculation, however, showed that ζ and δ remained approximately equal till the domain walls formed a closed hexagon as shown in Fig. 2(e).

The calculations were much simplified by assuming that $\zeta=\delta$. The waveform of H obtained analytically correlated well with that known experimentally. Eddy current loss for sinusoidal induction $L=0.0625\gamma\omega^2 B_s^2 t^2$ w per cubic meter, t is the thickness of the sheet and all variables are in MKS units. For 14 mil, 3.25% Si grain oriented steel sheets of resistivity $=46\,\mu$ ohm cm, the above equation gives the 60-cycle eddy loss $=0.555$ w per lb for an induction of 127 kilolines per sq in.

The values of eddy current loss were obtained from the difference between the ac loss and the equivalent loss of a dc hysteresis loop at various densities. Tests in one sample gave 0.42, 0.52, and 0.46 w/lb for 15, 17, and 18 Kg. Extrapolation to saturation would give a value within measurement tolerance of calculated value. The high values at lower densities may be attributed to the many degrees of freedom of domain wall motion in polycrystalline material, which results in higher domain wall velocity than obtained theoretically.

[2] C. D. Graham, Jr., "Domain wall observations in silicon iron," *Proceedings of the Conference on Magnetism and Magnetic Materials, Boston, 1956* (American Institute of Electrical Engineers, February, 1957), AIEE Spec. Publ. T-91, p. 410.

Ferrites and Oxides

The Role of Cation Vacancy in Magnetic Annealing of Iron-Cobalt Ferrites

SHŪICHI IIDA
Departmen of Physics, University of Tokyo, Tokyo, Japan

The kinetics of magnetic annealing effects in iron-cobalt ferrites is studied, based on a vacancy migration mechanism. First, a formal theory is developed, which makes clear the existence of a distribution of relaxation times in the phenomena. In order to get the distribution function of the relaxation time as a function of vacancy concentration and diffusion constants, a calculation based on a rather stochastic approach has been given. It is assumed that the dispersion in the relaxation time comes principally from the time required for the vacancies to migrate throughout the entire crystal lattice. The distribution function obtained is $f(\tau)=W\rho\tau/\tau_0 \times\exp(-W\rho\tau/\tau_0)$, where ρ is the density of vacancies, τ_0 is the mean relaxation time for the migration of a single vacancy, and W is a constant which depends on the lattice type, degree of short range ordering, and so on. On using this function the formation and the annihilation of the degree of directionality S_a is expressed as

$$\Delta S_a=\int_0^\infty f(\tau)\Delta S(\tau)d(\log\tau),\quad \Delta S(\tau)=[S(\tau)-S^e(T)](-\Delta t/\tau_0).$$

A quantitative calculation of the annihilation process of the magnetic annealing anisotropy in isothermal annealing accords exactly with the experimental results for iron-cobalt ferrites.

There is a short discussion of the equilibrium density of vacancies in iron-cobalt ferrites using the results of our statistical thermodynamical study of the same system. Discussions of several theoretical and experimental results of iron-cobalt ferrites recently carried out in Japan are also presented. From our results we conclude that the decrease in the degree of oxidation simply makes the scale of the time constant of the relaxation process longer, therefore it is not consistent with the suggestion previously made that only cobalt ions near vacancies can rearrange rapidly.

I. INTRODUCTION

THE magnetic annealing effects in iron-cobalt ferrites were first discovered in 1933 by Kato and Takei.[1] Since then many studies have been made in order to clarify the mechanism of the effects.[2–4] Several years ago, in collaboration with Sekizawa and Aiyama, we have reached two conclusions[5]—namely, (1) the effects originate in the internal directionality of the spinel structure itself and not in any secondary structures, and (2) the degree of oxidation, accordingly the amount of cation vacancies present in the spinel structure, has an essential influence to the effects. Recently Bickford et al.[6] and Slonczewski[7] have shown that at least in a region of small cobalt concentration, the expected directionality should be the preferential occupation of cobalt ions among the four different groups of sites of 16d in a spinel lattice. Since the agreement between the experimental results and the theoretical one is almost complete, there will be little doubt that the mechanism established is operating in such a region.

In the cobalt rich region it is necessary to consider some other mehcanism, especially in order to account for the presence and the predominance of the term F,[5,6] which could not be explained by the simple isolated model. Quite recently, Tachiki has made a calculation of the cubic anisotropy constant K_1 for the entire range of iron-cobalt ferrites based on a model in which the anisotropy is mainly due to the cobalt ions, which are under several kinds of low symmetry crystalline fields.[8] As shown later, the calculation gives a fairly good agreement with the experimental results. Therefore, it seems probable that the magnetic annealing effects in a cobalt rich region is also explained by a crystalline field model, i.e., by the difference in energy of cobalt ions in an exchange field and under various distorted crystalline field. In these cases, the mechanism would be caused by the presence of directional configurations of cobalt ions and iron ions in the 16d sites of the spinel lattice.

Previously, we presented also the mechanism of directional configuration of cations in 16d sites of spinel lattice with special emphasis on the deformed crystalline field caused by the presence of cation vacancies.[5] Although we think there is still some uncertainty about whether this type of mechanism takes some parts in the effect or not, we believe at present that at least the role of the cation vacancies present will be primarily their direct connection to the rate of diffusion of cations in the spinel lattice, in accordance with Bickford *et al.*

The magnetic field annealing effect is in itself a non-equilibrium problem. The uniaxial anisotropy is measured usually at low temperatures where the rate of diffusion of cations is very small. Therefore, the uniaxial anisotropy measured does not usually correspond to the final equilibrium state at this temperature, but to the average state in a certain high temperature range in which the specimen was annealed in a magnetic field, and the migration of the cations has ceased on cooling.

[1] Y. Kato and T. Takei, J. Inst. Elect. Engrs. (Japan) **53**, 408 (1933).
[2] I. Sugiura, J. Appl. Phys. (Japan) **19**, 198, 231 (1950); **20**, 98 (1951).
[3] C. Guillaud, Revs. Modern Phys. **25**, 64 (1953).
[4] R. M. Bozorth, E. F. Tilden, and A. J. Williams, Phys. Rev. **99**, 1788 (1955); H. J. Williams, R. D. Heidenreich, and E. A. Nesbitt, J. Appl. Phys. **27**, 885 (1956).
[5] S. Iida, H. Sekizawa, and Y. Aiyama, J. Phys. Soc. (Japan) **10**, 907 (1955); **13**, 58 (1958).
[6] R. F. Penoyer and L. R. Bickford, Jr., Phys. Rev. **108**, 271 (1957); J. M. Brownlow and R. F. Penoyer, J. Appl. Phys. **29**, 441 (1958).
[7] J. C. Slonczewski, Phys. Rev. **110**, 1341 (1958).
[8] M. Tachiki, presented at the Annual Meeting of the Physical Society of Japan (1959).

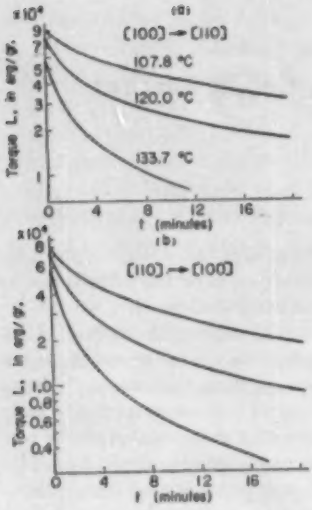

FIG. 1. Annihilation process of uniaxial anisotropy of a $Co_{0.25}Fe_{2.75}O_4$ single crystal. Annealing magnetic field is switched from [100] to [110] in (a) and from [1$\bar{1}$0] to [100] in (b).

The rate of diffusion determines this effective temperature range, and the rate of diffusion will exhibit a drastic change with the change in the number of cation vacancies.[5] Therefore, the density of cation vacancies should have an essential role in magnetic field annealing. It should be stressed that in order to advance the study more it is quite necessary to establish a suitable kinetic theory, which relates the magnetic annealing effect to the rate of diffusion or to the density of cation vacancies present. This paper deals mainly with this problem.

II. FORMAL THEORY OF CONFIGURATIONAL RELAXATION

In Fig. 1 we show the result of kinetic studies obtained by Aiyama[9] for a single crystal specimen. The specimen was annealed at higher temperatures long enough to attain equilibrium state in a magnetic field, then the direction of the magnetic field was switched to a new direction which is 45 deg from the original, and the torque required to maintain the specimen in the original position was measured continusously. The torque is considered to be proportional to the uniaxial anisotropy remaining in the original direction.

As shown in the figure, the curve cannot be represented by a simple relaxation formula, but by a complex formula,

$$K(t)=K^0(T)\exp[-t/(\tau_T+\alpha t^{\frac{1}{2}})]. \tag{1}$$

The formula was derived empirically by us[5] and it shows that the process has a spectrum in relaxation time as follows:

$$\exp(-t/(\tau_T+\alpha t^{\frac{1}{2}}))=\int_0^\infty f(\tau)\exp(-t/\tau)d(\log\tau). \tag{2}$$

We call $f(\tau)$ a distribution function of relaxation time in isothermal magnetic annealing.

[9] Y. Aiyama, Thesis, the University of Tokyo (1958).

First, in this section, we discuss quite formally the nature of $f(\tau)$. We shall assume hereafter the predominance of a vacancy diffusion mechanism and that the relevant ions are in 16d sites only. We assume that the specimen considered is composed of N independent crystallites, all of which are identical in the numbers of lattice points, cobalt ions, iron ions, and cation vacancies present. The crystallites may have various atomic configuration according to the different occupation of lattice points by each ion. Let these configurations be $A, B, C, \cdots, Q$.

Let $N_A, N_B, \cdots, N_C$ be the population (or the probability) of each configuration; for instance, N_A of N crystallites are in A configuration.

We define the vector $\mathbf{N}$ as

$$\mathbf{N}=\begin{bmatrix} N_A \\ N_B \\ N_C \\ \vdots \\ N_Q \end{bmatrix}. \tag{3}$$

Then

$$d\mathbf{N}/dt=-[D]\mathbf{N}=-D\mathbf{N} \tag{4}$$

can be written quite formally from a statistical consideration. Here, D is a matrix composed of various constants of vacancy diffusion. We put

$$D=\bar{D}+\delta \tag{5}$$

$$\mathbf{N}=\langle\mathbf{N}\rangle+\mathbf{n}, \tag{6}$$

where $\bar{D}$ is the component of D which is independent of the direction of magnetization, and it is assumed that

$$\bar{D}\gg\delta. \tag{7}$$

$\langle\mathbf{N}\rangle$ is defined so as to make

$$\bar{D}\langle\mathbf{N}\rangle=0, \quad \mathbf{n}\ll\mathbf{N}. \tag{8}$$

Then by neglecting $\delta\mathbf{n}$

$$d\mathbf{n}/dt=-\bar{D}\mathbf{n}-\delta\langle\mathbf{N}\rangle. \tag{9}$$

We define $\mathbf{n}^e$ as

$$\bar{D}\mathbf{n}^e+\delta\langle\mathbf{N}\rangle=0, \tag{10}$$

$$(d/dt)(\mathbf{n}-\mathbf{n}^e)=-\bar{D}(\mathbf{n}-\mathbf{n}^e). \tag{11}$$

On considering the physical nature of the matrix $\bar{D}$, $\bar{D}$ should satisfy the following mathematical equality[10]

$$\bar{D}\mathbf{m}_i=-\lambda_i\mathbf{m}_i. \tag{12}$$

Here, λ_i is a constant and will be positive physically, and $\mathbf{m}_i$ is an eigen-vector of $\bar{D}$ and should construct a complete set in the vector space $(\mathbf{n}-\mathbf{n}^e)$. Then

$$\mathbf{n}(t)-\mathbf{n}^e=\textstyle\sum_i a_i(t)\mathbf{m}_i \tag{13}$$

$$da_i(t)/dt=-\lambda_i a_i(t) \tag{14}$$

$$a_i(t)=a_i(0)\exp(-\lambda_i t). \tag{15}$$

[10] It is not necessary that $\bar{D}$ is Hermit. Therefore, the influence of short-range ordering on the element of $\bar{D}$ is well accounted for.

Thus we get a set of relaxation times $\tau_i=1/\lambda_i$ for the time change of a certain set of eigen-vectors $\mathbf{m}_i$ in the space $\mathbf{N}$.

As the uniaxial anisotropy should be represented by a proper linear combination of N_A, N_B, $\cdots$, N_Q, it should be expressed as

$$K_u(t)=\sum_i b_i^0(T)\exp(-\lambda_i t). \tag{16}$$

Here, $b_i^0(T)$ are determined according to the initial condition of the specimen. Thus, we could get a formal meaning of the distribution in relaxation times.

This is quite formal, but in the simplest case in which a regular tetrahedron having one cobalt ion, two iron ions, and a vacancy is treated as an elementary crystallite, we can get an exact solution of $\langle\mathbf{N}\rangle$, $\bar{D}$, $\mathbf{n}^e$ and λ_i. In this case, there are 12 λ_i in general, and under a simplification that the mean diffusion rate of cobalt ion is equal to that of iron ions we get effectively only four λ_i, i.e., $D/3$, D, $4D/3$, $5D/3$. It should be noticed that in this simplest case all ions always contact with a vacancy so that this gives an intrinsic distribution in relaxation times compared with that in the next section.

III. DISTRIBUTION FUNCTION FOR MIGRATING VACANCIES

The preceding theory is quite formal; however, what is physically the main origin of the dispersion in relaxation time? We have concluded that the principal part of the relaxation time will be the time required for the cations to have an opportunity to be able to move. It means that in order to move, it is necessary for a cation to have a cation vacancy as a nearest neighbor, and it will take much time for most of the cations to realize such a situation. Since the density of vacancies is so little in most of the crystals, it will take considerable time for the vacancies to migrate throughout the whole lattice points.

Of course there should be a dispersion in relaxation time owing to the cooperative nature of the atomic rearrangement as shown in the last part of the preceding section. But we think that the role of such an essential dispersion will have a minor contribution to the actual distribution function compared with the mechanism due to the migration of vacancies, and will neglect it hereafter.

We start from a simplest model in which there are L_0 lattice points, and $L_0\rho$ vacancies. At $t=0$, the vacancies are assumed to be distributed randomly over a whole points and we suppose the vacancies start a random walk at $t=0$. Let $L(t)$ be the number of lattice points that have been occupied by some of the vacancies at least once in the time from $t=0$ to $t=t$; these we will call nonvirgin lattice points, and their number will now be calculated. The differential increase of $L(t)$, $\Delta L(t)$ can be expressed as follows:

$$\Delta L(t)=L_0\rho\Delta t/\tau_0\cdot\{1-[L(t)/L_0]\}\cdot W_t, \tag{17}$$

where τ_0 is a relaxation time for a unit migration of a vacancy, and W_t is the probability that an arbitrary nearest neighbor point of a vacancy is a virgin point to the vacancy just considered. In Eq. (17), $L_0\rho\Delta t/\tau_0$ is the probable number of vacancies, which may migrate in the time interval Δt, $\{1-[L(t)/L_0]\}$ is the probability that a lattice point to which the vacancy will migrate has been a virgin lattice point for the other vacancies. W_t is the probability that the lattice point has been also a virgin lattice point to the same vacancy just considered. We should separate the foregoing probabilities and multiply, since we neglect the interaction of vacancies.

W_t can be calculated from τ_0 and W_N. Here, W_N means the probability that a lattice point nearest to a certain vacancy is still a virgin point after the random walk of N unit jumps of the same vacancy. It can be shown by a direct calculation and extrapolation that

$$W_N=W_\infty\exp\left[+\frac{2\alpha}{(N+\frac{1}{2})^{\frac{1}{2}}}\right] \tag{18}$$

with

$$W_\infty=0.591,\quad 2\alpha=0.431 \tag{19}$$

for the 16d sites of spinel lattice. Moreover it can be shown easily that, if $t/\tau_0\gtrsim 5$,

$$W_t\fallingdotseq W_\infty\exp[2\alpha/(t/\tau_0)^{\frac{1}{2}}]. \tag{20}$$

By using Eq. (20) $L(t)$ can be calculated easily.

We define $f(t)$ as

$$\Delta\frac{L(t)}{L_0}=\rho\frac{t}{\tau_0}\left(1-\frac{L(t)}{L_0}\right)\cdot W_t\cdot\Delta(\log t)=f(t)\Delta(\log t) \tag{21}$$

and assume physically that $f(\tau)$ is equal to the distribution function, which is defined previously and is now to be determined.

The assumption is not mathematically rigorous, but is to be justified physically from the good agreement of the conclusion with the experimental results.

Note added in proof. Quite recently we have obtained a single relaxation time in the same problem for the time change of the quantity $Q(t)$;

$$Q(t)=1/L_0\cdot\sum_i\exp[-k_i(t)/p],$$

where $k_i(t)$ is the number of the transits of vacancies on i lattice points from $t=0$ to $t=t$, the summation i extends over a whole lattice points, and p is a dimensionless constant. This result is quite consistent with the experimental results of single relaxation time in low cobalt concentration after Dr. Palmer (private communication) and Mr. Inoue which were obtained quite recently. Therefore, we now believe the presence of a distribution in relaxation time for cobalt rich region is due to a combined effect of the random walk of vacancies and the distribution of jumping probabilities of cobalt or iron ions among various microregions of a single matrix. The variety is introduced from the statistical scattering in the concentration of cobalt

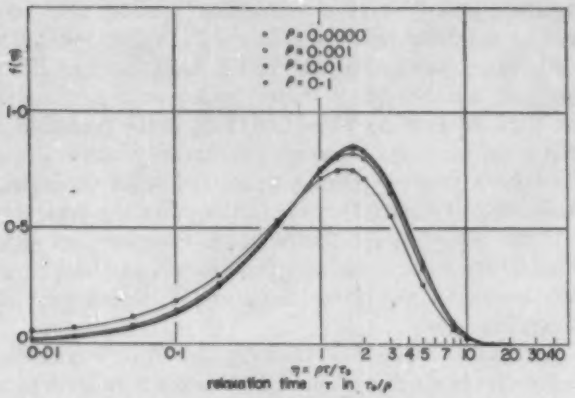

FIG. 2. Dispersion function of the relaxation time for atomic rearrangement, which is calculated from a model of migrating vacancies.

ions and also in the degree of short range ordering. The details will be published soon in J. Phys. Soc. Japan.

Calculation gives

$$f(\tau)=\rho W_\infty\frac{\tau}{\tau_0}\exp\left[-\rho W_\infty\frac{\tau}{\tau_0}\right]$$
$$\cdot\exp\left[-2\alpha\left\{\rho W_\infty\left(2\left(\frac{\tau}{\tau_0}\right)^{\frac{1}{2}}+1\right)-\left(\frac{\tau_0}{\tau}\right)^{\frac{1}{2}}\right\}\right], \quad (22)$$

where the last factor is a correction. The curves are shown in Fig. 2. We see that, when $\rho<0.01$, the correction term is actually negligible, and it corresponds to putting $W_t=W_\infty$ in Eq. (17).

The theory can be generalized easily to the real case in which short-range order is important. Let $L_{Co}{}^0$ be the number of cobalt ions present and $L_{Co}(t)$ be the number of the lattice points that are occupied by cobalt ions at $t=0$ and have been occupied by vacancies at $t=t$. Then,

$$\Delta L_{Co}(t)=L_0\rho\sum_{i,j}g_{ij}\left[w_{Co}{}^i(ij)W_{Coij}{}^i(\infty)\frac{\Delta t}{\tau_{Co}{}^i(ij)}\right.$$
$$\left.+w_{Co}{}^j(ij)W_{Coij}{}^j(\infty)\frac{\Delta t}{\tau_{Co}{}^j(ij)}\right]$$
$$\cdot\left[1-\frac{L_{Co}(t)}{L_{Co}{}^0}\right], \quad (23)$$

where g_{ij} means the probability that a vacancy is surrounded by i and j cobalt ions as nearest neighbors with i and j cobalt ions on the two groups of nearest neighbors, respectively (6 nearest neighbors of 16d lattice sites can be classified by symmetry, into two groups, each with 3 neighbors, so that i, j mean 0, 1, 2, or 3). $w_{Co}{}^i(ij)$ or $w_{Co}{}^j(ij)$ means the probability that the next migration of a vacancy is a replacement with a certain cobalt ion of i cobalt ions, or of j cobalt ions, $W_{Coij}{}^i(\infty)$ or $W_{Coij}{}^j(\infty)$ is a probability that a cobalt ion in an i or j group is a virgin lattice point under the assumption that the vacancy already has spent an infinite time for migration (we put $W_{Coij}{}^i(t)=W_{Coij}{}^i(\infty)$ according to the result of Fig. 2), and $\Delta t/\tau_{Co}{}^i(ij)$ is the probability of migration of the vacancy in the time interval Δt to one of the nearest neighbor i cobalt ions under the condition that the other kind of migration does not occur.

Although the actual calculation of g_{ij}, $w_{Co}{}^i(ij)$, $W_{Coij}{}^i(\infty)$, $\tau_{Co}{}^i$ will be quite complicated, it can be done at least in principle and we get a differential equation,

$$\langle\langle\tau\rangle\rangle_{Co}\frac{dL_{Co}}{dt}\Big/\left[1-\frac{L_{Co}(t)}{L_{Co}{}^0}\right]=L_0\rho\langle\langle w_{Co}W_{Co}(\infty)\rangle\rangle, \quad (24)$$

in which the double brackets indicate a mean value in a sense expressed in Eq. (24). Then,

$$f(\tau)=\frac{L_0\rho}{L_{Co}{}^0}\langle\langle w_{Co}W_{Co}(\infty)\rangle\rangle\langle\langle\tau\rangle\rangle_{Co}$$
$$\times\exp\left[-\frac{L_0\rho}{L_{Co}{}^0}\langle\langle w_{Co}W_{Co}(\infty)\rangle\rangle\langle\langle\tau\rangle\rangle_{Co}\right] \quad (25)$$

so that the distribution function is little changed, except for the replacement of the constant.

IV. KINETICS OF MAGNETIC ANNEALING

By using the distribution function $f(\tau)$, an analytical description of the magnetic annealing effect is easily made. The theory is quite general, and it can apply to alloys and also to the structural relaxation of every other property.

We first assume that S_u, the degree of directionality, can be defined as

$$K_u=S_u\cdot P(T). \quad (26)$$

In Bickford's model S_u is proportional to the differences in the occupation numbers of cobalt ions among four different groups of 16d sites. We assume further that

$$S_u=\int_0^\infty f(\tau)S(\tau)d(\log\tau) \quad (27)$$

$$\Delta S_u=\int_0^\infty f(\tau)\Delta S(\tau)d(\log\tau) \quad (28)$$

$$\Delta S(\tau)=[S(\tau)-S^e(T)](-\Delta t/\tau), \quad (29)$$

where $S(\tau)$ is defined as the degree of directional ordering of the region having a relaxation time τ. But of course there is no real definite portion in the crystal which relaxes with τ. We assume further $S^e(T)$ is independent of τ, and is equal to $S_u{}^e(T)$. Then in a magnetic field switching experiment,

$$S_u^R(t)=S^e(T)\int_0^\infty f(\tau)\exp(-t/\tau)d(\log\tau) \quad (30)$$

because, at $t=0$, $S(\tau)=S^e(T)$ along the direction R, and $S^{e,r}(T)=0$ after switching the magnetic field.

The results of numerical calculation are given in Fig. 3. It coincides completely with the experimental results of Fig. 1. We show also in Fig. 4 the comparable experimental results for a $CoFe_2O_4$ polycrystal.

Analytically, if we put

$$f(\tau)=a^2\tau\exp(-a^2\tau), \quad (31)$$

then

$$S_u^R(t)/S^e(T)=a^2\int_0^\infty \exp(-a^2\tau+t/\tau)d\tau$$
$$=2at^{\frac{1}{2}}K_1(2at^{\frac{1}{2}}), \quad (32)$$

where K_1 is a modified Bessel function.[11] Its asymptotic form at $t\to\infty$ is

$$(\pi a)^{\frac{1}{2}}\cdot t^{\frac{1}{4}}\cdot\exp[-2a(t)^{\frac{1}{2}}]\cdot\left[1+\frac{3}{8}\frac{1}{2a(t)^{\frac{1}{2}}}+\cdots\right], \quad (33)$$

and we get the exponential decrease in $t^{\frac{1}{2}}$.

The theory can apply to the magnetic field cooling experiment.

The dispersion function can be written generally

$$f(\tau)=W\rho\frac{\tau}{\tau_0}\exp\left(-W\rho\frac{\tau}{\tau_0}\right), \quad (34)$$

and the unit relaxation time τ_0 will be given approximately in quite a wide range of temperature as

$$\tau_0=\tau_0^\infty\exp(Q/kT). \quad (35)$$

By neglecting the temperature change of ρ, and putting

$$W\rho\frac{\tau}{\tau_0}=\eta, \quad \tau=\tau_\eta(T)=\frac{\tau_0\eta}{W\rho}, \quad (36)$$

then

$$\Delta S_u=\int_0^\infty f(\eta)(S_\eta-S^e(T))(-\Delta t/\tau_\eta(T))d(\log\eta). \quad (37)$$

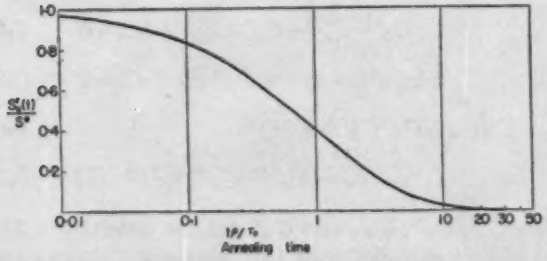

FIG. 3. Theoretical curve for annihilation of uniaxial anisotropy with time of annealing.

[11] This transformation is due to the suggestion by Professor Kubo and his collaborators.

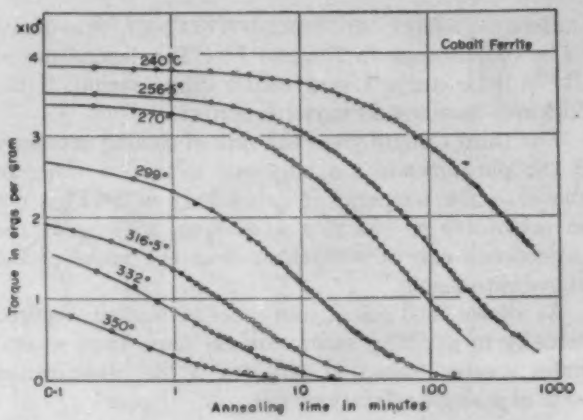

FIG. 4. Annihilation of uniaxial anisotropy of $CoFe_2O_4$ polycrystalline specimen with time of annealing at various temperatures.

In the magnetic field, cooling from $T=T_0$ to $T=T$,

$$T=T(t), \quad \Delta T=\Delta t/(dT(t)/dt) \quad (38)$$

$$S_u(T)=S_u^e(T)$$
$$-\int_0^\infty f(\eta)\left[\int_{x_0}^x G(\eta,x')\frac{dS^e(x')}{dx'}dx'\right]d(\log\eta), \quad (39)$$

where

$$G(\eta,x')=\exp\left(-K\int_{x'}^x e^{-x''}\frac{dt}{dx''}dx''\right) \quad (40)$$

$$x=Q/kT, \quad x_0=Q/kT_0 \quad (41)$$

$$K=W\rho/\eta\tau_0^\infty. \quad (42)$$

If we use a constant rate of cooling, then $G(\eta,x')$ becomes a step-like function.

As a result of the fact that the relaxation time has a distribution, the magnetic field cooling becomes more effective than the magnetic field annealing at constant temperature. This is shown numerically in Table I. It is assumed here that at the temperature considered, it takes about 180 min for S_u to get 99% saturation in isothermal annealing. The table shows the rate of cooling R necessary for getting 99% saturation of S_u at the same temperature after the magnetic field cooling from the higher temperature.

TABLE I. The rates of cooling required for getting 99% saturation in $S_u(T)$ at a certain temperature after a constant rate cooling from higher temperature are shown. It is assumed that 180 min are necessary to get 99% saturation in $S_u(T)$ in the isothermal annealing at the same temperature.

	R, the rate of cooling required in deg/min	
	$Q=1$ ev	$Q=1.6$ ev
If $S^e(T)\propto T^{-2}$	0.63	0.97
If $S^e(T)\propto T^{-1}$	1.1	1.7
If single τ	0.10	0.18

Here the temperature dependence of $S^e(T)$ is assumed to be proportional to T^{-2} and T^{-1}. The dependence of T^{-2} will be realized in a cobalt dilute region, if the Bickford-Slonczewski model is correct.

The third column gives the rate of cooling necessary if the phenomenon has only one relaxation time. In this case, the temperature dependence of $S^e(T)$ is not so responsive to the rate of cooling, so long as the dependence can be written or near the range of the above expressions.

As shown in Table I, the rates of cooling required actually to get 99% saturation are more than several times greater than that required if the phenomenon were of a single relaxation time.

V. PHASE DIAGRAM AND EQUILIBRIUM DENSITY OF CATION VACANCIES

Studies of the phase diagram of Fe-Co-O system are very few.[12-14] In Fig. 5 the phase diagram of Fe-O system by Darken and Gurry[15] is given in the partial pressure of oxygen temperature plane.[16] In the upper part of the figure, four border lines obtained by us[14] for the precipitation of αFe_2O_3 in $Co_xFe_{3-x}O_4$ system are shown. The lines correspond to $x=0$, 0.083, 0.167, and 0.250 respectively in order from the lowest line. The discrepancy of the results for $x=0$ are due to the difference of the atmosphere used (gas mixture by D. and G., vacuum by us).

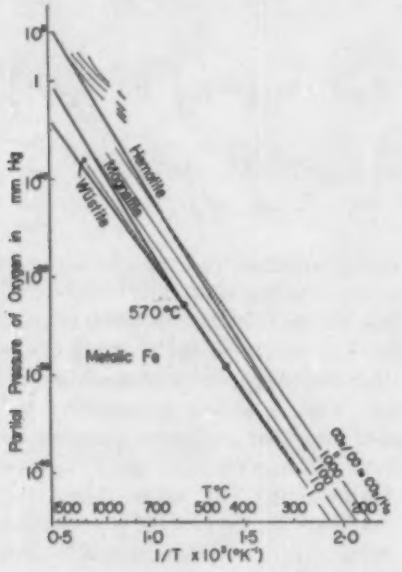

FIG. 5. Phase diagram of Fe-O system in the pressure of oxygen-temperature plane. Parallel lines show the expected partial pressures of oxygen for various gas mixtures indicated, as a function of temperature. A group of lines in the upper part of the figure shows the border line for the precipitation of αFe_2O_3 in $Co_xFe_{3-x}O_4$. The lines correspond to $x=0$, 0.083, 0.167, and 0.250, respectively, from lower to upper. The second group of small lines are expected from a simple statistical thermodynamical calculation.

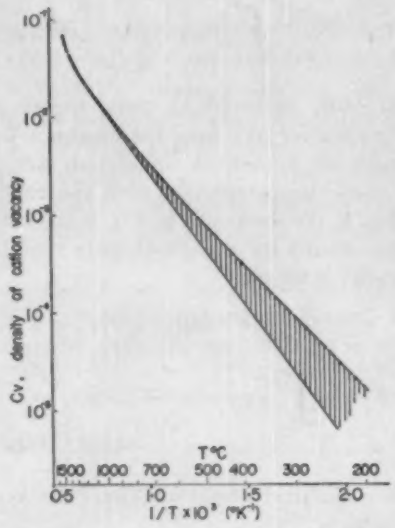

FIG. 6. Possible maximum equilibrium density of cation vacancies in magnetite. Experimental data exist only in the temperature region above 1000-C.

In Fig. 6 the most probable equilibrium density of vacancy is shown. The critical density C_v is expected to decrease exponentially as a function of $1/T$ according to our analysis by statistical thermodynamics.[17] Experimental data by Darken, Gurry, and Smiltens exist only in the high temperature region (above 900°C). It is expected in the temperature range of 500°C~600°C that the equilibrium density C_v of magnetite is less than $10^{-3}\sim10^{-6}$.

As for the equilibrium density of vacancies in iron cobalt ferrites, there are no available data at present, but we have studied theoretically,[17] assuming perfect inverse spinel structure, an approximation to a regular solution for 16d sites, using the Einstein approximation for the lattice vibration.

The results are as follows:

$$C_A'+C_A''+C_B'+C_B''+C_v=1 \qquad (43)$$

$$C_A'-C_A''+C_B'-C_B''+5C_v=0 \qquad (44)$$

$$C_A'x+C_B'(x-1)-C_B''+(8/3)xC_v=0 \qquad (45)$$

$$C_A'C_B''/C_A''C_B'=K(T)^* \qquad (46)$$

$$C_v=(C_A'^{8/3}/C_A''^{7/3})\cdot P^{1}\cdot J(T)^* \qquad (47)$$

where C_A', C_A'', C_B', and C_B'' are the densities in 16d sites of Fe^{2+} ions, Fe^{3+} ions, Co^{2+} ions, and Co^{3+} ions and cation vacancies. Equation (44) stands for the balance in the charge, Eq. (45) for the definition of the concentration of cobalt ion x, Eq. (46) for the balance of the

[12] J. Robin and J. Benard, C. R. **234**, 744, 956 (1952).
[13] J. Smiltens, Massachusetts Institute of Technology Tech. Rept. No. 115 (1957).
[14] S. Iida, J. Phys. Soc. (Japan) **11**, 846 (1956).
[15] L. S. Darken and R. W. Gurry, J. Am. Chem. Soc. **67**, 1398 (1946); **68**, 798 (1947).
[16] This figure has been replotted from the data of Darken and Gurry.
[17] S. Iida (to be submitted).

electron transfer reaction,

$$Fe^{2+}+Co^{3+} \leftrightarrows Fe^{3+}+Co^{2+}, \tag{52}$$

and Eq. (47) for the condition under which the pressure of oxygen and the degree of oxidation of the specimen are balanced.

If we assume C_v, $C_B''\ll 1$, as will be realized at lower temperatures, then we get

$$C_v=\frac{(1-x)^{8/3}}{2^{\frac{1}{3}}}\cdot P^{\frac{1}{6}}\cdot J(T), \tag{49}$$

showing the dependence on x as $(1-x)^{8/3}$ for fixed P and T. This is shown with curve (a) in Fig. 7.

For the initiation of hematite precipitates, the same treatment gives

$$C_v=L(T)/C_A''^{5}, \tag{50}$$

and if C_v, $C_B''\ll 1$

$$C_v=2^5\cdot L(T),^{18} \tag{51}$$

which is independent of x. It is shown with curve (b) in Fig. 11.

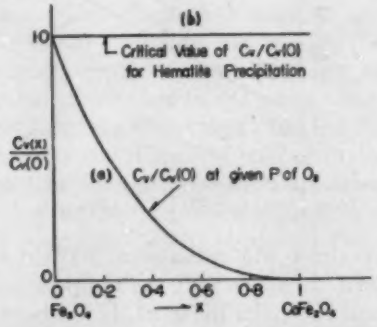

FIG. 7. Theoretical density of cation vacancies in iron-cobalt ferrites. (a) equilibrium density as a function of cobalt concentration at a given pressure of oxygen and temperature. (b) maximum equilibrium density of cation vacancies. The values correspond to the state just below the precipitation of αFe_2O_3.

[18] The actual expressions of the function used are as follows:

$$K(T)=\exp\left[-\frac{(q_F''-q_F')-(\gamma_F''-\gamma_F')}{kT}\right]\cdot\frac{u_A'\cdot u_B''}{u_A''u_B'}, \tag{A}$$

$$J(T)=\exp\left[\frac{8/3(q_F''-q_F')-\frac{8}{3}\epsilon_0-S_V}{kT}\right]\cdot\frac{h^2}{2\pi mkT}\cdot\frac{h^{4/3}}{[8\pi^2A(kT)^2]^{\frac{1}{3}}}(1-e^{-h\nu/kT})^{\frac{1}{3}}\cdot\left(\frac{\pi}{\nu}\right)^{\frac{1}{3}}\cdot\frac{1}{[1-\exp(\theta_0^F/T)]^4}\left[\frac{u_A''}{u_A'}\right]^{8/3}, \tag{B}$$

$$L(T)=\exp\left[-\frac{8(q_H''-q_F'')+S_V}{kT}\right]\cdot\frac{[1-\exp(-\theta_A^H/T)]^8}{[1-\exp(-\theta_A^F/T)]^8}\cdot\frac{[1-\exp(-\theta_0^H/T)]^9}{[1-\exp(-\theta_0^F/T)]^9}, \tag{C}$$

where q_F', q_F'', γ_F', γ_F'', and S_V are the heat of formation of $Fe^{2+}O^{2-}$, $Fe^{3+}O_{\frac{1}{2}}^{2-}$, $Co^{2+}O^{2-}$, $Co^{3+}O_{\frac{1}{2}}^{2-}$, and a cation vacancy in a spinel lattice, ϵ_0 denotes the heat of formation of oxygen molecule, m, A, and ν the constants of an oxygen molecule, u_A', u_A'', u_B', and u_B'' the electronic partition functions of Fe^{2+}, Fe^{3+}, Co^{2+} and Co^{3+} ions, and θ_A^H, θ_A^F, θ_0^H, and θ_0^F the Debye temperatures of a $Fe^{(+)}$ ion and a O^{2-} ion in hematite and magnetite, respectively.

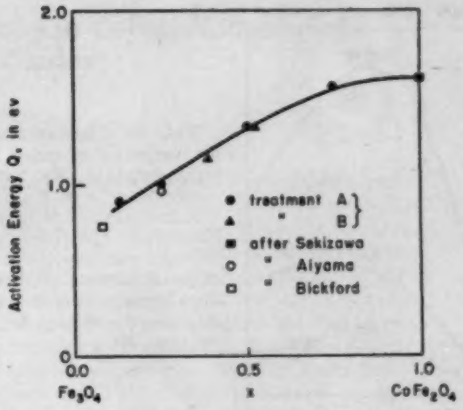

FIG. 8. Variation of activation energy Q with composition in $Co_xFe_{3-x}O_4$.

VI. SEVERAL EXPERIMENTAL RESULTS AND DISCUSSIONS

An important conclusion presented in this paper is that the relaxation time of the phenomena is simply proportional to the inverse of the density of vacancies ρ or C_v as well as to τ_0 of the diffusion constant, which decreases exponentially with the inverse of absolute temperature. Figure 8 shows the variation of the activation energy Q with the cobalt concentration x, which we obtained together with the result by Bickford *et al.* The situation is made clear in Fig. 9. Here the two groups of lines are drawn corresponding to the activation energy of 1.0 ev and 1.6 ev respectively, which represent the variation of relaxation time with temperature. Parallel lines correspond to the different vacancy density with the same activation energy, and the ratio of ρ between the two nearest lines is equal to 10^2. If we interpret that the disappearance of K_m, which was observed experimentally,[5] is induced only by the change in the diffusion rate associated with the change in the density of vacancy, Fig. 9 indicates that the decrease in ρ of about a factor $10^{-5}\sim 10^{-6}$ has proceeded with the vacuum heat

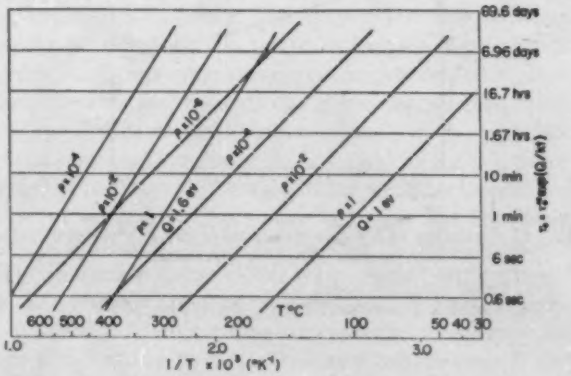

FIG. 9. Relaxation time as a function of temperature and density of cation vacancies. Two groups of lines correspond to two different activation energies: $Q=1.6$ ev for $CoFe_2O_4$ and $Q=1.0$ ev for $Co_{0.28}Fe_{2.72}O_4$.

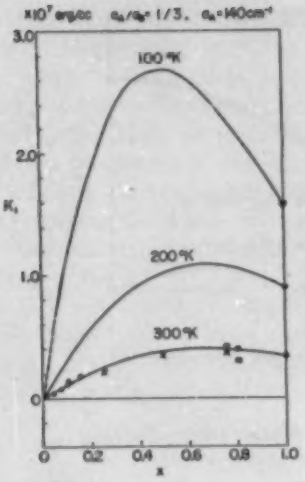

FIG. 10. Theoretical curves for variation of cubic anisotropy constant K_1 with the composition x in $Co_xFe_{3-x}O_4$. The temperature is taken as a parameter. The points plotted indicate the experimental results of various studies after Shenker, ●; Bozorth *et al.*, □; Bickford *et al.*, ○; and Aiyama, ×.

treatment at 750°C. Quite recently, we got the result[19] that there is no difference in $K_u^e(T)$ of the two carefully made specimens, which have the same composition but differ in relaxation times (about a factor of 20).

Bickford, Slonczewski *et al.*[6,7] get the result that the apparent final value of K_u is decreased during the progress of reduction. They presume that apparently the cobalt ions near a cation vacancy can move rapidly, but our study does not support this conclusion. Whether their result indicates an essential correlation of the uniaxial anisotropy to the density of vacancy or not is not clear. But we feel that the sample used by them in a reduced state might not be homogeneous concerning to the degree of oxidation.

Tachiki[20] of Osaka University has discussed this problem theoretically and asserts that the probability of having a direct pair of a cobalt ion and cation vacancy in 16d sites will be very small as a result of the effective charges of -0.5 e and -2.5 e, respectively. He has calculated recently the cubic anisotropy constant K_1 based on a crystalline field model.[5] In the calculation, the main part of the anisotropy comes from the Co^{2+} ions under several kinds of deformed crystalline fields. The deformation is assumed to be caused by the presence of one or two Co^{2+} ions as nearest neighbors. This result can describe well the experimental results obtained by Shenker,[21] Bozorth *et al.*,[4] Penoyer *et al.*,[22] and Aiyama[23] as shown in Fig. 10.

Although Tachiki did not calculate the amount of the uniaxial anisotropy K_u expected from his model, it is quite certain that the term F can be derived from the similar model. However, Aiyama, as a result of analysis of his experimental results still believes that the number of vacancies has a certain influence on the equilibrium value of K_u. Aiyama has made several experiments on the uniaxial anisotropy in a cobalt rich region. In Fig. 11, the variation of G and F is plotted against temperature. The specimen was annealed at 100°C for one hour and quenched. It shows that the temperature dependence of G and F is quite different. It has been found by Aiyama[9] that the relaxation time for the switching of the magnetic field from [100] to [110] is different from that for [110] to [100] by about a factor of two for a $Co_{0.28}Fe_{2.72}O_4$ specimen, as shown in Fig. 12.

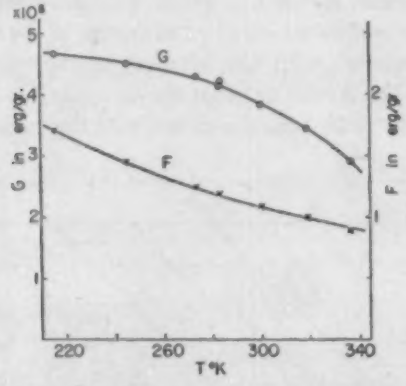

FIG. 11. Variation of the two constants G and F with temperature for $Co_{0.28}Fe_{2.72}O_4$ specimen.

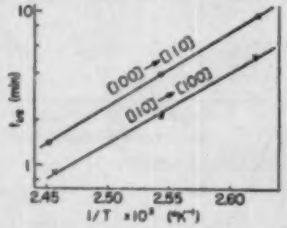

FIG. 12. Relaxation times for switching from [100] to [110], and from [110] to [100], $Co_{0.28}Fe_{2.72}O_4$.

ACKNOWLEDGMENTS

The author would like to express his appreciation to Dr. Y. Aiyama of The Electro-Technical Laboratory, Mr. M. Tachiki of the Ōsaka University, and also H. Sekizawa, T. Inoue, and H. Mizuta for permission to refer to their unpublished results. He extends his thanks to Professor R. Kubo and his collaborators for their valuable discussions.

[19] T. Inoue (unpublished).
[20] M. Tachiki, Busseiron Kenkyu, II, 4, 312 (1958).
[21] H. Shenker, Phys. Rev. **107**, 1247 (1957).
[22] L. R. Bickford, Jr., J. M. Brownlow, and R. F. Penoyer, Proc. Inst. Elec. Engrs. **104B** Suppl. 238 (1957).
[23] Y. Aiyama, presented at the Annual Meeting of the Physical Society of Japan (1959).

Intrinsic and Anneal-Induced Anisotropy in Cobalt-Substituted *W*-Type Hexagonal Oxides*

L. R. Bickford, Jr.
IBM *Research Laboratory, Poughkeepsie, New York*

The intrinsic and anneal-induced anisotropy of cobalt-substituted hexagonal ferrous *W* compounds containing some vacancies in lattice sites normally occupied by metal ions were measured by the torque method. Six oriented polycrystalline samples, corresponding to $y=0.03$, 0.06, 0.12, 0.24, 0.45, and 0.9 in the formula $BaCo_yFe_{17.9-y}O_{27}$, and one single crystal of composition $Ba_{0.27}Sr_{0.73}Co_{1.845}Fe_{16.155}O_{27}$, were investigated. The results confirm the prediction that the cobalt ions and vacancies would be located in the spinel portion of the *W* lattice and therefore respond to magnetic annealing in much the same way as in the ferrite system $Co_xFe_{3-x}O_4$. The contribution per cobalt ion to the anneal-induced anisotropy constant K_u was found to be approximately the same in the two systems (ca 3×10^{-16} erg/cobalt ion for annealing at 100°C). Other points of comparison include the dependence on cobalt concentration of K_u and the relaxation times characterizing the annealing process, the activation energy and the variation of K_u with temperature of anneal.

The first-order intrinsic hexagonal anisotropy constant K_1 becomes more negative with increasing cobalt concentration reaching a value of -4.35×10^6 erg/cc at 27°C for the single crystal. The value of K_3, the constant which determines the anisotropy in the basal plane, is much larger for this crystal than for any other hexagonal oxide reported so far ($K_3=-1.22\times10^4$ erg/cc at 27°C and $+1.35\times10^5$ erg/cc at −196°C). Two of the compositions ($y=0.45$ and 0.9) have cones of easy magnetization at −196°C.

THE addition of cobalt to ferrospinels is known to introduce a large positive contribution to their cubic ansiotropy, and at least in the case of iron ferrite it causes the ferrite to respond to magnetic annealing.[1,2] In the limit of low cobalt concentrations these effects have been interpreted in terms of a single ion model.[3] The octahedral cation sites in the spinel can be divided into four sublattices, each of which has a different cube body diagonal as the symmetry axis of the site's crystalline field. The energy of a cobalt ion depends upon the angle between its spin moment and the symmetry axis of the octahedral site it occupies. The annealing phenomenon amounts to a migration of cobalt ions through the lattice at elevated temperatures via octahedral vacancies in order to minimize their energy in the magnetic field. At room temperature, the cobalt ions have lost their mobility and their unequal distribution over the four numerically equivalent sublattices gives rise to the anneal-induced anisotropy.

In recent years, investigators at the Philips Research Laboratories have discovered new types of hexagonal ferrimagnetic oxides which have interesting anisotropy characteristics.[4] The structures of all these oxides can be described in terms of blocks of spinel structure (so oriented that a ⟨111⟩ of the spinel is parallel to the hexagonal c axis) separated by hexagonal oxide layers containing barium. In the compound designated as Me_2W, the spinel blocks are twice as thick as in any other hexagonal oxide. The octahedral sites of each spinel block of this compound exist in five layers parallel to the hexagonal basal plane. Since the outer two layers are adjacent to the hexagonal portion of the structure, only the sites on the inner three layers can be regarded as having essentially the same environment as in bulk spinel. All four spinel sublattices are represented in these three layers, although the sites with symmetry axis parallel to the hexagonal c axis are twice as numerous as those of any of the other three sublattices. Thus, the system $(Co_yFe_{2-y})W$ might be expected to have features in common with the system $Co_xFe_{3-x}O_4$. It was the object of this investigation to study the anisotropy of the *W* system, to determine whether it responds to magnetic annealing, and to compare the influence of cobalt on the anisotropy characteristics of the two systems.

The difficulty involved in fabricating single crystals of controlled composition necessitated the use of polycrystalline specimens for most of the experiments. These specimens were grain oriented; that is, the hexagonal c axes of the individual crystallites were well-aligned in one direction, whereas the other axes were oriented at random. The atmosphere during firing was closely controlled in order to oxidize the samples slightly, and thus create some vacancies in lattice sites normally occupied by cations. Six compositions, with $0.03\leq y\leq0.9$, and one single crystal with $y=1.845$ (actual composition $Ba_{0.27}Sr_{0.73}Co_{1.845}Fe_{16.155}O_{27}$), were studied. The annealing experiments were performed on disks cut normal to the c axis, in order that the large intrinsic anisotropy would not obscure the measurement.

The annealing experiments were carried out by heating the sample in a magnetic field, quenching it rapidly in the field, and measuring the uniaxial anisotropy at room temperature by the torque method. Although the growth of the anisotropy was not a simple exponential function of annealing time, it was possible to assign a characteristic relaxation time to the rate of final approach to saturation. As in the case of the spinels, the

* Based on experimental work performed while the author was guest scientist in the Philips Research Laboratories, N. V. Philips Gloeilampenfabrieken, Eindhoven, Netherlands.

[1] R. M. Bozorth, E. F. Tilden, and A. J. Williams, Phys. Rev. **99**, 1788 (1955).

[2] R. F. Penoyer and L. R. Bickford, Jr., Phys. Rev. **108**, 271 (1957).

[3] J. C. Slonczewski, Phys. Rev. **110**, 1341 (1958).

[4] J. Smit and H. P. J. Wijn, *Ferrites* (John Wiley & Sons, Inc., New York, 1959), Chap. IX, p. 177.

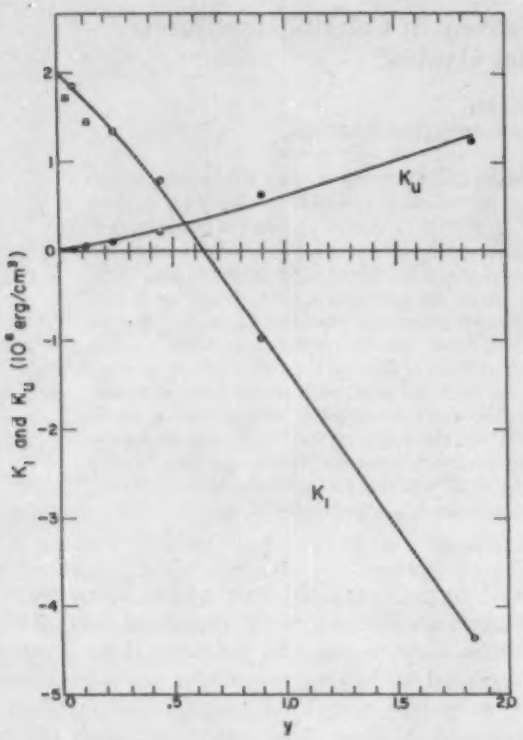

FIG. 1. Room temperature values of anneal-induced anisotropy constant K_u (for annealing at 100°C) and first-order hexagonal anisotropy constant K_1 as functions of cobalt concentration y in $(Co_yFe_{2-y})W$.

relaxation time at a given temperature increases with cobalt concentration. At 100°C it was found to be 10^4 hrs for $y=0.9$ and only a few minutes for $y\leq 0.12$. The former value was obtained by extrapolation of data measured at higher temperature, making use of the measured activation energy of 1.26 ev.

Figure 1 shows the variation with cobalt concentration of K_u, the uniaxial induced anisotropy constant, for annealing at 100°C. The values of K_u(100°C) for $y>0.5$ were obtained by extrapolation from results obtained at higher temperatures. K_u was found to vary inversely with the absolute temperature of annealing. The K_u vs y curve is approximately linear and resembles a corresponding curve for cobalt-iron ferrite.[1,2] (It should be noted that $y=2$ corresponds to the ferrite $Co_{0.5}Fe_{2.5}O_4$.) For purposes of quantitative comparison between the two systems it is convenient to use the parameter K_u/Co ion, which is obtained by dividing K_u(erg/cc) by the number of cobalt ions per cc. For the W system and annealing at 100°C, this parameter increases from 2.4 to 3.3×10^{-16} erg/Co, whereas in the ferrite system it increases from 2.0 to 3.4×10^{-16} erg/Co in a corresponding cobalt concentration range. Space limitations do not permit a critical analysis of the various approximations necessary to make this comparison. Whereas the actual agreement may not be as close as the above figures indicate, it is certainly sufficiently close to warrant the conclusion that a cobalt ion in the W structure contributes approximately the same amount to K_u as it does in the spinel.

The first-order intrinsic hexagonal anisotropy constant K_1 was obtained from torque curves measured on disks containing the c axis in their plane. The values of K_1 at room temperature vary with cobalt concentration as is shown in Fig. 1. The fact that this curve does not extrapolate to the value of $+3.0\times10^6$ reported[4] for Fe_2W is probably due to the incomplete orientation of the polycrystalline specimens. K_1 is negative for $y=0.9$ and 1.845, and these samples have planar anisotropy[4] at room temperature. Samples with $y=0.45$ and $y=0.90$ display cones[4] of easy magnetization at 77°K. The constant K_3, which characterizes the anisotropy in the basal plane, was determined from the single crystal. At 300°K, $K_3=-1.22\times10^4$ erg/cc, which is an order of magnitude larger than the value so far reported[4] for any other hexagonal oxide. The basal plane of the hexagonal crystal corresponds to a (111) plane of the spinel, in which the anisotropy is determined solely by the second order cubic anisotropy constant. Therefore, a comparison of K_3 with the second order anisotropy constant of the spinel provides an additional check on the relative influence of cobalt on the anisotropy of the two systems. K_3/Co in the W is -3.2×10^{-18} erg, and the equivalent parameter for the ferrite has the same numerical value but is a positive number. The preferred directions in the W basal plane correspond to ⟨110⟩ of the cubic crystal; whereas in the ferrite the preferred directions in (111) are ⟨112⟩. However, K_3 changes sign at ca 155°K, and reaches $+1.35\times10^5$ erg/cc at 77°K.

The results of this investigation tend to verify the assumption that the cobalt ions and cation vacancies are located in the spinel portion of the W structure, where they contribute to magnetic annealing in much the same way as they do in the ferrites. Cobalt has a very strong influence on the intrinsic anisotropy. In some respects, its influence is essentially what would be predicted, and in other respects is quite unexpected. A more complete report on this work will be published elsewhere.

ACKNOWLEDGMENTS

In conclusion, the author would like to express his sincere appreciation the staff and management of the Philips Research Laboratory for their hospitality and cooperation during the period this work was done. Particular thanks are due A. L. Stuijts, under whose direction the specimens were prepared. This investigation would not have been possible without his cooperation and ability to solve the difficult chemical problems posed by the system $(Co_yFe_{2-y})W$. The assistance of U. Enz in performing some of the measurements, and the general assistance and encouragement offered by J. Smit are also gratefully acknowledged.

Valence and Distribution of Manganese Ions in Ferrospinels

ARTHUR MILLER
RCA Laboratories, Princeton, New Jersey

Anomalous values of the magnetic moments observed for ferrospinels containing manganese have suggested that on octahedrally ligated spinel sites the ion pair [$Fe^{+2}Mn^{+3}$] is more stable than [$Fe^{+3}Mn^{+2}$]. Such behavior is opposed to that observed in aqueous solutions, and to what is usually expected in oxidic compounds. The magnetic measurements, however, cannot be interpreted unequivocally, since they can also be explained by invoking spin quenching, or deviations from the simple antiparallel spin-only coupling scheme such as Yafet-Kittel angular coupling.

A crystallographic rather than a magnetic criterion was devised to elucidate the valence behavior in these compounds. When a sufficient fraction of the octahedrally ligated spinel sites are occupied by Mn^{+3}, a macroscopic tetragonal distortion, due to the Jahn-Teller effect, occurs. For appropriately selected spinel systems, the compositions for which this distortion is observable at room temperature depend on whether [$Fe^{+3}Mn^{+2}$] or [$Fe^{+2}Mn^{+3}$] are the stably coexisting species. Various compositions in the system $Zn_{1-0.5x}Ge_{0.5x}[Fe_xMn_{2-x}]O_4$ were synthesized, and x-ray powder diffraction photographs were made to determine whether they were cubic or tetragonal. The findings confirmed that the stable ion pair on octahedrally ligated sites is indeed [$Fe^{+2}Mn^{+3}$]. Furthermore, the axial ratios observed for the tetragonal compositions are in good agreement with those calculated by Wojtowicz, provided that the valence assignment [$Fe^{+2}Mn^{+3}$] is assumed. The reversal of valence stability can be explained reasonably as arising from crystal field effects.

There is evidence that on octahedrally ligated spinel sites at elevated temperatures, and on tetrahedrally ligated sites, the ion pair [$Fe^{+3}Mn^{+2}$] is more stable than [$Fe^{+2}Mn^{+3}$]. The method of predicting the actual valence and ionic distributions in manganese-containing ferrospinels is discussed.

IN many spinels containing transition metal cations, it is not possible to assign valences unequivocally solely from considerations of stoichiometry and electroneutrality. It is usually assumed in these cases that the oxidation-reduction equilibria are the same as those observed for aqueous solutions, since the factors (such as crystal field stabilization) influencing thermodynamic properties are usually nearly the same for both oxides and hydrated ions. On this basis, the valence distribution in manganese ferrite would be $Mn^{+2}Fe_2^{+3}O_4$. However, in order to explain the saturation moment[1] at 0°K of 4.6 rather than 5.0 μ_B, it has been proposed[2] that the manganese on the octahedrally ligated spinel sites (*B*-sites) is trivalent, and that a corresponding amount, 0.2 formula unit, of iron on the *B*-sites is divalent.

Measurements of ferrimagnetic moments or of paramagnetic susceptibilities are not reliable criteria for assigning valence states, since phenomena such as orbital moment contributions, extremely high anisotropy fields, departures from the simple anti-parallel coupling scheme (e.g., Yafet-Kittel angular coupling), and spin-quenching can affect the observed moments and susceptibilities in much the same way as a change in valence states.

Recently, Krupička and Závěta[3] have demonstrated the existence of Fe^{+2} on the *B*-sites in manganese ferrite by measuring the dependence of the activation energies for electrical conductivity and magnetic relaxation on the oxygen content of the spinel. They account for the cation distribution in manganese ferrite by assuming that the oxidation in Mn^{+2} by Fe^{+3} cannot result in the formation of more than 0.2 formula unit of Mn^{+3} on the *B*-sites because of the inability of the spinel lattice to accommodate greater quantities of tetragonally distorted manganic ion.

The present investigation utilizes a method which unequivocally determines the valence of manganese, and includes those compositional regions where the amount of Mn^{+3} on the *B*-sites, formed by oxidation of Mn^{+2}, may exceed 0.2 formula unit.

Of the ions that can be present in manganese-containing ferrospinels, Mn^{+3} is unique in that it possesses a Jahn-Teller effect large enough to cause cooperative tetragonal distortions. Investigations of numerous systems[4] show that at room temperature, tetragonal distortions from cubic symmetry are observed in spinels when more than about 60% of the *B*-sites are occupied by Mn^{+3}. The system $Zn_{1-0.5x}Ge_{0.5x}[Fe_xMn_{2-x}]O_4$ (where the brackets enclose ions occupying the *B*-sites) is accordingly expected to be tetragonal for $0 \leqslant x < 0.4$ (and cubic for $x > 0.4$) if the stably coexisting valence states are predominantly Mn^{+2} and Fe^{+3} (Model I). On the other hand, tetragonality is expected for $0 \leqslant x < 0.8$ if the valence states are predominantly Mn^{+3} and Fe^{+2} (Model II), and for $0 \leqslant x < y$, where $0.4 < y < 0.8$ if all four ionic species can coexist in appreciable concentrations.

Representative compounds in this system were prepared by intimately mixing appropriate amounts of ZnO, GeO_2, Fe_2O_3, and Mn_2O_3, pressing the mixtures into pellets, and firing them for 90 minutes in air at 1150°C on single-crystal MgO plates. The lattice parameters of these preparations are shown in Table I below. The occurrence of tetragonal distortion at $x = 0.8$ suggests strongly that the ions exist almost wholly as Fe^{+2} and Mn^{+3}.

Wojtowicz[5,6] has shown by a theoretical treatment of cooperative distortions that the c/a ratios in spinels can be correlated with the amount of Mn^{+3} on the *B*-sites. Figure 1 shows a plot of the observed c/a ratios vs x,

[1] J. M. Hastings and L. M. Corliss, Phys. Rev. **104**, 329 (1956).
[2] F. W. Harrison, W. P. Osmond, and R. W. Teale, Phys. Rev. **106**, 865 (1957).
[3] S. Krupička, and K. Závěta, Czechoslov. J. Phys. **9**, 324 (1959).
[4] D. G. Wickham and W. J. Croft, J. Phys. Chem. Solids **7**, 351 (1958).
[5] P. J. Wojtowicz, J. Appl. Phys. **30**, 30S (1959).
[6] P. J. Wojtowicz, J. Phys. Rev. **116**, 32 (1959).

TABLE I. Lattice parameters and valence states in the system $Zn_{1-0.5x}Ge_{0.5x}[Fe_xMn_{2-x}]O_4$.

x	Model I	Model II	a_0, A	c_0, A	c/a
0.0[a]	Mn_2^{+3}	Mn_2^{+3}	8.076	9.225	1.142
0.4	$Fe_{0.4}^{+3}Mn_{0.4}^{+3}Mn_{1.2}^{+3}$	$Fe_{0.4}^{+3}Mn_{1.6}^{+3}$	8.20	9.12	1.11
0.5	$Fe_{0.5}^{+3}Mn_{0.5}^{+3}Mn^{+3}$	$Fe_{0.5}^{+3}Mn_{1.5}^{+3}$	8.238	8.965	1.088
0.8	$Fe_{0.8}^{+3}Mn_{0.8}^{+3}Mn_{1.2}^{+3}$	$Fe_{0.8}^{+3}Mn_{1.2}^{+3}$	8.37	8.724	1.042
1.0	$Fe^{+3}Mn^{+2}$	$Fe^{+2}Mn^{+3}$	8.470		cubic

[a] The crystallographic data for $Zn[Mn_2]O_4$ are taken from B. Mason, Am. Minerologist 32, 426 (1947).

with theoretical curves *I* and *II* calculated respectively for each of the aforementioned models. The calculations assume only that at room temperature distortion occurs when there is 60% or greater occupancy of the *B*-sites by Mn^{+3}, and the c/a ratio for a spinel whose *B*-sites are completely occupied by Mn^{+3} is about 1.144 (which has also been observed in numerous spinel systems). The observed values of c/a are decisive evidence for the correctness of the second of the alternative models.

Baltzer[7] has pointed out that the difference in oxidation-reduction behavior between aqueous solutions and spinels may be due to a larger value of crystal field parameter Dq for ions on the *B*-sites than for hydrated ions. This explanation is reasonable, since the observed moment and ionic distribution data require that the reversal does not take place on the tetrahedrally ligated sites (*A*-sites) at room temperature, or on the *B*-sites at temperatures greater than about 1000°K. In each of these cases, the value of Dq is smaller than what is expected for *B*-sites at room temperature.

Brož *et al.*[8] have proposed an alternative model for the ionic and valence distribution in the $MnFe_2O_4$-Mn_2FeO_4 system (which is a part of the Fe_3O_4-Mn_3O_4 system) which explains the observed ferrimagnetic moments on the basis of unquenched spin-only atomic moments and the usual Néel coupling scheme. They assume that the amount of Mn^{+3} on the *B*-sites remains constant at 0.2 formula unit, and that Fe^{+2}, Fe^{+3}, and Mn^{+4} also coexist on the *B*-sites in amounts varying linearly with the overall composition, and with the amount of Mn^{+4} ranging from none in $MnFe_2O_4$ to 0.818 formula units in Mn_2FeO_4. However, their model fails to take into account certain other considerations. It can be shown by thermodynamic arguments that in spinels expressions formally identical to chemical equilibrium expressions, such as $[Fe_B^{+3}][Mn_A^{+2}]/[Fe_A^{+3}] \times [Mn_B^{+2}] \approx K$ are valid, provided that there is no radical change in the free energy of the corresponding reaction as the overall composition of the system is varied. In the preceding expression, the bracketed quantities are the numbers of formula units of the respective ions on the *A*- or *B*-sites, as designated by the subscripts. There is no reason to assume that there is an abrupt change in the free energy of spinel systems when $[Mn_B^{+3}]=0.2$, since the present and other investigations[4,5] show that the formation of Mn^{+3} on the *B*-sites proceeds smoothly up to and past the composition where $[Mn_B^{+3}]=1.2$ and tetragonal distortion takes place.

If a given reaction involving Mn^{+3} and allowed by stoichiometry fails to proceed appreciably in one part of a compositional system, it should not be expected to begin abruptly in another part of the system closely similar to the first. Thus, it is not likely that the reaction $Fe^{+3}+Mn^{+3} \rightarrow Fe^{+2}+Mn^{+4}$, which does not occur to a measurable extent in $MnFe_2O_4$, should begin to take place when small amounts of Mn are replaced by Fe.

The "equilibrium constant" K which appears above, evaluated from the proposed high-temperature ionic distribution in manganese ferrite,

$$Mn_{0.8}^{+2}Fe_{0.2}^{+3}[Mn_{0.2}^{+2}Fe_{1.8}^{+3}]O_4,$$

is equal to about 36. In the system Fe_3O_4-Mn_3O_4, the composition[9] at which tetragonality begins corresponds very closely to Mn_2FeO_4. Using the value of K above the high temperature ionic distribution

$$Mn_{0.86}^{+2}Fe_{0.14}^{+3}[Mn^{+3}Mn_{0.14}^{+2}Fe_{0.86}^{+3}]O_4$$

and the corresponding room temperature distribution

$$Mn_{0.86}^{+2}Fe_{0.14}^{+3}[Mn_{1.14}^{+3}Fe_{0.14}^{+2}Fe_{0.72}^{+3}]O_4$$

are predicted. This result is consistent with the requirement[4] for tetragonality of about 60% or greater occupancy of the *B*-sites by Mn^{+3}. The alternative model, which assumes only 10% occupancy of the *B*-sites by Mn^{+3}, is clearly inconsistent with this requirement.

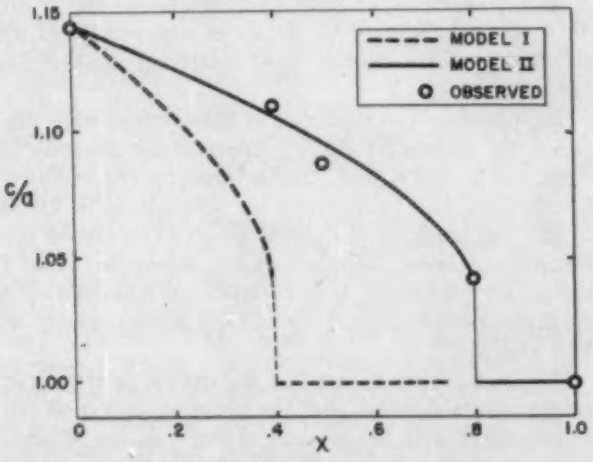

FIG. 1. Calculated and observed axial ratios in the $Zn_{1-0.5x}Ge_{0.5x}[Fe_xMn_{2-x}]O_4$ system.

ACKNOWLEDGMENTS

The author gratefully acknowledges the help of J. G. White and W. C. Roth, who performed the crystallographic measurements, and of R. E. Nielsen, who prepared most of the compounds discussed.

[7] P. K. Baltzer (private communication, 1957).

[8] J. Brož, S. Krupička, and K. Závěta, Czechoslov. J. Phys. 9, 481 (1959).

[9] G. I. Finch, A. P. B. Sinha, and K. P. Sinha, Proc. Roy. Soc. (London) A242, 28 (1957).

JOURNAL OF APPLIED PHYSICS SUPPLEMENT TO VOL. 31, NO. 5 MAY, 1960

High Field Magnetization Study of Ferrimagnetic Arrangements in Chromite Spinels*

I. S. JACOBS
General Electric Research Laboratory, Schenectady, New York

THE observation of a differential susceptibility at high magnetic fields and low temperatures in spinel-type compounds has been shown to be useful for detecting noncollinear ferrimagnetic arrangements. Such an increase in net magnetization with field is not expected for the Néel model model of tetrahedral A-site moments antiparallel to octahedral B-site moments. It is, however, expected for the triangular arrangements proposed by Yafet and Kittel in which the moments on one kind of site subdivide into two groups making angles with each other. The latter arrangements have frequently been suggested for chromium-containing spinels, usually on the basis of the observed anomalously low spontaneous magnetizations. Measurements of magnetization curves at 4.2°K in pulsed fields up to 140 kilo-oersteds reveal high field susceptibilities in $MnFe_{2-t}Cr_tO_4$, $t>0$; $CuCr_2O_4$; $FeCr_2O_4$; and $NiFe_{2-t}Cr_tO_4$, $t>1$. These are interpreted as triangular ferrimagnetic arrangements and choices are made between alternative triangular models. In some cases the sign of the dominant anisotropy is suggested. Néel antiparallel ferrimagnetic arrays are confirmed for $MnFe_2O_4$ and for $NiFe_{2-t}Cr_tO_4$, $t<1$. The present evidence for these conclusions is of a new and occasionally more direct type. A secondary conclusion is that particular care is required in the interpretation of magnetic data on powders of compounds with low crystal symmetry.

* A complete account of this work has been submitted to the *Journal of the Physics and Chemistry of Solids*.

JOURNAL OF APPLIED PHYSICS SUPPLEMENT TO VOL. 31, NO. 5 MAY, 1960

$GaFeO_3$: A Ferromagnetic-Piezoelectric Compound

J. P. REMEIKA
Bell Telephone Laboratories, Inc., Murray Hill, New Jersey

Piezoelectricity and ferromagnetism have been found to occur simultaneously in the compound $Ga_{(2-x)}Fe_xO_3$. Single crystals of approximately equimolar gallium to iron ratio have been grown from a flux consisting of Bi_2O_3 and B_2O_3. X-ray diffraction data on ceramic compositions have shown that the gallium to iron ratio can be varied between $x=0.7$ to $x=1.4$. Magnetic data showing the shift in magnetic Curie point vs Fe concentration and magnetization vs Fe concentration will be given.

INTRODUCTION

THIS report describes the discovery of a new and unusual crystal which is simultaneously piezoelectric and ferromagnetic. Preparative details and the results of various measurements are given for the system $Ga_{(2-x)}Fe_xO_3$. The ionic radii of Ga^{+3} and Fe^{+3} being very close, melts were made using Ga_2O_3 and Fe_2O_3, with Bi_2O_3 and B_2O_3 as the flux, in an attempt to form a compound which we hoped would have interesting magnetic properties. One of these melts resulted in rectangular prismatic crystals which were transparent in thin sections. Subsequent tests revealed that the crystals are magnetic below about 260°K and piezoelectric at room temperature and to the temperature of liquid nitrogen, the lowest temperature measured. Chemical analysis showed that the crystals were $GaFeO_3$.

PREPARATION AND PROPERTIES OF SINGLE CRYSTALS

Optimum conditions for the growth of single crystals were found to be the following:

By using a 100-cc platinum crucible as a container, the four oxides were weighted into it in the following proportions. The amounts given are in grams.

Ga_2O_3	6.50
Fe_2O_3	6.50
B_2O_3	4.00
Bi_2O_3	35.0.

The crucible was covered and placed in a glo-bar furnace at 1125°C and held 5 hrs. Cooling was carried out at a controlled rate of 4.0 to 7.0°C per hr to about 500°C, where the power was turned off. The resulting crystals were extracted from the solidified mass by immersing the entire crucible in a hot dilute solution of HNO_3 and H_2O. The ratio of Ga^{+3} to Fe^{+3} can be varied considerably in this compound, strongly affecting the properties. The above conditions produced crystals with magnetic Curie points between the temperature of liquid nitrogen and room temperature. The composition limits for piezoelectricity have not been so well established since all the crystals from this melt were piezoelectric

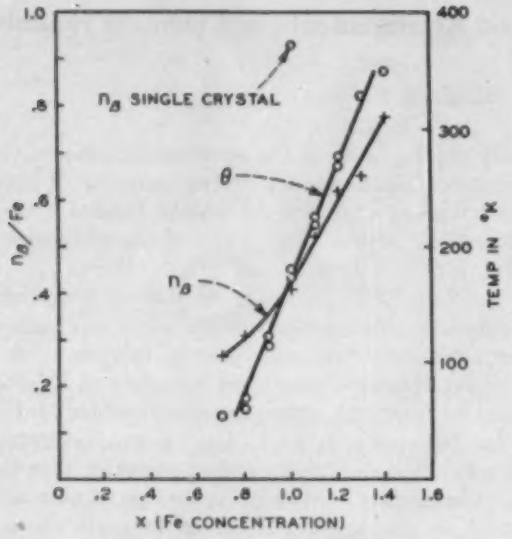

FIG. 1. Magnetization (at 4.2°K) n_B and Curie point θ in $Ga_{(2-x)}Fe_xO_3$.

from room temperature to liquid nitrogen. Chemical analysis of a group of crystals grown from a similar melt showed that under certain conditions (varying the ratio of Ga_2O_3 to Fe_2O_3 in the melt) crystals of very nearly equimolar proportions can be obtained with a magnetic Curie point at 260°K. By varying the ratio, it is equally possible to produce crystals which are magnetic and piezoelectric at and above room temperature.

E. A. Wood[1] has undertaken the structure determination. Preliminary work shows that the symmetry is orthorhombic. Lattice constants for a crystal grown under the following conditions are given below,

Ga_2O_3	12.50 g
Fe_2O_3	10.64 g
B_2O_3	14.00 g
Bi_2O_3	60.0 g.

This melt was held at 1100°C for 2 hrs; then cooled at 7.0°C per hr to 600°C, where the crucible was air quenched. The lattice constants are $a=8.77$ A, $b=9.44$ A, $c=5.08$ A.

Some piezoelectric constants have been measured on single crystals by D. L. White.[2] He finds the d_{31} constant to be 14.5×10^{-8} esu. A value of 6.8×10^{-8} esu is found for d_{11} in quartz.

The relative dielectric constant for a single crystal was about 5.0. No appreciable change in slope with temperature was seen. Tests for ferroelectricity in this compound have so far proved negative. Attempts to observe a ferroelectric hysteresis loop above room temperature were complicated by a rapid rise of conductivity. No ferroelectric loops were observed above the temperature of liquid nitrogen, the lowest temperature investigated.

PROPERTIES OF CERAMIC COMPOSITIONS

Twelve ceramic compositions were prepared at 0.1 mole increments from $Ga_{1.5}Fe_{0.5}O_3$ to $Ga_{0.4}Fe_{1.6}O_3$. The ceramics were prepared by the usual techniques.

X-ray powder diffraction photographs taken by V. B. Compton showed that a single phase of the orthorhombic symmetry persists between $Ga_{1.3}Fe_{0.7}O_3$ and $Ga_{0.6}Fe_{1.4}O_3$, with a regular change in lattice constant. Beyond these limits, free Fe_2O_3 is found in the iron rich specimens and free Ga_2O_3 in the gallium rich end. Attempts were made to produce isomorphous compounds, replacing Ga^{+3} with Al^{+3} and In^{+3}, Fe^{+3} with Cr^{+3} and Co^{+3}. In no case was an isomorphous structure found.

Figure 1 shows the change of magnetic Curie point vs composition and the magnetization in Bohr magnetons per iron atom vs composition for ceramic specimens of $Ga_{(2-x)}Fe_xO_3$. These measurements were made by R. M. Bozorth and D. Davis. A measurement on a single crystal shows a value twice that of a ceramic of the same composition. This may be qualitatively explained by the fact that the easy direction of magnetization is randomly distributed in the ceramic.

CONCLUSION

It is believed that the compound $Ga_{(2-x)}Fe_xO_3$ is the first single phase known to exhibit piezoelectricity and ferromagnetism simultaneously.[3] The compound can be prepared either as a single crystal or a ceramic body. Single crystals of a given composition may be grown by using constant temperature techniques.

[1] E. A. Wood, Acta Cryst. (to be published).
[2] D. L. White (to be published).
[3] A post-dated paper given at this conference by P. H. Fang and R. S. Roth on "Ferroelectric and ferrimagnetic properties of $(Ba_{6-2x}R_{2x})$ $(Nb_{9-x}Fe_{1+x})$ O_{30}" indicates that their compound is ferroelectric (thus also piezoelectric) and ferrimagnetic at the same time.

JOURNAL OF APPLIED PHYSICS SUPPLEMENT TO VOL. 31, NO. 5 MAY, 1960

High-Temperature Susceptibility of Ferrimagnetic Spinels

PETER J. WOJTOWICZ
RCA Laboratories, Radio Corporation of America, Princeton, New Jersey

Power series expansions of the susceptibility and its inverse in ascending powers of the exchange divided by the temperature have been obtained for ferrimagnetic spinels by using the methods of Rushbrooke and Wood. The Heisenberg form of exchange is assumed, and in this paper, interactions between neighboring spins from different sublattices ($A-B$ exchange) only are considered. The coefficients in the series are derived for arbitrary values of the spins on the two sublattices. The calculations have been carried out to terms including the fifth power of the exchange divided by the temperature; the molecular field theory by contrast is rigorously valid only to the first power term of its expansion. The explicit dependence of the Néel temperature on the spin values has also been deduced. The derived susceptibilities and Néel temperatures are compared to the results of earlier models. It is anticipated that these expansions will prove useful in the interpretation of accurate susceptibility data for the purpose of deriving meaningful values for the exchange interactions in the spinels.

THE theory of the high temperature susceptibility and Curie temperatures of the cubic Heisenberg ferromagnets has recently been advanced to a high degree of approximation through the introduction of exact series expansion methods by Brown and Luttinger[1] and by Rushbrooke and Wood.[2] The corresponding theory for the ferrimagnets has not yet reached this stage of development. The only attempt at a higher approximation than the molecular field theory is Smart's[3] extention of the Bethe-Weiss method to certain simple cases of ferrimagnetism with spins of $\frac{1}{2}$. The present communication describes progress in the derivation of a theory for the susceptibility of ferrimagnets which parallels the high degree of approximation already achieved for the simpler ferromagnets.

Power series expansions of the susceptibility and its inverse in ascending powers of the reciprocal temperature have been obtained for ferrimagnetic spinels by using the methods of Rushbrooke and Wood.[2] The Heisenberg form of exchange is assumed, and in this article, interactions between nearest neighboring spins from different sublattices ($A-B$ exchange) only are considered. The coefficients in the series are derived for general values of the spins on the two sublattices, but the g factors, though arbitrary, are assumed equal. The explicit dependence of the Néel temperature on the spin values has also been deduced. Unfortunately, space limitations permit the presentation of the results only; the detailed mathematical treatment of this and other more general cases of ferrimagnetism will be published elsewhere.

The system of interest is one formula weight of spinel, AB_2O_4 containing $3N$ transition metal cations distributed among two nonequivalent sublattices. The A sublattice has N tetrahedrally coordinated sites occupied by cations with spin S_A, while the B sublattice has $2N$ octahedrally coordinated sites occupied by cations with spin S_B. Each A site cation has twelve nearest neighbor B site cations with which strong indirect exchange interaction occur. Each B site cation has six nearest neighbor A sites with which it interacts. Interactions between neighboring A site cations are usually negligible; interactions between neighboring B site cations are sometimes significant, but will be neglected here. The spin Hamiltonian of this system in the presence of a magnetic field H_z has the form,

$$\mathcal{H}=-2J\mathbf{P}-g\mu H_z\mathbf{Q},$$
$$\mathbf{P}=\sum_{ij}\mathbf{S}_i\cdot\mathbf{S}_j,\quad \mathbf{Q}=\sum_i S_i^z+\sum_j S_j^z, \tag{1}$$

where μ is the Bohr-magneton, and where J is the magnitude of the indirect exchange interaction between neighboring A and B sites ($J<0$ for ferrimagnetism). The operator $\mathbf{P}$ is the sum of Heisenberg exchange operators for all nearest neighbor $A-B$ pairs in the lattice, while $-g\mu H_z\mathbf{Q}$ is the Zeeman energy operator for the entire system (i and j are summed over A and B sublattices, respectively).

The molar zero field susceptibility is expanded in a power series in the variable J/kT,

$$\chi=\frac{C}{T}\{1+\sum_{n=1} a_n(J/kT)^n\}, \tag{2}$$

where k is the Boltzmann constant and C the molar Curie constant. The first term is Curie's law for noninteracting spins, while succeeding terms represent increasing orders of the (statistical mechanical) perturbation of the exchange on the free ion paramagnetism. According to a straightforward statistical mechanical development analogous to that reported in reference 2, the coefficients a_n are given by

$$a_n=\frac{3\cdot 2^n\Gamma_N\langle\mathbf{P}^n\mathbf{Q}^2\rangle}{n!N(2\bar{B}+\bar{A})}, \tag{3}$$

where $\langle\mathbf{X}\rangle$ means $(2S_A+1)^{-N}(2S_B+1)^{-2N}$ times the Trace of the matrix representation of the operator $\mathbf{X}$, and where $\Gamma_N\langle\mathbf{X}\rangle$ means "that part of $\langle\mathbf{X}\rangle$ which is proportional to N". The quantity $\bar{A}$ is $S_A(S_A+1)$ while

[1] H. A. Brown and J. M. Luttinger, Phys. Rev. **100**, 685 (1955) and Phys. Rev. **104**, 624 (1956).
[2] G. S. Rushbrooke and P. J. Wood, Proc. Phys. Soc. (London) **A68**, 1161 (1955) and Molecular Phys. **1**, 257 (1958).
[3] J. S. Smart, Phys. Rev. **101**, 585 (1956).

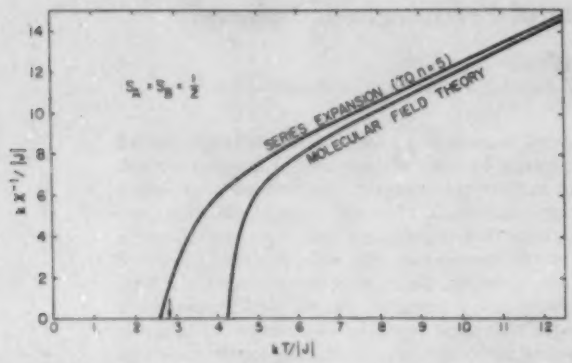

FIG. 1. Reduced inverse susceptibility vs reduced temperature for $S_A=S_B=\frac{1}{2}$ computed from Eq. (5) and from the molecular field theory.

$\bar{B}$ is $S_E(S_B+1)$. The most difficult and tedious part of the calculation is the evaluation of the $\Gamma_N\langle \mathbf{P}^n\mathbf{Q}^2\rangle$. This has been carried out to $n=5$ by using the scheme described in reference 2; the resulting a_n are

$$\begin{aligned}
a_1&=2D, \quad a_2=D(10\bar{A}+22\bar{B}-3)/3,\\
a_3&=2D(1088\bar{A}\bar{B}-81\bar{A}-171\bar{B}+12)/45,\\
a_4&=D(10280\bar{A}^2\bar{B}+23192\bar{A}\bar{B}^2-520\bar{A}^2-2473\bar{B}^2\\
&\qquad -8513\bar{A}\bar{B}+510\bar{A}+1068\bar{B}-45)/135, \quad (4)\\
a_5&=D(434258\bar{A}^2\bar{B}^2-97370\bar{A}^2\bar{B}-127658\bar{A}\bar{B}^2\\
&\qquad +30061\bar{A}\bar{B}+3135\bar{A}^2+14799\bar{B}^2\\
&\qquad -1214\bar{A}-2510\bar{B}+99)/405,
\end{aligned}$$

where $D=8\bar{A}\bar{B}/(2\bar{B}+\bar{A})$. Considerable care was taken to ensure the reliability of these results; at several stages in the computation the results were checked against those of Rushbrooke and Wood by removing the restriction that the spins and the sublattices be non-equivalent. The inverse susceptibility may also be expanded in a power series,

$$\chi^{-1}=\frac{T}{C}\{1+\sum_{n=1} b_n(J/kT)^n\}. \quad (5)$$

The b_n are too complex to reproduce here, but may be computed from the formula,

$$b_n=-\sum_{r=1}^{n} a_r b_{n-r}, \quad b_0=1.$$

The Néel temperature of a ferrimagnet, T_N may be defined as that temperature at which χ becomes infinite. Thus, the radius of convergence, R of the series expansion for χ, Eq. (2), may be used[2] to estimate T_N: $kT_N/|J|=R^{-1}$. The most suitable formula for R was found to be the limit, $n\to\infty$, of $(a_{n-2}/a_n)^{\frac{1}{2}}$. To determine T_N for given values of S_A and S_B, the quantities $(a_n/a_{n-2})^{\frac{1}{2}}$ were computed from Eq. (4) for $n=2, 3, 4, 5$ and plotted against $1/n$. Extrapolation to $1/n=0$ then gave estimates of R^{-1} to within a probable error of 1 to 2 percent. Twenty-five such estimates of R^{-1} were made (S_A and $S_B=\frac{1}{2}$ to $\frac{5}{2}$) in order to deduce the functional dependence of T_N on S_A and S_B. A least squares analysis demonstrates that the following equation summarizes the data with an rms relative deviation of less than 1%,

$$kT_N/|J|=4.55(\bar{A}-0.090)^{\frac{1}{2}}(\bar{B}-0.185)^{\frac{1}{2}}. \quad (6)$$

It is instructive to compare the functional form of Eq. (6) with the Rushbrooke and Wood[2] result for the cubic ferromagnets where T_C is found proportional to $[11S(S+1)-1]$, and with the molecular field formula for the spinel where $kT_N/|J|=4(2\bar{A}\bar{B})^{\frac{1}{2}}$. The similarity of Eq. (6) to these latter forms is quite striking.

A numerical comparison of our results with those obtained from other models can be made for the case, $S_A=S_B=\frac{1}{2}$. The predicted values of $kT_N/|J|$ from this investigation, the Bethe-Weiss model,[3] the Ising-Bethe model,[3] and the molecular field theory are 2.79, 3.36, 3.68, and 4.25, respectively. Numerical values of the inverse susceptibility for $S_A=S_B=\frac{1}{2}$ have also been computed from Eq. (5) and from the molecular field theory. These results are depicted in Fig. 1. The arrow indicates the value of T_N predicted by Eq. (6). The curve (as well as those for other S_A, S_B) should not be considered reliable below this point; higher order b_n begin to contribute significantly. The above comparisons make it quite clear that the use of molecular field expressions in the analysis of experimental data can lead to serious errors in the estimation of both $|J|$ and C.

The assistance of Richard I. Joseph in checking a number of the calculations is gratefully acknowledged.

Time Decrease of Initial Permeability in $Mn_xFe_{3-x}O_{4+y}$

W. A. CRAPO
IBM *Research Laboratory, Poughkeepsie, New York*

The time decrease of initial permeability has been measured for several stoichiometric and nonstoichiometric compositions of $Mn_xFe_{3-x}O_{4+y}$. The samples were in the form of polycrystalline toroids with compositions $x=0.5$, 0.7, 0.85, and 0.9. The stoichiometric compositions, $y=0$, were fired to maintain a metal-oxygen ratio of 3:4, while the nonstoichiometric samples were fired to produce the maximum vacancy concentration. The permeabilities were measured at a peak driving field of 0.002 oe in the temperature range $-15°$ to $+35°$C. The time decrease data was described by three relaxation times. Activation energies calculated on the basis of these relaxation times were within experimental error equal and independent of the Mn/Fe ratio, i.e., $Q=0.46\pm0.06$ ev. The activation energy for the nonstoichiometric samples was equal to that observed for the stoichiometric samples. The magnitude of the effect in the stoichiometric samples was found to decrease approximately linearly with the increasing Mn/Fe ratio.

THE decrease of initial permeability with increasing time following demagnetization has been found to occur in many ferro- and ferrimagnetic materials. This phenomenon is called disaccommodation. The explanation of this effect in alpha iron was given by Snoek[1] and Néel.[2] It was shown that diffusion of interstitial impurities such as carbon in the region of the Block walls creates a localized potential energy minima which restricts their mobility. An analogous explanation has been advanced to account for this effect in ferrites.[3] It is assumed that the time decrease in the initial permeability in these materials is caused by a transition of electrons between different ions.

This paper describes the results of an experimental study of the time decrease effect in some polycrystalline samples of manganese ferrous ferrite characterized by the formula $Mn_xFe_{3-x}O_{4+y}$. The stoichiometric samples ($y=0$) were fired to maintain a metal-oxygen ratio of 3:4 while the nonstoichiometric samples were fired to produce a maximum number of vacancies $y\cong0.025$. The compositions studied can be characterized by $x=0.5$, 0.70, 0.85, and 0.90.

The permeabilities were measured at a frequency of 10 kcps with a peak driving field of 0.002 oe in the temperature range of $-15°$ to $+35°$C. The signal was amplified, rectified and recorded. Demagnetization was accomplished with a 60-cps field, the peak magnitude of which was adjusted to be ten times the coercive force of the material.

The time decrease cannot be described in terms of a single relaxation time. In order to decompose this time decrease into its component relaxation times, we use a method described by Rathenau[4] in which the time dependence of the reluctivity r defined as the reciprocal of the permeability, is assumed to be

$$r=r_0+\sum_i r_i(1-e^{-t}/\tau_i). \qquad (1)$$

Here, τ_i and r_i are the characteristic relaxation time and reluctivity associated with the ith term. r_∞ is the value of the reluctivity measured when the decrease is complete. r_0 is obtained by extrapolating a curve of $\ln(r_\infty-r)$ to time zero.

A graph of the time decrease characteristics of $Mn_{0.5}Fe_{2.5}O_{4+y}$ for $y=0$ and $y\cong0.025$ is shown in Fig. 1 plotted as $\ln(r_\infty-r/r_\infty-r_0)$ *vs* time. The form of the curves presented is characteristic of all the compositions studied. Indicated on the graph is the longest time constant observed, τ_1, and its relative reluctivity $r_1/\sum r_i$. The contribution of the component characterized by τ_1 and $r_1/\sum r_i$ is subtracted from the data and the same procedure is used to calculate (τ_2, $r_2/\sum r_i$) etc. Three

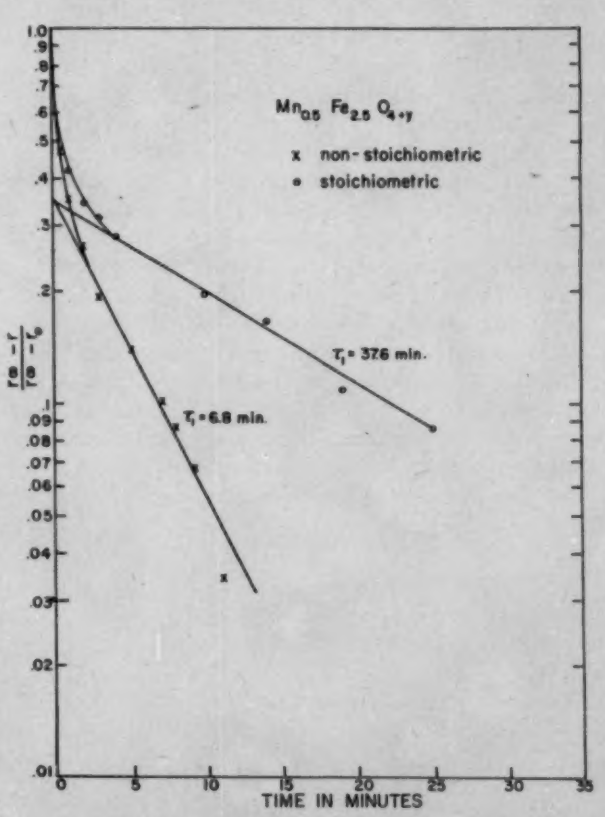

FIG. 1. Time decrease of initial permeability of stoichiometric ($y=0$) and nonstoichiometric ($y\cong0.025$) $Mn_{0.5}Fe_{2.5}O_{4+y}$ at 0°C.

[1] J. L. Snoek, Physica **5**, 663 (1938); **6**, 161 (1939).
[2] L. Néel, J. Phys. Radium **5**, 249 (1952); **11**, 49 (1950).
[3] U. Enz, Physica **24**, 609 (1958).
[4] G. W. Rathenau, J. Appl. Phys. **29**, 239 (1958).

TABLE I. A for various Mn/Fe ratios.

x	Mn/Fe	A at 25°C	A at 0°C
0.9	0.428	0.02	
0.85	0.395	0.06	0.05
0.70	0.304	0.13	0.11
0.50	0.200	0.23	0.25

TABLE II. Relaxation times (in minutes) obtained from the decomposition of the curves in Fig. 1.

	$y=0$			$y\cong 0.025$		
T°C	τ_1	τ_2	τ_3	τ_1	τ_2	τ_3
25	12.5	1.3	0.16	3.6	0.15	~0.03
0	37.6	4.65	0.54	6.8	0.72	0.08

relaxation times were sufficient to fit the data. Within the experimental error, the temperature dependence of these relaxation times could be represented by an equation of the form $\tau_i=\tau_{0i}\exp(Q/kT)$. The longest relaxation times observed, τ_1's, for the stoichiometric samples with $x=0.7$, 0.85, 0.90 showed the least scatter. The temperature dependence of these three compositions can be represented by the equation

$$\tau_1=\tau_{01}\exp(Q/kT);\quad Q=0.46\pm0.06 \text{ ev.}$$

The shorter relaxation times exhibited larger scatter, but within this error the activation energies for all compositions were the same, i.e., $Q=0.4\pm0.1$ ev. The relaxation times for the nonstoichiometric samples were consistently smaller and had a larger scatter than the corresponding relaxation times for the stoichiometric compositions. In order to compare the magnitude of the time decrease in different samples, it is necessary to normalize the results in order to eliminate the effect of differences in the permeabilities of the samples. The ratio $A=(\tau_\infty-\tau_0)/\tau_\infty$ was used for this purpose. The values of A for the stoichiometric samples are given in Table I. It can be seen that A is essentially independent of temperature.

There is a general decrease in A as the manganese iron ratio increases. This decrease is approximately linear for the stoichiometric samples. The value of A for the nonstoichiometric samples is, in general, larger but no linear relation exists.

Table II shows a comparison of the relaxation times for the composition shown in Fig. 1.

The magnitude of the relaxation times strongly suggest that the mechanism responsible for the pinning of the domain walls is the result of an electron diffusion process since the activation energies observed are consistent with an electron migration. Comparison of the stoichiometric and nonstoichiometric samples is somewhat difficult because of the large scatter in the nonstoichiometric results and because of the uncertainty in the number of vacancies present in the samples. Identical activation energies for both sets of samples indicate that the same processes are involved in both cases.

Any model proposed to account for this effect in these materials should explain the following experimental observations:

1. The same processes occur in both stoichiometric and nonstoichiometric compositions.
2. The magnitude of the effect, A, is larger and the relaxation times shorter in the nonstoichiometric compositions than in the stoichiometric compositions (vacancy effect).
3. The magnitude, A, decreases with increasing Mn/Fe ratio in the stoichiometric samples.

Since the magnitude of the effect is observed to decrease with increasing Mn/Fe ratio it is tempting to conclude that an electron exchange involving the Fe^{+2}, Fe^{+3} ions would be the most likely. However, it is known that these ions are basic to the conductivity mechanism in these materials and the activation energy measured is smaller than we observe. Similarly, it is known that in oxidized samples the amount of Fe^{+2} is reduced, which should result in a decrease in magnitude of the effect in nonstoichiometric samples rather than an increase. It cannot be concluded on the basis of these measurements whether the electronic processes responsible for the time decrease effect in these materials occur on any particular site or between sites in the crystal. Other ion combinations are being examined in the light of additonal observation of this type.

ACKNOWLEDGMENTS

The author is indebted to B. A. Calhoun for many helpful discussions and suggestions.

Square Loop Properties of Copper-Manganese Ferrites

R. S. Weisz and D. L. Brown
Telemeter Magnetics, Inc., Los Angeles, California

A survey of magnetic properties for the system $CuFe_2O_4-MnFe_2O_4-Mn_3O_4$ is reported. Saturation flux density, Curie temperature, coercivity, hysteresis loop squareness, and switching constant were determined for 60 compositions. A large compositional area having square loop properties was found. Apparently, both divalent Cu and trivalent mu contribute to squareness. Switching constant was found to decrease markedly with increasing manganese content to a low in the neighborhood of 0.6 oe-μsec.

Coincident-current memory cores made from appropriate Cu-Mn ferrites have properties very similar to conventional Mg-Mn ferrites but at significantly lowered driving currents.

INTRODUCTION

As part of a program aimed at improving ferrites used in high-speed magnetic core memories, an investigation of the copper oxide-manganese oxide-iron oxide system has been made. Square hysteresis loops are well known in ferrites containing (a) divalent Cu[1] or (b) trivalent Mn.[2] One would, therefore, expect that ferrites containing both of these elements together would be of unusual interest. Brief reports on Cu-Mn ferrites have already appeared,[3] but no detailed compositional survey of their magnetic properties seems to have been published. The present paper undertakes to fill this gap.

PREPARATION AND CHEMISTRY

Memory cores, 0.08 in. o.d.×0.05 in. i.d.×0.025 in. ht., were chosen for the measurements to be reported Approximately 60 compositions covering the $MnFe_2O_4-CuFe_2O_4-Mn_3O_4$ portion of the manganese oxide-copper oxide-iron oxide system were prepared from high purity raw materials using standard sintering techniques. Each composition was optimized for its square loop properties by varying firing temperature and oxygen pressure during sintering. The required oxygen pressure was directly proportional to the copper content. Typical oxygen pressures ranged from 10^{-3} to 1 atmos; typical firing temperatures were from 1000° to 1300°C.

All samples were cooled rapidly through the region 900° to 500°C to prevent transformation to a tetragonal phase. It is believed that samples so treated were in fact single phase spinels.

The exact oxygen content of manganese-iron spinels is known to vary with the temperature and oxygen pressure used during firing.[4] Instead of the conventional formula, $MnFe_2O_4$, one should, thus, write $Mn^{2+}_{0.914}Mn^{3+}_{0.086}Fe_2O_{4.043}$ for Mn ferrite in equilibrium with air at 1100°C. Similarly, in the present investigation it was found by chemical analysis that Cu-Mn-ferrites prepared in air had somewhat greater oxygen contents than correspond to the conventional formula, $xMnFe_2O_4 \cdot yCuFe_2O_4 \cdot zMn_3O_4$, which we use for convenience.

SUMMARY OF MAGNETIC PROPERTIES

The optimized sample of each composition was measured at 25°C for (1) technical saturation flux density, B_m; (2) coercivity, H_c; (3) Curie temperature, T_c; (4) hysteresis loop squareness; and (5) switching constant, S_w. Figure 1 is a plot of loop squareness and S_w as a function of mol % $MnFe_2O_4$, $CuFe_2O_4$, and Mn_3O_4.

Hysteresis loop squareness was determined both by pulse and dc hysteresis loop methods. The criterion adopted was that of the ratio, R_t, of the threshold or "knee" to the coercive force of the major hysteresis loop. To avoid ambiguity with materials having a rounded knee, the threshold was arbitrarily taken as that field which switched 10% of the total flux. Pulse and dc methods gave results in close agreement. Threshold ratios greater than 0.75 are found in a large area of the system adjacent to $MnFe_2O_4$. Apparently, divalent Cu and trivalent Mn can contribute to squareness either singly or together. Further contours of squareness are not shown, because of uncertainty as to whether every composition has been fully optimized.

Switching constant, S_w, was determined from the field dependence of the interval between 10 and 90% output voltage points. A large decrease in S_w with increasing content of $MnFe_2O_4$ is the most pertinent feature of this

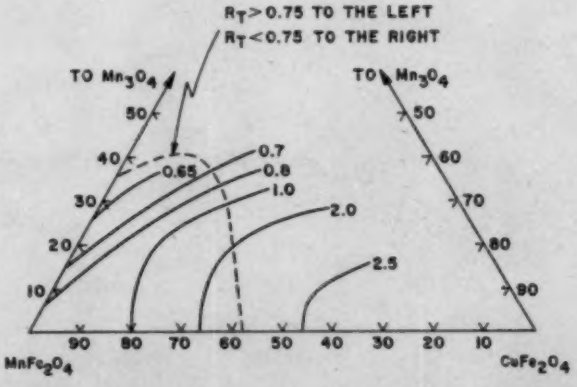

FIG. 1. Contours of S_w (full lines) and contour of $R_T=0.75$ (dashed line) for the system $CuFe_2O_4-MnFe_2O_4-Mn_3O_4$.

[1] A. P. Greifer and W. J. Croft, J. Appl. Phys. **30**, 34S (1959).
[2] P. K. Baltzer, Am. Inst. Elec. Engrs, **T-78** 247 (1955).
[3] H. P. J. Wijn, E. W. Gorter, C. J. Esveldt, and P. Geldermans, Philips Tech. Rev. **16**, 49 (1954); P. W. Beck and K. E. Matteson, U. S. Patent **2**, 818, 387 (1957).
[4] R. S. Weisz, J. Am. Ceram. Soc. **40**, 139 (1957).

plot. It is noteworthy that $S_w \leqslant 0.6$ oe-μsec was found in a region where the squareness is quite high. Conventional Mg-Mn ferrites have S_w of 0.8 to 1.0 oe-μsec. The decrease in S_w with increasing Mn content is apparently caused by the accompanying increase in saturation flux density.[5]

Technical saturation, which is usually at least 20% below true saturation,[6] was measured both on a dc loop tracer and by a pulse method at driving fields of 5 to 10 oe. The two methods were in close agreement. Technical saturation was a maximum at the composition $MnFe_2O_4$, for which $B_m = 3400$ gauss, and decreased both with increasing $CuFe_2O_4$ content and with increasing Mn_3O_4 content. Curie temperature varied from 305° for $MnFe_2O_4$ to 450°C for $CuFe_2O_4$, and decreased with increasing Mn_3O_4 content. Coercivity varied from 1.9 oe for $MnFe_2O_4$ to 5.6 for $CuFe_2O_4$, and again decreased with increasing Mn_3O_4 content to a minimum of about 1.0 oe. It was noted, incidentally, that pulse coercivity was always higher than dc by an amount which varied inversely with the magnitude of the coercivity. The difference is only appreciable at values considerably below 1 oe.

MEMORY CORE CHARACTERISTICS

The primary aim of this investigation having been a pragmatic one, to develop improved memory cores, we now give a single example of how the data of Fig. 1 can be combined to locate compositions favorable for making useful square-loop ferrites. A high threshold ratio and a low switching constant are necessary; low coercive force and high Curie temperature are also desirable. The latter two, however, are generally incompatible and a compromise must be made. A probable region is in the neighborhood of $0.8MnFe_2O_4 \cdot 0.1CuFe_2O_4 \cdot 0.1Mn_3O_4$.

TABLE I. Comparison of pulse response[a] of 80 mil o.d. memory cores of CuMn ferrite and MgMn ferrite.

Type	I_f/I_d (ma)	uV_1 (mv)	dV_s (mv)	T_p (μsec)	T_s (μsec)	I_t (ma)	I_t/I_f
CuMn ferrite	650/325	80	20	0.75	1.42	420	0.65
MgMn ferrite	800/400	100	18	0.70	1.40	480	0.60

[a] Pulses were 10 μsec wide with $t_r = 0.2$ μsec. Twenty disturb pulses, I_d, were used to test for noise, dV_s. The threshold current, I_t, was also determined with 20 repeats.

A promising composition having been chosen it can be further improved for coincident-current memory core operation. This is accomplished by studying minor loop pulse characteristics. By depending on engineering considerations, one or more parameters may be optimized. For example, it was found that Cu-Mn ferrites driven at lower current, I_f, give switching times as short as those of similar Mg-Mn ferrites. Table I shows this comparison. Aside from the approximately 20% lower driving field, other characteristics of the two cores such as output voltage, uV_1, noise, dV_s, and the temperature dependence of these parameters are quite similar.

To obtain the maximum advantage of the low switching constant characteristics of Cu-Mn ferrites one should operate them not by a coincident-current system but by a word-select system.[7] With the latter method of operation, memory cores can be interrogated by an arbitrarily large current pulse and therefore can switch proportionately fast. At the present time, we are investigating Cu-Mn ferrites for such memories.

[5] N. Menyuk and J. B. Goodenough, J. Appl. Phys. **26**, 8 (1955).
[6] T. J. Matcovich and C. J. Kriessman, J. Appl. Phys. **30**, 26S (1959).
[7] K. H. Olsen, Thesis, Massachusetts Institute of Technology (1953).

Temperature Dependence of the Saturation Magnetization of Ferrites with Magnetoplumbite Structure

G. HEIMKE
Physikalisches Institut, Hochschule für Verkehrswesen, Dresden, Germany

The anomaly in the saturation magnetization vs temperature dependence of ferrites with magnetoplumbite structure is supposed to be caused by the fact that the superexchange interactions of the five crystallographically distinguished sublattices may be of several kinds in a part of the unit cell. It is shown that the interaction chain can be made to be of one kind only by replacement of the iron ions of one sublattice by nonmagnetic ions, and the conditions under which this replacement can be effected are pointed out. Experimental evidence demonstrates that this can partly be achieved by using $BaTiO_3$ instead of $BaCO_3$ in the starting mixture, if special precautions as to the sintering conditions are taken.

INTRODUCTION

THE saturation magnetization of ferrites with magnetoplumbite structure decreases nearly linearly with increasing temperature.[1] As the remanence B_r is half of the saturation magnetization $4\pi J_s$, presuming the crystals are small enough and their directions of easy magnetization are distributed isotropically, this is the reason for the high temperature dependence of the remanence.

In this work, some possibilities for the alteration of the $4\pi J_s(T)$ dependence will be derived from a consideration of the interaction scheme of the five crystallographically distinguished sublattices. Experimental evidence will demonstrate that such an alteration can be realized.

LATTICE

The lattice of $BaO \cdot 6Fe_2O_3$ consists of layers of cubic and hexagonal close packed oxygen ions; in every fifth plane, one oxygen ion is replaced by a barium ion. The ferric ions are situated in the interstices between the oxygen ions. There are five kinds of interstices in this lattice distinguished by the arrangement of the surrounding oxygen ions.

The 24 Fe^{3+} ions per unit cell are the carriers of the magnetic moment. In Reference 1, the authors indicated an interaction scheme between different sublattices with which the experimental values for $T \to 0$ (and $H \to \infty$) can be explained [Fig. 1(a)].

$4\pi J_s(T)$ DEPENDENCE

A discussion of the possible superexchange interactions between the five sublattices on the basis of Anderson's theory shows that there are two more interaction schemes to be considered [Figs. 1(b) and 1(c)]. They differ in the interaction sequence of the $=12k=4f_2=2b=4f_2=12k=$ sublattices (notation according to footnote 2) as the $12k$ and $2b$ sublattices have interaction distances and angles which seem still favorable for superexchange interaction.[3] This sequence brings about the coupling through the layers containing barium.

For the understanding of the experimental $4\pi J_s(T)$ curve [Fig. 2(a)], one could suppose that there is a transition from a state according to Fig. 1(a) to one of the two others with rising temperature. In this case, it should be possible to alter the $4\pi J_s(T)$ dependence principally by suppressing two of the three rivalling interactions. Then, the interaction scheme will be completely unique and the $4\pi J_s(T)$ curve should be similar to a Langevin or one of the Néel curves.

This suppression can indeed be attained by getting non-magnetic ions on the sites of the $4f_2$ sublattice. The resulting magnetic moment per unit cell would then be $14 \uparrow +6 \downarrow = 8 \uparrow$. But as the remaining $12k=2b$ interaction, which then controls the coupling via the layers containing barium, has a much more unfavorable interaction distance and angle, the coupling across those layers can be disturbed more easily by thermal motion so that a material of this kind should have a lower Curie temperature.

If one can effect the replacement of only one of the two ions of sublattice $4f_2$ per barium layer, then there would be a resulting magnetic moment per unit cell of 6 ionic moments for the configuration of Fig. 1(b) and 10 for that of Fig. 1(c).

A replacement of the ions of sublattice $2b$ by nonmagnetic ions cannot have any success, as an interaction

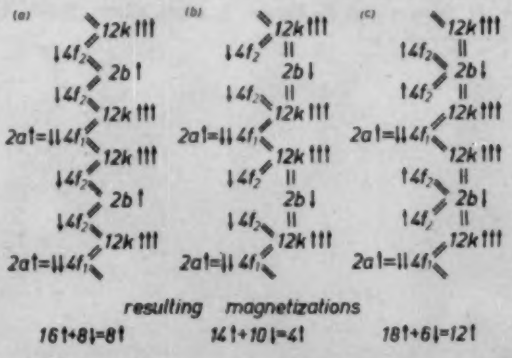

FIG. 1. The possible interaction schemes in the unit cell of the magnetoplumbite structure. Each arrow represents one ionic moment of $Fe^{3+}=5$ Bohr magnetons.

[1] J. J. Went, G. W. Rathenau, E. W. Gorter, and G. W. van Oosterhout, Philips' tech. Rundschau **13**, 361 (1952).
[2] V. Adelsköld, Arkiv Kemi, Mineralogi och Geologi **12A**, (1938).
[3] E. W. Gorter, Philips Research Repts. **9**, 295, 321, 403 (1954).

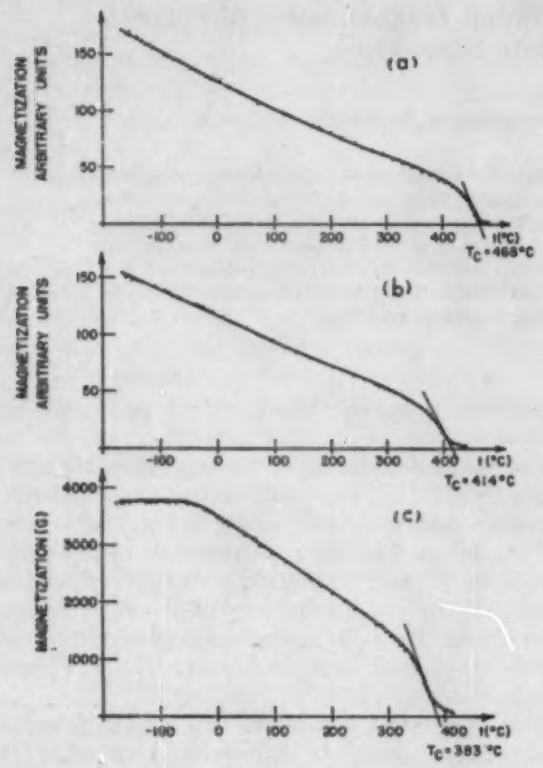

FIG. 2. $4\pi J_s(T)$ curves of (a) $BaO \cdot 6Fe_2O_3$, (b) $BaTiO_3 \cdot 6Fe_2O_3$, (c) $BaTiO_3 \cdot 6Fe_2O_3 + 1.5\%$ $CaSiO_3$.

$4f_2 = 4f_2$ is not possible and, therefore, the coupling across the layer containing barium would cease completely. This shows that the continuous and nearly linear decrease of the Curie temperature with increasing content of nonmagnetic ions until $x = 4[\text{in } (6-x)\ Fe_2O_3 \cdot x(M_2O_3) \cdot BaO)]$[4,5] can happen only if these ions are distributed statistically upon one or more sublattices. By replacing the magnetic ions of sublattice $2b$, the coupling through the barium layer would already be cut off completely for $x = 1$.

Sublattice $4f_2$ consists of octahedral sites. But there are 14 more octahedral sites per unit cell available (sublattices $12k$ and $2a$) and those of sublattice $4f_2$ are the most unfavorable energetically for two of the surrounding octahedra have one plane in common.[4]

The only way to get suitable nonmagnetic ions on the $4f_2$ sites seems to be to use the close neighborhood of the barium ion. The best results would be expected with a compound XM_2O_3 (X = Ba, Sr, or Pb and M a suitable ion), which does not dissociate at a temperature much below that at which the magnetoplumbite lattice begins to form.

Such a compound has not yet been found. But $BaTiO_3$ seems partly to fit into our conditions: The Ti can change from the four- to the trivalent state in which it carries one Bohr magneton only, it strongly prefers octahedral coordination and the compound itself is produced at temperatures in the neighborhood of that at which barium ferrite is formed.

EXPERIMENTAL RESULTS

Barium titanate and iron(III)oxide were mixed according to the formula $BaTiO_3 \cdot 5Fe_2O_3$ and worked into oxide magnets in the usual way. X-ray analysis showed that the samples had the magnetoplumbite structure. The $4\pi J_s(T)$ curve is reproduced in Fig. 2(b). The nature of the curve is not altered from that of the Ti free material, but the Curie temperature is lowered by about 50°C. This corresponds precisely to a statistical distribution in References 4 and 5 for $x = 0.5$.

By using former experiences on the enhancement of the reactivity during the formation of barium ferrite,[6] the experiment was repeated with the addition of 1.5% calcium silicate. Here, too, X-ray analysis showed the presence of the magnetoplumbite structure. The $4\pi J_s(T)$ curve [Fig. 2(c)] shows that the Curie temperature is lowered by another 30°C and its form below 0°C is altered completely.

The still remaining linear slope between 0°C and the Curie point is attributed to the fact that only one of the two ions of sublattice $4f_2$ per Ba-ion is replaced by Ti-ions so that the interaction chain is not yet quite unique.

[4] E. F. Bertaut, A. Deschamps, R. Pauthenet, and S. Pickart Colloque international de magnetisme, Grenoble, (1958), p. 340.
[5] A. H. Mones and E. Banks, J. Phys. Chem. Solids 4, 217 (1958).
[6] H. G. Müller and G. Heimke, *Berichte der Arbeitsgemeinschaft Ferromagnetismus* (Riederer-Verlag, Stuttgart, 1958), p. 101.

Magnetic Behavior in the Transition Region of a Hematite Single Crystal*

S. T. LIN
Massachusetts Institute of Technology, Cambridge, Massachusetts

The magnetic behavior in the transition region of a hematite single crystal from Elba has been investigated carefully. The remanence-temperature relationship and the thermal hysteresis effect (i.e., the remanence is a double-valued function of temperature) have been obtained for each of three mutually perpendicular directions of the crystal in the temperature range between 488° and 77°K. A graphical representation of the ferromagnetic state has been constructed to show the direction, the magnitude, and the turning of the remanent magnetization vector with the temperature in the transition region. Another experiment, which consists of measuring the remanence along different directions in the plane containing the [111] direction, and the projection of the remanent magnetization vector in the (111) plane for three different temperatures, also has been carried out. These experimental data show that the direction and the magnitude of the remanent magnetization vector changes continuously between the [111] direction and the (111) plane when the temperature changes through the transition region.

INTRODUCTION

BEFORE the appearance of the previous article,[1] it generally had been believed that the weak anisotropic ferromagnetism of hematite could not be observed along the rhombohedral axis,[2,3] and that if some ferromagnetism were to be observed along this axis, it could belong to the isotropic ferromagnetism.[2] But the magnetic behavior of the Elba single crystal[1] seems to be contradictory to this belief. The present investigation has been devoted to the study of the magnetic behavior in the transition region, and the data strongly supports the previous work.

EXPERIMENTAL RESULTS

A sphere about $\frac{3}{16}$ in. diam cut, from a single crystal of hematite from Elba, has been used for measuring the remanent magnetization of a virgin sample which had never been exposed to a magnetic field except the small earth field. The remanent magnetization was measured by measuring the vertical component of force in a vertical field gradient which was several oersteds per centimeter. The sphere was hung along the field gradient which was parallel to the basal plane perpendicular to the rhombohedral axis. The temperature was varied for several complete cycles between 488° and 77°K without applying any field, and the remanence was measured for a complete cycle of temperature between 488° and 77°K. The remanence-temperature $\sigma_R - T$ curve shown in curve 1, Fig. 1, formed a close loop in the transition region. This loop was reproducible if the temperature of the sample was varied for several cycles before measurement. The suspension was changed by 90° in the basal plane. The same procedure was carried out and another $\sigma_R - T$ loop obtained (curve 2, Fig. 1). The sphere then was suspended along the [111] direction. After making several cyclic changes of temperature and following the same procedure, a third loop was obtained and is shown in curve 3, Fig. 1. This loop is complementary to the other two.

These three loops together give the representation of the weak ferromagnetic state in the ascending and descending temperature between 488° and 77°K. Eventually a three-dimensional graphical representation in spherical coordination could be constructed to show the direction, the magnitude, and the turning of the remanent magnetization vector with the temperature in the whole temperature range. For clarity, a two-dimensional graphical representation of the ferromagnetic state has been made. This was done as follows: The resultant curve for the basal plane was obtained by combining the corresponding branch of curves 1 and 2. From this resultant curve, and curve 3, the direction and magnitude of the remanent magnetization vector at each temperature was calculated and the results were plotted in Fig. 2. This curve shows that at each temperature in the transition region, the remanent magnetization vector has a more or less definite orientation and magnitude, depending upon the ascending or descending temperature.

Another experiment has been carried out as follows: The spherical sample was rotated in the field gradient, and the remanent magnetization was measured along

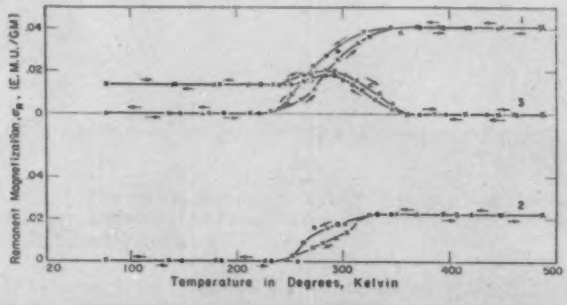

FIG. 1. Variation of remanent magnetization, with temperature and thermal hysteresis effect, of natural hematite single crystal: (1) along a direction x in the (111) plane, (2) along a direction y in the (111) plane and perpendicular to x, (3) along [111] direction.

* This work was carried out under contract with the U. S. Atomic Energy Commission.

[1] S. T. Lin, J. Appl. Phys. **30**, 306S (1959).
[2] L. Néel, Rev. Modern Phys. **25**, 58 (1953).
[3] I. E. Dzyaloshinsky, J. Phys. Chem. Solids **4**, 241 (1958); S. V. Vonsovsky and B. A. Turov, J. Appl. Phys. **30**, 9S (1959).

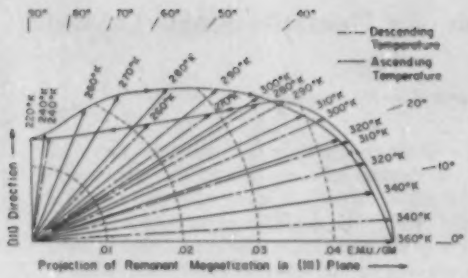

FIG. 2. Polar plot of the magnitude and direction with respect to the crystallographic axis of remanent magnetization vector as a function of temperature in the transition region of natural hematite single crystal.

different directions in the plane containing the [111] direction and the direction of the remanent magnetization in the (111) plane. The polar plot of the measured magnetization *vs* angle of observation gave a circle passing through the origin. The direction of the center point of this circle was the direction of magnetization, and the diameter of the circle was the magnitude of magnetization. The three magnetization vectors, at three different temperatures determined this way, fitted in Fig. 2 very well. For the sake of neatness, the three vectors are not shown in Fig. 2.

DISCUSSION

First of all, we would like to emphasize the following point. The sample used in the present case is a virgin material and the strength of the field gradient is only several oersteds per centimeter. Since the sample has never been disturbed by any magnetic field greater than several oersteds, the $\sigma_R - T$ curves (Fig. 1) obtained in this way should represent the true remanence-temperature relationship for each of the three mutually perpendicular directions of the sample. These curves are very similar to the spontaneous magnetization-temperature $\sigma_0 - T$ curves[1] except that the magnitude is much smaller. This similarity indicates that the method for obtaining the curves of footnote 1 is a proper procedure, and hence the conclusions drawn from them are correct.

The magnetization of a crystalline material is a three-dimensional problem. Without the determination of all its components, it would be difficult to understand its nature. Since in the present case, the three components have been obtained from a single spherical sample, there should be no uncertainty in the determination of the total vector. The most interesting effect is indicated in Fig. 2, which shows that when the temperature decreases through the transition region the remanent magnetization vector turns from the basal plane toward the [111] direction, and, at the same time, its magnitude shrinks. While the temperature increases through the transition region the vector would turn back from the [111] direction toward the basal plane, and, at the same time, its magnitude increases. This turning seems to be continuous through a temperature range of about 140°K.

What we have observed is the remanence of the weak ferromagnetism. If the weak ferromagnetism is interpreted as the result of the canted antiferromagnetism, as described in footnote 1, the mean direction of the antiferromagnetic spin of each sublattice would turn continuously between the [111] direction and the basal plane when the temperature changes through the transition region.

Another interesting phenomenon is seen in the thermal hysteresis loops shown in Fig. 1. In the case of the two loops for the basal plane, the magnitude of the remanence in the transition region is greater along the descending temperature segment, while, for the case of [111] direction loop, the magnitude of remanence is greater along the ascending temperature segment. The explanation for this hysteresis behavior of the $\sigma_R - T$ curves is not apparent.

ACKNOWLEDGMENTS

The author wishes to thank A. Pinella and C. J. Herman for their assistance in the experimental work.

Metamagnetic Behavior of Manganese Arsenide

D. S. RODBELL AND P. E. LAWRENCE
General Electric Research Laboratory, Schenectady, New York

Between 35° and 125°C there exists a threshold magnetic field strength at which the compound MnAs exhibits a large and steep increase of its net magnetization. At 35°C the threshold field is 40 koe. There is a large hysteresis associated with the magnetization change. This behavior resembles that exhibited by a material that is metamagnetic in the sense of Néel's description. We believe, however, that in this material the existence of a first-order phase transformation is sufficient to account for the magnetic behavior.

INTRODUCTION

THE compound MnAs exhibits certain interesting and unusual physical properties. At a temperature near 35°C it undergoes a first-order transformation that has associated with it a thermal hysteresis, a latent heat, a discontinuous change in the electrical resistivity and a discontinuous change in density. The magnetic state also changes in an interesting way as indicated by Bates[1] and Guillaud[2]; the interesting temperatures are 35° and 125°C. The ferromagnetism that exists at lower temperatures vanishes abruptly at 35°C. Above 125°C MnAs is paramagnetic. Since the early experiments on MnAs, this compound has been recognized as possessing unusual properties. The magnetic studies by Bates[1] and Guillaud[2] have established that interesting transitions occur near 35° and 125°C. The lower transition temperature (35°C) is sensitive to composition as Guillaud has shown, and this may account for discrepancies between quoted values in the literature. We have examined polycrystalline samples of MnAs obtained from two different sources.[3] Their behavior is qualitatively the same. The differences observed in critical temperature and net moment are in directions consistent with composition differences determined by chemical analysis. We report in the following the data corresponding to sample *a*, which we find to be Mn rich by a few percent. We limit the data presented here in lieu of a more extensive treatment in preparation.

EXPERIMENTAL

The magnetization curve (M vs H) taken at temperatures in the ferromagnetic range exhibits no[4] coercive force, but large fields are required to achieve saturation magnetization. In the interesting temperature range of 35° to 125°C a sufficiently large magnetic field can achieve large magnetizations compared to the magnetization observed at low fields. The data are shown in Fig. 1 and correspond to essentially adiabatic observations. Previous observations under isothermal con-

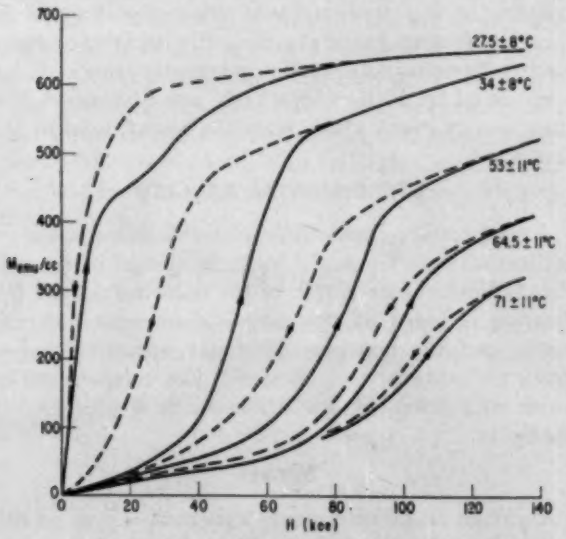

FIG. 1. The magnetization curves of a polycrystalline compact of MnAs (sample *a*) demonstrating the influence of high magnetic fields in accomplishing magnetization and also showing the large hysteresis associated with the magnetization cycle.

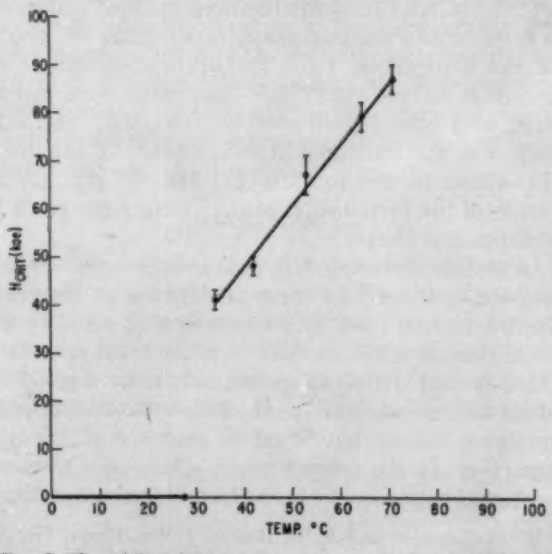

FIG. 2. The critical field as a function of temperature. The value of H_{crit} is arbitrarily taken as the break in M *vs* H curves of Fig. 1 on the increasing H portion.

[1] L. F. Bates, Phil. Mag. 8, 714 (1929).
[2] C. Guillaud, thesis, Strasbourg (1943).
[3] Samples kindly supplied by G. E. Bacon (British Atomic Energy Establishment, Harwell, England, sample *a*), and G. Fischer (National Research Council, Ottawa Canada, sample *b*).
[4] Less than 50 oersteds.

ditions were reported by Meyer and Taglang[5] using steady fields up to 30 koe.

We have arbitrarily picked the break in the magnetization *vs* field curve (increasing H) as a parameter called H_{crit}, and this is plotted *versus* the temperature in Fig. 2.

By application of hydrostatic pressure to the specimen in its magnetic state, we have accomplished the change in state with its associated loss of net magnetization. The value of the critical pressure required to accomplish the state change is consistent with the value of the critical field at the appropriate temperature.

[5] A. J. P. Meyer and P. Taglang, J. phys. radium **14**, 82 (1953).

CONCLUSIONS

Néel's "metamagnetic" material[6] has many interesting magnetic characteristics. Although MnAs resembles such a material in its magnetic behavior, this fact may be merely coincidental to the first order phase transformation exhibited by MnAs.[5,7]

[6] L. Néel, Bull. acad. sci. U.R.S.S. Sér. phys. **21**, 889 (1957).
[7] A. J. P. Meyer and P. Taglang, Compt. rend. **246**, 1820 (1958).

JOURNAL OF APPLIED PHYSICS SUPPLEMENT TO VOL. 31, NO. 5 MAY, 1960

Magnetic Properties of the $Li_xMn_{1-x}Se$ System

THOMAS R. MCGUIRE, *U. S. Naval Ordnance Laboratory, White Oak, Silver Spring, Maryland*

AND

ROBERT R. HEIKES, *Westinghouse Research Laboratories, Pittsburgh 35, Pennsylvania*

The details of the magnetic behavior of the $Li_xMn_{1-x}Se$ system are attributed to the double exchange interaction. At low temperatures, the hole, which is introduced by the Li^+, is bound to the Li^+ itself. Double exchange causes local distortions of the spin system. As the concentration is increased ($x=0.07$), these local distortions overlap sufficiently so that a magnetic field will induce a suitable moment. Finally at $x=0.10$ one finds that spontaneous magnetization develops below 110°K. As the temperature is lowered through 70°K, the spontaneous moment disappears and an antiferromagnetic state is found. This phase change is attributed to the binding of the holes to the Li^+.

INTRODUCTION

A MAGNETIC study has been made of manganese selenide with small amounts of lithium substituted for the manganese. Each Li substitution causes the formation of one Mn^{+++}ion. Specimens were investigated with composition $x=0.03$, 0.05, 0.07, and 0.10, where x is the fractional atomic amount of lithium as represented in the formula $Li_x^+Mn_x^{+++}Mn_{1-2x}^{++}Se$. Details of the preparation of the samples are given by Johnston and Heikes.[1]

An exchange mechanism, double exchange, has been proposed by Zener[2] for these mixed valency materials. This interaction leads to a ferromagnetic coupling and in addition, to a low metallic-type electrical resistance.

Heikes and Johnston[3–5] had originally looked for double exchange in various transition metal monoxides containing lithium but found no evidence of this type interaction. In the compound $Li_{0.10}Mn_{0.90}Se$, however, they found both metallic behavior and ferromagnetism.[6] As the behavior of the electrical resistivity at low temperatures indicated a "freezing out" of the current carriers and a consequent loss of double exchange coupling, it was predicted that this material would become antiferromagnetic at sufficiently low temperatures. Such a ferromagnetic-antiferromagnetic transition has been found by Pickart, Nathans, and Shirane.[7,8] It is these observations which form the background of this study.

[1] W. D. Johnston and R. R. Heikes, J. Am. Chem. Soc. **80**, 5904 (1958).
[2] C. Zener, Phys. Rev. **82**, 403 (1951).
[3] W. D. Johnston and R. R. Heikes, J. Am. Chem. Soc. **78**, 3255 (1956).
[4] R. R. Heikes and W. D. Johnston, J. Chem. Phys. **26**, 582 (1957).
[5] W. D. Johnston, R. R. Heikes, and D. Sestrich, J. Phys. Chem. Solids **7**, 1 (1958).
[6] R. R. Heikes and W. D. Johnston, Bull. Am. Phys. Soc. Ser. II, **3**, 98 (1958).

EXPERIMENTAL RESULTS

A temperature-composition phase diagram of the experimental data for the $Li_xMn_{1-x}Se$ system is shown in Fig. 1. With the exception of the point for MnSe, this diagram is based on our magnetic moment measurements and the neutron diffraction measurements of Pickart, Nathans, and Shirane.[9] The temperature at which each magnetic transition occurs is identified in the figure.

MnSe

Although no measurements were made by us on this material, its characteristics are important as the starting point of the system. MnSe is known to be antiferro-

[7] S. J. Pickart, R. Nathans, and G. Shirane, Bull. Am. Phys. Soc. Ser. II, **4**, 52 (1959).
[8] R. R. Heikes, T. R. McGuire, and R. J. Happel, Jr., Bull. Am. Phys. Soc. Ser. II, **4**, 52 (1959).
[9] S. J. Pickart, R. Nathans, and G. Shirane (to be published).

magnetic. The Néel point or temperature at which antiferromagnetic ordering sets in is about 110°K. Neutron diffraction studies by Shull, Strauser, and Wollen[10] show MnSe has a spin ordering of the second kind similar to MnO.

$Li_{0.03}Mn_{0.97}Se$

As lithium is added the Néel temperature drops slightly. For $x=0.03$ the $1/\chi$ vs T curve has the form of a hyperbola, but flattens out below 80°K. It is this break in the curve that is chosen as the Néel point. The shape of the susceptibility curve is, however, not typical of antiferromagnetism. At the present, time neutron diffraction measurements are not available for further confirmation of the exact Néel temperature.

$Li_{0.05}Mn_{0.95}Se$

Neutron diffraction results for this composition indicate that the sample is antiferromagnetic at all temperatures below 83°K. The magnetic measurements give the additional information that there is a small magnetic moment (unsaturated) of about 0.2 μ_B per molecular unit in a field of 7000 gauss at 77°K. At liquid helium temperatures, the magnetic susceptibility is constant with field ($\chi \approx 300 \times 10^{-6}$ emu/gm), which means that the magnetic moment present at higher temperatures has disappeared.

$Mn_{0.07}Mn_{0.93}Se$

We observe a magnetic moment in this sample for all temperatures below 100°K. For example, at 20°K a saturated moment of 0.6 μ_B per molecule is measured. The neutron diffraction results of Pickart et al.[9] are complex. As indicated in Fig. 1, there is an antiferromagnetic superlattice which appears at 73°K and a further change in spin axis at 42°K. In the presence of a magnetic field certain of the anitferromagnetic superlattice, peaks are reduced. This reduction is attributed to the field induced alignment of ferromagnetic clusters surrounding each Li ion.

$Li_{0.10}Mn_{0.90}Se$

The specimen with the highest lithium content showed good agreement between magnetic moment measurements and the neutron diffraction data. At 110°K, the material becomes ferromagnetic, while at 70°K there is a transition to antiferromagnetism. At 71°K the magnetic moment is 0.7 μ_B.

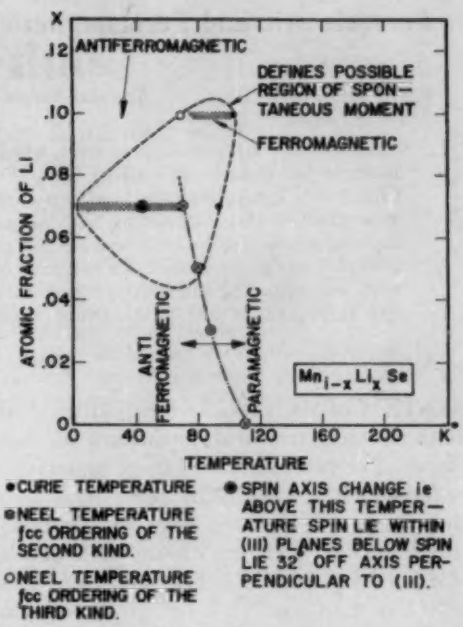

FIG. 1. Phase diagram showing temperatures at which various compositions have magnetic transitions.

The paramagnetic susceptibilities of the four compositions have been measured. In all cases, when the reciprocal susceptibility is plotted against temperature, there is a hyperbolic curvature as has been already described in connection with the $x=0.03$ composition. The molar-Curie constant calculated from the high temperature slope reveals that the trivalent manganese has zero moment if the divalent manganese is assumed to have five unpaired spins as it normally does.

CONCLUSIONS

Three characteristics of double exchange are found in these materials. The first is a metallic type electrical conductivity. The other two include the presence of ferromagnetism and the hyperbolic shape of the $1/\chi$ vs T curve. The latter is a shape predicted for double exchange by Anderson and Hasegawa[11] on a theoretical basis.

[10] C. G. Shull, W. A. Strauser, and E. O. Wollan, Phys. Rev. **83**, 333 (1951).

[11] P. W. Anderson and A. Hasegawa, Phys. Rev. **100**, 675 (1955).

Ferroelectric and Ferrimagnetic Properties of $(Ba_{6-2x}R_{2x})$ $(Nb_{9-x}Fe_{1+x})O_{30}$

P. H. Fang and R. S. Roth
National Bureau of Standards, Washington 25, D. C.

Materials which possess properties, which strongly suggest both ferroelectricity and ferrimagnetism, are found in the systems $(Ba_{6-2x}R_{2x})$ $(Nb_{9-x}Fe_{1+x})O_{30}$, where R is a trivalent rare earth ion and x can vary from 0 to 1. X-ray diffraction powder patterns indicate a single phase having the potassium tungsten bronze type structure also exhibited by $Ba_4Nb_8Zr_2O_{30}$. When R is Gd^{+3} and x is at a maximum for this system, the material appears to be both ferroelectric and ferrimagnetic at room temperature. The ferrimagnetism is indicated by the appearance of a remnant polarization and the ferroelectricity by the presence of a dielectric hysteresis loop. The magnetic susceptibility is of the order of 120 at room temperature and exhibits dispersion at frequencies near 20 Mc. Other properties of materials in these systems will also be discussed.

A SYSTEM of single phase compositions, which is both ferroelectric and ferrimagnetic, has been found by us. The composition of these materials can be represented by $(Ba_{6-2x}R_{2x})(Nb_{9-x}Fe_{1+x})O_{30}$, where R is a trivalent rare earth ion with large ionic radius: Nd^{+3}, Sm^{+3}, Eu^{+3} and Gd^{+3}. The maximum value of x is equal to one for Nd^{+3} and Sm^{+3}. For Eu^{+3} and Gd^{+3}, this value is slightly less than one. This system of compounds is an extension of a system of materials which was found to be ferroelectric.[1] The structure of this system of materials can be interpreted on the basis of the tungsten bronze structure.[2]

Ferroelectric properties are confirmed by the presence of the dielectric hysteresis loop and the piezoelectric resonance. The piezoelectric effect was measured on a previously polarized ceramic disk. Ferrimagnetic properties are verified by the presence of the remanent magnetization and the effect of the replacement of different rare earth ions on the ferrimagnetic Curie temperature.

There seems to be some correlation between the ferroelectric and ferrimagnetic properties. When the rare earth ion is Nd^{+3} both ferroelectric and ferrimagnetic properties exist only below room temperature. On the other hand, with the other rare earth ions, Sm^{+3}, Eu^{+3}, and Gd^{+3}, the materials are both ferroelectric and ferrimagnetic above room temperature. When the rare earth ion is La^{+3}, neither ferroelectric nor ferrimagnetic effects were observed down to liquid nitrogen temperatures. The relaxation dispersions of the dielectric permittivity and the magnetic permeability occurs in the same frequency region, around 20 Mc.

The ferroelectric coercive field shows a strong temperature dependence and large temperature hysteresis. The magnetic coercive field is near one thousand oersteds.

Smolenskii et al.[3] reported ferroelectricity in some compounds of perovskite structure containing Fe^{+3}, and proposed that both ferroelectric and ferromagnetic properties may be found among similar compounds possessing the perovskite structure. The present materials are the first substances, which are definitely shown to be simultaneously ferroelectric and ferrimagnetic.

An extension of the present work to modify the compositions by different crystallographic substitutions, will be reported at a later date.

ACKNOWLEDGMENTS

We would like to acknowledge the help of Dr. P. M. Pan of Westinghouse Electric Corporation for the magnetic measurements, Dr. J. H. Wasilik for the piezoelectric measurements, H. S. Schofer for dielectric measurements, and H. Johnson for specimen preparations.

[1] R. S. Roth, Bull. Am. Phys. Soc. 4, 63 (1959); P. H. Fang, R. S. Roth, and W. S. Brower, ibid 4, 64 (1959); P. H. Fang, R. S. Roth, and W. S. Brower, Bull. Am. Ceram. Soc. 38, 183 (1959); P. H. Fang, R. S. Roth, H. Johnson J. Am. Ceram. Soc. (to be published).

[2] A. Magnali, Arkiv Kemi 1, 213 (1949).

[3] G. A. Smolenskii and V. A. Joffe, paper presented at Colloque International de Magnetisme de Grenoble (1958); G. A. Smolenskii and A. I. Agranovskaia, J. Tech. Phys. (U.S.S.R.) 28, 1491 (1958) (Transl. Soviet Phys. Tech. Phys. 3, 1380, 1959); Smolenskii, Agranovskaia, and Popov Isupov, ibid 28, 2152 (1958) [Transl. ibid 3, 1981 (1959)].

Magnetic Films

Some Physical Properties of Thin Magnetic Films

A. C. Moore and A. S. Young
Royal Radar Establishment, Malvern, England

In films of nickel iron evaporated under suitable conditions, the magnetocrystalline anisotropy is averaged out by the random array of small crystallites. The stress in the films cannot be eliminated but its effect is made insignificant by using alloys whose mean magnetostriction is zero. In these particular films, no evidence is found of angle of incidence effect but it is shown that they may contain traces of oxide.

It is easier to obtain uniformity in magnetic properties of a number of elements in a plane if the magnetic film is made continuous and edge effects are excluded. No interaction takes place between adjacent areas when spaced ½ cm apart. This spacing can probably be reduced by a factor of at least two without interaction trouble.

THIN films about 1000 A thick of nickel iron (near 80/20) when formed by evaporation onto a heated glass substrate in a magnetic field in a manner similar to Blois[1] can show wide variation in magnetic properties. It was found that minimum coercivity in the preferred direction, H_c, occurred with substrate temperatures of 300°C; so, this condition was fixed and the films so produced were investigated.

COMPOSITION

The mean chemical composition of the films were measured with a polarograph. This gave an accuracy of about 1% for a 2 cm square 1000 A thick film and showed a degree of iron enrichment compared with the starting material of about 2% depending mainly on the rate of evaporation. A far more sensitive test for observing small changes in composition when working near the composition for zero mean magnetostriction lies in observing the effect of strain on the *BH* "loop" obtained at right angles to the preferred axis of magnetization.[2] It was found here that two successive evaporations from the same 10-g crucible charge could give two layers whose sign of magnetostriction changed from the iron rich side of zero in one to the nickel rich side in the next. The iron enrichment of the layers during evaporation was accompanied by nickel enrichment of the charge. In order to obtain zero mean magnetostriction films, it was therefore necessary to control the starting material to about 0.2% as well as control the conditions of evaporation.

The mean composition of the film over a 1-mm diam spot was estimated from the lattice parameter determined by x-rays. Back reflection Debye Scherrer and iron K_α radiation were used. The accuracy is limited by the broadening and corresponds to $\pm 1\frac{1}{2}\%$ in composition. The mean value obtained agreed with the chemical composition and no variation outside this limit was observed across these films.

PHYSICAL NATURE

The x-ray line broadening could be accounted for by a 10% variation in composition under the x-ray spot, or by strain variations a few times greater than the elastic limit of the bulk material, but the most plausible explanation lies in small crystallite size normal to the film and this is borne out by other observations which follow. The crystallite sizes are roughly estimated to vary from 200 to 1000 A in films 2000 A to 1 μ in thickness. In films less than 2000 A thick the x-ray reflections are too diffuse to register, but with prolonged annealing can be seen in 1000 A films.

The diffracted rings are all present at about the right relative intensities and are uniformly continuous. The angle of incidence of the x-ray beam was changed from 0° to 30° but no change was obtained in the pattern. There is therefore no evidence here for orientation of any sort in these films. Verderber[3] obtained variable results for the existence of a fibre axis in films evaporated onto a substrate at 300°C and supposed that some other undiscovered factor was controlling the nature of the film in this case.

The best illustration of the physical nature of thin films was obtained by stripping thinner films ~800 A thick from their glass substrate and examining them by direct transmission in an EM3 electron microscope. The results show small crystallites of dimensions about 1000 A in the plane of the film randomly oriented normal to it (the transmission of each crystallite differs from its neighbors). The film is unlikely to be more than one or two crystallites thick and there are signs of banding due to twinning or stresses. There is no sign of any dimensionally preferred direction as has been suggested by Wolfarth.[4]

In transmission electron diffraction, these films show rings with a graininess expected from crystallite sizes of a few hundred A. The rings are all there and of the right relative intensities; each ring is uniform and the pattern

[1] M. S. Blois, J. Appl. Phys. **26**, 975 (1955).
[2] D. O. Smith, J. Appl. Phys. **30**, 264S (1959).
[3] R. R. Verderber, J. Appl. Phys. **30**, 1360 (1959).
[4] E. P. Wohlfarth, Sheffield conference on magnetism (September, 1959).

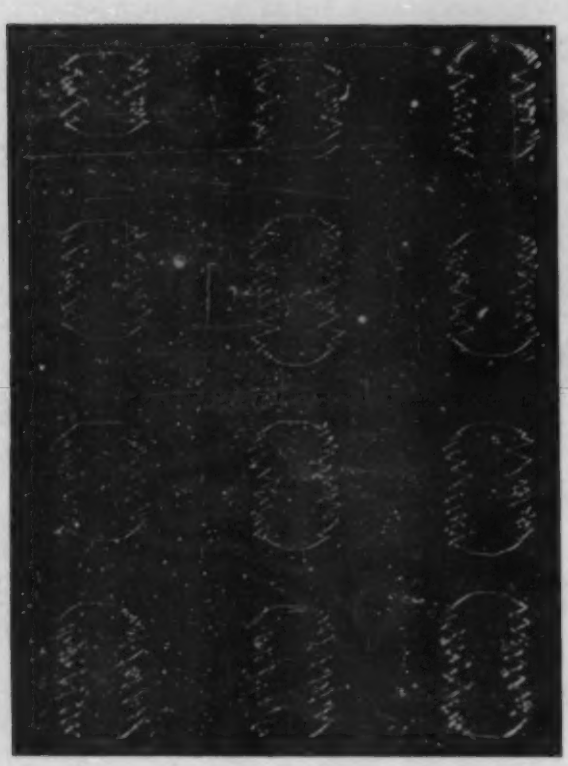

FIG. 1. Reversal of magnetization in selected areas of a continuous thin film using coincident current methods. The domain walls are marked by magnetic colloid. Scale ¼ cm between centers of elements.

is not changed by tilting the specimen in the electron beam. This agrees with the x-ray results in showing lack of orientation.

There were, however, two faint extra lines in the electron diffraction pattern. Heidenreich[5] has shown that oxygen can be preferentially absorbed in various magnetic materials so as to give rise to a preferred direction of magnetization, and that with larger amounts of oxygen oxides could be detected. The extra lines were therefore compared with the diffraction pattern of a thin film of nickel ferrite and were found to coincide with two of the three most intense lines in the ferrite pattern (440), (400). The third intense line from the ferrite (311) would be obscured by the central spot.This suggests the presence of oxides in these thin nickel iron films.

Although the film had a well defined magnetic axis, the extra diffraction rings showed no preferred orientation.

To sum up so far, these particular films are randomly orientated small polycrystalline layers with traces of oxides with no preferred shape or oxide distribution and with zero mean magnetostriction, but still show variation in their magnetic properties.

[5] R. D. Heidenreich, *et al.*, J. Appl. Phys. **30**, 995 (1959).

SUBSTRATE AND EDGE EFFECTS

Two external effects can cause variation in the films: First, by the substrate. It was found that fine polishing scratches on the substrate, if all in one direction, made that the preferred direction of magnetization with coercive force for rotation H_K up to 20 oe or more. A mat finish obtained by scratching in all directions gave a coercive force $\simeq$50 oe with no preferred direction in the plane of the film. Care was therefore taken to eliminate this trouble.

Secondly, the edges of the film had a marked effect on its magnetic properties. H_c and switching times at an angle of 20° to the preferred magnetic direction of the center of a strip 6×1 cm were measured. A 1-cm square cut from the center of this strip showed a reduction of H_c from 3 to 2 oe and an increase in switching time at the fields used in the first experiment.

The orientation of the preferred direction in 6×6 cm continuous sheets of magnetic film on glass was measured at various spots on the film by switching the magnetic vector out at right angles to the nominal preferred direction and observing which way it had fallen back. A pickup loop orthogonal to the drive loop was used. On early films with nonzero magnetostriction, variations up to 20° from the nominal direction were found. With a complete film of zero magnetostriction material, the orientation is now usually better than 1°, the limit of accuracy of this measurement. If a well aligned film is etched away so as to leave 1 cm diam spots on the surface, these spots now often show variation in preferred direction of up to 10° from their original direction and these variations are quite random over the sheet. There is no evidence of any symmetrical variation at the corners of the sheet, which might be caused by an angle of incidence effect.

It was therefore suggested that continuous sheets of film should be used for a storage plane of elements and the interaction between adjacent elements on one plane was investigated. A complete film was saturated in one preferred direction and a reversing field H such that $1/2H_c<H<H_c$ was applied to strips of the film ¼ cm apart by means of conductors laid along the surface of the film. A coincident field of equal magnitude was superimposed at ¼ cm intervals along the strips, but the conductor in this case was bent away from the film between elements. The results are shown in Fig. 1. There is no interaction between adjacent elements at this spacing. Measurements under pulse conditions using 2 μsec pulses again show no interaction between elements.

It is thought the spacing of the elements can be reduced by a factor of two at least without interaction.

Millimicrosecond Magnetization Reversal in Thin Magnetic Films

W. DIETRICH AND W. E. PROEBSTER
International Business Machines Corporation, Research Laboratory, Zurich, Switzerland

A special pulse equipment including a pulse sampling oscilloscope with an overall response time of 0.35 mμsec for the observation of the millimicrosecond flux reversal in thin permalloy films is described. Output signals as short as 1 mμsec have been obtained and are discussed with respect to the underlying reversal processes. Inverse switching times versus driving field curves have slopes of about 10^3/oe sec. Coherent rotation and oscillation of the magnetization have been clearly detected by picking up the flux change transverse to the driving field.

INTRODUCTION

SWITCHING times of about 1 mμsec for the coherent rotation of the magnetization in thin permalloy films with uniaxial anisotropy have been predicted from results of ferromagnetic resonance experiments.[1,2] The experimental problem is characterized by the display of the very short signals lying beyond the time resolution of the conventional measuring instruments. By means of oscilloscopes with distributed amplifiers and travelling wave oscilloscopes, film switching times have been measured down to 10 mμsec[3] and 3 mμsec[4] respectively. However, even these advanced techniques have not allowed a more detailed investigation of the very rapid processes. In the following, film switching measurements are reported, carried out by an improved technique based on a pulse sampling oscilloscope with an overall time resolution of 0.35 mμsec.

EXPERIMENTAL TECHNIQUES

A magnetic field pulse is generated in a balanced 50 Ω strip transmission line by the discharge of a 50 Ω cable over a coaxial mercury relay. The rise time of this pulse is less than 0.35 mμsec. The strip line is short-circuited, by which the magnetic field is doubled, due to the reflected wave. In addition to the pulse field, premagnetization and reset fields are provided in the plane of the film by two pairs of Helmholtz coils.

The longitudinal flux change of the film—the flux change in the direction of the pulse field—is picked up by a wire placed in the symmetry axis of the strip line (Fig. 1). The voltage induced by the air-flux is cancelled by matching the end of the pick-up wire by means of equal resistors connected to the two plates of the strip line. The capacitively picked-up disturbances caused by the step-wave in the strip line is reduced by the aforementioned short-circuiting of that line.

The transverse magnetic flux is linked by a wire placed normal to the axis of the strip line just above the film. One end of this wire can be short-circuited for the reduction of capacitive disturbances, as no air-flux is picked up.

The signals are repetitively produced at a rate of about 50 cps and fed over a wideband cable type RG 19 U with a delay of 140 mμsec to a pulse sampling oscilloscope.[5] This signal delay is necessary because of the delayed generation of the sampling pulse. The overall response time of the homemade oscilloscope[6] is about 0.35 mμsec.

The picked-up disturbances, which are mainly periodical, have been reduced by electronic subtraction of the disturbing signal from the disturbed switching signal generated alternatingly. The disturbing signal alone is produced by applying the driving pulse while the film is completely saturated, and, therefore, causes no flux change. A complete storing of the two waveforms is not necessary as the sampling oscilloscope allows a point by point subtraction.[7]

Switching signals longer than 10 mμsec have been measured with high sensitivity by means of Tektronix 517 A oscilloscope in connection with a 300-Mc/sec distributed amplifier type SKL 206. While the maximum sensitivity of the equipment with the sampling oscilloscope is at present 30 mv/cm, a sensitivity of 2 mv/cm can easily be obtained with the distributed amplifier setup.

RESULTS

The magnetization reversal of numerous permalloy films of thicknesses between 700 A and 3000 A, and of various anisotropy fields H_K has been investigated. Usually a pulse field H_S has been applied in the easy direction, with a dc field H_T in the hard direction. During the pulse intervals a reset field is provided oppositely to the pulse field.

Figures 2(a)–(d) show the longitudinal signals for increasing pulse fields H_S and constant transverse field H_T for a typical film. Starting from low-driving fields

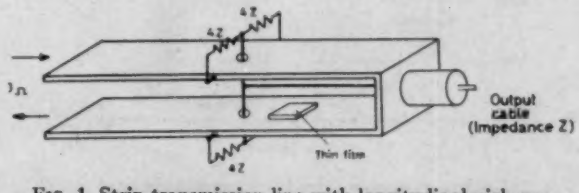

FIG. 1. Strip transmission line with longitudinal pick up.

[1] D. O. Smith, J. Appl. Phys. **29**, 264 (1958).
[2] P. R. Gillette and K. Oshima, J. Appl. Phys. **29**, 1465 (1958).
[3] C. D. Olson and A. V. Pohm, J. Appl. Phys. **29**, 274 (1958).
[4] D. O. Smith and G. P. Weiss, J. Appl. Phys. **29**, 290 (1958).
[5] R. Sugarman, Rev. Sci. Instr. **28**, 933 (1957).
[6] H. P. Schlaeppi and H. P. Louis, Helv. Phys. Acta **32**, 328 (1959).
[7] W. Dietrich and W. E. Proebster, IBM Journal **3**, 375 (1959).

we first observe a small output pulse about 1 mμsec long, caused by reversible rotation of the magnetization [Fig. 2(a)]. When H_S exceeds the coercive force H_c, this first short pulse is followed by a long pulse which is due to wall motion [Fig. 2(b)]. For increasing H_S, the length of this second pulse decreases while its amplitude increases [Figs. 2(c) and 2(d)]. At the same time, the amplitude of the first peak grows considerably larger. Evidently, while an increasing part of the film switches by fast rotation, the remaining part, which becomes smaller and smaller, switches still by wall motion [or possibly by slow incoherent rotation ($\tau > 5$ mμsec)].[8]

These figures and observations by the sampling oscilloscope show clearly that for irreversible flux change two switching times can be defined, whether we consider the first or the second part of the signal. Figure 2 shows the inverse switching times $1/\tau$ versus pulse field H_S, τ being defined as the time interval between the ten percent values of the corresponding output signals.

Another definition of the switching time would be based on the time interval between the 10 and 90% value of the total flux change. Such a definition leads to a continuous transition between the two branches of the $1/\tau$ vs H_S curve in Fig. 2, but entails a more difficult measurement.

Because of the low signal to noise ratio, the experimental error of the switching times for fast coherent rotation is rather high, so that the exact shape of the curves in Fig. 2 is still uncertain. Work is in progress to further decrease the noise level and to extend the measurements to higher pulse fields. If we assume straight lines for these curves, we obtain slopes of approximately 10^8/oe sec.

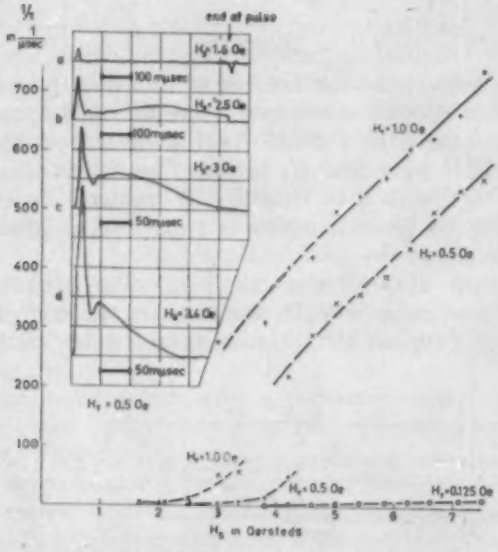

FIG. 2. Inverse switching time $1/\tau$ vs switching field H_S. (Film No. 215, 1500 A, 80/20 Ni-Fe, $H_c = 1.7$ oe, $H_K = 3$ oe.)

[8] F. B. Humphrey and E. M. Gyorgy, J. Appl. Phys. **30**, 935 (1959).

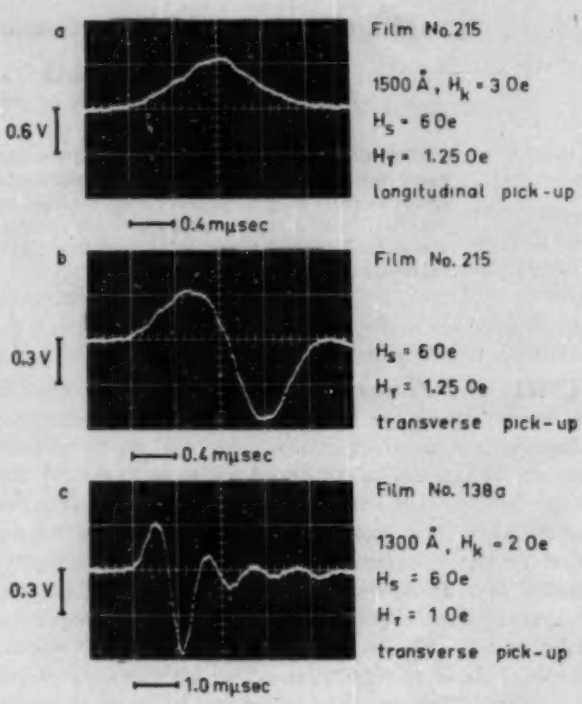

FIG. 3. Coherent rotational switching and oscillation of the magnetization.

The delay between the start of the driving pulse and the 10% value of the output pulse for the short switching times (<5 mμsec) in Fig. 2 is smaller than 1 mμsec. The delay decreases as expected when the pulse field H_S is increased.

The investigation of the transverse flux change allows the determination of the amount of flux rotating in a coherent mode. Figures 3(a) and (b) show longitudinal and transverse output signals for the same driving condition. From the voltage time integrals of the single pulse in Fig. 3(a) and the double pulse in Fig. 3(b), it can be concluded that the magnetization rotates in a coherent mode. Discrepancies still exist with respect to the theoretically expected total flux change and that observed by pulse measurements, caused probably by shielding effects in the strip transmission line.

A few films showed an oscillation of the transverse output signal [Fig. 3(c)]. This oscillation can be considered as the excitation of ferromagnetic resonance by the driving pulse. With increasing driving field, the resonance frequency is increased. Moreover, the oscillations are more pronounced the more the conditions for coherent rotation are approached. The damping parameter λ in the Landau-Lifschitz equation has been determined by ferromagnetic resonance measurements at 500 Mc/sec for the same films. The resulting λ agrees with that obtained from the decay of the observed oscillation.

Flux Reversal by Noncoherent Rotation in Magnetic Films*

K. J. HARTE†
Lincoln Laboratory, Massachusetts Institute of Technology, Lexington 73, Massachusetts

A model of magnetization reversal in thin ferromagnetic films is proposed. The model is based on a small angular dispersion (~3°) in the film plane of the axis of planar anisotropy. The dynamical effects of this dispersion are important when the switching field (H_s) is of the order of the anisotropy field, fall off rapidly with increasing H_s, and include a two- to threefold increase in the switching coefficient for bias field large enough to insure unidirectional rotation. In addition, it is shown that the transverse flux reaches its maximum before the longitudinal flux is one-half switched. These results are in reasonable agreement with experiment.

I. INTRODUCTION

THREE distinct modes of flux reversal in magnetic films have been inferred from observations, each mode characterized by a region of different slope in a plot of inverse switching time ($1/\tau$) *vs* switching field (H_s), at various transverse fields (H_1).[1,2] For the very high slope (fast) and very low slope (slow) regions, reversal mechanisms are generally considered to be coherent rotation[1,3,4] and domain wall motion,[5] respectively. Humphrey and Gyorgy[2] have suggested that in the intermediate speed region, where 0.1 μsec$\lesssim\tau\lesssim$0.5 μsec, flux reversal is by noncoherent rotation. This paper proposes a model of noncoherent rotation and discusses its predictions.

II. ROTATION MODEL

Measurements on thin Fe-Ni films by Crowther[6] indicate that the axis of planar anisotropy varies slightly from point to point in the film plane. The maximum amplitude of this variation was found to be ~3° for a variety of films, and the standard deviation of the distribution ~1½°. If exchange energy is small compared to anisotropy energy, the measured dispersion is the actual dispersion of the anisotropy axis; but if exchange effects are large, the actual dispersion may be much larger.

Consider a transverse field $H_\perp$ applied in the film plane at right angles to the mean anisotropy axis. In equilibrium the angle $\phi(\mathbf{r})$, between the local magnetization vector and the mean anisotropy axis, will be distributed $\pm\sim3°$ about a mean value slightly less than the value expected for coherent magnetization, i.e., $\phi=\arcsin h_\perp$, where $h_\perp=H_\perp/H_k$ for anisotropy field H_k [see Fig. 1(a)]. Now consider a switching field H' applied opposite the mean anisotropy axis. All segments of the film with equilibrium angles $\phi<\arcsin h_\perp$ will behave as if subject to a reduced bias field, and segments with $\phi>\arcsin h_\perp$ will experience an augmented field. Since the equilibrium distribution is skewed toward $\phi=0$, an increased switching coefficient (inverse slope of $1/\tau$ *vs* H_s curve) would seem likely. Calculation shows that this is indeed the case.

Note, however, that for $h_\perp$ less than the maximum dispersion, some fraction of the flux will reverse in the opposite sense from the main rotation, and for $h_\perp=0$, equal flux reversal should occur in both directions. These processes are fundamentally noncoherent for all H_s, and will be omitted from this treatment.

Another characteristic of noncoherent flux reversal is the following: Humphrey[7] has noted from transient waveforms that the transverse flux switched reaches a maximum considerably before half the longitudinal flux has reversed. According to the coherent rotation model, these points should be reached simultaneously at $\phi=\pi/2$. With the present model, this anomaly is easily explained. The longitudinal flux is half switched when the average over the film of the projections onto the

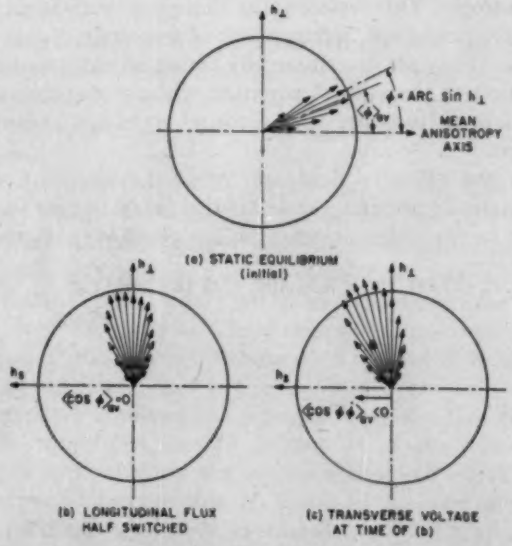
h⊥
φ = ARC sin h⊥
MEAN ANISOTROPY AXIS
(a) STATIC EQUILIBRIUM (initial)
(b) LONGITUDINAL FLUX HALF SWITCHED
(c) TRANSVERSE VOLTAGE AT TIME OF (b)

FIG. 1. Magnetization distribution: static and dynamic states.

* The work reported in this paper was performed by Lincoln Laboratory, a center for research operated by Massachusetts Institute of Technology with the joint support of the U. S. Army, Navy, and Air Force.

† National Science Foundation Predoctoral Fellow. Present address: Department of Physics, Harvard University, Cambridge, Massachusetts.

[1] C. D. Olson and A. V. Pohm, J. Appl. Phys. **29**, 274 (1958).
[2] F. B. Humphrey and E. M. Gyorgy, J. Appl. Phys. **30**, 935 (1959).
[3] R. L. Conger and F. C. Essig, Phys. Rev. **104**, 915 (1956).
[4] D. O. Smith, J. Appl. Phys. **29**, 264 (1958).
[5] N. Menyuk and J. B. Goodenough, J. Appl. Phys. **26**, 8 (1955).
[6] T. S. Crowther, Lincoln Laboratory Group Report No. 51-2, February 24, 1959 (to be published).
[7] F. B. Humphrey, J. Appl. Phys. **29**, 284 (1958).

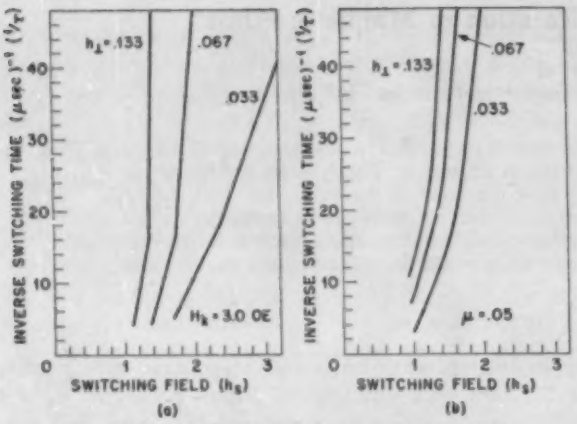

FIG. 2. Inverse switching time *vs* switching field. (a) Experimental.[3] (b) Theoretical.

mean anisotropy axis of the magnetization vectors vanish [see Fig. 1(b)]. The transverse flux, on the other hand, is a maximum when the transverse voltage transient is zero, or when the average of the projections onto the mean anisotropy axis of the magnetization vectors each multiplied by their respective velocities $\partial\phi/\partial t$ vanishes. But since $\partial\phi/\partial t$ increases with increasing ϕ at this stage of the switching process, the transverse voltage distribution will be skewed in the direction of increasing ϕ [see Fig. 1(c)], and the transverse voltage transient will lead the longitudinal flux.

III. CALCULATIONS AND RESULTS

One may question whether dispersive effects are large enough to alter coherent switching appreciably. However, calculations show that a small dispersion may have a large dynamical effect. A modification of the Gilbert[5] equation is used, in which the damping is assumed to be anisotropic. Furthermore, the damping coefficients are assumed constant, independent of the mode of flux reversal. They are determined by fitting an exact machine solution of the Gilbert equation without dispersion to the data of Humphrey and Gyorgy[2] in the fast, coherent region.

In the effective field are included anisotropy, demagnetizing, exchange, and applied fields, but for variations in the magnetization taking place over distances $\gg 10^{-4}$ cm, exchange fields may be ignored. Various configurations for $\phi(\mathbf{r},0)$ are assumed, and approximate solutions $\phi(\mathbf{r},t)$, satisfying appropriate boundary conditions, are found in terms of the first few coefficients of power series expansions in the maximum dispersion (μ) and $h_\perp(\ll 1)$.

Calculated switching curves (see Fig. 2) show a two- to threefold increase in the switching coefficient for $\tau \gtrsim 50$ mμsec. As $h_s(=H_s/H_k)$ increases, with $h_\perp$ held constant, noncoherent effects rapidly decrease, and the linear, coherent region is approached. Agreement with experiment is good except at very low or zero bias fields, e.g., $h_\perp=0.033$. For these cases, since $h_\perp<\mu$, it is expected that rotation will occur in both directions, with the appearance of as yet unknown dissipative processes.

The ratio of the time (t_1) for the transverse flux to reach its maximum, to the time (t_2) at which the longitudinal flux is half switched is found to be, for $h_s>1$,

$$t_1/t_2=\ln\left[\frac{h_s-1+\mu}{\mu h_s}\right]\Big/\ln\left[\frac{2(h_s-1)+\mu}{\mu h_s}\right].$$

For typical values of $h_s=1.1$ and $\mu=0.05$, $t_1/t_2=0.65$. This compares fairly well with experimental values, which range from $t_1/t_2=0.4$ to 0.8.[1,7]

IV. CONCLUSIONS

It is reasonable to conclude that for all rotational processes, angular dispersion is present; at high fields the effects are negligible. The present model predicts fairly accurately some of the characteristics of noncoherent switching. It seems likely that other mechanisms are also operative during a slow reversal process, e.g., scattering of energy from the coherent rotation into spin wave modes by film inhomogeneities. Also, oppositely directed rotations certainly play a major role at very low $h_\perp(\lesssim 0.04)$, where the simple dispersion model breaks down. Further experiments would be desirable, for example switching characteristics of films with abnormally high or low dispersions.

V. ACKNOWLEDGMENTS

The author wishes to thank D. O. Smith for suggestions, advice, and encouragement, and T. A. Kaplan for helpful discussions. Thanks are also due Mrs. Ann Sherman, who performed the machine calculations.

[5] T. L. Gilbert, Phys. Rev. **100**, 1243 (A) (1955).

JOURNAL OF APPLIED PHYSICS SUPPLEMENT TO VOL. 31, NO. 5 MAY, 1960

Magnetization Reversal in Uniaxial Films near to the Preferred Direction

E. M. BRADLEY AND M. PRUTTON
International Computers and Tabulators Limited, Stevenage Herfordshire, England

It is now well known that uniaxial thin magnetic films can be made which have almost ideal square hysteresis loops in the preferred direction and almost straight line hysteresis loops in the hard direction. For this type of film, which can be prepared by evaporation from ingots of approximately 81:19 NiFe alloy, it is found that the switching time constant of the reversal process which occurs when magnetic fields are applied exactly in the easy direction can be very large.

The switching process occurring when fields are applied at angle 10° to the preferred direction has been studied in detail, both by a new pulse response technique and by observation of the domain structure revealed by use of the Kerr magneto-optic effect.

In the latter experiment, short pulses have been applied to the specimen and photographs taken of the domain pattern after each pulse. It was found that the specimen breaks into small domains whose area increases after each pulse and that eventually the film could be completely reversed if the pulse amplitude was between certain critical values. Curves were plotted of the pulse amplitude against the proportion of the film switched found by measuring the reversed area in the photographs. It was shown that the process is very well approximated by an equation of the form $S_w = \tau(H-H_0)$, which implies a viscous damped process, and there is a critical nucleation field, which is less than the field required to move the walls.

In the pulse response experiments, the switching time has been derived from the response to a reset pulse which was applied after a variable number of set pulses of variable amplitude. It was found that in some films there can be a rapid switching process, which is complete after about 100 mμsec, followed by a slow process lasting up to 10 μsec under the same conditions. From the experiments performed, it has been possible to compute a switching time constant which can be very large in some films. This constant is found to be correlated with the ratio $p=H_e/H_k$, where H_e is the coercivity in the easy direction and H_k is the rotational coercivity. If the film obeyed the simple coherent rotational model the p ratio would be 1, and films which have $p=0.9$ have been found have $S_w=0.3\times10^{-6}$ oe μsec, whereas for $p=0.3$, $S_w=7\times10^{-6}$ oe μsec.

1. INTRODUCTION

IT is now well known that uniaxial thin magnetic films can be made which have almost ideal square hysteresis loops in the preferred or "easy" direction and almost straight line loops in the "hard" direction.[1-3] This type of film has been prepared here by evaporation from ingots of 81:19 NiFe alloy.

It has been found experimentally and predicted theoretically[3] that the switching time constant of the reversal process, which occurs when the anisotropic film is subjected to magnetic fields exactly in the easy direction can be very large. The long switching time thus observed precludes the exploitation of the easy direction square loop property in computer storage matrices. However, if the magnetic field is applied at a small angle to the easy direction, the switching process can be very much faster, and as the hysteresis loop does not depart significantly from the rectangular shape, it could still be used for the selection process.

With these considerations in mind, the switching process occurring when fields are applied at an angle of 10° to the preferred direction has been studied in detail, both by a new response technique and by observation of the domain structure revealed by use of the Kerr magneto-optic effect.[4,5] In the experiments reported, film specimens 1500 A thick and size 2.5 mm×10 mm with the easy axis parallel to the 2.5 mm side were used. The films were deposited onto 1 mm thick soda glass, and the required shape etched out by the photo resist process. The fields were applied by passing a current through a strip line placed at an angle of 10° to the long side of the specimen. The output flux was picked up in a small figure-eight loop with the specimen enclosed by one-half of the loop.

2. KERR EFFECT MAGNETO-OPTIC EXPERIMENTS

A series of magnetic field pulses of 0.5 μsec duration was applied to the specimen in these experiments. Photographs of the domain patterns were taken after each pulse, and when there was no further effect the experiment was repeated using pulses of different amplitudes.

It was found, if the pulse amplitude was between certain critical values, that the specimen breaks up into small domains whose area increases after each pulse and that eventually the film could be completely reversed.

Curves were plotted of the fraction of the film reversed, which was found by computing the reversed area from the photograph, against the magnetic pulse field amplitude and the number of pulses applied. From this data a curve was plotted of switching time vs drive field where the switching time was found from the number of pulses of known duration which will reverse 90% of the film.

The curve obtained is a straight line indicating that in the range 2–4 oe the process is of the viscous damped type obeying the equation $S_w=\tau(H-H_0)$. It is interesting to note that H_0 found in this way agrees well with the coercivity measured at 400 c/s and is nearly twice the field at which reversed domains first occur at the edges of the specimen, referred to as the nucleation field.

[1] M. S. Blois, J. Appl. Phys. **26**, 975 (1955).
[2] E. M. Bradley and M. Prutton, J. Electronics and Control **6**, 81 (1959).
[3] D. O. Smith, J. Appl. Phys. **29**, 264 (1958).
[4] C. A. Fowler, Jr., and E. M. Fryer, Phys. Rev. **100**, p. 746 (1955); C. A. Fowler, Jr., E. M. Fryer, and J. R. Stevens, Phys. Rev. **104**, p. 645 (1956).
[5] M. Prutton, Phil. Mag. **4**, 1063 (1959).

3. PULSE RESPONSE EXPERIMENTS

Pulse response measurements were made on many specimens whose p ratio varied from 0.3–0.95 (where $p=H_c/H_k$). The technique used was somewhat different from that previously reported[3] in that the response was measured to a reset pulse which was fixed in amplitude, while the amplitude of either set or unset pulses was varied. The film voltage response output to this fixed reset pulse was found to be proportional to the flux change since the switching time did not change for large variations of flux switched by the reset pulse.

Two pulse trains were used:

I. A two-pulse train in which the amplitude of the negative set pulse was varied and the voltage output to the reset pulse was measured.

II. A three-pulse train in which the negative set pulse was fixed in amplitude being followed first by a positive unset pulse whose amplitude could be varied, and second by a fixed amplitude positive reset pulse to which the response was measured. The single variable amplitude positive pulse could be changed to a train of pulses whose amplitudes were variable together.

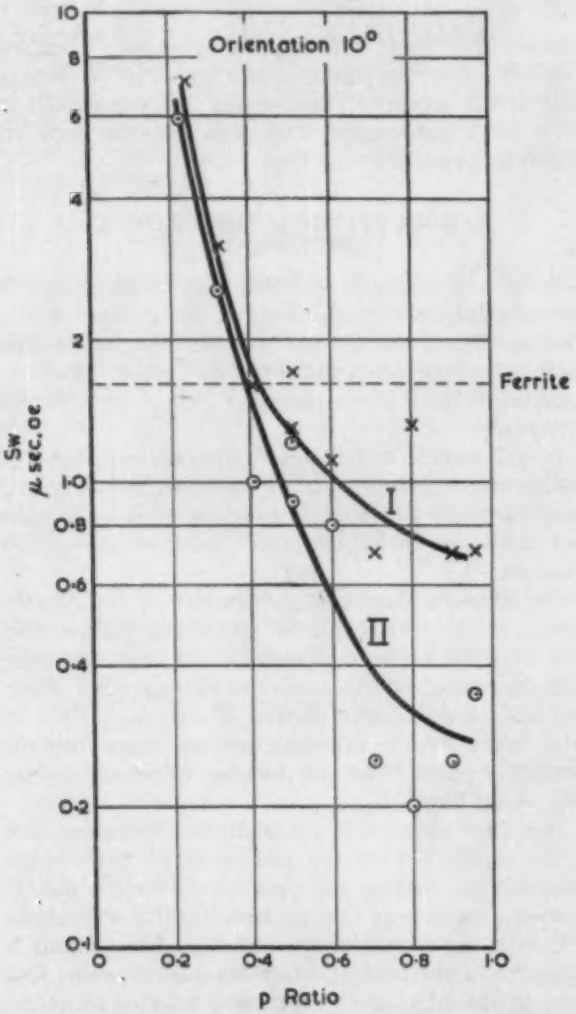

FIG. 1. Switching time constant vs p ratio for uniaxial films found using pulse trains I and II.

The amplitude of the pulse or series of pulses which caused the response to the fixed reset pulse to be either 90% or 10% of the saturation response for pulse trains I and II, respectively, was defined to be the field at which the switching process occurred in the total duration of the pulse or series of pulses. The switching time constant was computed from this measurement and from a measurement of the field required to produce switching using a train of 160 pulses in pulse train II. This latter field was assumed to be that required to switch the film in infinite time. The assumption is justified by the fact that the same field, within the experimental error, is required to effect switching if trains of 5000 or 80 pulses are used.

Values of switching time constant were obtained for a number of samples having a p ratio between 0.3 and 0.9. The samples with the lower p ratio had $H_k \sim 5$ oe and those with $p>0.6$ had $H_k \sim 3.5$ oe.

From the results obtained curves could be plotted of p ratio vs S_w. It was possible to see from the results that there was no correlation of S_w with H_k. The curves obtained are shown in Fig. 1. It can be seen that there are two separate curves corresponding to the results obtained from the pulse trains I and II. It is interesting to note that ferrite rings and thick electroplated coatings which were not highly anisotropic gave the same results for the pulse trains I and II.

Observations of the response to the variable positive pulses were made using pulse train II. It was found that there was a switching pulse in response to the first positive pulse, but the voltage output from the second and subsequent pulses could not be distinguished from the noise level.

Removal of these pulses resulted in a very large change in flux switched by the large reset pulse.

4. CONCLUSIONS

The switching process occurs in at least two steps. Firstly, a quick response process, which usually results in only a small fraction of the available flux being switched. This is followed by a much slower process which cannot easily be observed by the techniques used previously.

This complex switching behavior imposes a further restriction on the use of the square hysteresis loop for memory selection purposes because, if fast operation is required, not only must the film have a well defined square loop but it should also have a p ratio which is preferably greater than 0.7.

ACKNOWLEDGMENTS

The authors would like to thank the Directors of I.C.T. Ltd., for permission to publish this note, M. Kearton and J. Wells who made the measurements reported, and P. Astwood who made the films.

Influence of Nearby Conductors on Thin Film Switching

J. S. EGGENBERGER
IBM Research Laboratory, Poughkeepsie, New York

The usual concept of a thin film or other open flux path magnetic element consists of the material itself closely encircled by drive and sense conductors. Strips of conductor of width approximately that of the element are attractive for several reasons, i.e., low resistance, low skin effect, and low line impedance. However, these strips, being closely coupled to the element, can severely influence its dynamic properties by means of induced eddy currents.

These conductors manifest themselves in three ways:

1. A slowing of the switching due to the air return flux path of the element passing through a conductor and being damped.
2. A dynamic distortion of the air return flux due to shielding effects.
3. A dynamic distortion of an applied field due to shielding effects.

All of these effects can be detrimental to the operation of the element. In this paper, approximate calculations are presented to show the extent of these effects. The geometry considered is that of a "conventional" flat thin film element, driven and sensed by strip transmission lines. Several drive and sense configurations are considered, and experimental evidence is presented in support of these calculations. Although the cases considered are somewhat arbitrary, the methods and many of the results are applicable to other cases of utilization of open flux path elements.

I. INTRODUCTION

THE usual concept of a thin film memory or logic cell is that of a square or circular element of thin film surrounded by strip transmission lines, which supply drive fields and sense flux changes. Wide strip lines have many advantages over narrow conductors; for example, they yield a more uniform field at the bit location, lower field at other bit locations, lower skin effect for equivalent dc resistance, and lend themselves to greater ease of automated fabrication. The geometry of these strips, however, lends itself to large eddy current losses caused by a changing flux perpendicular to the strip, which can have a profound effect on the operational characteristics of the cell. This paper is an attempt to evaluate these effects for various geometries of drive and sense. In all cases, an applicational strip line will be understood to mean, rather arbitrarily, a strip line with a width of 0.1 cm, a separation of 0.01 cm, and a strip thickness of 0.001 cm.

II. PARALLEL STRIP LINES

The first geometry to be considered is that of two parallel strip lines, one included within the other [see Fig. 1(a)]. Since little flux produced by either line pierces the other, there is little shielding effect due to eddy currents. For applicational size lines, the shorted turn shielding effects are effective for times of less than 1 mμsec (because of the terminations at the ends of the line), providing that at least one termination is of the order of the line impedance.

Little flux from a square bit of thin film included within the inner strip line and magnetized perpendicular to it pierces either strip line, if the bit width is equal to or greater than, the line width. If the mode of reversal is disregarded, the film would appear to be undamped by eddy currents in the strip line. However, in a coherent rotational process, the flux would be required to pierce the strip in the intermediate state. Since induced eddy currents in the strip would make this mode of switching unfavorable for applicational dimensions, the flux lines tend to crowd between the strips in the intermediate state, resulting in a higher energy and hence an increased rotational threshold on a dynamic basis. A simplified model in which all the flux becomes crowded uniformly between the film and the line results in an increase in rotational threshold given by

$$\Delta H_r = 2B_m T/S \text{ (emu)}, \qquad (1)$$

where B_m = saturation flux density of the film, T = thickness of the film, and S = distance between the film and

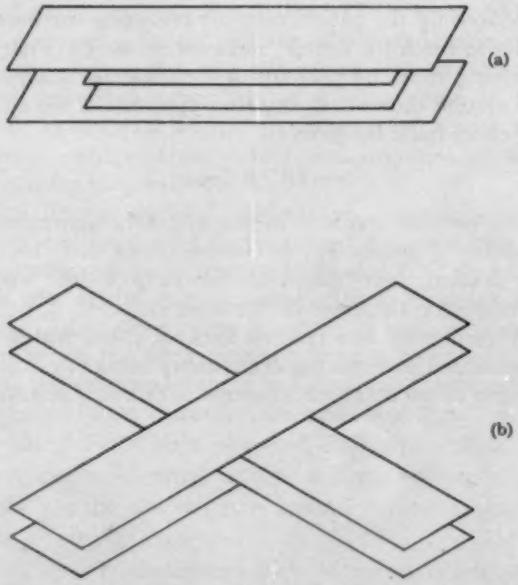

FIG. 1. (a) Parallel strip line cell. (b) Perpendicular strip line cell.

the nearest strip line. Switching plots made on a film included between copper drive lines for varying film to line spacings substantiate this analysis within a factor of two. A 500 A film included in an applicational drive line would experience an increase in rotational threshold of 20 oe, essentially prohibiting rotational switching. The switching in the region in which coherent rotation is prohibited appears to take place by an incoherent rotational process, with a switching coefficient of about 0.1 to 0.2 oe μsec, depending on perpendicualr bias field, and independent of strip line thickness. If the process were one of damped coherent, rotation, the energy losses, and hence the switching coefficient, would increase with increasing strip thickness.

It is of interest to note that a rotational switching process in the presence of a strip line should occur at a different rate than in an isolated sample. The initial rise of the magnetization out of the plane of the film would be constrained by the strip lines, giving a demagnetizing factor perpendicular to the plane of the film of greater than 4π on a dynamic basis. This additional constraint would serve to change the speed of a rotational switching. Experimental evidence of this effect is lacking due to the size of the effect in comparison with experimental accuracy.

A round sample included in parallel strip lines should show some damping for any switching process, since the flux pierces the strip in the static state. For applicational dimensions, however, this damping is negligible in comparison with the normal switching coefficients of the modes. The increase in rotational threshold is still in evidence.

III. PERPENDICULAR STRIP LINES

In the case of perpendicular strip lines, one included within the other [see Fig. 1(b)], it is seen that the field produced by the outer line must penetrate the inner in order to reach the center, and hence some eddy current damping must be present. A dimensional analysis of the system shows that any time constant of the shielding effect must be given by

$$\tau = kW/R \text{ (emu)}, \tag{2}$$

where τ = time constant in seconds; k = a dimensionless function of geometry; W = some linear dimension of the system, here taken as the strip width; and R = resistivity/thickness of the inner strip.

A system of two crossed lines of equal width was constructed, the spacing of the inner being one-half the spacing of the outer and centered within it. The average field in the region common to both lines was measured by means of a sense coil and an electronic integrator. It was found empirically that the field produced by a step function of current in the outer line is given to a good approximation by

$$H = H_s(1 - 1/2e^{-t/\tau}), \tag{3}$$

where H_s = steady state field produced by the current, t = time since application of the current, and τ is as defined in Eq. (2). The fall of the field is of the same form as the rise. The instantaneous increase to half the steady state value is evidently associated with fields coming in from the edges of the inner line, since it disappears when the inner line is replaced by an extended shield.

Experimental measurements of k as a function of the inner line impedance over a range of 5 to 50 ohms indicate values of 0.3 to 0.5, the lower limit being for lower impedance lines. For lines of 25 to 50 ohms, the value is essentially constant at 0.5. The time constant of an applicational line made from Cu is of the order of 30 μsec.

The increase in rotational threshold as described for parallel lines is again observed. No increase in switching coefficient could be observed for the low field switching modes for larger than applicational sized models. Since any increase in switching coefficient would become less pronounced with decreasing linear dimensions, the applicational size cell should also be free from these effects.

IV. CONCLUSIONS

The results of this investigation can be expressed as follows:

1. While the rotational mode of switching of a thin film element is attractive for memory and logical operations due to its speed and sensitivity to two directions of applied field, this mode of switching is difficult to achieve in a strip line configuration of reasonable size.
2. An appreciable dynamic shielding can result in a significantly longer rise time field at the bit location in a crossed strip line cell than in a parallel line cell.

V. ACKNOWLEDGMENTS

The author wishes to thank L. A. Russell for initially suggesting the problem, S. H. Charap for suggesting the dimensional analysis approach, and R. A. Middlebrook for his aid in construction of apparatus.

JOURNAL OF APPLIED PHYSICS SUPPLEMENT TO VOL. 31, NO. 5 MAY, 1960

Preferred Orientation and Ordering in Evaporated Films of Fe, Ni, and Fe-Ni*

R. F. Adamsky
Computer Products Division, Laboratory for Electronics, Inc., 1079 Commonwealth Avenue, Boston, Massachusetts

Studies of the effect of evaporation angle on orientation tendencies have shown the effect to be insignificant for certain evaporation conditions. Thickness gradients and particle size variations are the major effects of variation of incidence angle in these experiments. Slight degrees of preferred orientation in the form of [111] fiber axes have been found for Fe, Ni, and permalloy films deposited on heated substrates. Annealing experiments have shown the presence of superlattice ordering in permalloy films held for short periods of time at 200°C.

In studies of evaporated ferromagnetic films, an effect due to the angle of incidence between the substrate and the depositing beam has been observed to influence uniaxial anisotropy, and has been attributed by Knorr and Hoffman,[1] in the case of iron films, to the formation of a single texture axis inclined toward the incident beam. The development of texture axes has also been suggested by Smith[2] to be a contributing factor to angle of incidence effects on uniaxial anisotropy in films of permalloy.

The effect of angle of incidence on preferred orientation has been investigated for evaporated films of Fe, Ni, and alloys of Fe-Ni, by use of transmission electron diffraction and microscopy and by x-ray diffraction, for certain conditions of film formation.

The films generally were made by evaporation from tungsten boats at rates of 50 A/sec at pressures of 5×10^{-5} mm Hg, although evaporation from tungsten filaments and rates as slow as 2–3 A/sec were used as well. Substrates were Formvar, collodion or carbon films, and glass. The carbon and glass substrates were heated variously from room temperature to 300°C. Films could be removed from the glass for electron diffraction by flotation in water or with pressure sensitive tape in certain instances only, and only when the substrate was close to room temperature. Most of the electron diffraction results obtained apply, therefore, to films on carbon substrate.

In most cases, an aluminum grid holder containing ten evenly-spaced microscope grids was placed at a fixed distance above the tungsten boat, with the axis of the boat and holder at right angles. One grid was directly over the tungsten boat so that the angle of incidence was normal, and the angle of incidence for the remaining grids depended on the distance of the holder from the boat and the dimensions of the holder. This distance was varied from 2–6 in.; the angle of incidence for the tenth grid measured between the film normal, and the atom beam thus varied from 66° to 34°. In other cases, grids or glass slides were placed directly above the evaporant source, and the axis of the substrates tilted, with respect to the normal to the source. For the first arrangement, variation of boat to holder distance, as well as changing the angular relationship, changed the degree of heating of substrate and film due to radiation from the source. For distances of 2 in., this heating effect caused a temperature rise of 10–20°C for a thermocouple imbedded in the interior of the aluminum holder. The rise in surface temperature, while of short duration, is probably much higher than this, although the surface heating effect has not been measured accurately.

Specimens obtained in these experiments were examined chiefly by electron diffraction and microscopy, using, for the diffraction work, various angles of tilt of the film plane with respect to the electron beam to allow detection of possible fiber axes normal to the film plane. Microscopy was employed for examination of crystallite structure, grain size, film imperfections, and magnetic structure by observation of domain walls.

Film thickness for the electron diffraction studies was in the range of 200 to 800 A.

The results of the diffraction studies showed that the conditions of evaporation were significant in producing mainly random films; preferred orientation effects were always very slight and became apparent only at substrate temperatures above about 200°C. The most noticeable orientation effects were apparent for iron at substrate temperatures above 175°C, where [111] fiber axes normal to the film developed. It is estimated that the degree or orientation was less than 20%. Below this temperature, no orientation could be detected, in contrast to the experiments of Knorr and Hoffman, where strong orientation occurred at substrate temperatures of 75°C.

The effect of angle of incidence on orienting tendencies seemed to be very slight, being noticeable only for Fe films at substrate temperatures of 300°C, in which cases the texture axes departed slightly from the film normal. In addition, large amounts of iron oxide were observed on the films, apparently as a result of a reaction with residual oxygen in the vacuum system, and relatively large (several thousand angstrom) single crystals of Fe_2O_3 were observed through the film. No differences were noted for the various substrate materials, nor did the slower evaporation rates appear to cause noticeable changes.

Thickness gradients and partical size variations were significant effects produced by angle of incidence.

* This work was supported in part under contract with the Bell Helicopter Corporation.

[1] T. G. Knorr and R. W. Hoffman, Phys. Rev. 113, 1039 (1959).
[2] D. O. Smith, J. Appl. Phys. (Suppl.) 30, 264S (1959).

Thickness gradients are introduced by an increasing increment of area at high evaporation angle and also by the boat shape, which tends to limit and focus the atom beam to some extent. Thickness variations of 1000 A/in. were measured by interference methods for a Ni film of mean thickness 3800 A deposited on a substrate inclined at 20° to the horizontal. Particle size is greatest for normal incidence and decreases with decreasing film thickness. Part of the effect is due to radiation from the source, causing surface heating effects on the films closest to the tungsten boat.

Ni and permalloy films of larger thickness (3000–10 000 A) were examined by x-ray diffraction, and the presence of [111] fiber axes was noted for these films in cases where substrate temperature was above 250°C. The x-ray method was extended, by use of a scintillation counter with a pulse-height discriminator, to films of ~900 A thickness, and partial pole figures obtained for permalloy and Ni films. In addition to [111] fiber axes, some peculiar textures were observed which are not fully interpreted as yet.

In Fe-Ni alloys around the permalloy composition, ordered structures of the Ni_3Fe type may be formed. In evaporated films of permalloy, ordering is not detectable when the substrate is unheated and is distant from the heated source. When the temperature of the substrate is raised by a heater, or by radiation from the heated filament or boat, the increased mobility of the atoms increases the tendency to order. Regions which become ordered then may be considered inclusions of structurally and magnetically different material in the disordered lattice. In the case where ordering is nearly complete, regions of disorder are, likewise, inclusions in the ordered lattice.

The magnetic anisotropic properties of permalloy films are altered by the tendency to order, particularly if a magnetic field is applied during the ordering process. The presence of the field induces local changes in anisotropy considered to be due to a directional dependence of atomic order, leading, for example, to more Fe-Fe pairs in one direction than in another.[3] A uniaxial anisotropy superimposed on the crystalline anisotropy thus results from annealing in a magnetic field. The ordering temperature for $FeNi_3$ in the bulk phase is given by Josso[4] as about 505°C, while Leech and Sykes[5] obtained ordering by annealing Fe-Ni alloys for 500 hr at 370–490°C.

Experiments have been conducted which show that long-range ordering occurs in thin (~500-A) films of permalloy at 200°C for annealing periods of 15 min, and ordering is found in films evaporated onto a substrate heated to 250°C. The films used in the annealing experiments were deposited on carbon (100–200 A thick) substrates heated variously to 180–250°C±10°C at pressures of $1\text{-}5\times10^{-5}$ mm Hg, and at evaporation rates of about 50 A/sec. After evaporation, some of the films were annealed for short periods of time ranging up to 15 min (in the earth's magnetic field only). At the end of the annealing period, the heater was switched off, and the films then cooled at an average rate of 2 deg/min down to 100°C. For the films annealed for 15 min at temperatures of 200–225°C, superlattice lines are clearly visible in electron diffraction patterns.

The experiments indicate that extensive long-range ordering takes place at temperatures greater than 200°C, and it is very likely that lesser degrees of ordering occur at even lower temperatures. The existence of short-range order, or clustering, such as a directional ordering of Fe pairs in the Ni matrix, would require a detailed examination of the diffuse background scattering present in the diffraction patterns.

For most of the annealed films, the domain structure is exceedingly complex, probably as a result of highly stressed areas in the film caused by nonuniformity of the substrate. For some films, however, the domain pattern is simple, resembling that of nonannealed Permalloy, and indicating a well-defined easy axis in the film. Grain size in annealed permalloy films, as measured from electron micrographs is in the range 300–500 A.

[3] S. Chickazumi, J. Phys. Soc. Japan **11**, 551 (1956).

[4] E. Josso, Compt. rend. **230**, 1467 (1950).

[5] P. Leech and C. Sykes, Phil. Mag. **27**, 742 (1939).

JOURNAL OF APPLIED PHYSICS SUPPLEMENT TO VOL. 31, NO. 5 MAY, 1960

Investigations into the Origin of Anisotropy in Oblique-Incidence Films*

M. S. COHEN, E. E. HUBER, JR., G. P. WEISS, AND D. O. SMITH
Lincoln Laboratory, Massachusetts Institute of Technology, Lexington 73, Massachusetts

Experimental evidence is presented which shows that the magnetic anisotropy of oblique-incidence Permalloy and iron films is not caused by an inclined texture axis or anisotropic strain. Electron diffraction and microscopy have not yet revealed anisotropy in the crystalline microstructure of these films. These techniques have also thus far failed to reveal the existence of agglomeration of the crystallites into small groups having anisotropic geometric shapes. Magnetic anisotropy, on the other hand, was observed in Permalloy films deposited at normal incidence on non-magnetic metal films deposited at oblique incidence; this would suggest such an agglomeration mechanism. There is also some indication that oxygen may play a role in oblique-incidence magnetic anisotropy.

INTRODUCTION

WHEN a Permalloy or an iron film is made by vacuum deposition in such a way that the beam of incoming metal atoms makes a nonzero angle with the normal to the plane of the substrate, magnetic anisotropy of the film results, even though no magnetic field is applied during deposition.[1,2]

Some investigations that have been made into the origin, on a microscopic level, of the oblique-incidence effect are described here.

CRYSTALLOGRAPHIC TEXTURE STUDIES

Evans and Wilman[3] report crystallographic texture axes inclined toward the incident metal-vapor beam for oblique-incidence films. Smith[1] has shown that considerations of texture alone, linked with the magnetic crystallographic anisotropy, cannot explain the oblique-incidence effect. Knorr and Hoffman,[2] however, point out that a film having inclined crystallographic texture necessarily has associated with it an anisotropic magnetoelasticity; when this acts in conjunction with the high isotropic stress always present in thin films,[4] magnetic anisotropy can result. If the stress in the film is anisotropic and properly oriented, the magnetic anisotropy is, of course, reinforced; such anisotropic stress in iron films has been reported by Finegan and Hoffman.[5] Knorr and Hoffman have interpreted their experimental observations on iron in terms of this model. Experimental results, obtained in this laboratory, which are in contradiction with the Knorr and Hoffman model are discussed below.

Strain in both Permalloy and iron oblique-incidence films was measured by a Newton-ring technique.[5,6] The curvature of the soft glass substrate supporting a deposited film was thus observed; the film was then dissolved in acid and the curvature of the glass alone was measured. From these two observations the strain in the film alone could be deduced. Many films did indeed show a large anisotropic strain component, but no correlation was found between the direction of greatest strain and the easy-axis direction. Much less strain anisotropy was observed for films deposited on glass that was preselected for freedom from strain nonuniformities, however. It can therefore be concluded that the strain in Permalloy and iron films is isotropic; any anisotropy that was found was probably caused by residual strain non-uniformity in the glass substrates.

Several films of both Permalloy and iron were stripped from their glass substrates. Past experience has shown that films whose magnetic properties are highly stress-dependent change their magnetic character drastically when subjected to this treatment (e.g. "mottled" films[6]). The anisotropy field H_k of either iron or Permalloy oblique-incidence films, as measured by a hysteresis-loop tracer, was unaffected by the stripping process. The same result has been reported by Heidenreich and Reynolds.[7]

If the Knorr and Hoffman model holds for Permalloy films, the direction of the easy axis for oblique-incidence films having a positive magnetostriction constant (nickel content $<83\%$) should differ by 90° from that for films having a negative magnetostriction constant (nickel content $>83\%$). A shift in the easy-axis direction has indeed been observed, but at a composition of about 90% nickel[8]; this result is inconsistent with the Knorr and Hoffman model.

Oblique-incidence films of Permalloy on soft glass substrates were examined by reflection electron diffraction. Diffraction patterns were taken for a series of films of increasing thickness. Films of less than 1000 A thickness always showed ring patterns, i.e., no preferred crystallographic axis. Films having thicknesses in the

* The work reported in this paper was performed by Lincoln Laboratory, a center for research operated by Massachusetts Institute of Technology with the joint support of the U. S. Army, Navy, and Air Force.

[1] D. O. Smith, J. Appl. Phys. **30**, 264S (1959).
[2] T. G. Knorr and R. W. Hoffman, Phys. Rev. **113**, 1039 (1959).
[3] D. M. Evans and H. Wilman, Acta Cryst. **5**, 731 (1952).
[4] R. W. Hoffman, R. D. Daniels, and E. C. Crittenden, Proc. Phys. Soc. (London) **B67**, 497 (1954).
[5] J. D. Finegan and R. W. Hoffman, J. Appl. Phys. **30**, 597 (1959).
[6] E. E. Huber, Jr., and D. O. Smith, J. Appl. Phys. **30**, 267S (1959).
[7] R. D. Heidenreich and F. W. Reynolds, in *Structure and Properties of Thin Films*, edited by C. A. Neugebauer, J. B. Newkirk, and D. A. Vermilyea (John Wiley & Sons, Inc., New York, 1959), p. 402.
[8] D. O. Smith, E. E. Huber, Jr., M. S. Cohen, and G. P. Weiss, J. Appl. Phys. **31**, (1960).

range from about 1000 A to 3000 A often had a [110] texture axis; the texture was more pronounced for the thicker films. These results are consistent with those of Sachtler *et al.*[9] for nickel. Large magnetic anisotropy has, however, been observed in the thinner oblique-incidence films which show no texture.

OTHER POSSIBLE ORIGINS OF OBLIQUE-INCIDENCE ANISOTROPY

Some geometric anisotropy in crystallite size, shape, habit or position may conceivably be the cause of the magnetic anisotropy. To investigate this possibility, Permalloy films deposited at normal and oblique incidence on glass were observed by reflection electron diffraction; films deposited at normal and oblique incidence on thin carbon substrates were observed by transmission electron diffraction and electron microscopy. Electron microscopy revealed that films of compositions near 80% Ni and 20% Fe several hundred angstroms thick consist of crystallites several hundred angstroms in diameter; it may be concluded that, within the accuracy of the electron diffraction measurements made, the crystallites take the bulk Ni lattice. No differences in results for films deposited at normal or at oblique incidence have, however, yet been noted, and the patterns or pictures have revealed no directional anisotropy in structure.

It is well known that thin films contain high concentrations of structural defects.[10] It is possible that the geometric factors involved in an oblique-incidence evaporation cause a geometric anisotropy in the distribution of such defects, which in turn gives rise to magnetic anisotropy. To test this hypothesis, thin epitaxially deposited Permalloy films were examined by transmission electron diffraction. The patterns from both oblique and normal incidence films contained the satellite spots associated with repeated twinning of the lattice.[11] An anisotropy in the oblique-incidence film patterns has, however, not yet been detected; the patterns did not essentially differ from those for normal-incidence films.

Another possible origin of the oblique-incidence effect is the agglomeration of Permalloy crystallites at various sites in the film into groups having anisotropic geometric shapes which would, in turn, give rise to magnetic anisotropy. Such a mechanism would be consistent with the phenomenological model of oblique-incidence anisotropy presented by Smith *et al.*[8] Such agglomeration of crystallites has not yet been observed by electron microscopy. Furthermore, it is unlikely that the oblique-incidence effect is due to some simple small-scale shadowing effect since this phenomenon occurs about equally well for a wide variety of substrates having very different surface roughnesses. Magnetic anisotropy has, on the other hand, been observed in films made by evaporation of Permalloy at normal incidence on films of aluminum, gold, silver, or platinum which had previously been deposited at oblique incidence. The optical and resistive anisotropy shown by many non-magnetic metal films when deposited at oblique incidence[8] was somewhat transmitted to the overlying Permalloy films; the easiest way to explain such a transmission is in terms of the agglomeration mechanism mentioned above.

Heidenreich and Reynolds[7] suggest that the presence of oxygen is necessary for oblique-incidence anisotropy. To check this hypothesis, several oblique-incidence films having values of H_k of several hundred oersteds were subjected to various annealing treatments. Drastic decreases in H_k were found when the films were annealed in various gases that contained traces of oxygen, but little changes in H_k were observed for films annealed in vacuum. Reflection electron diffraction revealed the presence of oxide on those films subjected to long anneals or high temperature anneals in gases containing oxygen.

As a further examination of the role of oxygen, during the evaporation of Permalloy at normal incidence with no applied field, oxygen was slowly leaked into the vacuum system so that the oxygen stream was directed towards the substrate. The values of H_k and wall coercive force, H_c, were in the range to be expected for oblique-incidence films. The same experiment performed with argon instead of oxygen yielded films having values of H_k and H_c which would be expected for normal-incidence films.

Contrary to Heidenreich's[7] results, on the other hand, magnetic anisotropy was found for oblique-incidence Permalloy films whose reflection electron diffraction patterns showed no trace of oriented oxide.

[9] W. M. H. Sachtler, G. Dorgelo, and W. van der Knaap, J. chim. phys. **51**, 491 (1954).

[10] G. A. Bassett, J. W. Menter, and D. W. Pashley, International Conference on Structure and Properties of Thin Films, Lake George, New York, September 9–11, 1959 (to be published).

[11] H. Raether, *Handbuch der Physik* (Springer Verlag, Berlin, 1957) Vol. 32, p. 443.

Magnetic Anisotropy in Evaporated Iron Films

E. W. Pugh, J. Matisoo, D. E. Speliotis, and E. L. Boyd
IBM Research Laboratory, Poughkeepsie, New York

A torque method has been used to measure the magnetic anisotropy of iron films deposited from the vapor at various incident angles on glass substrates. The anisotropy is found to be largest in films prepared with large incident angles and low substrate temperatures. A theoretical calculation of the anisotropy expected in an iron film with a [111] fiber axis has been made for various angles of the fiber axis and as a function of stress in the film. The theoretically calculated values are not only an order of magnitude lower than most measured anisotropies, but they always have the worng sign. Iron films deposited on rocksalt exhibit anisotropies before and after removal from the substrate which indicate that the anisotropy is affected by cold-working but not by stress relief. It is concluded that the magnetic anisotropy in iron films is primarily related to the faulted regions formed in the films during deposition and not to stress or the proposed fiber axis structure.

A RELATIONSHIP between the angle of incidence of the vapor stream during deposition and the magnetic anisotropy of the resultant evaporated films was first reported in permalloy films[1]; however, the most detailed study of this effect has been made in iron films.[2] This later work suggests that a tilt toward the vapor source of the [111] texture axis of iron films combined with a suitable anisotropic stress yields a magnetic anisotropy of the correct order of magnitude. Such a texture axis tilt has been reported by Evans and Wilman[3] while the anisotropic stress was measured in an evaporated iron film by Finegan and Hoffman.[4] While such a model might be useful in iron, its applicability to Permalloy is highly questionable in view of Smith's observation that the direction of the easy axis in Permalloy films relative to the vapor source is the same whether a composition of negative or positive magnetostriction is chosen.[5] Further opposition to the texture axis model has been given recently by Heidenreich[6] who reports that the fiber axis observed in either iron or Permalloy films by reflection electron diffraction is actually an oxide structure and that transmission electron diffraction fails to reveal any texture axis in the metal. In contrast to this, however, recent x-ray diffraction work of Verderber indicates the existance of a [111] or a [113] fiber axis in Permalloy films representing up to 50% of the material.[7] In view of the somewhat confusing picture presented by the above references a detailed investigation of the angle of incidence effect and its possible relation of a fiber axis structure seems in order.

A series of iron films approximately 1000 A thick have been prepared in a vacuum of less than 10^{-6} mm Hg by vapor deposition from a tungsten source. The source distance from the film was fixed at five inches while the incident angle was varied from 0° to 40° and the substrate temperature ranged from 30°C to 350°C. The magnetic anisotropy of these films was then determined by a torque balance and the resulting family of curves is shown in Fig. 1. It will be noted that the largest anisotropies occur at the large incident angles and low temperatures. The scatter is not bad considering the fact that the films were made in separate evaporations extending over several months.

FIBER AXIS MODEL

To see how the measured anisotropies would compare with theoretically predicted values, the calculation of

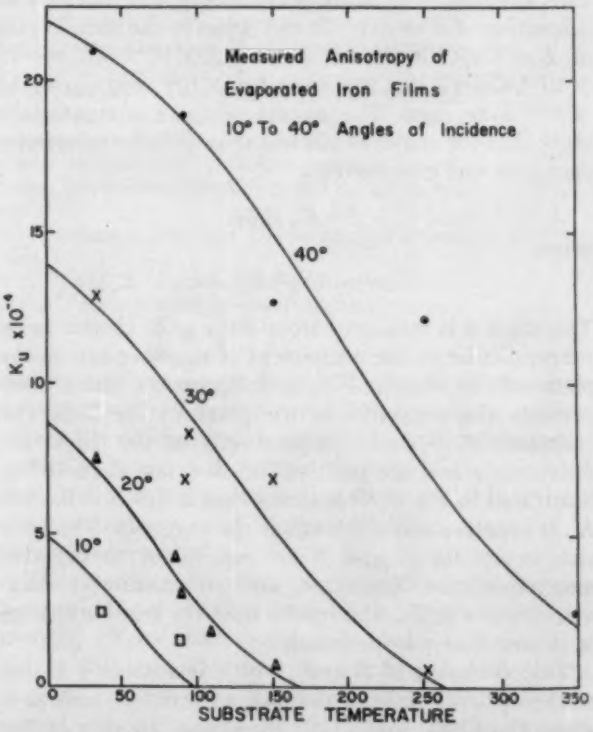

FIG. 1. Uniaxial anisotropy in iron films as a function of substrate temperature and incident angle of the vapor stream during deposition. The positive values for K_u indicate that the easy axis is perpendicular to the vapor stream.

[1] D. O. Smith, J. Appl. Phys. **30**, 264S (1958).
[2] T. G. Knorr and R. W. Hoffman, Phys. Rev. **113**, 1039 (1959).
[3] D. M. Evans and H. Wilman, Acta. Cryst. **5**, 731 (1952).
[4] J. D. Finegan and R. W. Hoffman, J. Appl. Phys. **30**, 597 (1959).
[5] D. O. Smith (private communication).
[6] R. D. Heidenreich, International Conference on Structure and properties of Thin Films, Bolton Landing, New York, September 9–11, 1959.
[7] R. R. Verderber, J. Appl. Phys. **30**, 1359 (1959).

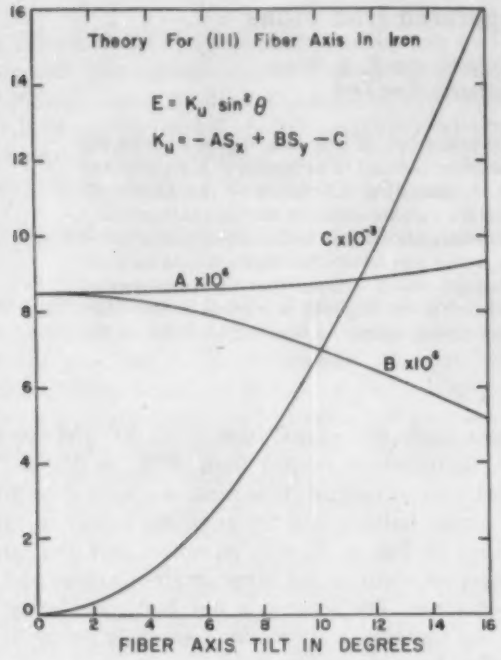

FIG. 2. Result of calculation of magnetic anisotropy in an iron film with a [111] fiber axis inclinded from the normal. S_x and S_y represent strains in the film perpendicular and parallel to the component of the fiber axis in the plane of the film.

Knorr and Hoffman was programed on a computer and computations were made of the magnetic anisotropy as a function of fiber axis tilt and stress in the film. Values of $K_1=4.8\times10^5$, $K_2=0$, $\lambda_{100}=+20\times10^{-6}$, $\lambda_{111}=-19\times10^{-6}$, $C_{11}=2.29\times10^{12}$, $C_{12}=1.34\times10^{12}$, and $C_{44}=1.14\times10^{12}$ were used. The results of these computations show that for angles of tilt less than 16° the anisotropy energy is well expressed by

$$E=K_u\sin^2\theta,$$

where

$$K_u=-AS_x+BS_y-C.$$

The angle θ is measured from the x axis, chosen to be perpendicular to the component of the fiber axis in the plane of the film, and S_x and S_y are the stress components also measured in the plane of the film. The constants A, B, and C depend only on the tilt of the fiber axis γ and are positive for all γ less than 16° as illustrated in Fig. 2. This shows that if $S_x=S_y=0$, then K_u is negative and the y axis is the easy axis. The positive values for A and B are equivalent to negative magnetostrictive constants, and an anisotropic magnetostriction in the film results from the relative change in A and B as γ is increased.

This deviation of B and A with increasing γ is due to the opposite signs of the magnetostrictive constants along the [100] and [111] directions. In view of the large differences between λ_{100} and λ_{111} it is surprising how well the effect of strain in the fiber axis model could be approximated by the simple isotropic model in which the approximation $\lambda_{100}=\lambda_{111}=\lambda_s$ is made. The effective magnetostrictive constant when $\gamma=0$ is $\lambda_{eff}=-5.7\times10^{-6}$ as compared to $\lambda_s=-7\times10^{-6}$ which is usually assumed for isotropic magnetostriction in iron.

Comparing the calculated K_u with the experimentally determined values, it is immediately evident that, for $S_x=S_y=0$ and the largest tilt angle reported of $\gamma=10°$, a theoretical value of $K_u=-7\times10^3$ is obtained, which is an order of magnitude less than most measured values. Even more important, theory predicts the y axis to be easy while experiment in all cases gives the x axis. Furthermore, since $A>B$, any isotropic stress would make K_u even more negative. Only a much larger stress in the y than the x direction could account for the positive K_u in a manner consistent with the fiber axis model and this is in conflict with the anisotropic stresses $S_x=8.0\times10^9$ and $S_y=6.4\times10^9$ dyne/cm² as reported by Finegan and Hoffman in a film evaporated at an incident angle.

SIMPLE STRESS MODEL

The possibility that a macroscopic anisotropic stress is responsible for the observed anisotropy in films has been completely eliminated by a series of experiments in which iron films were deposited on rocksalt below a temperature where significant epitaxy takes place. The values for K_u as a function of angle and substrate temperature were approximately the same as those obtained for films deposited on glass. The films were then floated off the NaCl in water and picked up on glass slides. In this manner any net macroscopic strain in the film resulting from the deposition would be removed. The direction of the easy axis was unchanged in all cases indicating that the major source of magnetic anisotropy is largely independent of macroscopic stress. It has been noted, however, that the change in magnitude of the anisotropy of the film is strongly affected by the amount of cold-working the film undergoes during the process of floating-off the rocksalt. When this is accomplished without bending the film by more than 20°, the anisotropy generally decreases by less than 30%; however, if the film bending is closer to 90°, changes as great as an 80% decrease or a 50% increase have been observed. Since a decrease in anisotropy is observed much more often than an increase, the possibility has been considered that at least this small portion is due to simple relief of macroscopic stress. However, because the greater stress has been measured to be in the x direction, stress relief could reduce anisotropy only if the effective magnetostriction of the films was positive; and torque measurements on our iron films as a function of applied strain clearly indicate that the magnetostrictive constant is negative.

THE ROLE OF IMPERFECTIONS

The above theoretical considerations and experimental work eliminate both the fiber axis and macroscopic strain as the major source of anisotropy in iron

films evaporated at an angle of incidence. The remaining possibilities are microscopic strains associated with imperfections in the films or with the imperfections themselves, and recent work in nickel and Permalloy films by two of the authors suggests that the latter of these is more likely.[8] In this work the easy axis of pure nickel films has been observed to be parallel to the vapor source direction rather than perpendicular as is observed for iron and Permalloy; and since the magnetostrictive constant is negative in both nickel and iron, this difference in easy axis direction would not be anticipated on a microscopic stress model.

The apparent importance of (111) faults for magnetic annealing in Perminvar and Permalloy[9] suggests that the important imperfections in the iron films may be the faulted regions between the crystallites. An anisotropy due to faults would intuitively be proportional to the difference of the faulted area in the xz plane to that in the yz plane. This difference is related to the shape of the crystallites, which we will assume to be controlled by the angle of incidence, and would be inversely proportional to the crystallite size. The decrease in K_u with increasing temperature is in good qualitative agreement with this model because of the known increase in crystallite size and film perfection with increasing substrate temperature during deposition. The importance of imperfections in the film is further evidenced by the effect of cold-working during removal from the substrate.

[8] E. W. Pugh and E. L. Boyd, IBM J. Research Develop. (to be published in Thin Films Issue, April, 1960).

[9] R. D. Heidenreich, E. A. Nesbitt, and R. D. Burbank, J. Appl. Phys. **30**, 995 (1959); E. A. Nesbitt and R. D. Heidenreich, J. Appl. Phys. **30**, 1000 (1959); E. A. Nesbitt, R. D. Heidenreich, and A. J. Williams, Magnetics Conference, 1959.

JOURNAL OF APPLIED PHYSICS SUPPLEMENT TO VOL. 31, NO. 5 MAY, 1960

Anisotropy and Inversion in Permalloy Films*

D. O. Smith, E. E. Huber, Jr., M. S. Cohen, and G. P. Weiss†
Lincoln Laboratory, Massachusetts Institute of Technology, Lexington 73, Massachusetts

A phenomenological model of field-induced and oblique-incidence anisotropy in Permalloy films is proposed. It is assumed that the field-induced structure does not introduce any local spatial dispersion in the macroscopic magnetization **M**; the opposite is assumed for oblique-incidence structure. In addition it is assumed that the oblique-incidence dispersion is anisotropic, being least when **M** is perpendicular to the depositing beam.

Support for the model comes from anisotropies, found for oblique-incidence films only, in the following measurements: resonance line width, transmission of polarized light, and resistivity. A primary success of the model is the prediction of a correlation between anisotropy and inversion ($H_w/H_k>1$). Inverted films can be made by crossing the field-induced and oblique-incidence anisotropies at 90°. Such films exhibit a "locked" state in which opposite rotation of **M** in local regions occurs; this implies centers of spatial dispersion and provides the connection with oblique-incidence anisotropy.

A method of inducing anisotropy by means of a moving substrate is described. The assumption of local dispersion is shown to apply to this type of anisotropy also.

Finally, a guide to understanding the interdependence of H_k and H_w is given in terms of the anisotropy model: field-induced structure does not have any effect on H_w, while oblique-incidence structure can be a primary determinant for H_w.

I. INTRODUCTION

ANISOTROPY can be induced in Permalloy films which are vacuum deposited onto glass substrates by two methods: (1) deposition in a unidirectional magnetic field in a vapor beam which is normal to the substrate,[1] and (2) deposition in a vapor beam which forms an oblique angle with the substrate.[2] The structure underlying these anisotropies is at present unknown with certainty. However, inference from a number of macroscopic observations allows the construction of a phenomenological model which serves not only to relate these observations but also to specify important characteristics which the underlying structure must possess. A primary success of the model is the prediction of a connection between oblique-incidence anisotropy and "inverted" films; inversion is defined below.

The ratio of wall coercive force to rotational coercive force H_w/H_k is usually about 0.5, although values approaching 1 are often found. Since rotational switching is very fast compared to wall switching, it follows that at 1000 cps the case $H_w/H_k>1$ should never be observed, since the film should switch by rotation at $H=H_k$ before the field H_w is obtained. However, experimentally it is found that films prepared in special ways do exhibit $H_w/H_k>1$, and hence additional fac-

* The work reported in this paper was performed by Lincoln Laboratory, a center for research operated by Massachusetts Institute of Technology with the joint support of the U. S. Army, Navy, and Air Force.

† Staff Members.

[1] M. S. Blois, Jr., J. Appl. Phys. **26**, 975 (1955).

[2] D. O. Smith, J. Appl. Phys. **30**, 264S (1959).

tors must be entering to cause a "locking" of the rotational state which prevents rotation at H_k. Films of this type are designated inverted, referring to the behavior of the H_w/H_k ratio. Inverted films have been previously reported by Kreissman, Belson, and Edelman,[3] and Wolf, Katz, and Brain[4]; locking has not been considered by these authors.

It is the purpose of this paper to describe a model which relates anisotropy to inversion and also to describe additional experimental results which either support the model or are at least consistent with it. A more detailed exposition will be given in a later publication.

II. PHENOMENOLOGICAL ANISOTROPY MODEL

It is assumed that no spatial dispersion in **M** is associated with the field-induced structure and that at all points the local and average directions of **M** would be the same.

A very different assumption is made regarding oblique-incidence structure. Here it is assumed that the local and average directions of **M** differ greatly, i.e., there is local spatial dispersion of **M** around oblique-incidence structure. Since the film is magnetically anisotropic, it is further assumed that the amount of dispersion of **M** near such structure depends on the average orientation of **M**, being least when **M** is perpendicular to the depositing beam.

An example of a structure which illustrates these ideas is a void in the shape of a needle. For the average **M** parallel to the needle local dispersion would be slight; however, for **M** perpendicular to the needle large demagnetizing effects set in and severe local dispersion will result. However, a simple representation of the source of oblique-incidence anisotropy as a collection of oriented demagnetizing needles is not able to explain in a straightforward way all of the experimental observations, particularly the compositional dependence of the effect.

III. ANISOTROPIC LINE WIDTH, BIREFRINGENCE, AND ANISOTROPIC RESISTIVITY

Direct support for needle-like dispersion centers is given by resonance line-width measurements for different orientations of the dc field in the plane of the film. An example is provided by a film made at a depositing-beam incidence of 30° from the normal and measured at 900 Mc. The line width with the dc field parallel to the easy axis was 6 oe; perpendicular to the easy axis the line width was 40 oe. This pronounced difference is interpreted as being due to the difference in internal demagnetizing fields parallel and perpendicular to a needle-like dispersion center.

Experiments with polarized light and resistivity measurements give support to the idea that field-induced and oblique-incidence anisotropies are due to different structural features. Von Kundt (1886)[5] studied the transmission of polarized light through sputtered films of Pt, Pd, Au, Ag, Fe, and Cu. The plane of polarization was rotated and a slight ellipticity was introduced. The significant point is that the effect was found to be anisotropic in the plane of the film; a reference axis related to the angle-of-incidence of the depositing beam was noted. Preliminary experiments have established this effect in oblique-incidence Permalloy films; no such effect has been observed for normal-incidence deposition in a magnetic field.

Normal incidence films have isotropic resistivity while oblique-incidence yields anisotropic resistivity. As an example 80% Ni-20% Fe Permalloy was evaporated at 45° incidence in narrow strips parallel and perpendicular to the vapor beam. The resistance of the perpendicular strips was about 75% of those parallel to the beam. Thus, the low resistance and easy magnetic directions coincide, as is expected from the model as exemplified by the idea of demagnetizing needles. Anisotropic resistance in oblique-incidence nickel films was first reported by Maurain (1906).[6]

IV. INVERTED FILMS

Insight into the locked state of inverted films can be obtained from Bitter pattern studies. For **H** antiparallel to **M** in a film previously saturated in the easy direction, the pattern which appears is sketched in Fig. 1(a). Disconnected line segments of colloid form perpendicular to the easy axis. This is interpreted as showing that **M** rotates in opposite directions on either side of these segments, as indicated in Fig. 1(a). Interaction between oppositely directed regions inhibits further rotation, and the film is locked until walls enter and complete the reversal. A photograph is shown in Fig. 1(b); the reversibility of locking is shown in Fig. 1(c). Similar Bitter patterns have been obtained for iron films by Fuller and Rubinstein.[7]

Locking suggests that with no field present dispersion centers exist in the film around which there is local distortion in the direction of **M**; application of a field enhances this distortion, leading to the locked state. Connection can now be made with the anisotropy model. Assume that the dispersion centers postulated for oblique-incidence anisotropy can also operate as the dispersion centers required for locking. Further consideration shows that for this to true it is necessary to cross the field-induced and oblique-incidence axes, optimally at 90°. Example of such crossed-axis inverted films have been made in accordance with this prediction.

Inverted films can be made in additional ways which do not necessarily involve oblique-incidence anisotropy.

[3] C. J. Kreissman, H. S. Belson and F. H. Edelman, J. Appl. Phys. **30**, 262S (1959).
[4] I. W. Wolf, H. W. Katz, and A. E. Brain, Proceedings of the 1959 Electronic Components Conference, Philadelphia, Pennsylvania, (May 6–8, 1959), p. 15.
[5] A. von Kundt, Ann. Physik **27**, 59 (1886).
[6] C. Maurain, Compt. rend. **142**, 870 (1906).
[7] H. W. Fuller and H. Rubinstein, J. Appl. Phys. **30**, 84S (1959).

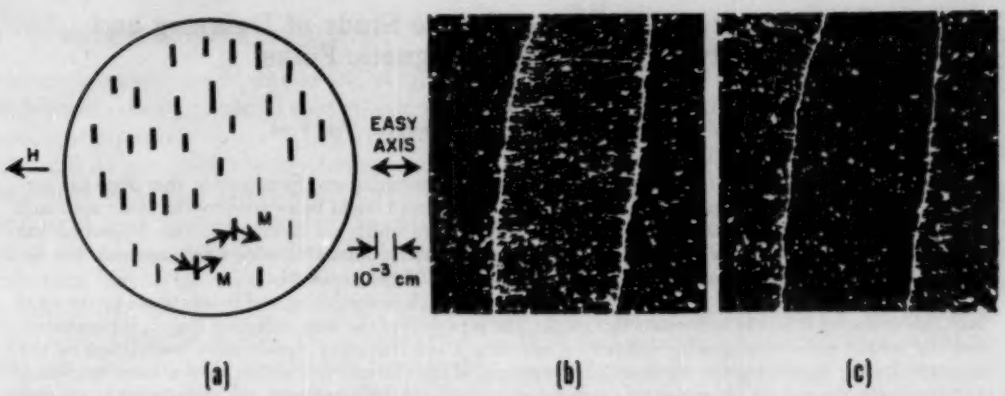

FIG. 1 (a) Sketch of the Bitter pattern of an inverted film in the "locked" state. Opposite rotation of M in local adjacent regions is postulated. (b) Locked and reversed regions of a film after walls have moved part way through the film. (c) Same as (b) but with the applied field reversed; this demonstrates the reversibility of locking.

Examples include: (1) slow evaporation (~1000 A/hour) onto "normally" cleaned glass substrates[8]; (2) fast (~1000 A/minute) or slow evaporation onto "specially" cleaned substrates[9]; (3) electrodeposition onto glass substrates which have an underlayer of sputtered Au when the sputtering voltage and pressure are held within certain limits.[4] A full discussion of these results cannot be given here, nor is the problem completely understood.

V. MOVING-SUBSTRATE ANISOTROPY

Magnetic anisotropy can be induced by deposition onto a substrate which is moving slowly back and forth behind a narrow linear slit which serves as an aperture for the depositing beam; an easy axis develops perpendicular to the direction of motion. The maximum aperture angle has been kept below 2° but it is still unclear if the effect is not simply a subtle manifestation of oblique-incidence anisotropy; alternatively, the sequential exposure to the depositing beam may be the important factor.

The same dispersive assumptions applied to oblique-incidence anisotropy are to be applied to moving-substrate anisotropy as demonstrated by the fact that if field-induced and moving substrate anisotropies are crossed at 90°, inverted films result.[8]

VI. INTERDEPENDENCE OF H_k AND H_w

Interdependence of H_w and H_k is a complex question and films have been made which show either slight or great interdependence. A guide to understanding is the assumed differences in field-induced and oblique-incidence structures. There will be no first-order influence on H_w coming from the nondispersive field-induced structure; however, the dispersion centers generated by oblique-incidence can be expected to increase H_w.

VII. COMPOSITIONAL DEPENDENCE

A complicating feature is the compositional dependence of oblique-incidence anisotropy. For a nickel content greater than ~90% the easy axis is parallel to the beam. The simplest form of the model postulates demagnetizing needles perpendicular to the beam. This orientation is dictated by the presence of large magnetic anisotropy at 81% Ni, the point of zero magnetostriction constant λ(λ positive for Ni<81%, negative for Ni>81%). A reasonable extension of the model to include the compositional shift of the easy axis is to postulate a strain field around the needles such that for negative λ the resultant magnetoelastic easy axis is perpendicular to the long needle axis. Since λ increases negatively with increasing nickel, this magnetoelastic component is presumed to eventually exceed the demagnetizing component and the easy axis changes direction.

VIII. CONCLUSION

A brief outline of a wide range of experimental observations on Permalloy films has been given, along with a unifying conception regarding the structure of these films. It is clear that the outstanding problem is an exact specification of the structures involved in the various anisotropies under consideration.

Note added in proof. The extreme anisotropy in resonance line-width reported in Section III has been shown to be due to slight sample misalignment; the anisotropy, if it exists, is only of the order of 20%. Other resonance behavior not reported here continue to support the dispersive models of anisotropy and inversion as described. Difficulty has been encountered in reproducing the experiments regarding crossed-axis inverted films; thus a simple and consistent connection between oblique-incidence anisotropy and inversion is in doubt.

[8] T. S. Crowther, M. I. T. Lincoln Laboratory (private communication).

[9] Normal substrate cleaning consists of washing in detergent (e.g., Alconox) and rinsing in distilled water agitated by ultrasound. If the detergent wash is followed by dipping in stannous chloride ($SnCl_2$) and then finally rinsed in distilled water, inverted films often result. This is also the case if certain detergents (e.g., Aerosol) are used, omitting the $SnCl_2$ dip.

Microcalorimetric Technique for the Study of Damping and Hysteresis in Ferromagnetic Films

J. R. MAYFIELD
IBM Research Laboratory, Poughkeepsie, New York

Experience with experimental techniques for the study of damping and hysteresis in thin films has suggested that many of the difficulties and complications encountered might be avoided by the direct approach of measuring the heat generated by the irreversible processes which are of interest. This suggestion has led to the development of a simple and reliable microcalorimetric apparatus with which accurate loss determinations may be made over a frequency range of about 100 cps to 100 Mc.

The loss detector employed is a thin-film thermocouple which developes an emf proportional to the total heat flux emerging from the ferromagnetic sample. The zero drift of the heat-detecting system is eliminated, and the overall noise level greatly reduced by imposing a low-frequency square-wave modulation on the magnetic losses, amplifying the resultant ac component of the thermal emf with a narrow-band amplifier, and rectifying the output by means of a commutator phase-synchronized with the modulator. It appears that losses as small as 10^6 erg/sec per cc of sample volume are readily detectable. The thermal method thus has a degree of sensitivity which compares favorably with that of other experimental techniques, and has the added advantage of providing a direct measure of energy loss.

I. INTRODUCTION

A MICROCALORIMETRIC method has been developed to measure energy losses in ferromagnetic films under a variety of experimental conditions including domain-wall hysteresis, rotational hysteresis, and VHF resonance. The loss detector is a thermocouple formed by evaporating two strip-shaped films of dissimilar metals onto the same substrate which supports the ferromagnetic film. These strips overlap on the surface of the sample film to form the "hot" junction (see Fig. 1). The strips are continued over the edge of the substrate and on to the bare side of the substrate, where they are connected to output leads by means of a silver conducting paint.

The largest temperature differences between different parts of the sample-detector assembly, or between any part of this assembly and its immediate surroundings, are very small compared with the absolute ambient temperature, and the modulations which are imposed on these differences are still smaller (less than 0.01°C). The heat flux between any two parts of the sample-detector assembly or its surroundings is therefore proportional to the temperature difference between them, regardless of the modes of heat transfer involved, and it is readily seen that the amplitude of the modulated thermal emf generated by the thermocouple should be directly proportional to the power which the rf magnetic field dissipates in the sample. The loss detector's response to a given rate of dissipation is unaffected by the magnetic field conditions giving rise to this dissipation, so that a change in the field conditions does not necessitate any rebalancing, phase adjustment, or recalibration of the detecting system.

Functionally, the system used in our experiments is closely analogous to an infra-red or microwave absorption spectrometer, and might be referred to as a "microcalorimetric loss (MCL) spectrometer." A simplified block diagram of this instrument is shown in Fig. 1. An 8-cps square wave of current provided by a constant-speed motor-driven switch controls two mercury-contact relays. One of these relays chops the radio-frequency magnetic field applied to the sample at a frequency of 8-cps, thus imposing a square-wave modulation on the ferromagnetic energy losses, while the other acts as a synchronous rectifier (commutator) for the 8-cps signal obtained by amplifying the output of the loss detector. The output from the commutating relay, smoothed by a ripple filter, provides a dc signal several volts in amplitude representing the losses. To record the losses as a function of the magnetic bias field, or as a function of the rf field amplitude, the gang switch is placed in position *A* or *B*, respectively. The slowly-swept control voltage supplied by a motor-driven helipot then controls the desired field parameter, and a voltage representing the instantaneous value of this parameter is supplied to the *X* input of the recorder. The same basic system is used for all types of loss measurements; in order to study rotational hysteresis, or to make resonance measurements at frequencies above 10 mc, the system shown in Fig. 1 is modified by making appropriate substitutions for the circuits and transmission lines controlled by the chopping relay.

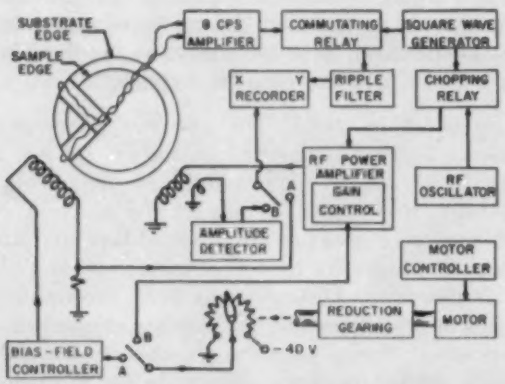

FIG. 1. Block diagram of MCL spectrometer.

II. THERMOCOUPLE DESIGN

The thermocouple strips are of copper and of an alloy of 2 atomic percent cobalt in gold. These metals give a large thermoelectric power (43 μv/°C), are convenient to evaporate, and do not exhibit either ferromagnetism or an anomalously large Hall coefficient. There is also some advantage in using copper as one of the materials in that one of the two points of connection to the external circuit then has no thermoelectric power.

In order that differential heating of the hot and cold junctions by eddy currents within the thermocouple itself should not produce any appreciable signal, the thermocouple strips must not be a great deal thicker than the ferromagnetic sample. On the other hand, these strips should be thick enough to very effectively short-circuit any galvanomagnetic potential differences along the surface of the sample. Experience shows that strip thicknesses from 1000 A to 10 000 A are quite satisfactory.

To avoid an unnecessarily high noise level, care must be taken to arrange the thermocouple strips and connecting wires so as to form a completely noninductive circuit. If this is not done, sharp transients of both **H** and **M**, which occur each time the rf field is turned on or off, induce in the thermocouple circuit signals containing a component with frequency equal to the chopping frequency. Since the phase of the rf field at the instant it is chopped is completely random, there is a random variation in the amplitudes of successive transients, and the voltages induced are finally recorded as noise.

A simplified configuration in which the evaporated copper strip was omitted and the hot junction was made by attaching one of the copper output leads directly to the "hot" end of the gold-cobalt strip was found to be unsatisfactory. Except in those cases where an insulating film of SiO was interposed between the sample and the thermocouple, large "spurious" signals were developed whenever there was any appreciable magnetic bias field normal to the plane of the sample. The manner in which the magnitude and sense of these objectionable signals have been observed to depend on various experimental conditions can be consistently explained in terms of the Nernst effect associated with the ferromagnetic film. However, there is also the possibility of explaining the observations on the basis of an interaction between the Hall and magnetoresistive effects, such as has been discussed by Seavey and Tannenwald.[1] Whatever the origin of the undesired emf, it appears to be effectively cancelled out in the conventional thermocouple design employing two opposed thermocouple strips.

[1] M. H. Seavey, Jr., and P. E. Tannenwald, J. Appl. Phys. **30**, 227S (1959).

III. PERFORMANCE OF THE APPARATUS

The ultimate loss sensitivity of the MCL spectrometer is determined by the electrical noise level, the thermoelectric power of the thermocouple, and the efficiency with which the loss modulations are converted to temperature variations between the thermocouple junctions. With the present noise level, equivalent to 0.0025 μv average peak-to-peak noise in the thermocouple circuit, and a thermoelectric power of 43 μv/°C, the ultimate temperature sensitivity is 6×10^{-5}°C. In measurements performed thus far, losses of 10^7 erg/sec per cc of sample were detectable, and indications are that the conversion efficiency of the sample-detector assembly can be improved sufficiently to permit detection of 10^6 erg/sec-cc or even substantially less. For a typical permalloy film ($H_c=3$ oe, $M=800$ erg/cc-oe), the latter quantity corresponds to about 1% of the longitudinal major-loop hysteresis loss at 100 cps, or to about 1% of the peak rotational hysteresis loss[2] at 500 cps. With respect to the sensitivity obtainable in resonance experiments in the frequency range 10 to 100 mc, the microcalorimetric technique appears comparable with methods employing an inductive pick-up loop as the detector.

To calibrate the MCL spectrometer, a hysteresis loop plotter, for which the flux sensitivity for samples of a given area has been accurately determined, is used to determine the energy loss per second in a particular sample when it is tracing a major longitudinal hysteresis loop at some frequency f_0. The sample is then allowed to describe the same hysteresis cycle, at the frequency f_0, in the MCL spectrometer. The ratio of the deflection recorded by the spectrometer to the dissipation rate deduced from the loop-plotter data furnishes the desired calibration factor. For some detector-sample assemblies, the equivalent of this procedure has been carried out at a number of frequencies (and therefore, a number of dissipation rates) and the expected linearity of the calibration has been verified.

ACKNOWLEDGMENTS

The author wishes to thank E. W. Pugh for his continued encouragement and helpful criticism and A. Hoag for his valuable assistance in every phase of the experimental work.

[2] J. R. Mayfield, J. Appl. Phys. **30**, 256S (1959).

Domain Wall Velocities in Thin Iron-Nickel Films

N. C. Ford, Jr.
IBM Research Laboratory, Poughkeepsie, New York

An apparatus based on the Kerr magneto-optical effect has been used to measure the velocity of domain walls in thin iron-nickel films. Polarized light, after being reflected by a film, is analyzed and detected by a photomultiplier tube. The slope of an oscilloscope trace resulting from the photomultiplier signal is directly proportional to the domain wall velocity, as the wall traverses a light spot of known size. Wall velocities are found to be well described by an equation of the form $v=m(H-H_0)$, where m is the wall mobility and $H-H_0$ the excess applied field. Measurements have been made on films varying in thickness from 4000 A to 700 A with corresponding mobilities of 0.5×10^4 cm/sec-oe for the thicker film and 4.9×10^4 cm/sec-oe for the thinner film. The wall mobility is found to be inversely proportional to $B_s\sigma d$ where σ is the electrical conductivity and d the film thickness. This is the dependence that is predicted on the basis of a simple eddy current model indicating that, even in films as thin as 700 A, the dominant loss mechanism in wall motion is caused by eddy currents rather than intrinsic damping of the Landau-Lifshitz type.

MEASUREMENTS of domain wall velocities have been reported in the literature for both nonconducting[1,2] and conducting[3–5] ferromagnetic materials. In nonconducting materials, these velocities are believed to be limited by an intrinsic damping mechanism of the Landau-Lifshitz type. In this case, the wall mobility, m, is given by the expression[1]

$$\frac{v}{H-H_0}=m=\frac{B_s\gamma^2 l}{4\pi\lambda}, \tag{1}$$

where v is the wall velocity, $H-H_0$ the excess applied field, γ the gyromagnetic ratio, B_s the saturation flux density, λ the relaxation frequency, and l the domain wall thickness. On the other hand, velocities in conducting materials agree with the theory based on eddy current damping which may be expressed as[6]

$$m=\frac{\pi^2 c^2}{32B_s\sigma d\sum_{n=1}^{\infty}(2n-1)^{-2}}, \tag{2}$$

where σ is the electrical conductivity and d the film thickness. By inserting numerical values for permalloy films into these equations, we find that $m=(5.5\times10^{-2})/\lambda$ cm/sec-oe for the first case and $m=(2.7\times10^{20})/B_s\sigma d$ cm/sec-oe for the second. In conducting films that are sufficiently thin, however, there should be an opportunity to observe both types of damping because the eddy current damped wall mobilities are inversely proportional to film thickness while the thickness dependence of wall mobilities limited by intrinsic damping is determined by the small variation of l with d. Since l is approximately[7] proportional to $d^{\frac{1}{2}}$, the effects due to the two types of damping are easily separable. In the remainder of this paper we shall neglect the thickness dependence of intrinsic damping losses because it is negligible over the range considered. With this approximation, the wall mobility is given by the expression

$$m=1/[a\lambda+b(B_s\sigma d)], \tag{3}$$

where a and b are related to Eqs. 1 and 2 such that m reduces to (1) for very thin films and (2) for very thick films. This paper reports wall velocities measured in iron-nickel films from 4000 A to 700 A thick in an attempt to learn how thin a film must be before intrinsic damping is important.

Kerr magneto-optical apparatus was used to make the measurements in a manner similar to that used by Lee and Callaby.[5] The Kerr apparatus has two advantages over other techniques: First, the portion of a film sample contributing to the data may be controlled by adjusting the size of the light spot, and second the domain patterns may be observed visually to assure that no more than one wall is present in the light spot during a magnetization reversal.

This apparatus has a 100-w zirconium lamp, the light from which is partially collimated and then passed through an adjustable mask with a glass reticle for measuring purposes. A second lens serves the dual purpose of focusing an image of the mask on the film sample and completing the collimation of the light beam. The light is then polarized, reflected from the film, and analyzed. A long focal length objective lens together with an eyepiece and a prism system form a telescope with a magnification adjustable from 20 to 100 times for visual observation of the domain pattern. A movable mirror allows either visual observation or photo-multiplier sensing for high speed measurements of changes of light intensity.

In order to make domain wall velocity measurements, a fast rise time field pulse from a small helmholtz coil is used to cause the magnetization to reverse by domain wall motion. As a domain wall traverses the Kerr light spot, the anode current from a photomultiplier tube placed in the analyzed light beam changes from one

[1] J. K. Galt, Phys. Rev. **85**, 664 (1952).
[2] K. H. Stewart, Proc. Phys. Soc. (London) **A63**, 761 (1950).
[3] K. J. Sixtus and L. Tonks, Phys. Rev. **37**, 930 (1931).
[4] D. S. Rodbell and C. P. Bean, Phys. Rev. **103**, 886 (1956).
[5] E. W. Lee and D. R. Callaby, Nature **182**, 254 (1958).
[6] H. J. Williams, W. Shockley, and C. Kittel, Phys. Rev. **80**, 1090 (1950).
[7] L. Néel, J. phys. radium **17**, 250 (1956).

steady state value to another with a slope that is proportional to the wall velocity. This slope is easily measured with an oscilloscope and may be plotted as a function of the applied field to determine the wall mobility.

The use of a photomultiplier tube as a sensing element leads to a noise level that is proportional to the square root of the frequency range utilized at the output of the tube. In other words, the noise is proportional to the square root of the reciprocal of the shortest time to be measured. The signal to noise ratio, therefore, may be improved by making the light spot wider in order to increase the time of transit of a domain wall. It may also be improved by increasing the total amount of light signal by increasing the height of the light spot.

The light spot used in most measurements was 2 mm wide and about 5 mm high, and was limited to this size by the necessity of having a single wall traverse the light spot. That this occurred was assured by visual observations before each measurement. To further complicate the situation, the domain patterns observed for slowly increasing fields are frequently very different from those observed when the applied field is in the form of pulses. Consequently, a region of the film was selected for the experiment such that a single wall would move across the light spot under the influence of a number of pulses without the intrusion of other walls.

It might be thought that the difficulties introduced by the use of a photomultiplier could be avoided by measuring the distance a wall moves during a single short pulse optically and dividing this distance by the pulse length. This method was investigated, but found to give erratic results, probably because the walls do not begin moving with the start of the pulse and move for some unknown distance after the end of the pulse. Indeed, this type of behavior has been observed by the photo-multiplier method, but in that case the instantaneous wall velocities are measured so that the final measurements are not affected.

In Fig. 1 domain wall mobility is plotted as a function of $1/B_s\sigma d$, where B_s and σ are the bulk values for the appropriate compositions and d was obtained by optical interferometry measurements. The crosses represent films for which the data are considered to be poor, either because the measured resistivity is more than two times the bulk value or because the domain patterns as observed visually were poor. The remaining data are seen to fit the curve $m=1.6\times10^{20}(1/B_s\sigma d)$ which may be compared with $m=2.7\times10^{20}(1/B_s\sigma d)$ as predicted by Eq. 1. It is tempting to explain the discrepancy in slope on the basis of the effect of intrinsic damping. The inclusion of such a term leads to a dependence of wall mobility on thickness given by Eq. 3 and shown by the dotted line in Fig. 1, where the value of $\lambda=10^8$ as reported by D. O. Smith has been used.[8] Although it would be possible to find a value of λ that would predict the observed slope within the limited

[8] D. O. Smith, J. Appl. Phys. 29, 264 (1958).

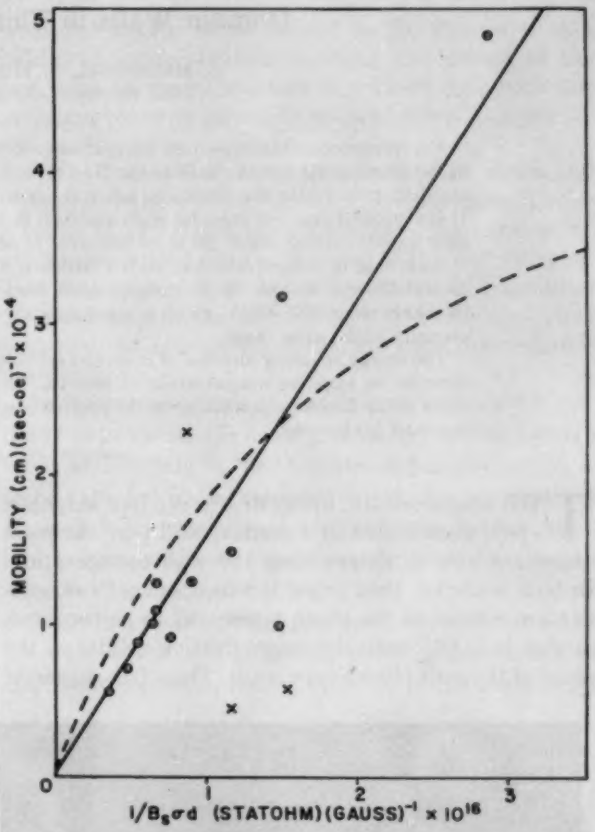

FIG. 1. Domain wall mobilities as measured in nickel-iron films 700 A to 4000 A thick.

thickness range studied, the extrapolation of the straight line to infinite film thickness would not pass through the origin as in the case for the data reported here. Consequently, it is believed that intrinsic damping is not significant for films as thin as 700 A and that lack of agreement with the eddy current theory is due to a combination of experimental error and the inadequacies of the theory with regard to the effects of film edges and imperfections. Unfortunately, it is not possible to measure velocities in films thinner than about 700 A because the magnetization reverses by the growth of domains in a mottled pattern rather than the motion of a small number of walls extending across the film.

The fact that no effect attributable to intrinsic damping has been observed in these data suggests that either the value of λ for the thinner films is less than half that used to calculate the dotted curve, or that the theory for the limiting of domain wall velccities by intrinsic damping is in error. A similar discrepancy has been observed in magnetite by J. K. Galt who reported that the value of λ calculated from domain wall velocities was a factor of five smaller than that reported for a microwave resonance measurement.

ACKNOWLEDGMENT

The author would like to thank R. E. Behringer and E. W. Pugh for many helpful discussions and suggestions.

JOURNAL OF APPLIED PHYSICS SUPPLEMENT TO VOL. 31, NO. 5 MAY, 1960

Domain Walls in Thin Magnetic Ni-Fe Films

S. Methfessel, S. Middelhoek, and H. Thomas
IBM Research Laboratory, Zurich, Switzerland

Néel proposed a transition from the normal type of domain wall (i.e., rotation of the magnetization vector in the plane of the domain wall) to the Néel type (i.e., rotation of the magnetization vector in the plane of the film) at a certain film thickness, which is due to the thickness dependence of the magnetostatic energy. It is suggested that the cross-tie walls observed in thin Ni-Fe films with uniaxial anisotropy correspond to such a transition, in which the cross ties serve to decrease the magnetostatic energy.

According to this explanation, such a structure should occur in a certain thickness range only. Experimental observations on Ni-Fe wedge-shaped films show the occurrence of the cross-tie structure in the thickness range 400–900 A, which is approximately that predicted by theory. The coercive force shows an anomaly in the same range.

The energy reducing function of cross ties is also shown by the Bitter patterns near scratches in the easy direction in negative magnetostrictive material. In a region along the scratch, the magnetization in the plane of the film is perpendicular to the original easy direction due to the local stresses and again a cross-tie structure is observed.

THE magnetostatic forces due to the free magnetic pole distribution in a domain wall play the most important role in determining the wall configuration. In bulk material, they cause the component of magnetization normal to the plane of the wall to be constant, so that in a 180°-wall the magnetization rotates in the plane of the wall (Bloch type wall). Thus, free magnetic poles occur only at the intersection of the wall with the surface of the sample, which is assumed to be at an infinite distance. The wall energy is determined only by anisotropy and exchange energy.

In thin films, the increasing magnetostatic energy of these free poles at the surface, gives rise to an increasing wall energy with decreasing film thickness. Néel[1] made

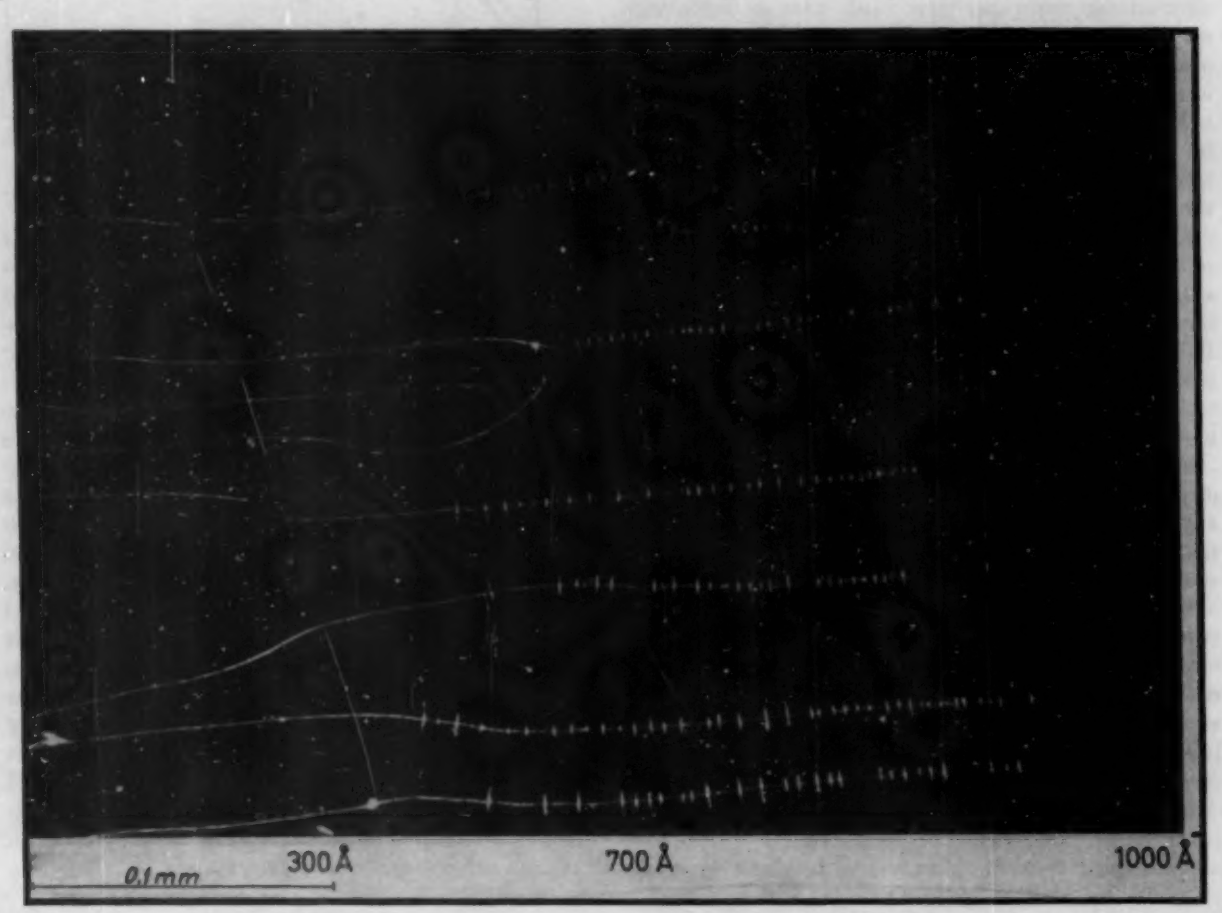

Fig. 1. Domain wall configurations in a wedge-shaped 80-20 Ni-Fe film.

[1] L. Néel, Compt. rend. **241**, 533 (1955).

a rough estimate of this energy and demonstrated that in very thin films it is more favorable, in terms of energy, if the component of magnetization normal to the plane of the film vanishes so that the magnetization then rotates in the plane of the film (Néel type wall), and free magnetic poles are created at the wall, inside the material. In this case, the wall energy decreases with decreasing film thickness.

A transition from one type of domain wall to the other is to be expected in the thickness region where the wall energies of both types are equal. The model which Huber, Smith and Goodenough[2] proposed as an explanation for the cross-tie walls observed in thin films represents such a transition between the two types. Alternation of Bloch and Néel wall segments of alternating polarity reduces the magnetostatic energy, which leads to a decrease in the total wall energy, even though more exchange energy is needed for the cross-ties. A quantitative treatment, for example a theoretical estimate of the cross-tie period, the length of the cross ties, etc. has not yet been given, due to the difficulties generally encountered in micromagnetics.

If this model is correct, cross-tie walls should exist only in a certain critical thickness region. Therefore, we investigated the domain wall types present in thin Ni-Fe films of varying thickness with the Bitter technique. In order to avoid uncontrollable changes in evaporation conditions, the whole thickness range was produced in one evaporation run. By suitable shadowing, 80/20 Ni-Fe films of a wedge-shaped cross section were evaporated onto heated glass substrates in a vacuum of 10^{-5} mm Hg. The film thickness, measured by the Tolansky method, varied between 0 and 1500 A along the sample. During evaporation, a magnetic field was present inducing an uniaxial anisotropy in the direction of the thickness gradient ($H_K \sim 3$ Oe), so that the effect of thickness can be studied on one 180° domain wall.

Figure 1 shows the Bitter pattern of such a film. The smooth parts of the wall at the thin and thick ends of the film have to be interpreted as pure Néel and Bloch walls, respectively; in the thickness range of 400 to 800 A the cross-tie wall represents a continuous transition between the two types.

The Néel wall is found to be much more visible than the Bloch wall. This may be due to the different direction of the magnetostatic field at the surface of the film in both cases. Above a Néel wall its direction is mainly horizontal, above a Bloch wall, mainly vertical, thus exerting different forces on the particles in the Bitter suspension.

The good visibility of the walls throughout the entire cross-tie region indicates, therefore, that a cross-tie wall consists of Néel wall segments of alternating polarity with only narrow transitions between them. Thus, the cross ties appear to be related to the free poles of a Néel wall inside the film material; the energy of the free poles at the intersection of a Bloch wall with the surface apparently cannot be reduced by such a cross-tie structure.

Figure 1 shows that the change between Bloch and Néel type walls occurs at about 900 A thickness. This is a factor of two larger than the critical thickness value extrapolated from Néel's estimates of the wall energies. This discrepancy is probably because Néel's formulas are valid only in the limit of very thin and very thick films and the extrapolation into the transition region is not justified.

As the coercive force H_c for domain wall motion certainly depends on the form and energy of the domain walls, an anomaly in the thickness dependence of H_c is to be expected in the cross-tie region. Measurement of H_c made in the same samples showed that the maximum in cross-tie density is always accompanied by a maximum in H_c.

According to the model proposed, the cross-tie walls are a consequence of an energy reducing flux-closure of Néel wall segments, i.e., of bars where the magnetiza-

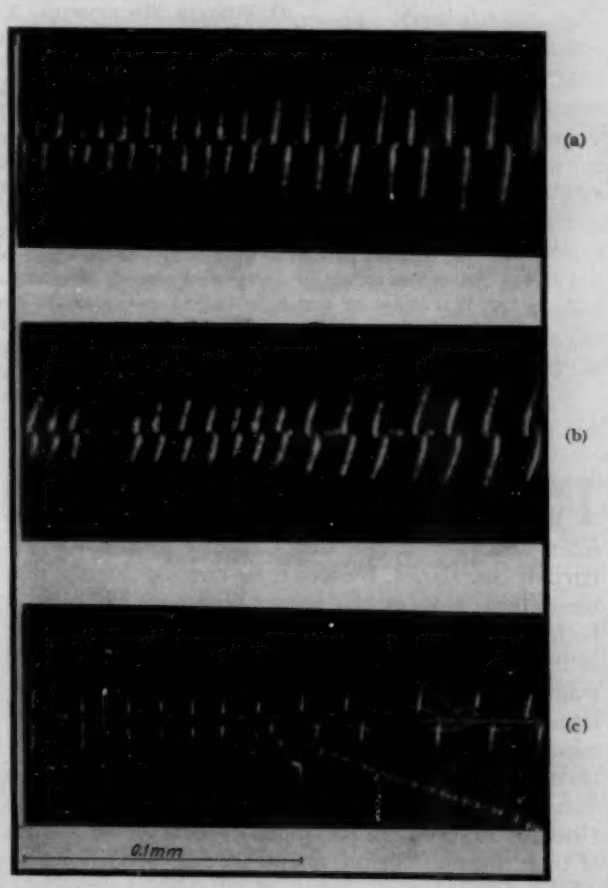

FIG. 2. Bitter patterns near scratches in negative magnetostrictive Ni-Fe films. (a) No external field. (b) With external field in the hard direction (3 Oe). (c) A domain wall joining a scratch.

[2] E. E. Huber, D. O. Smith, and J. B. Goodenough, J. Appl. Phys. 29, 294 (1958).

tion is perpendicular to the easy direction in the plane of the film. This hypothesis was confirmed by the observation of Bitter patterns along scratches parallel to the easy direction in thin Ni-Fe films with a negative magnetostriction. The deformed surroundings of a scratch are under a pressure perpendicular to the scratch (taken up by the glass substrate), which causes, in negative magnetostrictive material, a preferred direction also perpendicular to the scratch and thus perpendicular to the easy direction in the rest of the film. Therefore, the surroundings of the scratch resemble a Néel type wall with the only difference that the magnetization direction on both sides is now parallel instead of antiparallel. Again, a reduction of energy is possible by an alternating polarity of the magnetization in this region, which gives rise to a cross-wall structure. The cross-ties are equally spaced but now on alternate sides of the scratch. Figure 2(a) shows the Bitter pattern observed.

If this model is correct, an external field applied at right angles to the scratch, i.e., parallel to the hard direction of the film, should have two effects: Firstly, the part of the scratch region magnetized parallel to this field becomes more favorable, in terms of energy, than the part magnetized antiparallel to the field and, therefore, should grow at the expense of the latter part, so that the cross walls should move together in pairs Secondly, the magnetization on both sides of the scratch region is rotated into a new equilibrium position which should cause a bending of the cross-walls. Both effects are visible in Fig. 2(b).

If the scratch functions simultaneously as a domain wall, the cross-walls again stand opposite to one another, as can be seen from Fig. 2(c).

JOURNAL OF APPLIED PHYSICS SUPPLEMENT TO VOL. 31, NO. 5 MAY, 1960

Annular Uniaxially Magnetized Domains in Thin Ni-Fe Films*

O. William Muckenhirn, A. E. LaBonte, and P. J. Besser
Electrical Engineering Department, University of Minnesota, Minneapolis, Minnesota

Stable annular uniaxially magnetized domains have been observed in thin circular Ni-Fe films using both the Kerr and Faraday magneto-optic effects. The films exhibit unusual magnetic behavior in both the "easy" and "hard" directions. Generally the magnetization reversal begins at the circumference of the film with the appearance of a uniaxially magnetized annular domain whose inner radius then decreases with increasing applied field. In a number of films, the mechanism of magnetization reversal in an outer annular region appears to be distinctly different from that in the central region. In the annular region, the low-frequency magnetization reversal in the easy direction proceeds by wall motion with the Bloch walls approximately parallel to the direction of the applied field, but there is evidence that the reversal in the hard direction occurs by a rotational process. After the annular region is completely reversed, the center region is reversed by a radially inward motion of the circular boundary between the two concentric uniaxially magnetized domains. The magneto-optic observations are qualitatively correlated with 60 cps $d\phi_M/dt$ vs H and ϕ_M vs H loop data. Based on the assumptions of uniform magnetization per unit volume, M, and uniform film thickness, quantitative correlation of ϕ_M vs H as obtained from Kerr effect photographs and from normalized 60 cps hysteresis loop measurements have been made and are reported.

INTRODUCTION

IN the course of our investigations of thin magnetic films, circular films have been produced which exhibit uniaxially magnetized domains with concentric circular boundaries. Besides their unusual domain patterns, these films exhibit unusual magnetic behavior in both the easy and hard directions. The definite nature of the domains and their behavior under conditions of magnetization reversal suggested a study of the correlation of the relative volume magnetization as determined by domain areas from magneto-optic observations and as obtained from normalized ϕ_M vs H loop data. It is the function of this paper to describe these films and to serve as a preliminary report on our studies of their magnetic behavior and on the correlations established thus far.

* This investigation was conducted under a Graduate School Grant, University of Minnesota.

THE PHENOMENON

The reversal of magnetization of these films in the easy direction generally begins at the circumference of the film with the appearance of a uniaxially magnetized annular domain whose inner radius decreases with increasing applied field. This is illustrated by the sequence of Kerr photographs in Fig. 1(a) through 1(e), the arrows indicating the relative directions of M. The films have a reasonably high coercive force (10 to 20 oe) and relatively high ratios of applied field change to domain area change. The domain patterns therefore represent stable states and multiple ring patterns such as illustrated in Fig. 1(f) are readily generated in the easy direction by the application of alternate reverse fields with decreasing amplitude.

In a number of the films the mechanism of magnetization reversal appears to be distinctly different in an outer annular region from that in the inner region al-

though no macroscopic physical boundary was detected between the two regions. At a critical value of applied field in the easy direction, conventional "spike" domains with walls parallel or nearly parallel to the field appear at one side of the annular ring. With a small increase in applied field the walls move perpendicularly to the applied field until the annular region is traversed. Further increase in applied field results in a concentric shrinking of the inner circular domain proportional to the applied field. Qualitative correlation of this with the $d\phi_M/dt$ vs H loop (60 cps) is shown in Fig. 2(a) in which the voltage pulse at approximately 0.25 H_s represents the reversal of the annular ring and the ensuing low nearly constant voltage represents the relatively uniform shrinking of the inner domain. Likewise in the integrated loop (ϕ_M vs H) of Fig. 2(c) the steep slopes represent magnetization reversal in the annular region and the gradual slopes reversal in the inner region.

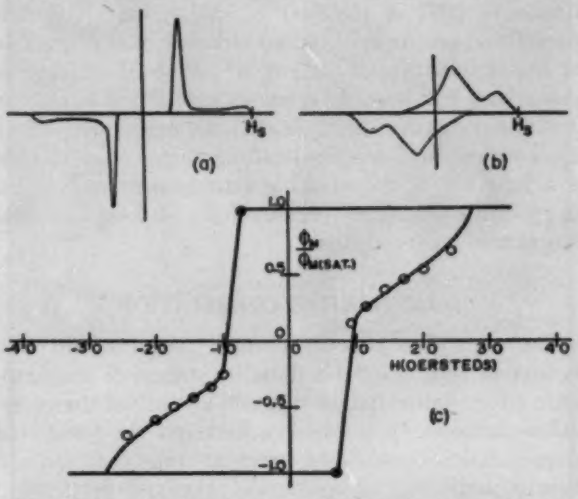

FIG. 2. Magnetization characteristics (line drawings taken from 60 cps loop tracer oscillographs—film 7E). (a) $d\phi_M/dt$ vs H—easy direction. (b) $d\phi_M/dt$ vs H—hard direction. (c) Normalized ϕ_M vs H—easy direction; circles represent normalized domain area measurements taken from Kerr magneto-optic effect photographs.

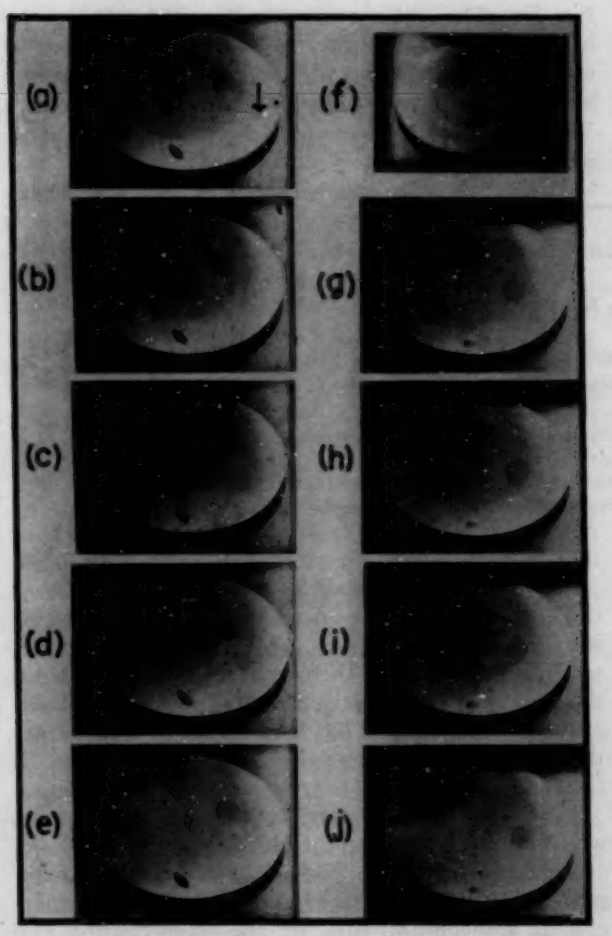

FIG. 1. Annular uniazially-magnetized domains as observed by the longitudinal Kerr magneto-optic effect. (a) through (e): easy direction magnetization reversal; applied fields of 0.3 H_s, 0.5 H_s, 0.7 H_s, 0.8 H_s, and H_s, respectively (film 7E). (f): Stable, multiple annular domains (film 13C). (g) through (j): hard direction magnetization reversal; applied field of 0, 0.2 H_s, 0.3 H_s, and H_s, respectively (film 7E).

In the hard direction the two distinct regions are also apparent. When a saturating applied field in the hard direction is reduced to zero, a low contrast appears between the regions as observed by Kerr magneto-optic effect, the inner region retaining its original intensity. As the applied field is increased in the reverse hard direction the contrast between the regions increases without domain boundary movement until the magnitude of applied field approaches the critical value for easy direction reversal in the annular region. This suggests that as the hard direction field is reduced to zero, the anisotropy is sufficient to rotate the M vector towards the easy direction in the annular region but not in the inner region. Further increase in the applied field yields no further changes in contrast between the two regions but results in a concentric shrinking of the inner circular domain until saturation is reached.

The photographic sequence Figs. 1(g) through 1(j) illustrates the hard direction domain dynamics. Because of photographic reproduction difficulties the contrast changes between Figs. 1(g) and 1(h) are not as vivid as observed visually. The corresponding $d\phi_M/dt$ vs H loop is shown in Fig. 2(b). Qualitative correlation again appears good. Figure 2(b) shows a voltage output for the near-zero applied fields indicating a time rate of change of magnetization corresponding to the Kerr effect contrast change and interpreted as some type of rotation process. The succeeding voltage output is due to inner domain shrinkage.

All of the films were prepared in a uniform magnetic field by evaporation from pure 10-mil thick, 2-inch wide, Ni-Fe alloy sheets on to ultrasonically cleaned, unheated glass substrates mounted in direct contact with a fixed aperture copper mask. The annular domain patterns have been observed in films of various compositions (70% Ni-30% Fe to 80% Ni-20% Fe) and of different

thickness (500 A to 2000 A) indicating that these parameters are not critical. No radial thickness gradient or radial substrate distortion, which could account for this effect, has been detected in any of the films. Our preliminary studies indicate that the mechanism which allows these high magnetostatic energy states to exist is a function of the masking arrangement and of the aging of the film. The specific nature of these functions is now under investigation.

QUANTITATIVE CORRELATION

The ability to observe domain patterns and wall motion in thin magnetic films by means of magneto-optic effects immediately suggests a study of the correlations between these observations and the associated magnetization curve.[1] The irregular spike patterns and their unpredictable movements as previously reported[2–4] have seriously hampered such studies. The well defined annular domains and the repeatable magnetic behavior of the films described above provided new encouragement in this direction. Correlations of the hysteresis loops in the easy direction were made on five different films in the following manner. The films were taken through a magnetization cycle from saturation in one direction to saturation in the opposite direction and back to the original saturated state. At selected values of applied field throughout the cycle, photographs of the Kerr domain patterns were taken. Since the domain patterns on both sides of the film were observed to be the same it was assumed that the domains extended through the thickness of the film.

On the basic assumptions of uniform magnetization through a domain region, uniform film thickness and circular domain boundaries, the total magnetization of a domain was considered to be directly proportional to the domain area. Therefore, the relative ϕ_M values of the hysteresis loop were determined in terms of the saturated value as the ratio of the domain area to film area for each designated value of applied field. These points are shown for a representative film as circles in Fig. 2(c). The continuous curve shows the values of the hysteresis loop taken directly from a transistorized 60 cps ϕ_M vs H loop tracer.[5] Within the limits of experimental measurements, the correlation appears good.

[1] N. C. Ford, Jr., and E. W. Pugh, J. Appl. Phys. **30**, 270S (1959).
[2] C. A. Fowler and E. M. Fryer, Phys. Rev. **100**, 746 (1955).
[3] C. D. Olson and A. D. Pohm, J. Appl. Phys. **29**, 274 (1958).
[4] R. W. Olmen and E. N. Mitchell, J. Appl. Phys. **30**, 258S (1959).
[5] E. C. Crittenden, A. A. Hudrinac, and R. L. Strough, Rev. Sci. Instr. **22**, 872 (1951).

JOURNAL OF APPLIED PHYSICS SUPPLEMENT TO VOL. 31, NO. 5 MAY, 1960

Cross-Tie Walls in Thin Films*

HARVEY RUBINSTEIN AND ROBERT J. SPAIN
Laboratory for Electronics, Inc., Computer Products Division, 1079 Commonwealth Avenue, Boston, Massachusetts

Various properties of cross-tie walls are summarized. Several new Bitter pattern experiments dealing with cross-tie walls are described. The first experiment firmly determines the magnetization distribution about a cross-tie, with the aid of an applied field at 45° to the wall. The second experiment tests the stability of cross-tie walls. It is shown in this experiment that another wall configuration is possible. This is discussed in light of the buckling mechanism of film switching.

THE observation of cross-tie walls in thin films has been reported by several investigators.[1–3] The model for the magnetization distribution in and about the wall has been set forth but as yet calculations and further corroborating experiments which would verify this description are lacking. In this report some general properties of cross-tie walls will be stated and several new experiments with cross-tie walls will be described. One of these experiments substantiates the present model.

Inspection of Bitter patterns on a number of films has indicated that on the average cross-tie walls possess the properties enumerated in the following.

(1) The spatial periodicity of cross-ties increases as the film's thickness is decreased over a range of 300–700 A.

(2) In a given film there exists a relation between the length of a cross-tie and the distance between cross-ties. Generally it has been found that the larger the spacing between cross-ties, the longer is the cross-tie.

(3) Cross-ties frequently are not found on walls which are not parallel to the film's easy direction.

Examination of the previously proposed cross-tie model[1] leads to a number of unanswered questions, including a theoretical basis for the magnetization distribution. The experimental work[1,2] which has been published appears only to indicate certain symmetries in the magnetization distribution. These experiments have not shown how the magnetization is directed. In this model, the magnetization circulates about a point

* This work was supported in part by the Office of Naval Research.
[1] Huber, Smith, and Goodenough, J. Appl. Phys. **29**, 294 (1958).
[2] R. M. Moon, J. Appl. Phys. **30**, 82S (1959).
[3] H. W. Fuller and H. Rubinstein, J. Appl. Phys. **30**, 84S (1959).

FIG. 1

FIG. 2

FIG. 1. Bitter pattern of walls and magnetization distribution of domains before applying field.

FIG. 2. Bitter pattern of walls and magnetization distribution of domains and walls after applying fields at 45° to walls.

midway between the cross-ties. Another model based on an energy minimization results in locating the circulating magnetization at the cross-tie and the published experimental observations can be interpreted to fit this model as well. To resolve this situation a Bitter pattern experiment was devised employing a film prepared from a 50-50 FeNi ingot having a thickness of 300–400 A. This film is characterized by long segments between cross-ties which facilitates this experiment. To obtain the magnetization distribution information a field is applied in the plane of the film and at an angle of 45° to the wall. The component normal to the wall is used to determine[4] the magnetization direction in the wall while the component parallel to the wall determines the domain and the cross-tie magnetization directions. First, a field which does not cause wall motion is applied while a domain pattern shown in Fig. 1 exists in the film. The result and interpretation, for the wall region, is shown in Fig. 2. Increasing the field causes the wall to move yielding the domain magnetization information. The decrease in length of the cross-tie between the arrows on the wall together with the indicated direction shows that magnetization does not curl about the cross-tie. The resulting distribution inferred from this experiment firmly establishes the magnetization distribution of the existing model.

Another question is whether the cross-tie wall is the only stable configuration, since cross-tie and simple walls frequently coexist in the same specimen. Experiments showed that in certain films (i.e., 50-50 Fe-Ni, 600 A thick), a variety of stable wall configurations could be formed. In Fig. 3 the effect is shown of a field applied in the plane of the film and normal to the

[4] H. Rubinstein and H. W. Fuller, J. Appl. Phys. (to be published).

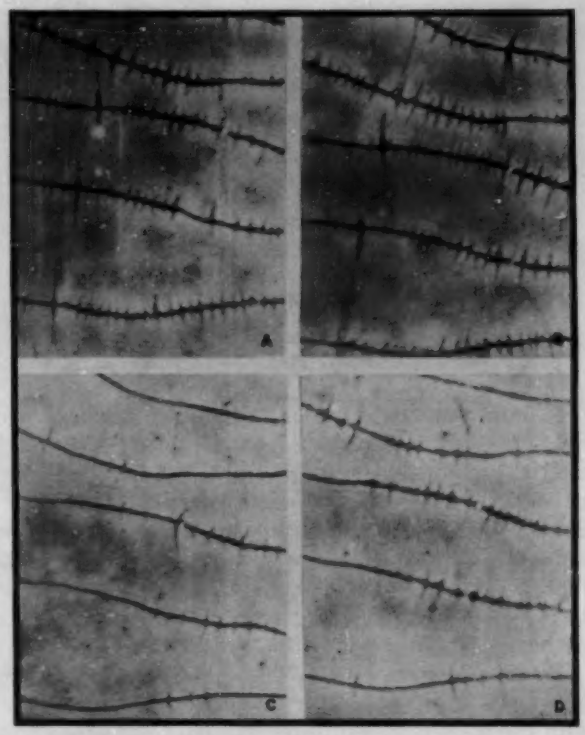

FIG. 3. Effects of applying field normal to cross-tie wall. (A) Before applying field. (B) Field increased. (C) Field further increased. (D) Field removed.

cross-tie wall. Increasing the field causes cross-ties to vanish, and a large fraction of cross-ties fail to reappear on removal of the field. The new stable wall configuration probably corresponds to the elimination of some of the magnetization rotations along the wall, since Néel-wall segments are not observed with maximum applied field. Application of a reversed field results in returning cross-ties that were removed.

The above experiment may be interpreted in terms of the buckling model.[3] If the cross-ties are a result of this mechanism of magnetization change, the application of a field normal to the wall should inhibit the buckling and the possibility of cross-tie formation.

It is also interesting to note the manner in which a cross-tie wall moves in various applied fields. If the applied field is parallel to the wall, the wall moves retaining the cross-ties, but with the intermediary regions moving first followed by the cross-ties, giving the appearance that the cross-ties are pinned in position. This interpretation is supported by the observed predilection of cross-ties to settle at a position on a wall where a visible film imperfection exists. On the other hand, if a field component exists normal to the wall of such magnitude as to make the cross-tie disappear, the entire wall moves uniformly.

The authors wish to acknowledge the work of M. Chollis in preparing the films and the valuable discussions with Dr. H. W. Fuller.

Static and Dynamic Studies of Magnetization Distribution in Thin Films by Electron Microscopy*

HARRISON W. FULLER AND MURRAY E. HALE
Computer Products Division, Laboratory for Electronics, Inc., Boston, Massachusetts

Several modes of operation of a transmission electron microscope are discussed which are useful for the observation of the magnetization distribution in thin films. Gross defocusing of the instrument provides great sensitivity to slow variations in static magnetization direction, while slight defocusing enables the measurement of rapid variations of magnetization at high resolution. The applications of electron microscopy to dynamic wall studies is discussed; this can be demonstrated by motion pictures. Some new ways of observing domains and walls at instrumental focus are described which utilize an opaque knife edge for intercepting a fraction of the deflected electron beam below the specimen.

THE methods used in observing domains and domain walls in thin ferromagnetic films with electron microscopy, and the types of observations that have been made will be summarized in this paper. Several modes of operation of an electron microscope for domain observations are now available, and in thin film investigations these methods of observation appear to be extensions and complements to the earlier Bitter pattern and magneto-optic methods.

When an electron passes through a thin magnetized film the electron undergoes a deflection by interaction with the magnetization of the specimen, in addition to random deflections by normal scattering processes. Taking the Lorentz force on the electron,

$$\mathbf{F}=-(e/c)(\mathbf{v}\times\mathbf{B}), \tag{1}$$

to describe this interaction appears to give at least semiquantitative agreement with experimental observations.

One general way of observing an image of the magnetization distribution in a thin film is to use a small-aperture illuminating source and to focus the instrument on a plane other than the specimen plane.[1] In the special but important case when the magnetization distribution in a region of the film is one dimensional (i.e., all simple wall models), and taking the magnetization of the specimen to be given by $M_y(x)$ in the x,y plane of the specimen, it can be shown[2] that the magnetic deflections of a parallel beam of normally incident electrons result in an electron intensity distribution at an X,Y observation plane given by the parametric equations

$$I(X)=I_0|1-(z\Phi/M_s)(\partial M_y/\partial x)|^{-1},$$
$$X=x-z\Phi M_y/M_s. \tag{2}$$

In Eq. (2), I_0 is the intensity of the incident electron beam, z is the distance of the X,Y observation plane from the x,y specimen plane, M_s is the saturation magnetization of the film material, and $\Phi=(4\pi\tau M_s/c)\times(e/2Vm)^{\frac{1}{2}}$ is the maximum possible deflection angle, with τ being the film thickness and V the electron accelerating potential. The expression neglects the effects of normal scattering processes and, also, the the magnification by lenses, but the latter is easily incorporated.

If the projector lens of an instrument alone is used to magnify the magnetization image, the mode of operation corresponds to a large defocusing distance z, in which case the beam displacement $z\Phi$ becomes large compared with, for example, usual domain wall widths. Domain walls with this mode of operation appear as relatively broad dark or light ribbons, and the resolution for observations of this kind is not great. A large z distance, on the other hand, results in an intensity pattern that is quite sensitive to even small and slow variations in the magnetization of the film. A phenomenon called "magnetization ripple" has been demonstrated in this way,[2] and it is believed that the intensity striations that result in the image furnish a very useful orthogonal map of the magnetization distribution of the entire film and permit the interpretation of complex domain patterns.

The large-z mode of operation, in the case of the Philips EM 75 B instrument, is convenient to photograph because of the high image intensity. It, accordingly, is a valuable method for observing domain walls in motion, where the adjustable stray fields of the objective lens or other inserted fields can be used for inducing wall motion. Among dynamic studies possible with the technique is that of the motion of cross-tie walls. Figure 1 shows a sequence of micrographs of wall motion derived by printing about every fifth frame of a motion picture that was taken of the viewing screen.[3] This is an interesting case in which a simple wall becomes a cross-tie bearing wall in its motion toward an apparently highly stressed region of a thin film.

Other subjects that benefit from dynamic electron

* This work was supported in part by the Office of Naval Research and Bell Helicopter Corporation.

[1] M. E. Hale, H. W. Fuller, and H. Rubinstein, J. Appl. Phys. 30, 789 (1959).

[2] H. W. Fuller and M. E. Hale, J. Appl. Phys. 31, 238 (1960).

[3] A motion picture showing a variety of wall motion studies was shown at the Fifth Conference on Magnetism and Magnetic Materials. The film was taken with an Arriflex 16 camera that allowed the operator to adjust all normal microscope controls while observing the image in a reflex viewer.

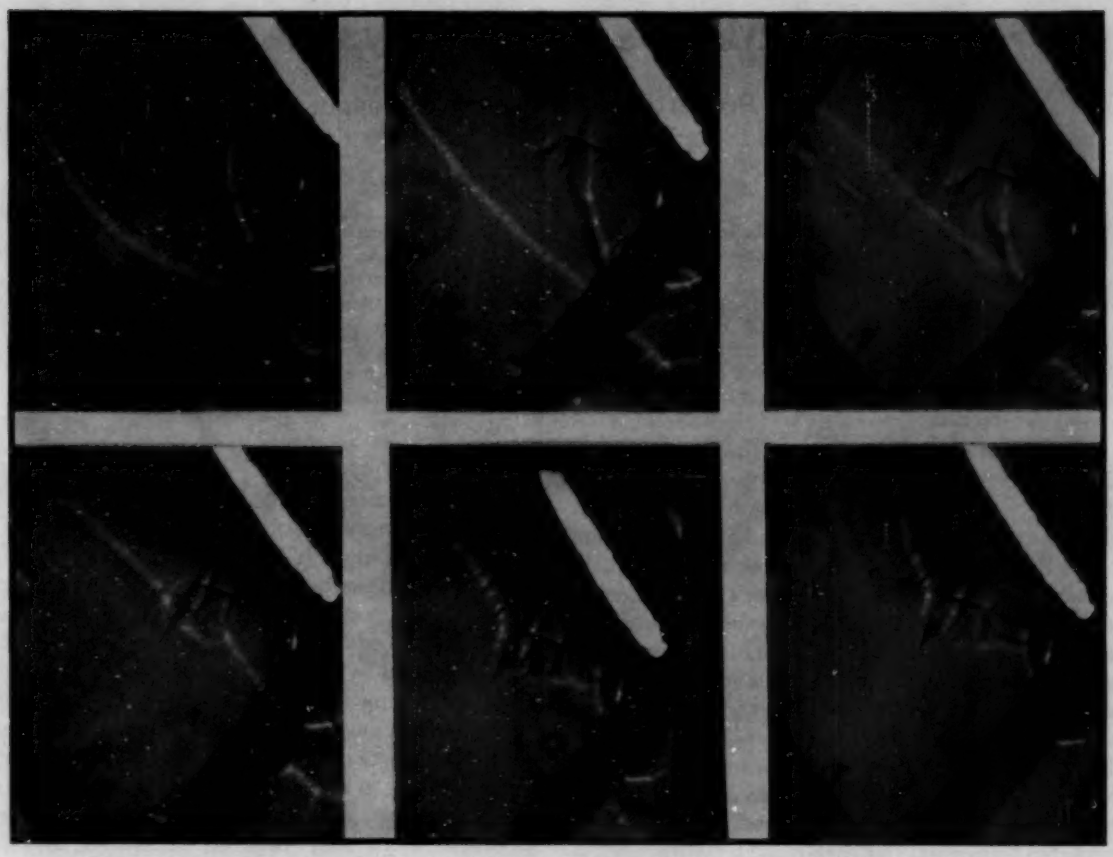

FIG. 1. Sequence of micrographs showing walls in motion in a thin film observed by electron microscopy. The sequence order is: top, left to right; bottom, left to right.

microscopic observations are the buckling mechanism of film switching,[4] and the change in grain structure and magnetic characteristics with rapid film heating in the electron beam.

The use of small values of z in Eq. (2) is possible by partial operation of the objective lens or by moving the specimen plane. For small z values, the sensitivity of the observation to slight magnetization changes is reduced, but the resolution for observations of domain walls approaches that of the instrument in normal use. It is by these means that the width of domain walls in thin films has been measured experimentally.[2] In certain cases the solution of Eq. (2) can be inverted to give a parametric integral equation solution for the magnetization distribution in a thin film from the measured intensity distribution of the image.[2]

The method of observing the magnetization distribution in a thin film that has been discussed so far has relied on defocusing the instrument to a greater or lesser extent. This is because the maximum angle of magnetic deflection is well within the normal angular aperture of the microscope lenses, so that at focus, all the rays leaving the specimen are returned to their correct image points in the image plane. Another means of imaging the magnetization distribution in the region of walls was proposed by the authors, which would permit operation at instrumental focus.[5] The method relies on the insertion of an opaque knife edge into the space a distance z below the specimen so as to intercept a portion of the magnetically deflected beam and to give an intensity distribution in the focused image in accordance with the wall distribution. The wall distribution itself then could be deduced by the variation in the image intensity pattern as a function of the knife-edge position.

A somewhat similar in-focus method of observation was discovered by the authors in connection with exploratory work with an electrostatically focusing microscope. In this case, however, the knife edge (objective diaphragm) is inserted at the back focal plane of the objective (or an optically equivalent position in the system), and the effect is to produce intensity contrast between entire domains of differing magnetization directions.[5] The micrographs resemble Faraday magneto-optic observations, where, however, the potential resolution and useful magnification of the electron microscope method is very great.

[4] H. W. Fuller and H. Rubinstein, J. Appl. Phys. **30**, 84S (1959).

[5] To be published.

Metals and Alloys

Magnetic Properties of Manganese Copper Alloys

R. STREET
Department of Physics, The University, Sheffield, England

The magnetic properties of the manganese-copper alloy system have been investigated by using a number of experimental techniques. Long range antiferromagnetic order occurs in alloys of high manganese concentration; the disappearance of ordering is associated with a face centered tetragonal → face centered cubic martensitic transformation. By extrapolation of the experimental results it is possible to derive the Néel temperature and magnetic moment of manganese ions in pure fct γ-manganese as approximately 390°K and 2.4±0.1 μ_B, respectively. At lower manganese concentrations, it is likely that short range antiferromagnetic ordering occurs and in addition at sufficiently low temperatures weak ferromagnetic behavior associated with high coercive force becomes apparent. These results and possible interpretations of them are discussed.

1. INTRODUCTION

THE phase diagram of the manganese copper system has been extensively studied, the most complete being that carried out by Dean et al.[1] The addition of Cu to Mn results in a depression of the $\gamma \rightarrow \alpha$ transformation temperature, and it is possible to retain the γ phase at room temperature by rapid quenching from temperatures in the γ field. At moderate temperatures, the unstable γ phase transforms very slowly into the equilibrium $(\alpha+\gamma)$ phases. Investigations of α phase alloys containing more than about 75 atomic percent Mn have shown that the low temperature structure is face centered tetragonal (fct with $c/a<1$), which undergoes a martensitic transformation to a face centered cubic structure at higher temperatures.[2]

For the investigations reported here the alloys were prepared by melting together spectroscopically pure manganese and copper in an argon arc furnace, followed by homogenization of the specimens by maintaining them at temperatures near the solidus, in some cases for several days. Chemical and spectrographic analyses showed that no detectable amounts of impurity were introduced by the methods of preparation.

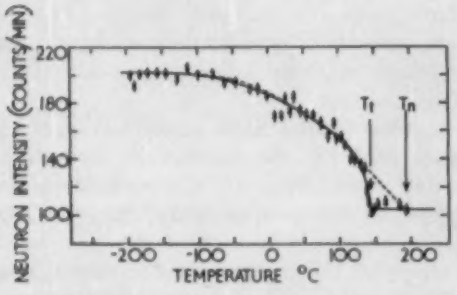

FIG. 1. The temperature variation of the intensity of the (110) magnetic reflection for a 90 atomic % Mn alloy: —— experimental curve, - - - - square of Brillouin function with $S=\frac{1}{2}$ and $T_N=461$°K.

The alloys were examined in a number of ways. Neutron diffraction measurements were made over the temperature range from 80°K upwards by using the neutron spectrometer described by Bacon et al.[3] The magnetic parameters were determined from the forces exerted on specimens placed in an inhomogeneous field. The forces were measured by means of a Sucksmith ring balance. Values of Young's modulus and decrement were measured by examining the resonance of longitudinal oscillation of composite oscillators consisting of quartz crystal bars cemented to bar specimens of the alloys. The resonant frequencies of longitudinal oscillation of the bar specimens alone may thus be calculated, and hence Young's modulus derived. Electron spin resonance measurements were made at frequencies of about 10 000 Mc/s by using finely divided powders of the alloys. Resistivities and specific heats were also measured by using conventional techniques.

2. FACE-CENTERED MANGANESE-RICH ALLOYS

At sufficiently low temperatures the neutron diffraction patterns of γ alloys containing more than about 75 atomic % Mn include a fairly intense magnetic (110) reflection and a (201) magnetic reflection of intensity about 14% that of the (110). This pattern is consistent with a magnetic structure of manganese-copper alloys in this composition range, first proposed by Meneghetti and Sidhu,[4] in which ions in 0 0 0 and $\frac{1}{2}\frac{1}{2}0$ positions have moments parallel to the c axis and the moments of ions in $\frac{1}{2}0\frac{1}{2}$ and $0\frac{1}{2}\frac{1}{2}$ positions are antiparallel. The moments of nearest neighboring ions are thus ordered antiferromagnetically in this structure. The intensity of the (110) magnetic reflection decreases with increasing temperature and first becomes zero at a critical temperature, characteristic of the alloy composition, at which long range antiferromagnetic ordering disappears. Within the limits of experimental error, antiferromagnetic ordering in alloys containing between 80 and 95

[1] R. S. Dean, J. R. Lang, T. R. Graham, E. V. Potter, and E. T. Hayes, Trans. Am. Soc. Metals **34**, 443 (1945).
[2] Z. S. Basinski and J. W. Christian, J. Inst. Metals **80**, 659 (1951).
[3] G. E. Bacon, J. A. G. Smith, and C. D. Whitehead, J. Sci. Instr. **27**, 330 (1950).
[4] D. Meneghetti and S. S. Sidhu, Phys. Rev. **105**, 130 (1957).

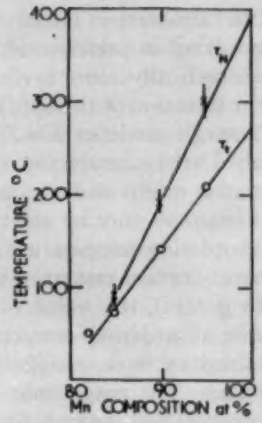

FIG. 2. The variation of the Néel temperature, T_N and the fct → fcc transformation temperature T_t as a function of alloy composition.

atomic % Mn disappears at the temperatures of transformation from the tetragonal to cubic structure (T_t) determined by x-ray techniques by Basinski and Christian.[2] For an antiferromagnetic exhibiting regular behavior the intensities of magnetic reflections vary with temperature as the square of the appropriate Brillouin function, B_s, which is a measure of the degree of antiferromagnetic order. It is possible to fit a B_s^2 function to the neutron diffraction results at lower temperatures, by treating the Néel temperature, T_N, as an adjustable parameter. This is shown in Fig. 1. The experimental results in the temperature region near T_t decrease more rapidly than expected from the B_s^2 function. The onset of the fct → fcc transformation, thus disorders the antiferromagnetic arrangement far more rapidly than the expected disordering due to thermal agitation alone. The extrapolated values of T_N and the observed values of T_t are plotted as functions of alloy composition in Fig. 2. Within the limits of experimental error, T_N varies linearly with manganese content and it appears to be justified to extrapolate to the value of about 390°C as the Néel temperature of pure fct γ Mn.

The intensities of the magnetic reflections have maximum values at $T=0$°K, at which antiferromagnetic ordering is complete. From the absolute intensity of the (110) reflection, extrapolated to $T=0$°K the average magnetic moment of all the atoms in the unit cell may be determined. On assuming that only the manganese ions have a resultant magnetic moment this may be determined from the value of the average moment by simple proportion since there is no preferential ordering

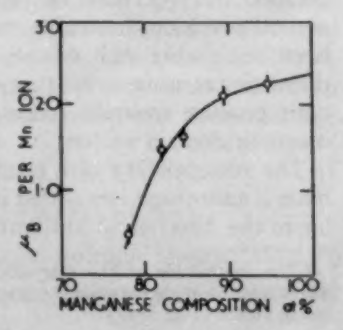

FIG. 3. The variation of the ionic moment, in Bohr magnetons, per Mn atom as a function of alloy composition.

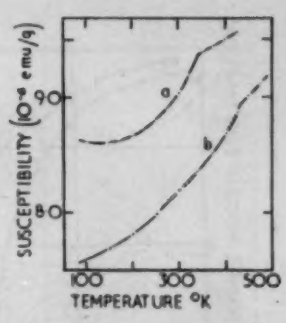

FIG. 4. The temperature variation of susceptibility of (a) 85 atomic % and (b) 90 atomic % Mn alloys.

or grouping of the Mn and Cu ions on the available atomic sites. The results obtained are shown in Fig. 3. Extrapolation gives a value of 2.4 ± 0.1 μ_B for the magnetic moment of the Mn ions in pure fct γ Mn.

The temperature variations of magnetic susceptibility shown in Fig. 4 are typical for manganese rich alloys. In the region of the fct → fcc transformation temperature there is a sharp rise in susceptibility; the susceptibility continues to increase at higher temperatures and no Curie-Weiss law behavior is observed. Higher temperature measurements are precluded by the transformation of the single γ phase states into the equilibrium mixed (α+γ) phases.

The resistivity vs temperature curves for alloys containing more than 80 atomic % Mn, plotted in Fig. 5 show characteristic discontinuities of slope at the spin disordering temperature. Friedel and de Gennes[5] have derived an expression for the "magnetic" contribution to resistivity (ρ_{mag}) resulting from interactions between conduction electrons and magnetic ions of half-integral

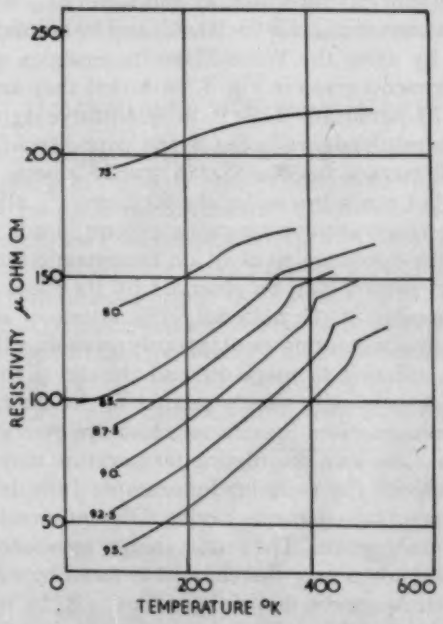

FIG. 5. The temperature variation of resistivity of γ MnCu alloys of the atomic % Mn compositions shown.

[5] J. Friedel and P. de Gennes, J. Phys. Chem. Solids 4, 71 (1958).

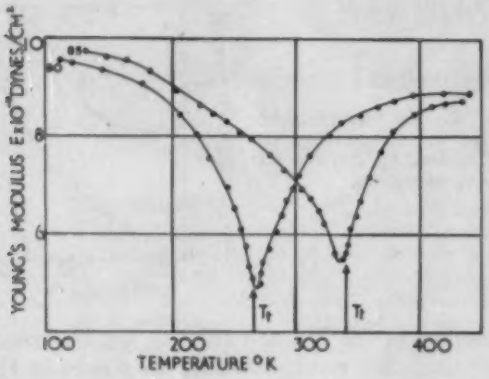

FIG. 6. The temperature variation of Young's modulus of γ MnCu alloys containing 80 and 85 atomic % Mn. The fct $\rightarrow$ fcc transformation T_t temperatures for the two alloys are indicated by vertical arrows.

spin. Weiss and Marrotta[6] consider that the Friedel analysis can be applied to metals of nonhalf integral spin by using a Van Vleck model in which the magnetic ions are in different spectroscopic states, the proportions p_i being determined by the magnetic moment of the metal as a whole. Analysis of the experimental results on transition metals and their alloys show that at temperatures above the spin disordering temperature $\rho_{mag}=C\sum_i p_i S_i(S_i+1)$, where C is a constant of value 30×10^{-6} ohm cm and S_i is the spin quantum number of the ith ion type. At low temperatures, the ionic moments approach a perfectly ordered state and $\rho_{mag}=0$. Thus, in general terms, the change in slope of the resistivity vs temperature curve will be more pronounced as the average spin quantum number and hence ρ_{mag} increases. Calculations of ρ_{mag} for 95, 90, 85, and 80 atomic % Mn alloys, by using the Weiss-Marrotta equation and the ionic moments given in Fig. 3, show that they are in the ratios 70:62:46:16. This is in qualitative agreement with the results shown in Fig. 5; the slope discontinuities are well marked for the 85, 90, and 95 atomic % Mn alloys, but much less so for the 80 atomic % alloy.

Long range antiferromagnetic ordering leads in general to the development of an antiferromagnetic domain structure which may be observed by its effect on the elastic moduli of the material.[7] The lattice of an antiferromagnetic deforms spontaneously on cooling through its spin ordering temperature and the direction of deformation is usually simply related to the direction of antiferromagnetism. Specimens which are monocrystalline above the spin disordering temperature may therefore subdivide (by twinning for example if the deformation is large) into domains having different directions of antiferromagnetism. The strain energy associated with an applied stress may therefore be reduced by a change in antiferromagnetic domain structure, e.g., by rotation of the direction of antiferromagnetism against crystalline anisotropy forces or by domain wall movement resulting in preferential growth of domains, which are energetically more favorably oriented with respect to the direction of the applied stress. At low temperatures, Young's modulus $E=Z/(\epsilon_e+\epsilon_m)$, where Z is the applied stress producing linear strain components ϵ_e of elastic origin and ϵ_m caused by redistribution of the domain vectors by the applied stress. Above the spin disordering temperature $\epsilon_m=0$, since the antiferromagnetic domain structure no longer exists and $E=Z/\epsilon_e'$. In general, the value of Young's modulus below the spin disordering temperature will be lower than obtained by back extrapolation of the high temperature values. The magnitude of the difference at any temperature will depend, for the case of antiferromagnetic domain wall movement, on the area and type of domain walls and on the displacement of the walls as a function of stress. The temperature variations of Young's modulus for 80 and 85 atomic percent Mn alloys, given in Fig. 6, are in qualitative agreement with expectations. Quantitative interpretation of the observed variation requires detailed information on domain structure which is not at present available.

The alignment of the directions of antiferromagnetism by applied stress may be demonstrated directly by neutron diffraction experiments on unstrained and plastically deformed alloys. Results for an alloy containing 85 atomic % Mn are shown in Fig. 7. Plastic deformation has resulted in reorientation such that for each crystallite the [100]-type direction lying most nearly parallel to the direction of compression is the (shorter) c axis, and hence the direction of antiferromagnetism. The considerably enhanced intensity of the (110) magnetic reflection in Fig. 7(b) is caused by the fact that the magnitude of the magnetic interaction vector[8] is increased for the (110) reflection under the conditions shown. There is also an increase in the number of c axes which lie along the specimen axis, and consequently there is an increased number of (200) planes and a reduced number of (002) planes available for reflection. For the conditions shown for Fig. 7(c) the spin moments tend to be aligned along the scattering vector, thus reducing the magnitude of the magnetic interaction vector to zero, and hence the intensity of the (110) magnetic reflection is virtually zero. Again there will be a marked increase in the number of (002) planes in a reflecting position and a decrease for (200). Although the experimental precision attainable was not great, it has also been reasonably well established by similar neutron diffraction measurements that stresses within the elastic limit produce *reversible* reorientation of the antiferromagnetic domain vectors.

The susceptibility of a single antiferromagnetic domain is anisotropic; measured in a direction perpendicular to the direction of antiferromagnetism, χ_1 is a con-

[6] R. J. Weiss and A. S. Marrotta, J. Phys. Chem. Solids **4**, 71 (1958).

[7] R. Street and B. Lewis, Nature **168**, 1036 (1951); Proc. Phys. Soc. London **72**, 604 (1958).

[8] The magnitude of the magnetic interaction vector is $\sin\alpha$, where α is the angle between the magnetic moments and the scattering vector [Fig. 7(a)].

stant independent of temperature. χ_{11}, the susceptibility measured parallel to the direction of antiferromagnetism, decreases monotonically to zero at $T=0°K$. Thus, it is to be expected that the plastically deformed specimens discussed above will also exhibit anisotropy of susceptibility. The results plotted in Fig. 8 confirm this. The susceptibility measured in a direction perpendicular to the compressive stress axis is denoted by $\chi_{\pi/2}$ and χ_0 is the susceptibility measured along the direction of compression. Below the spin ordering temperature, it is observed that $\chi_{\pi/2}>\chi_0$, which is to be expected from the preferential alignment of the direction of antiferromagnetism along [100] type axes lying most nearly parallel to the axis of compression. The results may be analyzed by assuming that the total susceptibility is the sum of two components, the first arising from the antiferromagnetic ordering of the ionic moments and the second an isotropic contribution caused

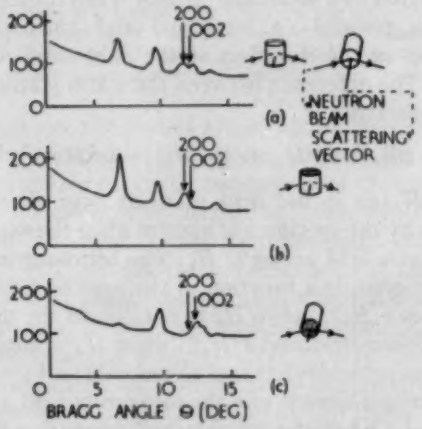

FIG. 7. Neutron diffraction patterns of 85 atomic % Mn alloy. (a) Unstrained specimen, cylinder axes either horizontal or vertical for neutron measurements. (b) After application of compressive stress of 40 Kg mm^{-2} along cylinder axis; scattering vector perpendicular to compression axis. (c) As for (b), but with scattering vector parallel to axis of compression.

by nonlocalized electrons. If a domain of mass m is aligned with its direction of antiferromagnetism inclined at angle ϕ to the measuring field H then the antiferromagnetic contribution to the induced moment is $mH(\chi_{11}\cos^2\phi+\chi_\perp\sin^2\phi)$. This expression may be combined with the distribution function for the number of crystallites in a polycrystalline material for which the [100] type axis most nearly parallel to a given direction is inclined at an angle lying between θ and $\theta+d\theta$ to that direction.[9] Hence, the total "antiferromagnetic" contributions to the susceptibility may be calculated by integration between limits appropriate to χ_0 and $\chi_{\pi/2}$. Hence,

$$\chi_0=\chi(T)+0.70\chi_{11}+0.30\chi_\perp,$$

$$\chi_{\pi/2}=\chi(T)+0.15\chi_{11}+0.85\chi_\perp,$$

where $\chi(T)$ is the assumed isotropic susceptibility. By

[9] K. Hoselitz and M. McCaig, Proc. Phys. Soc. London **B62**, 163 (1949).

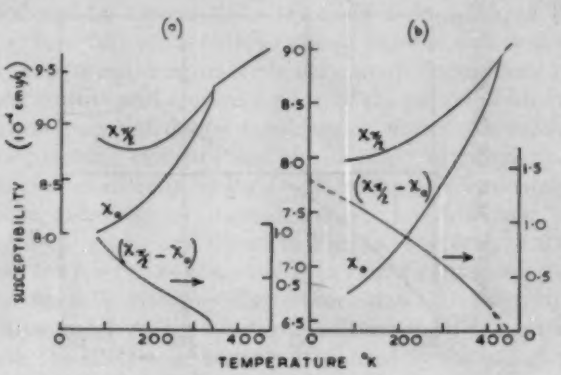

FIG. 8. The temperature variations of $\chi_{\pi/2}$, χ_0 and $(\chi_{\pi/2}-\chi_0)$ for (a) 85 and (b) 90 atomic % Mn alloys.

assuming that $\chi_\perp$ is temperature independent and $\chi_{11}=0$ at $T=0°K$ the value of $\chi_\perp$ and the values of χ_{11} and $\chi(T)$ as functions of temperature may be determined and these are shown in Fig. 9.

Finally, in this section, we note the influence of antiferromagnetic order on specific heat of the alloys. The results for an alloy containing 80 atomic % Mn, in which the magnetic moment of the manganese ions is 1.0 μ_B (Fig. 3), are shown in Fig. 10. The difference in the maximum and minimum values of the specific heat near the spin disordering temperature is 0.65 cal/g atom of Mn, which is smaller than the corresponding value for Ni near the Curie temperature (1.0–1.5 cal/g atom). For an 80 atomic % Mn alloy, the Néel temperature (T_N) and the fct → fcc transformation temperature (T_t) lie close together. If $T_N>T_t$ the maximum observed value of specific heat will be greater than that expected from simple thermal disordering of antiferromagnetic ordering.

3. MANGANESE-RICH ($\alpha+\gamma$) ALLOYS

Pure α manganese is extremely brittle and cannot be machined into regularly shaped specimens required for elastic modulus measurements. However, the elastic properties of α manganese have been indirectly investigated in the following way. γ phase copper manganese alloys containing as much as 95 atomic % Mn are relatively easily machined and it is possible to produce bar specimens suitable for Young's modulus measurements from them. They can then be transformed by heating to 600°C into α manganese with an admixture of γ

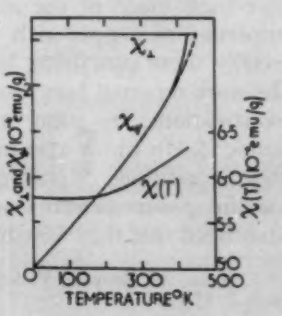

FIG. 9. The temperature variations of χ_{11}, $\chi_\perp$ and $\chi(T)$ calculated from the results of FIG. 8 for 90 atomic % Mn alloy.

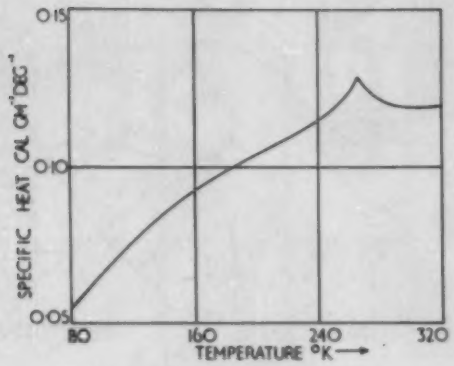

FIG. 10. The temperature variation of specific heat of 80 atomic % Mn γ phase alloy.

MnCu (of composition 40 atomic % Mn) with no deleterious effects on the form of the bar.

The results plotted in Fig. 11 were obtained with mixed $(\alpha+\gamma)$ phase specimens containing 90 and 95 atomic % Mn. The most significant feature of the curves is the relatively small, but well pronounced minimum in the Young's modulus at 104°K for both specimens. The Néel temperature of α manganese is approximately 100°K and there seems to be no doubt that the minimum is caused by the effect on the modulus of the antiferromagnetic ordering of ionic moments in α manganese. It follows that cooling below the Néel temperature should result in an anisotropic deformation of the lattice of α manganese, which is cubic at higher temperature. However, in view of the relatively small magnitude of the step in the Young's modulus at the Néel temperature, it is likely that the deformation would be correspondingly small. X-ray measurements using a 19 cm camera have been made at 80 and 290°K on pure α manganese and mixed $(\alpha+\gamma)$ phase CuMn alloys, but we could find no evidence of a departure from cubic symmetry at 80°K. More refined techniques are therefore necessary to detect the antiferromagnetostrictive strain in α manganese.

4. γ CuMn ALLOYS EXHIBITING NO LONG RANGE ANTIFERROMAGNETIC ORDER

Neutron diffraction measurements show that long range antiferromagnetic ordering, of the type discussed in Sec. 2 above, does not occur in alloys containing less than about 75 atomic % Mn. A number of investigations have been made of the magnetic and other physical properties of copper rich γ phase CuMn alloys, especially those containing less than 20 atomic % Mn.[10] The work reported here was carried out to extend these investigations, by using alloys containing up to 50 atomic % Mn which were prepared under carefully controlled conditions. Metallographic examination showed that the specimens were single phase and x-ray analysis established that they were fcc structures. Measurements of alloy properties were made as soon as possible after preparation in order to avoid segregation or ordering effects.[11]

The susceptibilities were usually determined, by using the method noted in Sec. 1, by first cooling the specimens to low temperature and observing the force exerted on the specimen placed in an inhomogeneous magnetic field as its temperature was allowed to increase. For a given specimen, the susceptibility vs temperature curves were of different form when initially cooled with or without a field acting. For cooling in zero field, there was a maximum in the susceptibility, which occurred at lower temperatures for decreasing manganese content. When the specimens were cooled in a magnetic field through the temperature of maximum susceptibility they acquired a remanent magnetic moment of direction parallel to that of the field applied during the cooling. In Fig. 12 are plotted the temperature variations of force exerted on a 40 atomic % alloy when the measuring field was parallel (p branches) and antiparallel (a branches) to the direction of the field applied during cooling. The difference between the a and p branches at any temperature, T, is

$$\Delta F_x = m(dH_y/dx)[\sigma(H_y^+) - \epsilon\sigma(H_y^-)],$$

where dH_y/dx is the field gradient over the volume occupied by the specimen of mass m when the magnitude of the mean field acting is H_y. The ferromagnetic moment per gram is a function of the applied field and is written as $\sigma(H_y^+)$ when H_y is parallel to the direction of the cooling field and $\sigma(H_y^-)$ when H_y is antiparallel to the cooling field. ϵ has two values only, ± 1; -1 when the magnetic moment and the measuring field are antiparallel, $+1$ when the moment and measuring field are

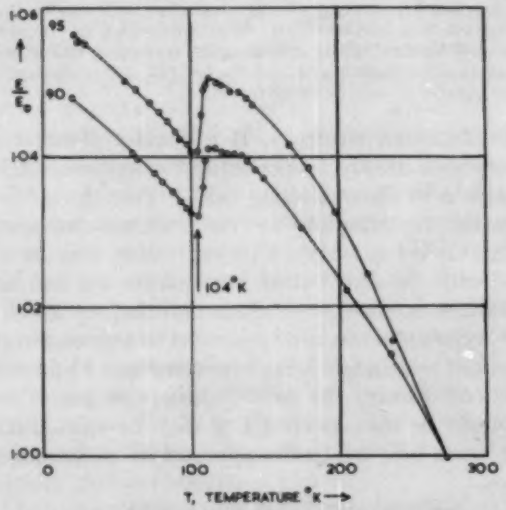

FIG. 11. The temperature variation of Young's Modulus of $(\alpha+\gamma)$ CuMn alloys containing 95 atomic % Mn (upper curve) and 90 atomic % Mn (lower curve). Ordinate E/E_0 where E = Young's modulus at temperature T°K, E_0 = Young's modulus at 0°C.

[10] J. Owen, M. Browne, V. Arp, and A. F. Kip, J. Phys. Chem. Solids 2, 85 (1956).

[11] E. Scheil and E. Wachtel, Z. Metallk. 48, 571 (1957).

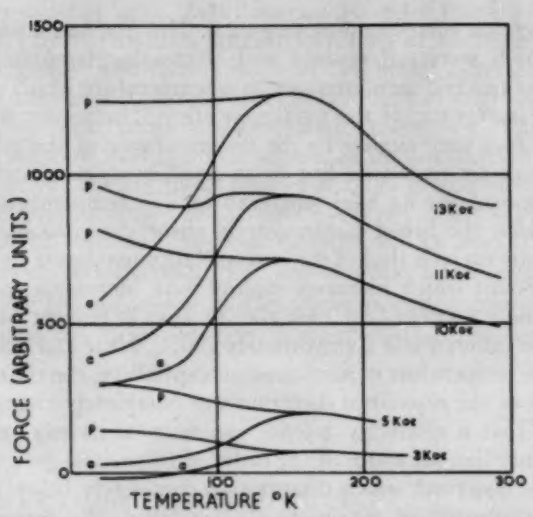

FIG. 12. The temperature variation of the force acting on a 40 atomic % Mn alloy after cooling to 20°K in a field of 10 koe. The magnitudes of the measuring fields are marked on the curves. The branches marked '*p*' were obtained with the measuring field parallel to field applied during cooling, those marked '*a*' were obtained with measuring field antiparallel.

parallel. Thus, the sign of ϵ will change from -1 to $+1$ when the measuring field passes through the coercive force of the ferromagnetic component of the magnetization of the alloy. For measuring fields which are insufficient to *saturate* the ferromagnetic component $\sigma(H_y^+)>\sigma(H_y^-)$: for these fields $\Delta F_x \neq 0$ and the *p* branch will lie above the *a* branch which is the case for all fields used in the measurements shown in Fig. 12. Absolute values of $\sigma(H_y^+)-\epsilon\sigma(H_y^-)$ may be obtained from the calibration constants of the apparatus. By extrapolation to zero field $[\sigma(H_y^+)-\epsilon\sigma(H_y^-)]_{(H_y\to 0)} = 2\sigma_r$ can be derived, where σ_r is the remanent intensity of magnetization produced by cooling in a magnetic field. The remanent moments depend on alloy composition and on temperature. We have observed remanent intensities of magnetization lying between 0.1 and 1 e.m.u. g^{-1} and we estimate the coercivity to lie between 10 and 20 koe.

An interesting feature of the ferromagnetism of the alloys is that the magnetization over some temperature range is strongly time dependent. Appreciable times are required for the magnetization to approach its equilibrium value following a change in the applied field. Typical results, for a specimen containing 30 atomic % Mn, are shown in Fig. 13. These were obtained by cooling the specimen to 78°K in the magnetic susceptibility apparatus with an applied forward field of 10 koe and measuring the time variation of the force acting on the specimen in a reverse measuring field of 10 koe applied at time $t=0$. The force is directly proportional to the magnetic moment of the specimen and hence the time variation of the specific intensity of magnetization may be derived. The change of intensity of magnetization over the time interval from 5–120 sec is 0.05 c.g.s. g^{-1} which is about 50% of the remanent magnetization produced by cooling this alloy to 78°K in a field of 10 koe. It is difficult to obtain entirely reproducible results in these measurements since very small fluctuations in temperature and applied field over the period of observation may introduce considerable errors. However, there is some evidence that the intensity of magnetization varies directly as $\log(t-t_0)$, where t_0 is a constant for a given set of measurements; the deflection vs $\log(t-t_0)$ graph also shown in Fig. 13 is typical, in this case $t_0=8$ sec. The observed behavior is very similar to the magnetic viscosity effect observed in high coercivity alloys under rather similar conditions.[12] In the latter case, the effect was shown to be caused by the influence of thermal agitation on the direction of domain magnetization vectors. Thermal energy may provide sufficient energy to allow a transition of vectors from positions of metastable to stable equilibrium. Analysis in these terms shows that the time variation of intensity of magnetization is proportional to $\log t$ when an applied field is changed to a constant value at time $t=0$. However, in practice, the time constant of an electromagnet circuit will not permit field changes to be made in this ideal way and the parameter t_0 depends on the time required for the field to reach a steady value. The time dependence is particularly marked at temperatures near and below that at which the susceptibility peak occurs and with reverse fields approximately equal to the coercive force. At very low temperatures, the time dependence is less marked and is not observed at all at temperatures above the susceptibility peak. There is thus strong evidence for the view that thermal agitation plays an important part in the magnetization of the ferromagnetic component of these alloys.

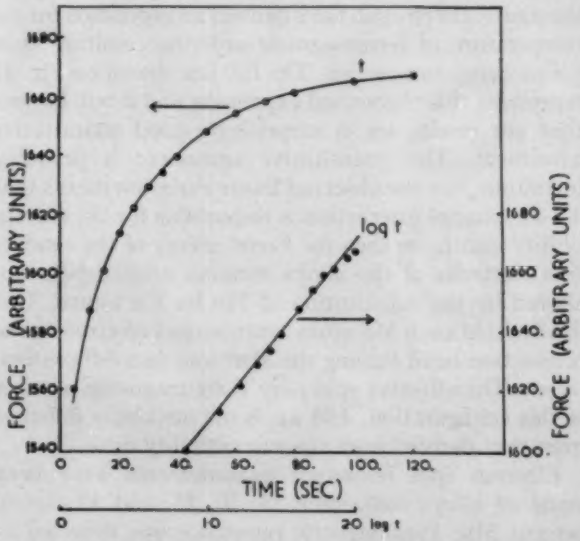

FIG. 13. The time variation of the force acting on a specimen containing 30 atomic % Mn. The specimen was originally cooled to 78°K in a forward field of 10 koe and measurements were made at 78°K in a reverse field of 10 koe applied at time $t=0$.

[12] R. Street and J. C. Woolley, Proc. Phys. Soc. (London) **B69**, 1189 (1956).

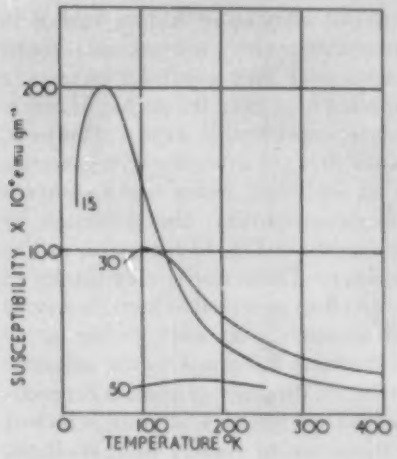

FIG. 14. The temperature variations of the susceptibility of γ MnCu alloys containing 15, 30, and 50 atomic % Mn.

The temperature variations of the susceptibility of three typical γ Mn Cu alloys cooled in zero field are shown in Fig. 14. It is not possible to obtain reliable higher temperature susceptibility measurements for the higher manganese-content alloys resulting from the formation of mixed (α+γ) phases. However, at lower Mn compositions, Curie-Weiss law behavior is observed from which the effective Bohr magneton numbers of the ions may be calculated at least approximately. The values obtained are in reasonable agreement with those derived by Myers,[13] obtained from measurements on these γ phase alloys at temperatures up to 1000°C, which lie between 4.3 and 4.9 μ_B. The temperature of the susceptibility maximum is plotted as a function of Mn content in Fig. 15. Our measurements do not appear to be in agreement with those of Owen et al.[14] on lower manganese composition alloys, which are also shown on the figure. Owen et al. have derived an expression for the temperature of ferromagnetic ordering resulting from *s-d* exchange interaction. The full line drawn on Fig. 15 represents this theoretical expression and it will be seen that our results are in surprisingly good quantitative agreement. The quantitative agreement is probably fortuitous, but the observed linear variation means that if *s-d* exchange interaction is responsible for the susceptibility maximum then the Fermi energy of the conduction electrons of the alloys remains substantially unaltered by the substitution of Mn for Cu atoms. This implies that each Mn atom contributes 1 electron to the conduction band leaving the Mn^+ ions in a $3d^6$ configuration. The effective spin only Bohr magneton number of this configuration, 4.91 μ_B, is not strikingly different from that derived from the susceptibility data.

Electron spin resonance measurements have been made on alloys containing 15, 20, 25, and 30 atomic percent Mn. Paramagnetic resonance was detected in all the alloys at sufficiently high temperatures; the lines were broad and usually distorted but with a peak absorption corresponding to $g=2.0$. This line had a width which increased rapidly with decreasing temperature and reached zero intensity at a temperature which was characteristic of the particular alloy. The results were in fact very similar to the disappearance of the paramagnetic resonance line in an antiferromagnetic when approaching its Néel temperature. The temperature at which the broad paramagnetic absorption line disappears exceeds that of the susceptibility maximum by an amount which increases rapidly with increasing manganese content, e.g., for the 30 atomic percent alloy this difference is approximately 200°C. Near and above the temperature of maximum susceptibliity, the character of the resonance spectrum was completely changed in that a relatively intense symmetrical narrow resonance line (of width of the order of 100 oe and $g=2.00$) was observed, which disappeared completely below the temperature of maximum susceptibility. We consider that this is a ferromagnetic resonance line. For some alloy compositions, it was possible to observe both the broad paramagnetic and the narrow ferromagnetic lines at certain temperatures.

It is possible to consider a model of these alloys containing less than 50 atomic percent Mn from a statistical point of view. On progressively reducing the temperature, short range antiferromagnetic order in small groups of manganese ions first occurs and the ordering temperature of a group will vary according to the number of ions cooperating in the group. Therefore, there will be no definite Néel temperature for the material as a whole since there will be a statistical distribution of group size. From the electron spin resonance results, it may be inferred that this short range antiferromagnetic ordering occurs in general at temperatures much higher than the

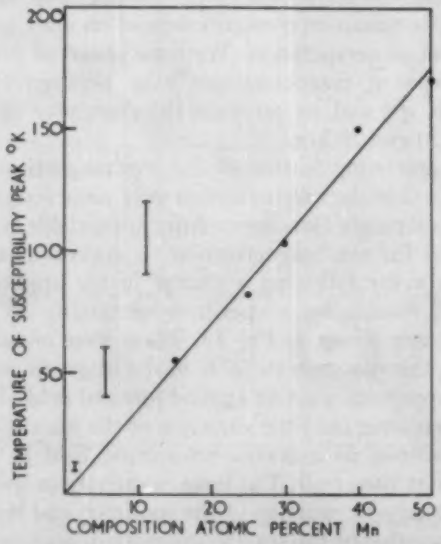

FIG. 15. The variation of the temperature of susceptibility maximum as a function of alloy composition. The vertical lines represent the results of Owen et al.[14] on similar alloys of lower Mn content.

[13] H. P. Myers, Can. J. Phys. 34, 527 (1956).
[14] J. Owen, M. Browne, W. D. Knight, and C. Kittel, Phys. Rev. 102, 1501, 1956.

susceptibility peak. Additional evidence for this is provided by the neutron diffraction results of Meneghetti and Sidhu[4] who considered that the broad diffraction line they observed near the (100) reflection angle was due to short range antiferromagnetic ordering. Their results show that this line persists at temperatures well above the susceptibility peak. For *small* groups of ions with spins arranged antiferromagnetically it is unlikely that the resultant magnetic moment will be zero. The observed ferromagnetic resonance line may be accounted for by the precession of this uncompensated moment around the field direction if magnetocrystalline anisotropy energy is low. At temperatures below that of the susceptibility peak the magnetic measurements show that the magnetocrystalline anisotropy energy of the uncompensated magnetic moment is large, which is perhaps caused by *s-d* exchange interaction, thus suppressing the electron spin resonance.

ACKNOWLEDGMENTS

I wish to acknowledge with thanks the help and assistance afforded by Dr. G. E. Bacon, J. H. Smith, Dr. J. M. Titman, M. G. Cornwall, and D. A. Read who have collaborated with me in this work.

JOURNAL OF APPLIED PHYSICS SUPPLEMENT TO VOL. 31, NO. 5 MAY, 1960

Mechanism of Antiferromagnetism in Dilute Alloys*

A. W. OVERHAUSER
Scientific Laboratory, Ford Motor Company, Dearborn, Michigan

A MECHANISM for the antiferromagnetic ordering of a dilute paramagnetic solute in a metal is proposed and discussed in relation to the phenomena that occur in Cu-Mn alloys. Long-range antiferromagnetic order results from a static spin density wave in the electron gas of the metal. This new state of the gas is dynamically self sustaining as a result of the exchange potentials arising from the spin density distribution. The paramagnetic solute atoms are then oriented by their exchange interaction with the spin density wave. The resulting interaction energy more than compensates the increase in energy associated with the formation of the spin density wave. The theory predicts correctly the magnitude and concentration dependence of the critical temperature, the anomalous low-temperature specific heat, and the anomalous electric and magnetic properties of the alloys.

* The text of this paper will appear in the J. Phys. Chem. Solids.

Long-Range Magnetic Interactions via Conduction Electrons

ARTHUR PASKIN
Materials Research Laboratory, Ordnance Materials Research Office, Watertown, Massachusetts

Yosida has shown that the long-range ferromagnetic term arising from the exchange interaction between conduction electrons and unfilled inner-shell electrons, does not appear explicitly when the calculation is extended to second-order perturbation (i.e. the magnetic interaction term to second-order perturbation is not long-range but decreases rapidly with distance). Upon re-examining the Yosida calculation, we find that the long-range magnetic term disappears because of noninteracting electron approximations made for the energy and density of states of the conduction electrons. Without the latter approximation but still to second-order, the long-range magnetic interaction appears with a coefficient proportional to $[(\partial^2 E/\partial n^2)^{-1}-\rho(E_f)]$ where $\rho(E_f)$ is the density of states evaluated at the Fermi energy; n, the number of conduction electrons (of a given spin); and E, their energy. This coefficient can be estimated both from theoretical calculations of Pines on electron interaction effects in metals as well as from nuclear magnetic resonance data. From the calculations of Pines, we conclude that the coefficient is such that the long-range magnetic interaction may not be neglected. On using nuclear magnetic resonance data, we estimate that the magnitude of the long-range term and the short-range interaction term are the same for the Cu-Mn alloys studied by Yosida.

INTRODUCTION

KASUYA[1] and Mitchell[2] have placed the Zener mechanism[3] of ferromagnetism arising from an exchange interaction between the conduction electrons and the unfilled inner-shell electrons on a more rigorous footing. Kasuya's work[1] was directed towards explaining the magnetic properties of the transition and rare-earth metals. Yosida[4] later applied Kasuya's calculation[1] to the magnetic and associated properties of dilute Cu-Mn alloys. In particular, Yosida[4] elaborated on the relationship between the second-order effect of the s-d exchange and the first-order effect which is directly the Zener interaction. Yosida[4] found that the long-range Zener interaction was incorporated in the second-order term and the resultant interaction is a spin coupling term that falls-off rapidly with the distance between spins. Yosida's work[4] does not elaborate on the conditions under which the long-range interaction vanishes and leaves a spin-coupling term that is essentially short-range relative to the Zener term. We have therefore re-examined the Yosida calculation[4] to see if the disappearance of the long-range interaction is a direct consequence of the exchange interaction via conduction electrons or results from some simplifying approximations made in the calculation. We find that the Yosida result is a consequence of neglecting electron interaction effects in parts of the calculation.[4] We shall here show that the long-range interaction does not vanish to second-order perturbation when electron interactions occur, but instead contributes a magnetic interaction of the same order of magnitude as the second-order term of Yosida.[4]

THEORY

We start with the energy of the conduction electron-inner electron interaction to second-order perturbation essentially as given by Kasuya[1] and Yosida.[4]

$$\begin{aligned}\mathcal{H}=&2E(n)-(E'')^{-1}\mathfrak{M}^2\\&+N^{-2}\sum_m\sum_t\sum_{\mathbf{k}}\sum'_{\mathbf{k}'}|J(\mathbf{k}-\mathbf{k}')|^2\\&\times\exp[i(\mathbf{k}-\mathbf{k}')\cdot\mathbf{R}_{mt}]\\&\times(E_k-E_{k'})^{-1}[2f_k(1-f_{k'})]S_m^{\,z}S_t^{\,z}\\&+N^{-2}\sum_m\sum_t\sum_{\mathbf{k}}\sum_{\mathbf{k}'}|J(\mathbf{k}-\mathbf{k}')|^2\\&\times\exp[i(\mathbf{k}-\mathbf{k}')\cdot\mathbf{R}_{mt}](E_k-E_{k'})^{-1}\\&\times[f_k(1-f_{k'})(S_m^{+}S_t^{-}+S_m^{-}S_t^{+})].\end{aligned}\quad(1)$$

Equation (1) was obtained by using equilibrium values of $n_\pm$ for all functions that depend explicitly on n_+ and n_-, the total number of conduction electrons with spin $+$ and $-$, respectively. $E(n_\pm)$ are the unperturbed energies that depend on $n_\pm$. The primed summation $\sum'_{\mathbf{k}'}$ for the z component, means to exclude $\mathbf{k}'=\mathbf{k}$. The essential difference between (1) and the energy terms of Kasuya[1] and Yosida[4] is that we have not limited ourselves to a noninteracting electron approximation of the $E(n)$. All other terms in (1) are essentially defined by Yosida,[4] namely, N is the total number of lattice sites; $J(\mathbf{k}-\mathbf{k}')$, the exchange integral between the conduction and inner-electrons; $\mathbf{k}$, the wave vector of the conduction electrons; $\mathbf{R}_m$, the site of the unpaired inner-electrons giving rise to the spin represented by the operator $\mathbf{S}_m$; $\mathbf{R}_{mt}=\mathbf{R}_m-\mathbf{R}_t$; f_k, the unperturbed Fermi distribution; and E_k, the energy of state k, assumed to depend only on the magnitude of k. The equilibrium values of $n_\pm$ used in (1) were obtained by minimizing the energy (to first order perturbation) and are given by

$$n_\pm-n=\pm\mathfrak{M}/[\partial^2 E(n_\pm)/\partial n_\pm^{\,2}]_{n_\pm=n}=\pm\mathfrak{M}(E'')^{-1},\quad(2)$$

where $\mathfrak{M}=N^{-1}J(0)\sum_m S_m^{\,z}$. On examining Yosida's work[4] we find that the long-range interaction term (the second term of (1)) vanishes when the $\mathbf{k}'=\mathbf{k}$ term of the z component is explicitly introduced into (1). Adding and subtracting the latter term, identically cancels the long-range term in the noninteracting electron approximation of Yosida.[4] We now examine this term without

[1] T. Kasuya, Progr. Theoret. Phys. (Kyoto) **16**, 45 (1956).
[2] A. H. Mitchell, Phys. Rev. **105**, 1439 (1957).
[3] C. Zener, Phys. Rev. **81**, 440 (1951).
[4] K. Yosida, Phys. Rev. **106**, 893 (1957); *ibid* **107**, 396 (1957).

making the latter approximation. We are therefore interested in evaluating

$$\sum_{\mathbf{k}} \lim_{\mathbf{k}'\to\mathbf{k}}\{|J(\mathbf{k}-\mathbf{k}')|^2 \times\exp[i(\mathbf{k}-\mathbf{k}')\cdot\mathbf{R}_{mt}](E_k-E_{k'})^{-1}[2f_k(1-f_{k'})]\}. \quad (3)$$

$f_k(1-f_{k'})$ differs from zero only in the vicinity of the Fermi energy E_f where $k=k_m\gg|\mathbf{k}'-\mathbf{k}|$. Keeping the first two terms of the Taylor's series expansion of $f_{k'}$ and $E_{k'}$ in the region $k'\cong k$, and setting $\mathbf{q}=\mathbf{k}'-\mathbf{k}$, we approximate (3) by

$$\sum_{\mathbf{k}} \lim_{q\to 0}\left\{\frac{2|J(\mathbf{q})|^2\exp(i\mathbf{q}\cdot\mathbf{R}_{mt})}{E_{k'}} \times\left[\frac{f_k(1-f_k)(2k)}{2\mathbf{k}\cdot\mathbf{q}-q^2}+f_kf'_k\right]\right\}. \quad (4)$$

where $f'_k=\partial f_k/\partial k$ and $E'_k=\partial E_k/\partial k$. The second term of (4) can be evaluated directly because of the separability of the k and q dependent factors. The first term can be put into a similar form by averaging over all directions of $\mathbf{k}$ relative to $\mathbf{q}$. We then find

$$\sum_{\mathbf{k}} \lim_{q\to 0}\{2|J(\mathbf{q})|^2\exp(i\mathbf{q}\cdot\mathbf{R}_{mt})(E'_k)^{-1} \times[-f_k(1-f_k)(2k)^{-1}+f_kf'_k]\}. \quad (5)$$

The q and k dependence of both terms in (5) are now separable and the limit may be taken. Further introducing the density of states $\rho(E_k)$, the sum over k is replaced by an integral over dE_k, and (5) in the limit $q\to 0$ is

$$2|J(0)|^2\int dE_k\rho(E_k)(E'_k)^{-1} \times[f_kf'_k-f_k(1-f_k)(2k)^{-1}]. \quad (6)$$

Making use of the form of f_k, and the delta-function like behavior of $(-\partial f_k/\partial E_k)$, the only contribution to (6) is at E_f. We thus write (6) as

$$-2|J(0)|^2\{\rho(E_k)[f_k+KT/(2kE'_k)]\}_{E_k=E_f} =-|J(0)|^2\rho(E_f), \quad (7)$$

where K = Boltzmann's constant and T = temperature. The final simplification is obtained by noting

$$KT/(2k_mE'_{km})\cong KT/E_f\ll\tfrac{1}{2}.$$

From (7) and (1), the energy to second-order perturbation is

$$\mathcal{H}=2E(n)-[(E'')^{-1}-\rho(E_f)]\mathfrak{M}^2 +N^{-2}\sum_m\sum_l\sum_{\mathbf{k}}\sum_{\mathbf{k}'}[J(\mathbf{k}-\mathbf{k}')|^2 \times\{\exp[i(\mathbf{k}-\mathbf{k}')\cdot\mathbf{R}_{mt}](E_k-E_{k'})^{-1} \times[2f_k(1-f_{k'})](\mathbf{S}_m\cdot\mathbf{S}_l)\}. \quad (8)$$

The long-range magnetic interaction term is thus proportional to the coefficient $C=[(E'')^{-1}-\rho(E_f)]$, and does not vanish identically to second-order perturbation.

MAGNITUDE OF C

C can be estimated from the electron interaction calculations of Pines.[5] For the alkali metals, C ranges from (0.2−0.8) times $\rho^0(E_f)$, the noninteracting electron value of $\rho(E_f)$. An alternate semi-empirical approach is to estimate C in terms of the fractional Knight shift $(\Delta H/H)$ and the spin-lattice relaxation time T_1. Pines[5] has shown that electron interactions alter the Korringa relationship[6] as follows:

$$[T_1(\Delta H/H)^2] \cong[T_1(\Delta H/H)^2]_{\text{free electron}}[1+2C/\rho^0(F_f)]. \quad (9)$$

From Korringa[6] we find that the calculated free-electron value for copper is 1.2×10^{-8} and from Redfield[7] and Knight[8] we find the experimental value is 1.8×10^{-8}. From (9) we find $C/\rho^0(E_f)=0.25$ for copper and thus for the Cu-Mn alloys treated by Yosida,[4] the long-range magnetic interaction is of the same order of magnitude as the short-range interaction. It might be noted that this estimate of the long-range magnetic interaction for dilute Cu-Mn alloys is compatible with the temperature dependent Knight shifts recently observed by Sugawara[9] whereas Owen, Browne, Knight, and Kittel[10] interpret their earlier Knight shift data as being in contradiction to the occurrence of significant long-range magnetic interactions in the Cu-Mn alloys.

EXTENSION OF CALCULATIONS

On decomposing the unperturbed energy into its interacting (s-s) and noninteracting (single particle) terms, we find the additional long-range term (to second-order perturbation) arises from the combined inner-outer (s-d) and (s-s) interactions. We are now extending the calculation to *higher-order perturbation* using the Gell-Mann and Brueckner formulation[11] to examine the generality of the present results.

ACKNOWLEDGMENT

I thank Dr. R. J. Harrison for many valuable discussions of the problem.

---

[5] D. Pines, Solid State Phys. **1**, 368 (1955).
[6] J. Korringa, Physica **16**, 601 (1950).
[7] A. G. Redfield, Phys. Rev. **101**, 67 (1956).
[8] W. D. Knight, Solid State Phys. **2**, 93 (1956).
[9] T. Sugawara, J. Phys. Soc. Japan **14**, 643 (1959).
[10] Owen, Browne, Knight, and Kittel, Phys. Rev. **102**, 1501 (1956).
[11] M. Gell-Mann and K. A. Brueckner, Phys. Rev. **106**, 364 (1957).

Hyperfine Interactions in Magnetic Materials by γ–γ Angular Correlation Measurements*

M. E. Caspari and S. Frankel
Department of Physics, University of Pennsylvania, Philadelphia, Pennsylvania

and

M. A. Gilleo
Lockheed Aircraft Corporation, Missile and Space Division, Palo Alto, California

A method for measuring hyperfine interactions in magnetic materials by $\gamma-\gamma$ angular correlation techniques is discussed. The change in the anisotropy of the 1415-122 Kev $\gamma-\gamma$ angular correlation following the K capture of Eu^{152} in neutron irradiated polycrystalline samples of Europium iron garnet enriched in Eu^{151} has been measured as a function of temperature without applied magnetic field, and the rotation of the angular correlation pattern has been observed when a magnetic field was applied perpendicular to the plane containing the γ counters. From these experiments, the effective magnetic field acting at the Europium nuclei immediately after the radioactive decay can be obtained.

IT is well known that in magnetic materials in the ordered phase paramagnetic resonance is unsuitable for the experimental determination of hyperfine interactions. Nuclear magnetic resonance on the paramagnetic ion in the ordered phase of magnetic materials has so far only been observed in very few cases.[1,2] Another measurement of hyperfine interactions in magnetic materials involves the determination of the degree of nuclear alignment at very low temperatures.[3]

The technique which will be described in this paper allows the measurement of the hyperfine interaction in ferro-, ferri-, and antiferromagnetic materials at any temperature below the Curie point and without the application of an external magnetic field, except possibly a field just strong enough to align the domains in ferro- or ferrimagnetic materials. At the same time, one also obtains information regarding the magnetic moments of short lived excited nuclear states. The method involves $\gamma-\gamma$ angular correlation measurements, which have long been employed for the determination of spins and parities of excited nuclear states.[4] In this technique, one studies the decay of a radioactive nucleus in which, following the β decay or K capture process, the ground state of the daughter nucleus is reached with the successive emission of two γ-rays via an intermediate excited nuclear state. In an angular correlation experiment, one measures the coincidence rate of the two γ rays as a function of the angle between them. The percentage difference between the coincidence rates at 90° and 180° is called the anisotropy. It is well known that correlation measurements are perturbed in many cases by magnetic and quadrupole interactions. In the case of ferro- or ferrimagnetic materials, when a sample is saturated by a magnetic field perpendicular to the plane containing the γ counters, the effective magnetic field acting at the nuclei, H_{eff}, also points in the same direction and produces a Larmor precession of the nuclear spin of the intermediate excited state, which can be detected by the change in the angular correlation pattern of the second γ ray relative to the first in a coincidence measurement. The correlation pattern turns through an angle $\theta=\frac{1}{2}\tan(2\omega\tau)$, where

$$\omega\tau=(\mu_n H_{eff}\tau/\hbar),$$

and where μ_n is the magnetic moment and τ the lifetime of the excited state. At the same time the anisotropy of the correlation is reduced by a factor which depends on $\{1+(\omega\tau)^2\}^{-1}$. Since H_{eff} is usually of the order 10^8–10^9 koe in the transition elements Fe, Co, Ni and somewhat larger in the rare earths[3] and since nuclear g factors fall in the range 0.1 to 6, this method is usually applicable to decay schemes involving such paramagnetic atoms or ions, which have a reasonably large anisotropy in the angular correlation, and in which the lifetimes of the intermediate states lie in the range 10^{-9} to 10^{-11} sec. The lifetimes of the excited nuclear states of the above order of magnitude are usually known from independent measurements. The experiment, therefore, determines H_{eff} if the g factor of the intermediate state is independently known. Conversely, if H_{eff} is known from any one of the techniques described in the beginning of this paper, the g values of short lived excited nuclear states can be determined. Even if H_{eff} is not known, ratios of g values of various excited states can be measured if suitable decay schemes involving more than one intermediate state exist in the same nucleus. In an antiferromagnetic crystal or in a multidomain ferro- or ferrimagnetic crystal or powder, there will be no rotation of the angular correlation pattern but there may be partial wipeout of the correlation which can be used to determine the hyperfine interaction. The same effect can also be expected in paramagnetic materials as long

* This work was supported in part by the Office of Ordnance Research, the Office of Naval Research, and the National Science Foundation.

[1] V. Jaccarino, Phys. Rev. Letters **2**, 163 (1959).
[2] A. C. Gossard and A. M. Portis, Phys. Rev. Letters **3**, 164 (1959).
[3] N. Kurti, J. Appl. Phys. **30**, S155 (1959).
[4] For a simple account of angular correlation measurements and the effect of extranuclear fields on the correlation, see for instance, Rolf M. Steffen, Phil. Mag. **4**, 293 (1955).

as the temperature is low enough so that H_{eff} does not average to zero over a period equal to the lifetime of the intermediate excited state. An obvious advantage of the technique is that it can be utilized to measure hyperfine interactions at the paramagnetic atom in very dilute solutions of paramagnetic atoms in a diamagnetic lattice as well as in the bulk of certain superconductors. In crystals where quadrupole effects exist, these can be studied separately above the Curie point.

Our first experiment demonstrating the validity of the technique is concerned with an investigation of the hyperfine interaction in the K capture decay of Eu^{152} in neutron irradiated polycrystalline samples of europium iron garnet enriched in Eu^{151} by studying the 1415-122 Kev $\gamma-\gamma$ correlation which involves the 2+ rotational state in Sm^{152}. This state is known to have a mean lifetime of 2×10^{-9} sec,[5] and the g factor has been determined independently and is reported to have a value of 0.2.[6] The anisotropy of the angular correlation as a function of temperature without applied magnetic field is shown in Fig. 1. Even well above the Néel point, there is a considerable wipeout in the anisotropy of the angular correlation which has tentatively been attributed to quadrupole effects. Well below the Néel point, the full magnetic effect on the angular correlation becomes apparent. This effect does not appear immediately below the Néel temperature because the sublattice magnetization of the europium ions is not large immediately below the Néel point. One can obtain the magnetic hyperfine interaction to first approximation by neglecting the quadrupole interactions if the square of the quadrupole interaction energy is much less than the square of the magnetic interaction energy. By neglecting the quadrupole interaction, we find $\omega\tau=1.5$, and we estimate that the inclusion of quadrupole effects will raise this value to 1.7. The detailed calculations of this effect are in progress. The value $\omega\tau=1.7$ leads to an effective magnetic field $H_{eff}=9\times10^5$ oe. When a magnetic field is applied perpendicular to the plane of the counters and the sample is saturated, the rotation of the angular correlation is observed. The rotation and the magnitude of the angular correlation pattern agree well with the value of $\omega\tau$ estimated above. It is, at present, impossible to say whether the hyperfine interaction is due to the europium or samarium ion or to some intermediate atomic configuration. Preliminary experiments on the β decay of Eu^{154} to Gd^{154} in neutron irradiated europium iron garnet samples enriched in Eu^{152} indicate that H_{eff} is much smaller in this case.

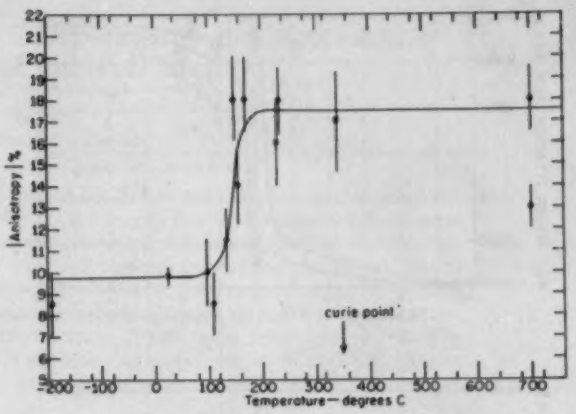

FIG. 1. Anisotropy of the 1415-122 kev $\gamma-\gamma$ angular correlation following the K capture of Eu^{152} in neutron irradiated polycrystalline samples of Europium iron garnet enriched in Eu^{151} as a function of temperature without applied magnetic field.

[5] A. W. Sunyar, Phys. Rev. **98**, 653 (1955).
[6] G. Goldring and R. P. Scharenberg, Phys. Rev. **110**, 701 (1958).

ACKNOWLEDGMENTS

During the stay of one of us (M. A. G.) at the Bell Telephone Laboratories, materials and services were generously provided for the synthesis of specimens by D. W. Mitchell. We would also like to express our gratitude to Dr. S. Geschwind of the Bell Telephone Laboratories for supplying us with further samples and for many helpful discussions.

JOURNAL OF APPLIED PHYSICS SUPPLEMENT TO VOL. 31, NO. 5 MAY, 1960

Magnetic Properties of Ferromagnetic Superconductors

R. M. BOZORTH AND D. D. DAVIS
Bell Telephone Laboratories, Murray Hill, New Jersey

Solid solutions of $GdRu_2$ in $CeRu_2$ are known to be superconducting and ferromagnetic. Magnetic measurements are reported for the 4 and 8% alloys; these show negative initial susceptibility (zero permeability) and hysteresis loops characteristic of superconductors. The 8% alloy shows typical ferromagnetic saturation and hysteresis at 5°K, and at 1.3° it appears to be both ferromagnetic and superconducting at the same time. Detection of ferromagnetism in the superconducting 4% alloy is difficult and could not be established.

IN studying the properties of solid solutions of $GdRu_2$ in $CeRu_2$ at low temperatures, Matthias, Suhl, and Corenzwit[1] have shown that these alloys are superconducting and ferromagnetic. The alloys become superconducting when the concentration is less than about 10% $GdRu_2$, those containing 6 to 30% $GdRu_2$ are ferromagnetic with a Curie point approximately proportional to the concentration.

[1] B. T. Matthias, H. Suhl, and E. Corenzwit, Phys. Rev. Letters **1**, 449 (1958).

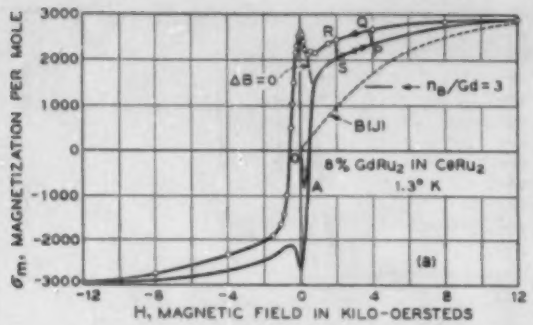

(a)

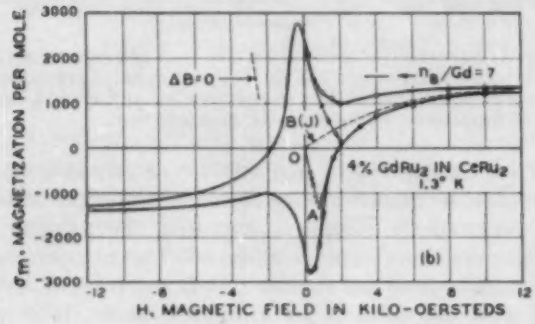

(b)

FIG. 1. Hysteresis loops of two $GdRu_2$-$CeRu_2$ alloys: (a) 8% $GdRu_2$, showing superconductivity and ferromagnetism; (b) 4%, showing superconductivity.

We have studied two of these alloys in some detail; the 8% alloy ($Gd_{0.08}Ce_{0.92}Ru_2$), which we find to become ferromagnetic at 6.2°K, is expected to become superconducting on cooling; the 4% alloy, which we find to be superconducting at 5°K, is expected to be ferromagnetic at about 3°K. The purpose of our work has been to show, by means of magnetic measurements, whether the expected behavior is followed or whether the previous existence of ferromagnetism (or superconductivity) modifies the occurrence of superconductivity (or ferromagnetism).

The most relevant data are the magnetization curves and hysteresis loops of Fig. 1, measured at 1.3°K. The 8% alloy [Fig. 1(a)] shows the initial negative magnetization (OA) and the increase of magnetization with decreasing field in the first quadrant of the hysteresis loop, both phenomena being characteristic of a superconductor. The data also indicate in two ways that the material is ferromagnetic at this temperature: (1) the magnetization curve lies well above that calculated, using the Brillouin function $B(J)$, for an ideal paramagnetic material of this gadolinium content, and (2) the remanence is well above that expected for a purely paramagnetic superconductor, a point now to be explained in more detail.

A superconductor when magnetized will show a change in magnetization[2] corresponding to zero change in the induction B ("frozen in" flux) so that

$$B=H+4\pi I=0, \quad I=\sigma_m d/M=-H/(4\pi),$$

where d and M are the density and molecular weight, respectively. When the field H is increased to the critical value H_{CR}, superconductivity will be destroyed, then on decrease of H will exist again from H_{CR} to $-H_{CR}$. The result is that the maximum negative value of σ_m on the initial curve (point A) should be no larger than the positive value of σ_m on the hysteresis loop at the point where the true field is zero (taking into account the demagnetizing factor), provided there is no ferromagnetic remanence. Figure 1(a) shows that there is a large such remanence in the 8% alloy and that this material is ferromagnetic.

The minor loop $PQRS$ shows that superconductivity exists in at least part of the alloy in fields of 4000 oe when the superconductivity of the specimen as a whole has been destroyed. This suggests that we have a mixture of domains of superconductivity and domains of ferromagnetism in the same specimen at the same temperature and field strength.

The same two criteria of ferromagnetism as applied to the 4% alloy do not give conclusive results. The difference between the frozen-in flux as measured on the initial curve and that for the hysteresis loop at a true field of zero is comparable with the error in measurement. Also, the magnetization curve calculated on the assumption that the Brillouin function applies to this material suggests that the material is paramagnetic with perhaps only weak ferromagnetism. Whether or not the Brillouin function can be applied is, of course, an open question. Ferromagnetism could not be established by either method within the experimental error.

Measurements of a 10% alloy give no sign of superconductivity at 1.3°. This alloy has a Curie point, θ, of about 8°, as determined by interpolation of the θ vs composition curve. Thus, the superconducting transition temperature, T_s, drops very suddenly around the 10% composition, probably as a result of the strong ferromagnetism ($\theta \gg T_s$). Conversely, the existence of strong superconductivity ($T_s \gg \theta$) appears to modify the ferromagnetism.

ACKNOWLEDGMENT

We are indebted to E. Corenzwit and A. J. Williams for preparation of the material and assistance with the measurements and to B. T. Matthias, H. Suhl, and P. W. Anderson for helpful discussions.

[2] D. Shoenberg, *Superconductivity* (University Press, Cambridge, England, 1952).

Strong Field Magnetization at Low Temperatures and Approach to Absolute Saturation of Thulium Metal

WARREN E. HENRY
United States Naval Research Laboratory, Washington, D. C.

Magnetization studies of metallic thulium have been carried out at low temperatures and in magnetic fields up to 70 000 gauss. Near 100°K, the magnetization (M) is linear in field and reaches 0.8 Bohr magnetons per atom of thulium at 70 000 gauss. At 4.2°K, a magnetization curve is traced in which the direction of concavity changes twice. In the high field range, $(\partial M/\partial H)$ is decreasing and between 60 000 and 70 000 gauss, it is very small. At 70 000 gauss, the magnetization reaches 3.4 Bohr magnetons per atom of thulium, suggesting the validity of the $^2F_{7/2}$ ground state assignment for metallic thulium. At 1.3°K, the magnetization is slightly lower at equivalent fields, but approaches the same 70 000 gauss value as at 4.2°K. The remanence is 0.3 Bohr magneton per atom at 4.2°K and 0.4 Bohr magneton per atom at 1.3°K. A pronounced hysteresis is observed in the liquid helium range. A sample motion technique is used in the measurements and the calibration carried out with pure nickel.

INTRODUCTION

FOR verifying results inferred from optical spectroscopy and quantum mechanics and obtaining results not fully delineated by them, there are two general conditions under which magnetic atomic constants are determined. These are (1) at low values of H/T and (2) at high values of H/T, where H is the magnetic field to which the atomic dipole is subjected and T is the absolute temperature. Under condition (1) there are two approaches: (a) through electronic paramagnetic resonance from which constants such as the Landé splitting factor, g, are arrived at; and (b) through susceptibility measurements from which the intrinsic magnetic moment, μ, is estimated from the equation

$$\mu = A[\chi(T-\theta)]^{\frac{1}{2}}, \qquad (1)$$

containing two arbitrary constants, A and θ. θ is sometimes an undetermined function of T the temperature, χ is the susceptibility. With condition (2), the saturation magnetization, gJ, can be directly determined and can be compared forthrightly with values determined by spectroscopy and quantum mechanical treatment.

Previous work on thulium has been limited to two investigations: one, corresponding to (1, *b*), by Klemm and Bommer,[1] and the other by Rhodes, Legvold, and Spedding[2] who verified the work of Klemm and Bommer and attempted condition (2). Klemm and Bommer, using a powdery mixture of thulium metal and alkali chloride, and magnetic fields of about 2000 gauss, deduced some properties for thulium. These included a ferromagnetic Curie point of 10° and susceptibilities which, when put into formula (1), were used to estimate an intrinsic moment, μ. They estimated that $[J(J+1)]^{\frac{1}{2}} = 7.6$ Bohr magnetons as the effective intrinsic magnetic moment in a range 90–291°K and in fields under 2000 gauss, where the susceptibility was field independent.

Direct magnetization measurements were made on thulium metal by Rhodes, Legvold and Spedding, who had temperatures avaialble down to 4.2°K and a magnetic field up to 18 000 gauss. Under these conditions, they were able to reach only 20% of saturation. They obtained a magnetization of less than one Bohr magneton per atom of thulium.

The gJ values of the rare earth trivalent ions have been worked out by Van Vleck[3] and his students; this quantity amounts to 7 Bohr magnetons per gadolinium ion, corresponding to an $^8S_{7/2}$ ground state. It turns out that the saturation magnetization of gadolinium is also 7 Bohr magnetons per atom of gadolinium. If it were assumed that the ground state of the thulium atom is the same as the thulium ion, $3\,H_6$, the gJ product would be 7 Bohr magnetons per atom of thulium. This value is inferred from the low field, high temperature susceptibility measurements mentioned above and the two-constant Eq. (1). On the other hand, spectroscopic data indicate a $^2F_{7/2}$ ground state for the thulium metal atom, leading to a gJ product of 4.0 Bohr magnetons per atom of thulium. It is of interest to measure magnetization in the saturation range to attempt to determine, by direct experimental measurement, the magnetic atomic constant, gJ, for thulium metal.

EXPERIMENTAL METHOD

The low temperature magnetization measurements were carried out on thulium metal by a method previously described[4] in which the sample is moved between the centers of two coils wound in series opposition and in series with a ballistic galvanometer, the deflection of which is proportional to the magnetic moment of the sample. The measuring system was calibrated with nickel. The low temperatures were produced in a metal dewar[5] for liquid helium and the magnetic fields were produced using a modified Bitter solenoid[6] energized by

[1] W. Klemm and H. Bommer, Z. anorg. u. allgem. Chem. **231**, 138 (1937).
[2] Rhodes, Legvold, and Spedding, Phys. Rev. **109**, 1547 (1958).
[3] J. H. Van Vleck, *The Theory of Electric and Magnetic Susceptibilities* (Oxford University Press, New York).
[4] W. E. Henry, Phys. Rev. **88**, 559 (1952).
[5] W. E. Henry and R. L. Dolecek, Rev. Sci. Instr. **21**, 496 (1950); W. E. Henry, J. Appl. Phys. **22**, 1439 (1951).
[6] F. M. Bitter, Rev. Sci. Instr. **10**, 373 (1939).

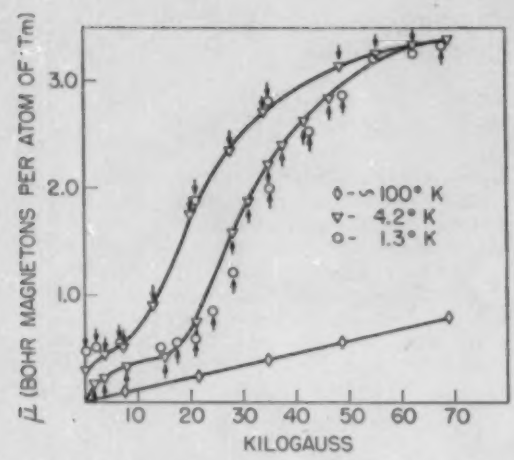

FIG. 1. Plot of magnetization against magnetic field (H) for thulium metal at 1.3°, 4.2° and in the range of 100°K. Arrows up indicate increasing field.

a 2 megawatt, controlled D. C. generator. The sample, a lump of metallic thulium, was obtained from City Chemical Company and had a purity of 99.8 per cent.

DISCUSSION OF RESULTS

Figure 1 shows a plot of isothermal magnetization of thulium metal against magnetic field for several fixed temperatures. At 100°K, the linear magnetization is 1.1×10^{-5} Bohr magneton per gauss-atom and reaches 0.75 Bohr magneton per atom of thulium at 70 000 gauss. At 4.2°K and at low magnetic fields, the shape of the magnetization curve is similar to that of Rhodes, Legvold, and Spedding in that $(\partial^2M/\partial H^2)_T$ is negative below about 13 000 gauss then goes positive. There is a rapid increase in the moment as a function of magnetic field in the range 13 000–18 000 gauss, just as was found in their results; however, at 18 000 gauss the magnetization of our sample amounted to 0.75 Bohr magneton per atom, whereas Rhodes, Legvold, and Spedding got 0.8 Bohr magneton per atom at 18 000 gauss and 4.2°K.

In this investigation, beyond 18 000 gauss, the magnetization continued to increase rapidly and at about 30 000 gauss $(\partial^2M/\partial H^2)_T$ went negative and the increase in magnetization decreased with increasing fields. At 70 000 gauss, the magnetization reached 3.4 Bohr magnetons per atom of thulium. A pronounced hysteresis was shown. For example, at 34 500 gauss, the magnetization for increasing fields is 2.2 Bohr magnetons per atom of thulium while for decreasing fields it is 2.7 Bohr magnetons per atom. At 20 000 gauss, the descending value is three times the ascending value.

At 1.3°K, the magnetization is slightly lower for equivalent low fields, perhaps indicating increased anisotropy, but the value at 70 000 gauss is about the same at 1.3°K as at 4.2°K. The remanence is 0.4 Bohr magneton per atom at 1.3°K, as compared with 0.3 Bohr magneton per atom at 4.2°K.

The average magnetization of thulium at liquid helium temperatures and 70 000 gauss (3.4 Bohr magneton per atom) is not quite the saturation magnetization although the slow rate of rise of the magnetization with field in this high field range suggests an extrapolated value perhaps a little less than 4.0 Bohr magnetons per atom of thulium and is in accord with a $^2F_{7/2}$ ground state for the $4f^{13}6s^2$ configuration of thulium metal. It is possible that this sluggish approach to saturation is caused by the joint action[7] of the crystalline electric field and spin-orbit coupling. If one should try to force the concept of a $^3H_6$ ground state for thulium metal by assuming $4d$ occupancy and thus ignoring the values of the screening constants deduced from experiment, the expected saturation magnetization (gJ) would be 7 Bohr magnetons per atom and the disagreement between theory and the approached saturation would be marked. This could be explained, however, by assuming an anisotropy in the gJ product. That is, if gJ is assumed to be 7 Bohr magnetons per atom in one crystalline direction and, due to pronounced splitting of the ground state, the Pauli principle is applied for the perpendicular plane, the average could be three Bohr magnetons per atom of thulium. Now, if there were a 5% nonrandom distribution of directions of crystalline axes an apparent saturation magnetization of about 3.7 Bohr magnetons would be expected.

This investigation has yielded high field magnetization at low temperatures which magnetization is approaching the absolute magnetic saturation of thulium metal. The value approached lends support to the theoretical model in which a $^2F_{7/2}$ ground state is assumed. The slowness of approach to absolute saturation is attributed to the combined effect of the crystalline electric field and spin-orbit coupling. The strong hysteresis and substantial remanence attest to the ferromagnetism in thulium metal at liquid helium temperatures.

[7] M. H. L. Pryce (private communication); J. H. Van Vleck (private communication).

Magnetic Behavior of Polycrystalline Neodymium, Holmium, and Erbium from 300 to 1500°K

SIGURDS ARAJS AND D. S. MILLER
Edgar C. Bain Laboratory for Fundamental Research, United States Steel Corporation, Research Center, Monroeville, Pennsylvania

The paramagnetic susceptibilities of polycrystalline Nd, Ho, and Er have been determined from about 300 to 1500°K by the Faraday method. The inverse paramagnetic susceptibility versus temperature ($1/\chi$ vs T) curve for Nd at high temperatures show two slight anomalies associated with a solid state phase transformation and the melting point, respectively. The paramagnetic susceptibility of hcp Nd does not satisfy the Weiss-Curie law due to the partial population of the energy levels above the ground state $^4I_{9/2}$. The paramagnetic susceptibility of Ho and Er is representable by the Weiss-Curie law. The experimental Bohr magneton numbers are in satisfactory agreement with those predicted by the Van Vleck theory.

MUCH experimental work has been done on the various physical properties of the rare earth metals from 1 to 300°K. However, the high temperature behavior of these metals has not been so thoroughly explored. Only in a few cases has the magnetic behavior of the rare earths been studied above 300°K. Such studies, however, would be of considerable value in understanding the origin of magnetism in these metals. Recently, we studied the magnetic behavior of rare earth metals at elevated temperatures by measuring magnetic susceptibility. This paper reports these measurements on Nd, Ho, and Er from 300 to 1500°K.

The polycrystalline Nd, Ho, and Er used in this investigation were all better than 99% pure, with less than 0.1% of other rare earths. Fe content was found to be 0.02% in Nd and less than 0.05% in Ho. There was no iron detected in the erbium. The magnetic susceptibility was measured with an experimental error of ±3% using the Faraday method.

The inverse paramagnetic susceptibility of Nd as a function of temperature is shown in Fig. 1. Our susceptibility values as a function of temperature are in satisfactory agreement (within ±5%) with the room temperature data of the previous low temperature work.[1–6] The only known high temperature studies on the magnetism in Nd are due to Owen[7] and Bates et al.,[8] extending to about 800 and 700°C, respectively. Our measurements are in very good agreement with those of Bates et al., but not with Owen's results, as can be seen in Fig. 1. Spedding et al.[9] have reported a phase transformation in Nd at 862°C and the melting point at 1024°C.[10] Our magnetic measurements show slight anomalies at about these temperatures (Fig. 1). It is interesting that neither the phase transformation nor the melting process gives rise to discontinuities in the plot of inverse magnetic susceptibility versus temperature. This observation is very different from that in Fe above its ferromagnetic Curie temperature, where the $\alpha-\gamma$ and the $\gamma-\delta$ transformation and the melting process produce discontinuities in the curve of inverse susceptibility vs temperature.[11] It appears that these effects indicate different models for magnetism in these materials. Although the electronic structure of bcc and fcc Fe and its relation to the magnetic behavior of Fe is not completely understood at the present time, the paramagnetism in metallic Nd can be approximately explained using the Nd^{3+} approximation and the Van Vleck theory of paramagnetism of the rare earth ions.[12] Since the energy levels of the lowest multiplet are relatively close together in comparison with the thermal

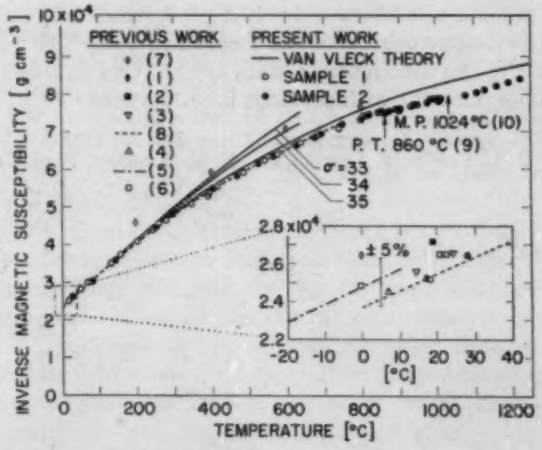

FIG. 1. Inverse paramagnetic susceptibility of Nd as a function of temperature.

[1] F. Trombe, Ann. Phys. **7**, 383 (1937).
[2] W. Klemm and H. Bommer, Z. anorg. allgem. Chem. **241**, 264 (1939).
[3] J. F. Elliott, S. Legvold, and F. H. Spedding, Phys. Rev. **94**, 50 (1954).
[4] D. R. Behrendt, S. Legvold, and F. H. Spedding, Phys. Rev. **106**, 723 (1957).
[5] J. M. Lock, Proc. Phys. Soc. (London) **B70**, 566 (1957).
[6] H. Leipfinger, *Magnetic Properties of Rare Earth Metals at Very Low Temperatures* (Physik. Inst. Tech. Hochs. München, 1957), Technical Rept. Z. Physik **150**, 415 (1958).
[7] M. Owen, Ann. Phys. **37**, 657 (1912).
[8] L. F. Bates, S. J. Leach, R. G. Losby, and K. W. H. Stevens, Proc. Phys. Soc. (London) **B68**, 181 (1955).
[9] F. H. Spedding, A. H. Daane, and K. W. Hermann, J. Metals **9**, 895 (1957).
[10] F. H. Spedding, S. Legvold, A. H. Daane, and L. D. Jennings, "Some Physical Properties of the Rare Earth Metals," in *Progress in Low Temperature Physics*, edited by C. J. Gorter (North-Holland Publishing Company, 1957), Vol. II, p. 368.
[11] Y. Nakagawa, J. Phys. Soc. (Japan) **11**, 855 (1956).
[12] J. H. Van Vleck, *The Theory of Electric and Magnetic Susceptibilities* (Oxford University Press, New York, 1932), p. 226.

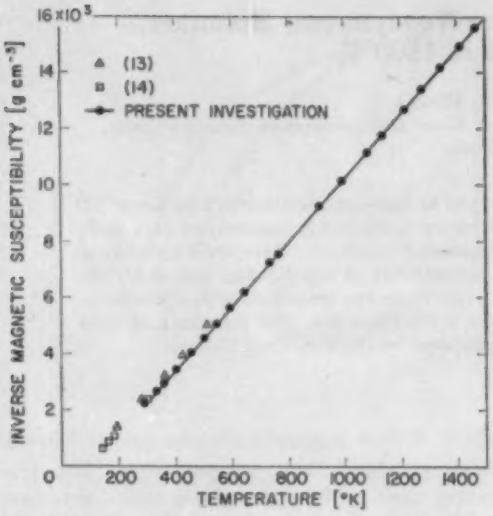

FIG. 2. Inverse paramagnetic susceptibility of Ho as a function of temperature.

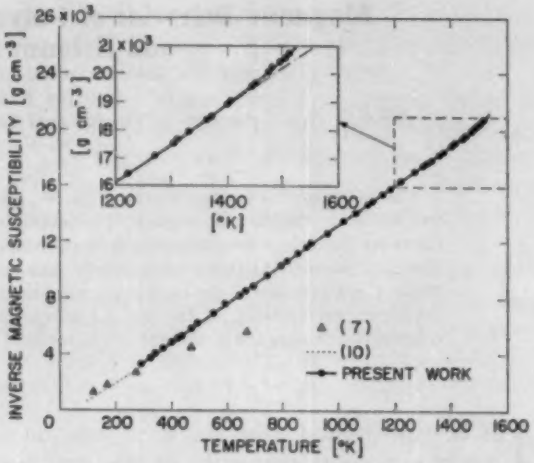

FIG. 3. Inverse paramagnetic susceptibility of Er as a function of temperature.

energy kT, the occupancy of the energy states above the ground state $4f^3\ {}^4I_{9/2}$ invalidates the Curie-Weiss law. The theoretical inverse paramagnetic susceptibility versus temperature curves calculated from the Van Vleck theory using various screening constants σ, and assuming the Russell-Saunders coupling are shown in Fig. 1. An approximate agreement with the experimental data for the hcp Nd is obtained for $\sigma=35$.

The inverse paramagnetic susceptibility *vs* temperature data for Ho obtained in this investigation are shown in Fig. 2. The Curie-Weiss law, $\chi=8.79\times10^{-3}/(T-87.7)$, where χ is the magnetic susceptibility per g and T the absolute temperature, is satisfied up to 1500°K. The effective Bohr magneton number obtained from these measurements is 10.8 ± 0.2, which is in satisfactory agreement with the theoretical value[12] 10.6 for Ho^{3+} in the spectroscopic state $4f^{10}\ {}^5I_8$. Our data are in good agreement with previous investigations.[13,14]

The inverse paramagnetic susceptibility of Er as a function of temperature is shown in Fig. 3. The Curie-Weiss law $\chi=7.16\times10^{-2}/(T-47.2)$ is obeyed up to about 1400°K. At this temperature, a very slight anomoly occurs whose origin is not understood at the present time. Our measurements are in agreement with those of Spedding et al.,[10] but do not agree with Owen's[7] work done on powdered Er. The experimental effective Bohr magneton number obtained from our data is 9.79 ± 0.15, which compares favorably with the theoretical value[12] 9.60 for Er^{3+} in the ground state $4f^{11}\ 4I_{15/2}$.

ACKNOWLEDGMENTS

We are indebted to R. W. Whitmore for the analysis of the experimental data by the method of least squares and computations with the IBM 650 computer. Stimulating discussions with R. A. Oriani and S. Legvold, and the technical assistance of A. D. Damick, have been greatly appreciated.

[13] H. Bommer, Z. anorg. allgem. Chem. **242**, 277 (1939).
[14] B. L. Rhodes, S. Legvold, and F. H. Spedding, Phys. Rev. **109**, 1547 (1958); B. L. Rhodes, "Magnetic Properties of Holmium and Thulium," U. S. Atomic Energy Commission Rept. ISC-701 (1955).

Analysis of Magnetic Interactions in Alloys of Platinum with Iron Group Transition Elements

HIROSHI SATO
Scientific Laboratory, Ford Motor Company, Dearborn, Michigan

The magnetic properties of alloys of platinum with iron group transition elements are analyzed and interpreted on the basis of an Ising model of ferromagnetism. It is found that in the wide ranges of compositions of the face-centered-cubic alloys of Ni, Co, Fe, Mn, and Cr with Pt there is systematic change with atomic number in the dependence of Curie temperature and saturation magnetization on concentration of magnetic atoms or on the formation of superlattices. Values of magnetic interactions in alloys, which also depend on the concentration, are estimated mainly from the Curie point by using the Cluster-Variation method. The magnetic moment of Pt atoms can be induced in alloys and this tendency becomes stronger as the *d*-shell radii of magnetic atoms increase. The analysis also indicates that the magnetic interactions of γ-Fe, γ-Mn and f.c.c. Cr change their signs from negative to positive by merely increasing the interatomic distance. This is most clearly shown in the case of γ-Fe. Further, it is suggested that the alloys Mn-Pt and Cr-Pt would show ferrimagnetic behavior as found in disordered Ni-Mn alloys. Based upon such analyses, a qualitative conclusion concerning the dependence of magnetic interactions upon distance is drawn. The general behavior of the interaction is consistent with the generally accepted picture of the location of these elements with respect to the "Bethe-Slater curve" of exchange interactions if the distances are short, but not if the distances are longer.

I. INTRODUCTION

SINCE the understanding of the interaction between magnetic moments in metals and alloys is still quite unsatisfactory, even a qualitative analysis of the relation between magnetic properties and simple physical variables would be important for a further sound theoretical treatment. The so-called "Pauling-Slater curve," which relates the saturation value of alloys to the number of electrons thus has stimulated a great deal of speculation and discussion. Alloys of platinum with each one of the Fe group transition metals (Ni to Cr) give a good example of this kind. These alloys form wide-range solid solutions with the face-centered cubic structure, and furthermore, superlattices of the same symmetries as those found in the Au-Cu system are formed in all of these systems. The magnetic interaction is extracted from the properties of these alloys using an Ising type model.[1] A localized approach has a certain advantage over a collective electron approach[2] in the present case, since the effect of local distribution of atoms can be more easily taken care of.

II. METHOD OF ANALYSIS

Although it is not justifiable to carry this kind of treatment to an extreme, its application would be safe in this case because the object is to point out a systematic change of magnetic properties in similar alloys depending on the species of alloying elements.

The analysis of the properties are made on the following bases:

(i) Curie point of the alloys. The Curie point of a disordered A-B alloy can be calculated by the Cluster-Variation method to be the temperature, which satisfies the following equation,

$$\begin{aligned}49[&(1-c)^2K_1/(K_1+1)+c^2K_3/(K_3+1)\\&+2(1-c)c\{K_1K_3/(K_1+1)(K_3+1)+K_2/(K_2+1)^2\}]\\&-28[c\{2K_3/(K_3+1)+1\}\\&+(1-c)\{2K_1/(K_1+1)+1\}]+32=0. \quad (1)\end{aligned}$$

Here, K_1, K_2, and K_3 are defined by

$$K_1=e^{J_{AA}/kT}, \quad K_2=e^{J_{AB}/kT}, \quad K_3=e^{J_{BB}/kT},$$

respectively. J_{AA}, J_{AB} and J_{BB} are the interaction between the spins A-A, A-B, and B-B pairs. c is the concentration of B atoms, here to be Pt atoms. For the case of simple dilution, ($J_{AB}=J_{BB}=0$), the result is already given.[3]

We can assume $J_{BB}=0$ from the analysis of magnetic properties of platinum. However, a moment can be induced in a platinum atom in alloys. Therefore we can assume a finite value for J_{AB} as well as a contribution to the saturation value of alloys from such platinum atoms.[4] Eq. (1) shows that a finite value of J_{AB}, irrespective of its sign, raises the Curie point above that of the simple dilution.

(ii) Critical concentration. Since J_{BB} is zero, the Curie point becomes zero at some point on the Pt side. This concentration is called the critical concentration. A simple calculation of the critical concentration based on Eq. (1) shows that it is 0.86 for simple dilution but it becomes 0.98 when the contribution from A-B pairs is taken into account for b.c.c. structure ($z=8$). For f.c.c. structure ($z=12$), the values are even higher.

(iii) Saturation value. If a magnetic moment is induced in a platinum atom, this will affect the saturation value of alloys.

(iv) Dependence of the Curie point upon the degree of order. If $J_{AA}>J_{AB}$, the Curie point of the ordered state

[1] H. Sato, Proc. Conference on Magnetism and Magnetic Materials, AIEE, New York (1955) p. 119; H. Sato, A. Arrott, Phys. Rev. **114**, 1427 (1959).
[2] E. P. Wohlfarth, Phil. Mag. **45**, 647 (1952).
[3] Sato, Arrott and Kikuchi, J. Phys. Chem. Solids **10**, 19 (1959).
[4] We retain $J_{BB}=0$ in alloys in calculation. This assumption can be justified within the degree of approximation of this treatment.

is lower than the disordered state and vice versa. This can be a check on the magnitude of J_{AB}.

(v) Temperature dependence of the saturation value. If $J_{AA}>J_{AB}$, the reduced saturation value of the disordered state would be higher than the ordered state at the same reduced temperature and vice versa.[5] This will also give another check on the value of J_{AB}.

(vi) Possible contribution from the next nearest A-A pairs. If the alloy AB_3 becomes ordered, there will be no A-A nearest neighbors. The change in properties thus gives a possibility of estimating the magnitude of A-A second nearest neighbor interactions.

III. RESULTS OF ANALYSIS

Ni-Pt.[6] The concentration dependence of the Curie temperature and the critical concentration suggest that $J_{AB}\neq 0$. The dependence of the Curie point on order of Ni_3Pt and NiPt supports this fact.

Co-Pt.[7] From the concentration dependence of the Curie temperature and the critical concentration, it can be concluded that there is a positive contribution of J_{AB}, but its magnitude is far smaller than J_{AA}. The dependence of the Curie point on the degree of order of Co_3Pt, CoPt, and $CoPt_3$ supports this conclusion. The difference of the temperature dependence of the saturation between ordered and disordered Pt_3Co, the only case investigated in detail[8] also confirms this conclusion.[9]

Fe-Pt.[10] There is indirect evidence, from the low temperature study of γ-phase iron alloys, that γ-Fe is slightly antiferromagnetic.[11] ($J_{AA}<0$). The onset of ferromagnetism on the Fe side is at about 20% Pt. The Curie point reaches a maximum at about 50% Pt and vanishes at very high concentration of Pt. This concentration dependence of the Curie point on the Pt side and the critical concentration indicates, however, that both J_{AA} and J_{AB} are positive. This fact is also borne out by the saturation value of alloys of high Pt content.[12]

The dependence of the Curie point on the degree of order reveals that $J_{AB}<J_{AA}$ in the concentration range $FePt_3$ and FePt but $J_{AB}>J_{AA}$ at Fe_3Pt. This fact strongly indicates that J_{AA} increases from a negative value to a large positive value with the addition of Pt and surpasses the value of J_{AB} at the concentration between Fe_3Pt and FePt. This assumption well explains the concentration dependence of the Curie point of Fe-Pt alloys.

Mn-Pt and Cr-Pt. Both of these systems are similar in behavior.[13,14] Since γ-Mn is actually antiferromagnetic, so would be f.c.c. Cr. ($J_{AA}<0$). However, the alloys are ferromagnetic on the platinum side. This is due to a strong positive J_{AB} contribution. The dependence of the Curie point of the concentration can be explained by these assumptions. Higher Curie points for ordered $MnPt_3$ and $CrPt_3$ than the disordered alloys also support this assumption. Further, by increasing Mn or Cr contents, the Curie point increases but the saturation value decreases passing through a maximum. This indicates that the alloys become ferrimagnetic at high concentrations because of the coexistence of positive J_{AB} and negative J_{AA} just as observed in disordered Ni-Mn.[1,15]

IV. SUMMARY

J_{AA} is positive for Ni and Co, but negative for γ-Mn and f.c.c. Cr. For γ-Fe, it is negative, but it becomes positive by the addition of Pt. If we plot this result against the ratio of atomic distance to d shell radius, R/r, in the conventional way in Fig. 1, we get a curve similar to the "Bethe-Slater" curve.[16] Since the lattice constant increases with the addition of Pt, the range is also shown in Fig. 1. This indicates also that J_{AA} of γ-Fe changes its sign by increasing the atomic distance. The estimated value of J_{AB} is also plotted in the figure. It clearly indicates that J_{AB} increases with the degree of overlapping of d electron wave function.

Analysis of second nearest neighbor interaction mainly from the properties of AB_3 type alloys shows that it is definitely negative for Fe, but positive for Mn or Cr. This conclusion agrees with the conclusion obtained

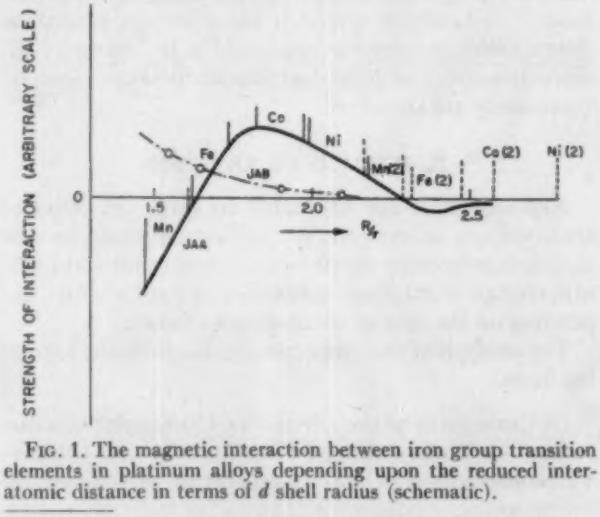

FIG. 1. The magnetic interaction between iron group transition elements in platinum alloys depending upon the reduced interatomic distance in terms of d shell radius (schematic).

[5] H. Sato, Sci. Rept. RITU **A1**, 71 (1949); Sec. Rept. Japan Inst. Metals **II**, 1 (1949).

[6] A. Kussmann and H. Nitka, Phys. Z. **39**, 373 (1938); V. Marian, Ann. phys. **7**, 459 (1937).

[7] E. Gebhardt and W. Köster, Z. Metallk. **32**, 253 (1940).

[8] A. W. Simpson and R. H. Tredgold, Proc. Phys. Soc. (London) **B67**, 38 (1954).

[9] Generally, the temperature dependence of the saturation value is less convex in the case of alloys as compared to pure metals. Went[9a] suggested that in the case of alloys statistical concentration fluctuation caused the effect, however, that in the ordered case, there would eventually be no concentration fluctuation and the situation would be similar to pure elements as actually observed in Ni_3Fe. Therefore, the case of $CoPt_3$, which is contrary to Ni_3Fe indicates that Went's interpretation is not necessarily true. The calculation based on the Ising model, however, explains this difference.

[9a] J. Went, Physica **17**, 596 (1951).

[10] A. Kussmann and G. v. Rittberg, Z. Metallk. **42**, 470 (1950).

[11] E. I. Kondorski and V. L. Sedov, Soviet Phys.—JETP **35**, 1104 (1958).

[12] J. Crangle, J. Phys. Rad. **20**, 435 (1959).

[13] M. Auswäter and A. Kussmann, Ann. Phys. **7**, 169 (1950).

[14] A. Kussmann and E. Friedlich, Phys. Z. **36**, 185 (1935).

[15] Kouvel, Graham, and Becker, J. Appl. Phys. **29**, 518 (1958).

[16] We used here a schematic plot on a single curve with an arbitrary scale instead of giving each curve for each element using calculated values.

from the dilute solution of Fe in precious metals and the ferromagnetism of manganese alloys and compounds. For Co and Ni, there seems to be no appreciable contributions. This relation is also plotted on the same curve in Fig. 1 although this may not be justifiable. It seems that the overall behavior shown in Fig. 1 cannot be explained without including an indirect exchange mechanism.

JOURNAL OF APPLIED PHYSICS SUPPLEMENT TO VOL. 31, NO. 5 MAY, 1960

Effect of Impurities on the Low-Temperature Spontaneous Magnetization of Cubic Ferromagnetic Crystals*

A. A. MARADUDIN†
Institute for Fluid Dynamics and Applied Mathematics, University of Maryland, College Park, Maryland
AND
P. A. DIXON
Physics Department, University of Maryland, College Park, Maryland

The effect of substitutional impurities on the low temperature spontaneous magnetization of cubic ferromagnetic crystals is investigated in the spin wave formalism with the aid of techniques developed previously for the study of defect problems in lattice dynamics. The impurities considered have an exchange integral with their nearest neighbors different from that between neighbors in the pure crystal. The results of these calculations show that the Bloch $T^{\frac{3}{2}}$ law is still obeyed, but that the coefficient of the $T^{\frac{3}{2}}$ term is a function of the impurity concentration whose form is determined in the limit of low impurity content.

IN this note, we would like to present a method for dealing with certain kinds of problems involving spin waves, and to illustrate this method by applying it to a particular problem.

The classical Bloch spin wave theory predicts that the spontaneous magnetization, $M(T)$, of a ferromagnet in the limit of low temperature and zero external magnetic field varies as $T^{\frac{3}{2}}$. The coefficient of $T^{\frac{3}{2}}$ is a function of the ferromagnet's crystal structure, spin, and most importantly, the exchange interaction. It is of interest to determine the value of this coefficient for crystals, which are more general than the perfect, monatomic, cubic structures usually studied in this approximation. Hence, our purpose in this work is to develop mathematical techniques which can be used to study the magnetic properties of lattices containing impurities, and to apply these techniques to the case of the primitive cubic lattices containing a particular kind of impurity. We display the details of the calculations for simple cubic lattices and merely state the corresponding results for body- and face-centered cubic lattices.

The result, which we obtain by the present method, can also be obtained by more direct methods, and in fact was first obtained by perturbation theory. A third method for obtaining this result has recently been communicated to us by Professor F. Keffer. Thus, the result, while new and of interest itself in that it provides quantitative verifaction of results expected from intuitive arguments, in the present discussion will play a secondary role to the arguments by which it is obtained. Our method, which is based on a theorem from the theory of contour integration and employs arguments from the theory of asymptotic expansions, will be applied first to a derivation of the well known Bloch $T^{\frac{3}{2}}$ law for perfect lattices, and will then be directed to the case of a lattice containing impurities.

In the usual Bloch theory in which isotropic spin coupling between nearest neighbor atoms only is assumed, the Hamiltonian for the spin system is

$$H_0=-g\mu\mathcal{H}\sum_{\mathbf{i}}\mathbf{S}_{\mathbf{i}}^{(z)}-2J\sum_{\substack{\mathbf{i},\mathbf{j}\\ n.n.}}\mathbf{S}_{\mathbf{i}}\cdot\mathbf{S}_{\mathbf{j}}, \qquad (1)$$

where g is the spectroscopic splitting factor and equals 2 approximately, μ is the Bohr magneton, $\mathcal{H}$ is the external magnetic field, $\mathbf{S}_{\mathbf{i}}$ is the spin vector of atom $\mathbf{i}$, and J is the exchange integral for the interaction between atoms $\mathbf{i}$ and $\mathbf{j}$. The ground state eigenfunction of this for a crystal of N atoms is $\psi_0=\prod_{\mathbf{i}}\alpha_{\mathbf{i}}$, where $\alpha_{\mathbf{i}}$ is the usual "spin-up" spin wave function and i represents the position vector of the ith atom in the crystal. The first excited state is characterized by the eigenfunction $\psi_{\mathbf{k}}=\sum_{\mathbf{j}}a_{\mathbf{j}}(\mathbf{k})\phi_{\mathbf{j}}$, where

$$\phi_{\mathbf{j}}=\alpha_1\alpha_2\cdots\alpha_{\mathbf{j}-1}\beta_{\mathbf{j}}\alpha_{\mathbf{j}+1}\cdots\alpha_{\mathbf{N}},$$

and $\beta_{\mathbf{j}}$ is the usual "spin down" spin wave function. It can be shown that with a proper choice of the $\{a_{\mathbf{j}}\}\psi_{\mathbf{k}}$ is equivalent to a spin wave with a wave vector $\mathbf{k}$. Interactions between spin waves are neglected in this linear theory, which is expected to be valid only at low temperatures.

By operating on $\psi_{\mathbf{k}}$ with H_0 leads to the following equations for the $a_{\mathbf{j}}$:

$$[E_{\mathbf{k}}+2zJNS^2-4zJS+2\mu\mathcal{H}NS-2\mu\mathcal{H}]a_{\mathbf{j}}+4JS\sum_{\boldsymbol{\rho}}a_{\mathbf{j}+\boldsymbol{\rho}}, \qquad (2)$$

where z is the coordination number of the lattice, and

* This research was supported by contracts with U. S. Air Force through the Air Force Office of Scientific Research.

† A portion of this work was carried out while this author was a consultant to the General Motors Research Laboratories.

$\mathbf{p}$ is a vector which links the atom at j to its nearest neighbors. By assuming solutions to Eq. (2) of the form $a_j = N^{-\frac{1}{2}} \exp(i\mathbf{k}\cdot\mathbf{j})$, the eigenvalues of H_0 are found to be

$$E(\mathbf{k}) = E_0 + 2\mu\mathcal{H} + 4JS \times (3 - \cos k_x a - \cos k_y a - \cos k_z a), \quad (3)$$

where a is the lattice parameter, and where the ground state energy is given by

$$E_0 = -2zJNS^2 - 2\mu NS\mathcal{H}. \quad (4)$$

The spontaneous magnetization at zero external field, $M(T)$, is obtained from the Helmholtz free energy through the relation

$$M(T) = -1/V(\partial F(T)/\partial\mathcal{H})_{\mathcal{H}=0}, \quad (5)$$

where V is the volume of the crystal.

At low temperatures the free energy can be written as

$$F(T) = E_0 - \beta^{-1} \sum_{n=1}^{\infty} \frac{1}{n} I_n(T) \quad (6)$$

with

$$I_n(T) = \sum_{\mathbf{k}} e^{-n\beta\Lambda(\mathbf{k})}, \quad (7)$$

where $\beta^{-1} = kT$ and $\Lambda(\mathbf{k}) = E(\mathbf{k}) - E_0$ are the excitation energies of the spin waves above the ground state.

The $\{\Lambda(\mathbf{k})\}$ are the eigenvalues of a matrix whose elements are the coefficients of the a_j in Eq. (2). Alternatively, they are the roots of a determinantal equation, which can be written as

$$|D_0(\Lambda)| = \prod_{\mathbf{k}} [\Lambda(\mathbf{k}) - \Lambda] = 0. \quad (8)$$

Thus, with the use of a well-known theorem from the theory of contour integration $I_n(T)$ can be expressed in the form

$$I_n(T) = (1/2\pi i) \int_c e^{-n\beta\Lambda} d\ln |D_0(\Lambda)|, \quad (9)$$

where c is a closed counterclockwise contour which encloses the zeros of $|D_0(\Lambda)|$. We choose for c the D-shaped contour which consists of a semi-circle of radius R in the right hand half-plane and the portion of the imaginary axis $(-iR, iR)$ in the limit as $R \to \infty$. In this limit, the contribution from the semi-circle vanishes, and we have that

$$I_n(T) = -(1/2\pi i) \int_{-\infty}^{\infty} e^{-in\beta x} d\ln |D_0(ix)|. \quad (10)$$

It follows from Eq. (3) and (8) that

$$\Delta(x) = \frac{\partial}{\partial\mathcal{H}} \left\{ \frac{d}{dx} \ln |D_0(ix)| \right\}_{\mathcal{H}=0} = i2\mu \frac{N}{\pi^3} \int\int\int_0^{\pi} \frac{d\phi_1 d\phi_2 d\phi_3}{[ix - 4JS(3 - \cos\phi_1 - \cos\phi_2 - \cos\phi_3)]^3}. \quad (11)$$

According to a theorem of Lighthill[1] the asymptotic behavior of $(\partial I_n(T)/\partial\mathcal{H})_{\mathcal{H}=0}$ in the limit as $T \to 0$ $\times(\beta \to \infty)$ is determined by the nature of the singularities of $\Delta(x)$. It can be shown that the only singularity of $\Delta(x)$ occurs at $x=0$, and leads to

$$\left(\frac{\partial I_n(T)}{\partial\mathcal{H}}\right)_{\mathcal{H}=0} \sim -\frac{N\mu}{\pi^{\frac{1}{2}}} \frac{1}{(4JS)^{\frac{1}{2}}} \frac{1}{(n\beta)^{\beta}} \quad \beta \to \infty. \quad (12)$$

On combining Eq. (5), (6) and (12) we obtain the result that for a perfect simple cubic lattice

$$M(T) = M(0)\left[1 - \frac{1}{S} \frac{2.612}{(4\pi)^{\frac{1}{2}}} \left(\frac{kT}{2JS}\right)^{\frac{1}{2}}\right], \qquad M(0) = \frac{2NS\mu}{V}. \quad (13)$$

Equation (13) just expresses the well-known Bloch $T^{\frac{1}{2}}$ law.

We now turn to the case in which a normal atom in the crystal is replaced by an impurity atom whose exchange integral with its nearest neighbors is $J' = (1-\epsilon)J$, where $\epsilon < 1$. It is assumed that the spin on the impurity atom is the same as on the normal atoms. This assumption is not an essential one but simplifies the calculations. The equations analogous to (2) for the a_j become

$$[E(\mathbf{k}) - E_0' - 2\mu\mathcal{H}]a_j + 2JS \sum_{\substack{\mathbf{p} \\ n.n.}} [a_{j+\mathbf{p}} - a_j] + 2S(J'-J)\delta_{j,0} \sum_{\substack{\mathbf{p} \\ n.n.}} [a_{j+\mathbf{p}} - a_j] + 2S(J'-J) \sum_{\substack{\mathbf{p} \\ n.n.}} [a_{j+\mathbf{p}} - a_j]\delta_{j+\mathbf{p},0} = 0, \quad (14)$$

where E_0' is the perturbed ground state energy

$$E_0' = -2zJ(N-1)S - 2zJ'S - 2\mu NS\mathcal{H}. \quad (15)$$

The excitation energies $\Lambda'(\mathbf{k}) = E(\mathbf{k}) - E_0'$ of the spin waves above the perturbed ground state are the eigenvalues of a matrix whose elements are the coefficients of the a_j in Eq. (14). The corresponding determinantal equation becomes

$$|D(\Lambda')| = |D_0(\Lambda') + \delta D(\Lambda')| = |D_0(\Lambda')||I + D_0^{-1}(\Lambda')\delta D(\Lambda')| = 0, \quad (16)$$

where $D_0(\Lambda')$ is given by Eq. (8), and $\delta D(\Lambda')$ represents the change due to the defect. The change in $I_n(T)$ is

$$\Delta I_n(T) = -(1/2\pi i) \int_{-\infty}^{\infty} e^{-in\beta x} d\ln |I + D_0^{-1}(ix)\delta D(ix)|. \quad (17)$$

[1] M. J. Lighthill, *An Introduction to Fourier Analysis and Generalized Functions* (Cambridge University Press, Cambridge, England, 1958), p. 43.

The elements of the matrix $D_0^{-1}(\Lambda)$ are

$$[D_0^{-1}(\Lambda)]_{i,j}=g(\mathbf{i}-\mathbf{j};\Lambda)=\frac{1}{\pi^3}\int\int_0^\pi\int\frac{\cos m_1\phi_1\cos m_2\phi_2\cos m_3\phi_3 d\phi_1 d\phi_2 d\phi_3}{\Lambda-2\mu\mathfrak{H}-4JS(3-\cos\phi_1-\cos\phi_2-\cos\phi_3)}, \quad (18)$$

where (m_1,m_2,m_3) are the relative coordinates of the points $(\mathbf{i},\mathbf{j})$ in units of the lattice parameter. The following approximation suffices to give us the term in $T^{\frac{1}{2}}$ exactly:

$$\ln|I+D_0^{-1}(ix)\delta D(ix)| \sim 2\epsilon[(ix-2\mu\mathfrak{H})g(0,0,0,ix)-1]. \quad (19)$$

The asymptotic behavior of $[(\partial/\partial\mathfrak{H})\Delta I_n(T)]_{\mathfrak{H}=0}$ in the limit as $\beta\to\infty$ is determined by the small x behavior of (19) so that

$$\left(\frac{\partial}{\partial\mathfrak{H}}\Delta I_n(T)\right)_{\mathfrak{H}=0}\sim-\frac{3}{(4\pi)^{\frac{1}{2}}}\frac{\epsilon\mu}{(2JS)^{\frac{1}{2}}}\frac{1}{(n\beta)^{\frac{1}{2}}},\ \beta\to\infty. \quad (20)$$

Since the change in the ground state energy due to the impurity is independent of $\mathfrak{H}$, from Eq. (6) and (20), we find that the change in the spontaneous magnetization per defect is given by

$$\Delta M(T)=-\frac{1}{V}\frac{3(2.612)}{4\pi^{\frac{1}{2}}}\epsilon\mu\left(\frac{kT}{2JS}\right)^{\frac{1}{2}}. \quad (21)$$

It should be emphasized that this is not a small ϵ result, but is valid for all $\epsilon<1$.

If n such defects are randomly distributed throughout the crystal, where $n\ll N$, then to terms linear in the concentration of the impurity atoms, $c=n/N$, the total change in the spontaneous magnetization can be shown to be n times the expression given by Eq. (21). Thus, to first order in c the spontaneous magnetization of the simple cubic lattice in the Bloch $T^{\frac{1}{2}}$ approximation becomes

$$M(T)=M(0)\left[1-\frac{1}{S}\frac{2.612}{(4\pi)^{\frac{1}{2}}}(1+3\epsilon c)\left(\frac{kT}{2JS}\right)^{\frac{1}{2}}\right]. \quad (22)$$

The corresponding expressions for the body- and face-centered cubic lattices differ from Eq. (22) only in that the coefficients of $T^{\frac{1}{2}}$ are multiplied by $\frac{1}{2}$ and $\frac{1}{4}$, respectively.

From Eq. (22) we see that if the impurities have a stronger exchange coupling with their neighbors than exists in the perfect lattice ($\epsilon<0$), the coefficient of the $T^{\frac{1}{2}}$ term is reduced, and the spontaneous magnetization at a given temperature is increased. The reverse is true if the impurities have weaker exchange interactions with their neighbors than exist in the perfect lattice.

These results agree with what one would expect from purely physical arguments. A stronger exchange coupling between a spin and its neighbors means that more thermal energy will have to be supplied to the crystal to invert that spin, leading to a larger spontaneous magnetization.

A more complete discussion of this problem will be published elsewhere.

JOURNAL OF APPLIED PHYSICS SUPPLEMENT TO VOL. 31, NO. 5 MAY, 1960

Antiferromagnetism of Iron in Face-Centered Crystalline Lattice and the Causes of Anomalies in Invar Physical Properties

E. I. KONDORSKY AND V. L. SEDOV
The Academy of Science of the U.S.S.R., State University of Moscow, Moscow, U.S.S.R.

The anomalies of electrical and magnetic properties in invars at low temperatures and the fact that these anomalies are observed in Fe-Ni alloys with the nickel content ranging from 30 to 40% are explained on the grounds of an assumption that the exchange integral of electrons of neighboring ions of iron in a face-centered lattice is negative which entails a "latent" antiferromagnetism in the invars. This assumption is founded on experimental data obtained by authors and proving that in an Fe alloy with a face-centered lattice, stable at low temperatures thanks to the presence of chromium and nickel alloying elements, an antiferromagnetic transformation occurs. The paper presents results of investigation of the influence of pressure upon the magnetic saturation σ_s and the residual resistivity ρ_0 of iron, nickel and Fe-Ni alloys at low temperatures. It is shown that the values $K_\sigma=(1/\sigma_s)(\Delta\sigma_s/\Delta P)$ and $K_\rho=(1/\rho_0)(\Delta\rho/\Delta P)$ in invar alloys at low temperatures and other Fe-Ni alloys; the ratios K_ρ/K_σ are approximately equal to the ratios $(1/\rho_0)(\Delta\rho_0/\Delta H)/(1/\sigma_s)(\Delta\sigma_s/\Delta H)$, which is in agreement with the conclusions of the suggested theory.

THE physical properties of Invar alloys have a number of anomalies[1]: the low heat expansion coefficient, a substantial value of electrical resistivity, comparatively big values of volume magnetostriction, magnetic susceptibility in the magnetic saturation region and the coefficient $K_\sigma=(\Delta\sigma_s/\sigma_s\Delta P)$ describing the pressure influence upon the specific magnetic saturation σ_s. It follows from the thermodynamic equality: $(1/V)(\partial V/\partial H)_P=-(\partial I_s/\partial P)_H$ that at big values of K_σ, big values of volume magnetostriction should be

[1] R. M. Bozorth, *Ferromagnetism* (D. Van Nostrand Company, Inc., Princeton, New Jersey, 1951).

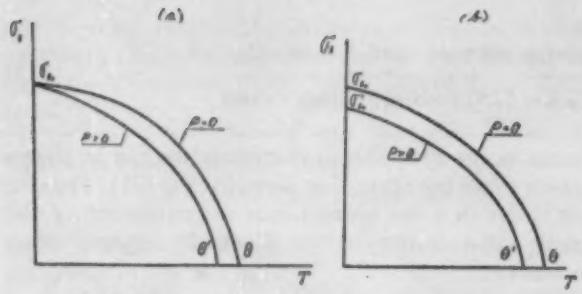

FIG. 1. Diagram of pressure influence upon spontaneous magnetization. (a) The spontaneous magnetization alters only due to Curie point shift. (b) The spontaneous magnetization alters due to Curie point shift and due to the change in the average atomic magnetic moments.

observed in Invars and as a consequence the heat expansion coefficient anomalies. The comparatively big values of K_σ in Invars have been explained heretofore[2–4] by the assumption that the exchange interaction energy between the electrons of neighboring ions in these alloys changes radically under the expansion or compression of the crystalline lattice. It was believed that the point corresponding to the mean exchange integral for ions in Invars is on the steep of the positive section of the Bethe-Slater curve, and it has been considered that the changes in the spontaneous magnetization of these alloys caused by pressure come as a consequence of the Curie point displacement which in its turn is related to the change in the exchange energy when the distance between the lattice ions shrinks or increases. Figure 1(a) shows how the spontaneous magnetization should change under the influence of pressure if the latter caused only the Curie point shift.

This explanation of the K_σ anomaly and of the related peculiarities of physical properties in Invar alloys can hardly be treated as a satisfactory one. It doesn't supply a direct answer as to why these anomalies are observed precisely in the Fe-Ni alloys with nickel concentration ranging from 30 to 45% or in Fe-Pt alloys at definite concentrations, and is not observed in these alloys with some other contents of nickel or platinum. There are also doubts as to the validity of comparing the dependence curve of Curie temperature upon the Ni concentration in Fe-Ni alloys with the Bethe-Slater curve. Finally, from the point of view of the above said concepts it is impossible to explain the high electrical resistivity and a number of anomalies in magnetic properties that have been found recently[5–7] in Invars at low temperatures. In their paper[7] the authors of the present work have shown that the limit value of magnetic saturation $\sigma_0 = (\sigma_s)_{T=0}$ and the residual resistivity ρ_0 change with hydrostatic compression, and that the coefficients $(K_\sigma)_{T=0}$ and $(K_\rho)_{T=0}$ do not turn into zero. Thus, the actual shape of the curve for the Invar alloys at $p>0$ is not as is shown in Fig. 1(a) outline, but follows the pattern of Fig. 1(b). Apparently, the changes of σ_s caused by the pressure in the low temperature region [the left part of the curve in Fig. 1(b)] cannot be explained by the Curie point displacement resulting from pressure.

In our paper[7] we have indicated the possible causes of pressure influence upon σ_0 and ρ_0, in particular that the changes of σ_0 and ρ_0 can be a result of the influence of pressure upon the values of the *d-d* exchange integrals provided certain exchange integrals are negative and their is a noncompensated antiferromagnetism in the alloy. The present work attempts to explain the anomalies of electrical and magnetic properties in Invars at low temperatures and that these anomalies are manifest precisely at a nickel content ranging from 30–40%, proceeding from the assumption that the exchange integral of the *d* electrons of the neighboring ions iron in a face-centered lattice is negative.

I. EXPERIMENTAL GROUNDS FOR SUPPOSING THAT IRON IS ANTIFERROMAGNETIC IN A FACE-CENTERED LATTICE

It has been shown by Weiss and Foex[8] that for the γ phase (face-centered cubic lattice) of iron in the temperature interval from 910–1400°C when the phase is stable, the Curie-Weiss law is valid, but with other values of the C and θ parameters than for the α phase (body-centered cubic lattice). In keeping with Weiss and Foex[8] the θ parameter for the γ iron phase is a

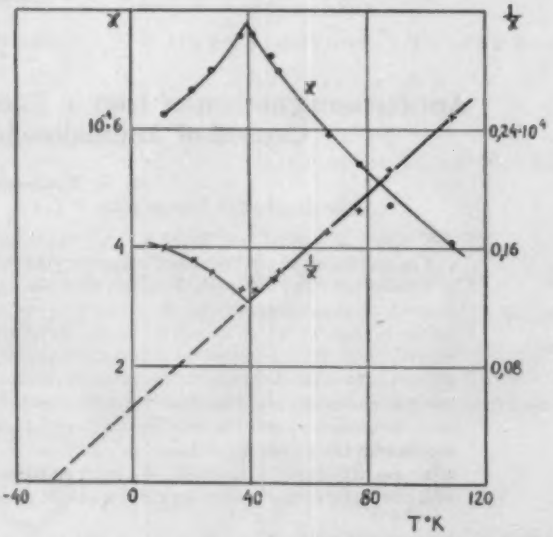

FIG. 2. The temperature dependence of the magnetic susceptibility and its inverse value in austenite steel with 18% Cr and 9% Ni. Fracture points indicating the antiferromagnetic transformation.

[2] M. Kornetzky Z. phys. **98**, 289 (1935).
[3] U. Dehlinger Z. Metallk. **28**, 194 (1936).
[4] K. P. Belov, Soviet Phys.-JETP **19**, 1032 (1949).
[5] D. Smit, Physica **17**, 612 (1951).
[6] K. P. Belov and A. V. Pedko, Doklady (S.S.S.R.) **2**, 214 (1958).
[7] E. I. Kondorsky and V. L. Sedov, Soviet Phys.-JETP **35**, 845 (1958).
[8] P. Weiss and G. Foex, J. phys. radium **1**, 744 (1911).

negative value ($\theta_\gamma = -1340°K$), which gives us grounds to suppose the absence of the ferromganetic transformation in this phase up to the absolute zero. In order to determine whether the γ phase of iron is paramagnetic or antiferromagnetic at low temperatures, we should prevent the $\gamma \rightarrow \alpha$ transition by introducing alloying elements and by appropriate heat treatment. Mott and Stevens[9] made a brief reference to the fact that according to the neutronographic analysis data the Fe-Mn alloys with a face-centered cubic lattice containing over 12% of manganese are antiferromagnetic. However, thus far no works have been published where these data would have been described.

We have investigated the temperature dependence of the magnetic susceptibility of an alloy with a face-centered lattice, containing 73% of Fe, 18% of Cr and 9% of Ni. No precipitate of the ferromagnetic α phase at low temperatures has been observed in the alloys of this content that have been aged at room temperature following their preparation.[10] The specific susceptibility x was measured by means of the procedure described by us.[7] The results are presented in Fig. 2. The antiferromagnetic transformation takes place at 40°K. The value of the paramagnetic Curie point proves to be $-28 \pm 3°K$.

The obtained results give grounds to suppose that the exchange interactions in a face-centered iron lattice would at low temperatures result in antiferromagnetism similarly to the neighboring elements Mn[11–12] and Cr.[13]

II. ANOMALIES IN INVAR ALLOYS MAGNETIC AND ELECTRICAL PROPERTIES AT LOW TEMPERATURES

The magnetic saturation I_S of Fe-Ni alloys at hydrogen temperatures has been studied in the work of Kondorsky and Fedotov.[14] In footnote (15) and in our our paper[7] the residual electrical resistivity of these alloys has been studied. Figure 3 presents the curves describing the dependence $I_0 = (I_S)_{T=0}$ and ρ_0 of Fe-Ni alloys upon Ni content. In the Invar alloy region, there takes place a decrease of I_0 and a radical growth of ρ_0 with the increase of the iron content.

In order to determine how far the $K_\sigma = (\Delta\sigma_s/\sigma_s \Delta P)$ and $K_\rho = (\Delta\rho/\rho\Delta P)$ differ for Invar alloys from the same values in the alloys of other content, we have studied the influence of pressure upon σ_0 and ρ_0 of Fe, Ni, and Fe-Ni alloys of different concentrations.

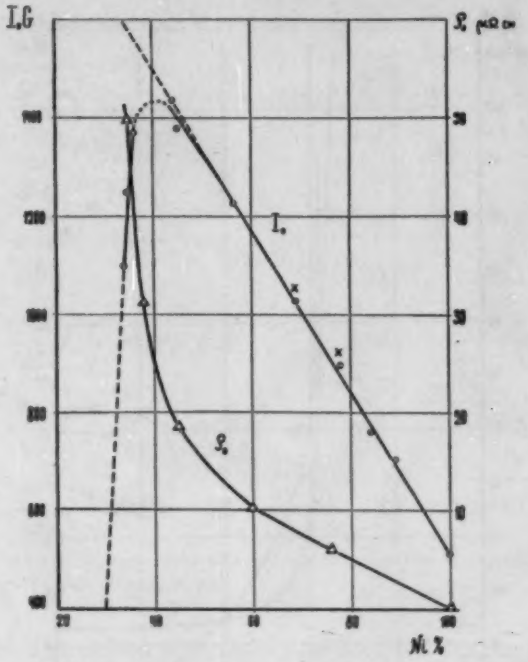

FIG. 3. Magnetic saturation at absolute zero point and residual resistivity of Fe-Ni alloys vs Ni content in alloys. 0, Δ, unordered alloys (data of authors and of Weiss and Foex[8]); x, ordered alloys (data of Weiss and Foex[8]).

A pressure of about 150 atmos was created by gaseous He, which was fed into a beryllium-bronze bomb from a gas tank through a capillar valve. The bomb with the specimen was in a field of a water-cooled solenoid. The measuring coils, the basic and the compensating one were placed outside the bomb and were in the circuit of the photoelectrical fluxmeter with the sensitivity of 5 Maxwell/deg. The error in measuring the value $(\Delta I_s/\Delta P)$ was $\pm 0.15.10^{-4}$ Gauss/atmos. The value was determined by the procedure described by Lazarev and Kan[16] and Brandt and Tomashuk.[17] In this case, the pressure was created by freezing a 3% aqueous solution of alcohol.

It turned out that within the accuracy limits of our measurements the values K_σ of the studied metals and alloys are not dependent on temperature in the range from 4.2 to 20.4°K, while in the same interval K_ρ values slowly diminish with temperature.

Figure 4 presents the curves describing the dependence of the K_σ and K_ρ limit values obtained by extrapolation to absolute zero, from the nickel content in the alloys. In the region of Invar alloys (30–40%), there takes place a radical increase of K_σ and a peak K_ρ. Thus, the *Ki* anomaly in the Invars takes place both at high and low temperatures.

[9] N. Mott and K. Stevens, Phil. Mag. **2**, 1364 (1957).
[10] T. Colombier Hochmann, *Aciers Inoxi Dobles* (Aciers Refractuires, Paris, 1955).
[11] T. B. McGuire and C. T. Kriessman, Phys. Rev. **85**, 452, 9, 1 (1952).
[12] C. G. Shull and M. K. Wilkinson, Phys. Rev. **86**, 599(A) (1952).
[13] C. G. Shull and M. K. Wilkinson, Revs. Modern Phys. **25**, 100 (1953).
[14] E. I. Kondorsky and L. N. Fedotov, Izvest. Akad. Nauk. S.S.S.R. (Phys.) **16**, 432 (1952).
[15] I. Shirakava, Sci. Repts.-Tohoku Imp. Univ. **27**, 485 (1939).
[16] B. G. Lazarev and L. S. Kan, Soviet Phys.-JETP **14**, 439 (1944).
[17] N. B. Brandt and A. K. Tomashuk, Soviet Phys.-JETP **2**, 113 (1958).

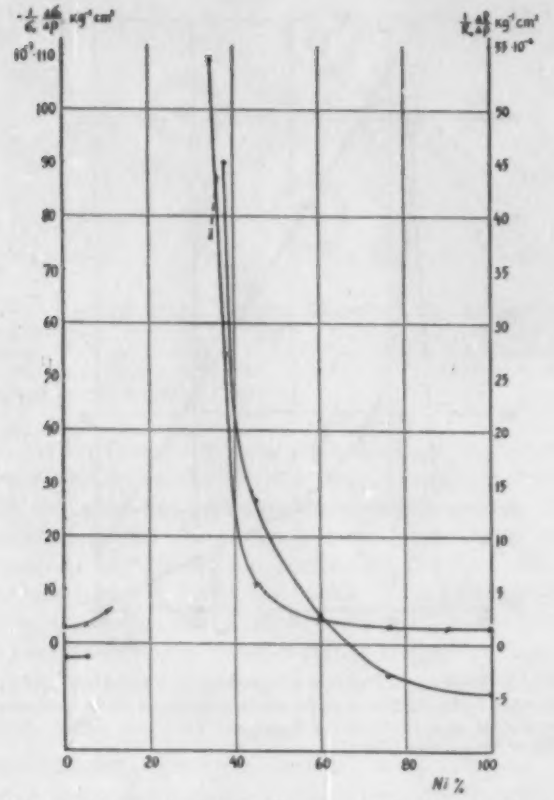

FIG. 4. Values of $K_\sigma=(\Delta\sigma_0/\sigma_0\Delta P)$, and $K_\rho=(\Delta\rho_0/\rho_0\Delta P)$ vs Ni content in Fe-Ni alloys. The curves exhibit the anomalies of K_σ and K_ρ in invars region.

III. FERROMAGNETISM-ANTIFERROMAGNETISM TRANSFORMATION IN IRON-NICKEL ALLOYS WITH FACE-CENTERED LATTICE AS THE CAUSE OF ANOMALIES IN MAGNETIC AND ELECTRICAL PROPERTIES OF INVARS

The quantum-mechanical calculation of the magnetic saturation of disordered alloys involves profound mathematical difficulties and thus far has not been carried out. A calculation of this type for the ordered AB and AB_3 alloys has been performed by Kondorsky and Pakhomov,[18] but the results cannot be applied to disordered alloys like Invars. Therefore, proceeding from the quasi-classical model, we shall try to make a rough estimate of the least nickel concentration in Fe-Ni alloys, at which these alloys can be ferromagnetic, provided that the exchange integral of the d electrons of the neighboring ions of iron is negative. Suppose F_1, F_{12}, and F_2 are exchange integrals between d electrons of neighboring ions of iron, iron and nickel and nickel, respectively; C_1 and C_2 are the concentrations of iron and nickel in the alloy ($C_1+C_2=1$). The concentrations of ions of iron and nickel with the right and left spins shall be denoted as C_1^+, C_2^+, C_1^- and C_2^-, respectively.

As has been indicated for the first time by Vonsovsky,[19] it is impossible to consider the spontaneous magnetization of parts of the lattice occupied by ions of nickel separately from the parts of the lattice occupied by the ions of iron, but rather only the full numbers of τ and l of right and left spins, respectively. Therefore, we should take $C_1^+=(\tau/2n)C_1$, $C_2^+=(\tau/2n)C_2$, $C_1^-=[1-(\tau/2n)]C_1$, $C_2^-=[1-(\tau/2n)]C_2$, where $2n=\tau+l$. Then considering the mean exchange energies of iron and nickel ions with right and left spins surrounded by Z neighbors, ($Z=12$) and taking into account only the interaction between the neighboring ions it is not difficult to obtain for the exchange energy W_a alloy from N ions,

$$W_a=-\frac{NZ}{2}\left(\frac{\tau}{n}-1\right)^2(C_1^2F_1+2C_1C_2F_{12}+C_2^2F_2)\cdots, \quad (1)$$

which coincides with the formula obtained for the first time in the work.[19]

It follows from Eq. (1) that at low temperatures antiferromagnetism is possible provided there are negative exchange integrals. The pure nickel is ferromagnetic, within an increase of the iron content up to 60% the magnetic moment of Fe-Ni alloys increases too. Hence, $F_2>0$, $F_{12}\geqslant 0$. In view of the experimental data that have been mentioned earlier, we may take $F_1<0$. Then, the state with $\tau=2n$, i.e., a ferromagnetic state, will correspond to the smallest values of the exchange energy W_a when the trinominal in the second brackets of formula (1) is positive. When this trinominal is negative, the least value of W_a is obtained at $\tau=n$, which corresponds to antiferromagnetism. Hence, if we have the $C_2>C_k$ concentration, the ferromagnetism is more advantageous from the energy point of view at low temperatures, if $C_2<C_k$, then under the same condition the antiferromagnetism is more advantageous. By taking the trinominal in the formula (1) as being equivalent to zero, we find that

$$C_k=\frac{F_{12}-F_1-(F_{12}^2-F_1F_2)^{\frac{1}{2}}}{2F_{12}-F_1-F_2}\cdots \quad (2)$$

in a special case when $-F_1\approx F_{12}\approx F_2$, $C_k\approx 0.3$, which apparently is a quite satisfactory result.

The random distribution of ions with antiparralel spins is more likely at high temperatures then at low ones when there should take place the groupings of spins (the closest magnetic order). Therefore, between the fully ferromagnetic and the antiferromagnetic, there should be alloys with some of the ions having the antiparallel spins. This type of "latent" antiferromagnetism should take place when the mean energy of the ion of iron with the left spin $W^-=Z(\tau/n-1)\times(F_1C_1+F_{12}C_2)$ is negative, i.e., at a nickel concentra-

[18] E. I. Kondorsky and A. S. Pahomov, Soviet Phys.-JETP **32**, 323 (1957).

[19] S. V. Vonsovsky, Doklady Akad. Nauk. S.S.S.R. **26**, 564 (1949).

tion of $C_2<C_0=-(F_1/F_{12}-F_1)$. Hence, at $-F_1\approx F_{12}$, $C_0\approx 0.5$. While $C_2>C_0$, the ferromagnetic moment of Fe-Ni alloys grows linearly with the increase in the iron content, at $C_2=C_0$ appears a deviation from linearity and at C_2 close to C_k there sets in a radical drop of I_0, thanks to an increase in the number of the antiparallel spins. As it is seen from Fig. 3, the change in the I_0 with the growth of iron content in the Fe-Ni alloys with the face-centered lattice occurs precisely in this way. Let us note that the deviation from the linearity on the curve I_0 occurs in the interval nickel content ranging from 50 to 40%, while with further decrease in nickel content, beginning with 40% a radical drop of I_0 is observed.

We believe that the latent antiferromagnetism should be regarded as the main cause of the anomalies in Invar physical properties. In fact, the presence of the antiparallel spins in these alloys explains the comparatively big values of the volume magnetistriction and the susceptibility in strong magnetic fields. Further, as it is seen from formula (1) the transitional concentration C_k grows with the increase in the absolute value F_1, which most likely grows at hydrostatic compression. Let us note that to explain the C_k "displacement" there is no necessity of assuming that any of exchange integrals correspond to the point on the steep part of the Bethe-Slater curve, and are more sensitive to the changes of the interatomic distances than others. For instance, from (2) at $-F_1=F_{12}=F_2$ and $dF_1/dP=dF_{12}/dP=dF_2/dP=dF/dP$, it follows that $dC_k/dP=-(1/2\sqrt{2}F_1)dF/dP$. Then, if $dF/dP<0$, we find $dC_k/dP>0$. An increase in C_k entails a shift of the steep part of the curve I_0 towards the nickel end, which should be accompanied by radical decrease in I_0 and σ_0 precisely of the Invars which are in the transition region. As it is seen from Fig. 4, the experimental data corroborate this conclusion.

In a similar way, it is possible to explain the anomaly of magnetic properties observed in Fe-Pt alloys at Pt content of 30–40%.

An indirect confirmation of "latent" antiferromagnetism in Invars is their great electrical resistivity,

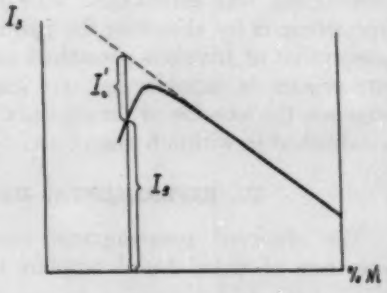

FIG. 5. Diagram illustrates the determination of I_0' and I_s.

TABLE I.

	Content of Ni in alloy 34.7%	38%
$\frac{1}{\rho_0}\frac{\Delta\rho_0}{\Delta C}\Big/\frac{1}{I_0}\frac{\Delta I_0'}{\Delta C}$	−3	−4
$\frac{1}{\rho_0}\frac{\Delta\rho_0}{\Delta H}\Big/\frac{1}{\sigma_0}\frac{\Delta\sigma_0}{\Delta H}$	—	−4.1
K_ρ/K_σ	−3.7	−7.4
$\frac{\Delta\rho_0}{\Delta C}\Big/\frac{\Delta\sigma'^{a}}{\Delta C}$ $\mu\Omega G^{-1}g\tau$ cm^{-6}	−0.9	−0.8
$\frac{\Delta\rho_0}{\Delta H}\Big/\frac{\Delta\sigma_0}{\Delta H}$ $\mu\Omega G^{-1}g\tau$ cm^{-3}	—	−0.8
$\frac{\Delta\rho_0}{\Delta P}\Big/\frac{\Delta\sigma_0}{\Delta P}$ $\mu\Omega G^{-1}g\tau$ cm^{-3}	−1.2	−1.4

[a] $\sigma_0'=I_0'/b\delta$ = density of alloy.

which we believe is caused by the conductivity electron scattering on the magnetic moment heterogeneities. With an increase in the iron content from 50%, the electrical resistivity begins to grow and particularly vigorously in the region of the magnetic moment drop. As a value describing the magnetic moment of antiparallel spins, we may regard $I_0'=I_0-I_s$, where I_0 is the spontaneous magnetization value corresponding to the ordinate obtained by extrapolating the linear part of the I_s curve on the iron end (Fig. 5). I_0 are the spontaneous magnetization values of alloys with x concentrations in real or hypothetical cases when all the spins are parallel. If we determine the $\Delta\rho_0$ electrical resistivity increments and the $\Delta I_0'$ spontaneous magnetization, which correspond to the increase in the iron concentration on ΔC, compose the ratios $\Delta\rho_0/\rho_0\Delta C/\Delta I_0'/I_0\Delta C$ and compare them with the ratios $\Delta\rho_0/\rho_0\Delta H/\Delta\sigma_0/\sigma_0\Delta H$ and K_ρ/K_σ for the alloys of the same concentrations, it turns out that all these ratios are approximately the same. Table I presents the values of these ratios for the alloys with the Ni content of 34.7% and 38%.

The value $(\Delta\rho_0/\rho_0\Delta H)$ in strong fields is negative in ferromagnetics, and ordinarily this has been associated with the fact that when the true magnetization grows in the strong fields the scattering of electrons on spin waves decreases. The "latent" antiferromagnetism considered by us in Invar alloys is reduced to the existence of spin waves at absolute zero. An approximate coincidence of the mentioned ratios may be regarded therefore as a confirmation of the assumption on the "latent" antiferromagnetism.

Magnetic Salts

Paramagnetic Resonance Absorption of Nickel in Sapphire

S. A. MARSHALL AND A. R. REINBERG
Physics Division, Armour Research Foundation, Chicago 16, Illinois

A paramagnetic resonance absorption spectrum which is in excess of that due to trivalent chromium and iron has been observed in sapphire single crystal. The spectrum is interpreted as being due to transitions between fine structure energy states of divalent nickel. Best fit constants to the spin Hamiltonian, obtained at room temperature, are given by $D=[1.385\pm0.002]$ cm^{-1}, $g_{\parallel}=2.196\pm0.004$, and $g_{\perp}=2.187\pm0.004$. Measurements made by progressive saturation of the resonance lines at 77°K give an average spin-lattice relaxation time of 6×10^{-6} sec.

I. INTRODUCTION

FREE divalent nickel ion has a ground term designation ^3F, which is a state of 21 fold degeneracy. As a consequence of the action of crystalline fields and spin-orbit interaction, the low lying states of divalent nickel can be treated as three effective spin states whose degeneracy has been partially lifted.[1-3]

The spin Hamiltonian generally employed in describing such a system of states is given by

$$\mathcal{H}=\beta H\cdot g\cdot S+D[S_z^2-\tfrac{1}{3}S(S+1)], \qquad (1)$$

where β is the Bohr magneton, H is the Zeeman field vector, g is the spectroscopic splitting tensor, S and S_z are spin operators, and D is the zero field splitting energy. For the case of three-fold rotation symmetry and the choice of crystal C axis as axis of quantization, the spin Hamiltonian takes the form,

$$\mathcal{H}=D[S_z^2-\tfrac{1}{3}S(S+1)]+g_{\parallel}\beta HS_z\cos\theta+\tfrac{1}{2}g_{\perp}\beta H\sin\theta[e^{i\varphi}\sigma^-+e^{-i\varphi}\sigma^+], \qquad (2)$$

where θ and φ are the polar and azimuthal angles, σ^- and σ^+ are the spin raising and lowering operators, and H is the magnitude of the Zeeman field vector.

The secular equation obtained by evaluating the Hamiltonian matrix elements in the spin states representation is given by

$$E^3-[(D^2/3)+g^2\beta^2H^2]E+\frac{D}{3}\left[\frac{2}{9}D^2+g^2\beta^2H^2\left(1-3\frac{g_{\parallel}^2}{g^2}\cos^2\theta\right)\right]=0, \qquad (3)$$

where $g^2=g_{\parallel}^2\cos^2\theta+g_{\perp}^2\sin^2\theta$. At $\theta=0°$ the roots to this equation are given by $E_{1,3}=\frac{1}{3}D\pm g_{\parallel}\beta H$ and $E_2=-\frac{2}{3}D$. For this orientation, the state functions are the unmixed spin vectors corresponding to the spin eigenvalues $S_z=0,\pm1$. At $\theta=90°$, the roots to Eq. 3 are given by $E_{1,3}=-\frac{1}{6}D\pm[(D/2)^2+(g_{\perp}\beta H)^2]^{\frac{1}{2}}$, and $E_2=\frac{1}{3}D$. In this case, the state functions are heavily mixed because of the noncommuting operators in the spin Hamiltonian and because of the large value of the zero field splitting energy. By measuring the resonance field strengths at $\theta=0°$, $\theta=90°$, and at an intermediate angle the three constants D, $g_{\parallel}$, and $g_{\perp}$ are determined.

II. EXPERIMENTAL PROCEDURE

The instrument used in this investigation is of conventional design utilizing a twelve inch electromagnet and a klystron oscillator locked to the specimen cavity frequency. The cavity is cylindrical operating in the TE_{011} mode, which makes it possible to unambiguously determine relative absorption intensity ratios since the static and microwave magnetic fields are always perpendicular. Frequency of the microwave power was determined by measuring the resonance absorption Zeeman field strength of 1, 1-diphenyl-2-picryl hydrazyl whose g value was taken as 2.0037.[4] Zeeman field strengths were in turn determined by measuring the resonance absorption frequency of hydrogen and lithium nuclei. A BC221 standardized to the 10 Mc/sec transmission of radio station WWV monitored the nuclear magnetic resonance frequencies.

Orientation of the sapphire crystal was accomplished by two methods, which provided the minimum tolerable orientation uncertainty. Preliminary orientation was obtained by a polarizing microscope which located the crystal C axis direction to within 15 min of arc. Final orientation was established with the crystal in the spectrometer by observing the paramagnetic resonance absorption of trivalent chromium and iron ions which are present in sapphire as trace impurities.[5-7] In this manner, the location of the crystal C axis direction was established to within 6 min of arc.

III. EXPERIMENTAL RESULTS

The observed paramagnetic resonance absorption spectrum of nickel doped sapphire is characterized by

[1] R. P. Penrose and K. W. H. Stevens, Proc. Phys. Soc. (London) **A63**, 29 (1949).
[2] B. Bleaney and K. W. H. Stevens, Rept. Progr. Phys. **16**, 108 (1953).
[3] K. D. Bowers and J. Owen, Rept. Progr. Phys. **18**, 304 (1955).
[4] C. A. Hutchison and R. C. Pastor, Phys. Rev. **81**, 282 (1951).
[5] J. E. Geusic, Phys. Rev. **102**, 1252 (1956).
[6] C. Kikuchi, J. Lambe, G. Makhov, and R. W. Terhune, J. Appl. Phys. **30**, 1061 (1959).
[7] L. S. Kornienko and A. M. Prokhorov, Soviet Phys.—JETP **6**, 620 (1958).

two fine structure lines uncomplicated by nuclear hyperfine interactions. These lines occur at 10 347 oe for $\theta=0°$ and 7151 oe for $\theta=90°$ when the microwave energy is 0.3151 cm^{-1}.

No low field lines are observed at either orientation, which suggests that the zero field crystal splitting energy is greater than the microwave energy. By working on this premise, we see that for the $\theta=0°$ solution to Eq. 3 only one transition $E_2 \leftrightarrow E_3$ is possible. The resonance Zeeman field of this transition depends upon which of the two states is lowest. Since only one resonance absorption is observed at this orientation, it is concluded that E_2 is the lower state. At $\theta=90°$, there appears to be no question that the 7151 oe line is due to the $E_2 \leftrightarrow E_1$ transition since $D>h\nu$ and since the energy levels diverge as the Zeeman field is increased.

The best fit constants for the spin Hamiltonian at room temperature are given by

$$D=[1.385\pm0.002]\ cm^{-1}$$
$$g_{\parallel}=\ 2.196\pm0.004$$
$$g_{\perp}=\ 2.187\pm0.004,$$

where the errors are due principally to the uncertainty in locating the peaks of the resonance absorption lines, which have half widths at half intensities of 36 to 45 oe. These are room temperature constants determined from data taken at several orientations. The resonance Zeeman field variation of one of the fine structure lines *vs* orientation is given in Fig. 2. The points in the figure are experimental and the solid curve is theoretically obtained from the constants of the spin Hamiltonian. Solution of the theoretical curve is obtained by effectively turning Eq. 3 inside out while imposing the condition $E_1-E_2=0.3151\ cm^{-1}$. At 77°K, the constants to the spin Hamiltonian are given by $D=[1.312\pm0.003]\ cm^{-1}$ and $g=2.156\pm0.004$. These changes are not surprising in view of similar observations made by Penrose and Stevens[1] and by Holden, Kittel, and Yager[8] on nickel fluosilicate.

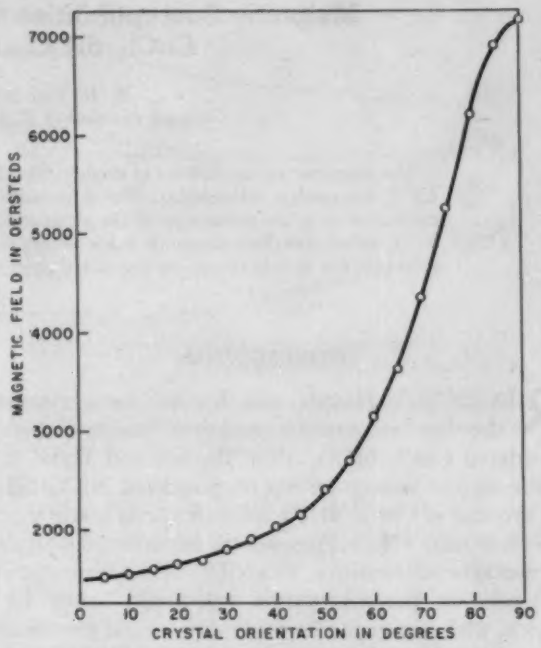

FIG. 1. Resonance field dependence of $E_2 \leftrightarrow E_1$ transition on orientation. The solid curve is theoretically predicted and the circles are experimental.

Spin-lattice relaxation time measurements were obtained at 77°K by observing the resonance absorption intensity diminution with increasing microwave power. By allowing for uncertainties in the measurement of cavity Q, microwave power, and possible cavity mode corruption due to the coupling iris and presence of the sapphire sample, the spin-lattice relaxation time is estimated to be 6×10^{-6} sec.

[8] A. N. Holden, C. Kittel, and W. A. Yager, Phys. Rev. **75**, 1443 (1949).

Magnetic Susceptibilities of Single Crystal $NiCl_2 \cdot 6H_2O$ and $CoCl_2 \cdot 6H_2O$ at Low Temperatures*

R. B. Flippen and S. A. Friedberg
Carnegie Institute of Technology, Pittsburgh 13, Pennsylvania

The magnetic susceptibilities of single crystal $NiCl_2 \cdot 6H_2O$ and $CoCl_2 \cdot 6H_2O$ have been measured down to 1.3°K for various orientations. The occurrence of antiferromagnetism in $CoCl_2 \cdot 6H_2O$ below ~2.3°K is confirmed as is the anisotropy of the g-factor of the Co^{++} ion over the whole range. It is concluded that $NiCl_2 \cdot 6H_2O$ is antiferromagnetic in the helium region and that the temperature-independence of the powder susceptibility here is caused by the fact that $\chi_\perp$ rises as T falls below T_N.

INTRODUCTION

RECENTLY Haseda and Kanda[1] have measured the low-temperature magnetic susceptibility of powdered $CoCl_2 \cdot 6H_2O$, while Haseda and Date[2] have made similar measurements on powdered $NiCl_2 \cdot 6H_2O$. In the case of $CoCl_2 \cdot 6H_2O$, a broad maximum in χ_{powder} was seen near 3°K, suggesting the occurrence of an antiferromagnetic transition. For $NiCl_2 \cdot 6H_2O$, temperature-independent paramagnetism was found below 4.2°K which, with higher temperature data, could presumably be explained without antiferromagnetism. Robinson and Friedberg,[3] however, have measured the specific heats of both salts between 1.4° and 20°K and find λ type anomalies in each case. The cooperative transitions with which these anomalies are associated are presumably antiferromagnetic, with Néel temperatures of 2.29°K for $CoCl_2 \cdot 6H_2O$ and 5.34°K for $NiCl_2 \cdot 6H_2O$. The latter is in a temperature region not covered in the χ_{powder} measurements.[2]

We have made measurements of the magnetic susceptibilities of single crystals of $CoCl_2 \cdot 6H_2O$ and $NiCl_2 \cdot 6H_2O$ in an attempt to: (1) understand the rather unusual behavior of χ_{powder} of $NiCl_2 \cdot 6H_2O$; (2) verify the conclusion that this salt becomes antiferromagnetic as does $CoCl_2 \cdot 6H_2O$; (3) determine the preferred direction of spin orientation in the antiferromagnetic state in both salts.

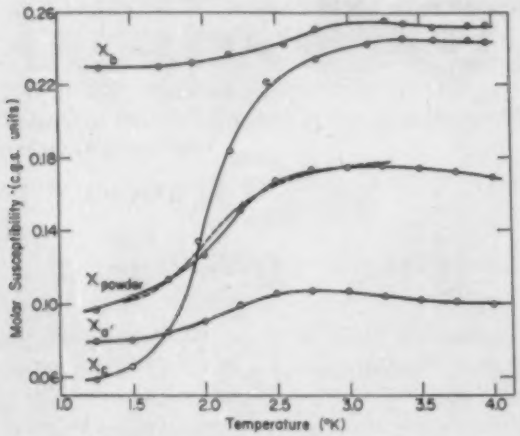

FIG. 1. The molar susceptibility of powdered and single crystal $CoCl_2 \cdot 6H_2O$ at liquid helium temperatures.

EXPERIMENTAL METHODS

Single crystals of $CoCl_2 \cdot 6H_2O$ and $NiCl_2 \cdot 6H_2O$ were grown from aqueous solution. These crystals are monoclinic and of the prismatic habit described by Groth.[4] The specimens were oriented using the data of Groth and the orientations confirmed by x-ray back-reflection photography. Susceptibilities were measured by observing the change in the mutual inductance of two coaxial coils produced by inserting a specimen. An electronic ac mutual inductance bridge similar to that described by Pillinger, Jastram, and Daunt[5] was used for this purpose, operating usually at 500 cps. The coils were immersed in the refrigerant and produced at the specimen a maximum field of ~3 gauss. The bridge was calibrated during each run with a manganous ammonium sulfate sample which could be substituted for the unknown.

Measurements were made on specimens of each material oriented so that the measuring field coincided with the crystallographic b and c axes, which are normal to each other, and with a third direction (a') perpendicular to b and c. a' is inclined about 32° from the a axis in both these isomorphous substances. Data were obtained in the temperature intervals 1.3 to 4.2°K and 14° to 21°K and at 78°K. Supplementary observations were made on powdered specimens of both salts at the same temperatures. The agreement of these results with the published values is very satisfactory.

RESULTS AND DISCUSSION

The results of the susceptibility measurements in the He range are shown for $CoCl_2 \cdot 6H_2O$ in Fig. 1 and $NiCl_2 \cdot 6H_2O$ in Fig. 2. In Fig. 1 it is evident that χ_b and χ_c may be identified as $\chi_\perp$ and $\chi_\parallel$, respectively, so that the direction of preferred alignment of ionic moments in $CoCl_2 \cdot 6H_2O$ is the c direction. The values of χ_b and χ_a, however, are significantly different over the whole

* Work supported in part by the Office of Naval Research, the National Science Foundation, and the Alfred P. Sloan Foundation.

[1] T. Haseda and E. Kanda, J. Phys. Soc. Japan **12**, 1051 (1957).
[2] T. Haseda and M. Date, J. Phys. Soc. Japan **13**, 175 (1958).
[3] W. K. Robinson and S. A. Friedberg, Bull. Am. Phys. Soc. Ser. II, **4**, 183 (1959); Phys. Rev. **117**, 402 (1960).
[4] P. Groth, Chem. Kryst. II, 247, 248 (1908).
[5] W. L. Pillinger, P. G. Jastram, and J. G. Daunt, Rev. Sci. Instr. **29**, 159 (1958).

range. These differences persist in the hydrogen range where each follows a Curie-Weiss law, from which a splitting factor, g, can be deduced for each direction. We find $g_{a'}=2.7$, $g_b=5.0$, and $g_c=4.9$. Recently, Dr. M. Date has kindly informed us of paramagnetic resonance observations on $CoCl_2 \cdot 6H_2O$ at 4.2°K, which yield $g_{a'}=2.9$, $g_b=5.0$, $g_c=4.0$. He also quotes unpublished single crystal susceptibility measurements by Haseda who finds the preferred direction to be the c axis and who gives $g_{a'}=2.7$, $g_b=4.9$, and $g_c=4.9$, in excellent agreement with the present results. This highly anisotropic behavior of the Co^{++} ion is consistent with findings on other cobaltous salts. By using the anisotropic g values and the single crystal susceptibility data, one can calculate values of χ_{powder} according to[6] $\chi_{powder}=(\frac{1}{3})[(g_{a'}/g)^2\chi_{a'}+(g_b/g)^2\chi_b+(g_c/g)^2\chi_c]$ where g is an equivalent scalar average value. These values are shown in Fig. 1 as a dashed curve and closely reproduce the observed quantities.

From the results for $NiCl_2 \cdot 6H_2O$ we note in Fig. 2 that χ_c and χ_b coincide while $\chi_{a'}$ deviates considerably from them. No anisotropy is found above 14°K ($g \sim 2.2$), in agreement with the usual behavior of the Ni^{++} ion. There is strong reason to believe, therefore, that the anisotropy below 4.2°K is due to cooperative interaction which, judging from the curves of Fig. 2, has become important at a temperature above 4.2°K and is antiferromagnetic in sign. This is consistent with the specific heat results which fix the Néel point at 5.34°K. $\chi_{a'}$ is evidently $\chi_{\parallel}$ so that the preferred direction for alignment of ionic moments is along the a' axis. It should be noted that $\chi_{\parallel}$ apparently does not go to zero with T for either the nickel or the cobalt salt.

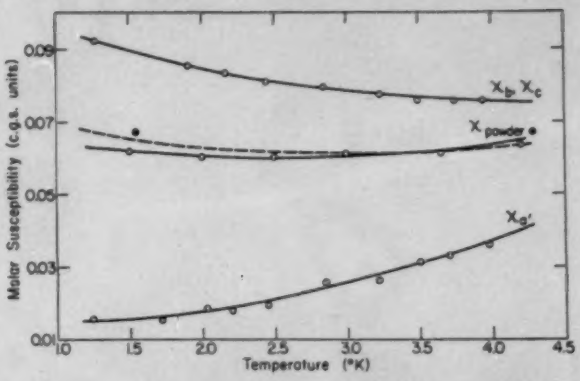

FIG. 2. The molar susceptibility of powdered and single crystal $NiCl_2 \cdot 6H_2O$ at liquid helium temperatures. The solid black circles are powder values due to Haseda and Date.

The near temperature-independence of χ_{powder} for $NiCl_2 \cdot 6H_2O$ below 4.2°K is explained by the fact that $\chi_{\perp}$, that is χ_b (or χ_c), rises with falling temperature. Such behavior can be understood qualitatively if finite anisotropy is included in the molecular field model.[6] Simple averaging of χ_c, χ_b, and $\chi_{a'}$ gives values of χ_{powder} (dashed curve Fig. 2) in good agreement with observation.

[6] T. Nagamiya, K. Yosida, and R. Kubo, Advances in Phys. 4, (1955).

JOURNAL OF APPLIED PHYSICS SUPPLEMENT TO VOL. 31, NO. 5 MAY, 1960

Properties of Manganese Ferrites Prepared at Various Oxygen Pressures

ALEKSANDER BRAGIŃSKI
Research Laboratory for Magnetic Materials "Polfer", Warsaw, Poland

MANGANESE ferrite solid solutions $Mn_yFe_{3-y}O_{4+\gamma}$, $0{,}87<y<1{,}14$, were investigated. The samples were sintered at various temperatures and then cooled at various oxygen pressures. It was shown that the lattice defects were formed during sintering facilitated both the reduction or oxidation processes during cooling depending upon the oxygen pressure applied. The concentration of defects at constant sintering temperature increased with the iron content, especially at $y<1$.

JOURNAL OF APPLIED PHYSICS SUPPLEMENT TO VOL. 31, NO. 5 MAY, 1960

Effect of Potassium Ions on the Reaction and Final Properties of Mn-Zn Ferrite

STEFAN MAKOLĄGWA
Research Laboratory for Magnetic Materials "Polfer," Warsaw, Poland

A Mn-Zn ferrite containing a slight iron excess is investigated. Small additions of potassium ions introduced into the initial mixture of raw oxides volatilize during sintering and accelerate the reaction process, thus facilitating the reduction or oxidation of the ferrite, which depends on the oxygen pressure applied. The basic magnetic properties are greatly influenced by this. The effect may be explained by the formation of lattice defects.

Magnetic Properties of Uranium Digermanide*

CLAYTON E. OLSEN
Los Alamos Scientific Laboratory, University of California, Los Alamos, New Mexico

Investigations on the magnetic properties of actinide element intermetallic compounds has disclosed that UGe_2 and $PuGe_2$ are ferromagnetic with magnetic moments greater than 0.803 and 0.144 Bohr magneton per molecule respectively at 4°K. Electrical resistivity measurements on UGe_2 indicate an interaction of the conduction electrons with the local spin which produces ferromagnetism. Also the electrical resistivity of USi_2, which is not ferromagnetic, was measured for comparison.

INTRODUCTION

INVESTIGATIONS on the magnetic properties of actinide element intermetallic compounds show uranium digermanide and plutonium digermanide[1] to be ferromagnetic. Electrical resistivity measurements on uranium digermanide indicate an interaction of the conduction electrons with the local spin which produces ferromagnetism. The magnetic properties of uranium disilicide and plutonium disilicide also were investigated and the electrical resistivity of uranium disilicide was measured to provide a comparison to the uranium digermanide.

EXPERIMENTAL PROCEDURES

The uranium disilicide and digermanide and the plutonium disilicide were made by arc melting stoichiometric amounts of the elements. The plutonium digermanide was made by induction melting stoichiometric amounts of the elements. The uranium disilicide and digermanide buttons were arc melted into rods which then were shaped on abrasive wheels.

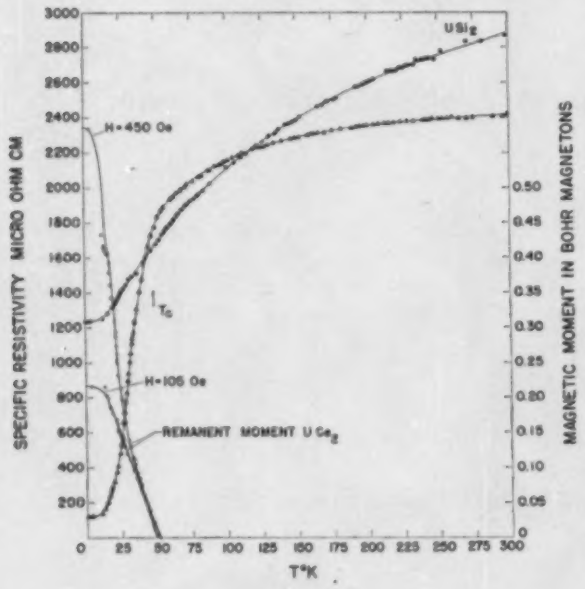

FIG. 1.

The magnetic measurements[2] were made ballistically in the usual way with the specimen mutual inductance mounted in a cryostat. A piece of high-purity, annealed nickel was used as a magnetic standard.

The electrical resistivity measurements[3] were made potentiometrically on bars with known probe separation and cross sectional area. Corrections were made for thermal emfs.

STRUCTURE OF THE COMPOUNDS

The structures of uranium disilicide and plutonium disilicide have been reported by Zachariasen.[4] The structure of plutonium digermanide has been reported by Ellinger.[5] All these compounds are reported to be isomorphous with $ThSi_2$. Results of x-ray diffraction work by the author on the USi_2 used in the resistivity measurement are in agreement with the results of Zachariasen. No x-ray work was done on the specimens of plutonium disilicide or digermanide used in the magnetic measurements.

Neither the structure nor the properties of uranium digermanide have been reported in the literature previously. Single crystal Weissenberg photographs taken on the material show it to be orthorhombic with the following parameters:

$$a = 4.08 \pm 1 \text{ A},$$
$$b = 3.96 \pm 1 \text{ A},$$
$$c = 15.43 \pm 2 \text{ A},$$
$$D_x = 10.21 \text{ g/cm}^3,$$
$$D_m = 10.29 \text{ g/cm}^3 \text{ at } 24°\text{C},$$
$$M = 4, Amm2.$$

All lines on the powder pattern can be indexed using the above parameters. Space group considerations and similarities in the powder patterns of USi_2 and UGe_2 suggest that UGe_2 is an orthorhombic distortion of the

* Work performed under the auspices of the U. S. Atomic Energy Commission.

[1] For ferromagnetism in the corresponding rare earth compounds see B. T. Matthias, E. Corenzwitt, and W. H. Zachariasen, Phys. Rev. 112, 89 (1958).

[2] F. K. Harris, *Electrical Measurements* (John Wiley & Sons, Inc., New York, 1952), pp. 362, 383.

[3] A. N. Gerritsen, *Handbuch der Physik* (Springer-Verlag, Berlin, Germany, 1956), Vol. 15, pp. 137–152; D. K. C. MacDonald, *ibid.*, Vol. 14, pp. 154–169.

[4] W. H. Zachariasen, Acta Cryst. 2, 94 (1949).

[5] A. S. Coffinberry and F. H. Ellinger, U. S. A. Rpt. A/Conf 8/p/826 (1955).

$ThSi_2$ structure. Work is under way to determine the structure of UGe_2 more completely.

EXPERIMENTAL RESULTS

The results of the electrical resistivity measurements on USi_2 and UGe_2 are shown in Fig. 1. Figure 1 shows the specific resistivity (uncorrected for thermal expansion) of USi_2 and UGe_2 plotted as a function of temperature and the magnetic moment of UGe_2 as a function of temperature. The resistivity measurements were repeated several times on each specimen. The results agreed within experimental error. There was no evidence for hysteresis in the electrical properties of USi_2 or UGe_2. In addition, magnetoresistivity measurements were made on UGe_2. With fields up to 1000 oe no magnetic effects were found within the limits of experimental error.

UGe_2 and $PuGe_2$ are extremely hard magnetically. If the material is cooled below the Curie point without an applied field, there is no evidence of ferromagnetism with fields up to 1000 oe (the highest obtainable in the present apparatus). If the material is cooled with an applied field it becomes permanently magnetized. However, within a few degrees of the Curie point, the materials become quite soft and it is also possible to determine the Curie point by means of field reversal.

Magnetization curves were obtained on UGe_2 and $PuGe_2$ by cooling the specimens from room temperature to 4°K in different fields and then measuring deflections obtained when the specimens were removed from the mutual inductance. The saturation magnetization for UGe was found to be larger than 0.803 Bohr magneton per molecule at 4°K with an applied field of 840 oe and for $PuGe_2$ was found to be larger than 0.144 Bohr magneton per molecule at 4°K with an applied field of 420 oe. The Curie temperatures for UGe_2 and $PuGe_2$ were 52.0°K and 34.5°K, respectively.

No evidence was found for any magnetic transitions in USi_2 or $PuSi_2$ down to 1.3°K and the electrical resistivity measurements on USi_2 confirm this.

DISCUSSION OF RESULTS

The electrical resistivity measurements on USi_2 show this material to conduct by the same mechanism over the temperature range 1.4° to 300°K. However, the measurements over the same temperature range on UGe_2 clearly show a magnetically dependent resistivity.

Comparison of the magnetic moment curves with the electrical resistivity curves show a close relationship between the magnetic moment and electrical resistivity of a type predicted theoretically[6] for a local spin conduction electron interaction. In addition the failure to find any magnetoresistivity effects is an indication of a strong local spin-conduction electron interaction. It appears that the ferromagnetism in UGe_2 and probably $PuGe_2$ originates in a local spin-conduction electron interaction.

Above the Curie point, UGe_2 almost shows the temperature-independent resistivity called for by a spin disorder[7] resistivity. However, there is a small temperature-dependent contribution to the resistivity from lattice scatter. A log log plot of resistivity vs temperature shows clearly that magnetic ordering in UGe_2 starts near 100°K even though the ferromagnetic ordering first becomes detectable at 52°K. Work now in progress on other ferromagnetic compounds of plutonium and uranium, which are isomorphous to each other, suggests that the crystal structure differences between UGe_2 and $PuGe_2$ are not responsible for the major differences in magnetic properties.

In the case of USi_2 it is not clear whether the low-temperature dependence of the resistivity has its origin in a spin disorder resistivity. The greater binding energy and greater covalent character of the bonding would lead one to anticipate a much smaller amount of local spin. The results do not rule out the possibility of USi_2 being antiferromagnetic with a Curie point above 300°K.

ACKNOWLEDGMENTS

The author would like to acknowledge the help of Vernon O. Struebing, CMF-5, who prepared the specimens of plutonium disilicide and digermanide. The author would also like to acknowledge the helpful discussions of Dr. B. T. Matthias, and Professor W. H. Zachariasen, consultants to the Laboratory.

[6] R. J. Weiss and A. S. Marotta, J. Phys. Chem. Solids **9**, 302 (1959).

[7] For review and references on this subject see B. R. Coles, *Advances in Phys.* **7**, 40 (1958).

Interpretation of the Magnetic and Crystallographic Properties of Several Iron, Nickel, and Iron-Nickel Nitrides*

J. B. GOODENOUGH, A. WOLD, AND R. J. ARNOTT†
Lincoln Laboratory, Massachusetts Institute of Technology, Cambridge, Massachusetts

The saturation moment at 4°K and the room-temperature structure of the following nitrides have been examined: $Fe_{4-x}Ni_xN$ with $0 \leqslant x \leqslant 3$ (Fe_4N-type structure); tetragonal, ordered FeNiN; hexagonal $Fe_{2-y}N$ with $0<y<1$; hexagonal $Ni_3N_{1.16}$; and orthorhombic Fe_2N. The atomic ordering, nitrogen solubility, and atomic moments of the system $Fe_{4-x}Ni_xN$ are interpreted from a model of the band structure of the f.c.c. transition elements of the first long period in which it is explicitly assumed that the crystalline fields split the d bands into separable components.

IN another report,[1] semiempirical arguments have been presented for the following model for fcc transition metals. (1) Spin correlations split the atomic $e_g(d_{z^2-y^2}, d_{z^2}$ pointing towards next-nearest neighbors) levels from the t_{2g} (d_{yz}, d_{zx}, d_{xy} pointing towards nearest neighbors) levels so that in first approximation the metallic d bands can be considered to be composed of discrete d subbands. (2) The e_g electrons are less perturbed and sufficiently localized that the narrow energy band may be split in two by intraatomic exchange. (3) The t_{2g} electrons form a broader energy band, and the stability of antiparallel correlation between electrons on neighboring atoms renders cubic symmetry stable at low temperatures only if the number of t_{2g} electrons is $5<n_{2g}\leq 6$. (It is not possible to propagate antiferromagnetic correlation of all near neighbors throughout a fcc lattice.) (4) The narrow, high-energy half of the split e_g sub-band overlaps the top of the t_{2g} band: holes in this e_g sub-band give rise to a localized magnetic moment that is capable of inducing magnetic polarization of the overlapping t_{2g} band. A spontaneous ferromagnetic moment results that is roughly equivalent to the total number of holes in the d bands times the Bohr magneton. (5) Available experimental data indicate that the outer-electron configurations for fcc iron and nickel are, respectively, $e_g^2t_{2g}^{6-\xi}s^{\xi}$ and $e_g^{4-\eta}t_{2g}^{6-\zeta}s^{\eta+\zeta}$, where $\xi\approx 1$ and $(\eta+\zeta)=0.6$ provide a measure of the amount of overlap of the s and d bands.

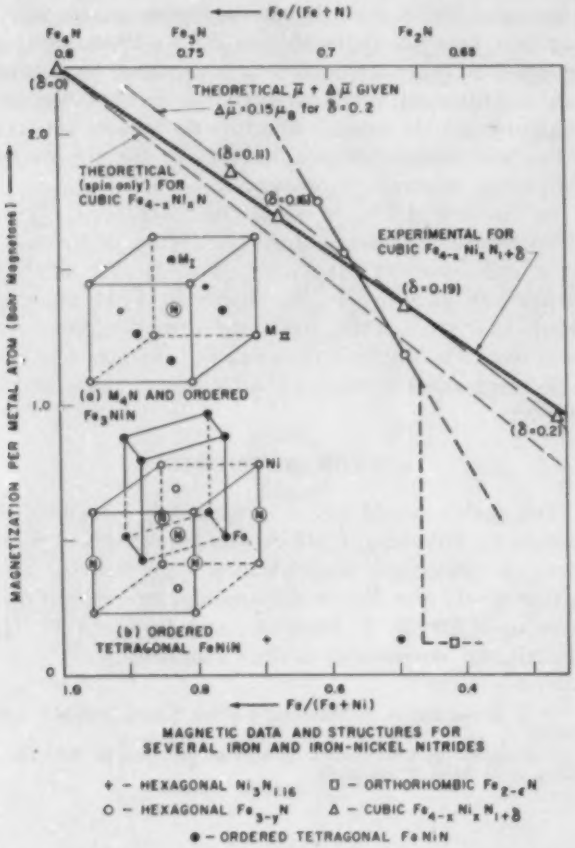

FIG. 1. Magnetic data and structure for several iron and iron-nickel nitrides.

In order to obtain further experimental information about the nature of the outer-electron configuration in the fcc transition metals, it was decided to prepare several nitrides. The nitrogen atom enters the lattice interstitially. Because it has the outer-electron configuration s^2p^3, it is readily stabilized in an octahedral interstice provided the metallic orbitals that strongly overlap the half-filled nitrogen p orbitals are themselves half or less filled. Antiferromagnetic correlation between the N atom and its six near-neighbor metal atoms provides a ferromagnetic correlation between these metal atoms. In Fig. 1(a), these are labeled M_I. If $n_{2g}>5$, the model[1] predicts ferromagnetic coupling between M_I and M_{II}. If $n_{2g}<5$, M_I and M_{II} may be coupled antiferromagnetically. In the cubic alloy systems under investigation here, it seems that $n_{2g}>5$, but that $n_{2g}\rightarrow 5$ in Fe_4N. Therefore, it is assumed that the number of iron s electrons is $n_s^{Fe}=1$, or $\xi=1$.

Experimentally, it is found that the cubic system $Fe_{4-x}Ni_xN_{1+\delta}$, where $0\leqslant x\leqslant 3.3$ and $0\leqslant\delta\leqslant 0.2$, can be

* The work reported in this paper was performed by Lincoln Laboratory a center for research operated by Massachusetts Institute of Technology with the joint support of the U. S. Army, Navy, and Air Force.

† Staff Members, Lincoln Laboratory, Massachusetts Institute of Technology.

[1] J. B. Goodenough, "On the band structure of the transition metals and their alloys," Lincoln Laboratory Tech. Rept. TR 208 (September 1, 1959).

prepared[2] by reducing the oxides with purified hydrogen followed by nitriding the finely divided powders for six hours in a stream of NH_3 or NH_3/H_2. As the nickel content is increased, the nitriding temperature must be reduced from 500° to 350°C. The unit cell size decreases from $a=3.797$ for Fe_4N to 3.755 for $Fe_{1.06}Ni_{2.96}N_{1.20}$, deviation from Vegard's law occuring for $x>2$. A small excess of nitrogen is present, δ increasing monotonically from 0.0 at Fe_4N to 0.19 at $Fe_2Ni_2N_{1.19}$ and remaining nearly constant for higher x. The M_4N structure is that shown in Fig. 1(a). It is not possible to prepare Ni_4N: a two-phase region of Ni_3N and M_4N exists from $x\sim3.3$ to almost 4. In the range $1.96\leqslant x\leqslant 2.06$, it was possible to produce the ordered, tetragonal phase FeNiN of Fig. 1(b).[2] By further nitriding the Fe_4N samples, it was possible to prepare hexagonal $Fe_{3-y}N$, with $0.64\leqslant y\leqslant 0.95$ and an orthorhombic $Fe_{1.92}N$. Crystallographic data for these structures are described by Jack.[3] Magnetization measurements at 4°K in fields up to 11 000 gauss were extrapolated to give the number of Bohr magnetons per metallic atom shown in Fig. 1.

According to the model, the Fe_{II} atoms do not interact with the N atoms, and therefore carry a localized atomic moment $\mu^{Fe\,II}=(2+\xi)\mu_B\approx 3\mu_B$, whereas the antiferromagnetic correlation between the nitrogen p electrons and the $Fe_I e_g$ electrons effectively pairs one e_g electron per Fe_I atom leaving $\mu^{Fe\,I}=[(2+\xi)-1]\mu_B\approx 2\mu_B$. This provides an average atomic moment per metal atom $\bar{\mu}=2.25\ \mu_B$, which is in good agreement with the experimental moment. The magnitudes of the individual moments are also in accord with recent neutron-diffraction data.[4]

If this interpretation is correct, it follows that substituted Ni atoms having e_g levels more than half filled will be stabilized in the M_{II} positions. Such an ordered structure for Fe_3NiN has also been proposed by Wiener and Berger[5] who reasoned from a different model. Such ordering has recently been confirmed.[2] It also follows from this model that for $x>1$, the additional Ni atoms enter the M_I position in a random manner. This prediction has also been verified.[2] In the M_I positions, the nickel atoms must have a half-filled d_z^2 orbital directed towards the two neighboring N atoms and therefore an outer-electron configuration $d_{x^2-y^2}{}^2 t_{2g}{}^6 d_{z^2}{}^1 s^1$, or $\eta=1$, $\zeta=0$. With such an orientation of the z axis, the other octahedral interstices adjacent to the Ni atoms are not available to the N atoms as the $d_{x^2-y^2}$ orbitals are more than half-filled: this means that the available diffusion paths for the nitrogen atoms are reduced and nitriding becomes more difficult. At the limit of pure Ni, diffusion of the N atoms through the cubic phase is almost completely suppressed so that there is little solubility of nitrogen in fcc nickel: it is necessary to diffuse the nitrogen into the nickel via the hexagonal Ni_3N phase. Thus the model provides some insight into the lack of an Ni_4N phase and into the forces responsible for order in Fe_3NiN.

When chemical analysis revealed that FeNiN had been prepared, it followed at once from the model that the structure must be ordered as shown in Fig. 1(b). In this configuration, the nickel atoms have two nitrogen near neighbors (nickel d_z^2 directed towards each), whereas the iron atoms with only two e_g electrons can have four coplanar nitrogen atoms. It also followed that the nitrogen p electrons paired the nickel d_z^2 and the two iron e_g electrons so that there could be no localized atomic moment to induce a magnetic polarization of the holes in the t_{2g} band. Therefore, FeNiN was predicted to be ordered, tetragonal, and paramagnetic. The ordered, tetragonal structure was confirmed[2] and the low saturation moment (see Fig. 1) is compatible with paramagnetism.

If $\xi\approx 1$, $\eta=1$ and $\zeta=0$ throughout the cubic system $Fe_{4-x}Ni_xN$, the model predicts the linear decrease in $\bar{\mu}$ shown in Fig. 1, the atomic moments being $\mu^{Fe\,II}\approx 3\mu_B$, $\mu^{Ni\,II}\approx 1\mu_B$, $\mu^{Fe\,I}\approx 2\mu_B$, $\mu^{Ni\,I}\approx 0\mu_B$. This prediction is somewhat lower than the experimental values. Whether the excess nitrogen ($\delta>0$) is responsible for this discrepancy is not known. Neither is it known why the excess nitrogen is present. Although excess nitrogen might be expected to decrease $\bar{\mu}$, extrapolation of hexagonal $Fe_{3-y}N$ suggests that in this phase the atomic moments are considerably larger for a comparable amount of nitrogen. The dotted line in Fig. 1 corresponding to $\Delta\bar{\mu}=0.15\mu_B$ for $\delta=0.2$ is suggestive of a regular increase in $\bar{\mu}$ with excess nitrogen.

ACKNOWLEDGMENT

The authors would like to thank N. Menyuk for making the magnetic measurements with the vibrating-coil magnetometer and R. Small for the chemical analyses.

[2] R. J. Arnott and A. Wold (to be published in J. Chem. Phys. Solids).
[3] K. H. Jack, Proc. Roy. Soc. (London) **A195**, 34 (1948).
[4] B. C. Frazer, Phys. Rev. **112**, 751 (1958).
[5] G. W. Wiener and J. A. Berger, J. Metals **7**, 360 (1955).

Magnetic Transitions in Ti_2O_3 and V_2O_3†

P. H. Carr and S. Foner
Lincoln Laboratory, Massachusetts Institute of Technology, Lexington 73, Massachusetts

The principal susceptibilities of single crystals of Ti_2O_3 and V_2O_3 have been measured from 4.2°K to 300°K by means of a vibrating sample magnetometer. In Ti_2O_3, $\chi_{\parallel}=9\times10^{-7}$ cgs/g and $\chi_{\perp}=8\times10^{-7}$ cgs/g, and both susceptibilities are nearly temperature independent. In V_2O_3, below the transition temperature T_0, $\chi_{\parallel}=6.9\times10^{-6}$ cgs/g and $\chi_{\perp}=5.9\times10^{-6}$ cgs/g and both are temperature independent. The small, almost equal, and temperature independent values of both $\chi_{\parallel}$ and $\chi_{\perp}$ below T_0 confirm recent neutron diffraction data which indicate no appreciable long-range antiferromagnetic order for these oxides. Van Vleck temperature independent paramagnetism can account for the observed values. It is concluded that the observed discontinuities of susceptibility and corresponding electrical conductivity changes are not due to long-range magnetic ordering effects.

INTRODUCTION

DISCONTINUITIES of the magnetic susceptibility have been observed in polycrystalline Ti_2O_3[1,2] and V_2O_3[3,4] at a transition temperature, T_0. It has been suggested that a long-range antiferromagnetic ordering at low temperatures would account for the observed sudden decrease in susceptibility.[3] In contrast with Cr_2O_3 (which is known to be an antiferromagnetic below about 308°K), in Ti_2O_3 and V_2O_3, the sudden change in magnetic susceptibility is accompanied by a marked change in electrical conductivity; as temperature is decreased, a metallic to semiconducting conductivity change is observed.[3,5] Morin has recently examined the electrical conductivity of several single crystal[6] titanium and vanadium oxides as a function of temperature. In order to explain the radical changes in conductivity, he assumed the existence of long-range antiferromagnetic ordering below T_0, and proposed that the periodicity of this antiferromagnetic ordering splits the "3*d*" band. The model is similar to that suggested by Slater.[7]

A sharp decrease in magnetic susceptibility is of course not sufficient to determine long-range antiferromagnetic ordering. We have therefore reexamined the magnetic susceptibility temperature dependence of single crystal[8] V_2O_3 and Ti_2O_3 over the range of 4.2°K to 300°K in order to detect any antiferromagnetic ordering. In both of these oxides, $\chi_{\parallel}$ and $\chi_{\perp}$, the magnetic susceptibility parallel and perpendicular to the *c*-axis respectively, are approximately temperature independent below T_0. These results suggest that, if long-range antiferromagnetic order is present, the localized moment at the metal ion is very small. These conclusions confirm recent neutron diffraction results, and favor a model proposed by Goodenough.[9]

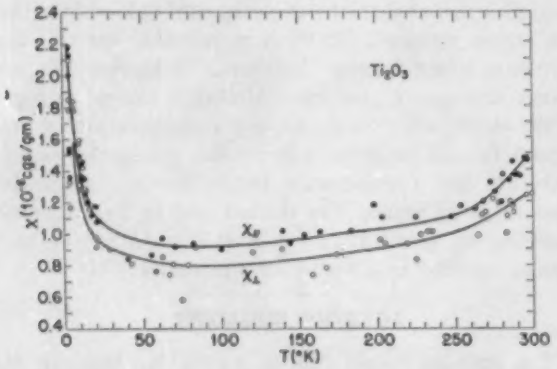

FIG. 1. Temperature dependence of magnetic susceptibility in single crystal Ti_2O_3.

EXPERIMENTAL RESULTS

The magnetic measurements were made in uniform magnetic fields of as much as 16 kilogauss with a vibrating-sample magnetometer.[10] Oriented samples of about 0.1 g cut from single crystals[8] grown by the flame fusion technique,[11] were used. The susceptibility was field independent, and showed no remanent magnetic moment for either Ti_2O_3 or V_2O_3.

The results for $Ti_2O_3(d^1)$ are shown in Fig. 1. The relatively large scatter of the data is due to the small susceptibility, which was comparable to the diamagnetic contribution of the sample support member.[10] The prominent increase in χ at lowest temperatures is attributed to paramagnetic impurities or lack of stoichiometry. The slight increase of χ above 250°K agrees in magnitude with available polycrystalline data

† The work reported in this paper was performed at Lincoln Laboratory, a center for research operated by Massachusetts Institute of Technology with the joint support of the U. S. Army, Navy, and Air Force.

[1] A. D. Pearson, J. Phys. Chem. Solids **5**, 316 (1958).
[2] M. Foex and J. Wucher, Compt. rend. **241**, 184 (1955).
[3] A summary of the properties of V_2O_3 is given in J. recherches centre natl. recherche sci. Labs. Bellevue (Paris) **21**, 237 (1952) *et seq.* by M. Foex, S. Goldsztaub, and R. Wey; J. Jaffray and R. Lyand; and J. Wucher.
[4] V. Hoschek and W. Klemm, Z. anorg. u. allgem. Chem. **242**, 63 (1939).
[5] F. J. Morin, Phys. Rev. Letters **3**, 34 (1959).
[6] F. J. Morin, Bell System Tech. J. **37**, 1047 (1958).
[7] J. C. Slater, *Handbuch der Physik* (Springer-Verlag, Berlin, 1956), Vol. 19
[8] The V_2O_3 single crystal material was obtained from Linde Air Products Company. The Ti_2O_3 single crystal was kindly furnished by Dr. R. Newnham now at the Massachusetts Institute of Technology Laboratory for Insulation Research.
[9] J. B. Goodenough, J. Appl. Phys. **31**, 359S (1960), this issue.
[10] S. Foner, Rev. Sci. Instr. **30**, 548 (1959).
[11] The stoichiometry was within 1% for V_2O_3 and within 5% for Ti_2O_3.

and indicates the onset of a broad lattice distortion region which occurs between 400 and 500°K.[1]

The more complex magnetic behavior of $V_2O_3(d^2)$ is shown in Fig. 2. It was found that once a single crystal sample was cooled below 150°K, the V_2O_3 crystal cracked extensively on warmup to room temperature, suggesting a radical crystallographic distortion. Alignment of the crystal fragments was maintained by a surrounding cement binder. Each of the curves in Fig. 2 were obtained with one crystal piece during warmup.[12] Thermal hysteresis of the sharp transition, observed during cooling, is indicated by T_1 in Fig. 2—corresponding hysteresis in conductivity has been noted earlier.[3,5] Warekois[13] has recently determined that a martensitic phase transformation occurs in this region.

No paramagnetic resonance of impurities or antiferromagnetic resonance was observed with pulsed field resonance experiments[14] with 36 kMcps radiation and fields of as much as 150 kilogauss.

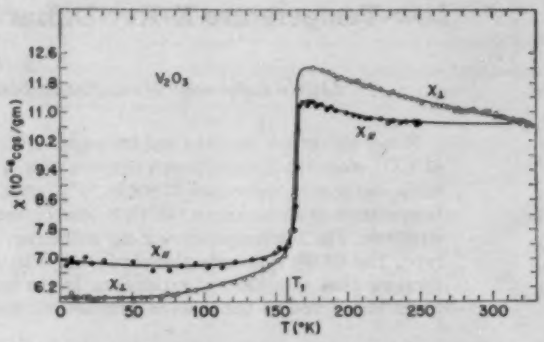

FIG. 2. Temperature dependence of magnetic susceptibility in single crystal V_2O_3.

DISCUSSION

We conclude that for Ti_2O_3, long-range antiferromagnetic order is not present. This conclusion is based on the fact that $\chi_{\parallel}$ and $\chi_{\perp}$ are *both* small, almost equal, and practically temperature independent up to 250°K. $\chi_{\parallel}$ and $\chi_{\perp}$ could be equal in an antiferromagnet if the anisotropy field were negligible, but this is not likely here since the ^2D ground state of Ti^{3+} is expected to have a large crystalline field interaction. If Ti_2O_3 were antiferromagnetic, molecular field calculations using the small value of χ would predict ordering far above the observed $T_0 \simeq 500$°K. Finally, recent neutron diffraction data[15,16] indicated that the localized moment at the Ti^{3+} is less than $0.5\,\mu_B$, thus confirming our point of view.

Similar arguments can be applied to the observations for V_2O_3. The sharp drop in χ is attributed to the phase transformation rather than to magnetic ordering. The larger magnitude of χ, and the more limited region over which χ is temperature-independent, do not permit conclusions as unambiguous as indicated for Ti_2O_3. However, the magnetic data indicates that any localized moment on the V^{3+} sites must be small, in agreement with neutron diffraction results which indicate less than $0.5\,\mu_B$ localized on these sites.

The residual low-temperature susceptibility including its anisotropy can be described by Van Vleck temperature independent paramagnetism in Ti_2O_3 and V_2O_3. Calculations which include estimates of orbital level splittings obtained from optical data of Ti^{3+} and V^{3+} in Al_2O_3[17] indicate this contribution would be of the correct magnitude. The qualitative magnetic behavior is in accord with the recent bonding theory proposed by Goodenough.[9]

Based on the examples of Ti_2O_3 and V_2O_3 discussed in the foregoing, it appears that there is not sufficient evidence for long-range antiferromagnetic ordering in other titanium and vanadium oxides. Re-examination by means of single crystal susceptibility and neutron diffraction measurements is therefore suggested.

ACKNOWLEDGMENTS

We have profited from informative discussions with J. B. Goodenough, E. P. Warekois, R. Newnham, and G. W. Pratt, Jr.; and from valuable assistance by B. Feldman and J. S. Coe in performing the experiments.

[12] Reproducibility was demonstrated by measurements with several samples.
[13] E. P. Warekois, J. Appl. Phys. **31**, 346S (1960).
[14] See for instance, S. Foner, J. phys. radium **20**, 336 (1959).
[15] G. Shirane, S. J. Pickart, and R. Newnham, J. Phys. Chem. Solids (to be published).
[16] A. Paoletti and S. J. Pickart, J. Phys. Chem. Solids (to be published).
[17] W. Low of the Hebrew University, Jerusalem, Israel (private communication).

Low-Temperature X-Ray Diffraction Studies on Vanadium Sesquioxide*

E. P. Warekois
Lincoln Laboratory, Massachusetts Institute of Technology, Lexington 73, Massachusetts

X-ray diffraction patterns and microphotographs were obtained from single crystals and powder samples of V_2O_3, cooled to liquid nitrogen temperatures. The c axis, in the hexagonal unit cell, expanded 5.8×10^{-6}/°C while the a axis contracted 22.9×10^{-6}/°C, over the range from room temperature to the transformation temperature of about minus 145°C. Below this temperature a microphotograph showed a typical martensitic structure. The low-temperature x-ray diffraction reflections split for all reflections except those of the (000l) type. The (000l) type reflections indicated a lattice contraction below the transformation. Those x-ray reflections that split showed expansions in the interplanar spacings. The low-temperature powder pattern could be indexed on the basis of a monoclinic unit cell; $a=8.57$, $b=4.98$ and $c=13.88$ A with $\beta=91.6°$.

EXPERIMENTAL data[1,2] have been presented that show marked changes in the electrical and magnetic properties of V_2O_3 at low temperatures. Theoretical considerations have proposed that these changes can be attributed to magnetic ordering phenomena[1] or to crystallographic transformations.[3] Gross changes in the x-ray diffraction patterns obtained from powder samples of V_2O_3 have been observed.[4] The present paper concerns itself with a more extensive investigation of the lattice distortions and the crystallography of the low temperature phase transformation.

Single crystals of V_2O_3,[5] grown by an arc fusion technique, were oriented and cut so as to expose the $(11\bar{2}0)$, $(10\bar{1}0)$, (0001), $(10\bar{1}1)$, $(11\bar{2}3)$, $(11\bar{2}6)$, and $(21\bar{3}4)$ crystallographic planes. Portions of the crystals were crushed and used for powder patterns. The x-ray reflections and powder patterns were then recorded on a Norelco diffractometer using copper radiation. The x-ray data were taken at room temperature and at suitable intervals down to liquid nitrogen temperatures. The crystals were cooled by passing precooled nitrogen gas over them. The temperatures were recorded by a thermocouple cemented to the back surface of the crystals. The microphotograph in Fig. 1 shows a typical martensitic structure at low temperature. This structure vanished when the crystal was brought back to room temperature but the fractures produced by the cooling are still visible.

The lattice parameters in the V_2O_3 hexagonal unit cell were obtained from the single crystal x-ray reflections recorded at suitable temperature intervals down to the transformation point. All reflections, except the

FIG. 1. Microphotographs V_2O_3 single crystal. (A) Room temperature before cooling. (B) In liquid nitrogen. (C) Room temperature after cooling.

* The work reported in this paper was performed by Lincoln Laboratory, a center for research operated by Massachusetts Institute of Technology with the joint support of the U. S. Army, Navy, and Air Force.

[1] F. J. Morin, Phys. Rev. Letters **3**, 34 (1959).
[2] P. H. Carr and S. Foner, J. Appl. Phys. **31**, 344S (1960).
[3] J. B. Goodenough, J. Appl. Phys. **31**, 359S (1960).
[4] M. Foex *et al.*, J. recherches centre natl. recherche Sci. Lab., Bellevue (Paris) **4**, 259 (1952).
[5] Supplied by the Linde Company, Speedway, Indiana.

(000l) type, shifted and showed a lattice contraction in the plane perpendicular to the c axis. The average coefficient of *contraction* was found to be 22.9×10^{-6} per °C. The lattice parameter parallel to the c axis had a coefficient of *expansion* of 5.8×10^{-6} per °C. New x-ray reflections appeared as the temperature was lowered. The crystallographic transformation occurred so rapidly that the transition temperature could only be estimated to be in the range of minus 145 to 160°C. The x-ray reflections taken at room temperature after the cooling cycle were consistent with the initial recordings.

The low-temperature x-ray diffraction powder pattern and single crystal reflections were characterized by a definite type of line splitting. The (000l) reflections from the low-temperature V_2O_3 phase did not split but did show a lattice contraction of about 0.34% relative to the room-temperature parameter. The (*hki*0) type reflections split into doublets, and the more general type of (*hkil*) reflections split into triplets. The splittings that were not observed on the powder pattern diagram because of the low intensity levels were confirmed by single crystal measurements.

If the crystallographic transformation is considered as one from a hexagonal to a pseudo-orthorhombic unit cell, then the hexagonal indices (*hkil*) can be expressed as pseudo-orthorhombic indices (*pqr*).[6] The relationship between the indices is given by $p=(k+2h)$, $q=k$, and $r=l$. This type of crystallographic transformation would require that (000l) reflections remain as singlets, the (*hki*0) and (*hhil*) reflections split into doublets, and the more general (*hkil*) reflections split into triplets. However, the most salient feature of the low-temperature x-ray diffraction powder pattern was the very strong triplet that appeared at the $(11\bar{2}6)$ reflection. Triplets were also observed from the $(11\bar{2}3)$ and $(11\bar{2}6)$ single crystal reflections. Therefore, in order to account for this experimental fact the structure was reconsidered as having monoclinic symmetry. Monoclinic symmetry requires that the (*hhil*) reflections split into triplets and the general reflections (*hkil*) become sextets.

The $(30\bar{3}0)$ and the $(11\bar{2}0)$ reflections become the (330):(600) and (310):(020) reflections in the monoclinic system, so that by using the appropriate line the a and b parameters could be determined. The c parameter was obtained from the single reflection at the (000l) position. The separation between the lines at the $(20\bar{2}2)$ is a direct measure of the monoclinic β angle. Since only one line was observed, the β angle was calculated by equating the interplanar spacings of the components of this reflection. The lattice parameters of the low temperature phase of V_2O_3 as determined from the single crystal data were: $a=8.57$, $b=4.98$, $c=13.88$ A, and $\beta=91.6°$. These parameters were then used to calculate the position of the possible reflections in the powder pattern. The relative intensities of the lines are indicated by the multiplicity factor for each type of reflection in any one general family. The data obtained from the powder pattern, supplemented by single crystal data when required, are given in Table I. The observed pattern agreed with the calculated pattern except for some lines where the instrumental resolution was not sufficient to completely resolve overlapping lines.

The present x-ray investigation has shown that V_2O_3 does indeed undergo a crystallographic transformation at low temperatures. The lattice distortions and subsequent transformations are in qualitative agreement with the theory proposed by Goodenough[3] to explain the electrical and magnetic transitions of this material.

TABLE I. V_2O_3 X-ray diffraction data.

Room temperature			Liquid nitrogen			Calculated (monoclinic)		
d(A)	*hkil*	I	d(A)	I		d(A)	*pqr*	*m*
			3.65	22		3.694	202	2
3.62	$01\bar{1}2$	60				3.683	112	4
			3.58	18		3.637	$\bar{1}12$	4
						3.603	$\bar{2}02$	2
			2.73	16		2.721	$\bar{1}14$	4
2.69	$10\bar{1}4$	80				2.693	$\bar{2}04$	2
			2.67	25		2.683	$\bar{1}14$	4
						2.660	$\bar{2}04$	2
2.45	$11\bar{2}0$	60	2.48	14	[a]	2.489	020	2
			2.47	24		2.479	310	4
2.32	0006	2	2.31	[a]	[b]	2.314	006	–
			2.23	[a](70)		2.207	$\bar{3}13$	4
2.17	$11\bar{2}3$	20	2.21	[a](70)	[b]	2.192	023	4
			2.18	[a](40)		2.163	313	4
2.03	$20\bar{2}2$	2	2.07	[a](25)	[b]	2.092	$\bar{2}22$	4
			2.05	[a](35)		2.064	(402) (222)	8
						2.032	402	2
1.82	$02\bar{2}4$	25	1.83	80		1.847	404	2
						1.841	224	4
						1.818	$\bar{2}24$	4
			1.79	18		1.801	$\bar{4}04$	2
			1.71	31		1.712	316	4
1.69	$11\bar{2}6$	100	1.69	29		1.695	026	4
			1.66	42		1.671	$\bar{3}16$	4
1.61	$12\bar{3}1$	2	...	...		Six calculated positions		
1.57	$01\bar{1}8$	3	...	...		Four calculated positions		
						1.484	514	4
			1.48	14		1.483	424	4
						1.478	134	4
1.46	$21\bar{3}4$	25	1.47	13		1.472	$\bar{1}34$	4
			1.45	9		1.459	$\bar{4}24$	4
						1.454	$\bar{5}14$	4
1.42	$30\bar{3}0$	30	1.43	[a](24)		1.435	330	4
			1.42	[a](13)		1.429	600	2

[a] Single crystal data.
[b] Second-order reflections recorded.
[c] Second- and third-order reflections recorded.

[6] C. S. Barrett, *Structure of Metals* (McGraw-Hill Book Company, Inc., New York, 1943), p. 11.

Ionic Ordering Effects in the Ferromagnetic Resonance of Lithium Ferrite Monocrystals

A. D. Schnitzler, V. J. Folen, and G. T. Rado
U. S. Naval Research Laboratory, Washington, 25, D. C.

Ferromagnetic resonance experiments on ordered and disordered lithium ferrite monocrystals are reported. The resonance line width ΔH, the g factor, and the magnetocrystalline anisotropy constants K_1 and K_2 were measured at temperatures ranging from 300°K to 4°K. Before an influence of ordering on ΔH could be observed, it was necessary to reduce drastically several spurious effects. These included a large and strongly anisotropic ΔH, which was attributed to a plastic deformation in a thin layer underlying the sample surface. After proper preparation of the samples, it was found that at all temperatures and crystallographic angles at which measurements were made, the value of ΔH is either increased or relatively unchanged as a result of long-range cation ordering. It is concluded that in lithium ferrite, at least, spin wave scattering resulting from cation disorder is not the dominant source of linewidth. The observations include a large peak of ΔH obtained in the [110] direction of the ordered samples at low temperatures, and a low value of ΔH (3 oe) obtained in the [111] direction of the disordered samples at 4°K.

It was the primary purpose of the experiments discussed in this paper to determine whether an effect of ionic ordering on the microwave resonance line width does exist in ferromagnetic insulators. Although this question is of considerable theoretical[1] and practical interest, no such effect has been observed previously in any material. It is known,[2] however, that in lithium ferrite a state of long-range order can be established among the octahedrally situated cations. This order can occur over a wide range of temperatures. In lithium ferrite, moreover, the degree of inversion is independent of the heat treatment, and in pure samples of this material all the magnetic ions are of the same kind. On the basis of these facts, we chose monocrystals of lithium ferrite for the work described below. Since resonance data on such monocrystals are not given in the literature, we measured the g factor and the first and second order magnetocrystalline anisotropy constants, K_1 and K_2, in addition to the resonance line width, ΔH.

The monocrystals were grown from a PbO flux and their chemical formula, based on an analysis of the cations, was found to be $Li_{0.85}Fe_{2.15}O_4$. Electrical conductivity measurements indicated that the ferrous ion content of these crystals is probably not zero, although it is small. The microwave measurements were made at temperatures of about 300, 196, 77 and 4°K with a tunable cavity operating at about 24 kmc/sec in the TE_{102} mode. Small spherical samples having diameters between 80 and 250 μ were ground[3] from the monocrystals and each sphere was mounted on a polystyrene post in the center of the cavity. The surface polish as well as heat treatment of the spheres was varied. Their degree of ionic order, described by the long-range order parameter S, was determined by x-ray analysis of lithium ferrite powder heat treated simultaneously with the spheres.

At first, it seemed impossible to observe an influence of ionic ordering on the line width because of large and unexpected effects of the heat treatments, which did not seem to be correlated with the long-range ordering parameter. In addition, a large and strongly anisotropic line width eas exhibited even by some of those spheres which had been subjected to the final polishing (using 0.1 μ sapphire particles), and appeared smooth under 300× magnification. We observed, for example, that at 300°K the line width is largest in the [111] direction, and that the value of ΔH (defined as the full width of the resonance curve between the points of half maximum of χ'') may range from 25 to 63 oe. These previously unreported spurious effects are evidently caused by something other than scratches and pits, in contrast to the surface effects observed by LeCraw[4] and others. We found it possible, however, to reduce the spurious effects drastically. One method for accomplishing this consists in prolonging the final polishing after the surface is smooth (as seen with 300× magnification) until ΔH ceases to be affected by further polishing. We observed, incidentally, that the simultaneous polishing of two or more spheres in an air-jet type of spheremaker[3] produces a distinct kind of spurious ΔH which is characterized by a peak in the [100] rather than [111] direction. Another method for drastically reducing the spurious effects consists in annealing the spheres at 700°C for about 30 min. The use of temperatures in excess of 800°C resulted in the sample surfaces having an "etched" appearance, presumably as a consequence of recrystallization. Since these two methods proved to be about equally effective, we attribute the spurious ΔH effects to a plastic deformation in a thin layer underlying the spherical surface.

The drastic reduction in the spurious effects led to reproducable observations of a difference between ΔH in the long-range ordered state ($S=1$) and in an almost disordered state ($S\approx 0.1$). It should be emphasized that this difference may arise both from the ionic rearrangement itself and from the resulting changes in the spontaneous lattice distortions. Phenomena caused by strains

[1] A. M. Clogston, H. Suhl, L. R. Walker, and P. W. Anderson, J. Phys. Chem. Solids **1**, 129–136 (1956); S. Geschwind and A. M. Clogston, Phys. Rev. **108**, 49–53 (1957); A. M. Clogston, J. Appl. Phys. **29**, 334–336 (1958).
[2] P. B. Braun, Nature **170**, 1123 (1952).
[3] W. L. Bond, Rev. Sci. Instr. **22**, 344–345 (1951).
[4] R. C. LeCraw, E. G. Spencer, and C. S. Porter, Phys. Rev. **110**, 1311–1313 (1958).

which originate in a "disordering" or "ordering" heat treatment must thus be regarded as belonging intrinsically to the order-disorder effect.

All the monocrystalline spheres used in the measurements were first heated in air at 950°C for about 10 min, and then quenched into water. This treatment apparently relieved all "historical" strains, including those caused by the grinding, and then established an almost disordered ($S\approx0.1$) cation distribution. Some of the spheres were subsequently prepolished (using 4/0 paper), and then subjected to the prolonged final polishing described earlier. The remaining spheres were exposed to an "ordering" heat treatment in which their temperature was lowered from 700° to 300°C during four hours, and from 300°C to room temperature during the cooling period of the furnace. These "ordered" spheres were then polished by the same method as the "disordered" spheres discussed above. (One of the fully prepared "ordered" spheres was reannealed to check on the absence of appreciable volume strains, and it was found that the resulting decrease in the anisotropy of ΔH is only about one oersted.) While the polishing technique used on the spheres cannot possibly be perfect, it is important to note that both sets of spheres did receive the same final surface treatment. The two sets differ, therefore, only in their volume properties and thus predominantly in effects arising from differences in their state of ionic order.

Figure 1 shows the angular dependence of the measured line widths for the ordered ($S=1$) and disordered ($S\approx0.1$) samples at various temperatures. The ionic ordering is seen to have an effect on ΔH. This effect is anisotropic, and its magnitude increases with decreasing temperature. It should further be noted that at all angles and temperatures the line width is either increased or relatively unchanged as a result of the ionic ordering. On the other hand, present theories of spin wave scattering by inhomogeneities predict a decreased line width upon ionic ordering. Thus we conclude that in lithium ferrite, at least, spin wave scattering resulting from cation disorder is not the dominant source of linewidth.

Interesting aspects of the $S=1$ curves at 77°K are the sharp peak of ΔH observed in the [110] direction and the three subsidiary ΔH-peaks observed in other directions. All these peaks disappear at 96°K. Preliminary data at 4°K in the vicinity of the [110] direction indicate that the main peak is at least as high and sharp as that observed at 77°K. In regard to the $S\approx0.1$ curves, we note that ΔH decreases with decreasing temperature. This is opposite to the temperature dependence usually observed in other disordered ferrites. The value $\Delta H=3$ oe obtained for $S\approx0.1$ at 4°K in the [111] direction is perhaps the narrowest line width observed in ferrites. In attempting to explain the changes in ΔH resulting from ionic ordering, we are investigating, among other possibilities, whether the mechanisms of Kittel[5] and

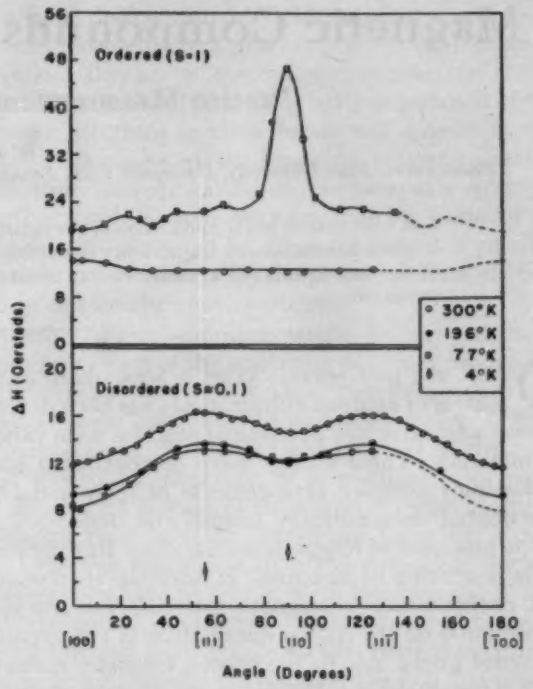

FIG. 1. Angular dependence of the resonance linewidth, ΔH, in the (110) plane for the ordered ($S=1$) and disordered ($S\approx0.1$) monocrystals of $Li_{0.55}Fe_{2.45}O_4$ at 24 kmc/sec and various temperatures.

co-workers are applicable to the present results. The main problem is the determination of the effects of order-induced alterations in the crystalline fields upon the relaxation times of possible impurity cations.

Note added in proof. The role of ferrous ion impurities was studied experimentally by oxidizing one of the ordered samples at 700°C for 20 hr and then restoring the $S=1$ state. The oxidation resulted in the disappearance of the ΔH-peak previously observed in the [110] direction at 77°K.

The resonance line shapes were found to be Lorentzian in all the measurements. Except for the $S=1$ samples at 77°K, where $g=2.012$ was obtained, the measured g values ranged between 2.003 and 2.006. The experimental values of K_2/M, where M is the saturation magnetization, are about -8 oe and -295 oe at 300°K and 77°K, respectively, for the $S=1$ samples. In the case of the $S\approx0.1$ samples, the K_2/M values are 2 oe at 300°K and -96 oe at 77°K. The microwave values of K_1/M for both states of order and the corresponding static values of K_1/M measured by Folen[6] are in very good agreement.

Further experimental and theoretical work on the line width and related problems in lithium ferrite is in progress.

[5] C. Kittel, Phys. Rev. 115, 1587–1590 (1959); de Gennes, Kittel and Portis, Phys. Rev. 116, 323–330 (1959); C. Kittel, Phys. Rev. Letters 3, 169–170 (1959) and Phys. Rev. (to be published). For possible applications of the Kittel mechanisms to ferrites, see R. L. White, Phys. Rev. Letters 2, 465–466 (1959).

[6] V. J. Folen, J. Appl. Phys. 31, 166S (1960), this issue.

Magnetic Compounds and Neutron Diffractions

Precise Measurement of Magnetic-Form Factors*

ROBERT NATHANS
Pennsylvania State University, University Park, Pennsylvania, and Brookhaven National Laboratory, Upton, New York†

A brief outline of the application of the polarized beam technique to studies of the magnetic-form factor is given. Limitations on the accuracy of the final data imposed by corrective factors are noted. A summary of the main results of the measurements taken to date and a discussion of the proposed investigations are presented.

OVER the past several years a large share of the efforts of neutron diffractionists has been devoted to magnetic structure determinations of a wide variety of materials. These studies have demonstrated some increasingly complex arrangements of spins and have contributed immeasurably toward the understanding of the processes of magnetic interactions. But the magnetic scattering of neutrons, in addition to revealing spin configurations in magnetic materials, can also yield information on the spatial distribution of the unpaired electrons giving rise to the atom's magnetic moment. This information is contained in the neutron magnetic form factor.

In making precise measurements of the magnetic form factor, one encounters experimental difficulties very similar to those which have limited the equivalent x-ray measurements. In fact, with unpolarized neutrons, the more rapid fall-off of the magnetic form factor with increasing scattering angle makes an accurate determination of the high angle magnetic scattering even more of a problem. It is fortunate that in the cases of ferromagnetic or ferrimagnetic materials, it is possible to turn to polarized neutron beams and to obtain enhanced sensitivity for such determinations. Studies of the properties of polarized neutron beams have been made by a large number of investigators. More recently, a standard neutron diffractometer has been modified and procedures investigated for obtaining accurate small magnetic scattering cross sections.[1,2]

The polarization of a neutron beam as well as the intensification of the effects of small magnetic amplitudes has its source in the interference effects between simultaneous occurring nuclear and magnetic scattering. By a suitable orientation of the atomic moments and the ability to control the spin directions of the incoming neutrons, one can alter the structure factors of the different Bragg reflections for the particular diffracting material in a manner indicated below:

$$F_{hkl}^{+} = (b_{hkl} + p_{hkl})$$
$$F_{hkl}^{-} = (b_{hkl} - p_{hkl}),$$

where the + and − refer to the situation in which the neutron spins and atomic moments are either parallel or antiparallel to each other. In theory, therefore, observation of the scattered intensities for the + and − arrangements, that is the polarization ratio affords a means of assessing the ratio of the magnetic to nuclear structure factors. If now one has some previous knowledge of the chemical structure, and therefore, the nuclear structure factors, the magnetic structure factor values in question follow.

In the actual collection of data for evaluation of the form factor, the test specimen, ordinarily a single crystal, is rotated until the maximum scattered intensity is registered in the counter which has been set at the Bragg angle. Only peak intensities, not integrated intensities are detected. The resonant oscillator, which reverses the polarization of the incoming neutrons, is then cycled on and off. Background levels are established by rotating crystal and counter off their Bragg settings. It is worth noting that since crystal and counter are in fixed positions during the course of the measurement, from an experimental viewpoint, the arrangement is a very favorable one. Such corrections as inhomogeneous beam distribution, absorption factors, long term fluctuations in beam intensities, and imperfect alignment of the diffracting crystal, all can be ignored to all intents and purposes.

There are, however, other corrections to be applied before the magnetic structure factor can be calculated from the observed polarization ratio. Depolarization of the neutron beam as it traverses the test specimen effectively brings about an uncertainty in the incident beam polarization. For single crystals in a well magnetized state this effect is small, although not negligible, and can be determined easily.[2] In addition, one may have half wavelength effects. Since the polarization of the $\lambda/2$ component is different from that of the primary beam, this introduces a certain amount of complication into estimating this correction. The use of filters or

* Work performed under the auspices of the U. S. Atomic Energy Commission and the National Security Agency.

† Present address: Lincoln Laboratory, Massachusetts Institute of Technology, Lexington 73, Massachusetts.

[1] The polarized beam experiments described in this paper represent the joint efforts of a group at Brookhaven National Laboratory working under the initial guidance of Prof. C. G. Shull and including from time to time Dr. Andresen, Dr. McReynolds, Dr. Paoletti, Dr. Pickart, Dr. Riste, Dr. Shirane, and the author.

[2] Nathans, Shull, Shirane, and Andresen, J. Phys. Chem. Solids **10**, 138 (1959).

analysis of the polarization ratio dependence on wavelength are available as means for securing the elimination or calculation of the necessary subtractive factor.

By far, the most bothersome correction is that caused by extinction. In addition to the familiar devices of making wavelength dependence study and altering of the sample thickness, it is possible to use a third method peculiar to polarized beam measurements. This involves study of the polarization ratio for different crystal orientations, the counter remaining fixed at the Bragg setting. As the crystal is turned off the Bragg angle fewer mosaics are available for scattering, and there is a resultant dimunition of secondary extinction effects.

Thus far, the form factors of nickel, iron, face-centered cobalt, and most recently ordered Fe_3Al have been obtained with polarized neutrons. Comparison of the general shape of these curves has shown that the variation from element to element follows along the lines of what one expects from the differences in their respective nuclear charges. A further examination of the similarities in shapes of the neutron form factors with the x-ray studies of the outer electron distributions in nickel and iron has brought out several further points of interest.[3] Finally, special attention has been directed to the high angle region where experimental evidence of asymmetries in the magnetic electron cloud have been demonstrated.[2,4,5] These effects have been analyzed according to a procedure given by Weiss and Freeman.[3] Because of the different symmetries of the e_g and t_{2g} wave functions, the relative population of the magnetic electrons in these bands will appear as systematic deviations of the magnetic scattering amplitudes from those predicted on the basis of a spherical distribution of electrons. By using then the values of the form factors calculated by these authors, it is possible to arrive at an estimate for the proper mixture of these two groups for the above materials.

A more direct approach would be to perform a Fourier inversion of the scattering data into projections of the magnetic electron density. Heretofore, such calculations were considered to be rather useless in view of limitations on the number and accuracy of the magnetic reflections. However, it is worthwhile to point out that for the outermost reflections of nickel magnetic scattering cross sections, which are down by almost four orders of magnitude from the equivalent nuclear cross sections were measured. With this sensitivity, and with the flexibility of using enriched isotopes to make the nuclear and magnetic amplitudes more comparable, it appears promising that future studies on the transition elements will allow meaningful magnetic electron density maps to be prepared.

[3] R. J. Weiss and A. J. Freeman, J. Phys. Chem. Solids **10**, 147 (1959); W. Marshall and R. J. Weiss, J. Appl. Phys. **30**, 2205 (1959).

[4] R. Nathans and A. Paoletti, Phys. Rev. Letters **2**, 254 (1959).

[5] S. J. Pickart and R. Nathans, J. Appl. Phys. **31**, 372S (1960).

Antiferromagnetic Structure and Domains in Single Crystal NiO

WALTER L. ROTH AND GLEN A. SLACK
General Electric Research Laboratory, Schenectady, New York

Single crystals of NiO have been annealed and stressed at room temperature to sweep out twin boundaries. Neutron diffraction and rotational torque studies have been made on a crystal which had only 1.3% of the twin orientation. The ferromagnetic sheet structure originally proposed in which the atomic moments lie in (111) planes is found to be correct. The anisotropy in the (111) plane is extremely small and at low fields the spins in the ferromagnetic sheet are locked in domains and the susceptibility is nearly isotropic. Rotation of the spins in (111) takes place at fields above 2400 oe.

PREVIOUS neutron diffraction measurements[1] on NiO showed the magnetic moments in antiferromagnetic NiO were probably arranged in ferromagnetic sheets in (111) planes, with reversed directions of magnetization in alternate sheets. The superexchange coupling between the Ni ions produces a lattice contraction and a rhombohedral crystal deformation[2] in otherwise cubic NiO below its Néel temperature of 525°K. This contraction ordinarily occurs along any of the four ⟨111⟩ cubic directions. Thus different regions of an antiferromagnetic NiO crystal possess different contraction axes, and are twinned to neighboring regions on {100} or {110} planes.

These twin walls are one type of antiferromagnetic domain wall. It has been shown previously[3,4] that at least some twin walls can be removed from NiO crystals by a high temperature stress-anneal with a [111] stress applied during cooling. In the present experiment, flame fusion grown NiO crystals have been well annealed at 1600°C in argon with no applied stress. After cooling to 25°C, a small (10^6 d/cm²) momentary stress along [111] will remove all twin walls from the crystal by sweeping them to the ends of the sample. After the stress is removed, the crystal remains untwinned. With momentary stresses in other ⟨111⟩ directions the contraction axis can be switched at will. At a twin wall, there is a small angular tilt between the atomic planes in NiO. Thus, the presence of a twin wall can be seen with reflected light on an optically polished surface of NiO. Both $(\bar{1}10)$ and $(11\bar{2})$ faces have been used to show all possible twin walls.

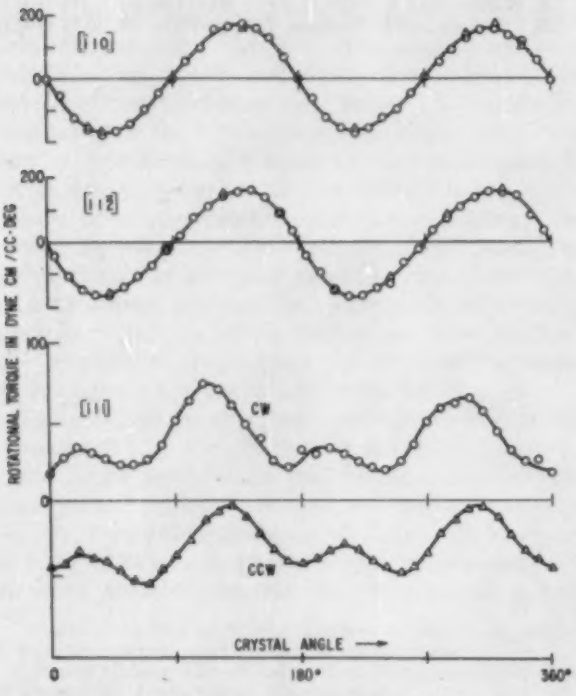

FIG. 1. Rotational torque of untwinned NiO crystal at room temperature in $H = 4800$ oe for three different rotational axes. The ○ and Δ refer to the torque measured in clockwise and counterclockwise rotations.

It was previously shown[1] that single (untwinned) crystal intensity measurements should differentiate between various antiferromagnetic structures which cannot be distinguished by powder neutron diffraction. From the present measurements of the magnetic reflections from an annealed and stressed crystal we prove the single spin axis structure for the ordered antiferromagnetic state of NiO* and show that in this crystal 98.7% of the ferromagnetic sheets are perpendicular to the compression axis.

The magnetic anisotropies were investigated by studying the torques of untwinned crystals in magnetic fields (Fig. 1). The torque curves obtained upon rotation about the $[\bar{1}10]$ and $[11\bar{2}]$ crystal axes in large fields suggest a nearly isotropic susceptibility in the (111) plane. The torque varies approximately with $H^2 \sin 2\theta$ as expected for an antiferromagnet. The rotational torques when the field is rotated in (111) are quite unusual. The torque is very small or zero at small fields. Above 2400 oe, the torque is composed of $\sin 2\theta$ and $\sin 4\theta$ components; the torque curve is a function of crystal shape and a nearly pure $\sin 4\theta$ curve obtains when the (111) cross section is square. Furthermore, the (111) torque shows rotational hysteresis which attains a maxi-

[1] W. L. Roth, Phys. Rev. **110**, 1333; **111**, 772 (1958).
[2] H. P. Rooksby, Acta Cryst. **1**, 226 (1948).
[3] J. R. Singer, Phys. Rev. **104**, 929 (1956).
[4] Kondoh, Uchida, Nakazumi, and Nagamiya, J. Phys. Soc. (Japan) **13**, 579 (1958).
* We understand from private communication that H. Alperin has arrived at similar conclusions from work performed at the U.S.N.O.L.

mum value of 375 ergs/cc-cycle at 8000 oe and decreases only slightly with fields as high as 16 000 oe.

Two alternative interpretations are suggested: (A) The spins are distributed among domains such that the average antiferromagnetic susceptibility in (111) is isotropic and given by $\frac{1}{2}(\chi_{\parallel}+\chi_{\perp})$ at all H fields. Then the (111) torque is not an intrinsic property of the antiferromagnetic state and may originate from small moments associated with domain walls and/or impurities. (B) The spins are locked in random domains for $H<2400$ oe. but larger fields rotate the moments within the (111) plane. The neutron diffraction experiments described below show that (B) is correct.

The intensity of magnetic scattering is proportional to the quantity q^2 which is a function of the angle between the scattering vector and the magnetic moment. The dependence of q^2 for various planes (hkl) upon the azimuthal angle of the magnetic moments in (111) is shown in Fig. 2. The $(11\bar{3})$ intensity was found to be a maximum when a field of 4200 oe was applied perpendicular to $(11\bar{3})$ and to decrease by 20% when the field was rotated nearly in (111) by an angle of about 25°. This agrees with the computed curve and shows that the antiferromagnetic spin system rotated normal to the applied field.

Our interpretation resembles a model proposed by Keffer and O'Sullivan[5] to explain the powder susceptibility of MnO. On assuming an average value for $\chi_{\perp}$ (whether parallel or perpendicular to the ferromagnetic sheet) and combining our data with those of Singer, we obtain as provisional estimates of the individual susceptibilities $\chi_{\perp}=71.5\times10^{-6}$ and $\chi_{\parallel}=57.1\times10^{-6}$ emu per cc).

Further experiments are planned to study the effects of magnetic fields on the thermal conductivity[6] and the rotation of magnetic moments in single domain NiO crystals.

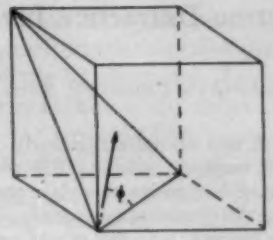

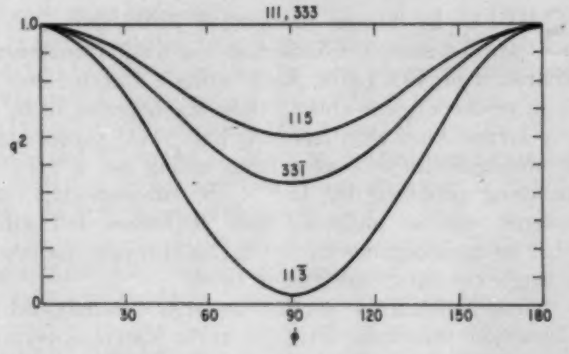

FIG. 2. Dependence of neutron scattering, q^2, from magnetic planes (hkl) as a function of the angular orientation, ϕ, of the magnetic moments in the (111) plane.

ACKNOWLEDGMENTS

We are grateful to J. M. Hastings for the use of the BNL spectrometer to obtain the effect of a magnetic field on the magnetic scattering. We also wish to thank J. Kouvel for some of the torque measurements, and R. Newman for growing the crystals.

[5] Keffer and O'Sullivan, Phys. Rev. **108**, 637 (1957).
[6] G. Slack and R. Newman, Phys. Rev. Letters **1**, 359 (1958).

Neutron Diffraction Investigation of the Magnetic Structure of Nickel Oxide

H. A. Alperin
University of Connecticut, Storrs, Connecticut, and U. S. Naval Ordnance Laboratory, Silver Spring, Maryland

A neutron diffraction study of nickel oxide was performed utilizing single crystal samples to investigate the magnetic structure. The results indicate the structure to have a single magnetic axis lying in a (111) plane, but within this plane there are domains such that the directions of the moments of these domains are distributed symmetrically. To fit the data required an effective spin value for the Ni^{++} atom of 0.8 and an isotropic form factor $\exp[-6(\sin\theta/\lambda)^2]$.

I. INTRODUCTION

SHULL[1] by means of neutron diffraction with a powder sample established the antiferromagnetic character of NiO. Later, Roth[2] using a spectrometer of high resolution was able to show the ordering to be of the second kind with ferromagnetic (111) planes antiferromagnetically coupled, thus ruling out a type of ordering proposed by Li.[3] Roth[4] subsequently considered various multiaxis spin structures indicating that for unambiguous interpretation of results one needs a single crystal sample free of twins.

Nickel oxide single crystals undergo a rhombohedral distortion[5] from cubic structure at the Néel temperature (~530°K). This results in crystallographic twins, the four possible rhombohedral axes being the four [111] directions. The crystals used in this work, which were grown by the flame fusion method, were twinned in this manner. The magnetic intensities one obtains from diffraction are thus greatly affected since the ferromagnetic (111) planes form perpendicular to the axis of distortion. Ideally, one would like to obtain a crystal free of all twinning, i.e., with a single rhombohedral axis.

II. EXPERIMENTAL

The present investigation follows the work of Singer,[6] who showed that it was possible to eliminate some of the twinning present by heating a nickel oxide crystal to 1000°C and then applying a compression along a [111] direction while the crystal cooled to room temperature. A crystal carefully prepared in this way was kindly lent to us by Professor Uchida of the University of Osaka Prefecture. Neutron diffraction measurements were performed on this crystal and a second one to be described later, utilizing the facilities of the Naval Research Laboratory reactor.

In order to calculate the expected intensities, the effect of absorption and secondary extinction in the crystal had to be taken into account. This calculation was made difficult due to the irregular shape of the crystal which was dictated by the requirements of the pressure annealing procedure. The crystal was in the shape of an elongated hexagonal slab with length, width and thickness approximately 0.76 cm, 0.53 cm, and 0.13 cm, respectively. The secondary extinction was particularly severe, e.g., the strongest nuclear reflection had a combined extinction-absorption factor of 0.32 and the strongest magnetic reflection had a value of 0.47 for this factor. No account was taken of primary extinction. The general procedure followed was the one described by Hamilton[7] and the calculation was programed for the IBM 704 computer. The magnetic intensities were first put on an absolute basis by using the nuclear reflections for calibration. The mean percentage probable error for the agreement between the observed and calculated nuclear reflections was 9%.

A similar procedure was adopted in regard to the magnetic reflections. The parameters determined from the nuclear reflections were now constants for the calculation of the magnetic intensities. Since the stress applied to the crystal during pressure annealing was in a [111] direction, one expects the resultant twin distribution to show the largest portion of the crystal to have its axis of rhombohedral distortion in the [111] direction, the remainder of the crystal having equal volumes distorted in the other three [111] directions. This parameter, the percentage of moments aligned in the (111) plane, together with the effective spin value for the Ni^{++} atom and the constant A in the relation for the isotropic magnetic form factor, $f=\exp[-A(\sin\theta/\lambda)^2]$ were used as parameters to fit the magnetic data. The assumed magnetic structure was a model where the spins lie within the (111) plane, but within this plane antiferromagnetic domains exist such that within each domain the spins are ferromagnetically aligned, but the directions of the domains themselves are distributed symmetrically within the plane.

III. RESULTS

The results for the first crystal indicate that 79.5% of the spins are aligned in the (111) plane, and 6.8% in each of the planes $(\bar{1}11)$, $(1\bar{1}1)$ and $(11\bar{1})$.

Table I shows a comparison of the observed and computed intensities for the magnetic reflections that were measured. The assumption of the domains in the (111)

[1] Shull, Strauser, and Wollan, Phys. Rev. **83**, 333 (1951).
[2] W. Roth, Phys. Rev. **110**, 1333 (1958).
[3] Y. Y. Li, Phys. Rev. **100**, 627 (1955).
[4] W. Roth, Phys. Rev. **111**, 772 (1958).
[5] H. P. Rooksby, Acta Cryst. **1**, 226 (1948).
[6] J. R. Singer, Phys. Rev. **104**, 929 (1956).
[7] W. Hamilton, Acta Cryst. **10**, 629 (1957).

TABLE I. Neutron intensities from NiO crystal.

hkl	Intensity Observed	Intensity Calculated	hkl	Intensity Observed	Intensity Calculated
111	1650	1674	131	39	40
$\bar{1}11$	192	209	113	35	40
$1\bar{1}1$	219	191	$3\bar{1}3$	412	399
$11\bar{1}$	212	191	$33\bar{1}$	414	399
333	313	314	313	27	28
$\bar{3}33$	23	24	331	25	28
$3\bar{3}3$	25	22	555	30	26
$33\bar{3}$	25	22	$55\bar{7}$	7	3
$\bar{3}11$	542	520	$5\bar{3}5$	46	34
$1\bar{3}1$	563	494	$55\bar{3}$	43	34
$11\bar{3}$	543	494	373	47	34
311	40	41	337	40	34

plane is necessitated by the equality of the observed values for the reflections $\bar{3}11$, $1\bar{3}1$ and $11\bar{3}$. If the spins were assumed to point in a preferred direction in the (111) plane (e.g., the direction $[\bar{1}10]$), then the $11\bar{3}$ reflection would have had approximately twice the value that was observed and the reflections $\bar{3}11$ and $1\bar{3}1$ approximately one-half the observed values.

Of the multiaxes spin structures considered in reference 4, the only one that could possibly fit the data is the one with the spins in the directions $[\bar{1}10]$ and $[\bar{2}11]$. One would still require domains in the (111) plane. However, in order for this model to represent the data for the reflections of the form {111} one must give up the physically reasonable assumption made earlier that there is an equal distribution of spins in the $(\bar{1}11)$, $(1\bar{1}1)$ and $(11\bar{1})$ planes. However, even if one does this, the multiaxis structure would require one of the weaker reflections of the {311} form (e.g., 311) to have an intensity approximately one-half that of the stronger reflection (e.g., $\bar{3}11$). This is not borne out by the data.

The best fit to the magnetic data is obtained with an effective spin value S for the Ni^{++} atom of 0.8. This value represents the observed temperature variation of the magnetic intensity[4] somewhat better than the value $S=1$, usually used for Ni^{++} (obtained by assuming a completely quenched orbital contribution to the magnetic moments of the $3d$ electrons). The constant A in the isotropic representation of the magnetic form factor is found to have the value 6. This yields a form factor falling off with $(\sin\theta/\lambda)^2$ much more slowly than that for the Mn^{++} atom[8] (the curve that is usually taken for Ni^{++} also). This form factor curve is quite close to that for Ni metal.

Torque measurements on the crystal described above were made by Kondoh *et al.*[9] The results of their measurements and the measurements described here are in very good agreement.

A second crystal[10] was also measured and its intensities can be represented by the same magnetic structure. This crystal had approximately 90% of the spins in the (111) plane, 0% in the $(\bar{1}11)$ plane, 3% in the $(1\bar{1}1)$ plane and 7% in the $(11\bar{1})$ plane. No pressure annealing was used in its preparation. It was annealed at 1500°C for 1 hr and then cooled slowly (~1°C/min).

The magnetic structure found here for NiO is in agreement with the model discussed by Keffer and O'Sullivan[11] for MnO, who ascribe the constraint of the moments to the (111) plane as being due to dipolar and exchange forces and the constraint of the moment within this plane to a threefold set of easy axes due to a much weaker anisotropy force.

ACKNOWLEDGMENTS

The author would like to thank L. Schmidt for help with the programing of the computations, S. Strong and R. Strakna for preparing data, Dr. E. Prince and G. Ferguson for many helpful discussions and Dr. T. R. McGuire and Dr. L. R. Maxwell for constant help and encouragement.

[8] L. Corliss and J. Hastings, Phys. Rev. **104**, 924 (1956).
[9] H. Kondoh, E. Uchida, Y. Nakazumi, and T. Nagamiya, J. Phys. Soc. (Japan) **13**, 579 (1958).
[10] This crystal was grown by Dr. E. J. Scott, U. S. Naval Ordnance Laboratory.
[11] F. Keffer and W. O'Sullivan, Phys. Rev. **108**, 637 (1957).

Neutron Diffraction Investigation of the $Fe_{1-\delta}S$ System*

J. T. Sparks, W. Mead, A. J. Kirschbaum, and W. Marshall†
University of California, Lawrence Radiation Laboratory, Livermore, California

The intensity of the purely magnetic (001) reflection has been investigated as a function of temperature for $Fe_{1-\delta}S$ samples with $\delta=0.02$, 0.066, 0.099 and 0.107. Samples from the antiferromagnetic α' phase, $\delta=0.02$, exhibit a spin reorientation at a temperature corresponding closely to that at which the susceptibility anomaly occurs (125°C). Preliminary measurements on a stoichiometric sample, $\delta=0$, suggest that for this composition, two distinct spin reorientations occur, one at 140°C corresponding to the abrupt change in susceptibility and the second at 160°C. The presence of a small (001) reflection at room temperature in the α'-phase samples, and the appearance of the x-ray powder diffraction photographs suggest that a mixed phase region may exist below the α' transition. Quenching from above the α' transition produces samples which show no room temperature peak, and whose x-ray patterns indicate only a single phase. An examination of the (001) reflection of samples for which $\delta=0.066$, 0.099 and 0.107, suggests that for these compositions the spins lie in the hexagonal planes from room temperature to the Néel temperature, 320°C. No anomalies were observed for $\delta=0.066$ at the α'' transition or in the γ region. Also no evidence of disorder occurring in the spin system below T_n was observed with either $\delta=0.099$ or $\delta=0.107$.

INTRODUCTION

OVER the last two decades, a number of experimental investigations and theoretical speculations have been made concerning the structure and unusual magnetic properties of the $Fe_{1-\delta}S$ system ($0\leq\delta\leq0.125$). Nevertheless, many of the most interesting properties are still open to interpretation because of a lack of knowledge of the detailed behavior of the spin system. In order to provide this information, we have undertaken a powder neutron diffraction investigation of the iron-sulfide system. This paper reports some of the preliminary results.

The $Fe_{1-\delta}S$ system consists of a series of compounds possessing the NiAs structure or closely related superstructures. The magnetic properties of these compounds have been studied extensively by Haraldsen,[1] Lotgering,[2] and Hirahara.[3] Susceptibility measurements show that the spin alignment is basically antiferromagnetic with a Néel temperature of 320°C. The sulfur-rich compounds exhibit unbalanced antiferromagnetism or ferrimagnetism. Sidhu[4] has verified the antiferromagnetic structure by means of neutron diffraction.

Of particular interest are the abrupt changes in susceptibility, which are observed between room temperature and the Néel temperature. Compounds in the range $0\leq\delta<0.08$ show a sharp increase in susceptibility in the vicinity of 100°C. In addition, a relatively large anomalous peak occurs in the γ region at about 180°C for $0.04<\delta<0.08$. Over the range $0.08<\delta<0.107$, an anomalous spontaneous magnetization occurs over a narrow temperature interval around 220°C. In the sulfur-rich region, $0.107\leq\delta\leq0.125$, the compounds possess a spontaneous magnetization from room temperature to about 280°C.

To explain the kink in the susceptibility curve at the α' transition for $\delta=0$, M. Shimizu[5] has postulated that at the transition the spins rotate from an alignment parallel to the c axis to an alignment perpendicular to it. K. Yosida[6] has postulated that the anomalous magnetic properties for sulfur-rich compositions arise from a preferential ordering of Fe^{2+} and Fe^{3+} ions on alternate hexagonal planes. On the other hand, Lotgering[2] has attempted to explain some of these properties by competitive ordering of spins and vacancies. Observation of the temperature dependence of the purely magnetic (001) reflection in the neutron diffraction spectra of these compounds should help to check these speculations, since the intensity of this peak is dependent on spin orientation and degree of order.

EXPERIMENTAL

A number of polycrystalline samples of iron sulfide were prepared following, in general, the procedure used by Haraldsen.[1] Baker and Adamson sulfur and iron wire were used. Spectrochemical analysis of the sulfur gave an impurity content of 0.08%. The stated purity of the iron wire was 99.90%. For examination in the spectrometer, the samples were sealed in evacuated 1-in. o.d. quartz tubes.

A simple furnace designed for use with the neutron spectrometer was used for the temperature-dependent magnetic scattering studies. The sample temperature was obtained from thermocouples attached to the wall of the sample tube.

The neutron diffraction spectrometer used to examine the samples is a simple "hand-driven" instrument. It has proven adequate, however, for measuring relative changes in intensity resulting from spin reorientations

* Printed for the U. S. Atomic Energy Commission.
† Theoretical Physics Division, Atomic Energy Research Establishment, Harwell, England.
[1] H. Haraldsen, Z. anorg. u. allgem. Chem. **231**, 78 (1937); **246**, 169 (1941); and **246**, 195 (1941).
[2] F. K. Lotgering, Philips Research Rept. **11**, 190 (1956).
[3] E. Hirahara, M. Murakami, J. Phys. Chem. Solids **7**, 281 (1958).
[4] S. S. Sidhu, D. Meneghetti, Phys. Rev. **91**, 435 (1953).
[5] M. Shimizu (original article in Japanese). Discussed by Yosida in reference 6.
[6] K. Yosida, Progr. Theoret. Phys. **6**, 356 (1951).

and structure changes. Peak widths of somewhat less than one degree, and count rates of several hundred counts per minute are obtainable with this instrument. The present instrument is to be replaced shortly by a new spectrometer more suitable for precision quantitative measurements.

RESULTS

The intensity of the purely magnetic (001) reflection was carefully examined from room temperature to above the Néel point for two $\delta=0.02$ samples. A large increase in intensity was observed between 120°–130°C. We have also made magnetic measurements on one of these samples using the Gouy method and have observed a sharp kink in the susceptibility at about 125°C in agreement with the results of other investigators.

Further investigation of the (001) reflection has revealed a significant room temperature peak for all $\delta=0.02$ samples that have been cooled slowly through the α' transition. Quenching from above the transition, however, removes the peak. Examination of the (001) reflection of a quenched sample as a function of temperature shows a rather broad α' transition with an apparent knee at about 100°C as shown in Fig. 1. If the samples are quenched or cooled slowly from the temperature of the knee, the intensity does not return to zero, but remains as a room temperature peak of about the same height as the knee.

Room temperature x-ray powder diffraction photographs were taken of both quenched and slow-cooled $\delta=0.02$ samples. The quenched pattern can be indexed on the α' superlattice and the calculated lattice parameters agree well with Haraldsen's.[1] The slow-cooled pattern, however, exhibited two sets of lines, which yield lattice parameters corresponding to Haraldsen's $\delta=0.01$ and $\delta=0.038$ (α'') parameters.

Two $\delta=0.066$ samples have been examined in an attempt to gain insight into the puzzling γ anomaly and also to check the spin orientation in the α'' region. A full-sized (001) reflection is present at room temperature and the intensity shows no obvious irregularities as the temperature is increased to the Néel point. Quenching from above the α'' transition does not affect the intensity of the room temperature peak.

Two samples in the sulfur-rich region, $\delta=0.099$ and $\delta=0.107$ were also prepared. The $\delta=0.099$ sample exhibited spontaneous magnetization from about 200° to 240°C and the $\delta=0.107$ sample showed this property at room temperature. The temperature dependence of the (001) reflection has been examined for both samples. No pronounced irregularities in the intensities were observed between room temperature and the Néel point, in apparent contradiction to Lotgering's[2] hypothesis of competitive ordering of spins and vacancies.

DISCUSSION

In view of the limited number of samples we have examined so far, only tentative conclusions are appropriate at this stage of the investigation. The abrupt change in the (001) intensity observed with the $\delta=0.02$ samples confirms the existence of a spin reorientation at the temperature of the susceptibility anomaly, $T_{\alpha'}$. Above the transition the spins lie in the hexagonal planes forming ferromagnetic sheets perpendicular to the c axis with antiparallel spin directions on adjacent planes.

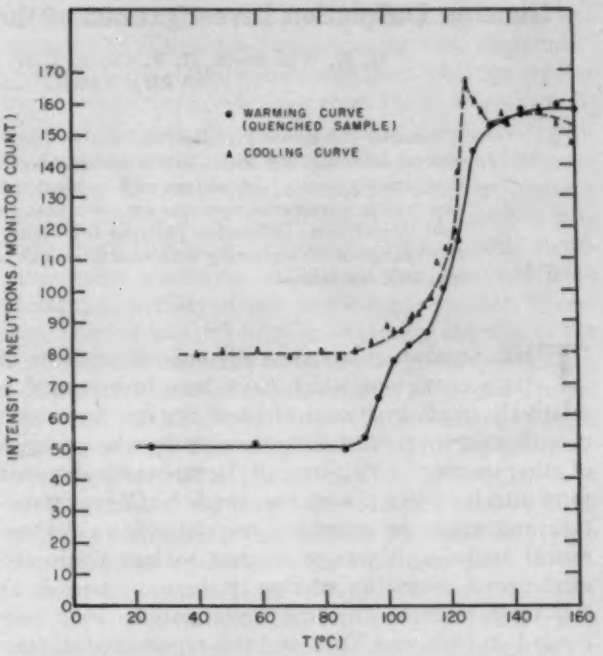

FIG. 1. Intensity of the (001) magnetic reflection as a function of temperature in the vicinity of the α' transition for $\delta=0.02$.

The question of the spin alignment below the α' transition requires further clarification. An arrangement similar to that above the transition, but with the spins aligned along the c axis, is consistent with the data obtained from the quenched α' samples. However, preliminary measurements with a stoichiometric sample ($\delta=0$) suggest that, for this composition at least, a third spin arrangement occurs between 140° and 160°C. The change to the the arrangement observed with $\delta=0.02$ samples above the α' transition, as shown by the abrupt appearance of the (001) reflection, does not occur until $T=160$°C.

The origin of the (001) room temperature peak observed with the $\delta=0.02$ samples is as yet uncertain. The x-ray results on these samples and the neutron results on $\delta=0.066$ samples suggest that a mixed phase region involving both α' and α'' phases may exist below the α-transition.

ACKNOWLEDGMENT

We express our gratitude to J. E. Harrar for the preparation of numerous iron sulfide samples and also thank Dr. Allen Zalkin for the x-ray analyses.

Neutron Diffraction Investigations of the Magnetic Ordering in Rare Earth Nitrides

M. K. Wilkinson, H. R. Child, J. W. Cable, E. O. Wollan, and W. C. Koehler
Oak Ridge National Laboratory, Oak Ridge, Tennessee

Neutron diffraction investigations on HoN and TbN at low temperatures show that both compounds become ferromagnetic with Curie temperatures of about 18°K and 43°K, respectively. Although the paramagnetic scattering is consistent with moment values calculated for the free trivalent rare earth ions, the observed ferromagnetic moments are lower than the calculated values and indicate the effect of crystalline field interactions. Diffraction patterns from both compounds at 1.3°K show considerable ferromagnetic short-range-order scattering with characteristics which are different from those associated with critical magnetic scattering.

THE number of magnetically-ordered systems of rare earth ions which have been investigated is relatively small, and most of these systems have been complicated by crystal distortions or by the presence of other magnetic ions. Since all the rare earth elements form nitrides which possess the simple NaCl-type structure and might be amenable to relatively easy theoretical analyses, it was of interest to investigate the existence of magnetic ordering in these compounds at low temperatures. The first investigations were performed on HoN and TbN, and this report contains the preliminary results which were obtained.

The compounds were prepared[1] from rare earth metals which had a spectroscopic purity of about 99.5%. The metals were first converted to the hydrides after which the nitrides were formed by reaction with NH_3 at temperatures from 850° to 1100°C. Quantitative chemical analyses for nitrogen indicated that only about 95% of the desired amount was present in the samples. Additional analyses suggest that this low value is not the result of nitrogen vacancies in the nitride lattice but is due to the presence of small amounts of rare earth oxides and carbides formed during the preparation from oxygen and carbon which were present in the metals.

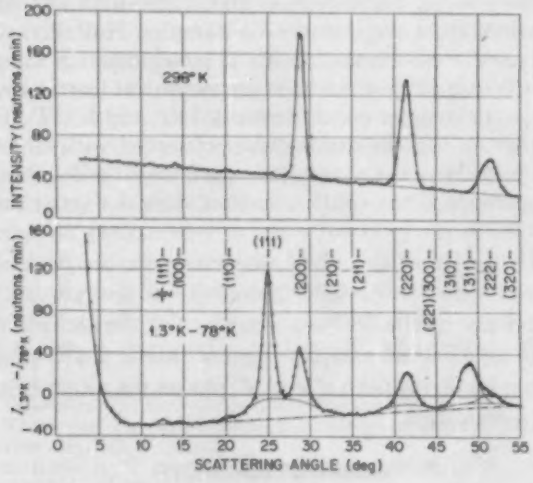

FIG. 1. Neutron diffraction patterns from HoN.

Neutron diffraction investigations have been performed on powdered specimens of both compounds at temperatures from 298°K to 1.3°K, and Fig. 1 shows diffraction patterns obtained from HoN. The pattern at room temperature shows the nuclear reflections superimposed on a very high paramagnetic diffuse scattering. The observed cross section of this paramagnetic scattering is in good agreement with that calculated for the paramagnetic moment (10.6 Bohr magnetons) of the free Ho^{+3} ion, and the angular variation of the scattering is consistent with the magnetic form factor which was obtained from investigations[2] on Ho_2O_3. Ferromagnetic reflections were observed in the diffraction patterns from HoN at liquid-helium temperatures, and these reflections are shown in Fig. 1b, where the data represent the difference in results obtained at 1.3°K and 78°K. It is interesting to note that the (111) and (311) magnetic reflections actually occur at positions where nuclear reflections would be expected, but the latter are missing because the nuclear scattering amplitudes of holmium and nitrogen are almost equal. The intensity of the (111) magnetic reflection was studied as a function of temperature, and it was found to exhibit a Brillouin-type dependence with a Curie temperature about 18°K. The very pronounced small-angle scattering and the large increase in diffuse scattering in the angular regions of the reflections are characteristic of the diffraction pattern at 1.3°K and indicate the presence of a short-range ferromagnetic correlation at temperatures far below the magnetic transition temperature. This small-angle scattering, which has been studied with well-collimated incident and reflected beams at scattering angles to one degree, occurs at temperatures above the Curie point and increases with decreasing temperatures down to 1.3°K. Therefore, it does not have the characteristics associated with critical magnetic scattering, and the mechanism for producing it is not yet understood.

The large variation in the diffuse scattering causes considerable uncertainty concerning the calculation of the ferromagnetic moment in the ordered lattice at low temperatures. However, if it is assumed that the long-range ferromagnetic order produces reflections with a

[1] We are very much indebted to D. E. LaValle, ORNL, for preparing these samples.

[2] W. C. Koehler, E. O. Wollan, and M. K. Wilkinson, Phys. Rev. **110**, 37 (1958).

resolution comparable to the nuclear reflections, then the background must be similar to that shown by the dotted lines in Fig. 1(b), and the ferromagnetic moment is about 6.8 Bohr magnetons per holmium ion. If the large humps in the background are included in the reflections, a value of about 8.6 Bohr magnetons per holmium ion is obtained. Since either calculation gives a moment which is smaller than the maximum ordered moment (10.0 μ_B) associated with the Ho^{+3} ion, these results indicate that the moment value is affected by crystalline field interactions. Recent calculations by Trammell[3] of the energy levels which result from these interactions are consistent with this interpretation. His calculations also predict that the magnetic moments in the ordered lattice are directed along the edges of the cubic unit cell and that relatively large energies are required to move them from this direction. This prediction was verified experimentally by measurements of the (200) and (111) magnetic intensities when a magnetic field was applied parallel to the scattering vectors of the corresponding reflecting planes. The magnetic contribution to the (200) reflection was almost eliminated by a magnetic field of 16 koe, but there was little effect on the (111) intensity by a field of this value. These results indicate that moderate magnetic fields can turn the atomic moments from one cube edge to another, but these fields are not sufficiently strong to rotate the moments to a direction parallel to the cube diagonal.

The neutron diffraction results from TbN are similar to those which were obtained from HoN. At room temperature, the paramagnetic scattering is consistent with that calculated for the trivalent Tb ion, and at low temperatures the compound becomes ferromagnetic with a Curie point about 43°K. Although the diffraction patterns from TbN at 1.3°K show a ferromagnetic short-range-order scattering similar to that observed from HoN, the intensity of this scattering is smaller. Therefore, there is less difficulty in obtaining the size of the ferromagnetic moment from the magnetic reflections, and these calculations give a value of 7.0 μ_B per Tb ion. This value is also lower than the maximum ordered moment (9.0 μ_B) associated with the Tb^{+3} ion and indicates the effect of the crystalline field. Investigations of the intensities of the magnetic reflections in an external magnetic field suggest that in TbN the direction of easy magnetization is parallel to the cube diagonal.

Additional experiments will be performed on HoN and TbN to investigate the nature of the small angle scattering from these compounds and to obtain a better magnetic form factor associated with the 4*f* electrons in these ions. Neutron scattering experiments will also be performed on the other rare earth nitrides which have sufficiently small absorption cross sections to permit analysis by this technique.

[3] G. T. Trammell (private communication).

JOURNAL OF APPLIED PHYSICS SUPPLEMENT TO VOL. 31, NO. 5 MAY, 1960

Direct Cation-Cation Interactions in Primarily Ionic Solids*

JOHN B. GOODENOUGH
Lincoln Laboratory, Massachusetts Institute of Technology, Lexington 73, Massachusetts

It is pointed out that there is considerable experimental evidence for direct cation-cation interactions in several primarily ionic solids containing transition-element cations with outer-electron configuration nd^m, where $m \leq 5$. Competitive indirect (cation-anion-cation) interactions are dominant if $m = 5$. Nevertheless, if cation-occupied octahedra share a common face, as in the corundum and NiAs-type structures, the direct (cation–cation) interactions may also significantly influence the physical properties of the material. If octahedral-site cations have $m \leq 3$, the cation-anion-cation interactions are weak and cation- -cation interactions may be dominant. The consequences of cation- -cation interactions are described and shown to be quite distinct from those of cation-anion-cation interactions so that the dominant mechanism can usually be distinguished. Data for several illustrative materials are presented.

I

THE purpose of this paper is to point out some of the electric, magnetic, and crystallographic consequences to be associated with cation- -cation (no anion intermediary) interactions in primarily ionic crystals and to review the experimental data on several compounds that appear to illustrate the importance of these effects.

Cation- -cation interactions are induced by the overlap of partially filled *d* orbitals of neighboring transition-element cations. In the illustrative examples of this effect, the interacting cations are located in octahedral (or distorted octahedral) interstices of an anion sublattice, so that cation- -cation interactions are possible if cation-occupied octahedra share either a common face or a common edge. In a cubic structure, crystalline

* The work reported in this paper was performed by Lincoln Laboratory, a center for research operated by Massachusetts Institute of Technology, with the joint support of the U. S. Army, Navy, and Air Force.

fields split the atomic d levels of an octahedral-site cation into a more stable, triply degenerate $t_{2g}(d_{yz}d_{zx}d_{xy})$ level and a less stable, double degenerate $e_g(d_{z^2}, d_{x^2-y^2})$ level. Partially filled anion-directed e_g orbitals induce strong cation-anion-cation interactions between cations making an obtuse angle α with an intervening anion,[1] whereas partially filled t_{2g}(empty e_g) orbitals induce only weak cation-anion-cation interactions. Since the purpose of this paper is to discuss cation- -cation interactions, the guiding rules that have been developed[2-4] for the competitive cation-anion-cation interactions are not repeated here.

As the cation-cation separation is increased, there should be an abrupt transition from cation- -cation interactions that induce delocalization of the electrons in overlapping t_{2g} orbitals to those that leave the electrons localized at the cation.[5] Cation- -cation interactions that induce delocalization of the electrons will be defined as strong, those that do not as weak, interactions. Whether the interactions are strong or weak, the entropy term in the free energy favors paramagnetism with localized atomic moments approaching those of the free ions. At low temperatures, strong interactions may lead to covalent-type bonding of cation pairs. These considerations and empirical data lead to the following rules for cation- -cation interactions in predominantly ionic crystals:

(1) Weak Interactions

If overlapping t_{2g} orbitals of cation neighbors are half or less filled, there exists a cation- -cation antiferromagnetic interaction that is weaker than strong, cation-anion-cation magnetic interactions but may be greater than weak, cation-anion-cation interactions. There is no contribution to metallic-type conductivity. If one or both of the overlapping orbitals is more than half-filled, the interaction is negligible.

(2) Strong Interactions

(a) *High Temperatures*

Partially filled t_{2g} orbitals form a partially filled band, and metallic-type conductivity results. The atomic moment approaches that for localized electrons as the temperature is increased.

(b) *Low Temperatures*

Covalent-type cation- -cation bonds may be formed that displace the cations from the center of symmetry of their anion interstice. This crystallographic transition may be noncooperative (lattice symmetry unchanged) and extend over a considerable range of temperature ($\Delta T \sim 100°C$), or cooperative, taking place at a discrete temperature and exhibiting thermal hysteresis.[6] Bonding electrons have paired spins and therefore contribute a negligible atomic moment unless unpaired, localized d electrons are simultaneously present. In this latter event, bonded cations are coupled antiferromagnetically, and the bonding electrons contribute a fraction of a Bohr magneton to the atomic moment. Electrons in covalent-type bonds do not contribute to metallic-type conducitivity.

II

In Table I are listed several physical properties of a few pertinent compounds. CrN, VO, $LiVO_2$, V_2O_3, Ti_2O_3, and VO_2 are believed to illustrate strong cation--cation interactions. In the corundum structure the most stable covalent-type bond is between c-axis pairs (neighboring octahedra share a common face), but less stable bonding can also occur in the basal plane (neighboring octahedra share a common edge). A noncooperative transition is to be associated with c-axis bonding, but a cooperative transition to orthorhombic symmetry with bonding by only one t_{2g} electron in the basal plane. Therefore two transitions are possible if the cation has two t_{2g} electrons, and the semiconducting $\rightleftharpoons$ metallic transition must accompany the lower-temperature, cooperative transition. Lack of magnetic scattering in neutron-diffraction experiments on low-temperature V_2O_3 and Ti_2O_3 is further evidence that the d electrons are paired in bonding. The magnetic order of CrN (to be contrasted with that of MnO) couples nearest-neighbor cations of the distorted lattice antiferromagnetically, and the atomic moment is reduced from its spin-only value. Since the low-temperature phase is compatible with bonding by only two of the three t_{2g} electrons, it is expected to be metallic ($\Delta\rho = 0$). The semiconducting low-temperature phase of isoelectric VO is expected to have a different symmetry in which three t_{2g} electrons are tied up in bonds. Low-temperature VO_2 is a distorted rutile with bonded cation pairs.[7] The small χ in the low-temperature phase also supports the direct-bonding hypothesis.

The other compounds of Table I illustrate weak cation- -cation interactions. In α-Fe_2O_3 and MnF_2, the e_g orbitals are half filled and the cation-anion-cation interactions are strong: therefore these determine the magnetic order. By contrast, Cr_2O_3 exhibits the magnetic order expected from cation- -cation interactions[8] and MnO_2 a magnetic order characteristic of a cation--cation interaction about 1.6 times stronger than the cation-anion-cation interaction.[8] The metallic, ferro-

[1] P. W. Anderson, Phys. Rev. **79**, 350 (1950).
[2] J. B. Goodenough, J. Phys. Chem. Solids **6**, 287 (1958).
[3] D. G. Wickham and J. B. Goodenough (to be published).
[4] P. W. Anderson, Phys. Rev. **115**, 2 (1959).
[5] N. F. Mott, Proc. Phys. Soc. (London) A62, 416 (1949).
[6] These phase transformations are to be distinguished from Jahn-Teller and spin-orbit distortions, which are due to cation-anion interactions. J. D. Dunitz and L. E. Orgel, J. Phys. Chem. Solids **3**, 20 (1957).
[7] A. Magnéli and G. Anderson, Acta Chem. Scand. **9**, 1378 (1955).
[8] A. Yoshimori, J. Phys. Soc. Japan **14**, 807 (1959).

TABLE I. Some Physical Properties of a Few Transition Element Compounds.[a]

Structure at high T	Compound	$n_{t_{2g}}$	$n_b(m)$	$\rho(\Omega\,\mathrm{cm})$ $T=T_t^+$	Cooperative transition T_t(°K)	$\Delta\rho(\Omega\,\mathrm{cm})$	$\Delta\chi/\chi_{T_t^+}$	T_N, T_C (°K)	Mag. order at low T	Noncooperative transition T_1, T_2(°K)	$\Delta\rho(\Omega\,\mathrm{cm})$	$\Delta\chi/\chi_{T_t^+}$	Refs.
Rocksalt	CrN	3	2(2)	Metal ?	~273	0	~0.6	273	4th kind $\mu^{Cr}=2.36\mu_B$	...	...	...	e
Rocksalt	VO	3	3?	Metal $10^{-1.9}$	114(c) 126(h)	$\sim10^{6}$	?	...?	?	...	...	...	f
Ordered rocksalt[b]	$LiVO_2$	2	2?	?	~450	?	~0.75	...?	?	...	...	...	g
Corundum	αFe_2O_3	5	–	Ins $\sim10^{14}$	...	...	...	948	+ − − + on c axis	~175–253	?	μ axis changes	h,i j,k
Corundum	Cr_2O_3	3	–	Ins ?	...	...	...	306	+ − + − on c axis	~220–306	?	d	l,m
Corundum	V_2O_3	2	1(1) 1(1)?	Metal $10^{-1.7}$	153(c) 165(h)	$>10^{3}$	~0.4	...	No Mag. scatter	380–530	Max. ρ ~525°K	Const. χ $T_1<T<T_2$	f,n
Corundum	Ti_2O_3	1	1(1)	Metal $10^{-1.3}$	...	...	...	...	$\mu^{T_t}<0.5\mu_B$	~300–500	$\sim10^{2}$	~0.5	f,o,p
Rutile	VO_2	1	1(1)	Metal $\sim10^{-2.4}$	~330(c) ~340(h)	$\sim10^{4}$	~0.9	...	?	...	...	...	f
Rutile	CrO_2	2	...	Metal[c] 10^{-2}	...	...	...	394	Ferro. $\mu^{Cr}=2.07\mu_B$	...	...	...	q,r
Rutile	MnO_2	3	...	?[c]	...	...	...	~72	Spiral	...	...	...	s,t
Rutile	MnF_2	5	...	Ins $\sim10^{20}$ (1kc)	...	...	...	~84	Cat subl antiferro	...	...	...	s,u,v

[a] Legend: $n_{t_{2g}}$ = number of cation t_{2g} electrons; $n_b(m)$ = number of bonding t_{2g} electrons in low-temperature phase and the multiplicity m of bonds in which each bonding electron participates; T_t^+ = temperature just above transition temperature T_t; $T_1 \leqslant T \leqslant T_2$ is temperature interval over which second-order transition takes place; T_N, T_C are Néel and Curie temperatures; $\chi_{T_t^+}$ is magnetic susceptibility just above T_t.

[b] Hexagonal or rhombohedral symmetry.

[c] Stoichiometry questionable. Max. ρ at T_C or T_N.

[d] Anomalous antiferromangetic-resonance effects in temperature interval of ~100°C below T_N.

[e] L. M. Corliss, N. Eliott, and J. M. Hastings, Brookhaven Natl. Lab. Rept. BNL4294 (1959).

[f] F. J. Morin, Phys. Rev. Letters **3**, 34 (1959).

[g] P. F. Bongers, Thesis, Univ. Leiden, July 4, 1957.

[h] F. J. Morin, Phys. Rev. **83**, 100 (1951).

[i] R. Chevallier, J. phys. radium **12**, 172 (1951).

[j] C. G. Shull, W. A. Strauser, and E. O. Wollan, Phys. Rev. **83**, 333 (1951).

[k] H. M. A. Urquart and J. E. Goldman, Phys. Rev. **101**, 1443 (1956).

[l] J. Jaffray and J. Viloteau, Compt. rend. **226**, 1701 (1948).

[m] B. N. Brockhouse, J. Chem. Phys. **21**, 961 (1953).

[n] A. Paoletti and S. J. Pickart (unpublished research).

[o] A. D. Pearson, J. Phys. Chem. Solids **5**, 316 (1958).

[p] G. Shirane, S. J. Pickart and R. Newnham (private communication).

[q] C. Guillaud, A. Michel, J. Bernard, and M. Fallot, Compt. rend. **219**, 58 (1944).

[r] G. H. Jonker (private communication).

[s] H. Bizette, J. Phys. radium **12**, 161 (1951).

[t] A. Yoshimori, J. Phys. Soc. Japan **14**, 807 (1959).

[u] W. Westphal (private communication).

[v] R. A. Erickson, Phys. Rev. **90**, 779 (1953).

magnetic properties of low-temperature CrO_2 are not characteristic of cation- -cation interactions. Removal of cation- -cation interaction by t_{2g} electron ordering (Cr^{4+} has $t_{2g}^2 e_g^0$) would also induce ferromagnetic cation-anion-cation interactions since the anion orbitals then overlap half-filled cation orbitals on one side of anion, empty cation orbitals on the other.[2]

In closing, it should be noted that the anomalous magnetic properties of the chromite spinels and the different magnetic order[9] of $MnTiO_3$ from that of $FeTiO_3$ and $NiTiO_3$ can be attributed to the influence of weak cation- -cation interactions.

[9] G. Shirane, S. J. Pickart, R. Nathans, and Y. Ishikawa, J. Phys. Chem. Solids **10**, 35 (1959); and (to be published).

Theory of the Low Lying States of Some Rare Earth Compounds

G. T. TRAMMELL
Oak Ridge National Laboratory, Oak Ridge, Tennessee

The "electrostatic" crystalline torques acting on the magnetic ions in the rare earth nitrides are likely larger than those due to exchange. Some of the consequences of this are discussed.

IN the rare earth compounds, the splitting of the rare earth levels in the crystalline field may be comparable to, or larger than, the exchange energy. Thus, in the rare earth nitrides studied by Wilkinson, Wollan, Cable, and Child,[1] the field has cubic symmetry and may be estimated to give overall splittings of some hundreds of wave numbers, whereas the observed Curie points indicate exchange energies corresponding to some tens of wave numbers. The interplay of the electrostatic crystalline forces with the exchange forces leads to interesting results. Generally, the ordered magnetic moment in the ground state is less than the full value, and superimposed on the static, long range order is a dynamic, short range, spin correlation. The short range correlation is presumably responsible for the "humps" in the neutron diffraction patterns in the vicinity of the coherent Bragg peaks, and analysis of them leads to the tentative conclusion that the exchange force in these substances extends over many neighbors. The time average magnetic moment induced by a given exchange field usually depends markedly on the direction of the field relative to the crystal axes; this should lead to sharp domain boundaries.

If we assume the exchange integral is the same in holmium and terbium, and if we assume that the crystalline potential energy of an electron in the 4*f* shell of either atom is the same,[2] then we may adjust the ratios of the exchange integral and the sixth order potential to the fourth order potential to yield the observed ordered moments (7 μ_B for both).[1] This gives a sixth to fourth order potential ratio fifty times larger than the naive value obtained by assuming an electrostatic field due to neighboring, spherically symmetric, nitrogen ions, and the radial distribution of the 4*f* electrons that of a hydrogen atom with $Z^*=23(\langle r^4\rangle=.67a_0^4,\langle r^6\rangle=.92a_0^6)$. This could be due to "streamers" in the electron distribution between the rare earths and the nitrogens or to a small admixture of "itinerant" character to the 4*f* electrons.[3] This gives a sixth order splitting of about the same size as the fourth order splitting in holmium, but the sixth order potential is still relatively small in terbium.

We assume

$$H=\sum_i V_{ci}-\tfrac{1}{2}\sum_{i,j}\mathcal{J}_{ij}^*\mathbf{S}_i\cdot\mathbf{S}_j, \tag{1}$$

$$=\sum_i V_{ci}-\tfrac{1}{2}\sum_{i,j}\mathcal{J}_{ij}\mathbf{J}_i\cdot\mathbf{J}_j, \tag{2}$$

where in (1) the first sum represents the crystalline field energy, and the second the exchange energy of the rare earth ions. We assume that the effective exchange integral $\mathcal{J}_{ij}^*$ is isotropic and the same for all rare earth ions. For (2) we have assumed that J^2 is a good quantum number. We rewrite (2)

$$H=\sum_i(V_{ci}-\sum_j\mathcal{J}_{ij}\langle J_z\rangle J_{zi})$$
$$-\tfrac{1}{2}\sum_{i,j}[(J_{zi}-\langle J_z\rangle)(J_{zj}-\langle J_z\rangle)$$
$$+J_{zi}J_{zj}+J_{yi}J_{yj}]\mathcal{J}_{ij}, \tag{3}$$

where $(V_c-\sum_z\mathcal{J}_{ij}\langle J_z\rangle J_z)w_m=e_mw_m$ with $\langle J_z\rangle=(w_0,J_zw_0)$ and the z direction and w_0 are chosen to minimize e_0. The self consistent field solution, $\pi_i w_{0,i}$, is then the best product wave function approximation to the ground state.

The second sum in (3) gives configuration mixing, which yields a separation dependent contribution to $\langle\mathbf{J}_i\cdot\mathbf{J}_j\rangle$ in the ground state. We use the Bogoliubov[4] approximation scheme to take account of the configuration interaction.

By using the w_n's as bases the operators $\mathbf{J}$ are written out explicitly,

$$J_\mu(i)=\langle n|J_\mu|m\rangle\bar{a}_n{}^i a_m{}^i, \tag{4}$$

where μ is x, y, or z, i indicates a particular rare earth ion, and $\bar{a}_n{}^i$ and $a_m{}^i$ are creation and destruction operators for the states n and m of the ith atom. The substitutions (4) are made in (3) and the terms not quadratic in the a_0, $\bar{a}_0$'s are dropped. After replacing $\bar{a}_0{}^i a_0{}^i$ by $1-\bar{a}_1{}^i a_1{}^i-\cdots$, a_0 and $\bar{a}_0$ are replaced by 1, and the $\bar{a}_n$, a_n's are treated as Bose operators.[4] For the case V_c negligible, the resulting approximation to (3) is identical to the usual spin-wave approximation. With these replacements, H becomes quadratic in the field amplitudes and may be diagonalized in the usual manner by introducing normal mode coordinates.

There will generally be several w_n's such that

[1] Wilkinson *et al.*, preceding paper. The 7 μ_B ordered moment assignments are based on the assumption that the short range correlation, which causes the humps in the diffraction patterns, is due to the dynamic spin correlations. If the correlation is due to an alternation of the static moment direction, then the estimate of the strength of the sixth order potential which we make would not be valid.

[2] C. A. Hutchison, Jr. and E. Wong, J. Chem. Phys. **29**, 754 (1958).

[3] B. R. Judd, Proc. Roy. Soc. (London) **A251**, 134 (1959).

[4] N. N. Bogoliubov and S. V. Tiablikov, Izvest. Akad. Nauk S.S.S.R. Ser. Fiz. Vol. 21, No. 6 (June, 1957).

$(w_n, J_\mu, w_0) \neq 0$, therefore several independent cooperative modes of oscillation, however those modes for which,

$$|(w_n, J_\mu w_0)| \ll \sum_j \mathcal{J}_{ij} \ll e_n - e_0 \tag{5}$$

will have frequencies independent of wave number, and hence, just represent independent oscillations under the electrostatic torques.

In order to obtain the w_m's and e_m's (Eq. 3′) the levels in the crystalline field alone are first determined. On following Elliot and Stevens,[5] the effect of the crystalline potential on the rare earth ion can be represented by

$$V_c = A_4\langle r^4\rangle S_4(\mathbf{J}) + A_6\langle r^6\rangle S_6(\mathbf{J}), \tag{6}$$

if we assume J remains a good quantum number. S_4 and S_6 are polynomials[5] of the fourth and sixth order, respectively, in the components of J, which are invariant under the cubic group. The labor of obtaining the eigenvalues and eigenfunctions of (6) is lightened considerably if one takes advantage of the symmetry of the problem and uses $2J+1$ bases of irreducible representation of the cubic group, rather than eigenfunctions of J_z. This can be done immediately in terms of the even eigenfunctions of J_x, J_y, J_z (for integral J's). The eigenfunctions and eigenvalues for *Tb*, *Tu*, and *Ho* in a general cubic potential have been evaluated in this manner.

We have not yet made an absolute determination of the coefficients in (6). For the following discussion, only the ratio of $A_6\langle r^6\rangle$ and the exchange integral to $A_4\langle r^4\rangle$ enter. For definiteness, we take $A_4\langle r^4\rangle$ the naive value mentioned above. The three lowest levels of *Tb* are then $\Gamma_1, -83\ \text{cm}^{-1}$; $\Gamma_4, -63\ \text{cm}^{-1}$; $\Gamma_5, -40\ \text{cm}^{-1}$. The levels of *Tb* are very insensitive to $A_6\langle r^6\rangle$ changing by only one or two cm^{-1} in going from $A_c\langle r_6\rangle = 0.63\ \text{cm}^{-1}$ (naive value) to 30 cm^{-1} (value indicated by experiment). $\Gamma_1+\Gamma_4$ has an isotropic susceptibility (arbitrary field magnitude); further, for terbium the maximum $\langle \mathbf{J}\cdot\boldsymbol{\tau}\rangle$ is $(14)^{\frac{1}{2}} = 3.74$, whereas the observed ordered moment corresponds to $\langle \mathbf{J}\cdot\boldsymbol{\tau}\rangle = 4.5$, therefore the exchange integral must be large enough to cause a considerable admixture of Γ_5. The smallest $\sum_j \mathcal{J}_{ij}$* to obtain $\langle \mathbf{J}\cdot\boldsymbol{\tau}\rangle = 4.5$ is obtained for $\boldsymbol{\tau}$ in the body diagonal direction and is $\sum_j \mathcal{J}_{ij}^* = 5.6\ \text{cm}^{-1}$ (relative to the naive value $A_4\langle r^4\rangle = 1850$). That *Tb* should have its moment along the body diagonal was expected since in (6), $V_{c4} \sim +(J_x^4 + J_y^4 + J_z^4)$, in *Ho* on the other hand $V_{c4} \sim -(J_x^4 + J_y^4 + J_z^4)$ and its moment would be expected along the cube edge.

If we take for $A_6\langle r^6\rangle$, the naive value in the case of holmium, the three lowest levels are $\Gamma_1 = -70\ \text{cm}^{-1}$, $\Gamma_3 = -63\ \text{cm}^{-1}$, $\Gamma_4 = -65\ \text{cm}^{-1}$. These six states are 8_z, 8_{-z}, $8_y \cdots$, where 8_z is the state having eigenvalue $8 (= J$ for holmium) for J_z. The above exchange integral would give the full eight units of angular momentum along a cube edge, whereas only 5.5 units are observed. It is necessary to increase the ratio of $(A_6\langle r^6\rangle / A_4\langle r^4\rangle)$ by a factor of 50 over the naive value to achieve the smaller moment. This changes the above energy value to the following, $\Gamma_1 = -36\ \text{cm}^{-1}$, $\Gamma_3 = -234\ \text{cm}^{-1}$, $\Gamma_4 = -217\ \text{cm}^{-1}$.

These parameters when applied to thulium predict that the ground state will not order at all. This is consistent with the experimental result of no ordering at 1.3°K.

The calculations on the short range correlation are not completed.

ACKNOWLEDGMENTS

I am indebted to Dr. M. K. Wilkinson and Dr. E. O. Wollan for many useful discussions.

[5] B. Bleaney and K. W. H. Stevens, Repts. Progr. in Phys. **16**, 108 (1953).

Classical Theory of Spin Configurations in the Cubic Spinel*

T. A. KAPLAN†
Lincoln Laboratory, Massachusetts Institute of Technology, Lexington 73, Massachusetts

It recently has been pointed out that the Yafet-Kittel triangular spin configurations do not minimize the classical Heisenberg exchange energy in the cubic spinel. A perturbation calculation for determining the ground configuration is described in the present paper. We consider only nearest neighbor A-B and B-B interactions (J_{AB} and J_{BB}), one spin magnitude S_A for the A sites, and one S_B for the B sites. The method consists of first determining the largest value, y_0, of $y=J_{BB}S_B/J_{AB}S_A$, for which the Néel configuration is stable with respect to sufficiently small spin deviations. One then looks for solutions of the extremum equations as power series in $y-y_0(\geq 0)$, such that the spin deviations from the Néel configuration are small when $y-y_0$ is small. The detailed calculations lead to the following conclusions: 1. Equilibrium configurations exist which have, simultaneously, nonzero angles between spins on the A sites and between those on the B sites. 2. The ground state in the cubic spinel will probably be a long-range-ordered canted-spin arrangement, for at least some finite range of $y-y_0$. The significance of these conclusions in connection with experiments on $MnCr_2O_4$ and Mn_3O_4, and with Anderson's remarks concerning spin configurations in spinels, is discussed.

CLASSICAL THEORY OF SPIN CONFIGURATIONS IN THE CUBIC SPINEL

IT has recently been pointed out[1] that the Yafet-Kittel[2] triangular spin configurations do not minimize the classical Heisenberg exchange energy, E, in the cubic spinel. In other words, knowledge as to the type of spin configuration to be expected when the B-B and A-B interactions are comparable is nonexistent. In this paper, we describe a method for determining the ground state, its application being discussed in sufficient detail to allow some general conclusions of physical interest to be drawn.

The problem is to determine the set of vectors, $\mathbf{S}_i^A$, $\mathbf{S}_j^B$, associated with each point of the tetrahedral and octahedral sublattices, respectively, that minimizes

$$E=2J_{AB}S_AS_B\{\sum_{\langle i,j\rangle}\boldsymbol{\sigma}_i^A\cdot\boldsymbol{\sigma}_j^B+y\sum_{\langle i,j\rangle}\boldsymbol{\sigma}_i^B\cdot\boldsymbol{\sigma}_j^B\}, \quad (1)$$

where

$$\boldsymbol{\sigma}_i^\Gamma=\mathbf{S}_i^\Gamma/S_\Gamma,\ \Gamma=A,B, \quad (2)$$

$$y=J_{BB}S_B/J_{AB}S_A\geq 0, \quad (3)$$

J_{AB} and J_{BB} are positive (for antiferromagnetic interactions), $S_\Gamma=|\mathbf{S}_j^\Gamma|$, and $\sum\langle i,j\rangle$ indicates a sum over nearest neighbor (n.n.) A-B or B-B pairs. We neglect A-A interactions both for simplicity and because they are expected to be small.

When $y=0$, it is easy to see from the lattice properties that the Néel configuration C_0 (given when the z components, $\sigma_i^{Az}=1$, $\sigma_i^{Bz}=-1$) allows each term in E (i.e., for each n.n. A-B pair) to have its minimum value. For any nonzero value of y, no such rigor is possible. (The only fairly general method[3] for rigorously determining the ground state breaks down here, since there are spins on nonequivalent lattice sites.) However, as y increases from zero, C_0 will remain locally stable until y reaches a critical value, y_0, C_0 becoming unstable when y exceeds y_0. By "locally stable" we mean the following. By using

$$\sigma_i^{\Gamma z}=\pm[1-(\sigma_i^{\Gamma x})^2-(\sigma_i^{\Gamma y})^2]^{\frac{1}{2}}$$
$$=\pm\{1-(\tfrac{1}{2})[(\sigma_i^{\Gamma x})^2+(\sigma_i^{\Gamma y})^2]-\cdots\}, \quad (4)$$

(+ when $\Gamma=A$, − when $\Gamma=B$), valid for small deviations, $\sigma_i^{\Gamma u}$, $u=x,y$, from C_0, we obtain an expansion for the energy,

$$E=E_0+E_2+E_4+\cdots, \quad (5)$$

where E_n is of nth order in the deviations. C_0 is locally stable if the quadratic form, E_2, is positive definite. It seems reasonable to assume that when C_0 is locally stable it is the minimum energy state, and that when $y-y_0\equiv\eta$ is small and positive the ground state will deviate only slightly from C_0. The latter assumption is implemented by looking for solutions of the extremum equations,

$$\partial E/\partial\sigma_i^{\Gamma u}=0, \quad (6)$$

in the form

$$\sigma_i^{\Gamma u}=\eta^\alpha\sum_{n=0}^{\infty}C_{i\Gamma u}^{(n)}\eta^n,\ \eta\geq 0,\ \alpha>0,\ (u=x,y). \quad (7)$$

(The restriction $\alpha>0$ gives $\sigma_i^{\Gamma u}\to 0$ as $\eta\to 0$.) If the assumptions are correct, then the lowest energy solution (7) will give the ground state.

Detailed calculation gives the results $y_0=\frac{3}{4}$ (which may be compared to the corresponding critical value of $\frac{3}{4}$ found previously[2]) and $\alpha=\frac{1}{2}$ (which may be understood on the basis of a simple analogue of our problem, $E=-\eta\sigma^2+e\sigma^4$, $e>0$).

It is convenient to describe the spin configuration in terms of the normal modes of the system defined by the quadratic form E_2 (the normal modes diagonalize E_2 by a unitary transformation). The solutions of (6), in lowest order, are linear combinations of the normal

* The work reported in this paper was performed by Lincoln Laboratory, a center for research operated by Massachusetts Institute of Technology with the joint support of the U. S. Army, Navy, and Air Force.

† Staff Member, Lincoln Laboratory, Massachusetts Institute of Technology, Lexington 73, Massachusetts.

[1] T. A. Kaplan, to appear in Physical Review.

[2] Y. Yafet and C. Kittel, Phys. Rev. 87, 290 (1952).

[3] J. M. Luttinger and L. Tisza, Phys. Rev. 70, 954 (1946); J. M. Luttinger, Phys. Rev. 81, 1015 (1952).

modes, defined at $\eta=0$, with minimum E_2 (i.e., those modes corresponding to a zero eigenvalue of the matrix of E_2). In one of these modes, the spins are all parallel to one plane and the spin deviations on any one of the face-centered-cubic lattices containing spins vary sinusoidally with lattice position. The wave vector, $\mathbf{k}_0$, characterizing this sine wave is in the [110] direction, with magnitude, k_0, given by

$$\cos^2(k_0 a/4\sqrt{2})=\tfrac{3}{8},$$

where a is the lattice constant. This gives a wavelength $\lambda_0=(0.861)\ (a\sqrt{2})$ ($=0.861\times$twice the primitive translation in [110]). The relative amplitudes for the sine waves on the different fcc lattices are definite, and such that there are nonzero angles between A spins and between B spins. This mode is degenerate only with the corresponding modes of the same wavelength, with $\mathbf{k}$ in $[1\bar{1}0]$, etc.[4]

In particular, any one of these modes gives a solution of (6) to lowest order in η, the absolute amplitudes being determined uniquely (by E_2 and E_4). Thus, we definitely have an equilibrium configuration (for small enough η) with angles occurring simultaneously between A spins and between B spins (in contrast with the contrary conclusion[2,5] drawn rigorously from the Yafet-Kittel assumptions). Further, any linear combination of the modes described above will exhibit long-range-order. Since we have only a very small degeneracy, these results suggest that the exchange energy will cause long range ordering. This is to be contrasted with Anderson's[6] remarks: He showed that there is an enormous number of ways of placing a given number of +'s and −'s on the octahedral lattice, all with the same short range order. By identifying the +'s and −'s with the projections on the x-y plane of the canted spins (in the Yafet-Kittel picture), he was led to suggest that there would be no long-range-ordering of these components. This, of course, assumed that the Yafet-Kittel configuration gave the minimum energy whereas our results show the inadequacy of this assumption in general.[7]

Our general conclusions are in agreement with the neutron diffraction results of Corliss and Hastings[8] on the cubic spinel $MnCr_2O_4$, which indicate that there are long-range-ordered "angles," with angles simultaneously on the A and on the B sites. However, the results of our calculations, which were made only in the lowest order of approximation, do not agree in detail. This points up the need for carrying the present calculations to higher orders, and, more important, to show that our assumptions are (or are not) correct.

Our results appear to have interesting possibilities in connection with recent experiments on hausmannite (Mn_3O_4). Kaspar[9] and Jacobs[10] apparently have shown that there must be canted spins in this material. The former has shown that there is a doubling of the magnetic unit cell in the [110] direction, and has proposed a particular model to explain his diffraction intensities. However, Menyuk and Dwight[11] have pointed out that there is no energy difference between Kaspar's model (which has angles only on the B lattice) and another one, obtained simply from this, which does not double the unit cell. Our result, that the important mode approximately doubles the cell in [110], is therefore quite suggestive in this connection. We plan to investigate the effect of the tetragonal distortion which characterizes Mn_3O_4.

A paper giving a more detailed account of the present considerations is in preparation.

---

[4] With the exception of the uniform rotation ($k=0$) mode.
[5] F. K. Lotgering, Philips Research Rept. **11**, 190 (1956).
[6] P. W. Anderson, Phys. Rev. **102**, 1008 (1956).
[7] An exception occurs for $J_{AB}=0$, our results (to be published) being consistent with Anderson's in this case.
[8] L. Corliss and J. Hastings (unpublished).
[9] J. S. Kaspar, Bull. Am. Phys. Soc. **II**, 4, 178 (1959).
[10] I. S. Jacobs, Bull. Am. Phys. Soc. **II**, 4, 178 (1959).
[11] N. Menyuk and K. Dwight (private communication). These authors have also shown that the Yafet-Kittel theory cannot be applied consistently to their experimental results on Mn_3O_4 (to be published); this is, of course, significant in connection with the theoretical instability[1] of the Yafet-Kittel ground state.

Magneto Structural Studies on Gadolinium-Iron Alloys

R. C. Vickery, W. C. Sexton, V. Novy, and E. V. Kleber
Research Chemicals Division, Nuclear Corporation of America, Burbank, California

Magnetic and constitutional data have been established for a series of alloys in the gadolinium-iron system, ranging from 2–98% Fe. Seven intermetallic compounds have been found and some correlation has been derived between their crystal structures and magnetic properties. The cubic Gd_2Fe_3 compound has been found to exhibit highest magnetization values of the intermetallics and comparison of data on the Gd-Co and Gd-Ni compounds suggests that presence of the 2:3 structure (not found in the Gd-Ni system) is necessary for the development of ferromagnetism in these systems.

THE increasing availability of pure rare earth metals has stimulated studies of their magnetic properties and already an appreciable amount of information is available. Much less information is, however, available on the magnetic properties of alloys based upon the rare earths. Such data can be of much interest, not only to workers in the rare earths field, but to a wider group because it would seem to provide a definitive contribution to our understanding of the development of ferro or antiferromagnetism in systems possessing unfilled orbitals of such an inaccessible level that their configurations are found to be only mildly perturbed by the most stringent of crystal field forces.

Nesbitt, Wernick, and Corenzwit[1] recently presented the results of studies on the magnetic moments of compositions in the Gd-Co and Gd-Fe systems. The data obtained were rationalized on the basis of antiferromagnetic exchange coupling. In work carried out for the Bureau of Ships, both structural and magnetic findings for these systems have been extended and compared with similar data on the Gd-Ni system. In this report however, we shall refer to systems containing nickel and cobalt only for the purpose of final correlation.

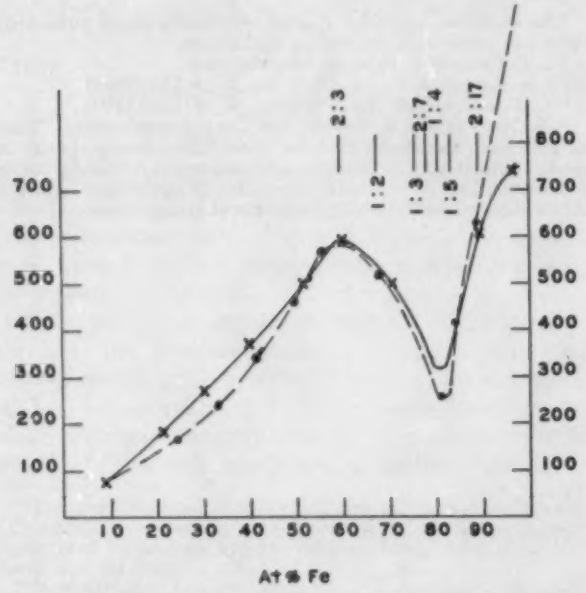

FIG. 1. Gadolinium-iron system. Saturation magnetization per unit volume (K_0) at 0°K vs composition ○ - - - - ○. Curie temperature vs composition × - - - - ×.

[1] E. A. Nesbitt, J. H. Wernick, and E. Corenzwit, J. Appl. Phys. 30, 365 (1959).

In the Gd-Fe system, seven intermetallic compounds have been established having Gd:Fe ratios of 2:3, 1:2, 1:3, 2:7, 1:4, 1:5, and 2:17. These have been observed and confirmed by X-ray, density, differential thermal analysis and metallographic techniques. Crystal structures and lattice parameters of these compounds are shown in Table I.

TABLE I. Intermetallic compounds in the Gd-Fe system.

Compound	Composition % Fe	Structure	Lattice parameters
Gd_2Fe_3	34.9	Cubic	a:8.25
$GdFe_2$	41.7	Cubic	a:7.53
$GdFe_3$	51.8	Rhomb	a:4.72 α=39°42′
Gd_2Fe_7	55.6	ortho	a:5.71 b:6.78 c:7.15
$GdFe_4$	58.7	hex	a:5.15 c:6.64
$GdFe_5$	64.1	hex	a:4.92 c:4.11
Gd_2Fe_{17}	75.3	hex	a:8.39 c:8.53

Figure 1 illustrates the variation of magnetization and Curie point with composition and some comparison of structure can also be made. The normal cubic iron structure changes to hexagonal near to the 2:17 compound and, with a small decrease of cell parameters, hexagonal structures persist to the 1:4 intermetallic. At the 1:3 composition a tetragonal structure exists and the unit cell, though increasing in volume, has a higher molecular density. It would seem that this increase in the packing of these molecules is associated with a minimum in magnetization. With increasing gadolinium contents the cell expands, and changes to a large cell cubic structure with a much lower molecular density.

There would appear to be some correlation between Curie temperature and magnetization value curves; the "peaking" of both at the 2:3 composition suggests that the increase in magnetization at this point is attributable to an increase in interaction energy rather than alignment of moments.

Good agreement is found between magnetization values now presented and those reported earlier by Nesbitt *et al.*—although these workers did not extend studies into the high gadolinium area.

Two points remain for this brief discussion. If it is assumed that gadolinium and iron electron moments are always aligned antiparallel, complete cancellation of spins should be effected at a 2:7 composition. At this point, however, an observed magneton number of approximately 0.65 is found. Several explanations could be presented for this behavior but all require further experimentation, possibly by neutron diffraction, before any finality can be suggested.

When considering interatomic distances in the two important lattices—Gd_2Fe_3 and $GdFe_4$, we have found in the former that the internuclear distance between nearest neighbor atoms is of the order 2.8 A and the diameter of the unfilled (4f) orbital, 0.912 A; i.e. a radius ratio of 3.08 is obtained. In the $GdFe_4$ compound, however, internuclear distance appears somewhat shorter—of the order 2.35 A—and this closer approximation of atoms would seem to destroy any spin exchange coupling and force the spins to align antiparallel or at least cant away from any parallelity induced in the 2:3 compound. The enhancement of magnetization values at the 2:3 compound might, however, be attributable not to a Gd-Gd exchange but to Fe-Fe coupling. Again, further work is required to establish this point.

Similar behavior may be considered to occur in the Gd-Co system which presents a maximum at the 2:3 compound and a minimum at the hexagonal 1:5 compound (Fig. 2). Here again absolute cancellation of spins does not seem to occur. A point of note in this system is that magnetization values increase anomalously with increase in temperature.

The Gd-Ni system does not appear to have been examined hitherto and is found to present quite different characteristics from systems of gadolinium with iron and cobalt. The addition of gadolinium to nickel decreases magnetization values linearly to the 1:5 compound. Magnetization values then remain low and no maximum develops equivalent to that in systems containing cobalt or iron. The absence of such a maximum seems associated with the absence of a 2:3 compound in the Gd-Ni system.

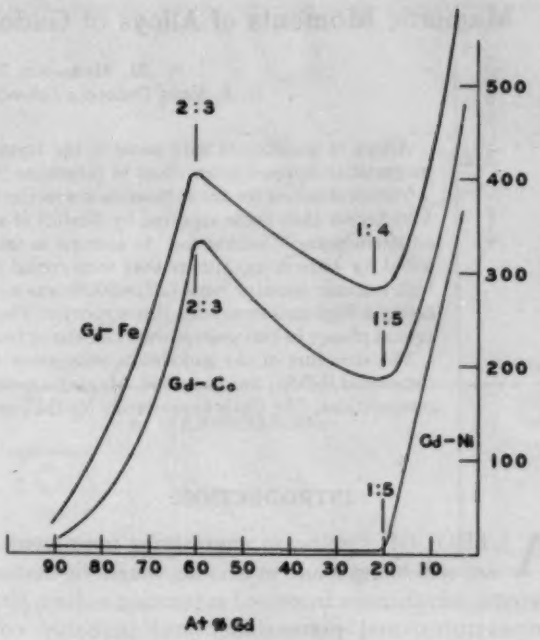

FIG. 2. Gd-Fe, Gd-Co, Gd-Ni systems. Magnetization per unit volume (K) at 300°K vs composition

ACKNOWLEDGMENTS

This work has been performed under sponsorship of the Bureau of Ships and was administered by G. W. Sorkin of the Materials Development Section. The advice and assistance of Lieutenant Commander F. W. Anders and Earl L. Palmer of the Bureau of Ships is also acknowledged.

Magnetic Moments of Alloys of Gadolinium with Some of the Transition Elements

W. M. Hubbard, E. Adams, and J. V. Gilfrich
U. S. Naval Ordnance Laboratory, White Oak, Silver Spring, Maryland

Alloys of gadolinium with some of the transition elements were prepared and examined by x-ray and magnetic techniques in an effort to determine their structure, Curie temperatures and magnetic moments.

Values obtained for the saturation magnetization for some compositions in the gadolinium-cobalt system were higher than those reported by Nesbitt et al., but the data agree qualitatively with their theory of an antiferromagnetic interaction. An increase in saturation magnetization at room temperature and below was noted for some compositions that were cooled from their Curie points in a magnetic field. An extremely high intrinsic coercive force ($_IH_c$=8000) was measured on the powdered hexagonal compound $GdCo_8$ indicating a high anisotropy for this structure. The lattice parameters for a face centered cubic and two hexagonal phases in this system were calculated from the x-ray data.

The structure of the gadolinium-manganese system was found to be extremely complex, and only the compound $GdMn_2$ was identified. Magnetic moment *vs* temperature values were also determined for various compositions. The Curie temperature for the composition $Gd_{0.2}Mn_{0.8}$ was found to be approximately 250°C.

INTRODUCTION

ALTHOUGH significant engineering improvements are still being made in existing magnetic material systems, advances in increased saturation values, Curie temperatures, and permeability will probably come from efforts on new material systems.

One approach to the development of new material systems has been to use the now available rare earths, since their measured uncompensated spin values are close to the theoretical limit. This agreement with theory is presumably due to the fact that the important electronic level in these materials is the 4*f* level, and it is well shielded from the levels that enter the bonding process. If the rare earths can be alloyed with one of the transition elements to lower the atomic weight of the alloy and at the same time increase the effective moment of the transition element, then a high saturation material should be forthcoming; provided a radical decrease in density does not accompany the other changes. The magnetic moments of gadolinium alloyed with chromium, manganese, and cobalt were therefore measured along with other properties for a few chosen compositions.

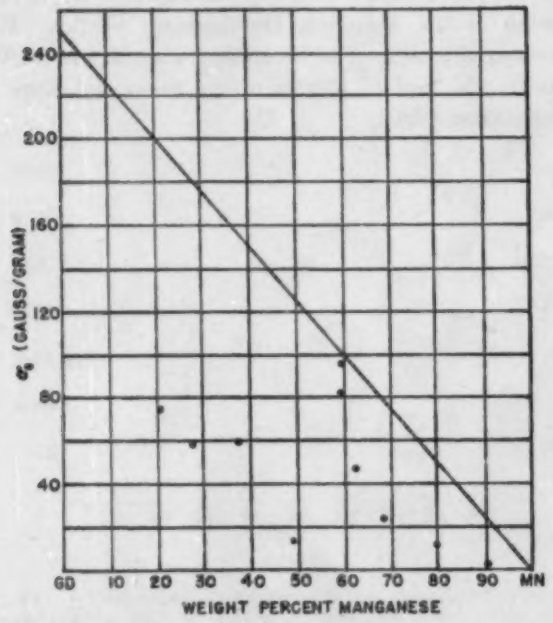

FIG. 1. Saturation magnetization for various compositions of gadolinium manganese alloys (solid curve—values to be expected from dilution effect).

GADOLINIUM-CHROMIUM SYSTEM

The samples for this system, covering the entire composition range from 0 to 100 weight % chromium in 10% increments were prepared by arc melting 99.92% chromium and 99+% gadolinium metal.

No alloying was detected in this system. The saturation moments per gram were linear functions of the composition, the Curie temperatures of all the melts were approximately 300°K, and no changes in the lattice parameter of chromium were observed.

GADOLINIUM-MANGANESE SYSTEM

The samples for this system were prepared by melting 99.95% electrolytic manganese and 99+% gadolinium metal under one and one-half atmosphere pressure of helium. The melts were slow cooled and during cooling, time-temperature curves were run in an effort to establish the phase diagram. Because of insufficient sensitivity of the apparatus it was not possible to define the phase diagram, but a strong thermal arrest at 1070°C was observed for all compositions from 30 to 90 weight % manganese, and indications of an order-disorder region were observed between 20 and 50% Mn at temperatures below 900°C.

The number of lines in the x-ray pattern for each melt was quite large and, except for the composition corresponding to the compound $GdMn_2$, could not be indexed as a single compound. The lattice parameter measured for the $GdMn_2$ was a=7.74 A, in good agreement with the data of Endter and Klemm.[1]

[1] F. Endter and W. Klemm, Z. anorg. Chem. **252**, 377 (1943–4).

The magnetic moment measurements on $GdMn_2$ gave 0.95 Bohr magnetons per atom at 0°K with a Curie point of approximately 300°K. Magnetic moment measurements on a sample containing 62.3 weight % manganese showed the presence of two phases; one having a Curie point of approximately 150°K, the other having a Curie temperature of approximately 500°K. Values for the moment per gram for various compositions are presented in Fig. 1.

GADOLINIUM-COBALT SYSTEM

The samples for this system were prepared by arc melting 99.0% Co and 99+% Gd metal in helium. The samples were rapidly cooled and received no heat treatment prior to pulverization.

X-ray examination indicated the presence of the compound $GdCo_2$ having a face centered cubic structure with $a=7.27$ A; $GdCo_5$ having a hexagonal structure with $a=4.98$ A, $c=4.00$ A; another hexagonal structure having $a=4.84$ A, $c=4.07$ A consisting of a saturated solid solution of cobalt in $GdCo_5$; and at least two other phases that have not been isolated as yet.

The magnetic moment measurements gave approximately the same results as those previously reported by Nesbitt[2] ($\sigma_{30°}=16$ gauss/gm), except in the region 60 to 70 weight % Co. In this region, the values obtained were slightly higher ($\sigma_{30°}=32$ gauss/gm), increased more rapidly, and exhibited what was first thought to be a magnetic annealing effect. This unexpected effect is now believed to be due to the sample reacting at temperatures above approximately 500°C, with residual nitrogen from the helium atmosphere or leaks in the apparatus to give free cobalt and gadolinium nitride. The gadolinium nitride was volatile at the higher temperatures and therefore the magnetic moment on return to room temperature reflected a mixture of Co and $GdCo_5$, the relative proportions varying with particle size of sample and time exposed.

The disagreement in values for the magnetic moment in the 60 to 70% Co region may be due to differences in level of saturation. It was observed that loose powders free to orient in the measuring field gave consistently higher results than immobilized unoriented powders. The latter samples would approximate the conditions in the cast samples used by Nesbitt. It was also noted that the magnetization curves for cast samples in this composition range behaved as if the samples were beginning to saturate in fields as low as 2000 gauss. However, if the fields were increased further the magnetization curve again turned upward at approximately 24 000 oe and was still rising at the highest fields available in this laboratory. For the composition $GdCo_5$ the (B-H) value was 5500 gauss at $H=28\,000$ oe. Preliminary experiments by Dr. Warren E. Henry[3] using the high field facility at the Naval Research Laboratory indicate that fields in excess of 30 000 oe are required to achieve saturation.

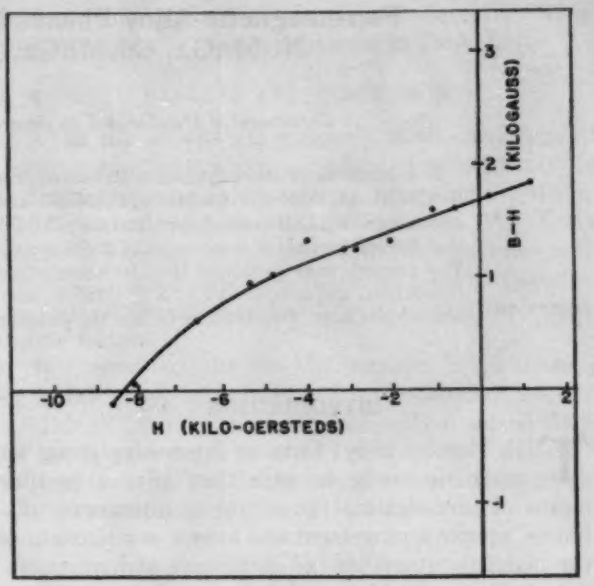

FIG. 2. Demagnetization curve for −100 mesh +200 mesh $GdCo_5$ powder suspended in wax.

The compositions between approximately 60 and 70 weight % Co also exhibited large intrinsic coercive forces. These coercive forces are presumably due to a large magnetocrystalline anisotropy in the hexagonal phase, but no simple explanation has yet been found to explain the magnitude of this effect in the as-cast samples ($_IH_c=800$ oe). Studies of the variation of the intrinsic coercive force with particle size of the pulverized material have been inconclusive as yet, possibly because of the reactive nature of the small particles, but values of $_IH_c=8000$ oe have been consistently obtained, as shown in Fig. 2. Meaningful values of $(BH)_{max}$ have not been obtained because of the lack of a field large enough to saturate the sample during test.

X-ray examination of a powdered $GdCo_5$ sample that had been magnetically aligned indicated that the easy direction of magnetization is parallel to the hexagonal axis.

ACKNOWLEDGMENTS

The authors wish to acknowledge the continuing interest of Dr. T. R. McGuire and Emil P. Wenzel for the magnetic moment measurements.

[2] E. A. Nesbitt, J. H. Wernick, and E. Corenzwit, J. Appl. Phys. 30, 365–7 (1959).

[3] Private communication.

Ferromagnetic-Alloy Phases Near the Compositions Ni_2MnIn, Ni_2MnGa, Co_2MnGa, Pd_2MnSb, and PdMnSb*

F. A. Hames
Department of Metallurgical Engineering, Queen's University, Kingston, Ontario

In a search for further examples of Heusler-type alloys, ferromagnetic alloys were found near the composition Ni_2MnIn, Ni_2MnGa, Co_2MnGa, Pd_2MnSb, and PdMnSb. The first four alloys are tentatively identified as having the $L2_1$(Heusler)-type structure; PdMnSb, the Cl_1-type structure. Previous work has indicated that ferromagnetism in these types of alloys is associated with Mn-Mn distances in the range 4.17–4.37 A. The present work indicates that ferromagnetism persists with Mn-Mn distances as small as 4.08 A (Co_2MnGa) and as large as 4.42 A (PdMnSb); and that ferromagnetism disappears if the Mn-Mn distances become too large. Pd_2MnSb, with Mn-Mn distance 4.55 A, is only feebly magnetic at room temperature.

INTRODUCTION

THE Heusler alloys form an interesting group for magnetic study because they offer a possible means of investigating the effects of interatomic distances, atomic arrangement and atomic environment of the magnetic atoms on the occurrence of ferromagnetism on the one hand, and of deducing alloying valences of the metals from measured magnetic moments on the other hand.

The classical Heusler alloys are the ferromagnetic copper-manganese-aluminum alloys based on the beta phase (body-centered cubic structure) of the binary copper-aluminum system. They have a rather wide composition range, which includes the composition Cu_2MnAl. They have an ordered cubic structure under suitable conditions of heat treatment. Maximum degree of order is obtained at composition Cu_2MnAl and the atomic arrangement in this alloy is usually assumed to be that proposed by Bradley and Rogers.[1] The structure may be described in terms of the atoms occupying four types of atom sites, herein designated *A*, *B*, *C*, and *D*, whose coordinates are

A			*B*			*C*			*D*		
0	0	0	$\frac{1}{4}$	$\frac{1}{4}$	$\frac{1}{4}$	$\frac{1}{2}$	$\frac{1}{2}$	$\frac{1}{2}$	$\frac{3}{4}$	$\frac{3}{4}$	$\frac{3}{4}$
$\frac{1}{2}$	$\frac{1}{2}$	0	$\frac{3}{4}$	$\frac{3}{4}$	$\frac{1}{4}$	0	0	$\frac{1}{2}$	$\frac{1}{4}$	$\frac{3}{4}$	$\frac{3}{4}$
$\frac{1}{2}$	0	$\frac{1}{2}$	$\frac{3}{4}$	$\frac{1}{4}$	$\frac{3}{4}$	0	$\frac{1}{2}$	0	$\frac{1}{4}$	$\frac{3}{4}$	$\frac{1}{4}$
0	$\frac{1}{2}$	$\frac{1}{2}$	$\frac{1}{4}$	$\frac{3}{4}$	$\frac{3}{4}$	$\frac{1}{2}$	0	0	$\frac{3}{4}$	$\frac{1}{4}$	$\frac{1}{4}$.

In Cu_2MnAl, *A* and *C* are occupied by Cu; *B* by Mn; and *D* by Al atoms. This arrangement corresponds with space group O_h^5-*Fm3m* and is the prototype of the "Strukturbericht" $L2_1$ structure.

Other examples of this structure are found in ferromagnetic manganese alloys having the ideal composition M_2MnX, where M is Cu, Ni, or Co, and *X* is a *B* sub-group metal. Pearson[2] lists the following examples (lattice constant, *a*, in parentheses).

Cu_2MnAl (5.937); Cu_2MnGa (?); Cu_2MnIn (6.1865); Cu_2MnSn (6.1608); Ni_2MnSb (6.001); Ni_2MnSn (6.036); Co_2MnSn (5.977).

Cl_1 structures (space group T_d^2–$F\bar{4}3m$) of ideal composition $MMnX$ are obtained in some instances by leaving half of the M atoms out of the Heusler alloy. This leaves one set of sites (the C sites, for example) unoccupied. NiMnSb (5.903) and CoMnSn (5.956) are in this category.

CoMnSb (5.888) is described as having a Cl_1-fluorite structure with Co ordered in the *A* sites, but Mn and Sb occupying the *B* and *D* sites randomly.

It is not certain that all of the Heusler alloys listed above have an atomic arrangement analogous to that described for Cu_2MnAl, i.e., *M* in *A* and *C*; Mn in *B*; and *X* in *D*; space group O_h^5–*Fm3m*. An alternative arrangement is: *M* in *A* and *B*; Mn in *C*; and X in *D*; space group T_d^2–$F\bar{4}3m$. Determination of the correct arrangement by x-ray diffraction alone is difficult if differences between atomic scattering factors of the atoms are not favorable. Castelliz[3] has discussed this problem and has suggested a method of distinguishing between the two arrangements, making use of measured magnetic moments.

It is of interest to inquire as to the roles of various atoms in the Heusler alloy as regards contribution to magnetic moment. The *B* sub-group metal appears to be unimportant, except possibly for its size and valence. These might be important in determining the structure of the alloy and whether or not there is a superlattice, according to the alloying concepts of Hume-Rothery.

It is generally assumed that the magnetic moment is due entirely to manganese, although Slater[4] has suggested that copper may also be contributing to the magnetization in the copper-manganese-aluminum Heusler alloy. Mn-Mn distances appear to be significant. Coles, Hume-Rothery, and Myers,[5] comparing Cu_2MnAl with Cu_2MnIn, note a decreasing Curie point with increasing interatomic distance and suggest that in Cu_2MnIn the critical ratio of interatomic distance to *3d* electron shell

* The research for this paper was supported in part by the Defence Research Board of Canada.

[1] A. J. Bradley and J. W. Rodgers, Proc. Roy. Soc. (London), A144, 340 (1934).

[2] W. B. Pearson, *A Handbook of Lattice Spacings and Structures of Metals and Alloys* (Pergamon Press, New York, 1958).

[3] L. Castelliz, Z. Metallk. 46, 198 (1955).

[4] J. Slater, Phys. Rev. 36, 57 (1930).

[5] B. R. Coles, W. Hume-Rothery, and H. P. Myers, Proc. Roy. Soc. (London) A196, 125 (1949).

TABLE I. Structure of the alloys (tentative). *Q* and *FC* indicate quenching and cooling in the furnace, respectively, after 24 hrs at the temperature indicated.

Ideal composition	*a*,*A*	Mn-Mn distance,*A*	Treatment
$L2_1$ (Heusler) Structures			
Ni_2MnIn	6.07	4.29	*Q* 810°C
	6.08	4.30	FC
Ni_2MnGa	5.86	4.14	*Q* 940°C
	5.83	4.12	FC
Co_2MnGa	5.77	4.08	*Q* 940°C
	5.78	4.09	FC
Pd_2MnSb	6.38	4.51	*Q* 590°C
	6.43	4.55	FC
Cl_1 Structure			
PdMnSb	6.25	4.42	*Q* 620°C

diameter is being approached at which ferromagnetism will disappear.

When transition metals such as nickel and cobalt are substituted for copper, the problem of the interpretation of measured magnetic moments is complicated because of the presence of two kinds of potentially magnetic atoms. There is then the question of the relative importance of M-M, M-Mn, and Mn-Mn interactions in determining ferromagnetism; and the associated question of the relative importance of M-M, M-Mn, and Mn-Mn distances.

The question of the correct atomic arrangement (O_h^5 vs T_d^2) in the various Heusler alloys is perhaps not significant if it is only the Mn-Mn distances that are important; in both arrangements the shortest Mn-Mn distance is $[(2)^{\frac{1}{2}}/2]a$. On the other hand, if M-Mn or M-M distances are significant, knowledge of the correct arrangement is desirable. In O_h^5 M-M$=a/2$; M-Mn $=[(3)^{\frac{1}{2}}/4]a$, In T_d^2, M-M$=[(3)^{\frac{1}{2}}/4]a$, M-Mn$=a/2$. This question has been discussed by Castelliz[3] in the same reference noted above.

As an aid to resolving questions of the relative importance of atomic arrangement, interatomic distances, and the environment of the magnetic atoms on the occurrence of ferromagnetism, a search for further examples of Heusler alloys has been undertaken. Some preliminary results are summarized in Table I.

RESULTS AND DISCUSSION

All of the alloys were magnetic in all conditions of heat treatment examined, as indicated by attraction to a magnet; attraction was strong, excepting Pd_2MnSb.

The structures indicated are tentative. The X-ray patterns were not inconsistent with the structures indicated, but other structures would give similar patterns, in view of the unfavorable differences in atomic scattering factors.

It is noted that the Mn-Mn distances in the strongly magnetic alloys range from 4.08 A (Co_2MnGa) to 4.42 A (PdMnSb), the distances for previously reported alloys of these types range from 4.17 A (NiMnSb) to 4.37 A (Cu_2MnIn). In Pd_2MnSb, which is weakly magnetic, the corresponding distance is 4.55 A.

CONCLUSIONS

1. Ni_2MnIn, Ni_2MnGa, Co_2MnGa, and Pd_2MnSb are tentatively identified as having the $L2_1$(Heusler) structure; PdMnSb the Cl_1 structure.
2. Ferromagnetism is strong in the alloys with Mn-Mn distances in the range 4.08 to 4.42 A.
3. Ferromagnetism is weak (at room temperature, at least) in Pd_2MnSb, Mn-Mn 4.55 A.
4. Although it appears that ferromagnetism might be associated with a critical range of Mn-Mn distances, it is not possible at present to separate this effect from the possible ferromagnetism of Ni or Co interactions.

ACKNOWLEDGMENTS

The writer wishes to acknowledge assistance received from the International Nickel Company. The indium was donated by the Consolidated Mining and Smelting Company of Canada, Limited; and the nickel and cobalt by Sherritt Gordon Mines Limited. Donald Lea and Brian Stevens assisted with the experiments.

The permission of the Defence Research Board of Canada to publish this paper is gratefully acknowledged.

Magnetic-Form Factor of Fe_3Al†

S. J. PICKART, *U. S. Naval Ordnance Laboratory, White Oak, Silver Spring, Maryland, and Brookhaven National Laboratory, Upton, New York*

AND

R. NATHANS,* *Pennsylvania State University, University Park, Pennsylvania, and Brookhaven National Laboratory, Upton, New York*

A polarized neutron study carried out on the high angle superlattice reflections of ordered Fe_3Al shows that the near neighbor environment influences not only the average moment per Fe atom, but also the spatial symmetry of the *d* electron charge distribution. Preliminary analysis of the form factor indicates that the magnetic electrons of the Fe atom surrounded by 8 Fe near neighbors (which has a moment $\mu=2.1\mu_B$) preferentially occupy the doubly degenerate e_g orbitals, while those of the Fe atom with 4 Fe and 4 Al near neighbors ($\mu=1.5\mu_B$) favor the triply degenerate t_{2g} orbitals.

INTRODUCTION

A CHARACTERISTIC of the ordered alloy Fe_3Al that makes it of interest magnetically is the fact that iron atoms are found in two widely differing environments. The structure is a face-centered cubic supercell[1] with half the body-centered iron atoms replaced by aluminum. One type of iron atom in the superlattice, designated Fe(I), has only iron near neighbors; the other, Fe(II), is surrounded by four aluminum and four iron atoms in a tetrahedral configuration.

An earlier polarized neutron study on Fe_3Al by Nathans, Pigott, and Shull[2] up to the (400) reflection established a negligible moment for the Al atoms, and significantly different magnetic scattering amplitudes for the iron atoms, corresponding to an average moment of 2.15 μ_B for Fe(I) and 1.46 for Fe(II). One possible conclusion is that the near neighbor configuration determines the moment, the localized moment of Fe(II) being reduced by bonding with Al. The effect has also been attributed to a greater amount of thermal disorder within the Fe(II) sublattice at room temperature[3] or to some antiparallelism in the Fe(II) spins.[4]

The form factor of higher angle superlattice reflections will display any difference in the *d* electron charge distribution of the two iron types. In addition, the more numerous reflections, with varying crystallographic directions, should provide an ideal means of detecting asphericities in the spin density, which, as Weiss and Freeman[5] have shown, can radically affect the form factor at higher values of $\sin\theta/\lambda$.

EXPERIMENTAL

The apparatus, which uses a resonant spin-flipping rf coil to reverse the neutron polarization direction during alternate intervals, has been described previously.[2] The present measurements were made on a pillar of square cross section 20×2×2 mm cut with the long axis [110], along which a field of 6500 oe is applied. The observed ratio of the intensities for incoming neutron spin parallel and antiparallel to the analyzing field, after correction for extinction, depolarization and oscillator efficiency, gives $(1+\gamma)^2/(1-\gamma)^2$, where $\gamma=p/b$, the ratio of the magnetic to the known nuclear structure amplitude. Corrections for depolarization and oscillator efficiency were determined directly. Extinction was shown to be negligible for the superlattice reflections, which are relatively weak, by measuring the polarization ratio as a function of Bragg missetting[6]; data for the fundamental reflections were obtained by this method and by using polycrystalline material.

Structure factors for the superlattice reflections are of two types:

$$h, k, l \text{ odd}: \quad F\sim a_{Fe(I)}-a_{Al}$$

$$h, k, l \text{ even}, \frac{h+k+l}{2} \text{ odd}: \quad F\sim 2a_{Fe(II)}-a_{Fe(I)}-a_{Al},$$

where *a* is the magnetic or nuclear scattering amplitude. Results obtained so far are listed in Table I, and plotted as a function of $\sin\theta/\lambda$ in Fig. 1. The scattering amplitude in the forward direction is obtained by normalizing the first three reflections to the spherical Fe form factor,[5] since the usual method of normalizing to the observed moment is inapplicable; however, the calculated asymmetry effects in this region are small. The quoted limits are the standard deviations of repeated runs, and include the effect of averaging over the different members of the form $\{h\bar{h}l\}$ accessible in the zone. Scatter of the points at higher angles is quite apparent, in fact, for (511, 333) or (600, 442) which are at equal $\sin\theta/\lambda$, the

† Work performed under the auspices of the U. S. Atomic Energy Commission and the National Security Agency.

* Present address: Massachusetts Institute of Technology Lincoln Laboratory, Lexington, Massachusetts.

[1] A. J. Bradley and A. H. Jay, Proc. Roy. Soc. (London) **136**, 210 (1932).

[2] R. Nathans, M. T. Pigott, and C. G. Shull, J. Phys. Chem. Solids **6**, 38 (1958).

[3] H. Sato and A. Arrott, J. Appl. Phys. **29**, 515 (1958).

[4] J. B. Goodenough, Lincoln Tech. Rept. 208.

[5] R. J. Weiss and A. J. Freeman, J. Phys. Chem. Solids **10**, 147 (1959).

[6] R. Nathans, C. G. Shull, G. Shirane, and A. Andresen, J. Phys. Chem. Solids **10**, 138 (1959).

TABLE I. Results of polarized neutron measurements on Fe_3Al.

hkl	γ_{hkl}	p_{hkl}	f_{hkl}
111	0.845±0.010	0.477	0.816±0.009
200	0.252±0.003	0.135	0.767±0.009
220	0.261±0.001	0.852	0.604±0.003
311	0.531±0.004	0.295	0.506±0.004
222	0.161±0.001	0.0867	0.492±0.004
400	0.183±0.002	0.597	0.428±0.005
331	0.310±0.002	0.171	0.293±0.002
422	0.101±0.003	0.326	0.234±0.007
333	0.215±0.001	0.119	0.204±0.002
511	0.252±0.002	0.139	0.238±0.002
440	0.062±0.001	0.200	0.143±0.003
442	0.061±0.002	0.0326	0.185±0.006
600	0.032±0.001	0.0171	0.097±0.003
533	0.097±0.001	0.0532	0.091±0.001
622	0.033±0.001	0.0176	0.100±0.003
444	0.042±0.001	0.135	0.097±0.002
711	0.108±0.001	0.0592	0.101±0.001
553	0.022±0.002	0.0121	0.021±0.002

differences are upwards of ten times the standard deviation.

DISCUSSION

The Fe(I) and Fe(II) moments obtained by the foregoing procedure agree well with the previous report.[2] As a start in analyzing the higher angle data we have calculated the form factors expected if the magnetic electrons are exclusively in either the doubly degenerate (e_g) or the triply degenerate (t_{2g}) levels, using the tabulated principal scattering factors of Weiss and Freeman.[5] Comparison with the observations illustrates a general tendency for the superlattice reflections: for (111) type reflections the observed value lies closer to $f(e_g)$, while for (200) type, closer to $f(t_{2g})$. Treating the degree of admixture of t_{2g} and e_g wave functions as a parameter, we find that the first group represents roughly 70% e_g, the latter, 90% t_{2g}.

These numbers, of course, depend on the theoretically calculated form factors,[5] and on the model used for the iron spin density distribution[7–9]; nevertheless, the fact that they are different is relatively independent of these uncertainties, and allow us to conclude that the outer electrons of the Fe(I) and Fe(II) atoms have different spatial symmetry. Moreover, the observation of different f values for reflections having reciprocal lattice vectors of equal magnitude but different orientation indicates unequivocally that the spin density in the unit cell is not spherical. Finally, we note that only the Fe(I) atoms contribute to the (111) type reflections if the aluminum moment is zero and that the observed Fe form factor[5,6] favored e_g symmetry; the fact that Fe(I) has the same near neighbor environment, the same outer electron configuration, and the same net spin as pure Fe, seems to support a redistribution of the electrons in the d shells of the Fe(II) atoms induced by the tetrahedral coordination of near neighbor aluminum atoms.[10]

Further data are in the process of being collected, and it is hoped that enough reflections can be examined to make a two-dimensional projection of the spin density feasible. These results will be reported in detail elsewhere.

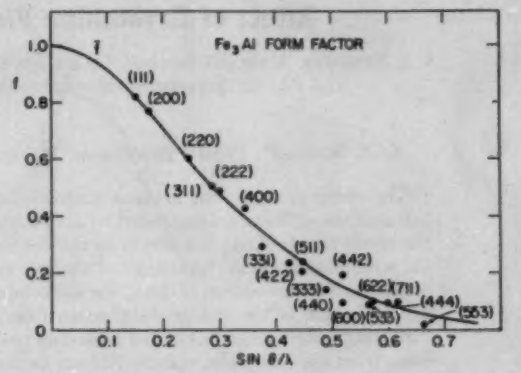

FIG. 1. The form factor of Fe_3Al. The uncertainties in the data are less than the size of the experimental points. The solid curve f is the spherical form factor for iron calculated by Weiss and Freeman.[5]

[7] Y. Komura, Y. Tomiie, and R. Nathans, Phys. Rev. Letters 3, 268 (1959).
[8] R. J. Weiss and J. J. DeMarco, Revs. Modern Phys. 30, 59 (1958).
[9] B. Batterman, Phys. Rev. 115, 81 (1959).
[10] A. Taylor and R. M. Jones, J. Phys. Chem. Solids 6, 16 (1958).

JOURNAL OF APPLIED PHYSICS SUPPLEMENT TO VOL. 31, NO. 5 MAY, 1960

Effect of Crystalline Fields on Magnetic-Form Factors

A. J. FREEMAN, *Materials Research Laboratory, Ordnance Materials Research Office, Watertown, Massachusetts, and Physics Department, Massachusetts Institute of Technology, Cambridge, Massachusetts*

AND

R. E. WATSON*, *Physics Department, Massachusetts Institute of Technology, Cambridge, Massachusetts*

The effects of crystalline fields on magnetic-form factors are discussed on the basis of recent Hartree-Fock calculations of Watson augmented by an analysis of experimental optical absorption data. It is shown that the crystalline field has two effects on the free ion 3*d* wave functions and hence on their form factors as well: (1) a differentiation or "splitting" of the two types of cubic 3*d* functions by an expansion of the t_{2g} (or e_g) orbital and a contraction of the e_g (or t_{2g}) orbital resulting in two different radial charge densities and (2) a net expansion of the charge distribution from the free ion value. The magnetic-form factor due to this "splitting" effect when calculated according to the methods of Weiss and Freeman shows measurable deviations from the free atom results. A form factor for Mn^{+2} based on optical absorption data shows a large expansion of the 3*d* charge density, in agreement with the measurements of Hastings, Elliott, and Corliss.

INTRODUCTION

WEISS and Freeman[1] have calculated the effect on form factors of non-spherical charge distributions in various crystalline environments. They showed that large measurable deivations from the usual spherical approximation resulted, and that a theoretical analysis of these "bumps" in measured form factor data led to a new technique for determining the spatial symmetry of the spin densities in magnetic materials. By applying this technique to the precise polarized neutron measurements of Shull, Nathans, and collaborators,[2] they were able to determine the angular distribution of the 3*d* spin densities in Fe, Ni, and (fcc) Co in terms of a mixing of the two types of 3*d* wave functions in a cubic field (i.e., a triply degenerate set, called t_{2g} and a doubly degenerate set, called e_g). Recently Pickart and Nathans[3] have carried out a similar analysis of their detailed measurements of the Fe_3Al form factor. In these papers[1,2] the usual assumption of a single radial wave function for both the t_{2g} and e_g electrons about a given atom site was made. (For Fe_3Al, which has two types of Fe atom sites at which the Fe atoms have different magnetic moments and hence different spin densities, a distinct radial wave function for each site was of course needed to analyze the measured magnetic form factor.[3])

The purpose of this paper is to investigate the effects of crystalline fields on the free atom wave functions and in turn on the theoretical form factors. Our discussion is specialized to the case of a transition metal ion in an ionic compound where the effects of a crystalline field are expected to be large.

WAVE FUNCTIONS FOR AN ION IN A CRYSTALLINE FIELD

If, in an ionic crystal of cubic symmetry, we computed the potential at the site of a metal ion due to the rest of the ions in the crystal and then used this (external) potential in a calculation of the metal ion's wave functions, two effects would be observed. First, there would be a differentiation or "splitting" of the two types of cubic 3*d* functions (by an expansion of the t_{2g} (or e_g) orbital and a contraction of the e_g(or t_{2g}) orbital) with respect to their common free ion value, resulting in two different *radial* charge densities. Second, this splitting would be accompanied by a net expansion of the ion's charge distribution as compared with the free ion's charge distribution—the expansion being most noticeable in the outermost electron shell (namely the 3*d* shell in our case.)

One of us,[4] has recently carried out a Hartree-Fock calculation for the $Mn^{+2}(3d^5)$ ion in an external cubic point charge field. In what follows, we use the results of this calculation, augmented by experimental optical absorption data, to estimate and discuss the variation in form factors due to both the effects mentioned above.

EFFECT OF 3*d* SHELL SPLITTING ON THE MAGNETIC FORM FACTOR

In the Hartree-Fock calculation, the external potential was due to an octahedral array of negative point charges. The individual electrons were taken to have cubic symmetry (the "strong field" approximation) and different radial wave functions were obtained for the two types of cubic 3*d* electrons. We have calculated the effect of this "splitting" on the magnetic form factor using the methods described by Weiss and Freeman[1] thus taking full account of the angular distribution of the one-electron wave functions as well. As a reference frame for our considerations we use the results of a free ion Hartree-Fock calculation[5] for Mn^{+2} in all our comparisons.

As observed in earlier work[1] the form factors for the individual t_{2g} and e_g electrons calculated at the Bragg

* The research done by this author was supported jointly by the U. S. Army, Navy, and Air Force under contract with the Massachusetts Institute of Technology.

[1] R. J. Weiss and A. J. Freeman, J. Phys. Chem. Solids **10**, 147 (1959).

[2] Nathans, Shull, Shirane, and Andreson, J. Phys. Chem. Solids **10**, 133 (1959); R. Nathans and A. Paoletti, Phys. Rev. Letters **2**, 254 (1959).

[3] S. Pickart and R. Nathans, J. Appl. Phys. **31**, 372S (1960).

[4] R. E. Watson, Quarterly Progress Reports, Solid State and Molecular Theory Group, MIT, July 15, 1959, p. 3 (unpublished), and Phys. Rev. **117**, 742 1960.

[5] R. E. Watson, "Iron series Hartree-Fock calculations," Tech. Rept. No. 12, Solid State and Molecular Theory Group, MIT, Cambridge, Massachusetts, June, 1959 (unpublished), and Phys. Rev. (submitted).

reflections in a cubic crystal fail to lie on a smooth curve. The use of different radial wave functions gives rise to further deviations or "bumps" from the smooth form factor curve at the observed Bragg peaks (which are due to the radial charge differences alone). These "new" deviations cannot be described by a simple scaling of the free atom results since for some reflections the "bumps" are increased while for others they are diminished. These deviations from the free atom values have a magnitude of the order of 0.02 electron units (which is well above the experimental uncertainty in current polarized neutron measurements[2]) or of the order of some "bumps" due to free atom nonsphericity alone. From this, we see that in these cases a single form factor for both the e_g and t_{2g} electrons cannot give a unique determination of the spatial symmetry of the outer electrons.[6]

Mn^{+2}, with its half-filled 3*d* shell is a rather special case. As a free ion, its ground state is $(3d)^5\ {}^6S$, which has a spherical charge distribution, and hence its form factor would be the usual (spherically symmetric) smooth curve. The "splitting" effect however results in a non-spherical charge distribution which gives a form factor which shows deviations from a smooth curve even though three t_{2g} orbitals and two e_g orbitals are occupied (i.e., a half-filled shell). The "bumps" in the total form factor for these five cubic 3*d* electrons, which is the least favorable case that could be considered, are not as large as the ones discussed earlier for the separate t_{2g} or e_g form factors—they are just outside of experimental uncertainty—and hence would be hard to observe. For transition metals ions with non-closed (but *not* half-filled) 3*d* shells this effect would however be more readily observed.[8]

EFFECT OF WAVE FUNCTION EXPANSION ON MAGNETIC-FORM FACTOR

Since a point charge cubic field does not produce a charge density expansion in a half-filled 3*d* shell ion (a more accurate crystalline field would do this), the results of the calculation based on the octahedral array of point charges described earlier cannot be used to discuss the effect of charge density expansion on the form factor. For this reason we have looked into the information available from optical absorption data[9] for transition metal ions in crystalline environments.

In both the free ion and crystalline ion absorption work two parameters are interpreted to be integrals involving the 3*d* wave functions *alone*. These are the Slater $F^k(3d,3d)$ integrals. These integrals are found to be substantially smaller for the crystalline ions and this can be interpreted as representing a substantial expansion of the atomic 3*d* radial function. We have taken a typical observed variation (about 15%) in the $F^k(3d,3d)$ integrals for Mn^{+2} and from theoretical $F^k(3d,3d)$ integrals for the ion series ions[5] we have selected 3*d* wave functions which show this same percentage change from the theoretical Mn^{+2} value. The V^{+2} and Mn^{+} 3*d* functions satisfy this requirement. Their form factors, and that for the free Mn^{+2} ion, are plotted in Fig. 1. The shaded region between V^{+2} and Mn^{+} indicates a range in predicted form factor due to the expansion effect of the crystalline field. If we now also plot the observed Mn^{+2} magnetic-form factor,[8] we see that there is good agreement with our crude estimate derived from the optical absorption data. This suggests that both the optical absorption data and the neutron diffraction data are due to an expansion of the 3*d* wave function from its free ion value.

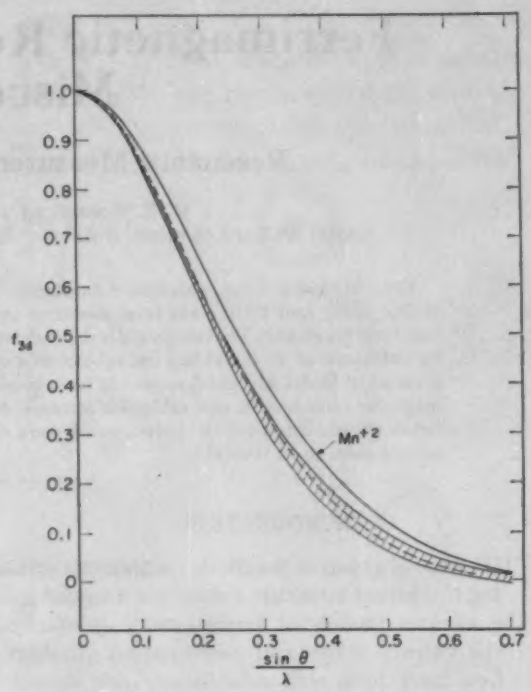

FIG. 1. The calculated free ion 3*d* form factor for Mn^{+2}; the predicted crystalline form factor for Mn^{+2} (shaded region); and the measured magnetic-form factor for Mn^{+2} (dashed curve) of Hastings, Elliott, and Corliss.

A complete account of this work will be given in a forthcoming publication.

ACKNOWLEDGMENTS

We are indebted to Professor C. G. Shull and Dr. R. J. Harrison for helpful discussions and to Dr. J. M. Hastings for making his data available to us.

[6] Professor G. F. Koster has pointed out to us that this 3*d* "splitting" mechanism may explain an observed[7] absorption line in a manganous pechlorate solution.

[7] Heidt, Koster, and Johnson, J. Am. Chem. Soc. **80**, 6471 (1958).

[8] Deviations from a smooth form factor have been observed [J. M. Hastings, N. Elliott, and L. M. Corliss, Phys. Rev. **115**, 13 (1959)] for Mn^{+2} in several ionic compounds. Their relevancy with respect to the "splitting" effect of the crystalline field is being investigated.

[9] For example, see C. K. Jørgensen, Discussions Faraday Soc. **26**, 110 (1958).

Ferrimagnetic Resonance Effects and Miscellaneous

Resonance Measurements in Magnetic Garnets*

G. P. Rodrigue,† H. Meyer,‡ and R. V. Jones
Gordon McKay Laboratory, Division of Engineering and Applied Physics, Harvard University

The effective g value, anisotropy constants, and line widths of single crystals of YIG, GdIG, SmIG, HoIG, ErIG, and YbIG have been measured over a range of temperatures from 1.5°K to 550°K by ferrimagnetic resonance. The temperature dependence of K_1 in both YIG and GdIG is satisfactorily represented by the model of an individual ion subject to a crystalline field in addition to a Weiss molecular field. The g values of HoIG and ErIG appear to be in good agreement with the estimations of Kittel et al. for a ferrimagnetic system with one sublattice strongly damped. It has been found that SmIG and YbIG do not follow the predictions of the Kittel model, since different relative strengths of exchange and relaxation interactions seem to be involved.

INTRODUCTION

THE general group of magnetic compounds exhibiting the garnet structure constitute a valuable test for the various models of ferrimagnetic interactions. Since the valence states and coordination numbers of these ions have been well established,[1] one should be able to make reliable predictions of the energy level schemes associated with each magnetic ion. Due to the many possible chemical substitutions, these isomorphic compounds provide a range of interactions between $4f$ and $3d$ magnetic ions in various combinations.[2] To gain insight into the interactions involved in the iron-garnet series (i.e., $5Fe_2O_3 \cdot 3M_2O_3$ usually labelled MIG) the ferrimagnetic absorption of single garnet crystals has been measured over a range in temperatures from 1.5° to 550°K. The resonances were observed in a conventional X-band reflection spectrometer.[3] The temperature of the microwave cavity was maintained by an electronic control system which provided, electrically, a heat flow to balance the heat lost to a refrigerant bath. The crystals were grown by the lead oxide flux method[4] and ground into highly polished spheres.[5] The results of preliminary measurements have been reported earlier.[6] A summary of more extensive measurements on yttrium-, gadolinium-, samarium-, holmium-, erbium-, and ytterbium-iron garnet are presented here.

If it is assumed that the resonance behavior of a multisublattice system such as the garnets can be described by the ferromagnetic torque equation, then for various principal axes of the crystal the magnetic field required for resonance will be given in terms of the effective anisotropy constants, K_1 and K_2, and the effective g value.[7] Wangness[8] has demonstrated the conditions under which this assumption is valid and has interpreted these effective resonance parameters in terms of the magnetic properties of the individual sublattices. For the case of two sublattices, A and B, and negligible damping, the effective resonance parameters are given by

$$g_{eff}=g_Ag_B(M_A-M_B)/(g_BM_A-g_AM_B), \qquad (K_1)_{eff}=(K_1)_A+(K_1)_B, \qquad (1)$$

where the M's specify the magnitudes of sublattice magnetizations. However, Kittel[9] has pointed out that for certain rare earth-iron garnets the damping of the rare earth sublattice is not negligible. In accounting for the preliminary resonance data on ErIG and HoIG, he found that although the rare earth ions contribute to the magnetization, and presumably to the free energy, the rare earth contributions to the gyroscopic characteristics of the magnetic system are damped out.[10] Under the assumption of large damping of the rare earth ions, the effective parameters become

$$g_{eff}=g_A(M_A-M_B)/M_A, \quad (K_1)_{eff}=(K_1)_A+(K_1)_B. \qquad (2)$$

YTTRIUM-IRON GARNET

The magnetization of the simplest iron garnet, YIG, has been interpreted by Pauthenet[11] in terms of a net

* Research jointly sponsored by an Air Force Cambridge Research Center contract and a National Security Agency contract.
† Present address: Sperry Microwave Electronics Division, Tampa, Florida.
‡ Present address: Department of Physics, Duke University.
[1] F. Bertaut and F. Forrat, Compt. Rend. 242, 382 (1956); M. L. Keith and R. Roy. Am Mineralogist 39, 1 (1954); H. S. Yoder and M. L. Keith, Am. Mineralogist 36, 519 (1951).
[2] M. A. Gilleo and S. Geller, Phys. Rev. 110, 73 (1958).
[3] J. O. Artman and P. E. Tannenwald, J. Appl. Phys. 26, 1124 (1955).
[4] J. W. Nielsen and E. F. Dearborn, J. Phys. Chem. Solids 5, 202 (1958).
[5] W. L. Bond, Rev. Sci. Instr. 22, 344 (1951).
[6] R. V. Jones, G. P. Rodrigue, and W. P. Wolf, J. Appl. Phys. 29, 434 (1958).
[7] C. Kittel, Phys. Rev. 73, 155 (1948); L. R. Bickford, Technical Rept. No. 23, ONR Contract N5 ori-07801, Laboratory of Insulation Research, M.I.T. (1949); J. F. Dillon, Jr., S. Geschwind, and V. Jaccarino, Phys. Rev. 100, 750 (1955).
[8] R. K. Wangsness, Phys. Rev. 91, 1085 (1953); 93, 68 (1954); 95, 339 (1954); Am. J. Phys. 24, 60 (1956).
[9] C. Kittel, Phys. Rev. 115, 1587 (1959).
[10] It should be noted that Wangsness had previously derived the appropriate expressions for the effective parameters of a ferrimagnetic system with damping, Phys. Rev. 111, 813 (1958).
[11] R. Pauthenet, Ann. Phys. 13, Series 1, 424 (1958).

antiferromagnetic coupling of the ferric ions on the 24 d sites with those on the 16a sites. Dillon has reported extensive measurements on the resonance behavior of YIG.[12–14] His work has dramatized the importance of small amounts of rare earth impurities in producing "anomalously" large line widths and anisotropies. The emphasis of the YIG work presented here has been directed towards the understanding of the "normal" or nonimpurity dependent contributions to the anisotropy energy. These are the contributions associated with the ferric ions in ^6S states.

Several authors have suggested that the magnetocrystalline anisotropy of S state ions may be associated with the splitting of these states[15–17] by the local crystalline field of the ion site. The spin Hamiltonian appropriate to this problem has been given by Bleaney and Trenam[18] in terms of the cubic field constant "a" and the second and fourth order trigonal field constants D and F. If we assume that exchange forces which act on the magnetic ion are presented by a Weiss molecular field, and use the energy levels derived from the spin Hamiltonian, the partition function and, hence, the free energy of the system can be evaluated. Yosida and Tachiki,[17] and independently, Wolf[16] have carried out such a calculation and have evaluated the sublattice anisotropy energy in terms of functions of the sublattice magnetization. These functions, $r(T)$ and $t(T)$, have been conveniently tabulated by Wolf[16] and the first order cubic anisotropy constant can be expressed as

$$K_1(T)=N[(a+(7/12)\gamma F)r(T)+(D^2/kT)\gamma t(T)], \quad (3)$$

where N is the number of magnetic ions per unit volume. The axial field contributions to the cubic anisotropy come about through the averaging of the local distortions over all of the nonequivalent sites of the cubic structure ($\cos^4\theta=\gamma(l^2m^2+m^2n^2+n^2l^2)$, where θ and (l,m,n) denote the orientation of the magnetization relative to respectively the trigonal and cubic axes).

The experimental variation of K_1 with temperature is presented in Fig. 1. The K_2 term makes a negligible contribution to the anisotropy energy of YIG. The data for K_1 does not show the rapid rise below 100°K, which was observed in the early work of Dillon,[12] and which must be attributed to rare earth impurities. The fitted curve in Fig. 1 represents a sum of appropriately weighted $r(T)$ functions for the two types of ferric sites. The sublattice magnetizations given by Pauthenet[11] have been used in determining the $r(T)$'s. The value of the weighting factor leads to an estimate of the constant

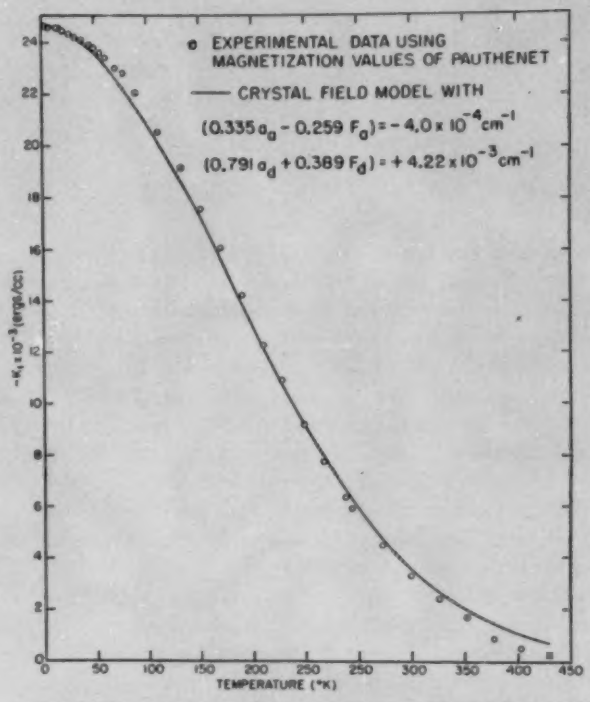
EXPERIMENTAL DATA USING MAGNETIZATION VALUES OF PAUTHENET
CRYSTAL FIELD MODEL WITH
$(0.335\,a_a - 0.259\,F_a) = -4.0\times10^{-4}\,cm^{-1}$
$(0.791\,a_d + 0.389\,F_d) = +4.22\times10^{-3}\,cm^{-1}$
$-K_1\times10^{-3}$ (ergs/cc)
TEMPERATURE (°K)

FIG. 1. Temperature variation of K_1 in YIG. Cubic crystalline terms have been used in the temperature fit with the indicated parameters.

$(a+7\gamma F/12)$. However, in the garnets, as pointed out by Wolf[16] and Cooper,[19] the local cubic anisotropy energy associated with a given site is reduced when averaged over all sites since the local cubic axes are not parallel to the cubic axes of the unit cell. The octahedral a site is oriented with its three-fold axis along the various $\langle111\rangle$ axes of the unit cell. By using the structural data of Geller and Gilleo,[20] the reduction factor associated with the cubic field of the a site is $+0.335$ and for a $\langle111\rangle$ distortion $\gamma=+4/9$. The twofold axis of the d site lies along the various $\langle100\rangle$ axes of the unit cell. One finds for this case, a reduction factor of $+0.78$ and for a $\langle100\rangle$ distortion $\gamma=-\frac{2}{3}$. The weighting factors used in Fig. (1) are presented in Table (I) and are compared with the splitting constants determined by Geschwind[21] from measurements of the paramagnetic resonance of ferric ions in a yttrium-gallium garnet host crystal. From Geschwind's values of the D constant, one can estimate the second term in Eq. (3) to be about 1/25 of the first and, hence, the (D^2/k) term has been ignored in the temperature fit. If the F terms are neglected, one would need to invoke a particularly small and negative a_a to explain the observed data. The fact that the anisotropy can be explained in terms of a positive sign of the a constants for both the tetrahedral and octahedral sites is particularly satisfying. All reported paramagnetic resonance data [18,21,22] seems to be consistently in agree-

[12] J. F. Dillon, Jr., Phys. Rev. **105**, 759 (1957).
[13] J. F. Dillon, Jr., Phys. Rev. **111**, 1476 (1958).
[14] J. F. Dillon and J. W. Nielson, Phys. Rev. Letters **3**, 30 (1959).
[15] G. T. Rado and V. J. Folen, Bull. Am. Phys. Soc. Ser. II, **1**, 132 (1956).
[16] W. P. Wolf, Phys. Rev. **108**, 1152 (1957).
[17] K. Yosida and M. Tachiki, Progr. Theoret. Phys. **17**, 331 (1957).
[18] B. Bleaney and R. S. Trenam, Proc. Roy. Soc. (London) **A223**, 1 (1954).
[19] B. R. Cooper, Phys. Rev. **112**, 395 (1959).
[20] S. Geller and M. A. Gilleo, J. Phys. and Chem. Solids **3**, 30 (1957).
[21] S. Geschwind, Phys. Rev. Letters **3**, 208 (1959).
[22] G. D. Watkins, Phys. Rev. **110**, 986 (1958).

TABLE I. Yttrium-iron garnet.

Site	Weighting factor (i.e., coef. of $r(T)$ in Eq. 3)	g	a	F (Data of Geschwind[21])	D
a	$0.335a-0.259F=-4.0\times10^{-4}$ cm^{-1}	2.003	$+1.94\times10^{-2}$ cm^{-1}	$+0.27\times10^{-2}$ cm^{-1}	-0.1356 cm^{-1}
d	$0.791a+0.389F=+4.22\times10^{-3}$ cm^{-1}	2.0047	$+0.65\times10^{-2}$ cm^{-1}	-0.42×10^{-2} cm^{-1}	$+0.0929$ cm^{-1}

ment with the Watanabe[23] theory, which predicts a positive constant for all coordinations. However, the reported values required to fit the anisotropy of spinel ferrites have disagreed with this prediction.[15,17,24] It would appear that the F terms are perhaps important for the interpretation of the spinel data as well.[24a] It is not surprising that the a and F values required for the interpretation of the anisotropy of data in YIG should be somewhat different from those found for Fe^{3+} in yttrium-gallium garnet since the lattice constant of YIG is 0.8% greater than that of YGaG[2]. The splitting constants should be sensitive functions of the lattice and oxygen parameters. For example, Kaminow has found that the anisotropy of YIG increases by 7% in a 0.5% volume change.[25,26] One may conclude that the normal anisotropy behavior of YIG can be well accounted for in terms of the model of an individual ferric ion interacting with its local crystalline field and a Weiss molecular field.

It is seen from Fig. 6 that the effective g value for YIG is essentially independent of temperature. It varies only from 2.006 ± 0.002 at 480°K to 2.001 ± 0.002 at 1.5°K. These values are in good agreement with Geschwind's[21] results which are quoted in Table (I). Equation (1) combined with the sublattice magnetization data of Pauthenet[11] and the g values of Geschwind predicts that there should be a slight decrease in g_{eff} at low temperatures.

The highly polished samples used in the YIG experiments exhibited what might be termed "normal"[14] anisotropic behavior in the line width. The "normal" behavior, which has been observed for most of the ferrites, gives the broadest line width when the magnetic field is parallel to an easy axis and the narrowest when it is parallel to a hard axis. The temperature variation of the principal line widths is given in Fig. 2. The peak in this curve at 50°K has been studied extensively by the workers at Bell Telephone Laboratories.[14,27] Kittel

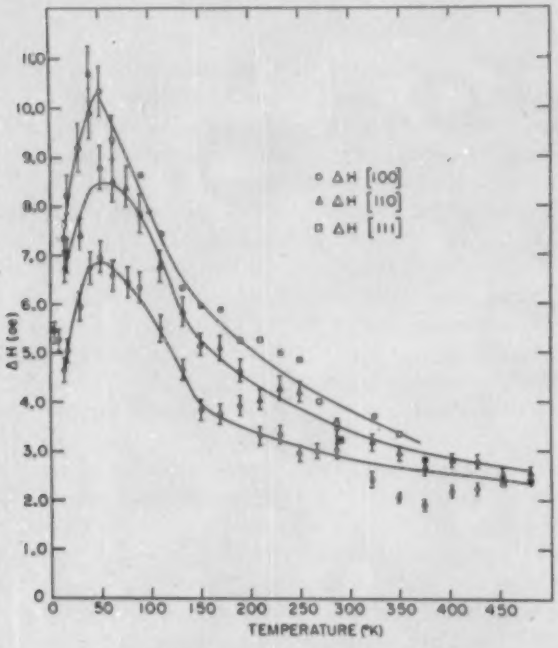

FIG. 2. Temperature variation of ΔH in highly polished YIG crystals.

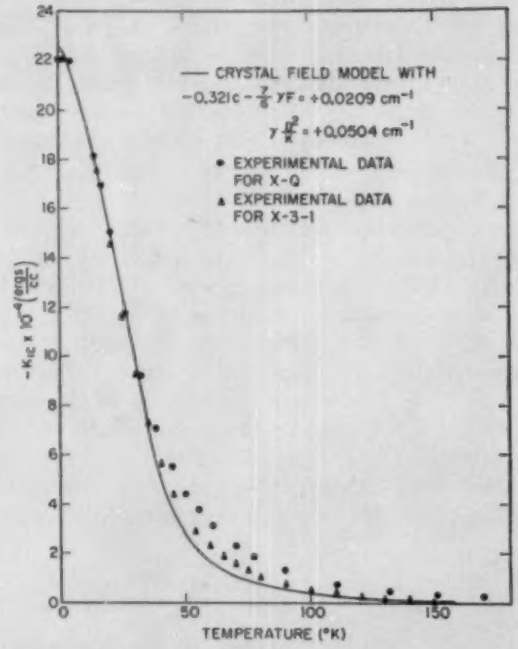

FIG. 3. Temperature variation of K_1 in GdIG. Cubic and axial crystalline field terms have been used in the temperature fit.

[23] H. Watanabe, Progr. Theoret. Phys. (Kyoto) 18, 405 (1957).
[24] V. J. Folen and G. T. Rado, J. Appl. Phys. 29, 438 (1958).
[24a] *Note added in proof.* V. J. Folen, J. Appl. Phys. 31, 166S (1960), notes this same possibility.
[25] I. Kaminow, W. Paul, and R. V. Jones, Bull. Am. Phys. Soc. Ser. II, 4, 177 (1959).
[26] The values quoted in this reference are in error and should be corrected to: $-(K_1/M)=44.7$ oe$+(3.2\times10^{-4}$ oe/kg cm$^{-3})P$. $4\pi M=1776$ gauss$+(1.7\times10^{-3}$ gauss/kg cm$^{-3})P$. K_2 and g did not change significantly with pressure.
[27] E. G. Spencer, R. C. LeCraw, and A. M. Clogston, Phys. Rev. Letters 3, 32 (1959).

TABLE II. Gadolinium-iron garnet.

GdIG		Gd^{3+} in CaF_2	
Weighting factors (c site)	g_e	a	g
$0.321a+\frac{7}{12}\gamma F=-4.18\times10^{-2}$ cm^{-1}	1.994±0.005 (480°K)	9.25×10^{-3} cm^{-1} (Low[30])	1.991 (Low[30])
$\frac{\gamma D^2}{k}=+5.04\times10^{-2}$ cm^{-1}	1.999±0.005 (4.2°K)	9.35×10^{-3} cm^{-1} (Ryter[31])	1.9918 (Ryter[31])

and coworkers[28] have proposed that this maximum occurs at the point where the Weiss field acting on a given rare earth impurity becomes comparable with the damping forces on this impurity. Above the peak the ΔH varies directly as the relaxation time, τ, of the impurity and below inversely with τ. The maximum value of 7 oe, would indicate an impurity content of the order of 0.1%. Such an impurity level would not affect the considerations of cubic anisotropy given above. However, such impurities did in several cases lead to the "giant anomalies" in the anisotropy energy as observed by Dillon[13] and discussed by Kittel.[29]

GADOLINIUM-IRON GARNET

The magnetization of GdIG has been attributed to the weak coupling of the rare earth ions on the 24 c sites with the ferric ions.[11] The problem is usually treated by assuming the coupling of the a and d sites is so strong that one may treat the iron sublattices as unaffected by the presence of the rare earth ions. Since the gadolinium ion is in a ^8S state, one may assume that it is not strongly damped,[30,31] and hence the early interpretation by Wangness[8] of ferrimagnetic resonance may be assumed to hold. The anisotropy constants and the g value associated with the c sublattice may be obtained from Eq. (1) by using the known values for the a-d iron sublattices determined from the YIG measurements.

A subtraction of the first order anisotropy constant of YIG from that of GdIG yields the contributions to K_1 from the rare earth sublattice. The experimental variation of this $(K_1)_c$ is plotted in Fig. 3 where the magnetization data of Pauthenet[11] have been used. Also the fact that Gd^{3+} is in an S state enables one to apply the crystalline field model of anisotropy discussed in connection with Eq. (3).[15–17] In comparison with YIG, one would expect that the D term would be more important for GdIG even if the constant has the same value in both cases. At $T=0$°K, this term varies as $D^2/g\beta H_{eff}$ where H_{eff} is the Weiss molecular field at the given ion. The Weiss field at the ferric ions is of the order of ten times that at the gadolinum ions and therefore the D contribution to the anisotropy of the gadolinium sublattice cannot be ignored. The experimental points in Fig. 3 have been fitted by a weighted combination of the $r(T)$ and $t(T)$ functions from Wolf's paper[16] and magnetization data taken from Pauthenet.[11] The c site has three two-fold axes which are permutated in orientation along respectively two ⟨110⟩ axes and one ⟨100⟩ axis of the unit cell. Since the local cubic axes are not aligned with the unit cell axes, the local contributions to the cubic anisotropy will be again reduced.[16,19] In this case, the reduction factor will be −0.321. The appropriate direction of the distortion axis of the c site is not clear to the authors. The weighting factors required for Fig. 3 are presented in Table (II) and are compared with typical a constants taken from paramagnetic resonance data on Gd^{3+} in a calcium fluoride cubic host crystal.[30–32] A positive sign for the a constant of Gd^{3+} in GdIG would not be unreasonable. However, the noncubic terms for this case become quite important.

The temperature variation of the g_{eff} of two GdIG samples is shown in Fig. 4. On referring to Eq. (1),

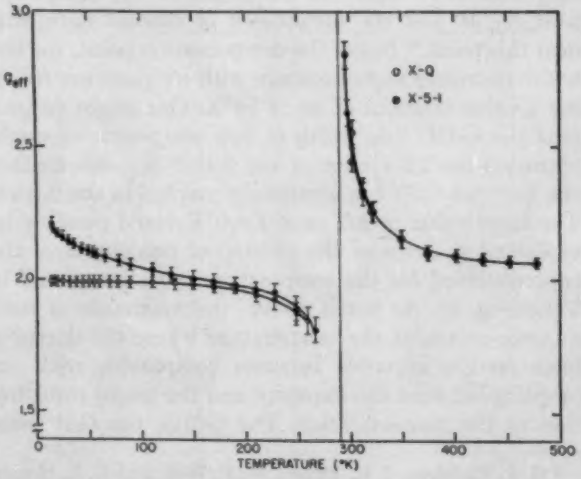

FIG. 4. Effective g factors as a function of temperature in GdIG.

[28] P. G. deGennes, C. Kittel, and A. M. Portis, Phys. Rev. **116**, 323 (1959).
[29] C. Kittel, Phys. Rev. Letters **3**, 169 (1959); also Phys. Rev. (to be published).
[30] W. Low, Phys. Rev. **109**, 265 (1958). (The c used in this reference is 2a of reference 18).
[31] C. Ryter, Helv. Physica Acta **30**, 354 (1957).
[32] J. M. Baker, B. Bleaney, and W. Hayes, Proc. Roy. Soc. (London) **A247**, 141 (1958). (The authors of this reference were unable to interpret the paramagnetic spectrum in terms of a cubic term.)

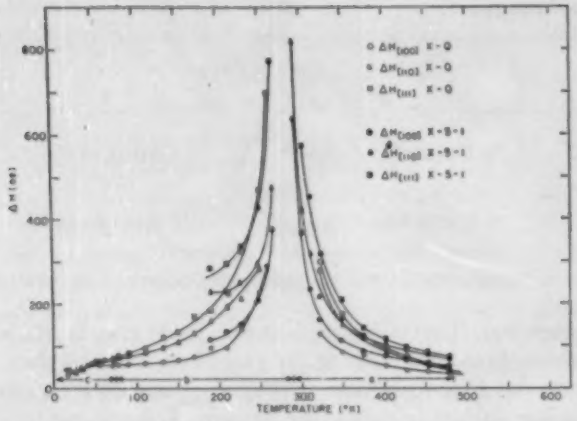

FIG. 5. Temperature variation of ΔH in GdIG.

one sees, as indicated in earlier work,[33–35] that the compensation point for the angular momentum must occur at a temperature higher than that of the magnetization in order to account for the dispersive shape of the curve near the compensation point (~295°K). By using Eq. (1) and magnetization data,[11] one finds that the g value of the c sublattice, g_c, is essentially independent of temperature for the purer crystals. It ranges from 1.994 ± 0.005 at 480°K to 1.999 ± 0.005 at 4.2°K, remaining approximately constant through the compensation point. The higher values previously reported by Calhoun and coworkers[35] may probably be attributed to impurities. For comparison, the g values of Gd^{3+} from paramagnetic resonance in calcium fluoride have been given in Table II.[30,31]

The line width of GdIG (Fig. 5) shows the "normal" anisotropy mentioned above and an enormous broadening at the compensation point. This broadening is probably associated with the rapid rise in the anisotropy field K_1/M and the breakdown of dipolar narrowing near this point.[36] Below the compensation point, the line width decreases monotonically with temperature reaching a value of about 45 oe at 14°K. One might suspect that the GdIG line width at low temperatures would approach the YIG value of less than 5 oe, since neither the Fe^{3+} nor Gd^{3+} ion is strongly coupled to the lattice. The large value of ΔH near $T=0$°K could possibly be explained in terms of the overlap of two curves of the type observed for the temperature variation of ΔH in YIG (Fig. 2). As noted above, the maximum of such a curve occurs at the temperature where the damping force on the impurity becomes comparable with the coupling between the impurity and the major contribution to the magnetization. For GdIG, the Gd^{3+} sublattice at low temperatures is the major contributor and the coupling is much less.[11] Hence, the temperature at which the peak occurs decreases. Therefore, the peaks from the Gd^{3+} and the Fe^{3+} sublattices should wash out to give the fairly flat region c in Fig. 5. The "giant anisotropy anomalies"[13,29] were also observed at the lowest temperatures.

ERBIUM AND HOLMIUM-IRON GARNET

As mentioned earlier Kittel and coworkers[9,28] have constructed a theory of ferrimagnetic resonance for particular garnets in order to account for early data on HoIG, ErIG, and DyIG.[32,6,34] The essence of this theory lies in the observation that at temperatures near 300°K the rare earth ions, which have a nonvanishing orbital angular momentum will individually be more strongly coupled to the lattice than to the other ferric and rare earth ions. The calculation of resonance under these conditions leads to Eq. (2) for the g_{eff}[9] and to an approximate expression for the line width[28]

$$\Delta H/H=H_{ex}(\gamma\tau). \tag{4}$$

This expression applies above the temperature at which the damping field (represented by $1/\gamma\tau$) and the exchange field (represented by H_{ex}) are comparable.

Figure 6 presents the experimental temperature variations of the g_{eff} in both polycrystal and single crystal samples of HoIG and ErIG. The curves both have a downward slope near room temperature as predicted by Eq. (2) and the magnetization data.[11] In fact, one would always expect a positive slope of the g_{eff} curve near room temperature since there all measured rare earth garnets have $(M_A-M_B)/M_A$ increasing with temperature. The dotted curve indicates the shape of the variation predicted by Eq. (2). The 5% discrepancy in the results could be easily attributed to errors in the magnetization values. The "damped c sublattice" model[9,28] seems to give a rather good account of the behavior of ErIG and HoIG g values.

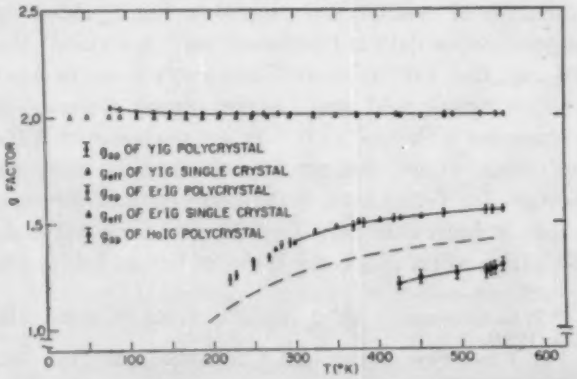

FIG. 6. Effective g factors as a function of temperature in YIG, ErIG, and HoIG. Upper curve YIG. Middle two curves ErIG. (Dashed curve theoretical. See text.) Lower curve HoIG.

[33] G. P. Rodrigue, J. E. Pippin, W. P. Wolf, and C. L. Hogan, Inst. Radio Engrs. Trans. PGMTT **6**, 83 (1958).
[34] B. Dreyfus, Compt. Rend. **241**, 552 (1955).
[35] B. A. Calhoun, W. V. Smith, and J. Overmeyer, J. Appl. Phys. **29**, 427 (1958).
[36] A. M. Clogston, J. Appl. Phys. **29**, 3, 334 (1958); S. Geschwind and A. M. Clogston, Phys. Rev. **108**, 49 (1957); E. Schlömann, J. Phys. Chem. Solids **6**, 242 (1958).

The temperature variation of the K_1 values of ErIG are presented in Fig. 7. It was found that the second order term K_2 is generally negligible over the temperature range considered. It would be difficult to make any definite statement about the interpretation of the rapid temperature rise of K_1 until the distribution of the energy levels of the $I_{15/2}$ state of Er^{3+} has been made clear. This distribution will be primarily dependent on the magnitude of the zero field splitting of the Er^{3+} manifold by the crystalline field of the c site. Although White and Andelin,[37] and independently, Ayant and Thomas[38] have to some extent clarified the level disposition, there still remain several undetermined parameters in the calculations. Therefore, an evaluation of the system's free energy in terms of these energy levels would not seem meaningful at present.

The dependence of ΔH on T for ErIG and HoIG has been plotted in Fig. 8 and Table III lists the approximate slopes of $\log\Delta H$ *vs* $\log T$. For both ErIG and HoIG the line width seems to be, roughly, inversely proportional to T^2. deGennes, Kittel, and Portis[28] have assumed that H_{ex} varies as $(1/T)$ for these garnets. From Eq. (4), our experimental results would imply a $(1/T)$ dependence for τ at temperatures near 300°K.

SAMARIUM- AND YTTERBIUM-IRON GARNET

The magnetization of both YbIG and SmIG exhibit unusual characteristics. The temperature variation and absolute magnitude of the magnetic moment of SmIG is virtually identical with that of YIG.[11] The negligible contribution of Sm^{3+} ions to the magnetization of SmIG is probably attributable to the small effective moment of the Sm^{+3} ions in the ground state.[39] A calculation of the magnetization of YbIG below $T=80$°K based on Pauthenet's data[11] reveals particularly large exchange coupling constants for Yb^{3+}. This calculation yields $n'=29$ (c-c coupling) and $n=76$ (ad-c coupling) compared to much smaller values calculated by Pauthenet for other rare earths (see Fig. 8 in reference 11). It seems clear from these considerations that the assumed sublattice dynamics of the Kittel model[9] may not be appropriate to SmIG and YbIG, since the exchange frequency may no longer be very much less than $1/\tau$.

TABLE III. Approximate slopes of linear portions of log ΔH vs log T curves.

Garnet	YIG (above 50°K)	GdIG (below 300°K)	YbIG	SmIG	HoIG	ErIG
100 direction	−0.84	+4.8	−1.8	−1.3		−1.8
111 direction	−0.87		−4.0			−2.1
Polycrystal			−2.0		−2.1	−2.0

[37] R. L. White and J. P. Andelin, Phys. Rev. **115**, 1435 (1959).
[38] Y. Ayant and J. Thomas Compt. Rend. **248**, 1955 (1959).
[39] J. H. Van Vleck, *The Theory of Electric and Magnetic Susceptibilities* (Oxford University Press, New York, 1932).

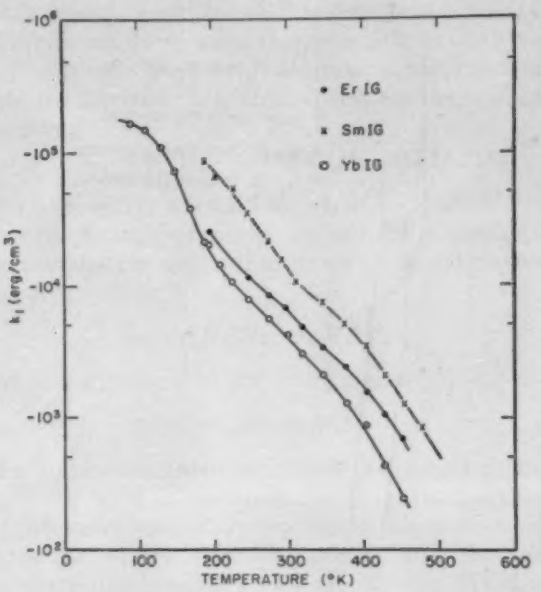

FIG. 7. Temperature variation of K_1 in YbIG, ErIG, and SmIG.

The temperature variation of the g_{eff} for these garnets, as shown in Fig. (9), does not particularly follow the prediction of Eq. (2). Both materials show a slight decrease in g_{eff} with decreasing temperature and indicates some of the Kittel interaction.[9] However, the magnitude of the decrease for YbIG is by no means large enough. The rapid rise at approximately 200°K does not fit the behavior of Eq. (2) at all. The rise for YbIG could be explained by using Eq. (1) and assuming that the magnetic compensation point, which is at approximately $T=0$°K for YbIG, lies below the angular momentum compensation point. If one considers the splitting of the Yb^{3+} state in a cubic field[37,40] this assumption is not

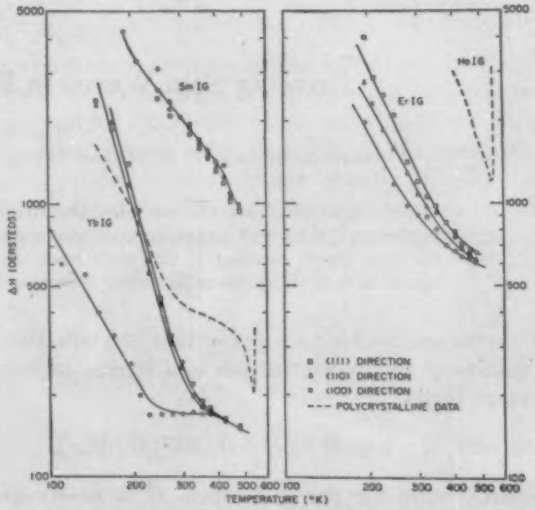

FIG. 8. Temperature variation of ΔH in YbIG, SmIG, ErIG, and HoIG.

[40] Y. Ayant and J. Thomas, Compt. Rend. **248**, 387 (1959).

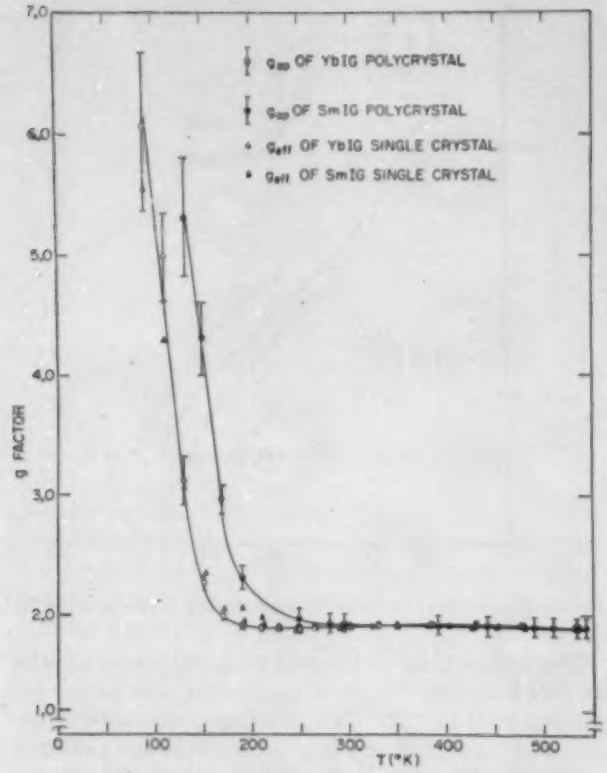

FIG. 9. Effective g factors as a function of temperature in SmIG and YbIG.

unreasonable since it appears that the angular momentum of Yb^{3+} will approach compensation much more rapidly than will the magnetic moment. Equation (1) indicates that g_e stays at a fairly constant value of approximately 3.9 near room temperature and drops to a value of approximately 1.0 at low temperatures. If the lowest two levels of Yb^{3+} in a cubic field are the only ones populated at low temperatures then the g tensor should be isotropic and equal to the Landé g value of 8/7. Since paramagnetic resonance measurements of Yb^{3+} in YGaG yield a fairly isotropic g value[41] at low temperatures, it seems that one is justified to first approximation in using the results of the cubic field calculations. No explanation for the g_{eff} behavior of SmIG is offered.

As in the case of the ErIG anisotropy data presented above, further clarification of the appropriate energy level systems must be available before one could hope to explain the temperature dependence of the K_1's of SmIG and YbIG, presented in Fig. 7. Again, the K_2 term did make a significant contribution to the anisotropy over the range of temperatures measured.

From Fig. 8 and Table III it may be noted that the variation in the YbIG line width along the hard and easy axes have considerably different temperature dependencies. For SmIG, there is a striking lack of anisotropy in the line width. There seems to be no definitive interpretation of these observations at the present time.

ACKNOWLEDGMENTS

The authors would like to express their appreciation for the interest and participation of Dr. C. L. Hogan and Dr. W. P. Wolf in the early phases of this work. Discussions with Professor N. Bloembergen have been invaluable.

[41] D. Boakes, G. Garton, D. Ryan, and W. P. Wolf, Proc. Phys. Soc. (London) (to be published); J. W. Carson and R. L. White, J. Appl. Phys. 31, 53S (1960).

JOURNAL OF APPLIED PHYSICS SUPPLEMENT TO VOL. 31, NO. 5 MAY, 1960

Growing Spin Waves in Ferrites in Unstable Equilibrium*

TOR SCHAUG-PETTERSEN
Microwave Laboratory, W. W. Hansen Laboratories of Physics, Stanford University, Stanford, California

This paper demonstrates that when the direction of the magnetic field in a saturated ferrite is inverted, spin waves occur which have an aperiodic exponential growth. The fastest growing of these waves have the time factor $\exp(\Omega_M t/2)$ and their wave vector is oriented at right angles to the magnetic field. The significance of these waves for ferrite switching and microwave pulse generation is discussed briefly.

IT seems reasonable to suppose that the equation of motion of the magnetization in a ferrite, including exchange forces,

$$d\bar{M}/dt = -\gamma \cdot \bar{M} \times [\bar{H} + H_{ex} l^2 \nabla^2 (\bar{M}/M_0)], \quad (1)$$

is equally valid for the case when $\bar{M}$ is nearly antiparallel to $\bar{H}$ as when it is nearly parallel to $\bar{H}$. The former case arises when a ferrite sample is saturated and the external field is suddenly reversed in direction, as in ferrite switching, or when 180° pulsing is used in the ferrite pulse generator proposed by Pound and analyzed by Silver and Levinthal[1] and by Morgenthaler.[2]

* This research was supported in part by a U. S. Air Force contract, monitored by the Air Force Office of Scientific Research of the Air Research and Development Command.

[1] S. Silver and E. C. Levinthal, Levinthal Rept. No. 106, Levinthal Electronics Products (1956).

[2] F. Morgenthaler, Inst. Radio Engrs. Trans. MTT-7, 1, 6–11 (1959).

In particular, the linear approximation for small deviations of $\bar{M}$ from the antiparallel direction must lead to Suhl's dispersion relation,[3]

$$\omega_k^2=\gamma^2(H_0-N_zM_0+H_{ex}l^2k^2)\times(H_0-N_zM_0+H_{ex}l^2k^2+4\pi M_0\sin^2\theta). \quad (2)$$

for plane spin waves traveling at an angle θ with the dc field.

The interesting point is that when $H_0-N_zM_0<0$, ω_k^2 can take on negative values. If $\omega_k^2=-\Omega_k^2$, the corresponding spin wave has the time factor $e^{\Omega_k t}$ or $e^{-\Omega_k t}$, depending on the initial condition. These waves are nontraveling; their components behave as $\cos(\bar{k}\cdot\bar{r})e^{\pm\Omega_k\cdot t}$, which cannot be resolved into traveling waves as in the case of a real ω_k.

The growing exponential $e^{\Omega_k\cdot t}$ is by no means excluded, energetically or otherwise. In fact, these spin waves do not gain or lose energy as they change their amplitude. As the spins move from their initial position antiparallel to the dc field, they lose potential energy, but this is compensated for by the volume demagnetizing fields and, for shorter wavelengths, by the exchange fields. The situation is very similar to the aperiodic motion of an inverted pendulum.

We shall now calculate the rate of growth of these unstable spin waves, putting $N_z=0$ for simplicity. Then

$$\omega_k^2=\gamma^2(H_0+H_{ex}l^2k^2)(H_0+H_{ex}l^2k^2+4\pi M_0\sin^2\theta). \quad (3)$$

For $0>H_0>-2\pi M_0$ the minimum of ω_k^2 occurs at $k=0$, $\theta=\pi/2$, and is

$$(\omega_k^2)_{\min}=4\pi\gamma^2H_0M_0=-|\omega_H\omega_M/2|, \quad (0>H_0>-2\pi M_0). \quad (4)$$

For $H_0<-2\pi M_0$, the minimum occurs at $H_0+H_{ex}l^2k^2+2\pi M_0=0$, and is

$$(\omega_k^2)_{\min}=-4\pi^2\gamma^2M_0^2=(\omega_M^2/4), \quad (H_0<-2\pi M). \quad (5)$$

For the latter case, the spin waves grow extremely rapidly. If $4\pi M_0=2000$ gauss, the amplitude grows by a factor e in about 0.05 μsec. Also, the number of unstable spin wave modes is extremely large, even for moderate field strengths. In a cylinder of 1-mm diam and 10-mm length, there are $\sim10^{13}$ unstable spin wave modes when $H_0=-10$ oe and $4\pi M_0$ has the above value.

For $0>H_0-N_zM_0>-4\pi M_0$, the unstable region reaches down to $k=0$, and we therefore should expect to find exponentially growing magnetostatic modes. It is easily seen that these exist. To take a particular example, the 200 mode in a ferrite sphere has the resonant frequency

$$\omega_{200}=\gamma[(H_0-4\pi M_0/3)(H_0+28\pi M_0/15)]^{\frac{1}{2}},$$

which is imaginary when $0>H_0-4\pi M_0/3>-8\pi M_0/15$. As another example, consider the uniform precession in a circular disk, magnetized in its own plane. The resonance frequency is

$$\omega_r=\gamma[H_0(H_0+4\pi M_0)]^{\frac{1}{2}},$$

which is imaginary over the entire region

$$0>H_0>-4\pi M_0.$$

If a suitable magnetostatic mode is strongly excited before the field is inverted, the magnetization will probably move in a pattern resembling this mode during a large part of the "switching period," and this may give interesting possibilities for experiments. When instead the spin waves all grow from their thermal amplitudes, the magnetostatic modes are too few to have much influence, and the plane wave approximation may be used.

It is possible by the spin-wave theory to calculate the dynamic behavior of the average magnetization during the first part of the switching period, and such calculations will be presented on a later occasion. Here we shall only observe that the fastest growing spin waves always have $\theta=90°$. Thus after the initial thermal disturbances have had time to grow for a while, the direction of the magnetization tends to vary much more rapidly in the $\theta=90°$ direction than in the $\theta=0$ direction. This indicates that later in the switching period it may be a valid approximation to assume that the direction of the magnetization is constant along $\theta=0$. This fact lends some support to the type of switching model suggested by W. L. Shevel.[4]

In conclusion, the presence of exponentially growing spin waves in a ferrite in unstable equilibrium has been demonstrated. These spin waves seem to offer a partial explanation to the short switching times observed in ferrites, in that they show how rapidly an initial disturbance develops. Their presence also seems to make the ferrite pulse generator with 180° pulsing impractical.

[3] H. Suhl, J. Phys. Chem. 1, 209–227 (1957).

[4] W. L. Shevel, J. Appl. Phys. 30, 475 (1959).

Nucleation Experiments on Thin Magnetic MnBi Films*

LUDWIG MAYER
Mechanical Division, General Mills, Inc., Minneapolis, Minnesota

Experiments devised to provide information about the nucleation probability of ferromagnetic MnBi films are described. These experiments revealed that uniform magnetic MnBi films grow from only a few randomly distributed nucleation sites. Thus nucleation is of considerable importance in the preparation of magnetic MnBi films. Further studies aimed at controlling this nucleation behavior are therefore indicated. First experiments directed toward this goal showed that 100% nucleation occurs if the Mn-Bi layer which is to be transformed is deposited on an already formed magnetic MnBi film. The magnetic field of this premagnetized MnBi film substrate is the cause for the development of extremely large domains but the high efficiency of nucleation seems to stem simply from the direct contact with the already finished MnBi film substrate.

OBSERVATIONS made during the vacuum heat treatment necessary to develop ferromagnetic MnBi films from their nonmagnetic constituents[1] suggested that the nucleation behavior of this transformation might be one of the causes for the poor reproducibility in the preparation of MnBi films. Experiments were therefore devised to provide information about the nucleation probability in such films. For that purpose two types of films were prepared after Williams *et al.*[2] on glass disks of 25 mm diameter. One type of film contained the Mn-Bi layer uniformly deposited across the entire area of the disk; the other type consisted of a two-dimensional array of small squares (0.4×0.4 mm^2) of this Mn-Bi double layer prepared by vacuum evaporation through a grid. All the disks of these two types were deposited in one and the same evaporation run and together were subjected to the same vacuum heat treatment. In successful heat treating runs the disks containing uniform Mn-Bi double layers were transformed completely into perfect homogeneous ferromagnetic MnBi films across the entire disk area. However, only a few randomly distributed squares of the two-dimensional array were transformed at the same time into squares of ferromagnetic MnBi film. The micrograph of Fig. 1 shows an example in which only about 75 randomly distributed squares of the total of 1060 squares had become ferromagnetic. (The magnetic squares have been made visible by a kind of deterioration—nondeterioration effect described in a previous article.[1] This discrimination method was used here because the equipment available did not permit viewing of the entire disk with a Kerr magneto-optic arrangement.) Figure 2 shows by means of the Kerr magneto-optic effect two micrographs of one area containing one square of magnetic MnBi surrounded by squares which remained nonmagnetic. In Fig. 2(a) the analyzer was set approximately $+5°$ off the crossed analyzer-polarizer position; in Fig. 2(b) the setting was about $-5°$. The disk containing this square had been subjected to a magnetic field capable of magnetizing the MnBi film to saturation. This had been done because the comparatively small antiparallel domains in the magnetic square would have required a large magnification, thus restricting the area which could be viewed to only a portion of one square.

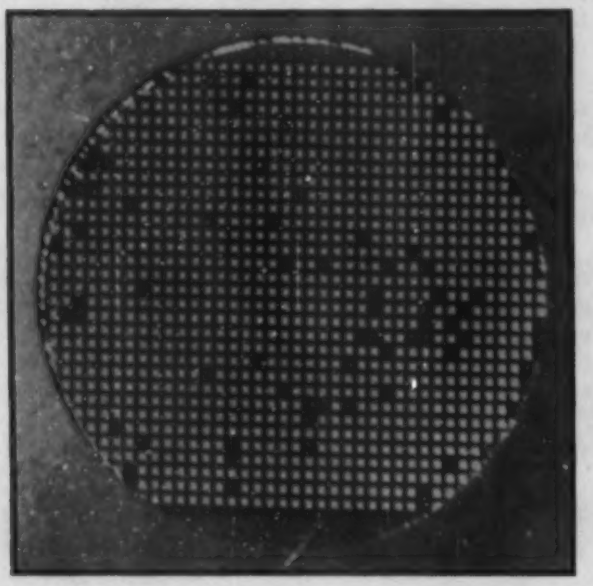

FIG. 1. Randomly distributed nucleation of magnetic MnBi films. Magnification approximately 2.7X.

From the experimental evidence described one must conclude that the nucleation behavior is of considerable importance in the preparation of magnetic MnBi films because such films apparently nucleate on only a few randomly distributed sites. From these sites a MnBi film can then grow uniformly across an entire disk. If this growth is inhibited on borders, as in the array of squares, most of the Mn-Bi layer will not be transformed into magnetic MnBi films, despite the fact that the evaporation procedure and vacuum heat treatment are identical for all squares of one disk and all disks of one run.

A few more experiments were made as first steps toward the goal of controlling the nucleation behavior. In these experiments the Mn-Bi layer squares were

* This research was supported by the Aeronautical Research Laboratory WCLJL, WADC.

[1] Ludwig Mayer, J. Appl. Phys. 31, 346 (1960).

[2] H.J. Williams, R.C. Sherwood, F. G. Foster, and E. M. Kelley, J. Appl. Phys. 28, 1181 (1957).

deposited on a previously prepared uniform ferromagnetic MnBi film magnetized to saturation. This time all the newly deposited Mn-Bi squares became ferromagnetic, exhibiting extremely large domains, i.e., domains with dimensions approaching the size of the squares. Figure 3 shows a micrograph of magnetic MnBi film squares with domains sometimes covering nearly an entire square. Because in this experiment all newly deposited Mn-Bi layer squares had been transformed into a magnetic MnBi film, the substrate, i.e., the previously prepared magnetic MnBi film, had apparently seeded the layer above. One could argue that the magnetic field of the magnetized MnBi film substrate might be responsible for the 100% nucleation. That this is not the case can be shown by repeating the experiment after evaporating a SiO coating between the Mn-Bi layer of the squares and the magnetic MnBi film substrate. Despite the fact that the magnetic field at the Mn-Bi layer squares remained practically unaltered by such a thin SiO layer, the number of squares transformed into a magnetic MnBi film was now again far from 100%, although there were more transformed squares than when only the glass had been the substrate. The increase in the number of transformed squares may have its explanation in the fact that SiO layers often contain submicroscopic holes which allow nucleation through such holes from the ferromagnetic MnBi substrate. The dimensions of the antiparallel domains again approached in this case the size of the squares. In conclusion, one can state that magnetic MnBi films grow from a few randomly distributed nucleation sites. Nucleation as such is not influenced by the magnetic field originating in a substrate film; the size of the magnetic domains may well depend on such fields, however.

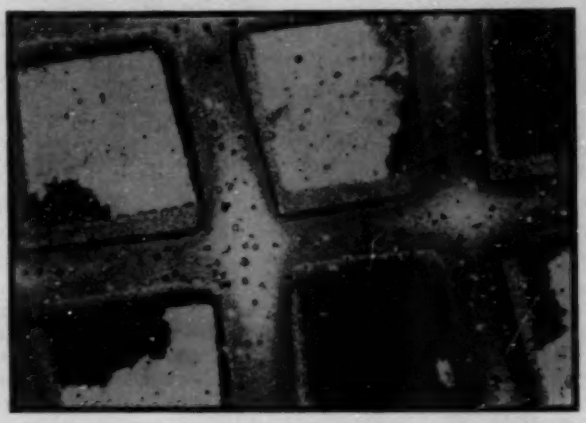

FIG. 3. Large antiparallel magnetic domains in MnBi film squares above previously prepared and premagnetized MnBi film. Magnification approximately 50X.

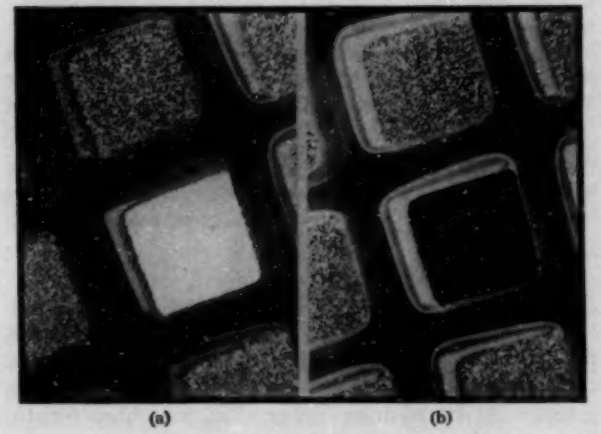

(a) (b)

FIG. 2. One premagnetized MnBi film square [bright in 2(a), dark in 2(b)] surrounded by Mn-Bi squares which remained nonmagnetic. Observation by means of the Kerr magneto-optic effect with a setting of +5° [in 2(a)] and −5° [in 2(b)] from the crossed analyzer-polarizer setting. Magnification approximately 40X.

Recent Developments in Ferromagnetic Resonance at High Power Levels

E. SCHLÖMANN
Raytheon Company, Waltham, Massachusetts

J. J. GREEN*†
Gordon McKay Laboratory, Harvard University, Cambridge, Massachusetts

AND

U. MILANO
Raytheon Company, Waltham, Massachusetts

The influence of inhomogeneities on the saturation of the ferromagnetic resonance is investigated. In the region of moderate power levels, the susceptibility at resonance χ'' varies linearly with the square of the rf field h. The magnitude of the slope $\partial\chi''/\partial h^2$ depends on the nature of the dominant scattering mechanism. If the uniform mode scatters primarily to spin waves of very large wavelength, the slope should be negative. Scattering to spin waves of short wavelength gives a positive contribution to the slope and can lead to a reversal of the sign. The theoretical predictions agree with measurements at X band on various polycrystalline garnets and ferrites.

At very high power levels the opening angle of the precessing magnetization vector approaches a limiting value, which is related to the "line width" ΔH_k of z directed spin waves having the same frequency as the uniform mode. Experiments on single crystals and polycrystals of rare earth substituted garnets show that ΔH_k increases approximately linearly with the rare earth content. The materials investigated contain Gd, Yb, Er, Sm, Dy, Ho, or Tb and for a given ratio of substitution ΔH_k increases in that order. The line width ΔH_k of z directed spin waves is found to be approximately proportional to the line width ΔH of the uniform mode as measured in single crystals.

Experimental results on cobalt and zinc substituted nickel ferrite are reported. ΔH_k increases linearly with the cobalt content. For the nickel-zinc ferrites with a large magnetic moment the saturation curve (χ'' vs h^2) measured at X band shows a maximum well below the initial onset of nonlinearity. A theoretical explanation for this extraordinary behavior is given.

A new nonlinear effect arising from spin wave instability in a microwave magnetic field applied parallel to the dc field has been observed. Spin waves which propagate in directions perpendicular to the dc field are most susceptible to this instability. The observed variation of the critical rf field strength agrees well with the theoretical predictions. It indicates that the spin-wave line width increases with increasing wave number and decreasing angle between propagation direction and dc magnetic field.

I. INTRODUCTION

IT has been known since the works of Damon[1] and of Bloembergen and Wang[2] that at sufficiently high power levels the phenomena of ferromagnetic resonance are quite different from those observed at low power levels. It is generally observed that the height of the absorption maximum decreases with increasing power level, and in addition a subsidiary absorption peak has been noticed at a dc field strength below that required for resonance. These effects were explained in a very satisfactory way by H. Suhl.[3] According to his theory the nonlinear effects are caused by the fact that some of the spin waves become unstable as soon as the amplitude of the uniform mode (which is driven by the applied microwave field) exceeds a certain critical value. Two possible mechanisms may be distinguished. For one of them, the unstable spin waves have half the frequency of the applied signal; for the other, they have the same frequency as the applied signal. In the following, these mechanisms will be referred to as nonlinear of first and second order. It has been shown by Suhl that the first order process is not allowed at resonance if the signal frequency exceeds a "characteristic frequency,"

$$\omega_c = 2N_\perp\omega_M. \tag{1}$$

Here, it is assumed that the sample is a spheroid magnetized along its axis, $\omega_M = \gamma 4\pi M$ (γ = gyromagnetic ratio, M = saturation magnetization), and $N_\perp$ is the transverse demagnetizing factor (equal to $\frac{1}{3}$ for a sphere). At frequencies higher than the characteristic frequency ω_c, the first-order process gives rise to the subsidiary absorption peak and the second-order process accounts for the saturation of the main resonance.

Suhl's theory has been very successful in accounting for many of the observed saturation effects. Thus, the critical field at which spin-wave instability sets in has been found to be much smaller at frequencies smaller than ω_c than it is at frequencies larger than ω_c.[4–6] The observed location of the subsidiary absorption peak agrees quite well with the theoretical prediction. For the case in which the first-order nonlinear process accounts for the saturation of the resonance, Suhl's theory predicts that the resonance susceptibility should fall off inversely proportional to the rf field strength. This behavior has also been confirmed experimentally.[3,6,7]

During the last year considerable progress has been made in understanding the saturation effects arising from the second order nonlinear process. In Suhl's original work[3] only the instability threshold had been

* The portion of the work performed by J. J. Green was supported by the Air Force Cambridge Research Center.

† Present address: Raytheon Company, Waltham, Massachusetts.

[1] R. W. Damon, Revs. Modern Phys. **25**, 239 (1953).

[2] N. Bloembergen and S. Wang, Phys. Rev. **93**, 72 (1954).

[3] H. Suhl, J. Phys. Chem. Solids **1**, 209 (1957); Proc. Inst. Radio Engrs. **44**, 1270 (1956); J. Appl. Phys. **29**, 416 (1958).

[4] E. G. Spencer, R. C. LeCraw, and C. S. Porter, J. Appl. Phys. **29**, 429 (1958).

[5] R. C. LeCraw, E. G. Spencer, and C. S. Porter, J. Appl. Phys. **29**, 326 (1958).

[6] E. Schlömann, J. H. Saunders, and M. H. Sirvetz, Trans. Inst. Radio Engrs. MTT-8, 96 (1960).

[7] E. G. Spencer, R. C. LeCraw, and C. S. Porter, *Symposium on Solid State Physics in Electronics and Telecommunications*, Brussels, 1958 (Academic Press, to be published).

calculated for this case. Recent extensions of the theory[9–10] have made it possible to analyze the complete saturation curve (the susceptibility at resonance as a function of the power level).

The physical idea which forms the basis of much of the recent work is very simple. It has been known that inhomogeneities contribute significantly to the width of the ferromagnetic resonance line.[11–13] This linebroadening can be understood as a scattering of energy from the uniform mode which is driven by the rf magnetic field to higher order modes of excitation (spin waves) that have the same frequency. The inhomogeneities that give rise to this scattering may be due to the randomness in the distribution of the various ions over the available sites[11] (this source is absent in single crystals of garnets, which contain only one type of rare earth ions or yttrium), to polycrystallinity in conjunction with crystalline anisotropy,[12,13] to nonmagnetic inclusions,[14–17] and to surface roughness.[18] Because of this scattering, those spin waves that have the right frequency are slightly excited by a uniform microwave field even at very low power levels, their amplitude being proportional to the driving field. At higher power levels the same spin waves are simultaneously subject to a time-varying coupling produced by the large amplitude of the uniform mode. The excitation of some of the spin waves (mainly those that propagate in the direction of the dc field and have the same frequency as the uniform mode) is greatly enhanced by this time-varying coupling. Even at powers below those required for instability, some of the spin waves are excited to a comparatively high level. The excitation varies smoothly as the power is increased beyond the point at which instability would occur in the absence of inhomogeneity broadening. The saturation curve, therefore, also does not exhibit a sharp threshold in the presence of appreciable inhomogeneity broadening.

It should be noticed that inhomogeneity broadening has a strong influence on the saturation of the resonance only in the case of the second-order nonlinear process. The spin waves which are important for the first-order nonlinear process have frequencies equal to half the signal frequency, and they therefore are not excited by inhomogeneities.

If the presence of inhomogeneities is taken into account in the theory, the calculated saturation curves agree quite well with the experimental results. At moderate power levels, the resonance susceptibility changes gradually, and finally decreases inversely proportional to the amplitude of the driving field at high power levels. Careful experiments on small samples of single crystals of yttrium garnet and gadolinium garnet have shown that the saturation curve exhibits a fine structure, superimposed on the general decline of the resonance susceptibility with increasing power level.[19] This fine structure can also be understood in terms of the existing theory[10] and arises from the fact that the spin-wave spectrum is discrete rather than continuous. From a quantitative interpretation of the fine structure the "exchange field" which characterizes the curvature of the spin wave band at $k=0$ can be inferred. The numerical value obtained in this way agrees closely with the value obtained from measurements of the specific heat at low temperatures.[20,21]

In the present paper, theoretical as well as experimental results concerning various aspects of ferromagnetic resonance at high power levels will be presented. In Sec. 2 the onset of saturation effects at moderate power levels will be discussed. It is shown that the resonance susceptibility should vary linearly with the square of the rf field strength in this range. The magnitude of the slope $\partial\chi''_{res}/\partial h^2$ depends on the nature of the dominant scattering mechanism. Experiments on polycrystalline samples are reported in which the scattering mechanism is modified by changing the composition of the sample, the grain size, and the location of the uniform mode with respect to the spin-wave band. In Sec. 3 the behavior at very high power levels is discussed. Experimental results on polycrystals and single crystals of yttrium garnet with rare earth substitutions are presented. Section 4 contains similar results on polycrystalline nickel-cobalt ferrites and nickel-cobalt ferrite-aluminates. In Sec. 5 we present a brief theoretical discussion of the unusual situation, in which the signal frequency is very close to the characteristic frequency given by Eq. (1). Experiments on polycrystalline nickel-zinc ferrites are reported. It is shown in Sec. 6 that at sufficiently high power levels a microwave magnetic field applied parallel to the dc field can also give rise to unstable growth of certain spin waves. Experiments on single crystals of yttrium garnet and manganese ferrite agree well with the theoretical predictions.

2. ONSET OF SATURATION EFFECTS AT THE MAIN RESONANCE

In the present section, we shall discuss the saturation behavior at moderate power levels for the case in which

[8] E. Schlömann, Bull. Am. Phys. Soc. Ser. II, **4**, 53 (1959).
[9] H. Suhl, J. Appl. Phys. **30**, 1961 (1959).
[10] E. Schlömann, Phys. Rev. **116**, 828 (1959).
[11] A. M. Clogston, H. Suhl, L. R. Walker, and P. W. Anderson, J. Phys. Chem. Solids **1**, 129 (1956).
[12] S. Geschwind and A. M. Clogston, Phys. Rev. **108**, 49 (1957); A. M. Clogston, J. Appl. Phys. **29**, 334 (1958).
[13] E. Schlömann, J. Phys. Chem. Solids **6**, 242 (1958).
[14] S. L. Blum, J. E. Zneimer, and H. Zlotnick, J. Am. Ceram. Soc. **40**, 143 (1957).
[15] E. Schlömann, Proc. Conf. Magnetism and Magnetic Materials (Boston, Massachusetts, Oct., 1956), p. 600.
[16] G. P. Rodriguez, J. E. Pippin, W. P. Wolf, and C. L. Hogan, Trans. Inst. Radio Engr. MTT-**6**, 83 (1958); W. P. Wolf and G. P. Rodrigue, J. Appl. Phys. **29**, 105 (1958).
[17] J. Snieder, Appl. Sci. Research **B7**, 185 (1958).
[18] R. C. LeCraw, E. G. Spencer, and C. S. Porter, Phys. Rev. **110**, 1311 (1958).
[19] E. Schlömann and J. J. Green, Phys. Rev. Letters **3**, 129 (1959).
[20] D. T. Edmonds and R. G. Petersen, Phys. Rev. Letters **2**, 499 (1959); **4**, 92 (1960).
[21] H. Meyer and A. B. Harris, J. Appl. Phys. **31**, 49S (1960).

$\omega > \omega_c$, so that the second order nonlinear process accounts for the saturation. It will be shown that in this range the susceptibility depends linearly on the square of the rf magnetic field,

$$\chi''/\chi_0'' = 1 - C(h/\Delta H)^2 + \cdots \text{(higher powers of } h/\Delta H). \quad (2)$$

Here χ'' is the negative imaginary part of the susceptibility at resonance, χ_0'' the value of χ'' realized at low power levels, ΔH the line width (full width), and h the amplitude of the microwave magnetic field, which will be assumed to be linearly polarized.

Equation (2) will later be derived on the basis of a microscopic theory, which will also lead to estimates of the magnitude of C. It is interesting to note, however, that the phenomenological equations proposed by Bloch[22] also lead to a result of the form (2). According to Bloch the saturation curve should be given by (see also footnote 2)

$$\frac{\chi''}{\chi_0''} = \frac{1}{1+\frac{1}{4}\gamma^2 h^2 T_1 T_2}, \quad (3)$$

where T_1 and T_2 are the longitudinal and transverse relaxation times, respectively.[23] Equation (2) is obviously a consequence of Eq. (3) and since $\gamma \Delta H = 2/T_2$, the constant C would equal

$$C_{\text{Bloch}} = T_1/T_2. \quad (4)$$

The experimentally observed values of C are typically between 10 and 100. This agrees in order of magnitude with theoretical expectations based on Eq. (4). It will be shown, however, that details of the experimental results, such as the dependence of C on the nature of the scattering mechanism, cannot be understood in terms of the phenomenological theory. In particular, C has been observed to be negative under certain conditions. This can certainly not be understood on the basis of Eq. (4), but it is consistent with the microscopic theory described below. In this paper, only a brief outline of the theory is presented. Details are given in footnote 10 and in a recent technical report.[24]

For convenience, a canonical formulation of the equations of motion is used. The Hamiltonian which determines the motion of the magnetization is

$$\mathcal{H} = \sum_k \omega_k u_k^* u_k + \frac{1}{2}\sum_{k\neq 0} g_k (u_0^2 u_k^* u_{-k}^* + \text{c.c.}) + \frac{1}{2}\sum_{k,k'\neq 0} \ell_{kk'} u_k^* u_{-k}^* u_k u_{-k'} + \sum_{kk'} P_{kk'} u_k^* u_{k'} - \gamma(h_0 u_0^* + \text{c.c.}), \quad (5)$$

where c.c. denotes the complex conjugate of the expression preceding it. The dynamic variables u_k are the amplitudes of spin waves, characterized by the propagation vector $\mathbf{k}$, and the equations of motion are

$$u_k = i\partial\mathcal{H}/\partial u_k^*. \quad (6)$$

The first term in Eq. (5) gives rise to the usual linear equations of motion and the ω_k are the spin-wave frequencies. The second term represents the important part of the nonlinear interaction between spin waves (with $k \neq 0$) and the uniform mode. Similarly, the third term represents the nonlinear interaction between spin-wave pairs. The coefficients g_k and $\ell_{kk'}$ are coupling constants which characterize the strength of this interaction. The fourth term arises from inhomogeneities. The coefficients $P_{kk'}$ form a hermitian matrix and are related to the Fourier components of certain random functions which describe the inhomogeneities present in the sample. The last term of Eq. (5) is the contribution of the rf magnetic field to the Hamiltonian. Here, $h_0 = h_{0x} + ih_{0y}$ represents the transverse components of the applied rf field.

The steady state solution of the equations of motion (6) can readily be obtained for the case in which the rf field is circularly polarized i.e., $h_0 \sim e^{i\omega t}$. As far as the uniform mode is concerned the result can be expressed in the form,

$$(\Omega_{0\text{eff}} - \omega) u_0 = \gamma h_0, \quad (7)$$

where $\Omega_{0\text{eff}}$ is an effective complex resonance frequency, which depends among other things on $|u_0|^2$. For the interpretation of most high power experiments, only the imaginary part of $\Omega_{0\text{eff}}$ is important, because the observations are performed at resonance where the real part of $\Omega_{0\text{eff}} - \omega$ vanishes. The susceptibility at resonance is then

$$\chi'' = \gamma M / \text{Im}\Omega_{0\text{eff}}. \quad (8)$$

In the range of moderate power levels, the effective resonance frequency can be expanded in powers of $|u_0|^2$. In this way, one obtains from the equations of motion as derived from Eqs. (5) and (6),

$$\text{Im}\Omega_{0\text{eff}} = \tilde{\eta}_0 (1 + C|u_0|^2), \quad (9)$$

where higher powers of $|u_0|^2$ are neglected. Here, $\tilde{\eta}_0$ is the decay constant of the uniform mode at low powers and contains an intrinsic part (η_0) and a contribution arising from inhomogeneities (η_0')

$$\tilde{\eta}_0 = \eta_0 + \eta_0'$$
$$\eta_0' = \pi \textstyle\sum_k |P_{k0}|^2 \delta(\omega_k - \omega), \quad (10)$$

where $\delta(\omega_k - \omega)$ is the Dirac delta function. The constant C can be expressed in terms of the coupling constants g_k and $\ell_{kk'}$, the spin-wave frequencies ω_k and the scattering coefficients P_{k0} as

$$C = C_1 + C_2$$
$$C_1 = \frac{\pi}{\tilde{\eta}_0} \sum_k g_k |P_{k0}|^2 \delta'(\omega_k - \omega)$$
$$C_2 = \frac{\pi^2}{\tilde{\eta}_0} \sum_{k'} \frac{\ell_{kk'}}{\eta_k} |P_{k0}|^2 |P_{k'0}|^2 \delta(\omega_k - \omega)\delta'(\omega_{k'} - \omega), \quad (11)$$

[22] F. Bloch, Phys. Rev. **70**, 460 (1946).

[23] P. E. Seiden and H. J. Shaw (J. Appl. Phys., this issue) have derived a similar result on the basis of the phenomenological equations proposed by H. B. Callen [J. Phys. Chem. Solids **4**, 256 (1958)].

[24] E. Schlömann, Technical Rept., No. R-48, Research Division, Raytheon Company (1959).

where $\delta'(\omega_k-\omega)$ is the derivative of the Dirac delta function, and η_k is the decay constant of a spin wave with propagation constant $\mathbf{k}$.

The deduction of Eqs. (9), (10), and (11) from the equations of motion (6) is quite straightforward and involves only one nontrivial approximation. This approximation consists of the neglect of scattering which does not involve the uniform mode. This is probably a good approximation in this range of power levels and it has generally been adopted in previous calculations.[11,13]

The susceptibility at resonance is now, according to Eqs. (8) and (9),

$$\frac{\chi''}{\chi_0''}=\frac{1}{1+C|u_0|^2}\approx 1-C|u_0|^2\approx 1-C\left(\frac{h}{\Delta H}\right)^2, \quad (12)$$

where the rf field is assumed linearly polarized and where higher powers of $h/\Delta H$ are neglected. The constant C of Eqs. (9), (11), and (12) is thus identical to that of Eq. (2).

A calculation of the coupling constants g_k and $\ell_{kk'}$ shows that both are of the same order of magnitude. The ratio of C_2 to C_1 is, therefore, approximately η_0'/η_k. In most cases of interest, this ratio is very large so that C_1 can be neglected in comparison with C_2. In order to obtain a numerical estimate of C_2 (and hence C), we shall discuss two limiting cases. At first, the scattering from the uniform mode will be assumed to be limited to spin waves with long wavelength. Later on, the scattering will be assumed to be essentially equally strong for all spin waves degenerate with the uniform mode.

If the coefficients $|P_{k0}|^2$ are appreciably different from zero only in the range of small wave numbers the uniform mode scatters only to spin waves of very long wavelength. Under typical experimental conditions, the important spin waves (those with large $|P_{k0}|^2$) then propagate in directions more or less perpendicular to the direction of the dc field.[25] It can be shown that the important coupling constants $\ell_{kk'}$ are, under these conditions,

$$\ell_{kk'}\approx-\omega_M/2. \quad (13)$$

From Eqs. (10), (11), and (13), therefore,

$$C\approx(\omega_M\eta_0'/2\bar{\eta}_0\eta_k)(\partial\eta_0'/\partial\omega). \quad (14)$$

In order to further simplify this expression, a theoretical estimate of the frequency dependence of η_0' can be used. It may be seen from Fig. 2 of reference 13 that $\partial\eta_0'/\partial\omega$ is >0 if the frequency of the uniform mode lies inside the spin wave band (extrapolated to $k=0$). A typical value is $4\eta_0'/\omega_M$. By using this estimate, therefore,

$$C\approx(2\eta_0'^2/\bar{\eta}_0\eta_k)\approx(2\eta_0'/\eta_k). \quad (15)$$

In the last step, we have assumed that $\bar{\eta}_0\approx\eta_0'$, an assumption that is frequently justified. It is interesting to note that the estimate (15) is quite similar to the theoretical prediction of the Bloch equation [Eq. (4)].

[25] An exception to this rule is the case of a thin disk magnetized perpendicular to its plane.

Consider now the other extreme in which the uniform mode scatters to all spin waves regardless of the wavelength. In this case, the inhomogeneity contribution to the line width is proportional to the total number of spin waves per unit frequency, which are degenerate with the uniform mode. It is known that this function increases with increasing ω in the range of interest. The coupling constants $\ell_{kk'}$ for nearly z directed spin waves can be shown to be

$$\ell_{kk'}\approx\omega_M(2N_\perp+1)/4. \quad (16)$$

The coupling constants $\ell_{kk'}$ are thus in part positive [Eq. (16)] and in part negative [Eq. (13)]. Thus, the constant C should be reduced as compared with the previous situation. Since the nearly z directed spin waves occupy a comparatively large volume of k space (they have the largest wave number of all spin waves degenerate with the uniform mode), it may be expected that the constant C can become negative under suitable conditions.

The theoretical treatment that has been described is based on the Hamiltonian (5). This Hamiltonian is approximate and neglects terms that are believed to be unimportant in the present context. It is not obvious that all terms which contribute significantly to C are taken into account. In particular, the scattering part of the Hamiltonian should, in general, contain terms of higher than the second order in the spin wave amplitudes. Such terms contribute to C. It can be shown, however, that this contribution is of order unity and can, therefore, probably be neglected to a good approximation.

The results concerning the magnitude of C can thus be summarized as follows: Scattering to spin waves with long wavelength leads to large positive values of C (approximately 10–100), if the uniform mode lies within the spin-wave band at $k=0$. Scattering to spin waves with shorter wavelength tends to decrease C and can lead to a reversal of the sign.

In a recent paper, H. Suhl[9] has discussed the influence of inhomogeneity scattering on the saturation curve. His approach is quite similar to the one described above. In the evaluation of his results, however, Suhl has introduced certain approximations, not used in the preceding discussion. As a consequence of these approximations, Suhl finds that the first deviation of χ'' from χ_0'' should be proportional to the fourth rather than the second power of h.

The linear dependence of the resonance susceptibility on the square of the rf field has previously been confirmed experimentally by Schlömann et al.[6] These experiments were performed at 1300 Mc on polycrystalline samples of a nickel ferrite-aluminate and various yttrium-gadolinium garnets. It has also been confirmed by Green and Schlömann[26] and by Seiden and Shaw[27] through measurements at X band on polycrystalline garnets. In order to test the theory in more detail, we

[26] J. J. Green and E. Schlömann, Trans. Inst. Radio Engr. MTT-8, 100 (1960).

[27] P. E. Seiden and H. J. Shaw, J. Appl. Phys. 31, 224S (1960).

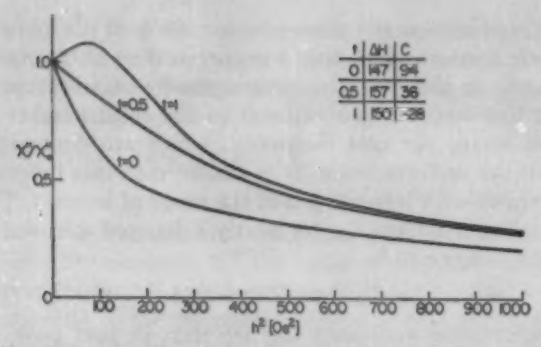

FIG. 1. Suceptibility at resonance as a function of power level for spherical samples of polycrystalline $5Fe_2O_3 \cdot 3Y_{2-t}Gd_tO_3$ ($t=0, 0.5, 1.0$) measured at X band. The materials chosen for this comparison have approximately the same line width.

have performed high power resonance experiments at X band on various ferrites and garnets. The scattering mechanism was modified in three ways:

1. Substitution of ions in a "pure" material (one in which all equivalent lattice sites are occupied by identical ions) by ions of a different kind. Example: Substitution of yttrium by gadolinium in yttrium garnet. The foreign ions provide an additional scattering mechanism which extends to relatively high wave numbers as compared to the anisotropy scattering in polycrystals. Hence, C should decrease with increasing substitution.

2. Variation of the grain size. Reduction of the grain size increases the scattering to z directed spin waves and should lead to a decrease of C.

3. Variation of the relative position of the uniform mode with respect to the spin wave band. This was achieved by using samples in the shape of long cylinders, and varying the orientation of the cylinder in the dc magnetic field. With the dc field along the axis of the rod, the uniform mode lies outside the spin wave band. When the rod is rotated the uniform mode enters the spin wave band and lies well within when the dc field is perpendicular to the axis of the rod. C should be

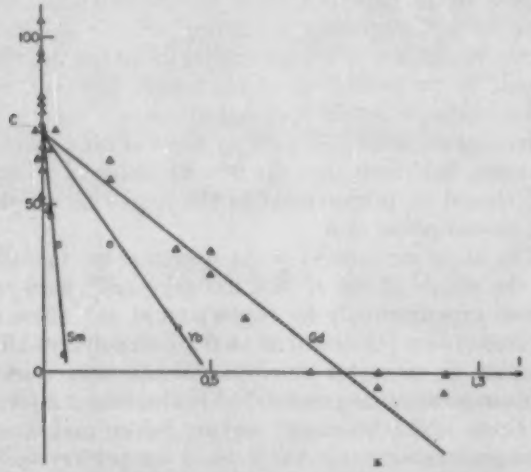

FIG. 2. Dependence of the constant C of Eq. (2) on the rare earth content of polycrystalline garnets of the type $5Fe_2O_3 \cdot 3Y_{2-t}Me_tO_3$, where Me=Gd(Δ), Yb(○), or Sm(□). Measured at X band on spherical samples.

largest when the uniform mode is degenerate with the upper edge of the spin wave band and should fall off towards both sides.

Figure 1 shows three saturation curves obtained at X band on spherical samples of polycrystalline yttrium-gadolinium garnets. Here the susceptibility is plotted vs the square of the rf field strength on a linear scale in order to demonstrate the validity of Eq. (2). The three samples differed in their gadolinium content as indicated in the figure. For a given gadolinium content, the line width of these materials can be varied appreciably by changing the firing conditions, and most of this additional linebroadening is apparently due to nonmagnetic inclusions (such as pores) in the sample.

It is evident from Fig. 1 that the constant C decreases with increasing gadolinium content, and has become negative for the sample with the highest gadolinium content. This is demonstrated more clearly in Fig. 2, which summarizes the results of a large number of measurements on mixed garnets containing gadolinium, ytterbium and samarium as substitutes for yttrium. Here, the constant C is plotted as a function of the composition characterized by the parameter t. The tendency of C to decrease with increasing t is quite apparent. It is also apparent, however, that other factors also influence the magnitude of C, since the measured points for a given composition cover an appreciable range. Similar results have been obtained with mixed nickel-cobalt ferrites.

The influence of the grain size on the magnitude of C has been studied in spherical samples of yttrium garnet. The grain size was varied by changing the particle size of the unreacted starting material and by changing the firing conditions. The results are summarized in Fig. 3. A small increase of C with grain size was observed in agreement with the theoretical predictions. The line width of polycrystalline yttrium garnet is apparently primarily caused by porosity.[18] Anisotropy broadening should be relatively unimportant. For this reason, the magnitude of C should primarily be correlated with the average pore size rather than the average grain size. It appears reasonable to assume that pore size and grain size are to some extent proportional. Under those conditions, a correlation between C and the grain size would be expected. It is conceivable that the deviations of the experimental points of Fig. 3 from a smooth curve can in part be explained by considerations of this kind.

Experimental results obtained at X band on a rod-shaped sample of yttrium-gadolinium garnet containing equal amounts of yttrium and gadolinium are summarized in Fig. 4. It can be shown that under resonance conditions for an infinitely long cylinder, the uniform mode lies above the spin-wave band if the angle between the magnetization vector and the rod axis is less than ϑ_0, where

$$\sin\vartheta_0=[1+(2\omega/\omega_M)]^{-\frac{1}{2}}. \qquad (17)$$

In general, the direction of the magnetization vector (ϑ) does not coincide with that of the magnetic field

(θ in Fig. 4). The difference is small, however, and can be taken into account. The arrow in Fig. 4 indicates the angle at which the uniform mode enters the spin wave band. It is seen that C goes through a maximum in the vicinity of this point in agreement with the theoretical predictions. The line width also varies significantly with the orientation. It is larger for those orientations for which the uniform mode is inside the spin wave band (extrapolated to $k=0$). This behavior is also predicted by the theory[12,13] and has previously been observed by C. R. Buffler[28] in experiments on spherical samples of yttrium garnet at frequencies in the vicinity of 3 kMc.

The data shown in Fig. 4 were taken on a rod with a length to diameter ratio of 10:1. Spherical samples of the same material exhibited a negative C of the order of -30. Very similar results have been obtained with a rod of yttrium garnet. In this case, C was positive for all orientations. C as well as ΔH showed the expected variation with orientation. Compared to the data on yttrium-gadolinium garnet the maxima occurred at slightly higher angles θ in agreement with Eq. (17).

3. SATURATION AT HIGH POWER LEVELS IN YTTRIUM GARNETS CONTAINING RARE EARTH SUBSTITUTIONS

It has generally been observed that at sufficiently high power levels, the resonance susceptibility decreases inversely proportional to the rf field strength. The behavior in this range of power levels can thus be characterized by a critical rf field strength h_w defined by

$$\chi''/\chi_0''=h_w/h. \tag{18}$$

This equation should be understood to be applicable only at sufficiently high power levels. Since the precession angle of the uniform mode is proportional to $\chi'' h$, Eq. (18) implies that the precession angle is not dependent on the power level. In order to determine h_w, it is convenient to plot χ'' vs $1/h$. The experimental results at high power levels, if plotted in this way, can usually be represented quite well by a straight line which extrapolates to the origin. In some cases, it was observed that with increasing power level the precession angle reaches a maximum and then decreases again. In these cases h_w was determined in such a way that

$$u_{0_{max}}=h_w/\Delta H \tag{19}$$

is the maximum precession angle. According to Suhl's theory[3] and the recent extensions of this theory[9,10,24] the square of the precession angle is proportional to the decay constant of the unstable (z directed) spin waves,

$$u_{0_{max}}{}^2=\Delta H_k/4\pi M. \tag{20}$$

Equation (20) neglects the effects of crystalline anisotropy. It is shown in reference 24 that in the presence of crystalline anisotropy a correction term proportional to the anisotropy field and dependent on the direction of the dc field with respect to the crystal axes must be added to the denominator on the right of Eq. (20).

Kittel and his collaborators[29] have shown that the presence of rare earth ions other than gadolinium in yttrium garnet leads to a rapid relaxation of the magnetic moment. This effect can be observed by noting the changes in the line width produced by rare earth substitution.[30,31] For polycrystals and at small degrees of substitution, this method is not reliable because the line width is then primarily determined by inhomogeneity broadening (arising from anisotropy, nonmag-

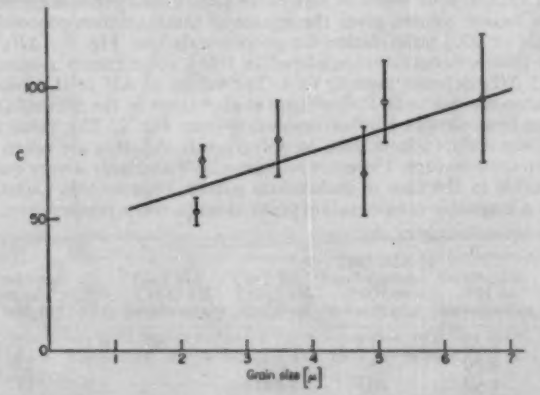

FIG. 3. Dependence of the constant C of Eq. (2) on the grain size for polycrystalline yttrium garnet. Measured at X band on spherical samples.

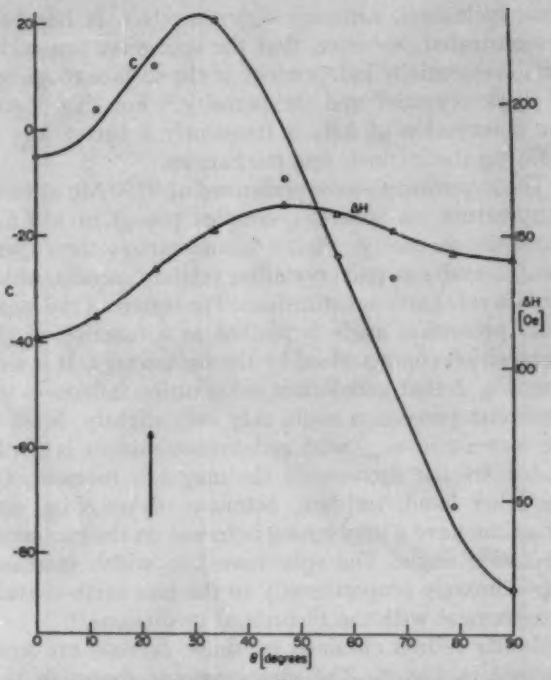

FIG. 4. Line width ΔH and C [Eq. (2)] as measured in a polycrystalline rod of $5Fe_2O_3 \cdot 3YGdO_3$ at X band. θ is the angle between the rod axis and the direction of the dc magnetic field. The arrow indicates the angle at which the uniform mode is degenerate with the upper edge of the spin-wave band.

[28] C. R. Buffler, J. Appl. Phys. **30**, 172S (1959).

[29] C. Kittel, Phys. Rev.; **115**, 1587 (1959). C. Kittel, and A. M. deGennes, C. Kittel, and A. M. Portis, Phys. Rev. **116**, 323 (1959).

[30] M. H. Sirvetz and J. E. Zneimer, J. Appl. Phys. **29**, 431 (1958).

[31] J. F. Dillon, Jr. and J. W. Nielsen, Phys. Rev. Letters **3**, 30 (1959).

netic inclusions, surface roughness, etc.). It has been demonstrated, however, that the spin-wave line width ΔH_k is essentially independent of the surface roughness of single crystals[32] and the porosity.[26] For this reason, the observation of ΔH_k is frequently a better way of studying the intrinsic loss mechanism.

The experiments were performed at 9250 Mc at room temperature on spherical samples placed in a TE_{202} transmission cavity. Figure 5 summarizes the experimental results on polycrystalline yttrium garnets, which contain rare earth substitutions. The square of the maximum precession angle is plotted as a function of the composition characterized by the parameter t. It is seen from Fig. 5 that gadolinium substitution influences the maximum precession angle only very slightly. Most of the increase in $u_{0_{max}}$ with gadolinium content is attributable to the decrease of the magnetic moment. On the other hand, terbium, holmium, dysprosium, and samarium have a very strong influence on the maximum precession angle. The spin-wave line width increases approximately proportionally to the rare earth content in agreement with the theoretical predictions.[29]

Similar results obtained on single crystals are summarized in Fig. 6. The measurements shown in this figure were carried out with the dc field along the [111] direction, which is the easy direction of magnetization. In some cases, the measurements were repeated with the dc field along the [100] direction. It was generally observed that the maximum precession angle was smaller in the latter case (typically by a factor of approximately 0.8). The observed dependence of $u_{0_{max}}$ on the direction of the dc field can in part be attributed to the anisotropy corrections mentioned in connection with Eq. (20) (see also reference 24). In part they must be attributed to an anisotropy in the spin-wave line width ΔH_k.

Comparison of Figs. 5 and 6 shows that in single crystals the rare earth substitutions are apparently more effective in enhancing ΔH_k than in polycrystals. This impression is a little misleading because measure-

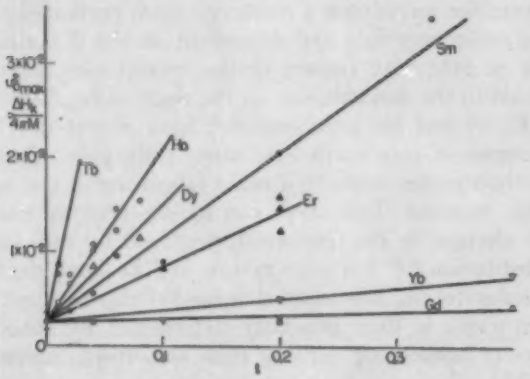

FIG. 5. Square of the maximum precession angle for polycrystalline garnets of the type $5Fe_2O_3 \cdot 3Y_{2-t}Me_tO_3$, where Me = Tb(■), Ho(○), Dy(△), Sm(●), Er(▲), Yb(▽), or Gd(□). Measurements on spherical samples at X band.

[32] R. C. LeCraw and E. G. Spencer, J. Appl. Phys. 30, 185S (1959).

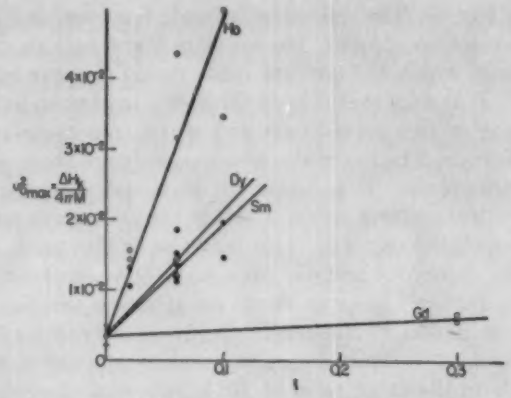

FIG. 6. Square of the maximum precession angle for single crystals of yttrium garnets containing rare earth substitutions. Symbols are the same as in Fig. 5.

ments on single crystals with the dc field along the [100] direction gave smaller values for $u_{0_{max}}^2$ which agreed fairly well with the data taken on polycrystals. The reasons for the rather large scatter of the experimental results obtained on single crystals are not completely understood. It is conceivable, however, that different crystals have received different amounts of the rare earth impurity.

Figure 7 shows the line width of single crystals of rare earth substituted yttrium garnets measured at room temperature. The line width of single crystals is found to be essentially proportional to the rare earth content. If the data on polycrystals were included in the present figure, the points would be scattered over an extremely broad region, particularly for small rare earth contents. This indicates that the line width of polycrystals is strongly dependent on physical parameters other than the rare earth content.

In Table I, the line width data on rare earth substituted yttrium garnets are summarized. The values of ΔH_k refer to z directed spin waves degenerate with the uniform mode in spherical samples. The sixth column shows that ΔH_k and ΔH are approximately proportional.

TABLE I. Line width in rare earth substituted yttrium garnets. The second column gives the square of the maximum precession angle at 10% substitution for polycrystals (see Fig. 5). ΔH_k in the third column is extrapolated to 100% substitution assuming that ΔH_k depends linearly on t. The values of ΔH in the fourth column are due to G. P. Rodrigue et al.,[33] those in the fifth column have been obtained by extrapolation from Fig. 7. The value for Tb was deduced from data on polycrystals. All data are taken at room temperature. The extrapolation of ΔH and ΔH_k is very questionable in the case of gadolinium garnet, because this material has a magnetic compensation point close to room temperature.

Me	$u_{0_{max}}^2 \times 10^3$ at 10% substitution	ΔH_k [oe] extrapolated to 100% substitution	ΔH [oe] $\mathbf{H} \parallel$ [111] Rodrigue	ΔH [oe] $H \parallel$ [111] extrapolated	$\frac{\Delta H}{\Delta H_k}$	Number of 4f electrons in Me^{3+}
Gd	0.33	13		80	6.1	7
Yb	0.50	47	270		5.7	13
Er	1.42	203	1200		5.9	11
Sm	2.06	318	1900	1800	5.8	5
Dy	2.75	407		3200	7.9	9
Ho	3.91	603		5000	8.3	10
Tb	11.45	1910		16 000	8.4	8

At the present time no detailed explanation for the variation of ΔH observed in the rare earth garnets is available. It has been pointed out by Kittel[29] that the line width of gadolinium garnet should be much smaller than that of the other rare earth garnets. The Gd^{3+}-ion contains seven $4f$ electrons which combine according to Hund's rule in such a way that the ion has no orbital angular momentum. The spin-orbit interaction will, therefore, be very small and cannot lead to a rapid relaxation as in the case of the other rare earth ions. The number of $4f$ electrons in the triply ionized rare earth ions is given in the last column of the table.

4. NICKEL-COBALT FERRITES

It has previously been observed that in polycrystalline nickel-cobalt ferrites the line width decreases with increasing cobalt content in the range of small degrees of substitution. The line width reaches a minimum at approximately 3% substitution and then increases again. This has been attributed to the fact that small cobalt substitutions tend to decrease the effects of crystalline anisotropy.[15,34,35] Since nickel ferrite has a negative anisotropy constant K_1 and cobalt ferrite has a very large positive one, a compensation of the crystalline anisotropy is expected in the range of a few percent substitution. Figure 8 shows the extraordinary dependence of ΔH on the cobalt content, which was described above. $u_{0_{max}}{}^2$, however, (and, therefore, ΔH_k since M is nearly constant) increases approximately linearly with the cobalt content. C decreases with increasing cobalt content in agreement with the theoretical predictions described in Sec. 2.

Similar results have been obtained in a series of related materials in which the iron was partially replaced by aluminum. These materials have a lower saturation magnetization. Line width and maximum precession angle depend on the cobalt content in the same manner as for the nickel-cobalt ferrites shown in Fig. 8.

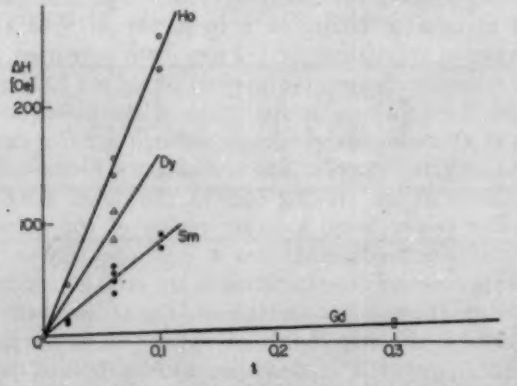

FIG. 7. Line width of spherical single crystals of yttrium garnets containing rare earth substitutions. Symbols are the same as in Fig. 5. Measured at X band with the dc field along a [111] direction.

[33] G. P. Rodrigue, H. Meyer, and R. V. Jones, J. Appl. Phys. 31, 376S (1960).
[34] M. H. Sirvetz and J. H. Saunders, Phys. Rev. 102, 366 (1956).
[35] J. E. Pippin and C. L. Hogan, Trans. Inst. Radio Engrs. MTT-6, 77 (1958).

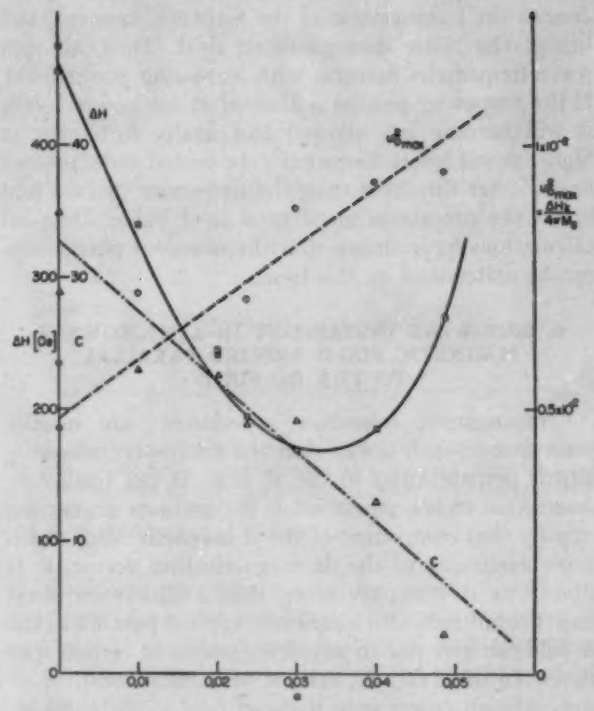

FIG. 8. Line width ΔH(□), square of the maximum precession angle $u_{0_{max}}{}^2$(○), and C [Eq. (2)] (△) for spherical samples of polycrystalline $Ni_{1-a}Co_aFe_{1.9}Mn_{0.02}O_4$ as a function of the composition.

5. NICKEL-ZINC FERRITES

It is known that zinc substitution in nickel ferrite increases the low temperature saturation magnetization and decreases the Curie temperature.[36] The saturation magnetization measured at room temperature at first increases with the zinc content, then reaches a maximum and finally decreases again. In the range between 30 and 50% substitution, the saturation magnetization is large enough to permit saturation through the first order nonlinear process in spherical samples at our signal frequency of 9.25 kMc [see Eq. (1)]. If the first order nonlinear process is only barely allowed, as is the case here, the saturation curve (χ''_{res} vs h) exhibits unusual properties. In the first order region ($\omega<\omega_c$) the susceptibility has usually been found to decrease as $1/h$ in all of the nonlinear range.[3,7] We have found that if ω is only slightly smaller than ω_c, the susceptibility decreases with power level less rapidly than $1/h$, reaches a plateau or even a maximum and then decreases approximately as $1/h$ at very high power levels.

This behavior is quite consistent with the theory we have described (see also footnotes 10 and 24). It is necessary, however, to take into account the fact that all spin wave frequencies are dependent on the excitation of the uniform mode and that of all other spin waves. This consideration is also important in the interpretation of the fine structure[19] mentioned in Sec. 1. The physical origin is the fact that the excitation de-

[36] E. W. Gorter, Phillips Research Rept. 9, 295–365 and 403–443 (1959).

creases the z component of the magnetic moment, and hence, the static demagnetizing field. Thus, all spin wave frequencies increase with increasing power level. If the first-order process is allowed at low power levels, it will become less allowed and finally forbidden at higher power levels. Eventually the second-order process has a lower threshold than the first-order process and limits the precession angle to a fixed value. Detailed calculations have shown that the observed phenomena can be understood on this basis.

6. SPIN-WAVE INSTABILITY IN A MICROWAVE MAGNETIC FIELD APPLIED PARALLEL TO THE DC FIELD

Ferromagnetic resonance experiments are usually performed in such a way that the microwave magnetic field is perpendicular to the dc field. It can readily be shown that at low power levels the resonance is excited only by that component of the rf magnetic field, which is perpendicular to the dc magnetization vector. It is interesting to note, therefore, that a microwave magnetic field of sufficient amplitude applied parallel to the dc field can give rise to unstable growths of certain spin waves. In this case, the sample will, under ideal conditions, absorb power only if the rf field exceeds the instability threshold.

This instability occurs by virtue of the fact that for some of the elementary excitations (spin waves) the precessing magnetization vector follows an ellipsoidal rather than a circular cone. A simple derivation of the stability criterion may be obtained by considering the equation of motion for the uniform magnetization of a thin disk magnetized in its plane. If α_x and α_y are the directional cosines of the magnetization vector with respect to the x and y axes, the equations of motion are

$$\begin{aligned}\dot{\alpha}_x &= -\gamma(H+4\pi M)\alpha_y - \gamma H_1 \cos\omega t\,\alpha_y \\ \dot{\alpha}_y &= \gamma H\alpha_x + \gamma H_1 \cos\omega t\,\alpha_x.\end{aligned} \tag{21}$$

Here we have assumed that the plane of the disk is the xz plane and that the dc field H and the rf field H_1 are applied along the z direction. It is convenient to introduce a new dynamic variable

$$\alpha = (H)^{\frac{1}{2}}\alpha_x + i(H+4\pi M)^{\frac{1}{2}}\alpha_y \tag{22}$$

in terms of which the equations of motion become

$$\dot{\alpha} = i\{\omega_0\alpha + c\cos\omega t\,\alpha^*\}, \tag{23}$$

where $\omega_0=\gamma[H(H+4\pi M)]^{\frac{1}{2}}$ is the resonance frequency, the asterisk denotes the complex conjugate, and

$$c=\gamma H_1\omega_M/2\omega_0. \tag{24}$$

In Eq. (23) a time-varying term proportional to $\cos\omega t\,\alpha$ has been omitted because it does not lead to instability. By following the arguments described by Suhl[3] (see also reference 24) it is easily shown that Eq. (23) has an exponentially growing solution as soon as $c/2$ exceeds the decay constant η of the mode under consideration, provided that the resonance frequency of this mode equals half the signal frequency ω. The critical field is thus in the present case,

$$H_{\text{crit}}=\omega\Delta H/\omega_M, \tag{25}$$

where ΔH is the line width characteristic of the potentially unstable mode.

It is shown in reference 24 that, in general, the critical field for spin-wave instability in a microwave magnetic field applied parallel to the dc field is

$$H_{\text{crit}}=\frac{\omega}{\omega_M}\min\frac{\Delta H_k}{\sin^2\theta_k}, \tag{26}$$

where the minimum must be taken subject to the side condition,

$$\omega_k=\omega/2. \tag{27}$$

θ_k is the angle between the propagation direction and the field direction. Spin waves which propagate in directions perpendicular to the dc field (xy directed spin waves) are most susceptible to instability in the present case. At low internal dc field strengths, such spin waves have a finite wave number. As the internal dc field increases, the wave number decreases and becomes zero at a characteristic dc (internal) field strength

$$H_c=-2\pi M+[(2\pi M)^2+(\omega/2\gamma)^2]^{\frac{1}{2}}. \tag{28}$$

For internal fields larger than H_c the frequency condition (27) cannot be satisfied for xy directed spin waves. According to Eq. (26), the critical field should, therefore, increase with increasing dc field in this range ($H>H_c$). The dependence of the critical field on the dc field for $H<H_c$ is strongly influenced by the variation of ΔH_k with the wave number k. If ΔH_k increases with increasing k (as the experimental results indicate) the critical field has a minimum at $H=H_c$.[37]

The predicted spin-wave instability has been observed at room temperature in single crystals of yttrium garnet and manganese ferrite at a frequency of 9.42 kMc. Samples of approximately 1–2 mm diam were used, and the magnetic fields were applied along a [100] axis. Figure 9 shows oscilloscope traces of the pulses transmitted at various power levels through a TE_{102} cavity containing the sample. The nonlinearity becomes first noticeable at the trailing edge of the pulse. With increasing power level, a larger region of the pulse is affected. The nonlinearity sets in quite abruptly so that the experimental determination of the critical field from the scope traces is not ambiguous. The critical field determined in this way $H_1(\tau)_{\text{crit}}$ is dependent on the pulse length τ, however. It decreases with increasing pulse length in such a way that

$$H_1(\tau)_{\text{crit}}-H_{\text{crit}}\sim 1/\tau. \tag{29}$$

[37] It should be noticed that for $H>H_c$ the plane wave analysis predicts that the unstable modes have zero wave numbers. Under these conditions the plane wave analysis is not adequate since the normal modes are strongly influence by surface dipolar fields. A reqned calculation should be based on the exact mode spectrum.

Here, H_{1crit} is the critical field at infinite pulse length, and should according to the theory be given by Eq. (26).

Figure 10 shows a comparison of the experimental and theoretical dependence of the critical field on the dc field. The experimental points are obtained with a pulse length of 4μsec and a duty cycle of 8×10^{-4}. The pulse length correction of Eq. (29) has not been applied to the data. Preliminary measurements indicate that it would reduce the critical field by approximately 40%. The theoretical curves of Fig. 10 are based on the assumption that ΔH_k does not depend on the dc magnetic field. If this assumption is justified the observed variation of critical rf field with the dc field allows us to infer the variation of ΔH_k with the direction and magnitude of the propagation vector. On the low field side of the minimum of H_{1crit} at 1690 oe, the unstable spin waves have $k\neq0$ and $\theta_k=\pi/2$. The theoretical curve for $H<1690$ oe is based on the assumption that (for $\theta_k=\pi/2$) $\Delta H_k=A+Bk^2$. On the high field side of the minimum, the unstable spin waves have $k=0$ and $\theta_k<\pi/2$. The broken line is a theoretical curve based on the assumption that ΔH_k is not dependent on the direction of propagation. The full line is calculated with the assumption that (for $k=0$) $\Delta H_k=A+C\cos^4\theta$, where $C/A=0.86$. Thus, ΔH_k increases with decreasing θ_k. The theoretical curve of Fig. 10 incorporates a small correction arising from crystalline anisotropy. In the absence of anisotropy, the minimum of H_{1crit} should, according to Eq. (28), occur at an applied dc field of 1610 oe. Under the influence of crystalline anisotropy, the minimum is shifted towards higher field by the amount $-2K_1/M_s$ if the field is applied in the [100] direction.

The line width of xy-directed spin waves of long wavelength in yttrium garnet as inferred from these experiments is approximately 0.35 oe. The critical field for the onset of Suhl's subsidiary absorption[3] has also been measured on the same sample and was found to be approximately 1.05 oe (linearly polarized). The line

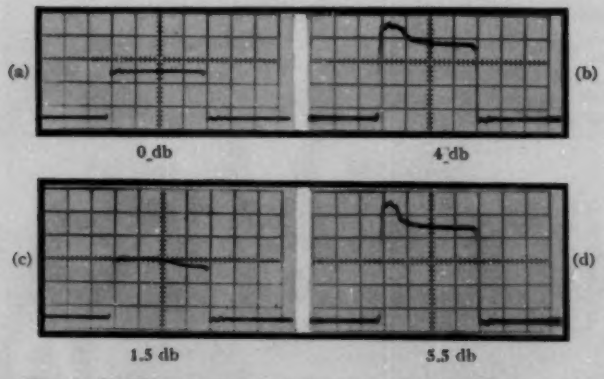

FIG. 9. Oscilloscope traces of the transmitted pulse at various power levels. The microwave magnetic field is applied parallel to the dc field. The spin-wave instability reduces the pulse height at the trailing edge. The numbers refer to the input power level.

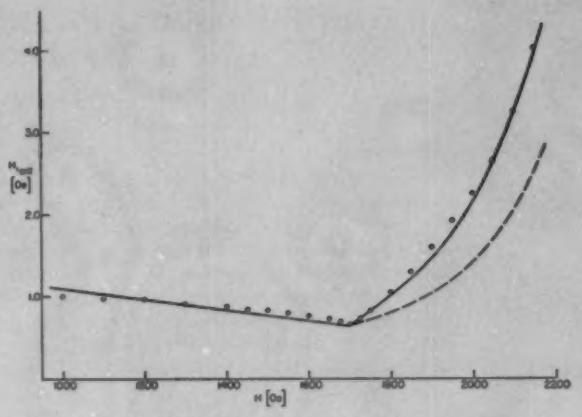

FIG. 10. Critical field for spin-wave instability as a function of the external dc field. Measurements on a spherical single crystal of yttrium garnet at a frequency of 9.42 kMc with the magnetic fields parallel to a [100] direction. The significance of the theoretical curves is explained in the text.

width of long wavelength spin waves with $\theta_k\approx45$ deg as inferred from the subsidiary absorption is approximately 0.52 oe. This agrees quite well with the value obtained from measurements with the rf field parallel to the dc field.

The line width of z directed spin waves of relatively short wavelength (approximately 1.4×10^{-5} cm) can be inferred from the maximum precession angle at the main resonance [see Eq. (20)]. Measurements on small spherical samples (polycrystals as well as single crystals) gave a line width ΔH_k of approximately 4 oe. The spin wave line width thus increases quite rapidly with the wave number. This agrees at least qualitatively with the dependence of ΔH_k on the wave number observed for xy-directed spin waves (see Fig. 10).

It should be noticed that in the present experiment it is not possible to distinguish between a field dependence and a k dependence of ΔH_k. For this reason, our conclusions concerning the k dependence of ΔH_k must remain tentative at the present time. It is conceivable that similar experiments at different frequencies will make it possible to determine unambiguously both the field and the k dependence of the spin wave decay constants.

ACKNOWLEDGMENTS

The samples used in the experiments were in part prepared at Harvard University by L. Lin, F. Molea, and C. Quadros, and in part in the Raytheon Research Division by Dr. S. L. Blum, W. Griffin, and A. E. Paladino. The determination of the grain size was carried out by D. A. Belforti. The authors are particularly grateful to Dr. M. H. Sirvetz and Prof. R. V. Jones for many stimulating discussions. J. J. Green is greatly indebted to Dr. L. C. Hogan for his original suggestion to investigate the high power phenomena in ferrites and garnets.

Transfer Function and Error Probability of a Digital Magnetic Tape Recording System

JOHN WENCHUNG HUNG
IBM Product Development Laboratory, Poughkeepsie, New York

In spite of the complexities of the digital magnetic recording system, it has been discovered that the output of the system for the input of a unit step of current can be approximated by a Gaussian probability function $A\exp[-a(x-d)^2]$. The value "a" in $A\exp[-a(x-d)^2]$ is a figure of merit of the system.

This yields an analytic expression for the transfer function of the system. Experimental results correlate quite well with those based on this approximate transfer function.

Using this transfer function, the output of the system for any *Nonreturn to Zero* recording method can be predicted. For example, the reduction in system output with increasing bit densities is established. In addition, when Gaussian noise is introduced into the system, the error probability is obtained. The effect of the input rise time to the output amplitude is discussed.

I. INTRODUCTION

THE performance of the digital magnetic recording system can be judged by its transfer function. Generally, this transfer function gives information about the gain of the system with respect to bit density. Once the transfer function is known, the output voltages and waveforms may be evaluated for any desired form of digital recording.

II. A TRANSFER FUNCTION

A transfer function of a system can be expressed as the ratio of Laplace transform of the output to that of the input. When a unit step function is applied to the input of the magnetic recording system, the output can be approximated by a Gaussian function $A\exp[-a(x-d)^2]$ as shown in Fig. 1.

The solid line output in Fig. 1 indicates the experimental system output, while the dotted line shows the calculated waveform of $A\exp[-a(x-d)^2]$. The value a in $A\exp[-a(x-d)^2]$ is a figure of merit and is a function of many parameters such as: permeability of head material, magnetic surface characteristics, spacing between head, and recording medium as well as write current; d is the delay between input and output. A large value of figure of merit a is necessary to make the resolution of the recording system good. Then in terms of the Laplace transform, a transfer function $G(s)$ is given by[1]:

$$G(s)=A(\pi/a)^{\frac{1}{2}}s\cdot\exp(s^2/4a)\exp(-ds). \quad (1)$$

The factor s in the transfer function represents a differentiating process which is commonly used in describing the simplest model of a recording system. That is, the voltage induced in the read coil is proportional to the rate of change of flux caused by recorded magnetization on the tape. This term by itself would indicate that the output voltage amplitude should increase with frequency. In contrast the term $\exp(s^2/4a)$, in addition to affecting the shape of the output, results in a decrease of the output amplitude with frequency. A similar transfer function $G'(s)$ can be obtained when the input has a rise time T,

$$G'(s)=A(\pi/a)^{\frac{1}{2}}s\cdot\exp(s^2/4a)\exp(-ds)/[1-(1/4s^2T^2)]. \quad (2)$$

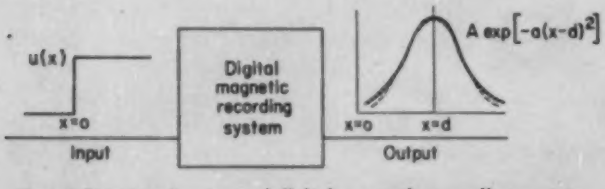

FIG. 1. Input and output of digital magnetic recording system.

To test the concept of a transfer function the output of a digital magnetic recording system was obtained both theoretically and experimentally. For this purpose magnetic tape was magnetized to saturation in alternate directions each time a *one* was recorded but allowed to remain in the previous state of saturation each time a *zero* was recorded. This method of recording is called *Modified Nonreturn to Zero*.[2] For information consisting of *ones*, only, the input to the recording system is a constant current square wave whose pulse width δ corresponds to the reciprocal of bit density. For this case, using the transfer function and assuming that superposition of pulses is valid, the output voltage of the magnetic recording system is:

$$e_{out}(\delta)=A\sum_{n=-\infty}^{\infty}(-1)^{n-1}\exp(-an^2\delta^2). \quad (3)$$

Similar expressions can be obtained for different inputs to the recording system and different recording methods. These results could also have been obtained directly by superposition.

The theoretical results correlate quite well with those obtained by experiment (curves 1 and 1*A*, Fig. 2), and thus the concept of superposition of pulses appears to be a valid one. Superposition is implied here only in a

[1] J. Laning and R. Battin, *Random Processes in Automatic Control* (McGraw-Hill Book Company, Inc., New York, 1956).

[2] Footnote 1, p. 330.

limited sense. Due to the nonlinearities of the magnetic recording system different output waveforms will be obtained, for example, for different write current amplitudes. Thus, this method will predict the performance of the system only if the parameters in the transfer function are adjusted in accordance with the shape of a single output pulse for a particular set of conditions. It is, therefore, not surprising that a transfer function which can predict quite accurately the behavior of a digital recording system fails to do so for sinusoidal recording (curve 3, Fig. 2). For this case, only qualitative results can be obtained.

III. ERROR PROBABILITY

At high recording densities the bit length is small. This causes the output pulses to overlap and the

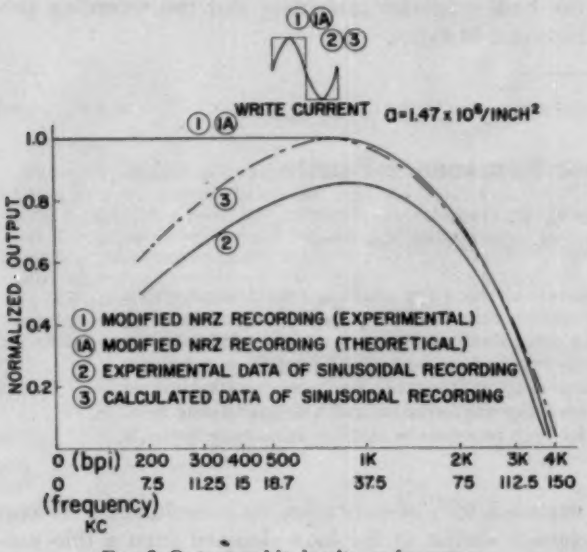

FIG. 2. Output *vs* bit density or frequency.

amplitude to decrease (curve 1, Fig. 2). In the presence of noise this reduction in amplitude may cause errors in the information.

The mathematical formulation of noise in a magnetic tape system is made difficult by the fact that noise and defects in the magnetic surface produce a complex error dependence. In this analysis only Gaussian noise was assumed together with amplitude sensing.

The probability of the normalized noise n/σ (σ is rms noise), exceeding a given μ_0 is given by the expression[3,4]:

$$p=\int_{u^0}^{\infty}(2\pi)^{-1}\exp(-u^2/2)du, \tag{4}$$

[3] R. K. Richards, *Digital Computer Components and Circuits* (D. Van Nostrand Company, Inc., Princeton, New Jersey, 1957).
[4] G. Goldman, *Frequency Analysis, Modulation and Noise* (McGraw-Hill Book Company, Inc., New York, 1948).

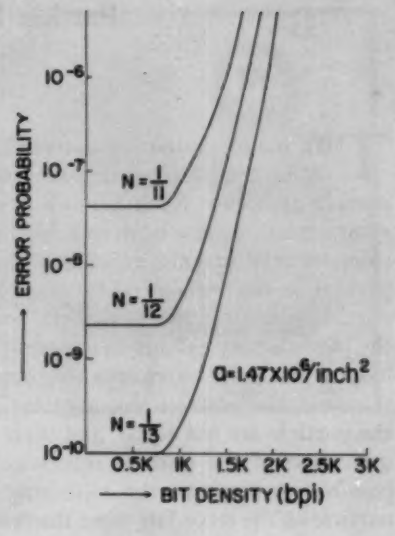

FIG. 3. Error probability as a function of bit density for modified *NRZ* recording.

and let

$$\mu_0=(e_{out}-e_T)/\sigma, \tag{5}$$

where e_T = amplitude of the sensing level.

There are two kinds of errors involved: (1) failing to detect a pulse when one is present and (2) detecting a pulse when one is absent. In order to have an equal probability for the above two types of errors (a symmetric channel), the sensing level e_T is set to $e_{out}/2$.

$$\mu_0=(e_{out}-e_T)/\sigma=e_{out}/2\sigma=(\text{signal-to-noise ratio})/2. \tag{6}$$

Since the relationship between the output amplitude and bit density is shown in Fig. 2, error probability *vs* bit density for the constant normalized rms noise σ can be evaluated and is shown in Fig. 3. For this particular value of a ($a=1.47\times10^6/\text{in.}^2$) the error probability remains unchanged under 800 bpi due to the fact that the output amplitude is constant up to this density.

IV. CONCLUSIONS

The output of the digital magnetic tape recording system due to the unit step function can be approximated by $A\exp[-a(x-d)^2]$. The transfer function of the system was derived, and output with respect to bit densities for *Nonreturn to Zero* recording was obtained. It was found that the theoretical results correlate quite well with the experimental results but that the transfer function is not valid for the sinusoidal recording. The error probabilities due to Gaussian noise were also evaluated.

V. ACKNOWLEDGMENT

The author is gratefully indebted to Dr. E. G. Newman for many valuable discussions and constant encouragement.

JOURNAL OF APPLIED PHYSICS SUPPLEMENT TO VOL. 31, NO. 5 MAY, 1960

Particle Interaction in Magnetic Recording Tapes

J. G. Woodward and E. Della Torre
RCA Laboratories, Princeton, New Jersey

THE magnetic coating of recording tape is assumed to be composed of an assemblage of small, single-domain particles. Each particle is assumed to having symmetrical, square hysteresis loop when the reversible component of magnetization is neglected and when the particle is not influenced by the fields of neighboring particles. When influenced by the fields of its neighbors, the particle may exhibit an asymmetrical loop when the loop is plotted relative to an external applied field. In this case, the positive and negative switching fields for the particle are not equal, and their difference gives an indication of the particle interaction. While it is not possible to measure the switching fields of a single particle on the recording tape, the distribution of switching fields in the assemblage of particles can be measured, along with the distribution of magnetic moments associated with the switching fields. The two switching fields and the magnetic moment define a 3-dimensional distribution function which describes the magnetic properties of the tape, and in terms of which both dc and anhysteretic magnetization processes may be described.

The distribution functions have been measured for two recording tapes. While the functions for the two tapes are markedly different in detail both show that particle interaction is very appreciable in recording tapes and that it is a significant factor in determining the bulk magnetic properties and the recording performance of tapes.

JOURNAL OF APPLIED PHYSICS SUPPLEMENT TO VOL. 31, NO. 5 MAY, 1960

Switching Behavior of Low Remanence Ferrite

F. B. Hagedorn and E. M. Gyorgy
Bell Telephone Laboratories, Incorporated, Murray Hill, New Jersey

Switching studies have been made on a low remanence ferrite. By using a sampling oscilloscope with a response time less than 5×10^{-10} second, switching times shorter than 5×10^{-9} second have been measured. About half of the flux in this ferrite appears to switch by nonuniform rotation, but even in small fields the remaining flux switches substantially faster than would be expected on the basis of nonuniform rotational reversal. This observation is interpreted as further evidence of the existence of a ferrite flux reversal process in which switching is speeded up by an interaction between the magnetization and a demagnetizing field. In contrast to square loop ferrites, the threshold field for both processes in this low remanence ferrite is approximately zero.

INTRODUCTION

A SEMIQUANTITATIVE description of high-speed flux reversal has been developed in recent years.[1] It has been shown that, in general, dynamic flux reversal occurs by domain wall motion in small applied fields, by nonuniform rotation in intermediate fields, and by uniform rotation in larger fields. The helical mode has been recently suggested as an illustrative model of the uniform rotational flux reversal in ferrite toroids.[2,3] In order to extend the experimental study of this high-speed mode, we have measured the switching characteristics of a low remanence ferrite. This material was selected for measurement because of the apparent high-speed switching properties of the reversible flux in square loop ferrites.

EXPERIMENT

The remanent induction of the ferrite used for these measurements is 6% of saturation ($B_s=2000$ gauss), and the induction resulting from an applied field of 3 oersteds is 95% of saturation. As a result, the B–H loop appears similar to the loop obtained from a thin anisotropic Permalloy film when the field is applied in the hard direction. The nominal ferrite composition is $Ni_{0.3}Zn_{0.7}Fe_2O_4$.

Switching times were measured as a function of the applied field for two initial magnetic states: remanence and saturation. The final state was saturation in both cases. For both measurements, the toroid was mounted coaxially in a coaxial transmission line. A coaxial mercury relay in the line was used to generate pulses with a rise time of about 5×10^{-10} second. When an initially saturated state was desired, the incoming pulse switched the toroid from remanence to saturation, and the leading edge of a reflected pulse was made to arrive at the toroid simultaneously with the trailing edge of the incoming pulse. The toroid was then switched from one saturated state to the other by the reflected pulse. Due to dispersion, attenuation, and reflection of the pulses by nonidealized components, the minimum transition time from the initial field pulse to the reflected field pulse was about 1.5×10^{-9} second.

A pickup loop encircled the toroid and came through a small hole in the wall of the coaxial line. A signal

[1] For a review of dynamic flux reversal processes, see E. M. Gyorgy, J. Appl. Phys. 31, 110S (1960).
[2] W. Lee Shevel, Jr., J. Appl. Phys. 30, 47S (1959).
[3] E. M. Gyorgy and F. B. Hagedorn, J. Appl. Phys. 30, 1368 (1959).

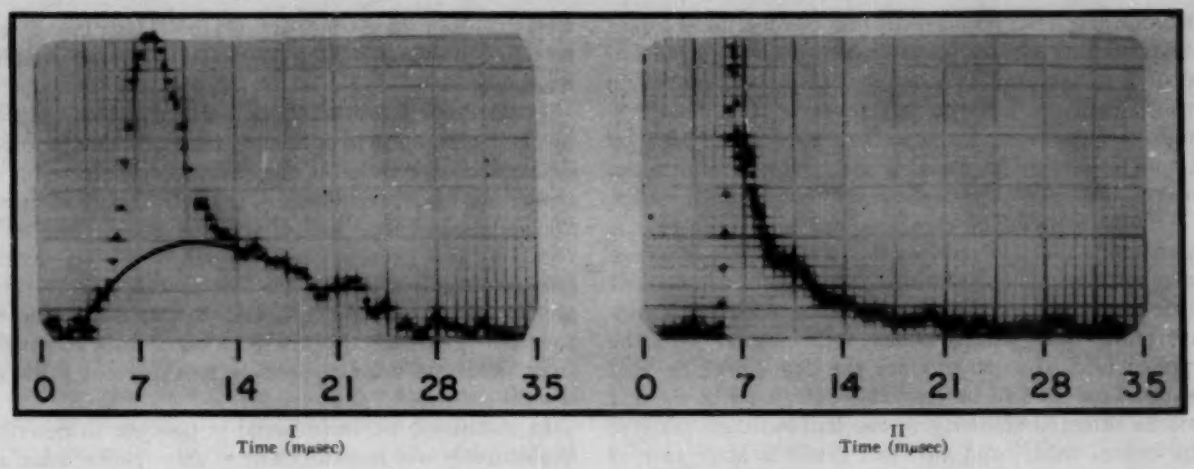

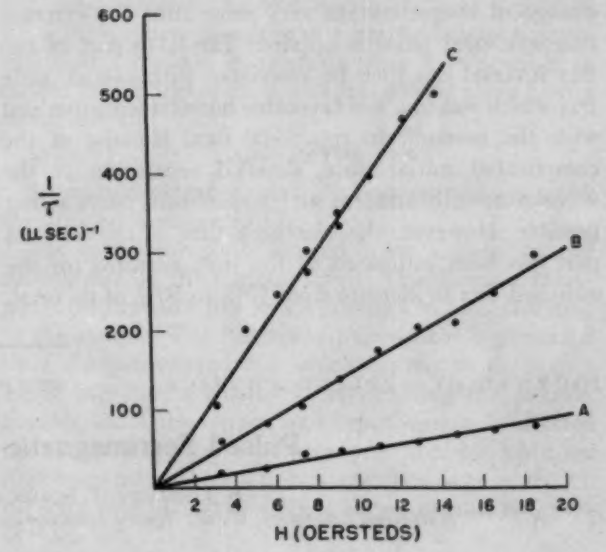

FIG. 1. Reciprocal switching time of a low remanence ferrite plotted as a function of the applied field. Curves A and B correspond to switching from one saturated state to the other, and inset I is a waveform typical for this process. Curve C is for switching from remanence to saturation, and the waveform associated with this process is shown in inset II. The applied field was 14.0 oersteds and the sweep speed was 3.5 mμsec for 5 small divisions for both insets. The solid line in inset I is an empirical separation of the waveform which is discussed in the text.

proportional to the time rate of change of magnetization of the toroid was generated on this loop, and this signal was displayed on a sampling oscilloscope whose effective response time was less than 5×10^{-10} second.

RESULTS

Typical signals are shown in insets I and II of Fig. 1. The waveform shown in I is characteristic of switching from one saturated state to the other while that shown in II is typical of switching from remanence to saturation. For both waveforms, the applied field was 14.0 oersteds and the sweep speed was 3.5 millimicroseconds for five divisions. The waveform in I apparently is composed of two parts. The solid line seen in I is an empirical separation of these two. Graphical integration of each as a function of externally applied field has shown that the flux is about equally divided between the two portions from 3 to 20 oersteds. The time required for the flux in each portion to increase from 10% to 90% of its respective total was then obtained from the integrals, and the reciprocals of these times are plotted in Fig. 1. Plot *A* corresponds to the slower process evident in inset I while plot *B* pertains to the faster.

An obvious division of the waveform shown in II into two parts is not apparent. It is to be noted, however, that the maximum rate of flux change occurs within the rise time of the applied field pulse and that a substantial portion of the flux is switched in a relatively short time. Reciprocals of the time required for the switched flux to increase from 10% to 50% of its total have been plotted as *C* in Fig. 1.

DISCUSSION

Several interesting features are apparent in Fig. 1. Plot A has a switching coefficient of 0.21 oersted-microsecond, in good agreement with the minimum value predicted by the nonuniform rotational model of flux reversal.[4] Plot B, which pertains to the faster process apparent in inset I, has a switching coefficient of 0.065 oersted-microsecond. It has been suggested previously[2,3] that the flux reversal process most likely responsible for such fast switching is similar to the uniform rotational reversal of thin films in that the bulk of the magnetization involved precesses around an internal de-

[4] E. M. Gyorgy, J. Appl. Phys. 28, 1011 (1957).

magnetizing field. As a result, it is possible to interpret the switching of this low remanence ferrite from one saturated state to the other as a composite process in which about half of the flux reverses by a relatively uniform mode while the other half goes more slowly by a nonuniform mode. Possibly material nonuniformities are responsible for this division into two reversal modes.

Using this point of view, one can also interpret the results obtained by switching the ferrite from remanence to saturation. The essentially demagnetized remanent state is probably composed of a complicated flux configuration, only part of which will interact with the applied field so as to produce the demagnetizing field required for the fast process. However, some of the flux will be oriented similarly to the half-switched state of the helical mode, and this will create a large rate of change of magnetization very soon after the external magnetic field pulse is applied. The later part of the flux reversal can then be associated with helical mode flux which was in a less favorable initial orientation and with the nonuniform rotational flux. Because of the complicated initial state, detailed separation of the waveforms into uniform and nonuniform parts is not possible. However, the switching time of the uniform part has been estimated as the time required for the switched flux to increase from 10% to 50% of its total. Reciprocals of these times are plotted as C in Fig. 1, and this plot has a switching coefficient of 0.026 oersted-microsecond.

Unfortunately, the presence of about half of the flux in the nonuniform rotational mode obscures a more detailed interpretation of the faster process in terms of the helical mode. Nonetheless, this ferrite is an interesting material in that half of the flux is switched by a relatively fast process even in small fields. The extrapolated threshold field of the fast process is, therefore, approximately zero. In contrast, the fast component in square loop ferrites appears to be small until relatively large fields are applied, leading to threshold fields of several oersteds.[2,3]

In summary, we have found it possible to describe qualitatively our measurement of flux reorientation in a low remanence ferrite by an equal combination of uniform and nonuniform rotation. Nonuniformity in the ferrite has been suggested as the cause for this division. Although this division obscures the detailed interpretation of the faster process in terms of the helical mode, the results given herein are additional evidence of the existence of a flux reversal process in ferrite in which the switching is speeded up by an interaction with a demagnetizing field.

We want to thank F. J. Schnettler for supplying the ferrite used for these measurements.

JOURNAL OF APPLIED PHYSICS SUPPLEMENT TO VOL. 31, NO. 5 MAY, 1960

Pulsed Ferrimagnetic Microwave Generator*

B. J. Elliott, T. Schaug-Pettersen, and H. J. Shaw
Microwave Laboratory, W. W. Hansen Laboratories of Physics, Stanford University, Stanford, California

The idea of making a solid-state generator using a ferrimagnetic material to convert energy from a pulsed dc magnetic field into microwave radiation has been studied by several workers. Recent theoretical studies have disclosed serious basic problems for such devices. This paper describes initial experiments on a device which avoids the principal difficulties. It uses an rf input signal together with a pulsed dc magnetic field to generate microwave pulses at a frequency higher than the input frequency. An input signal at 2.4 kMc/sec and a pulsed magnetic field of 150 gauss were used to generate a pulsed output signal at 2.8 kMc/sec.

INTRODUCTION

THE first specific idea for a pulsed microwave generator using ferrimagnetic material appears to have been made by R. V. Pound.[1] In this case, a large pulsed magnetic field was to be applied to a ferrite, at right angles to a dc saturating field. The pulsed field was to rise to its peak value in a time short compared to the ferrite relaxation time, and establish, on a transient basis, a large angle θ between the total magnetic field and the uniform magnetization in the ferrite. The magnetization would then execute a uniform precession about the magnetic field thereby radiating its stored energy into a suitably designed microwave circuit.

Silver and Levinthal[2] and Heard[3] reported engineering studies of this scheme with particular attention to the microwave circuit and pulsed field generation problems. More recently, Morgenthaler[4] published a theoretical analysis showing that the magnetization will closely follow the changing direction of the magnetic field during pulsing, and a significant angle θ will not result, unless the rise time of the magnetic field is short compared to the precession period, which constitutes an impracticable requirement. Morgenthaler pointed out that this problem might be avoided by orienting the pulsed field at an angle of nearly 180° to the dc saturating field.

* The research reported in this document was supported by the U. S. Army Signal Corps. Engineering Laboratories.

[1] R. V. Pound, U. S. Patent No. 2,873,370.

[2] S. Silver and E. C. Levinthal, Levinthal Electronics Inc., Rept. No. 106, (November, 1956).

[3] H. G. Heard, Levinthal Electronics Inc., Rept. No. 104 (1955).

[4] F. R. Morgenthaler, IRE Trans., MTT-7, 6 (1959).

Recent theoretical work of Schaug-Pettersen[5] indicates that when the magnetic field is inverted in this way, the magnetization of the material will rapidly break up into a random pattern such that coherent radiation into a microwave circuit cannot be expected. The calculated time constant for this breakup is typically a few tenths of a millimicrosecond, which would again require pulse time scales that cannot be met in practice. It should be mentioned that the growing spin waves described by Suhl[6] have a similar effect and would constitute a further problem for the 90° pulsing technique. For 180° pulsing, however, the breakup just referred to would be expected to be predominant.

In this paper we will describe initial experiments with a device designed to avoid the above problems. This device suggested itself by analogy with recent pulsed maser generators[7] and, it is found, was also suggested by Morgenthaler.[4]

PRINCIPLES OF OPERATION

In the present device an rf input signal of frequency ω_p is applied to a garnet sphere which is adjusted for gyromagnetic resonance by means of a magnetic field H_0, thus establishing a uniform precession with precession angle θ. A pulsed field H_p is applied along the direction of H_0 so that the resonant frequency of the spins is increased to

$$\omega=\omega_p+\gamma H_p. \tag{1}$$

The pulsed field exerts no forces tending to change θ, so if the rise time is short compared to the garnet relaxation time T, θ will be preserved during the rise of H_p. The energy stored in the spin system at the peak of H_p will then be

$$E=(H_0+H_p)M(1-\cos\theta), \tag{2}$$

where M is the garnet magnetization. The spins no longer absorb energy from the input signal, but instead execute uniform free precession at the higher frequency ω and radiate their energy as a microwave pulse into a suitable circuit.

By making the duration of the rf pulses short compared with the intrinsic relaxation time of the material, the conversion efficiency of magnetic stored energy to rf energy can be made to approach 100%. The most interesting case occurs when the output frequency is much higher than the input frequency. The energy in the output pulse is then derived mainly from the pulsed field, while the energy derived from the rf input signal can be kept small in comparison.

To avoid spin-wave excitation θ may be held below the critical value given by Suhl.[6] Using this condition, the peak pulsed power output may be obtained by time differentiation of Eq. (2) giving

$$P_{\max}=(\Delta H_k/\gamma T_\tau)fV/2 \tag{3}$$

where V is the sample volume, ΔH_k is the linewidth of the potentially unstable spin wave, and T_τ is the time constant of the output pulse. Using parameters appropriate for yttrium-iron garnet, $T\sim10^{-7}$ sec, $T_\tau\sim10^{-8}$ sec, $\Delta H_k\sim1$ gauss, we find maximum peak power of 4.5 w for a sphere diameter of 1 mm and output wavelength of 1 cm. On a transient basis it is possible to exceed the critical angle θ, and this should allow higher power output.

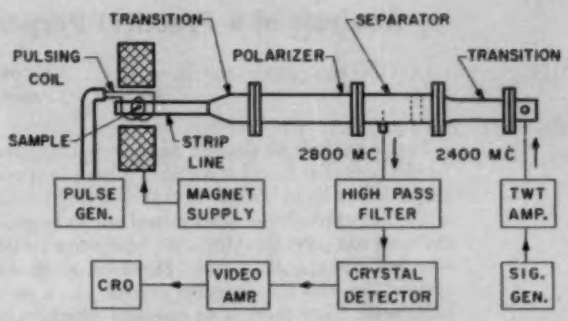

FIG. 1. Block diagram of ferrite generator experiment.

APPARATUS

A preliminary experiment has been carried out using the apparatus shown in Fig. 1.

The garnet sample is located inside a dielectric rod surrounded by three metal strips. This forms a three-phase transmission line which provides suitable coupling to the sample. The fast rising pulsed field is produced by a charged coaxial line which discharges through a spark gap into a small coil surrounding the sample. Separation of the output and input signals is affected by the polarization separator and the 2.5 kMc/sec high-pass filter. The latter is matched into a crystal detector and video system having an overall rise time of 5 mμ sec.

EXPERIMENTAL RESULTS

Using a 30-mil diam sample of single crystal YIG with a line width ΔH of 1.2 oe, 1 w of input power at 2.4 kMc/sec, and a pulsed field of 150 gauss with a rise time of 5 mμ sec, the output pulse power is about 1 mw peak at 2.8 kMc/sec. The rf output envelope rises quickly to the peak value, then decays exponentially with a time constant of 20 mμ sec. A larger output signal of approximately 1-w peak is obtained by using a larger sphere (diam=120 mils, $\Delta H=2$ oe), but the output pulse is extremely short in this case because of stronger coupling to the circuit. Polycrystalline samples with $\Delta H=45$ oe have been used successfully but with reduced power output and pulse length because of higher internal losses.

The frequency change in this initial experiment was kept intentionally small as the object was simply to prove the principle. Experiments to study performance capability at higher frequencies are being planned. As a first step an S-band to K-band (3-kMc input, 20-kMc output) generator is being designed. It is hoped that millimeter waves may eventually be generated by this method.

[5] T. Schaug-Pettersen, J. Appl. Phys. **31**, 382S (1960).
[6] H. Suhl, Proc. Inst. Radio Engrs., **44**, 1271 (1956).
[7] S. Foner *et al.*, Phys. Rev. Letters, **3**, 36 (1959).

Analysis of a Practical Perpendicular Head for Digital Purposes

GEORGE J. Y. FAN
Ampex Corporation, Redwood City, California

In this analysis we studied the potential field around a perpendicular recording head by a Fourier method. As this potential function obtained is easy to operate, the wavelength response of the head can be calculated and is shown to be similar to that of a ring head for a recorded sine wave. The first term of our expansion of the flux through the head turned out to be $\sin x/x$. This term is nominally not affected by spacing; thus, the head has good reliability. We built some perpendicular recording heads and obtained a reasonably good response curve as illustrated. However, we find the main drawback of such a head, in a standard tape system, lies with the recording process, i.e., a wavelength loss on tape rather than a limitation of the playback head. Since there is no essential difference between sine-wave and digital recording, the analysis can easily be extended to a digital system.

THE head under investigation has a configuration as shown in Fig. 1 where region B is the pole piece. We assign a potential H_0 to the pole piece.

Outside of Region B we have $\nabla^2\phi(x,y)=0$.

We may break the outside region into region A and region C. By the symmetry of the problem:

$$\phi_A(x,y)=\sum_1^\infty A_n \sin n\pi y \cosh n\pi(L+x)+H_0 y, \quad (1)$$

$$\phi_C(x,y)=\int_0^\infty C(k)\sin ky e^{-kx}dk. \quad (2)$$

By matching the potential at $x=0$,

$$\int_0^\infty C(k)\sin ky dk=\begin{cases} H_0 & \text{when } \infty>y>1 \\ H_0 y+\sum_1^\infty A_n \sin n\pi y \cosh n\pi L & \text{when } y<1. \end{cases} \quad (3)$$

By operating (3) with $\int \sin\lambda y dy$, we get

$$\frac{\pi}{2}C(\lambda)=\frac{H_0\sin\lambda}{\lambda^2}+\sum_1^\infty A_n \cosh n\pi L(-1)^n n\pi\frac{\sin\lambda}{\lambda^2-(n\pi)^2}. \quad (4)$$

By matching the derivatives, we obtain

$$-\int_0^\infty C(k)\sin ky k dk=\sum_1^\infty A_n n\pi \sin n\pi y \sinh n\pi L \quad \text{when } y<1; \quad (5)$$

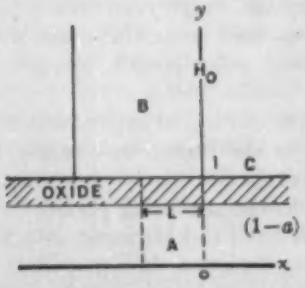

FIG. 1. Perpendicular recording head.

and by operating (5) with $\int \sin m\pi y dy$ gives

$$(-1)^{m+1}\int_0^\infty C(k)\frac{k\sin k}{k^2-(m\pi)^2}dk=\frac{A_m \sinh m\pi L}{2}. \quad (6)$$

By combining Eqs. (4) and (6),

$$H_0\int_0^\infty \frac{\sin^2 k(-1)^{m+1}}{k[k^2-(m\pi)^2]}dk+\sum_1^\infty A_n \cosh n\pi(-1)^{n+m+1}n\pi \times\int_0^\infty \frac{k\sin^2 k dk}{[k^2-(n\pi)^2][k^2-(m\pi)^2]}=\frac{\pi A_m \sinh m\pi L}{2}. \quad (7)$$

It has been evaluated that

$$\int_0^\infty \frac{\sin^2 k dk}{k[k^2-(m\pi)^2]}=-\frac{1}{2(m\pi)^2}[\gamma+\ln 2m\pi-Ci(2m\pi)]$$

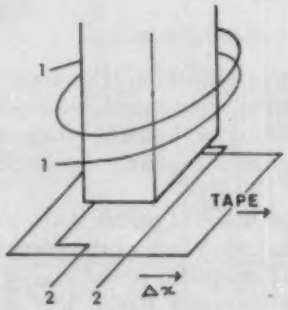

FIG. 2. Illustration for reciprocity.

and

$$\int_0^\infty \frac{\sin^2 k\, k dk}{[k^2-(m\pi)^2][k^2-(n\pi)^2]}=\begin{cases} \frac{1}{2m\pi}Si(2m\pi) & \text{when } n=m \\ \frac{1}{2\pi^2(n^2-m^2)}\left[\ln\frac{m}{n}-Ci(2m\pi)+Ci(2n\pi)\right] & \text{when } n\neq m; \end{cases}$$

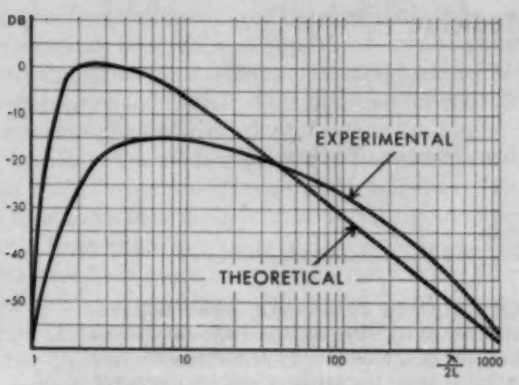

FIG. 3. Wavelength response of perpendicular recording head $L=0.7$ mil.

where

$$Ci(2m\pi)=-\int_{2m\pi}^{\infty}\frac{\cos x}{\lambda}dx \text{ and } \gamma \text{ is Euler's Constant.}$$

By inserting these values into Eq. (7), we get a set of n algebraic equations for A's from which A's can be estimated for a given configuration. If these values are inserted into Eq. (1), and

$$\phi_c(x,y)=\frac{2H_0}{\pi}\int_0^{\infty}\frac{\sin k\sin ky}{k^2}e^{-kz}dk+\frac{2}{\pi}\sum_1^{\infty}A_n \times\cosh n\pi L(-1)^n n\pi\int_0^{\infty}\frac{\sin k\sin kye^{-kz}dk}{k^2-(n\pi)^2} \quad (8)$$

is obtained from Eqs. (2) and (4), the potential of the whole plane can be calculated.

Once the potential function is evaluated, we can predict the sine wave response of such a head by applying the theorem of reciprocity. In so doing, we replace the magnetization on the tape by an equivalent current loop (Fig. 2) which is properly oriented about the tape position to reproduce the same external field. The sensing or recording winding is between terminals 1–1 (Fig. 2).

Then, the flux through the perpendicular reproducing head Φ_1 can be found as[1]:

$$\Phi_1=\frac{1}{H_0}\int_{1-a}^{1}dy\int_{-L}^{+L}\frac{\partial\phi_A(x,y)}{\partial y}M_y dx; \quad (9)$$

[1] W. K. Westmijze, "Studies on magnetic recording," Philips Research Reports (April, 1953).

where for a sine-wave recording,

$$M_y=M\cos(\pi x/\lambda)\cos(\pi Vt/\lambda). \quad (10)$$

Because of symmetry we can neglect the odd components of M_y, because they will make no net contribution to the flux in the reproduce head.

$$\Phi_1=M\cos\frac{\pi Vt}{\lambda}\left\{2aL\frac{\sin 2\pi L/\lambda}{2\pi L/\lambda}+\sum_1^{\infty}\frac{A_n(-1)^n\cosh n\pi\sin n\pi a}{H_0\pi(n^2+1/\lambda^2)}\left[n\sinh hn\pi L\cos\frac{\pi L}{\lambda}+\frac{1}{\lambda}\sin\frac{\pi L}{\lambda}\cosh n\pi L\right]\right\}. \quad (11)$$

Equation (11) gives the wavelength response of the perpendicular reproducing head for sinusoidal recorded flux.

The analysis can be extended to digital recording without formal difficulty. The essential difference is that instead of writing a sine wave for Eq. (10), the magnetization is represented by a Fourier series. For a square wave, the series would be

$$\sum_{n=1}^{\infty}\frac{1}{2n-1}\cos(2n-1)\frac{\pi x}{\lambda},$$

and the corresponding output could be synthesized from Fig. 3.

An experimental head was built with $L=0.1$, and its response is plotted with the calculated curve in Fig. 3. The discrepancy between the two is probably due to frequency effect and wavelength loss on tape during the recording process.

ACKNOWLEDGMENT

Thanks are due Eric Daniels and Nelson Yew for reading the script and many helpful suggestions. I am particularly indebted to Dr. E. T. Jaynes for his guidance in my study of potential theory.

Magnetism in Medicine

M. W. FREEMAN
Detroit, Michigan

A. ARROTT
Scientific Laboratory, Ford Motor Company, Dearborn, Michigan

AND

J. H. L. WATSON
Edsel B. Ford Institute for Medical Research, Henry Ford Hospital, Detroit, Michigan

The applications of magnetic materials and magnetic fields in medicine are reviewed. Direct biological effects of magnetic fields, clinical uses of the mechanical force exerted by magnets, and magnetic analysis as a tool in biochemistry are considered. The authors' applications of the technology of fine particle iron to the treatment of cancer and mental disease, for investigation of basic biochemistry and for diagnostic purposes are discussed. A significant step in these applications has been the discovery of sublingual assimilation of fine particle iron.

IF not with the marriage of magnetism and medicine, this paper is at least concerned with an affair between these two different fields. This affair is really an old one, which goes back to the first important scientific study of magnetism, that which was carried out by Gilbert of Colchester, Court Physician to Elizabeth I. His most important contribution was the clear recognition of the earth's role as a big magnet. The use of magnets in clinical medicine has a long and dramatic history which we will touch upon, i.e., when objects such as nails or open safety pins are accidentally swallowed and become lodged in the body passages or when a steel splinter enters the eye, the ideal surgical tool for their removal is a magnetic field gradient. In the 19th Century, there were periodic fads of "magnetic healing." The resulting controversies make interesting reading from which one might conclude that magnets can be used to attract not only iron and steel, but also money from the gullible. We are only just beginning to know something of the biological effects of magnetic fields. These we will discuss as well as a third use of magnetism in medicine, namely the applications of magnetic analysis in biochemistry. In discussing our own work with fine particles of iron, we will bring together all three of these uses of magnetism in medicine.

The use of bar magnets for the removal of iron from the body has been documented as far back as the 17th Century. By the end of the 19th Century the electromagnet was in clinical use. The development of alnico has allowed dramatic removals of dangerous objects from previously inaccessible body passages.[1] Alnico magnets have been used in artificial eyes.[2]

The most frequent application of magnetism in medicine occurs in the treatment of traumatic gastritis in cattle, or as it is known, "hardware" disease. The most common cause is bailing wire in the feed. The result is anything from an upset stomach to death. Often 50% of a herd will be afflicted. The remedy is to have the cow swallow an alnico magnet and periodically remove it.[3] The hardware it collects can amount to more than twice the weight of the magnet. It turns out that this is more economical than to use magnetic separation of the feed of the cattle.

Essential to the life process are the changes back and forth from ferric to ferrous iron. In the study of such chemical changes, magnetic analysis can be applied. For example, a certain key protein molecule known as transferrin contains two iron ions. If one does a magnetic analysis using the Curie-Weiss law for the interpretation of results, one can obtain the valance of both of these iron ions and also the strength of the interaction between them. This problem has been attacked by magnetic analysis,[4] but the results were only carried out at one temperature, therefore, the maximum information in the Curie-Weiss law was not obtained.

Magnetic resonance is just now beginning to show its potentialities as a tool in biochemical and medical analysis. As an example, we cite the study of the recombination rate of free radicals which have been induced by radiation in living cells.[5]

A different sort of application of magnetism in analysis is illustrated by the process where micron size iron particles are coated with starch and are grabbed by the white blood cells.[6] The white cells can then be separated by applying a magnetic field gradient.

The first definitive study of the direct biological effects of the magnetic field were carried out by experimenters in Edison's Laboratory in 1892.[7] They subjected a dog and five of the experimenters themselves to magnetic fields of the order of several thousand gauss. They were not able to sense any effects. They concluded

[1] Murdock Equen, *Magnetic Removal of Foreign Bodies* (Charles C. Thomas, Springfield, Illinois, 1957).
[2] *Applied Magnetics* (Indiana Steel Products Company, October, 1956).
[3] R. E. Carroll, J. Am. Vet. Med. Assoc. **129**, 376 (1956).
[4] A. Ehrenberg and C. B. Laurell, Acta Chem. Scand. **9**, 68 (1955).
[5] Zimmer, Ehrenberg and Ehrenberg, Strahlentherapie **103**, 3 (1957).
[6] Sumner Levine, Science **123**, 186 (1956).
[7] Peterson and Kennelly, N. Y. Med. J. (December 31, 1892).

that previous "miracle cures" worked with bar magnets and solenoids resulted from psychic or suggestive effects rather than from direct effects of the magnetic fields. This research provided sufficient ammunition for the medical profession to fight the charlatans selling "magnetic healing" devices. The medical profession has used these somewhat limited experiments too well for they have fostered the unwarranted statement that there are no biological effects from the application of magnetic field. Though there have been sporadic attempts over the last 50 yrs to show various effects of magnetic fields,[8] the really convincing set of experiments are those carried out quite recently at the University of Illinois by the Barnothys.[9] With controlled experiments of statistical significance, they have shown that mice when kept in a field of 4000 gauss become less demonstrative. They note a drop in temperature and an increase in food consumption and, rather strikingly, a 40% decrease in the white cell count. They say that if mice are kept in a field for several weeks during their youth and then removed from the field they will show a considerably greater activity, a lower food consumption, and appear to be younger to a very old age. They notice that the white cell count recovered after removal from the magnetic field and actually went up to twice the usual white cell count. They applied this knowledge to counteracting the influence of irradiation, which normally causes death through a decrease of white cell count.

Our work centers around the application of the technology of fine particle iron to medical problems. We have in mind in particular the treatment of cancer, of mental disease, of investigations of basic biochemistry, and the use of magnetic analysis in diagnosis. The Fe crystals, which are produced by the Freeman process, have been thoroughly studied by electron microscopy and discussed previously at these conferences.[10] The particles are available with various morphologies reflecting different degrees of dendritic growth. The different classes of particles range in size from 50 to 1000 A. When properly conditioned, any of these will pass through the smallest capillaries in the body (~50 000 A diam). Thus, we can transport fine particles through the vascular system and concentrate them at a particular point in the body with the aid of magnetic fields. The iron particles thus become a means for transporting radiation or some healing chemical to a particular spot in the body. That is, the particles can be alloyed with the proper choice of radioactive element or they can be coated with an adsorbed layer of a therapeutic agent.

The interaction of fine particle iron with the blood system is of interest in itself for several reasons. The local fields surrounding single domain particles can be greater than those for which biological effects have already been demonstrated. There is the possibility of increased catalytic or enzymic activity arising from the large surface of a metal with holes in the electronic *d* band. As iron ions play an essential role in the blood cycle, there is the question of the influence of fine particle metallic iron on the iron kinetics. And finally, it is not known how the blood system would react to a metallic particle of such small size.

It is known that about 8 mg of intravenous iron salt immediately induces toxic reaction in the blood. In our initial studies, we have had patients adsorb up to 120 mg of alpha iron under the tongue without any ill effects. In fact, the patients have had some very pleasant side reactions. As our results are limited to six patients, we cannot as yet recommend iron particles for the improvement of one's well being or his sex status. The first patient, to our knowledge, anywhere in the world who took alpha iron particles under the tongue was a 6½ year old boy suffering from Idiopathic Thrombocytopenic Purpura. Despite the remarkable course of recovery of the boy, we cannot claim a direct relationship between the recovery and the administration of the iron crystals. However, we can say that after each treatment within ten minutes and more significantly after one hour, there was a manifestation in the patient's blood; serum iron increased by over 70%. An effect has been noted in all six patients. This appears to be a new phenomenon in a living organism and as such poses an interesting biochemical problem in which magnetic analysis should be utilized. Of immediate interest is the value of this phenomenon in the carrying out of our program in which we will bring the technology of magnetism and magnetic materials to bear on medical problems.

[8] Bibliography available on request to Scientific Laboratory.
[9] J. M. Barnothy and M. F. Barnothy, *Medical Physics* (Year Book Publ. Co.) 1959 edition, (to be published); also Nature **177**, 577 (1956) and Nature **181**, 1785 (1958).
[10] J. H. L. Watson and M. W. Freeman, Proc. of Conference on Magnetism and Magnetic Materials (Am. Inst. of Elect. Engrs.) **150** (1955) and **163** (1956); also with A. Arrott, J. Appl. Phys. **306** (1958).

Blood Flow Measurements Using Dynamical Paramagnetic Relaxation Times and Paramagnetic Tracer Techniques

J. R. SINGER
University of California, Berkeley, California

The effect of flow on the paramagnetic relaxation time of fluids is discussed. The saturation or magnetization inversion of a group of nuclear moments constitutes a short-lived tracer for these moments permitting flow velocity measurements. For long-lived tracers, a given set of molecules with a well-known nuclear or electron paramagnetic resonance spectrum may be employed. Experimental measures of blood flow velocity in mice are discussed.

INTRODUCTION

THE longitudinal relaxation time of paramagnetic materials (either electrons or nuclei) depends upon the coupling of the elemental paramagnets to the surrounding substance. For strong coupling, relaxation times are short, and the converse also holds. In the case of hydrogen protons in pure water, the coupling is relatively weak, and the relaxation time is the order of 2.3 sec.[1] On the supposition that the relaxation time of the protons in blood would be almost this long, we deduced that the measurement of blood flow velocity in vivo by means of nuclear resonance techniques would be feasible, and they did indeed so prove as our experimental results will show. The relaxation time of protons in blood is the order of four tenths of a second by our measurements.

We consider the present method of flow velocity measurement as a tracer system. An example will illustrate this point of view. If the nuclei of a group of molecules are saturated in the sense that magnetic level populations are equalized, nuclear resonance absorption is decreased in these molecules for a time the order of T_1 (the longitudinal relaxation time). Consequently, the saturated nuclei are tracers for that amount of time. If on the other hand, it is desirable to use a tracer for a longer time than is readily obtained from a relaxation method, one may inject a material with a well established nuclear or electron resonance spectrum into the flow channel and determine the presence of this substance at various positions along the channel by noting the presence of its resonance absorption. The tracer material will be useful as long as it is not uniformly distributed in the flow channel.

NMR TECHNIQUE

Our early experimental procedure consists of measuring the relaxation time indirectly by determination of the saturation parameter. This scheme provides a very fast measurement, and is particularly useful when the flow rate varies with time since the variation may then be measured. In particular, the method has important application to measuring blood flow at much faster intervals than the heart pump rate. This may be accomplished as described below.

When measuring magnetic resonance absorption with an r-f level sufficient to approach notable saturation, the absorption level is reduced by a factor Z given by

$$Z=[1+(\tfrac{1}{2})\gamma^2H_1^2T_1g(\nu)]^{-1}, \tag{1}$$

where γ is the gyromagnetic ratio of the spins, H_1 is the r-f magnetic field, and $g(\nu)$ is the shape function of the resonance line.

For convenience, we define

$$Z=[1+sT_1]^{-1} \tag{2}$$

with obvious relationships to equation (1).

If the observed material is a flowing fluid, with average velocity $\bar{V}$ observed in a region L_r, the relaxation time observed is not the same as the static relaxation time but is[2]

$$(T_1)'=T_1L_r/(L_r+T_1\bar{V}), \tag{3}$$

provided that the measurement is concerned with the time to return to the equilibrium magnetization of the *flowing fluid*.

The reason for the existence of $(T_1)'$ is easy to explain. Suppose that a region of flow is saturated by a burst of rf energy. The return to a normal magnetization state can occur much more rapidly than with a static fluid since unsaturated fully magnetized nuclei replace the saturated nuclei by reason of the flow. The derivation of Eq. (3) is explicitly given in reference 2.

The saturation factor for the flowing fluid is, then

$$Z=[1+sT_1L_r/(L_r+T_1\bar{V})]^{-1}. \tag{4}$$

Consequently, with partial saturation, the amplitude of the signal is increased with more flow velocity. If the amplitude of the resonance absorption without flow is denoted by A, and that with flow by A_f, a convenient equation to describe the flow velocity is

$$\frac{A_f-A}{A}=\frac{s[1-L_r/(L_r+\bar{V}T_1)]}{1+s[L_r/(L_r+\bar{V}T_1)]}. \tag{5}$$

Certain assumptions are implicit in this equation; these will now be explicitly enumerated:

(1) The flowing spins are in the magnetic field long

[1] E. Hahn, Phys. Rev. **80**, 580 (1950).

[2] J. R. Singer, J. Appl. Phys. **31**, 125 (1960).

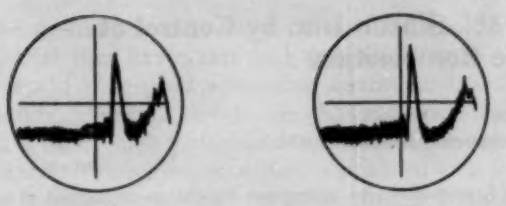

(a) (b)

FIG. 1. NMR signals of protons in mice blood in *vivo*. In (a) the tail was constricted with a tourniquet at the base of the tail; in (b) blood flow was unhampered. Note the change in amplitude of the signal. The mouse was sedated with ether fumes.

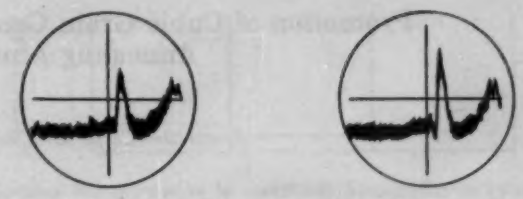

(a) (b)

FIG. 2. NMR signals of protons in mice blood in *vivo*. The same situation applies as in Fig. 1, except that the mouse was administered sodium pentothal for ease of handling.

enough to reach their equilibrium magnetization before entering the resonance absorption region. (Otherwise, a comparison of amplitudes requires a more complicated expression.)

(2) No extraneous material exhibits resonance absorption, i.e., the measurement involves only the absorption due to spins in a fluid at rest and then in motion.

In the case of biological measurements, the second assumption is not always justifiable. If we consider proton absorption, the normal water in the tissues provides absorption which leads to inaccuracies when measuring the static absorption amplitude. However, chemical shifts may result in these lines being resolved. If the resolution does not occur, the only blood flow measurement is a comparative measure. For example, one may find the average flow velocity on the same subject when subjected to various physiological or psychological stimuli and compare relative flow rates. In this case, the "noise" due to water in the tissues will cancel out.

Equation (5) may be simplified to

$$(A_f - A)/A \approx (\bar{V} T_1 / L_r) \qquad (6)$$

if s is much larger than unity. The amplitude comparisons for blood flow rates may readily be performed by measuring the resonant absorption amplitude with a tourniquet to obtain A and with tourniquet removed to observe A_f. Since the same region is observed in both measurements, extraneous water in the tissues only alters the denominator. If the subject is now perturbed and the relative change in flow velocity is to be measured, this is achieved by using

$$[(A_f - A)_1/(A_f - A)_2] = \bar{V}_1/\bar{V}_2 \qquad (7)$$

thus, relative measurements of flow may be achieved with considerable sensitivity and precision. Furthermore, changes in flow rate are immediately apparent from changes in the rf absorption amplitude curves.

Examples of the observation of such changes in blood flow in mice tails are shown in Figs. 1 and 2. These are traces of oscilloscope patterns of the NMR patterns of protons in mice blood observed by placing the mouse tail in an NMR induction spectrometer. It appears that the chemical shift resolves the water protons from bound protons; however further experiments are needed to establish this with certainty.

The figures illustrate the difference in NMR amplitudes observed for proton resonance in the mouse tail when (b) the blood was flowing and (a) when a tourniquet about the base of the tail prevented flow. In one of the illustrations, the mouse was sedated with ether fumes, in the second an injection of sodium pentothal was utilized to permit ease of handling. No attempt has been made to obtain absolute measures of flow velocity, but relative flow rates varied by a factor of five dependent upon the applied sedative. Experiments are continuing with improvements in our experimental design. Absolute measurements of flow velocities are theoretically feasible, and should be within the capabilities of our future experiments. An outline of the experimental arrangements for continued work is given in reference 2.

ACKNOWLEDGMENT

It is a pleasure to thank Dr. Erminio Lombardi for his assistance in the early experiments, and Prof. Melvin Calvin for several useful suggestions.

Promotion of Cubic Grain Growth in 3% Silicon Iron by Control of Annealing Atmosphere Composition

DALE KOHLER
Armco Steel Corporation, Research Laboratories, Middletown, Ohio

Under certain special conditions of processing and annealing, silicon iron can be made to have cubic orientation. This phenomenon was first reported by Assmus et al.

The driving force for the growth of the cubic grains has been determined by several investigators to be surface energy. We have found that by controlling the concentration of impurities in the annealing atmosphere the growth of grains having the (100) plane parallel to the sheet surface can be greatly improved. Calculations of the surface energies in the body-centered system show that the surface energy of atomic planes are (110), (100) and (111) in order of ascending values. From this orientation dependency of the surface energy, there results a discrepancy between theory and the observed fact of (100) surface energy growth.

It is proposed that adsorption by the metal surface of atmosphere constituents in a very special manner can accomplish a change in relative surface energy so that the (100) plane becomes the lowest energy crystal plane.

Data on some atmosphere composition effects on transformation to cube texture of silicon iron 2 to 14 mils thick were obtained.

The degree of transformation was found to be closely related to the concentration of certain compounds that are added to the atmosphere. The degree of cube growth reaches a maximum at a certain small concentration of impurity.

These effects were studied in both metal and ceramic annealing tubes. With proper additives excellent cube growth can be obtained in either type annealing tube.

INTRODUCTION

IT has been shown by many investigators that it is possible to produce silicon iron with a cubic orientation.[1–6] It also has been shown that the driving force for the growth of grains having the (100) plane parallel, or within less than about 5° from parallelism with the sheet surface, is the lower surface energy of these crystals. It has been reported that it is also possible to cause grains having the (110) plane parallel to the sheet surface to grow by the same mechanism.[6] We have found in our laboratory that grains having the (111) and other low index planes parallel to the sheet surface can also grow by a surface energy mechanism.

Most theoretical calculations of crystal surface energy are based on the principle that an atom at the surface is at higher energy than an atom in the interior of a crystal because the surface atom has a smaller number of nearest neighbors and hence, less chance for complete resonant bonding.[7] We would, therefore, expect that surface energy would be a function of the density of packing of the crystal plane. From this point of view, we would find that the surface energy of the (110) crystal face should be less than the (100) and followed by the (111) and other less densely packed plane. We have here, then, an anomaly that planes other than the lowest energy plane grow by surface energy. Similar discrepancies between theory and practice are found in other processes which are orientation dependent; for example, the growth and solution of crystals, evaporation and oxidation.

We propose that in order to explain the discrepancies, one must consider not only the crystal surface but the adsorbed layer on it. The nature of this adsorbed layer is largely a function of furnace atmosphere composition.

To investigate the effect of atmosphere composition on surface energy grain growth, materials were added to the furnace atmosphere in controlled amounts and the effect on grain growth was measured.

EXPERIMENTAL PROCEDURES

In choosing a material that would be most effective as an additive, we would avoid elements or compounds that would form a very stable compound at annealing temperatures; since these would be likely to form con-

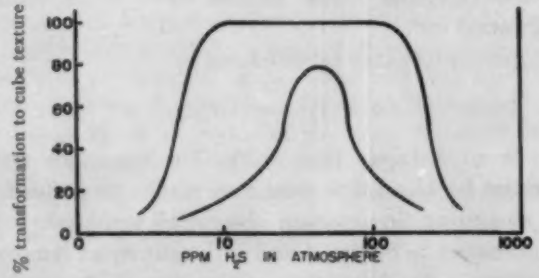

FIG. 1. Effect of hydrogen sulfide atmosphere addition on percent transformation to cube texture in a quartz annealing tube.

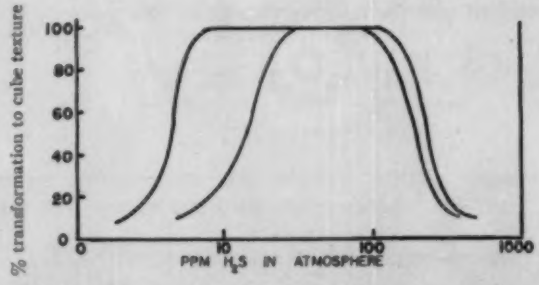

FIG. 2. Effect of hydrogen sulfide atmosphere addition on percent transformation to cube texture in an inconel annealing tube.

[1] K. J. Sixtus, Physica **6**, 105 (1935).
[2] H. E. Mobius, German Patent 1,009,214.
[3] Assmus, et al., Z. Metallk. **48**, 341 (1957).
[4] Walters et al., J. Appl. Phys. **29**, 363 (1958).
[5] Wiener et al., J. Appl. Phys. **29**, 366 (1958).
[6] J. L. Walter and C. G. Dunn, Trans. Am. Inst. Met. Engrs. **215**, (1959).
[7] J. Friedel et al., Acta Met. **1**, (1953).

tinuous surface films. At the same time, we would wish a material that has rather high polarizability so that they would have good adsorption characteristics. For this study, hydrogen sulfide was chosen as an additive because of its high polarizability and ease of experimentation. The hydrogen sulfide was added to a very pure dry hydrogen atmosphere by passing the hydrogen over iron sulfide or manganese sulfide in a pretreating furnace. The temperature of the pretreating furnace is a sensitive control of the concentration of the hydrogen sulfide in the gas stream. Chemical analyses of the gas stream were made on the exit gas, after the annealing furnace had cooled to room temperature. We have also found it possible to add compounds to the annealing separator that will decompose at high temperature and supply hydrogen sulfide to the atmosphere.

Samples were prepared from 3.15% silicon iron commercial open hearth heats. The sample size was 30.5×3 cm, and they were annealed in 2½ in. diam tubes. A gas flow rate of 5 cu ft/hr was maintained. The annealing time was 8 hours, and the temperature was 2200°F. Approximately 5 hrs was required to reach temperature.

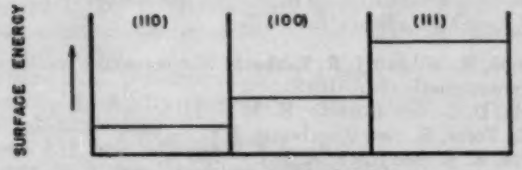

FIG. 3. Diagram of surface energies of low index crystal planes for a "clean" metal surface.

EXPERIMENTAL RESULTS

Figure 1 shows the effect of the addition on 12 mil steel and 1.8 mil steel. Samples of both thicknesses were annealed in a quartz tube. Here, we see that the samples would not undergo good cubic recrystallization unless the impurity concentration was kept within narrow limits. The 12 mil steels did not completely transform, probably due to the contamination of the surface of the sample due to the hydrogen atmosphere reducing the silica of the annealing tube. This reaction precedes at an appreciable rate at these temperatures.

Figure 2 shows the effect in an inconel tube. Here, the 12 mil steel also completely transforms.

We have found that the optimum hydrogen sulfide concentration will vary slightly depending on the size of the change, tube material, spacing of samples, sulfur content of steel, and gas flow rate.

Other additions, such as compounds of carbon, also have been found to be beneficial. These have the disadvantage of carbon pickup in the steel. Sulfur and carbon compounds have been successfully added to argon and helium, and with the same growth promoting effect on cubic grains. It is important, when using argon and helium, to remember that if these gases are thoroughly purified, we have no longer a method to add

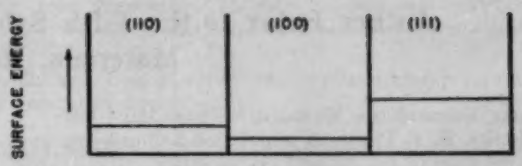

FIG. 4. Diagram of surface energies of low index crystal planes for a "slightly contaminated" metal surface.

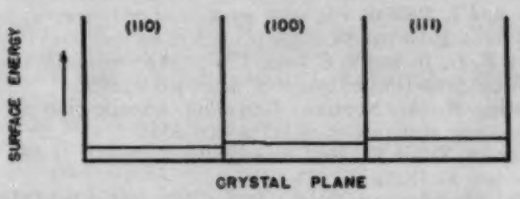

FIG. 5. Diagram of surface energies of low index crystal planes for a "severely contaminated" metal surface.

impurities by the technique described above. It has also been shown that these additions are effective in vacuum anneals.[8]

DISCUSSION OF RESULTS

The following three sketches of possible surface conditions will be useful in presenting the proposed theory for surface energy growth. Figure 3 shows the surface energy of low index crystal planes as a function of packing density for a clean adsorption-free surface. Figure 4 shows a condition that might be possible in a slightly contaminating atmosphere. Here, since the high index or lower density atomic planes have the highest energy, they will adsorb the few contaminating atoms or molecules first and preferentially to the lower energy planes. It is possible to observe this preferential adsorption or combination of sulfur with various crystallographic planes by making a sulfur print of the surface of samples freshly annealed in hydrogen containing hydrogen sulfide. Low energy planes show much less sulfur than higher energy planes. We propose that it is possible to achieve the condition shown in this diagram, where an already fairly low energy crystallographic plane can, by adsorption of atmosphere impurities, become the lowest energy crystal plane. Figure 5 shows the condition of a highly contaminating atmosphere. Here, the crystallographic effect of surface energy is nearly blotted out by the strongly adsorbed layers or the compounds formed at the surface.

From this proposed model, we can predict that the (110) growth would occur under very clean surface conditions and (100) growth under slightly contaminating conditions. If the surface is highly contaminated, no surface energy growth would occur.

ACKNOWLEDGMENT

In conclusion, grateful acknowledgment is made to John M. Jackson for many discussions and valuable suggestions.

[8] Unpublished work of G. W. Wiener.

Author Index to the Fifth Symposium on Magnetism and Magnetic Materials, November 16-19, 1959

Adams, Edmond (see Hubbard, William M.)—368S
Adamsky, R. F. Preferred orientation and ordering in evaporated films of Fe, Ni, and Fe-Ni—289S
Agarwal, Paul D. and D. C. Graham. Effect of eddy currents on domain wall behavior configurations, wall motion and loss for a domain model of cube-on-edge material—249S
—— **and L. Rabins.** Rigorous solution of eddy current losses in rectangular bar for single plane domain wall model—246S
Alley, R. E., Jr. and V. E. Legg. Effects of hydrostatic pressure on the properties of magnetic materials—239S
Alperin, H. A. Neutron diffraction investigation of the magnetic structure of nickel oxide—354S
Anderson, Elmer E. (see Cunningham, Richard J.)—45S
—— (see McDuffie, G. E.)—47S
Arajs, Sigurds and D. S. Miller. Magnetic behavior of polycrystalline neodymium, holmium, and erbium from 300 to 1500°K—325S
Arnott, R. J. (see Goodenough, J. B.)—342S
Arrott, Anthony (see Freeman, Michael W.)—404S
Auld, B. A. Finite amplitude electromagnetic waves in gyromagnetic media—106S

Baer, G., D. Ganz, and H. Thomas. Secondary recrystallization in vacuum annealed silicon iron—235S
Bailey, P. C. Absorption and reflectivity measurements on some rare earth garnets and α-Fe_2O_3—39S
Barker, R. C. and R. M. Brownell. DC measurements on tape-wound cores—243S
Belov, K. P. and A. V. Pedko. Magnetostriction of gadolinium iron garnets—55S
——, **G. I. Katayev, and R. Z. Levitin.** Internal friction anomalies in ferromagnetics and antiferromagnetics near the Curie point—153S
Bennett, Glenn E. Harmonic generation in a ferrimagnetic disk—97S
Bennion, David R. New multi-aperture magnetic logic element—129S
Besser, P. J. (see Muckenhirn, Wm. O.)—304S
Bickford, L. R., Jr. Intrinsic and anneal-induced anisotropy in cobalt-substituted *W*-type hexagonal oxides—259S
Bockemuehl, R. R. and W. E. Sargeant. Practical hysteresigraph—180S
Bohlmann, M. A. (see Kronenberg, K. J.)—82S
Boyd, E. L. (see Pugh, E. W.)—293S
Bozorth, R. M. and D. D. Davis. Magnetic properties of ferromagnetic superconductors—321S
Bradley, E. M. and M. Prutton. Magnetization reversal in uniaxial films near to the preferred direction—285S
Bragiński, Aleksander. Properties of manganese ferrites prepared at various oxygen pressures—339S
Bratina, W. J., U. M. Martius, and D. Mills. Magnetic contribution to the ultrasonic attenuation in annealed and deformed steel (SAE 1020)—241S
Brown, D. L. (see Weisz, R. S.)—269S
Brown, W. F., Jr., J. P. Hanton, and A. H. Morrish. Initial-permeability spectra of microscopic iron-oxide particles—214S
Brownell, R. M. (see Barker, R. C.)—243S
Brownlow, J. M., W. L. Shevel, Jr., and O. A. Gutwin. Ferrite films—new logic and storage devices—121S
Buffler, C. R. Effects of surface irregularities on single crystal resonance parameters—222S

Cable, J. W. (see Wilkinson, M. K.)—358S
Callen, Earl R. Anisotropic magnetization—149S
Carr, P. H. and S. Foner. Magnetic transitions in Ti_2O_3 and V_2O_3—344S
Carson, John W. and Robert L. White. Paramagnetic resonance of Yb^{+++} in aluminum and gallium garnets—53S
Carter, R. E. (see Meiklejohn, W. H.)—164S
Caspari, M. E., S. Frankel, and M. A. Gilleo. Hyperfine interactions in magnetic materials by γ-γ angular correlation measurements—320S
Chang, H. (see Shevel, W. L., Jr.)—125S
Chikazumi, Soshin. Roll magnetic anisotropy of iron-aluminum crystals—158S
Child, H. R. (see Wilkinson, M. K.)—358S
Clogston, A. M. Interaction of magnetic crystals with radiation in the range 10^4–10^5 cm^{-1}—198S
Coale, Franklin S. High-speed ferrite rotating half-wave plate—170S
Cohen, M. S., E. E. Huber, Jr., G. P. Weiss, and D. O. Smith. Investigations into the origin of anisotropy in oblique-incidence films—291S
—— (see Smith, D. O.)—295S
Coleman, Paul D. (see Steier, Wm. H.)—99S
Crapo, W. A. Time decrease of initial permeability in $Mn_xFe_{3-x}O_{4+y}$—267S
Cunningham, J. Richard, Jr., and Elmer E. Anderson. Samarium substitutions in yttrium iron garnet—45S
—— (see McDuffie, G. E.)—47S

Damon, R. W. and J. R. Eshbach. Magnetostatic modes of a ferromagnetic slab—104S
Davis, D. D. (see Bozorth, R. M.)—321S
Della Torre, E. (see Woodward, J. G.)—398S
deVos, K. J. (see Koch, A. J. J.)—75S
Dietrich, W. and W. E. Proebster. Millimicrosecond magnetization reversal in thin magnetic films—281S
Dillon, J. F. and J. W. Nielsen. Ferrimagnetic resonance in impurity doped yttrium iron garnet (YIG)—43S
Dixon, P. A. (see Maradudin, A. A.)—329S

Eggenberger, J. S. Influence of nearby conductors on thin film switching—287S
Eichbaum, Barlane R. Development of high-speed coincident current memory cores—117S
Elliott, B. J., T. Schaug-Pettersen, and H. J. Shaw. Pulsed ferrimagnetic microwave generator—400S
Enz, U. (see Smit, J.)—137S
Eshbach, J. R. (see Damon, R. W.)—104S

Fan, George J. Y. Analysis of a practical perpendicular head for digital purposes—402S
Fang, P. H. and R. S. Roth. Ferroelectric and ferrimagnetic properties of $(Ba_{3-2x}R_{2x})(Nb_{9-x}Fe_{1+x})O_{30}$—278S
Fletcher, R. C. (see LeCraw, R. C.)—95S
Fletcher, P. C. (see Solt, I. H.)—100S
Flippen, R. B. and S. A. Friedberg. Magnetic susceptibilities of single crystal $NiCl_2 \cdot 6H_2O$ and $CoCl_2 \cdot 6H_2O$ at low temperatures—338S
Folen, V. J. Influence of ionic order on the magnetocrystalline anisotropy and crystalline field parameters in lithium ferrite monocrystals—166S
—— (see Schnitzler, A. D.)—348S
Foner, S. (see P. H. Carr)—344S
Ford, N. C., Jr. Domain wall velocities in thin iron-nickel films—300S
Foster, K. and J. J. Kramer. Effect of directional orientation on the magnetic properties of cube-oriented magnetic sheets—233S
—— (see Pavlovic, D.)—231S

Foy, J. E. and R. J. Parker. Permanent magnet leakage permeance evaluation based on polar radiation analogy —188S
Frankel, S. (see Caspari, M. E.)—320S
Freeman, A. J. and R. E. Watson. Effect of crystalline fields on magnetic-form factors—374S
Freeman, Michael W. (M.D.), Anthony Arrott, and John H. L. Watson. Magnetism in medicine—404S
Friedberg, S. A. (see Flippen, R. B.)—338S
Fuller, Harrison W. and Murray E. Hale. Static and dynamic studies of magnetization distribution in thin films by electron microscopy—308S

Ganz, D. (see Baer, G.)—235S
Geiszler, T. D. and R. A. Henschke. Broadband reciprocal ferrite phase shifters—174S
Geller, S. Magnetic interactions and distribution of ions in the garnets—30S
Gilfrich, John V. (see Hubbard, William M.)—368S
Gilleo, M. A. (see Caspari, M. E.)—320S
Giron, V. S. (see Néel, L.)—27S
Goodenough, John B. Direct cation-cation interactions in primarily ionic solids—359S
——, **A. Wold, and R. J. Arnott.** Interpretation of the magnetic and crystallographic properties of several iron, nickel, and iron-nickel nitrides—342S
Gossard, A. C. (see Portis, A. M.)—205S
Gottlieb, Peter. Double pump degenerate ferrite amplifier —172S
Graham, C. D., Jr. Temperature dependence of anisotropy and saturation magnetization in iron and iron-silicon alloys —150S
Graham, D. C. (see Agarwal, P. D.)—249S
Granath, J. A. Instrumentation applications of inverse-Wiedemann effect—178S
Green, J. J. (see Schlömann, E.)—385S
Gutwin, O. A. (see Brownlow, J. M.)—121S
Gyorgy, E. M. Flux reversal in soft ferromagnetics—110S
—— (see Hagedorn, F. B.)—398S

Hagedorn, F. B. and E. M. Gyorgy. Switching behavior of low remanence ferrite—398S
Hale, Murray E. (see Fuller, Harrison W.)—308S
Hall, R. C. Magnetic anisotropy and magnetostriction of ordered and disordered cobalt-iron alloys—157S
Hames, F. A. Ferromagnetic-alloy phases near the compositions Ni_2MnIn, Ni_2MnGa, Co_2MnGa, Pd_2MnSb, and PdMnSb—370S
Hanton, J. P. (see Brown, W. F.)—214S
Harris, A. B. (see Meyer, Horst)—49S
Harte, K. J. Flux reversal by noncoherent rotation in magnetic films—283S
Heidenreich, R. D. (see Nesbitt, E. A.)—228S
Heikes, Robert R. (see McGuire, Thomas R.)—276S
Heimke, G. Temperature dependence of the saturation magnetization of ferrites with magnetoplumbite structure —271S
Henry, Warren E. Strong field magnetization at low temperatures and approach to absolute saturation of thulium metal—323S
Henschke, R. A. (see Geiszler, T. D.)—174S
Herring, Conyers. State of *d* electrons in transition metals—3S
Heuer, A. (see Straley, R.)—126S
Hokkeling, P. (see Koch, A. J. J.)—75S
Hooper, E. T., Jr. (see Krall, A. D.)—178S
Hubbard, William M., Edmond Adams, and John V. Gilfrich. Magnetic moments of alloys of gadolinium with some of the transition elements—368S
Huber, E. E. (see Cohen, M. S.)—291S
—— (see Smith, D. O.)—295S
Hung, John Wenchung. Transfer function and error probability of a digital magnetic tape recording system—396S

Iida, Shuichi. Role of cation vacancy in magnetic annealing of iron-cobalt ferrites—251S

Jacobs, I. S. High field magnetization study of ferrimagnetic arrangements in chromite spinels—263S
Jones, R. V. (see Rodrique, G. P.)—376S
Joseph, L. (see Tompkins, J. E.)—176S

Kaminow, I. P. Volume dependence of ferrimagnetic resonance properties in $Ni_{1-x}Co_xFe_2O_4$—220S
Kanamori, Junjiro. Crystal distortion in magnetic compounds —14S
Kane, B. (see Straley, R.)—126S
Kaplan, T. A. Classical theory of spin configurations in the cubic spinel—364S
Katayev, G. I. (see Belov, K. P.)—153S
Kelley, Clinton M. (see Wiechec, Walter)—131S
Kirschbaum, Albert J. (see Sparks, Joseph T.)—356S
Kiseda, J. R. (see Seelbach, W. C.)—135S
Kittel, C. Microwave resonance in rare earth iron garnets—11S
Kleber, E. V. (see Vickery, R. C.)—366S
Koch, A. J. J., P. Hokkeling, M. G. v.d. Steeg, and K. J. deVos. New material for permanent magnets on a base of Mn and Al—75S
Koehler, W. C. (see Wilkinson, M. K.)—358S
Kohler, Dale. Promotion of cubic grain growth in 3% silicon iron by control of annealing atmosphere composition—408S
Kolbe, C. L. and D. L. Martin. Hot working of Alnico 5 alloys —84S
Kondorsky, E. I. and V. L. Sedov. Antiferromagnetism of iron in face-centered crystalline lattice and the causes of anomalies in Invar physical properties—331S
Kouvel, J. S. Exchange anisotropy in Cu-Mn and Ag-Mn alloys—142S
—— (see Pry, R. H.)—162S
Krall, A. D. and E. T. Hooper, Jr. Ferromagnetic powders in waveguides at elevated temperatures—178S
Kramer, J. J. (see Foster, K.)—233S
Kronenberg, K. J. Transmission electron diffraction of Alnico V—80S
—— **and M. A. Bohlmann.** Long-term magnetic stability of Alnico and barium ferrite magnets—82S

LaBonte, A. E. (see Muckenhirn, O. William)—304S
Lauriente, M. and G. E. Lynn. Characteristics of Supermendur at 500°C—237S
Lawrence, P. E. (see Rodbell, D. S.)—275S
LeCraw, R. C., R. C. Fletcher, and E. G. Spencer. Electron spin relaxation in ferromagnetic insulators—95S
Legg, V. E. (see Alley, R. E., Jr.)—239S
Levitin, R. Z. (see Belov, K. P.)—153S
Lin, S. T. Magnetic behavior in the transition region of a hematite single crystal—273S
Long, T. R. Electrodeposited memory elements for a nondestructive memory—123S
Lotgering, F. K. (see Smit, J.)—137S
Luborsky, F. E. and T. O. Paine. Angular variation of the magnetic properties of elongated single-domain iron particles—66S
—— **and T. O. Paine.** Coercive force and remanence of 25-A to 2000-A diameter cobalt, iron, and iron-cobalt alloy—68S
—— (see Paine, T. O.)—78S
Lynn, G. E. (see Lauriente, M.)—237S

McDuffie, G. E., Jr., J. Richard Cunningham, and Elmer E. Anderson. Initial permeability characteristics of mixed yttrium-gadolinium iron garnets—47S

McGuire, Thomas R. and Robert R. Heikes. Magnetic properties of the $Li_xMn_{1-x}Se$ system—276S
McKay, R. W. and K. C. Smith. Effect of previous history on switching rate in ferrites—133S

Makolagwa, Stefan. Effect of potassium ions on the reaction and final properties of Mn-Zn ferrite—339S
Maradudin, A. A. and P. A. Dixon. Effect of impurities on the low-temperature spontaneous magnetization of cubic ferromagnetic crystals—329S
Maringer, R. E. Effects of directional ordering on the damping of zone-melted iron—229S
Marshall, S. A. and A. R. Reinberg. Paramagnetic resonance absorption of nickel in sapphires—336S
Marshall, Walter (see Sparks, Joseph T.)—356S
Martin, D. L. (see Kolbe, C. L.)—84S
Martius, U. M. (see Bratina, W. J.)—241S
Masters, Joseph I. Instability of magnetic resonance in single crystal spheres of yttrium iron garnet—41S
Matisoo, J. (see Pugh, E. W.)—293S
Matthias, Bernd. Relations between superconductors and ferromagnets—23S
Mayer, Ludwig. Nucleation experiments in thin magnetic MnBi films—384S
Mayfield, J. R. Microcalorimetric technique for the study of damping and hysteresis in ferromagnetic films—298S
Mead, Warren (see Sparks, Joseph T.)—356S
Meiklejohn, W. H. and R. E. Carter. Exchange anisotropy in rock magnetism—164S
Mendelsohn, L. I. Rictometer system for calibrating transmitters of remote indicating compasses—183S
Methfessel, S., S. Middelhoek, and H. Thomas. Domain walls in thin magnetic Ni-Fe films—302S
Meyer, Horst and A. B. Harris. Specific heat of some rare earth iron garnets and YIG at low temperatures—49S
—— (see Rodrique, G. P.)—376S
Middelhoek, S. (see Methfessel, S.)—302S
Miksch, E. S. (see Pry, R. H.)—162S
Milano, U. (see Schlömann, E.)—385S
Miller, Arthur. Valence and distribution of manganese ions in ferrospinels—261S
Miller, D. S. (see Arajs, Sigurds)—325S
Mills, D. (see Bratina, W. J.)—241S
Moore, A. C. and A. S. Young. Some physical properties of thin magnetic films—279S
Morgenthaler, Frederic R. Survey of ferromagnetic resonance in small ferrimagnetic ellipsoids—95S
—— (see Stiglitz, Martin R.)—37S
Morrish, A. H. (see Brown, W. F., Jr.)—214S
—— (see Watt, L. A. K.)—71S
Muckenhirn, O. William, A. E. LaBonte, and P. J. Besser. Annular uniaxially magnetized domains in thin Ni-Fe films—304S

Nathans, Robert. Precise measurement of magnetic-form factors—350S
—— (see Pickart, S. J.)—372S
Néel, L., R. Pauthenet, G. Rimet, and V. S. Giron. On the laws of magnetization of ferromagnetic single crystals and polycrystals. Application to uniaxial compounds—27S
Nesbitt, E. A., R. D. Heidenreich, A. J. Williams. Necessary factor for heat treatment of the permalloys in a magnetic field—228S
Neugebauer, C. A. Temperature dependence of the saturation magnetization of nickel films of thickness less than 100 A—152S
Neurath, P. W. Simple recording torque magnetometer—184S
Nielsen, J. W. Improved method for the growth of yttrium-iron and yttrium-gallium garnets—51S
—— (see Dillon, J. F., Jr.)—43S
Novy, V. F. (see Vickery, R. C.)—366S

Olsen, Clayton E. Magnetic properties of uranium digermanide—340S
Osborne, John A. Preface—1S
Overhauser, A. W. Mechanism of antiferromagnetism in dilute alloys—317S

Paine, T. O. and F. E. Luborsky. "Interaction anisotropy" model of the structure of Alnico magnet alloys—78S
—— (see Luborsky, F. E.)—66S, 68S
Parker, R. J. (see Foy, J. E.)—188S
Paskin, Arthur. Long-range magnetic interactions via conduction electrons—318S
Pauthenet, R. (see Néel, L.)—27S
Pavlovic, D. and K. Foster. Study of heat treatments for low coercive force 14 to 17 percent aluminum iron alloys—231S
Pearson, R. F. Magnetic anisotropy in ferrimagnetic crystals—160S
Pedko, A. V. (see Belov, K. P.)—55S
Pickart, S. J. and R. Nathans. Magnetic-form factor of Fe_3Al—372S
Pohm, A. V., A. A. Read, R. M. Stewart, Jr., and R. F. Schauer. Operation of magnetic film parametrons in the 100- to 500-Mc regions—119S
Portis, A. M. and A. C. Gossard. Nuclear resonance in ferromagnetic cobalt—205S
Proebster, W. E. (see Dietrich, W.)—281S
Prutton, M. (see Bradley, E. M.)—285S
Pry, R. H., J. S. Kouvel, and E. S. Miksch. Exchange anisotropy in the system $Mn_{(1-x)}Cr_xSb$—162S
Pugh, E. W., J. Matisoo, D. E. Speliotis, and E. L. Boyd. Magnetic anisotropy in evaporated iron films—293S

Rabins, L. (see Agarwal, Paul D.)—246S
Rado, G. T. (see Schnitzler, A. D.)—348S
Radus, R. J. Magnetic field measurement using ultrasonics—186S
Read, A. A. (see Pohm, A. V.)—119S
Reggia, F. (see Tompkins, J. E.)—176S
Reinberg, A. R. (see Marshall, S. A.)—336S
Remeika, J. P. $GaFeO_3$: A ferromagnetic-piezoelectric compound—263S
Rimet, G. (see Néel, L.)—27S
Rodbell, D. S. and P. E. Lawrence. Metamagnetic behavior of manganese arsenide—275S
Rodrique, G. P., H. Meyer, and R. V. Jones. Resonance measurements in magnetic garnets—376S
Roth, R. S. (see Fang, P. H.)—278S
Roth, Walter L. and Glen A. Slack. Antiferromagnetic structure and domains in single crystal NiO—352S
Rubinstein, Harvey and Robert J. Spain. Cross-tie walls in thin films—306S

Saenz, A. W. Spin waves in complex exchange-coupled lattices and neutron scattering—108S
Sagnis, James C., Jr., Michael Teig, and Robert L. Ward. Effect of geometry on thick film toroids—190S
Salkovitz, E. I. (see Schindler, A. I.)—245S
Sargeant, W. E. (see Bockemuehl, R. R.)—180S
Sato, Hiroshi. Analysis of magnetic interactions in alloys of platinum with iron group transition elements—327S
Schauer, R. F. (see Pohm, A. V.)—119S
Schaug-Petterson, Tor. Growing spin waves in ferrites in unstable equilibrium—382S
—— (see Elliott, B. J.)—400S
Schenk, H. L. (see Young, F. J.)—194S

Schindler, A. I. and E. I. Salkovitz. Effect of applying a magnetic field during neutron irradiation on the magnetic properties of Fe-Ni alloys—245S
Schlömann, E., J. J. Green, and U. Milano. Recent developments in ferromagnetic resonance at high power levels —386S
Schnitzler, A. D., V. J. Folen, and G. T. Rado. Ionic ordering effects in the ferromagnetic resonance of lithium ferrite monocrystals—348S
Seavey, M. H., Jr. Galvanomagnetic effects in ferromagnetic resonance—216S
Sedov, V. L. (see Kondorsky, E. I.)—331S
Seelbach, W. C. and J. R. Kiseda. Elastic switching properties of some square loop materials in toroidal structures—135S
Seiden, P. E. and H. J. Shaw. Saturation effects in ferrimagnetic resonance—225S
Sexton, W. C. (see Vickery, R. C.)—366S
Shaw, H. J. (see Elliott, B. J.)—400S
—— (see Seiden, P. E.)—225S
Shevel, W. L., Jr., and H. Chang. New approach to high-speed storage—low flux density materials—125S
—— (see Brownlow, J. M.)—121S
Shtrikman, S. and D. Treves. Internal structure of Bloch walls—147S
—— **and D. Treves.** On the remanence of ferromagnetic powders—58S
—— **and D. Treves.** On the resolution of Brown's paradox —72S
Singer, J. R. Blood flow measurements using dynamical paramagnetic relaxation times, and paramagnetic tracer techniques—406S
Slack, Glen A. (see Roth, Walter L.)—352S
Slaten, Lynore E. Precipitation of dispersed fine-particle magnetite—74S
Smit, J., F. K. Lotgering, and U. Enz. Anisotropy properties of hexagonal ferrimagnetic oxides—137S
Smith, D. O., E. E. Huber, Jr., M. S. Cohen, and G. P. Weiss. Anisotropy and inversion in Permalloy films—295S
—— (see Cohen, M. S.)—291S
Smith, K. C. (see McKay, R. W.)—133S
Soden, R. R. (see Van Uitert, L. G.)—226S
Solt, I. H. and P. C. Fletcher. Magnetic anisotropy from the magnetostatic modes—100S
Soohoo, R. F. Initial susceptibility spectra of Permalloy films —218S
Spain, Robert J. (see Rubinstein, Harvey.)—306S
Sparks, Joseph T., Warren Mead, Albert J. Kirschbaum, and Walter Marshall. Neutron diffraction investigation of the $Fe_{1-\delta}S$ system—356S
Speliotis, D. E. (see Pugh, E. W.)—293S
Spencer, E. G. (see LeCraw, R. C.)—95S
Stadler, H. L. Localized field permanent magnet arrays—196S
v.d. Steeg, M. G. (see Koch, A. J. J.)—75S
Steier, Wm. H. and Paul D. Coleman. Theory and application of dipolar ferrite modes—99S
Stewart, R. M., Jr. (see Pohm, A. V.)—119S
Stiglitz, Martin P. and Frederic R. Morgenthaler. Resonance experiments with single crystal yttrium iron garnets in pulsed magnetic fields—37S
Straley, R., A. Heuer, B. Kane, and G. Tkach. Miniature memory planes for extreme environmental conditions—126S
Street, R. Magnetic properties of manganese copper alloys —310S
Swanekamp, F. W. (see Van Uitert, L. G.)—226S

Teig, Michael (see Sagnis, James C.)—190S
Thomas, H. (see Baer, G.)—235S
—— (see Methfessel, S.)—302S
Tkach, G. (see Straley, R.)—126S
Tompkins, J. E., F. Reggia, and L. Joseph. Multimode propagation in gyromagnetic rods and its application to traveling-wave devices—176S
Trammell, G. T. Theory of the low lying states of some rare earth compounds—362S
Treves, D. (see Shtrikman, S.)—58S, 72S, 147S

Van Uitert, L. G., R. R. Soden, and F. W. Swanekamp. Resonance line widths of sintered nickel ferrites having low porosities—226S
Vickery, R. C., W. C. Sexton, V. F. Novy, and E. V. Kleber. Magneto structural studies on gadolinium-iron alloys—366S

Ward, Robert L. Experimental flux pattern determination in magnetic cores—192S
—— (see Sagnis, James C.)—190S
Warekois, E. P. Low-temperature x-ray diffraction studies on vanadium sesquioxide—346S
Watson, John H. L. (see Freeman, Michael W.)—404S
Watson, R. E. (see Freeman, A. J.)—374S
Watt, L. A. K. and A. H. Morrish. Comparison of the critical single-domain size for Fe_3O_4 and γ-Fe_2O_3—71S
Weiss, G. P. (see Cohen, M. S.)—291S
—— (see Smith, D. O.)—295S
Weiss, Jerald A. Tetrahedral junction—168S
Weiss, M. T. Ferrimagnetic resonance at high power—103S
Weisz, R. S. and D. L. Brown. Square loop properties of copper-manganese ferrites—269S
White, Robert L. Use of magnetostatic modes as a research tool—86S
—— (see Carson, John W.)—53S
Wiechec, Walter and Clinton M. Kelley. Fast switching by domain walls in ferrites—131S
Wilkinson, M. K., H. R. Child, J. W. Cable, E. O. Wollan, and W. C. Koehler. Neutron diffraction investigations of the magnetic ordering in rare earth nitrides—358S
Williams, A. J. (see Nesbitt, E. A.)—228S
Wojtowicz, Peter J. High-temperature susceptibility of ferrimagnetic spinels—265S
Wold, A. (see Goodenough, J. B.)—342S
Wollan, E. O. (see Wilkinson, M. K.)—358S
Woodward, J. G. and E. Della Torre. Particle interaction in magnetic recording tapes—398S

Young, A. S. (see Moore, A. C.)—279S
Young, F. J. and H. L. Schenk. Method for measuring iron losses in elliptically polarized magnetic fields—194S

Subject Index to the Fifth Symposium on Magnetism and Magnetic Materials, November 16–19, 1959

Magnetism, General and Theory

"Interaction anisotropy" model of the structure of alnico magnet alloys. T. O. Paine and F. E. Luborsky—78S

Interpretation of the magnetic and crystallographic properties of several iron, nickel, and iron-nickel nitrides. J. B. Goodenough, A. Wold, and R. J. Arnott—342S

Analysis of magnetic interactions in alloys of platinum with iron group transition elements. Hiroshi Sato—327S

Anisotropic magnetization. Earl R. Callen—149S

Antiferromagnetism of iron in face-centered crystalline lattice and the causes of anomalies in Invar physical properties. E. I. Kondorsky and V. L. Sedov—331S

Classical theory of spin configurations in the cubic spinel. T. A. Kaplan—364S

Effect of crystalline fields on magnetic-form factors. A. J. Freeman and R. E. Watson—374S

Effect of eddy currents on domain wall configurations, wall motion, and loss for a domain model of cube-on-edge material. P. D. Agarwal and D. C. Graham—249S

Effects of hydrostatic pressure on the properties of magnetic materials. R. E. Alley, Jr. and V. E. Legg—239S

Effect of impurities on the low-temperature spontaneous magnetization of cubic ferromagnetic crystals. A. A. Maradudin and P. A. Dixon—329S

Exchange anisotropy in Cu-Mn and Ag-Mn alloys. J. S. Kouvel—142S

Exchange anisotropy in rock magnetism. W. H. Meiklejohn and R. E. Carter—164S

Exchange anisotropy in the system $Mn_{(1-x)}Cr_xSb$. R. H. Pry, J. S. Kouvel, and E. S. Miksch—162S

Finite amplitude electromagnetic waves in gyromagnetic media. B. A. Auld—106S

Flux reversal in soft ferromagnetics. E. M. Gyorgy—110S

Hyperfine interactions in magnetic materials by $\gamma - \gamma$ angular correlation measurements. M. E. Caspari, S. Frankel, and M. A. Gilleo—320S

Initial-permeability spectra of microscopic iron-oxide particles. W. F. Brown, Jr., J. F. Hanton, and A. M. Morrish—214S

Interaction of magnetic crystals with radiation in the range 10^4–10^8 cm^{-1}. A. M. Clogston—198S

Internal structure of Bloch walls. S. Shtrikman and D. Treves—147S

Long-range magnetic interactions via conduction electrons. Arthur Paskin—318S

Magnetic-form factor of Fe_3Al. S. J. Pickart and R. Nathans—372S

Magnetic interactions and distribution of ions in the garnets. S. Geller—30S

Magnetic properties of ferromagnetic superconductors. R. M. Bozorth and D. D. Davis—321S

Magneto structural studies on gadolinium-iron alloys. R. C. Vickery, W. C. Sexton, V. F. Novy, and E. V. Kleber—366S

Mechanism of antiferromagnetism in dilute alloys. A. W. Overhauser—317S

Microwave resonance in rare earth iron garnets. C. Kittel—11S

Nuclear resonance in ferromagnetic cobalt. A. M. Portis and A. C. Gossard—205S

Direct cation-cation interactions in primarily ionic solids. John B. Goodenough—359S

Internal friction anomalies in ferromagnetics and antiferromagnetism near the Curie point. K. P. Belov, G. I. Katayev, and R. Z. Levitin—153S

On the laws of magnetization of ferromagnetic single crystals and polycrystals. Application to uniaxial compounds. L. Neel, R. Pauthenet, G. Rimet, and V. S. Giron—27S

On the resolution of Brown's paradox. S. Shtrikman and D. Treves—72S

Precise measurement of magnetic-form factors. Robert Nathans—350S

Relations between superconductors and ferromagnets. Bernd Matthias—23S

Rigorous solution of eddy current losses in rectangular bar for single plane domain wall model. Paul D. Agarwal and L. Rabins—246S

Specific heat of some rare earth iron garnets and YIG at low temperatures. Horst Meyer and A. B. Harris—49S

State of *d* electrons in transition metals. Conyers Herring—3S

Theory of the low lying states of some rare earth compounds. G. T. Trammell—362S

Use of magnetostatic modes as a research tool. Robert L. White—86S

Ferromagnetism and Antiferromagnetism; Metals and Alloys

Analysis of magnetic interactions in alloys of platinum with iron group transition elements. Hiroshi Sato—327S

Angular variation of the magnetic properties of elongated single-domain iron particles. F. E. Luborsky and T. O. Paine—66S

Anisotropy and inversion in permalloy films. D. O. Smith, E. E. Huber, Jr., M. S. Cohen, and G. P. Weiss—295S

Annular uniaxially magnetized domains in thin Ni-Fe films. O. William Muckenhirn, A. E. LaBonte, and P. J. Besser—304S

Antiferromagnetism of iron in face-centered crystalline lattice and the causes of anomalies in Invar physical properties. E. I. Kondorsky and V. L. Sedov—331S

Characteristics of Supermendur at 500°C. M. Lauriente and G. E. Lynn—237S

Coercive force and remanence of 25-A to 2000-A diameter cobalt, iron, and iron-cobalt alloy. F. E. Luborsky and T. O. Paine—68S

Cross-tie walls in thin films. Harvey Rubinstein and Robert J. Spain—306S

Domain wall velocities in thin iron-nickel films. N. C. Ford, Jr.—300S

Domain walls in thin magnetic Ni-Fe films. S. Methfessel, S. Middlehoek, and H. Thomas—302S

Effect of applying a magnetic field during neutron irradiation on the magnetic properties of Fe-Ni alloys. A. I. Schindler and E. I. Salkovitz—245S

Effect of impurities on the low-temperature spontaneous magnetization of cubic ferromagnetic crystals. A. A. Maradudin and P. A. Dixon—329S

Electrodeposited memory elements for a nondestructive memory. T. R. Long—123S

Exchange anisotropy in Cu-Mn and Ag-Mn alloys. J. S. Kouvel—142S

Exchange anisotropy in rock magnetism. W. H. Meiklejohn and R. E. Carter—164S

Exchange anisotropy in the system $Mn_{(1-x)}Cr_xSb$. R. H. Pry, J. S. Kouvel, and E. S. Miksch—162S

Ferromagnetic-alloy phases near the compositions Ni_2MnIn, Ni_2MnGa, Co_2MnGa, Pd_2MnSb, and PdMnSb. F. A. Hames—370S

Ferromagnetic powders in waveguides at elevated temperatures. A. D. Krall and E. T. Hooper, Jr.—178S

Flux reversal in soft ferromagnetics. E. M. Gyorgy—110S

Hyperfine interactions in magnetic materials by $\gamma-\gamma$ angular correlation measurements. M. E. Caspari, S. Frankel, and M.A. Gilleo—320S
"Interaction anisotropy" model of the structure of alnico magnet alloys. T. O. Paine and F. E. Luborsky—78S
Interpretation of the magnetic and crystallographic properties of several iron, nickel, and iron-nickel nitrides. J. B. Goodenough A. Wold, and R. J. Arnott—342S
Investigations into the origin of anisotropy in oblique-incidence films. M. S. Cohen, E. E. Huber, Jr., G. P. Weiss, and D. O. Smith—291S
Long-range magnetic interactions via conduction electrons. Arthur Paskin—318S
Magnetic anisotropy in evaporated iron films. E. W. Pugh, J. Matisoo, D. E. Speliotis, and E. L. Boyd—293S
Magnetic anisotropy and magnetostriction of ordered and disordered cobalt-iron alloys. R. C. Hall—157S
Magnetic behavior of polycrystalline neodymium, holmium, and erbium from 300 to 1500°K. Sigurds Arajs and D. S. Miller—325S
Magnetic-form factor of Fe_2Al. S. J. Pickart and R. Nathans—372S
Magnetic moments of alloys of gadolinium with some of the transition elements. William M. Hubbard, Edmond Adams, and John V. Gilfrich—368S
Magnetic properties of ferromagnetic superconductors. R. M. Bozorth and D. D. Davis—321S
Magnetic properties of manganese copper alloys. R. Street—310S
Magnetostatic modes of a ferromagnetic slab. R. W. Damon and J. R. Eshbach—104S
Magneto structural studies on gadolinium-iron alloys. R. C. Vickery, W. C. Sexton, V. F. Novy, and E. V. Kleber—366S
Mechanism of antiferromagnetism in dilute alloys. A. W. Overhauser—317S

Ferrimagnetism and Antiferrimagnetism; Compounds

Microcalorimetric technique for the study of damping and hysteresis in ferromagnetic films. J. R. Mayfield—298S
Necessary factor for heat treatment of the permalloys in a magnetic field. E. A. Nesbitt, R. D. Heidenriech, and A. J. Williams—228S
New material for permanent magnets on a base of Mn and Al. A. J. J. Koch, P. Hokkeling, M. G. v.d. Steeg, and K. J. deVos—75S
Nuclear resonance in ferromagnetic cobalt. A. M. Portis and A. C. Gossard—205S
On internal friction anomaly in ferromagnetics and antiferromagnetics near the Curie point. K. P. Belov, G. I. Katayev, and R. Z. Levitin—153S
On the remanence of ferromagnetic powders. S. Shtrikman and D. Treves—58S
Operation of magnetic film parametrons in the 100 to 500 Mc region. A. V. Pohm, A. A. Read, R. M. Stewart, and R. F. Schauer—119S
Preferred orientation and ordering in evaporated films of Fe, Ni, and Fe-Ni. R. F. Adamsky—289S
Promotion of cubic grain growth in 3% silicon iron by control of annealing atmosphere composition. Dale Kohler—408S
Recent developments in ferromagnetic resonance at high power levels. E. Schlömann, J. J. Green, and U. Milano—386S
Relations between superconductors and ferromagnets. Bernd Matthias—23S
Roll magnetic anisotropy of iron-aluminum crystals. Soshin Chikazumi—158S
Secondary recrystallization in vacuum annealed silicon iron. G. Baer, D. Ganz, and H. Thomas—235S
State of *d* electrons in transition metals. Conyers Herring—3S
Strong field magnetization at low temperatures and approach to absolute saturation of thulium metal. Warren E. Henry—323S
Study of heat treatments for low coercive force 14–17% aluminum iron alloys. D. Pavlovic and K. Foster—231S
Temperature dependence of anisotropy and saturation magnetization in iron and iron-silicon alloys. C. D. Graham, Jr.—150S
Temperature dependence of the saturation magnetization of nickel films of thickness less than 100 A. C. A. Neugebauer—152S
Absorption and reflectivity measurements on some rare-earth iron garnets and on α-Fe_2O_3. P. C. Bailey—39S
Anisotropy properties of hexagonal ferrimagnetic oxides. J. Smit, F. K. Lotgering, and U. Enz—137S
Antiferromagnetic structure and domains in single crystal NiO. Walter L. Roth and Glen A. Slack—352S
Broadband reciprocal ferrite phase shifters. T. D. Geiszler and R. A. Henschke—174S
Comparison of the critical single-domain size for Fe_3O_4 and γ-Fe_2O_3. L. A. K. Watt and A. H. Morrish—71S
Crystal distortion in magnetic compounds. Junjiro Kanamori—14S
Development of high-speed coincident current memory cores. Barlane R. Eichbaum—117S
Double pump degenerate ferrite amplifier. Peter Gottlieb—172S
Effect of potassium ions on the reaction and final properties of Mn-Zn ferrite. Stefan Makolagwa—339S
Effect of previous history on switching rate in ferrites. R. W. McKay and K. C. Smith—133S
Electron spin relaxation in ferromagnetic insulators. R. C. LeCraw, R. C. Fletcher, and E. G. Spencer—95S
Exchange anisotropy in rock magnetism. W. H. Meiklejohn and R. E. Carter—164S
Fast switching by domain walls in ferrites. Walter Wiechec and Clinton M. Kelley—131S
Ferrite films—new logic and storage devices. J. M. Brownlow, W. L. Shevel, Jr., and O. A. Gutwin—121S
Ferrimagnetic resonance at high power. M. T. Weiss—103S
Ferrimagnetic resonance in impurity doped yttrium iron garnet (YIG). J. F. Dillon, Jr., and J. W. Nielsen—43S
Ferroelectric and ferrimagnetic properties of $(Ba_{4-2x}R_{2x})(Nb_{9-x}Fe_{1+x})O_{30}$. P. H. Fang and R. S. Roth—278S
$GaFeO_3$: A ferromagnetic-piezoelectric compound. J. P. Remeika—263S
Growing spin waves in ferrites in unstable equilibrium. Tor Schaug-Pettersen—382S
Harmonic generation in a ferrimagnetic disk. Glenn E. Bennett—97S
High field magnetization study of ferrimagnetic arrangements in chromite spinels. I. S. Jacobs—263S
High-speed ferrite rotating half-wave plate. Franklin S. Coale—170S
High-temperature susceptibility of ferrimagnetic spinels. Peter J. Wojtowicz—265S
Hyperfine interactions in magnetic materials by $\gamma-\gamma$ angular correlation measurements. M. E. Caspari, S. Frankel, and M. A. Gilleo—320S
Improved method for the growth of yttrium-iron and yttrium-gallium garnets. J. W. Nielsen—51S
Influence of ionic order on the magnetocrystalline anisotropy and crystalline field parameters in lithium ferrite monocrystals. V. J. Folen—166S
Initial permeability characteristics of mixed yttrium-gadolinium iron garnets. G. E. McDuffie, Jr., J. Richard Cunningham, and Elmer E. Anderson—47S

Ferrimagnetism and Antiferrimagnetism; Compounds (*continued*)
Initial-permeability spectra of microscopic iron-oxide particles. W. F. Brown, Jr., J. P. Hanton, and A. H. Morrish—214S
Instability of magnetic resonance in single crystal spheres of yttrium iron garnet. Joseph I. Masters—41S
Interaction of magnetic crystals with radiation in the range 10^4–10^5 cm^{-1}. A. M. Clogston—198S
Interpretation of the magnetic and crystallographic properties of several iron, nickel, and iron-nickel nitrides. J. B. Goodenough, A. Wold, and R. J. Arnott—342S
Intrinsic and anneal-induced anisotropy in cobalt-substituted *W*-type hexagonal oxides. L. R. Bickford, Jr.—259S
Ionic ordering effects in the ferromagnetic resonance of lithium ferrite monocrystals. A. D. Schnitzler, V. J. Folen, and G. T. Rado—348S
Long-term magnetic stability of alnico and barium ferrite magnets. K. J. Kronenberg and M. A. Bohlmann—82S
Low-temperature x-ray diffraction studies on vanadium sesquioxide. E. P. Warekois—346S
Magnetic anisotropy in ferrimagnetic crystals. R. F. Pearson—160S
Magnetic behavior in the transition region of a hematite single crystal. S. T. Lin—273S
Magnetic interactions and distribution of ions in the garnets. S. Geller—30S
Magnetic properties of the $Li_xMn_{1-x}Se$ system. Thomas R. McGuire and Robert R. Heikes—276S
Magnetic transitions in Ti_2O_3 and V_2O_3. P. H. Carr and S. Foner—344S
Magnetic properties of uranium digermanide. Clayton E. Olsen—340S
Magnetostriction of gadolinium iron garnets. K. P. Belov and A. V. Pedko—55S
Metamagnetic behavior of manganese arsenide. D. S. Rodbell and P. E. Lawrence—275S
Microwave resonance in rare earth iron garnets. C. Kittel—11S
Miniature memory planes for extreme environmental conditions. R. Straley, A. Heuer, B. Kane, and G. Tkach—126S
Neutron diffraction investigations of the magnetic ordering in rare earth nitrides. M. K. Wilkinson, H. R. Child, J. W. Cable, E. O. Wollan, and W. C. Koehler—358S
Neutron diffraction investigation of the magnetic structure of nickel oxide. H. A. Alperin—354S
Neutron diffraction investigation of the $Fe_{1-\gamma}S$ system. Joseph T. Sparks, Warren Mead, Albert J. Kirschbaum, and Walter Marshall—356S
New approach to high-speed storage—low-flux density materials. W. L. Shevel, Jr., and H. Chang—125S
Direct cation-cation interactions in primarily ionic solids. John B. Goodenough—359S
On the laws of magnetization of ferrimagnetic single crystals and polycrystals. Application to uniaxial compounds. L. Néel, R. Pauthenet, G. Rimet, and V. S. Giron—27S
Paramagnetic resonance absorption of nickel in sapphires. S. A. Marshall and A. R. Reinberg—336S
Paramagnetic resonance of Yb^{+++} in aluminum and gallium garnets. John W. Carson and Robert L. White—53S
Properties of manganese ferrites prepared at various oxygen pressures. Aleksander Bragiński—339S
Pulsed ferrimagnetic microwave generator. B. Elliot, T. Schaug-Petterson, and H. J. Shaw—400S
Resonance experiments with single crystal yttrium iron garnets in pulsed magnetic fields. Martin R. Stiglitz and Frederic R. Morgenthaler—37S
Resonance line widths of sintered nickel ferrites having low porosities. L. G. Van Uitert, R. R. Soden, and F. W. Swanekamp—226S
Resonance measurements in magnetic garnets. G. P. Rodrique, H. Meyer, and R. V. Jones—376S
Role of cation vacancy in magnetic annealing of iron-cobalt ferrites. Shuichi Iida—251S
Samarium substitutions in yttrium iron garnet. J. Richard Cunningham, Jr., and Elmer E. Anderson—45S
Specific heat of some rare earth iron garnets and YIG at low temperatures. Horst Meyer and A. B. Harris—49S
Square loop properties of copper-manganese ferrites. R. S. Weisz and D. L. Brown—269S
Survey of ferromagnetic resonance in small ferrimagnetic ellipsoids. Frederic R. Morgenthaler—95S
Switching behavior of low remanence ferrite. F. B. Hagedorn and E. M. Gyorgy—398S
Temperature dependence of the saturation magnetization of ferrites with magnetoplumbite structure. G. Heimke—271S
Theory and application of dipolar ferrite modes. William H. Steier and Paul D. Coleman—99S
Time decrease of initial permeability in $Mn_xFe_{3-x}O_{4+\gamma}$. W. A. Crapo—267S
Valence and distribution of manganese ions in ferrospinels. Arthur Miller—261S
Spin and Spin Waves
Classical theory of spin configurations in the cubic spinel. T. A. Kaplan—364S
Growing spin waves in ferrites in unstable equilibrium. Tor Schaug-Pettersen—382S
Mechanism of antiferromagnetism in dilute alloys. A. W. Overhauser—317S
Spin waves in complex exchange-coupled lattices and neutron scattering. A. W. Saenz—108S
Theory of the low lying states of some rare earth compounds. G. T. Trammell—362S
Anisotropy
An isotropic magnetization. Earl R. Callen—149S
Anisotropy properties of hexagonal ferrimagnetic oxides. J. Smit, F. K. Lotgering, and U. Enz—137S
Effect of directional orientation on the magnetic properties of cube-oriented magnetic sheets. K. Foster and J. J. Kramer—233S
Effects of directional ordering on the damping of zone-melted iron. R. E. Maringer—229S
Exchange anisotropy in Cu-Mn and Ag-Mn alloys. J. S. Kouvel—142S
Exchange anisotropy in rock magnetism. W. H. Meiklejohn and R. E. Carter—164S
Exchange anisotropy in the system $Mn_{(1-x)}Cr_xSb$. R. H. Pry, J. S. Kouvel, and E. S. Miksch—162S
Flux reversal by noncoherent rotation in magnetic films. K. J. Harte—283S
High field magnetization study of ferrimagnetic arrangements in chromite spinels. I. S. Jacobs—263S
Influence of ionic order on the magnetocrystalline anisotropy and crystalline field parameters in lithium ferrite monocrystals. V. J. Folen—166S
"Interaction anisotropy" model of the structure of alnico magnet alloys. T. O. Paine and F. E. Luborsky—78S
Intrinsic and anneal-induced anisotropy in cobalt-substituted *W*-type hexagonal oxides. L. R. Bickford, Jr.—259S
Investigations into the origin of anisotropy in oblique-incidence films. M. S. Cohen, E. E. Huber, Jr., G. P. Weiss, and D. O. Smith—291S
Magnetic anisotropy in ferrimagnetic crystals. R. F. Pearson—160S
Magnetic anisotropy and magnetostriction of ordered and disordered cobalt-iron alloys. R. C. Hall—157S

Magnetic anisotropy from the magnetostatic modes. I. H. Solt, Jr., and P. C. Fletcher—100S
Magnetization reversal in uniaxial films near to the preferred direction. E. M. Bradley and M. Prutton—285S
Magnetostriction of gadolinium iron garnet. K. P. Belov and A. V. Pedko—55S
Preferred orientation and ordering in evaporated films of Fe, Ni, and Fe-Ni. R. F. Adamsky—289S
Role of cation vacancy in magnetic annealing of iron-cobalt ferrites. Shuichi Iida—251S
Roll magnetic anistropy of iron-aluminum crystals. Soshin Chikazumi—158S
Square loop properties of copper-manganese ferrites. R. S. Weisz and D. L. Brown—269S
Temperature dependence of anisotropy and saturation magnetization in iron and iron-silicon alloys. C. D. Graham, Jr.—150S
Temperature dependence of the saturation magnetization of nickel films of thickness less than 100A. C. A. Neugebauer—152S
Theory and application of dipolar ferrite modes. William H. Steier and Paul D. Coleman—99S

Resonance

Applications, Techniques, and Devices, Misc.

Effects of surface irregularities on single crystal resonance parameters. C. R. Buffler—222S
Electron spin relaxation in ferromagnetic insulators. R. C. LeCraw, R. C. Fletcher, and E. G. Spencer—95S
Ferrimagnetic resonance at high power. M. T. Weiss—103S
Ferrimagnetic resonance in impurity doped yttrium iron garnet (YIG). J. F. Dillon, Jr., and J. W. Nielsen—43S
Galvanomagnetic effects in ferromagnetic resonance. M. H. Seavey, Jr.—216S
Ionic ordering effects in the ferromagnetic resonance of lithium ferrite monocrystals. A. D. Schnitzler, V. J. Folen, and G. T. Rado—348S
Instability of magnetic resonance in single crystal spheres of yttrium iron garnet. Joseph I. Masters—41S
Magnetic anisotropy from the magnetostatic modes. I. H. Solt, Jr. and P. C. Fletcher—100S
Magnetostatic modes of a ferromagnetic slab. R. W. Damon and J. R. Eshbach—104S
Microwave resonance in rare earth iron garnets. C. Kittel—11S
Nuclear resonance in ferromagnetic cobalt. A. M. Portis and A. C. Gossard—205S
Paramagnetic resonance absorption of nickel in sapphires. S. A. Marshall and A. R. Reinberg—336S
Paramagnetic resonance of Yb^{+++} in aluminum and gallium garnets. John W. Carson and Robert L. White—53S
Recent developments in ferromagnetic resonance at high power levels. E. Schlömann, J. J. Green, and U. Milano—386S
Resonance experiments with single crystal yttrium iron garnets in pulsed magnetic fields. Martin R. Stiglitz and Frederic R. Morgenthaler—37S
Resonance line widths of sintered nickel ferrites having low porosities. L. G. Van Uitert, R. R. Soden, and F. W. Swanekamp—226S
Resonance measurements in magnetic garnets. G. P. Rodrique, H. Meyer, and R. V. Jones—376S
Saturation effects in ferrimagnetic resonance. P. E. Seiden and H. J. Shaw—224S
Survey of ferromagnetic resonance in small ferrimagnetic ellipsoids. Frederic R. Morgenthaler—95S
Theory and application of dipolar ferrite modes. William H. Steier and Paul D. Coleman—99S
Use of magnetostatic modes as a research tool. Robert L. White—86S
Volume dependence of ferrimagnetic resonance properties in $Ni_{1-x}Co_xFe_2O_4$. I. P. Kaminow—220S

Magnetic Films

Absorption and reflectivity measurements on some rare earth iron garnets and on α-Fe_2O_3. P. C. Bailey—39S
Analysis of a practical perpendicular head for digital purposes. George J. Y. Fan—402S
Blood flow measurements using dynamical paramagnetic relaxation times, and paramagnetic tracer techniques. J. R. Singer—406S
Broadband reciprocal ferrite phase shifters. T. D. Geiszler and R. A. Henschke—174S
dc measurements on tape-wound cores. R. C. Barker and and R. M. Brownell—243S
Development of high-speed coincident current memory cores. Barlane R. Eichbaum—117S
Double pump degenerate ferrite amplifier. Peter Gottlieb—172S
Effect of applying a magnetic field during neutron irradiation on the magnetic properties of Fe-Ni alloys. A. I. Schindler and E. I. Salkovitz—245S
Effect of geometry on thick film toroids. James C. Sagnis, Jr., Michael Teig, and Robert L. Ward—190S
Effect of potassium ions on the reaction and final properties of Mn-Zn ferrite. Stefan Makolagwa—339S
Effect of previous history on switching rate in ferrites. R. W. McKay and K. C. Smith—133S
Effects of hydrostatic pressure on the properties of magnetic materials. R. E. Alley, Jr., and V. E. Legg—239S
Elastic switching properties of some square loop materials in toroidal structures. W. C. Seelbach and J. R. Kiseda—135S
Electrodeposited memory elements for a nondestructive memory. T. R. Long—123S
Exchange anisotropy in rock magnetism. W. H. Meiklejohn and R. E. Carter—164S
Experimental flux pattern determination in magnetic cores. Robert L. Ward—192S
Fast switching by domain walls in ferrites. Walter Wiechec and Clinton M. Kelley—131S
Ferrite films—new logic and storage devices. J. M. Brownlow, W. L. Shevel, Jr., and O. A. Gutwin—121S
Ferromagnetic powders in waveguides at elevated temperatures. A. D. Krall and E. T. Hooper, Jr.—178S
Finite amplitude electromagnetic waves in gyromagnetic media. B. A. Auld—106S
Flux reversal by noncoherent rotation in magnetic films. K. J. Harte—283S
$GaFeO_3$: Ferromagnetic-piezoelectric compound. J. P. Remeika—263S
Harmonic generation in a ferrimagnetic disk. Glenn E. Bennett—97S
High-speed ferrite rotating half-wave plate. Franklin S. Coale—170S
Hot working of Alnico V alloys. C. L. Kolbe and D. L. Martin—84S
Improved method for the growth of yttrium-iron and yttrium-gallium garnets. J. W. Nielsen—51S
Influence of nearby conductors on thin film switching. J. S. Eggenberger—287S
Instrumentation applications of inverse-Wiedemann effect. J. A. Granath—178S
Long-term magnetic stability of Alnico and barium ferrite magnets. K. J. Kronenberg and M. A. Bohlmann—82S
Magnetic anisotropy and magnetostriction of ordered and disordered cobalt-iron alloys. R. C. Hall—157S
Magnetic contribution to the ultrasonic attenuation in annealed and deformed steel (SAE 1020). W. J. Bratina, U. M. Martius and D. Mills—241S
Magnetic field measurement using ultrasonics. R. J. Radus. 186S
Magnetization reversal in uniaxial films near to the preferred direction. E. M. Bradley and M. Prutton—285S

Magnetic Films (*continued*)
Magnetism in medicine. Michael W. Freeman, M.D., Anthony Arrott, John H. L. Watson—404S
Method for measuring iron losses in elliptically polarized magnetic fields. F. J. Young and H. L. Schenk—194S
Microcalorimetric technique for the study of damping and hysteresis in ferromagnetic films. J. R. Mayfield—298S
Millimicrosecond magnetization reversal in thin magnetic films. W. Dietrich and W. E. Proebster—281S
Miniature memory planes for extreme environmental conditions. R. Straley, A. Heuer, B. Kane, and G. Tkach—126S
Multimode propagation in gyromagnetic rods and its application to traveling-wave devices. J. E. Tompkins, F. Reggia and L. Joseph—176S
Necessary factor for heat treatment of the permalloys in a magnetic field. E. A. Nesbitt, R. D. Heidenriech, and A. J. Williams—228S
New approach to high-speed storage—low flux density materials. W. L. Shevel, Jr. and H. Chang—125S
New multi-aperture magnetic logic element. David R. Bennion—129S
Operation of magnetic film parametrons in the 100- to 500-Mc region. A. V. Pohm, A. A. Read, R. M. Stewart, and R. F. Schauer—119S
Particle interaction in magnetic recording tapes. J. G. Woodward and E. DellaTorre—398S
Practical hysteresigraph. R. R. Bockemuehl and W. E. Sargeant—180S
Precipitation of dispersed fine-particle magnetite. Lynore E. Slaten—74S
Precise measurement of magnetic-form factors. Robert Nathans—350S
Promotion of cubic grain growth in 3% silicon iron by control of annealing atmosphere composition. Dale Kohler—408S
Properties of magnanese ferrites prepared at various oxygen pressures. Aleksander Bragiński—339S
Pulsed ferrimagnetic microwave generator. B. Elliot, T. Schaug-Petterson, and H. J. Shaw—400S
Rictometer system for calibrating transmitters of remote indicating compasses. L. I. Mendelsohn—183S
Roll magnetic anisotropy of iron-aluminum crystals. Soshin Chikazumi—158S
Secondary recrystallization in vacuum annealed silicon iron. G. Baer, D. Ganz, and H. Thomas—235S
Simple recording torque magnetometer. P. W. Neurath—184S
Specific heat of some rare earth iron garnets and YIG at low temperatures. Horst Meyer and A. B. Harris—49S
Study of heat treatments for low coercive force 14–17% aluminum iron alloys. D. Pavlovic and K. Foster—231S
Survey of ferromagnetic resonance in small ferrimagnetic ellipsoids. Frederic R. Morgenthaler—95S
Switching behavior of low remanence ferrite. F. B. Hagedorn and E. M. Gyorgy—398S
Tetrahedral junction. Jerald A. Weiss—168S
Theory and application of dipolar ferrite modes. William H. Steier and Paul D. Coleman—99S
Transfer function and error probability of a digital magnetic tape recording system. John Wenchung Hung—396S
Anisotropy and inversion in permalloy films. D. O. Smith, E. E. Huber, Jr., M. S. Cohen, and G. P. Weiss—295S
Annular uniaxially magnetized domains in thin Ni-Fe films. O. William Muckenhirn, A. E. LeBonte, and P. J. Besser—304S
Cross-tie walls in thin films. Harvey Rubinstein and Robert J. Spain—306S
Domain wall velocities in thin iron-nickel films. N. C. Ford, Jr.—300S
Domain walls in thin magnetic Ni-Fe films. S. Methfessel, S. Middlehoek, and H. Thomas—302S
Electrodeposited memory elements for a nondestructive memory. T. R. Long—123S
Ferrite films—new logic and storage devices. J. M. Brownlow, W. L. Shevel, Jr., and O. A. Gutwin—121S
Flux reversal by noncoherent rotation in magnetic films. K. J. Harte—283S
Influence of nearby conductors on thin film switching. J. S. Eggenberger—287S
Investigations into the origin of anisotropy in oblique-incidence films. M. S. Cohen, E. E. Huber, Jr., G. P. Weiss, and D. O. Smith—291S
Initial susceptibility spectra of permalloy films. R. F. Soohoo—218S
Magnetic anisotropy in evaporated iron films. E. W. Pugh, J. Matisoo, D. E. Speliotis, and E. L. Boyd—293S
Magnetization reversal in uniaxial films near to the preferred direction. E. M. Bradley and M. Prutton—285S
Microcalorimetric technique for the study of damping and hysteresis in ferromagnetic films. J. R. Mayfield—298S
Millimicrosecond magnetization reversal in thin magnetic films. W. Dietrich and W. E. Proebster—281S
Nucleation experiments on thin magnetic MnBi films. Ludwig Mayer—384S
Operation of magnetic film parametrons in the 100- to 500-Mc region. A. V. Pohm, A. A. Read, R. M. Stewart and R. F. Schauer—119S
Preferred orientation and ordering in evaporated films of Fe, Ni, and Fe-Ni. R. F. Adamsky—289S
Some physical properties of thin magnetic films. A. C. Moore and A. S. Young—279S
Static and dynamic studies of magnetization distribution in thin films by electron microscopy. Harrison W. Fuller and Murray E. Hale—308S
Temperature dependence of the saturation magnetization of nickel films of thickness less than 100A. C. A. Neugebauer—152S

Paramagnetism
Classical theory of spin configurations in the cubic spinel. T. A. Kaplan—364S
High-temperature susceptibility of ferrimagnetic spinels. Peter J. Wojtowicz—265S
Hyperfine interactions in magnetic materials by $\gamma-\gamma$ angular correlation measurements. M. E. Caspari, S. Frankel, and M. A. Gilleo—320S
Magnetic susceptibilities of single crystal $NiCl_2 \cdot 6H_2O$ and $CoCl_2 \cdot 6H_2O$ at low temperatures. R. B. Flippen and S. A. Friedberg—338S
Theory of the low lying states of some rare earth compounds. G. T. Trammell—362S

Diamagnetism

Domains
Angular variation of the magnetic properties of elongated single-domain iron particles. F. E. Luborsky and T. O. Paine—66S
Anisotropy and inversion in permalloy films. D. O. Smith, E. E. Huber, Jr., M. S. Cohen, and G. P. Weiss—295S
Annular uniaxially magnetized domains in thin Ni-Fe films. O. William Muckenhirn, A. E. LeBonte, and P. J. Besser—304S
Comparison of the critical single-domain size for Fe_3O_4 and γ-Fe_2O_3. L. A. K. Watt and A. H. Morrish—71S
Cross-tie walls in thin films. Harvey Rubinstein and Robert J. Spain—306S
Domain wall velocities in thin iron-nickel films. N. C. Ford, Jr.—300S

Domain walls in thin magnetic Ni-Fe films. S. Methfessel, S. Middlehoek, and H. Thomas—302S
Effect of eddy currents on domain wall configurations, wall motion and loss for a domain model of cube-on-edge material. P. D. Agarwal and D. G. Graham—249S
Effects of directional ordering on the damping of zone-melted iron. R. E. Maringer—229S
Fast switching by domain walls in ferrites. Walter Wiechec and Clinton M. Kelley—131S
Flux reversal in soft ferromagnetics. E. M. Gyorgy—110S
Internal structure of Bloch walls. S. Shtrikman and D. Treves—147S
Investigations into the origin of anisotropy in oblique-incidence films. M. S. Cohen, E. E. Huber, Jr., G. P. Weiss, and D. O. Smith—291S
Magnetic anisotropy in evaporated iron films. E. W. Pugh, J. Matisoo, D. E. Speliotis, and E. L. Boyd—293S
Microcalorimetric technique for the study of damping and hysteresis in ferromagnetic films. J. R. Mayfield—298S
Preferred orientation and ordering in evaporated films of Fe, Ni, and Fe-Ni. R. F. Adamsky—289S
Rigorous solution of eddy current losses in rectangular bar for single plane domain wall model. Paul D. Agarwal and L. Rabins—246S
Static and dynamic studies of magnetization distribution in thin films by electron microscopy. Harrison W. Fuller and Murray E. Hale—308S

Structure

Antiferromagnetic structure and domains in single crystal NiO. Walter L. Roth and Glen A. Slack—352S
Crystal distortion in magnetic compounds. Junjiro Kanamori—14S
Effect of directional orientation on the magnetic properties of cube-oriented magnetic sheets. K. Foster and J. J. Kramer—233S
Effects of directional ordering on the damping of zone-melted iron. R. E. Maringer—229S
Influence of ionic order on the magnetocrystalline anisotropy and crystalline field parameters in lithium ferrite monocrystals. V. J. Folen—166S
Ionic ordering effects in the ferromagnetic resonance of lithium ferrite monocrystals. A. D. Schnitzler, V. J. Folen, and G. T. Rado—348S
Low-temperature x-ray diffraction studies on vanadium sesquioxide. E. P. Warekois—346S
Magnetic transitions in Ti_2O_3 and V_2O_3. P. H. Carr and S. Foner—344S
Neutron diffraction investigation of the $Fe_{1-\delta}S$ system. Joseph T. Sparks, Warren Mead, Albert J. Kirschbaum, and Walter Marshall—356S
Neutron diffraction investigation of the magnetic structure of nickel oxide. H. A. Alperin—354S
Neutron diffraction investigations of the magnetic ordering in rare earth nitrides. M. K. Wilkinson, H. R. Child, J. W. Cable, E. O. Wollan, and W. C. Koehler—358S
Precise measurement of magnetic-form factors. Robert Nathans—350S
Spin waves in complex exchange-coupled lattices and neutron scattering. A. W. Saenz—108S
Transmission electron diffraction of Alnico V. K. J. Kronenberg—80S

Permanent Magnets

Angular variation of the magnetic properties of elongated single-domain iron particles. F. E. Luborsky and T. O. Paine—66S
Coercive force and remanence of 25-A to 2000-A diameter cobalt, iron, and iron-cobalt alloy. F. E. Luborsky and T. O. Paine—68S
Comparison of the critical single-domain size for Fe_3O_4 and γ-Fe_2O_3. L. A. K. Watt and A. H. Morrish—71S
Hot working of Alnico V alloys. C. L. Kolbe and D. L. Martin—84S
"Interaction anisotropy" model of the structure of Alnico magnet alloys. T. O. Paine and F. E. Luborsky—78S
Localized field permanent magnet arrays. H. L. Stadler—196S
Long-term magnetic stability of Alnico and barium ferrite magnets. K. J. Kronenberg and M. A. Bohlmann—82S
New material for permanent magnets on a base of Mn and Al. A. J. J. Koch, P. Hokkeling, M. G. v.d. Steeg, and K. J. deVos—75S
On the remanence of ferromagnetic powders. S. Shtrikman and D. Treves—58S
Permanent magnet leadage permeance evaluation based on polar radiation analogy. J. E. Foy and R. J. Parker—188S
Precipitation of dispersed fine-particle magnetite. Lynore E. Slaten—74S
Transmission electron diffraction of Alnico V. K. J. Kronenberg—80S

CONFERENCE ORGANIZATION

General Conference Chairman

C. L. Hogan

Technical Program Committee

J. E. Goldman, *Chairman*
A. Arrott
J. J. Becker
H. B. Callen
L. R. Himmel
C. L. Hogan
C. Kittel
J. A. Krumhansl
J. S. Smart
H. Suhl

Local Conference Committee

D. M. Grimes, *Chairman*
H. R. Armstrong
J. Bergstrom
J. Betts
F. R. Bryan
R. H. Campbell
J. J. Lambe
D. C. Ray
G. G. Scott
O. L. Tiffany

Manager of Exhibits

John Leslie Whitlock Associates

Publications

J. A. Osborn, *Chairman*

H. Brooks
J. E. Goldman
C. L. Hogan
J. A. Krumhansl

AIEE Subcommittee on Magnetics

C. L. Hogan, *Chairman*
A. C. Beiler
L. R. Bickford
E. Both
R. M. Bozorth
F. G. Brockman
H. Brooks
R. A. Chegwidden
E. A. Gaugler
J. E. Goldman
I. S. Jacobs
V. E. Legg
M. F. Littman
L. R. Maxwell
C. A. Maynard
W. H. Meiklejohn
W. Morrill
J. A. Osborn
T. O. Paine
G. T. Rado

Society Representatives

American Institute of Electrical Engineers
R. S. Gardner
American Physical Society
J. E. Goldman
American Institute of Mining, Metallurgical and Petroleum Engineers
J. J. Becker
American Institute of Radio Engineers
L. J. Giacoletto
Office of Naval Research
W. R. Gruner